SANDIA REPORT

SAND98–0365
Unlimited Release
Printed September 1998

Uncertainty and Sensitivity Analysis Results Obtained in the 1996 Performance Assessment for the Waste Isolation Pilot Plant

J. C. Helton, J. E. Bean, J. W. Berglund, F. J. Davis, K. Economy, J. W. Garner, J. D. Johnson, R. J. MacKinnon, J. Miller, D. G. O'Brien, J. L. Ramsey, J. D. Schreiber, A. Shinta, L. N. Smith, D. M. Stoelzel, C. Stockman, and P. Vaughn

Prepared by
Sandia National Laboratories
Albuquerque, New Mexico 87185 and Livermore, California 94550

Sandia is a multiprogram laboratory operated by Sandia Corporation, a Lockheed Martin Company, for the United States Department of Energy under Contract DE-AC04-94AL85000.

Sandia National Laboratories

Issued by Sandia National Laboratories, operated for the United States Department of Energy by Sandia Corporation.

Available to DOE and DOE contractors from
Office of Scientific and Technical Information
P.O. Box 62
Oak Ridge, TN 37831

Prices available from (615) 576-8401, FTS 626-8401

Available to the public from
National Technical Information Service
U.S. Department of Commerce
5285 Port Royal Rd
Springfield, VA 22161

NTIS price codes
Printed copy: A24
Microfiche copy: A01

SAND98-0365
Unlimited Release
Printed September 1998

Uncertainty and Sensitivity Analysis Results Obtained in the 1996 Performance Assessment for the Waste Isolation Pilot Plant

J.C. Helton[a], J.E. Bean[b], J.W. Berglund[b], F.J. Davis, K. Economy[c], J.W. Garner[d], J.D. Johnson[e], R.J. MacKinnon, J. Miller, D.G. O'Brien[f], J.L. Ramsey, J.D. Schreiber[d], A. Shinta[g], L.N. Smith[h], D.M. Stoelzel, C. Stockman, and P. Vaughn

WIPP Performance Assessment Departments
Sandia National Laboratories
P.O. Box 5800
Albuquerque, NM 87185

Abstract

The Waste Isolation Pilot Plant (WIPP) is located in southeastern New Mexico and is being developed by the U.S. Department of Energy (DOE) for the geologic (deep underground) disposal of transuranic (TRU) waste. A detailed performance assessment (PA) for the WIPP was carried out in 1996 and supports an application by the DOE to the U.S. Environmental Protection Agency (EPA) for the certification of the WIPP for the disposal of TRU waste. The 1996 WIPP PA uses a computational structure that maintains a separation between stochastic (i.e., aleatory) and subjective (i.e., epistemic) uncertainty, with stochastic uncertainty arising from the many possible disruptions that could occur over the 10,000 yr regulatory period that applies to the WIPP and subjective uncertainty arising from the imprecision with which many of the quantities required in the PA are known. Important parts of this structure are (1) the use of Latin hypercube sampling to incorporate the effects of subjective uncertainty, (2) the use of Monte Carlo (i.e., random) sampling to incorporate the effects of stochastic uncertainty, and (3) the efficient use of the necessarily limited number of mechanistic calculations that can be performed to support the analysis. The use of Latin hypercube sampling generates a mapping from imprecisely known analysis inputs to analysis outcomes of interest that provides both a display of the uncertainty in analysis outcomes (i.e., uncertainty analysis) and a basis for investigating the effects of individual inputs on these outcomes (i.e., sensitivity analysis). The sensitivity analysis procedures used in the PA include examination of scatterplots, stepwise regression analysis, and partial correlation analysis. Uncertainty and sensitivity analysis results obtained as part of the 1996 WIPP PA are presented and discussed. Specific topics considered include two phase flow in the vicinity of the repository, radionuclide release from the repository, fluid flow and radionuclide transport in formations overlying the repository, and complementary cumulative distribution functions used in comparisons with regulatory standards (i.e., 40 CFR 191, Subpart B).

---

[a] Department of Mathematics, Arizona State University, Tempe, AZ 85287
[b] New Mexico Engineering Research Institute, Albuquerque, NM 87106
[c] Ecodynamics Research Associates, Albuquerque, NM 87106
[d] Piru Associates, Albuquerque, NM 87106
[e] GRAM, Inc., Albuquerque, NM 87112
[f] Solutions Engineering, Lakewood, CO 80232
[g] Applied Physics, Albuquerque, NM 87106
[h] Comforce, Albuquerque, NM 87110

CONTENTS

FIGURES

TABLES

1. Introduction

The Waste Isolation Pilot Plant (WIPP) is located in southeastern New Mexico and is being developed by the U.S. Department of Energy (DOE) for the geologic (deep underground) disposal of transuranic (TRU) waste (U.S. DOE 1980, 1990, 1993). Waste disposal will take place in panels excavated in bedded salt approximately 2,000 ft below the land surface. As part of the development process for the WIPP, a sequence of performance assessments (PAs) has been carried out by Sandia National Laboratories (SNL) to organize knowledge currently available about the WIPP and to provide guidance for future research and development efforts (Marietta et al. 1989; Bertram-Howery et al. 1990; WIPP PA 1991-1992, 1992-1993). The structure of these PAs derives from the U.S. Environmental Protection Agency's (EPA's) regulation for the geologic disposal of radioactive waste: 40 CFR 191, Subpart B: *Environmental Radiation Protection Standards for the Management and Disposal of Spent Nuclear Fuel, High-Level and Transuranic Radioactive Wastes* (U.S. EPA 1985, 1993a; Helton 1993a; Helton et al. 1997). The most recent iteration of these PAs was completed in the summer of 1996 and supports an application, designated the Compliance Certification Application (CCA), by the DOE to the EPA for the certification of the WIPP for the disposal of TRU waste (U.S. DOE 1996). This report presents a summary of uncertainty and sensitivity analysis results obtained as part of the 1996 WIPP PA.

The report is organized as follows. The overall conceptual structure of the 1996 WIPP PA is described in Chapter 2. This structure involves three basic entities: (1) A probabilistic characterization of different futures that could occur at the WIPP site over the next 10,000 yr, (2) Models for the physical processes that take place at the WIPP site and for the estimation of potential radionuclide releases that may be associated with these processes, and (3) A probabilistic characterization of the uncertainty in the models and parameters that underlie the WIPP PA.

The probabilistic characterization of different futures is discussed in more detail in Chapter 3. This characterization plays an important role in the construction of the complementary cumulative distribution function (CCDF) specified in 40 CFR 191.13. Regulatory guidance and extensive review of the WIPP site resulted in exploratory drilling for natural resources and the mining of potash being identified as the only significant disruptions at the WIPP site with the potential to affect radionuclide releases to the accessible environment. Topics considered in Chapter 3 include drilling intrusion time, drilling location, penetration of excavated/nonexcavated areas of the repository, penetration of pressurized brine in the Castile Formation, borehole plugging patterns, activity level of waste penetrated by a drilling intrusion, and time at which potash mining occurs.

Models for the physical processes that take place at the WIPP and for the estimation of potential radionuclide releases are discussed in Chapter 4. These models are used in the construction of the CCDF specified in 40 CFR 191.13. Topics considered in Chapter 4 include two-phase (i.e., gas and brine) flow in the vicinity of the repository, radionuclide transport in the vicinity of the repository, releases to the surface at the time of a drilling intrusion due to

cuttings and cavings, releases to the surface at the time of a drilling intrusion due to spallings, releases to the surface at the time of a drilling intrusion due to direct brine flows, brine flow in the Culebra Dolomite, and radionuclide transport in the Culebra Dolomite.

The probabilistic characterization of parameter uncertainty is discussed in Chapter 5. It is this uncertainty that gives rise to the uncertainty and sensitivity analysis results presented in this report. Further, this is the uncertainty that must be considered in assessing the confidence that the CCDF specified in 40 CFR 191.13 will meet applicable regulatory standards. Topics considered in Chapter 5 include uncertain variables incorporated into the 1996 WIPP PA, the distributions assigned to these variables, and the correlations between variables.

Computational procedures that underlie the uncertainty and sensitivity analysis results presented in this report are discussed in Chapter 6. Topics considered include sampling techniques (i.e., random, importance, and Latin hypercube sampling), correlation control, sample size, statistical confidence for mean CCDF, generation of Latin hypercube samples (LHSs), generation of individual 10,000 yr futures, construction of CCDFs, the Kaplan/Garrick ordered triple representation for risk, calculations performed with the models discussed in Chapter 4, and the sensitivity analysis techniques in use.

Uncertainty and sensitivity analysis results for two-phase flow in the vicinity of the repository under undisturbed conditions are presented and discussed in Chapter 7. The primary emphasis is on conditions within the repository. The topics considered include brine inflow, gas generation, repository pressure, brine saturation, and brine and gas outflow.

Uncertainty and sensitivity analysis results for two-phase flow in the vicinity of the repository under disturbed conditions (i.e., subsequent to one or more drilling intrusions) are presented and discussed in Chapter 8. Several different patterns of drilling intrusion are considered: (1) a single drilling intrusion that does not penetrate pressurized brine in the Castile Formation (i.e., an E2 intrusion), (2) a single drilling intrusion that penetrates pressurized brine in the Castile Formation (i.e., an E1 intrusion), (3) an intrusion that does not penetrate pressurized brine followed by an intrusion that does penetrate pressurized brine (i.e., an E2E1 intrusion), and (4) multiple E1 intrusions. Uncertainty and sensitivity analysis results are presented for brine inflow, gas generation, repository pressure, brine saturation, brine and gas outflow, and behavior of brine pockets in the Castile Formation subsequent to a drilling intrusion.

Uncertainty and sensitivity analysis results for releases to the surface environment due to cuttings and cavings and also to spallings are presented and discussed in Chapter 9. Results are presented for initial intrusions into the repository and also for intrusions subsequent to an earlier intrusion. The procedures used to construct CCDFs resulting from the cuttings and cavings releases and also from the spallings releases are described. The CCDFs that

result from use of these procedures are presented, and the results of uncertainty and sensitivity analyses performed with these CCDFs are described.

Uncertainty and sensitivity analysis results for releases to the surface environment due to direct brine flow (i.e., direct brine releases) are presented and discussed in Chapter 10. Results are presented for initial intrusions into the repository and also for intrusions subsequent to an earlier intrusion. The procedures used to construct CCDFs resulting from direct brine releases are described. The CCDFs that result from use of these procedures are presented, and the results of uncertainty and sensitivity analyses performed with these CCDFs are described.

Uncertainty and sensitivity analysis results for dissolved and colloidal radionuclide releases from the repository to the overlying Culebra Dolomite are presented and discussed in Chapter 11. Releases due to E1, E2 and E2E1 intrusions are considered. Further, the procedures used to construct CCDFs for radionuclide releases from the repository to the Culebra are described. The CCDFs that result from use of these procedures are presented, and the results of uncertainty and sensitivity analyses performed with these CCDFs are described.

Uncertainty and sensitivity analysis results for radionuclide transport in the Culebra Dolomite are presented and discussed in Chapter 12. No significant transport through the Culebra to the accessible environment occurred, with the result that meaningful sensitivity studies were not possible for radionuclide transport through the Culebra with the initial transport calculations performed for the 1996 WIPP PA. To provide a basis for sensitivity analysis for radionuclide transport in the Culebra, a second set of transport calculations was performed on a much higher resolution computational grid. Uncertainty and sensitivity analysis results obtained for these calculations are presented. Further, the procedures developed to construct CCDFs for radionuclide transport through the Culebra are described, although these procedures were not used in the 1996 WIPP PA due to the absence of radionuclide transport through the Culebra to the accessible environment.

Uncertainty and sensitivity analysis results for the CCDFs used for comparison with the boundary line specified in 40 CFR 191.13 are presented and discussed in Chapter 13. These CCDFs are based on all release modes considered in the 1996 WIPP PA, although only the cuttings and cavings, spallings, and direct brine release modes produced nonzero releases to the accessible environment. The total release CCDFs tend to be dominated by the cuttings and cavings component, although the spalling component also has the potential to contribute significantly to the total release. The distribution of CCDFs associated with all release modes falls substantially below the boundary line specified in 40 CFR 191.13, which indicates a high degree of confidence that the WIPP satisfies this regulatory requirement.

2. Conceptual Structure of Analysis

2.1 Regulatory Requirements

The conceptual structure of the 1996 PA for the WIPP ultimately derives from the regulatory requirements imposed on this facility. The primary regulation determining this structure is the U.S. EPA's standard for the geologic disposal of radioactive waste, *Environmental Radiation Protection Standards for the Management and Disposal of Spent Nuclear Fuel, High-Level and Transuranic Radioactive Wastes* (40 CFR 191) (U.S. EPA 1985, 1993a), which is divided into three parts. Subpart A applies to a disposal facility prior to decommissioning and limits annual radiation doses to members of the public from waste management and storage operations. Subpart B applies after decommissioning and sets probabilistic limits on cumulative releases of radionuclides to the accessible environment for 10,000 yr (40 CFR 191.13) and assurance requirements to provide confidence that 40 CFR 191.13 will be met (40 CFR 191.14). Subpart B also sets limits on radiation doses to members of the public in the accessible environment for 10,000 yrs of undisturbed performance (40 CFR 191.15). Subpart C limits radioactive contamination of certain sources of groundwater for 10,000 yr after disposal (40 CFR 191.24). The DOE must provide a reasonable expectation that the WIPP will comply with the requirements of Subparts B and C of 40 CFR 191.

The following is the central requirement in 40 CFR 191, Subpart B, and the primary determinant of the conceptual structure of the 1996 WIPP PA (p. 38086, U.S. EPA 1985):

> § 191.13 Containment requirements:
>
> (a) Disposal systems for spent nuclear fuel or high-level or transuranic radioactive wastes shall be designed to provide a reasonable expectation, based upon performance assessments, that cumulative releases of radionuclides to the accessible environment for 10,000 years after disposal from all significant processes and events that may affect the disposal system shall:
>
> (1) Have a likelihood of less than one chance in 10 of exceeding the quantities calculated according to Table 1 (Appendix A); and
>
> (2) Have a likelihood of less than one chance in 1,000 of exceeding ten times the quantities calculated according to Table 1 (Appendix A).
>
> (b) Performance assessments need not provide complete assurance that the requirements of 191.13(a) will be met. Because of the long time period involved and the nature of the events and processes of interest, there will inevitably be substantial uncertainties in projecting disposal system performance. Proof of the future performance of a disposal system is not to be had in the ordinary sense of the word in situations that deal with much shorter time frames. Instead, what is required is a reasonable expectation, on the basis of the record before the implementing agency, that compliance with 191.13(a) will be achieved.

Containment Requirement 191.13(a) refers to "quantities calculated according to Table 1 (Appendix A)," which means a normalized radionuclide release to the accessible environment based on the type of waste being disposed of, the initial waste inventory, and the release that takes place (App. A, U.S. EPA 1985). Table 1 (Appendix A) specifies allowable releases (i.e., release limits) for individual radionuclides and is reproduced as Table 2.1.1 of this presentation. The WIPP is intended for transuranic waste, which is defined to be "waste containing more than 100 nanocuries of alpha-emitting transuranic isotopes, with half-lives greater than twenty years, per gram of waste" (p. 38084, U.S. EPA, 1985). Specifically, the normalized release R for transuranic waste is defined by

$$R = \sum_i \left(\frac{Q_i}{L_i} \right) \left(1 \times 10^6 \text{ Ci} / C \right), \tag{2.1.1}$$

where Q_i is the cumulative release of radionuclide i to the accessible environment during the 10,000-yr period following closure of the repository (Ci), L_i is the release limit for radionuclide i given in Table 2.1.1 (Ci) and C is the amount of transuranic waste emplaced in the repository (Ci). In the 1996 WIPP PA, $C = 3.44 \times 10^6$ Ci (Sanchez et al. 1997). Further, accessible environment means (1) the atmosphere, (2) land surfaces, (3) surface waters, (4) oceans, and (5) all of the lithosphere that is beyond the controlled area; and controlled area means (1) a surface location, to be identified by passive institutional controls, that encompasses no more than 100 square kilometers and extends horizontally no more than five kilometers in any direction from the outer boundary of the original location of the radioactive wastes in a disposal system and (3) the subsurface underlying such a surface location.

To help clarify the intent of 40 CFR 191, the EPA also published 40 CFR 194, *Criteria for the Certification and Re-Certification of the Waste Isolation Pilot Plant's Compliance With the 40 CFR Part 191 Disposal Regulations; Final Rule* (U.S. EPA 1996). There, the following elaboration on the intent of 40 CFR 191.13 is given (pp. 5242-5243, U.S. EPA 1996):

> § 194.34 Results of performance assessments.
>
> (a) The results of performance assessments shall be assembled into "complementary, cumulative distributions functions" (CCDFs) that represent the probability of exceeding various levels of cumulative release caused by all signficant processes and events.
>
> (b) Probability distributions for uncertain disposal system parameter values used in performance assessments shall be developed and documented in any compliance application.
>
> (c) Computational techniques, which draw random samples from across the entire range of the probability distributions developed pursuant to paragraph (b) of this section, shall be used in generating CCDFs and shall be documented in any compliance application.

Table 2.1.1. Release Limits for the Containment Requirements (Table 1, App. A, U.S. EPA 1985)

Radionuclide	Release Limit L_i per 1000 MTHM[a] or other unit of waste[b]
Americium-241 or -243	100
Carbon 14	100
Cesium-135 or -137	1,000
Iodine-129	100
Neptunium-237	100
Plutonium-238, -239, -240, or -242	100
Radium-226	100
Strontium-90	1,000
Technetium-99	10,000
Thorium-230 or -232	10
Tin-126	1,000
Uranium-233, -234, -235, -236, or -238	100
Any other alpha-emitting radionuclide with a half-life greater than 20 yrs	100
Any other radionuclide with a half-life greater than 20 yrs that does not emit alpha particles	1,000

[a] Metric tons of heavy metal exposed to a burnup between 25,000 megawatt-days per metric ton of heavy metal (MWd/MTHM) and 40,000 MWd/MTHM

[b] An amount of transuranic wastes containing one million curies of alpha-emitting transuranic radionuclides with half-lives greater than 20 yrs

> (d) The number of CCDFs generated shall be large enough such that, at cumulative releases of 1 and 10, the maximum CCDF generated exceeds the 99th percentile of the population of CCDFs with at least a 0.95 probability.
>
> (e) Any compliance application shall display the full range of CCDFs generated.
>
> (f) Any compliance application shall provide information which demonstrates that there is at least a 95 percent level of statistical confidence that the mean of the population of CCDFs meets the containment requirements of § 191.13 of this chapter.

When viewed at a high level, three basic entities (EN1, EN2, EN3) underlie the results required in 191.13 and 194.34 and ultimately determine the conceptual and computational structure of the 1996 WIPP PA:

EN1, a probabilistic characterization of the likelihood of different futures occurring at the WIPP site over the next 10,000 yr,

EN2, a procedure for estimating the radionuclide releases to the accessible environment associated with each of the possible futures that could occur at the WIPP site over the next 10,000 yr,

EN3, a probabilistic characterization of the uncertainty in the parameters used in the definition of EN1 and EN2.

Together, EN1 and EN2 give rise to the CCDF specified in 191.13(a) (Fig. 2.1.1), and EN3 corresponds to the distributions indicated in 194.34(b).

The preceding entities arise from an attempt to answer three questions about the WIPP,

Q1: What occurrences could take place at the WIPP site over the next 10,000 yr?

Q2: How likely are the different occurrences that could take place at the WIPP site over the next 10,000 yr?

Q3: What are the consequences of the different occurrences that could take place at the WIPP site over the next 10,000 yr?

and one question about the WIPP PA,

Q4: How much confidence should be placed in answers to the first three questions?

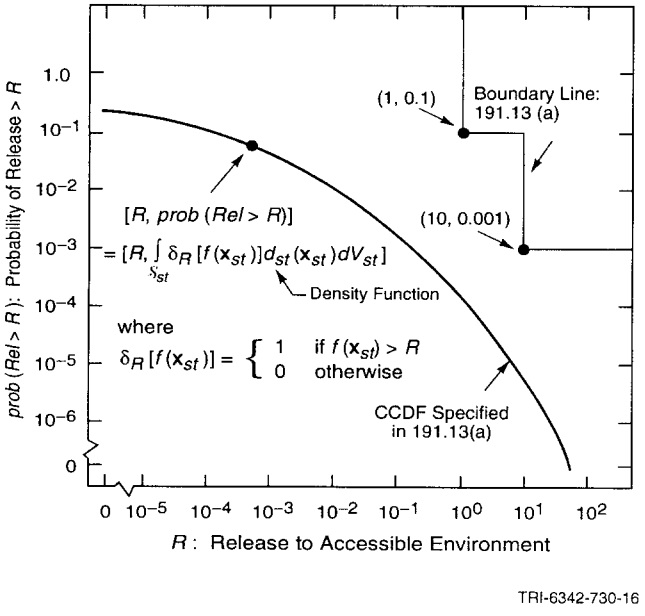

Fig. 2.1.1. Boundary line and associated CCDF specified in 40 CFR 191, Subpart B.

In the WIPP PA, EN1 provides answers to Q1 and Q2, EN2 provides an answer to Q3, and EN3 provides an answer to Q4. The nature of EN1, EN2 and EN3 and the role that they play in the 1996 WIPP PA are elaborated on in the next three sections.

2.2 EN1: Probabilistic Characterization of Different Futures

The entity EN1 is the outcome of the scenario development process for the WIPP and provides a probabilistic characterization of the likelihood of different futures that could occur at the WIPP site over the next 10,000 yr, with the period of 10,000 yr specified in 40 CFR 191. When viewed formally, EN1 is defined by a probability space ($\mathcal{S}_{st}$, $\mathcal{A}_{st}$, p_{st}), with the sample space $\mathcal{S}_{st}$ given by

$$\mathcal{S}_{st} = \{\mathbf{x}_{st}\text{: } \mathbf{x}_{st} \text{ is a possible 10,000 yr sequence of occurrences at the WIPP}\}. \tag{2.2.1}$$

The subscript *st* refers to stochastic (i.e., aleatory) uncertainty and is used because ($\mathcal{S}_{st}$, $\mathcal{A}_{st}$, p_{st}) is providing a probabilistic characterization of occurrences that may take place in the future (Helton 1997).

As a reminder, a probability space ($\mathcal{S}$, $\mathcal{A}$, p) consists of three components: a set $\mathcal{S}$ that contains everything that could occur for the particular "universe" under consideration, a suitably restricted set $\mathcal{A}$ of subsets of $\mathcal{S}$ and a function p defined for elements of $\mathcal{A}$ that actually defines probability (p. 116, Feller 1971). In the terminology of probability theory, $\mathcal{S}$ is the sample space, the elements of $\mathcal{S}$ are elementary events, the subsets of $\mathcal{S}$ contained in $\mathcal{A}$ are events, and p is a probability measure. In most applied problems, the function p defined on $\mathcal{A}$ is replaced by a probability density function (PDF) d (e.g., d_{st} in Fig. 2.1.1).

The scenario development process for the WIPP identified exploratory drilling for natural resources as the only disruption with sufficient likelihood and consequence for inclusion in the definition of EN1 (App. SCR, U.S. DOE 1996). In addition, 40 CFR 194 specifies that the occurrence of mining within the land withdrawal boundary must be included in the analysis. As a result, the elements $\mathbf{x}_{st}$ of $\mathcal{S}_{st}$ are vectors of the form

$$\mathbf{x}_{st} = [\underbrace{t_1, l_1, e_1, b_1, p_1, \mathbf{a}_1}_{1^{st}\text{ intrusion}}, \underbrace{t_2, l_2, e_2, b_2, p_2, \mathbf{a}_2}_{2^{nd}\text{ intrusion}}, \ldots, \underbrace{t_n, l_n, e_n, b_n, p_n, \mathbf{a}_n}_{n^{th}\text{ intrusion}}, t_{min}] \tag{2.2.2}$$

in the 1996 WIPP PA, where n is the number of drilling intrusions, t_i is the time (yr) of the i^{th} intrusion, l_i designates the location of the i^{th} intrusion, e_i designates the penetration of an excavated or nonexcavated area by the i^{th} intrusion, b_i designates where or not the i^{th} intrusion penetrates pressurized brine in the Castile Formation, p_i designates the plugging procedure used with the i^{th} intrusion (*i.e.*, continuous plug, two discrete plugs, three discrete plugs), $\mathbf{a}_i$ designates the type of waste penetrated by the i^{th} intrusion (*i.e.*, no waste, contact-handled (CH) waste, remotely-handled (RH) waste), and t_{min} is the time at which potash mining occurs within the land withdrawal boundary. In the development of ($\mathcal{S}_{st}$, $\mathcal{A}_{st}$, p_{st}), the probabilistic characterization of n, t_i, l_i and e_i derives from the

assumption that drilling intrusions occur randomly in time and space (i.e., follow a Poisson process), the probabilistic characterization of b_i derives from assessed properties of brine pockets, the probabilistic characterization of $\mathbf{a}_i$ derives from the properties of the waste to be emplaced at the WIPP, and the probabilistic characterization of p_i derives from current drilling practices in the sedimentary basin (i.e., the Delaware Basin) in which the WIPP is located. A vector notation is used for $\mathbf{a}_i$ because it is possible for a given drilling intrusion to penetrate several different types of waste. Further, the probabilistic characterization for t_{min} follows from the guidance in 40 CFR 194 that the occurrence of potash mining within the land withdrawal boundary should be assumed to occur randomly in time (i.e., follow a Poisson process with a rate constant of $\lambda_m = 10^{-4}$ yr^{-1}), with all commercially viable potash reserves within the land withdrawal boundary being extracted at time t_{min}.

With respect to the previously indicated questions, $\mathcal{S}_{st}$ provides an answer to Q1, while $\mathscr{A}_{st}$ and p_{st} provide an answer to Q2. In practice, Q2 will be answered by specifying distributions for n, t_i, l_i, e_i, b_i, p_i, $\mathbf{a}_i$, and t_{min}, which in turn lead to definitions for $\mathscr{A}_{st}$ and p_{st}. The CCDF in 40 CFR 191 will be obtained by evaluating an integral involving ($\mathcal{S}_{st}$, $\mathscr{A}_{st}$, p_{st}) (Fig. 2.1.1). The definition of ($\mathcal{S}_{st}$, $\mathscr{A}_{st}$, p_{st}) is discussed in more detail in Chapter 3.

2.3 EN2: Estimation of Releases

The entity EN2 is the outcome of the model development process for the WIPP and provides a way to estimate radionuclide releases to the accessible environment for the different futures (i.e., elements $\mathbf{x}_{st}$ of $\mathcal{S}_{st}$) that could occur at the WIPP. Estimation of environmental releases corresponds to evaluation of the function f in Fig. 2.1.1. Release mechanisms associated with f include direct removal to the surface at the time of a drilling intrusion (i.e., cuttings, spallings, brine flow) and release subsequent to a drilling intrusion due to brine flow up a borehole with a degraded plug (i.e., groundwater transport).

The primary computational models used in the 1996 WIPP PA are indicated in Fig. 2.3.1. Most of these models involve the numerical solution of partial differential equations used to represent material deformation, fluid flow and radionuclide transport. It is the models indicated in Fig. 2.3.1 that actually define the function f in Fig. 2.1.1.

The models in Fig. 2.3.1 are too complex to permit a closed form evaluation of the integral in Fig. 2.1.1 that defines the CCDF specified in 40 CFR 191. Rather, a Monte Carlo procedure is used in the 1996 WIPP PA. Specifically, elements $\mathbf{x}_{st,i}$, $i = 1, 2, \ldots, nS$, are randomly sampled from $\mathcal{S}_{st}$ in consistency with the definition of ($\mathcal{S}_{st}$, $\mathscr{A}_{st}$, p_{st}). Then, the integral in Fig. 2.1.1, and hence the associated CCDF, is approximated by

$$prob(Rel > R) = \int_{\mathcal{S}_{st}} \delta_R\left[f(\mathbf{x}_{st})\right] d_{st}(\mathbf{x}_{st})\, dV_{st} \doteq \sum_{i=1}^{nS} \delta_R\left[f(\mathbf{x}_{st,i})\right] / nS, \tag{2.3.1}$$

where $\delta_R[f(\mathbf{x}_{st})] = 1$ if $f(\mathbf{x}_{st}) > R$ and 0 if $f(\mathbf{x}_{st}) \leq R$ (Helton and Shiver 1996). The models in Fig. 2.3.1 are too computationally intensive to permit their evaluation for every element $\mathbf{x}_{st,i}$ of $\mathcal{S}_{st}$ in Eq. (2.3.1). Due to this constraint, the models in Fig. 2.3.1 are evaluated for representative elements of $\mathcal{S}_{st}$ and then the results of these evaluations are used to construct values of f for the large number of $\mathbf{x}_{st,i}$ (e.g., $nS = 10{,}000$) in Eq. (2.3.1).

With respect to the previously indicated questions, the models in Fig. 2.3.1 are providing an answer to Q3. The models in Fig. 2.3.1, and hence the function f in Eq. (2.3.1), are discussed in more detail in Chapter 4.

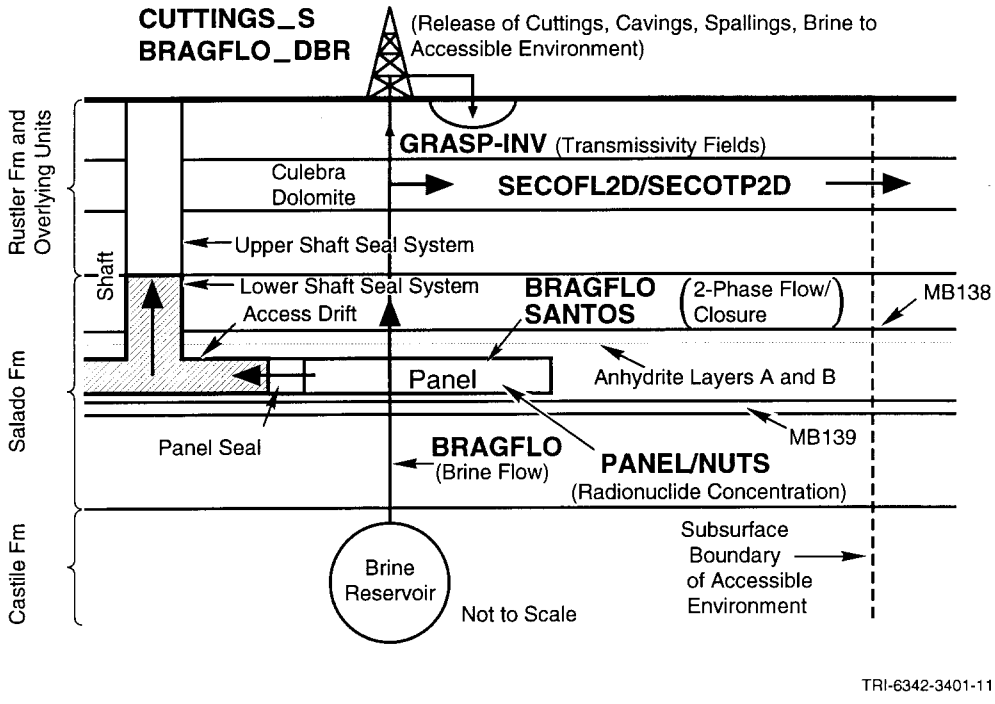

Fig. 2.3.1. Models used in 1996 WIPP PA.

2.4 EN3: Probabilistic Characterization of Parameter Uncertainty

The entity EN3 is the outcome of the data development effort for the WIPP and provides a probabilistic characterization of the uncertainty in the parameters that underlie the WIPP PA. When viewed formally, EN3 is defined by a probability space $(\mathcal{S}_{su}, \mathcal{A}_{su}, p_{su})$, with the sample space $\mathcal{S}_{su}$ given by

$$\mathcal{S}_{su} = \{\mathbf{x}_{su}: \quad \mathbf{x}_{su} \text{ is possibly the correct vector of parameter values to use in the WIPP PA models}\}. \tag{2.4.1}$$

The subscript *su* refers to subjective (i.e., epistemic) uncertainty and is used because $(\mathcal{S}_{su}, \mathcal{A}_{su}, p_{su})$ is providing a probabilistic characterization of where the appropriate inputs to use in the WIPP PA are believed to be located (Helton 1997). In practice, some elements of $\mathbf{x}_{su}$ could affect the definition of $(\mathcal{S}_{st}, \mathcal{A}_{st}, p_{st})$ (e.g., the rate constant λ used to define the Poisson process for drilling intrusions or the probability that a randomly placed drilling intrusion will penetrate pressurized brine in the Castile Formation) and other elements could relate to the models in Fig. 2.3.1 that determine the function f in Fig. 2.1.1 and Eq. (2.3.1) (e.g., radionuclide solubilities in Castile brine or fracture spacing in the Culebra Dolomite).

If the value for $\mathbf{x}_{su}$ was precisely known, then the CCDF in Fig. 2.1.1 could be determined with certainty and compared with the boundary line specified in 40 CFR 191. However, given the complexity of the WIPP site and the 10,000 yr time period under consideration, $\mathbf{x}_{su}$ can never be known with certainty. Rather, uncertainty in $\mathbf{x}_{su}$ as characterized by $(\mathcal{S}_{su}, \mathcal{A}_{su}, p_{su})$ will lead to a distribution of CCDFs (Fig. 2.4.1), with a different CCDF resulting for each possible value that $\mathbf{x}_{su}$ can take on. The proximity of this distribution to the boundary line in Fig. 2.1.1 provides an indication of the confidence with which 40 CFR 191 will be met.

The distribution of CCDFs in Fig. 2.4.1 can be summarized by distributions of exceedance probabilities conditional on individual release values (Fig. 2.4.2). For a given release value R, this distribution is defined by a double integral over $\mathcal{S}_{su}$ and $\mathcal{S}_{st}$ (Helton 1996, 1997). In practice, this integral is too complex to permit a closed-form evaluation. Instead, the WIPP PA uses Latin hypercube sampling (McKay et al. 1979) to evaluate the integral over $\mathcal{S}_{su}$ and, as indicated in Eq. (2.3.1), simple random sampling to evaluate the integral over $\mathcal{S}_{st}$. Specifically, a Latin hypercube sample $\mathbf{x}_{su,k}$, $k = 1, 2, \ldots, nLHS$, is generated from $\mathcal{S}_{su}$ in consistency with the definition of $(\mathcal{S}_{su}, \mathcal{A}_{su}, p_{su})$ and a random sample $\mathbf{x}_{st,i}$, $i = 1, 2, \ldots, nS$, is generated from $\mathcal{S}_{st}$ in consistency with the definition of $(\mathcal{S}_{st}, \mathcal{A}_{st}, p_{st})$. The probability $prob(p \le P|R)$ in Fig. 2.4.2 is then approximated by

$$prob(p \le P|R) \doteq 1 - \sum_{k=1}^{nLHS} \delta_P \left[\sum_{i=1}^{nS} \delta_R \left[f\left(\mathbf{x}_{st,i}, \mathbf{x}_{su,k}\right) \right] / nS \right] / nLHS. \tag{2.4.2}$$

The result of the preceding calculation is typically displayed by plotting percentile values (e.g., $P_{0.1}$, $P_{0.5}$, $P_{0.9}$ from Fig. 2.4.2) and also mean values for exceedance probabilities above the corresponding release values (i.e., R) and

then connecting these points to form continuous curves (Fig. 2.4.3). The proximity of these curves to the indicated boundary line provides an indication of the confidence with which 40 CFR 191 will be met.

With respect to the previously indicated questions, ($\mathcal{S}_{su}$, $\mathcal{A}_{su}$, p_{su}) and results derived from ($\mathcal{S}_{su}$, $\mathcal{A}_{su}$, p_{su}) (e.g., the distributions in Figs. 2.4.1 - 2.4.3) are providing an answer to Q4. The definition of ($\mathcal{S}_{su}$, $\mathcal{A}_{su}$, p_{su}) is discussed in more detail in Chapter 5.

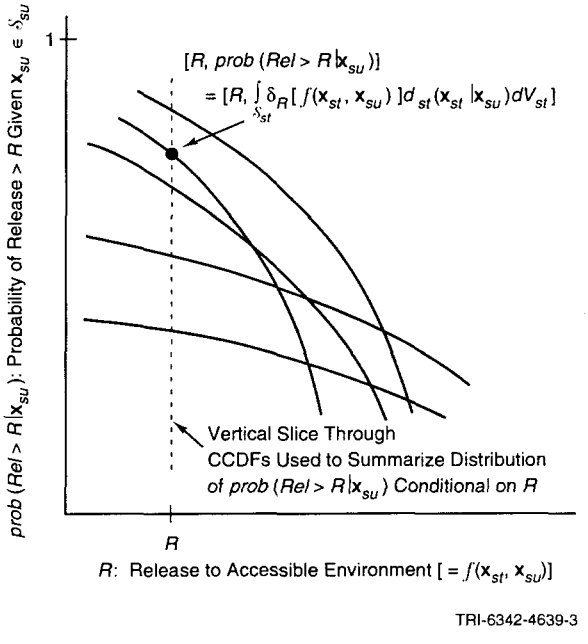

Fig. 2.4.1. Distribution of CCDFs resulting from possible values for $\mathbf{x}_{su} \in \mathcal{S}_{su}$.

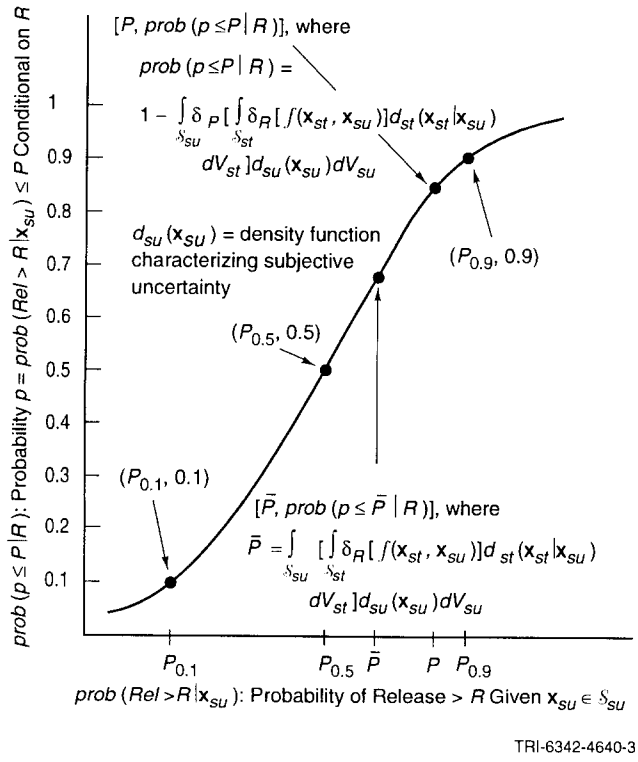

Fig. 2.4.2. Distribution of exceedance probabilities due to subjective uncertainty.

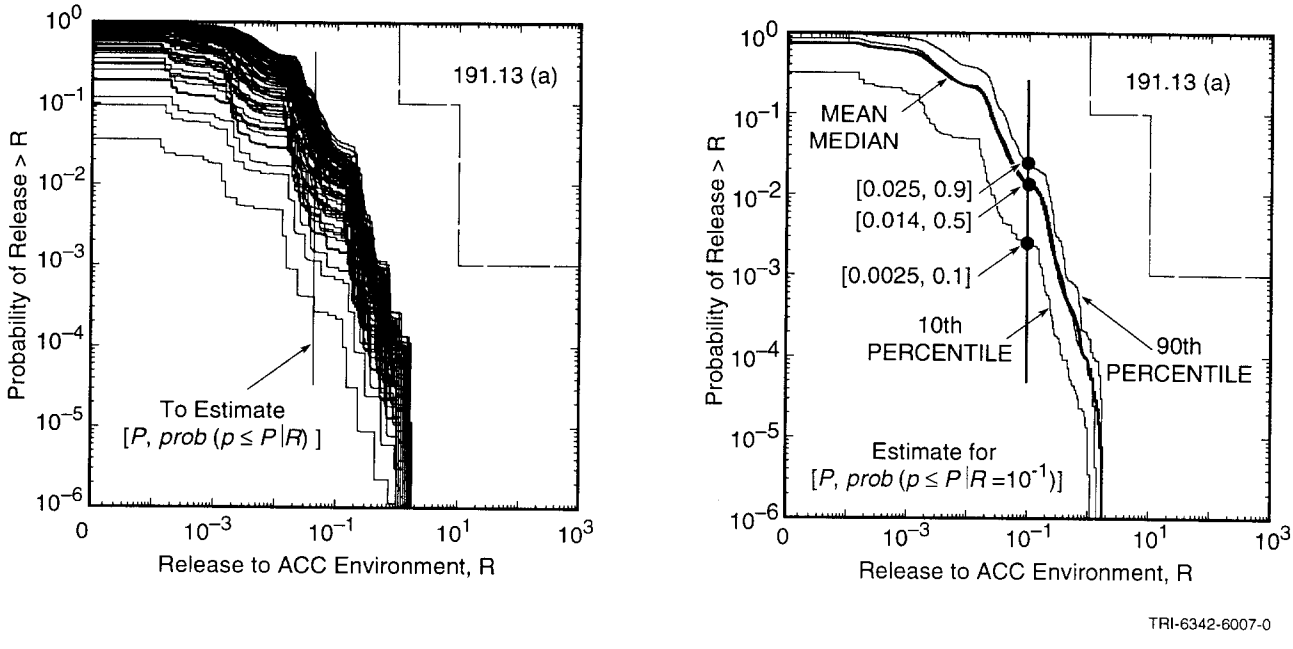

Fig. 2.4.3. Example CCDF distribution from 1992 WIPP PA.

2.5 Historical Perspective (Adapted from Helton and Burmaster 1996)

The importance of identifying, characterizing and displaying the uncertainty in the outcomes of analyses for complex systems is now widely recognized: The EPA's requirements for such results are explicitly stated in the quotes from 40 CFR 191 and 40 CFR 194 in Sect. 2.1. As other examples, the following statements are made in the indicated documents:

Risk Assessment in the Federal Government: Managing the Process (p. 148, NRC 1983)

> Preparation of fully documented written risk assessments that explicitly define the judgments made and attendant uncertainties clarifies the agency decision-making process and aids the review process considerably.

Safety Goals for the Operation of Nuclear Power Plants (p. 30031, U.S. NRC 1986)

> The Commission is aware that uncertainties are not caused by use of quantitative methodology in decisionmaking but are merely highlighted through use of the quantification process. Confidence in the use of probabilistic and risk assessment techniques has steadily improved since the time these were used in the Reactor Safety Study. In fact, through use of quantitative techniques, important uncertainties have been and continue to be brought into better focus and may even be reduced compared to those that would remain with sole reliance on deterministic decisionmaking. To the extent practicable, the Commission intends to ensure that the quantitative techniques used for regulatory decisionmaking take into account the potential uncertainties that exist so than an estimate can be made on the confidence level to be ascribed to the quantitative results.

Issues in Risk Assessment (p. 329, NRC 1993)

- *A discussion of uncertainty should be included in any ecological risk assessment.* Uncertainties could be discussed in the methods section of a report, and the consequences of uncertainties described in the discussion section. End-point selection is an important component of ecological risk assessment. Uncertainties about the selection of end points need to be addressed.

- *Where possible, sensitivity analysis, Monte Carlo parameter uncertainty analysis, or another approach to quantifying uncertainty should be used.* Reducible uncertainties (related to ignorance and sample size) and irreducible (aleatory) uncertainties should be clearly distinguished. Quantitative risk estimates, if presented, should be expressed in terms of distributions rather than as point estimates (especially worst-case scenarios).

An SAB Report: Multi-Media Risk Assessment for Radon, Review of Uncertainty Analysis of Risks Associated with Exposure to Radon (pp. 24–25, U.S. EPA 1993b)

> The Committee believes strongly that the explicit disclosure of uncertainty in quantitative risk assessment is necessary any time the assessment is taken beyond a screening calculation. ...
>
> The need for regulatory action must be based on more realistic estimates of risk. Realistic risk estimating, however, requires a full disclosure of uncertainty. The disclosure of uncertainty

enables the scientific reviewer, as well as the decision-maker, to evaluate the degree of confidence that one should have in the risk assessment. The confidence in the risk assessment should be a major factor in determining strategies for regulatory action.

Large uncertainty in the risk estimate, although undesirable, may not be critical if the confidence intervals about the risk estimate indicate that risks are clearly below regulatory levels of concern. On the other hand, when these confidence intervals overlap the regulatory levels of concern, consideration should be given to acquiring additional information to reduce the uncertainty in the risk estimate by focusing research on the factors that dominate the uncertainty. The dominant factors controlling the overall uncertainty are readily identified through a sensitivity analysis conducted as an integral part of quantitative uncertainty analysis. Acquiring additional data to reduce the uncertainty in the risk estimates is especially important when the cost of regulation is high. Ultimately, the explicit disclosure (of the uncertainty) in the risk estimate should be factored into analyses of the cost-effectiveness of risk reduction as well as in setting priorities for the allocation of regulatory resources for reducing risk.

Science and Judgment in Risk Assessment (NRC 1994)

A distinction between uncertainty (i.e., degree of potential error) and inter-individual variability (i.e., population heterogeneity) is generally required if the resulting quantitative risk characterization is to be optimally useful for regulatory purposes, particularly insofar as risk characterizations are treated quantitatively.

- The distinction between uncertainty and individual variability ought to be maintained rigorously at the level of separate risk-assessment components (e.g., ambient concentration, uptake and potency) as well as at the level of an integrated risk characterization. (p. 242)

When reporting estimates of risk to decision-makers and the public, EPA should report not only point estimates of risk but also the sources and magnitudes of uncertainty associated with these estimates. (p. 263)

Because EPA often fails to characterize fully the uncertainty in risk assessments, inappropriate decisions and insufficiently or excessively conservative analyses can result. (p. 267)

Guiding Principles for Monte Carlo Analysis (p. 3, Risk Assessment Forum 1997)

... the basic goal of a Monte Carlo analysis is to characterize, quantitatively, the uncertainty and variability in estimates of exposure or risk. A secondary goal is to identify key sources to the overall variance and range of model results.

Consistent with EPA principles and policies, an analysis of variability and uncertainty should provide its audience with clear and concise information on the variability in individual exposures and risks; it should provide information on population risk (extent of harm in the exposed population); it should provide information on the distribution of exposures and risks to highly exposed or highly susceptible populations; it should describe qualitatively and quantitatively the scientific uncertainty in the models applied, the data utilized, and the specific risk estimates that are used.

When viewed at a high level, the uncertainty referred to in 40 CFR 191, 40 CFR 194 (Sect. 2.1) and also in the preceding quotes can usually be divided into two types: stochastic (i.e., aleatory) uncertainty, which arises because the system under study can behave in many different ways and is thus a property of the system, and subjective (i.e., epistemic) uncertainty, which arises from a lack of knowledge about the system and is thus a property of the analysts performing the study. When a distinction between stochastic and subjective uncertainty is not maintained, the deleterious events associated with a system, the likelihood of such events, and the confidence with which both likelihood and consequences can be estimated become commingled in a way that makes it difficult to draw useful insights. Due to the pervasiveness and importance of these two types of uncertainty, they have attracted many investigators (e.g., Kaplan and Garrick 1981; Vesely and Rasmuson 1984; Paté-Cornell 1986, 1996; Whipple 1986; Silbergeld 1987; Parry 1988; Apostolakis 1989, 1990; IAEA 1989; Finkel 1990; McKone and Bogen 1991; Breeding et al. 1992; Anderson et al. 1993; Helton 1993a, 1994, 1997; Kaplan 1993; Hoffman and Hammonds 1994; Brattin et al. 1996; Frey and Rhodes 1996; Rai et al. 1996) and also many names (e.g., aleatory, type A, irreducible, and variability as alternatives to the designation stochastic, and epistemic, type B, reducible, and state of knowledge as alternatives to the designation subjective). Indeed, this distinction can be traced back to the beginnings of the formal development of probability theory in the seventeenth century (Hacking 1975).

As an example, probabilistic risk assessments (PRAs) for nuclear power plants and other complex engineered facilities involve stochastic uncertainty due to the many different types of accidents that can occur and subjective uncertainty due to the inability of the analysts involved to precisely determine the frequency and consequences of these accidents. The recent reassessment of the risk from nuclear power plants conducted by the U.S. Nuclear Regulatory Commission (NUREG-1150) provides an example of a very large analysis in which an extensive effort was made to separate stochastic and subjective uncertainty (U.S. NRC 1990-1991, Breeding et al. 1992). This analysis was instituted in response to criticisms that the Reactor Safety Study (U.S. NRC 1975) had inadequately characterized the uncertainty in its results (Lewis et al. 1978). Similarly, the EPA's standard for the geologic disposal of radioactive waste (Sect. 2.1) can be interpreted as requiring (1) the estimation of a CCDF, which arises from the different disruptions that could occur at a waste disposal site and is thus a summary of the effects of stochastic uncertainty (Sect. 2.2), and (2) the assessment of the uncertainty associated with the estimation of this CCDF, with this uncertainty deriving from a lack of knowledge on the part of the analysts involved and thus providing a representation for the effects of subjective uncertainty (Sect. 2.4). Conceptually, similar problems also arise in the assessment of health effects within a population exposed to a carcinogenic chemical or some other stress, where variability within the population can be viewed as stochastic uncertainty and the inability to exactly characterize this variability and estimate associated exposures and health effects can be viewed as subjective uncertainty (e.g., Bogen and Spear 1987, Hattis and Silver 1994, McKone 1994, Allen et al. 1996, NCRP 1996, Price et al. 1996, Thompson and Graham 1996). Other examples also exist of analyses that maintain a separation of stochastic and aleatory uncertainty (e.g., PLG 1982, 1983; Payne 1992; Payne et al. 1992a, b, c; Fogarty et al. 1992; MacIntosh et al. 1994). Thus, by maintaining a separation between stochastic and subjective uncertainty as indicated

in Sects. 2.2-2.4 and described in more detail in the remainder of this presentation, the 1996 WIPP Pa is in the main stream of current analyses for complex systems.

Many individuals believe that the boundary line associated with 40 CFR 191.13 and illustrated in Fig. 2.1.1 is a novel concept. Actually, this construction is an example of the Farmer limit line approach to the definition of acceptable risk (Farmer 1967, Cox and Baybutt 1982, Munera and Yadigaroglu 1986). A similar construction was used in the NUREG-1150 analyses (U.S. NRC 1990-1991, Breeding et al. 1992) to implement the proposed large release safety goal for reactor accidents (U.S. NRC 1986, Helton and Breeding 1993). Thus, again, the 1996 WIPP PA involves widely used ideas, although the actual scale of the analysis is much larger than that of a typical PA.

3. Probabilistic Characterization of Different Futures

3.1 Probability Space ($\mathcal{S}_{st}$, $\mathcal{A}_{st}$, p_{st})

The first entity that underlies the 1996 WIPP PA is a probabilistic characterization of the likelihood of different futures occurring at the WIPP site over the next 10,000 yr. As discussed in Sect. 2.2, this entity is defined by a probability space ($\mathcal{S}_{st}$, $\mathcal{A}_{st}$, p_{st}) that characterizes stochastic uncertainty. The individual elements $\mathbf{x}_{st}$ of $\mathcal{S}_{st}$ are vectors of the form shown in Eq. (2.2.2). The manner in which the individual components t_i, l_i, e_i, b_i, p_i, $\mathbf{a}_i$ and t_{min} of $\mathbf{x}_{st}$ are defined is now described (Sects. 3.2 - 3.8). The definition of these components and their associated probability distributions gives rise to the probability space ($\mathcal{S}_{st}$, $\mathcal{A}_{st}$, p_{st}) for stochastic uncertainty. The concept of a scenario as a subset of the sample space $\mathcal{S}_{st}$ for stochastic uncertainty is discussed in Sect. 3.9. Further, the procedure used to sample the individual elements $\mathbf{x}_{st,i}$ of $\mathcal{S}_{st}$ indicated in Eq. (2.3.1) is described in Sect. 6.6.

3.2 Drilling Intrusion Time t_i

Drilling intrusions in the 1996 WIPP PA are assumed to occur randomly in time and space (i.e., follow a Poisson process). Specifically, the base drilling rate considered within the area marked by a berm as part of the system for passive institutional controls (Fig. 3.2.1) is 46.8 intrusions/km^2/10^4 yr (App. DEL, U.S. DOE 1996). Further, active institutional controls are assumed to result in no possibility of a drilling intrusion for the first 100 yr after the decommissioning of the WIPP (Chapt. 7, U.S. DOE 1996), and passive institutional controls are assumed to reduce the base drilling rate by two orders of magnitude between 100 and 700 yrs after decommissioning (Trauth et al. 1996).

For the computational implementation of the 1996 WIPP PA, it is convenient to represent the Poisson process for drilling intrusions by its corresponding rate term $\lambda_d(t)$ for intrusions into the area marked by the berm. Specifically,

$$\lambda_d(t) = 0 \text{ yr}^{-1} \qquad \text{for } 0 \le t \le 100 \text{ yr} \tag{3.2.1}$$

$$= (0.01)\,(0.6285 \text{ km}^2)\,(46.8/\text{km}^2/10^4 \text{ yr}) = 2.94 \times 10^{-5} \text{ yr}^{-1} \tag{3.2.2}$$

$$\text{for } 100 < t \le 700 \text{ yr}$$

$$= (0.6285 \text{ km}^2)\,(46.8/\text{km}^2/10^4 \text{ yr}) = 2.94 \times 10^{-3} \text{ yr}^{-1} \tag{3.2.3}$$

$$\text{for } 700 < t \le 10000 \text{ yr}$$

where 0.6285 km^2 is the area of the berm (Trauth 1996) and t is elapsed time since decommissioning of the WIPP.

The function $\lambda_d(t)$ defines the part of the probability space ($\mathcal{S}_{st}$, $\mathcal{A}_{st}$, p_{st}) in Sect. 2.2 that corresponds to t_i. In the computational implementation of the analysis, $\lambda_d(t)$ is used to define the distribution of time between drilling

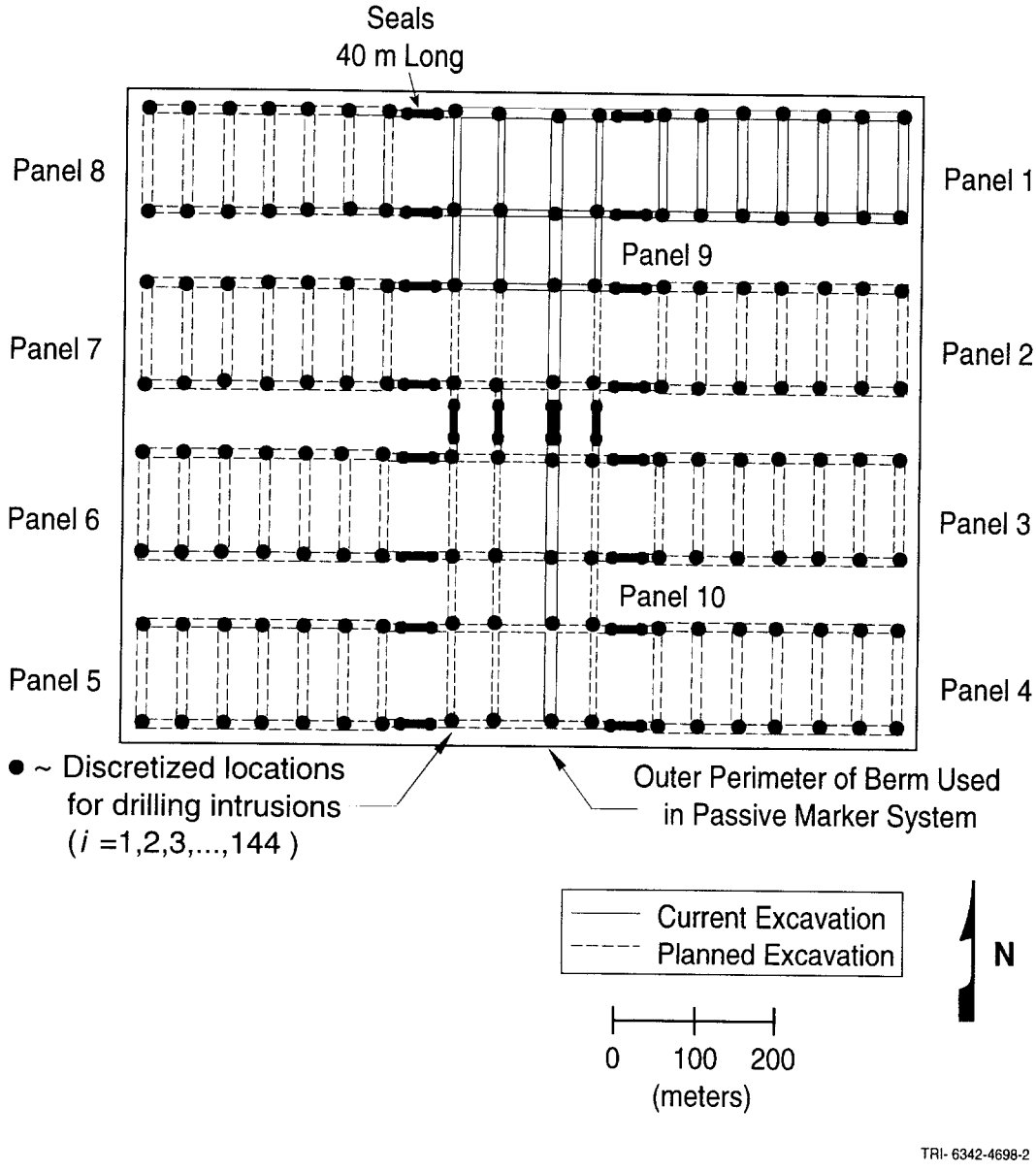

Fig. 3.2.1. Location of berm used in passive marker system.

intrusions (Fig. 3.2.2). As a reminder, the occurrence of one event in a Poisson process has no effect on the occurrence of the next event. Thus, the cumulative distributions in Fig. 3.2.2 can be used to define the time from one drilling event to the next (see Sect. 6.6). Due to the 10,000 yr regulatory period specified in 40 CFR 191.13, t_i is assumed to be bounded above by 10,000 yr in the definition of $\mathcal{S}_{st}$. Further, t_i is assumed to be bounded below by 0 yr, although drilling intrusions prior to 100 yr cannot occur with $\lambda_d(t)$ as defined in Eqs. (3.2.1) - (3.2.3).

The function $\lambda_d(t)$ also determines the probability $prob(nBH = n|[a, b])$ that a future will have exactly n drilling intrusions in the time interval $[a, b]$ (Helton 1993b), where

$$prob(nBH = n|[a,b]) = \left[\left(\int_a^b \lambda_d(t)dt\right)^n / n!\right] \exp\left(-\int_a^b \lambda_d(t)dt\right). \tag{3.2.4}$$

Further, the probability $prob(nBH \geq n\,|[a, b])$ that a future will have greater than or equal to n drilling intrusions in the time interval $[a, b]$ is given by

$$\begin{aligned} prob(nBH \geq n|[a,b]) &= 1 && \text{for } n = 0 \\ &= 1 - \sum_{m=0}^{n-1} prob(nBH = m|[a,b]) && \text{for } n > 0. \end{aligned} \tag{3.2.5}$$

Example probabilities for drilling intrusions within the berm (i.e., for $\lambda_d(t)$ as defined in Eqs. (3.2.1) - (3.2.3)) and also for drilling intrusions into the nonexcavated and excavated areas beneath the berm are given in Table 3.2.1. The excavated area beneath the berm corresponds to the area in which waste disposal takes place.

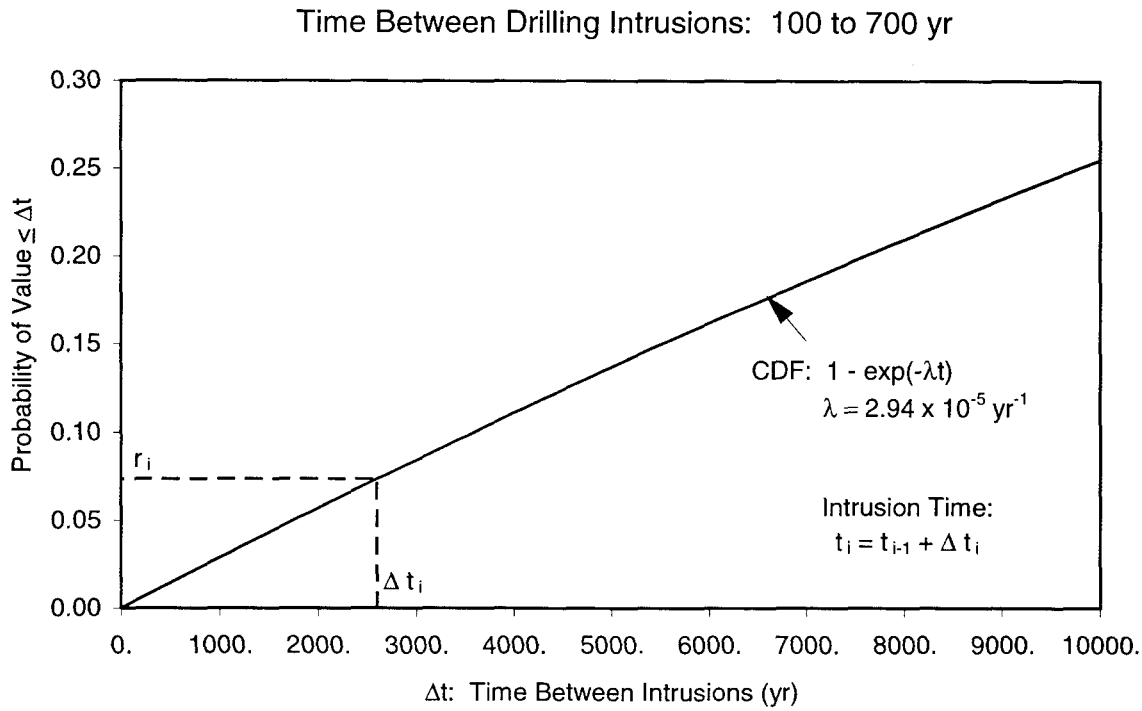

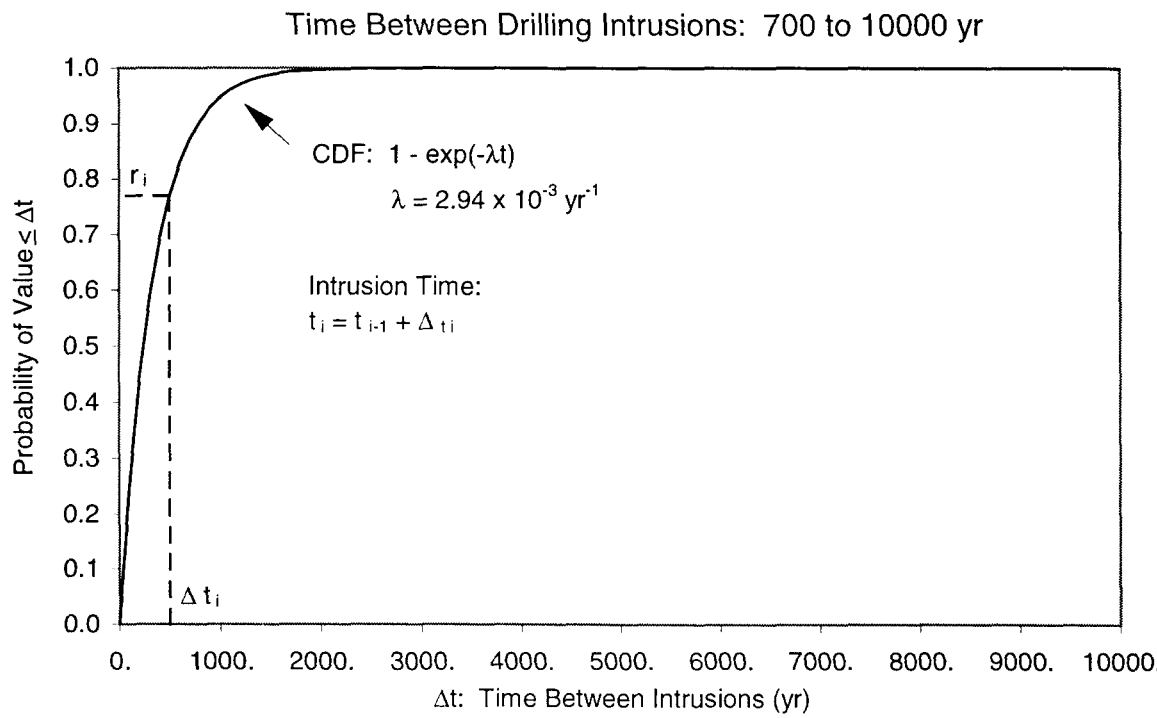

Fig. 3.2.2. Cumulative distribution functions for time between drilling intrusions into area marked by the berm used as part of the passive marker system (Fig. 3.2.1).

Table 3.2.1 Probabilities for Futures with Different Numbers of Drilling Intrusions into the Total Area Marked by the Berm (i.e., for $\lambda_d(t)$ in Eqs. (3.2.1) - (3.2.3)) and into the Nonexcavated (i.e., $\lambda_n(t) = 0.791\,\lambda_d(t)$; see Sect. 3.4) and Excavated (i.e., $\lambda_e(t) = 0.209\,\lambda_d(t)$; see Sect. 3.4) Areas beneath the Berm

During Passive Institutional Controls: 1.00E+02 to 7.00E+02 yr

Number of Intrusions	Nonexcavated (λ_n =2.33E–05/yr)		Excavated (λ_e =6.15E–06/yr)		Total (λ_d =2.94E–05/yr)	
(n)	(=n)	(≥n)	(=n)	(≥n)	(=n)	(≥n)
0	9.86E–01	1.00E+00	9.96E–01	1.00E+00	9.83E–01	1.00E+00
1	1.38E–02	1.39E–02	3.68E–03	3.68E–03	1.73E–02	1.75E–02
2	9.61E–05	9.65E–05	6.78E–06	6.79E–06	1.53E–04	1.54E–04
3	4.47E–07	4.49E–07	8.34E–09	8.35E–09	9.00E–07	9.04E–07

After Passive Institutional Controls: 7.00E+02 to 1.00E+04 yr

Number of Intrusions	Nonexcavated (λ_n=2.33E–03/yr)		Excavated (λ_e=6.15E–04/yr)		Total (λ_d=2.94E–03/yr)	
(n)	(=n)	(≥n)	(=n)	(≥n)	(=n)	(≥n)
0	4.02E–10	1.00E+00	3.28E–03	1.00E+00	1.32E–12	1.00E+00
1	8.69E–09	1.00E+00	1.88E–02	9.97E–01	3.61E–11	1.00E+00
2	9.40E–08	1.00E+00	5.37E–02	9.78E–01	4.93E–10	1.00E+00
3	6.78E–07	1.00E+00	1.02E–01	9.24E–01	4.50E–09	1.00E+00
4	3.67E–06	1.00E+00	1.46E–01	8.22E–01	3.08E–08	1.00E+00
5	1.59E–05	1.00E+00	1.67E–01	6.76E–01	1.68E–07	1.00E+00
6	5.72E–05	1.00E+00	1.60E–01	5.08E–01	7.67E–07	1.00E+00
7	1.77E–04	1.00E+00	1.30E–01	3.49E–01	3.00E–06	1.00E+00
8	4.78E–04	1.00E+00	9.32E–02	2.18E–01	1.02E–05	1.00E+00
9	1.15E–03	9.99E–01	5.92E–02	1.25E–01	3.12E–05	1.00E+00
10	2.49E–03	9.98E–01	3.39E–02	6.60E–02	8.52E–05	1.00E+00
11	4.89E–03	9.96E–01	1.76E–02	3.21E–02	2.12E–04	1.00E+00
12	8.82E–03	9.91E–01	8.40E–03	1.45E–02	4.83E–04	1.00E+00
13	1.47E–02	9.82E–01	3.70E–03	6.09E–03	1.02E–03	9.99E–01
14	2.27E–02	9.67E–01	1.51E–03	2.39E–03	1.99E–03	9.98E–01
15	3.27E–02	9.45E–01	5.76E–04	8.82E–04	3.62E–03	9.96E–01
16	4.43E–02	9.12E–01	2.06E–04	3.06E–04	6.19E–03	9.93E–01
17	5.63E–02	8.68E–01	6.92E–05	1.00E–04	9.96E–03	9.86E–01
18	6.77E–02	8.11E–01	2.20E–05	3.12E–05	1.51E–02	9.76E–01
	...		...		...	
48	3.96E–07	7.01E–07	5.98E–28	0.00E+00	1.01E–04	2.22E–04
49	1.75E–07	3.05E–07	6.98E–29	0.00E+00	5.63E–05	1.21E–04
50	7.56E–08	1.30E–07	7.98E–30	0.00E+00	3.08E–05	6.49E–05

During Regulatory Period: 1.00E+02 to 1.00E+04 yr

Number of Intrusions	Nonexcavated[a] (λ_n=2.19E–03/yr)		Excavated[a] (λ_e=5.78E–04/yr)		Total[a] (λ_d =2.76E–03/yr)	
(n)	(=n)	(≥n)	(=n)	(≥n)	(=n)	(≥n)
0	3.96E–10	1.00E+00	3.27E–03	1.00E+00	1.30E–12	1.00E+00
1	8.58E–09	1.00E+00	1.87E–02	9.97E–01	3.54E–11	1.00E+00
2	9.29E–08	1.00E+00	5.35E–02	9.78E–01	4.85E–10	1.00E+00

Table 3.2.1 Probabilities for Futures with Different Numbers of Drilling Intrusions into the Total Area Marked by the Berm (i.e., for $\lambda_d(t)$ in Eqs. (3.2.1) - (3.2.3)) and into the Nonexcavated (i.e., $\lambda_n(t) = 0.791\,\lambda_d(t)$; see Sect. 3.4) and Excavated (i.e., $\lambda_e(t) = 0.209\,\lambda_d(t)$; see Sect. 3.4) Areas beneath the Berm (continued)

During Regulatory Period: 1.00E+02 to 1.00E+04 yr

Number of Intrusions	Nonexcavated (λ_n=2.19E–03/yr)		Excavated (λ_e=5.78E–04/yr)		Total (λ_d=2.76E–03/yr)	
(n)	(=n)	(≥n)	(=n)	(≥n)	(=n)	(≥n)
3	6.70E–07	1.00E+00	1.02E–01	9.24E–01	4.43E–09	1.00E+00
4	3.63E–06	1.00E+00	1.46E–01	8.22E–01	3.03E–08	1.00E+00
5	1.57E–05	1.00E+00	1.67E–01	6.76E–01	1.66E–07	1.00E+00
6	5.67E–05	1.00E+00	1.60E–01	5.09E–01	7.57E–07	1.00E+00
7	1.75E–04	1.00E+00	1.30E–01	3.49E–01	2.96E–06	1.00E+00
8	4.74E–04	1.00E+00	9.33E–02	2.19E–01	1.01E–05	1.00E+00
9	1.14E–03	9.99E-01	5.94E–02	1.26E–01	3.08E–05	1.00E+00
10	2.47E–03	9.98E-01	3.40E–02	6.62E–02	8.43E–05	1.00E+00
11	4.86E–03	9.96E-01	1.77E–02	3.22E–02	2.10E–04	1.00E+00
12	8.77E–03	9.91E-01	8.43E–03	1.46E–02	4.78E–04	1.00E+00
13	1.46E–02	9.82E-01	3.71E–03	6.12E–03	1.01E–03	9.99E–01
14	2.26E–02	9.67E-01	1.52E–03	2.41E–03	1.97E–03	9.98E–01
15	3.26E–02	9.45E-01	5.79E–04	8.88E–04	3.59E–03	9.96E–01
16	4.41E–02	9.12E-01	2.07E–04	3.08E–04	6.15E–03	9.93E–01
17	5.61E–02	8.68E-01	6.98E–05	1.01E–04	9.90E–03	9.86E–01
18	6.75E–02	8.12E-01	2.22E–05	3.15E–05	1.51E–02	9.77E–01
		...		...		...
48	4.03E–07	7.13E–07	6.14E–28	7.45E–17	1.02E–04	2.25E–04
49	1.78E–07	3.11E–07	7.18E–29	7.45E–17	5.71E–05	1.23E–04
50	7.70E–08	1.33E–07	8.22E–30	7.45E–17	3.13E–05	6.59E–05

[a] Rate (i.e., λ_n, λ_e, λ_d) is time-dependent; indicated rate is equivalent time-averaged rate (e.g., 2.76×10^{-3} yr^{-1} = (600 yr/9900 yr) (2.94×10^{-5} yr^{-1}) + (9300 yr/9900 yr)(2.94×10^{-3} yr^{-1}))

3.3 Drilling Location l_i

Drilling locations are discretized to the 144 locations in Fig. 3.2.1. Given that a drilling intrusion occurs within the berm, it is assumed to be equally likely to occur at each of these 144 locations. Thus, the (conditional) probability pL_j that drilling intrusion i will occur at location L_j, j = 1, 2, ..., 144, in Fig. 3.2.1 is

$$pL_j = 1/144 = 6.94 \times 10^{-3}. \tag{3.3.1}$$

The probabilities pL_j define the part of $(\mathcal{S}_{st}, \mathcal{A}_{st}, p_{st})$ in Sect. 2.2 associated with l_i.

3.4 Penetration of Excavated/Nonexcavated Area e_i

The variable e_i is a designator for whether or not the i^{th} drilling intrusion penetrates an excavated area of the repository (i.e., e_i = 0, 1 implies penetration of nonexcavated, excavated area, respectively). The corresponding probabilities pE_0 and pE_1 for $e_i = 0$ and $e_i = 1$ are

$$pE_1 = 0.1314 \text{ km}^2/0.6285 \text{ km}^2 = 0.209 \tag{3.4.1}$$

$$pE_0 = 1 - pE_1 = 0.791, \tag{3.4.2}$$

where 0.1314 km^2 and 0.6285 km^2 are the excavated area of the repository (Vol. 3, WIPP PA 1992-1993) and the area of the berm (Trauth 1996), respectively. The probabilities pE_0 and pE_1 define the part of ($\mathcal{S}_{st}$, $\mathcal{A}_{st}$, p_{st}) in Sect. 2.2 associated with e_i. The probabilities of different numbers of drilling intrusions into excavated and nonexcavated areas beneath the berm are illustrated in Table 3.2.1.

3.5 Penetration of Pressurized Brine b_i

The variable b_i is a designator for whether or not the i^{th} drilling intrusion penetrates pressurized brine (i.e., b_i = 0, 1 implies nonpenetration, penetration of pressurized brine). The corresponding probabilities pB_0 and pB_1 for b_i = 0 and b_i = 1 are 0.92 and 0.08, respectively (Powers, Sigda and Holt 1996). The rationale for defining the probability of penetrating pressurized brine for individual drilling intrusions is based on the belief that the fractures in the Castile Formation that are capable of supplying significant quantities of brine are a small fraction (i.e., 0.08) of the area encompassed by the berm (Powers, Sigda and Holt 1996). The probabilities pB_0 and pB_1 define the part of ($\mathcal{S}_{st}$, $\mathcal{A}_{st}$, p_{st}) in Sect. 2.2 that corresponds to b_i.

Example probabilities for futures with different numbers of drilling intrusions that penetrate pressurized brine within the berm (Fig. 3.2.1) and also within the nonexcavated and excavated areas beneath the berm are given in Table 3.5.1. The defining equations for these probabilities are the same as those in Eqs. (3.2.4) and (3.2.5) with $\lambda_d(t)$ replaced by the appropriate drilling rate into pressurized brine. In particular, these rates are the original drilling rates (i.e., the rates used in the generation of Table 3.2.1) multiplied by 0.08.

Table 3.5.1 Probabilities for Futures with Different Numbers of Drilling Intrusions that Penetrate Pressurized Brine in the Total Area Marked by the Berm (i.e., for the drilling rate $\tilde{\lambda}_d$ into pressurized brine defined by $\lambda_d(t)$ in Eqs. (3.2.1) - (3.2.3) multiplied by 0.08) and into the Nonexcavated (i.e., $\tilde{\lambda}_n(t) = (0.08)(0.791)\lambda_d(t)$) and Excavated (i.e., $\tilde{\lambda}_e(t) = (0.08)(0.209)\lambda_d(t)$) Areas beneath the Berm

During Passive Institutional Controls: 1.00E+02 to 7.00E+02 yr

Number of Intrusions (n)	Nonexcavated ($\tilde{\lambda}_n$ =1.86E–06/yr)		Excavated ($\tilde{\lambda}_e$ =4.92E–07/yr)		Total ($\tilde{\lambda}_d$ =2.35E–06/yr)	
	(=n)	(≥n)	(=n)	(≥n)	(=n)	(≥n)
0	9.99E–01	1.00E+00	1.00E+00	1.00E+00	9.99E–01	1.00E+00
1	1.12E–03	1.12E–03	2.95E–04	2.95E–04	1.41E–03	1.41E–03
2	6.23E–07	6.23E–07	4.36E–08	4.36E–08	9.95E–07	9.96E–07

After Passive Institutional Controls: 7.00E+02 to 1.00E+04 yr

Number of Intrusions (n)	Nonexcavated ($\tilde{\lambda}_n$ =1.86E–04/yr)		Excavated ($\tilde{\lambda}_e$ =4.92E–05/yr)		Total ($\tilde{\lambda}_d$ =2.35E–04/yr)	
	(=n)	(≥n)	(=n)	(≥n)	(=n)	(≥n)
0	1.77E–01	1.00E+00	6.33E–01	1.00E+00	1.12E–01	1.00E+00
1	3.07E–01	8.23E–01	2.90E–01	3.67E–01	2.45E–01	8.88E–01
2	2.65E–01	5.16E–01	6.63E–02	7.76E–02	2.68E–01	6.43E–01
3	1.53E–01	2.51E–01	1.01E–02	1.14E–02	1.96E–01	3.74E–01
4	6.62E–02	9.78E–02	1.16E–03	1.27E–03	1.07E–01	1.78E–01
5	2.29E–02	3.16E–02	1.06E–04	1.14E–04	4.69E–02	7.12E–02
6	6.61E–03	8.69E–03	8.07E–06	8.63E–06	1.71E–02	2.44E–02
7	1.64E–03	2.07E–03	5.27E–07	5.59E–07	5.35E–03	7.26E–03
8	3.54E–04	4.36E–04	3.02E–08	3.18E–08	1.46E–03	1.91E–03
9	6.80E–05	8.20E–05	1.53E–09	1.61E–09	3.56E–04	4.52E–04
10	1.18E–05	1.39E–05	7.02E–11	7.32E–11	7.78E–05	9.67E–05

During Regulatory Period: 1.00E+02 to 1.00E+04 yr

Number of Intrusions (n)	Nonexcavated[a] ($\tilde{\lambda}_n$ =1.75E–04/yr)		Excavated[a] ($\tilde{\lambda}_e$ =4.63E–05/yr)		Total[a] ($\tilde{\lambda}_d$ =2.21E–04/yr)	
	(=n)	(≥n)	(=n)	(≥n)	(=n)	(≥n)
0	1.77E–01	1.00E+00	6.33E–01	1.00E+00	1.12E–01	1.00E+00
1	3.06E–01	8.23E–01	2.90E–01	3.67E–01	2.45E–01	8.88E–01
2	2.65E–01	5.17E–01	6.63E–02	7.77E–02	2.68E–01	6.43E–01
3	1.53E–01	2.51E–01	1.01E–02	1.14E–02	1.96E–01	3.75E–01
4	6.63E–02	9.80E–02	1.16E–03	1.27E–03	1.07E–01	1.79E–01
5	2.30E–02	3.17E–02	1.06E–04	1.15E–04	4.70E–02	7.14E–02
6	6.63E–03	8.71E–03	8.10E–06	8.66E–06	1.71E–02	2.44E–02
7	1.64E–03	2.08E–03	5.30E–07	5.62E–07	5.36E–03	7.28E–03
8	3.55E–04	4.38E–04	3.03E–08	3.19E–08	1.47E–03	1.92E–03
9	6.84E–05	8.24E–05	1.54E–09	1.62E–09	3.57E–04	4.54E–04
10	1.18E–05	1.40E–05	7.06E–11	7.37E–11	7.82E–05	9.72E–05

[a] Rate (i.e., $\tilde{\lambda}_d$) is time-dependent; indicated rate is equivalent time-averaged rate (e.g., 2.21×10^{-4} yr^{-1} = (600 yr/9900 yr) (2.35×10^{-6} yr^{-1}) + (9300 yr/9900 yr)(2.35×10^{-4} yr^{-1}))

3.6 Plugging Pattern p_i

Three plugging patterns are considered in the 1996 WIPP PA: (1) p_1, which corresponds to a full concrete plug through Salado Formation to Bell Canyon Formation with a permeability of 5×10^{-17} m^2, (2) p_2, which corresponds to a two plug configuration with concrete plugs at Rustler/Salado interface and Castile/Bell Canyon interface, and (3) p_3, which corresponds to a three plug configuration with concrete plugs at Rustler/Salado, Salado/Castile and Castile/Bell Canyon interfaces (Thompson et al. 1996; App. DEL, U.S. DOE 1996). The probability that a given drilling intrusion will be sealed with plugging pattern p_j, j = 1, 2, 3, is given by pPL_j, where pPL_1 = 0.02, pPL_2 = 0.68 and pPL_3 = 0.30 (App. DEL, U.S. DOE 1996). The probabilities pPL_j define the part of (S_{st}, $\mathcal{J}_{st}$, p_{st}) in Sect. 2.2 that corresponds to p_i.

3.7 Activity Level a_i

The waste intended for disposal at the WIPP is divided in 570 distinct waste streams (Table 3.7.1), with 569 of these waste streams designated as contact-handled (CH)-TRU waste and one waste stream designated as remotely-handled (RH)-TRU waste. Each waste drum emplaced at the WIPP will contain waste from a single CH-TRU stream. Given that the CH-TRU drums will be stacked three high, each drilling intrusion through CH-TRU waste will intersect three waste streams. In contrast, there is only one waste stream for RH-TRU waste, and so each drilling intrusion through RH-TRU waste will intersect this single waste stream.

The concentrations and conditional probabilities for individual CH-TRU streams are indicated in Table 3.7.1. However, the large number of waste streams makes a complete display of this information cumbersome. A more compact summary of the probabilities and concentrations for the CH-TRU streams is provided by CCDFs for concentration at individual times (Fig. 3.7.1). Each CCDF in Fig. 3.7.1 summarizes the probability and concentration data indicated in Table 3.7.1 for CH-TRU waste at a specific time (i.e., 100, 125, ..., 10,000 yr).

The vector $\mathbf{a}_i$ characterizes the type of waste penetrated by the i^{th} drilling intrusion. Specifically,

$$\mathbf{a}_i = a_i = 0 \tag{3.7.1}$$

if $e_i = 0$ (i.e., if the i^{th} drilling intrusion does not penetrate an excavated area of the repository);

$$\mathbf{a}_i = a_i = 1 \tag{3.7.2}$$

if $e_i = 1$ and RH-TRU is penetrated; and

$$\mathbf{a}_i = \left[2, iCH_{i1}, iCH_{i2}, iCH_{i3}\right] \tag{3.7.3}$$

Table 3.7.1. Concentrations and Conditional Probabilities for Individual Waste Streams Associated with CH- and RH-TRU Waste (Sanchez et al. 1997)

Waste Stream[a]	Cond Prob[b]	Concentration (EPA units/m^3) at Indicated Times (yr) 100	125	175	350	1000	3000	5000	7500	10000
					CH Waste					
1	7.282E–05	4.844E–03	4.654E–03	4.295E–03	3.244E–03	1.144E–03	4.630E–05	1.873E–06	3.400E–08	6.172E–10
2	1.359E–05	3.243E–03	3.159E–03	3.001E–03	2.648E–03	2.162E–03	1.702E–03	1.456E–03	1.214E–03	1.022E–03
3	2.963E–04	3.164E–03	3.133E–03	3.074E–03	2.910E–03	2.574E–03	2.244E–03	2.068E–03	1.880E–03	1.716E–03
4	9.715E–04	3.157E–03	3.126E–03	3.068E–03	2.903E–03	2.568E–03	2.239E–03	2.063E–03	1.876E–03	1.711E–03
5	5.555E–05	6.320E–03	6.258E–03	6.141E–03	5.812E–03	5.141E–03	4.482E–03	4.131E–03	3.755E–03	3.427E–03
6	4.036E–06	8.418E–01	6.934E–01	4.716E–01	1.287E–01	1.421E–02	1.281E–02	1.213E–02	1.133E–02	1.058E–02
7	1.246E–06	2.780E–-1	2.290E–01	1.557E–01	4.249E–02	4.691E–03	4.228E–03	4.002E–03	3.737E–03	3.491E–03
					...					
567	1.642E–04	4.657E+00	3.826E+00	2.584E+00	6.629E–01	1.971E–02	1.307E–02	1.206E–02	1.105E–02	1.021E–02
568	1.890E–04	3.024E+00	2.484E+00	1.676E+00	4.270E–01	8.839E–03	4.744E–03	4.296E–03	3.889E–03	3.571E–03
569	3.086E–06	3.468E–01	3.465E–01	3.460E–01	3.443E–01	3.379E–01	3.190E–01	3.011E–01	2.802E–01	2.607E–01
SUM=	1.000E+00[c]									
					RH Waste					
1	1.000E+00	1.021E–02	9.421E–03	8.569E–03	7.488E–03	5.883E–03	4.659E–03	4.200E–03	3.742E–03	3.356E–03
SUM=	1.000E+00									

[a] Waste stream for indicated waste type (i.e., CH-TRU or RH-TRU)

[b] Probability of waste stream conditional on occurrence of indicated waste type (i.e., pCH_j, j = 1, 2, ..., 569, for CH-TRU waste and pRH, for RH-TRU waste)

[c] Sum of conditional probabilities

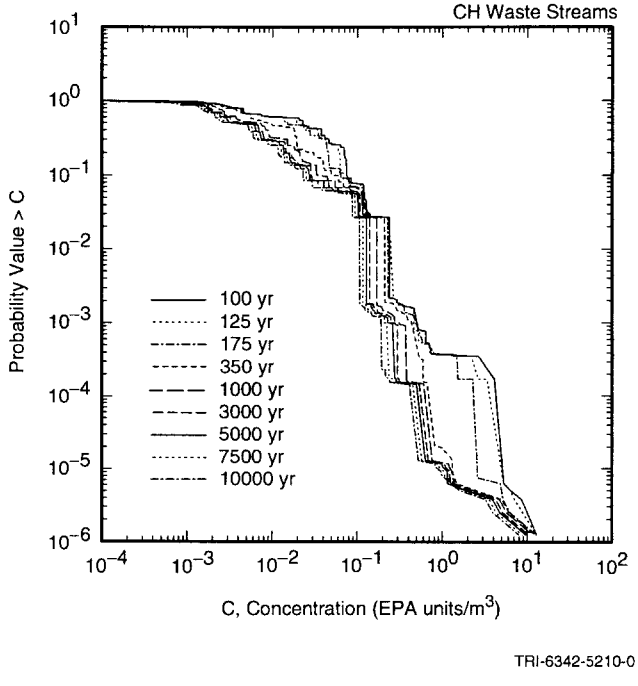

Fig. 3.7.1. Distribution of radionuclide concentration (EPA units/m^3) in CH-TRU waste streams at selected times (Sanchez et al. 1997).

if $e_i = 1$ and CH-TRU is penetrated, where iCH_{i1}, iCH_{i2} and iCH_{i3} are integer designators for the CH-TRU waste streams intersected by the i^{th} drilling intrusion (i.e., each of iCH_{i1}, iCH_{i2} and iCH_{i3} is an integer between 1 and 569).

Whether the i^{th} intrusion penetrates a nonexcavated or excavated area is determined by the probabilities pE_0 and pE_1 discussed in Sect. 3.4. Given that the i^{th} intrusion penetrates an excavated area, the probabilities pCH and pRH of penetrating CH- and RH-TRU waste are given by

$$pCH = aCH / aEX = \left(1.115 \times 10^5 \text{ m}^2\right) / \left(1.273 \times 10^5 \text{ m}^2\right) = 0.876 \tag{3.7.4}$$

$$pRH = aRH / aEX = \left(1.576 \times 10^4 \text{ m}^2\right) / \left(1.273 \times 10^5 \text{ m}^2\right) = 0.124, \tag{3.7.5}$$

where aCH is the excavated area used for disposal of CH-TRU waste (i.e., 1.115×10^5 m^2), aRH is the excavated area used for disposal of RH-TRU waste (i.e., 1.576×10^4 m^2), and $aEX = aCH + aRH$ (i.e., 1.273×10^5 m^2) (Vol. 3, WIPP PA 1992-1993). The excavated area of 1.314×10^5 m^2 used in Eq. (3.4.1) is slightly larger than the excavated area of 1.273×10^5 m^2 used in Eqs. (3.7.4) and (3.7.5) due to the inclusion of a seal area of 4.133×10^3 m^2 in the definition of the area 1.314×10^5 m^2 but not the area 1.273×10^5 m^2.

As indicated in this section, the probabilistic characterization of $\mathbf{a}_i$ in $(\mathcal{S}_{st}, \mathcal{J}_{st}, p_{st})$ depends on a number of individual probabilities. Specifically, pE_0 and pE_1 determine whether a nonexcavated or excavated area is penetrated (Sect. 3.4); pCH and pRH determine whether CH- or RH-TRU waste is encountered given penetration of an excavated area; and the individual waste stream probabilities in Table 3.7.1 (i.e., pCH_j, $j = 1, 2, \ldots, 569$) determine the waste streams encountered given a penetration of CH-TRU waste.

3.8 Mining Time t_{min}

Consistent with guidance in 40 CFR 194, full mining of known potash reserves within the land withdrawal boundary is assumed to occur at time t_{min}. In 40 CFR 194, the occurrence of mining within the land withdrawal boundary in the absence of institutional controls is specified as following a Poisson process with a rate of $\lambda_m = 1 \times 10^{-4}$ yr^{-1}. However, this rate can be reduced by active and passive institutional controls. Specifically, active institutional controls are assumed to result in no possibility of mining for the first 100 yr after decommissioning of the WIPP (Chapt. 7, U.S. DOE 1996), and passive institutional controls are assumed to reduce the base mining rate by two orders of magnitude between 100 and 700 yr after decommissioning (Trauth et al. 1996).

The preceding requirements lead to a time-dependent mining rate $\lambda_m(t)$. Specifically,

$$\lambda_m(t) = 0 \text{ yr}^{-1} \qquad \text{for } 0 \le t \le 100 \text{ yr} \tag{3.8.1}$$

$$= (0.01)\left(1 \times 10^{-4} \text{ yr}^{-1}\right) = 1 \times 10^{-6} \text{ yr}^{-1} \qquad \text{for } 100 < t \le 700 \text{ yr} \tag{3.8.2}$$

$$= 1 \times 10^{-4}\ \mathrm{yr}^{-1}, \qquad \text{for } 700 < t \leq 10000\ \mathrm{yr} \tag{3.8.3}$$

where t is elapsed time since decommissioning of the WIPP. The function $\lambda_m(t)$ defines the part of ($\mathcal{S}_{st}$, $\mathcal{J}_{st}$, p_{st}) that corresponds to t_{min}. In the computational implementation of the analysis, $\lambda_m(t)$ is used to define the distribution of time to mining (Fig. 3.8.1). The use of $\lambda_m(t)$ to characterize t_{min} is analogous to the use of λ_d to characterize the t_i except that only one mining event is assumed to occur (i.e., $\mathbf{x}_{st}$ contains only one value for t_{min}) in consistency with guidance given in 40 CFR 194 that mining within the land withdrawal boundary should be assumed to remove all economically viable potash reserves. Due to the 10,000 yr regulatory period specified in 40 CFR 191.13, t_{min} is assumed to be bounded above by 10,000 yr in the definition of $\mathcal{S}_{st}$. Further, t_{min} is assumed to be bounded below by 0 yr, although mining cannot occur prior to 100 yr with $\lambda_m(t)$ as defined in Eqs. (3.8.1) - (3.8.3).

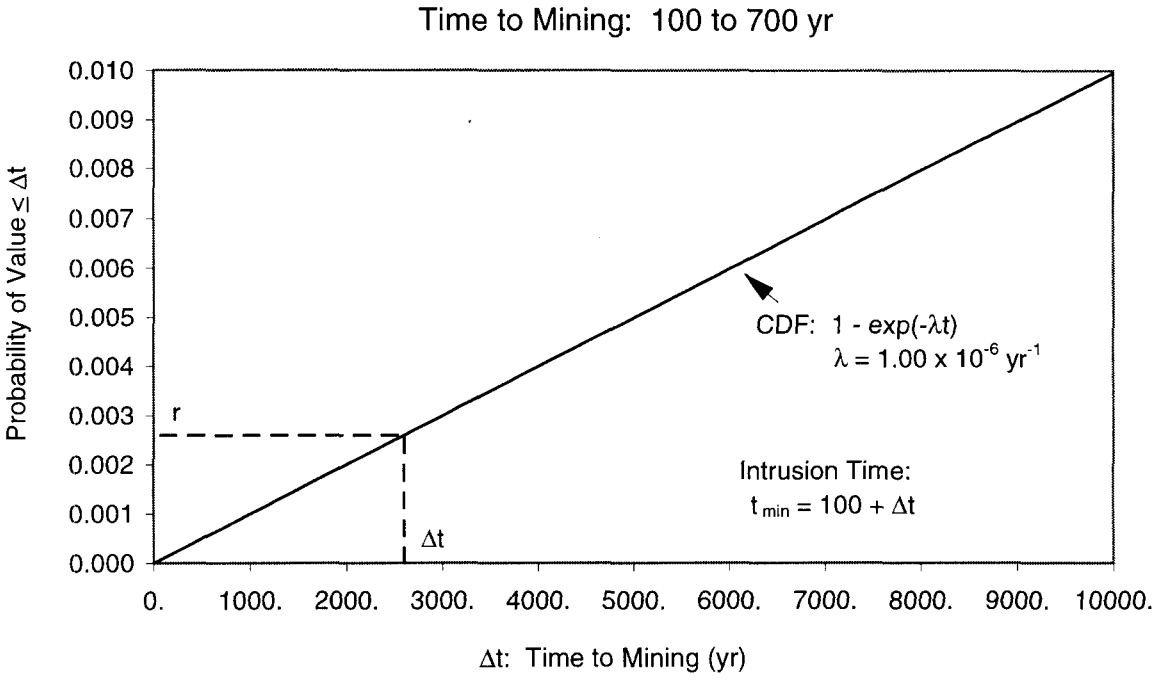

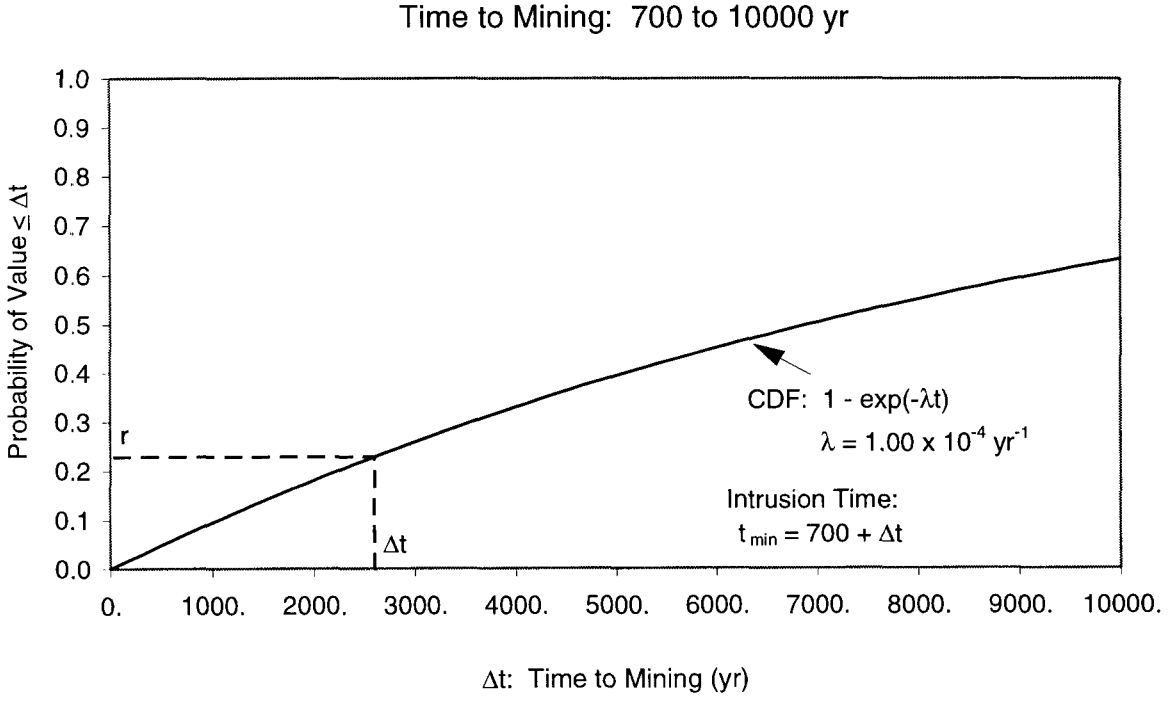

Fig. 3.8.1. Cumulative distribution functions for time to mining.

3.9 Scenarios and Scenario Probabilities

In the formal development of the 1996 WIPP PA, a scenario is a subset $\mathcal{S}$ of the sample space $\mathcal{S}_{st}$ for stochastic uncertainty. More specifically, a scenario is an element $\mathcal{S}$ of the set $\mathcal{A}_{st}$ in the probability space $(\mathcal{S}_{st}, \mathcal{A}_{st}, p_{st})$ for stochastic uncertainty, and the probability of $\mathcal{S}$ is given by $p_{st}(\mathcal{S})$. Thus, a scenario is what is called an event in the usual terminology of probability theory.

Given the complexity of the elements $\mathbf{x}_{st}$ of $\mathcal{S}_{st}$ (see Eq. (2.2.2)), infinitely many different scenarios can be defined. Several examples follow:

$\mathcal{S}_0 = \{\mathbf{x}_{st}$: $\mathbf{x}_{st}$ involves no drilling intrusion through an excavated area of the repository (i.e., $n = 0$ or $e_i = 0$ in Eq. (2.2.2) for $i = 1, 2, \ldots, n > 0)\}$ (3.9.1)

$\mathcal{S}_1 = \{\mathbf{x}_{st}$: $\mathbf{x}_{st}$ involves exactly one drilling intrusion through an excavated area of the repository, with this intrusion penetrating pressurized brine in the Castile Fm (i.e., $n > 0$ in Eq. (2.2.2) and there exists an integer i such that $1 \le i \le n$, $e_i = 1$, $b_i = 1$, and $e_j = 0$ for $j \ne i$ and $1 \le j \le n)\}$ (3.9.2)

$\mathcal{S}_2 = \{\mathbf{x}_{st}$: $\mathbf{x}_{st}$ involves exactly one drilling intrusion through an excavated area of the repository, with this intrusion not penetrating pressurized brine in the Castile Fm (i.e., $n > 0$ in Eq. (2.2.2) and there exists an integer i such that $1 \le i \le n$, $e_i = 1$, $b_i = 0$, and $e_j = 0$ for $j \ne i$ and $1 \le j \le n)\}$ (3.9.3)

$\mathcal{S}_3 = \{\mathbf{x}_{st}$: $\mathbf{x}_{st}$ involves exactly one drilling intrusion through an excavated area of the repository (i.e., $n > 0$ in Eq. (2.2.2) and there exists an integer i such that $1 \le i \le n$, $e_i = 1$, and $e_j = 0$ for $j \ne i$ and $1 \le j \le n)\}$. (3.9.4)

The definitions of the preceding four scenarios are quite simple. In general, scenarios can be defined on the basis of any possible characterization of the properties of the individual elements of $\mathbf{x}_{st}$, which can lead to very complex scenario definitions.

The immediately preceding sentence implies that $\mathcal{A}_{st}$ can be defined to be all possible subsets of $\mathcal{S}_{st}$. This is correct at an intuitive level and, for practical purposes, $\mathcal{A}_{st}$ can be thought of as containing all subsets of $\mathcal{S}_{st}$. However, to obtain a mathematically rigorous development of probability (p. 116, Feller 1971), $\mathcal{A}_{st}$ and p_{st} must have the following properties: (1) if $\mathcal{E} \in \mathcal{A}_{st}$, then $\mathcal{E}^c \in \mathcal{A}_{st}$, where the superscript c is used to denote the complement of $\mathcal{E}$, (2) if $\{\mathcal{E}_i\}$ is a countable collection of elements of $\mathcal{A}_{st}$, then $\cup_i \mathcal{E}_i$ and $\cap_i \mathcal{E}_i$ are also elements of $\mathcal{A}_{st}$, (3) $p_{st}(\mathcal{S}_{st}) = 1$, (4) if $\mathcal{E} \in \mathcal{A}_{st}$, then $0 \le p_{st}(\mathcal{E}) \le 1$, and (5) if $\mathcal{E}_1, \mathcal{E}_2, \ldots$ is a sequence of disjoint sets from $\mathcal{A}_{st}$ (i.e., $\mathcal{E}_i \cap \mathcal{E}_j = \varnothing$ if $i \ne j$), then $p_{st}(\cup_i \mathcal{E}_i) = \sum_i p_{st}(\mathcal{E}_i)$. Properties (1) - (5) are describing characteristics that are intuitively expected of scenarios. Specifically, Property (1) implies that, if the occurrence of event $\mathcal{E}$ is a scenario, then the nonoccurrence of event $\mathcal{E}$ is also a scenario; Property (2) implies that, if the occurrence of each of the events $\mathcal{E}_1, \mathcal{E}_2, \ldots$ is a scenario, then the occurrence of $\mathcal{E}_1$ or $\mathcal{E}_2$ or ... is a scenario, and similarly the occurrence of $\mathcal{E}_1$ and $\mathcal{E}_2$

and ... is also a scenario, where the indicated sequence of scenarios (i.e., $\mathcal{E}_1$, $\mathcal{E}_2$, ...) can be finite or infinite; Property (3) implies that the sample space $\mathcal{S}_{st}$ contains everything that could possibly occur (i.e., the sample space $\mathcal{S}_{st}$ is a scenario that has a probability of 1); Property (4) implies that all scenarios have probabilities between 0 and 1; and Property (5) implies that, if $\mathcal{E}_1$, $\mathcal{E}_2$, ... is a sequence of mutually exclusive scenarios (i.e., $\mathcal{E}_i$ and $\mathcal{E}_j$ cannot both occur if $i \neq j$), then the probability of $\mathcal{E}_1$ occurring or $\mathcal{E}_2$ occurring or ... is the sum of the probabilities for $\mathcal{E}_1$, $\mathcal{E}_2$, ..., where the indicated sequence of scenarios can be finite or infinite. With considerable mathematical ingenuity, subsets of $\mathcal{S}_{st}$ can be constructed such that it is not possible to define a function p_{st} satisfying Properties (3) - (5) (Sect. 1.29, Romano and Siegel 1986); thus, in a formal mathematical development, $\mathcal{A}_{st}$ cannot consist of all possible subsets of $\mathcal{S}_{st}$. However, subsets of $\mathcal{S}_{st}$ that do not permit a suitable definition for p_{st} are so esoteric that their exclusion from $\mathcal{A}_{st}$ by the requirement that Properties (1) - (5) be satisfied does not result in the removal of any scenarios of potential interest in PA.

In the terminology of the 1996 WIPP PA, $\mathcal{S}_0$ is typically called the E0 scenario (i.e., no drilling intrusions through the repository), $\mathcal{S}_1$ is typically called the E1 scenario (i.e., a single drilling intrusion through the repository that penetrates pressurized brine), and $\mathcal{S}_2$ is typically called the E2 scenario (i.e., a single drilling intrusion through the repository that does not penetrate pressurized brine). Another important scenario is defined by

$$\mathcal{S}_{21} = \{\mathbf{x}_{st}:\ \mathbf{x}_{st} \text{ involves exactly two drilling intrusions through excavated areas of the repository, with the first intrusion not penetrating pressurized brine and the second intrusion penetrating pressurized brine (i.e., } n \geq 2 \text{ in Eq. (2.2.2) and there exist integers } i, j \text{ such that } 1 \leq i < j \leq n,\ e_i = 1,\ b_i = 0,\ e_j = 1,\ b_j = 1, \text{ and } e_k = 0 \text{ for } k \neq i, j \text{ and } 1 \leq k \leq n)\} \tag{3.9.5}$$

In the terminology of the 1996 WIPP PA, $\mathcal{S}_{21}$ is typically called the E2E1 scenario.

The scenarios $\mathcal{S}_0$, $\mathcal{S}_1$, $\mathcal{S}_2$, $\mathcal{S}_3$ and $\mathcal{S}_{21}$ are elements of $\mathcal{A}_{st}$, and their probabilities are formally represented by $p_{st}(\mathcal{S}_0)$, $p_{st}(\mathcal{S}_1)$, $p_{st}(\mathcal{S}_2)$, $p_{st}(\mathcal{S}_3)$, and $p_{st}(\mathcal{S}_{21})$, with these probabilities deriving from the probability distributions assigned to the individual elements of $\mathbf{x}_{st}$. For example,

$$\begin{aligned} p_{st}(\mathcal{S}_0) &= \exp\left(-\int_a^b pE_1\lambda_d(t)dt\right) \\ &= 3.27 \times 10^{-3} \end{aligned} \tag{3.9.6}$$

$$\begin{aligned} p_{st}(\mathcal{S}_1) &= \left[\left(\int_a^b pE_1\lambda_d(t)dt\right)^1 \Big/ 1!\right]\left[\exp\left(-\int_a^b pE_1\lambda_d(t)dt\right)\right]\left[pB_1\right] \\ &= 1.50 \times 10^{-3} \end{aligned} \tag{3.9.7}$$

$$p_{st}(\mathcal{S}_2) = \left[\left(\int_a^b pE_1\lambda_d(t)dt\right)^1 \Big/ 1!\right]\left[\exp\left(-\int_a^b pE_1\lambda_d(t)dt\right)\right]\left[pB_0\right]$$
$$= 1.72 \times 10^{-2} \tag{3.9.8}$$

$$p_{st}(\mathcal{S}_3) = \left[\left(\int_a^b pE_1\lambda_d(t)dt\right)^1 \Big/ 1!\right]\left[\exp\left(-\int_a^b pE_1\lambda_d(t)dt\right)\right]$$
$$= 1.87 \times 10^{-2}, \tag{3.9.9}$$

where $[a, b]$ = [0, 10,000 yr], $pE_1 = 0.209$ (see Sect. 3.4), $pB_0 = 0.08$ (see Sect. 3.5), $pB_1 = 0.92$ (see Sect. 3.5), $\lambda_d(t)$ is defined in Eqs. (3.2.1) - (3.2.3), and the probabilities in Eqs. (3.9.6) - (3.9.9) are based on the relationship in Eq. (3.2.4).

The expressions defining $p_{st}(\mathcal{S}_0)$, $p_{st}(\mathcal{S}_1)$, $p_{st}(\mathcal{S}_2)$ and $p_{st}(\mathcal{S}_3)$ are relatively simple because the scenarios $\mathcal{S}_0$, $\mathcal{S}_1$, $\mathcal{S}_2$ and $\mathcal{S}_3$ are relatively simple. The scenario $\mathcal{S}_{21}$ is more complex and, as a result, $p_{st}(\mathcal{S}_{21})$ is also more complex. Specifically,

$$p_{st}(\mathcal{S}_{21}) = \int_a^b p_{[a,t]}(nI = 1, nB = 0)[pB_1 pE_1\lambda_d(t)]p_{[t,b]}(nI = 0)dt$$
$$= \int_a^b \left[\int_a^t pB_0 pE_1\lambda_d(\tau)d\tau\right]\left[\exp\left(-\int_a^t pE_1\lambda_d(\tau)d\tau\right)\right]\left[pB_1 pE_1\lambda_d(t)\right]\left[\exp\left(-\int_t^b pE_1\lambda_d(\tau)d\tau\right)\right]dt$$
$$= pB_0 pB_1 pE_1^2\left[\int_a^b\left(\int_a^t \lambda_d(\tau)d\tau\right)\lambda_d(t)dt\right]\left[\exp\left(-\int_a^b pE_1\lambda_d(t)dt\right)\right], \tag{3.9.10}$$

where

$[a, b]$ = [0, 10,000 yr]

$p_{[a, t]}(nI = 1, nB = 0)$ = probability that exactly one intrusion (i.e., $nI = 1$) will penetrate an excavated area of the repository during the time interval $[a, t]$, with this intrusion not penetrating pressurized brine (i.e., $nB = 0$)

$$= \left[\left(\int_a^t pB_0 pE_1\lambda_d(\tau)d\tau\right)^1 \Big/ 1!\right]_1\left[\exp\left(-\int_a^t pB_0 pE_1\lambda_d(\tau)d\tau\right)\right]_2$$
$$\left[\exp\left(-\int_a^t pB_1 pE_1\lambda_d(\tau)d\tau\right)\right]_3$$

$$= \left[\int_a^t pB_0 pE_1\lambda_d(\tau)d\tau\right]\left[\exp\left(-\int_a^t pE_1\lambda_d(\tau)d\tau\right)\right] \tag{3.9.11}$$

$p_{[t,\,b]}(nI = 0)$ = probability that no intrusions (i.e., nI = 0) will penetrate an excavated area of the repository during the time interval $[t, b]$

$$= \exp\left(-\int_t^b pE_1\lambda_d(\tau)d\tau\right) \tag{3.9.12}$$

and the derivation of Eq. (3.9.10) generally follows the ideas in the derivation of Eq. (22) in Helton (1993b). In the definition of $p_{[a,t]}(nI = 1,\ nB = 0)$ in Eq. (3.9.11), the product $[\sim]_1\ [\sim]_2$ gives the probability that exactly one intrusion through an excavated area of the repository that does not penetrate pressurized brine will occur during the time interval $[a, t]$, and $[\sim]_3$ gives the probability that no intrusions that penetrate pressurized brine will occur during $[a, t]$.

More complex scenarios can be defined but with a corresponding increase in the complexity of the closed-form representation for scenario probability (Helton 1993b). For example, consider the following relatively simple scenario:

$\mathcal{S}_4$ = {$\mathbf{x}_{st}$: $\mathbf{x}_{st}$ involves exactly two drilling intrusions in the time interval $[a, b]$ and the mining event (i.e., t_{min}) also occurs in $[a, b]$, with the first drilling intrusion penetrating pressurized brine, using plugging pattern 2 and failing to penetrate an excavated area of the repository and the second drilling intrusion penetrating pressurized brine, an excavated area of the repository and RH waste and using plugging pattern 3 (i.e., $n \geq 2$ in Eq. (2.2.2), $a \leq t_{min} \leq b$, and there exists an integer i such that $1 \leq i < n$, $a \leq t_i \leq t_{i+1} \leq b$, $e_i = 0$, $b_i = 1$, $p_i = 2$, $\mathbf{a}_i = 0$, $e_{i+1} = 1$, $b_{i+1} = 1$, $p_{i+1} = 3$, $\mathbf{a}_{i+1} = 1$, and $t_k < a$ or $b < t_k$ for $k \neq i$, i+1 and $1 \leq k \leq n$)} (3.9.13)

The corresponding probability is given by

$$\begin{aligned}
p_{st}(\mathcal{S}_4) &= \left\{\int_a^b p_{[a,t]}(nI = 1, nB = 1)[pB_1\,pE_1\,pRH\,\lambda_d(t)]p_{[t,b]}(nI = 0)dt\right\}\left\{p_{[0,a]}(nM = 0)\ \ p_{[a,b]}(nM \geq 1)\right\} \\
&= \left\{\int_a^b \left[\int_a^t pB_1\,pE_0\lambda_d(\tau)d\tau\right]\left[\exp\left(-\int_a^t \lambda_d(\tau)d\tau\right)\right]\left[pB_1\,pE_1\,pRH\,\lambda_d(t)\right]\left[\exp\left(-\int_t^b \lambda_d(\tau)d\tau\right)\right]dt\right\} \\
&\quad \left\{\left[\exp\left(-\int_0^a \lambda_m(t)dt\right)\right]\left[1-\exp\left(-\int_a^b \lambda_m(t)dt\right)\right]\right\} \\
&= \left\{\int_a^b\left[\int_a^t \lambda_d(\tau)d\tau\right]\lambda_d(t)dt\right\}\left\{\exp\left(-\int_a^b \lambda_d(t)dt\right)\right\}\left\{pB_1^2\,pE_0\,pE_1\,pRH\right\} \\
&\quad \left\{\exp\left(-\int_0^a \lambda_m(t)dt\right)-\exp\left(-\int_0^b \lambda_m(t)dt\right)\right\},
\end{aligned} \tag{3.9.14}$$

where

$p_{[a,\,t]}(nI = 1, nB = 1)$ = probability that exactly one intrusion (i.e., $nI = 1$) will penetrate the area marked by the berm during the time interval $[a, b]$, with this intrusion penetrating pressurized brine (i.e., $nB = 1$) but failing to penetrate an excavated area of the repository

$$= \left[\left(\int_a^t pB_1 pE_0 \lambda_d(\tau)d\tau\right)^1 \Big/ 1!\right]\left[\exp\left(-\int_a^t pB_1 pE_0 \lambda_d(\tau)d\tau\right)\right]$$
$$\left[\exp\left(-\int_a^t (pB_0 pE_0 + pE_1)\lambda_d(\tau)d\tau\right)\right]$$

$$= \left[\int_a^t pB_1 pE_0 \lambda_d(\tau)d\tau\right]\left[\exp\left(-\int_a^t \lambda_d(\tau)d\tau\right)\right] \tag{3.9.15}$$

$p_{[t,\,b]}(nI = 0)$ = probability that no intrusions (i.e., $nI = 0$) will penetrate the area marked by the berm during the time interval $[t, b]$

$$= \exp\left(-\int_t^b \lambda_d(\tau)d\tau\right) \tag{3.9.16}$$

$p_{[0,\,a]}(nM = 0)$ = probability that no mining (i.e., $nM = 0$) will occur during the time interval $[0, a]$

$$= \exp\left(-\int_0^a \lambda_m(t)dt\right) \tag{3.9.17}$$

$p_{[a,\,b]}(nM \geq 1)$ = probability that mining will occur (i.e., $nM \geq 1$) during the time interval $[a, b]$

$$= 1 - \exp\left(-\int_a^b \lambda_m(t)dt\right) \tag{3.9.18}$$

and the development of Eq. (3.9.15) is similar to that indicated for Eq. (3.9.11).

The consideration of more complex scenarios will result in more complex formulas for scenario probability. Closed-form formulas for the probabilities of quite complex scenarios can be derived but they are very complicated and involve large numbers of iterated integrals (Helton 1993b). Thus, p_{st} can be defined in concept but does not have a simple form that can be easily displayed.

The example scenarios $\mathcal{S}_0$, $\mathcal{S}_1$, $\mathcal{S}_2$, $\mathcal{S}_3$, $\mathcal{S}_{21}$ and $\mathcal{S}_4$ have infinitely many elements and nonzero probabilities. However, scenarios involving drilling intrusions that occur at specific times will have a probability of zero. For example, the scenario

$$\mathcal{S}_5 = \{\mathbf{x}_{st}: \ \mathbf{x}_{st} = [t_1 = 350 \text{ yr}, l_1, e_1 = 1, b_1 = 1, p_1 = 2, \mathbf{a}_1, t_{min}], \text{ with } l_1, \mathbf{a}_1 \text{ and } t_{min} \text{ unrestricted}\} \quad (3.9.19)$$

contains infinitely many futures (i.e., infinitely many $\mathbf{x}_{st}$ meet the criteria to belong to $\mathcal{S}_5$ due to the infinite number of values that t_{min} can assume) and also has a probability of zero (i.e., $p_{st}(\mathcal{S}_5) = 0$) because t_1 is restricted to a single value. Sets that contain single elements of $\mathcal{S}_{st}$ are also scenarios, but such scenarios will typically have a probability of zero. In particular, the only single element scenario that has a nonzero probability contains the future that has no drilling intrusions and no mining.

The probabilities for a large number of relatively simple scenarios are given in Tables 3.2.1 and 3.5.1. Each of these scenarios can be expressed in the set notation used in this section. For example, Table 3.2.1 gives a probability of 0.102 for the scenario that involves exactly three drilling intrusions into an excavated area of the repository during the regulatory period. The corresponding scenario is

$\mathcal{S} = \{\mathbf{x}_{st}$: $\mathbf{x}_{st}$ involves exactly three drilling intrusions through an excavated area of the repository (i.e., $n \geq 3$ in Eq. (2.2.2) and there exist integers i, j, k such that $1 \leq i < j < k \leq n$, 100 yr $< t_i$, $e_i = e_j = e_k = 1$, and $e_l = 0$ for $l \neq i, j, k$ and $1 \leq l \leq n$)$\}$. (3.9.20)

In the definition of $\mathcal{S}$, no restrictions are placed on l_m, b_m, p_m and $\mathbf{a}_m$ for $m = 1, 2, \ldots, n$ nor on t_{min} because these elements of $\mathbf{x}_{st}$ are not specified and thus can take on any values in their allowable ranges (i.e., $l_m = 1, 2, \ldots, 144$; $b_m = 0, 1$; $p_m = 1, 2, 3$; $\mathbf{a}_m$ as defined in Eqs. (3.7.1) - (3.7.3); $0 \leq t_{min} \leq 10{,}000$ yr). If one or more of these characteristics is restricted to a subset of its range, then a new scenario will be produced that is a subset of $\mathcal{S}$ and has, in most cases, a smaller probability than $\mathcal{S}$.

The 1991 and 1992 WIPP PAs used an approach to the construction of the CCDF specified in 40 CFR 191.13 based on the exhaustive division of $\mathcal{S}_{st}$ into a collection of mutually exclusive scenarios $\mathcal{S}_{st,i}$, $i = 1, 2, \ldots, nS$ (Helton and Iuzzolino 1993). A probability $p_{st}(\mathcal{S}_{st,i})$ and a normalized release R_i were then calculated for each scenario $\mathcal{S}_{st,i}$ and used to construct the CCDF specified in 40 CFR 191.13. Due to the complexity of the elements $\mathbf{x}_{st}$ of $\mathcal{S}_{st}$ (see Eq. (2.2.2)), this approach was not used in the 1996 WIPP PA. In particular, the decomposition of $\mathcal{S}_{st}$ into a suitable and defensible collection of scenarios $\mathcal{S}_{st,i}$, $i = 1, 2, \ldots, nS$, is quite difficult. Further, once these scenarios are defined, it is necessary to calculate their probabilities $p_{st}(\mathcal{S}_{st,i})$, which is also not easy. Although the calculation of the probabilities $p_{st}(\mathcal{S}_{st,i})$ is difficult, the development of an appropriate and acceptable decomposition of $\mathcal{S}_{st}$ into the scenarios $\mathcal{S}_{st,i}$ is probably the greater challenge. By using the Monte Carlo approach to CCDF construction indicated in Eq. (2.3.1) and described in more detail in Sects. 6.6 and 6.7, the 1996 WIPP PA avoided the difficulties associated with decomposing $\mathcal{S}_{st}$ into a collection of mutually exclusive scenarios and then calculating the probabilities of these scenarios. Additional discussion of the concept of a scenario is given in Sect. 5.5.

4. Estimation of Releases

4.1 Results for Specific Futures

The second entity that underlies the 1996 WIPP PA is a procedure for estimating the radionuclide releases to the accessible environment associated with each of the possible futures $\mathbf{x}_{st}$ that could occur at the WIPP site over the next 10,000 yr. As discussed in Sect. 2.3, this procedure can be represented by the function $f(\mathbf{x}_{st})$ in Eq. (2.3.1). In practice, f is quite complex and is based on the models implemented in the computer programs indicated in Fig. 2.3.1. In the context of these models, f has the form

$$\begin{aligned} f(\mathbf{x}_{st}) = {} & f_C(\mathbf{x}_{st}) + f_{SP}\left[\mathbf{x}_{st}, f_B(\mathbf{x}_{st})\right] + f_{DBR}\left\{\mathbf{x}_{st}, f_{SP}\left[\mathbf{x}_{st}, f_B(\mathbf{x}_{st})\right], f_B(\mathbf{x}_{st})\right\} \\ & + f_{MB}\left[\mathbf{x}_{st}, f_B(\mathbf{x}_{st})\right] + f_{DL}\left[\mathbf{x}_{st}, f_B(\mathbf{x}_{st})\right] + f_S\left[\mathbf{x}_{st}, f_B(\mathbf{x}_{st})\right] \\ & + f_{S-T}\left\{\mathbf{x}_{st,0}, f_{S-F}(\mathbf{x}_{st,0}), f_{N-P}\left[\mathbf{x}_{st}, f_B(\mathbf{x}_{st})\right]\right\}, \end{aligned} \tag{4.1.1}$$

where

$\mathbf{x}_{st}$ ~ particular future under consideration,

$\mathbf{x}_{st,0}$ ~ future involving no drilling intrusions but a mining event at the same time t_{min} as in $\mathbf{x}_{st}$,

$f_C(\mathbf{x}_{st})$ ~ cuttings and cavings release to accessible environment for $\mathbf{x}_{st}$ calculated with CUTTINGS_S,

$f_B(\mathbf{x}_{st})$ ~ results calculated for $\mathbf{x}_{st}$ with BRAGFLO; in practice, $f_B(\mathbf{x}_{st})$ is a vector containing a large amount of information,

$f_{SP}\left[\mathbf{x}_{st}, f_B(\mathbf{x}_{st})\right]$ ~ spallings release to accessible environment for $\mathbf{x}_{st}$ calculated with the spallings model contained in CUTTINGS_S; this calculation requires BRAGFLO results (i.e., $f_B(\mathbf{x}_{st})$) as input,

$f_{DBR}\left\{\mathbf{x}_{st}, f_{SP}\left[\mathbf{x}_{st}, f_B(\mathbf{x}_{st})\right], f_B(\mathbf{x}_{st})\right\}$ ~ direct brine release to accessible environment for $\mathbf{x}_{st}$ calculated with a modified version of BRAGFLO designated BRAGFLO_DBR; this calculation requires spallings results obtained from CUTTINGS_S (i.e., $f_{SP}[\mathbf{x}_{st}, f_B(\mathbf{x}_{st})]$) and BRAGFLO results (i.e., $f_B(\mathbf{x}_{st})$) as input,

$f_{MB}[\mathbf{x}_{st}, f_B(\mathbf{x}_{st})]$ ~ release through anhydrite marker beds to accessible environment for $\mathbf{x}_{st}$ calculated with NUTS; this calculation requires BRAGFLO results (i.e., $f_B(\mathbf{x}_{st})$) as input,

$f_{DL}[\mathbf{x}_{st}, f_B(\mathbf{x}_{st})]$ ~ release through Dewey Lake Red Beds to accessible environment for $\mathbf{x}_{st}$ calculated with NUTS; this calculation requires BRAGFLO results (i.e., $f_B(\mathbf{x}_{st})$) as input,

$f_S[\mathbf{x}_{st}, f_B(\mathbf{x}_{st})]$ ~ release to land surface due to brine flow up a plugged borehole for $\mathbf{x}_{st}$ calculated with NUTS or PANEL; this calculation requires BRAGFLO results (i.e., $f_B(\mathbf{x}_{st})$) as input,

$f_{S-F}(\mathbf{x}_{st,0})$ ~ flow field calculated for $\mathbf{x}_{st,0}$ with SECOFL2D,

$f_{N-P}[\mathbf{x}_{st}, f_B(\mathbf{x}_{st})]$ ~ release to Culebra for $\mathbf{x}_{st}$ calculated with NUTS or PANEL as appropriate; this calculation requires BRAGFLO results (i.e., $f_B(\mathbf{x}_{st})$) as input,

$f_{S-T}\{\mathbf{x}_{st,0}, f_{S-F}(\mathbf{x}_{st,0}), f_{N-P}[\mathbf{x}_{st}, f_B(\mathbf{x}_{st})]\}$ ~ groundwater transport release through Culebra to accessible environment calculated with SECOTP2D; this calculation requires SECOFL2D results (i.e., $f_{S-F}(\mathbf{x}_{st,0})$) and NUTS or PANEL results (i.e., $f_{N-P}[\mathbf{x}_{st}, f_B(\mathbf{x}_{st})]$) as input; $\mathbf{x}_{st,0}$ is used as an argument to f_{S-T} because drilling intrusions are assumed to cause no perturbations to the flow field in the Culebra.

This chapter describes the mathematical structure of the mechanistic models that underlie the component functions of f in Eq. (4.1.1) (i.e., the mathematical models incorporated into the programs in Fig. 2.3.1).

The Monte Carlo CCDF construction procedure indicated in Eq. (2.3.1) and implemented by CCDFGF (Smith et al. 1996, Johnson 1997) used a sample of size nS = 10,000 in the 1996 WIPP PA. The individual programs in Fig. 2.3.1 do not run fast enough to allow this number of evaluations of f. As a result, it was necessary to evaluate the programs in Fig. 2.3.1 for a limited number of futures (Sect. 6.9) and then to use this limited number of evaluations to construct the releases for the large number of futures that must be considered in Eq. (2.3.1). These constructions are described in Chapters 9, 10, 11, 12 and 13, and produce the evaluations of f that are actually used in Eq. (2.3.1). Thus, a two-step procedure is being used in the definition of f in the numerical evaluation of the integral in Eq. (2.3.1). First, f and its component functions are evaluated with the procedures (i.e., models) described in this chapter for a group of preselected futures (Sect. 6.9). Second, values of $f(\mathbf{x}_{st,i})$ for the randomly selected futures $\mathbf{x}_{st,i}$ used in the numerical evaluation of the integral in Eq. (2.3.1) are then constructed from results obtained in the first step (Chapts. 9-13).

For notational simplicity at later points in this presentation, the functions on the right hand side of Eq. (4.1.1) will typically be written with only $\mathbf{x}_{st}$ as an argument (e.g., $f_{SP}(\mathbf{x}_{st})$ will be used instead of $f_{SP}[\mathbf{x}_{st}, f_B(\mathbf{x}_{st})]$). However, the underlying dependency on the other arguments will still be present.

The major topics considered in this chapter are two phase flow in the vicinity of the repository as modeled by BRAGFLO (i.e., f_B) (Sect. 4.2), radionuclide transport in the vicinity of the repository as modeled by NUTS (i.e., f_{MB}, f_{DL}, f_S, f_{N-P}) (Sect. 4.3), radionuclide transport in the vicinity of the repository as modeled by PANEL (i.e., f_S, f_{N-P}) (Sect. 4.4), cuttings and cavings releases to the surface as modeled by CUTTINGS_S (i.e., f_C) (Sect. 4.5), spallings releases to the surface as modeled by CUTTINGS_S (i.e., f_{SP}) (Sect. 4.6), direct brine releases to the surface as modeled by BRAGFLO_DBR (i.e., f_{DBR}) (Sect. 4.7), brine flow in Culebra as modeled by SECOFL2D (i.e., f_{S-F}) (Sect. 4.8), and radionuclide transport in the Culebra as modeled by SECOTP2D (Sect. 4.9).

4.2 Two-Phase Flow: BRAGFLO (i.e., f_B)

4.2.1 Mathematical Description

Two-phase flow in the vicinity of the repository is represented by the following system of two conservation equations, two constraint equations, and three equations of state:

Gas Conservation
$$\nabla \bullet \left[\frac{\alpha \rho_g \mathbf{K}_g k_{rg}}{\mu_g} \left(\nabla p_g + \rho_g g \nabla h \right) \right] + \alpha q_{wg} + \alpha q_{rg} = \alpha \frac{\partial \left(\phi \rho_g S_g \right)}{\partial t} \tag{4.2.1}$$

Brine Conservation
$$\nabla \bullet \left[\frac{\alpha \rho_b \mathbf{K}_b k_{rb}}{\mu_b} \left(\nabla p_b + \rho_b g \nabla h \right) \right] + \alpha q_{wb} + \alpha q_{rb} = \alpha \frac{\partial \left(\phi \rho_b S_b \right)}{\partial t} \tag{4.2.2}$$

Saturation Constraint
$$S_g + S_b = 1 \tag{4.2.3}$$

Capillary Pressure Constraint
$$p_C = p_g - p_b = f\left(S_b\right) \tag{4.2.4}$$

Gas Density
ρ_g determined by Redlich-Kwong-Soave equation of state (see Eqs. (4.2.30), (4.2.31))

Brine Density
$$\rho_b = \rho_0 \exp\left[\beta_b \left(p_b - p_{b0}\right)\right] \tag{4.2.5}$$

Formation Porosity
$$\phi = \phi_0 \exp\left[\beta_f \left(p_b - p_{b0}\right)\right] \tag{4.2.6}$$

where

g = acceleration due to gravity (m/s^2)
h = vertical distance from a reference location (m)
$\mathbf{K}_l$ = permeability tensor (m^2) for fluid l ($l = g$ ~ gas, $l = b$ ~ brine)
k_{rl} = relative permeability (dimensionless) to fluid l
p_C = capillary pressure (Pa)
p_l = pressure of fluid l (Pa)
q_{rl} = rate of production (or consumption, if negative) of fluid l due to chemical reaction (kg/m^3/s)
q_{wl} = rate of injection (or removal, if negative) of fluid l (kg/m^3/s)

S_l = saturation of fluid l (dimensionless)
t = time (s)
α = geometry factor (m in 1996 WIPP PA)
ρ_l = density of fluid l (kg/m^3)
μ_l = viscosity of fluid l (Pa s)
ϕ = porosity (dimensionless)
ϕ_0 = reference (i.e., initial) porosity (dimensionless)
p_{b0} = reference (i.e., initial) brine pressure (Pa), constant in Eq. (4.2.5) and spatially variable in Eq. (4.2.6)
ρ_0 = reference (i.e., initial) brine density (kg/m^3)
β_f = pore compressibility (Pa^{-1})
β_b = brine compressibility (Pa^{-1})

and the capillary function f is defined by the right hand sides of Eqs. (4.2.9), (4.2.18), and (4.2.21) as appropriate. The conservation equations are valid in one (i.e., $\nabla = [\partial/\partial x]$), two (i.e., $\nabla = [\partial/\partial x, \partial/\partial y]$) and three (i.e., $\nabla = [\partial/\partial x, \partial/\partial y, \partial/\partial z]$) dimensions. In the 1996 WIPP PA, the preceding system of equations is used to model two-phase fluid flow within the two-dimensional region shown in Fig. 4.2.1. Details of this system are now elaborated on.

The α term in Eqs. (4.2.1) and (4.2.2) is a dimension dependent geometry factor and is specified by

$$\begin{aligned} \alpha &= \text{area normal to flow direction in one-dimensional flow (i.e., } \Delta y \Delta z\text{; units = m}^2\text{),} \\ &= \text{thickness normal to flow plane in two-dimensional flow (i.e., } \Delta z\text{; units = m),} \\ &= 1 \text{ in three-dimensional flow (dimensionless).} \end{aligned} \tag{4.2.7}$$

The 1996 WIPP PA uses a two-dimensional geometry for computation of two-phase flow in the vicinity of the repository, and as a result, α is the thickness of the modeled region (i.e., Δz) normal to the flow plane (Fig. 4.2.1). Due to the use of the two-dimensional grid in Fig. 4.2.1, α is spatially dependent, with the values used for α defined in the column labeled "element depth" in Fig. 4.2.2. Specifically, α increases with distance away from the repository in both directions to incorporate the increasing pore volume through which fluid flow occurs.

The h term in Eqs. (4.2.1) and (4.2.2) defines vertical distance from a reference point. In the 1996 WIPP PA, this reference point is taken to be the center of MB 139 at the location of the shaft (i.e., (x_{ref}, y_{ref}) = (23664.9 m, 378.685 m), which is the center of cell 644 in Fig. 4.2.3). Specifically, h is defined by

$$h(x, y) = (x - x_{ref}) \sin \theta + (y - y_{ref}) \cos \theta, \tag{4.2.8}$$

where θ is the inclination of the formation in which the point (x,y) is located. In the 1996 WIPP PA, the Salado Formation is modeled as having an inclination of 1° from north to south, and all other formations are modeled as being horizontal. Thus, $\theta = 1°$ for points within the Salado, and $\theta = 0°$ otherwise. Treating the Salado as an inclined formation and treating the Castile Formation, brine reservoir, Rustler Formation, and overlying units as horizontal creates discontinuities in the grid at the lower and upper boundaries of the Salado. However, this treatment does not create a computational problem as the Salado is isolated from vertical flow by the impermeable Unnamed Lower

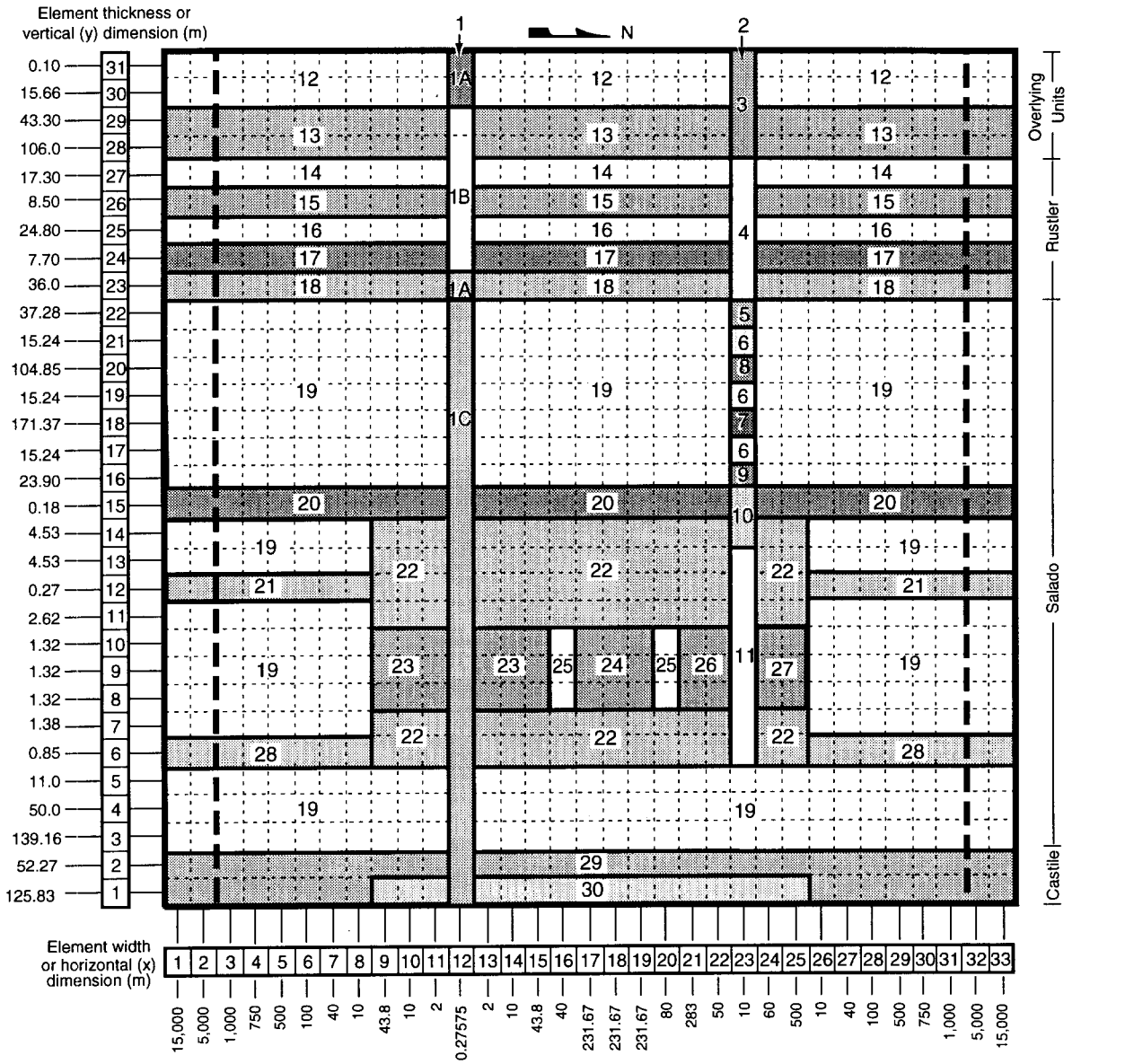

1. Borehole (first 200 years)
   1A. Borehole concrete plug
   1B. Upper unrestricted borehole
   1C. Lower unrestricted borehole
2. Shaft
3. Earth fill
4. Rustler compacted clay column
5. Asphalt
6. Concrete
7. Crushed salt (compacted salt column)
   Boundary of accessible environment
8. Upper Salado compacted clay column
9. Lower Salado compacted clay column
10. Lower clay component
11. Concrete monolith
12. Units above the Dewey Lake
13. Dewey Lake
14. Forty-niner
15. Magenta
16. Tamarisk
17. Culebra
18. Unnamed lower member
19. Impure halite
20. MB138
21. Anhydrite layer a and b
22. Disturbed rock zone
23. Waste panel
24. Rest of repository
25. Panel closures
26. Operation region
27. Experimental area
28. MB139
29. Castile
30. Brine reservoir

TRI-6342-5288-0

Fig. 4.2.1. Computational grid used in BRAGFLO to represent two phase flow in 1996 WIPP PA subsequent to a drilling intrusion. Same formulation is used in the absence of a drilling intrusion except that regions 1A, 1B and 1C have the same properties as the regions to either side.

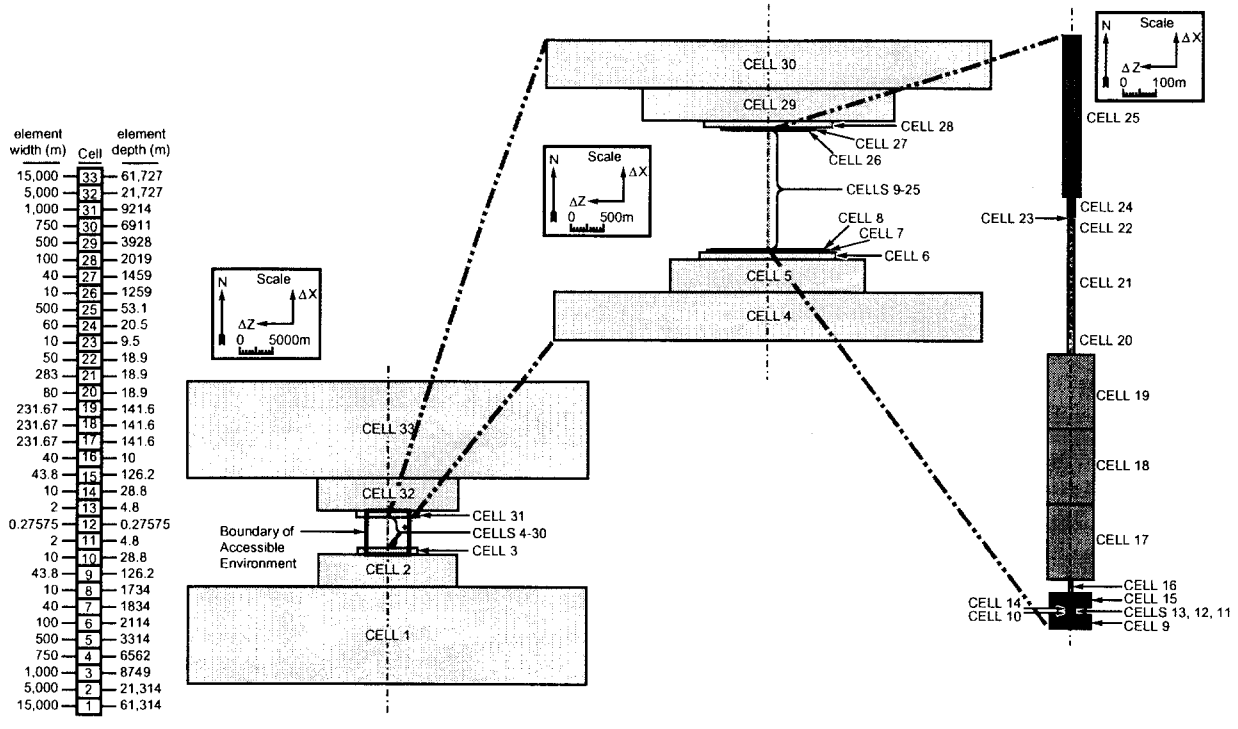

Note: This view illustrates the variation in element depth present in the model for simulation of radially convergent flow.

TRI-6342-5242-0

Fig. 4.2.2. Definition of element depth (i.e., element thickness normal to flow plane) in computational implementation of two-phase flow in 1996 WIPP PA. Cells 1 to 33 correspond to the 33 grid cells indicated in the x direction in Fig. 4.2.1; the indicated depths of these cells define the factor α in Eqs. (4.2.1) and (4.2.2).

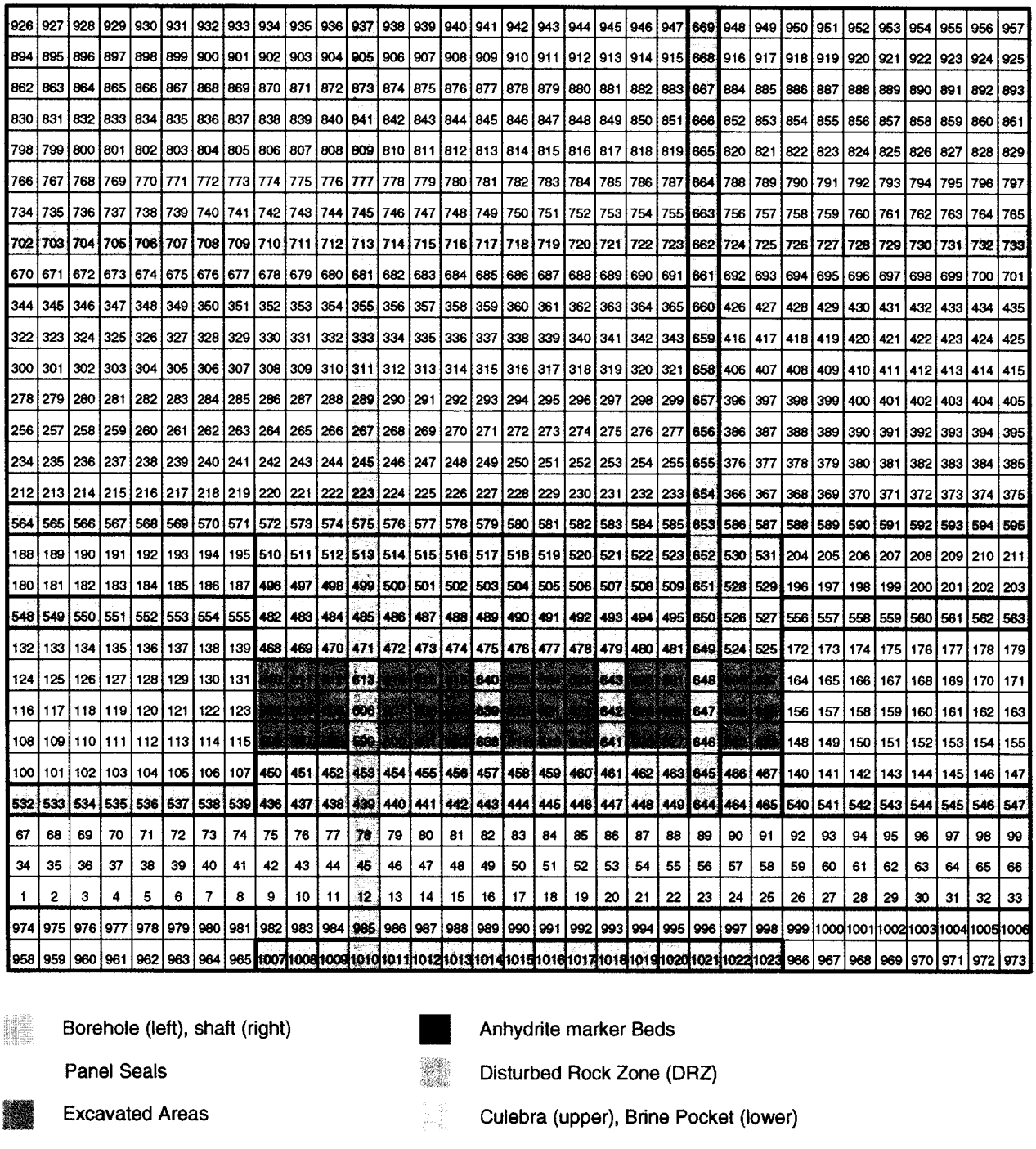

Fig. 4.2.3. Identification of individual cells in computational grid used with BRAGFLO to represent two phase flow in 1996 WIPP PA.

Member of the Rustler Formation at its upper boundary and by the impermeable Castile Formation at its lower boundary.

The primary model used in the 1996 WIPP PA for capillary pressure p_C and relative permeability k_{rl} is a modification of the Brooks-Corey model (Brooks and Corey 1964). Specifically, p_C, k_{rb} and k_{rg} are defined by

$$p_C = p_t(k) / S_{e2}^{1/\lambda} \tag{4.2.9}$$

$$k_{rb} = S_{e1}^{(2+3\lambda)/\lambda} \tag{4.2.10}$$

$$k_{rg} = \left(1 - S_{e2}\right)^2 \left(1 - S_{e2}^{(2+\lambda)/\lambda}\right), \tag{4.2.11}$$

where

λ = pore distribution parameter (dimensionless)

$p_t(k)$ = capillary threshold pressure (Pa) as a function of intrinsic permeability k (Webb 1992)

$$= a\ k^{\eta} \tag{4.2.12}$$

S_{e1} = effective brine saturation (dimensionless) without correction for residual gas saturation

$$= \left(S_b - S_{br}\right) / \left(1 - S_{br}\right) \tag{4.2.13}$$

S_{e2} = effective brine saturation (dimensionless) with correction for residual gas saturation

$$= \left(S_b - S_{br}\right) / \left(1 - S_{gr} - S_{br}\right). \tag{4.2.14}$$

The values used for λ, a, η, S_{br}, S_{gr} and k are summarized in Tables 4.2.1 and 4.2.2. The statement that the Brooks-Corey model is in use means that p_C, k_{rb} and k_{rg} are defined by Eqs. (4.2.9) - (4.2.11).

In the solution of Eqs. (4.2.1) and (4.2.2), S_b and S_g change as functions of location and time. Thus, p_C, k_{rb} and k_{rg} are functions of the form $p_C\ (x, y, t)$, $k_{rb}(x, y, t)$ and $k_{rg}(x, y, t)$. In the computational implementation of the solution of the preceding equations, flow of phase l out of a computational cell (Fig. 4.2.3) cannot occur when $S_l\,(x, y, t) \le S_{lr}(x, y, t)$, where S_{lr} denotes the residual saturation for phase l. The values used for S_{lr}, $l = b, g$, are summarized in Table 4.2.1.

Table 4.2.1. Parameter Values Used in Representation of Two Phase Flow

Material: I; R; N[a]	Material Description	λ	a	η	S_{br}	S_{gr}	ϕ_0	β_f
1; 2; S_HALITE	Undisturbed Salado Fm halite	0.7	0.56	−0.346	0.3	0.2	*HALPOR*[b]	*f(HALCOMP*[b]*)*[d]
2; 22; DRZ_0	Disturbed rock zone, −5 - 0 yr	0.7	0.0	0.0	0.0	0.0	*f(HALPOR)*[c]	6.286054×10^{-8}
3; 28; S_MB139	MB 139 in Salado Fm	*ANHBCEXP*[b]	0.26	−0.348	*ANRBSAT*[b]	*ANRGSSAT*[b]	0.01	*f(ANHCOMP*[b]*)*[d]
4; 21; S_ANH_AB	Anhydrite layers a & b in Salado Fm	*ANHBCEXP*[b]	0.26	−0.348	*ANRBSAT*[b]	*ANRGSSAT*[b]	0.01	*f(ANHCOMP*[b]*)*[d]
5; 20; S_MB138	MB 138 in Salado Fm	*ANHBCEXP*[b]	0.26	−0.348	*ANRBSAT*[b]	*ANRGSSAT*[b]	0.01	*f(ANHCOMP*[b]*)*[d]
6; 23; CAVITY_1	Excavated waste panel, −5 - 0 yr	0.7	0.0	0.0	0.0	0.0	1.0	0.0
7; 24; CAVITY_2	Excavated rest of repository, −5 - 0 yr	0.7	0.0	0.0	0.0	0.0	1.0	0.0
8; 26; CAVITY_3	Excavated operations & exp'tl region, −5 - 0 yr	0.7	0.0	0.0	0.0	0.0	1.0	0.0
9; 27; CAVITY_4	Excavated shaft and panel closures, −5 - 0 yr	0.7	0.0	0.0	0.0	0.0	1.0	0.0
10; 29; IMPERM_Z	Castile Fm impermeable material	0.7	0.0	0.0	0.0	0.0	0.005	0.0
11; 30; CASTILER	Castile Fm brine reservoir	0.7	0.56	−0.346	0.2	0.2	*f(BPVOL)*[e]	*f(BPCOMP*[b]*)*[d]
12; 23; WAS_AREA	Single waste panel in repository	2.89	0.0	0.0	*WRBRNSAT*[b]	*WRGSSAT*[b]	0.848	0.0
13; 24; REPOSIT	Rest of waste repository (minus one panel)	2.89	0.0	0.0	*WRBRNSAT*[b]	*WRGSSAT*[b]	0.848	0.0
14; 18; UNNAMED	Unnamed Mbr of Rustler Fm	0.7	0.0	0.0	0.2	0.2	0.181	0.0
15; 17; CULEBRA	Culebra Mbr of Rustler Fm	0.6436	0.26	−0.348	0.08363	0.07711	0.151	6.622517×10^{-10}
16; 16; TAMARISK	Tamarisk Mbr of Rustler Fm	0.7	0.0	0.0	0.2	0.2	0.064	0.0
17; 15; MAGENTA	Magenta Mbr of Rustler Fm	0.6436	0.26	−0.348	0.08363	0.07711	0.138	1.915942×10^{-9}
18; 14; FORTYNIN	Fortyniner Mbr of Rustler Fm	0.7	0.0	0.0	0.2	0.2	0.082	0.0
19; 13; DEWYLAKE	Dewey Lake Redbeds	0.6436	0.0	0.0	0.08363	0.07711	0.143	6.993007×10^{-8}
20; 12; SANTAROS	Santa Rosa Fm	0.6436	0.0	0.0	0.08363	0.07711	0.175	5.714286×10^{-8}
21; 26; OPS_AREA	Excavated region between shafts & repository	0.7	0.0	0.0	0.0	0.0	0.18	0.0
22; 27; EXP_AREA	Excavated region north of shafts	0.7	0.0	0.0	0.0	0.0	0.18	0.0
23; 3; EARTH	Earth backfill at top of shaft	*SHBCEXP*[b]	0.0	0.0	*SHRBRSAT*[b]	*SHRGSSAT*[b]	0.32	3.10×10^{-8}
24; 4; CLAY_RUS	Clay seal in shaft through Rustler Fm	*SHBCEXP*[b]	0.0	0.0	*SHRBRSAT*[b]	*SHRGSSAT*[b]	0.24	1.96×10^{-9}
25; 5; ASPHALT	Asphalt shaft seal	*SHBCEXP*[b]	0.0	0.0	*SHRBRSAT*[b]	*SHRGSSAT*[b]	0.01	2.97×10^{-8}
26; 6; CONC_T1	Concrete shaft seal, 0 - 400 yr	*SHBCEXP*[b]	0.0	0.0	*SHRBRSAT*[b]	*SHRGSSAT*[b]	0.05	2.64×10^{-9}
27; 6; CONC_T2	Concrete shaft seal, 400 - 10000 yr	*SHBCEXP*[b]	0.0	0.0	*SHRBRSAT*[b]	*SHRGSSAT*[b]	0.05	2.64×10^{-9}
28; 8; CL_M_T1	Upper Salado clay shaft seal, 0 - 10 yr	*SHBCEXP*[b]	0.0	0.0	*SHRBRSAT*[b]	*SHRGSSAT*[b]	0.24	1.81×10^{-9}
29; 8; CL_M_T2	Upper Salado clay shaft seal, 10 - 25 yr	*SHBCEXP*[b]	0.0	0.0	*SHRBRSAT*[b]	*SHRGSSAT*[b]	0.24	1.81×10^{-9}
30; 8; CL_M_T3	Upper Salado clay shaft seal, 25 - 50 yr	*SHBCEXP*[b]	0.0	0.0	*SHRBRSAT*[b]	*SHRGSSAT*[b]	0.24	1.81×10^{-9}
31; 8; CL_M_T4	Upper Salado clay shaft seal, 50 - 100 yr	*SHBCEXP*[b]	0.0	0.0	*SHRBRSAT*[b]	*SHRGSSAT*[b]	0.24	1.81×10^{-9}
32; 8; CL_M_T5	Upper Salado clay shaft seal, 100 - 10000 yr	*SHBCEXP*[b]	0.0	0.0	*SHRBRSAT*[b]	*SHRGSSAT*[b]	0.24	1.81×10^{-9}
33; 9; CL_L_T1	Lower Salado clay shaft seal, 0 - 10 yr	*SHBCEXP*[b]	0.0	0.0	*SHRBRSAT*[b]	*SHRGSSAT*[b]	0.24	1.59×10^{-9}

Table 4.2.1. Parameter Values Used in Representation of Two Phase Flow (continued)

Material: I; R; N[a]	Material Description	λ	a	η	S_{br}	S_{gr}	ϕ_0	β_f
34; 9; CL_L_T2	Lower Salado clay shaft seal, 10 - 25 yr	*SHBCEXP*[b]	0.0	0.0	*SHRBRSAT*[b]	*SHRGSSAT*[b]	0.24	1.59×10^{-9}
35; 9; CL_L_T3	Lower Salado clay shaft seal, 25 - 50 yr	*SHBCEXP*[b]	0.0	0.0	*SHRBRSAT*[b]	*SHRGSSAT*[b]	0.24	1.59×10^{-9}
36; 9; CL_L_T4	Lower Salado clay shaft seal, 50 - 10000 yr	*SHBCEXP*[b]	0.0	0.0	*SHRBRSAT*[b]	*SHRGSSAT*[b]	0.24	1.59×10^{-9}
37; 7; SALT_T1	Crushed salt shaft backfill, 0 - 10 yr	*SHBCEXP*[b]	0.0	0.0	*SHRBRSAT*[b]	*SHRGSSAT*[b]	0.05	1.60×10^{-9}
38; 7; SALT_T2	Crushed salt shaft backfill, 10 - 25 yr	*SHBCEXP*[b]	0.0	0.0	*SHRBRSAT*[b]	*SHRGSSAT*[b]	0.05	1.60×10^{-9}
39; 7; SALT_T3	Crushed salt shaft backfill, 25 - 50 yr	*SHBCEXP*[b]	0.0	0.0	*SHRBRSAT*[b]	*SHRGSSAT*[b]	0.05	1.60×10^{-9}
40; 7; SALT_T4	Crushed salt shaft backfill, 50 - 100 yr	*SHBCEXP*[b]	0.0	0.0	*SHRBRSAT*[b]	*SHRGSSAT*[b]	0.05	1.60×10^{-9}
41; 7; SALT_T5	Crushed salt shaft backfill, 100 - 200 yr	*SHBCEXP*[b]	0.0	0.0	*SHRBRSAT*[b]	*SHRGSSAT*[b]	0.05	1.60×10^{-9}
42; 7; SALT_T6	Crushed salt shaft backfill, 200 - 10000 yr	*SHBCEXP*[b]	0.0	0.0	*SHRBRSAT*[b]	*SHRGSSAT*[b]	0.05	1.60×10^{-9}
43; 10; CLAY_BOT	Lower (bottom) clay shaft seal	*SHBCEXP*[b]	0.0	0.0	*SHRBRSAT*[b]	*SHRGSSAT*[b]	0.24	1.59×10^{-9}
44; 25; PAN_SEAL	Panel seal	0.94	0.56	–0.346	0.2	0.2	0.075	2.64×10^{-9}
45; 11; CONC_MON	Concrete shaft station monolith	*SHBCEXP*[b]	0.0	0.0	*SHRBRSAT*[b]	*SHRGSSAT*[b]	0.05	2.64×10^{-9}
46; 22; DRZ_1	Disturbed rock zone	0.7	0.0	0.0	0.0	0.0	*f(HALPOR)*[c]	6.286054×10^{-8}
47; 1A; CONC_PLG	Concrete borehole plug	0.94	0.0	0.0	0.0	0.0	0.32	0.0
48; 1B,C; BH_OPEN	"Open" borehole	0.7	0.0	0.0	0.0	0.0	0.32	0.0
49; 1A,B,C; BH_SAND	Sand-filled borehole	0.94	0.0	0.0	0.0	0.0	0.32	0.0
50; 1C; BH_CREEP	Sand-filled borehole after creep closure	0.94	0.0	0.0	0.0	0.0	0.32	0.00

[a] Material identifier, where I ~ integer identifier, R ~ region in Fig. 4.2.1, N ~ material name.

[b] See Sect. 5.2.

[c] See Eq. (4.2.15).

[d] See Eq. (4.2.17); ϕ_0 can also be defined by an uncertain variable.

[e] See Eq. (4.2.16).

Table 4.2.2. Values Used for Intrinsic Permeability k in Representation of Two-Phase Flow

Material: I; R; N[a]	k, m^2	Material: I; R; N[a]	k, m^2
1; 2; S_HALITE	10^x, $x = HALPRM$[b]	26; 6; CONC_T1	10^x, $x = SHPRMCON$[b]
2; 22; DRZ_0	9.999999×10^{-18}	27; 6; CONC_T2	1.0×10^{-14}
3; 28; S_MB139	10^x, $x = ANHPRM$[b]	28; 8; CL_M_T1	$f(SHPRMCLY, SHPRMDRZ, HALPRM)$[c]
4; 21; S_ANH_AB	10^x, $x = ANHPRM$[b]	29; 8; CL_M_T2	$f(SHPRMCLY, SHPRMDRZ, HALPRM)$[c]
5; 20; S_MB138	10^x, $x = ANHPRM$[b]	30; 8; CL_M_T3	$f(SHPRMCLY, SHPRMDRZ, HALPRM)$[c]
6; 23; CAVITY_1	1.0×10^{-10}	31; 8; CL_M_T4	$f(SHPRMCLY, SHPRMDRZ, HALPRM)$[c]
7; 24; CAVITY_2	1.0×10^{-10}	32; 8; CL_M_T5	$f(SHPRMCLY, SHPRMDRZ, HALPRM)$[c]
8; 26; CAVITY_3	1.0×10^{-10}	33; 9; CL_L_T1	10^x, $x = SHPRMCLY$[b]
9; 27; CAVITY_4	1.0×10^{-10}	34; 9; CL_L_T2	$f(SHPRMCLY, SHPRMDRZ, HALPRM)$[c]
10; 29; IMPERM_Z	9.999999×10^{-36}	35; 9; CL_L_T3	$f(SHPRMCLY, SHPRMDRZ, HALPRM)$[c]
11; 30; CASTILER	10^x, $x = BPPRM$[b]	36; 9; CL_L_T4	$f(SHPRMCLY, SHPRMDRZ, HALPRM)$[c]
12; 23; WAS_AREA	1.702158×10^{-13}	37; 7; SALT_T1	$f(SHPRMDRZ, SHPRMHAL, HALPRM)$[c]
13; 24; REPOSIT	1.702158×10^{-13}	38; 7; SALT_T2	$f(SHPRMDRZ, SHPRMHAL, HALPRM)$[c]
14; 18; UNNAMED	9.999999×10^{-36}	39; 7; SALT_T3	$f(SHPRMDRZ, SHPRMHAL, HALPRM)$[c]
15; 17; CULEBRA	2.098938×10^{-14}	40; 7; SALT_T4	$f(SHPRMDRZ, SHPRMHAL, HALPRM)$[c]
16; 16; TAMARISK	9.999999×10^{-36}	41; 7; SALT_T5	$f(SHPRMDRZ, SHPRMHAL, HALPRM)$[c]
17; 15; MAGENTA	6.309576×10^{-16}	42; 7; SALT_T6	$f(SHPRMDRZ, SHPRMHAL, HALPRM)$[c]
18; 14; FORTYNIN	9.999999×10^{-36}	43; 10; CLAY_BOT	10^x, $x = SHPRMCLY$[b]
19; 13; DEWYLAKE	5.011881×10^{-17}	44; 25; PAN_SEAL	1.0×10^{-15}
20; 12; SANTAROS	1.0×10^{-10}	45; 11; CONC_MON	1.0×10^{-14}
21; 26; OPS_AREA	1.0×10^{-11}	46; 22; DRZ_1	1.0×10^{-15}
22; 27; EXP_AREA	1.0×10^{-11}	47; 1A; CONC_PLG	5.000339×10^{-17}
23; 3; EARTH	1.0×10^{-14}	48; 1B,C; BH_OPEN	1.0×10^{-9}
24; 4; CLAY_RUS	10^x, $x = SHPRMCLY$[b]	49; 1A,B,C; BH_SAND	10^x, $x = BHPRM$[b]
25; 5; ASPHALT	$f(SHPRMASP)$[c]	50; 1C; BH_CREEP	$10^x/10$, $x = BHPRM$[b]

[a] Material identifier, where I ~ integer identifier, R ~ region in Fig. 4.2.1, N ~ material name. See Table 4.2.1 for more detailed material descriptions.

[b] See Sect. 5.2.

[c] See Eqs. (4.2.34), (4.2.35).

Values for ϕ_0 and β_f (Eq. 4.2.6) are also given in Table 4.2.1. Initial porosity ϕ_0 for the disturbed rock zone (DRZ) is a function of initial halite porosity ϕ_{0H} (i.e., *HALPOR* in Sect. 5.2) and is given by (Martell 1996a; Chapt. 4, Bean et al. 1996)

$$\phi_0 = \phi_{0H} + 0.0029. \tag{4.2.15}$$

This representation is used because the DRZ and halite porosities are correlated, with the high, low and median porosity values for the DRZ being 0.0029 higher than the corresponding undisturbed halite values. Initial porosity ϕ_0 for regions of pressurized brine in the Castile is a function of brine pocket volume and is given by

$$\phi_0 = V_{brn}/V_{tot}\,, \tag{4.2.16}$$

where V_{brn} is the volume of pressurized brine (i.e., 32,000, 64,000, 96,000, 128,000 or 160,000 m^3 as defined by *BPVOL* in Sect. 5.2) and V_{tot} is the total volume associated with the region in Fig. 4.2.1 used to represent pressurized brine (i.e., region 30, which has a total volume of 1.8389×10^7 m^3).

The compressibilities β_f in Eq. (4.2.6) and Table 4.2.1 are pore compressibilities. These compressibilities were treated as uncertain for Salado anhydrite, Salado halite, and regions of pressurized brine in the Castile (see *ANHCOMP*, *HALCOMP*, *BPCOMP* in Sect. 5.2). However, the sampled values for these variables corresponded to bulk compressibilities rather than to the pore compressibilities actually used in the calculation. The conversion from bulk compressibility β_{fB} to pore compressibility β_f is approximated by

$$\beta_f = \beta_{fB}/\phi_0, \tag{4.2.17}$$

in the 1996 WIPP PA, where ϕ_0 is the initial porosity in the region under consideration.

The Brooks-Corey model is used for all materials with the following two exceptions (Table 4.2.3). First, whether to use the Brooks-Corey model or the van Genuchten-Parker model is treated as a subjective uncertainty for the anhydrite marker beds. Specifically, the variable *ANHBCVGP* (see Sect. 5.2) is used as a flag to determine whether the Brooks-Corey or van Genuchten-Parker model will be used in the representation of two-phase flow in the marker beds. Second, a linear model is used in the representation of two-phase flow in an open borehole (i.e., for the first 200 yr after a drilling intrusion for plugging patterns p_2 and p_3 (see Sect. 3.6)). Each of these alternatives to the Brooks-Corey model is now discussed.

Table 4.2.3. Models Used in Representation of Relative Permeability and Capillary Pressure for Two-Phase Flow

Material: *I*; *R*; *N*[a]	Relative Permeability[b]	Capillary Pressure[c]	Material: *I*; *R*; *N*[a]	Relative Permeability[b]	Capillary Pressure[c]
1; 2; S_HALITE	4	2	26; 6; CONC_T1	4	1
2; 22; DRZ_0	4	1	27; 6; CONC_T2	4	1
3; 28; S_MB139	*ANHBCVGP*	*2*	28; 8; CL_M_T1	4	1
4; 21; S_ANH_AB	*ANHBCVGP*	*2*	29; 8; CL_M_T2	4	1
5; 20; S_MB138	*ANHBCVGP*	*2*	30; 8; CL_M_T3	4	1
6; 23; CAVITY_1	4	1	31; 8; CL_M_T4	4	1
7; 24; CAVITY_2	4	1	32; 8; CL_M_T5	4	1
8; 26; CAVITY_3	4	1	33; 9; CL_L_T1	4	1
9; 27; CAVITY_4	4	1	34; 9; CL_L_T2	4	1
10; 29; IMPERM_Z	4	1	35; 9; CL_L_T3	4	1
11; 30; CASTILER	4	2	36; 9; CL_L_T4	4	1
12; 23; WAS_AREA	4	1	37; 7; SALT_T1	4	1
13; 24; REPOSIT	4	1	38; 7; SALT_T2	4	1
14; 18; UNNAMED	4	1	39; 7; SALT_T3	4	1
15; 17; CULEBRA	4	2	40; 7; SALT_T4	4	1
16; 16; TAMARISK	4	1	41; 7; SALT_T5	4	1
17; 15; MAGENTA	4	2	42; 7; SALT_T6	4	1
18; 14; FORTYNIN	4	1	43; 10; CLAY_BOT	4	1
19; 13; DEWYLAKE	4	1	44; 25; PAN_SEAL	4	2
20; 12; SANTAROS	4	1	45; 11; CONC_MON	4	1
21; 26; OPS_AREA	4	1	46; 22; DRZ_1	4	1
22; 27; EXP_AREA	4	1	47; 1A; CONC_PLG	4	1
23; 3; EARTH	4	1	48; 1B,C; BH_OPEN	5	1
24; 4; CLAY_RUS	4	1	49; 1A,B,C; BH_SAND	4	1
25; 5; ASPHALT	4	1	50; 1C; BH_CREEP	4	1

[a] Material identifier, where *I* ~ integer identifier, *R* ~ region in Fig. 4.2.1, *N* ~ material name. See Table 4.2.1 for more detailed material descriptions.

[b] Relative permeability model, where 1 ~ van Genuchten-Parker model (Eqs. 4.2.18 - 4.2.20), 4 ~ Brooks-Corey model (Eqs. 4.2.9 - 4.2.11), 5 ~ linear model (Eq. 4.1.18), and *ANHBCVGP* ~ use of Brooks-Corey or van Genuchten-Parker model treated as a subjective uncertainty (see Sect. 5.2).

[c] Capillary pressure model, where 1 ~ $p_C = 0$ Pa, 2 ~ p_C bounded above by 1×10^8 Pa as S_b approaches S_{br}.

In the van Genuchten-Parker model, p_C, k_{rb} and k_{rg} are defined by (van Genuchten 1978)

$$p_C = p_{VGP}\left(S_{e2}^{-1/m} - 1\right)^{1-m} \tag{4.2.18}$$

$$k_{rb} = S_{e1}^{1/2}\left[1 - \left(1 - S_{e1}^{1/m}\right)^{m}\right]^2 \tag{4.2.19}$$

$$k_{rg} = \left(1 - S_{e2}\right)^{1/2}\left(1 - S_{e2}^{1/m}\right)^{2m}, \tag{4.2.20}$$

where $m = \lambda/(1 + \lambda)$ and the capillary pressure parameter p_{VGP} is determined by requiring that the capillary pressures defined in Eqs. (4.2.9) and (4.2.18) are equal at an effective brine saturation of $S_{e2} = 0.5$ (Webb 1992). The statement that the van Genuchten-Parker model is in use means that p_C, k_{rb} and k_{rg} are defined by Eqs. (4.2.18) - (4.2.20). The van Genuchten-Parker model is only used for the anhydrite marker beds in the Salado Formation (i.e., Regions 20, 21, 28 in Fig. 4.2.1) and uses the same values for λ, S_{br} and S_{gr} as the Brooks-Corey model (Table 4.2.1).

Capillary pressure p_C for both the van Genuchten-Parker and Brooks-Corey models becomes unbounded as brine saturation S_b approaches the residual brine saturation S_{br}. To avoid unbounded values, p_C is capped at 1×10^8 Pa in selected regions (Table 4.2.3).

In the linear model, p_C, k_{rb} and k_{rg} are defined by (WIPP PA 1996a)

$$p_C = 0,\ k_{rb} = S_{e1},\ k_{rg} = 1 - S_{e1}. \tag{4.2.21}$$

As previously indicated, this model is only used for fluid flow in an open borehole.

The saturation and capillary pressure constraints (i.e., Eqs. 4.2.3, 4.2.4) permit a reduction of the number of equations to be solved from four (i.e., Eqs. 4.2.1 - 4.2.4) to two. In particular, the constraint equations are used to reformulate Eqs. (4.2.1) and (4.2.2) so that the unknown functions are gas saturation S_g and brine pressure p_b. Specifically, the saturation constraint in Eq. (4.2.3) allows S_b to be expressed as

$$S_b = 1 - S_g \tag{4.2.22}$$

and thus allows S_{e1} and S_{e2} in Eqs. (4.2.13) and (4.2.14) to be reformulated as

$$S_{e1} = \left(1 - S_g - S_{br}\right) / \left(1 - S_{br}\right) \tag{4.2.23}$$

$$S_{e2} = \left(1 - S_g - S_{br}\right) / \left(1 - S_{gr} - S_{br}\right). \tag{4.2.24}$$

Further, the capillary pressure constraint in Eq. (4.2.4) allows p_g to be expressed as

$$\begin{aligned} p_g &= p_b + p_C \\ &= p_b + p_t(k) / S_{e2}^{1/2} \qquad \text{for Brooks-Corey model, Eq. (4.2.9)} \qquad (4.2.25) \\ &= p_b + p_{VGP}\left(S_{e2}^{-1/m} - 1\right)^{1-m} \qquad \text{for van Genuchten-Parker model, Eq. (4.2.18)} \qquad (4.2.26) \end{aligned}$$

$= p_b$ for linear model, Eq. (4.2.21). (4.2.27)

The equalities in Eqs. (4.2.23) - (4.2.27) allow the transformation of Eqs. (4.2.1) and (4.2.2) into two equations whose unknown functions are S_g and p_b, which are the equations that are actually solved in BRAGFLO (Fig. 4.2.4). Once S_g and p_b are known, S_b and p_g can be obtained from Eq. (4.2.22) and Eqs. (4.2.25) - (4.2.27), respectively.

All materials are assumed to be isotropic in the 1996 WIPP PA (Howarth and Christian-Frear 1997). Thus, the tensor $\mathbf{K}_l$ in Eqs. (4.2.1) and (4.2.2) has the form

$$\mathbf{K}_l = \begin{bmatrix} k_l & 0 \\ 0 & k_l \end{bmatrix}, \tag{4.2.28}$$

where k_l is the permeability to fluid l for the particular material under consideration. For brine (i.e., fluid $l = b$), the permeability k_b is the same as the intrinsic permeability k in Table 4.2.2. For gas (i.e., fluid $l = g$), the permeability k_g is obtained by modifying the intrinsic permeability k to account for the Klinkenberg effect (Klinkenberg 1941). Specifically,

$$k_g = k\left(1 + b\, k^a / p_g\right), \tag{4.2.29}$$

where $a = a_{klink}$ and $b = b_{klink}$ are gas- and formation-dependent constants. For the 1996 WIPP PA, values of $a_{klink} = -0.3410$ and $b_{klink} = 0.2710$ were determined from data obtained for MB 139 (Christian-Frear 1996b), with these values used for all regions in Fig. 4.2.1. For fluid flow in the vicinity of the shaft, an averaging procedure was used to calculate k that incorporates the permeability of the DRZ that surrounds portions of the shaft (see Sect. 4.2.2). Further, a pressure-dependent modification of k is used in the anhydrite marker beds in the presence of pressure-induced fracturing (see Sect. 4.2.4).

Gas density is computed using the Redlich-Kwong-Soave (RKS) equation of state, with the gas assumed to be pure hydrogen in the 1996 WIPP PA. For a pure gas, the RKS equation of state has the form (pp. 43-54, Walas 1985)

$$p_g = \frac{RT}{V - b} - \frac{a\alpha}{V(V + b)}, \tag{4.2.30}$$

where

R = gas constant = 8.31451 J mol^{-1} K^{-1},
T = temperature (K) = 300.15 K (= 30° C),
V = molar volume (m^3 mol^{-1}),
a = $0.42747\, R^2 T_c^2 / P_c$,
b = $0.08664\, RT_c / P_c$,

Gas Conservation

$$p_g = p_b + p_C \text{ (see Eqs 4.2.25 - 4.2.27)}$$

$$\nabla \bullet \left[\frac{\alpha \rho_g \mathbf{K}_g k_{rg}}{\mu_g} \left(\nabla p_g + \rho_g g \nabla h \right) \right] + \alpha q_{wg} + \alpha q_{rg} = \alpha \frac{\partial \left(\phi \rho_g S_g \right)}{\partial t}$$

Brine Conservation

$$S_b = 1 - S_g \text{ (see Eq. 4.2.3)}$$

$$\nabla \bullet \left[\frac{\alpha \rho_b \mathbf{K}_b k_{rb}}{\mu_b} \left(\nabla p_b + \rho_b g \nabla h \right) \right] + \alpha q_{wb} + \alpha q_{rb} = \alpha \frac{\partial \left(\phi \rho_b S_b \right)}{\partial t}$$

Fig. 4.2.4. Reduction of gas and brine conservation equations to system of two equations in two unknowns (i.e., S_g and p_b) for numerical solution.

α = $[1 + (0.48508 + 1.55171\omega - 0.15613\omega^2)(1 - T_r^{0.5})]^2$
= $1.202\exp(-0.30288T_r)$ for hydrogen (Graboski and Daubert 1979),
T_c = critical temperature (K),
P_c = critical pressure (Pa),
$T_r = T/T_c$ = reduced temperature,
ω = acentric factor
= 0 for hydrogen (Graboski and Daubert 1979).

For hydrogen, pseudo-critical temperature and pressure values of T_c = 43.6 K and $P_c = 2.047 \times 10^6$ Pa are used instead of the true values of these properties (Prausnitz 1969). Eq. (4.2.30) is solved for molar volume V. Then, the gas density ρ_g is given by

$$\rho_g = M_{w,H_2} / V, \tag{4.2.31}$$

where M_{w,H_2} is the molecular weight of hydrogen (i.e., 2.01588×10^{-3} kg/mol; see p. B-26, Weast et al. 1969).

Brine density ρ_b is defined by Eq. (4.2.5), with $\rho_0 = 1230.0$ kg/m^3 at a pressure of $p_{b0} = 1.0132 \times 10^5$ Pa and $\beta_b = 2.5 \times 10^{-10}$ Pa^{-1} (Roberts 1996). Porosity ϕ as defined by Eq. (4.2.6) is used with two exceptions: in the repository (see Sect. 4.2.3) and in the marker beds subsequent to fracturing (see Sect. 4.2.4). The values of ϕ_0 and β_f used in conjunction with Eq. (4.2.6) are listed in Table 4.2.1. The reference pressure p_{b0} in Eq. (4.2.6) is spatially-variable and corresponds to the initial pressures $p_b(x, y, -5 \text{ yr})$ in Table 4.2.4. The gas and brine viscosities μ_l, $l = g$, b, in Eqs. (4.2.1) and (4.2.2) were assumed to have values of $\mu_g = 8.92 \times 10^{-6}$ Pa•s (Vargaftik 1975) and $\mu_b = 2.1 \times 10^{-3}$ Pa•s (McTigue 1993).

Table 4.2.4. Initial Conditions for p_b and S_g at (x, y, –5 yr) and Reset Conditions[a] for p_b and S_g at (x, y, 0 yr)

Initial Conditions: Brine Pressure $p_b(x, y, -5\text{ yr})$

1) Rustler Fm and overlying units (except in the shaft). Modeled as horizontal with spatially constant initial pressure in each layer (see Fig. 4.2.1 and Table 4.2.2).

Mesh Layer (Fig. 4.2.1)	Material Index (Table 4.2.2)	Region Index (Fig. 4.2.1)	Name	p_b (x, y, –5), Pa
31	20	12	Santa Rosa Fm	1.013250×10^5
30	20	12	Santa Rosa Fm	1.013250×10^5
29	19	13	Dewey Lake	1.013250×10^5
28	19	13	Dewey Lake	7.345482×10^5
27	18	14	Forty-Niner	1.471170×10^6
26	17	15	Magenta	9.170000×10^5
25	16	16	Tamarisk	1.824205×10^6
24	15	17	Culebra	8.220000×10^5
23	14	18	Unnamed	2.279613×10^6

2) Salado Fm (Mesh Layers 3 - 22) The Salado is assumed to dip uniformly $\theta = 1°$ downward from north to south. Except in repository excavations and shaft, brine is assumed initially (i.e., at –5 yr) to be in hydrostatic equilibrium relative to an uncertain initial pressure $p_{b,ref}$ (see *SALPRES* in Sect. 5.2) at a reference point located at center of shaft at elevation of midpoint of MB 139 (i.e., at $(x_{ref}, y_{ref}) = (23664.9\text{ m}, 379.685\text{ m})$), which is the center of cell 644 in Fig. 4.2.3), which gives rise to the condition

$$p_b(x, y, -5) = p_{b0} + (1/\beta_b)\ln\left[\rho_b(x, y, -5)/\rho_{b0}\right]$$

where

$$\rho_b(x, y, -5) = \frac{1}{g\,\beta_b\left[y_e - \Phi\left(x_{ref}, y_{ref}, -5\right) + \dfrac{1}{g\,\beta_b\,\rho_{b0}}\right]}$$

$$\Phi\left(x_{ref}, y_{ref}, -5\right) = y_{ref} + \frac{1}{g\,\beta_b}\left[\frac{1}{\rho_{b0}} - \frac{1}{\rho_b\left(x_{ref}, y_{ref}, -5\right)}\right]$$

$$\rho_b\left(x_{ref}, y_{ref}, -5\right) = \rho_{b0}\exp\left[-\beta_b\left(p_{b,ref} - p_{b0}\right)\right]$$

$$y_e = y_{ref} + h(x, y) = y_{ref} + \left(x - x_{ref}\right)\sin\theta + \left(y - y_{ref}\right)\cos\theta \quad \text{(See Eq. (4.2.8))}$$

$\rho_{b0} = 1220\text{ kg/m}^3$, $\beta_b = 3.1 \times 10^{-10}\text{ Pa}^{-1}$, $g = 9.79\text{ m/s}^2$, $p_{b0} = 1.01325 \times 10^5\text{ Pa}$

3) Castile Fm (Mesh Layers 1 and 2). The Castile is modeled as horizontal, and initial brine pressure is spatially constant in each layer, except that the brine reservoir is treated as a different material from rest of Castile and has a different initial pressure. Specifically,

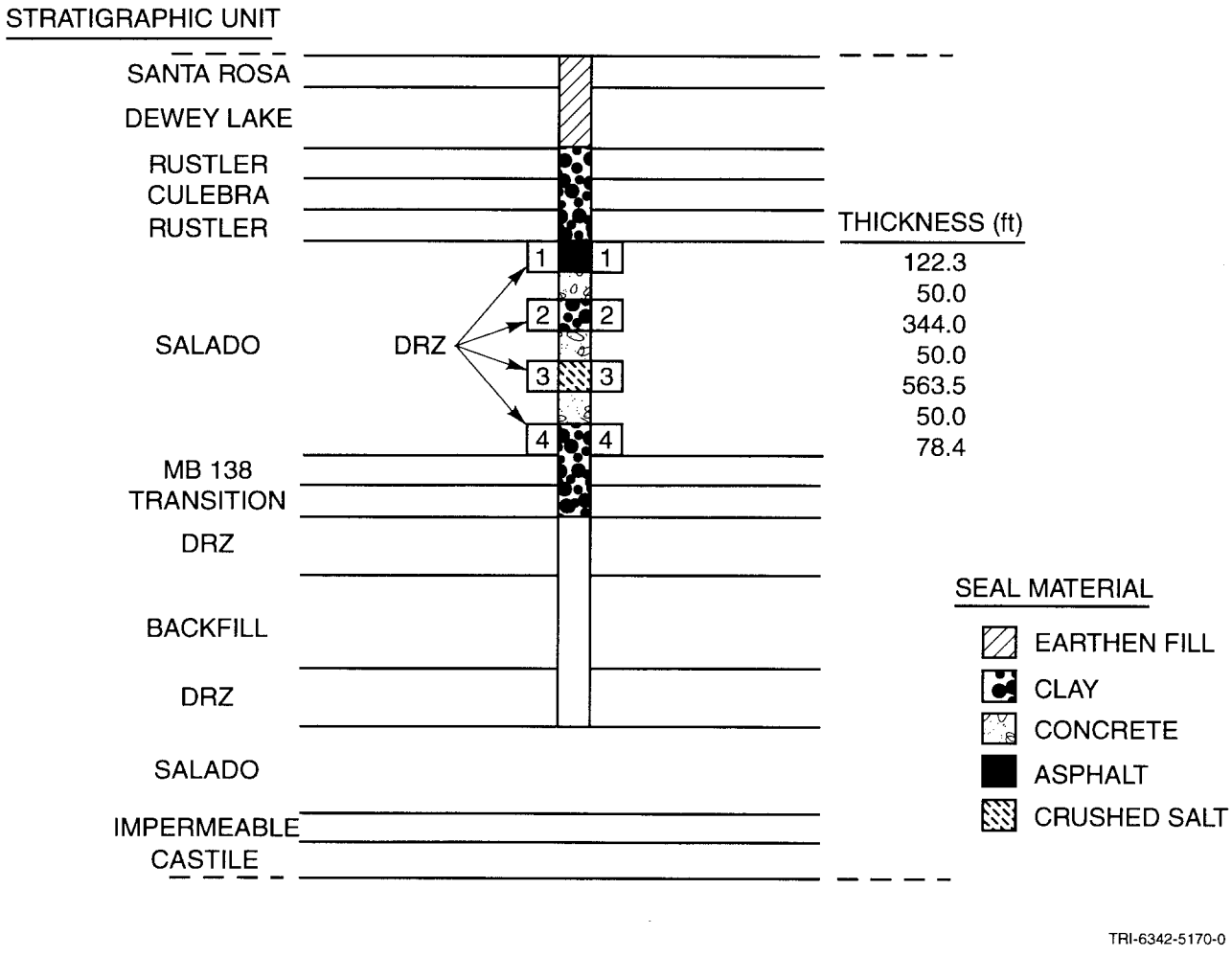

Fig. 4.2.5. Conceptual representation of shaft-seal system used in definition of model parameters for use in conjunction with regions 3 - 11 of Fig. 4.2.1.

Table 4.2.5. Treatment of Transient Permeability Associated with Shaft Seals

Material	Transient Seal Permeability	DRZ Present	Transient DRZ Permeability
Earthen Fill (region 3, Fig. 4.2.1)	No	No	N/A
Rustler Clay Column (region 4, Fig. 4.2.1)	No	No	N/A
Asphalt Column (region 5, Fig. 4.2.1)	No	Yes	No
Salado Concretes (region 6, Fig. 4.2.1)	Yes	No	N/A
Salado Clay Columns (regions 8, 9, Fig. 4.2.1)	No	Yes	Yes
Salado Salt Column (region 7, Fig. 4.2.1)	Yes	Yes	Yes

Table 4.2.6. Times at Which Permeabilities are Changed for Shaft Seal and DRZ Materials

Material	Permeability Changes
All Concretes (region 6, Fig. 4.2.1)	400 years
DRZ, Upper Salado Clay Column (region 8, Fig. 4.2.1; DRZ-2 in Fig. 4.2.5)	10, 25, 50 & 100 years
Salado Salt Column (region 7, Fig. 4.2.1)	50, 100 & 200 years
DRZ, Salado Salt Column (region 7, Fig. 4.2.1; DRZ-3 in Fig. 4.2.5)	10 & 25 years
DRZ, Lower Salado Clay Column (region 8, Fig. 4.2.1; DRZ-4 in Fig. 4.2.5)	10, 25 & 50 years

Table 4.2.5 summarizes the seal and DRZ materials assumed to have transient permeabilities. In the conceptualization of the behavior of the shaft seals and their associated DRZs, the effective DRZ permeabilities are transient because the DRZ radii are transient, not because their intrinsic permeability changes with time. Table 4.2.6 summarizes the times at which permeabilities are changed for shaft seal and DRZ materials.

The effects of shaft and DRZ permeabilities are incorporated into the analysis for each shaft component through an effective permeability k_e defined by

$$k_e = \left(k_s \sum_{i=1}^{4} A_{si} + k_d \sum_{i=1}^{4} A_{di} \right) / \left(\sum_{i=1}^{4} A_{si} \right), \tag{4.2.34}$$

where

k_s = permeability (m^2) for shaft component under consideration,

A_{si} = cross-sectional area (m^2) for shaft i,

k_d = permeability (m^2) for DRZ associated with shaft component under consideration,

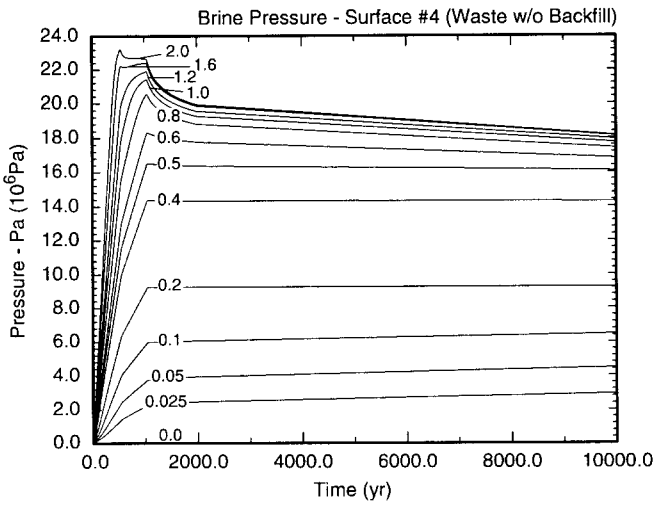

Fig. 4.2.6. Disposal room pressure for different values of the gas generation scale factor (f). Individual curves correspond to the functions $p(t, f)$ in Eq. (4.2.38) and were obtained from calculations performed with SANTOS.

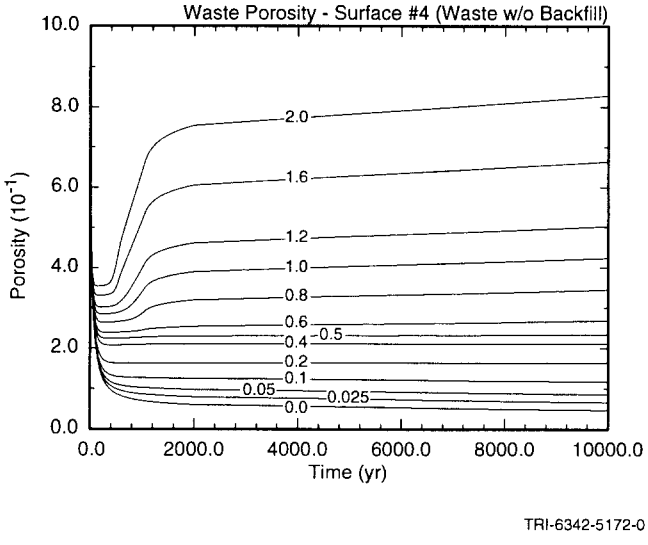

Fig. 4.2.7. Disposal room porosity curves for different values of the gas generation scale factor (f). Individual curves correspond to the functions $\phi(t, f)$ in Eq. (4.2.40) and define porosities for use in BRAGFLO on the basis of calculations performed with SANTOS.

for $0 \le t \le 10000$ yr and $f = 0, 0.025, \ldots, 2$ (see Figs. 4.2.6, 4.2.7). The pressure and porosity curves in Figs. 4.2.6 and 4.2.7 are calculated with the indicated values for $r_g(t, f)$ as described in Freeze et al. (1995).

The porosities calculated by SANTOS are defined relative to a dynamically changing excavated volume. In contrast, the porosities used in BRAGFLO are defined relative to a fixed excavated volume. The pressures in Fig. 4.2.6 are pressures calculated by SANTOS. However, the porosities in Fig. 4.2.7 are porosities for use in BRAGFLO and are obtained from porosities calculated by SANTOS in a manner that results in the excavated volumes in SANTOS and BRAGFLO having equal pore volumes. Specifically, $\phi_S h_S = \phi_B h_B$, where ϕ_S and ϕ_B are the porosities associated with SANTOS and BRAGFLO and h_S and h_B are the heights (m) of the excavated volume in SANTOS and BRAGFLO.

Brine pressures $p_b(t)$ obtained in the waste disposal regions are used in conjunction with the results in Figs. 4.2.6 and 4.2.7 to estimate porosity in regions 23 and 24 of Fig. 4.2.1 in the numerical solution of Eqs. (4.2.1) and (4.2.2). Given a value for $p_b(t)$, values f_1 and f_2 are determined such that

$$p(t, f_1) \le p_b(t) < p(t, f_2), \tag{4.2.38}$$

where $p(t, f)$ denotes the pressure (Pa) at time t obtained with gas generation rate $r_g(t, f)$ (see Fig. 4.2.6). An f value associated with $p_b(t)$ is then given by

$$\hat{f} = f_1 + \left(\frac{p_b(t) - p(t, f_1)}{p(t, f_2) - p(t, f_1)} \right) (f_2 - f_1), \tag{4.2.39}$$

with $\hat{f}$ being estimated by linear interpolation on f_1 and f_2. With $\hat{f}$ determined, a corresponding porosity $\hat{\phi}$ for use with $p_b(t)$ is obtained from the porosity results in Fig. 4.2.7. Specifically,

$$\hat{\phi} = \phi(t, f_1) + \left(\frac{\hat{f} - f_1}{f_2 - f_1} \right) \left(\phi(t, f_2) - \phi(t, f_1) \right), \tag{4.2.40}$$

where $\phi(t, f)$ denotes the porosity at time t obtained with gas generation rate $r_g(t, f)$ (see Fig. 4.2.7).

4.2.4 Interbed Fracturing

Fracturing within the anhydrite marker beds (i.e., regions 20, 21, 28 in Fig. 4.2.1) is assumed to occur at pressures slightly below lithostatic pressure and is implemented through a pressure-dependent compressibility $\beta_f(p_b)$. Specifically, the following assumptions are made (Mendenhall and Gerstle, 1995): (1) Fracturing of the marker beds begins at a brine pressure of

$$p_{bi} = p_{b0} + \Delta p_i, \tag{4.2.41}$$

where p_{bi} and p_{b0} are spatially dependent (i.e., $p_{b0} = p_b(x, y, -5)$ in Table 4.2.4) and $\Delta p_i = 2 \times 10^5$ Pa. (2) Fracturing ceases at a pressure of

$$p_{ba} = p_{bi} + \Delta p_a \tag{4.2.42}$$

and a fully-fractured porosity of

$$\phi(p_{ba}) = \phi_a = \phi_0 + \Delta\phi_a, \tag{4.2.43}$$

where $\Delta p_a = 3.8 \times 10^6$ Pa, ϕ_0 is spatially dependent (i.e., $\phi_0 = \phi_0(x, y, -5)$ in Table 4.2.4), and $\Delta\phi_a = 0.04$, 0.24 and 0.04 for MB 138, MB A&B and MB 139, respectively (i.e., $\phi_a = 0.05$, 0.25. 0.05 for MB 138, MB A&B, MB 139). (3) Compressibility β_f is a linear function

$$\beta_f(p_b) = \beta_f + \left(\frac{p_b - p_{bi}}{p_{ba} - p_{bi}}\right)(\beta_{fa} - \beta_f) \tag{4.2.44}$$

of brine pressure for $p_{bi} \le p_b \le p_{ba}$, with β_{fa} defined so that the solution ϕ of

$$d\phi / dp_b = \beta_f(p_b)\,\phi, \quad \phi(p_{bi}) = \phi_0 \exp\left[\beta_f(p_{bi} - p_{b0})\right] \tag{4.2.45}$$

satisfies $\phi(p_{ba}) = \phi_a$; specifically, β_{fa} is given by

$$\beta_{fa} = \beta_f\left[1 - \frac{2(p_{ba} - p_{b0})}{p_{ba} - p_{bi}}\right] + \left[\frac{2}{p_{ba} - p_{bi}}\right]\ln\left(\frac{\phi_a}{\phi_0}\right). \tag{4.2.46}$$

(4) The permeability $k_f(p_b)$ of fractured material at brine pressure p_b is related to the permeability k of unfractured material at brine pressure p_{bi} by

$$k_f(p_b) = \left[\phi(p_b) / \phi(p_{bi})\right]^n k, \tag{4.2.47}$$

where k is the permeability of unfractured material (i.e., at p_{bi}) and n is defined so that $k_f(p_{ba}) = 1 \times 10^{-9}$ m^2 (i.e., n is a function of k, which is an uncertain input to the analysis; see *ANHPRM* in Sect. 5.2). When fracturing occurs, $k_f(p_b)$ is used instead of k in the definition of the permeability tensor $\mathbf{K}_l$ in Eq. (4.2.28) for the fractured areas of the anhydrite marker beds.

4.2.5 Gas Generation

Gas production is assumed to result from anoxic corrosion of steel and microbial degradation of cellulosics, plastics and rubbers. Thus, the gas generation rate q_{rg} in Eq. (4.2.1) is of the form

$$q_{rg} = q_{rgc} + q_{rgm}\,, \tag{4.2.48}$$

where q_{rgc} is the rate of gas production due to anoxic corrosion of steel (kg/m^3/s) and q_{rgm} is the rate of gas production due to microbial degradation of cellulosics, plastics and rubbers (kg/m^3/s). Gas generation takes place only within the waste disposal region (i.e., regions 23, 24 of Fig. 4.2.1) and all the generated gas is assumed to have the same properties as H_2. Furthermore, q_{rb} in Eq. (4.2.2) is used to describe the consumption of brine during the corrosion process.

The rates q_{rgc}, q_{rb} and q_{rgm} are defined by

$$q_{rgc} = \left(R_{ci} S_{b,eff} + R_{ch}\, S_g^*\right) D_s\, \rho_{Fe}\, X_c(\mathrm{H_2|Fe})\, M_{H_2} \tag{4.2.49}$$

$$q_{rb} = -\left(q_{rgc} / M_{H_2}\right) X_c(\mathrm{H_2O|H_2})\, M_{H_2O} \tag{4.2.50}$$

$$q_{rgm} = \left(R_{mi}\, S_{b,eff} + R_{mh}\, S_g^*\right) D_c\, y(\mathrm{H_2|C})\, M_{H_2} \tag{4.2.51}$$

where

D_s = surface area concentration of steel in the repository ((m^2 surface area steel) / (m^3 disposal volume)),

D_c = mass concentration of cellulosics in the repository ((kg biodegradable material) / (m^3 of disposal volume)),

M_{H_2} = molecular weight of H_2 ((kg H_2) / (mol H_2)),

M_{H_2O} = molecular weight of H_2O ((kg H_2O) / (mol H_2O)),

R_{ci} = corrosion rate under inundated conditions (m/s),

R_{ch} = corrosion rate under humid conditions (m/s),

R_{mi} = rate of cellulose biodegradation under inundated conditions (mol CH_2O/kg CH_2O/s),

R_{mh} = rate of cellulose biodegradation under humid conditions (mol CH_2O/kg CH_2O/s),

$S_{b,eff}$ = effective brine saturation due to capillary action in the waste materials (see Eq. (4.2.71) in Sect. 4.2.6),

S_g^* = $1 - S_{b,eff}$ if $S_{b,eff} > 0$

= 0 if $S_{b,eff} = 0$,

$X_c(\mathrm{H_2|Fe})$ = stoichiometric coefficient for gas generation due to corrosion of steel, i.e., moles of H_2 produced by the corrosion of 1 mole of Fe ((mol H_2)/(mol Fe)),

$X_c(\mathrm{H_2O|H_2})$ = stoichiometric coefficient for brine consumption due to corrosion of steel, i.e., moles of H_2O consumed per mole of H_2 generated by corrosion ((mol H_2O/(mol H_2)),

$y(\mathrm{H_2|C})$ = average stoichiometric factor for microbial degradation of cellulose, i.e., the moles of H_2 generated per mole of carbon consumed by microbial action ((mol H_2) / (mol CH_2O)),

ρ_{Fe} = molar density of steel (mol/m^3).

The products $R_{ci}\, D_s\, \rho_{Fe}\, X_c$, $R_{ch}\, D_s\, \rho_{Fe}\, X_c$, $R_{mi}\, D_c\, y$ and $R_{mh}\, D_c\, y$ in Eqs. (4.2.49) and (4.2.51) define constant rates of gas generation (mol/m^3/s) that continue until the associated substrate (i.e. steel or cellulose) is exhausted (i.e., zero order kinetics). The terms $S_{b,eff}$ and S_g^* in Eqs. (4.2.49) and (4.2.51), which are functions of location and time, correct for the amount of substrate that is exposed to inundated and humid conditions, respectively. All the corrosion and microbial action is assumed to cease when no brine is present, which is the reason that 0 replaces $S_g = 1$ in the definition of S_g^*. In the 1996 WIPP PA, R_{ch} = 0 and R_{ci}, R_{mh} and R_{mi} are defined by uncertain variables (see *WGRCOR, WGRMICH, WGRMICI* in Sect. 5.2). Further, M_{H_2} = 2.02 × 10^{-3} kg/mol (pp. **1**-7, **1**-8, Lide 1991), M_{H_2O} = 1.80 × 10^{-2} kg/mol (pp. **1**-7, **1**-8, Lide 1991), ρ_{Fe} = 1.41 × 10^5 mol/m^3 (Telander and Westerman 1993), and D_s,D_c, $X_c(\mathrm{H_2O \mid H_2})$, $X_c(\mathrm{H_2 \mid Fe})$ and $y(\mathrm{H_2 \mid C})$ are discussed below.

The concentration D_s in Eq. (4.2.49) is defined by

$$D_s = A_d n_d / V_R\,, \tag{4.2.52}$$

where

A_d = surface area of steel associated with a waste disposal drum (m^2/drum),
V_R = initial volume of the repository (m^3),
n_d = number of waste drums required to hold all the waste emplaced in the repository (drums).

In the 1996 WIPP PA, A_d = 6 m^2/drum (Vol. 3, WIPP PA 1991-1992), V_R = 436,023 m^3 (Schreiber 1991), and n_d = 814,044 drums (Schreiber 1991; pp. 51-53, Nowak et al. 1990; Bechtel National 1986).

The biodegradable materials to be disposed at the WIPP consist of cellulosics, rubbers, and both waste plastics and container plastics. Cellulosics have been demonstrated experimentally to be the most biodegradable among these

materials (Francis et al. 1997). The occurrence of significant microbial gas generation in the repository will depend on: (1) whether microbes capable of consuming the emplaced organic materials will be present and active; (2) whether sufficient electron acceptors will be present and available; and (3) whether enough nutrients will be present and available. Given the uncertainties in these factors, a probability of 0.5 is assigned to the occurrence of microbial gas generation (see *WMICDFLG* in Sect. 5.2). Furthermore, two factors may increase the biodegradability of plastics and rubbers: long time scale and cometabolism. Over a time scale of 10,000 yr, the chemical properties of plastics and rubbers may change, increasing their biodegradability. Cometabolism means that microbes may degrade organic compounds, but do not use them as a source of energy, which is derived from other substrates. Both of these factors are highly uncertain and therefore a probability of 0.5 is assigned to biodegradation of plastics and rubbers conditional on the occurrence of biodegradation of cellulose (see *WMICDFLG* in Sect. 5.2). In cases where biodegradation of rubbers and plastics occurs, rubbers and plastics are converted to an equivalent quantity of cellulosics based on their carbon equivalence (Wang and Brush 1996a). This produces the density calculation

$$D_c = \begin{cases} m_{cel} / V_R & \text{for biodegradation of cellulosics only} \\ \left(m_{cel} + m_r + 1.7\, m_p\right) / V_R & \text{for biodegradation of cellulosics, rubber, plastics,} \end{cases} \tag{4.2.53}$$

where m_{cel} is mass of cellulosics (kg), m_r is the mass of rubbers (kg), and m_p is the mass of plastics (kg). The factor of 1.7 converts all plastics to an equivalent quantity of cellulosics based on carbon equivalence. In the 1996 WIPP PA, $m_{cel} = 9.25 \times 10^6$ kg, $m_r = 1.71 \times 10^6$ kg and $m_p = 1.03 \times 10^7$ kg (U.S. DOE 1995a).

The most plausible corrosion reactions after closure of the WIPP are believed to be (Wang and Brush 1996a)

$$Fe + 2H_2O = Fe(OH)_2 + H_2 \tag{4.2.54}$$

and

$$3Fe + 4H_2O = Fe_3O_4 + 4H_2. \tag{4.2.55}$$

When linearly weighted by the factors x and $1 - x$ ($0 \le x \le 1$), the two preceding reactions become

$$Fe + \left(\frac{4+2x}{3}\right)H_2O = \left(\frac{4-x}{3}\right)H_2 + xFe(OH)_2 + \left(\frac{1-x}{3}\right)Fe_3O_4, \tag{4.2.56}$$

where x and $1 - x$ are the fractions of iron consumed in the reactions in Eqs. (4.2.54) and (4.2.55), respectively. Although magnetite (Fe_3O_4) has been observed to form on iron as a corrosion product in low-Mg anoxic brines at elevated temperatures (Telander and Westerman 1997) and in oxic brine (Haberman and Frydrych 1988), there is no evidence that it will form at WIPP repository temperatures. If Fe_3O_4 were to form, H_2 would be produced (on a molar basis) in excess of the amount of Fe consumed. However, anoxic corrosion experiments (Telander and

Westerman 1993) did not indicate the production of H_2 in excess of the amount of Fe consumed. Therefore, the stoichiometric factor x in Eq. (4.2.56) is set to 1.0 (i.e., $x = 1$) in the 1996 WIPP PA, which implies that Eq. (4.2.54) represents corrosion. Thus, the stoichiometric factor for corrosion is

$$X_c(\mathrm{H_2|Fe}) = (4 - x)/3 = 1 \text{ mol / mol}, \tag{4.2.57}$$

which implies that one mole of H_2 is produced for each mole of iron consumed, and the stoichiometric factor for brine consumption is

$$X_c(\mathrm{H_2O|Fe}) = (4 + 2x)/3 = 2 \text{ mol / mol}, \tag{4.2.58}$$

which implies that two moles of H_2O are consumed for each mole of H_2 produced.

The most plausible biodegradation reactions after closure of the WIPP are believed to be (Wang and Brush 1996a)

reaction 1 (denitrification): $\mathrm{C_6H_{10}O_5 + 4.8H^+ + 4.8NO_3^- = 7.4H_2O + 6CO_2 + 2.4N_2}$ (4.2.59)

reaction 2 (sulfate reduction): $\mathrm{C_6H_{10}O_5 + 6H^+ + 3SO_4^{2-} = 5H_2O + 6CO_2 + 3H_2S}$ (4.2.60)

reaction 3 (methanogenesis): $\mathrm{C_6H_{10}O_5 + H_2O = 3CH_4 + 3\ CO_2}$. (4.2.61)

The accumulation of CO_2 produced by the above reactions will decrease pH and thus increase actinide solubility in the repository (Wang and Brush 1996b). To improve WIPP performance, a sufficient amount of MgO will be added to the repository as backfill to remove CO_2 and buffer pH (Bynum et al. 1997). The consumption of CO_2 by MgO in the repository takes place by the reaction

$$\mathrm{MgO + CO_2 = MgCO_3}. \tag{4.2.62}$$

Given the current waste inventory estimates, the minimum amount of MgO sufficient to remove all CO_2 is estimated to be 4×10^8 mol, which is about 4% of total transuranic waste volume (U.S. DOE 1995a). The amount recommended for use in the WIPP is 2×10^9 mol (App. Source Term, U.S. DOE 1996). The effect of CO_2 consumption by MgO on fluid is explicitly represented by a negative gas generation rate q_{rg}. Rather, the effect of CO_2 consumption is accounted for by modifying the stoichiometry of Eqs. (60) - (62).

The average stoichiometry of Eqs. (4.2.59) - (4.2.61) is

$$\mathrm{C_6H_{10}O_5} + \text{unknown} = 6y \text{ (mol) gas} + \text{unknowns}. \tag{4.2.63}$$

The average stoichiometric factor y in Eq. (4.2.63) depends on the extent of the individual biodegradation pathways in Eqs. (4.2.59) - (4.2.61) and the consumption of CO_2 by MgO. This factor is based on estimates of the transuranic waste to be emplaced in the WIPP (U.S. DOE 1995a, Drez 1996) and is derived as follows (Wang and Brush 1996a,b).

Estimates of the maximum quantities M_{cel} and M_{Fe} (mol) of cellulosics (i.e., CH_2O) and steels that can be potentially consumed in 10,000 yr are given by

$$M_{cel} = \min\left\{\frac{6000 m_{cel}}{162}, 3.2 \times 10^{11} R_m m_{cel}\right\} \tag{4.2.64}$$

$$M_{Fe} = \min\left\{\frac{1000 m_{Fe}}{56}, 4.4 \times 10^{16} R_{ci} A_d n_d\right\}, \tag{4.2.65}$$

where

$$R_m = \max\left\{R_{m,i}, R_{m,h}\right\} \tag{4.2.66}$$

and m_{cel} and m_{Fe} are the masses (kg) of cellulosics (see Eq. 4.2.53) and steels initially present in the repository ($m_{Fe} = 7.13 \times 10^7$ kg; see U.S. DOE 1995a). The terms 6000 m_{cel}/162 and 1000 m_{Fe}/56 in Eqs. (4.2.64) and (4.2.65) equal the inventories in moles of cellulosics and steel, respectively. The terms 3.2×10^{11} $R_m m_{cel}$ and 4.4×10^{16} $R_{ci} A_d n_d$ equal the maximum amounts of cellulosics and steel that could be consumed over 10,000 yr. In Eq. (4.2.64), $3.2 \times 10^{11} \doteq (3.15569 \times 10^7$ s/yr) (10^4 yr). In Eq. (4.2.65), $A_d n_d$ is the total surface area of all drums (m^2) and the factor $4.4 \times 10^{16} \doteq (3.15569 \times 10^7$ s/yr) (10^4 yr) (1.41×10^5 mol/ m^3), where $\rho_{Fe} = 1.41 \times 10^5$ mol/m^3 (see Eq. 4.2.49) (Telander and Westerman 1993), converts the corrosion rate from m/s to mol/m^2/s.

A range of possible values for the average stoichiometric factor y in Eq. (4.2.63) can be obtained by considering individual biodegradation pathways involving M_{cel} and accounting for the removal of CO_2 according to Eq. (4.2.62). Two extreme cases corresponding to the maximum and minimum values of y exist: (1) there is no reaction of microbially produced H_2S with ferrous metals and metal corrosion products, and (2) there is a complete reaction of microbially produced H_2S with ferrous metals and metal corrosion products. If no H_2S is consumed by reactions with iron and iron corrosion products, the maximum quantity of microbial gas will be retained in the repository and therefore the maximum value for y results. Thus, the maximum value of y can be estimated by averaging the gas yields for all reaction pathways to produce

$$y_{max} = \frac{\frac{2.4 M_{NO_3}}{4.8} + \frac{3 M_{SO_4}}{3} + 0.5\left(M_{cel} - \frac{6 M_{NO_3}}{4.8} - \frac{6 M_{SO_4}}{3}\right)}{M_{cel}}, \tag{4.2.67}$$

where M_{NO_3} and M_{SO_4} are the quantities of NO_3^- and SO_4^{2-} (in moles) initially present in the repository. Specifically, $M_{NO_3} = 2.61 \times 10^7$ mol and $M_{SO_4} = 6.59 \times 10^6$ mol (Drez 1996).

If H_2S reacts with iron and iron corrosion products, a significant quantity or perhaps all of the microbially produced H_2S would be consumed to produce FeS, which would result in the minimum value of y. Specifically,

$$y_{min} = \frac{\frac{2.4M_{NO_3}}{4.8} + \frac{3M_{SO_4}}{3} + 0.5\left(M_{cel} - \frac{6M_{NO_3}}{4.8} - \frac{6M_{SO_4}}{3}\right) - G}{M_{cel}} = y_{max} - \frac{G}{M_{cel}}, \tag{4.2.68}$$

where

$$G = \min\left\{\frac{3M_{SO_4}}{3}, M_{Fe}\right\}. \tag{4.2.69}$$

The stoichiometric factor y value is believed to be located within the interval $[y_{min}, y_{max}]$. That is,

$$y = y_{min} + \beta(y_{max} - y_{min}), \; 0 \le \beta \le 1. \tag{4.2.70}$$

The variable β in the preceding equation is treated as an uncertain quantity in the 1996 WIPP PA (see *WFBETCEL* in Sect. 5.2).

4.2.6 Capillary Action in the Waste

Capillary action (wicking) refers to the ability of a material to carry a fluid by capillary forces above the level it would normally seek in response to gravity. In the current analysis, this phenomena is accounted for by defining an effective saturation given by

$$\begin{aligned} S_{b,eff} &= S_b + S_{wick} && \text{if } 0 < S_b < 1 - S_{wick} \\ &= 0 && \text{if } S_b = 0 \\ &= 1 && \text{if } S_b > 1 - S_{wick} \end{aligned} \tag{4.2.71}$$

where

$S_{b,eff}$ = effective brine saturation,
S_b = brine saturation,
S_{wick} = wicking saturation.

The effective saturation is used on a grid block basis (Fig. 4.2.1) within all waste regions. The wicking saturation, S_{wick}, is treated as an uncertain variable (see *WASTWICK* in Sect. 5.2). The effective brine saturation $S_{b,eff}$ is only used in the calculation of the corrosion of steel (Eq. (4.2.49)) and the microbial degradation of cellulose (Eq. (4.2.51)) and does not directly affect the two phase flow calculations indicated in Eqs. (4.2.1) - (4.2.6).

4.2.7 Borehole Model

The major disruptive event in the 1996 WIPP PA is the penetration of the repository by a drilling intrusion. Such an intrusion is modeled by modifying the permeability of region 1 in Fig. 4.2.1 (Table 4.2.8). Further, the drilling intrusion is assumed to produce a borehole with a diameter of 12.25 in. (0.31 m) (Vaughn 1996a, Howard 1996); borehole fill is assumed to be incompressible; capillary effects are ignored; residual gas and brine saturations are set to zero, and porosity is set to 0.32 (see materials 47, 48, 49, 50 in Table 4.2.1). When a borehole that penetrates pressurized brine in the Castile Fm is under consideration (i.e., an E1 intrusion), the permeability modifications indicated in Table 4.2.8 extend from the land surface (i.e., grid cell 937 in Fig. 4.2.3) to the base of the pressurized brine (i.e., grid cell 1010 in Fig. 4.2.3). When a borehole that does not penetrate pressurized brine in the Castile Fm is under consideration (i.e., an E2 intrusion), the permeability modifications indicated in Table 4.2.8 stop at the bottom of the lower DRZ (i.e., grid cell 439 in Fig. 4.2.3).

4.2.8 Numerical Solution

Determination of gas and brine flow in the vicinity of the repository requires the numerical solution of the two nonlinear partial differential equations in Fig. 4.2.4 on the computational domain in Fig. 4.2.1 together with evaluation of appropriate auxiliary conditions (i.e., Eqs. 4.2.3 - 4.2.6, 4.2.25 - 4.2.27). The actual unknown functions in this solution are p_b and S_g, although the constraint conditions also give rise to values for p_g and S_b. As two dimensions in space and one dimension in time are in use, p_b, p_g, S_b and S_g are functions of the form $p_b(x, y, t)$, $p_g(x, y, t)$, $S_b(x, y, t)$ and $S_g(x, y, t)$.

The solution of the equations in Fig. 4.2.4 requires both initial value and boundary value conditions for p_b and S_g. The initial value conditions for p_b and S_g are given in Table 4.2.4. As indicated there, the calculation starts at time $t = -5$ yr, with a possible resetting of values at $t = 0$ yr, which corresponds to final waste emplacement and sealing of the repository. The boundary conditions are such that no brine or gas moves across the exterior grid boundary (Table 4.2.9). This Neumann-type boundary condition is maintained for all time. Further, BRAGFLO allows the user to specify pressure and/or saturation at any grid block. This feature is used to specify Dirichlet-type conditions at the surface grid blocks ($i = 1, 2, \ldots, 33, j = 31$, Fig. 4.2.1) and at the far field locations in the Culebra and Magenta formations ($i = 1, 33, j = 24$ and $i = 1, 33, j = 26$ in regions 17 and 15, Fig. 4.2.1) These auxiliary conditions are summarized in Table 4.2.10).

Table 4.2.8. Permeabilities Used with BRAGFLO Calculations for Drilling Intrusions Through the Repository (see materials 47, 48, 49, 50 in Table 4.2.2)

Time After Intrusion	Assigned Permeabilities
0 - 200 yr	Concrete plugs assumed to be emplaced at the Santa Rosa Fm (i.e., a surface plug with a length of 15.76 m; corresponds to grid cells 905, 937 in Fig. 4.2.3) and the Unnamed Mbr of the Rustler Fm (i.e., a plug at top of Salado Fm with a length of 36 m; corresponds to grid cell 681 in Fig. 4.2.3). Concrete plugs assumed to have a permeability of $k = 5 \times 10^{-17}$ m^2; remainder of borehole assumed to have a permeability of 1×10^{-9} m^2.
200 - 1200 yr	Concrete plugs are assumed to fail after 200 yr (U.S. DOE 1995b) and entire borehole is assigned a permeability typical of silty sand, i.e., $k = 10^x$ m^2, $x = BHPRM$, where $BHPRM$ is an uncertain input to the analysis (see Sect. 5.2).
> 1200 yr	Permeability reduced by one order of magnitude in Salado Fm beneath repository due to creep closure of borehole (Thompson et al. 1996) (i.e., $k = 10^x/10$, $x = BHPRM$, in grid cells 1010, 985, 12, 45, 78, 439, 453 of Fig. 4.2.3). No changes are made within and above the lower DRZ.

Table 4.2.9. Boundary Value Conditions for p_g and p_b, with the Imposed Conditions Resulting in No Flow Across the System Boundaries

Boundaries below ($y = 0$ m) and above ($y = 1039$ m)[a] system for $0 \le x \le 46630$ m and -5 yr $\le t$	
$(\nabla p_g + \rho_g g \nabla h)\|_{(x, y, t)} \bullet \mathbf{j} = 0$ Pa/m	no gas flow condition
$(\nabla p_b + \rho_b g \nabla h)\|_{(x, y, t)} \bullet \mathbf{j} = 0$ Pa/m	no brine flow condition
Boundaries at left ($x = 0$ m) and right ($x = 46630$ m) of system for $0 \le y \le 1039$ m and -5 yr $\le t$	
$(\nabla p_g + \rho_g g \nabla h)\|_{(x, y, t)} \bullet \mathbf{i} = 0$ Pa/m	no gas flow condition
$(\nabla p_b + \rho_b g \nabla h)\|_{(x, y, t)} \bullet \mathbf{i} = 0$ Pa/m	no brine flow condition

[a]Height of grid for disturbed (i.e., E1, E2) calculations; a grid with a height of 911 m used for undisturbed (i.e., E0) calculations.

Table 4.2.10. Auxiliary Dirichlet Conditions for p_b and S_g

Surface Grid Blocks	
$S_g(i, j, t) = 0.08363$	$i = 1, 2, \ldots, 33, j = 31, -5$ yr $\le t$
$p_b(i, j, t) = 1.01 \times 10^5$ Pa	$i = 1, 2, \ldots, 33, j = 31, -5$ yr $\le t$
Culebra and Magenta Far Field	
$p_b(i, 24, t) = 8.22 \times 10^5$ Pa	$i = 1$ and $33, j = 24, -5$ yr $\le t$ (Culebra)
$p_b(i, 26, t) = 9.17 \times 10^5$ Pa	$i = 1$ and $33, j = 26, -5$ yr $\le t$ (Magenta)

A fully implicit finite difference procedure is used to solve the two partial differential equations in Fig. 4.2.4. The associated discretization of the gas mass balance equation is given by

$$\frac{1}{\Delta x_i}\left\{\frac{1}{x_{i+1}-x_i}\left[\frac{\alpha\rho_g k_x k_{rg}}{\mu_g}\right]_{i+1/2,j}^{n+1}\left(\Phi_{gi+1,j}^{x-}-\Phi_{gi,j}^{x+}\right)^{n+1}-\frac{1}{x_i-x_{i-1}}\left[\frac{\alpha\rho_g k_x k_{rg}}{\mu_g}\right]_{i-1/2,j}^{n+1}\left(\Phi_{gi,j}^{x-}-\Phi_{gi-1,j}^{x+}\right)^{n+1}\right\}$$

$$+\frac{1}{\Delta y_j}\left\{\frac{1}{y_{j+1}-y_j}\left[\frac{\alpha\rho_g k_y k_{rg}}{\mu_g}\right]_{i,j+1/2}^{n+1}\left(\Phi_{gi,j+1}^{y-}-\Phi_{gi,j}^{y+}\right)^{n+1}-\frac{1}{y_j-y_{j-1}}\left[\frac{\alpha\rho_g k_y k_{rg}}{\mu_g}\right]_{i,j-1/2}^{n+1}\left(\Phi_{gi,j}^{y-}-\Phi_{gi,j-1}^{y+}\right)^{n+1}\right\}$$

$$+\alpha_{i,j}q_{wgi,j}^{n+1}+\alpha_{i,j}q_{rgi,j}^{n+1}-\frac{\left(\alpha\phi\rho_g S_g\right)_{i,j}^{n+1}-\left(\alpha\phi\rho_g S_g\right)_{i,j}^{n}}{\Delta t}=0, \qquad (4.2.72)$$

where Φ represents the phase potentials given by

$$\Phi_{gi,j}^{x+}=p_{gi,j}+\rho_{gi+1/2,j}gh_{i,j},\quad \Phi_{gi,j}^{x-}=p_{gi,j}+\rho_{gi-1/2j}gh_{i,j}$$

$$\Phi_{gi,j}^{y+}=p_{gi,j}+\rho_{gi,j+1/2}gh_{i,j},\quad \Phi_{gi,j}^{y-}=p_{gi,j}+\rho_{gi,j-1/2}gh_{i,j},$$

the subscripts are defined by

i	= x-direction grid index
j	= y-direction grid index
$i\pm1/2$	= x-direction grid block interface
$j\pm1/2$	= y-direction grid block interface
x_i	= grid block center in the x-coordinate direction (m)
y_j	= grid block center in the y-coordinate direction (m)
Δx_i	= grid block length in the x-coordinate direction (m)
Δy_j	= grid block length in the y-coordinate direction (m),

the superscripts are defined by

n	= index in the time discretization, known solution time level
$n+1$	= index in the time discretization, unknown solution time level,

and the interblock densities are defined by

$$\rho_{gi+1/2,j} = \frac{\Delta x_{i+1,j}}{\Delta x_{i,j} + \Delta x_{i+1,j}} \rho_{gi,j} + \frac{\Delta x_{i,j}}{\Delta x_{i,j} + \Delta x_{i+1,j}} \rho_{gi+1,j}$$

$$\rho_{gi-1/2,j} = \frac{\Delta x_{i,j}}{\Delta x_{i-1,j} + \Delta x_{i,j}} \rho_{g,i-1,j} + \frac{\Delta x_{i-1,j}}{\Delta x_{i-1,j} + \Delta x_{i,j}} \rho_{gi,j}$$

$$\rho_{gi,j+1/2} = \frac{\Delta y_{i,j+1}}{\Delta y_{i,j} + \Delta y_{i,j+1}} \rho_{gi,j} + \frac{\Delta y_{i,j}}{\Delta y_{i,j} + \Delta y_{i,j+1}} \rho_{gi,j+1}$$

$$\rho_{gi,j-1/2} = \frac{\Delta y_{i,j}}{\Delta y_{i,j-1} + \Delta y_{i,j}} \rho_{gi,j-1} + \frac{\Delta y_{i,j-1}}{\Delta y_{i,j-1} + \Delta y_{i,j}} \rho_{gi,j}$$

The interface values of k_{rg} in Eq. (4.2.72) are evaluated using upstream weighted values (i.e., the relative permeabilities at each grid block interface are defined to be the relative permeabilities at the center of the adjacent grid block that has the highest potential). Further, interface values for $\alpha\rho_g k_x/\mu_g$ and $\alpha\rho_g k_y/\mu_g$ are obtained by harmonic averaging of adjacent grid block values for these expressions (WIPP PA 1996a).

The discretization of the brine mass balance equation is obtained by replacing the subscript for gas, g, by the subscript for brine, b. As a reminder, p_g and S_b are replaced in the numerical implementation with the substitutions indicated in Fig. 4.2.4. For the 1996 WIPP PA, wells are not used in the conceptual model. Thus, the terms q_{wg} and q_{wb} are zero. For this analysis, the wellbore is not treated by a well model, but rather is explicitly modeled within the grid as a distinct material region (i.e., region 1 in Fig. 4.2.1).

The resultant coupled system of nonlinear brine and gas mass balance equations is integrated in time using the Newton Raphson method with upstream weighting of the relative permeabilities as previously indicated. The primary unknowns at each computational cell center are brine pressure and gas saturation.

4.2.9 Gas and Brine Flow across Specified Boundaries

The Darcy velocity vectors $\mathbf{v}_g(x, y, t)$ and $\mathbf{v}_b(x, y, t)$ for gas and brine flow ($(m^3/m^2)/s$ = m/s) are defined by the expressions

$$\mathbf{v}_g(x,y,t) = \mathbf{K}_g k_{rg}(\nabla p_g + \rho_g g \nabla h)/\mu_g \tag{4.2.73}$$

$$\mathbf{v}_b(x,y,t) = \mathbf{K}_b k_{rb}(\nabla p_b + \rho_b g \nabla h)/\mu_b \tag{4.2.74}$$

in Eqs. (4.2.1) and (4.2.2). Values for $\mathbf{v}_g$ and $\mathbf{v}_b$ are obtained and saved as the numerical solution of Eqs. (4.2.1) - (4.2.6) is carried out. Cumulative flows of gas, $C_g(t, \mathcal{B})$, and brine, $C_b(t, \mathcal{B})$, from time 0 to time t across an arbitrary boundary $\mathcal{B}$ in the domain of Eqs. (4.2.1) - (4.2.6) (i.e., Figs. 4.2.1 and 4.2.3) is then given by

$$C_l(t,\mathcal{B}) = \int_0^t \left[\int_{\mathcal{B}} \alpha(x,y)\, \mathbf{v}_l(x,y,t) \bullet \mathbf{n}(x,y) ds \right] dt \tag{4.2.75}$$

for $l = g, b$, where $\alpha(x, y)$ is the geometry factor defined in Fig. 4.2.2, $\mathbf{n}(x, y)$ is an outward pointing unit normal vector, and $\int_{\mathcal{B}} \sim ds$ denotes a line integral. As an example, $\mathcal{B}$ could correspond to the boundary of the waste disposal regions in Fig. 4.2.1. The integrals defining $C_g(t, \mathcal{B})$ and $C_b(t, \mathcal{B})$ can be evaluated from results calculated and saved during the numerical solution of Eqs. (4.2.1) - (4.2.6). Due to the dependence of gas volume on pressure, $C_g(t, \mathcal{B})$ is typically calculated in moles or in m^3 at standard temperature and pressure, which requires an appropriate change of units for $\mathbf{v}_g$ in Eq. (4.2.75).

4.2.10 Additional Information

Additional information on BRAGFLO and its use in the 1996 WIPP PA can be found in the BRAGFLO users manual (WIPP PA 1996a) and in the analysis package for the Salado flow calculations (Bean et al. 1996).

4.3 Radionuclide Transport in Vicinity of the Repository: NUTS (i.e., $f_{MB}, f_{DL}, f_S, f_{N\text{-}P}$)

4.3.1 Mathematical Description

The following system of partial differential equations is used to model radionuclide transport in the vicinity of the repository for E0, E1 and E2 conditions:

$$-\nabla \bullet \alpha \mathbf{v}_b C_{bl} + \alpha S_l = \alpha \frac{\partial}{\partial t}(\phi S_b C_{bl}) + (\alpha \phi S_b C_{bl})\lambda_l - \alpha \phi S_b \sum_{p \in \mathcal{P}(l)} C_{bp} \lambda_p \tag{4.3.1}$$

$$-S_l = \frac{\partial}{\partial t}(C_{sl}) + C_{sl}\lambda_l - \sum_{p \in \mathcal{P}(l)} C_{sp} \lambda_p \tag{4.3.2}$$

for $l = 1, 2, \ldots, nR$, where

- $\mathbf{v}_b$ = Darcy velocity vector ($(m^3/m^2)/s = m/s$) for brine (supplied by BRAGFLO from solution of Eqs. (4.2.1) - (4.2.6))
- C_{bl} = concentration (kg/m^3) of radionuclide l in brine
- C_{sl} = concentration (kg/m^3) of radionuclide l in solid phase (i.e., not in brine), with concentration defined with respect to total (i.e., bulk) formation volume (only used in repository, see Fig. 4.2.1)
- S_l = linkage term ($(kg/m^3)/s$) due to dissolution/precipitation between radionuclide l in brine and in solid phase (see Eqs. (4.3.3) - (4.3.6))
- ϕ = porosity (supplied by BRAGFLO from solution of Eqs. (4.2.1) - (4.2.6))
- S_b = brine saturation (supplied by BRAGFLO from solution of Eqs. (4.2.1) - (4.2.6))
- λ_l = decay constant (s^{-1}) for radionuclide l
- $\mathcal{P}(l)$ = $\{p$: radionuclide p is a parent of radionuclide $l\}$
- nR = number of radionuclides

and α is the dimension dependent geometry factor in Eq. (4.2.7). The 1996 WIPP PA uses a 2-dimensional representation for fluid flow and radionuclide transport in the vicinity of the repository with α defined by the element depths in Fig. 4.2.2. Although omitted from the notation for brevity, the terms α, $\mathbf{v}_b$, C_{bl}, C_{sl}, S_l, ϕ and S_b are functions $\alpha(x, y)$, $\mathbf{v}_b(x, y, t)$, $C_{bl}(x, y, t)$, $C_{sl}(x, y, t)$, $S_l(x, y, t)$, $\phi(x, y, t)$ and $S_b(x, y, t)$ of time t and the spatial variables x, y. The two preceding equations are defined and solved on the same computational grid used with BRAGFLO for the solution of Eqs. (4.2.1) - (4.2.6) (Fig. 4.2.1).

Radionuclides are present in both brine (Eq. (4.3.1)) and in an immobile solid phase (Eq. (4.3.2)). Radionuclide transport takes place only by brine flow (Eq. (4.3.1)). A maximum radionuclide concentration in brine is assumed for each element (see $S_T(Br, Ox, El)$ in Table 4.3.1). Then, each individual radionuclide equilibrates between the brine and solid phases on the basis of the maximum concentration of its associated element and the mole fractions of other isotopes of this element that are included in the calculation. The linkage between the brine and solid phases in Eqs. (4.3.1) and (4.3.2) is accomplished by the term S_l, where

$$S_l = \delta(\tau - t) Dif(S_T, C_{b,El(l)}) MF_{sl} \qquad (4.3.3)$$
$$\text{if } 0 \le Dif(S_T, C_{b,El(l)}) \le C_{s,El(1)} / (\phi S_b),\ 0 < S_b$$

$$= \delta(\tau - t)[C_{s,El(l)} / (\phi S_b)] MF_{sl} \qquad (4.3.4)$$
$$\text{if } 0 \le C_{s,El(l)} / (\phi S_b) < Dif(S_T, C_{b,El(l)}),\ 0 < S_b$$

$$= \delta(\tau - t) Dif(S_T, C_{b,El(l)}) MF_{bl} \qquad (4.3.5)$$
$$\text{if } Dif(S_T, C_{b,El(l)}) < 0,\ 0 < S_b$$

$$= 0 \quad \text{otherwise} \qquad (4.3.6)$$

with

$S_T[Br(t), Ox(l), El(l)]$ = maximum concentration (kg/m^3) of element $El(l)$ in oxidation statement $Ox(l)$ in brine type $Br(t)$, where $El(l)$ denotes the element of which radionuclide l is an isotope, $Ox(l)$ denotes the oxidation state in which element $El(l)$ is present, and $Br(t)$ denotes the type of brine present in the repository at time t (see Table 4.3.1 for definition of $S_T(Br, Ox, El)$ in units of mol/l; a conversion to kg/m^3 is required for use in conjunction with Eqs. (4.3.3) - (4.3.6) through the definition of $Dif(S_T, C_{b,El(l)})$ in Eq. (4.3.7))

$C_{b,El(l)}$ = concentration (kg/m^3) of element $El(l)$ in brine (i.e., sum of concentrations of radionuclides that are isotopes of same elements as radionuclide l, where $k \in \mathcal{E}(l)$ only if k is an isotope of element $El(l)$)

Table 4.3.1. Definition of Elemental Solubilities for Salado and Castile Brines (See Stockman et al. 1996 for additional information).

Dissolved Solubility $S_D(Br, Ox, El)$ (mol/l) as a Function of Type of Brine (Br ~ Salado, Castile), Oxidation State (Ox ~ +3, +4, +5, +6) and Element (El ~ americium, plutonium, uranium and thorium)

$S_D(Br, Ox, El) = S_{FMT}(Br, Ox)\ 10^{UF(Br,Ox,El)}$

where

$S_{FMT}(Br, Ox)$ = dissolved solubility (mol/l) calculated by FMT model (Siegel 1996) for brine type Br and oxidation state Ox (definition given below)

$UF(Br, Ox, El)$ = logarithm (base 10) of uncertainty factor for solubilities calculated by FMT expressed as a function of brine type Br, oxidation state Ox and element El (definition given below)

Dissolved Solubilities $S_{FMT}(Br, Ox)$ Calculated with FMT (mol/l)

Br/Ox	+3	+4	+5	+6
Salado	5.83×10^{-7}	4.4×10^{-6}	2.3×10^{-6}	8.7×10^{-6}
Castile	6.52×10^{-8}	6.0×10^{-9}	2.2×10^{-6}	8.8×10^{-6}

Uncertainty Factor $UF(Br, Ox, El)$ for Solubilities Calculated by FMT

Br/Ox, El	+3, Am	+3, Pu	+4, Pu	+4, U	+6, U	+4, Th
Salado	*WSOLAM3S*[a]	*WSOLPU3S*[a]	*WSOLPU4S*[a]	*WSOLU4S*[a]	*WSOLU6S*[a]	*WSOLTH4S*[a]
Castile	*WSOLAM3C*[a]	*WSOLPU3C*[a]	*WSOLPU4C*[a]	*0*	*WSOLU6C*[a]	*0*

Total (Colloidal and Dissolved) Solubility $S_T(Br, Ox, El)$ (mole/l) as a Function of Type of Brine (Br), Oxidation State (Ox) and Element (El)

$S_T(Br, Ox, El) = S_D(Br, Ox, El) + S_{Hum}(Br, Ox, El) + S_{Mic}(Br, Ox, El) + S_{Act}(El) + S_{Mn}$

where

$S_{Hum}(Br, Ox, El)$ = solubility (i.e., concentration expressed in mol/l) in brine type Br of element El in oxidation state Ox resulting from formation of humic colloids

= $min\{SF_{Hum}(Br, Ox, El)\ S_D(Br, Ox, El), UB_{Hum}\}$

$SF_{Hum}(Br, Ox, El)$ = scale factor used as a multiplier on $S_D(Br, Ox, El)$ in definition of $SF_{Hum}(Br, Ox, El)$ (definition given below)

UB_{Hum} = upper bound (i.e., cap) on solubility (i.e., concentration expressed in mol/l) of individual actinide elements resulting from formation of humic colloids

= 1.1×10^{-5} mol/l

$S_{Mic}(Br, Ox, El)$ = solubility (i.e., concentration expressed in mol/l) in brine type Br of element El in oxidation state Ox resulting from formation of microbial colloids

Table 4.3.1. Definition of Elemental Solubilities for Salado and Castile Brines (continued)

= $min\{SF_{Mic}(Ox, El)\ S_D(Br, Ox, El), UB_{Mic}(Ox, El)\}$

$SF_{Mic}(Ox, El)$ = scale factor used as multiplier on $S_D(Br, Ox, El)$ in definition of $S_{Mic}(Br, Ox, El)$ (definition given below)

$UB_{Mic}(Ox, El)$ = upper bound (i.e., cap) on solubility (i.e., concentration expressed in mol/l) of element El in oxidation state Ox resulting from formation of microbial colloids (definition given below)

$S_{Act}(El)$ = solubility (i.e., concentration expressed in mol/l) of element El resulting from formation of actinide intrinsic colloids

$$= \begin{cases} 1 \times 10^{-9} \text{ mol/l} & \text{if } El \sim \text{plutonium} \\ 0 \text{ mol/l} & \text{otherwise} \end{cases}$$

S_{Mn} = solubility (i.e., concentration expressed in mol/l) of individual actinide element resulting from formation of mineral fragment colloids

= 2.6×10^{-8} mol/l

Scale Factor $SF_{Hum}(Br, Ox, El)$ Used in Definition of $S_{Hum}(Br, Ox, El)$

Br/Ox, El	+3, Am	+3, Pu	+4, Pu	+4, U	+6, U	+4, Th
Salado	0.19	0.19	6.3	6.3	0.12	6.3
Castile	*WPHUMOX3*[a]	*WPHUMOX3*[a]	6.3	6.3	0.51	6.3

Scale Factor $SF_{Mic}(Ox, El)$ and Upper Bound $UB_{Mic}(Ox, El)$ (mol/l) Used in Definition of $S_{Mic}(Br, Ox, El)$

	+3, Am	+3, Pu	+4, Pu	+4, U	+6, U	+4, Th
$SF_{Mic}(Ox, El)$	3.6	0.3	0.3	2.1×10^{-3}	2.1×10^{-3}	3.1
$UB_{Mic}(Ox, El)$	1	6.8×10^{-5}	6.8×10^{-5}	2.1×10^{-3}	2.1×10^{-3}	1.9×10^{-3}

[a] See Sect. 5.2.

$$= \sum_{k \in \mathcal{E}(l)} C_{bk} \tag{4.3.7}$$

$Dif(S_T, C_{b,El(l)})$ = difference (kg/m^3) between maximum concentration of element $El(l)$ in brine and existing concentration of element $El(l)$ in brine

$$= S_T[Br(t), Ox(l), El(l)] - C_{b,El(l)} \tag{4.3.8}$$

MF_{pl} = mole fraction of radionuclide l in phase p, where $p = b$ ~ brine and $p = s$ ~ solids

$$= C_{pl} CM_l \Big/ \sum_{k \in \mathcal{E}(l)} C_{bk} CM_k \tag{4.3.9}$$

CM_l = conversion factor (mole/kg) from kilograms to moles for radionuclide l

$\delta(\tau - t)$ = Dirac delta function (s^{-1}) (i.e., $\delta(\tau - t) = 0$ if $\tau \neq t$ and $\int_{-\infty}^{\infty} \delta(\tau - t) d\tau = 1$).

Although omitted for brevity, the terms S_l, $C_{b,El(l)}$, $C_{s,El(l)}$, MF_{sl}, MF_{bl}, ϕ and S_b are functions of time t and spatial variables x, y. The Dirac delta function, $\delta(\tau - t)$, appears in Eqs. (4.3.3) - (4.3.5) to indicate that the adjustments to concentration are implemented instantaneously within the numerical solution of Eqs. (4.3.1) - (4.3.2) whenever a concentration imbalance is observed.

The velocity vector $\mathbf{v}_b$ in Eq. (4.3.1) is defined in Eq. (4.2.74) and is obtained from the numerical solution of Eqs. (4.2.1) - (4.2.6). If $\mathcal{B}$ denotes an arbitrary boundary (e.g., the land withdrawal boundary) in the domain of Eq. (4.3.1) (i.e., Fig. 4.2.1), then the cumulative transport of $C_l(t, \mathcal{B})$ of radionuclide l from time 0 to time t across $\mathcal{B}$ is given by

$$C_l(t, \mathcal{B}) = \int_0^t \left[\int_{\mathcal{B}} \mathbf{v}_b(x,y,t) C_l(x,y,t) \alpha(x,y) \bullet \mathbf{n}(x,y) ds \right] dt, \tag{4.3.10}$$

where $\mathbf{n}(x, y)$ is an outward pointing unit normal vector and $\int_{\mathcal{B}} \sim ds$ denotes a line integral over $\mathcal{B}$.

The system in Eqs. (4.3.1) - (4.3.2) models advective radionuclide transport due to the velocity vector $\mathbf{v}_b$. Although the effects of solubility limits are considered, no chemical or physical retardation is included in the model. Also, molecular diffusion is not included in the model, with this omission having little effect as the radionuclides under consideration have molecular diffusion coefficients on the order of 10^{-10} m^2/s and thus can be expected to move approximately 10 m over 10,000 yr due to molecular diffusion. Mechanical dispersion is also not included, with this omission having little effect on the final results due to the uniform initial radionuclide concentrations assumed within the repository and the use of time-integrated releases in assessing compliance with 40 CFR 191.13.

4.3.2 Radionuclides Transported

The WIPP is projected to contain 135 distinct radionuclides (U.S. DOE 1995a, Sanchez et al. 1997). Of these, 47 are regulated by 40 CFR 191, with 25 having more than 0.001 EPA units at some point in time over the 10,000 yr regulatory period (Table 4.3.2). In addition, several unregulated isotopes with short halflives exist that have significant inventory and decay to regulated radionuclides. Inclusion of these radionuclides resulted in a list of 33 radionuclides for possible radionuclide transport in the vicinity of the repository (Table 4.3.2).

Table 4.3.2. Radionuclides Considered for Transport in the Vicinity of the Repository in the 1996 WIPP PA with Time 0 yr Corresponding to Year 2033 (Sanchez et al. 1997)

Isotope	Half life (years)	Release Limit	0 years Ci	0 years EPA Units	100 years EPA Units	350 years EPA Units	10000 years EPA Units	MAX EPA Units
Pu-238	8.77E+01	344	1.94E+06	5.63E+03	2.55E+03	3.54E+02	1.32E-22	5.63E+03
Pu-239	2.41E+04	344	7.95E+05	2.31E+03	2.30E+03	2.29E+03	1.73E+03	2.31E+03
Am-241	4.32E+02	344	4.88E+05	1.42E+03	1.24E+03	8.31E+02	1.55E-01	1.42E+03
Pu-240	6.54E+03	344	2.14E+05	6.23E+02	6.17E+02	6.01E+02	2.16E+02	6.23E+02
Cs-137	3.00E+01	3440	9.31E+04	2.71E+01	2.68E+00	8.32E-03	0.00E+00	2.71E+01
Sr-90	2.91E+01	3440	8.73E+04	2.54E+01	2.35E+00	6.12E-03	0.00E+00	2.54E+01
U -233	1.59E+05	344	1.95E+03	5.67E+00	5.66E+00	5.66E+00	5.44E+00	5.67E+00
U -234	2.45E+05	344	7.51E+02	2.18E+00	3.28E+00	4.07E+00	4.09E+00	4.09E+00
Th-230	7.70E+04	34	3.06E-01	8.88E-03	3.41E-02	1.20E-01	3.56E+00	3.56E+00
Pu-242	3.76E+05	344	1.17E+03	3.40E+00	3.40E+00	3.40E+00	3.34E+00	3.40E+00
Th-229	7.34E+03	344	9.97E+00	2.90E-02	8.19E-02	2.12E-01	3.40E+00	3.40E+00
Np-237	2.14E+06	344	6.49E+01	1.89E-01	2.32E-01	3.15E-01	4.82E-01	4.82E-01
Cm-245	8.53E+03	344	1.15E+02	3.33E-01	3.31E-01	3.24E-01	1.48E-01	3.33E-01
Ra-226	1.60E+03	344	1.14E+01	3.32E-02	3.19E-02	2.94E-02	2.77E-01	2.77E-01
Pb-210	2.23E+01	344	8.75E+00	2.54E-02	3.19E-02	2.96E-02	2.77E-01	2.77E-01
U -238	4.47E+09	344	5.01E+01	1.46E-01	1.46E-01	1.46E-01	1.46E-01	1.46E-01
U -236	2.34E+07	344	6.72E-01	1.95E-03	3.79E-03	8.29E-03	1.16E-01	1.16E-01
Am-243	7.37E+03	344	3.25E+01	9.45E-02	9.36E-02	9.14E-02	3.69E-02	9.45E-02
U -235	7.04E+08	344	1.75E+01	5.08E-02	5.10E-02	5.16E-02	7.06E-02	7.06E-02
Cm-243	2.91E+01	344	2.07E+01	6.03E-02	5.30E-03	1.21E-05	0.00E+00	6.03E-02
U -232	6.89E+01	344	1.79E+01	5.21E-02	1.99E-02	1.79E-03	0.00E+00	5.21E-02
C -14	5.72E+03	344	1.28E+01	3.72E-02	3.68E-02	3.57E-02	1.11E-02	3.72E-02
Th-232	1.41E+10	34	1.01E+00	2.92E-02	2.92E-02	2.92E-02	2.92E-02	2.92E-02
Ac-227	2.18E+01	344	5.05E-01	1.47E-03	1.43E-03	1.69E-03	1.28E-02	1.28E-02
Pa-231	3.28E+04	344	4.67E-01	1.36E-03	1.46E-03	1.72E-03	1.28E-02	1.28E-02
Cm-248	3.39E+05	344	3.72E-02	3.72E-04	3.72E-04	3.71E-04	3.64E-04	3.72E-04
Pu-244	8.26E+07	344	1.51E-06	1.51E-08	1.54E-08	1.61E-08	4.34E-08	4.34E-08
Sm-147	1.06E+11	344	4.55E-10	4.55E-12	4.55E-12	4.55E-12	4.55E-12	4.55E-12
Pm-147	2.62E+00		8.10E-04					
Ra-228	5.75E+00		1.00E+00					
Cf-252	2.64E+00		1.72E-04					
Cm-244	1.81E+01		7.44E+03					
Pu-241	1.44E+01		3.94E+05					

With the exceptions of ^{14}C, ^{137}Cs, ^{147}Pm, ^{90}Sr and ^{232}U, the radionuclides in Table 4.3.2 belong to the following decay chains:

$$^{242}Pu \rightarrow {}^{238}U \rightarrow {}^{234}U \rightarrow {}^{230}Th \rightarrow {}^{226}Ra \rightarrow {}^{210}Pb \quad (4.3.11)$$

$$^{243}Am \rightarrow {}^{239}Pu \rightarrow {}^{235}U \rightarrow {}^{231}Pa \rightarrow {}^{227}Ac \quad (4.3.12)$$

$$^{252}Cf \rightarrow {}^{248}Cm \rightarrow {}^{244}Pu \rightarrow {}^{240}Pu \rightarrow {}^{236}U \rightarrow {}^{232}Th \rightarrow {}^{228}Ra \quad (4.3.13)$$

$$^{245}Cm \rightarrow {}^{241}Pu \rightarrow {}^{241}Am \rightarrow {}^{237}Np \rightarrow {}^{233}U \rightarrow {}^{229}Th. \quad (4.3.14)$$

As solution of Eqs. (4.3.1) - (4.3.2) for this many radionuclides and decay chains is a very time-consuming process, the number of radionuclides for direct inclusion in the analysis had to be reduced. To this end, the indicated radionuclides and decay chains were carefully examined to determine the minimum number of radionuclides required to appropriately assess the WIPP's compliance with 40 CFR 191.

Initially, radionuclides with low EPA inventories or short half-lives were dropped from consideration. In particular, radionuclides having maximum EPA inventories less than or equal to the maximum inventory of ^{237}Np were dropped from consideration. The *sum* of the *maximum* EPA units dropped from consideration was 1.6 EPA units, which is approximately 0.01% of the total EPA units in the repository. Nearly the entire inventory of these radionuclides would have to be released from the repository to produce a situation with the potential to cause a violation of 40 CFR 191. If conditions occurred that could cause such a large release of these radionuclides, then large releases of other more important radionuclides would also occur and dominate the size of the total release.

Although ^{137}Cs and ^{90}Sr have large initial inventories, they were dropped from consideration because of the rapidity with which their initial inventories decayed to less than 1 EPA unit (i.e., 136 yr for ^{137}Cs and 128 yr for ^{90}Sr). Short-lived, and therefore unregulated radionuclides, at the top of decay chains were examined to determine if their decay could significantly increase the inventory of important radionuclides, with this examination resulting in the decision to retain ^{241}Pu for inclusion in the analysis. At this point, the following 10 radionuclides accounting for 98.9% of the initial EPA units in the waste remained (Fig. 4.3.1):

$$^{238}Pu \rightarrow {}^{234}U \rightarrow {}^{230}Th \quad (4.3.15)$$

$$^{241}Pu \rightarrow {}^{241}Am \rightarrow {}^{233}U \rightarrow {}^{229}Th \quad (4.3.16)$$

$$^{242}Pu, {}^{240}Pu, {}^{239}Pu. \quad (4.3.17)$$

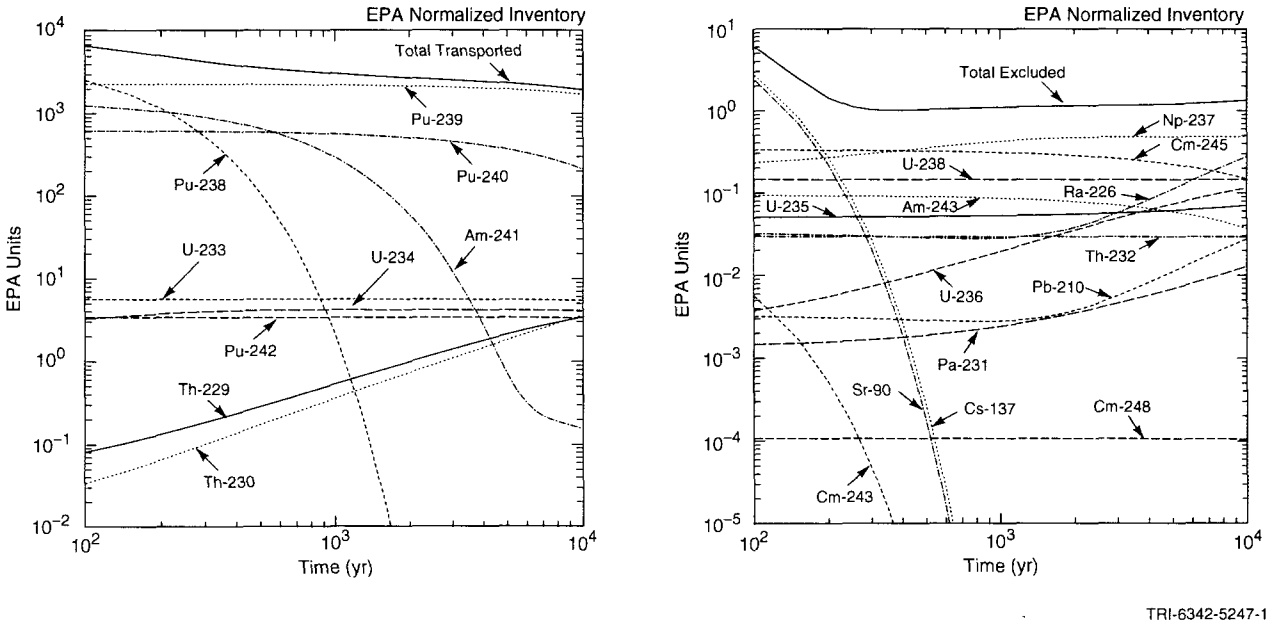

Fig. 4.3.1. Time-dependent radionuclide inventories expressed in EPA units (i.e., the normalized units used in showing compliance with 191.13(a)) for entire repository (Sanchez et al. 1997). Left frame shows radionuclides included in groundwater transport calculations; right frame shows radionuclides not included in groundwater transport because of low inventory or short half-life. All radionuclides shown are included in estimates of cuttings and cavings and spallings; direct brine releases included all except Sr-90, Cs-137, Pb-210, Ra-226, and Pa-231.

The remaining 10 radionuclides were then further reduced by combining radionuclides that have similar decay and transport properties. In particular, ^{234}U, ^{230}Th and ^{239}Pu were used as surrogates for the groups {^{234}U, ^{233}U}, {^{230}Th, ^{229}Th} and {^{242}Pu, ^{239}Pu, ^{240}Pu}, with the initial inventories of ^{234}U, ^{230}Th and ^{239}Pu being redefined to account for the additional radionuclide(s) in each group. In redefining the initial inventories, the individual radionuclides were combined on either a mole or Curie basis (i.e., moles added and then converted back to Curies or Curies added directly). In each case, the method that maximized the combined inventory was used, i.e.; ^{233}U was Curie added to ^{234}U, ^{240}Pu was Curie added to ^{239}Pu, ^{242}Pu was mole added to ^{239}Pu, and ^{229}Th was Curie added to ^{230}Th. In addition, ^{241}Pu was mole added to ^{241}Am because it has a half life of 14 years and will quickly decay to ^{241}Am, and neglect of this ingrowth would underestimate the ^{241}Am inventory by about 3% (Table 4.3.3). The outcome of this process was the following 5 radionuclides and 3 simplified decay chains:

$$^{241}\text{Am}, \; ^{238}\text{Pu} \rightarrow ^{234}\text{U} \rightarrow ^{230}\text{Th}, \; ^{239}\text{Pu}, \tag{4.3.18}$$

Table 4.3.3. Construction of Initial Inventories Associated with Reduction of 10 Radionuclides to 5 Radionuclides

Conversions	Conversion Procedure	New Inventory $A(0)$
$^{233}U \rightarrow ^{234}U$	1.95×10^3 Ci $^{233}U \rightarrow 1.95 \times 10^3$ Ci $^{234}U = 1.33 \times 10^3$ mol ^{234}U	2.70×10^3 Ci ^{234}U
	Original: 7.51×10^2 Ci $^{234}U = 5.14 \times 10^2$ mol ^{234}U	4.32×10^2 kg ^{234}U
$^{240}Pu \rightarrow ^{239}Pu$	2.14×10^5 Ci $^{240}Pu \rightarrow 2.14 \times 10^5$ Ci $^{239}Pu = 1.44 \times 10^4$ mol ^{239}Pu	1.03×10^6 Ci ^{239}Pu
$^{242}Pu \rightarrow ^{239}Pu$	1.23×10^3 mol $^{242}Pu \rightarrow 1.23 \times 10^3$ mol $^{239}Pu = 1.83 \times 10^4$ Ci ^{239}Pu	1.65×10^4 kg ^{239}Pu
	Original: 5.35×10^4 mol $^{239}Pu = 7.95 \times 10^5$ Ci ^{239}Pu	
$^{229}Th \rightarrow ^{230}Th$	9.97×10^0 Ci $^{229}Th \rightarrow 9.97 \times 10^0$ Ci $^{230}Th = 2.15 \times 10^0$ mol ^{230}Th	1.03×10^1 Ci ^{230}Th
	Original: 6.57×10^{-2} mol $^{230}Th = 3.05 \times 10^{-1}$ Ci ^{230}Th	5.09×10^{-1} kg ^{230}Th
$^{241}Pu \rightarrow ^{241}Am$	1.59×10^1 mol $^{241}Pu \rightarrow 1.59 \times 10^1$ mol $^{241}Am = 1.31 \times 10^4$ Ci ^{241}Am	5.01×10^5 Ci ^{241}Am
	Original: 5.89×10^2 mol $^{241}Am = 4.87 \times 10^5$ Ci ^{241}Am	1.46×10^2 kg ^{241}Am

which were then used with Eqs. (4.3.1) - (4.3.2) for transport in the vicinity of the repository and also for transport in the Culebra Dolomite (Sect. 4.9), with Pu-238 omitted from transport in the Culebra due to its short half life (i.e., 87.7 yr).

4.3.3 Numerical Solution

Eqs. (4.3.1) - (4.3.2) are numerically solved by the NUTS program (WIPP PA 1996b; Stockman et al. 1996) on the same computational grid (Fig. 4.2.1) used by BRAGFLO in the solution of Eqs. (4.2.1) - (4.2.6). In the solution procedure, Eq. (4.3.1) is numerically solved with $S_l = 0$ for each time step, with the instantaneous updating of concentrations indicated in Eqs. (4.3.3) - (4.3.6) and the appropriate modification to C_{sl} in Eq. (4.3.2) taking place after the time step. The solution is carried out for the 5 radionuclides indicated in Eq. (4.3.16).

The initial value and boundary value conditions used with Eqs. (4.3.1) - (4.3.2) are given in Table 4.3.4. At time $t = 0$ (i.e., year 2033), the total inventory of each radionuclide is assumed to be in brine; the solubility constraints associated with Eqs. (4.3.3) - (4.3.6) then immediately adjust the values for $C_{bl}(x, y, t)$ and $C_{sl}(x, y, t)$ for consistency with the constraints imposed by $S_T[Br(t), Ox(l), El(l)]$ and available radionuclide inventory.

Table 4.3.4. Initial Value and Boundary Value Conditions for $C_{bl}(x, y, t)$ and $C_{sl}(x, y, t)$

Initial Value Conditions for $C_{bl}(x, y, t)$ and $C_{sl}(x, y, t)$	
$C_{bl}(x, y, 0) = A_l(0)/V_b(0)$	if x, y point in repository (i.e., in regions 23, 24 of Fig. 4.2.1), where $A_l(0)$ is the amount (kg) of radionuclide l present at time $t = 0$ (Table 4.3.3) and $V_b(0)$ is the amount (m^3) of brine in repository at time $t = 0$ (from solution of Eqs. (4.2.1) - (4.2.6) with BRAGFLO) for all x, y.
$= 0$	otherwise
$C_{sl}(x, y, 0) = 0$	if x, y point in repository
Boundary Value Conditions for $C_{bl}(x, y, t)$	
$f_l(\mathcal{B}, t) = \int_{\mathcal{B}} \mathbf{v}_b(x,y,t) C_{bl}(x,y,t) \alpha(x,y) \bullet \mathbf{n}(x,y) ds$, where $\mathcal{B}$ is any subset of the outer boundary of the computational grid in Figs. 4.2.1 and 4.2.3, $f_l(\mathcal{B}, t)$ is the flux (kg/s) at time t of radionuclide l across $\mathcal{B}$, $\mathbf{v}_b(x, y, t)$ is the Darcy velocity ($(m^3/m^2)/s$) of brine at (x, y) on $\mathcal{B}$ and is obtained from the solution of Eqs. (4.2.1) - (4.2.6) by BRAGFLO, $\mathbf{n}(x, y)$ denotes an outward-pointing unit normal vector, and $\int_{\mathcal{B}} \sim ds$ denotes a line integral along $\mathcal{B}$	

The *nR* partial differential equations in Eq. (4.3.1) are discretized in two dimensions and then developed into a linear system of algebraic equations for numerical implementation. The following conventions are used in the representation of each discretized equation:

- the subscript b is dropped from C_{bl}, with the result that the unknown function is represented by C_l,
- a superscript n denotes time (t_n), with the assumption that the solution C_l is known at time t_n and is to be advanced (i.e., computed) at time t_{n+1},
- the grid indices are i in the x-direction, j in the y-direction, and are identical with the BRAGFLO grid indices; fractional indices refer to quantities evaluated at grid block interfaces,
- each time step by NUTS is equal to 20 BRAGFLO time steps, which results because BRAGFLO reported (i.e., stored) results (i.e., $\mathbf{v}_b$, ϕ, S_b) every 20 time steps.

The following finite difference discretization is used for the l^{th} equation in each grid block i, j:

$$q^{n+1}_{b,i+1/2,j}C^{n+1}_{l,i+1/2,j} - q^{n+1}_{b,i-1/2,j}C^{n+1}_{l,i-1/2,j} + q^{n+1}_{b,i,j+1/2}C^{n+1}_{l,i,j+1/2} - q^{n+1}_{b,i,j-1/2}C^{n+1}_{l,i,j-1/2} =$$

$$\frac{V_{R,i,j}}{\Delta t}\left[\left\{\phi_{i,j}S_{b_{i,j}}C_{l,i,j}\right\}^{n+1} - \left\{\phi_{i,j}S_{b_{i,j}}C_{l,i,j}\right\}^{n}\right] + V_{R,i,j}\left\{\phi_{i,j}S_{b_{i,j}}C_{l,i,j}\right\}^{n+1}\lambda_l - V_{R,i,j}\left(\phi_{i,j}S_{b_{i,j}}\right)^{n+1}\sum_{p\in\mathcal{P}(l)}C^{n+1}_{p,i,j}\lambda_p,$$

(4.3.19)

where q_b is the grid block interfacial brine flow rate (m^3/s) and V_R is the grid block volume (m^3). The quantity q_b is based on $\mathbf{v}_b$ and α in Eq. (4.3.1), and the quantity V_R is based on grid block dimensions (Fig. 4.2.1) and α.

The interfacial values of concentration in Eq. (4.3.18) are discretized using the one-point upstream weighting method (Aziz and Settari 1979), which results in

$$q^{n+1}_{b,i+1/2,j}\left(\omega_{i+1}C^{n+1}_{l,i,j} + (1-\omega_{i+1})C^{n+1}_{l,i+1,j}\right) - q^{n+1}_{b,i-1/2,j}\left(\omega_i C^{n+1}_{l,i-1,j} + (1-\omega_i)C^{n+1}_{l,i,j}\right)$$

$$+q^{n+1}_{b,i,j+1/2}\left(\omega_{j+1}C^{n+1}_{l,i,j} + (1-\omega_{j+1})C^{n+1}_{l,i,j+1}\right) - q^{n+1}_{b,i,j-1/2}\left(\omega_j C^{n+1}_{b,i,j-1} + (1-\omega_j)C^{n+1}_{l,i,j}\right)$$

$$= \frac{V_{R,i,j}}{\Delta t}\left[\left\{\phi_{i,j}S_{b_{i,j}}C_{l,i,j}\right\}^{n+1} - \left\{\phi_{i,j}S_{b_{i,j}}C_{l,i,j}\right\}^{n}\right] + V_{R,i,j}\left\{\phi_{i,j}S_{b_{i,j}}C_{l,i,j}\right\}^{n+1}\lambda_l$$

$$-V_{R,i,j}\left(\phi_{i,j}S_{b_{i,j}}\right)^{n+1}\sum_{p\in\mathcal{P}(l)}C^{n+1}_{p,i,j}\lambda_p, \qquad (4.3.20)$$

where ω derives from the upstream weighting for flow between adjacent grid blocks and is defined by

$$\omega_i = \begin{cases} 1 & \text{if flow is from grid block } i-1, j \text{ to grid block } i, j \\ 0 & \text{otherwise} \end{cases}$$

$$\omega_j = \begin{cases} 1 & \text{if flow is from grid block } i, j-1 \text{ to grid block } i, j \\ 0 & \text{otherwise.} \end{cases}$$

By collecting similar terms, Eq. (4.3.19) can be represented by the linear equation

$$AC^{n+1}_{l,i,j-1} + BC^{n+1}_{l,i-1,j} + DC^{n+1}_{l,i,j} + EC^{n+1}_{l,i+1,j} + FC^{n+1}_{l,i,j+1} = R_{l,i,j}, \qquad (4.3.21)$$

where

$$A = -\omega_j q^{n+1}_{b,i,j-1/2},\ B = -\omega_i q^{n+1}_{b,i-1/2,j},\ E = (1-\omega_{i+1}) q^{n+1}_{b,i+1/2,j},\ F = (1-\omega_{j+1}) q^{n+1}_{b,i,j+1/2},$$

$$D = -(1-\omega_j) q^{n+1}_{b,i,j-1/2} - (1-\omega_i) q^{n+1}_{b,i-1/2,j} + \omega_{j+1} q^{n+1}_{b,i,j+1/2} + \omega_{i+1} q^{n+1}_{b,i+1/2,j}$$

$$- \frac{V_{R,i,j}}{\Delta t} \left\{ \phi_{i,j} S_{b_{i,j}} \right\}^{n+1} + V_{R,i,j} \left\{ \phi_{i,j} S_{b_{i,j}} \right\}^{n+1} \lambda_l$$

$$R_{l,i,j} = -\frac{V_{R,i,j}}{\Delta t} \left\{ \phi_{i,j} S_{b_{i,j}} C_{l,i,j} \right\}^{n} - V_{R,i,j} \left(\phi_{i,j} S_{b_{i,j}} \right)^{n+1} \sum_{p \in \mathfrak{R}(l)} C^{n+1}_{p,i,j} \lambda_p .$$

Given the form of Eq. (4.3.21), the solution of Eq. (4.3.1) has now been reduced to the solution of $nR \times nG$ linear algebraic equations in $nR \times nG$ unknowns, where nR is the number of equations for each grid block (i.e., the number of radionuclides) and nG is the number of grid blocks into which the spatial domain is discretized (Fig. 4.2.1).

The system of partial differential equations in Eq. (4.3.1) is strongly coupled because of the contribution from parental decay to the equation governing the immediate daughter. Consequently, a sequential method is used to solve the system in which radionuclide concentrations are solved for by starting at the top of a decay chain and working down from parent to daughter. This implies that when solving Eq. (4.3.21) for the l^{th} isotope concentration, all parent concentrations occurring in the right hand side term R are known. The resulting system of equations is then linear in the concentrations of the l^{th} isotope. As a result, solution of Eq. (4.3.1) is reduced from the solution of one algebraic equation at each time step with $nR \times nG$ unknowns to the solution of nR algebraic equations each with nG unknowns at each time step, which can result in a significant computational savings.

The matrix resulting from one-point upstream weighting has the following structural form for a 3×3 system of grid blocks and a similar structure for a larger number of grid blocks:

	1	2	3	4	5	6	7	8	9
1	X	X	0	X					
2	X	X	X	0	X				
3	0	X	X	0	0	X			
4	X	0	0	X	X	0	X		
5		X	0	X	X	X	0	X	
6			X	0	X	X	0	0	X
7				X	0	0	X	X	0
8					X	0	X	X	X
9						X	0	X	X

where X designates possible nonzero matrix entries, and 0 designates zero entries. Entries outside of the banded structure are zero. Because of this structure, a banded direct elimination solver (Sect. 8.2.1, Aziz and Settari 1979) is used to solve the linear system for each radionuclide. The bandwidth is minimized by indexing equations first in

the coordinate direction having the minimum number of grid blocks. The coefficient matrix is stored in this banded structure and all infill coefficients calculated during the elimination procedure are contained within the band structure. Therefore, for the matrix system in two dimensions, a pentadiagonal matrix of dimension $IBW \times nG$ is inverted instead of a full $nG \times nG$ matrix, where IBW is the band width.

The numerical implementation of Eq. (4.3.2) enters the solution process through an updating of the radionuclide concentrations in Eq. (4.3.20) between each time step as indicated in Eqs. (4.3.3) - (4.3.6).

The numerical solution of Eqs. (4.3.1) and (4.3.2) also generates the concentrations required for the numerical evaluation of the integral that defines $C_l(t, \mathcal{B})$ in Eq. (4.3.10).

4.3.4 Additional Information

Additional information on NUTS and its use in the 1996 WIPP PA can be found in the NUTS users manual (WIPP PA 1996b) and in the analysis package for Salado transport calculations (Stockman et al. 1996). Further, additional information on dissolved and colloidal actinides is given in Stockman and Moore (1998).

4.4 Radionuclide Transport in Vicinity of Repository: PANEL (i.e., f_S, f_{N-P})

4.4.1 Mathematical Description

A relatively simple mixed-cell model is used for radionuclide transport in the vicinity of the repository when connecting flow between two drilling intrusions into the same waste panel is assumed to take place (i.e., an E2E1 intrusion). With this model, the amount of radionuclide l contained in a waste panel is represented by

$$dA_l / dt = -r_b C_{bl} - \lambda_l A_l + \sum_{p \in \mathcal{P}(l)} \lambda_p A_p \tag{4.4.1}$$

where

$A_l(t)$ = amount (mol) of radionuclide l in waste panel at time t

$C_{bl}(t)$ = concentration (mol/m^3) of radionuclide l in brine in waste panel at time t (see Eqs. (4.4.2) - (4.4.3))

$r_b(t)$ = rate (m^3/s) at which brine flows out of the repository at time t (supplied by BRAGFLO from solution of Eqs. (4.2.1) - (4.2.6)),

and λ_l and $\mathcal{P}(l)$ are defined in conjunction with Eqs. (4.3.1) - (4.3.2).

The brine concentration C_{bl} in Eq. (4.4.1) is defined by

$$C_{bl}(t) = S_T[Br(t), Ox(l), El(l)]\, MF_l(t) \quad \text{if } S_T[Br(t), Ox(l), El(l)] \le \sum_{k \in \mathcal{E}(l)} A_k(t) / V_b(t) \tag{4.4.2}$$

$$= A_l(t) / V_b(t), \quad \text{if } \sum_{k \in \mathcal{E}(l)} A_k(t) / V_b(t) < S_T[Br(t), Ox(l), El(l)] \tag{4.4.3}$$

where

$MF_l(t)$ = mole fraction of radionuclide l in waste panel at time t

$$= A_l(t) / \sum_{k \in \mathcal{E}(l)} A_k(t) \tag{4.4.4}$$

$V_b(t)$ = volume (m^3) of brine in waste panel at time t (supplied by BRAGFLO from solution of Eqs. (4.2.1) - (4.2.6)),

and $S_T[Br(t), Ox(l), El(l)]$ and $\mathcal{E}(l)$ are defined in conjunction with Eqs. (4.3.3) - (4.3.7). For use in Eqs. (4.4.2) and (4.4.3), $S_T[Br(t), Ox(l), El(l)]$ must be expressed in units of mol/l. In words, $C_{bl}(t)$ is defined to be the maximum brine concentration specified in Table 4.3.1 if there is sufficient radionuclide inventory in the waste panel to generate this concentration (Eq. (4.4.2)); otherwise, $C_{bl}(t)$ is defined by the concentration that results when all the relevant element in the waste panel is placed in solution (Eq. (4.4.3)).

Given r_b and C_{bl}, evaluation of the integral

$$R_l(t) = \int_0^t r_b C_{bl} dt \tag{4.4.5}$$

provides the cumulative release $R_l(t)$ of radionuclide l from the waste panel through time t.

The preceding model was used in two ways in the 1996 WIPP PA. First, Eq. (4.4.5) was used to estimate releases associated with E2E1 intrusions (Sect. 11.1). Second, with r_b set to a very small number and V_b set to a fixed value, Eqs. (4.4.2) - (4.4.3) were used to estimate radionuclide concentrations for use in the estimation of direct brine releases (Sects. 10.1, 10.2).

4.4.2 Radionuclides Transported

When used for E2E1 intrusions, the results in Eqs. (4.4.1) - (4.4.5) were calculated for all isotopes of americium, curium, neptunium, plutonium, thorium and uranium in Table 4.3.2. Then, the release was converted to

^{234}U, ^{239}Pu, ^{230}Th and ^{241}Am as indicated in Table 4.3.3 for transport in the Culebra. When used to support the calculation of direct brine releases, Eqs. (4.4.1) - (4.4.3) were used to obtain time-dependent concentrations for all isotopes of the preceding elements in Table 4.3.2 that have EPA release limits. Then, these individual concentrations were used to obtain an overall concentration (EPA units/m^3).

4.4.3 Numerical Solution

The results in Eqs. (4.4.1) - (4.4.5) are numerically evaluated by the PANEL model (WIPP PA 1996c). For E2E1 intrusions, the initial values are the inventories of the isotopes of americium, curium, neptunium, plutonium, thorium and uranium in Table 4.3.2 at the time of the E1 intrusion; these inventories for intrusions at 100, 350 and 10,000 yr are listed in Table 4.3.2. For use as part of the direct brine release calculations, the initial values are the values for A_l (0) (i.e., for $t = 0$ yr) in Table 4.3.2 for the radionuclides with EPA release limits.

A discretization based on 50 yr or smaller time steps is used by PANEL to evaluate the results in Eqs. (4.4.1) - (4.4.5). Specifically, Eq. (4.4.1) is evaluated with the approximation

$$A_l(t_{n+1}) = A_l(t_n) - \left[\int_{t_n}^{t_{n+1}} r_b(\tau)d\tau\right] C_{bl}(t_n) - A_l(t_n)\exp(-\lambda_l \Delta t) + G_l(t_n, t_{n+1}), \tag{4.4.6}$$

where

$G_l(t_n,t_{n+1})$ = gain in radionuclide l due to the decay of precursor radionuclides between t_n and t_{n+1} (see Eq. (4.4.7))

Δt = $t_{n+1} - t_n = 50$ yr.

As the solution progresses, values for $C_{bl}(t_n)$ are updated in consistency with Eqs. (4.4.2) - (4.4.3) and the products $r_b(t_n)C_{bl}(t_n)$ are accumulated to provide an approximation to R_l in Eq. (4.4.5).

The term $G_l(t_n,t_{n+1})$ in Eq. (4.4.6) is evaluated with the Bateman equations (Bateman 1910), with PANEL programmed to handle up to 4 succeeding generations of a given radionuclide (i.e., decay chains of length 5). As a single example, if radionuclide l is the third radionuclide in a decay chain (i.e., $l = 3$) and the two preceding radionuclides in the decay chain are designated by $l = 1$ and $l = 2$, then

$$\begin{aligned} G_3(t_n,t_{n+1}) = {} & \lambda_2 A_2(t_n)[\exp(-\lambda_2\Delta t) - \exp(-\lambda_3\Delta t)]/(\lambda_3 - \lambda_2) \\ & + \lambda_1\lambda_2 A_1(t_n)\{[\exp(-\lambda_1\Delta t)]/[(\lambda_2\lambda_1)(\lambda_3\lambda_1)] \\ & + [\exp(-\lambda_2\Delta t)]/[(\lambda_3 - \lambda_2)(\lambda_1 - \lambda_2)] \\ & + [\exp(-\lambda_3\Delta t)]/[(\lambda_1 - \lambda_3)(\lambda_2 - \lambda_3)]\} \end{aligned} \tag{4.4.7}$$

in Eq. (4.4.6).

4.4.4 Additional Information

Additional information on PANEL and its use in the 1996 WIPP PA calculations can be found in the PANEL users manual (WIPP PA 1996c) and the analysis package for Salado transport calculations (Stockman et al. 1996).

4.5 Cuttings and Cavings to Surface: CUTTINGS_S (i.e., f_C)

4.5.1 Release Mechanisms for Solid Waste

Three separate release modes, cuttings, cavings and spallings, are believed to determine the quantity of solid waste brought to the ground surface as the result of a drilling intrusion through a waste panel, where cuttings designates the waste contained in the cylindrical volume created by the cutting action of the drill bit passing through the waste, cavings designates the waste that erodes from the borehole in response to the upward-flowing drilling fluid within the borehole, and spallings designates the waste introduced into the borehole by the release of waste-generated gas escaping to the lower-pressure borehole. The releases associated with these processes are computed within the CUTTINGS_S code (WIPP PA 1996d). The mathematical representations used for the first two processes, cuttings and cavings, are described in the present section (Sect. 4.5). Then, the representation used for spallings is described in Sect. 4.6.

4.5.2 Cuttings

The uncompacted volume of cuttings removed and transported to the surface in the drilling mud, V_{cut}, is given by

$$V_{cut} = AH_i = \pi D^2 H_i / 4, \tag{4.5.1}$$

where H_i is the initial (i.e., uncompacted) repository height (m), A is the drill bit area (m^2), and D is the drillbit diameter (m). In the 1996 WIPP PA, D = 12.25 in. = 0.31115 m and H_i = 3.96 m (Sect. 7.0, Berglund 1996a). For drilling intrusions through RH-TRU waste, H_i = 0.509 m is used (Tierney 1996b). The size of the cuttings release is independent of the conditions that exist in the repository at the time of a drilling intrusion, with the result that the cuttings volume V_{cut} is a lower bound on the quantity of material removed by a drilling intrusion.

4.5.3 Cavings (adapted from Sect. 3.5 of Helton et al. 1995a)

The cavings component of the direct surface release is caused by the shearing action of the drilling fluid (mud) on the waste as the mud flows up the borehole annulus. As is the case for the cuttings release, the cavings release is assumed to be independent of the conditions that exist in the repository at the time of a drilling intrusion.

The final diameter of the borehole will depend on the diameter of the drill-bit and on the extent to which the actual borehole diameter exceeds the drill-bit diameter. Although a number of factors affect erosion within a

borehole (Broc 1982), the most important factor is believed to be the fluid shear stress on the borehole wall (i.e., the shearing force per unit area, (kg m/s^2/m^2) resulting from circulating drilling fluids (Darley 1969, Walker and Holman 1971). As a result, the 1996 WIPP PA estimates cavings removal with a model based on the effect of shear stress on the borehole diameter. In particular, the borehole diameter is assumed to grow until the shear stress on the borehole wall is equal to the shear strength of the waste (i.e., the limiting shear stress below which the erosion of the waste ceases).

The final eroded diameter D_f (m) of the borehole through the waste determines the volume V (m^3) of uncompacted waste that will be removed to the surface by circulating drilling fluid. Specifically,

$$V = V_{cut} + V_{cav} = \pi D_f^2 H_i / 4, \tag{4.5.2}$$

where V_{cav} is the volume (m^3) of waste removed as cavings.

Most borehole erosion is believed to occur in the vicinity of the drill collar (Fig. 4.5.1) (Rechard et al. 1990, Letters 1a and 1b, App. A). An important determinant of the extent of this erosion is whether the flow of the drilling fluid in the vicinity of the collar is laminar or turbulent. The 1996 WIPP PA uses Reynolds numbers to distinguish between the occurrence of laminar flow and turbulent flow. The Reynolds number is the ratio between inertial and viscous (i.e., shear) forces in a fluid and can be expressed as

$$R_e = \frac{\rho_f \|\mathbf{v}\| D_e}{\eta}, \tag{4.5.3}$$

where R_e is the Reynolds number (dimensionless), ρ_f is the fluid density (kg m^{-3}), D_e is the equivalent diameter (m), $\mathbf{v}$ is the fluid velocity (m s^{-1}), and η is the fluid viscosity (kg m^{-1} s^{-1}).

Typically, ρ, $\mathbf{v}$ and η are averages over a control volume with an equivalent diameter of D_e. In the 1996 WIPP PA, $\rho_f = 1.21 \times 10^3$ kg m^{-3} (Sect. 7.0, Berglund 1996a), $\|\mathbf{v}\| = 0.7089$ m s^{-1} (based on 40 gallons/min per inch of drill diameter, Sect. 2.3, Berglund 1992), and $D_e = 2\,(R - R_i)$ as shown in Fig. 4.5.1. The diameter of the drill collar (i.e., $2R_i$ in Fig. 4.5.1) is 8.0 in = 0.2032 m (Sect. 7.0, Berglund 1996a). The determination of η is discussed below. Reynolds numbers less than 2100 are assumed to be associated with laminar flow, while Reynolds numbers greater than 2100 are assumed to be associated with turbulent flow (Walker 1976).

Drilling fluids are non-Newtonian fluids, which means that the viscosity η is a function of the shear rate within the fluid (i.e., the rate at which the fluid velocity changes normal to the flow direction, ((m/s)/m). The 1996 WIPP PA uses a model proposed by Oldroyd (1958) to estimate the viscosity of drilling fluids. As discussed by Broc (1982), this model leads to the following expression for the Reynolds number associated with the helical flow of a drilling fluid within an annulus:

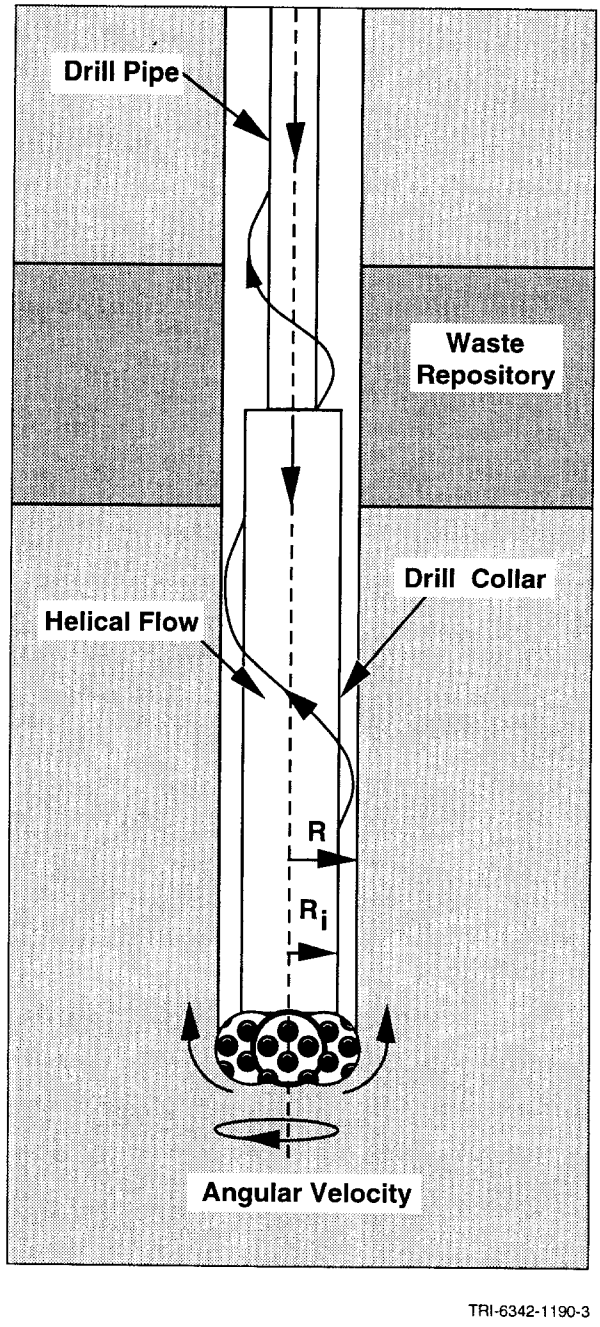

Fig. 4.5.1. Detail of rotary drill string adjacent to drill-bit (Fig. 7.3, Vol. 2, WIPP PA 1991-1992; Fig. 13, Helton et al. 1995a)

$$R_e = \frac{0.8165\, D_e \|\mathbf{v}\| \rho_f}{\eta_\infty}, \tag{4.5.4}$$

where D_e, $\|\mathbf{v}\|$ and ρ_f are defined in conjunction with Eq. (4.5.3), and η_∞ is the asymptotic value for the derivative of the shear stress (τ, kg m^{-1} s^{-2}) with respect to the shear rate (Γ, s^{-1}) obtained as the shear rate increases (i.e., $\eta_\infty = d\tau/d\Gamma$ as $\Gamma \rightarrow \infty$). The 1996 WIPP PA uses Eq. (4.5.4) to obtain the Reynolds numbers that are used to determine whether drilling fluids in the area of the drill collar are undergoing laminar or turbulent flow.

The Oldroyd model assumes that the shear stress τ is related to the shear rate Γ by the relationship

$$\tau = \eta_0 \left(\frac{1+\sigma_2 \Gamma^2}{1+\sigma_1 \Gamma^2} \right) \Gamma, \tag{4.5.5}$$

where η_0 is the asymptotic value of the viscosity (kg m^{-1} s^{-1}) that results as the shear rate Γ approaches zero, and σ_1, σ_2 are constants (s^2). The expression leads to

$$\eta_\infty = \eta_0 \left(\frac{\sigma_2}{\sigma_1} \right). \tag{4.5.6}$$

The 1996 WIPP PA uses values of $\eta_0 = 1.834 \times 10^{-2}$ kg m^{-1} s^{-1}, $\sigma_1 = 1.082 \times 10^{-6}$ s^2 and $\sigma_2 = 5.410 \times 10^{-7}$ s^2 (Table 2-1, Sect. 7.0, Berglund 1996a; Berglund 1992), and a resultant value of $\eta_\infty = 9.17 \times 10^{-3}$ kg m^{-1} s^{-1}. The quantity η_∞ is comparable to the plastic viscosity of the fluid (Broc 1982).

As previously indicated, different models are used to determine the eroded diameter of a borehole (i.e., $2R$ in Fig. 4.5.1, with $R = D_f/2$ in Eq. (4.5.2)) depending on whether flow in the vicinity of the drill collar is laminar or turbulent. The model for borehole erosion in the presence of laminar flow is described next, and is then followed by a description of the model for borehole erosion in the presence of turbulent flow.

As shown by Savins and Wallick (1966), the shear stresses associated with the laminar helical flow of a non-Newtonian fluid can be expressed as

$$\tau(R,\rho) = \left\{ \left[\frac{C}{\rho^2} \right]^2 + \left[\frac{RJ}{2} \left(\frac{\rho^2 - \lambda^2}{\rho} \right) \right]^2 \right\}^{1/2} \tag{4.5.7}$$

for $R_i/R \le \rho \le 1$, where R_i and R are the inner and outer radii within which the flow occurs as indicated in Fig. 4.5.1; $\tau(R, \rho)$ is the shear stress (kg m^{-1} s^{-2}) at a radial distance ΔR beyond the inner boundary (i.e., at $\rho = (R_i + \Delta R)/R$); and the quantities C, J and λ are functions of R that satisfy conditions indicated below. The shear stress at the outer boundary (i.e., R) is given by

$$\tau(R,1) = \left\{ C^2 + \left[\frac{RJ}{2}\left(1-\lambda^2\right) \right]^2 \right\}^{1/2} . \tag{4.5.8}$$

As previously indicated, the borehole radius R is assumed to increase as a result of erosional processes until a value of R is reached at which $\tau(R, 1)$ is equal to the shear strength of the waste. In the 1996 WIPP PA, the shear strength of the waste is treated as an uncertain input variable (see *WTAUFAIL* in Sect. 5.2). Computationally, determination of the eroded borehole diameter R associated with a particular waste shear strength requires repeated evaluation of $\tau(R, 1)$, as indicated in Eq. (4.5.8), until a value of R is determined for which $\tau(R, 1)$ equals that shear strength.

The quantities C, J and λ must satisfy the following three conditions (Savins and Wallick 1966) for the expression in Eq. (4.5.8) to be valid:

$$0 = \int_{R_i/R}^{1} \left(\frac{\rho^2 - \lambda^2}{\rho\eta} \right) d\rho, \tag{4.5.9}$$

$$0 = C\int_{R_i/R}^{1} \left(\frac{1}{\rho^3\eta} \right) d\rho - \Delta\Omega, \tag{4.5.10}$$

and

$$0 = \frac{4Q}{\pi R^3} + 2RJ \int_{R_i/R}^{1} \left[\frac{(R_i/R)^2 - \rho^2}{\eta} \right] \left[\frac{\rho^2 - \lambda^2}{\rho} \right] d\rho, \tag{4.5.11}$$

where η is the drilling fluid viscosity (kg m^{-1} s^{-1}) and is a function of R and ρ, $\Delta\Omega$ is the drill string angular velocity (rad s^{-1}), and Q is the drilling fluid flow rate (m^3 s^{-1}).

The viscosity η in Eqs. (4.5.9) - (4.5.11) is introduced into the analysis through the assumption that the drilling fluid follows the Oldroyd model for shear stress in Eq. (4.5.5). In particular, because

$$\tau = \eta\Gamma \tag{4.5.12}$$

as a result of the definition of the viscosity η and

$$\Gamma^2 = \frac{(\eta - \eta_0)}{(\eta_0\sigma_2 - \eta\sigma_1)} \tag{4.5.13}$$

from Eq. (4.5.5), the expression in Eq. (4.5.7) can be reformulated as

$$\frac{\eta^2(\eta-\eta_0)}{(\eta_0\sigma_2-\eta\sigma_1)}=\left[\frac{C}{\rho^2}\right]^2+\left[\frac{RJ}{2}\left(\frac{\rho^2-\lambda^2}{\rho}\right)\right]^2. \tag{4.5.14}$$

As discussed by Savins and Wallick (1966) and also by Berglund (1992), the expressions in Eqs. (4.5.9) - (4.5.11) and (4.5.14) can be numerically evaluated to obtain C, J and λ for use in Eqs. (4.5.7) and (4.5.8). In the 1996 WIPP PA, $\Delta\Omega = 7.8$ rad s^{-1} (Sect. 7.0, Berglund 1996a),

$$Q=\|\mathbf{v}\|\left(\pi R^2-\pi R_i^2\right) \tag{4.5.15}$$

where $\|\mathbf{v}\| = 0.7089$ m s^{-1} as used in Eq. (4.5.3), and η_0, σ_1 and σ_2 are defined in conjunction with Eq. (4.5.6).

The model for borehole erosion in the presence of turbulent flow is now described. Unlike the theoretically derived relationship for erosion in the presence of laminar flow, the model for borehole erosion in the presence of turbulent flow is empirically based. In particular, pressure loss for axial flow in an annulus under turbulent flow conditions can be approximated by (Broc 1982)

$$\Delta P=\frac{2fL\rho_f\|\mathbf{v}\|^2}{0.8165D_e}, \tag{4.5.16}$$

where ΔP is the pressure change (Pa), L is distance (m) over which pressure change ΔP occurs, f is the Fanning friction factor (dimensionless), and ρ_f, $\|\mathbf{v}\|$ and D_e are defined in conjunction with Eq. (4.5.3).

For pipe flow, f is empirically related to the Reynolds number R_e and a roughness term ε by (Whittaker 1985)

$$\frac{1}{f^{1/2}}=-4\log_{10}\left(\frac{\varepsilon}{3.72D}+\frac{1.255}{R_e f^{1/2}}\right), \tag{4.5.17}$$

where D is the inside diameter (m) of the pipe and ε is the average depth (m) of pipe wall irregularities. In the absence of a similar equation for flow in an annulus, Eq. (4.5.17) is used in the 1996 WIPP PA to define f for use in Eq. (4.5.16), with D replaced by the effective diameter $D_e = 2(R - R_i)$ and ε equal to the average depth of irregularities in the waste-borehole interface. In the present analysis, $\varepsilon = 0.025$ m (Sect. 7.0, Berglund 1996a), which exceeds the value often chosen for use in calculations involving very rough concrete or riveted steel piping (Streeter 1958). Further, the Reynolds number R_e is defined in Eq. (4.5.4).

The pressure change ΔP in Eq. (4.5.16) and the corresponding shear stress τ at the walls of the annulus are approximately related by

$$\Delta P\left[\pi\left(R^2 - R_i^2\right)\right] = \tau\left[2\pi L\left(R + R_i\right)\right], \tag{4.5.18}$$

where $\pi(R^2 - R_i^2)$ is the cross-sectional area of the annulus (see Fig. 4.5.1) and $2\pi L\,(R + R_i)$ is the total (i.e., interior and exterior) surface area of the annulus. Rearrangement of Eq. (4.5.18) and use of the relationship in Eq. (4.5.16) yields

$$\tau = \frac{f\rho_f \|\mathbf{v}\|^2}{2(0.8165)}, \tag{4.5.19}$$

which was used in the 1991 and 1992 WIPP PAs to define the shear stress at the surface of a borehole of radius R. As a reminder, R enters into Eq. (4.5.9) through the use of $D = 2(R-R_i)$ in the definition of f in Eq. (4.5.17). As in the case for laminar flow, the borehole radius R is assumed to increase until a value of τ (actually, $\tau(R)$) is reached that equals the shear strength of the waste (i.e., the uncertain analysis input *WTAUFAIL* in Sect. 5.2). Computationally, the eroded borehole diameter is determined by solving Eq. (4.5.19) for R under the assumption that τ equals the assumed shear strength of the waste.

In the 1996 WIPP PA, a slight modification to the definition of τ in Eq. (4.5.19) was made to account for drillstring rotation when fluid flow in the vicinity of the drill collars is turbulent (Abdul Khader and Rao 1974, Bilgen et al. 1973). Specifically, an axial flow velocity correction factor (i.e., a rotation factor), F_r, was introduced into the definition of τ. The correction factor F_r is defined by

$$F_r = \|\mathbf{v}_{2100}\| / \|\mathbf{v}\|, \tag{4.5.20}$$

where $\|\mathbf{v}_{2100}\|$ is the norm of the flow velocity required for the eroded diameters to be the same for turbulent and laminar flow at a Reynolds number of 2100 and is obtained by solving

$$\tau_{fail} = \frac{f\rho_f \|\mathbf{v}_{2100}\|^2}{2(0.8165)} \tag{4.5.21}$$

for $\|\mathbf{v}_{2100}\|$ with D in the definition of f in Eq. (4.5.17) assigned the final diameter value that results for laminar flow at a Reynolds number of $R_e = 2100$ (i.e., the D in $D_e = 2(R-R_i) = D-2R_i$ obtained from Eq. (4.5.4) with $R_e = 2100$). The modified definition of τ is

$$\tau = \frac{f\rho_f (F_r \|\mathbf{v}\|)^2}{2(0.8165)} \tag{4.5.22}$$

and results in turbulent and laminar flow having the same eroded diameter at a Reynolds number of 2100, which is the Reynolds number at which a transition between turbulent and laminar flow is assumed to take place.

The following algorithm was used to determine the final eroded radius R_f of a borehole and incorporates the possible occurrence of a transition from turbulent to laminar fluid flow within a borehole:

Step 1. Use Eq. (4.5.4) to determine an initial Reynolds number R_e, with R set to the drill-bit radius (i.e., R_0). In the 1996 WIPP PA, R_0 = 12.25 in (Sect. 7.0, Berglund 1996a).

Step 2. If $R_e < 2100$, then the flow is laminar and the procedures discussed in conjunction with Eqs. (4.5.7) and (4.5.8) are used to determine R_f. Because any increase in the borehole diameter will cause the Reynolds number to decrease, the flow will remain laminar and there is no need to consider the possibility of turbulent flow as the borehole diameter increases, with the result that R_f determined in this step is the final eroded radius of the borehole.

Step 3. If $R_e \geq 2100$, then the flow is turbulent and the procedures discussed in conjunction with Eqs. (4.5.19) and (4.5.22) are used to determine R_f. Once R_f is determined, the associated Reynolds number R_e is calculated with Eq. (4.5.4) and $R = R_f$. If $R_e > 2100$, then a transition from turbulent to laminar flow cannot take place, and the final eroded radius is R_f determined in this step.

Step 4. If the Reynolds number R_e determined in Step 3 satisfies the inequality $R_e \leq 2100$, then a transition from turbulent to laminar flow is assumed to have taken place. In this case, the calculation of R_f is redone for laminar flow, with the outer borehole radius R initially defined to be the radius at which the transition from turbulent to laminar flow occurs (i.e., the radius associated with $R_e = 2100$). In particular, the initial value for R is given by

$$R = R_i + \frac{2100\eta_\infty}{2(0.8165)\|\mathbf{v}\|\rho} \tag{4.5.23}$$

which is obtained from Eq. (4.5.4) by solving for R with $R_e = 2100$. A new value for R_f is then calculated with the procedures discussed in conjunction with Eqs. (4.5.7) and (4.5.8) for laminar flow, with this value of R_f replacing the value from step 3 as the final eroded diameter of the borehole.

Step 5. Once R_f is known, the amount of waste removed to the surface is determined by Eq. (4.5.2) with $D_f = 2R_f$.

4.5.4 Additional Information

Additional information on CUTTINGS_S and its use in the 1996 WIPP PA to determine cuttings and cavings releases can be found in the CUTTINGS_S users manual (WIPP PA 1996d) and in the analysis package for cuttings and spallings releases (Berglund 1996a).

4.6 Spallings to Surface: CUTTINGS_S (i.e., f_{SP})

4.6.1 Volume Removed by Spallings

The spallings model used in the 1996 WIPP PA estimates the release of solid material carried to a borehole by venting gas after a drilling intrusion. Such releases are assumed to have the potential to occur when the pressure in the repository at the time of a drilling intrusion exceeds 8 MPa, which is the pressure exerted by a column of brine-saturated drilling fluid at the depth of the repository (Stoelzel and O'Brien 1996). If repository pressure is less than 8 MPa, then no gas venting into the borehole, and hence no spallings release, is assumed.

Results from steady state flow experiments through granular material in a cylindrical geometry indicate that a pattern of channels would be formed in the waste by venting gas in the vicinity of an intruding borehole (Lenke et al. 1996). Based on these results, the following conceptual model for spallings releases at pressures above 8 MPa was formulated: (1) Immediately after a drilling intrusion, pressure gradients associated with the flow of gas towards the borehole fracture the porous waste material, thus permitting the escaping gas to flow within the fractures rather than through the porous waste. Consequently, the waste permeability does not affect gas flow, and the gas pressure at the borehole entrance can be assumed to be the initial (i.e., the time of the intrusion) gas pressure in the repository. (2) The gas flow velocity up the borehole is determined by the properties of isothermal gas flow in a long tube of a given cross-sectional area, tube roughness, and gas pressure at the borehole entrance. (3) The total mass flow rate of gas in the fractures at any radial distance from the borehole is equal to the mass flow rate of gas up the borehole. (4) Erosion of solid material occurs within the fractures when the gas velocity exceeds a fracture erosion velocity v_e. (5) The fracture erosion velocity v_e is related to drag forces on a particle and the cohesive strength that results from moisture and cementation in the matrix. (6) The development of the fracture system is not limited by the amount of gas available for venting.

The mathematical implementation of the preceding conceptual model is now described. With the assumption that gas pressure, and hence gas density, is approximately constant throughout the waste, conservation of mass requires that

$$2\pi r v_a(r) H = A_{BH} v_{BH} \tag{4.6.1}$$

or, equivalently, that

$$v_a(r) = A_{BH} v_{BH} / (2\pi r H), \tag{4.6.2}$$

where $v_a(r)$ is the average gas velocity (m/s) in the waste at a distance r (m) from the borehole, H is the height (m) of a repository room at the time of the intrusion, A_{BH} is the area (m^2) of the annulus between the drill pipe and the borehole wall (Fig. 4.5.1), and v_{BH} is the gas velocity (m/s) up the borehole. The determination of v_{BH} is discussed

later. As the gas flow is assumed to take place predominately within the induced fracture system, the gas velocity $v_f(r)$ (m/s) within the fractures is given by

$$v_f(r) = v_a(r) / \phi_f(r), \tag{4.6.3}$$

where $\phi_f(r)$ is the fracture porosity at a distance r from the borehole.

The fractures are assumed to grow in size until the gas velocity within them is reduced to the minimum velocity v_e (m/s) required to cause erosion of the fracture surfaces. When v_e is reached at a given distance r from the borehole, erosion of material from the fractures will cease. Thus, the final (i.e., maximum) fracture porosity $\phi_{fe}(r)$ at a distance r from the borehole is given by

$$\phi_{fe}(r) = v_a(r) / v_e = (A_{BH} v_{BH}) / (2\pi r H v_e). \tag{4.6.4}$$

The velocity v_e is a property of the waste and its derivation will be discussed later. Given that v_e is known, the solid volume V_{sol} (m^3) eroded (i.e., spalled) from the fractures is

$$V_{sol} = \int_0^{2\pi} \int_0^{r_0} H(1-\phi)\phi_{fe}(r) r dr d\theta = A_{BH} v_{BH} r_0 (1-\phi) / v_e, \tag{4.6.5}$$

where ϕ is the bulk porosity of the waste at the time of the intrusion and r_0 is the equivalent radius (m) of a waste disposal room. The presence of $1-\phi$ in Eq. (4.6.5) results in the spallings volume V_{sol} being taken only from the solid components of the waste. The porosity ϕ is obtained from solution of Eqs. (4.2.1) - (4.2.6) by BRAGFLO and is a function of intrusion time. Further, in the 1996 WIPP PA, $A_{BH} = 4.36 \times 10^{-2}$ m^2 (i.e., $\pi(r_b - r_c)^2$, where r_b = (0.311 m)/2 is the drillbit radius and r_p = (0.2032 m)/2 is the drill pipe radius) and $r_0 = 17.1$ m (Sect. 7.0, Berglund 1996a).

The volume V_{sol} in Eq. (4.6.5) is the volume of solid material removed by spallings. The equivalent volume of original uncompacted material can be obtained from the equality

$$\phi_i = (V_i - V_{sol}) / V_i, \tag{4.6.6}$$

where ϕ_i is the original (i.e., uncompacted) porosity of the waste and V_i is the original volume (m^3) of material that gave rise to a spallings release of size V_{sol}. In turn,

$$V_i = V_{sol} / (1-\phi_i) = (A_{BH} v_{BH} r_0 / v_e)(1-\phi) / (1-\phi_i). \tag{4.6.7}$$

In the 1996 WIPP PA, radionuclide concentrations were calculated for original uncompacted waste, and so V_i rather than V_{sol} was used in the determination of the normalized releases due to spallings.

Two important quantities, v_e and v_{BH}, used in the calculation of V_i and V_{sol} remain to be discussed. The determination of v_e is described first (Sect. 4.6.2) and then followed by a description of the determination of v_{BH} (Sect. 4.6.3).

4.6.2 Fracture Erosion Velocity

The fracture erosion velocity v_e is the gas velocity in a fracture required to erode the fracture walls. One possibility is to define v_e to be the terminal velocity of a falling spherical particle as this is the velocity at which the weight of the particle equals the drag forces on the particle. As discussed by Cheremisinoff and Cheremisinoff (p. 30, 1984), this results in the relationship

$$v_e^2 = \frac{4gd(\rho_s - \rho_g)}{3C_D[R_e(v_e)]\rho_g}, \tag{4.6.8}$$

where g is the acceleration due to gravity (m/s^2), d is the particle diameter (m), ρ_s is the particle density (kg/m^3), ρ_g is the gas density (kg/m^3), and $C_D[R_e(v_e)]$ is the coefficient of drag and a function of the Reynolds number $R_e(v_e)$. In turn, $R_e(v_e)$ and $C_D[R_e(v_e)]$ are defined empirically (p. 406, Fox and McDonald 1973) by

$$R_e(v_e) = \rho_g v_e d / \mu \tag{4.6.9}$$

$$\log_{10}\{C_D[R_e(v_e)]\} = \log_{10}[24 / R_e(v_e)] \qquad \text{if } R_e(v_e) < 0.4 \tag{4.6.10}$$

$$= \sum_{i=0}^{6} a_i [\log_{10} R_e(v_e)]^i \qquad \text{if } 0.4 \le R_e(v_e) \le 2 \times 10^5 \tag{4.6.11}$$

$$= \log_{10}(0.2), \qquad \text{if } R_e(v_e) \ge 2 \times 10^5 \tag{4.6.12}$$

where μ is the gas viscosity (Pa • s) and the a_i in Eq. (4.6.11) are empirically determined from the relationship given by Fox and McDonald, using the program GRAPHER, Version 1.23, from Golden Software Inc., Golden CO, to be (Sect. 7.0, Berglund 1996a)

$a_0 = 1.3918$, $a_1 = -0.907723$, $a_2 = 0.136371$, $a_3 = 0.0165093$
$a_4 = -0.0285484$, $a_5 = 0.00933281$, $a_6 = -0.000897166$.

The velocity v_e can then be determined by numerical solution of Eq. (4.6.8) subject to the constraints in Eqs. (4.6.9) - (4.6.12).

The use of Eq. (4.6.8) to determine v_e results in drag being the only resistance to particle movement. In reality, the tensile strength of the waste also resists erosion in fractures by flowing gas and should be incorporated into the derivation of v_e. As now described, one way to do this is by replacing the gravity term g in Eq. (4.6.8) by an effective gravity force g_{eff} that derives from both drag and the tensile strength of the waste.

The parting force p_f (kg m/s^2) on a particle can be expressed as

$$\sigma = \frac{p_f}{p_a} = \frac{mg_t}{\pi R^2} = \frac{4\pi R^3 \rho_s g_t / 3}{\pi R^2} = 4\rho_s g_t R / 3, \tag{4.6.13}$$

where σ is the tensile strength (kg/ms^2), p_a is the effective particle area (i.e., πR^2) (m), m is the particle mass (kg), R is the particle radius (m), ρ_s is the particle density (kg/m^3), and g_t is the force (kg/ms^2) (i.e., the effective acceleration due to gravity) necessary to generate a particle weight equal to the parting force p_f. Solution of Eq. (4.6.13) for g_t then yields

$$g_t = 3\sigma / (4\rho_s R) . \tag{4.6.14}$$

An effective acceleration due to gravity g_{eff}(m/s^2) that accounts for both drag and tensile strength can now be defined by

$$\begin{aligned} g_{eff} &= g + g_t \\ &= g + 3\sigma / (4\rho_s R) \\ &= g + 3\sigma_p / (4\rho_s R) + 3\sigma_c / (4\rho_s R), \end{aligned} \tag{4.6.15}$$

with the last equality following from the assumption that $\sigma = \sigma_p + \sigma_c$ has a component σ_p resulting from pore water and a component σ_c resulting from intergranular cementation.

The value for g_{eff} in Eq. (4.6.15) was obtained for an unconstrained system. For the determination of spallings releases, g_{eff} will be used for flow in channels. In this situation, it is desirable to add effectiveness factors (Lenke et al. 1996) to account for the constrained conditions associated with flow in small channels. When this is done, g_{eff} becomes

$$g_{eff} = F_{ge} g + 3F_{pe}\sigma_p / (4\rho_s R) + 3F_{ce}\sigma_c / (4\rho_s R), \tag{4.6.16}$$

where F_{ge}, F_{pe} and F_{ce} are empirically-determined effectiveness factors for drag forces, shear strength associated pore water and shear strength associated with intergranular cementation, respectively (Lenke et al. 1996).

In the 1996 WIPP PA, g_{eff} as defined in Eq. (4.6.16) was used instead of g in Eq. (4.6.8) in the numerical determination of v_e. In this determination, the following additional values were also used (Sect. 7.0, Berglund

1996a): ρ_s = 2650 kg/m^3, ρ_g = 0.0726 kg/m^3, $\mu = 9.2 \times 10^{-6}$ Pa•s, σ_p = 0 kg/ms^2, σ_c = 6895 kg/ms^2, F_{ge} = 18.1, F_{pe} = 0, F_{ce} = 1.0, $R = d/2$, and the particle diameter d was an uncertain analysis input (see *WPRTDIAM* in Sect. 5.2).

4.6.3 Gas Velocity in Borehole

The velocity v_{BH} is given by

$$v_{BH} = C\, M_i, \tag{4.6.17}$$

where $C = (KRT)^{1/2}$ is the local sound speed (m/s), T is the absolute temperature (°K), R = 4123 J/(kg s) is the universal gas constant for hydrogen (p. 541, Obert 1948), K is the ratio of specific heat of hydrogen at constant pressure to specific heat of hydrogen at constant volume, and M_i is the inlet Mach number (Binder 1958).

In turn, the inlet Mach number is computed based on flow in the borehole annulus with the assumption that the borehole is free of drilling fluid. Compressible, isothermal flow of a gas in a channel (i.e., the borehole annulus) is characterized by the following equation (Binder 1958):

$$fL / D = (1 - P_o^2 / P_i^2)(KM_i^2)^{-1} - 2\ln(P_i / P_o), \tag{4.6.18}$$

where f is the friction factor (dimensionless), D is the channel diameter (m), L is the channel length (m), and P_i and P_o are the inlet and outlet gas pressures (Pa). In this analysis, D is the effective diameter for the borehole annulus (i.e., the diameter of a circle that has the same area as the borehole annulus).

Due to the difference in D depending on whether flow is in the area of the drill collar or the drill pipe (Fig. 4.5.1), Eq. (4.6.18) must be applied over two intervals (i.e., the drill collar and the much longer drill pipe) in the estimation of M_i for use in the determination of v_{BH}. This division produces the following two equations:

$$fL_c / D_c = (1 - P_{c\text{-}p}^2 / P_i^2)(KM_i^2)^{-1} - 2\ln(P_i / P_{c\text{-}p}) \tag{4.6.19}$$

$$fL_p / D_p = (1 - P_o^2 / P_{c\text{-}p}^2)[KM_i^2 (P_i / P_{c\text{-}p})^2 (D_c / D_p)^4]^{-1} - 2\ln(P_{c\text{-}p} / P_o), \tag{4.6.20}$$

where L_c and L_p are the lengths (m) of the drill collar and the drill pipe, D_c and D_p are the effective diameters (m) for the annuli associated with the drill collar and the drill pipe, and $P_{c\text{-}p}$ is the gas pressure (Pa) at the interface between the drill collar and the drill pipe.

The two preceding equations were numerically solved to obtain M_i and $P_{c\text{-}p}$. In this solution, f = 0.08, L_c = 182.88 m, L_p = 472.12 m, D_c = 0.2032 m, D_p = 0.1143 m, K = 1.41, P_i = pressure (Pa) in waste at time of drilling

intrusion (obtained from numerical solution of Eqs. (4.2.1) - (4.2.6) by BRAGFLO) and P_o equals atmospheric pressure (i.e., 89465 Pa) or, if applicable, the pressure that corresponds to the condition that the rate of change of pressure with respect to length is unbounded (i.e., $dp/dl \rightarrow \infty$ at the pipe exit) (Sect. 7.0, Berglund 1996a). Once obtained, M_i is then used in Eq. (4.6.17) to determine v_{BH}.

4.6.4 Additional Information

Additional information on CUTTINGS_S and its use in the 1996 WIPP PA to determine spallings releases can be found in the CUTTINGS_S users manual (WIPP PA 1996d) and in the analysis package for cuttings and spallings releases (Berglund 1996a).

4.7 Direct Brine Release to Surface: BRAGFLO_DBR (i.e., f_{DBR})

4.7.1 Overview

Direct brine releases are the releases of brine to the surface at the time of a drilling intrusion. Such releases have the potential to occur when the pressure in the repository at the time of a drilling intrusion exceeds 8 MPa, which is the pressure exerted by a column of brine-saturated drilling fluid at the depth of the repository (Stoelzel and O'Brien 1996). For repository pressures less than 8 MPa, no direct brine releases are assumed to occur. However, even if the repository pressure exceeds 8 MPa at the time of a drilling intrusion, a direct brine release is not assured as there may not be sufficient mobile brine in the repository to result in brine movement to the intruding borehole.

Direct brine releases are determined for the following cases: (1) an initial intrusion into the repository into a downdip panel, (2) an initial intrusion into the repository into an updip panel, (3) an intrusion into a waste panel that has been preceded by an E1 intrusion into the same waste panel, (4) an intrusion into a waste panel that has been preceded by an E1 intrusion into a different waste panel, (5) an intrusion into a waste panel that has been preceded by an E2 intrusion into the same waste panel, and (6) an intrusion into a waste panel that has been preceded by an E2 intrusion into a different waste panel (see Sect. 6.9). To determine releases for the above cases, the direct brine release calculations use a computational grid that explicitly includes all 10 waste panels (Fig. 4.7.1).

The direct brine releases take place over a relatively short period of time (i.e., 3 to 11 days) following the drilling intrusion under consideration. The initial value conditions for use in the determination of direct brine releases are obtained by mapping solutions of Eqs. (4.2.1) - (4.2.6) obtained with the computational grid in Fig. 4.2.1 onto the grid in Fig. 4.7.1 (Sect. 4.7.2).

In concept, the direct brine release for a drilling intrusion has the form

$$DBR = \int_0^{t_e} rDBR(t)dt, \tag{4.7.1}$$

where

DBR = direct brine release (m^3) for drilling intrusion,

$rDBR(t)$ = rate (m^3) at time t at which brine flows up intruding borehole,

t = elapsed time (s) since drilling intrusion,

t_e = time (s) at which direct brine release ends.

The definition of $rDBR(t)$ is discussed in Sects. 4.7.3 - 4.7.6 and is based on the two-phase flow relationships in Eqs. (4.2.1) - (4.2.6) and use of the Poettmann-Carpenter correlation (Poettmann and Carpenter 1952) to determine a

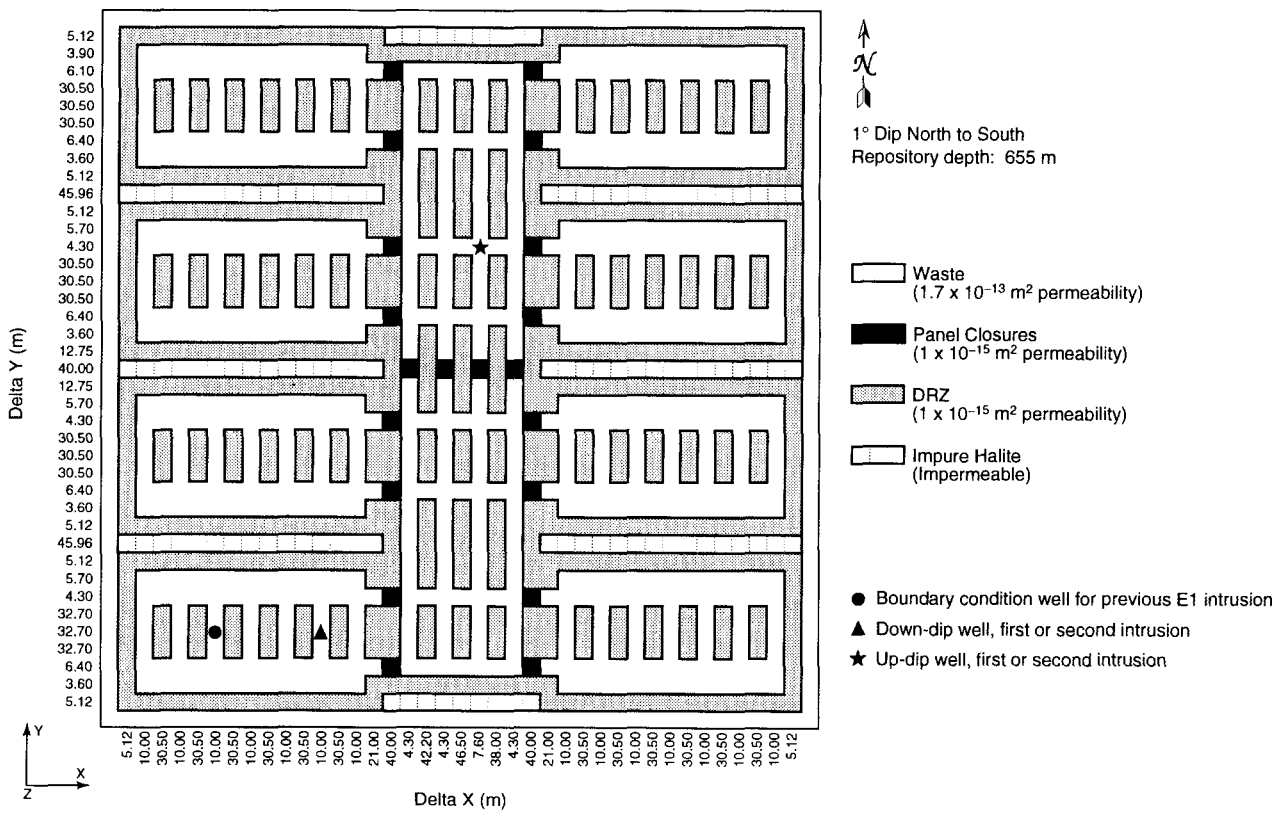

Note: Model cells are not to scale. The actual dimensions of the grid blocks are indicated along the edge of the diagram.

TRI-6342-5432-3

Fig. 4.7.1. Direct brine release (BRAGFLO_DBR) mesh.

boundary pressure at the connection between the intruding borehole and the repository. The time t_e is based on current drilling practices in the Delaware Basin (Sect. 4.7.7).

4.7.2 Linkage to Solution of Eqs. (4.2.1) - (4.2.6)

The mesh in Fig. 4.7.1 was linked to the mesh in Fig. 4.2.1 by subdividing the waste disposal area in the mesh in Fig. 4.2.1 into four regions (Fig. 4.7.2). Region 1 represents the farthest updip repository grid blocks in Fig. 4.2.1 that contained waste. Region 4 represents the farthest downdip repository grid blocks in Fig. 4.2.1 that contained waste and thus corresponds to the downdip waste panel. Similar subdivisions are made for regions 2 and 3. The linkage between the solutions to Eqs. (4.2.1) - (4.2.6) and the direct brine release calculations was made by assigning properties calculated by BRAGFLO for each region in Figure 4.2.1 to the corresponding waste region in Fig. 4.7.1.

The height of the grid in Fig. 4.7.1 was assigned a value that corresponded to the crushed height h (m) of the waste as predicted by the solution of Eqs. (4.2.1) - (4.2.6). Specifically,

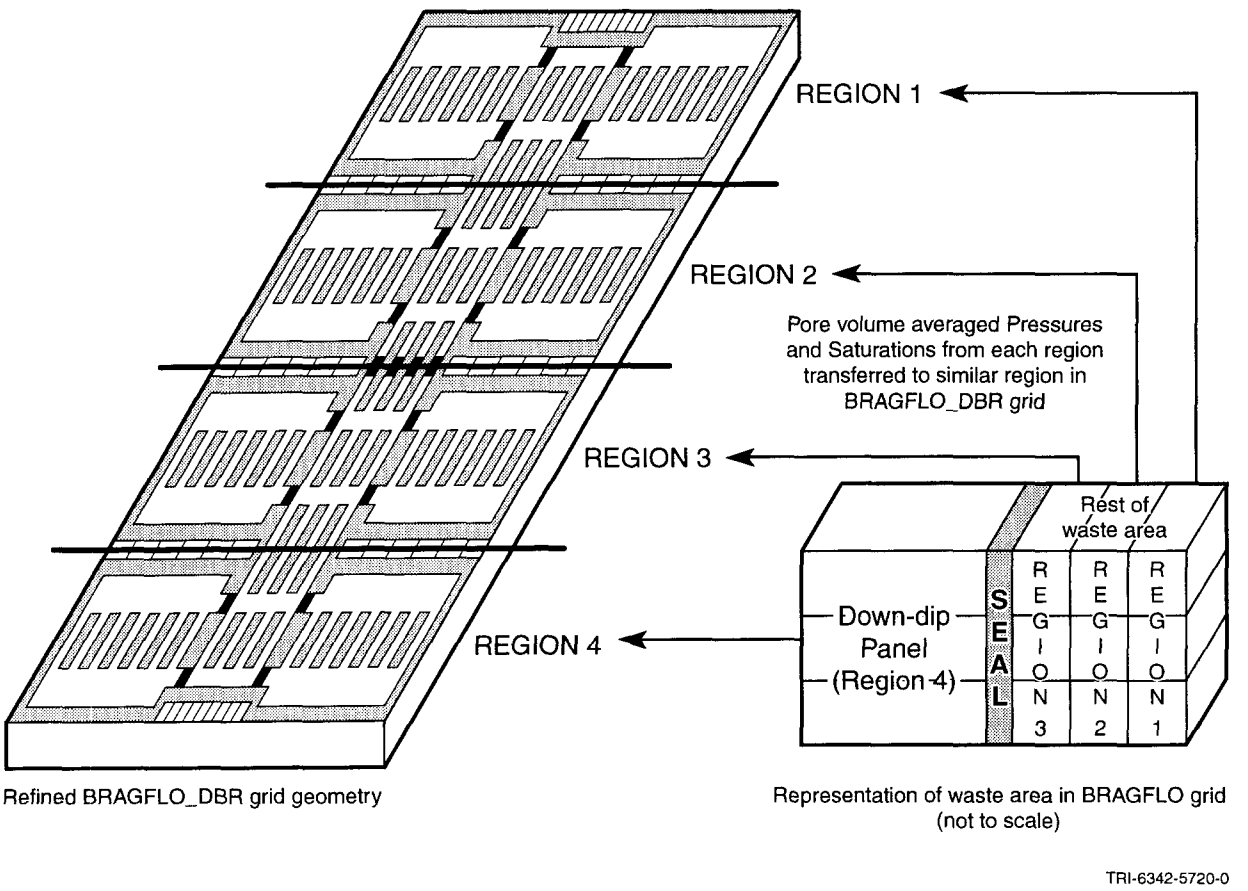

Fig. 4.7.2. Representation of coupling between grids in Figs. 4.2.1 and 4.7.1 to obtain initial conditions for direct brine release calculation at each intrusion time.

$$h = h_i\,(1 - \phi_i)/(1 - \phi), \tag{4.7.2}$$

where h_i and ϕ_i are the initial height (m) and porosity of the waste and ϕ is the volume-averaged porosity of the waste at the particular time under consideration as predicted by the SANTOS calculations (Sect. 4.2.3). The areas designated panel seals, DRZ and impure halite in Fig. 4.7.1 were assigned the same pressures and saturations as the corresponding waste areas and were assigned porosities that resulted in a conservation of the initial pore volumes used for these areas in the solution of Eqs. (4.2.1) - (4.2.6) on the grid in Fig. 4.2.1 (Table 4.7.1). Specifically, the pore volumes associated with the panel seals, DRZ and impure halite do not change with time, with this constancy implemented by the definitions of $\phi(x, y, 0)$ in the lower half of Table 4.7.1.

4.7.3 Conceptual Representation for Flow Rate *rDBR(t)*

The driving force that gives rise to the direct brine release *DBR* is the difference between waste panel pressure, p_w (Pa), and the flowing bottomhole pressure in the borehole, p_{wf} (Pa), at the time of the intrusion. The flowing bottomhole pressure p_{wf}, defined as the dynamic pressure at the inlet of the intruding borehole to the waste panel, is less than the static pressure p_w due to elevation, friction and acceleration effects. The rate at which brine and gas are transported up the intruding borehole is determined by the difference $p_w - p_{wf}$ and a productivity index J_p for the intruded waste panel (p. 79, Mattax and Dalton 1990):

$$q_p(t) = J_p\left[p_w(t) - p_{wf}\right], \tag{4.7.3}$$

where

$q_p(t)$ = flow rate (m^3/s) at time t for phase p ($p = b$ ~ brine, $p = g$ ~ gas),

J_p = productivity index (m^3/Pa·s) for phase p,

and p_w and p_{wf} are defined above. As indicated by the inclusion/exclusion of a dependence on t, the terms J_p and p_{wf} are constant during the determination of $q_p(t)$ for a particular drilling intrusion in the present analysis, and $p_w(t)$ changes as a function of time.

The determination of J_p is now discussed. Then, the numerical determination of p_w and *DBR* is discussed in Sect. 4.7.4, and the determination of p_{wf} is discussed in Sects. 4.7.5 - 4.7.6. In concept, the direct brine release *DBR* is given by

$$DBR = \int_0^{t_e} rDBR(t)dt = \int_0^{t_e} J_b\left[p_w(t) - p_{wf}\right]dt \tag{4.7.4}$$

Table 4.7.1 Initial Definition (i.e., Initial Value Conditions) for Brine Pressure p_b (x, y, 0), Gas Saturation S_g (x, y, 0) and Porosity ϕ (x, y, 0) for Computational Grid in Fig. 4.7.1, where (x, y) Designates a Point in the Grid and t = 0 yr Corresponds to Time at which Drilling Intrusion Occurs

Values for p_b (x, y, 0) and S_g (x, y, 0)

$$p_b(x, y, 0) = \int_R \tilde{p}_b(\tilde{x}, \tilde{y}, t_{int})dV / \int_R dV$$

$$S_g(x, y, 0) = \int_R \tilde{S}_g(\tilde{x}, \tilde{y}, t_{int})dV / \int_R dV$$

where $\tilde{p}_b$ and $\tilde{S}_g$ denote solutions to Eqs. (4.2.1 - (4.2.6), $\tilde{x}$ and $\tilde{y}$ denote the variables of integration, t_{int} is the time at which the drilling intrusion occurs (Note: t_{int} defines a time in the solution of Eqs. (4.2.1) - (4.2.6); t = 0 defines the start time for the direct brine release calculation and corresponds to t_{int} in the solution of Eqs. (4.2.1) - (4.2.6)), and R corresponds to the region in the computational grid for BRAGFLO that is mapped into the region in the computational grid for BRAGFLO_DBR that contains the point (x, y) (Fig. 4.7.2)

Values for ϕ (x, y, 0)

$\phi(x, y, 0)$	=	$1 - h_i(1 - \phi_{WP,i})/ h(t_{int})$	(x, y) in waste panel in Fig. 4.7.1
	=	$h_{DRZ,i}\, \phi_{DRZ,i}/ h(t_{int})$	(x, y) in DRZ in Fig. 4.7.1
	=	$h_{PS,i}\, \phi_{PS,i}/ h(t_{int})$	(x, y) in panel seal in Fig. 4.7.1
	=	$h_{H,i}\, \phi_{H,i}/ h(t_{int})$	(x, y) in undisturbed halite in Fig. 4.7.1

where h_i is initial height of waste panels (3.96 m), $\phi_{WP,i}$ is initial porosity of waste panels (0.848), $h(t_{int})$ is height of repository at time of intrusion (typically 1 to 1.5 m; corresponds to h in Eq. (4.7.2)), $h_{DRZ,i}$ is initial height for DRZ that results in DRZ in Fig. 4.7.1 having the same pore volume as the initial pore volume of the DRZ in Fig. 4.2.1 (8.98 m), $\phi_{DRZ,i}$ is initial porosity of DRZ (0.0129) (Note: $h_{DRZ,i}\, A_{DRZ}\, \phi_{DRZ,i}$ is equal to pore volume of DRZ in Fig. 4.2.1, where A_{DRZ} is area associated with DRZ in Fig. 4.7.1), $h_{PS,i}$ is initial height of panel seals (3.96 m), $\phi_{PS,i}$ is initial porosity of panel seals (0.075) (Note: $h_{PS,i}\, A_{PS}\, \phi_{PS,i}$ is equal to pore volume of panel seals in Fig. 4.2.1, where A_{PS} is area associated with panel seals in Fig. 4.7.1), $h_{H,i}$ is initial height of undisturbed halite in Fig. 4.7.1 (arbitrarily taken to be same as $h_{DRZ,i}$, which is 8.98 m), and $\phi_{H,i}$ is initial porosity of halite (0.01) (Note: due to its low permeability (3.16×10^{-23} m^2), undisturbed halite has little effect on results calculated over a short time period with the computational grid in Fig. 4.7.1 and so no effort was made to preserve halite pore volume when mapping from the computational grid in Fig. 4.2.1 to the computational grid in Fig. 4.7.1).

once J_p, p_w and p_{wf} are determined. The associated gas release is given by the corresponding integral with J_g rather than J_b. In the computational implementation of the analysis, *DBR* is determined as part of the numerical solution of the system of partial differential equations that defines p_w (Sect. 4.7.4).

In a radial drainage area with uniform saturation, which is assumed to be valid throughout the direct brine release, the following representation for J_p can be determined from Darcy's law (p. 79, Mattax and Dalton 1990; Williamson and Chappelear 1981, Chappelear and Williamson 1981):

$$J_p = \frac{k k_{rp} h}{\mu_p \left[\ln(r_e / r_w) + s + c\right]}, \tag{4.7.5}$$

where

- k = absolute permeability (assumed to be constant through time at 1.7×10^{-13} m^2),
- k_{rp} = relative permeability to phase p (calculated with modified Brooks-Corey model in Eqs. (4.2.10) - (4.2.11) and brine and gas saturations, S_g and S_b, obtained by mapping solutions of Eqs. (4.2.1) - (4.2.6) obtained with grid in Fig. 4.2.1 onto grid in Fig. 4.7.1),
- h = crushed panel height (Eq. (4.7.2)),
- μ_p = viscosity of fluid phase (assumed to be constant through time with $\mu_b = 1.8 \times 10^{-3}$ Pa·s, and $\mu_g = 8.92 \times 10^{-6}$ Pa·s (Kaufmann 1960)),
- r_e = external drainage radius (for use with the rectangular gridblocks in Fig. 4.7.1, r_e is taken to be the equivalent areal radius; see Eq. (4.7.6)),
- r_w = wellbore radius (assumed to be constant through time at 0.1556 m (Table 14.7, Gatlin 1960)),
- c = −0.50 for pseudo steady-state flow,
- s = skin factor, which is used to incorporate flow stimulation caused by spallings release (see Eq. (4.7.7)).

In the present analysis,

$$r_e = \sqrt{(10)(32.7)/\pi} = 10.2 \text{ m} \tag{4.7.6}$$

results from the gridblock dimensions of 10 m × 32.7 m for the gridblock in Fig. 4.7.1 that contains the downdip borehole.

The skin factor s is derived from the spallings release through the following petroleum engineering well testing relationship (pp. 5-7, Lee 1982):

$$s = \left(\frac{k}{k_s} - 1\right) \ln\left(\frac{r_s}{r_w}\right), \tag{4.7.7}$$

where

k_s = permeability (m^2) of an open channel as a result of spallings releases (assumed to be infinite),

r_s = effective radius (m) of the wellbore with spallings volume removed.

The effective radius r_s is obtained by converting the spallings volume release V_i in Eq. (4.6.7) into an equivalent areal release A_i through the relationship

$$A_i = V_i / h_i. \tag{4.7.8}$$

Then,

$$r_s = \sqrt{A_i / \pi}, \tag{4.7.9}$$

and substitution of r_s into Eq. (4.7.7) with $k_s = \infty$ yields

$$s = -\ln[\sqrt{A_i / \pi} / r_w], \tag{4.7.10}$$

which is used as the skin factor in the calculation of direct brine releases.

4.7.4 Determination of Waste Panel Pressure $p_w(t)$ and Brine Release *DBR*

The repository pressure $p_w(t)$ in Eq. (4.7.4) after a drilling intrusion is determined with the same system of nonlinear partial differential equations discussed in Sect. 4.2. Indeed, what is referred to as the BRAGFLO_DBR program is actually the BRAGFLO program used with the computational grid in Fig. 4.7.1 and assumptions (i.e., parameter values, initial value conditions, and boundary value conditions) that are appropriate for representing brine flow to an intruding borehole over a relatively short time period immediately after the intrusion (i.e., 3-11 days). Due to the short time periods under consideration, the model for direct brine release does not include gas generation due to either corrosion or microbial action and also does not include changes in repository height due to creep closure. Further, to stabilize the calculation and thus allow longer time steps in the numerical solution, the capillary pressure was assigned a value of 0 Pa in all modeled regions (Fig. 4.7.1); in the analysis of the full system in Sect. 4.2, capillary pressure had a value of 0 Pa in the waste regions and the DRZ but a nonzero value in the panel seals (Table 4.2.3). Use of a capillary pressure of 0 Pa results in the brine pressure p_b (x, y, t) and the gas pressure p_g (x, y, t) being equal, with the pressure $p_w(t)$ in Eq. (4.7.4) given by

$$p_w(t) = p_b\,(x, y, t). \tag{4.7.11}$$

Although the determination of *DBR* can be conceptually represented by the integral in Eq. (4.7.1), in the numerical implementation of the analysis *DBR* is determined within the numerical solution of the system of partial differential equations that defines $p_b\,(x, y, t)$.

With the specific assumptions for direct brine release, Eqs. (4.2.1) - (4.2.6) become

Gas Conservation
$$\nabla \bullet \left[\frac{\alpha \rho_g \mathbf{K}_g k_{rg}}{\mu_g} \left(\nabla p_g + \rho_g g \nabla h \right) \right] = \alpha \frac{\partial \left(\phi \rho_g S_g \right)}{\partial t} \tag{4.7.12}$$

Brine Conservation
$$\nabla \bullet \left[\frac{\alpha \rho_b \mathbf{K}_b k_{rb}}{\mu_b} \left(\nabla p_b + \rho_b g \nabla h \right) \right] = \alpha \frac{\partial \left(\phi \rho_b S_b \right)}{\partial t} \tag{4.7.13}$$

Saturation Constraint
$$S_g + S_b = 1 \tag{4.7.14}$$

Capillary Pressure Constraint
$$0 = p_g - p_b \tag{4.7.15}$$

Gas Density
ρ_g determined by Redlich-Kwong-Soave equation of state (Eq. (4.2.30))

Brine Density
$$\rho_b = \rho_0 \exp\left[\beta_b \left(p_b - p_{b0} \right) \right] \tag{4.7.16}$$

Formation Porosity
$$\phi = \phi_0 \exp\left[\beta_f \left(p_b - p_{b0} \right) \right] \tag{4.7.17}$$

with all symbols having the same definitions as in Eqs. (4.2.1) - (4.2.6).

The same parameter values described in Sect. 4.2 for the waste regions, panel seals and DRZ are used with Eqs. (4.7.12) - (4.7.17) to model direct brine releases with the following exceptions: α is a function of the computational grid and is determined by the outcome of the calculations described in Sect. 4.2 (i.e., $\alpha = h$ as defined in Eq. (4.7.2)), the pore distribution parameter λ used in the definition of k_{rg} and k_{rb} (see Eqs. (4.2.10) - (4.2.11)) is assigned a value of 0.7 for the waste regions, panel seals and DRZ (values of $\lambda = 0.7$, 0.94 and 2.89 were used for the waste regions, panel seals and DRZ in the calculations described in Sect. 4.2), and the initial porosity ϕ_0 and initial pressure p_{b0} were set on the basis of the calculations described in Sect. 4.2 (Sect. 4.7.2). In particular, the intrinsic permeability k used in the definitions of $\mathbf{K}_g$ and $\mathbf{K}_b$ (Eq. (4.2.28)) is given by $k = 1.7 \times 10^{-13}$ m^2, 1.0×10^{-15} m^2 and 1.0×10^{-15} m^2 in the waste regions, panel seals and DRZ, respectively, and the relative permeabilities k_{rg} and k_{rb} are defined in Eqs. (4.2.10) - (4.2.11). The uncertain parameters *WRBRNSAT* ($\sim S_{br}$) and *WRGSSAT* ($\sim S_{gr}$) (see Sect. 5.2) directly enter the direct brine release calculations through the definitions of p_C, k_{rg} and k_{rb} in Eqs. (4.2.9) - (4.2.14).

The primary differences between the BRAGFLO calculations described in Sect. 4.2 and the BRAGFLO_DBR calculations described in this section are in the computational meshes used (i.e., the mesh in Fig. 4.7.1 for the

solution of Eqs. (4.7.12) - (4.7.17) and the mesh in Fig. 4.2.1 for the solution of Eqs. (4.2.1) - (4.2.6), the initial values used (Table 4.7.1), and the boundary values used (Table 4.7.2). In particular, the appropriate assignment of boundary value conditions is used to incorporate brine and gas flow associated with intruding boreholes into the model. Specifically, brine flow up an intruding borehole is incorporated into Eqs. (4.7.12) - (4.7.17) by using the Poettmann-Carpenter wellbore model to determine the pressure at the outflow point in a waste panel (Fig. 4.7.1), with this pressure entering the calculation as a boundary value condition (Table 4.7.2). The details of this determination are discussed in Sect. 4.7.5. Further, should a calculation involve a prior E1 intrusion, the effects of this intrusion are also incorporated into the analysis as a pressure specified as a boundary value condition (Table 4.7.2). The determination of this pressure is discussed in Sect. 4.7.6.

For perspective, the following provides a quick comparison of the assumptions that underlie the solution of Eqs. (4.2.1) - (4.2.6) on the mesh in Fig. 4.2.1 (i.e., the BRAGFLO mesh) and the solution of Eqs. (4.7.12) - (4.7.17) on the mesh in Fig. 4.7.1 (i.e., the BRAGFLO_DBR mesh): (1) The BRAGFLO_DBR mesh is defined in the areal plane with the z-dimension (height) one element thick; the BRAGFLO mesh is defined as a cross-section, with multiple layers in height and the thickness (y-dimension) one element thick. (2) The BRAGFLO_ DBR model represents flow only in the waste area. The BRAGFLO model includes the surrounding geology as well as the entire WIPP excavation (including operations, experimental, and shaft regions). (3) Local scale heterogeneities are

Table 4.7.2. Boundary Value Conditions for p_b and S_g in Solution of Eqs. (4.7.12) - (4.7.17) with Computational Grid in Fig. 4.7.1 (see Tables 4.2.9, 4.2.10)

(x, y) on Upper (Northern) or Lower (Southern) Boundary in Fig. 4.7.1, $0 \le t$	
$(\nabla p_g + \rho_g g \nabla h)\|_{(x, y, t)} \bullet \mathbf{j} = 0$ Pa/m	no gas flow condition
$(\nabla p_b + \rho_b g \nabla h)\|_{(x, y, t)} \bullet \mathbf{j} = 0$ Pa/m	no brine flow condition
(x, y) on Right (Eastern) or Left (Western) Boundary in Fig. 4.7.1, $0 \le t$	
$(\nabla p_g + \rho_g g \nabla h)\|_{(x, y, t)} \bullet \mathbf{i} = 0$ Pa/m	no gas flow condition
$(\nabla p_b + \rho_b g \nabla h)\|_{(x, y, t)} \bullet \mathbf{i} = 0$ Pa/m	no brine flow condition
(x, y) at Location of Drilling Intrusion under Consideration (see indicated points in Fig. 4.7.1), $0 \le t$	
$p_b\,(x, y, t) = p_{wf}$ (see Sect. 4.7.5)	
(x, y) at Location of Prior Drilling Intrusion into Pressurized Brine (see indicated point in Fig. 4.7.1), $0 \le t$	
$p_b\,(x, y, t) = p_{wE1}$ (see Sect. 4.7.6)	

included in the BRAGFLO_ DBR model, including the salt pillars, rooms, panel seals, and passageways which contain waste. These are not fully represented in the BRAGFLO mesh. (4) The BRAGFLO_ DBR mesh uses constant thickness, while BRAGFLO rectangularly flares the element thickness to account for 3-dimensional volumes in a 2-dimensional grid (Fig. 4.2.2). (5) The DRZ is included in both models, but exists above and below the excavated regions in the BRAGFLO model, whereas the DRZ surrounds the waste rooms on the sides for the BRAGFLO_ DBR model. (6) Both models include a one degree formation dip through the excavated regions (Eq. 4.2.8).

4.7.5 Boundary Value Pressure p_{wf}

The boundary value pressure p_{wf} at the inlet of the intruding borehole is defined by a system of equations of the following form:

$$dp/dh = F\{q_b[p(0)], q_g[p(0)], p(h), h\}, 0 \le h \le 655 \text{ m} \tag{4.7.18}$$

$$p(655) = 1.013 \times 10^5 \text{ Pa} \tag{4.7.19}$$

$$q_b[p(0)] = J_b[p_w - p(0)] \tag{4.7.20}$$

$$q_g[p(0)] = J_g[p_w - p(0)], \tag{4.7.21}$$

where $p(h)$ is pressure (Pa) at elevation h (m) in the borehole with $h = 0$ m corresponding to the entry point of the borehole into the waste panel and $h = 655$ m corresponding to the land surface (Fig. 4.7.3), F is a function (Pa/m) characterizing the change of pressure with elevation in the borehole, $p(655)$ is an initial value condition requiring that pressure at the land surface (i.e., the outlet point of the borehole) be equal to atmospheric pressure, $q_b[p(0)]$ and $q_g[p(0)]$ define brine and gas flow rates (m^3/s) into the borehole (see Eq. (4.7.3)), J_b and J_g are productivity indexes (m^3/Pa s) (see Eq. (4.7.5)), and p_w is the pressure (Pa) in the repository at the time of the drilling intrusion.

The boundary value pressure p_{wf} is defined by

$$p_{wf} = p(0). \tag{4.7.22}$$

Thus, p_{wf} is determined by the numerical solution of Eq. (4.7.18) for $p(0)$ subject to the constraints in Eqs. (4.7.19) - (4.7.21).

The pressure p_w corresponds to the pressure $p_w(0)$ in Eq. (4.7.11) and is obtained from the solution of Eqs. (4.2.1) - (4.2.6) with the computational grid in Fig. 4.2.1 (see Sect. 4.7.2). The production indexes J_b and J_g are defined in Eq. (4.7.5). Thus, the only quantity remaining to be specified in Eqs. (4.7.18) - (4.7.21) is the function F.

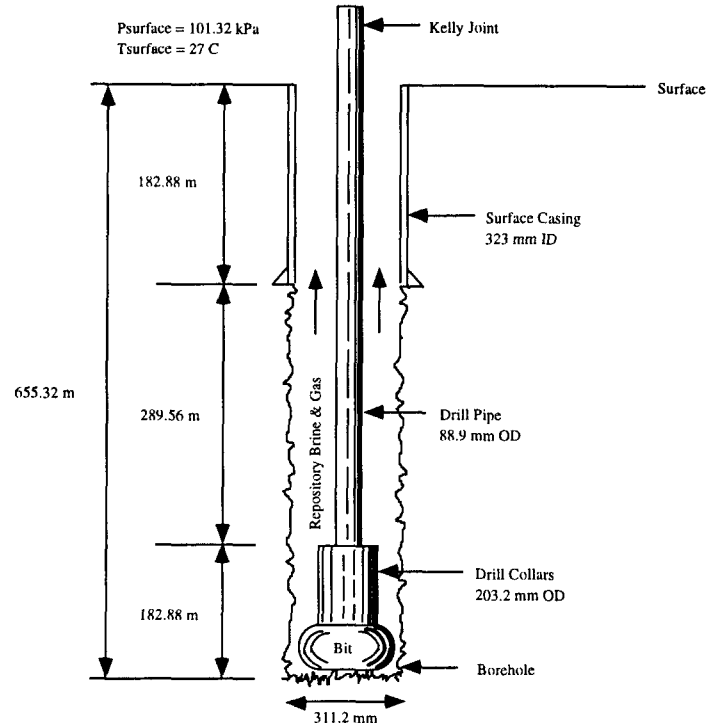

Fig. 4.7.3. Borehole representation used for Poettmann-Carpenter correlation.

Brine and gas flow up a borehole is governed by complex physics dependent on frictional effects and two-phase fluid properties. This phenomena has been widely studied in the petroleum industry and many modeling procedures (i.e., empirical correlations) have been developed to predict flow rates and pressures in vertical two-phase pipe flow (i.e., to define F in Eq. (4.7.18)) (Brill and Beggs 1986). For this analysis, the Poettmann-Carpenter model (Poettmann and Carpenter 1952, Welchon et al. 1962) was used to define F because it accounts for multi-phase frictional effects based on empirical (i.e., field) data from flowing wells, is one of the few modeling approaches that included annular flow data in its development, and is relatively easy to implement. Specifically, the Poettmann-Carpenter model defines F by

$$F\{q_b[p(0)],\, q_g[p(0)],\, p(h),h\} = gm(h) + f'\{m(h),D(h),q_b[p(0)]\}gm(h)F^2(h) / D^5(h), \tag{4.7.23}$$

where

g = acceleration due to gravity (9.8 m/s^2)

$m(h)$ = density (kg/m^3) of fluids (i.e., gas and brine) in wellbore at elevation h (Note: $m(h)$ is a function of $q_b[p(0)]$ and $q_g[p(0)]$; see Eq. (4.7.24) below),

$f'\{m(h), D(h)q_b[p(0)]\}$ = empirically defined scale factor (m/s^2) (Note: f' is the scale factor in the Poettmann-Carpenter model for fluid flow in a wellbore (Poettmann and Carpenter 1952); see discussion below),

$F(h)$ = flow rate (m^3/s) of fluids (i.e., gas and brine) in wellbore at elevation h (Note: $F(h)$ is a function of $q_b\,[p(0)]$ and $q_g\,[p(0)]$; see Eq. (4.7.25) below),

$D(h)$ = effective diameter (m) of wellbore (see Eq. (4.7.28) below).

The first term, $gm(h)$, in Eq. (4.7.23) results from the contribution of elevation to pressure; the second term results from frictional effects (Poettmann and Carpenter 1952). The original development of Eq. (4.7.23) (Poettmann and Carpenter 1952) and also the numerical implementation in the 1996 WIPP PA (Stoelzel and O'Brien 1996) used oilfield units. However, for consistency with the other model descriptions in this presentation, the terms in this equation are given in SI units.

The fluid density $m(h)$ at elevation h is given by

$$m(h) = \{q_b[p(0)]\rho_b[p(0)] + q_g[p(0)]\rho_g[p(0)]\} / F(h), \tag{4.7.24}$$

where

$$F(h) = q_b[p(0)] + [z(h)p(h) / p(0)]q_g[p(0)], \tag{4.7.25}$$

$\rho_b[p(0)]$ = density (kg/m^3) of brine at pressure $p(0)$ and temperature 300.1°K, which is fixed at 1230 kg/m^3,

$\rho_g[p(0)]$ = density (kg/m^3) of H_2 at pressure $p(0)$ and temperature 300.1°K (see Eq. (4.7.26) below),

$z(h)$ = z-factor for compressibility of H_2 at elevation h (Note: $z(h)$ is a function of $p(h)$; see Eq. (4.7.27) below), and $q_b[p(0)]$ and $q_g[p(0)]$ are defined in Eqs. (4.7.20) and (4.7.21).

The gas density in Eq. (4.7.24) is obtained from the universal gas law, $PV = nRT$, by

$$\rho_g[p(0)] = C_{m,kg}(n / V) = C_{m,kg}(P / RT), \tag{4.7.26}$$

where n is the amount of gas (mol) in a volume V, $C_{m,kg}$ is the conversion factor from moles to kilograms for H_2 (i.e., 2.02×10^{-3} kg/mol), $P = p(0)$, $R = 8.3145$ kg $m^2/mol°K\ s^2$, and $T = 300.1°K$. The z-factor is given by

$$z(h) \doteq 1 + (8.54 \times 10^{-8}\, Pa^{-1})p(h) \tag{4.7.27}$$

and was obtained from calculations performed with the SUPERTRAPP program (Ely and Huber 1992) for pure H_2 and a temperature of 300.1°K (Fig. 4.7.4, Stoelzel and O'Brien 1996). The preceding approximation to $z(h)$ was obtained by fitting a straight line between the results for pressures of 0 psia and 3000 psia and a hydrogen mole fraction of 1 in Fig. 4.7.4 of Stoelzel and O'Brien (1996); the actual calculations used the more complex, but numerically similar, regression model given in Fig. 4.7.4 of Stoelzel and O'Brien (1996). The numerator and denominator in Eq. (4.7.24) involve rates, with the time units canceling to give $m(h)$ in units of kg/m^3.

The effective diameter $D(h)$ in Eq. (4.7.23) is defined with the hydraulic radius concept. Specifically,

$$D^5(h) = [D_i(h) + D_o(h)]^2 [D_i(h) - D_o(h)]^3 , \tag{4.7.28}$$

where $D_i(h)$ and $D_o(h)$ are the inner and outer diameters (m) of the wellbore at elevation h(m) (see Fig. 4.7.3).

The factor f' in Eq. (4.7.23) is a function of $m(h)$, $D(h)$ and $q_b[p(0)]$. In the original development by Poettmann and Carpenter (Fig. 4, 1952), f' is defined in terms of quantities commonly used to measure production from oil and gas wells (Note: Poettmann and Carpenter use the symbol f rather than the symbol f' used in many subsequent treatments). The result is that f' is expressed in quantities that are unfamiliar outside of the oil and gas industry. For clarity, Eq. (4.7.23) and the quantities contained in it are expressed in SI units. However, to allow use of the original correlations developed by Poettmann and Carpenter to define f', the calculations within the 1996 WIPP PA (Stoelzel and O'Brien 1996) were performed in the same oilfield units originally used by Poettmann and Carpenter.

The following iterative procedure based on Euler's method was used to approximate solutions to Eqs. (4.7.18) - (4.7.21) for $p(0)$:

Step 1. Make initial or updated estimate of $p(0)$ as appropriate. (Initial guess for $p(0)$ is midpoint $p_w/2$ of interval $[0, p_w]$, where p_w is the pressure in the repository at the time of the drilling intrusion used in Eqs. (4.7.20), (4.7.21). Next guess for $p(0)$ is at midpoint of $[0, p_w/2]$ or $[p_w/2, p_w]$ depending on whether resultant approximation to $p(655)$ is above or below atmospheric pressure. Subsequent guesses for $p(0)$ are made in a similar manner.

Step 2. Use $p(0)$, known values for J_b, J_g and p_w, and Eqs. (4.7.20) - (4.7.21) to determine $q_b[p(0)]$ and $q_g[p(0)]$.

Step 3. Use Euler's method with Δh = 25 ft = 7.62 m and appropriate changes in annular diameter (Fig. 4.7.3) to determine $p(655)$ [i.e., $p(h + \Delta h) = p(h) + F\{q_b[p(0)], q_g[p(0)], p(h), h\}\Delta h$].

Step 4. Stop if $p(655)$ is within 0.07% of atmospheric pressure (i.e., if $|1.013 \times 10^5$ Pa $- p(655)| \leq 71$ Pa). Otherwise, return to Step 1 and repeat process.

The preceding procedure is continued until the specified error tolerance (i.e., 0.07%) has been met or 26 iterations have been performed. If the specified error tolerance has not been met after 26 iterations, the procedure is repeated with the error tolerance increased to 5%.

The computational design of the 1996 WIPP PA had the potential to require 15,600 separate direct brine release calculations (Sect 6.9). In concept, each of these cases requires the solution of Eqs. (4.7.18) - (4.7.21) with the iterative procedure just presented to obtain the boundary value condition $p_{wf} = p(0)$ for use in conjunction with Eqs. (4.7.12) - (4.7.17) (Table 4.7.2). To help hold computational costs down, Eqs. (4.7.18) - (4.7.21) were solved for $p(0)$ for approximately 2000 randomly-generated vectors of the form

$$\mathbf{v} = [p_w, h, S_{br}, S_{gr}, S_b, A_i], \tag{4.7.29}$$

where p_w is the repository pressure (used in definition of $q_b[p(0)]$, $q_g[p(0)]$ in Eqs. (4.7.20), (4.7.21)), h is the crushed height of the repository (used in definition of J_p in Eq. (4.7.5)), S_{br} and S_{gr} are the residual saturations for gas and brine in the repository (used in definition of k_{rp} in Eq. (4.7.5)), S_b is the saturation of brine in the repository (used in definition of k_{rp} in Eq. (4.7.5)), and A_i is the equivalent area of material removed by spallings (used in definition of skin factor s in Eq. (4.7.10)). The outcomes of these calculations were divided into three cases: (1) mobile brine only (i.e., $k_{rg} = 0$ in Eq. (4.2.11)), (2) brine-dominated flow (i.e., $\log (k_{rg}/k_{rb}) \leq 0$), and (3) gas-dominated flow (i.e., $\log (k_{rg}/k_{rb}) > 0$). Then, regression procedures were used to fit algebraic models that can be used to estimate $p(0)$ (Figs. 4.7.4 - 4.7.6). These regression models were then used to determine $p(0)$, and hence p_{wf}, in the 1996 WIPP PA.

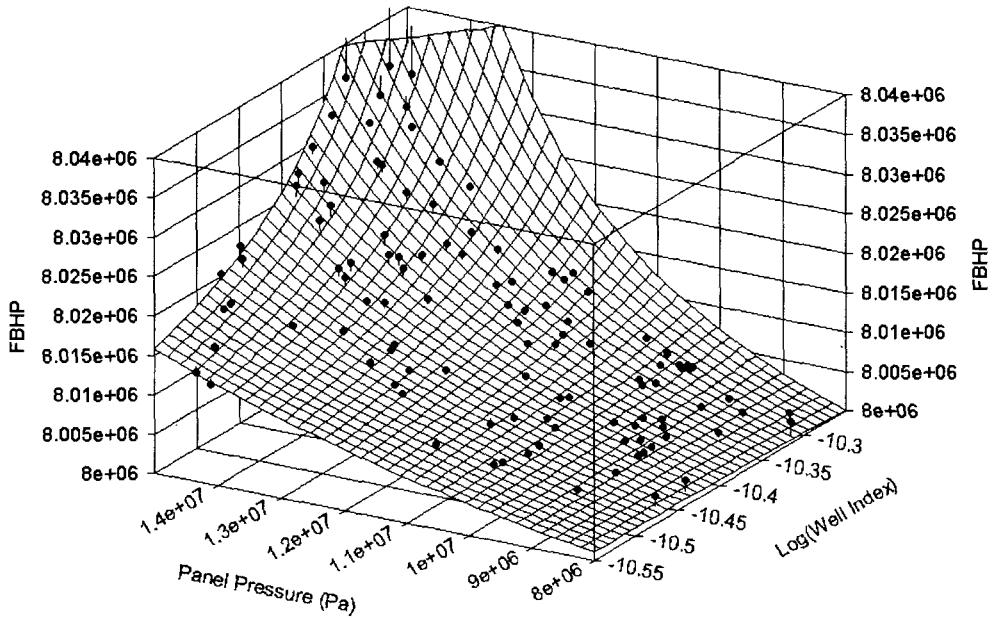

Fig. 4.7.4. Flowing bottom hole pressure (FBHP) (i.e., p_{wf} in Eq. (4.7.22)) as a function of brine well index (i.e., J_b in Eq. (4.7.5)) and panel pressure for a system with only mobile brine (i.e., $k_{rg} = 0$) (Fig. B1, Stoelzel and O'Brien 1996).

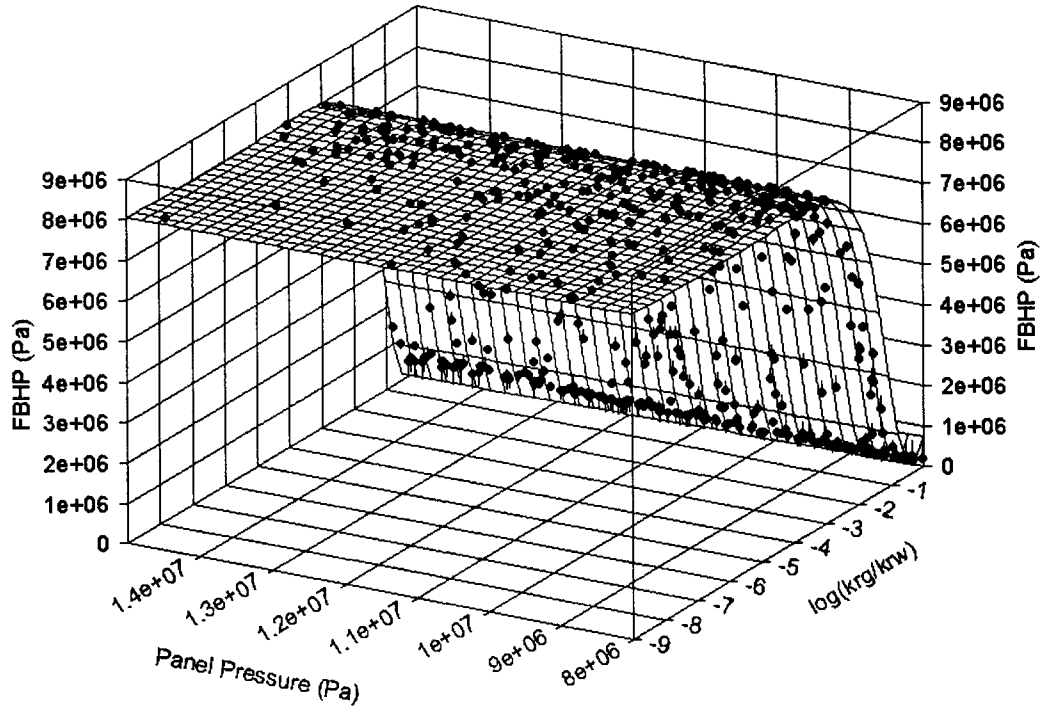

Fig. 4.7.5. Flowing bottom hole pressure (FBHP) (i.e., p_{wf} in Eq. (4.7.22)) as a function of relative permeabilities and panel pressure for a brine dominated system (i.e., log $(k_{rg}/k_{rb}) \leq 0$) (Fig. B2, Stoelzel and O'Brien 1996).

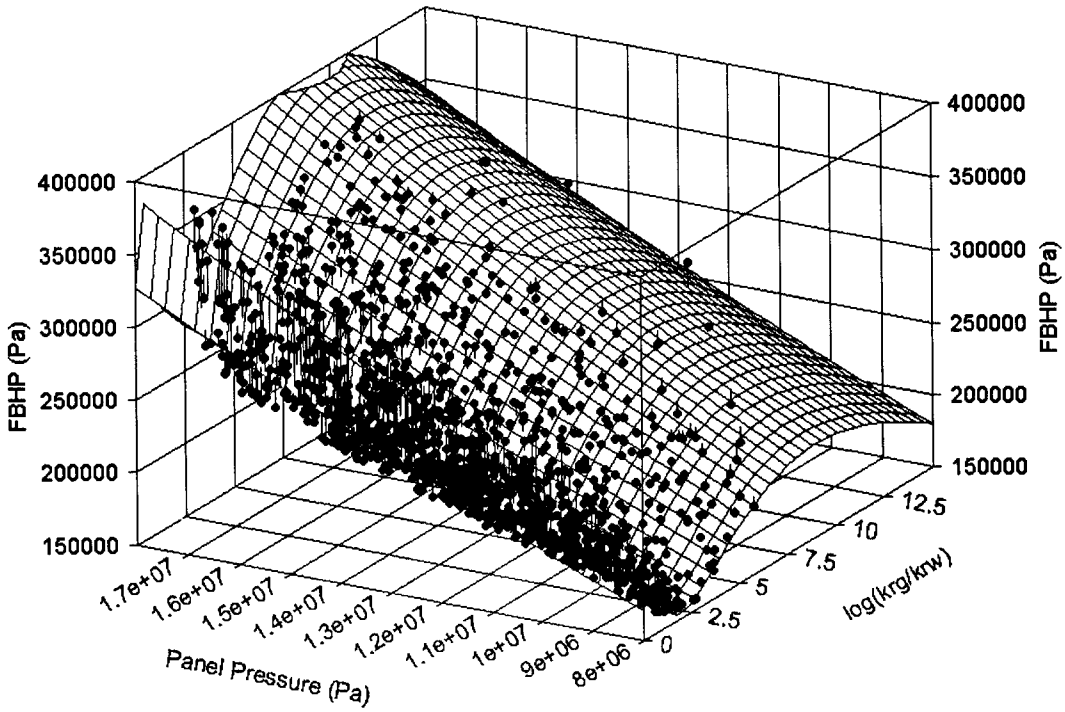

Fig. 4.7.6. Flowing bottom hole pressure (FBHP) (i.e., p_{wf} in Eq. (4.7.22)) as a function of relative permeabilities and panel pressure for a gas dominated system (i.e., log $(k_{rg}/k_{rb}) > 0$) (Fig. B3, Stoelzel and O'Brien 1996).

4.7.6 Boundary Value Pressure p_{wE1}

Some of the calculations for direct brine release are for a drilling intrusion that has been preceded by an E1 intrusion in either the same waste panel or a different waste panel (Sects. 4.7.1, 6.9). The effects of these prior E1 intrusions are incorporated into the solution of Eqs. (4.7.12) - (4.7.17), and hence into the direct brine release *DBR*, by the specification of a boundary pressure p_{wE1} at the location of the E1 intrusion into the repository (Table 4.7.2).

Two cases are considered for the definition of p_{wE1}: (1) an open borehole between the brine pocket and the repository, and (2) a borehole between the brine pocket and the repository filled with material with properties similar to silty sand. The first case corresponds to the situation in which the drilling intrusion under consideration has occurred within 200 yr of a prior drilling intrusion that penetrated the pressurized brine pocket, and the second case corresponds to the situation in which the drilling intrusion under consideration has occurred more than 200 yr after a prior drilling intrusion that penetrated the pressurized brine pocket (Table 4.2.8).

Case 1: Open Borehole. A derivation follows for the flowing well pressure at the inlet to the repository associated with a drilling intrusion that penetrates the repository and a brine pocket under the assumption that an open borehole exists between the brine pocket and the repository. The value for this pressure is then assigned to p_{wE1} for the case under consideration (Table 4.7.2). This determination is made by developing a system of equations of the following form:

$$Q = f_1 (p_{BP}, p_{wfBP}) \tag{4.7.30}$$

$$Q = f_2 (p_{wfBP}, p_{wfBI}) \tag{4.7.31}$$

$$Q = f_3 (p_{wfBI}, p_{wfBO}) \tag{4.7.32}$$

where

p_{BP} = pressure (Pa) in brine pocket,

p_{wfBP} = flowing well pressure (Pa) at outlet from brine pocket,

p_{wfBI} = flowing well pressure (Pa) at inlet to repository from brine pocket,

p_{wfBO} = flowing well pressure (Pa) at outlet from repository due to intruding borehole (Note: The boreholes associated with p_{wfBI} and p_{wfBO} arise from different drilling intrusions and hence are at different locations; see Fig. 4.7.1),

Q = brine flow rate (m^3/s) from brine pocket to repository, through repository, and then to surface,

and f_1, f_2 and f_3 are linear functions of their arguments. In the development, p_{BP} and p_{wfBO} are assumed to be known, with the result that Eqs. (4.7.30) - (4.7.32) constitute a system of three linear equations in three unknowns (i.e., p_{wfBP}, p_{wfBI}, Q) that can be solved to obtain p_{wfBI}. In the determination of $p_{wfBI} = p_{wE1}$ for use in a particular solution of Eqs. (4.7.12) - (4.7.17), p_{BP} is the pressure in the brine pocket at the time of the intrusion obtained from the solution of Eqs. (4.2.1) - (4.2.6) with BRAGFLO, and p_{wfBO} is the flowing well pressure obtained from conditions at the time of the intrusion (from the solution of Eqs. (4.2.1) - (4.2.6)) and the solutions of the Poettmann-Carpenter model embodied in Figs. 4.7.4 - 4.7.6. (i.e., given pressure, k_{rg} and k_{rb} at the time of the intrusion from the solution of Eqs. (4.2.1) - (4.2.6) with BRAGFLO and J_b from both the solution of Eqs. (4.2.1)- (4.2.6) with BRAGFLO and the evaluation of the spallings release with CUTTINGS_S, p_{wfBO} is determined from the regression models indicated in Figs. 4.7.4 - 4.7.6).

The definition of Eqs. (4.7.30) - (4.7.32) is now discussed. Eq. (4.7.30) characterizes flow out of the brine pocket into an open borehole and has the form (Williamson and Chappelear 1981, Chappelear and Williamson 1981):

$$Q = \left(\frac{k_{BP} h_{BP}}{\mu[\ln(r_{eBP} / r_w) - 0.5]} \right) \left(p_{BP} - p_{wfBP} \right) \tag{4.7.33}$$

where

k_{BP} = brine pocket permeability (m^2),

h_{BP} = effective brine pocket height (m),

r_{eBP} = effective brine pocket radius (m),

r_w = wellbore radius (m),

μ = brine viscosity (Pa s).

In the present analysis, k_{BP} is an uncertain analysis input (see *BPPRM* in Sect. 5.2), h_{BP} = 12.34 m (Stoelzel and O'Brien 1996), r_{eBP} = 114 m (Stoelzel and O'Brien 1996), which corresponds to the size of the largest brine pocket that could fit under one waste panel, r_w = (8.921 in) /2 = 0.1133 m, which is the inside radius of a 9 5/8 in outside diameter casing (Table 14.7, Gatlin 1960), $\mu = 1.8 \times 10^{-3}$ Pa s, and p_{BP} is determined from the solution of Eqs. (4.2.1) - (4.2.6) as previously indicated.

Eq. (4.7.31) characterizes flow up an open borehole from the brine pocket to the repository and is based on Poiseuille's Law (Eqs. 7-21, 7-22, Prasuhn 1980). Specifically, Eq. (4.7.31) has the form

$$Q = \left[\frac{\pi D^4}{128\mu(y_{BP} - y_{rep})}\right]\left[\left(p_{wfBP} - p_{wfBI}\right) + g\rho\left(y_{rep} - y_{BP}\right)\right] \tag{4.7.34}$$

where

D = wellbore diameter (m),

y_{rep} = elevation of repository (m) measured from surface,

y_{BP} = elevation of brine pocket (m) measured from surface,

g = acceleration due to gravity (9.8 m/s^2),

ρ = density of brine (kg/m^3),

and the remaining symbols have already been defined.

In the present analysis, D = $2r_w$ = 0.2266 m, ρ = 1230 kg/m^3, and $y_{rep} - y_{BP}$ = 247 m. With the preceding values,

$$128\mu(y_{BP} - y_{rep})/\pi D^4 = 6.87 \times 10^3 \text{ Pa s/m}^3 \tag{4.7.35}$$

$$g\rho(y_{rep} - y_{BP}) = -2.98 \times 10^6 \text{ Pa.} \tag{4.7.36}$$

Thus,

$$p_{wfBI} \doteq p_{wfBP} - 2.98 \times 10^6 \text{ Pa} \tag{4.7.37}$$

when Q is small ($\leq$ 0.1 m^3/s). When appropriate, this approximation can be used to simplify the construction of solutions to Eqs. (4.7.30) - (4.7.32).

Eq. (4.7.32) characterizes flow from the brine pocket inlet point to the repository to the outlet point associated with the drilling intrusion under consideration and has the same form as Eq. (4.7.33). Specifically,

$$Q = \left(\frac{k_{rep} h_{rep}}{\mu[\ln(r_{e,rep} / r_w) - 0.5]}\right)\left(p_{wfBI} - p_{wfBO}\right), \tag{4.7.38}$$

where

k_{rep} = repository permeability (m^2),

h_{rep} = repository height (m),

$r_{e,rep}$ = effective repository radius (m),

and the remaining symbols have already been defined. In the present analysis, $k_{rep} = 1.7 \times 10^{-13}$ m^2; h_{rep} at the time of the drilling intrusion under consideration is obtained from the solution of Eqs. (4.2.1) - (4.2.6) (see Eq. (4.7.2)); and $r_{e,rep}$ is the same as the radius r_e defined in Eq. (4.7.6) (i.e., $r_{e,rep}$ = 10.2 m). As previously indicated, p_{wfBO} is obtained from the solutions to the Poettmann-Carpenter model summarized in Figs. 4.7.4 - 4.7.6.

Three equations (i.e., Eqs. (4.7.33), (4.7.34) and (4.7.38)) in three unknowns (i.e., p_{wfBP}, p_{wfBI} and Q) have now been developed. Solution is straight forward (e.g., use Cramer's Rule or a simple numerical procedure). It is the solution for p_{wfBI} that is of primary interest because p_{wfBI} defines the initial value p_{wE1} in Table 4.7.2. When the simplification in Eq. (4.7.37) is used, the resultant solution for p_{wfBI} is

$$p_{wfBI} = (p_{wfBO} + K_1 p_{BP} - 2.98 \times 10^6 K_1) / (1 + K_1), \tag{4.7.39}$$

where

$$K_1 = \{k_{BP} h_{BP} \ln[(r_{e,rep} / r_w) - 0.5]\} / \{k_{rep} h_{rep} \ln[(r_{eBP} / r_w) - 0.5]\} \tag{4.7.40}$$

and -2.98×10^6 comes from Eq. (4.7.36). The expression in Eq. (4.7.40) was used to define p_{wE1} in the 1996 WIPP PA in the determination of direct brine releases for a drilling intrusion that occurred within 200 yr of a preceding E1 intrusion (see Table 4.2.8).

Case 2: Sand-Filled Borehole. The determination of the pressure p_{wfBI} with the assumption that a borehole filled with material with properties similar to silty sand connects the brine pocket and the repository is now considered. The approach is similar to that used for the open borehole except that Eqs. (4.7.30) - (4.7.31) are replaced by a single equation based on Darcy's Law. Specifically, flow from the brine pocket to the repository is represented by

$$Q = k_{BH} A_{BH} [(p_{wfBP} - p_{wfBI}) + g\rho(y_{rep} - y_{BP})] / [\mu(y_{BP} - y_{rep})], \tag{4.7.41}$$

where

k_{BH} = borehole permeability (m^2),

A_{BH} = borehole cross-sectional area (m^2),

and the remaining symbols have been defined previously. In the present analysis, k_{BH} is an uncertain input (see *BHPRM* in Sect. 5.2) and A_{BH} is defined by the assumption that the borehole diameter is the same as the drillbit diameter (i.e., 12.25 in. = 0.311 m).

The representation for flow from the brine pocket inlet point to the repository to the outlet point associated with the drilling intrusion under consideration remains as defined in Eq. (4.7.38). Thus, two equations (i.e., Eqs. (4.7.41) and (4.7.38)) and two unknowns (i.e., p_{wfBI} and Q) are under consideration. Solution for p_{wfBI} is straight forward and yields

$$p_{wfBI} = (p_{wfBO} + K_2 p_{BP} - 2.98 \times 10^6 K_2)/(1 + K_2), \tag{4.7.42}$$

where

$$K_2 = \pi k_{BH} r_w^2 [\ln(r_{eBP}/r_w) - 0.5]/[h_{rep} k_{rep} (y_{BP} - y_{rep})] \tag{4.7.43}$$

and -2.98×10^6 comes from Eq. (4.7.36). The expression in Eq. (4.7.42) was used to define p_{wE1} in the determination of direct brine releases for a drilling intrusion that occurred more than 200 yr after a preceding E1 intrusion (see Table 4.2.8).

4.7.7 End of Direct Brine Release t_e

The 1996 WIPP PA involved 15600 cases that potentially required solution of Eqs. (4.7.12) - (4.7.17) to obtain the direct brine release *DBR* (Sect. 6.9). However, the direct brine release was set to zero without solution of Eqs. (4.7.12) - (4.7.17) when there was no possibility of a release (i.e., the intruded waste panel at the time of the intrusion had either a pressure less than 8 MPa or a brine saturation below the residual brine saturation S_{br}, which was defined by the uncertain analysis input *WRBRNSAT* (Sect. 5.2)).

For the remaining cases, Eqs. (4.7.12) - (4.7.17) were solved for a time period of 50 days, although the value used for t_e was always less than 50 days. The minimum value used for t_e was 3 days, which is an estimate of the time required to drill from the repository through the Castile Formation and then cement the intermediate casing. If there is little or no gas flow associated with brine inflow into the borehole during drilling in the Salado Formation, current industry practice is to allow the brine to "seep" into the drilling mud and be discharged to the mud pits until the salt section is cased.

If there is a significant amount of gas flow, then it is possible that the driller will lose control of the well. In such cases, direct brine releases will take place until the gas flow is brought under control. Two possibilities exist: (1) the driller will regain control of the well when the gas flow drops to a manageable level, and (2) aggressive measures will be taken to shut off the gas flow before it drops to a manageable level. In the 1996 WIPP PA, the

driller was assumed to be able to regain control of the well when the gas flow dropped to a "cut-off" rate of 1×10^5 standard cubic feet per day (SCF/d in commonly used oil field units). Experience at the South Culebra Bluff Unit #1, which blew out in January 1978, suggests that approximately 11 days are needed to bring a well under control before the gas flow drops to a manageable level (i.e., 1×10^5 SCF/d). In particular, 11 days was the time required to assemble the necessary equipment and personnel and then bring that well under control.

Given the preceding, t_e is defined by

$$t_e = \begin{cases} \max\{3\text{ d}, t_f\} & \text{if } t_f \le 11\text{ d} \\ 11\ d & \text{if } t_f > 11\text{ d} \end{cases} \tag{4.7.44}$$

in the 1996 WIPP PA, where t_f is the time at which the gas flow out of the well drops below 1×10^5 SCF/d. As a reminder, gas flow out of the repository in the intruding borehole, and hence t_f, is determined as part of the solution to Eqs. (4.7.12) - (4.7.17).

4.7.8 Numerical Solution

As previously indicated, the BRAGFLO_DBR program used to solve Eqs. (4.7.12) - (4.7.17) is just the BRAGFLO program used with the computational grid in Fig. 4.7.1, the initial value and boundary value conditions in Tables 4.7.1 and 4.7.2, and parameter values appropriate for modeling direct brine releases. Thus, the numerical procedures in use are the same as those described in Sect. 4.2.8 for the solution of Eqs. (4.2.1) - (4.2.6).

In this solution, the boundary value conditions associated with drilling intrusions (i.e., p_{wf} and p_{wE1} in Table 4.7.2) are implemented through the specification of fluid withdrawal terms (i.e., q_{wg} and q_{wb} in Eqs. (4.2.1) and (4.2.2)) rather than as defined boundary value conditions. With this implementation, the representations in Eqs. (4.7.12) and (4.7.13) for gas and brine conservation become

$$\nabla \bullet \left[\frac{\alpha \rho_g \mathbf{K}_g k_{rg}}{\mu_g} \left(\nabla p_g + \rho_g g \nabla h \right) \right] + \alpha q_{wg} = \alpha \frac{\partial \left(\phi \rho_g S_g \right)}{\partial t} \tag{4.7.45}$$

$$\nabla \bullet \left[\frac{\alpha \rho_b \mathbf{K}_b k_{rb}}{\mu_b} \left(\nabla p_b + \rho_b g \nabla h \right) \right] + \alpha q_{wb} = \alpha \frac{\partial \left(\phi \rho_b S_b \right)}{\partial t} \tag{4.7.46}$$

and the constraints in Eqs. (4.7.14) - (4.7.17) remain unchanged. All quantities appearing in Eqs. (4.7.45), (4.7.46), (4.7.14) - (4.7.17) except q_{wg} and q_{wb} have been defined (see paragraph following Eqs. (4.7.12) - (4.7.17)).

The definitions of q_{wg} and q_{wb} are now considered. As used in Eqs. (4.7.45) and (4.7.46), q_{wg} and q_{wb} are independent of the computational grid in use (Fig. 4.7.1). In practice, q_{wg} and q_{wb} are defined with a productivity

index (see Eq. (4.7.5)) that is a function of the specific computational grid in use, with the result that these definitions are only meaningful in the context of the computational grid that they are intended to be used with. This specificity results because q_{wg} and q_{wb} as used in Eqs. (4.7.45) and (4.7.46) are defined on a much smaller scale than can typically be implemented with a reasonable-sized computational grid. As a result, the values used for q_{wg} and q_{wb} in the numerical solution of Eqs. (4.7.45) and (4.7.46) must incorporate the actual size of the grid in use.

In the solution of Eqs. (4.7.45) and (4.7.46) with the computational grid in Fig. 4.7.1, q_{wg} is used to incorporate gas flow out of the repository and q_{wb} is used to incorporate both brine inflow to the repository from a pressurized brine pocket and brine flow out of the repository. For gas flow out of the repository,

$$q_{wg}(x,y,t) = \frac{kk_{rg}(x,y,t)[p_g(x,y,t) - p_{wf}]}{\mu_g[\ln(r_e / r_w) + s + c]} \tag{4.7.47}$$

if (x, y) is at the center of the grid cell containing the drilling intrusion (Fig. 4.7.1) and q_{wg} $(x, y, t) = 0$ (kg/m^3)/s otherwise, where k, k_{rg}, μ_g, r_e, r_w, s and c are defined in conjunction with Eq. (4.7.5), p_g is gas pressure, and p_{wf} is the flowing well pressure at the outlet borehole (i.e., the boundary value condition in Table 4.7.2). The factor h in Eq. (4.7.5) is the crushed height of the repository as indicated in Eq. (4.7.2) and defines the factor α in Eqs. (4.7.45) and (4.7.46). In the numerical solution of Eqs. (4.7.45) and (4.7.46), $q_{wg}(x, y, t)$ defines $q^{n+1}_{wgi,j}$ in Eq. (4.2.72), with $q^{n+1}_{wgi,j}$ having a nonzero value only when i, j correspond to the grid cell containing the borehole through which gas outflow is taking place (i.e., the grid cells containing the down-dip and up-dip wells in Fig. 4.7.1).

For brine flow,

$$q_{wb}(x,y,t) = \frac{kk_{rb}(x,y,t)[p_b(x,y,t) - p_{wf}]}{\mu_b[\ln(r_e / r_w) + s + c]} \tag{4.7.48}$$

if (x, y) is at the center of the grid cell containing the drilling intrusion through which brine outflow from the repository is taking place (Fig. 4.7.1);

$$q_{wb}(x,y,t) = \frac{kk_{rb}(x,y,t)[p_{wE1} - p_b(x,y,t)]}{\mu_b[\ln(r_e / r_w) + c]} \tag{4.7.49}$$

if (x, y) is at the center of the grid cell containing a prior drilling intrusion into a pressurized brine pocket (Fig. 4.7.1), where p_{wE1} is the boundary value condition defined in Table 4.7.2; and $q_{wb}(x, y, t) = 0$ otherwise. In the numerical solution of Eqs. (4.7.45) and (4.7.46), $q_{wb}(x, y, t)$ defines $q^{n+1}_{wbi,j}$ in a discretization for Eq. (4.7.46) that is equivalent to the discretization for Eq. (4.7.45) shown in Eq. (4.2.72), with $q^{n+1}_{wbi,j}$ having a nonzero value only when i, j correspond to the grid cell containing the borehole through which brine outflow is taking place (i.e., the grid cells containing the down-dip and up-dip wells in Fig. 4.7.1; in which case, Eq. (4.7.48) defines $q^{n+1}_{wbi,j}$) or to the grid cell

containing the borehole through which brine inflow to the repository from a pressurized brine pocket is taking place (i.e., the grid cell containing the E1 intrusion in Fig. 4.7.1; in which case, Eq. (4.7.49) defines $q^{n+1}_{wbi,j}$).

4.7.9 Additional Information

Additional information on BRAGFLO_DBR (actually BRAGFLO) and its use in the 1996 WIPP PA to determine direct brine releases can be found in the analysis package for direct brine release (Stoelzel and O'Brien 1996) and in the BRAGFLO users manual (WIPP PA 1996a)

4.8 Brine Flow in Culebra: SECOFL2D (i.e., f_{S-F})

4.8.1 Mathematical Description

Groundwater flow in the Culebra Dolomite is represented by the equation

$$S\left(\frac{\partial h}{\partial t}\right) = \nabla \bullet (b\mathbf{K}\nabla h) - Q, \tag{4.8.1}$$

where

S = medium storativity (dimensionless),
h = hydraulic head (m),
t = time (s),
b = aquifer thickness (m),
$\mathbf{K}$ = hydraulic conductivity tensor (m/s),
Q = source/sink term expressed as the volumetric flux per unit area ($(m^3/m^2)/s$ =m/s).

Further, the Culebra is assumed to be isotropic, and as a result, $\mathbf{K}$ is defined by

$$\mathbf{K}(x, y) = k(x, y)\begin{bmatrix} 1 & 0 \\ 0 & 1 \end{bmatrix}, \tag{4.8.2}$$

where $k(x, y)$ is the hydraulic conductivity (m/s) at the point (x, y).

The following additional simplifying assumptions are also made: fluid flow in the Culebra is at steady state (i.e., $\partial h/\partial t = 0$), and source/sink effects arising from borehole intrusions and infiltration are negligible (i.e., $Q = 0$). Given these assumptions, Eq. (4.8.1) simplifies to

$$\nabla\bullet(b\mathbf{K}\nabla h) = 0, \tag{4.8.3}$$

which is the equation actually solved to obtain fluid flow (i.e., $\mathbf{K}\nabla h$) in the Culebra. In the 1996 WIPP PA, $b = 4$ m (Meigs and McCord 1996a), and $k(x, y)$ in Eq. (4.8.2) is a function of an imprecisely-known transmissivity field as discussed in Sect. 4.8.2.

4.8.2 Implementation

The first step in the analysis of fluid flow in the Culebra was to generate transmissivity fields $t(x, y)$ (m^2/s) for the Culebra and to characterize the uncertainty in these fields. This was accomplished by generating a large number of plausible transmissivity fields with WIPP-site data and geostatistical analysis with the program GRASP-INV (LaVenue 1996). Each generated transmissivity field $t(x, y)$ is a representation of spatial variability of transmissivity in the Culebra that is consistent with measured field data. A total of 100 equally-plausible transmissivity fields were generated for use in the analysis and correspond to the variable *CTRAN* in Sect. 5.2.

The hydraulic conductivity $k(x, y)$ in Eq. (4.8.2) was defined in terms of the transmissivity fields $t(x, y)$ by

$$k(x, y) = t(x, y)/b. \tag{4.8.4}$$

The original construction of the functions $t(x, y)$ used a Culebra thickness of 7.75 m (LaVenue 1996). However, flow was subsequently determined to take place primarily in the lower 4 m of the Culebra (Meigs and McCord 1996a) and so a value of $b = 4$ m was used in Eq. (4.8.4), which results in a conservation of transmissivity.

Fluid flow (i.e., $\mathbf{K}\nabla h$) is determined by solving Eq. (4.8.3) for two different cases (Wallace 1996a): (1) mining of potash deposits outside the land withdrawal boundary (Fig. 4.8.1), and (2) mining of potash deposits inside and outside the land withdrawal boundary (Fig. 4.8.2). As specified by guidance in 40 CFR 194 (p. 5229, U.S. EPA 1996), potash mining increases the hydraulic conductivity in the Culebra in the vicinity of such mining by an uncertain factor with a value between 1 and 1000 (see *CTRANSFM* in Sect. 5.2). The mining of economic potash reserves outside the land withdrawal boundary (Fig. 4.8.1) is assumed to have always occurred by 100 yr after decommissioning of the WIPP (i.e., by the end of the assumed 100 yr period of active institutional control). As specified in 40 CFR 194.32(b), the occurrence of potash mining within the land withdrawal boundary (Fig. 4.8.2) follows a Poisson process with a rate constant of $\lambda_m = 1 \times 10^{-4}$ yr^{-1} (see Sect. 3.7).

The preceding cases result in the following two modifications of the definition of $k(x, y)$ in Eq. (4.8.4):

$$k_1(x, y) = \begin{cases} SFM\ k(x, y) & \text{if } (x, y) \text{ corresponds to a point impacted by mining in Fig. 4.8.1} \\ k(x, y) & \text{otherwise,} \end{cases} \tag{4.8.5}$$

$$k_2(x, y) = \begin{cases} SFM\ k(x, y) & \text{if } (x, y) \text{ corresponds to a point impacted by mining in Fig. 4.8.2} \\ k(x, y) & \text{otherwise,} \end{cases} \tag{4.8.6}$$

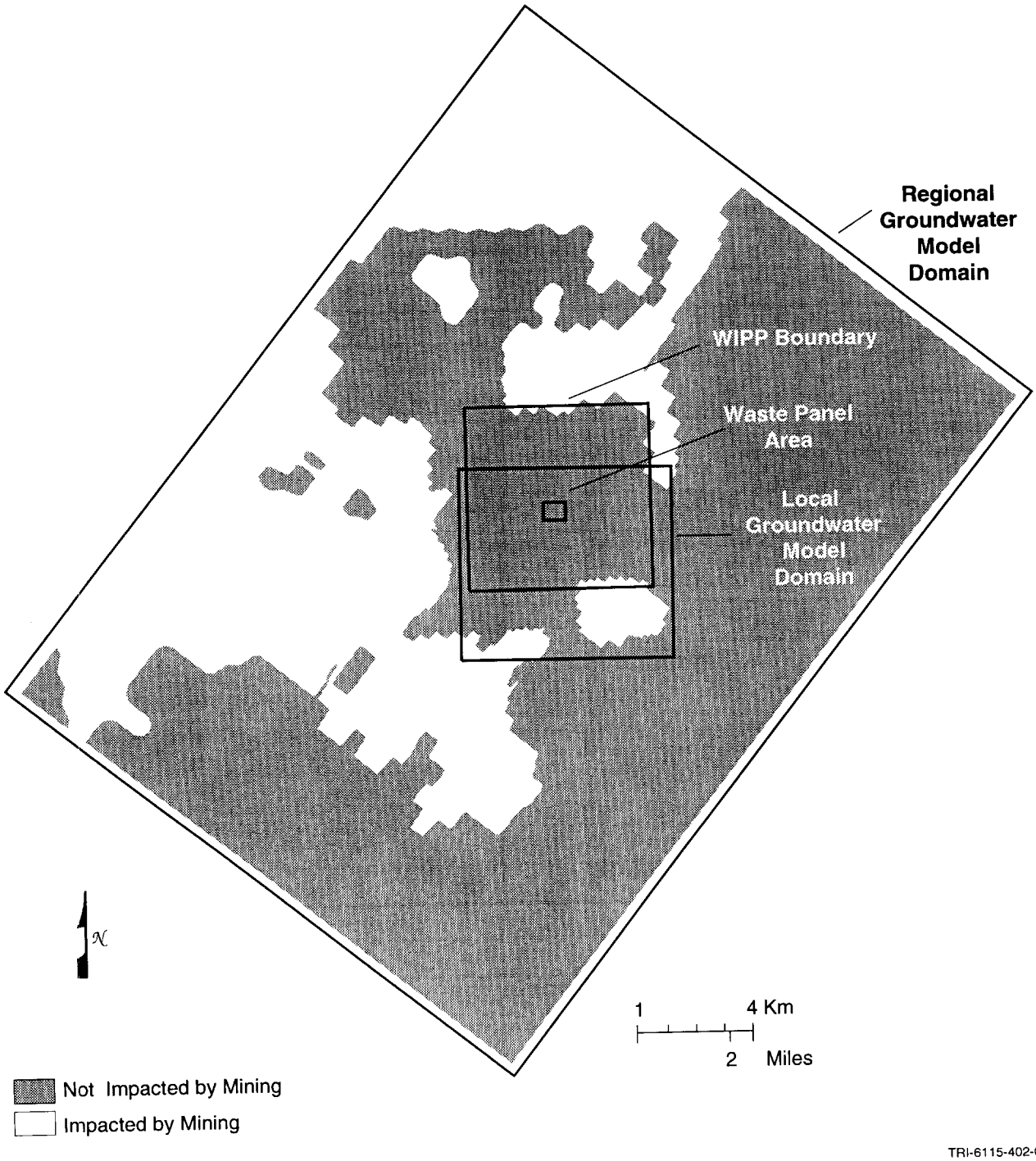

Fig. 4.8.1. Extent of impacted area in the Culebra Dolomite from mining in the McNutt potash zone outside the land withdrawal boundary (Wallace 1996a).

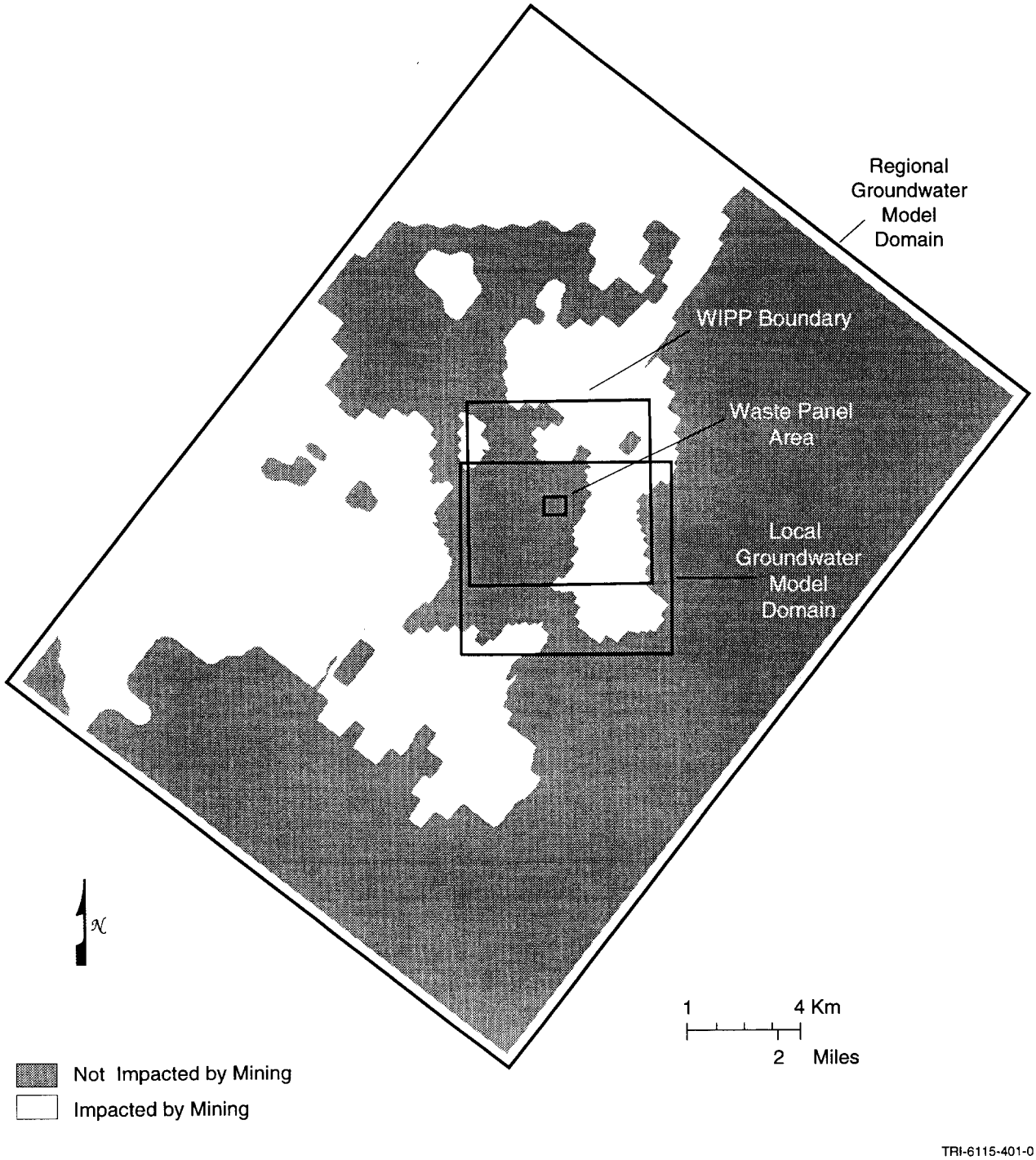

Fig. 4.8.2. Extent of impacted area in the Culebra Dolomite from mining in the McNutt potash zone inside and outside the land withdrawal boundary (Wallace 1996a).

where *SFM* is the scale factor for hydraulic conductivity due to potash mining that is specified in 40 CFR 194 (p. 5229, U.S. EPA 1996; see *CTRANSFM* in Sect. 5.2).

In turn, $k_1(x, y)$ and $k_2(x, y)$ result in the following definitions for the hydraulic conductivity tensor $\mathbf{K}$:

$$\mathbf{K}_i(x, y) = k_i(x, y)\begin{bmatrix} 1 & 0 \\ 0 & 1 \end{bmatrix}, \quad i = 1, 2 . \tag{4.8.7}$$

In the analysis, Eq. (4.8.3) is solved with each of the preceding definitions of $\mathbf{K}_i$ to obtain characterizations of fluid flow in the Culebra under partially-mined conditions (i.e., $\mathbf{K}_1\nabla h$) and fully-mined conditions (i.e., $\mathbf{K}_2\nabla h$).

The determination of fluid flow in the Culebra through the solution of Eq. (4.8.3) does not incorporate the potential effects of climate change on fluid flow. Such effects are incorporated into the analysis by the use of an uncertain scale factor (see *CULCLIM* in Sect. 5.2) to introduce the potential effects of climate change into the analysis (Corbet and Swift 1996a,b). Specifically, the Darcy fluid velocity $\mathbf{v}_i(x, y)$ actually used in the radionuclide transport calculations is given by

$$\mathbf{v}_i(x, y) = [u_i(x, y), v_i(x, y)] = SFC\,[\mathbf{K}_i(x, y)\nabla h_i(x, y)]^T, \tag{4.8.8}$$

where $u_i(x, y)$ and $v_i(x, y)$ represent Darcy fluid velocities (m/s) at the point (x, y) in the x and y directions, respectively, $\nabla h_i(x, y)$ is obtained from Eq. (4.8.3) with $\mathbf{K} = \mathbf{K}_i$, and *SFC* is a scale factor used to incorporate the uncertainty that results from possible climate changes (see *CULCLIM* in Sect. 5.2).

4.8.3 Computational Grids and Boundary Value Conditions

The representation for fluid flow in the Culebra in Eq. (4.8.3) is evaluated on both a regional and a local scale (Fig. 4.8.3). The regional scale simulations were performed over a large problem domain (Fig. 4.8.3) and used a relatively coarse computational grid (Fig. 4.8.4). The results of the regional scale simulations were used to define boundary value conditions for the local scale simulations. This analysis approach allows the use of a high resolution computational grid (Fig. 4.8.5) in the region of interest (i.e., close to the repository), and the incorporation of natural flow boundaries on a much larger scale.

The regional domain is approximately 22 × 30 km and aligned with the axis of Nash Draw along a portion of the western boundary (Fig. 4.8.3). Nash Draw is a topographic low created by the dissolution of halite beneath the Rustler Formation. As a consequence of this dissolution, the Rustler has subsided and the contact between the Rustler and Salado Formations consists of an unstructured residuum of gypsum, clay, and sandstone. This residuum is highly conductive and known to discharge to the surface into saline lakes (Hunter 1985). Test wells in the southern portion of Nash Draw produced brine from this interval, and it has become known as the brine aquifer

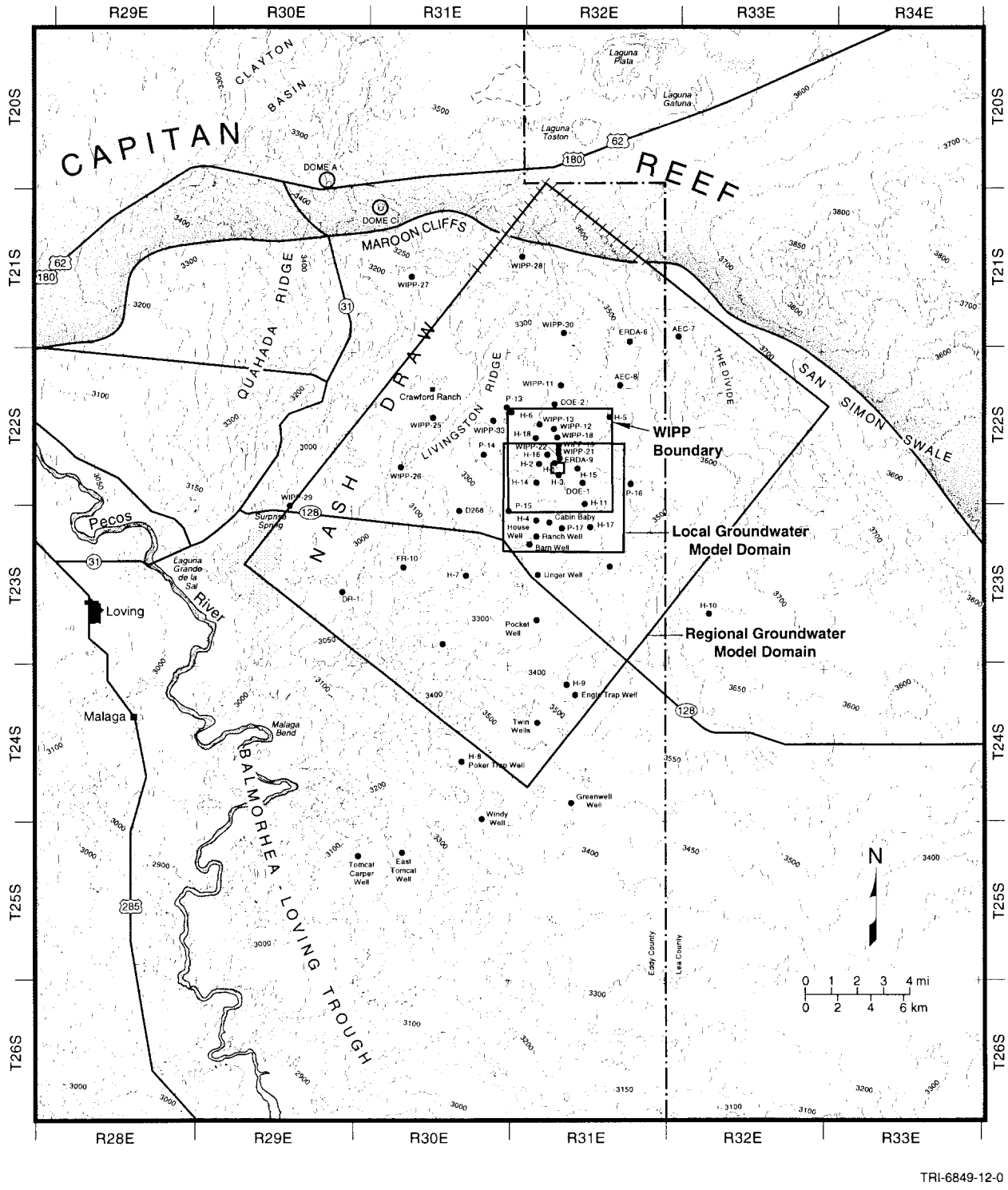

Fig. 4.8.3. Regional and local domains used in representation of groundwater flow in the Culebra Dolomite.

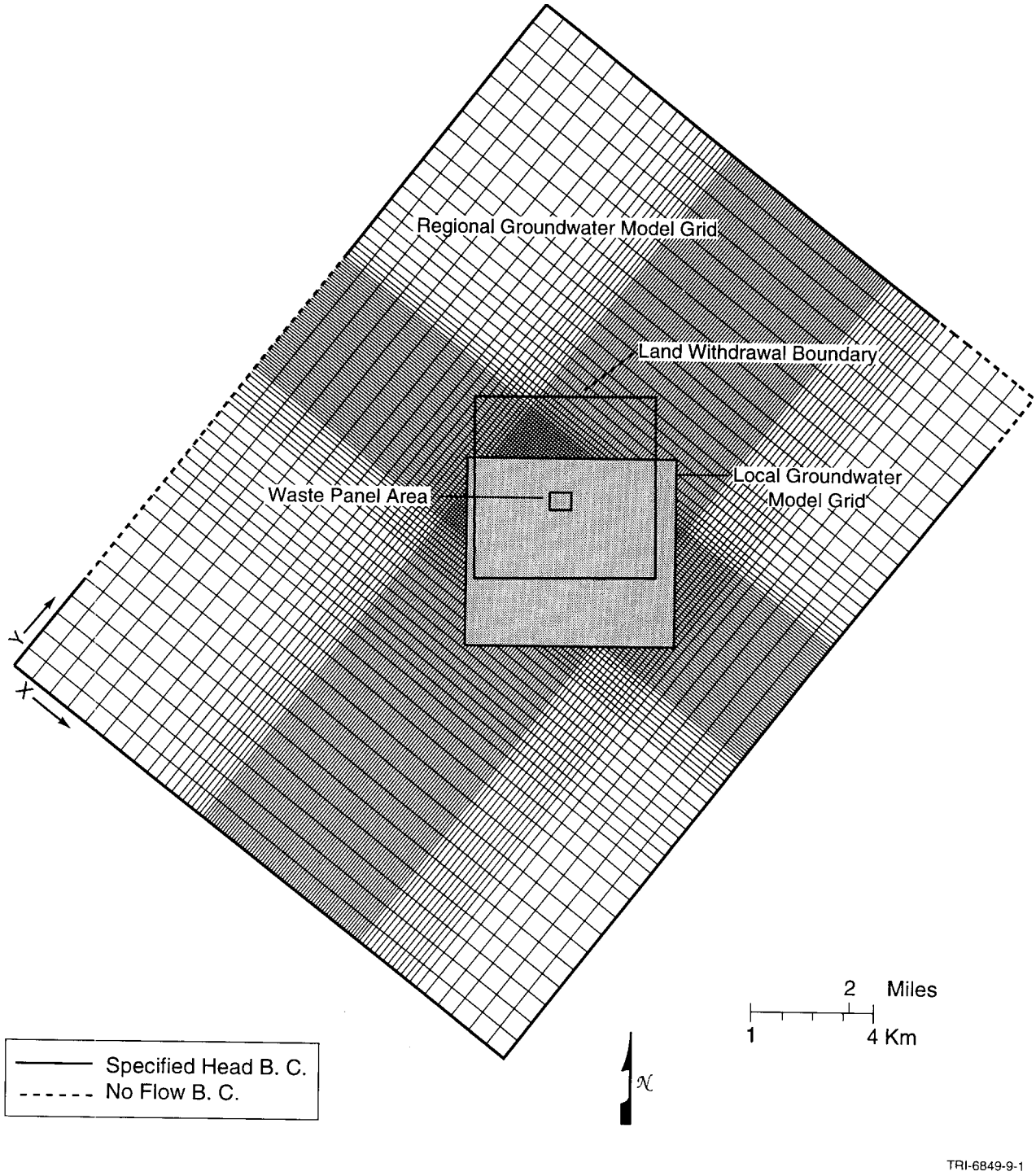

Fig. 4.8.4. Regional model domain spatial discretization and type of boundary conditions for groundwater flow in the Culebra Dolomite.

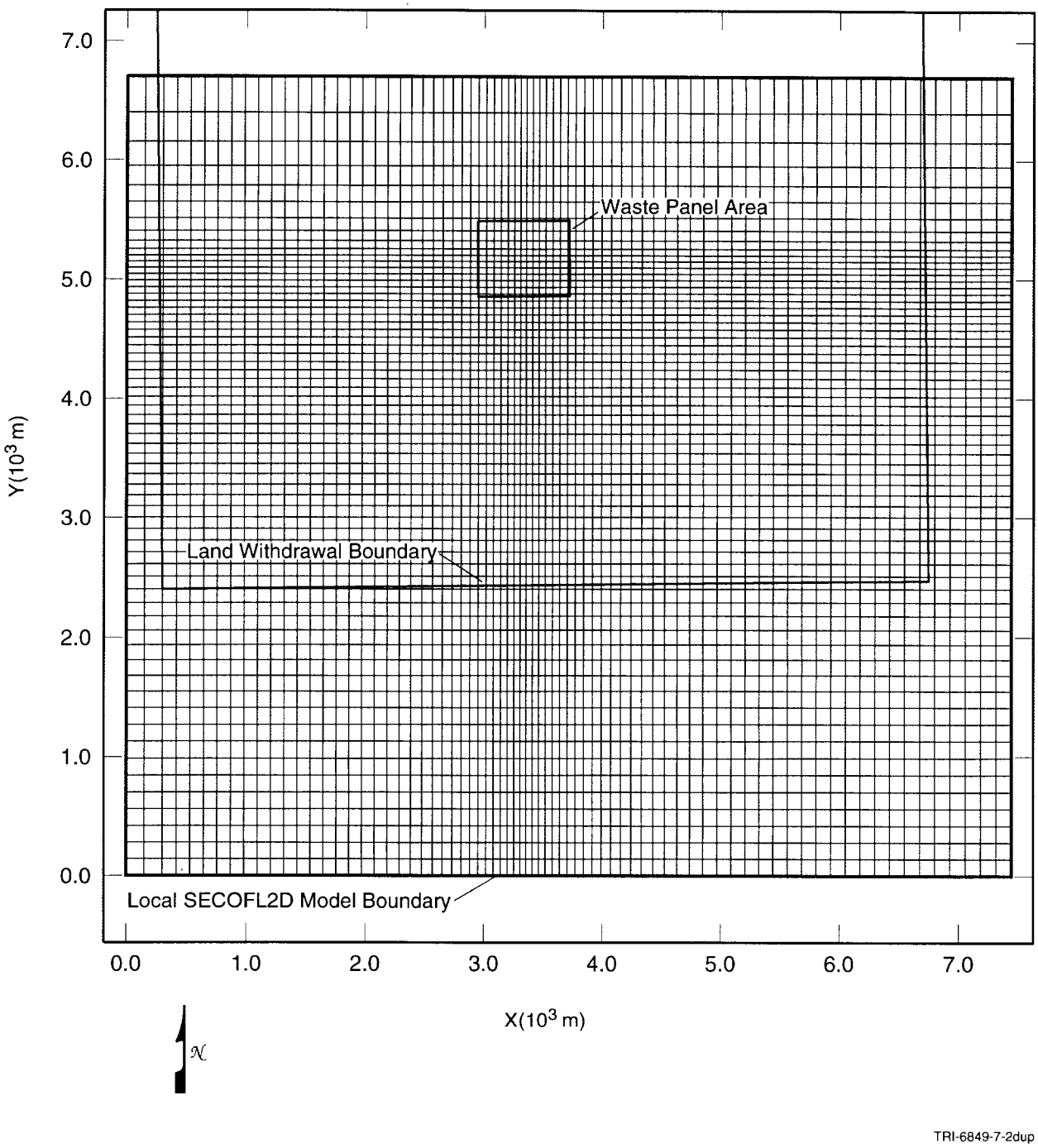

Fig. 4.8.5. Local domain spatial discretization for groundwater flow in the Culebra Dolomite.

(Robinson and Lang 1938). Robinson and Lang (1938) described the brine aquifer and suggested that the structural conditions that caused the development of Nash Draw may control the occurrence of brine. Thus, the brine aquifer boundary may coincide with the topographic surface elevations of Nash Draw. Drilling associated with the WIPP hydrogeologic studies in the northern half of Nash Draw support this theory (p. 50, Mercer 1983).

Groundwater divides are boundaries across which it is assumed that no groundwater flow occurs. The known topographic and geologic discharge features of Nash Draw suggest that it is a groundwater divide. Thus, the axis of Nash Draw is assumed to behave hydraulically as a discharge-type groundwater divide. Consequently, the portion of the western boundary of the regional domain (Figs. 4.8.3, 4.8.4) oriented along the axis of Nash Draw is modeled using a no flow boundary condition (Table 4.8.1).

The remaining regional boundary conditions are not as well defined. When possible, they were positioned to align with topographic highs or other geologic features such as San Simon Swale on the northeastern boundary (Fig. 4.8.3). Due to their uncertainty, the boundaries are positioned a large distance from the local problem domain (Fig. 4.8.3). Due to the relative abundance of head data near the site, Dirichlet (i.e., constant head) boundary conditions were imposed at all boundary locations other than Nash Draw and the northeastern corner of the problem domain (Table 4.8.1). No-flow boundary conditions were assumed in the northeastern corner due to low transmissivities and the coincidence with San Simon Swale, another topographic low (Table 4.8.1).

The boundary value conditions in Table 4.8.1 were used in all solutions of Eq. (4.8.3) on the regional domain in Figs. 4.8.3 and 4.8.4. As steady state solutions were being calculated, there was no need to specify initial value conditions.

The local domain boundaries (Fig. 4.8.5) were selected to capture important flow paths and facilitate the computation of integrated discharges across the land withdrawal boundary. The local domain is approximately 7×7 km. The computational grid contains 75 columns and 65 rows, resulting in 4875 grid blocks. Dirichlet (i.e., constant head) boundary conditions were imposed on the local domain and were derived from the solution for h on the regional domain with a bi-linear interpolation procedure. Unlike the constant head boundary conditions on the regional domain, the constant head boundary conditions on the local domain change for each calculation due to changes in value for $\mathbf{K} = \mathbf{K}_i$. As for the regional domain, steady state solutions to Eq. (4.8.3) were calculated on the local domain and so there was no need to specify initial value conditions.

4.8.4 Numerical Solution

The flow model in Eq. (4.8.3) is evaluated with a second-order difference procedure (McDonald and Harbaugh 1988, Roache 1972) on the computational grids in Figs. 4.8.4 and 4.8.5. Specifically, the discretized form of Eq. (4.8.3) is

Table 4.8.1. Boundary Value Conditions Used for h in solution of Eq. (4.8.3) on Regional Model Domain Shown in Figs. 4.8.3 and 4.8.4

	No Flow Boundaries
$\partial h/\partial x = 0$	Dashed boundary on left and right in Fig. 4.8.4
$\partial h/\partial y = 0$	Dashed boundary on top in Fig. 4.8.4
	Constant Head Boundaries
$h(x, y)$	Specified on solid boundary in Fig. 4.8.4; see Fig. 4.8.6 for example of specification on lower boundary in Fig. 4.8.4.

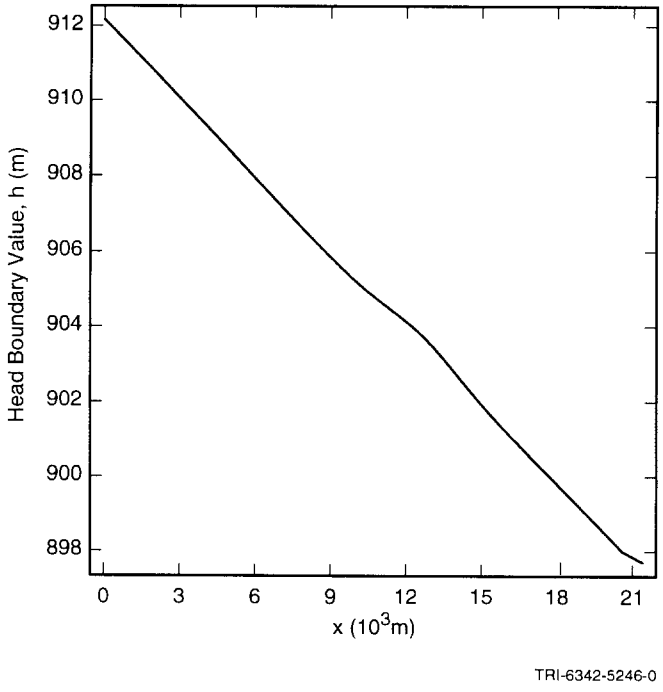

Fig. 4.8.6. Constant boundary values (m) specified for h on lower boundary in Fig. 4.8.4 for use in solution of Eq. (4.8.3) (LaVenue 1996).

$$0 = \frac{1}{\Delta x_i}\left[\frac{t_{i+1/2,j}(h_{i+1,j}-h_{i,j})}{(\Delta x_{i+1}+\Delta x_i)/2} - \frac{t_{i-1/2,j}(h_{i,j}-h_{i-1,j})}{(\Delta x_i+\Delta x_{i-1})/2}\right]$$

$$+\frac{1}{\Delta y_j}\left[\frac{t_{i,j+1/2}(h_{i,j+1}-h_{i,j})}{(\Delta y_{j+1}+\Delta y_j)/2} - \frac{t_{i,j-1/2}(h_{i,j}-h_{i,j-1})}{(\Delta y_j+\Delta y_{j-1})/2}\right] \tag{4.8.9}$$

where

$$t_{ij} = b_{ij}k_{ij},\ t_{i-1/2,j} = 2t_{ij}t_{i-1,j}/(t_{ij}+t_{i-1,j}),\ t_{i+1/2,j} = 2t_{i+1,j}t_{ij}/(t_{i+1,j}+t_{ij})$$
$$t_{i,j-1/2} = 2t_{ij}t_{i,j-1}/(t_{ij}+t_{i,j-1}),\ t_{i,j+1/2} = 2t_{i,j+1}t_{ij}/(t_{i,j+1}+t_{ij})$$

and b_{ij} and k_{ij} are the aquifer height (Eq. (4.8.1)) and hydraulic conductivity (Eq. (4.8.2)) at node (i, j). In the 1996 WIPP PA, b_{ij} = 4 m and k_{ij} enters the analysis through the specification of an uncertain, spatially-variable transmissivity (see Eqs. (4.8.4) - (4.8.7)).

The determination of h is then completed by the solution of the linear system of equations in Eq. (4.8.9) for the unknown heads h_{ij}. This solution is accomplished by using a semi-coarsening multigrid solver (Dendy et al. 1989, 1992) to make an initial estimate of the solution of the system in Eq. (4.8.9). Then, this estimate is used as the starting point in the construction of the solution by a successive over-relaxation (SOR) iterative method (Roache 1972). As the h_{ij} are determined, the Darcy velocities in Eq. (4.8.8) are also obtained and saved for use in later radionuclide transport calculations. Additional information on the numerical procedures in use is available in the user's manual for SECOFL2D (Sects. 3.1 - 3.3, Roache et al. 1996).

4.8.5 Additional Information

Additional information on SECOFL2D and its use in the 1996 WIPP PA to determine fluid flow patterns in the Culebra Dolomite can be found in the SECOFL2D users manual (Roache et al. 1996) and in the analysis package for fluid flow and radionuclide transport in the Culebra Dolomite (Ramsey et al. 1996).

4.9 Radionuclide Transport in Culebra: SECOTP2D (i.e., f_{S-T})

4.9.1 Mathematical Description

A dual porosity model is used to represent radionuclide transport in the Culebra Dolomite (Meigs and McCord 1996a). In this model, one system of partial differential equations (see Eq. (4.9.1)) is used to represent radionuclide transport in fractures within the Culebra Dolomite (i.e., advective transport) and another system of partial differential equations (see Eq. (4.9.6)) is used to represent radionuclide movement and sorption in the matrix that surrounds the fractures (i.e., diffusive transport).

The system used to represent advective transport in fractures is given by (WIPP PA 1997)

$$\nabla \bullet \left[\phi \mathbf{D}_k \nabla C_k - \mathbf{v} C_k\right] = \phi R_k \left(\frac{\partial C_k}{\partial t}\right) + \phi R_k \lambda_k C_k - \phi R_{k-1} \lambda_{k-1} C_{k-1} - Q_k - \Gamma_k \tag{4.9.1}$$

for $k = 1, 2, \ldots, nR$, where

nR = number of radionuclides under consideration,

C_k = concentration of radionuclide k in brine (kg/m^3),

$\mathbf{D}_k$ = hydrodynamic dispersion tensor (m^2/s),

$\mathbf{v}$ = Darcy velocity (i.e., specific discharge) of brine (m/s = (m^3/m^2)/s),

ϕ = advective (i.e., fracture) porosity (dimensionless),

R_k = advective retardation coefficient (dimensionless),

λ_k = decay constant for radionuclide k (s^{-1}),

Q_k = injection rate of radionuclide k per unit bulk volume of formation ((kg/s)/m^3) (Note: $Q_k > 0$ corresponds to injection into the fractures),

Γ_k = mass transfer rate of radionuclide k per unit bulk volume of formation due to diffusion between fractures and surrounding matrix ((kg/s)/m^3) (Note: $\Gamma_k > 0$ corresponds to diffusion into fractures).

The Darcy velocity $\mathbf{v}$ is obtained from the solution of Eq. (4.8.3); specifically, $\mathbf{v}$ is defined by the relationship in Eq. (4.8.8). The advective (i.e., fracture) porosity ϕ is an uncertain analysis input (Meigs and McCord 1996b; see *CFRCPOR* in Sect. 5.2).

The hydrodynamic dispersion tensor is defined by (WIPP PA 1997, Bear 1972)

$$\mathbf{D}_k = \frac{1}{\|\mathbf{v}\|\phi}\begin{bmatrix} u & -v \\ v & u \end{bmatrix}\begin{bmatrix} \alpha_L & 0 \\ 0 & \alpha_T \end{bmatrix}\begin{bmatrix} u & v \\ -v & u \end{bmatrix} + \tau D_k^* \begin{bmatrix} 1 & 0 \\ 0 & 1 \end{bmatrix}, \tag{4.9.2}$$

where α_L and α_T are the longitudinal and transverse dispersivities (m); u and v are the x and y components of $\mathbf{v}$ (i.e., $\mathbf{v} = [u, v]$); D_k^* is the free water molecular diffusion coefficient (m^2 s^{-1}) for radionuclide k, and $\tau = L/L_e$ is the advective tortuosity, where L denotes the length of the porous medium (m) and L_e denotes the flow path length of a fluid particle (m). In the 1996 WIPP PA, $\alpha_L = \alpha_T = 0$ m (McCord 1996). The diffusion coefficient D_k^* equals 3×10^{-10} m^2/s for radionuclides in the +3 oxidation state (i.e., Am^{+3}, Pu^{+3}), 1.53×10^{-10} m^2/s for radionuclides in the +4 oxidation state (i.e., Pu^{+4}, Th^{+4}, U^{+4}) and 4.26×10^{-10} m^2/s for radionuclides in the +6 oxidation state (i.e., U^{+6}) (Brush 1998a); the existence of plutonium in the +3 or +4 oxidation state (i.e., as Pu^{+3} or Pu^{+4}) and the existence of uranium in the +4 or +6 oxidation state (i.e., as U^{+4} or U^{+6}) is determined by an uncertain analysis input (see *WOXSTAT* in Sect. 5.2) (Brush 1996a). Further, $\tau = 1$ (Wallace 1996d). Thus, the definition of $\mathbf{D}_k$ reduces to

$$\mathbf{D}_k = D_k^* \begin{bmatrix} 1 & 0 \\ 0 & 1 \end{bmatrix} \tag{4.9.3}$$

in the 1996 WIPP PA.

The advective retardation coefficient R_k is defined by

$$R_k = 1 + (1-\phi)\rho_A K_{Ak} / \phi, \tag{4.9.4}$$

where

ρ_A = surface area density of fractures in Culebra (m^2/m^3 = 1/m) (i.e., surface area of fractures (m^2) divided by volume of fractures (m^3)),

K_{Ak} = surface area distribution coefficient ((kg/m^2)/(kg/m^3) = m) (i.e., concentration of radionuclide k sorbed on fracture surfaces (kg/m^2) divided by concentration of radionuclide k dissolved in brine within fractures (kg/m^3)).

In the 1996 WIPP PA, K_{Ak} = 0 m and thus R_k = 1 (Brush and Storz 1996).

The nR = 5 radionuclides transported in the Culebra (i.e., ^{241}Am, ^{238}Pu $\rightarrow$ ^{234}U$\rightarrow$^{230}Th, ^{239}Pu) are discussed in Sect. 4.3 (see Eq. (4.3.18) and Table 4.3.3). In concept, the term Q_k in Eq. (4.9.1) provides the link between the releases to the Culebra calculated with NUTS (Sect. 4.3) and PANEL (Sect. 4.4) and transport within the Culebra. In the computational implementation of the 1996 WIPP PA, radionuclide transport calculations in the Culebra were performed for unit radionuclide releases to the Culebra and then the outcomes of these calculations were used to construct the release to the accessible environment associated with time-dependent releases into the Culebra derived from NUTS and PANEL calculations (see Sect. 12.2). The definition of Q_k is discussed in more detail in Sect. 4.9.2.

If $\mathcal{B}$ denotes an arbitrary boundary (e.g., the land withdrawal boundary) in the domain of Eq. (4.9.1) (i.e., Fig. 4.8.5), then the cumulative transport of $C_k(t, \mathcal{B})$ of radionuclide k from time 0 to time t across $\mathcal{B}$ is given by

$$C_k(t, \mathcal{B}) = \int_0^t \left[\int_{\mathcal{B}} \left\{ \mathbf{v}(x,y) C_k(x,y,\tau) - \phi \mathbf{D}_k(x,y,t) \nabla C_k(x,y,\tau) \right\} b \bullet \mathbf{n}(x,y)\, ds \right] d\tau, \tag{4.9.5}$$

where b = 4 m is the thickness of the Culebra assumed for transport calculations (Meigs and McCord 1996a), ϕ is a constant in the context of the preceding integral in the 1996 WIPP PA, $\mathbf{n}(x, y)$ is an outward pointing unit normal vector, and $\int_{\mathcal{B}} \sim ds$ denotes a line integral over $\mathcal{B}$.

The system used to represent diffusive transport in the matrix surrounding the fractures is given by (WIPP PA 1997)

$$\frac{\partial}{\partial z}\left(\phi' D'_k \frac{\partial C'_k}{\partial z}\right) = \phi' R'_k \left(\frac{\partial C'_k}{\partial t}\right) + \phi' R'_k \lambda_k C'_k - \phi' R'_{k-1} \lambda_{k-1} C'_{k-1}\,, \tag{4.9.6}$$

where z is the spatial coordinate in Fig. 4.9.1, D'_k is the matrix diffusion coefficient (m^2/s) for radionuclide k defined by $D'_k = D^*_k \tau'$, and τ' is the matrix tortuosity. The remaining terms have the same meaning as those in Eq. (4.9.1) except that the prime denotes properties of the matrix surrounding the fractures. The matrix (i.e., diffusive) tortuosity τ' is defined by $\tau' = 0.11$ (Meigs 1996e). The matrix (i.e., diffusive) porosity ϕ' is an uncertain input to the analysis (see *CMTRXPOR* in Sect. 5.2). The matrix retardation R'_k is defined by

$$R'_k = 1 + (1 - \phi')\rho_s K_{dk} / \phi', \tag{4.9.7}$$

where ρ_s is the particle density (kg/m^3) of the matrix and K_{dk} is the distribution coefficient ((Ci/kg)/(Ci/m^3) = m^3/kg) for radionuclide k in the matrix. The density ρ_s is assigned a value of 2.82×10^3 kg/m^3 (Martell 1996b). The distribution coefficients K_{dk} are uncertain inputs to the analysis and dependent on the uncertain oxidation state of the relevant element (see *CMKDAM3*, *CMKDPU3*, *CMKDPU4*, *CMKDTH4*, *CMKDU4*, *CMKDU6*, *WOXSTAT* in Sect. 5.2).

The initial and boundary value conditions used in the formulation of Eq. (4.9.6) are

$$C'_k(x, y, z, 0) = 0 \text{ kg/m}^3 \tag{4.9.8}$$

$$\partial C'_k(x, y, 0, t) / \partial z = 0 \text{ kg/m}^2 \tag{4.9.9}$$

$$C'_k(x, y, B, t) = C_k(x, y, t), \tag{4.9.10}$$

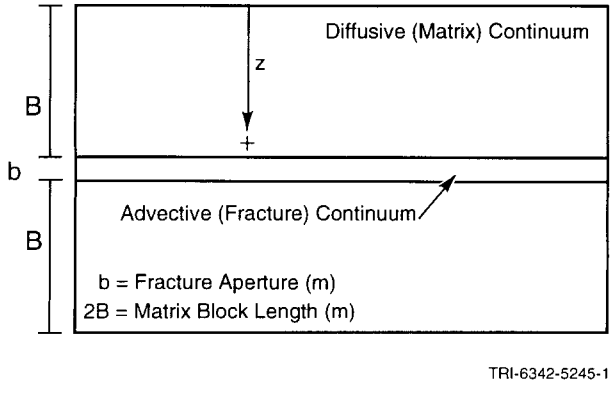

Fig. 4.9.1. Parallel plate dual porosity conceptualization.

where (x, y) corresponds to a point in the domain on which Eq. (4.9.1) is solved and B is the matrix half block length (m) in Fig. 4.9.1 (i.e., $2B$ is the thickness of the matrix between two fractures). The initial value condition in Eq. (4.9.8) says that no radionuclide is present in the matrix at the beginning of the calculation. The boundary value condition in Eq. (4.9.9) says that no radionuclide movement can take place across the centerline of a matrix block separating two fractures. The boundary value condition in Eq. (4.9.10) says that the dissolved radionuclide concentration in the matrix at the boundary with the fracture is the same as the dissolved radionuclide concentration within the fracture. The matrix half block length B is an uncertain input to the analysis (see *CFRCSP* in Sect. 5.2).

The linkage between Eqs. (4.9.1) and (4.9.6) is accomplished through the term Γ_k, with Γ_k defining the rate at which radionuclide k diffuses across the boundary between a fracture and the adjacent matrix (Fig. 4.9.1). Specifically,

$$\Gamma_k = -\frac{2\phi}{b}\left(\phi' D_k' \left.\frac{\partial C_k'}{\partial z}\right|_{z=B}\right), \tag{4.9.11}$$

where b is the fracture aperture (m) defined by

$$b = \phi B / (1-\phi). \tag{4.9.12}$$

The linkage term Γ_k appears directly in Eq. (4.9.1); further, it enters Eq. (4.9.6) through the specification of the boundary value condition in Eq. (4.9.10), with this condition affecting the value of $\left.\partial C_k' / \partial z\right|_{z=B}$ in the definition of Γ_k in Eq. (4.9.11).

4.9.2 Numerical Solution

Eqs. (4.9.1) and (4.9.6) are numerically solved using the spatial discretizations in Figs. 4.8.5 and 4.9.2. The initial and boundary value conditions used for Eq. (4.9.6) in this solution are given in Eqs. (4.9.8) - (4.9.10). For Eq. (4.9.1), the initial value condition is

$$C_k(x, y, 0) = 0 \text{ kg/m}^3. \tag{4.9.13}$$

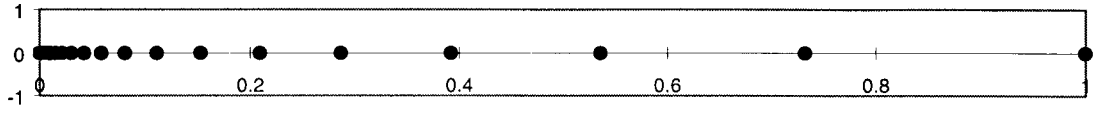

Fig. 4.9.2. Illustration of stretched grid used for discretization of matrix (i.e., diffusive) domain into points z_i, with points close together at the fracture-matrix interface and farther apart at greater distances from this interface.

Further, the boundary value conditions for Eq. (4.9.1) are defined at individual points on the boundary of the grid in Fig. 4.8.5 on the basis of whether the flow vector $\mathbf{v} = [u, v]$ defines a flow entering the grid or leaving the grid. The following Neumann boundary value condition is imposed at points (x, y) where flow leaves the grid:

$$\nabla C_k(x, y, t) \bullet \mathbf{n}(x, y) = 0 \text{ (kg/m}^3\text{)/m}, \tag{4.9.14}$$

where $\mathbf{n}(x, y)$ is an outward pointing unit normal vector defined at (x, y). The following Dirichlet boundary value condition is imposed at points (x, y) where flow enters the grid:

$$C_k(x, y, t) = 0 \text{ kg/m}^3. \tag{4.9.15}$$

As already indicated, Eqs. (4.9.1) and (4.9.6) were solved for unit radionuclide releases to the Culebra. Specifically, a release of 1 kg of each radionuclide under consideration was assumed to take place over a time interval from 0 to 50 yr, with this release taking place into the computational cell in Fig. 4.8.5 with center at the point (x = 3331.5 m, y = 5173.2 m). This cell (i.e., Cell (35, 55) is located at the center of the "Waste Panel Area" in Fig. 4.8.5 and has dimensions of 50 m × 50 m. Cell (35, 55) has a volume V of

$$V = (50\text{ m})(50\text{ m})(4\text{ m}) = 1\times10^4\text{ m}^3, \tag{4.9.16}$$

where 4 m is the assumed thickness of the Culebra Dolomite (Meigs and McCord 1996a). As a result, $Q_k(x, y, t)$ has the form

$$\begin{aligned} Q_k(x, y, t) &= (1\text{ kg})/[(1 \times 10^4\text{ m}^3)(50\text{ yr})(3.16 \times 10^7\text{ s/yr})] \\ &= 6.33 \times 10^{-14}\text{ (kg/m}^3\text{)/s} \end{aligned} \tag{4.9.17}$$

for $0 \le t \le 50$ yr and $(x, y) \in$ Cell (35, 55) in Fig. 4.8.5 and $Q_k(x, y, t) = 0$ (kg/m^3)/s otherwise.

A high level description of the numerical procedures used to solve Eqs. (4.9.1) and (4.9.6) follows, with more detail available in WIPP PA (1997). The fracture domain is discretized in space using the block centered finite difference method indicated in Fig. 4.9.3. In this formulation, cell concentrations are defined at grid block centers while velocities are defined on grid cell faces. Ghost cells are placed outside the problem domain for the purpose of implementing boundary conditions. The dispersive term, $\nabla\bullet(\phi\mathbf{D}_k\nabla C_k)$, in Eq. (4.9.1) is approximated using a second-order central difference formula (Fletcher 1988), and the advective term, $\nabla\bullet\mathbf{v}C_k$, is approximated using the Total Variation Diminishing (TVD) method (Sweby 1984). Temporal derivatives are approximated using a first-order backwards difference formula.

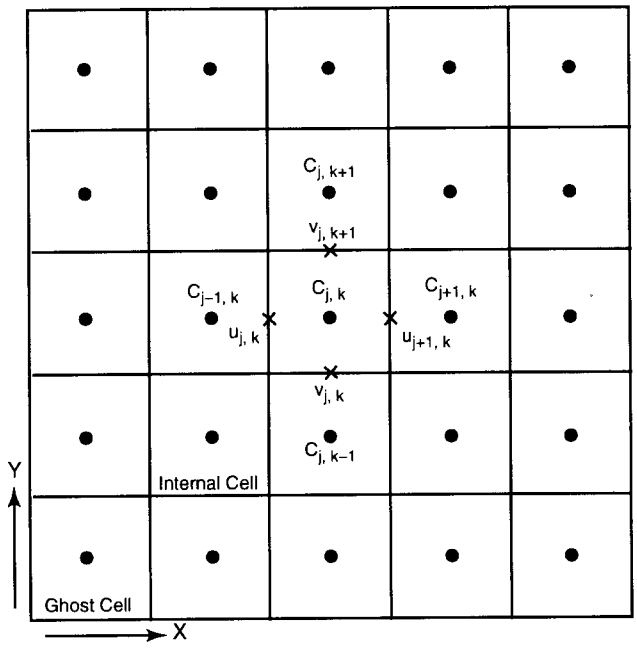

Fig. 4.9.3. Schematic of finite volume staggered mesh showing internal and ghost cells. Concentrations, C, are defined at cell centers and velocities, $\mathbf{v} = [u, v]$, at cell faces (Fig. 2, WIPP PA 1997).

The TVD method provides a way of accurately resolving advection dominated transport problems without the occurrence of nonphysical oscillations commonly present in second order solutions. This method invokes a weighted upstream differencing scheme that locally adjusts the weighting to prevent oscillatory behavior and maximize solution accuracy. The weighting parameters are known as the TVD flux limiters $\Phi(x,y,r)$, where r is a function of the concentration gradient and direction of flow. In the 1996 WIPP PA, the van Leer TVD limiter was used (p. 1005, Sweby 1984), which is defined as

$$\Phi(x,y,r) = \max\left\{0, \min\left\{2r, \frac{r+|r|}{1+|r|}\right\}\right\}. \tag{4.9.18}$$

At locations where u (i.e., the Darcy velocity in the x direction) is positive, r is defined at the $j-1/2$, k interface by

$$r_{j-1/2,k} = \frac{\partial C/\partial x\big|_{j-3/2,k}}{\partial C/\partial x\big|_{j-1/2,k}}, \tag{4.9.19}$$

and at locations where u is negative, r is defined by

$$r_{j-1/2,k} = \frac{\partial C/\partial x|_{j+1/2,k}}{\partial C/\partial x|_{j-1/2,k}} . \tag{4.9.20}$$

Similar definitions are made for r at the j, $k-1/2$ interface in the y-direction with v (i.e., the Darcy velocity in the y direction) used instead of u.

Because Φ_k is a function of C_k, the discretized set of equations is nonlinear. This nonlinearity is addressed by treating the flux limiters explicitly (i.e., time lagged). Explicit treatment of the limiter functions, however, can lead to oscillatory and sometimes unstable solutions when the Courant number exceeds unity ($Cr > 1$), where Cr is defined by

$$Cr_x = |u|\Delta t/\phi\Delta x \; , \; Cr_y = |v|\Delta t/\phi\Delta y \tag{4.9.21}$$

To avoid this behavior, the application of the TVD method is restricted to regions in which the Courant numbers are less than one. In regions where $Cr > 1$, a first order full upwinding scheme is invoked, which is unconditionally stable and non-oscillatory.

The discretized form of Eq. (4.9.1) can be expressed in a delta formulation as

$$\left(\mathbf{I} + \mathbf{L}_{xx} + \mathbf{L}_{yy} + \mathbf{S}\right)\Delta\mathbf{C}^{n+1} = \mathbf{RHS}^n, \tag{4.9.22}$$

where $\mathbf{I}$ is the identity matrix, $\mathbf{L}_{xx}$ and $\mathbf{L}_{yy}$ are finite difference operators in the x and y directions, $\mathbf{S}$ is an implicit source term that accounts for decay and mass transfer between the matrix and the fracture, **RHS** consists of the right hand side known values at time level n, and $\Delta\mathbf{C}^{n+1} = \mathbf{C}^{n+1} - \mathbf{C}^n$. Direct inversion of Eq. (4.9.22) for a typical Culebra transport problem is very computationally intensive and requires large amounts of memory and CPU time. To reduce these requirements, the operator in Eq. (4.9.22) is factored as follows:

$$\left(\mathbf{I} + \mathbf{L}_{xx} + \alpha_x\mathbf{S}\right)\left(\mathbf{I} + \mathbf{L}_{yy} + \alpha_y\mathbf{S}\right)\Delta\mathbf{C}^{n+1} = \mathbf{RHS}^n, \tag{4.9.23}$$

where α_x and α_y are constants that must sum to one (i.e., $\alpha_x + \alpha_y = 1$). The left hand sides in Eqs. (4.9.23) and (4.9.22) are not equivalent, with the result that the factorization of Eq. (4.9.22) in Eq. (4.9.23) is referred to as an "approximate factorization" (Fletcher 1988). The advantage of approximately factoring Eq. (4.9.22) is that the resulting equation consists of the product of two finite difference operators that are easily inverted independently using a tridiagonal solver. Hence, the solution to the original problem is obtained by solving a sequence of problems in the following order:

$$\left(\mathbf{I} + \mathbf{L}_{xx} + \alpha_x\mathbf{S}\right)\Delta\overline{\mathbf{C}} = \mathbf{RHS}^n \tag{4.9.24}$$

$$\left(\mathbf{I}+\mathbf{L}_{yy}+\alpha_y\mathbf{S}\right)\Delta\mathbf{C}^{n+1}=\Delta\overline{\mathbf{C}} \tag{4.9.25}$$

$$\mathbf{C}^{n+1}=\mathbf{C}^{n}+\Delta\mathbf{C}^{n+1}. \tag{4.9.26}$$

The equation for matrix transport, Eq. (4.9.6), is coupled implicitly to and solved simultaneously with the equation for fracture transport, Eq. (4.9.1). Second-order central differencing is used to approximate the spatial derivatives, and a first-order backwards differencing is used to approximate temporal derivatives. The implicit coupling is accomplished using a technique developed by Huyakorn et al. (1983). A detailed description of this technique and its implementation in the 1996 WIPP PA is given in the SECOTP2D user's manual (App. I, WIPP PA 1997).

The cumulative transport $C_k(t, \mathcal{B})$ of individual radionuclides across specified boundaries indicated in Eq. (4.9.5) is also accumulated during the numerical solution of Eqs. (4.9.1) and (4.9.6).

4.9.3 Additional Information

Additional information on SECOTP2D and its use in the 1996 WIPP PA to determine radionuclide transport in the Culebra Dolomite can be found in the SECOTP2D users manual (WIPP PA 1997) and in the analysis package for fluid flow and radionuclide transport in the Culebra Dolomite (Ramsey et al. 1996).

5. Probabilistic Characterization of Parameter Uncertainty

5.1 Probability Space ($\mathcal{S}_{su}$, $\mathcal{A}_{su}$, p_{su})

The third entity that underlies the 1996 WIPP PA is a probabilistic characterization of the uncertainty in important variables used as input to the analysis. As discussed in Sect. 2.4, this entity is defined by a probability space ($\mathcal{S}_{su}$, $\mathcal{A}_{su}$, p_{su}) that characterizes subjective uncertainty. The individual elements of $\mathcal{S}_{su}$ are vectors $\mathbf{x}_{su}$ of the form

$$\mathbf{x}_{su} = [x_1, x_2, ..., x_{nV}], \tag{5.1.1}$$

where each x_j is an imprecisely-known input to the analysis and nV is the number of such inputs.

The uncertainty in the x_j, and hence in $\mathbf{x}_{su}$, is characterized by developing a distribution

$$D_j, j = 1, 2, ..., nV, \tag{5.1.2}$$

for each x_j. Each distribution is based on all available knowledge about the corresponding variable and describes a degree of belief as to where the appropriate value to use for this variable is located. This degree of belief is conditional on the numerical, spatial and temporal resolution of the models selected for use in the 1996 WIPP PA (Chapt. 4). When appropriate, correlations between imprecisely-known variables are also possible, with such correlations indicating a dependency in the knowledge about the correlated variables. It is the distributions in Eq. (5.1.2) and any associated correlations between the x_j that define ($\mathcal{S}_{su}$, $\mathcal{A}_{su}$, p_{su}).

The uncertain variables (i.e., x_j) incorporated into the 1996 WIPP PA are discussed in Sect. 5.2. Then, the distributions and correlations assigned to these variables are described in Sects. 5.3 and 5.4. Finally, a discussion of the concept of a scenario is given in Sect. 5.5.

5.2 Uncertain Variables

The 1996 WIPP PA selected $nV = 57$ imprecisely-known variables for inclusion in the analysis (Table 5.2.1). The individual variables in Table 5.2.1 (i.e., *ANHBCEXP*, *ANHBCVGP*, ..., *WTAUFAIL*) correspond to the elements x_j of the vector $\mathbf{x}_{su}$ in Eq. (5.1.1). Several criteria were used in the selection process, including observed importance in past analyses, perceived importance with respect to the present analysis, and general level of interest in the variable. All uncertain variables incorporated into the 1996 WIPP PA are used as input to the models discussed in Sect. 2.3 and Chapt. 4. Specifically, none of the uncertain variables affect the definition of the probability space ($\mathcal{S}_{st}$, $\mathcal{A}_{st}$, p_{st}) discussed in Sect. 2.2 and Chapt. 3, although there is no conceptual reason that excludes ($\mathcal{S}_{su}$, $\mathcal{A}_{su}$, p_{su}) from containing such variables.

Table 5.2.1 Uncertain Variables Incorporated into 1996 WIPP PA (See App. PAR, U.S. DOE 1996 for additional information)

Variable	Description
ANHBCEXP	Brooks-Corey pore distribution parameter for anhydrite (dimensionless). Used in BRAGFLO. Defines λ in Eqs. (4.2.9) - (4.2.11) for regions 20, 21, 28 of Fig. 4.2.1 for use with Brooks-Corey model; defines λ in $m = \lambda/(1+\lambda)$ in Eqs. (4.2.18) - (4.2.20) for use with van Genuchten-Parker model in same regions. See *ANHBCVGP*. Distribution: Student's with 5 degrees of freedom. Range: 0.491 to 0.842. Mean, Median: 0.644. Database identifiers: 587 (S_MB139, PORE_DIS), 527 (S_ANH_AB, POR_DIS), 566 (S_MB138, PORE_DIS). Variable 25 in LHS. Additional information: Howarth and Christian-Frear 1997; WIPP PA 1992-1993 Vol. 3, p. 2-54.
ANHBCVGP	Pointer variable for selection of relative permeability model for use in anhydrite. Used in BRAGFLO. See *ANHBCEXP*. Distribution: Discrete with 60% 0, 40% 1. Value of 0 implies Brooks-Corey model defined by Eqs. (4.2.9)-(4.2.11); value of 1 implies van Genuchten-Parker model defined by Eqs. (4.2.18)-(4.2.20). Data base identifiers: 596 (S_MB139, RELP_MOD), 536 (S_ANH_AB, RELP_MOD, 575 (S_MB138, RELP_MOD). Variable 22 in LHS. Additional information: Howarth and Christian-Frear 1997; WIPP PA 1992-1993 Vol. 3, p. A-149.
ANHCOMP	Bulk compressibility of anhydrite (Pa^{-1}). Used in BRAGFLO. Pore compressibility β_f in Eq. (4.2.6) defined by *ANHCOMP* divided by initial porosity (i.e., ϕ_0 in Table 4.2.1) for use in regions 20, 21, 28 of Fig. 4.2.1. Distribution: Student's with 3 degrees of freedom. Range: 1.09×10^{-11} to 2.75×10^{-10} Pa^{-1}. Mean, Median: 8.26×10^{-11} Pa^{-1}. Correlation: –0.99 rank correlation with *ANHPRM*. Data base identifiers: 580 (S_MB139, COMP_RCK), 521 (S_ANH_AB, COMP_RCK), 560 (S_MB138, COMP_RCK). Variable 21 in LHS. Additional information: Saulnier et al. 1991, Stensrud et al. 1992.

Table 5.2.1 Uncertain Variables Incorporated into 1996 WIPP PA (Continued)

Variable	Description
ANHPRM	Logarithm of intrinsic anhydrite permeability (m^2). Used in BRAGFLO. Defines permeability tensors $\mathbf{K}_g$, $\mathbf{K}_b$ in Eqs. (4.2.1), (4.2.2) for regions 20, 21, 28 in Fig. 4.2.1. Specifically, the anhydrite is assumed to be isotropic, with result that *ANHPRM* is the logarithm of the diagonal elements of $\mathbf{K}_b$ for the indicated regions and similarly defines the diagonal elements of $\mathbf{K}_g$ after a correction is made for the Klinkenberg effect as shown in Eq. (4.2.29). Distribution: Student's with 5 degrees of freedom. Range: –21.0 to –17.1 (i.e., permeability range is 1×10^{-21} to $1 \times 10^{-17.1}$ m^2). Mean, Median: –18.9. Correlation : –0.99 rank correlation with *ANHCOMP*. Data base identifiers: 570 (S_MB138, PRMX_LOG), 571(S-MB138, PRMY_LOG), 572(S_MB138, PRMZ_LOG), 531 (S_ANH_AB, PRMX_LOG), 532 (S_ANH_AB, PRMY_LOG), 533(S_ANH_AB, PRMZ_LOG), 591 (S_MB139, PRMX_LOG), 592 (S_MB139, PRMY_LOG), 593 (S_MB139, PRMZ_LOG). Variable 20 in LHS. Additional information: Howarth and Christian-Frear 1997, Saulnier et al. 1991, Stensrud et al. 1992.
ANRBRSAT	Residual brine saturation in anhydrite (dimensionless). Used in BRAGFLO. Defines S_{br} in Eqs. (4.2.13) - (4.2.14) for use in regions 20, 21, 28 of Fig. 4.2.1. Distribution: Student's with 5 degrees of freedom. Range: 7.85×10^{-3} to 1.74×10^{-1}. Mean, Median: 8.36×10^{-2}. Data base identifiers: 598 (S_MB139, SAT_RBRN), 538 (S_ANH_AB, SAT_RBRN), 577(S_MB138, SAT_RBRN). Variable 23 in LHS. Additional information: Howarth and Christian-Frear 1997; WIPP PA 1992-1993 Vol. 3, p. 2-52.
ANRGSSAT	Residual gas saturation in anhydrite (dimensionless). Used in BRAGFLO. Defines S_{gr} in Eq. (4.2.14) for use in regions 20, 21, 28 of Fig. 4.2.1. Distribution: Student's with 5 degrees of freedom. Range: 1.39×10^{-2} to 1.79×10^{-1}. Mean, median: 7.71×10^{-2}. Database identifiers: 599 (S_MB139, SAT_RGAS), 539 (S_ANH_AB, SAT_RGAS), 578 (S_MB138, SAT_RGAS). Variable 24 in LHS. Additional information: Howarth and Christian-Frear 1997; WIPP PA 1992-1993 Vol. 3, p. 2-53.

Table 5.2.1 Uncertain Variables Incorporated into 1996 WIPP PA (Continued)

Variable	Description
BHPRM	Logarithm of intrinsic borehole permeability (m^2). Used in BRAGFLO. Defines permeability tensors $\mathbf{K}_g$, $\mathbf{K}_b$ in Eqs. (4.2.1), (4.2.2) for region 1 in Fig. 4.2.1 when borehole with properties similar to silty sand is present. Specifically, the borehole is assumed to be isotropic, with result that *BHPRM* is the logarithm of the diagonal elements of $\mathbf{K}_b$ for the indicated region and similarly defines the diagonal elements of $\mathbf{K}_g$ after a correction is made for the Klinkenberg effect as shown in Eq. (4.2.29). Distribution: Uniform. Range: −14 to −11 (i.e., permeability range is 1×10^{-14} to 1×10^{-11} m^2). Mean, median: −12.5. Data base identifiers: 3184 (BH_SAND, PRMX_LOG), 3190 (BH_SAND, PRMY_LOG). Variable 30 in LHS. Additional information: Thompson et al. 1996.
BPCOMP	Logarithm of bulk compressibility of brine pocket (Pa^{-1}). Used in BRAGFLO. Pore compressibility β_f in Eq. (4.2.6) defined by 10^{BPCOMP} divided by initial porosity (i.e., ϕ_0 in Table 4.2.1) for use in region 30 of Fig. 4.2.1. Distribution: Triangular. Range: −11.3 to −8.00 (i.e., bulk compressibility range is $1 \times 10^{-11.3}$ to 1×10^{-8} Pa^{-1}). Mean, mode: −9.80, −10.0. Correlation: −0.75 rank correlation with *BPPRM*. Data base identifier: 61 (CASTILER, COMP_RCK). Variable 29 in LHS. Additional information: Freeze 1996a.
BPINTPRS	Initial pressure in brine pocket (Pa). Used in BRAGFLO. Defines p_b (x, y, −5) in Table 4.2.4 for region 30 in Fig. 4.2.1. Distribution: Triangular. Range: 1.11×10^7 to 1.70×10^7 Pa. Mean, mode: 1.36×10^7 Pa, 1.27×10^7 Pa. Data base identifier: 66 (CASTILER, PRESSURE). Variable 27 in LHS. Additional information: Freeze and Larson 1996; WIPP PA 1992-1993 Vol. 3, Sect. 4.3.

Table 5.2.1 Uncertain Variables Incorporated into 1996 WIPP PA (Continued)

Variable	Description
BPPRM	Logarithm of intrinsic brine pocket permeability (m^2). Used in BRAGFLO. Defines permeability tensors $\mathbf{K}_g$, $\mathbf{K}_b$ in Eqs. (4.2.1), (4.2.2) for region 30 in Fig. 4.2.1. Specifically, the brine pocket is assumed to be isotropic, with result that *BPPRM* is the logarithm of the diagonal elements of $\mathbf{K}_b$ for the indicated region and similarly defines the diagonal elements of $\mathbf{K}_g$ after a correction is made for the Klinkenberg effect as shown in Eq. (4.2.29). Distribution: Triangular. Range: –14.7 to –9.80 (i.e., permeability range is $1 \times 10^{-14.7}$ to $1 \times 10^{-9.80}$ m^2). Mean, mode: –12.1, –11.8. Correlation: –0.75 with *BPCOMP*. Data base identifiers: 67 (CASTILER, PRMX_LOG), 68 (CASTILER, PRMY_LOG). Variable 28 in LHS. Additional information: Freeze 1996b, Popielak et al. 1983.
BPVOL	Pointer variable for selection of brine pocket volume. Used in BRAGFLO. Distribution: Discrete, with integer values 1, 2, ..., 32 equally likely. Originally intended to select from 32 equally-likely brine pocket maps obtained by assuming five regions beneath repository, with each region either containing or not containing pressurized brine. This produces 32 (i.e., 2^5) possible brine pocket maps. This approach was abandoned when more information on brine pockets became available (Powers et al. 1996) and the only role that *BPVOL* now plays is to determine volume of brine (m^3) contained in the brine pocket. Specifically, the volumes are 32,000, 64,000, 96,000, 128,000 and 160,000 m^3 if the original maps contained 0 or 1, 2, 3, 4 or 5 brine pockets, and the corresponding probabilities are 0.1875, 0.3125, 0.3125, 0.15625 and 0.03125. The indicated volumes define V_{brn} in Eq. (4.2.16) and thus define ϕ_0 for region 30 in Fig. 4.2.1; in addition, the number of drilling intrusions nD required to deplete the pressurized brine beneath the repository is defined by $nD = 2V_{brn}/32{,}000$ (i.e., 2, 4, 6, 8 or 10 intrusions depending on whether the associated brine volume is 32,000, 64,000, 96,000, 128,000 or 160,000 m^3; see nD in Table 6.6.2 of Sect. 6.6). For the presentation of sensitivity analysis results, *BPVOL* is assigned the brine volumes that correspond to the sampled integer values. Data base identifiers: 3194 (CASTILER, GRIDFLO). Variable 31 in LHS. Additional information: Larson 1997, Swift et al. 1996, Powers et al. 1996.

Table 5.2.1 Uncertain Variables Incorporated into 1996 WIPP PA (Continued)

Variable	Description
CFRCPOR	Culebra fracture (i.e., advective) porosity (dimensionless). Used in SECOTP2D. Defines ϕ in Eq. (4.9.1). Distribution: Loguniform. Range: 1.00×10^{-4} to 1.00×10^{-2}. Mean, median: 2.10×10^{-3}, 1.00×10^{-3}. Data base identifier: 3487 (CULEBRA, APOROS). Variable 50 in LHS. Additional information: Meigs and McCord 1996b, Meigs 1996a.
CFRCSP	Culebra fracture spacing (m). Used in SECOTP2D. Equal to half the distance between fractures (i.e., the Culebra half matrix block length). Defines B in Eq. (4.9.10) and Fig. 4.9.1. Distribution: Uniform. Range: 0.05 to 0.5 m. Mean, median: 0.275 m, 0.275 m. Data base identifier: 3485 (CULEBRA, HMBLKLT). Variable 49 in LHS. Additional information: Meigs 1996b, Meigs and McCord 1996c.
CMKDAM3	Matrix distribution coefficient (m^3/kg) for americium in +3 oxidation state. Used in SECOTP2D. Defines K_{dk} in Eq. (4.9.7) for Am^{3+}. Distribution: Uniform. Range: 0.02 to 0.5 m^3/kg. Mean, median: 0.26 m^3/kg, 0.26 m^3/kg. Data base identifier: 3482 (AM+3, MKD_AM). Variable 57 in LHS. Additional information: Brush 1998b.
CMKDPU3	Same as *CMKDAM3* but for plutonium in +3 oxidation state. Distribution: Uniform. Range: 0.02 to 0.5 m^3/kg. Mean, median: 0.26 m^3/kg, 0.26 m^3/kg. Data base identifier: 3480 (PU+3, MKD_PU). Variable 54 in LHS.
CMKDPU4	Same as *CMKDAM3* but for plutonium in +4 oxidation state. Distribution: Uniform. Range: 0.9 to 20 m^3/kg. Mean, median: 10.0 m^3/kg, 10.0 m^3/kg. Data base identifier: 3481 (TH+4, MKD_PU). Variable 55 in LHS.
CMKDTH4	Same as *CMKDAM3* but for thorium in +4 oxidation state. Distribution: Uniform. Range: 0.9 to 20 m^3/kg. Mean, median: 10.0 m^3/kg, 10.0 m^3/kg. Data base identifier: 3478 (TH+4, MKD_TH). Variable 56 in LHS.
CMKDU4	Same as *CMKDAM3* but for uranium in +4 oxidation state. Distribution: Uniform. Range: 0.9 to 20 m^3/kg. Mean, median: 10.0 m^3/kg, 10.0 m^3/kg. Data base identifier: 3479 (U+4, MKD_U). Variable 53 in LHS.

Table 5.2.1 Uncertain Variables Incorporated into 1996 WIPP PA (Continued)

Variable	Description
CMKDU6	Same as *CMKDAM3* but for uranium in +6 oxidation state. Distribution: Uniform. Range: 3.0×10^{-5} to 3.0×10^{-2} m^3/kg. Mean, median: 1.50×10^{-2} m^3/kg, 1.50×10^{-2} m^3/kg. Data base identifier: 3475 (U+6, MKD_U). Variable 52 in LHS.
CMTRXPOR	Culebra matrix (i.e., diffusive) porosity (dimensionless). Used in SECOFL2D and SECOTP2D. Defines ϕ' in Eq. (4.9.6). Distribution: Piecewise uniform. Range: 0.01 to 0.25. Mean, median: 0.16, 0.16. Data base identifier: 3486 (CULEBRA, DPOROS). Variable 51 in LHS. Additional information: Meigs 1996c,d.
CTRAN	Pointer variable for selecting transmissivity field. Used in SECOFL2D. Distribution: Discrete, with integer values 1, 2, ..., 100 equally likely. Each integer value identifies one of 100 transmissivity fields constructed with GRASP_INV for use in analysis. Transmissivity fields define $t(x, y)$ in Eq. (4.8.4). Data base identifier: 225 (GLOBAL, TRANSIDX). Variable 35 in LHS. Additional information: LaVenue 1996; WIPP PA 1992-1993 Vol. 3, p. 2-91.
CTRANSFM	Multiplier on transmissivity field in presence of mining of potash reserves within the land withdrawal boundary (dimensionless). Used in SECOFL2D. Transmissivity field selected by *CTRAN* is multiplied by *CTRANSFM* to obtain values for $k_1(x, y)$ and $k_2(x, y)$ in Eqs. (4.8.5) and (4.8.6); defines *SFM* in Eqs (4.8.5) and (4.8.6) for mining. Distribution: Uniform. Range: 1 to 1000. Mean, median: 500.5, 500.5. Data base identifier: 3419 (CULEBRA, MINP_FAC). Variable 34 in LHS. Additional information: Wallace 1996a-c.
CULCLIM	Climate scale factor for Culebra flow (i.e., velocity) field (dimensionless). Used in SECOTP2D. Culebra flow field is multiplied by *CULCLIM* to obtain $\mathbf{v}_i(x, y)$ in Eq. (4.8.8); defines *SFC* in Eq. (4.8.8). Distribution: Piecewise uniform. Range: 1 to 2.25. Mean, median: 1.31, 1.17. Data base identifier: 223 (GLOBAL, CLIMTIDX). Variable 48 in LHS. Additional information: Corbet and Swift 1996a,b.

Table 5.2.1 Uncertain Variables Incorporated into 1996 WIPP PA (Continued)

Variable	Description
HALCOMP	Bulk compressibility of halite (Pa^{-1}). Used in BRAGFLO. Pore compressibility β_f in Eq. (4.2.6) defined by *HALCOMP* divided by initial porosity (i.e., ϕ_0 in Table 4.2.1) for use in region 19 of Fig. 4.2.1. Distribution: Uniform. Range: 2.94×10^{-12} to 1.92×10^{-10} Pa^{-1}. Mean, median: 9.75×10^{-11} Pa^{-1}, 9.75×10^{-11} Pa^{-1}. Correlation: –0.99 rank correlation with *HALPRM*. Data base identifier: 541 (S_HALITE, COMP_RCK). Variable 19 in LHS. Additional information: Christian-Frear 1996a.
HALPOR	Halite porosity (dimensionless). Used in BRAGFLO. Defines ϕ_0 in Eq. (4.2.6) for region 19 in Fig. 4.2.1. Distribution: Piecewise uniform. Range: 1.0×10^{-3} to 3×10^{-2}. Mean, median: 1.28×10^{-2}, 1.00×10^{-2}. Data base identifier: 544 (S_HALITE, POROSITY). Variable 17 in LHS. Additional information: Howarth 1996; WIPP PA 1992-1993 Vol. 3, p. 2-41.
HALPRM	Logarithm of halite permeability (m^2). Used in BRAGFLO. Defines permeability tensors $\mathbf{K}_g$, $\mathbf{K}_b$ in Eqs. (4.2.1), (4.2.2) for region 19 in Fig. 4.2.1. Specifically, the halite is assumed to be isotropic, with result that *HALPRM* is the logarithm of the diagonal elements of $\mathbf{K}_b$ for the indicated region and similarly defines the diagonal elements of $\mathbf{K}_g$ after a correction is made for the Klinkenberg effect as shown in Eq. (4.2.29). Distribution: Uniform. Range: –24 to –21 (i.e., permeability range is 1×10^{-24} to 1×10^{-21} m^2). Mean, median: –22.5, –22.5. Correlation: –0.99 rank correlation with *HALCOMP*. Data base identifiers: 547 (S_HALITE, PRMX_LOG), 548 (S_HALITE, PRMY_LOG). Variable 18 in LHS. Additional information: Davies and Beauheim 1996, Domski 1996a, Christian-Frear 1996b.
SALPRES	Initial brine pressure, without the repository being present, at a reference point located in the center of the combined shafts at the elevation of the midpoint of MB 139 (Pa). Used in BRAGFLO. Defines p_{b0}, which is used to define $p_b(x, y, 0)$ (Table 4.2.4). With respect to computational cells in Fig. 4.2.1, defines initial brine pressure at location of cell (23,6). Distribution: Uniform. Range: 1.104×10^7 to 1.389×10^7 Pa. Mean, median: 1.247×10^7 Pa, 1.247×10^7 Pa. Data base identifier: 546 (S_HALITE, PRESSURE). Variable 26 in LHS. Additional information: Domski 1996b; WIPP PA 1992-1993 Vol. 3, p. 2-38.

Table 5.2.1 Uncertain Variables Incorporated into 1996 WIPP PA (Continued)

Variable	Description
SHBCEXP	Brooks-Corey pore distribution parameter for shaft (dimensionless). Used in BRAGFLO. Defines λ in Eqs. (4.2.9) - (4.2.11) for regions 3-11 in Fig. 4.2.1. Distribution: Piecewise uniform. Range: 0.11 to 8.10. Mean, median: 2.52, 0.94. Data base identifiers: 2516 (SALT_T1, PORE_DIS), 2533 (SALT_T2, POR_DIS), 2550 (SALT_T3, POR_DIS), 2567 (SALT_T4, POR_DIS), 2809 (SALT_T5, POR_DIS), 2989 (SALT_T6, POR_DIS), 2499 (EARTH, POR_DIS), 3006 (CLAY_RUS, POR_DIS), 2330 (CL_L_T1, POR_DIS), 2347 (CL_L_T2, POR_DIS), 2364 (CL_L_T3, POR_DIS), 3076 (CL_L_T4, POR_DIS), 2381 (CL_M_T1, POR_DIS), 2398 (CL_M_T2, POR_DIS), 2415 (CL_M_T3, POR_DIS), 2432 (CL_M_T4, POR_DIS), 2449 (CL_M_T5, POR_DIS), 2313 (CLAY_BOT, POR_DIS), 2466 (CONC_T1, POR_DIS), 2483 (CONC_T2, PORDIS), 3057 (CONC_MON, POR_DIS), 2279 (ASPHALT, POR_DIS). Variable 16 in LHS. Additional information: Kelley et al. 1996a,b; Hurtado 1996.
SHPRMASP	Logarithm of intrinsic permeability (m^2) of asphalt component of shaft seal (m^2). Used in BRAGFLO. Permeability tensors $\mathbf{K}_g$, $\mathbf{K}_b$ in Eqs. (4.2.1), (4.2.2) for region 5 in Fig. 4.2.1 are functions of asphalt permeability (i.e., $k_s = 10^x$, x = *SHPRMASP*, in Eq. (4.2.34)), halite permeability (i.e., $k_{out} = 10^x$, x = *HALPRM*, in Eq. (4.2.35), and shaft DRZ permeability (i.e., $k_{in} = 10^x$, x = *SHPRMDRZ*, in Eq. (4.2.35)), with diagonal elements of $\mathbf{K}_b$ defined by k_e in Eq. (4.2.34) and the diagonal elements of $\mathbf{K}_g$ defined similarly after a correction is made for the Klinkenberg effect as shown in Eq. (4.2.29). Distribution: Triangular. Range: −21 to −18 (i.e., permeability range is 1×10^{-21} to 1×10^{-18} m^2). Mean, mode: −19.7, −20.0. Data base identifiers: 2283 (ASPHALT, PRMX_LOG), 2284 (ASPHALT, PRMY_LOG). Variable 11 in LHS. Additional information: Kelley et al. 1996a,b; Repository Isolation Systems Department 1996.

Table 5.2.1 Uncertain Variables Incorporated into 1996 WIPP PA (Continued)

Variable	Description
SHPRMCLY	Logarithm of intrinsic permeability (m^2) for clay components of shaft. Used in BRAGFLO. Defines permeability tensors $\mathbf{K}_g$, $\mathbf{K}_b$ in Eqs. (4.2.1), (4.2.2) for regions 4, 10 in Fig. 4.2.1; specifically, the clay component is assumed to be isotropic, with result that *SHPRMCLY* is the logarithm of the diagonal elements of $\mathbf{K}_b$ for the indicated regions and the diagonal elements of $\mathbf{K}_g$ are defined similarly after a correction is made for Klinkenberg effect as shown in Eq. (4.2.29). Plays same role in definition of $\mathbf{K}_g$, $\mathbf{K}_b$ for regions 8, 9 in Fig. 4.2.1 as *SHPRMASP* does in the definition of $\mathbf{K}_g$, $\mathbf{K}_b$ for region 5 in Fig. 4.2.1, with result that $\mathbf{K}_g$, $\mathbf{K}_b$ are functions of *SHPRMCLY*, *HALPRM* and *SHPRMDRZ*. Distribution: Triangular. Range: −21 to −17.3 (i.e., permeability range is 1×10^{-21} to $1 \times 10^{-17.3}$ m^2). Mean, mode: −18.9, −18.3. Data base identifiers: 2334 (CL_L_T1, PRMX_LOG), 2335 (CL_L_T1, PRMY_LOG), 3009 (CLAY_RUS, PRMX_LOG), 3010 (CLAY_RUS, PRMY_LOG), 2334 (CL_L_T1, PRMX_LOG), 2335 (CL_L_T1, PRMY_LOG), 2351 (CL_L_T2, PRMX_LOG), 2352 (CL_L_T2, PRMY_LOG), 2368 (CL_L_T3, PRMX_LOG), 2369 (CL_L_T3, PRMY_LOG), 3078 (CL_L_T4, PRMX_LOG), 3079 (CL_L_T4, PRMY_LOG), 2385 (CL_M_T1, PRMX_LOG), 2386 (CL_M_T1, PRMY_LOG), 2402 (CL_M_T2, PRMX_LOG), 2403 (CL_M_T2, PRMY_LOG), 2419 (CL_M_T3, PRMX_LOG), 2420 (CL_M_T3, PRMY_LOG), 2436 (CL_M_T4, PRMX_LOG), 2437 (CL_M_T4, PRMY_LOG), 2453 (CL_M_T5, PRMX_LOG), 2454 (CL_M_T5, PRMY_LOG), 2317 (CLAY_BOT, PRMX_LOG), 2318 (CLAY_BOT, PRMY_LOG), 3009 (CLAY_RUS, PRMX_LOG), 3010 (CLAY_RUS, PRMY_LOG). Variable 9 in LHS. Additional information: Kelley et al. 1996a,b; Repository Isolation Systems Department 1996.
SHPRMCON	Same as *SHPRMCLY* (as used for regions 4, 10 in Fig. 4.2.1) but for concrete component of shaft seal (i.e., region 6 in Fig. 4.2.1) for 0 to 400 yr. Distribution: Triangular. Range: −17.0 to −14.0 (i.e., permeability range is 1×10^{-17} to 1×10^{-14} m^2). Mean, mode: −15.3, −15.0. Data base identifiers: 2470 (CONC_T1, PRMX_LOG), 2471 (CONC_T1, PRMY_LOG). Variable 10 in LHS. Additional information: Kelley et al. 1996a,b; Repository Isolation Systems Department 1996.

Table 5.2.1 Uncertain Variables Incorporated into 1996 WIPP PA (Continued)

Variable	Description
SHPRMDRZ	Logarithm of intrinsic permeability (m^2) of DRZ surrounding shaft. Used in BRAGFLO. Defines k_{in} in Eq. (4.2.35). Used in definition of effective permeability for shaft in regions 5, 8, 7 and 9 of Fig. 4.2.1. See *SHPRMASP*, *SHPRMCLY*, *SHPRMHAL*. Distribution: Triangular. Range: −17.0 to −14.0 (i.e., permeability range is 1×10^{-17} to 1×10^{-14} m^2). Mean, mode: −15.3, −15.0. Data base identifier: 3133 (SHFT_DRZ, PRMX_LOG). Variable 12 in LHS. Additional information: Kelley et al. 1996a,b; Knowles et al. 1998.
SHPRMHAL	Pointer variable (dimensionless) used to select intrinsic permeability in crushed salt component of shaft seal at different times. Used in BRAGFLO. Distribution: Uniform. Range: 0 to 1. Mean, mode: 0.5, 0.5. A distribution of permeability (m^2) in the crushed salt component of the shaft seal (i.e., region 7 in Fig. 4.2.1) is defined for each of the following time intervals: [0, 10 yr], [10, 25 yr], [25, 50 yr], [50, 100 yr], [100, 200 yr], [200, 10,000 yr] (see Table 2, Kelley et al. 1996a). *SHPRMHAL* is used to select a permeability value from the cumulative distribution function for permeability for each of the preceding time intervals with result that a rank correlation of 1 exists between the permeabilities used for the individual time intervals. Once selected, crushed salt permeabilities are used to define $\mathbf{K}_g$, $\mathbf{K}_b$ in Eqs. (4.2.1), (4.2.2). For region 7 (Fig. 4.2.1) in the same manner as SHPRMASP is used to define $\mathbf{K}_g$, $\mathbf{K}_b$ for region 5 (Fig. 4.2.1). Data base identifier: 2939 (SALT_T1, CUMPROB). Variable 13 in LHS. Additional information: Kelley et al. 1996a,b; Vaughn and McArthur 1996.

Table 5.2.1 Uncertain Variables Incorporated into 1996 WIPP PA (Continued)

Variable	Description
SHRBRSAT	Residual brine saturation in shaft (dimensionless). Used in BRAGFLO. Defines S_{br} in Eqs. (4.2.23) - (4.2.24) for regions 3-11 in Fig. 4.2.1. Distribution: Uniform. Range: 0 to 0.4. Mean, median: 0.2, 0.2. Data base identifiers: 2528 (SALT_T1, SAT_RBRN), 2545 (SALT_T2, SAT_RBRN), 2562 (SALT_T3, SAT_RBRN), 2579 (SALT_T4, SAT_RBRN), 2596 (SALT_T5, SAT_RBRN), 2992 (SALT_T6, SAT_RBRN), 2511 (EARTH, SAT_RBRN), 3014 (CLAY_RUS, SAT_RBRN), 2342 (CL_L_T1, SAT_RBRN), 2359 (CL_L_T2, SAT_RBRN), 2376 (CL_L_T3, SAT_RBRN), 3082 (CL_L_T4, SAT_RBRN), 2393 (CL_M_T1, SAT_RBRN), 2410 (CL_M_T2, SAT_RBRN), 2427 (CL_M_T3, SAT_RBRN), 2444 (CL_M_T4, SAT_RBRN), 2461 (CL_M_T5, SAT_RBRN), 2325 (CLAY_BOT, SAT_RBRN), 2478 (CONC_T1, SAT_RBRN), 2494 (CONC_T2, SAT_RBRN), 3063 (CONC_MON, SAT_RBRN), 2291 (ASPHALT, SAT_RBRN). Variable 15 in LHS. Additional information: Kelley et al. 1996a,b.
SHRGSSAT	Residual gas saturation in shaft (dimensionless). Used in BRAGFLO. Defines S_{gr} in Eq. (4.2.24) for regions 3-11 in Fig. 4.2.1. Distribution: Uniform. Range: 0 to 0.4. Mean, median: 0.2, 0.2. Data base identifiers: 2529 (SALT_T1, SAT_RGAS), 2546 (SALT_T2, SAT_RGAS), 2563 (SALT_T3, SAT_RGAS), 2580 (SALT_T4, SAT_RGAS), 2597 (SALT_T5, SAT_RGAS), 2993 (SALT_T6, SAT_RGAS), 2512 (EARTH, SAT_RGAS), 3015 (CLAY_RUS, SAT_RGAS), 2543 (CL_L_T1, SAT_RGAS), 2360 (CL_L_T2, SAT_RGAS), 2377 (CL_L_T3, SAT_RGAS), 3083 (CL_L_T4, SAT_RGAS), 2394 (CL_M_T1, SAT_RGAS), 2411 (CL_M_T2, SAT_RGAS), 2428 (CL_M_T3, SAT_RGAS), 2445 (CL_M_T4, SAT_RGAS), 2462 (CL_M_T5, SAT_RGAS), 2326 (CLAY_BOT, SAT_RGAS), 2479 (CONC_T1, SAT_RGAS), 2495 (CONC_T2, SAT_RGAS), 3064 (CONC_MON, SAT_RGAS), 2292 (ASPHALT, SAT_RGAS). Variable 14 in LHS. Additional information: Kelley et al. 1996a,b; Mayer et al. 1992.
WASTWICK	Increase in brine saturation of waste due to capillary forces (dimensionless). Used in BRAGFLO. Defines S_{wick} in Eq. (4.2.71) for regions 23, 24 in Fig. 4.2.1. Distribution: Uniform. Range: 0 to 1. Mean, median: 0.5, 0.5. Data base identifier: 2231 (WAS_AREA, SAT_WICK), 2138 (REPOSIT, SAT_WICK). Variable 8 in LHS.

Table 5.2.1 Uncertain Variables Incorporated into 1996 WIPP PA (Continued)

Variable	Description
WFBETCEL	Scale factor used in definition of stoichiometric coefficient for microbial gas generation (dimensionless). Used in BRAGFLO. Defines β in Eq. (4.2.70) for regions 23, 24 in Fig. 4.2.1. Distribution: Uniform. Range: 0 to 1. Mean, median: 0.5, 0.5. Data base identifier: 2994 (CELLULS, FBETA). Variable 5 in LHS. Additional information: Wang and Brush 1996a,b.
WGRCOR	Corrosion rate for steel under inundated conditions in the absence of CO_2 (m/s). Used in BRAGFLO. Defines R_{ci} in Eq. (4.2.49) for regions 23, 24 in Fig. 4.2.1. Distribution: Uniform. Range: 0 to 1.58×10^{-14} m/s. Mean, median: 7.94×10^{-15} m/s, 7.94×10^{-15} m/s. Data base identifier: 2907 (STEEL, CORRMCO2). Variable 1 in LHS. Additional information: Wang and Brush 1996a.
WGRMICH	Microbial degradation rate for cellulose under humid conditions (mol/kg•s). Used in BRAGFLO. Defines R_{mh} in Eq. (4.2.51) for regions 23, 24 in Fig. 4.2.1. Distribution: Uniform. Range: 0 to 1.27×10^{-9} mol/kg•s. Mean, median: 6.34×10^{-10} mol/kg•s, 6.34×10^{-10} mol/kg•s. Data base identifier: 656 (WAS_AREA, GRATMICH), 2127 (REPOSIT, GRATMICH). Variable 4 in LHS. Additional information: Wang and Brush 1996a.
WGRMICI	Microbial degradation rate for cellulose under inundated conditions (mol/kg•s). Used in BRAGFLO. Defines R_{mi} in Eq. (4.2.51) for regions 23, 24 in Fig. 4.2.1. Distribution: Uniform. Range: 3.17×10^{-10} to 9.51×10^{-9} mol/kg•s. Mean, median: 4.92×10^{-9} mol/kg•s, 4.92×10^{-9} mol/kg•s. Data base identifier: 657 (WAS_AREA, GRATMICI), 2128 (REPOSIT, GRATMICI). Variable 3 in LHS. Additional information: Wang and Brush 1996a.
WMICDFLG	Pointer variable for microbial degradation of cellulose. Used in BRAGFLO. Distribution: Discrete, with 50% 0, 25% 1, 25% 2. WMICDFLG = 0, 1, 2 implies no microbial degradation of cellulose, microbial degradation of only cellulose, microbial degradation of cellulose, plastic and rubber. Data base identifier: 2823 (WAS_AREA, PROBDEG), 2824 (REPOSIT, PROBDEG). Variable 2 in LHS. Additional information: Tierney 1996a.

Table 5.2.1 Uncertain Variables Incorporated into 1996 WIPP PA (Continued)

Variable	Description
WPRTDIAM	Waste particle diameter (m). Used in CUTTINGS_S. Defines d in Eqs. (4.6.8) and (4.6.9). Distribution: Loguniform. Range: 4.0×10^{-5} to 2.0×10^{-1} m. Mean, median: 2.35×10^{-2} m, 2.80×10^{-2} m. Data base identifier: 3246 (BRAGFLO_DBR, PARTDIA). Variable 32 in LHS. Additional information: Berglund 1996a,b.
WOXSTAT	Pointer variable for elemental oxidation states (dimensionless). Solubilities obtained with *WOXSTAT* used in NUTS, PANEL (see Eqs. (4.3.3)-(4.3.6) and Table 4.3.1); retardations obtained with *WOXSTAT* used in SECOTP2D (see Eq. (4.9.7)). Distribution: Uniform. Range: 0 to 1. Mean, median: 0.5, 0.5. Reset to *WOXSTAT* = 0, 1 for *WOXSTAT* $\leq$ 0.5, 0.5 < *WOXSTAT* $\leq$ 1. *WOXSTAT* = 0 implies use of *CMKDPU3, CMKDU4, WSOLPU3C, WSOLPUS, WSOLU4S; WOXSTAT* = 1 implies use of *CMKDPU4, CMKDU6, WSOLPU4C, WSOLPU4S, WSOLU6C, WSOLU6S.* Data base identifier: 3417 (GLOBAL, OXSTAT). Variable 47 in LHS. Additional information: Weiner 1996, Stockman 1996a.
WPHUMOX3	Ratio of concentration of actinides attached to humic colloids to dissolved concentration of actinides for oxidation state III in Castile brine (dimensionless). See SF_{Hum} (*Br, Ox, El*) in Table 4.3.1. Distribution: Piecewise uniform. Range: 0.065 to 1.60. Mean, median: 1.10, 1.37. Data base identifier: 3429 (PHUMOX3, PHUMCIM). Variable 46 in LHS. Additional information: Papenguth 1996, Papenguth and Moore 1996a, b.
WRBRNSAT	Residual brine saturation in waste (dimensionless). Used in BRAGFLO. Defines S_{br} in Eqs. (4.2.13) - (4.2.14) for use in regions 23, 24 in Fig. 4.2.1. Also used in BRAGFLO_DBR; see Sect. 4.7.4. Distribution: Uniform. Range: 0 to 0.552. Mean, median: 0.276, 0.276. Data base identifiers: 670 (WAS_AREA, SAT_RBRN), 2741 (REPOSIT, SAT_RBRN). Variable 7 in LHS. Additional information: Vaughn 1996a.

Table 5.2.1 Uncertain Variables Incorporated into 1996 WIPP PA (Continued)

Variable	Description
WRGSSAT	Residual gas saturation in waste (dimensionless). Used in BRAGFLO. Defines S_{gr} in Eq. (4.2.14) for use in regions 23, 24 in Fig. 4.2.1. Also used in BRAGFLO_DBR; see Sect. 4.7.4. Distribution: Uniform. Range: 0 to 0.15. Mean, median: 0.075, 0.075. Data base identifiers: 671 (WAS_AREA, SAT_RGAS), 2137 (REPOSIT, SAT_RGAS). Variable 6 in LHS. Additional information: Solutions Engineering 1995.
WSOLAM3C	Logarithm of scale factor used to define solubility in Castile brine of americium in oxidation state III (dimensionless). Solubility calculated from *WSOLAM3C* used in NUTS, PANEL. Defines *UF(Br, Ox, El)* in Table 4.3.1, which is a multiplier on solubility prediction with FMT (Siegel 1996). Distribution: Piecewise uniform. Range: –2.00 to 1.40. Mean, median: 0.18, –0.09. Data base identifier: 3263 (SOLAM3, SOLCIM). Variable 37 in LHS. Additional information: Stockman 1996b; Bynum 1996.
WSOLAM3S	Same as *WSOLAM3C* but for Salado brine. Data base identifier: 3262 (SOLAM3, SOLSIM). Variable 36 in LHS. Note: *WSOLAM3C, WSOLAM3S, WSOLPU3C, WSOLPU3S, WSOLPU4C, WSOLPU4S, WSOLTH4S, WSOLU4S, WSOLU6C, WSOLU6S* have same distribution (see *WSOLAM3C*) but are sampled independently.
WSOLPU3C	Same as *WSOLAM3C* but for plutonium. Data base identifier: 3264 (SOLPU3, SOLCIM). Variable 39 in LHS.
WSOLPU3S	Same as *WSOLAM3C* but plutonium in Salado brine. Data base identifier: 3265 (SOLPU3, SOLSIM). Variable 38 in LHS.
WSOLPU4C	Same as *WSOLAM3C* but for plutonium in oxidation state IV. Data base identifier: 3389 (SOLPU4, SOLCIM). Variable 41 in LHS.
WSOLPU4S	Same as *WSOLAM3C* but for plutonium in oxidation state IV in Salado brine. Data base identifier: 3266 (SOLPU4, SOLSIM). Variable 40 in LHS.
WSOLTH4S	Same as *WSOLAM3C* but for thorium in oxidation state IV in Salado brine. Data base identifier: 3393 (SOLTH4, SOLSIM). Variable 45 in LHS.

Table 5.2.1 Uncertain Variables Incorporated into 1996 WIPP PA (Continued)

Variable	Description
WSOLU4S	Same as *WSOLAM3C* but for uranium in oxidation state IV in Salado brine. Data base identifier: 3390 (SOLU4, SOLSIM). Variable 42 in LHS.
WSOLU6C	Same as *WSOLAM3C* but for uranium in oxidation state VI. Data base identifier: 3392 (SOLU6, SOLCIM). Variable 44 in LHS.
WSOLU6S	Same as *WSOLAM3C* but for uranium in oxidation state VI in Salado brine. Data base identifier: 3391 (SOLU6, SOLSIM). Variable 43 in LHS.
WTAUFAIL	Shear strength of waste (Pa). Used in CUTTINGS_S. Defines $\tau(R,1)$ in Eq. (4.5.8). Distribution: Uniform. Range: 0.05 to 10 Pa. Mean, median: 5.03 Pa, 5.03 Pa. Data base identifier: 2254 (BOREHOLE, TAUFAIL). Variable 33 in LHS. Additional information: Berglund 1996c.

5.3 Variable Distributions

A distribution that characterizes subjective uncertainty is indicated for each of the variables in Table 5.2.1. These distributions characterize a degree of belief as to where the appropriate value to use for each variable is located and correspond to the distributions D_j in Eq. (5.2.1). Examples of four of these distributions are provided in Fig. 5.3.1; further, all 57 distributions are presented in App. A. The truncations associated with *ANHCOMP* result from the restriction that the defined distribution cannot contain values that fall outside the observed range for the variable.

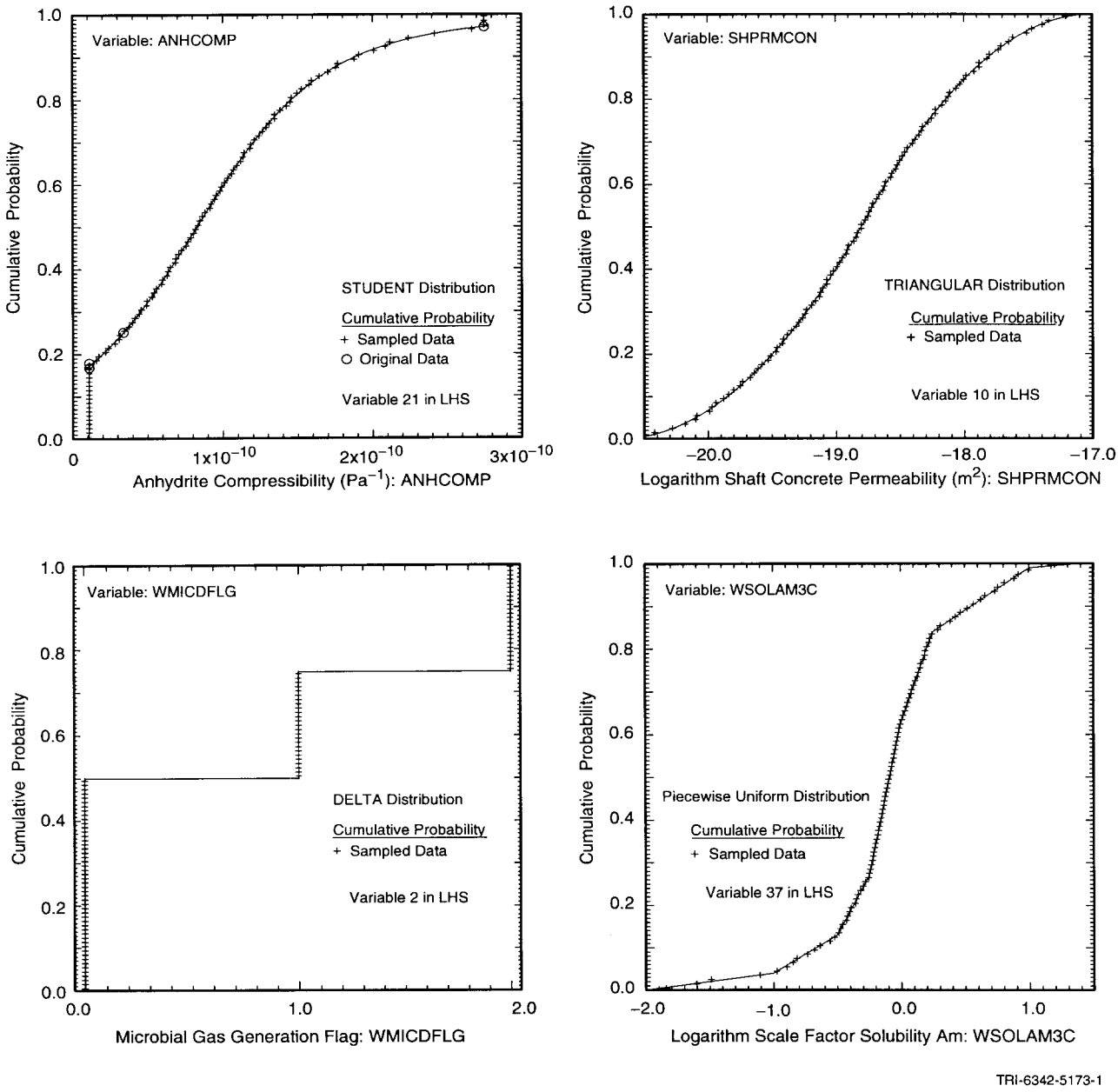

Fig. 5.3.1 Examples of uncertain variables, their associated distributions, and sampled values obtained with a Latin hypercube sample (McKay et al. 1979; see Sects. 6.1, 6.5) of size 100.

5.4 Correlations

Most of the variables in Table 5.2.1 are assumed to be uncorrelated. However, the pairs (*ANHCOMP, ANHPRM*), (*HALCOMP, HALPRM*) and (*BPCOMP, BPPRM*) are assumed to have rank correlations of –0.99, –0.99 and –0.75, respectively (Fig. 5.4.1). These correlations result from a belief that the underlying physics implies that a large value for one variable in a pair should be associated with a small value for the other variable in the pair. The scatterplots in Fig. 5.4.1 result from the Latin hypercube samples described in Sect. 6.5, with the rank correlations within the pairs (*ANHCOMP, ANHPRM*), (*HALCOMP, HALPRM*) and (*BPCOMP, BPPRM*) induced with the Iman and Conover (1982) restricted pairing technique (see Sect. 6.2).

The distributions and associated correlations indicated in Table 5.2.1 and Figs. 5.3.1 and 5.4.1 define the probability space ($\mathcal{S}_{su}$, $\mathcal{J}_{su}$, P_{su}) for subjective uncertainty in Sect. 2.4. The vector $\mathbf{x}_{su}$ in Eqs. (2.4.1) and (5.1.1) has the form

$$\mathbf{x}_{su} = [ANHBCEXP, ANHBCVGP, ..., WTAUFAIL], \tag{5.4.1}$$

where the individual elements of $\mathbf{x}_{su}$ are the variables described in Table 5.2.1.

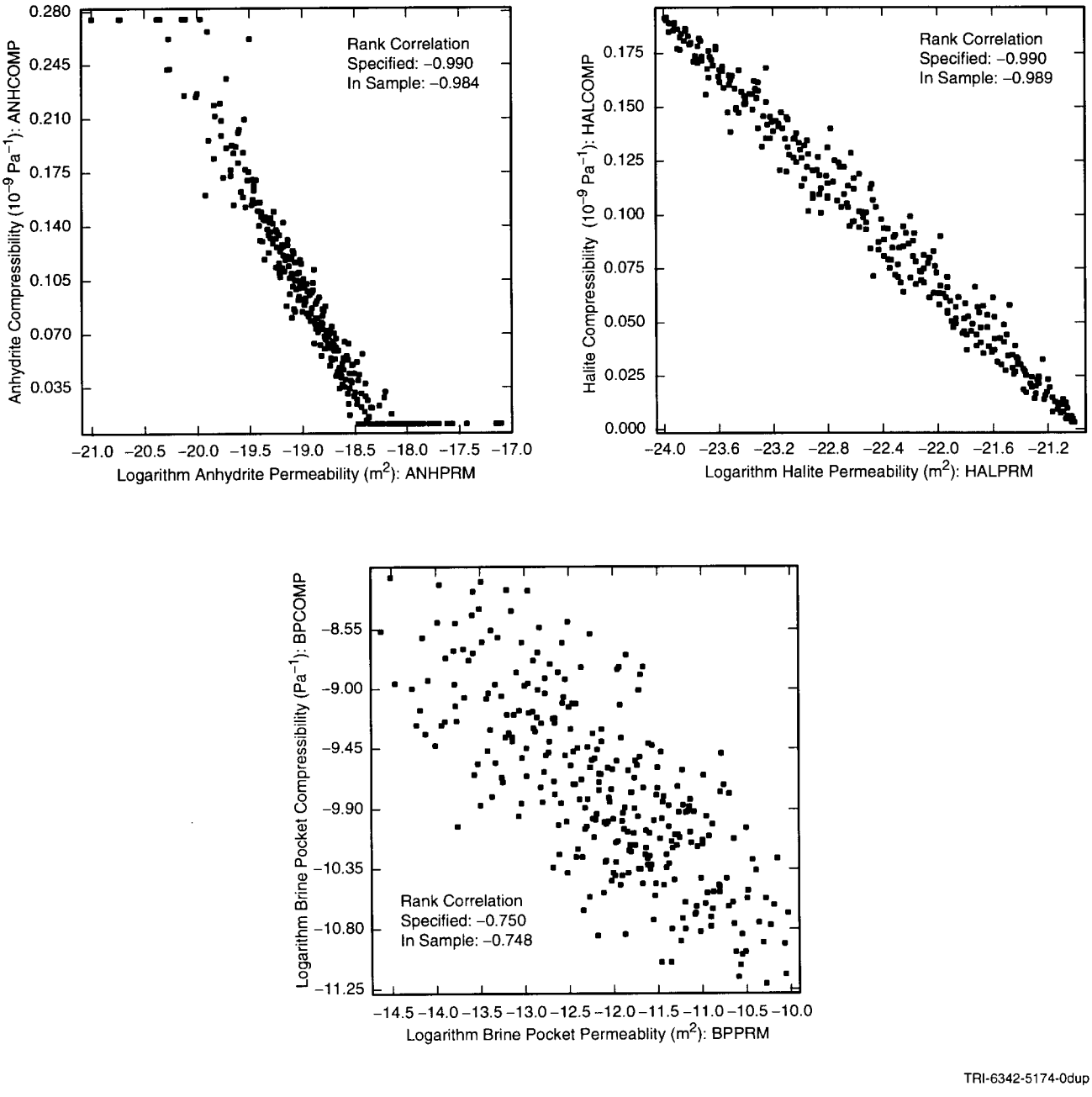

Fig. 5.4.1. Scatterplots illustrating correlations within the pairs (*ANHCOMP*, *ANHPRM*), (*HALCOMP*, *HALPRM*) and (*BPCOMP*, *BPPRM*).

5.5 Scenarios Involving Stochastic and Subjective Uncertainty

Scenarios are usually defined to be subsets $\mathcal{E}_{st}$ of the sample space S_{st} for stochastic uncertainty, and scenario probabilities $p_{st}(\mathcal{E}_{st})$ are defined by the function p_{st} associated with the probability space $(S_{st}, \mathcal{S}_{st}, p_{st})$ for stochastic uncertainty (Sect. 3.9). This definition is consistent with the concept that a scenario is something that could happen in the future. However, this definition is also consistent with the broader concept that a scenario is simply a subset of the sample space S associated with an arbitrary probability space $(S, \mathcal{S}, p)$; or to be technically correct, a scenario is an element of the set $\mathcal{S}$ associated with the probability space $(S, \mathcal{S}, p)$ (Sect. 3.9).

A probability space $(S_{su}, \mathcal{S}_{su}, p_{su})$ for subjective uncertainty has now been introduced (Sect. 5.1). Consistent with the concept that scenarios are subsets of the sample space associated with an arbitrary probability space, scenarios could also be defined to be subsets $\mathcal{E}_{su}$ of S_{su} (i.e., elements of $\mathcal{S}_{su}$), with corresponding probabilities given by $p_{su}(\mathcal{E}_{su})$.

Although a subset $\mathcal{E}_{st}$ of S_{st} and also a subset $\mathcal{E}_{su}$ of S_{su} can be formally thought of as being scenarios in the sense of being subsets of the sample space associated with a particular probability space, $\mathcal{E}_{st}$ and $\mathcal{E}_{su}$ are very different entities. In particular, $\mathcal{E}_{st}$ contains vectors $\mathbf{x}_{st}$ of the form defined in Eq. (2.2.2), and $\mathcal{E}_{su}$ contains vectors $\mathbf{x}_{su}$ of the form defined in Eqs. (5.1.1) and (5.4.1). Further, the probability $p_{st}(\mathcal{E}_{st})$ for $\mathcal{E}_{st}$ characterizes the likelihood that a vector $\mathbf{x}_{st}$ in $\mathcal{E}_{st}$ will match the occurrences that will take place at the WIPP over the next 10,000 yr, and the probability $p_{su}(\mathcal{E}_{su})$ for $\mathcal{E}_{su}$ characterizes a degree of belief that a vector $\mathbf{x}_{su}$ in $\mathcal{E}_{su}$ contains the appropriate values for the 57 variables in Table 5.2.1 for use in the 1996 WIPP PA. Given the difference between scenarios derived from S_{st} and scenarios derived from S_{su}, a careful specification of what is meant by a scenario is always necessary in an analysis that involves multiple probability spaces.

The probability spaces $(S_{st}, \mathcal{S}_{st}, p_{st})$ and $(S_{su}, \mathcal{S}_{su}, p_{su})$ can be combined to produce an additional probability space $(S, \mathcal{S}, p)$, where the elements $\mathbf{x}$ of the sample space S are vectors of the form

$$\mathbf{x} = [\mathbf{x}_{st}, \mathbf{x}_{su}], \mathbf{x}_{st} \in S_{st}, \mathbf{x}_{su} \in S_{su}. \tag{5.5.1}$$

Thus, under the convention that scenarios are subsets of the sample space associated with an arbitrary probability space, scenarios could also be defined to be sets of vectors of the form defined in Eq. (5.5.1). In this case, the definition of a scenario would involve the specification of what could occur in the future (i.e., the part of $\mathbf{x}$ defined by $\mathbf{x}_{st}$) and the specification of fixed but unknown values for parameters required in the analysis (i.e., the part of $\mathbf{x}$ defined by $\mathbf{x}_{su}$).

The probability space $(\mathcal{S}, \mathcal{A}, p)$ can be developed from $(\mathcal{S}_{st}, \mathcal{A}_{st}, p_{st})$ and $(\mathcal{S}_{su}, \mathcal{A}_{su}, p_{su})$ by defining each element $\mathcal{E}$ of $\mathcal{A}$ by

$$\begin{aligned}\mathcal{E} &= \mathcal{E}_{st} \times \mathcal{E}_{su} \\ &= \{\mathbf{x}: \mathbf{x} = [\mathbf{x}_{st}, \mathbf{x}_{su}], \mathbf{x}_{st} \in \mathcal{E}_{st}, \mathbf{x}_{su} \in \mathcal{E}_{su}\},\end{aligned} \tag{5.5.2}$$

where $\mathcal{E}_{st} \in \mathcal{A}_{st}$ and $\mathcal{E}_{su} \in \mathcal{A}_{su}$. If the probability spaces $(\mathcal{S}_{st}, \mathcal{A}_{st}, p_{st})$ and $(\mathcal{S}_{su}, \mathcal{A}_{su}, p_{su})$ are independent (i.e., the occurrence of a particular element $\mathbf{x}_{st}$ of $\mathcal{S}_{st}$ does not affect the definition of $(\mathcal{S}_{su}, \mathcal{A}_{su}, p_{su})$, and the occurrence of a particular element $\mathbf{x}_{su}$ of $\mathcal{S}_{su}$ does not affect the definition of $(\mathcal{S}_{st}, \mathcal{A}_{st}, p_{st})$), then

$$p(\mathcal{E}) = p(\mathcal{E}_{st} \times \mathcal{E}_{su}) = p_{st}(\mathcal{E}_{st})\, p_{su}(\mathcal{E}_{su}). \tag{5.5.3}$$

If $(\mathcal{S}_{st}, \mathcal{A}_{st}, p_{st})$ and $(\mathcal{S}_{su}, \mathcal{A}_{su}, p_{su})$ are not independent, then a more complicated definition for p is required, with the exact nature of this definition being a function of the dependencies that exist between $(\mathcal{S}_{st}, \mathcal{A}_{st}, p_{st})$ and $(\mathcal{S}_{su}, \mathcal{A}_{su}, p_{su})$.

In the 1996 WIPP PA, $(\mathcal{S}_{st}, \mathcal{A}_{st}, p_{st})$ and $(\mathcal{S}_{su}, \mathcal{A}_{su}, p_{su})$ are independent, with the result that the relationship in Eq. (5.5.3) holds. This would not be the case if a parameter required in the definition of $(\mathcal{S}_{st}, \mathcal{A}_{st}, p_{st})$ was treated as being uncertain and thus included in $\mathbf{x}_{su}$. For example, a more complex definition for p in Eq. (5.5.3) would be required if the drilling rate in Eqs. (3.2.1) - (3.3.3) was treated as being uncertain. Although none of the quantities used in the definition of $(\mathcal{S}_{st}, \mathcal{A}_{st}, p_{st})$ in the 1996 WIPP PA were considered to be uncertain, such uncertainties were considered in a verification analysis performed at SNL for the U.S. EPA (MacKinnon, Freeze and Jow 1997); in particular, the probability that a drilling intrusion would penetrate pressurized brine (Sect. 3.5) was treated as being uncertain and included in the definition of $\mathbf{x}_{su}$.

As described in conjunction with the probability spaces $(\mathcal{S}_{st}, \mathcal{A}_{st}, p_{st})$, $(\mathcal{S}_{su}, \mathcal{A}_{su}, p_{su})$ and $(\mathcal{S} = \mathcal{S}_{st} \times \mathcal{S}_{su}, \mathcal{A}, p)$, the concept of a scenario is consistent in the sense of being a subset of a sample space and yet can involve quite different entities due to the different probability spaces potentially under consideration. Thus, when the use of scenarios is discussed, it is important to specify clearly which of many possible probability spaces is under consideration.

Unless specified otherwise, use of the term scenario in the 1996 WIPP PA refers to subsets of the sample space $\mathcal{S}_{st}$ for stochastic uncertainty (Sect. 3.9). However, due to the use of Monte Carlo procedures to incorporate the effects of stochastic and subjective uncertainty into the 1996 WIPP PA, the use of terminology related to scenarios does not play a large role in the description of this analysis.

6. Computational Procedures

6.1 Sampling Procedures

As indicated in Chapter 2, extensive use is made of sampling procedures in the 1996 WIPP PA. In particular, random sampling is used in the generation of individual CCDFs (i.e., for integration over the probability space ($\mathcal{S}_{st}$, $\mathcal{A}_{st}$, p_{st}) for stochastic uncertainty; see Sect. 2.3) and Latin hypercube sampling is used for the assessment of the effects of imprecisely-known analysis inputs (i.e., for integration over the probability space ($\mathcal{S}_{su}$, $\mathcal{A}_{su}$, p_{su}) for subjective uncertainty; see Sect. 2.4). Due to the importance of sampling procedures in the 1996 WIPP PA, brief descriptions are given for random sampling, importance sampling and Latin hypercube sampling, which are probably the most widely used sampling techniques. For notational convenience, assume that the variable under consideration is represented by

$$\mathbf{x} = [x_1, x_2, ..., x_{nV}] \tag{6.1.1}$$

and that the corresponding probability space is ($\mathcal{S}$, $\mathcal{A}$, p).

In random sampling, sometimes also called simple random sampling, the observations

$$\mathbf{x}_k = [x_{k1}, x_{k2}, ..., x_{k,nV}], \quad k = 1, 2, ..., nR, \tag{6.1.2}$$

where nR is the sample size, are selected according to the joint probability distribution for the elements of $\mathbf{x}$ as defined by ($\mathcal{S}$, $\mathcal{A}$, p). In practice, ($\mathcal{S}$, $\mathcal{A}$, p) is defined by specifying a distribution D_j for each element x_j of $\mathbf{x}$. Points from different regions of the sample space $\mathcal{S}$ occur in direct relationship to the probability of occurrence of these regions. Further, each sample element is selected independently of all other sample elements. As illustrated in Fig. 6.1.1 for $x_1 = U$, $x_2 = V$, $nV = 2$ and $nR = 5$, the numbers $RU(1)$, $RU(2)$, ..., $RU(5)$ are sampled from a uniform distribution on [0, 1] and in turn lead to a sample $U(1)$, $U(2)$, ..., $U(5)$ from U based on the cumulative distribution function (CDF) for U. Similarly, the numbers $RV(1)$, $RV(2)$, ..., $RV(5)$ lead to a sample $V(1)$, $V(2)$, ..., $V(5)$ from V. The pairs

$$\mathbf{x}_k = [U(k), V(k)], \; k = 1, 2, ..., nR = 5, \tag{6.1.3}$$

then constitute a random sample from $\mathbf{x} = [U, V]$, where U has a normal distribution on [−1, 1] and V has a triangular distribution on [0, 4].

Random samples are generated in an analogous manner when $\mathbf{x}$ has a dimensionality greater than 2 (e.g., nV = 100). Specifically, if the elements of $\mathbf{x}$ are represented by U, V, ..., W and a random sample of size nR is to be generated, then random numbers $RU(1)$, $RU(2)$, ..., $RU(nR)$ are sampled uniformly from [0,1] and used to obtain

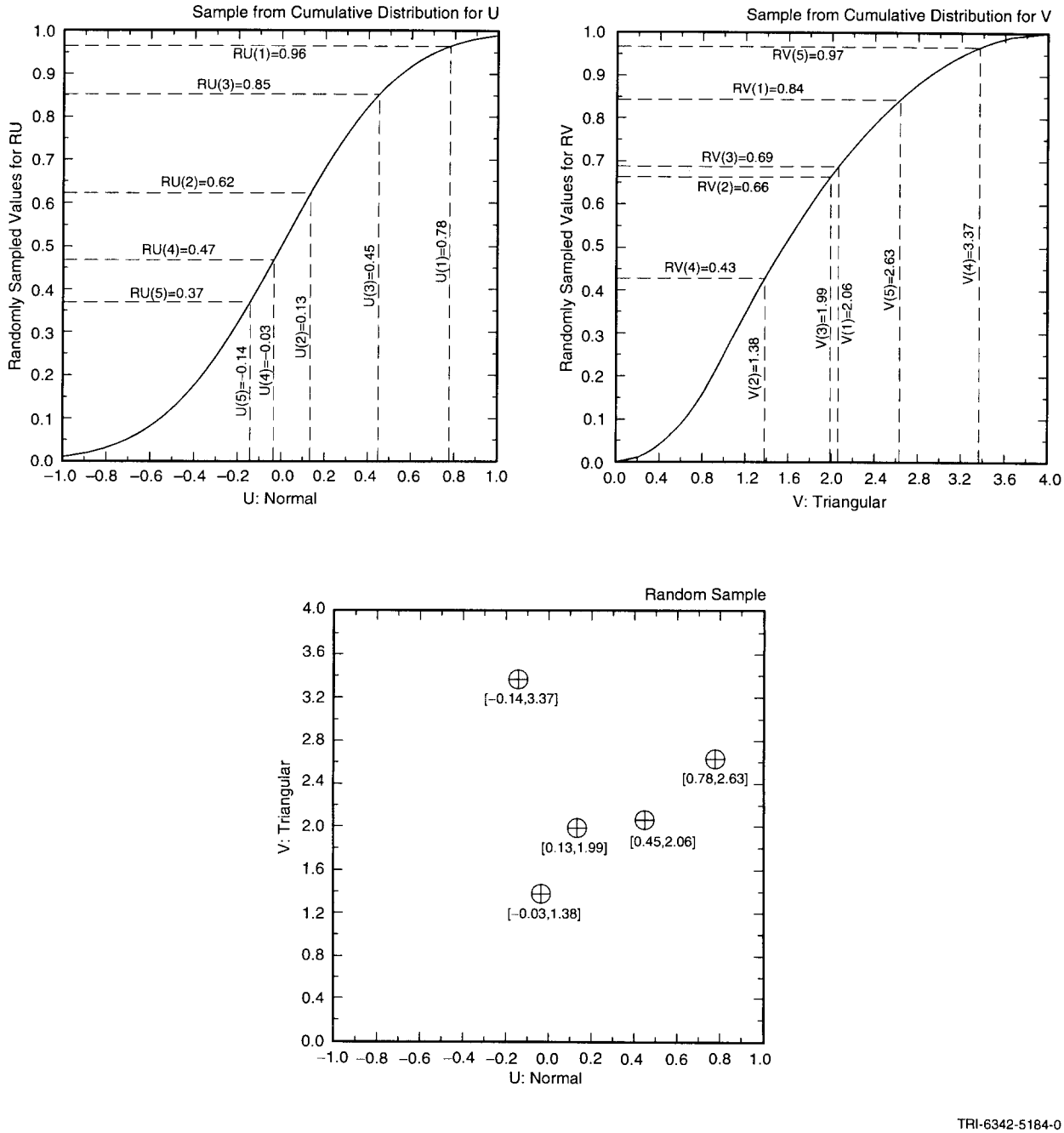

Fig. 6.1.1. Example of random sampling to generate a sample of size $nR = 5$ from $\mathbf{x} = [U, V]$ with U normal on $[-1, 1]$ (mean = 0, 0.01 quantile = −1, 0.99 quantile = 1) and V triangular on $[0, 4]$ (mode = 1).

corresponding values $U(1)$, $U(2)$, ..., $U(nR)$ for U; random numbers $RV(1)$, $RV(2)$, ..., $RV(nR)$ are sampled uniformly from [0,1] and used to obtain corresponding values $V(1)$, $V(2)$, ..., $V(nR)$ for V, and so on, with the process continuing through all elements of $\mathbf{x}$ and ending with the selection of random numbers $RW(1)$, $RW(2)$, ..., $RW(nR)$ from [0,1] and the generation of the corresponding values $W(1)$, $W(2)$, ..., $W(nR)$ for W. The vectors

$$\mathbf{x}_k = [U(k), V(k), ..., W(k)], k = 1, 2, ..., nR, \tag{6.1.4}$$

then constitute a random sample from $\mathbf{x} = [U,V, ..., W]$.

In random sampling, there is no assurance that points will be sampled from any given sub-region of the sample space $\mathcal{S}$. Also, it is possible for an inefficient sampling of $\mathcal{S}$ to occur due to several sampled values falling very close together. The preceding problems can be partially ameliorated by using importance sampling. With this technique, $\mathcal{S}$ is exhaustively divided into a number of nonoverlapping subregions (i.e., strata) $\mathcal{S}_i$, $i = 1, 2, ..., nS$. Then, nS_i values for $\mathbf{x}$ are randomly sampled from $\mathcal{S}_i$, with the random sampling carried out in consistency with the definition of $(\mathcal{S}, \mathcal{A}, p)$ and the restriction of $\mathbf{x}$ to $\mathcal{S}_i$. The resultant vectors

$$\mathbf{x}_k = [x_{k1}, x_{k2}, ..., x_{k,nV}], \; k = 1, 2, ..., \sum_{i=1}^{nS} nS_i \; , \tag{6.1.5}$$

then constitute an importance-based sample from $\mathcal{S}$ (i.e., a sample obtained by importance sampling). Typically, only one value is sampled from each $\mathcal{S}_i$, with the result that the sample has the form

$$\mathbf{x}_k = [x_{k1}, x_{k2}, ..., x_{k,nV}], \; k = 1, 2, ..., nS. \tag{6.1.6}$$

The name importance sampling derives from the fact that the $\mathcal{S}_i$ are in part defined on the basis of how important the $\mathbf{x}$'s contained in each set are to the final outcome of the analysis. Often, importance sampling is used to assure the inclusion in an analysis of $\mathbf{x}$'s that have high consequences but low probabilities (i.e., the probabilities $p(\mathcal{S}_i)$ are small for the $\mathcal{S}_i$ that contain such $\mathbf{x}$'s). When importance sampling is used, the probabilities $p(\mathcal{S}_i)$ and number of observations nS_i taken from each $\mathcal{S}_i$ must be folded back into the analysis before results can be meaningfully presented.

Several examples of importance sampling for $\mathbf{x} = [U, V]$ are given in Fig. 6.1.2. The two top frames are for strata of equal probability (i.e., all $p(\mathcal{S}_i)$ are equal). For two uniform distributions, this results in all strata having the same area (upper left frame). For two nonuniform distributions, different strata can have different areas even though they have the same probability (upper right frame). The two lower frames are for strata of unequal probability. In this case, the variable distributions and the strata probabilities interact to determine the area of the strata. However, it is important to recognize that specifying variable distributions, number of strata and strata probabilities does not

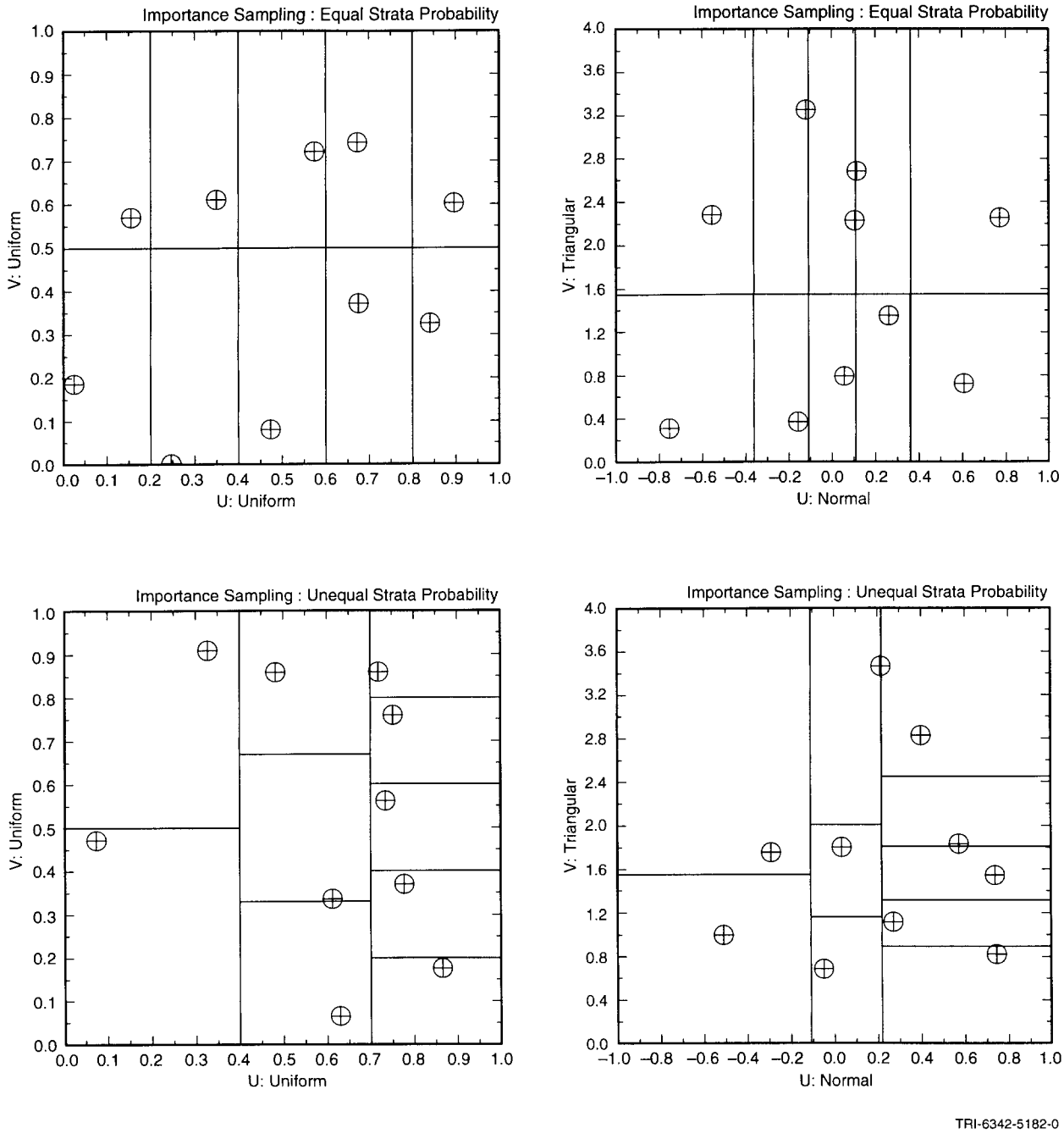

Fig. 6.1.2. Examples of importance sampling with ten strata (i.e., $nS = 10$), one random sample per strata (i.e., $nS_i = 1$), equal strata probability (i.e., $p(S_i) = 1/10$, upper frames), unequal strata probability (i.e., $p(S_i) = 0.2, 0.2, 0.1, 0.1, 0.1, 0.06, 0.06, 0.06, 0.06, 0.06$, lower frames), U and V uniform on [0, 1] (left frames) and U normal on [−1, 1] (mean = 0, 0.01 quantile = −1, 0.99 quantile = 1) and V triangular on [0, 4] (mode = 1) (right frames).

uniquely define an importance sampling procedure; rather, there are many ways in which the strata S_i can be defined that are consistent for the preceding constraints. In particular, appropriate definition of strata will depend on specific properties of individual analyses. Similar ideas also hold for more than two variables, in which case the strata become volumes in a space with the same dimension as **x**.

Importance sampling operates to ensure the full coverage of specified regions in the sample space. This idea is carried farther in Latin hypercube sampling (McKay et al. 1979) to ensure the full coverage of the range of each variable. Specifically, the range of each variable (i.e., the x_j) is divided into *nLHS* intervals of equal probability and one value is selected at random from each interval. The *nLHS* values thus obtained for x_1 are paired at random without replacement with the *nLHS* values obtained for x_2. These *nLHS* pairs are combined in a random manner without replacement with the *nLHS* values of x_3 to form *nLHS* triples. This process is continued until a set of *nLHS* nV-tuples is formed. These nV-tuples are of the form

$$\mathbf{x}_k = [x_{k1}, x_{k2}, ..., x_{k,nV}], \quad k = 1, ..., nLHS, \tag{6.1.7}$$

and constitute the Latin hypercube sample (LHS). The individual x_j must be independent for the preceding construction procedure to work; a method for generating Latin hypercube and random samples from correlated variables has been developed by Iman and Conover (1982) and will be discussed in Sect. 6.2. Latin hypercube sampling is an extension of quota sampling (Steinberg 1963) and can be viewed as an n-dimensional randomized generalization of Latin square sampling (pp. 206-209, Raj 1968).

The generation of an LHS of size *nLHS* = 5 from **x** = [U, V] is illustrated in Fig. 6.1.3. Initially, the ranges of U and V are subdivided into five intervals of equal probability, with this subdivision represented by the lines that originate at 0.2, 0.4, 0.6 and 0.8 on the ordinates of the two upper frames in Fig. 6.1.3, extend horizontally to the CDFs, and then drop vertically to the abscissas to produce the 5 indicated intervals. Random values $U(1)$, $U(2)$, ..., $U(5)$ and $V(1)$, $V(2)$, ..., $V(5)$ are then sampled from these intervals. The sampling of these random values is implemented by (1) sampling $RU(1)$ and $RV(1)$ from a uniform distribution on [0, 0.2], $RU(2)$ and $RV(2)$ from a uniform distribution on [0.2, 0.4], and so on and (2) then using the CDFs to identify (i.e., sample) the corresponding U and V values, with this identification represented by the dashed lines that originate on the ordinates of the two upper frames in Fig. 6.1.3, extend horizontally to the CDFs, and then drop vertically to the abscissas to produce $U(1)$, $U(2)$, ..., $U(5)$ and $V(1)$, $V(2)$, ..., $V(5)$. The generation of the LHS is then completed by randomly pairing (without replacement) the resulting values for U and V. As this pairing is not unique, many possible LHSs can result. Two such *LHS*s are shown in the lower two frames in Fig. 6.1.3, with one LHS resulting from the pairings [$U(1)$, $V(5)$], [$U(2)$, $V(1)$], [$U(3)$, $V(2)$], [$U(4)$, $V(3)$], [$U(5)$, $V(4)$] (lower left frame) and the other LHS resulting from the pairings [$U(1)$, $V(3)$], [$U(2)$, $V(2)$], [$U(3)$, $V(3)$], [$U(4)$, $V(5)$], [$U(5)$, $V(1)$] (lower right frame).

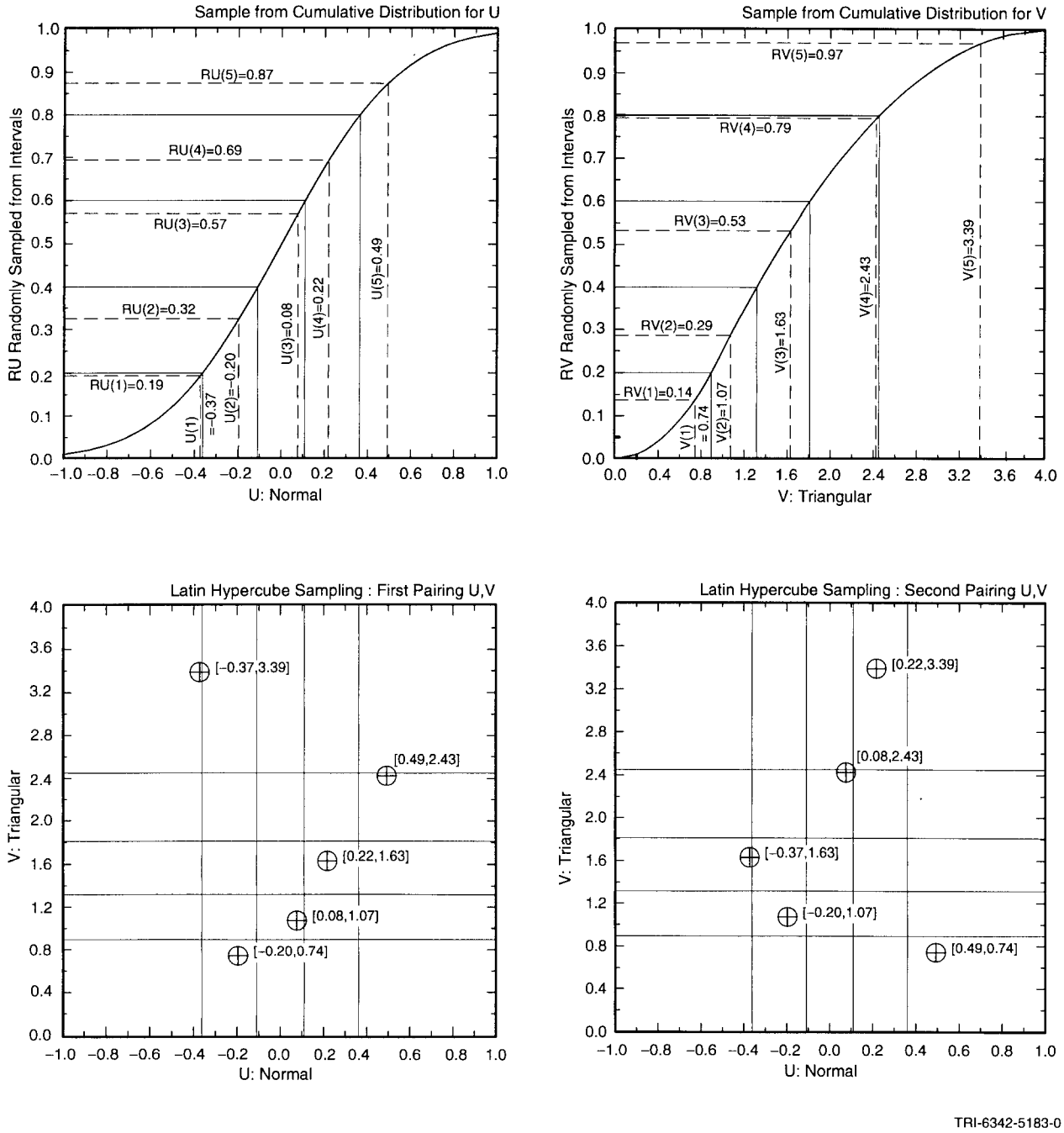

Fig. 6.1.3. Example of Latin hypercube sampling to generate a sample of size $nLHS = 5$ from $\mathbf{x} = [U, V]$ with U normal on [−1, 1] (mean = 0, 0.01 quantile = −1, 0.99 quantile = 1) and V triangular on [1, 4] (mode = 1).

The generation of an LHS for $nV > 2$ proceeds in a manner similar to that shown in Fig. 6.1.3 for $nV = 2$. The sampling of the individual variables for $nV > 2$ takes place in exactly the same manner as shown in Fig. 6.1.3. However, the nV variables define an nV-dimensional solid rather than a 2-dimensional rectangle in the plane. Thus, the two lower frames in Fig. 6.1.3 would involve a partitioning of an nV-dimensional solid rather than a rectangle.

Random sampling is the preferred technique when sufficiently large samples are possible because it is easy to implement, easy to explain, and provides unbiased estimates for means, variances and distribution functions. The possible problems with random sampling derive from the rather vague phrase "sufficiently large" in the preceding sentence. When the underlying models are expensive to evaluate (e.g., many hours of CPU time per evaluation) or estimates of extreme quantiles are needed (e.g., the 0.999999 quantile), the required sample size to achieve a specific purpose may be too large to be computationally practicable. In the 1996 WIPP PA, random sampling is used for the estimation of CCDFs (i.e., integration over $(\mathcal{S}_{st}, \mathcal{J}_{st}, p_{st})$) because it was possible to develop a computational strategy that allowed the use of a sample of size $nS = 10{,}000$ to estimate an exceedance probability of 0.001 (i.e., the 0.999 quantile of the distribution of normalized releases to the accessible environment).

When random sampling is not computationally feasible for the estimation of extreme quantiles, importance sampling is often employed. However, the use of importance sampling on nontrivial problems is not easy due to the difficulty of defining the necessary strata and also of calculating the probabilities of these strata. For example, the fault and event tree techniques used in probabilistic risk assessments for nuclear power stations and other complex engineered facilities can be viewed as algorithms for defining importance sampling procedures. The bottom line is that the definition and implementation of an importance sampling procedure is not easy. Further, without extensive *a priori* knowledge, the strata may end up being defined much more finely than is necessary, with the result that the importance sampling procedure ends up requiring more calculations than the use of random sampling to calculate the same outcomes. For example, the number of strata in the importance sampling procedure used to estimate CCDFs in the 1991 and 1992 WIPP PAs (Helton and Iuzzolino 1993) greatly exceeds the size of the random samples used in the 1996 WIPP PA to estimate CCDFs. The unequal strata probabilities also make the outcomes of analyses based on importance sampling inconvenient for use in sensitivity analyses (e.g., how does one interpret a scatterplot or a regression analysis derived from results obtained from an importance sampling procedure). For the preceding reasons, importance sampling was not used in the 1996 WIPP PA.

Latin hypercube sampling is used when large samples are not computationally practicable and the estimation of very high quantiles is not required. The preceding is typically the case in uncertainty and sensitivity studies to assess the effects of subjective uncertainty. First, the models under consideration are often computationally demanding, with the result that the number of calculations that can be performed to support the analysis is necessarily limited. For example, the totality of the model calculations (i.e., BRAGFLO, NUTS, PANEL, GRASP_INV, SECOFL2D, SECOTP2D, CUTTINGS_S, BRAGFLO_DBR) in the 1996 WIPP PA is too extensive to permit the generation of 1000's of CCDFs in an uncertainty/sensitivity study to assess the effects of subjective uncertainty on compliance

with 40 CFR 191.13. Second, the estimation of very high quantiles is generally not required in an analysis to assess the effects of subjective uncertainty. Typically, a 0.90 or 0.95 quantile is adequate to establish where the available information indicates a particular analysis outcome is likely to be located; in particular, a 0.99, 0.999 or 0.9999 quantile is usually not needed in assessing the effects of subjective uncertainty.

Desirable features of Latin hypercube sampling include unbiased estimates for means and distribution functions and dense stratification across the range of each sampled variable (McKay et al. 1979). In particular, uncertainty and sensitivity analysis results obtained with Latin hypercube sampling have been observed to be quite robust even when relatively small samples (i.e., $nLHS = 50$ to 200) are used (Iman and Helton 1988, 1991; Helton et al. 1995b).

For perspective, Latin hypercube and random sampling are illustrated in Fig. 6.1.4 for two different distribution pairs. To facilitate comparisons, the grid that underlies the LHSs is also shown for the random samples, although it plays no role in the actual generation of these samples. The desirability of Latin hypercube sampling derives from the full coverage of the range of the sampled variables; specifically, each equal probability interval for U and also each equal probability interval for V has exactly one value sampled from it. In contrast, the random sampling makes less efficient use of the sampled points, with the possibility existing that significant parts of a variable's range will be omitted (e.g., only one value below the 0.5 quantile for U and in the lower left frame and no values for U below the 0.19 quantile nor above the 0.85 quantile in the lower right frame) and that other parts will be overemphasized (e.g., 5 out of 10 values for U fall between the 0.5 and 0.7 quantiles for U in the lower left frame, and two pairs of sampled points fall close together in the lower right frame). The enforced stratification in Latin hypercube sampling prevents such inefficient samplings while still providing unbiased estimates for means and distribution functions.

The outcome of the enforced stratification associated with Latin hypercube sampling is that estimates of means and distribution functions tend to be more stable when generated by Latin hypercube sampling than by random sampling. Here, stability refers to the amount of variation between results obtained with different samples generated by the particular sampling technique under consideration. This stability can be illustrated by comparison of estimates of the CDF for the simple function

$$f(U, V) = U + V + UV \tag{6.1.8}$$

obtained with Latin hypercube and random sampling under the assumption that U and V are uniformly distributed on [0, 2]. In particular, each sampling technique is used to generate 100 samples of size 10 and also 100 samples of size 100 from U and V. Each sample gives rise to an estimated CDF for f (Fig. 6.1.5). The goal is to compare the variability between the estimates obtained with Latin hypercube and random sampling. Presenting plots similar to those in Fig. 6.1.5 for 100 CDFs at a time is not very informative because the CDFs tend to turn into a solid black

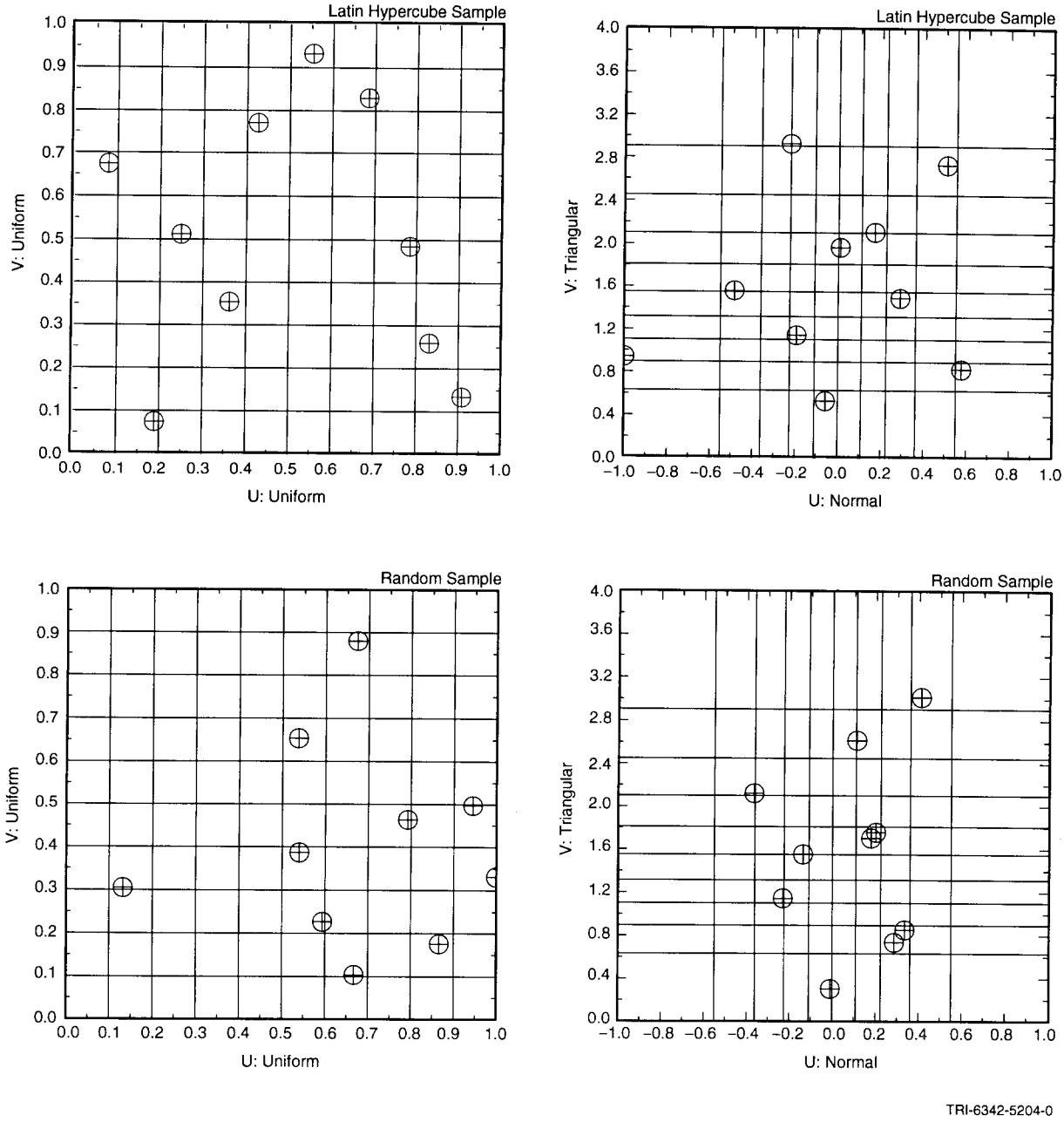

Fig. 6.1.4. Examples of Latin hypercube and random sampling to generate a sample of size 10 from variables U and V with (1) U and V uniform on [−1, 1], and (2) U normal on [−1, 1] (mean = 0, 0.01 quantile = −1, 0.99 quantile = 1) and V triangular on [0, 4] (mode = 1).

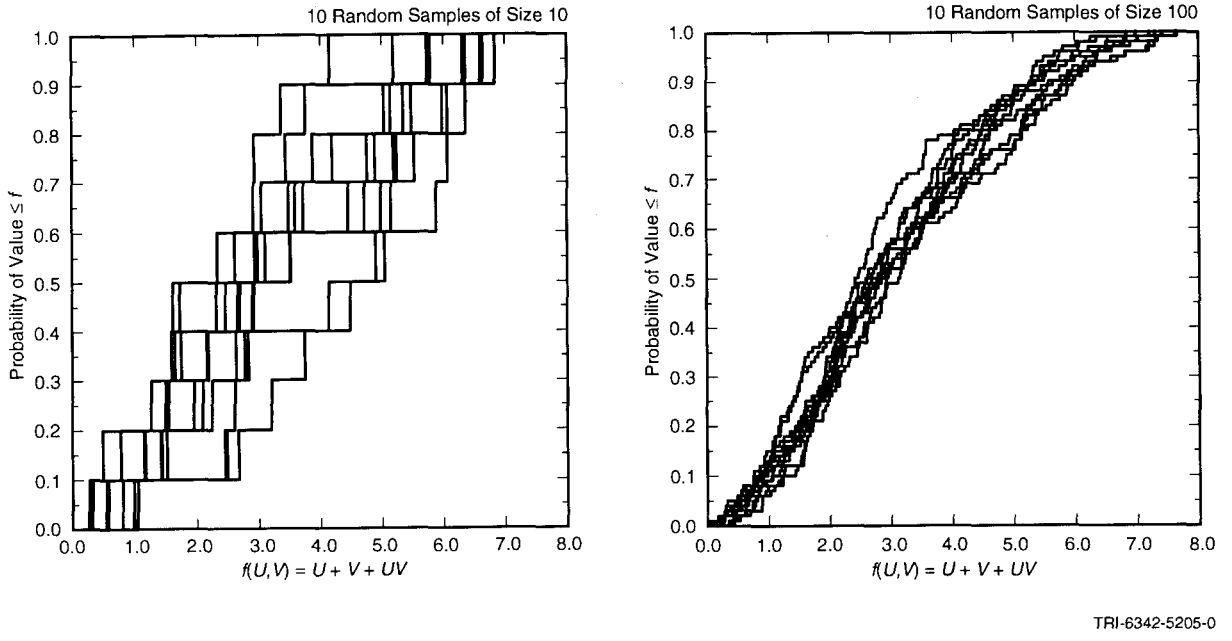

Fig. 6.1.5. Example CDFs for $f(U, V) = U + V + UV$ estimated with random samples of size 10 and 100 under the assumption that U and V are uniformly distributed on [0, 2].

mass. A more informative presentation is to summarize the distributions of CDFs with mean and percentile curves in a manner similar to that already discussed in Sect. 2.4. The location of the percentile curves then provides an indication of how stable the estimates of the CDFs are. In particular, limited separation between low and high percentiles (e.g., the 10th and 90th) indicates that the sampling procedure is providing stable estimates of the CDF (i.e., there is little variability in the estimated CDF from one sample to the next); in contrast, a large spread between low and high percentiles indicates that the sampling procedure is not providing stable estimates of the CDF (i.e., there is substantial variability in the estimated CDF from one sample to the next). The previously indicated 100 samples of size 10 and 100 are summarized in this manner in Fig. 6.1.6. Further, the analysis was replicated three times to give three estimates of the 10th percentile, three estimates of the 50th percentile, and so on.

As examination of Fig. 6.1.6 shows, Latin hypercube sampling is producing CDF estimates that are more stable than those produced by random sampling (i.e., the spread between the 10th and 90th percentile curves is tighter for Latin hypercube sampling than for random sampling). The stability of the mean and percentile estimates across the three replicates indicates that the observed stability is real rather than a chance occurrence associated with a particular set of 100 Latin hypercube or random samples.

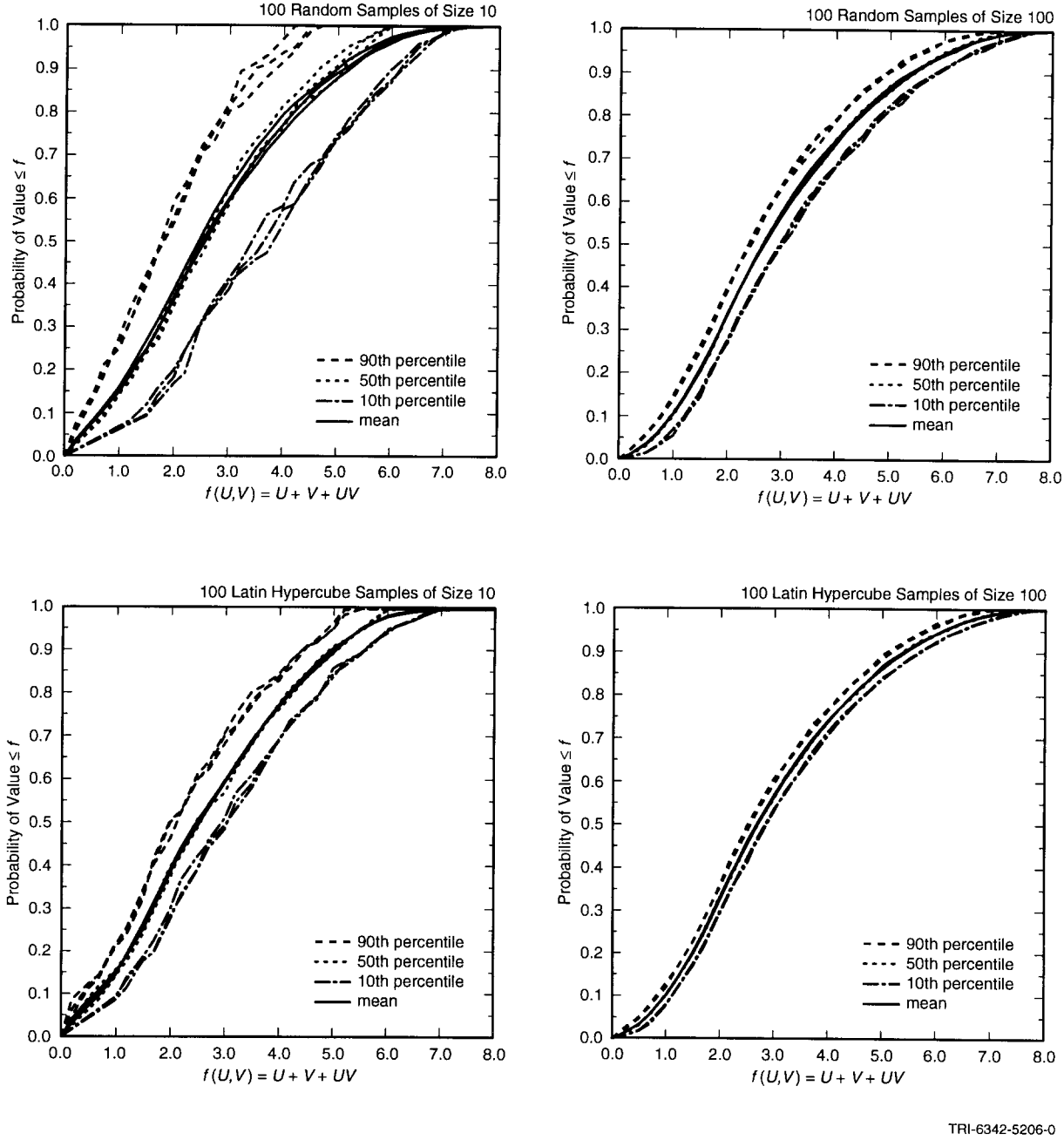

Fig. 6.1.6. Summary of distribution of CDFs for $f(U, V) = U + V + UV$ estimated with 3 replications of 100 Latin hypercube samples and 100 random samples of size 10 and 100 under the assumption that U and V are uniformly distributed on [0, 2].

From the perspective of uncertainty and sensitivity analysis, the full stratification over the range of each sampled variable is a particularly desirable property of Latin hypercube sampling. In a large analysis such as the 1996 WIPP PA, there are potentially 100's of predicted variables that will be examined at some point in the uncertainty and sensitivity analysis. Further, it is likely that almost every sampled variable will be important with respect to at least one of these predicted variables. With Latin hypercube sampling, every variable gets equal treatment (i.e., full stratification) within the sample; should a variable be important with respect to a particular output variable, it has been sampled in a way that will permit this importance to be identified. In contrast, it is very difficult to design an importance sampling procedure that provides acceptable results for a large number of sampled and predicted variables. In some sense, Latin hypercube sampling can be viewed as a compromise importance sampling procedure when *a priori* knowledge of the relationships between the sampled and predicted variables is not available. When random sampling is used with a small sample size in an analysis that involves a large number of sampled and predicted variables, the possibility exists that the chance structure of the sample will result in a poor representation of the relationships between some of the sampled and predicted variables. Such poor relationships can also occur for Latin hypercube sampling when several sampled variables affect a given predicted variable, but are less likely to do so than is the case with random sampling.

For reasons just outlined, the 1996 WIPP PA uses Latin hypercube sampling to determine the effects of subjective uncertainty (i.e., to integrate over $(S_{su}, \mathcal{S}_{su}, p_{su})$). In particular, Latin hypercube sampling is felt to be the most appropriate procedure to use to meet the requirement in 40 CFR 194.34(b) that "Computational techniques, which draw random samples from across the entire range of the probability distributions developed pursuant to paragraph (b) of this section, shall be used in generating CCDFs and shall be documented in any compliance application."

6.2 Correlation Control (Adapted from Sect. 3.2 of Helton 1993c)

Control of correlation within a sample can be very important. If two or more variables are correlated, then it is necessary that the appropriate correlation structure be incorporated into the sample if meaningful results are to be obtained in subsequent uncertainty/sensitivity studies. On the other hand, it is equally important that variables do not appear to be correlated when they are really independent.

It is often difficult to induce a desired correlation structure on a sample. Indeed, most multivariate distributions are incompatible with the majority of correlation patterns that might be proposed for them. Thus, it is fairly common to encounter analysis situations where the proposed variable distributions and the suggested correlations between the variables are inconsistent; that is, it is not possible to have both the desired variable distributions and the requested correlations between the variables.

In response to this situation, Iman and Conover (1982) have proposed a method of controlling the correlation structure in random and Latin hypercube samples that is based on rank correlation (i.e., on rank-transformed variables) rather than sample correlation (i.e., on the original untransformed data). With their technique, it is possible to induce any desired rank-correlation structure onto the sample. This technique has a number of desirable properties: (1) It is distribution free. That is, it may be used with equal facility on all types of distribution functions. (2) It is simple. No unusual mathematical techniques are required to implement the method. (3) It can be applied to any sampling scheme for which correlated input variables can logically be considered, while preserving the intent of the sampling scheme. That is, the same numbers originally selected as input values are retained; only their pairing is affected to achieve the desired rank correlations. This means that in Latin hypercube sampling the integrity of the intervals is maintained. If some other structure is used for selection of values, that same structure is retained. (4) The marginal distributions remain intact.

For many, if not most, uncertainty/sensitivity analysis problems, rank-correlation is probably a more natural measure of congruent variable behavior than is the more traditional sample correlation. What is known in most situations is some idea of the extent to which variables tend to move up or down together; more detailed assessments of variable linkage are usually not available. It is precisely this level of knowledge that rank correlation captures.

The following discussion provides an overview of the Iman/Conover procedure for inducing a desired rank correlation structure on either a random or a Latin hypercube sample. A more detailed discussion of the procedure is given in the original article. The procedure begins with a sample of size m from the n input variables under consideration. This sample can be represented by the $m \times n$ matrix

$$\mathbf{X} = \begin{bmatrix} x_{11} & x_{12} & \cdots & x_{1n} \\ x_{21} & x_{22} & \cdots & x_{2n} \\ \vdots & \vdots & & \vdots \\ x_{m1} & x_{m2} & \cdots & x_{mn} \end{bmatrix} \tag{6.2.1}$$

where x_{ij} is the value for variable j in sample element i. Thus, the rows of $\mathbf{X}$ correspond to sample elements, and the columns of $\mathbf{X}$ contain the sampled values for individual variables.

The procedure is based on rearranging the values in the individual columns of $\mathbf{X}$ so that a desired rank correlation structure results between the individual variables. For convenience, let the desired correlation structure be represented by the $n \times n$ matrix

$$\mathbf{C} = \begin{bmatrix} c_{11} & c_{12} & \cdots & c_{1n} \\ c_{21} & c_{22} & \cdots & c_{2n} \\ \vdots & \vdots & & \vdots \\ c_{n1} & c_{n2} & \cdots & c_{nn} \end{bmatrix} \tag{6.2.2}$$

where c_{kl} is the desired rank correlation between variables x_k and x_l.

Although the procedure is based on rearranging the values in the individual columns of **X** to obtain a new matrix **X*** that has a rank correlation structure close to that described by **C**, it is not possible to work directly with **X**. Rather, it is necessary to define a new matrix

$$\mathbf{S} = \begin{bmatrix} s_{11} & s_{12} & \cdots & s_{1n} \\ s_{21} & s_{22} & \cdots & s_{2n} \\ \vdots & \vdots & & \vdots \\ s_{m1} & s_{m2} & \cdots & s_{mn} \end{bmatrix} \tag{6.2.3}$$

that has the same dimensions as **X**, but is otherwise independent of **X**. Each column of **S** contains a random permutation of the m van der Waerden scores (Conover 1980) $\Phi^{-1}(i/m + 1)$, $i = 1, 2, \ldots, m$, where Φ^{-1} is the inverse of the standard normal distribution. The matrix **S** is then rearranged to obtain the correlation structure defined by **C**. This rearrangement is based on the Cholesky factorization (Golub and van Loan 1983) of **C**. That is, a lower triangular matrix P is constructed such that

$$\mathbf{C} = \mathbf{P}\mathbf{P}^T. \tag{6.2.4}$$

This construction is possible because **C** is a symmetric, positive-definite matrix (Golub and van Loan 1983, p. 88).

If the correlation matrix associated with **S** is the $n \times n$ identity matrix (i.e., if the correlations between the values in different columns of **S** are zero), then the correlation matrix for

$$\mathbf{S}^* = \mathbf{S}\mathbf{P}^T \tag{6.2.5}$$

is **C** (Anderson 1984, p. 25). At this point, the success of the procedure depends on the following two conditions: (1) that the correlation matrix associated with **S** be close to the $n \times n$ identity matrix; and (2) that the correlation matrix for **S*** be approximately equal to the rank correlation matrix for **S***. If these two conditions hold, then the desired matrix **X*** can be obtained by simply rearranging the values in the individual columns of **X** in the same rank order as the values in the individual columns of **S***. This is the first time that the variable values contained in **X** enter into the correlation process. When **X*** is constructed in this manner, it will have the same rank correlation matrix as **S***. Thus, the rank correlation matrix for **X*** will approximate **C** to the same extent that the rank correlation matrix for **S*** does.

The condition that the correlation matrix associated with **S** be close to the identity matrix is now considered. For convenience, the correlation matrix for **S** will be represented by **E**. Unfortunately, **E** will not always be the identity matrix. However, it is possible to make a correction for this. The starting point for this correction is the Cholesky factorization for **E**:

$$\mathbf{E} = \mathbf{Q}\mathbf{Q}^T. \tag{6.2.6}$$

This factorization exists because **E** is a symmetric, positive-definite matrix. The matrix **S*** defined by

$$\mathbf{S}^* = \mathbf{S}(\mathbf{Q}^{-1})^T\mathbf{P}^T \tag{6.2.7}$$

has **C** as its correlation matrix. In essence, multiplication of **S** by $(\mathbf{Q}^{-1})^T$ transforms **S** into a matrix whose associated correlation matrix is the $n \times n$ identity matrix; then, multiplication by $\mathbf{P}^T$ produces a matrix whose associated correlation matrix is **C**. As it is not possible to be sure that **E** will be an identity matrix, the matrix **S*** used in the procedure to produce correlated input should be defined in the corrected form shown in Eq. (6.2.7) rather than in the uncorrected form shown in Eq. (6.2.5).

The condition that the correlation matrix for **S*** be approximately equal to the rank correlation matrix for **S*** depends on the choice of the scores used in the definition of **S**. On the basis of empirical investigations, Iman and Conover (1982) found that van der Waerden scores provided an effective means of defining **S**, and these scores are incorporated into the rank correlation procedure in the widely used LHS program (Iman and Shortencarier 1984). Other possibilities for defining these scores exist, but have not been extensively investigated. The user should examine the rank correlation matrix associated with **S*** to ensure that it is close to the target correlation matrix **C**. If this is not the case, the construction procedure used to obtain **S*** can be repeated until a suitable approximation to **C** is obtained. Results given in Iman and Conover (1982) indicate that the use of van der Waerden scores leads to rank correlation matrices for **S*** that are close to the target matrix **C**.

Additional information on the Iman/Conover (i.e., restricted pairing) technique to induce a desired rank-correlation structure is given in the original article. The results of various rank-correlation assumptions are illustrated in Iman and Davenport (1982). The LHS program generates both random and Latin hypercube samples with user-specified rank correlations between variables.

6.3 Sample Size for Incorporation of Subjective Uncertainty

The guidance in 40 CFR 194.34(d) states that "The number of CCDFs generated shall be large enough such that, at cumulative releases of 1 and 10, the maximum CCDF generated exceeds the 99th percentile of the population of CCDFs with at least a 0.95 probability." For a Latin hypercube or random sample of size n, the preceding guidance is equivalent to the inequality

$$1 - 0.99^n > 0.95, \tag{6.3.1}$$

which results in a minimum value of 298 for n. In consistency with the preceding result, the 1996 WIPP PA uses an LHS of size 300 to integrate over the probability space $(\mathcal{S}_{su}, \mathcal{S}_{su}, p_{su})$ for subjective uncertainty. Actually, as

discussed in the next section, three replicated LHSs of size 100 each are used, which results in a total sample size of 300.

6.4 Statistical Confidence on Mean CCDF

The guidance in 40 CFR 194.34(f) states that "Any compliance assessment shall provide information which demonstrates that there is at least a 95 percent level of statistical confidence that the mean of the population of CCDFs meets the containment requirements of § 191.13 of this chapter." Given that Latin hypercube sampling is to be used, the confidence intervals required in 194.34(f) can be obtained with a replicated sampling technique proposed by Iman (1982). In this technique, the LHS in Eq. (6.1.7) is repeatedly generated with different random seeds. These samples lead to a sequence $\overline{P}_r(R), r = 1, 2, \ldots, nR$, of estimated mean exceedance probabilities, where $\overline{P}_r(R)$ defines the mean CCDF obtained for sample r (i.e., $\overline{P}_r(R)$ is the mean probability that a normalized release of size R will be exceeded; see Sect. 2.4) and nR is the number of independent LHSs generated with different random seeds. Then,

$$\overline{P}(R) = \sum_{r=1}^{nR} \overline{P}_r(R) / nR \tag{6.4.1}$$

and

$$SE(R) = \left\{ \sum_{r=1}^{nR} \left[\overline{P}_r(R) - \overline{P}(R) \right]^2 / nR(nR-1) \right\}^{1/2} \tag{6.4.2}$$

provide an additional estimate of the mean CCDF and an estimate of the standard error associated with the mean exceedance probabilities. The t-distribution with $nR-1$ degrees of freedom can be used to place confidence intervals around the mean exceedance probabilities for individual R values (i.e., around $\overline{P}(R)$). Specifically, the $1-\alpha$ confidence interval is given by $\overline{P}(R) \pm t_{1-\alpha/2}\, SE(R)$, where $t_{1-\alpha/2}$ is the $1-\alpha/2$ quantile of the t-distribution with $nR-1$ degrees of freedom (e.g., $t_{1-\alpha/2} = 4.303$ for $\alpha = 0.05$ and $nR = 3$). The same procedure can also be used to place pointwise confidence intervals around percentile curves.

6.5 Generation of LHSs

The LHS program (Iman and Shortencarier 1984) was used to produce three independently generated LHSs of size $nLHS = 100$ each, for a total of 300 sample elements. Each individual replicate is an LHS of the form

$$\mathbf{x}_{su,k} = [x_{k1}, x_{k2}, \ldots, x_{k,nV}],\ k = 1, 2, \ldots, nLHS = 100. \tag{6.5.1}$$

In the context of the replicated sampling procedure described in Sect. 6.4, $nR = 3$ replicates are being used, with each replicate of size 100. For notational convenience, the replicates are designated by R1, R2 and R3 for replicates 1, 2 and 3, respectively.

At the beginning of the analysis, only the 31 variables in Table 5.2.1 that are used as input to BRAGFLO had been fully specified (i.e., their distributions D_j had been unambiguously defined); the remaining variables now listed in Table 5.2.1 were still under development. To allow the calculations with BRAGFLO to proceed, the previously indicated LHSs were generated from $nV = 75$ variables, with the first 31 variables being the then specified inputs to BRAGFLO and the remaining 44 variables being assigned uniform distributions on [0, 1]. Later, when the additional variables in Table 5.2.1 were fully specified, the uniformly distributed variables were used to generate sampled values from them consistent with their assigned distributions. This procedure allowed the analysis to go forward while maintaining the integrity of the Latin hypercube sampling procedure for the overall analysis.

With $nV = 75$ in the LHSs and 31 variables already assigned, 44 additional variables were available for incorporation into the analysis. To assure that the number of available positions in the LHSs was not exceeded, each group of investigators developing characterizations of variable uncertainty was assigned a maximum number of variables that they could elect to have incorporated into the analysis, with the sum of these maximums being less than 44. Ultimately, 26 additional variables were selected for incorporation into the analysis, which produced the 57 variables in Table 5.2.1.

The restricted pairing technique described in Sect. 6.2 was used to induce requested correlations and also to assure that uncorrelated variables had correlations close to zero. Due to the sequential manner in which the variables were developed, it was actually only the first 31 variables used as input to BRAGFLO that could have specified non-zero correlations. The correlations for the remaining variables were controlled in the sense that they were forced to be close to zero.

The variable pairs (*ANHCOMP*, *ANHPRM*), (*HALCOMP*, *HALPRM*) and (*BPCOMP*, *BPPRM*) were assigned rank correlations of –0.99, –0.99 and –0.75, respectively (Sect. 5.4). Further, all other variable pairs were assigned rank correlations of zero. The restricted pairing technique was quite successful in producing these correlations (Table 6.5.1). Specifically, the correlated variables have correlations that are close to their specified values and uncorrelated variables have correlations that are close to zero.

Table 6.5.1 Example Correlations in Replicate 1

WGRCOR	1.0000							
WMICDFLG	0.0198	1.0000						
HALCOMP	0.0011	0.0235	1.0000					
HALPRM	–0.0068	–0.0212	–0.9879	1.0000				
ANHCOMP	0.0080	0.0336	–0.0123	–0.0025	1.0000			
ANHPRM	0.0049	–0.0183	0.0037	0.0113	–0.9827	1.0000		
BPCOMP	0.0242	0.1071	–0.0121	0.0057	–0.0184	0.0078	1.0000	
BPPRM	–0.0514	–0.0342	0.0035	0.0097	0.0283	–0.0202	–0.7401	1.0000
	WGRCOR	*WMICDFLG*	*HALCOMP*	*HALPRM*	*ANHCOMP*	*ANHPRM*	*BPCOMP*	*BPPRM*

6.6 Generation of Individual Futures

Random sampling (Sect. 6.1) is used to generate elements $\mathbf{x}_{st}$ of S_{st} for use in CCDF construction. The drilling rate λ_d is used to generate the times at which drilling intrusions occur. For a Poisson process with a constant λ_d (i.e., a stationary process), the cumulative distribution function (CDF) for the time Δt between the successive events is given by (Ross 1987, p. 113)

$$prob(t \le \Delta t) = 1 - \exp(-\lambda_d \Delta t). \tag{6.6.1}$$

A uniformly distributed random number is selected from [0, 1]. Then, solution of

$$r_1 = 1 - \exp(-\lambda_d t_1) \tag{6.6.2}$$

for t_1 gives the time of the first drilling intrusion (Fig. 6.6.1). If 100 yr of administrative control is assumed, then 100 yr would be added to the t_1 obtained in Eq. (6.6.2) to obtain the time of the first drilling intrusion. Selection of a second random number r_2 and solution of

$$r_2 = 1 - \exp(-\lambda_d \Delta t_1) \tag{6.6.3}$$

for Δt_1 gives the time interval between the first and second drilling intrusions, with the outcome that $t_2 = t_1 + \Delta t_1$. This process can be continued until a time t_{n+1} is generated that exceeds 10,000 yr. The times t_1, t_2, ..., t_n then constitute the drilling times in $\mathbf{x}_{st}$ in Eq. (2.2.2). A detailed description of the algorithm for generating individual drilling intrusion times is given in Table 6.6.1. The mining time t_{min} is sampled in a similar manner. Additional uniformly distributed random numbers from [0, 1] are used to generate the elements l_i, e_i, b_i, p_i, $\mathbf{a}_i$, $i = 1, 2, \ldots, n$, of $\mathbf{x}_{st}$ from their assigned distributions (see Chapt. 3). A detailed description of the algorithm for generating individual futures is given in Table 6.6.2.

The 1996 WIPP PA assumed that drilling intrusions within the berm used as part of the passive marker system (Fig. 3.2.1) and potash mining within the land withdrawal boundary (Fig. 4.8.3) are the only events involved in the definition of $\mathbf{x}_{st}$ in Eq. (2.2.2) and hence in the definition of the sample space $\mathcal{S}_{st}$ for stochastic uncertainty. The inclusion of additional potential occurrences in the definition of $(\mathcal{S}_{st}, \mathcal{J}_{st}, p_{st})$ presents no conceptual problem. Such occurrences could be incorporated into the definition of $\mathbf{x}_{st}$ and their associated probabilities used in the sampling process described in the preceding paragraph. For example, if deemed sufficiently important to the calculation of normalized releases, climatic change could be incorporated into the definition of $\mathbf{x}_{st}$ and hence $(\mathcal{S}_{st}, \mathcal{J}_{st}, p_{st})$.

The algorithm in Table 6.6.2 describes how random sampling was used to generate a single future $\mathbf{x}_{st}$ in the 1996 WIPP PA. For each LHS element $\mathbf{x}_{su,k}$, $k = 1, 2, \ldots, 300$, used in the analysis, $nS = 10{,}000$ individual futures

$$\mathbf{x}_{st,i} = [t_{i1}, l_{i1}, e_{i1}, b_{i1}, p_{i1}, \mathbf{a}_{i1}, t_{i2}, l_{i2}, e_{i2}, b_{i2}, p_{i2}, \mathbf{a}_{i2}, \ldots, t_{in}, l_{in}, e_{in}, b_{in}, p_{in}, \mathbf{a}_{in}, t_{i,min}], \; i = 1, 2, \ldots, nS = 10{,}000, \tag{6.6.4}$$

were randomly sampled and used in the construction of all CCDFs for that LHS element. A different random seed was used to initiate the sampling of $\mathbf{x}_{st}$ for each LHS element, with the result that each LHS element uses different values for $\mathbf{x}_{st}$ in CCDF construction. As 300 LHS elements are used in the analysis and 10,000 futures are sampled for each LHS element, the total number of futures $\mathbf{x}_{st}$ used in the analysis in CCDF construction is 3×10^6.

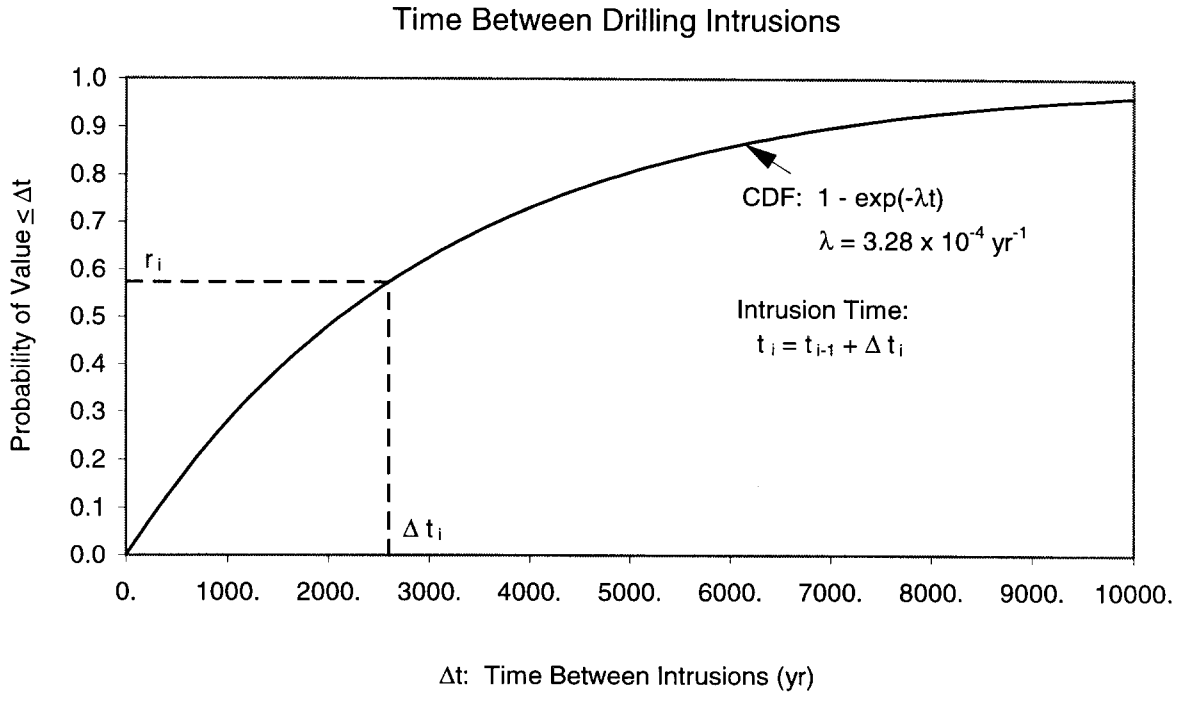

Fig. 6.6.1. Sampling of time intervals between drilling intrusions from cumulative distribution function (CDF) associated with drilling rate $\lambda = \lambda_d$ (Note: $\lambda = 3.28 \times 10^{-4}$ yr^{-1} is drilling rate used in the 1991 and 1992 WIPP PAs).

Table 6.6.1. Algorithm to Sample Time of a Drilling Intrusion with

$$\lambda(t) = \begin{cases} \mu = fPICD\,\lambda & \text{for } tA \le t \le tA + tPICD \\ \lambda & \text{for } tA + tPICD < t \end{cases}$$

where *tA* = 100 Yr is the Time at which Administrative Control Ends, *fPICD* = 0.01 is the Fractional Reduction in the Drilling Rate due to Passive Institutional Controls, and *tPICD* = 600 Yr is the Time over which Passive Institutional Controls are Effective in Deterring Drilling Intrusions.

---

1. Sample random number r from uniform distribution on [0, 1]. Then,

   $r = 1 - \exp(-\mu \Delta t_1) \Rightarrow \Delta t_1 = [-\ln(1-r)]/\mu.$

   Two cases, with $t_0 = tA$ to facilitate description of the algorithm:

   1.1 If $t_0 + \Delta t_1 \le tA + tPICD$, then $t_1 = t_0 + \Delta t_1$.

   1.2 If $t_0 + \Delta t_1 > tA + tPICD$, then sample *new* random number r and determine *new* Δt_1:

   $r = 1 - \exp(-\lambda \Delta t_1) \Rightarrow \Delta t_1 = [-\ln(1-r)]/\lambda.$

   Then, $t_1 = tA + tPICD + \Delta t_1$.

2. Repeat process to obtain t_2. Two cases:

   2.1 If $t_1 < tA + tPICD$, then identical to Step 1 except that t_0 is replaced by t_1 and the random number sampled at the start of the step produces an increment of time Δt_2. The two cases are then based on the inequalities

   $t_1 + \Delta t_2 \le tA + tPICD$ and $t_1 + \Delta t_2 > tA + tPICD$.

   2.2 If $t_1 > tA + tPICD$, then identical to Step 1.2 except that $tA + tPICD$ is replaced by t_1 in the definition of t_2 (i.e., $t_2 = t_1 + \Delta t_2$.

3. Repeat Step 2 to obtain $t_3, t_4, \ldots, t_{n+1}$, where t_{n+1} is the first time to exceed *tM* (=10,000 yr). Then, $t_1, t_2, \ldots, t_n$ are the desired times.

Table 6.6.2. Algorithm to Generate (i.e., Sample) Single Future $\mathbf{x}_{st}$ from $\mathcal{S}_{st}$

1. Sample t_1 (see Table 6.6.1) with a time dependent λ_d given by

$$\lambda_d(t) = 0 \qquad \text{if } 0 \le t \le tA$$

$$= fPICD\,\lambda_d \qquad \text{if } tA < t \le tA + tPICD$$

$$= \lambda_d \qquad \text{if } t > tA + tPICD$$

where tA = 100 yr (i.e., time at which administrative control ends), $tPICD$ = 600 yr (i.e., time over which passive institutional controls are effective), $fPICD$ = 0.01 (i.e., fractional reduction in drilling rate due to passive institutional controls) and $\lambda_d = 2.94 \times 10^{-3}$ yr^{-1} (see Sect. 3.2).

2. Sample l_1 with a probability of $pL_j = 6.94 \times 10^{-3}$ for each of the j = 1, 2, ..., 144 nodes in Fig. 3.2.1 (see Sect. 3.3).

3. Sample e_1 with a probability of $pE_0 = 0.791$ that the intrusion will be in an unexcavated area and a probability of $pE_1 = 0.209$ that the intrusion will be in an excavated area (see Sect. 3.4).

4. Sample b_1 with a probability of $pB_0 = 0.92$ that the intrusion will not penetrate pressurized brine and a probability of $pB_1 = 0.08$ that the intrusion will penetrate pressurized brine (see Sect. 3.5).

5. Sample p_1 with probabilities of $pPL_1 = 0.02$, $pPL_2 = 0.68$ and $pPL_3 = 0.30$ that plugging pattern 1, 2 or 3, respectively, will be used (see Sect. 3.6).

6. Sample $\mathbf{a}_1$ (see Sect. 3.7)

   6.1 Penetration of nonexcavated area (i.e., $e_1 = 0$): $\mathbf{a}_1 = a_1 = 0$.

   6.2 Penetration of excavated area (i.e., $e_1 = 1$): Sample to determine if intrusion penetrates RH or CH waste with probabilities of $pRH = 0.124$ and $pCH = 0.876$ of penetrating RH and CH waste, respectively.

   6.3 Penetration of RH waste: $\mathbf{a}_1 = a_1 = 1$.

   6.4 Penetration of CH waste: Use probabilities pCH_j of intersecting waste stream j, j = 1, 2, ..., 569, (see Table 3.7.1) to independently sample three intersected waste streams iCH_{11}, iCH_{12}, iCH_{13} (i.e., each of iCH_{11}, iCH_{12}, iCH_{13} is an integer between 1 and 569). Then, $\mathbf{a}_1 = [2, iCH_{11}, iCH_{12}, iCH_{13}]$.

7. Repeat steps 1 - 6 to determine properties (i.e., t_2, l_2, e_2, b_2, p_2, $\mathbf{a}_2$) of 2nd drilling intrusion.

8. Continue until $t_{n+1} > 10{,}000$ yr; the 1st n intrusions define the drilling intrusions associated with $\mathbf{x}_{st}$.

9. Sample t_{min} (see Table 6.6.1) with a time dependent λ_m given by

$$\lambda_m(t) = 0 \qquad \text{if } 0 \le t \le tA$$

$$= fPICM\,\lambda_m \qquad \text{if } tA < t \le tA + tPICM$$

$$= \lambda_m \qquad \text{if } tA + tPICM < t$$

where tA = 100 yr, $tPICM$ = 600 yr, $fPICM = 0.01$, $\lambda_m = 1 \times 10^{-4}$ yr^{-1} (see Sect. 3.8) and $tPICM$ and $fPICM$ are defined the same as $tPICD$ and $fPICD$ except for applying to mining rather than drilling.

6.7 Construction of CCDFs

The 1996 WIPP PA uses the sampled futures $\mathbf{x}_{st,i}$ in Eq. (6.6.4) to construct CCDFs for many different quantities (e.g., cuttings and cavings releases, spallings releases, direct brine releases, ...). The construction process is the same for each quantity. For notational convenience, assume that the particular quantity under consideration can be represented by a function $f(\mathbf{x}_{st,i})$, with the result that 10,000 values

$$f(\mathbf{x}_{st,i}),\ i = 1, 2, \ldots, 10{,}000 \tag{6.7.1}$$

are available for use in CCDF construction. Formally, the resultant CCDF is defined by the expression in Eq. (2.3.1). In practice, the indicator function δ_R is not directly used and the desired CCDF is obtained after an appropriate ordering of the $f(\mathbf{x}_{st,i})$ (i.e., from smallest to largest or largest to smallest) as described below.

In concept, the easiest way to construct the desired CCDF is to order the $f(\mathbf{x}_{st,i})$ from smallest to largest and then directly construct the CCDF with a weight of 10^{-4} assigned to each $f(\mathbf{x}_{st,i})$ (Fig. 6.7.1). However, this approach is cumbersome because it requires the $f(\mathbf{x}_{st,i})$ to be sorted from smallest to largest and also results in 10,000 plot points for each CCDF. As an aside, the included and excluded points appear in Fig. 6.7.1 because a CCDF gives the probability of exceeding a value. In practice, CCDFs are usually plotted with the distinction between included and excluded points omitted and vertical lines added at the discontinuities associated with these points (Fig. 6.7.2).

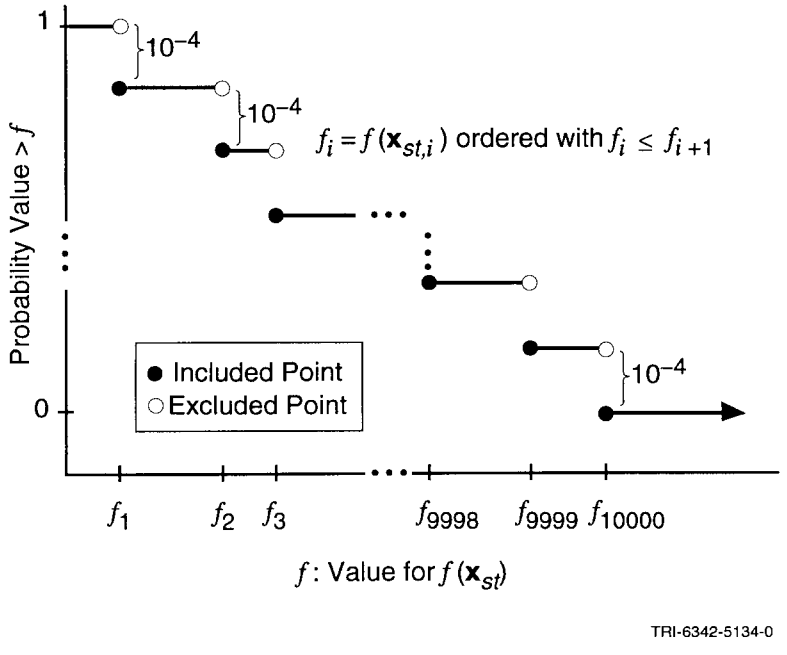

Fig. 6.7.1. Example CCDF construction from 10,000 values for $f(\mathbf{x}_{st,i})$.

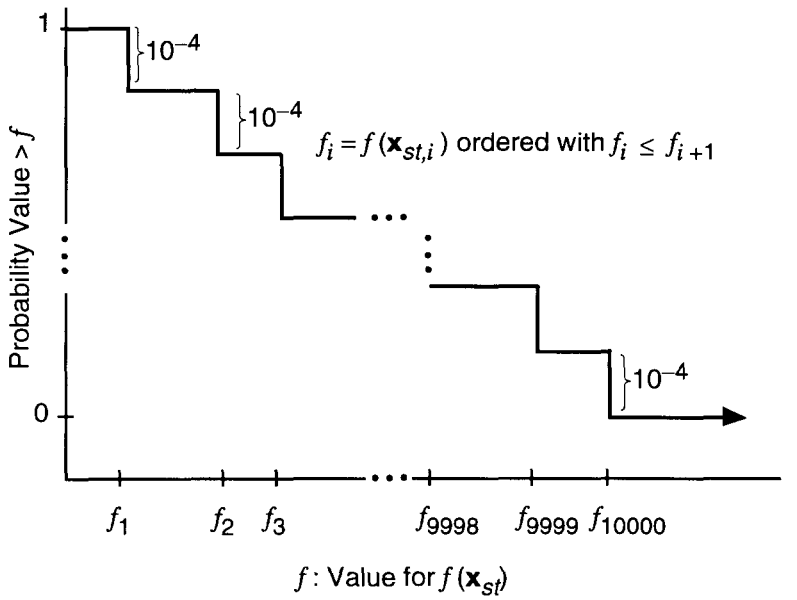

Fig. 6.7.2. Example CCDF construction from 10,000 values for $f(\mathbf{x}_{st,i})$ with vertical lines added at discontinuities (i.e., between the locations of included and excluded points in Fig. 6.7.1).

The 1996 WIPP PA uses a binning procedure in CCDF construction to simplify sorting the individual $f(\mathbf{x}_{st,i})$ and to reduce the number of plot points. Specifically, the range of f is divided into intervals (i.e., bins) by the specified points

$$f_{min} = b_0 < b_1 < b_2 < \ldots < b_n = f_{max}, \tag{6.7.2}$$

where f_{min} is the minimum value of f to be plotted (typically 10^{-6} or 10^{-5} when an EPA normalized release is under consideration), f_{max} is the maximum value of f to be plotted (typically 100 when an EPA normalized release is under consideration), n is the number of bins in use, and the b_i are typically loguniformly placed with 20 values per order of magnitude. A counter nB_j is used for each interval $[b_{j-1}, b_j]$. All counters are initially set to zero. Then, as individual values $f(\mathbf{x}_{st,i})$ are generated, the counter nB_j is incremented by 1 when the inequality

$$b_{j-1} < f(\mathbf{x}_{st,i}) \leq b_j \tag{6.7.3}$$

is satisfied. As an aside, the indicated procedure is dynamic in the 1996 WIPP PA in the sense that, if necessary, f_{max} will be increased in value so that the inequality $f(\mathbf{x}_{st,i}) < f_{max}$ will always be satisfied. Once the 10,000 values for $f(\mathbf{x}_{st,i})$ have been generated, a value of nB_j will exist for each interval $[b_{j-1}, b_j]$. The nB_j satisfy the inequality

$$\sum_{j=1}^{n} nB_j \leq 10{,}000 \tag{6.7.4}$$

because some of the $f(\mathbf{x}_{st,i})$ may satisfy the inequality $f(\mathbf{x}_{st,i}) < f_{min}$.

The quotient

$$pB_j = nB_j / 10{,}000 \tag{6.7.5}$$

provides an approximation to the probability that $f(\mathbf{x}_{st})$ will have a value that falls in the interval $[b_{j-1}, b_j]$. The resultant CCDF is then defined by the points

$$(b_j, prob(value > b_j)) = (b_j, \sum_{k=j+1}^{n} pB_k) \tag{6.7.6}$$

for $j = 0, 1, 2, \ldots, n-1$, where $prob(value > b_j)$ is the probability that a value greater than b_j will occur (Fig. 6.7.3).

The omitted points in the CCDF in Fig. 6.7.3 produce plots that are hard to read. This is especially true when multiple CCDFs appear in a single plot frame. One possibility is to add vertical lines at the discontinuities as indicated in Fig. 6.7.3. However, this can also produce plots that are hard to read when multiple CCDFs appear in a single plot frame due to the running together of the horizontal components of individual CCDFs at the discretized probability levels (e.g., at integer multiples of 10^{-4}), which makes it difficult to follow a single CCDF in the plot; this behavior can be seen in the CDFs in Fig. 6.1.5. Further, in most situations a stairstep CCDF should converge to a continuous CCDF as additional points (i.e., elements $\mathbf{x}_{st}$ of $\mathcal{S}_{st}$) are used in its construction. For the preceding reasons, the 1996 WIPP PA "smooths" its CCDFs by drawing diagonal lines from included point to included point (i.e., from the left end of one bin to the left end of the next bin; see Fig. 6.7.4).

When multiple CCDFs appear in a single plot, the bottom of the plot can become very congested as the individual CCDFs drop to zero on the abscissa. For this reason, the CCDFs for comparison with the EPA release limits contained in this presentation stop at the largest observed consequence value (e.g., a point in the interval $[b_{n-3}, b_{n-2}]$ in Fig. 6.7.4 as illustrated in Fig. 6.7.5). Stopping at the largest consequence value rather than the left bin boundary of the bin that contains this value (e.g., b_{n-3} in Fig. 6.7.4) permits the CCDF to explicitly show the largest observed consequence. However, given that 20 bins per order of magnitude are in use, this convention has no significant effect on the appearance of the resultant CCDFs.

Due to the use of a sample size of 10,000 in the generation of CCDFs for comparison with the EPA release limits, the last nonzero exceedance probability in the resultant CCDFs is typically 10^{-4} (Fig. 6.7.6). Specifically, the

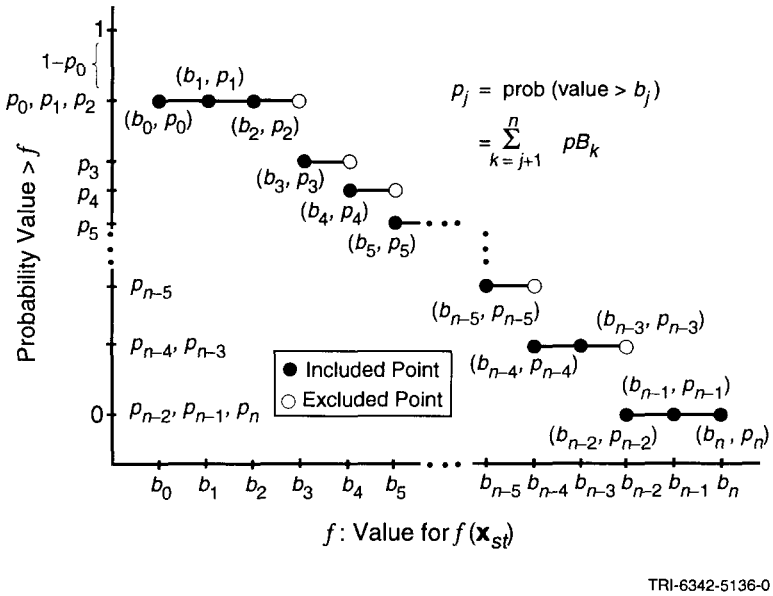

Fig. 6.7.3. Example CCDF construction based on subdivision of range of $f(\mathbf{x}_{st,i})$ into bins.

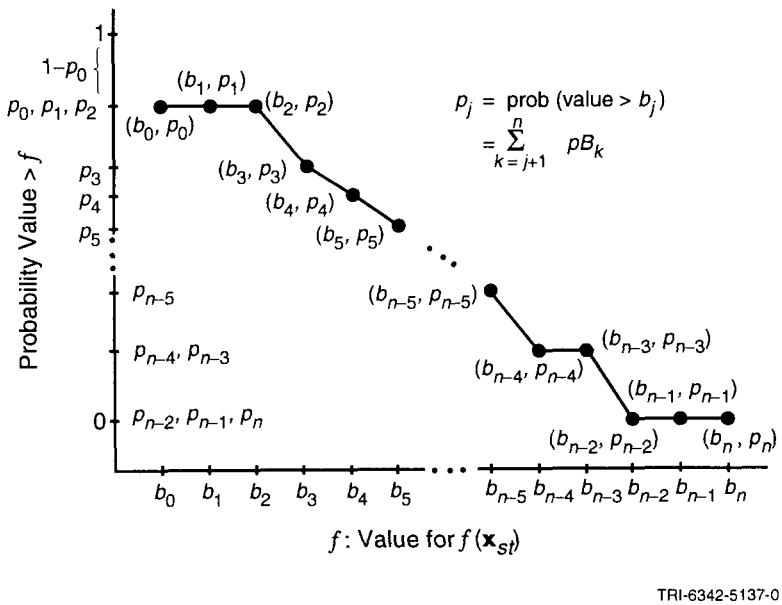

Fig. 6.7.4. Example CCDF construction based on subdivision of range of $f(\mathbf{x}_{st,i})$ into bins and connection of included points.

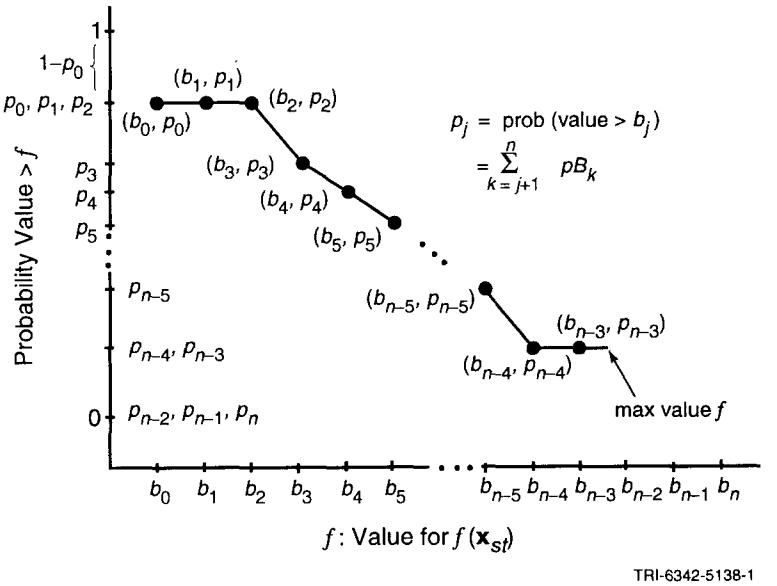

Fig. 6.7.5. Example CCDF construction based on subdivision of range of $f(\mathbf{x}_{st,i})$ into bins, connection of included points, and termination of CCDF at largest observed consequence value (i.e., maximum value for $f(\mathbf{x}_{st})$).

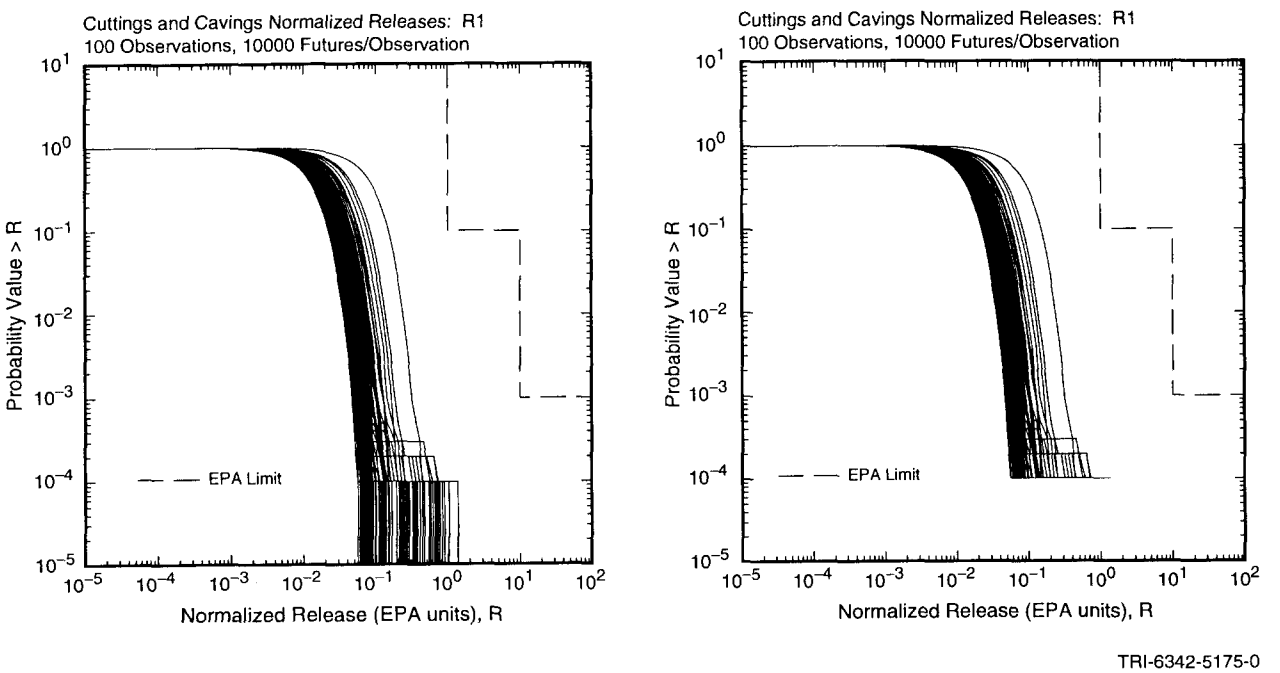

Fig. 6.7.6. Comparison of plots of multiple CCDFs with individual CCDFs continued to largest observed consequence value and then extended to the abscissa (left frame) and individual CCDFs terminated at largest observed consequence value (right frame).

left frame of Fig. 6.7.6 shows what the CCDFs would look like if the plots dropped to zero from the largest observed value, and the right frame in Fig. 6.7.6 shows what the same CCDFs would look like with the convention of stopping at the largest observed consequence value. The only difference in the CCDFs in the left and right frames of Fig. 6.7.6 are the vertical lines between exceedance probabilities of 10^{-4} and 10^{-5}, where 10^{-5} is being used as a surrogate for an exceedance probability of zero. As already indicated, the plotting convention in the right frame of Fig. 6.7.6 will be used in this presentation. The horizontal lines near the bottom of the CCDFs in Fig. 6.7.6 result when the largest observed consequence value is preceded by several unpopulated bins. Further, the appearance of these horizontal lines is accentuated by the discretized probability values (i.e., integer multiples of 10^{-4}), which results in horizontal sections of different CCDFs running together; this same pattern can be seen in Fig. 6.1.5.

In the 1996 WIPP PA, the sampling of individual futures (Sect. 6.6) and associated CCDF construction is carried out by the CCDFGF program (Smith et al. 1996, Johnson 1997).

6.8 Kaplan/Garrick Ordered Triple Representation for Risk

The 1991 and 1992 WIPP PAs (WIPP PA 1991-1992, 1992-1993) used the Kaplan and Garrick (1981) ordered triple representation for risk as a basis for CCDF construction (Helton and Iuzzolino 1993). In this representation, risk is characterized by a set $\mathfrak{R}$ of the form

$$\mathfrak{R} = \{(\mathcal{S}_j, pS_j, \mathbf{cS}_j), j = 1, 2, \ldots, nS\}, \tag{6.8.1}$$

where $\mathcal{S}_j$ is a subset of the sample space $\mathcal{S}_{st}$ for stochastic uncertainty (i.e., an element of $\mathcal{J}_{st}$), the $\mathcal{S}_j$ have no futures in common (i.e., $\mathcal{S}_j \cap \mathcal{S}_k = \emptyset$ if $j \neq k$), the $\mathcal{S}_j$ are all inclusive in the sense that $\mathcal{S}_{st} = \cup_j \mathcal{S}_j$, pS_j is the probability of $\mathcal{S}_j$ (i.e., $pS_j = p_{st}(\mathcal{S}_j)$), $\mathbf{cS}_j$ is a vector of consequence values associated with $\mathcal{S}_j$ (e.g., one of the many elements cS_j of $\mathbf{cS}_j$ would be the EPA normalized release specified in 40 CFR 191.13(a)), and nS is the number of sets (i.e., scenarios) into which $\mathcal{S}_{st}$ is decomposed. The construction of a CCDF for a particular consequence contained in **cS** proceeds in exactly the same manner as described in Figs. 6.7.1 - 6.7.4 except that each consequence value cS_j has a probability of pS_j rather than a fixed probability as is the case when random sampling is used to select the futures for which consequence results will be calculated (e.g., a probability of 10^{-4} when a sample of size 10,000 is used). As an aside, it is technically incorrect to refer to probabilities for elements of random samples. These numbers (i.e., probabilities) are actually weights that are used in estimating distributions and related quantities; the individual sample elements typically have probabilities of zero.

The 1991 and 1992 WIPP PAs used an importance sampling procedure to subdivide $\mathcal{S}_{st}$ into the sets $\mathcal{S}_j$, to determine the probabilities pS_j, and to calculate the consequences in $\mathbf{cS}_j$ (Helton 1993b, Helton and Iuzzolino 1993). By the 1996 WIPP PA, the elements $\mathbf{x}_{st}$ of $\mathcal{S}_{st}$ had become too complex to be amendable to the use of an importance sampling procedure (see Sect. 3.9). Therefore, the PA switched to a Monte Carlo procedure (i.e., simple random

sampling) for integration over $\mathcal{S}_{st}$ to produce the CCDF specified in 40 CFR 191.13(a). However, it is still possible to express the results in the Kaplan/Garrick representation in Eq. (6.8.1) by appropriately defining the sets $\mathcal{S}_j$ in terms of the bin boundaries b_j, $j = 0, 1, 2, \ldots, n$, in Eq. (6.7.2). Specifically, the sets $\mathcal{S}_0$, $\mathcal{S}_1$, $\mathcal{S}_2$, ..., $\mathcal{S}_n$ are defined by

$$\mathcal{S}_0 = \{\mathbf{x}_{st}: f(\mathbf{x}_{st}) \le b_0\} \tag{6.8.2}$$

and

$$\mathcal{S}_j = \{\mathbf{x}_{st}: b_{j-1} < f(\mathbf{x}_{st}) \le b_j\}, j = 1, 2, \ldots, n, \tag{6.8.3}$$

where $f(\mathbf{x}_{st})$ is the normalized release associated with $\mathbf{x}_{st}$. The sets $\mathcal{S}_0$, $\mathcal{S}_1$, $\mathcal{S}_2$, ..., $\mathcal{S}_n$ in Eqs. (6.8.2) and (6.8.3) correspond to the sets $\mathcal{S}_j$, $j = 1, 2, \ldots, nS$, in Eq. (6.8.1). Further, approximations to the probabilities of these sets are given by

$$pS_j = p_{st}(\mathcal{S}_j) \doteq pB_j, j = 1, 2, \ldots, n, \tag{6.8.4}$$

and

$$pS_0 = p_{st}(\mathcal{S}_0) \doteq 1 - \sum_{j=1}^{n} pB_j, \tag{6.8.5}$$

where pB_j is defined in Eq. (6.7.5). Finally, the sets $\mathcal{S}_j$ are assigned the consequence

$$cS_0 = 0 \text{ and } cS_j = b_{j-1}, j = 1, 2, \ldots, n. \tag{6.8.6}$$

The preceding assignments for $\mathcal{S}_j$, pS_j and cS_j in the definition of the set $\mathfrak{R}$ in Eq. (6.8.1) results in the same CCDF as the construction procedure used in the 1996 WIPP PA and described in conjunction with Figs. 6.7.4 and 6.7.5.

Although the procedure for CCDF construction used in the 1996 WIPP PA and the procedure used in the 1991 and 1992 WIPP PAs can both be formally represented in terms of the Kaplan/Garrick representation for risk, there is an underlying difference in approach. The 1991 and 1992 PAs defined the sets $\mathcal{S}_j$ entirely on the basis of properties of $\mathbf{x}_{st}$. This approach has already been referred to as a form of importance sampling because of the division of $\mathcal{S}_{st}$ into sets and the assignment of probabilities to these sets. However, it can also be viewed as an integration problem in the spirit of the Riemann integral in the sense that it is based on laying a systematic grid on the space that is being integrated over (i.e., $\mathcal{S}_{st}$). The 1996 WIPP PA defined the sets $\mathcal{S}_j$ on the basis of the values assumed by $f(\mathbf{x}_{st})$, which results in the possibility that a given set $\mathcal{S}_j$ will contain elements $\mathbf{x}_{st}$ from very different regions of $\mathcal{S}_{st}$. This can also be viewed as an integration problem, but it is now an integration problem in the spirit of the Lebesgue integral, as sets based on the range of f rather than simply on a partitioning of $\mathcal{S}_{st}$ are under consideration (App. B, Sokolnikoff

and Redheffer 1966). In consistency with the concept of Lebesgue integration, the determination of pS_j can be viewed as the estimation of a probability measure (i.e., a probabilistic size) for $\mathcal{S}_j$. However, when appropriately implemented, both approaches lead to approximations of the same CCDF.

The individual randomly sampled futures can also be used in the following expression with the same structure as the Kaplan/Garrick ordered triple representation for risk:

$$\mathcal{R} = \{(\mathbf{x}_{st,i},\ 1/nS,\ \mathbf{f}(\mathbf{x}_{st,i})),\ i = 1, 2, \ldots, nS\}, \tag{6.8.7}$$

where nS = 10,000 in the 1996 WIPP PA and $\mathbf{f}(\mathbf{x}_{st,i})$ is a vector of consequence values associated with $\mathbf{x}_{st,i}$. Although the preceding representation leads to approximations of the same CCDFs as the representation in Eq. (6.8.1), the individual terms are different. Specifically, the $\mathcal{S}_j$ in Eq. (6.8.1) are disjoint sets such that $\mathcal{S}_{st} = \cup_j \mathcal{S}_j$; in contrast, the $\mathbf{x}_{st,i}$ in Eq. (6.8.7) are elements randomly sampled from $\mathcal{S}_{st}$ with $\mathcal{S}_{st} \neq \cup_i \{\mathbf{x}_{st,i}\}$. The pS_j in Eq. (6.8.1) are the probabilities of the sets $\mathcal{S}_j$; in contrast, $1/nS$ in Eq. (6.8.7) is a weight used in estimating CCDFs but is not equal to the probability of $\mathbf{x}_{st,i}$. The $\mathbf{cS}_j$ in Eq. (6.8.1) are representative of the consequences associated with $\mathcal{S}_j$ and, as such, might be calculated for a single representative element $\mathbf{x}_{st,j}$ of $\mathcal{S}_j$ or, more appropriately but very unlikely in practice, might be the expected consequences associated with $\mathcal{S}_j$; in contrast, $\mathbf{f}(\mathbf{x}_{st,i})$ in Eq. (6.8.7) is calculated specifically for $\mathbf{x}_{st,i}$.

6.9 Mechanistic Calculations

The computational strategy used in the 1996 WIPP PA was to perform calculations with the models described in Chapt. 4 for selected elements of $\mathcal{S}_{st}$ and then to use the results of these calculations to determine the releases to the accessible environment for the large number (i.e., 10,000) of randomly sampled futures used in the estimation of individual CCDFs. The same set of mechanistic calculations was performed for each LHS element (Table 6.9.1). The manner in which these calculations were used to construct releases for the randomly sampled elements $\mathbf{x}_{st,i}$ of $\mathcal{S}_{st}$ is described in Sect. 9.2 (cuttings and cavings), Sect. 9.4 (spallings), Sect. 10.3 (direct brine release), Sect. 11.2 (release to Culebra), Sect. 12.2 (transport in Culebra), and Sect. 13.1 (total release to accessible environment).

Four categories of calculations are indicated in Table 6.9.1 as being performed with BRAGFLO (i.e., E0, E1, E2, E2E1). In turn, the calculations associated with these categories can be viewed as being performed for specific elements $\mathbf{x}_{st}$ of $\mathcal{S}_{st}$. In particular, the E0 calculation is performed for

$\mathbf{x}_{st,0}$ = element of $\mathcal{S}_{st}$ that corresponds to no drilling intrusions and no mining (Note: $\mathbf{x}_{st,0}$ as defined here is different from $\mathbf{x}_{st,0}$ in Eq. (4.1.1)). (6.9.1)

Table 6.9.1. Mechanistic Calculations Performed to Support CCDF Construction in the 1996 WIPP PA.

BRAGFLO: 1800 Calculations
E0 (i.e., undisturbed conditions)
E1 at 350, 1000 yr (i.e., drilling intrusion through repository that penetrates pressurized brine in the Castile Fm)
E2 at 350, 1000 yr (i.e., drilling intrusion through repository that does not penetrate pressurized brine in the Castile Fm)
E2E1 with E2 intrusion at 800 yr and E1 intrusion at 2000 yr
Total calculations = 6 *nR nLHS* = 6 • 3 • 100 = 1800
Note: All intrusions are represented by region 1 in Fig. 4.2.1.
CUTTINGS_S: 15600 Calculations
Intrusion into lower waste panel in previously unintruded (i.e., E0 conditions) repository at 100, 350, 1000, 3000, 5000, 10,000 yr
Intrusion into upper waste panel in previously unintruded repository at 100, 350, 1000, 3000, 5000, 10,000 yr
Initial E1 intrusion at 350 yr followed by a second intrusion into the same waste panel at 550, 750, 2000, 4000 or 10,000 yr
Initial E1 intrusion at 350 yr followed by a second intrusion into a different waste panel at 550, 750, 2000, 4000 or 10,000 yr
Initial E1 intrusion at 1000 yr followed by a second intrusion into the same waste panel at 1200, 1400, 3000, 5000 or 10,000 yr
Initial E1 intrusion at 1000 yr followed by a second intrusion into a different waste panel at 1200, 1400, 3000, 5000 or 10,000 yr
Initial E2 intrusion at 350 yr followed by a second intrusion into the same waste panel at 550, 750, 2000, 4000 or 10,000 yr
Initial E2 intrusion at 350 yr followed by a second intrusion into a different waste panel at 550, 750, 2000, 4000 or 10,000 yr
Initial E2 intrusion at 1000 yr followed by a second intrusion into the same waste panel at 1200, 1400, 3000, 5000 or 10,000 yr
Initial E2 intrusion at 1000 yr followed by a second intrusion into a different waste panel at 1200, 1400, 3000, 5000 or 10,000 yr
Total calculations = 52 *nR nLHS* = 52 • 3 • 100 = 15600
Note: The calculations for two intrusions into the same waste panel assume that the intrusions are into the lower waste panel (i.e., region 23 in Fig. 4.2.1); the calculations for two intrusions into different waste panels assume that the first intrusion is into the lower waste panel (i.e., region 23 in Fig. 4.2.1) and that the second intrusion is into an upper waste panel (i.e., region 24 in Fig. 4.2.1).
BRAGFLO_DBR: 15600 Calculations
Same computational cases as for CUTTINGS_S

Table 6.9.1. Mechanistic Calculations Performed to Support CCDF Construction in the 1996 WIPP PA (continued).

NUTS: 594 Calculations
E0
E1 at 100, 350, 1000, 3000, 5000, 7000, 9000 yr
E2 at 100, 350, 1000, 3000, 5000, 7000, 9000 yr
Screening calculations = 5 *nR nLHS* = 1500
NUTS calculations = 594
Note: An initial screening calculation was initially performed for each computational case (i.e., E0, E1 at 350 and 1000 yr, E2 at 350 and 1000 yr, which produces the multiplier of 5 in the calculation of the number of screening calculations) to determine if the potential for a radionuclide release existed, with a full NUTS calculation only being performed when such a potential existed. For the three replicates 9, 62, 67, 18 and 18 sample elements were screened in for full NUTS calculations for the cases E0, E1 at 350 yr, E1 at 1000 yr, E2 at 350 yr and E2 at 1000 yr, respectively. In turn, this led to 9 + 62(2) + 67(5) + 18(2) + 18(5) = 594 full NUTS calculations, where the multipliers of 2 and 5 appear due to the use of intrusion results at 350 yr for NUTS calculations for intrusions at 100 and 350 yr (i.e., a multiplier of 2) and the use of intrusion results at 1000 yr for NUTS calculations for intrusions at 1000, 3000, 5000, 7000 and 9000 yr (i.e., a multiplier of 5).
PANEL: 2100 Calculations
E2E1 at 100, 350, 1000, 2000, 4000, 6000, 9000 yr
Total calculations: 7 *nR nLHS* = 7 • 3 • 100 = 2100
Note: Additional PANEL calculations were also performed at 100, 125, 175, 350, 1000, 3000, 5000, 7500 and 10,000 yr for Salado-dominated brines and also for Castile-dominated brines to determine dissolved radionuclide concentrations for use in the determination of direct brine releases.
SECOFL2D: 600 Calculations
Partially mined conditions in vicinity of repository
Fully mined conditions in vicinity of repository
Total calculations = 2 *nR nLHS* = 2• 3 • 100 = 600
Note: Only 100 unique transmissivity fields were constructed with GRASP_INV for use in the analysis.
SECOTP2D: 600 Calculations
Partially mined conditions in vicinity of repository
Fully mined conditions in vicinity of repository
Total calculations = 2 *nR nLHS* = 2 • 3 • 100 = 600
Note: Each calculation is for four radionuclides: Am-241, Pu-239, Th-230, U-234. Further, calculations are done for unit releases at time 0 yr, which can then be used to construct transport results for the Culebra for arbitrary time-dependent release rates into the Culebra (Sect. 12.2).

Similarly, the E1 calculations are performed for

$$\mathbf{x}_{st,1} = [t_1 = 350 \text{ yr}, l_1, e_1 = 1, b_1 = 1, p_1 = 2, \mathbf{a}_1] \tag{6.9.2}$$

$$\mathbf{x}_{st,2} = [t_1 = 1000 \text{ yr}, l_1, e_1 = 1, b_1 = 1, p_1 = 2, \mathbf{a}_1], \tag{6.9.3}$$

where t_1 = 350, 1000 yr indicates the time of the drilling intrusion (Sect. 3.2), e_1 = 1 indicates that an excavated area of the repository is penetrated by the drilling intrusion (Sect. 3.4), b_1 = 1 indicates that pressurized brine is penetrated by the drilling intrusion (Sect. 3.5), p_1 = 2 indicates that plugging pattern 2 is used (Sect. 3.6), the absence of specific values for drilling location l_1 (Sect. 3.3) and activity level $\mathbf{a}_1$ (Sect. 3.7) indicates that exact values for these characteristics are not specified, and the absence of a value for mining time t_m (Sect. 3.8) indicates that mining does not take place.

Although drilling location l_1 is not specified in Eqs. (6.9.2) and (6.9.3), some specification is required for the BRAGFLO calculations. If equivalent grids were used in the definition of $\mathbf{x}_{st}$ (Fig. 3.2.1) and in the numerical solution of the partial differential equations on which BRAGFLO is based (Fig. 4.2.1), the location of the drilling intrusion used in the BRAGFLO calculations could be specified as a specific value for l_1, which in turn would correspond to one of the 144 locations in Fig. 3.2.1 that are designated by l in the definition of $\mathbf{x}_{st}$. However, as these grids are not the same, a unique pairing between a value for l_1 and the location of the drilling intrusion used in the computational grid employed with BRAGFLO is not possible. The BRAGFLO computational grid divides the repository into a single lower (i.e., down dip) waste panel and a composite of the 9 upper (i.e., up dip) waste panels, with the drilling intrusion taking place through the center of the lower panel (Fig. 4.2.1). Thus, in the context of the locations in Fig. 3.2.1 potentially indexed by l_1, the drilling intrusion takes place at a location in Panel 4, 5 or 10 (i.e., at a location in one of the three most down dip waste panels).

The E2 calculations with BRAGFLO are performed for

$$\mathbf{x}_{st,3} = [t_1 = 350 \text{ yr}, l_1, e_1 = 1, b_1 = 0, p_1 = 2, \mathbf{a}_1] \tag{6.9.4}$$

$$\mathbf{x}_{st,4} = [t_1 = 1000 \text{ yr}, l_1, e_1 = 1, b_1 = 0, p_1 = 2, \mathbf{a}_1], \tag{6.9.5}$$

with $\mathbf{x}_{st,3}$ and $\mathbf{x}_{st,4}$ the same as $\mathbf{x}_{st,1}$ and $\mathbf{x}_{st,2}$ in Eqs. (6.9.2) and (6.9.3) except for the absence of a penetration of pressurized brine (i.e., b_1 = 0 rather than b_1 = 1). As in the BRAGFLO calculations for $\mathbf{x}_{st,1}$ and $\mathbf{x}_{st,2}$, the computational implementation of the analysis assumes that the drilling intrusion takes place through the center of the lower waste panel in Fig. 4.2.1.

The E2E1 calculations with BRAGFLO are performed for

$$\mathbf{x}_{st,5} = [t_1 = 800 \text{ yr}, l_1, e_1 = 1, b_1 = 0, p_1 = 2, \mathbf{a}_1, t_2 = 2000 \text{ yr}, l_2, e_2 = 1, b_2 = 1, p_2 = 2, \mathbf{a}_2]. \quad (6.9.6)$$

As for the E1 and E2 intrusions, the locations l_1 and l_2 of the drilling intrusions are assumed to correspond to the center of the lower waste panel in Fig. 4.2.1, with the effects of the two drilling intrusions and their associated plugging patterns being implemented through assumptions involving the time-dependent behavior of borehole permeability (Sect. 8.10).

Ten categories of calculations are indicated in Table 6.9.1 as being performed with CUTTINGS_S: (1) intrusion into lower waste panel in previously unintruded (i.e., E0 conditions) repository at 100, 350, 1000, 3000, 5000, 10,000 yr; (2) intrusion into upper waste panel in previously unintruded repository at 100, 350, 1000, 3000, 5000, 10,000 yr; (3) initial E1 intrusion at 350 yr followed by a second intrusion into the same waste panel at 550, 750, 2000, 4000 or 10,000 yr; (4) initial E1 intrusion at 350 yr followed by a second intrusion into a different waste panel at 550, 750, 2000, 4000 or 10,000 yr; (5) initial E1 intrusion at 1000 yr followed by a second intrusion into the same waste panel at 1200, 1400, 3000, 5000 or 10,000 yr; (6) initial E1 intrusion at 1000 yr followed by a second intrusion into a different waste panel at 1200, 1400, 3000, 5000 or 10,000 yr; (7) initial E2 intrusion at 350 yr followed by a second intrusion into the same waste panel at 550, 750, 2000, 4000 or 10,000 yr; (8) initial E2 intrusion at 350 yr followed by a second intrusion into a different waste panel at 550, 750, 2000, 4000 or 10,000 yr; (9) initial E2 intrusion at 1000 yr followed by a second intrusion into the same waste panel at 1200, 1400, 3000, 5000 or 10,000 yr; (10) initial E2 intrusion at 1000 yr followed by a second intrusion into a different waste panel at 1200, 1400, 3000, 5000 or 10,000 yr. Categories (1) and (2) involve elements $\mathbf{x}_{st}$ of $\mathcal{S}_{st}$ of the form

$$\mathbf{x}_{st,6} = [t_1, l_1, e_1 = 1, b_1, p_1, \mathbf{a}_1], \quad (6.9.7)$$

where t_1 = 100, 350, 1000, 3000, 5000 or 10,000 yr, l_1 corresponds to an intrusion into the lower waste panel (i.e., Panel 4, 5 or 10 in Fig. 3.2.1 and region 23 in Fig. 4.2.1) for Category (1) and into the upper waste panels (i.e., Panel 1, 2, 3, 6, 7, 8 or 9 in Fig. 3.2.1 and region 24 in Fig. 4.2.1) for Category (2), e_i = 1 indicates that the intrusion takes place into an excavated area of the repository, b_1 and p_1 are unspecified because these characteristics do not affect results calculated by CUTTINGS_S for use in the 1996 WIPP PA, and $\mathbf{a}_1$ corresponds to the penetration of CH-TRU waste (i.e., $\mathbf{a}_1$ = [2, CH_{11}, CH_{12}, CH_{13}], although only the property that CH-TRU waste is penetrated is used in the calculation with CUTTINGS_S). The characteristics specified by b_1 and p_1 (i.e., penetration of pressurized brine and plugging pattern) are not relevant to the determination of cuttings and spallings releases because these releases take place at the time that the drilling intrusion penetrates the repository. The penetration of CH-TRU waste is important because this determines the material properties used in the cavings and spallings calculations; the penetration of RH-TRU waste is assumed to result in no cavings and spallings releases. The actual locations at which the intrusions are assumed occur correspond to the points in Fig. 4.7.1 designated "Down-dip well, first or second intrusion" for Category (1) intrusions and "Up-dip well, first or second intrusion" for Category (2) intrusions. As

described in conjunction with Fig. 4.7.2, pressures for use at the indicated points in Fig. 4.7.1 are obtained from calculations performed with BRAGFLO on the computational grid in Fig. 4.2.1.

Categories (3) - (6) for the calculations performed with CUTTINGS_S involve elements $\mathbf{x}_{st}$ of $\mathcal{S}_{st}$ of the form

$$\mathbf{x}_{st,7} = [t_1, l_1, e_1 = 1, b_1 = 1, p_1 = 2, \mathbf{a}_1, t_2, l_2, e_2 = 1, b_2, p_2, \mathbf{a}_2], \tag{6.9.8}$$

where t_1 = 350 yr for Categories (3) and (4), t_1 = 1000 yr for Categories (5) and (6), t_2 = 550, 750, 2000, 4000 and 10,000 yr for Categories (3) and (4), t_2 = 1200, 1400, 3000, 5000 and 10,000 yr for Categories (5) and (6), l_1 and l_2 correspond to intrusions into the same waste panel (Fig. 3.2.1) for Categories (3) and (5), l_1 and l_2 correspond to intrusions into different waste panels for Categories (4) and (6), $e_1 = e_2 = 1$ indicates that both intrusions take place into excavated areas of the repository, $b_1 = 1$ indicates that the first intrusion penetrates pressurized brine, $p_1 = 2$ indicates that plugging pattern 2 is used with the first intrusion, $\mathbf{a}_1$ and $\mathbf{a}_2$ correspond to the penetration of CH-TRU waste (i.e., $\mathbf{a}_i$ = [2, CH_{i1}, CH_{i2}, CH_{i3}], i = 1,2, although only the property that CH-TRU waste is penetrated is used in the calculation with CUTTINGS_S), and p_2 is unspecified. In the computational implementation of the analysis, intrusions into different waste panels are implemented by assuming that the first and second intrusions occur at the locations in Fig. 4.7.1 designated "Down-dip well, first or second intrusion" and "Up-dip well, first or second intrusion," respectively, and intrusions into the same waste panel are implemented by assuming that both intrusions occur at the location in Fig. 4.7.1 designated "Down-dip well, first or second intrusion." Thus, intrusions into different waste panels are implemented computationally as an initial intrusion into a lower (i.e., down dip) waste panel followed by a second intrusion into an upper (i.e., up dip) waste panel, and intrusions into the same waste panel are implemented computationally as two intrusions into the same lower (i.e., down dip) waste panel.

Categories (7) - (10) for the calculations performed with CUTTINGS_S involve elements $\mathbf{x}_{st}$ of $\mathcal{S}_{st}$ of the form

$$\mathbf{x}_{st,8} = [t_1, l_1, e_1 = 1, b_1 = 0, p_1 = 2, \mathbf{a}_1, t_2, l_2, e_2 = 1, b_2, p_2, \mathbf{a}_2]. \tag{6.9.9}$$

The vectors $\mathbf{x}_{st,8}$ associated with Categories (7) - (10) are the same as the vectors $\mathbf{x}_{st,7}$ associated with Categories (4) - (6) except for the use of $b_1 = 0$ instead of $b_1 = 1$, which implies that the first intrusion associated with $\mathbf{x}_{st,7}$ penetrates pressurized brine while the first intrusion associated with $\mathbf{x}_{st,8}$ does not penetrate pressurized brine.

As described in Sects. 9.2 and 9.4, the results obtained with CUTTINGS_S for the elements of $\mathcal{S}_{st}$ indicated in Eqs. (6.9.7) - (6.9.9) are then used in conjunction with algebraic procedures to construct releases due to cuttings and cavings and also due to spallings for arbitrary elements $\mathbf{x}_{st}$ of $\mathcal{S}_{st}$ sampled in the Monte Carlo construction of CCDFs for comparison with the boundary line specified in 40 CFR 191.13.

Calculations are performed for BRAGFLO_DBR for the same ten categories as for CUTTINGS_S (Table 6.9.1). Thus, the elements of $\mathcal{S}_{st}$ in Eqs. (6.9.7) - (6.9.9) also characterize the elements of $\mathcal{S}_{st}$ for which

BRAGFLO_DBR calculations are performed. Further, BRAGFLO_DBR also uses the spallings releases calculated by CUTTINGS_S for these elements of $\mathcal{S}_{st}$ as input (Sect. 4.7.3). As described in Sect. 10.3, the results obtained with BRAGFLO_DBR are then used in conjunction with algebraic procedures to construct direct brine releases for arbitrary elements $\mathbf{x}_{st}$ of $\mathcal{S}_{st}$ sampled in the Monte Carlo construction of CCDFs for comparison with the boundary line specified in 40 CFR 191.13.

Three categories of calculations are indicated in Table 6.9.1 as being performed with NUTS (i.e., E0, E1, E2). The E0 calculation is performed for the vector $\mathbf{x}_{st,0}$ in Eq. (6.9.1). The E1 calculations are performed for vectors of the form appearing in Eqs. (6.9.2) and (6.9.3) with t_1 = 100, 350, 1000, 3000, 5000, 7000 and 9000 yr. Similarly, the E2 calculations are performed for vectors of the form appearing in Eqs. (6.9.4) and (6.9.5) with t_1 = 100, 350, 1000, 3000, 5000, 7000 and 9000 yr. The BRAGFLO flow fields calculated for intrusions at 350 yr are moved back in time to 100 yr to support the NUTS calculations for t_1 = 100 yr; similarly, the BRAGFLO flow fields calculated for intrusions at 1000 yr are moved forward in time to support the NUTS calculations for t_1 = 3000, 5000, 7000 and 9000 yr.

One category of calculations is indicated in Table 6.9.1 as being performed with PANEL (i.e., E2E1). The associated calculations are performed for vectors $\mathbf{x}_{st,5}$ of the form appearing in Eq. (6.9.6). The PANEL calculations are based on the E2E1 BRAGFLO calculation in which t_1 = 800 yr and t_2 = 2000 yr in $\mathbf{x}_{st,5}$. The PANEL calculations are for t_2 = 100, 350, 1000, 2000, 4000, 6000 and 9000 yr in $\mathbf{x}_{st,5}$. The single BRAGFLO calculation for $\mathbf{x}_{st,5}$ as defined in Eq. (6.9.6) supports the PANEL calculations by having the flow fields calculated by BRAGFLO moved forward or backward in time as appropriate to match the value for t_2 in the PANEL calculations. In concept, this can be viewed as having the corresponding values for t_1 in $\mathbf{x}_{st,5}$ for the PANEL calculations assigned values of

$$t_1 = \max\{100\text{ yr}, t_2 - 1200\text{ yr}\}, \tag{6.9.10}$$

where the restriction that t_1 cannot be less than 100 yr results because the definition of $\mathbf{x}_{st}$ does not allow negative intrusion times and the assumption of 100 yr of administrative control (i.e., $\lambda_d(t) = 0\ \text{yr}^{-1}$ for $0 \le t \le 100$ yr; see Eq. (3.2.1)) results in a probability of zero for intrusion times between 0 and 100 yr. Under this convention, what is specified in concept by the definition of $\mathbf{x}_{st,5}$ for the PANEL calculations differs from what is actually done computationally because t_1 does indeed precede t_2 by 1200 yr in the BRAGFLO calculation.

As described in Sect. 11.2, the results obtained with NUTS and PANEL for elements of $\mathcal{S}_{st}$ of the form indicated in Eqs. (6.9.1) - (6.9.6) are then used in conjunction with algebraic procedures to construct time-dependent releases to the Culebra for arbitrary elements $\mathbf{x}_{st}$ of $\mathcal{S}_{st}$ sampled in the Monte Carlo construction of CCDFs for comparison with the boundary line specified in 40 CFR 191.13.

The SECOFL2D calculations are performed for two categories of conditions (Table 6.9.1): partially mined conditions in the vicinity of the repository (Fig. 4.8.1) and fully mined conditions in the vicinity of the repository (Fig. 4.8.2). As a reminder, partially mined conditions are assumed to always exist by the end of the period of administrative control (i.e., at 100 yr) in assessing compliance with 40 CFR 191.13 (Wallace 1996a, U.S. EPA 1996). The SECOFL2D calculations for partially mined conditions are performed for the element $\mathbf{x}_{st,0}$ of $\mathcal{S}_{st}$ defined in Eq. (6.9.1). The SECOFL2D calculations for fully mined conditions are performed for the element $\mathbf{x}_{st,m}$ of $\mathcal{S}_{st}$ given by

$$\mathbf{x}_{st,m} = [t_{min} = 100 \text{ yr}], \tag{6.9.11}$$

which corresponds to the future in which no drilling intrusion occurs and full mining occurs at t_{min} = 100 yr.

The SECOTP2D calculations are performed for the same two categories of conditions as the SECOFL2D calculations (Table 6.9.1). Thus, the SECOTP2D calculations are performed for the elements $\mathbf{x}_{st,0}$ and $\mathbf{x}_{st,m}$ of $\mathcal{S}_{st}$ defined in Eqs. (6.9.1) and (6.9.11), with the flow fields required in these calculations supplied by the calculations with SECOFL2D for $\mathbf{x}_{st,0}$ and $\mathbf{x}_{st,m}$. As described in Sect. 12.2, the results obtained for $\mathbf{x}_{st,0}$ and $\mathbf{x}_{st,m}$ with SECOTP2D are then used in conjunction with algebraic procedures to construct Culebra transport results for arbitrary elements $\mathbf{x}_{st}$ of $\mathcal{S}_{st}$ sampled in the Monte Carlo construction of CCDFs for comparison with the boundary line specified in 40 CFR 191.13.

6.10 Sensitivity Analysis (Adapted from Sect. 3.5 of Helton 1993c)

6.10.1 Mapping from Input to Output

Evaluation of one or more of the models discussed in Chapt. 4 with the LHS in Eq. (6.5.1) (Table 6.9.1) creates a mapping

$$[\mathbf{x}_{su,k}, \mathbf{y}(\mathbf{x}_{su,k})], k = 1, 2, \ldots, nLHS, \tag{6.10.1}$$

from analysis inputs (i.e., $\mathbf{x}_{su,k}$) to analysis results (i.e., $\mathbf{y}(\mathbf{x}_{su,k})$), where $\mathbf{y}(\mathbf{x}_{su,k})$ denotes the results obtained with the model or models under consideration. A vector notation is used for $\mathbf{y}$ because, in general, a large number of predicted results is produced by each of the models used in the 1996 WIPP PA. In addition, $\mathbf{y}(\mathbf{x}_{su,k})$ could also correspond to a CCDF for normalized release constructed from model results associated with $\mathbf{x}_{su,k}$. Sensitivity analysis involves an exploration of the mapping in Eq. (6.10.1) to determine how the uncertainty in individual elements of $\mathbf{x}_{su}$ affects the uncertainty in individual elements of $\mathbf{y}(\mathbf{x}_{su})$.

The numerical implementation of the sensitivity analysis techniques used in this report involves the investigation of the effects of elements of $\mathbf{x}_{su}$ on single elements of $\mathbf{y}(\mathbf{x}_{su})$. For notational convenience in the description of these techniques, the mapping in Eq. (6.10.1) will be represented by

$$[\mathbf{x}_k, y_k],\ k = 1, 2, \ldots, nLHS, \tag{6.10.2}$$

where

$$\mathbf{x}_k = [x_{k1}, x_{k2} \ldots, x_{k,nV}] \tag{6.10.3}$$

and y_k corresponds to one element of $\mathbf{y}(\mathbf{x}_k)$. The vector $\mathbf{x}_k$ corresponds to the vector $\mathbf{x}_{su,k}$ in Eq. (6.10.1) with the subscript *su* dropped to produce a less cumbersome notation.

To make efficient use of all available information, most of the sensitivity analysis results contained in this report are based on a pooling of the results obtained for the three replicated LHSs (i.e., R1, R2, R3) discussed in Sect. 6.5. Thus, the mapping in use is actually of the form

$$[\mathbf{x}_k, y_k],\ k = 1, 2, \ldots, 3 \bullet nLHS, \tag{6.10.4}$$

where $k = 1, 2, \ldots, 100$ corresponds to results from replicate R1, $k = 101, 102, \ldots, 200$ corresponds to results from replicate R2, and $k = 201, 202, \ldots, 300$ corresponds to results from replicate R3. The discussions in this section will refer to the simpler mapping in Eq. (6.10.2) rather than the mapping in Eq. (6.10.4), although the numerical examples will actually be generated with the mapping in Eq. (6.10.4).

6.10.2 Scatterplots

The generation of scatterplots is undoubtedly the simplest sensitivity analysis technique and only involves plotting the points

$$(x_{kj}, y_k),\ k = 1, 2, \ldots, nLHS, \tag{6.10.5}$$

for each element x_j of $\mathbf{x}$ for $j = 1, 2, \ldots, nV$ (see Eq. (6.10.3)). This produces nV scatterplots that can then be examined for relationships between y and the elements of $\mathbf{x}$ (i.e., the x_j). As an example, the scatterplot in Fig. 6.10.1 shows a nonlinear but monotonic relationship between borehole permeability (*BHPRM*) and cumulative brine flow down an intruding borehole, with no brine flow taking place for small values of *BHPRM* and brine flow increasing rapidly for larger values of *BHPRM* (see Sect. 8.2 for additional discussion). As another example, the scatterplot in Fig. 6.10.2 shows a complex relationship between *BHPRM* and repository pressure that is both nonlinear and nonmonotonic, with repository pressure decreasing as *BHPRM* increases and then undergoing a sudden jump at $BHPRM \doteq -11.7$ (i.e., at a permeability of $10^{-11.7}\ m^2 \doteq 2 \times 10^{-12}\ m^2$) (see Sect. 8.4 for additional

discussion). In contrast to the well-defined patterns in Figs. 6.10.1 and 6.10.2, the individual points will be randomly spread over the plot when there is no relationship between y and a particular x_j.

Sometimes scatterplots alone will completely reveal the relationships between model input (i.e., elements of **x**) and model predictions (i.e., y). This is often the case when only one or two inputs dominate the outcome of the analysis. Further, scatterplots often reveal nonlinear relationships, thresholds and variable interactions that facilitate the understanding of model behavior and the planning of more sophisticated sensitivity studies. Iman and Helton (1988) provide an example where the examination of scatterplots revealed a rather complex pattern of variable interactions. The examination of scatterplots is always a good starting point in a sensitivity study. The examination of such plots when Latin hypercube sampling is used can be particularly revealing due to the full stratification over the range of each input variable.

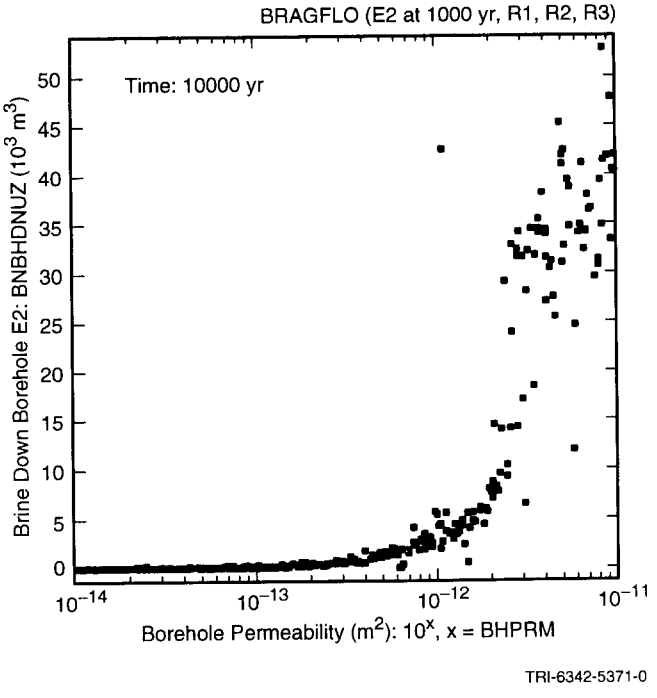

Fig. 6.10.1. Scatterplot for cumulative brine flow through borehole into upper DRZ over 10,000 yr for E2 intrusion at 1000 yr into lower waste panel versus borehole permeability (*BHPRM*).

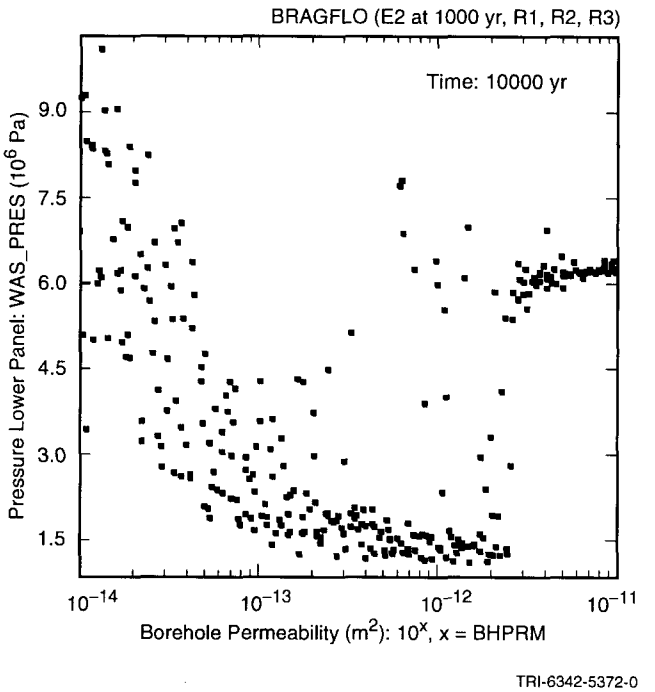

Fig. 6.10.2. Scatterplot for repository pressure (Pa) at 10,000 yr versus borehole permeability (*BHPRM*) for E2 intrusion at 1000 yr into lower waste panel.

6.10.3 Regression Analysis

A more formal investigation of the mapping in Eq. (6.10.2) can be based on regression analysis. In this approach, a model of the form

$$y = b_0 + \sum_{j=1}^{n} b_j \, x_j \tag{6.10.6}$$

is developed from the mapping between analysis inputs and analysis results shown in Eq. (6.10.2), where the x_j are the input variables under consideration and the b_j are coefficients that must be determined. The coefficients b_j and other aspects of the construction of the regression model in Eq. (6.10.6) can be used to indicate the importance of the individual variables x_j with respect to the uncertainty in y.

The construction of the regression model in Eq. (6.10.6) is considered first. To keep the notation from becoming unwieldy, n will be used to denote the number of independent variables under consideration (i.e., $n = nV$ as used in Eq. (6.10.3)) and m will be used to denote the number of observations under consideration (i.e., $m = nLHS$ or $3 \bullet nLHS$ as used in Eqs. (6.10.2) or (6.10.4)). As shown in Eq. (6.10.2), there exists a sequence y_k, $k = 1, ..., m$, of values for the output variable. When expressed in the form of the model in Eq. (6.10.6), each y_k becomes

$$y_k = b_0 + \sum_{j=1}^{n} b_j \, x_{kj} + \varepsilon_k \quad , \quad k = 1, \ldots, m, \tag{6.10.7}$$

where the error terms ε_k, $k = 1, ..., m$, equal the difference between the observed value y_k and the corresponding predicted value $\hat{y}_k$ defined by Eq. (6.10.6). At this point, the b_j are still unknown. What is desired is to determine the b_j in some suitable manner. The method of least squares is widely used and will be employed here (Harter 1983, Eisenhart 1964). As a result of its extensive use, there exist a number of excellent textbooks on least squares regression analysis (Myers 1986, Weisberg 1985, Seber 1977, Draper and Smith 1981, Daniel et al. 1980, Neter and Wasserman 1974). The purpose of the following discussion is to present just enough information to be able to describe some of the applications of regression-based techniques in sensitivity analysis. The indicated textbooks, as well as many others, provide far more information on regression analysis than can be presented here.

To determine the b_j, it is convenient to use the following matrix representation for the equalities in Eq. (6.10.7):

$$\mathbf{y} = \mathbf{X}\mathbf{b} + \varepsilon, \tag{6.10.8}$$

where

$$\mathbf{y} = \begin{bmatrix} y_1 \\ \vdots \\ y_m \end{bmatrix}, \quad \mathbf{X} = \begin{bmatrix} 1 & x_{11} & \cdots & x_{1n} \\ \vdots & \vdots & & \vdots \\ 1 & x_{m1} & \cdots & x_{mn} \end{bmatrix}, \quad \mathbf{b} = \begin{bmatrix} b_0 \\ \vdots \\ b_n \end{bmatrix} \quad \text{and} \quad \varepsilon = \begin{bmatrix} \varepsilon_1 \\ \vdots \\ \varepsilon_m \end{bmatrix}.$$

In the least squares approach, the intent is to determine the b_j such that the sum

$$S(\mathbf{b}) = \sum_{k=1}^{m} \left(y_k - b_0 - \sum_{j=1}^{n} b_j x_{kj} \right)^2 = (\mathbf{y} - \mathbf{X}\mathbf{b})^T \, (\mathbf{y} - \mathbf{X}\mathbf{b}) \tag{6.10.9}$$

is a minimum. Put another way, the b_j are determined such that the sum $\sum_k \varepsilon_k^2$ involving the error terms is a minimum. The determination of the b_j in the least squares approach is just an exercise in calculus and is based on consideration of the first derivatives of $S(\mathbf{b})$ with respect to the individual b_j (Draper and Smith 1981).

This derivation leads to the following matrix equation that defines the coefficient vector **b** for which the sum $S(\mathbf{b})$ given in Eq. (6.10.9) is a minimum:

$$\mathbf{X}^T\mathbf{X}\mathbf{b} = \mathbf{X}^T\mathbf{y}. \tag{6.10.10}$$

For the analysis to produce a unique value for the coefficient vector **b**, it is necessary that the matrix $\mathbf{X}^T\mathbf{X}$ be invertible. Then, **b** is given by

$$\mathbf{b} = (\mathbf{X}^T\mathbf{X})^{-1}\,\mathbf{X}^T\mathbf{y}. \tag{6.10.11}$$

The matrix $\mathbf{X}^T\mathbf{X}$ will always be invertible when the columns of **X** are linearly independent. This usually is the case in a sampling-based study in which the number of sample elements (i.e., m) exceeds the number of independent variables (i.e., n).

The following identity holds for the least squares regression model and plays an important role in assessing the adequacy of such models:

$$\sum_{k=1}^{m}(y_k-\bar{y})^2 = \sum_{k=1}^{m}(\hat{y}_k-\bar{y})^2 + \sum_{k=1}^{m}(\hat{y}_k-y_k)^2, \tag{6.10.12}$$

where $\hat{y}_k$ denotes the estimate of y_k obtained from the regression model and $\bar{y}$ is the mean of the y_k (Draper and Smith, 1981). Since

$$\sum_{k=1}^{m}(\hat{y}_k-y_k)^2 \tag{6.10.13}$$

provides a measure of variability about the regression model, the ratio

$$R^2 = \sum_{k=1}^{m}\left(\hat{y}_k-\bar{y}_k\right)^2 \Big/ \sum_{k=1}^{m}\left(y_k-\bar{y}\right)^2 \tag{6.10.14}$$

provides a measure of the extent to which the regression model can match the observed data. Specifically, when the variation about the regression model is small (i.e., when $\Sigma_k(\hat{y}_k - y_k)^2$ is a small relative to $\Sigma_k(\hat{y}_k - \bar{y})^2$), then the corresponding R^2 value is close 1, which indicates that the regression model is accounting for most of the uncertainty in the y_k. Conversely, an R^2 value close to zero indicates that the regression model is not very successful in accounting for the uncertainty in the y_k. Another name for R^2 is the coefficient of multiple determination.

An important situation occurs when the rows of the matrix **X** (i.e., the variable values at which the model is evaluated) are selected so that $\mathbf{X}^T\mathbf{X}$ is a diagonal matrix. In this case, the columns of **X** are said to be orthogonal, and the estimated regression coefficients are given by

$$\mathbf{b} = (\mathbf{X}^T\mathbf{X})^{-1}\,\mathbf{X}^T\mathbf{y}$$

$$= \begin{bmatrix} d_0 & 0 & \cdots & 0 \\ 0 & d_1 & & 0 \\ \vdots & \vdots & & \vdots \\ 0 & 0 & \cdots & d_n \end{bmatrix}^{-1} \begin{bmatrix} 1 & 1 & \cdots & 1 \\ x_{11} & x_{21} & \cdots & x_{m1} \\ \vdots & \vdots & & \vdots \\ x_{1n} & x_{2n} & \cdots & x_{mn} \end{bmatrix} \begin{bmatrix} y_1 \\ y_2 \\ \vdots \\ y_m \end{bmatrix} \tag{6.10.15}$$

and so each element b_j of **b** is given by

$$b_j = \sum_{k=1}^{m} x_{kj} y_k \,/\, d_j = \sum_{k=1}^{m} x_{kj} y_k \Big/ \sum_{k=1}^{m} x_{kj}^2 \quad . \tag{6.10.16}$$

The important point to recognize is that the estimate of the regression coefficient b_j for the variable x_j depends only on the values for x_j in the design matrix **X** (i.e., x_{1j}, ..., x_{mj}). This is true regardless of the number of variables included in the regression. As long as the design is orthogonal, the addition or deletion of variables from the model will not change the regression coefficients. Further, when the design matrix **X** is orthogonal, the R^2 value for the regression can be expressed as

$$R^2 = \sum_{k=1}^{m} \left(\hat{y}_k - \bar{y}\right)^2 \Big/ \sum_{k=1}^{m} \left(y_k - \bar{y}\right)^2 = R_1^2 + R_2^2 + \cdots + R_n^2 \,, \tag{6.10.17}$$

where R_j^2 is the R^2 value that results from regressing y on only x_j (Eq. (III-74) Helton et al. 1991). Thus, R_j^2 is equal to the contribution of x_j to R^2 when the design matrix **X** is orthogonal.

The regression model in Eq. (6.10.6) can be algebraically reformulated as

$$\left(y - \bar{y}\right) / \hat{s} = \sum_{j=1}^{n} \left(b_j \hat{s}_j \,/\, \hat{s}\right)\left(x_j - \bar{x}_j\right) \Big/ \hat{s}_j \,, \tag{6.10.18}$$

where

$$\bar{y} = \sum_{k=1}^{m} y_k \,/\, m, \qquad \hat{s} = \left[\sum_{k=1}^{m} \left(y_k - \bar{y}\right)^2 \Big/ (m-1)\right]^{1/2} ,$$

$$\bar{x}_j = \sum_{k=1}^{m} x_{kj} / m, \qquad \hat{s}_j = \left[\sum_{k=1}^{m} \left(x_{kj} - \bar{x}_j \right)^2 / (m-1) \right]^{1/2}.$$

The coefficients $b_j \hat{s}_j / \hat{s}$ appearing in Eq. (6.10.18) are called standardized regression coefficients (SRCs). When the x_j are independent, the absolute value of the SRCs can be used to provide a measure of variable importance. Specifically, the coefficients provide a measure of importance based on the effect of moving each variable away from its expected value by a fixed fraction of its standard deviation while retaining all other variables at their expected values. Calculating SRCs is equivalent to performing the regression analysis with the input and output variables normalized to mean zero and standard deviation one.

An example regression analysis is now given. The output variable (i.e., y) is pressure (Pa) in the repository at 10,000 yr under undisturbed (i.e., E0) conditions (i.e., the pressure values above 10,000 yr in Fig. 6.10.3). To keep the example at a convenient size, 3 independent variables (i.e., x_j) will be considered (Table 5.2.1): pointer variable for microbial degradation of cellulose (*WMICDFLG*), halite porosity (*HALPOR*), and corrosion rate for steel (*WGRCOR*). The following regression model is obtained using the preceding three variables and the pooled LHS in Eq. (6.10.4) (i.e., $n = 3$ and $m = 300$):

$$y = 5.72 \times 10^6 + 2.46 \times 10^6 \bullet WMICDFLG + 1.55 \times 10^8 \bullet HALPOR + 1.52 \times 10^{20} \bullet WGRCOR. \qquad (6.10.19)$$

The coefficients in the preceding model show the effect of a one unit change in an input variable (i.e., an x_j) on the output variable (i.e., y). The sign of a regression coefficient indicates whether y tends to increase (a positive regression coefficient) or tends to decrease (a negative regression coefficient) as the corresponding input variable increases. Thus, y tends to increase as each of *WMICDFLG*, *HALPOR* and *WGRCOR* increases.

It is hard to assess variable importance from the regression coefficients in Eq. (6.10.19) because of the effects of units and distribution assumptions. In particular, the regression coefficient for *WGRCOR* is much larger than the regression coefficients for *WMICDFLG* and *HALPOR*, which does not necessarily imply that *WGRCOR* has greater influence on the uncertainty in y than *WMICDFLG* or *HALPOR*. Variable importance is more clearly shown by the following reformation of Eq. (6.10.19) with SRCs:

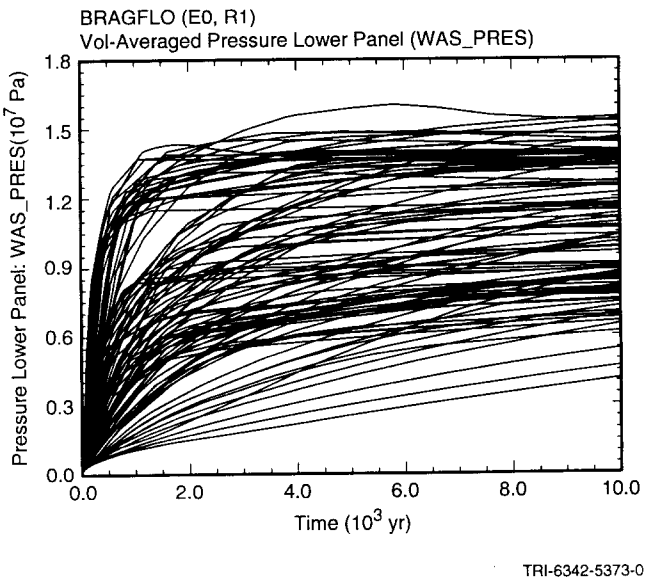

Fig. 6.10.3 Pressure (Pa) in lower waste panel under undisturbed conditions.

$$y = 0.722\ WMICDFLG + 0.468\ HALPOR + 0.246\ WGRCOR. \tag{6.10.20}$$

The SRCs in Eq. (6.10.20) provide a better characterization of variable importance than the unstandardized coefficients in Eq. (6.10.19). For perturbations equal to a fixed fraction of their standard deviation, the impact of *WMICDFLG* is approximately 50% larger than the impact of *HALPOR* (i.e., (0.722 – 0.468)/0.468 = 0.54) and almost 200% larger than the impact of *WGRCOR* (i.e., (0.722 – 0.246)/0.246 = 1.96). Both regression models have an R^2 value of 0.79 and thus can account for approximately 79% of the uncertainty in y.

6.10.4 Correlation and Partial Correlation

The ideas of correlation and partial correlation are useful concepts that often appear in sampling-based uncertainty/sensitivity studies. For a sequence of observations (x_i, y_i), $i = 1, ..., m$, the (sample) correlation r_{xy} between x and y is defined by

$$r_{xy} = \frac{\sum_{k=1}^{m} (x_k - \bar{x})(y_k - \bar{y})}{\left[\sum_{k=1}^{m} (x_k - \bar{x})^2\right]^{1/2} \left[\sum_{k=1}^{m} (y_k - \bar{y})^2\right]^{1/2}} \tag{6.10.21}$$

where $\bar{x}$ and $\bar{y}$ are defined in conjunction with Eq. (6.10.18). The correlation coefficient r_{xy} provides a measure of the linear relationship between x and y.

The nature of the correlation coefficient r_{xy} is most readily understood by considering the regression

$$y = b_0 + b_1 x. \tag{6.10.22}$$

The definition of r_{xy} in Eq. (6.10.21) is equivalent to the definition

$$r_{xy} = \text{sign}(b_1)(R^2)^{1/2}, \tag{6.10.23}$$

where $\text{sign}(b_1) = 1$ if $b_1 \geq 0$, $\text{sign}(b_1) = -1$ if $b_1 < 0$, and R^2 is the coefficient of determination that results from regressing y on x. With respect to interpretation, the correlation coefficient r_{xy} provides a measure of the linear relationship between x and y, and the regression coefficient b_1 characterizes the effect that a unit change in x will have on y.

When more than one input variable is under consideration, partial correlation coefficients (PCCs) can be used to provide a measure of the linear relationships between the output variable y and the individual input variables. The PCC between y and an individual variable x_p is obtained from the use of a sequence of regression models. First, the following two regression models are constructed:

$$\hat{y} = b_0 + \sum_{\substack{j=1 \\ j \neq p}}^{n} b_j x_j \quad \text{and} \quad \hat{x}_p = c_0 + \sum_{\substack{j=1 \\ j \neq p}}^{n} c_j x_j \ . \tag{6.10.24}$$

Then, the results of the two preceding regressions are used to define the new variables $y - \hat{y}$ and $x_p - \hat{x}_p$. By definition, the PCC between y and x_p is the correlation coefficient between $y - \hat{y}$ and $x_p - \hat{x}_p$. Thus, the PCC provides a measure of the linear relationship between y and x_p with the linear effects of the other variables removed. The preceding provides a rather intuitive development of what a PCC is. A formal development of PCCs and the relationships between PCCs and SRCs is provided by Iman et al. (1985).

The PCC characterizes the strength of the linear relationship between two variables after a correction has been made for the linear effects of the other variables in the analysis, and the SRC characterizes the effect on the output variable that results from perturbing an input variable by a fixed fraction of its standard deviation. Thus, PCCs and SRCs provide related, but not identical, measures of variable importance. In particular, the PCC provides a measure of variable importance that tends to exclude the effects of other variables, the assumed distribution for the particular input variable under consideration, and the magnitude of the impact of an input variable on an output variable. In contrast, the value for an SRC is significantly influenced by both the distribution assigned to an input variable and the impact that this variable has on an output variable. However, when the input variables in an analysis are uncorrelated, an ordering of variable importance based on either the absolute value of SRCs or the absolute value of

PCCs will yield the same ranking of variable importance, even though the SRCs and PCCs for individual variables may be quite different (Iman et al. 1985).

Many output variables are functions of time or location. A useful way to present sensitivity results for such variables is with plots of PCCs or SRCs. An example of such a presentation for the pressure curves in Fig. 6.10.3 is given in Fig. 6.10.4, which displays two sets of curves. The left set contains SRCs plotted as a function of time; the right set contains PCCs plotted in a similar manner. For both sets of curves, the dependent variables are pressures at fixed times, and each curve displays the values of SRCs or PCCs relating these pressures to a single input variable as a function of time.

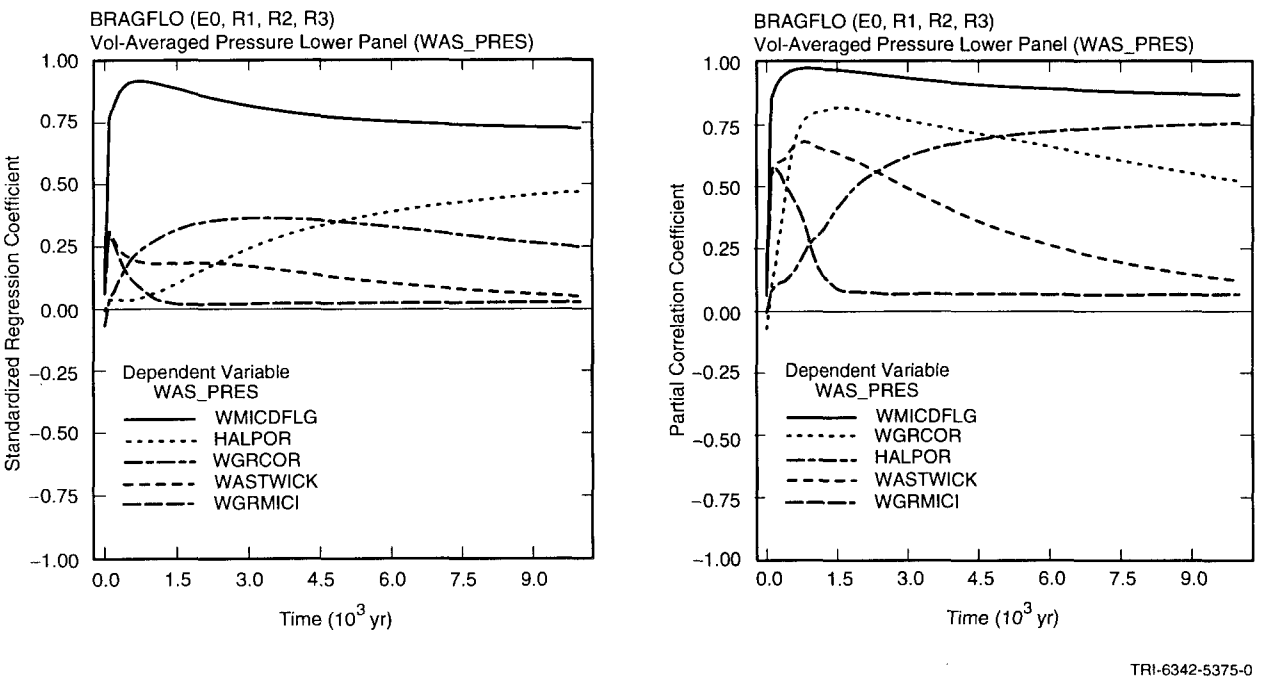

Fig. 6.10.4. Standardized regression coefficients (SRCs) and partial correlation coefficients (PCCs) for five variables having the largest PCCs, in absolute value, with pressure (Pa) in lower waste panel under undisturbed conditions.

6.10.5 Stepwise Regression Analysis

When many input variables are involved, the direct construction of a regression model containing all input variables as shown in Eq. (6.10.6) may not be the best approach for several reasons. First, the large number of variables makes the regression model tedious to examine and unwieldy to display. Second, it is often the case that only a relatively small number of input variables have an impact on the output variable. As a result, there is no reason to include the remaining variables in the regression model. Third, correlated variables result in unstable regression coefficients (i.e., coefficients whose values are sensitive to the specific variables included in the regression model). When this occurs, the regression coefficients in a model containing all the input variables can give a misleading representation of variable importance. As a side point, if several input variables are highly correlated, consideration should be given to either removing all but one of the correlated variables or transforming the variables to correct for (i.e., remove) the correlations between them. Fourth, an overfitting of the data can result when variables are arbitrarily forced into the regression model. This phenomenon occurs when the regression model attempts to match the predictions associated with individual sample elements rather than match the trends shown by the sample elements collectively.

Stepwise regression analysis provides an alternative to constructing a regression model containing all the input variables. With this approach, a sequence of regression models is constructed. The first regression model contains the single input variable that has the largest impact on the uncertainty in the output variable (i.e., the input variable that has the largest correlation with the output variable y). The second regression model contains the two input variables that have the largest impact on the output variable: the input variable from the first step plus whichever of the remaining variables has the largest impact on the uncertainty not accounted for by the first variable (i.e., the input variable that has the largest correlation with the uncertainty in y that cannot be accounted for by the first variable). The third regression model contains the three input variables that have the largest impact on the output variable: the two input variables from the second step plus whichever of the remaining variables has the largest impact on the uncertainty not accounted for by the first two variables (i.e., the input variable that has the largest correlation with the uncertainty in y that cannot be accounted for by the first two variables). Additional models in the sequence are defined in the same manner until a point is reached at which further models are unable to meaningfully increase the amount of the uncertainty in the output variable that can be accounted for. Further, at each step of the process, the possibility exists for an already selected variable to be dropped out if it no longer has a significant impact on the amount of uncertainty in the output variable that can be accounted for by the regression model; this only occurs when correlations exist between the input variables.

Several aspects of stepwise regression analysis provide insights on the importance of the individual variables. First, the order in which the variables are selected in the stepwise procedure provides an indication of their importance, with the most important variable being selected first, the next most important variable being selected second, and so on. Second, the R^2 values (see Eq. (6.10.14)) at successive steps of the analysis also provide a

measure of variable importance by indicating how much of the uncertainty in the dependent variable can be accounted for by all variables selected through each step. When the input variables are uncorrelated, the differences in the R^2 values for the regression models constructed at successive steps equals the fraction of the total uncertainty in the output variable that can be accounted for by the individual input variables being added at each step (see Eq. (6.10.17)). Third, the absolute values of the SRCs (see Eq. (6.10.18)) in the individual regression models provide an indication of variable importance. Further, the sign of an SRC indicates whether the input and output variable tend to increase and decrease together (a positive coefficient) or tend to move in opposite directions (a negative coefficient).

An important situation occurs when the input variables are uncorrelated. In this case, the orderings of variable importance based on order of entry into the regression model, size of the R^2 values attributable to the individual variables, the absolute values of the SRCs, and the absolute values of the PCCs are the same. In situations where the input variables are believed to be uncorrelated, one of the important applications of the previously discussed restricted pairing technique of Iman and Conover (Sect. 6.2) is to ensure that the correlations between variables within a Latin hypercube or random sample are indeed close to zero. When variables are correlated, care must be used in the interpretation of the results of a regression analysis since the regression coefficients can change in ways that are basically unrelated to the importance of the individual variables as correlated variables are added to and deleted from the regression model (see Sect. 7.2 for an example of the effects of correlated variables on the outcomes of a regression analysis).

When the stepwise technique is used to construct a regression model, it is necessary to have some criteria to stop the construction process. When there are many independent variables, there is usually no reason to let the construction process continue until all the variables have been used. It is also necessary to have some criteria to determine when a variable is no longer needed and thus can be dropped from the regression model. As indicated earlier, this latter situation only occurs when the input variables are correlated.

The usual criterion for making the preceding decisions is based on whether or not the regression coefficient associated with an input variable appears to be significantly different from zero. Specifically, the *t*-test is used to determine the probability that a regression coefficient as large as or larger than the one constructed in the analysis would be obtained if, in reality, there was no relationship between the input and output variable, and, as a result, the apparent relationship that led to the constructed regression coefficient was due entirely to chance (Sect. 7.5, Neter and Wasserman 1974). The probability of exceeding a regression coefficient due to chance variation is often referred to as an α-value. The actual derivation of the α-value depends on assumptions involving normality and random variation that are not satisfied in sampling-based sensitivity studies for computer models since there is no variation in the predictions for a fixed set of input. However, the *t*-test and the associated α-value still constitute a useful criterion for adding or deleting variables from a regression model in a sensitivity study since they provide a measure of how viable the relationship between the input and output variable would appear to be in a study in which

this relationship could possibly have arisen from random variation. Sensitivity studies often use an α-value of 0.01 or 0.02 to add a variable to a regression model and a somewhat larger value to drop a variable from the model.

As models involving more variables are developed in a stepwise regression analysis, the possibility exists of overfitting the data. Overfitting occurs when the regression model in essence "chases" the individual observations rather than following an overall pattern in the data. For example, it is possible to obtain a good fit to a set of points by using a polynomial of high degree. However, in doing so, it is possible to overfit the data and produce a spurious model that makes poor predictions.

To protect against overfit, the Predicted Error Sum of Squares (PRESS) criterion can be used to determine the adequacy of a regression model (Allen 1971). For a regression model containing q variables and constructed from m observations, PRESS is computed in the following manner. For $k = 1,2,...,m$, the kth observation is deleted from the original set of m observations and then a regression model containing the original q variables is constructed from the remaining $m - 1$ observations. With this new regression model, the value $\hat{y}_q(k)$ is estimated for the deleted observation y_k. Then, PRESS is defined from the preceding predictions and the m original observations by

$$PRESS_q = \sum_{k=1}^{m} \left(y_k - \hat{y}_q(k)\right)^2. \tag{6.10.25}$$

The regression model having the smallest PRESS value is preferred when choosing between two competing models, as this is an indication of how well the basic pattern of the data has been fitted versus an overfit or an underfit. In particular, PRESS values will decrease in size as additional variables are added to the regression model without an overfitting of the data (i.e., $PRESS_q > PRESS_{q+1}$), with an increase in the PRESS values (i.e., $PRESS_q < PRESS_{q+1}$) indicating an overfitting of the data. In addition to PRESS, there are also a number of other diagnostic tools that can be used to investigate the adequacy of regression models (Cook and Weisberg 1982, Belsley et al. 1980).

It is important to use scatterplots, PRESS values and other procedures to examine the reasonableness of regression models. This is especially true when regression models are used for sensitivity analysis. Such analyses often involve many input variables and large uncertainties in these variables. The appearance of spurious patterns is a possibility that must be checked for.

An example stepwise regression analysis is now presented for repository pressure at 10,000 yr under undisturbed conditions (Fig. 6.10.3). The following 31 variables from Table 5.2.1 and contained in the three replicated LHSs indicated in Eq. (6.5.1) are used as input to calculations performed with BRAGFLO in the 1996 WIPP PA: *ANHBCEXP*, *ANHBCVGP*, *ANRBRSAT*, *ANHCOMP*, *ANHPRM*, *ANRGSSAT*, *BHPRM*, *BPCOMP*, *BPINTPRS*, *BPPRM*, *BPVOL*, *HALCOMP*, *HALPOR*, *HALPRM*, *SALPRES*, *SHBCEXP*, *SHPRMASP*, *SHPRMCLY*,

SHPRMCON, *SHPRMDRZ*, *SHPRMHAL*, *SHRBRSAT*, *SHRGSSAT*, *WASTWICK*, *WFBETCEL*, *WGRCOR*, *WGRMICH*, *WGRMICI*, *WMICDFLG*, *WRBRNSAT* and *WRGSSAT*. Variables within the pairs (*ANHCOMP*, *ANHPRM*) and (*HALCOMP*, *HALPOR*) have rank correlations of −0.99 (Table 5.2.1, Fig. 5.4.1), which creates instabilities in regression results (Sect. 7.2). Therefore, to avoid the distracting effects that result from the presence of highly correlated variables, *ANHCOMP* and *HALCOMP* will not be included as independent variables in the following example. Thus, the data available for analysis are of the form

$$[x_{k1}, x_{k2}, \ldots, x_{k,29}, y_k],\ k = 1, 2, \ldots, m = 300, \tag{6.10.26}$$

where y_k is the value for pressure obtained with the kth sample element (i.e., y = *WAS_PRES* at 10,000 yr in Fig. 6.10.3), the x_{kj}, j = 1, 2, ..., 29, correspond to the variables indicated above with *ANHCOMP* and *HALCOMP* omitted, and a value of m = 300 results from pooling the three replicated LHSs (i.e., R1, R2, R3).

The variables *BHPRM*, *BPCOMP*, *BPINTPRS*, *BPPRM* and *BPVOL* do not effect repository pressure under undisturbed conditions and thus could be omitted from consideration. However, they are left in this example to increase the number of variables that must be considered in the stepwise process. Also, leaving such variables in an analysis can be beneficial from an analysis verification perspective. In particular, an error in the implementation of the analysis is indicated if such unimportant variables show up as having identifiable effects. Similarly, errors are indicated when variables are identified as having effects that are inconsistent with their known usage within the analysis.

The first step selects the input variable x_j that has the largest impact on the output variable y. Specifically, this is defined to be the variable that has the largest correlation, in absolute value, with y (see Eqs. (6.10.21) and (6.10.23)). Thus, it is necessary to calculate the correlations between y and each of the 29 input variables under consideration. For illustration, Table 6.10.1 shows the 7 × 7 correlation matrix for y and the six input variables ultimately selected in the stepwise regression, although the full correlation matrix would actually be (29 + 1) × (29 + 1). Each element in the correlation matrix is the correlation between the variables in the corresponding row and column. As examination of the correlation matrix in Table 6.10.1 shows, the variable *WMICDFLG* has the highest correlation with waste pressure, which is denoted by *WAS_PRES*. Thus, the first step in the analysis selects the variable *WMICDFLG*. A regression model relating y to *WMICDFLG* is then developed as shown in Eq. (6.10.11) with n = 1 and m = 300. The resultant regression model is

$$\hat{y} = 8.94 \times 10^6 + 2.43 \times 10^6 \bullet WMICDFLG, \tag{6.10.27}$$

which has an R^2 value of 0.508, an α-value of 0.0000, an SRC of 0.712 and a PRESS value of 1.20×10^{15}. This model is summarized in Table 6.10.2.

Table 6.10.1. Correlation Matrix for Variables Selected in Stepwise Regression Analysis for Pressure in the Repository at 10,000 yr Under Undisturbed Conditions (i.e., y = *WAS_PRES* at 10,000 yr in Fig. 6.10.3)

WMICDFLG	1.0000						
HALPOR	–0.0348	1.0000					
WGRCOR	0.0272	0.0216	1.0000				
ANHPRM	0.0008	–0.0039	0.0130	1.0000			
SHRGSSAT	–0.0026	0.0395	–0.0171	–0.0042	1.0000		
SALPRES	0.0560	–0.0072	0.0010	–0.0117	0.0061	1.0000	
WAS_PRES	0.7124	0.4483	0.2762	0.1303	0.0820	0.0993	1.0000
	WMICDFLG	*HALPOR*	*WGRCOR*	*ANHPRM*	*SHRGSSAT*	*SALPRES*	*WAS_PRES*

Table 6.10.2. Results of Stepwise Regression Analysis for Pressure in the Repository at 10,000 yr Under Undisturbed Conditions (i.e., y = *WAS_PRES* at 10,000 yr in Fig. 6.10.3)

Step[a]	Variables[b]	SRC[c]	α-Values[d]	R^2 Values[e]	PRESS[f]
1	*WMICDFLG*	0.712	0.0000	0.508	1.20×10^{15}
2	*WMICDFLG*	0.729	0.0000	0.732	6.59×10^{14}
	HALPOR	0.474	0.0000		
3	*WMICDFLG*	0.722	0.0000	0.792	5.14×10^{14}
	HALPOR	0.468	0.0000		
	WGRCOR	0.246	0.0000		
4	*WMICDFLG*	0.722	0.0000	0.809	4.79×10^{14}
	HALPOR	0.469	0.0000		
	WGRCOR	0.245	0.0000		
	ANHPRM	0.128	0.0000		
5	*WMICDFLG*	0.722	0.0000	0.814	4.70×10^{14}
	HALPOR	0.466	0.0000		
	WGRCOR	0.246	0.0000		
	ANHPRM	0.129	0.0000		
	SHRGSSAT	0.070	0.0056		
6	*WMICDFLG*	0.718	0.0000	0.818	4.63×10^{14}
	HALPOR	0.466	0.0000		
	WGRCOR	0.246	0.0000		
	ANHPRM	0.129	0.0000		
	SHRGSSAT	0.070	0.0055		
	SALPRES	0.063	0.0012		

[a] Steps in the analysis

[b] Variables selected at each step with *ANHCOMP* and *HALCOMP* excluded from entry into the regression model

[c] Standardized regression coefficients (SRCs) for variables in the regression model at each step

[d] α-values for variables in the regression model at each step

[e] R^2 value for the regression model at each step

[f] Predicted error sum of squares (PRESS) value for the regression model at each step

The second step selects the input variable x_j that has the largest impact on the uncertainty in the output variable y that cannot be accounted by *WMICDFLG*, the variable selected in the first step. This selection is made by defining a new variable

$$\tilde{y} = y - \hat{y} = y - (8.94 \times 10^6 + 2.43 \times 10^6 \bullet WMICDFLG), \tag{6.10.28}$$

where $\hat{y}$ is defined in Eq. (6.10.27), and then calculating the correlations between $\tilde{y}$ and the remaining variables. The variable with the largest correlation, in absolute value, with $\tilde{y}$ is selected as the second variable for inclusion in the model. In this example, the selected variable is *HALPOR*. The regression model at this step will thus involve the two variables *WMICDFLG* and *HALPOR* and is constructed as shown in Eq. (6.10.11) with $n = 2$ and $m = 300$. The resultant regression model is

$$\hat{y} = 6.89 \times 10^6 + 2.49 \times 10^6 \bullet WMICDFLG + 1.57 \times 10^8 \bullet HALPOR. \tag{6.10.29}$$

This model is summarized in Table 6.10.2.

The third step selects the input variable x_j that has the largest impact on the uncertainty in the output variable y that cannot be accounted for by *WMICDFLG* and *HALPOR*, the two variables from the second step. This selection is made by defining a new variable

$$\tilde{y} = y - \hat{y} = y - (6.89 \times 10^6 + 2.49 \times 10^6 \bullet WMICDFLG + 1.57 \times 10^8 \bullet HALPOR), \tag{6.10.30}$$

where $\hat{y}$ is defined in Eq. (6.10.29). The variable with the largest correlation, in absolute value, with $\tilde{y}$ is selected as the third variable for inclusion in the model. In this example, the selected variable is *WGRCOR*. The regression model for this step will thus involve the three variables *WMICDFLG*, *HALPOR* and *WGRCOR*. The resultant regression model is summarized in Table 6.10.2.

As shown in Table 6.10.2, the stepwise procedure then continues in the same manner through a total of six steps, until no more variables can be found with an α-value less than 0.02. At this point, the stepwise procedure stops.

At each step, the stepwise procedure also checks to see if any variable selected at a prior step now has an α-value that exceeds a specified level, which is 0.05 in this analysis. If such a situation occurs, the variable will be dropped from the analysis, with the possibility that it may be reselected at a later step as other variables are added and deleted from the model. This type of behavior only occurs when there are correlations between the input variables. As shown in the example correlation matrix in Table 6.10.2, the restricted pairing technique has been successful in keeping the correlations between the input variables close to zero. Thus, no variables meet the criterion to be dropped from the regression model once they have been selected at a prior step.

Another result of this lack of correlation is that the regression coefficients do not change significantly as additional variables are added to the regression model. As examination of Table 6.10.2 shows, the regression coefficients for a specific variable are essentially the same in all regression models containing that variable. Further, as indicated in Eq. (6.10.17), the R^2 values obtained for successive models can be subtracted to obtain the contribution to the uncertainty in y due to the newly added variable. Thus, for example, *WMICDFLG* accounts for approximately 51% of the uncertainty in y (i.e., $R^2 = 0.508$), while *WMICDFLG* and *HALPOR* together account for approximately 73% of the uncertainty (i.e., $R^2 = 0.732$). As a result, *HALPOR* by itself accounts for approximately 73% – 51% = 22% of the uncertainty in y. Similar results hold for the other variables selected in the analysis.

Table 6.10.2 also reports the PRESS values for the regression models obtained at the individual steps in the analysis. A decreasing sequence of PRESS values indicates that the regression models are not overfitting the data on which they are based. An increase in the PRESS values suggests that a model is overfitting the data, and thus that the stepwise procedure should probably be stopped at the preceding step. As shown by the decreasing PRESS values in Table 6.10.2, the regression models in this analysis are probably not overfitting the data from which they were constructed.

Typically, a certain amount of discretion is involved in selecting the exact point at which to stop a stepwise regression analysis. Certainly, α-values and the behavior of PRESS values provide two criteria to consider in selecting a stopping point. Other criteria include the changes in the R^2 values that take place as additional variables are added to the regression models and whether or not spurious variables are starting to enter the regression models. When only very small changes in R^2 values are taking place (e.g., ≤ 0.01), there is often little reason to continue the stepwise process. When α-values approach or exceed 0.01 and a large number of input variables are being considered, it is fairly common to start getting spurious variables in the regression. Such variables appear to have a small effect on the output variable which, in fact, is due to chance variation. In such situations, a natural stopping point may be just before spurious variables start being selected. Another possibility is to delete spurious variables from the regression model.

When the input variables are uncorrelated, a display of the results of a stepwise regression analysis as shown in Table 6.10.2 contains a large amount of redundant information. A more compact display can be obtained by listing the variables in the order that they entered in the regression model, the R^2 values obtained with the entry of successive variables into the regression model, and the SRCs for the variables contained in the final model. Table 6.10.3 shows what this summary looks like for the stepwise regression analysis presented in Table 6.10.2.

Table 6.10.3. Compact Summary of Stepwise Regression Analyses for Pressure in the Repository at 10,000 yr Under Undisturbed Conditions (i.e., y = *WAS_PRES* at 10,000 yr in Fig. 6.10.3).

Step[a]	Variable[b]	SRC[c]	R^{2d}
1	*WMICDFLG*	0.718	0.508
2	*HALPOR*	0.466	0.732
3	*WGRCOR*	0.246	0.792
4	*ANHPRM*	0.129	0.809
5	*SHRGSSAT*	0.070	0.814
6	*SALPRES*	0.063	0.818

[a] Steps in stepwise analysis.

[b] Variables listed in the order of selection in regression analysis with *ANHCOMP* and *HALCOMP* excluded from entry into regression model.

[c] Standardized regression coefficients (SRCs) for variables in final regression model.

[d] Cumulative R^2 value with entry of each variable into regression model.

6.10.6 The Rank Transformation

Regression and correlation analyses often perform poorly when the relationships between the input and output variables are nonlinear. This is not surprising since such analyses are based on developing linear relationships between variables. The problems associated with poor linear fits to nonlinear data can often be avoided by use of the rank transformation (Iman and Conover 1979). The rank transformation is a simple concept: data are replaced with their corresponding ranks and then the usual regression and correlation procedures are performed on these ranks. Specifically, the smallest value of each variable is assigned the rank 1, the next largest value is assigned the rank 2, and so on up to the largest value, which is assigned the rank m, where m denotes the number of observations. The analysis is then performed with these ranks being used as the values for the input and output variables.

Example regression analyses with raw (i.e., untransformed) and rank-transformed data follow. The output variable (i.e., y) is cumulative brine flow over 10,000 yr under undisturbed (i.e., E0) conditions from the anhydrite marker beds (MBs) to the disturbed rock zone (DRZ, see Fig. 4.2.3) that surrounds the repository (i.e., the cumulative flow values above 10,000 yr in Fig. 6.10.5). The results of the stepwise regression analyses with raw and rank-transformed data can be summarized in the compact form illustrated in Table 6.10.3 and show that the analysis with rank-transformed data is outperforming the analysis with raw data (Table 6.10.4). In particular, the analysis with rank-transformed data can account for approximately 87% of the uncertainty in y (i.e., $R^2 = 0.869$), while the analysis with raw data can account for only 50% of the uncertainty in y (i.e., $R^2 = 0.496$). Further, the regression with rank-transformed data indicates a stronger effect for *WMICDFLG* (i.e., $R^2 = 0.425$) than is indicated by the regression with raw data (i.e., $R^2 = 0.423 - 0.320 = 0.103$).

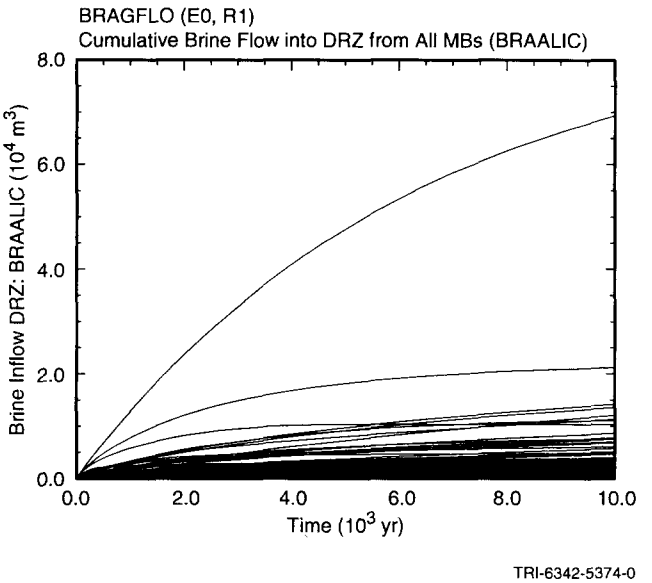

Fig. 6.10.5 Cumulative brine flow (m^3) into disturbed rock zone (DRZ) from all anhydrite marker beds (MBs) under undisturbed (i.e., E0) conditions.

Table 6.10.4. Comparison of Stepwise Regression Analyses with Raw and Rank-Transformed Data for Cumulative Brine Flow over 10,000 yr under Undisturbed Conditions from the Anhydrite Marker Beds to the Disturbed Rock Zone that Surrounds the Repository (i.e., y = *BRAALIC* at 10,000 yr in Fig. 6.10.5).

	Raw Data			Rank-Transformed Data		
Step[a]	Variable[b]	SRC[c]	R^{2d}	Variable[b]	SRRC[e]	R^{2d}
1	*ANHPRM*	0.562	0.320	*WMICDFLG*	–0.656	0.425
2	*WMICDFLG*	–0.309	0.423	*ANHPRM*	0.593	0.766
3	*WGRCOR*	–0.164	0.449	*HALPOR*	–0.155	0.802
4	*WASTWICK*	–0.145	0.471	*WGRCOR*	–0.152	0.824
5	*ANHBCEXP*	–0.120	0.486	*HALPRM*	0.143	0.845
6	*HALPOR*	–0.101	0.496	*SALPRES*	0.120	0.860
7				*WASTWICK*	–0.010	0.869

[a] Steps in stepwise regression analysis.
[b] Variables listed in order of selection in regression analysis with *ANHCOMP* and *HALCOMP* excluded from entry into regression model.
[c] Standardized regression coefficient (SRCs) in final regression model.
[d] Cumulative R^2 value with entry of each variable into regression model.
[e] Standardized rank regression coefficients (SRRCs) in final regression model.

The analysis with rank-transformed data is more effective than the analysis with raw data because the rank transformation tends to linearize the relationships between the independent variables (i.e., the x_j's) and the dependent variable (i.e., y). In particular, both *WMICDFLG* and *ANHPRM* show a better defined linear relationship with y after the rank transformation (Fig. 6.10.6). The rank transformation improves the analysis when nonlinear but monotonic relationships exist between the independent variables and the dependent variable. When more complex relationships exist, the rank transformation may do little to improve the quality of an analysis. In such cases, more sophisticated procedures may be required. For example, the chi square test can be used to test for deviations from randomness in scatterplots; other techniques also exist (Hamby 1994, Saltelli and Marivoet 1990).

As is the case for stepwise regression analyses, analyses wth SRCs and PCCs of the type presented in Fig. 6.10.4 can often be improved with the use of rank-transformed data. When the rank transform is used, the resultant plots will contain standardized rank regression coefficients (SRRCs) and partial rank correlation coefficients (PRCCs). As an example, the results of analyzing the cumulative brine inflows in Fig. 6.10.5 with both raw and rank-transformed data are presented in Fig. 6.10.7, with each plot frame showing the five variables with the largest, in absolute value, SRCs, PCCs, SRRCs and PRCCs as appropriate. As in the comparisons of stepwise regression analyses with raw and rank-transformed data (Table 6.10.4), the analyses with rank-transformed data in Fig. 6.10.7 produce outcomes that indicate stronger effects for individual variables than is the case for the analyses with raw data.

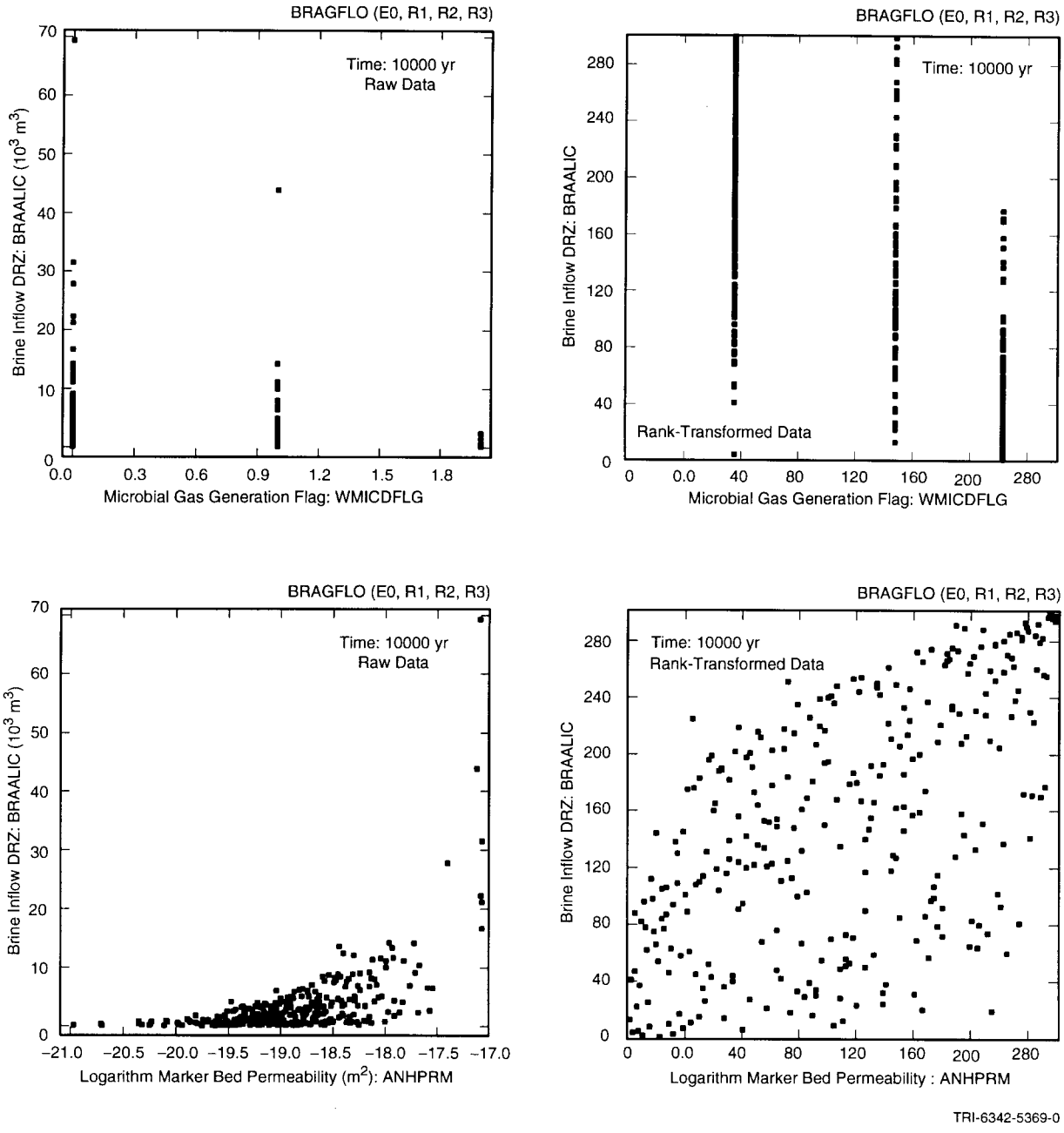

Fig. 6.10.6. Scatterplots for cumulative brine discharge (m^3) from the marker beds over 10,000 yr under undisturbed conditions versus microbial gas generation flag (*WMICDFLG*) and marker bed permeability (*ANHPRM*) with raw (i.e., untransformed) and rank-transformed data.

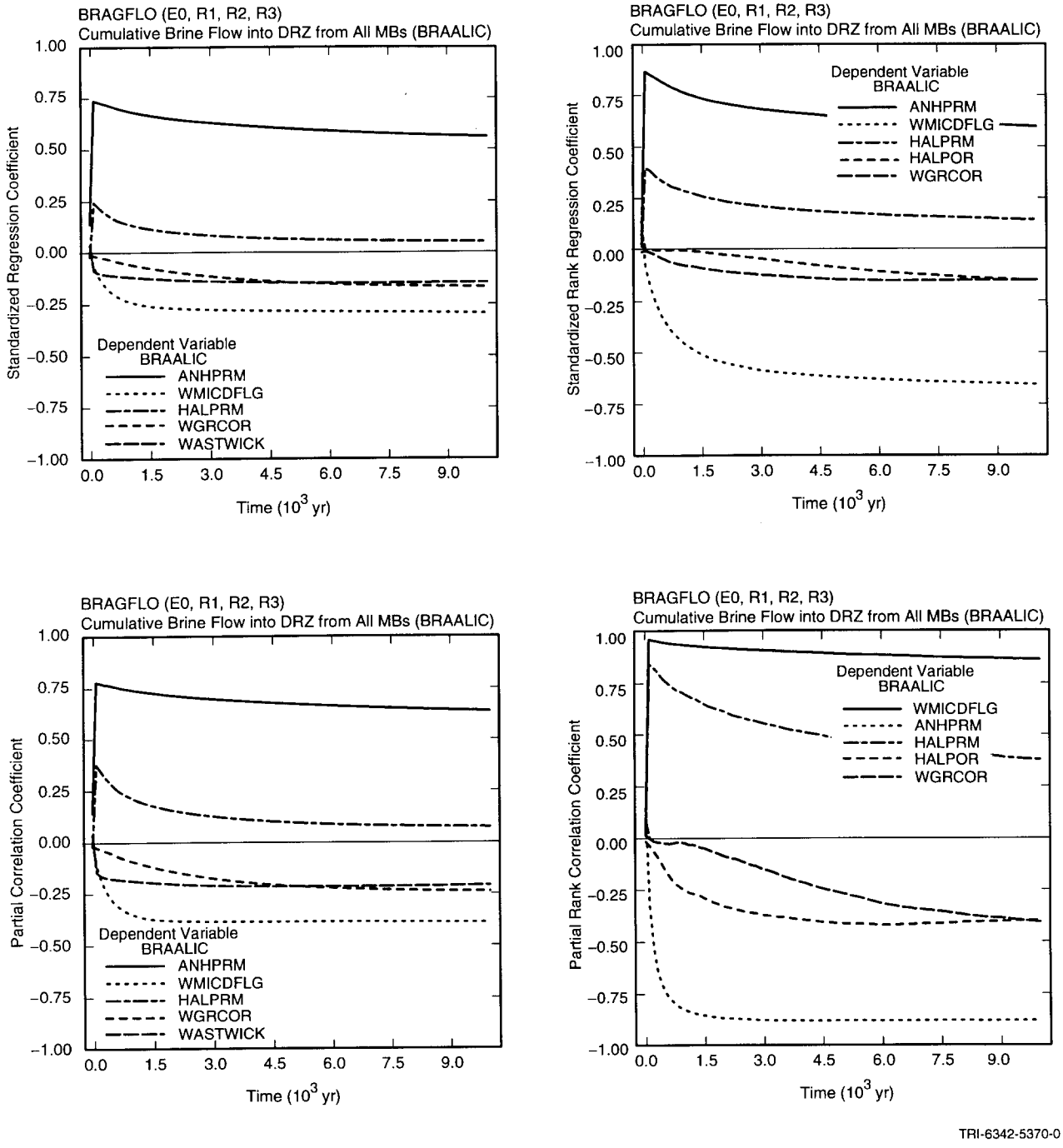

Fig. 6.10.7. Standardized regression coefficients and partial correlation coefficients calculated with raw and rank-transformed data for cumulative brine flow from anhydrite marker beds to disturbed rock zone (DRZ) under undisturbed conditions (i.e., y = *BRAALIC* in Fig. 6.10.5) with *ANHCOMP* and *HALCOMP* excluded from calculation.

7. Fluid Flow in Vicinity of Repository: Undisturbed Conditions

7.1 Overview

This chapter presents uncertainty and sensitivity analysis results for fluid flow in the vicinity of the repository under undisturbed conditions. These results were calculated with BRAGFLO for the three replicated samples (i.e., R1, R2, R3) indicated in Eq. (6.5.1). In particular, the results under consideration are the outcomes of the 300 E0 BRAGFLO calculations indicated in Table 6.9.1. The topics considered are brine inflow (Sect. 7.2), gas generation (Sect. 7.3), pressure (Sect. 7.4), brine saturation (Sect. 7.5), and brine and gas outflow (Sect. 7.6). In each section, a number of specific results calculated by BRAGFLO are examined with techniques based on examination of scatterplots, partial correlation coefficients, and stepwise regression analyses (Sect. 6.10). The specific BRAGFLO results considered in Chapt. 7 are listed in Table 7.1.1, which can be used to obtain exact definitions of the individual variables under consideration.

The sensitivity analysis results presented in this chapter and in other similar chapters will be based on all 300 observations (i.e., replicates R1, R2 and R3 will be pooled for the performance of sensitivity analyses with scatterplots, correlation coefficients and stepwise regression analyses). This will permit the sensitivity analysis results to be based on all available information. Similarly, summaries of uncertainty based on box plots will also use all 300 observations. In contrast, distributions of time-dependent results, and also CCDFs in later chapters, will typically be shown for only replicate R1 to avoid the presentation of plots with so many individual curves that they are unreadable. However, mean and percentile curves will typically be obtained from all 300 observations.

Table 7.1.1. Results Calculated by BRAGFLO Considered in Uncertainty and Sensitivity Analyses for Fluid Flow in the Vicinity of the Repository under Undisturbed (i.e., E0) Conditions

Result	Description
BRAABNIC	Cumulative brine flow (m^3) out of north anhydrites A and B into DRZ (i.e., from Cell 556 to Cell 527 in Fig. 4.2.3)
BRAABNLW	Cumulative brine flow (m^3) in north anhydrites A and B across land withdrawal boundary (i.e., from Cell 561 to Cell 562 in Fig. 4.2.3)
BRAABNOC	Cumulative brine flow (m^3) out of DRZ into north anhydrites A and B (i.e., from Cell 527 to Cell 556 in Fig. 4.2.3)
BRAABSLW	Cumulative brine flow (m^3) in south anhydrites A and B across land withdrawal boundary (i.e., from Cell 550 to Cell 549 in Fig. 4.2.3)
BRAABSOC	Cumulative brine flow (m^3) out of DRZ into south anhydrites A and B (i.e., from Cell 482 to Cell 555 in Fig. 4.2.3)

Table 7.1.1. Results Calculated by BRAGFLO Considered in Uncertainty and Sensitivity Analyses for Fluid Flow in the Vicinity of the Repository under Undisturbed (i.e., E0) Conditions (Continued)

Result	Description
BRAALLW	Cumulative brine flow (m^3) in all MBs across land withdrawal boundary (i.e., *BRM38NLW* + *BRAABNLW* + *BRM39NLW* + *BRM38SNLW* + *BRAABNLW* + *BRM39SLW*)
BRAALOC	Cumulative brine flow (m^3) out of DRZ into all MBs (i.e., *BRM38NOC* + *BRAABNOC* + *BRM39NOC* + *BRM38SNOC* + *BRAABNOC* + *BRM39SOC*)
BRM38NLW	Cumulative brine flow (m^3) in north MB138 across land withdrawal boundary (i.e., from Cell 593 to Cell 594 in Fig. 4.2.3)
BRM38NOC	Cumulative brine flow (m^3) out of DRZ into north MB138 (i.e., from Cell 587 to Cell 588 in Fig. 4.2.3)
BRM38SIC	Cumulative brine flow (m^3) out of south MB138 into DRZ (i.e., from Cell 571 to Cell 572 in Fig. 4.2.3)
BRM38SLW	Cumulative brine flow (m^3) in south MB138 across land withdrawal boundary (i.e., from Cell 566 to Cell 565 in Fig. 4.2.3)
BRM38SOC	Cumulative brine flow (m^3) out of DRZ into south MB138 (i.e., from Cell 572 to Cell 571 in Fig. 4.2.3)
BRM39NIC	Cumulative brine flow (m^3) out of north MB139 into DRZ (i.e., from Cell 540 to Cell 465 in Fig. 4.2.3)
BRM39NLW	Cumulative brine flow (m^3) in north MB139 across land withdrawal boundary (i.e., from Cell 545 to Cell 546 in Fig. 4.2.3)
BRM39NOC	Cumulative brine flow (m^3) out of DRZ into north MB139 (i.e., from Cell 465 to Cell 540 in Fig. 4.2.3)
BRM39SIC	Cumulative brine flow (m^3) out of south MB139 into DRZ (i.e., from Cell 539 to Cell 436 in Fig. 4.2.3)
BRM39SLW	Cumulative brine flow (m^3) in south MB139 across land withdrawal boundary (i.e., from Cell 534 to Cell 533 in Fig. 4.2.3)
BRM39SOC	Cumulative brine flow (m^3) out of DRZ into south MB139 (i.e., from Cell 436 to Cell 539 in Fig. 4.2.3)
BRN_DNSH	Cumulative brine flow (m^3) down shaft at upper boundary of DRZ (i.e., from Cell 654 to Cell 653 in Fig. 4.2.3)
BRN_RMV	Cumulative brine (m^3) consumed in repository by corrosion (i.e., in Cells 596-625 in Fig. 4.2.3)
BRNVOL_R	Brine volume (m^3) in upper waste panels (i.e., in Cells 617-625 in Fig. 4.2.3)
BRNVOL_W	Brine volume (m^3) in lower waste panels (i.e., in Cells 596-616 in Fig. 4.2.3)

Table 7.1.1. Results Calculated by BRAGFLO Considered in Uncertainty and Sensitivity Analyses for Fluid Flow in the Vicinity of the Repository under Undisturbed (i.e., E0) Conditions (Continued)

Result	Description
BRNREPTC	Cumulative brine flow (m^3) into repository (ie., into region corresponding to Cells 596-625, 638-640 in Fig. 4.2.3)
BRNSHUC	Cumulative brine flow (m^3) up shaft at boundary between Salado and Rustler Formations (i.e., from Cell 660 to Cell 661 in Fig. 4.2.3)
BSCL8AOC	Cumulative brine flow (m^3) up shaft at boundary of DRZ and intact halite (i.e., from Cell 653 to Cell 654)
CELL_KG	Mass of cellulose (kg) in repository (i.e., in Cells 596-625 in Fig. 4.2.3)
CELL_M_H	Cumulative gas generation (mol) in repository due to microbial degradation of cellulose under inundated conditions (i.e., in Cells 596-625 in Fig. 4.2.3)
CELL_M_I	Cumulative gas generation (mol) in repository due to microbial degradation of cellulose under inundated conditions (i.e., in Cells 596-625 in Fig. 4.2.3)
CELL_MOL	Cumulative gas generation (mol) in repository due to microbial degradation of cellulose (i.e., CELL_M_H + CELL_M_I)
FE_KG	Mass of steel (kg) in repository (i.e., in Cells 596-625 in Fig. 4.2.3)
FE_MOLE	Cumulative gas generation (mol) in repository due to corrosion (i.e., in Cells 596-625 in Fig. 4.2.3)
FEREM_R	Fraction of steel remaining in upper waste panels (i.e., in Cells 617-625 in Fig. 4.2.3)
FEREM_W	Fraction of steel remaining in lower waste panel (i.e., in Cells 596-616 in Fig. 4.2.3)
FRACXABN	Length (m) of fractured zone in north anhydrites A and B (i.e., in Cells 556-563 in Fig. 4.2.3)
FRACXABS	Length (m) of fractured zone in south anhydrites A and B (i.e., in Cells 548-555 in Fig. 4.2.3)
FRACX38N	Length (m) of fractured zone in north MB 138 (i.e., in Cells 588-595 in Fig. 4.2.3)
FRACX38S	Length (m) of fractured zone in south MB 138 (i.e., in Cells 564-571 in Fig. 4.2.3)
FRACX39N	Length (m) of fractured zone in north MB 139 (i.e., in Cells 540-547 in Fig. 4.2.3)
FRACX395	Length (m) of fracturez zone in south MB 139 (i.e., in Cells 532-539 in Fig. 4.2.3)
GAS_MOLE	Total cumulative gas generation in repository (i.e., FE_MOLE + CELL_MOL)
GASMOL_R	Cumulative gas generation (mol) in upper waste panels due to corrosion and microbial degradation (i.e., in Cells 617-625 in Fig. 4.2.3)
GASMOL_W	Cumulative gas generation (mol) in lower waste panel due to corrosion and microbial degradation (i.e., in Cells 596-616 in Fig. 4.2.3)

Table 7.1.1. Results Calculated by BRAGFLO Considered in Uncertainty and Sensitivity Analyses for Fluid Flow in the Vicinity of the Repository under Undisturbed (i.e., E0) Conditions (Continued)

Result	Description
GSAABNIM	Cumulative gas flow (mol) out of north anhydrites A and B into DRZ (i.e., from Cell 556 to Cell 527 in Fig. 4.2.3)
GSAABNOC	Cumulative gas flow (mol) out of DRZ into north anhydrites A and B (i.e., from Cell 527 to Cell 556 in Fig. 4.2.3)
GSAABSIM	Cumulative gas flow (mol) out of south anhydrites A and B into DRZ (i.e., from Cell 555 to Cell 482 in Fig. 4.2.3)
GSAABSOC	Cumulative gas flow (mol) out of DRZ into south anhydrites A and B (i.e., from Cell 482 to Cell 555 in Fig. 4.2.3)
GSAALIM	Cumulative gas flow (mol) out of all MBs into DRZ (i.e., *GSM38NIM* + *GSAABNIM* + *GSM39NIM* + *GSM38SNIM* + *GSAABNIM* + *GSM39SIM*)
GSAALOM	Cumulative gas flow (mol) out of DRZ into all MBs (i.e., *GSM38NOC* + *GSAABNOC* + *GSM39NOC* + *GSM38SNOC* + *GSAABNOC* + *GSM39SOC*)
GSM38NIM	Cumulative gas flow (mol) out of north MB138 into DRZ (i.e., from Cell 588 to Cell 587 in Fig. 4.2.3)
GSM38NOC	Cumulative gas flow (mol) out of DRZ into north MB138 (i.e., from Cell 587 to Cell 588 in Fig. 4.2.3)
GSM38SIM	Cumulative gas flow (mol) out of south MB138 into DRZ (i.e., from Cell 571 to Cell 572 in Fig. 4.2.3)
GSM38SOC	Cumulative gas flow (mol) out of DRZ into south MB138 (i.e., from Cell 572 to Cell 571 in Fig. 4.2.3)
GSM39NIM	Cumulative gas flow (mol) out of north MB139 into DRZ (i.e., from Cell 540 to Cell 465 in Fig. 4.2.3)
GSM39NOC	Cumulative gas flow (mol) out of DRZ into north MB139 (i.e., from Cell 465 to Cell 540 in Fig. 4.2.3)
GSM39SIM	Cumulative gas flow (mol) out of south MB139 into DRZ (i.e., from Cell 539 to Cell 436 in Fig. 4.2.3)
GSM39SOC	Cumulative gas flow (mol) out of DRZ into south MB139 (i.e., from Cell 436 to Cell 539 in Fig. 4.2.3)
GSMSHUPC	Cumulative gas flow (mol) up shaft at boundary between Salado and Rustler Formations (i.e., from Cell 660 to Cell 661 in Fig. 4.2.3)
PORVOL_R	Pore volume (m^3) in upper waste panels (i.e., in Cells 617-625 in Fig. 4.2.3)
PORVOL_T	Total pore volume (m^3) in repository (i.e., in Cells 596-625 in Fig. 4.2.3)
PORVOL_W	Pore volume (m^3) in lower waste panels (i.e., in Cells 596-616 in Fig. 4.2.3)

Table 7.1.1. Results Calculated by BRAGFLO Considered in Uncertainty and Sensitivity Analyses for Fluid Flow in the Vicinity of the Repository under Undisturbed (i.e., E0) Conditions (Continued)

Result	Description
PVOLI_T	Pore volume increase (m^3) due to fracturing in all MBs (i.e., *PVOLI38N* + *PVOLIABN* + *PVOLI39N* + *PVOLI38S* + *PVOLIABS* + *PVOLI39S*)
PVOLIABN	Pore volume increase (m^3) due to fracturing in north anhydrites A and B (i.e., in Cells 556-563 in Fig. 4.2.3)
PVOLIABS	Pore volume increase (m^3) due to fracturing in south anhydrites A and B (i.e., in Cells 548-555 in Fig. 4.2.3)
PVOLI38N	Pore volume increase (m^3) due to fracturing in north MB138 (i.e., in Cells 588-595 in Fig. 4.2.3)
PVOLI38S	Pore volume increase (m^3) due to fracturing in south MB138 (i.e., in Cells 564-571 in Fig. 4.2.3)
PVOLI39N	Pore volume increase (m^3) due to fracturing in north MB139 (i.e., in Cells 540-547 in Fig. 4.2.3)
PVOLI39S	Pore volume increase(m^3) due to fracturing in south MB139 (i.e., in Cells 532-539 in Fig. 4.2.3)
REP_PRES	Pressure (Pa) in upper waste panels (i.e., average pressure calculated over Cells 617-625 in Fig. 4.2.3)
REP_SATB	Brine saturation in upper waste panels (i.e., average brine saturation calculated over Cells 617-625 in Fig. 4.2.3)
WAS_PRES	Pressure (Pa) in lower waste panel (i.e., average pressure calculated over Cells 596-616 in Fig. 4.2.3)
WAS_SATB	Brine saturation in lower waste panel (i.e., average brine saturation calculated over Cells 596-616 in Fig. 4.2.3)

7.2 Undisturbed Conditions: Brine Inflow

The anhydrite marker beds (Fig. 4.2.1) provide the only significant pathway by which brine can flow from the Salado Formation to the repository from areas beyond the DRZ, with this flow tending to take place at a relatively constant rate (Fig. 7.2.1). However, the dominant source of brine into the repository is drainage from the DRZ, which primarily takes place over the first 50 to 100 yr of the calculation due to the enhanced permeability of the DRZ (i.e., 1×10^{-15} m^2) over that of the original, undisturbed halite (i.e., *HALPRM*) (Fig. 7.2.1). The highest cumulative brine inflow in Fig. 7.2.1 results for the sample element (i.e., element 23 in replicate R1) that has the

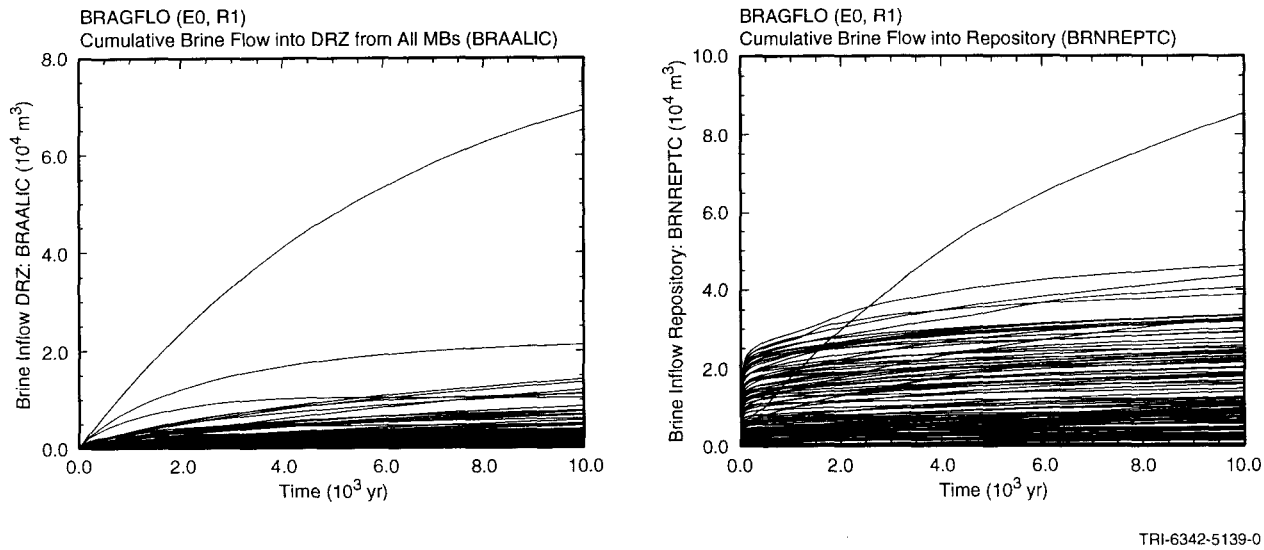

Fig. 7.2.1 Cumulative brine flow into DRZ (*BRAALIC*) and into repository (*BRNREPTC*) under undisturbed conditions.

second highest value for anhydrite permeability (i.e., *ANHPRM* = 7.94×10^{-18} m^2) and also one of the higher brine far-field pore pressures (i.e., *SALPRES* = 1.31×10^7 Pa).

The brine inflows from the anhydrite marker beds can occur from MB 138, anhydrites a and b, and MB 139 at both the northern and southern ends of the computational grid (Fig. 4.2.1). As shown by the box plots (Iman and Conover 1983) in Fig 7.2.2, the flow from MB 139 exceeds the flow from anhydrites a and b, which in turn exceeds the flow from MB 138. For a given marker bed, the flows from the north tend to be smaller than the flows from the south (Fig. 7.2.2). As already noted, total inflow to the repository exceeds total flow from the marker beds because of drainage from the DRZ.

Box plots (Fig. 7.2.2) provide an alternative way to display the information in a distribution function. The endpoints of the boxes are formed by the lower and upper quartiles of the data, that is $x_{0.25}$ and $x_{0.75}$. The vertical line within the box represents the median, $x_{0.50}$. The mean is identified by the large dot. The bar on the right of the box extends to the minimum of $x_{0.75} + 1.5(x_{0.75} - x_{0.25})$ and the maxium value. In a similar manner, the bar on the left of the box extends to the maximum of $x_{0.25} - 1.5(x_{0.75} - x_{0.25})$ and the minimum value. The observations falling outside of these bars are shown with crosses. In symmetric distributions, these values would be considered outliers. Box plots contain the same information as a distribution function, but in a somewhat reduced form. Further, their flattened shape makes it convenient to place many distirbutions on a single plot and also to compare different distirbutions.

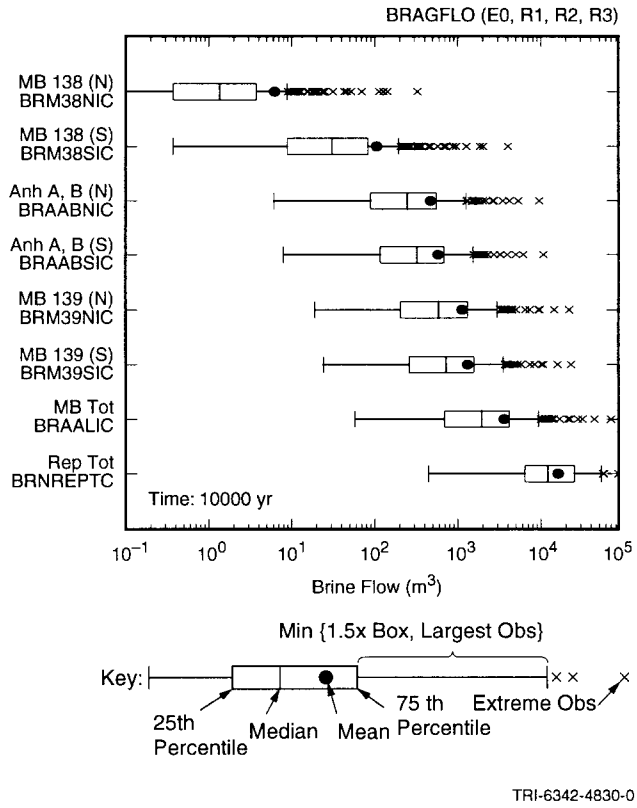

Fig. 7.2.2 Cumulative brine flow over 10,000 yr into DRZ (*BRM38NIC*, *BRM38SIC*, *BRAABNIC*, *BRAABSIC*, *BRM39NIC*, *BRM39SIC*, and *BRAALIC*) and into repository (*BRNREPTC*) under undisturbed conditions.

As examination of Figs. 7.2.1 and 7.2.2 shows, considerable uncertainty exists with respect to the amount of brine that will flow out of the marker beds and into the repository. The performance of a regression analysis between cumulative brine flow (Fig. 7.2.2) and variables in the LHS provides one way to assess the contribution of individual variables to this uncertainty, with variable importance being indicated by the order in which variables enter the regression model, the changes in R^2 values as additional variables enter the regression model, and the standardized regression coefficients of the variables in the final regression model (Table 7.2.1). The candidate independent variables for the regression analyses in Table 7.2.1 consist of the 31 variables in Table 5.2.1 that are used as input to BRAGFLO (i.e., *ANHBCEXP*, *ANHBCVGP*, *ANRBRSAT*, *ANHCOMP*, *ANHPRM*, *ANRGSSAT*, *BHPRM*, *BPCOMP*, *BPINTPRS*, *BPPRM*, *BPVOL*, *HALCOMP*, *HALPOR*, *HALPRM*, *SALPRES*, *SHBCEXP*, *SHPRMASP*, *SHPRMCLY*, *SHPRMCON*, *SHPRMDRZ*, *SHPRMHAL*, *SHRBRSAT*, *SHRGSSAT*, *WASTWICK*, *WFBETCEL*, *WGRCOR*, *WGRMICH*, *WGRMICI*, *WMICDFLG*, *WRBRNSAT* and *WRGSSAT*). Further, the outcomes of all three replicates were pooled, with the result that the individual regression analyses are based on 300 observations. For the results presented in Table 7.2.1 and other similar tables, variables were required to be significant at the 0.02 α-level to enter a regression model and to remain significant at the 0.05 α-level to be retained in a regression model.

Table 7.2.1. Stepwise Regression Analyses with Rank-Transformed Data for Cumulative Brine Flow over 10,000 yr into DRZ (*BRM38NIC, BRM38SIC, BRAABNIC, BRAABSIC, BRM39NIC, BRM39SIC, BRAALIC*) and into repository (*BRNREPTC*) under Undisturbed Conditions

	MB 138 North: *BRM38NIC*			MB 138 South: *BRM38SIC*			Anh a and b North: *BRAABNIC*			Anh a and b South: *BRAABSIC*		
Step[a]	Variable[b]	SRRC[c]	R^{2d}	Variable	SRRC	R^2	Variable	SRRC	R^2	Variable	SRRC	R^2
1	*ANHPRM*	0.75	0.54	*ANHPRM*	0.73	0.51	*WMICDFLG*	−0.66	0.43	*WMICDFLG*	−0.66	0.43
2	*WMICDFLG*	−0.52	0.80	*WMICDFLG*	−0.55	0.80	*ANHPRM*	0.60	0.79	*ANHPRM*	0.59	0.77
3	*HALCOMP*	0.21	0.84	*HALCOMP*	0.18	0.83	*HALPOR*	−0.15	0.81	*HALPOR*	−0.16	0.80
4	*HALPOR*	−0.11	0.86	*WGRCOR*	−0.13	0.85	*WGRCOR*	−0.16	0.84	*WGRCOR*	−0.16	0.83
5	*WGRCOR*	−0.12	0.87	*HALPOR*	−0.11	0.86	*SALPRES*	0.11	0.85	*SALPRES*	0.11	0.84
6	*SALPRES*	0.11	0.88	*SALPRES*	0.10	0.87	*WASTWICK*	−0.09	0.86	*HALPRM*	0.54	0.85
7	*WASTWICK*	−0.08	0.89	*WASTWICK*	−0.08	0.88	*HALPRM*	0.49	0.87	*WASTWICK*	−0.09	0.86
8	*WGRMICI*	−0.06	0.89	*WGRMICI*	−0.06	0.88	*HALCOMP*	0.40	0.87	*HALCOMP*	0.43	0.86
9	*SHRGSSAT*	−0.04	0.90	*SHRGSSAT*	−0.05	0.88	*SHRGSSAT*	−0.05	0.87	*SHRGSSAT*	−0.05	0.87

	MB 139 North: *BRM39NIC*			MB 139 South: *BRM39SIC*			MBs Total: *BRAALIC*			Repository Total: *BRNREPTC*		
Step	Variable	SRRC	R^2	Variable	SRRC	R^2	Variable	SRRC	R^2	Variable	SRRC	R^2
1	*WMICDFLG*	−0.65	0.42	*WMICDFLG*	−0.65	0.43	*WMICDFLG*	−0.65	0.43	*HALPOR*	0.88	0.77
2	*ANHPRM*	0.59	0.78	*ANHPRM*	0.57	0.75	*ANHPRM*	0.59	0.78	*WMICDFLG*	−0.26	0.85
3	*HALPOR*	−0.16	0.80	*HALPRM*	0.55	0.79	*HALPOR*	−0.16	0.80	*ANHPRM*	0.60	0.88
4	*HALPRM*	0.52	0.83	*HALPOR*	−0.16	0.81	*WGRCOR*	−0.15	0.82	*HALCOMP*	−0.09	0.89
5	*WGRCOR*	−0.15	0.85	*WGRCOR*	−0.15	0.84	*HALPRM*	0.51	0.85	*WRBRNSAT*	−0.09	0.89
6	*SALPRES*	0.12	0.86	*SALPRES*	0.12	0.85	*SALPRES*	0.12	0.86	*WGRCOR*	−0.08	0.90
7	*WASTWICK*	−0.10	0.87	*WASTWICK*	−0.10	.086	*WASTWICK*	−0.10	0.87	*ANHCOMP*	0.43	0.91
8	*HALCOMP*	0.37	0.88	*HALCOMP*	0.37	0.86	*HALCOMP*	0.37	0.87	*WASTWICK*	−0.06	0.91

[a] Steps in stepwise regression analysis.

[b] Variables listed in order of selection in regression analysis.

[c] Standardized rank regression coefficients in final regression model.

[d] Cumulative R^2 value with entry of each variable into regression model.

The regression analyses in Table 7.2.1 are all relatively successful in the sense that they have R^2 values between 0.86 and 0.91. However, close inspection of the individual regression analyses indicates that there is an undesirable complication that results from the rank correlations of −0.99 that are assigned to the variable pairs (*ANHPRM, ANHCOMP*) and (*HALPRM, HALCOMP*) (Table 5.2.1). When no correlations exist between the sampled variables in the regression model, the regression coefficients will decrease monotonically in absolute value. In this case, an ordering of the variables by the absolute value of their regression coefficients provides a way to rank variable importance. However, when correlated variables are included in a regression model, the sizes and even the signs of the associated regression coefficients may not properly indicate the effects of these variables. This behavior appears in Table 7.2.1 for the pair (*HALPRM, HALCOMP*) in the regressions for Anhydrites a and b North, Anhydrites a and b South, MB 139 North, MB 139 South and MBs Total, and for the pair (*ANHPRM, ANHCOMP*) in the regression for Repository Total. In particular, the existence of the strong correlations within the pairs (*HALPRM, HALCOMP*) and (*ANHPRM, ANHCOMP*) results in a nonmonotonic behavior of the associated regression coefficients.

As a more detailed example, explicit representations of the following three regression analyses for MBs total are shown in Table 7.2.2: (1) all 31 sampled variables allowed as candidates for inclusion in the regression model, (2) *ANHCOMP* and *HALCOMP* excluded as candidates for inclusion in the regression model, and (3) *ANHPRM* and *HALPRM* excluded as candidates for inclusion in the regression model. When all sampled variables are included as candidates, the regression coefficients decrease monotonically until Step 8, when *HALCOMP* enters the regression model. With entry of *HALCOMP*, the regression coefficient for *HALPRM* jumps from a value of 0.14 at Step 7 to a value of 0.51; further, *HALCOMP* has a regression coefficient of 0.37 even though it has essentially no effect on the R^2 value for the regression model (i.e., $R^2 = 0.86889$ at Step 7 and $R^2 = 0.87203$ at Step 8). When *ANHCOMP* and *HALCOMP* are excluded as candidates for entry into the regression model, a sequence of 7 regression models are produced that are identical to the first 7 regression models that are produced when all variables are allowed as candidates for inclusion. However, a different sequence of regression models is constructed when *ANHPRM* and *HALPRM* are excluded. In this case, *ANHPRM* and *HALPRM* are replaced in the regression models with *ANHCOMP* and *HALCOMP* and the signs of the regression coefficients are reversed. Thus, *ANHCOMP* and *HALCOMP* appear with negative regression coefficients where *ANHPRM* and *HALPRM* appear with positive regression coefficients. In contrast, *HALPRM* and *HALCOMP* both have positive regression coefficients when they appear together in the regression model constructed at Step 8 when all variables are included as candidates for entry into the analysis. Thus, care must be used in interpreting regression analyses that involve highly correlated variables.

For perspective, Tables 7.2.3 and 7.2.4 present regression analyses for the same cumulative brine flows considered in Table 7.2.1, but with *ANHCOMP* and *HALCOMP* excluded in Table 7.2.3 and *ANHPRM* and *HALPRM* excluded in Table 7.2.4. In general, the variables in the pairs (*ANHPRM*, *ANHCOMP*) and (*HALPRM*, *HALCOMP*) tend to be exchangeable with a reverse in the sign of the regression coefficient. Due to their important role in influencing fluid flow, the two permeabilities *ANHPRM* and *HALPRM* are probably the more basic variables. Therefore, the following discussion of sensitivity will emphasize the results in Table 7.2.3. However, with the assigned correlations of −0.99, the variables in the pairs (*ANHPRM*, *ANHCOMP*) and (*HALPRM*, *HALCOMP*) are almost interchangeable in a sensitivity analysis.

For brine inflow from the marker beds, the two dominant variables in the regression analyses in Table 7.2.3 are *WMICDFLG* and *ANHPRM*. The negative effect indicated for *WMICDFLG* results because increasing *WMICDFLG* increases gas generation and thus pressure in the repository, which in turn increases resistance to brine flow out of the marker beds. The positive effect indicated for *ANHPRM* results from decreased resistance to brine flow in the marker beds. Small negative effects are indicated for *HALPOR*, *WASTWICK*, *WGRCOR* and *WGRMICI*, with these effects resulting because each of these variables tends to increase gas generation and thus resistance to brine flow out of the marker beds due to increased repository pressure. The variable *HALPOR* will be discussed in more detail in

Table 7.2.2. Detailed Stepwise Regression Analyses with Rank-Transformed Data for Cumulative Brine Flow From all Marker Beds (*BRAALIC*) over 10,000 yr under Undisturbed Conditions

All Variables Included		*ANHCOMP* *HALCOMP* Excluded		*ANHPRM* *HALPRM* Excluded	
Variable[a]	SRRC[b]	Variable	SRRC	Variable	SRRC
Step 1					
WMICDFLG	−0.65	*WMICDFLG*	−0.65	*WMICDFLG*	−0.65
R^{2c}	0.43	R^2	0.43	R^2	0.43
Step 2					
WMICDFLG	−0.66	*WMICDFLG*	−0.66	*WMICDFLG*	−0.67
ANHPRM	0.59	*ANHPRM*	0.59	*ANHCOMP*	−0.58
R^2	0.77	R^2	0.77	R^2	0.76
Step 3					
WMICDFLG	−0.66	*WMICDFLG*	−0.66	*WMICDFLG*	−0.67
ANHPRM	0.59	*ANHPRM*	0.59	*ANHCOMP*	−0.58
HALPOR	−0.16	*HALPOR*	−0.16	*HALPOR*	−0.16
R^2	0.80	R^2	0.80	R^2	0.79
Step 4					
WMICDFLG	−0.66	*WMICDFLG*	−0.66	*WMICDFLG*	−0.66
ANHPRM	0.60	*ANHPRM*	0.60	*ANHCOMP*	−0.58
HALPOR	−0.16	*HALPOR*	−0.16	*HALPOR*	−0.16
WGRCOR	−0.15	*WGRCOR*	−0.15	*WGRCOR*	−0.15
R^2	0.82	R^2	0.82	R^2	0.81
Step 5					
WMICDFLG	−0.65	*WMICDFLG*	−0.65	*WMICDFLG*	−0.66
ANHPRM	0.59	*ANHPRM*	0.59	*ANHCOMP*	−0.58
HALPOR	−0.16	*HALPOR*	−0.16	*HALPOR*	−0.16
WGRCOR	−0.15	*WGRCOR*	−0.15	*WGRCOR*	−0.15
HALPRM	0.15	*HALPRM*	0.15	*HALCOMP*	−0.14
R^2	0.85	R^2	0.85	R^2	0.83

All Variables		*ANHCOMP* *HALCOMP* Excluded		*ANHPRM* *HALPRM* Excluded	
Variable	SRRC	Variable	SRRC	Variable	SRRC
Step 6					
WMICDFLG	−0.66	*WMICDFLG*	−0.66	*WMICDFLG*	−0.66
ANHPRM	0.59	*ANHPRM*	0.59	*ANHCOMP*	−0.59
HALPOR	−0.16	*HALPOR*	−0.16	*HALPOR*	−0.16
WGRCOR	−0.15	*WGRCOR*	−0.15	*WGRCOR*	−0.15
HALPRM	0.14	*HALPRM*	0.14	*HALCOMP*	−0.14
SALPRES	0.12	*SALPRES*	0.12	*SALPRES*	0.13
R^2	0.86	R^2	0.86	R^2	0.85
Step 7					
WMICDFLG	−0.66	*WMICDFLG*	−0.66	*WMICDFLG*	−0.66
ANHPRM	0.59	*ANHPRM*	0.59	*ANHCOMP*	−0.58
HALPOR	−0.16	*HALPOR*	−0.16	*HALPOR*	−0.16
WGRCOR	−0.15	*WGRCOR*	−0.15	*WGRCOR*	−0.15
HALPRM	0.14	*HALPRM*	0.14	*HALCOMP*	−0.14
SALPRES	0.12	*SALPRES*	0.12	*SALPRES*	0.13
WASTWICK	−0.10	*WASTWICK*	−0.10	*WASTWICK*	−0.09
R^2	0.87	R^2	0.87	R^2	0.85
Step 8					
WMICDFLG	−0.65				
ANHPRM	0.59				
HALPOR	−0.16				
WGRCOR	−0.15				
HALPRM	0.51				
SALPRES	0.12				
WASTWICK	−0.10				
HALCOMP	0.37				
R^2	0.87				

[a] Variables in regression model

[b] Standardized rank regression coefficients for variables in regression model

[c] R^2 values for regression model

Table 7.2.3 Stepwise Regression Analyses with Rank-Transformed Data for Cumulative Brine Flow over 10,000 yr into DRZ (*BRM38NIC*, *BRM38SIC*, *BRAABNIC*, *BRAABSIC*, *BRM39NIC*, *BRM29SIC*, *BRAALIC*) and into repository (*BRNREPTC*) under Undisturbed Conditions with Variables *ANHCOMP* and *HALCOMP* Excluded from Entry into Regression Model

	MB 138 North: *BRM38NIC*			MB 138 South: *BRM38SIC*			Anh a and b North: *BRAABNIC*			Anh a and b South: *BRAABSIC*		
Step[a]	Variable[b]	SRRC[c]	R^{2d}	Variable	SRRC	R^2	Variable	SRRC	R^2	Variable	SRRC	R^2
1	*ANHPRM*	0.75	0.54	*ANHPRM*	0.73	0.51	*WMICDFLG*	−0.72	0.43	*WMICDFLG*	−0.66	0.43
2	*WMICDFLG*	−0.52	0.80	*WMICDFLG*	−0.55	0.80	*ANHPRM*	0.60	0.79	*ANHPRM*	0.59	0.77
3	*HALPRM*	−0.20	0.84	*HALPRM*	−0.18	0.83	*HALPOR*	−0.15	0.81	*HALPOR*	−0.16	0.80
4	*HALPOR*	−0.12	0.86	*WGRCOR*	−0.12	0.85	*WGRCOR*	−0.16	0.84	*WGRCOR*	−0.16	0.83
5	*WGRCOR*	−0.12	0.87	*HALPOR*	−0.11	0.86	*SALPRES*	0.12	0.85	*SALPRES*	0.11	0.84
6	*SALPRES*	0.11	0.88	*SALPRES*	0.10	0.87	*WASTWICK*	−0.09	0.86	*HALPRM*	0.11	0.85
7	*WASTWICK*	−0.08	0.89	*WASTWICK*	−0.08	0.88	*HALPRM*	0.09	0.87	*WASTWICK*	−0.09	0.86
8	*WGRMICI*	−0.06	0.89	*WGRMICI*	−0.06	0.88	*SHRGSSAT*	−0.05	0.87	*SHRGSSAT*	−0.05	0.86

	MB 139 North: *BRM39NIC*			MB 139 South: *BRM39SIC*			MBs Total: *BRAALIC*			Repository Total: *BRNREPTC*		
Step	Variable	SRRC	R^2	Variable	SRRC	R^2	Variable	SRRC	R^2	Variable	SRRC	R^2
1	*WMICDFLG*	−0.65	0.42	*WMICDFLG*	−0.65	0.43	*WMICDFLG*	−0.66	0.43	*HALPOR*	0.88	0.77
2	*ANHPRM*	0.60	0.78	*ANHPRM*	0.57	0.75	*ANHPRM*	0.59	0.75	*WMICDFLG*	−0.26	0.85
3	*HALPOR*	−0.16	0.80	*HALPRM*	0.19	0.79	*HALPOR*	−0.16	0.80	*ANHPRM*	0.18	0.88
4	*HALPRM*	0.15	0.83	*HALPOR*	−0.16	0.81	*WGRCOR*	−0.15	0.82	*WRBRNSAT*	−0.09	0.89
5	*WGRCOR*	−0.15	0.85	*WGRCOR*	−0.15	0.84	*HALPRM*	0.14	0.85	*HALPRM*	0.09	0.89
6	*SALPRES*	0.12	0.86	*SALPRES*	0.12	0.85	*SALPRES*	0.12	0.86	*WGRCOR*	−0.08	0.90
7	*WASTWICK*	−0.10	0.87	*WASTWICK*	−0.10	0.86	*WASTWICK*	−0.10	0.87	*WASTWICK*	−0.06	0.90

[a] Steps in stepwise regression analysis.

[b] Variables listed in order of selection in regression analysis.

[c] Standardized rank regression coefficients in final regression model.

[d] Cumulative R^2 value with entry of each variable into regression model.

conjunction with total brine flow into the repository. A small positive effect is indicated for *SALPRES*, with this effect resulting because increasing *SALPRES* tends to increase the pressure gradient between the marker beds and the repository.

The variable *HALPRM* appears with negative regression coefficients for brine flow out of MB 138 North and MB 138 South and appears with positive regression coefficients for brine flow out of Anhydrites a and b North, Anhydrites a and b South, MB 139 North and MB 139 South. The reason for this behavior is not immediately apparent but is probably related to the assigned correlations between permeability and compressibility and the complex interactions between permeability and compressibility in determining brine flow into and through the marker beds. All things being equal, increasing *HALPRM* should reduce resistance to flow in the halite and, as a result, increase brine inflow to the marker beds and thus to the repository. Similarly, increasing *HALCOMP* should increase brine discharge from the halite for a given drop in pressure and, as a result, increase brine inflow to the marker beds and thus to the repository. Thus, *HALPRM* and *HALCOMP* should both have positive effects on brine

discharge from the marker beds to the repository. The appearance of *HALPRM* in Table 7.2.3 with both positive and negative effects on brine discharge probably results from the –0.99 rank correlation between *HALPRM* and *HALCOMP*, which produced a complex pattern of correlations between *HALPRM*, *HALCOMP* and brine discharge (Table 7.2.5).

It is not immediately apparent why *SHRGSSAT* appears in Table 7.2.3 for brine flow out of Anhydrites a and b. The effect of *SHRGSSAT* is very small (i.e., the change in the R^2 values with its addition is < 0.01) and its selection may be due to effects related to brine and gas movement across the part of the computational grid that corresponds to the shaft in the repository and DRZ (i.e., regions 10, 11 in Fig. 4.2.1). It is also possible that the effect may be spurious.

Table 7.2.4. Stepwise Regression Analyses with Rank-Transformed Data for Cumulative Brine Flow over 10,000 yr into DRZ (*BRM38NIC*, *BRM38SIC*, *BRAABNIC*, *BRAABSIC*, *BRM39NIC*, *BRM29SIC*, *BRAALIC*) and into repository (*BRNREPTC*) under Undisturbed Conditions with Variables *ANHPRM* and *HALPRM* Excluded from Entry into the Regression Model

	MB 138 North: *BRM38NIC*			MB 138 South: *BRM38SIC*			Anh a and b North: *BRAABNIC*			Anh a and b South: *BRAABSIC*		
Step[a]	Variable[b]	SRRC[c]	R^2[d]	Variable	SRRC	R^2	Variable	SRRC	R^2	Variable	SRRC	R^2
1	*ANHCOMP*	–0.74	0.52	*ANHCOMP*	–0.72	0.50	*WMICDFLG*	–0.66	0.43	*WMICDFLG*	–0.66	0.43
2	*WMICDFLG*	–0.53	0.79	*WMICDFLG*	–0.55	0.79	*ANHCOMP*	–0.59	0.77	*ANHCOMP*	–0.58	0.76
3	*HALCOMP*	0.20	0.83	*HALCOMP*	0.17	0.82	*HALPOR*	–0.16	0.80	*HALPOR*	–0.16	0.79
4	*SALPRES*	0.12	0.84	*WGRCOR*	–0.12	0.83	*WGRCOR*	–0.15	0.82	*WGRCOR*	–0.16	0.81
5	*HALPOR*	–0.12	0.86	*HALPOR*	–0.12	0.84	*SALPRES*	0.13	0.84	*SALPRES*	0.12	0.83
6	*WGRCOR*	–0.12	0.87	*SALPRES*	0.11	0.86	*WASTWICK*	–0.09	0.85	*HALCOMP*	–0.11	0.84
7	*WASTWICK*	–0.07	0.87	*WASTWICK*	–0.07	0.86	*HALCOMP*	–0.09	0.85	*WASTWICK*	–0.09	0.85
8	*WGRMICI*	–0.06	0.88	*WGRMICI*	–0.06	0.87						

	MB 139 North: *BRM39NIC*			MB 139 South: *BRM39SIC*			MBs Total: *BRAALIC*			Repository Total: *BRNREPTC*		
Step	Variable	SRRC	R^2	Variable	SRRC	R^2	Variable	SRRC	R^2	Variable	SRRC	R^2
1	*WMICDFLG*	–0.66	0.42	*WMICDFLG*	–0.66	0.43	*WMICDFLG*	–0.66	0.43	*HALPOR*	0.88	0.77
2	*ANHCOMP*	–0.59	0.76	*ANHCOMP*	–0.56	0.74	*ANHCOMP*	–0.58	0.76	*WMICDFLG*	–0.26	0.85
3	*HALPOR*	–0.16	0.79	*HALCOMP*	–0.18	0.77	*HALPOR*	–0.16	0.79	*ANHCOMP*	–0.16	0.87
4	*HALCOMP*	–0.15	0.81	*HALPOR*	–0.16	0.80	*WGRCOR*	–0.15	0.81	*HALCOMP*	–0.09	0.88
5	*WGRCOR*	–0.15	0.83	*WGRCOR*	–0.15	0.82	*HALCOMP*	–0.14	0.83	*WRBRNSAT*	–0.09	0.89
6	*SALPRES*	0.14	0.85	*SALPRES*	0.13	0.84	*SALPRES*	0.13	0.85	*WGRCOR*	–0.08	0.89
7	*WASTWICK*	–0.09	0.86	*WASTWICK*	–0.09	0.85	*WASTWICK*	–0.09	0.85	*WASTWICK*	–0.06	0.90

[a] Steps in stepwise regression analysis.

[b] Variables listed in order of selection in regression analysis.

[c] Standardized rnak regression coefficients in final regression model.

[d] Cumulative R^2 value with entry of each variable into regression model.

Table 7.2.5 Rank Correlations between *ANHPRM*, *ANHCOMP*, *HALPRM*, *HALCOMP* and Cumulative Brine Flow from the Marker Beds over 10,000 yr under Undisturbed Conditions

ANHPRM	1.0000			
ANHCOMP	−0.9887	1.0000		
HALPRM	0.0131	−0.0026	1.0000	
HALCOMP	−0.0084	−0.0021	−0.9836	1.0000
BRM38NIC	0.7343	−0.7222	−0.1670	0.1773
BRM38SIC	0.7162	−0.7036	−0.1384	0.1496
BRAABNIC	0.5890	−0.5740	0.1314	−0.1160
BRAABSIC	0.5769	−0.5621	0.1518	−0.1355
BRM39NIC	0.5840	−0.5670	0.1931	−0.1775
BRM39SIC	0.5599	−0.5429	0.2274	−0.2115
BRAALIC	0.5804	−0.5640	0.1850	−0.1694
	ANHPRM	*ANHCOMP*	*HALPRM*	*HALCOMP*

For total brine inflow to the repository, the dominant variable in the regression analysis is *HALPOR* (Table 7.2.3). The positive effect indicated for *HALPOR* results because increasing *HALPOR* increases the amount of brine in the DRZ that is available to drain downward into the repository. This increased brine results in greater gas generation due to corrosion and hence higher pressures in the repository. The association of higher pressures with increasing values for *HALPOR* is why *HALPOR* has a negative effect on brine flow from the marker beds to the repository. Specifically, increased repository pressure reduces the gradient between the marker beds and the repository and thus reduces the rate at which brine flows out of the marker beds. Smaller effects are indicated for *WMICDFLG* and *ANHPRM*. As previously discussed, increasing *WMICDFLG* reduces brine inflow from the marker beds by increasing pressure in the repository and increasing *ANHPRM* increases brine inflow from the marker beds by decreasing resistance to flow.

An alternative way to assess the sensitivity of analysis outcomes to uncertain inputs is by calculating partial rank correlation coefficients (PRCCs) between analysis outcomes and uncertain inputs. When the predicted outcomes are time dependent, the change in the PRCCs through time will indicate changing variable importance. The outcome of such an analysis for the brine flows in Fig. 7.2.1 is shown in Fig. 7.2.3. The variables *ANHCOMP* and *HALCOMP* have been excluded from the calculation of the PRCCs in Fig. 7.2.3. Due to the −0.99 rank correlation within the pairs (*ANHPRM*, *ANHCOMP*) and (*HALPRM*, *HALCOMP*), neither variable within a pair would appear in an analysis based on PRCCs. Fig. 7.2.3 and other similar figures in this presentation show the PRCCs for all variables whose PRCC exceeds 0.5 in absolute value at some point in time.

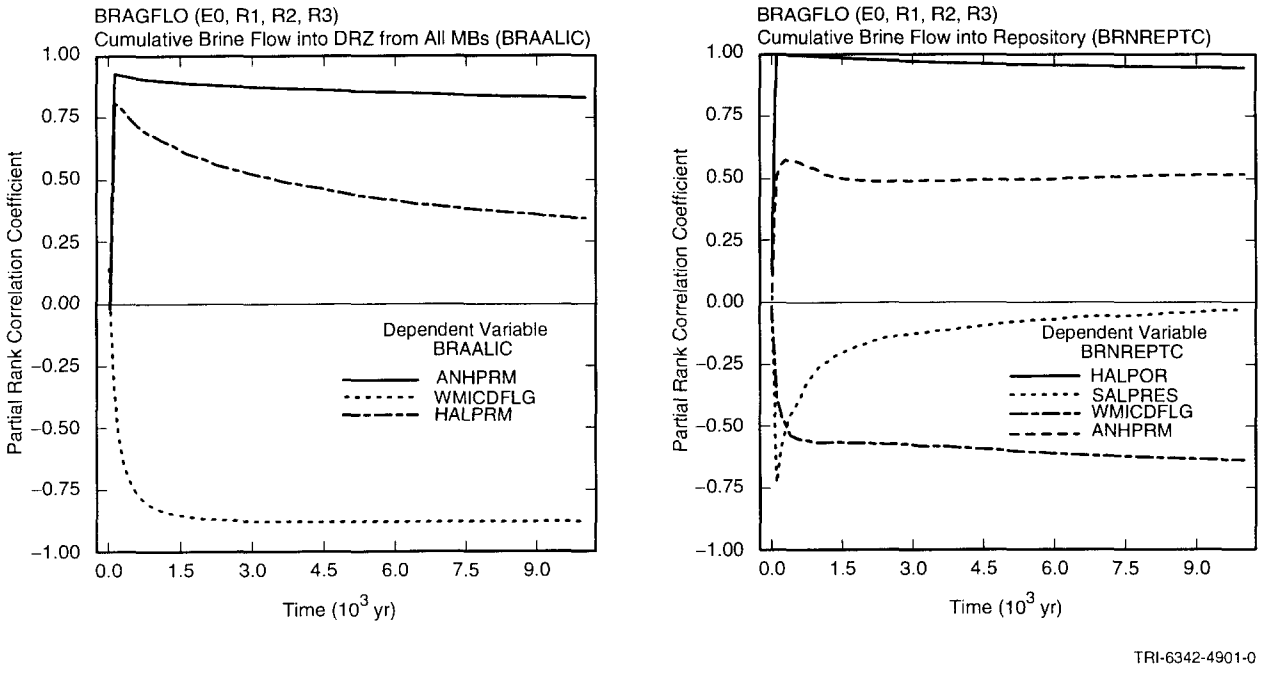

Fig. 7.2.3 Partial rank correlation coefficients for cumulative brine flow from marker beds (*BRAALIC*) and cumulative brine flow into repository (*BRNREPTC*) under undisturbed conditions with *ANHCOMP* and *HALCOMP* excluded from calculation.

The dominant variables for cumulative brine outflow from the marker beds identified with PRCCs are *ANHPRM*, *WMICDFLG* and *HALPRM* (Fig. 7.2.3), which is consistent with the results obtained in the regression analysis (Table 7.2.3). The positive effects for *ANHPRM* and *HALPRM* result because of reduced resistance to flow in the marker beds and in the Salado halite, respectively. The negative effect for *WMICDFLG* results because of increased pressure in the repository and hence an increased resistance to flow out of the marker beds.

The dominant variables for cumulative brine flow into the repository identified with PRCCs are *HALPOR*, *WMICDFLG* and *ANHPRM*, which is also consistent with the results obtained in the regression analysis (Table 7.2.3). The negative effect indicated for *SALPRES* at very early times may be spurious. As a reminder, PRCCs provide a measure of the linear relationship between two variables after a correction has been made for the effects of all other variables under consideration. As *HALPOR* has a PRCC of approximately 1 when *SALPRES* appears to have a negative effect, the amount of uncertainty being accounted for by *SALPRES* or any other variable is actually quite small after the correction is made for the effects of *HALPOR*. In the regression analysis, *SALPRES* is not identified as having a discernible effect on brine inflow to the repository over 10,000 yr (Table 7.2.3). The positive effects indicated for *HALPOR* and *ANHPRM* result from increased brine drainage from the DRZ and

increased brine flow from the marker beds, respectively. The negative effect for *WMICDFLG* results from increased pressure in the repository and hence increased resistance to flow out of the marker beds.

The examination of scatterplots provides an additional way to assess the effects of uncertain variables on analysis outcomes of interest. The two most important variables identified in Table 7.2.3 and Fig. 7.2.3 for brine outflow from the marker beds are *WMICDFLG* and *ANHPRM*. The corresponding scatterplots show well-defined relationships between these two variables and cumulative brine outflow from the marker beds over 10,000 yr (Fig. 7.2.4). Similarly, the dominant variable for cumulative brine inflow to the repository over 10,000 yr is *HALPOR*, with the corresponding scatterplot again showing a well-defined relationship (Fig. 7.2.5).

Flow down the shaft constitutes another possible brine inflow pathway to the repository. However, the amount of brine entering the repository by flow out of the shaft (Fig. 7.2.6) is insignificant relative to other sources of brine inflow (Fig. 7.2.2). Specifically, flow out of the shaft is on the order of a few 10's of cubic meters of brine (Fig. 7.2.6) while flow out of the marker beds is on the order of 1,000's to 10,000's of cubic meters of brine (Fig. 7.2.2).

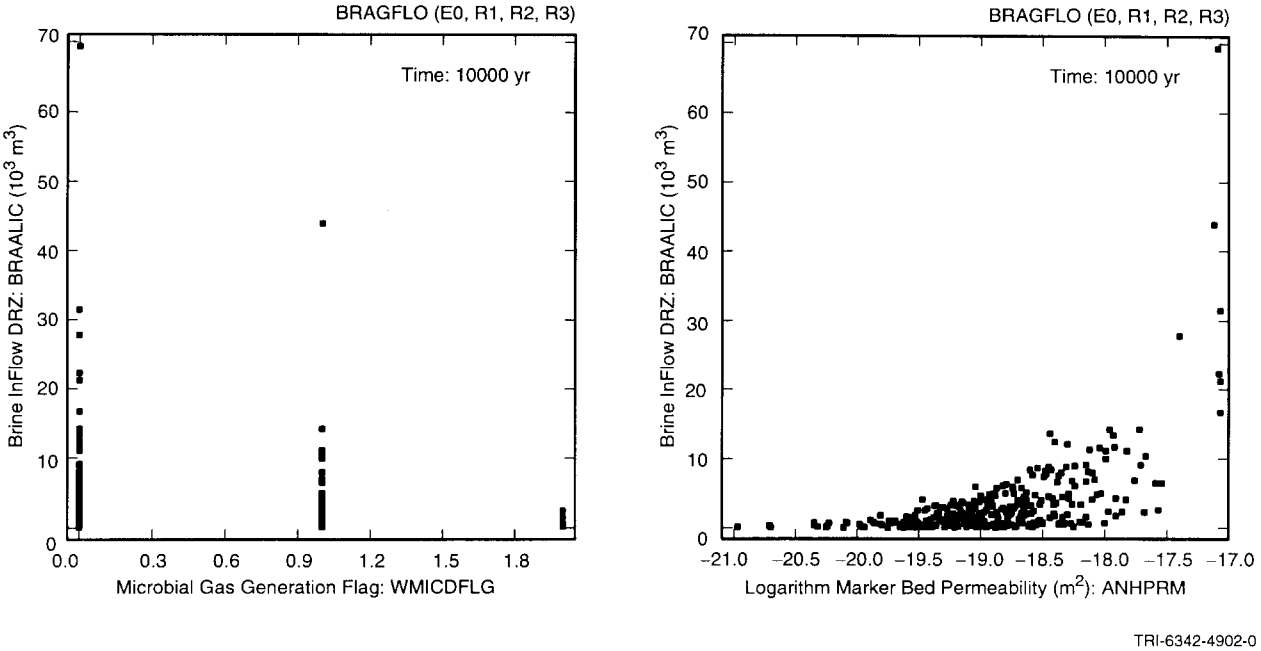

Fig. 7.2.4. Scatterplots for cumulative brine discharge from the marker beds (*BRAALIC*) over 10,000 yr under undisturbed conditions versus *WMICDFLG* and *ANHPRM*.

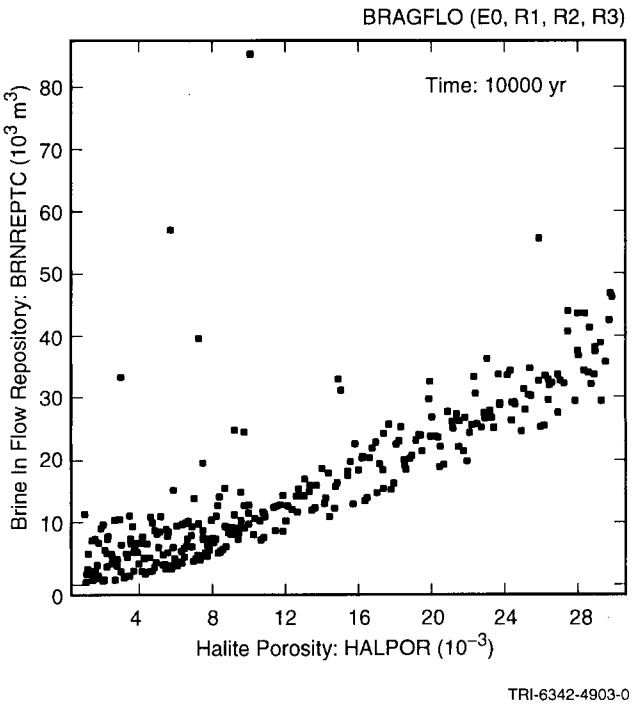

Fig. 7.2.5. Scatterplot for cumulative brine inflow to the repository (*BRNREPTC*) over 10,000 yr under undisturbed conditions versus *HALPOR*.

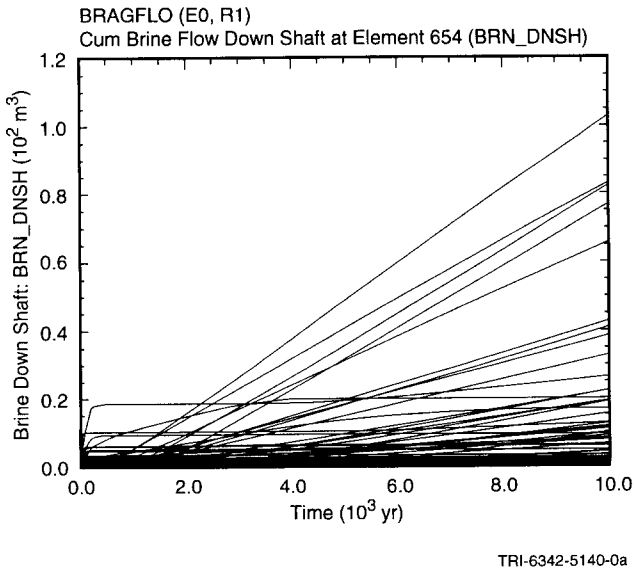

Fig. 7.2.6. Cumulative brine flow down the shaft at the upper boundary of the DRZ (*BRN_DNSH*) under undisturbed conditions.

7.3 Undisturbed Conditions: Gas Generation

Gas generation results from the corrosion of steel and the microbial degradation of cellulose (Fig. 7.3.1). The discretized character of cumulative gas generation for microbial degradation derives from the variable *WMICDFLG*, which takes on three values. Specifically, one value, which has a probability of 0.25, specifies the inclusion of rubber and plastics in the inventory of cellulose available for microbial degradation and results in the upper group of curves in Fig. 7.3.1; one value, which also has a probability of 0.25, specifies the exclusion of rubber and plastics from the inventory of cellulose available for microbial degradation and results in the middle group of curves in Fig. 7.3.1; and one value, which has a probability of 0.5, specifies that no microbial degradation of cellulose will take place and results in the lower group of curves in Fig. 7.3.1. The leveling off of the curves for microbial gas generation in Fig. 7.3.1 results from exhaustion of the cellulose inventory (Fig. 7.3.2).

Microbial gas generation takes place at different rates under humid and inundated conditions. Overall, more gas generation takes place under inundated than humid conditions (Fig. 7.3.3). However, the occurrence of gas generation under humid or inundated conditions does not affect the total amount of gas generated by microbial action as indicated by the lack of variability around the two asymptotes in Fig. 7.3.1.

Total gas generation is obtained by combining gas generation due to corrosion and gas generation due to microbial degradation (Fig. 7.3.4), with the larger contribution coming from corrosion (Fig. 7.3.1). However, microbial degradation still makes a substantial contribution to the total uncertainty in gas generation.

As already indicated, gas generation due to microbial degradation is dominated by *WMICDFLG*. For gas generation due to corrosion, the dominant variables are *WGRCOR* and *HALPOR*, with a smaller effect indicated for *WASTWICK* (left frame, Fig. 7.3.5). The variables *WGRCOR* and *WASTWICK* are important at early times because increasing each of these variables increases the rate at which gas is generated. However, over the longer term, the amount of gas generated by corrosion depends on the amount of steel undergoing corrosion, which in turn depends on the amount of brine available for the corrosion process. As a reminder, brine is consumed in the corrosion process, with the result that the amount of gas generated by corrosion can be limited by the amount of brine present in the repository. The positive effect indicated for *HALPOR* results because *HALPOR* is the dominant variable with respect to the amount of brine entering the repository (Table 7.2.3, Figs. 7.2.3, 7.2.5).

For total gas generation due to corrosion of steel and microbial degradation of cellulose, the dominant variables are *WMICDFLG* and *HALPOR*, with *WMICDFLG* controlling the uncertainty in the amount of gas generated by microbial degradation and *HALPOR* controlling the uncertainty in the amount of gas generated by corrosion (right frame, Fig. 7.3.5). Smaller positive effects are indicated for *WGRCOR* and *WASTWICK*, which affect the rate at which corrosion takes place, with these effects becoming less important with increasing time.

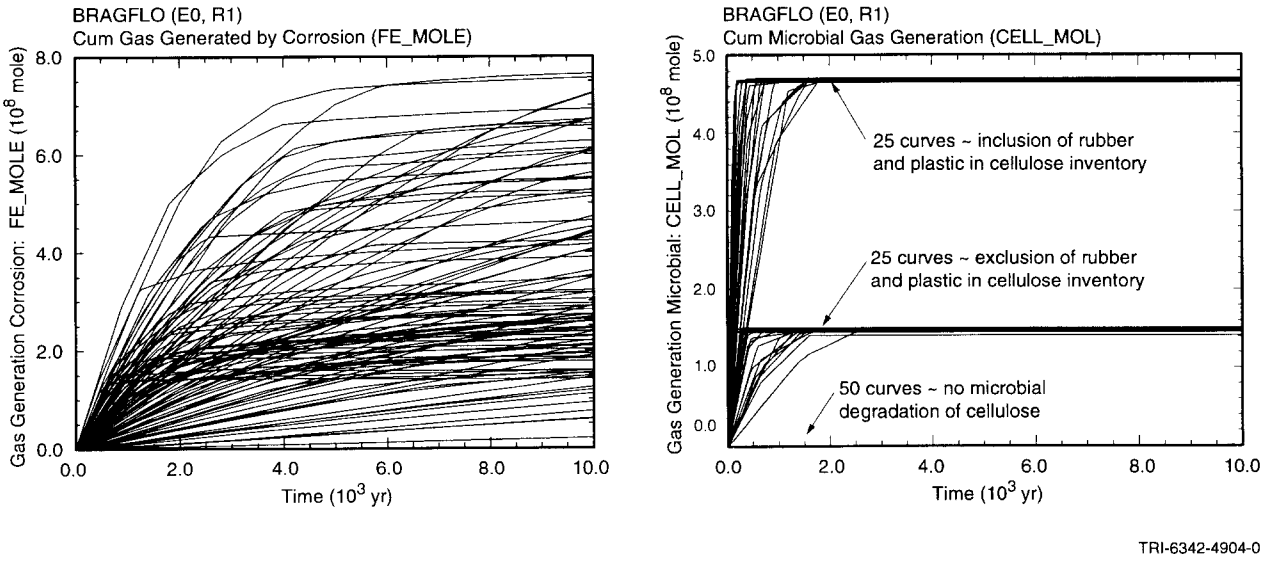

Fig. 7.3.1. Cumulative gas generation due to corrosion (*FE_MOLE*) and microbial degradation of cellulose (*CELL_MOL*) under undisturbed conditions.

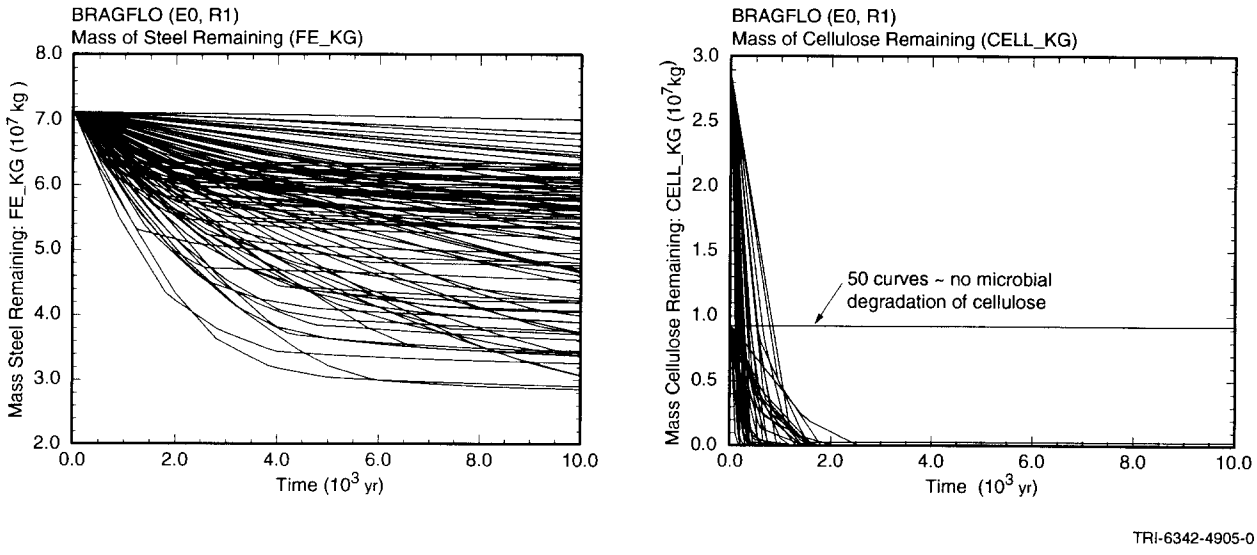

Fig. 7.3.2. Time-dependent masses of steel (*FE_KG*) and cellulose (*CELL_KG*) in repository under undisturbed conditions.

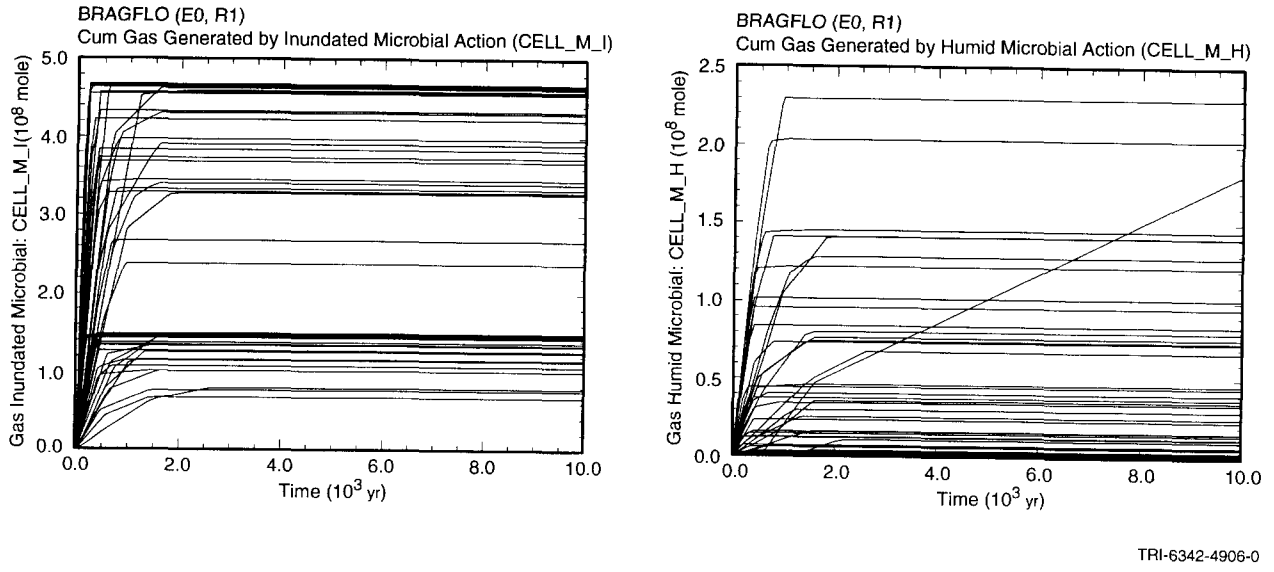

Fig. 7.3.3. Cumulative gas generation due to microbial degradation of cellulose under inundated (*CELL_M_I*) and humid (*CELL_M_H*) conditions for undisturbed conditions.

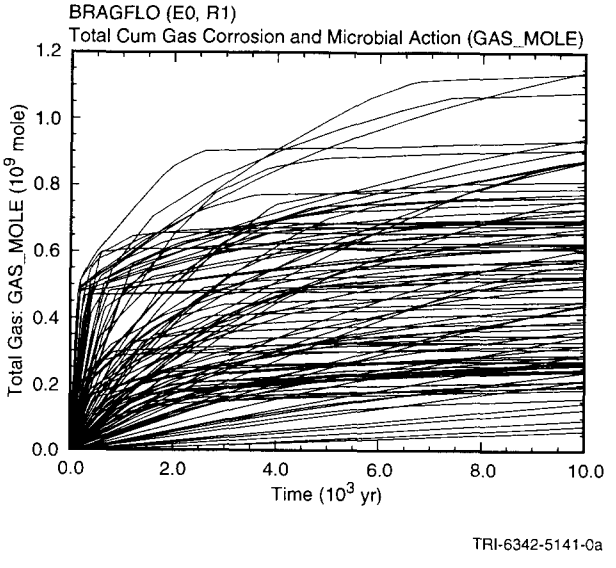

Fig. 7.3.4. Cumulative gas generation due to both corrosion and microbial degradation of cellulose (*GAS_MOLE*) under undisturbed conditions.

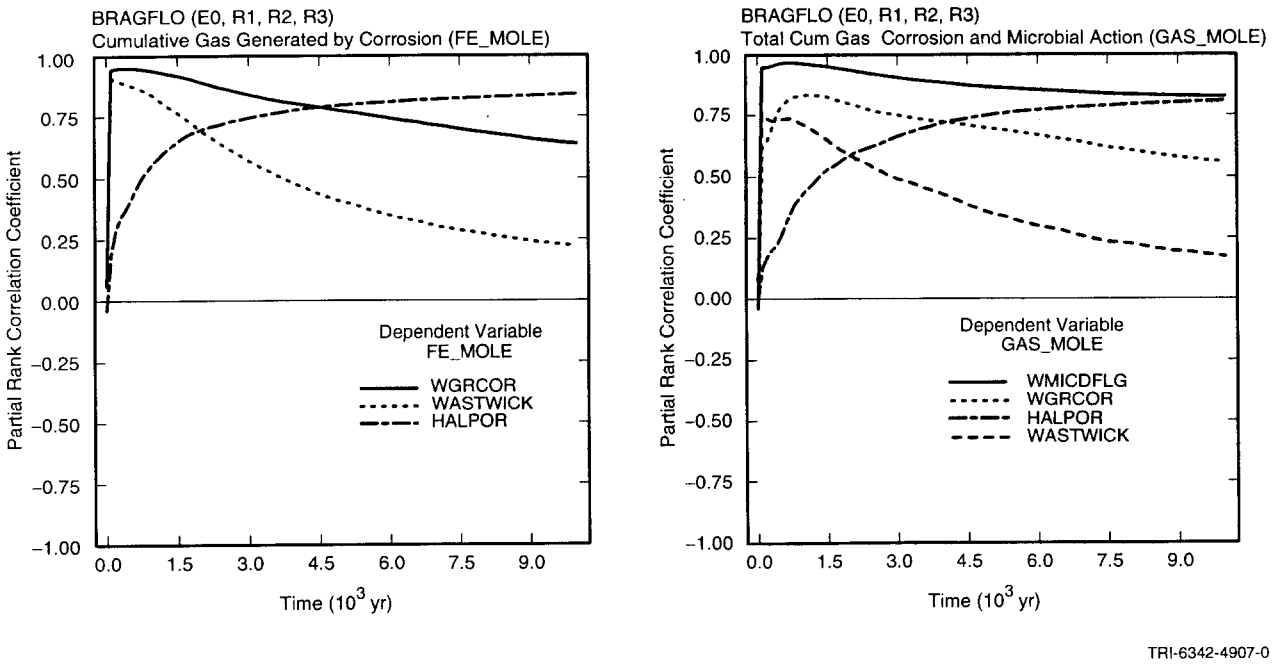

Fig. 7.3.5. Partial rank correlation coefficients for cumulative gas generation due to corrosion of steel (*FE_MOLE*) and cumulative gas generation due to corrosion of steel and microbial degradation of cellulose (*GAS_MOLE*) under undisturbed conditions with *ANHCOMP* and *HALCOMP* excluded from calculation.

Stepwise regression analysis provides an alternative way to investigate the uncertainty in gas generation (Table 7.3.1). For cumulative gas generation over 10,000 yr due to corrosion, the dominant variable is *HALPOR*, which controls the amount of brine entering the repository. Positive effects are also indicated for *WGRCOR* and *WASTWICK* due to their role in increasing the rate of corrosion. The variable *WMICDFLG* appears in the regression model with a negative regression coefficient due to its role in reducing brine inflow to the repository (Table 7.2.3, Figs. 7.2.3, 7.2.4). The variable *ANHPRM* also appears in the regression model with a positive regression coefficient, which is consistent with its role in increasing brine flow into the repository (Table 7.2.3, Figs. 7.2.3, 7.2.4). The appearance of *BPINTPRS* at the final step of the analysis is spurious, as may also be the case for the selection of *SHRGSSAT* at Step 5. However, it is also possible that *SHRGSSAT* affects gas and brine flow patterns within the repository. The exclusion of *SHRGSSAT* and *BPINTPRS* from the regression analysis reduces the R^2 value of the final regression model from 0.76 to 0.75.

Table 7.3.1. Stepwise Regression Analyses with Rank-Transformed Data for Cumulative Gas Generation over 10,000 yr due to Corrosion of Steel (*FE_MOLE*) and to Corrosion of Steel and Microbial Degradation of Cellulose (*GAS_MOLE*) under Undisturbed Conditions

	Corrosion of Steel: *FE_MOLE*			Corrosion of Steel and Microbial Degradation of Cellulose: *GAS_MOLE*		
Step[a]	Variable[b]	SRRC[c]	R^{2d}	Variable	SRRC	R^2
1	*HALPOR*	0.73	0.55	*WMICDFLG*	0.62	0.39
2	*WGRCOR*	0.39	0.69	*HALPOR*	0.57	0.72
3	*WMICDFLG*	−0.20	0.73	*WGRCOR*	0.28	0.80
4	*WASTWICK*	0.11	0.74	*ANHPRM*	0.08	0.81
5	*SHRGSSAT*	0.09	0.75	*WASTWICK*	0.07	0.81
6	*ANHPRM*	0.09	0.76	*SHRGSSAT*	0.07	0.82
7	*BPINTPRS*	0.07	0.76			

[a] Steps in stepwise regression analysis.

[b] Variables listed in order of selection in regression analysis with *ANHCOMP* and *HALCOMP* excluded from entry into regression model.

[c] Standardized rank regression coefficients in final regression model.

[d] Cumulative R^2 value with entry of each variable into regression model.

As discussed in conjunction with Fig. 7.3.1, *WMICDFLG* completely controls the amount of gas generation due to microbial degradation. For total gas generation due to corrosion and microbial degradation, *WMICDFLG* is also the dominant variable (Table 7.3.1). After *WMICDFLG*, the regression analysis for total gas generation selects variables also selected in the regression analysis for gas generation due to corrosion (i.e., *HALPOR, WGRCOR, WASTWICK, SHRGSSAT, ANHPRM*). The two dominant variables with respect to total gas generation are *WMICDFLG* and *HALPOR*, with these two variables producing patterns that are easily identified in scatterplots (Fig. 7.3.6). The three bands of points in the scatterplot for *HALPOR* result from the effects of the three values that *WMICDFLG* can take on.

The analysis outcomes amount of gas generated by corrosion (Fig. 7.3.1), amount of steel remaining in the repository (Fig. 7.3.2) and amount of brine consumed by corrosion (Fig. 7.3.7) are highly correlated (Fig. 7.3.8). Thus, the sensitivity analysis results for amount of gas generated by corrosion (Fig. 7.3.3, Table 7.3.1) are also indicative of the variables affecting amount of steel remaining in the repository and amount of brine consumed by corrosion.

The computational grid used in the 1996 WIPP PA is based on dividing the repository into a single lower, or downdip, waste panel and nine upper waste panels, with the panel closures placed between these two groups of panels (Figs. 4.2.1, 4.2.3). For disturbed conditions, BRAGFLO calculations are performed with the assumption that the associated drilling intrusion takes place into the single lower panel. Further, spallings and direct brine release calculations distinguish between drilling intrusions into upper and lower waste panels. The rationale for this selection was based on the belief that intrusions into a downdip panel might be somewhat worse from a release

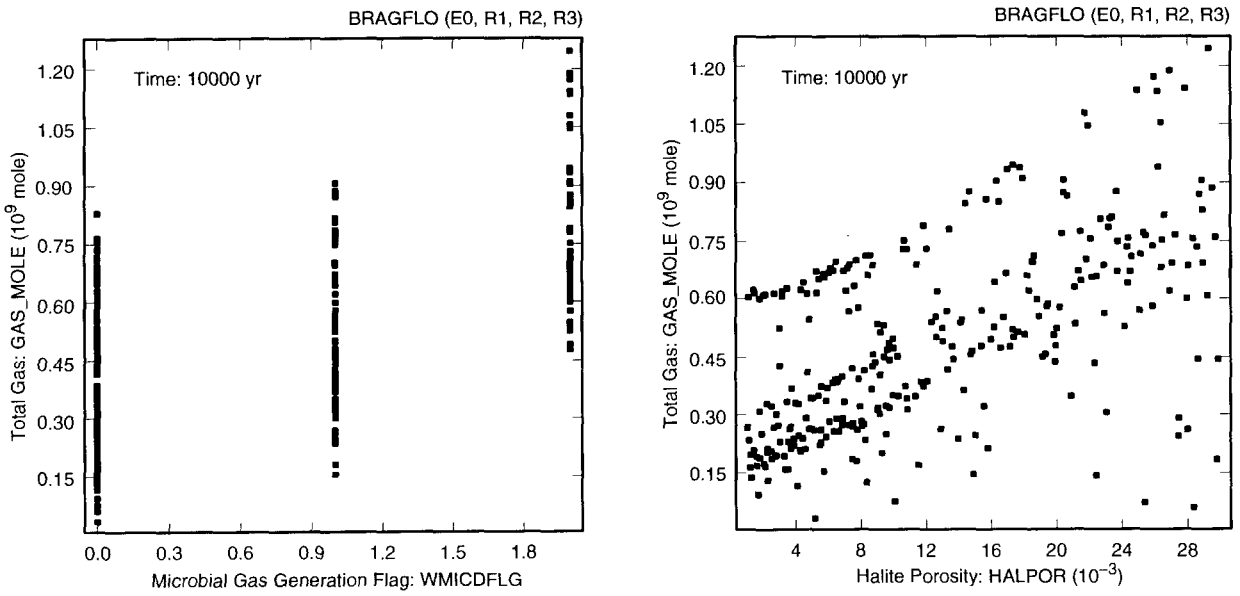

Fig. 7.3.6. Scatterplots for total gas generation over 10,000 yr due to corrosion of steel and microbial degradation of cellulose (*GAS_MOLE*) under undisturbed conditions versus *WMICDFLG* and *HALPOR*.

perspective than intrusions into an updip panel due to brine flow down the 1° dip on which the repository is constructed. Given the role that distinctions between intrusions into upper and lower waste panels will play in the release calculations, it is useful to examine the differences in conditions in these two sets of panels.

On a fractional basis, more steel is consumed in the lower waste panel than in the upper waste panels (Fig. 7.3.9). This pattern occurs because the lower waste panel receives more brine inflow relative to its volume than the upper waste panels. As indicated by the many level curves for fraction of steel in the upper waste panels, the corrosion of steel ceases for many sample elements due to brine depletion. In contrast, this behavior is less pronounced for the lower waste panel, which receives more brine inflow from the marker beds relative to its volume than does the upper waste panels. Also, the lower waste panel receives brine that initially enters the upper waste panels and then flows down dip into the lower waste panel.

The variables *WGRCOR*, *WASTWICK* and *HALPOR* have negative effects on the amount of steel remaining in both the upper and lower waste panels (Fig. 7.3.9). That is, increasing each of these variables tends to decrease the fraction of steel remaining. The variable *WMICDFLG* also appears in the analysis for the lower waste panel

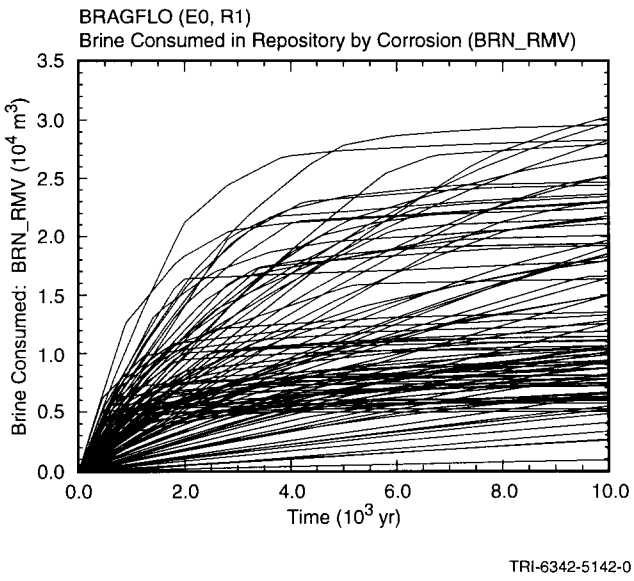

Fig. 7.3.7. Cumulative volume of brine consumed by corrosion (*BRN_RMV*) under undisturbed conditions.

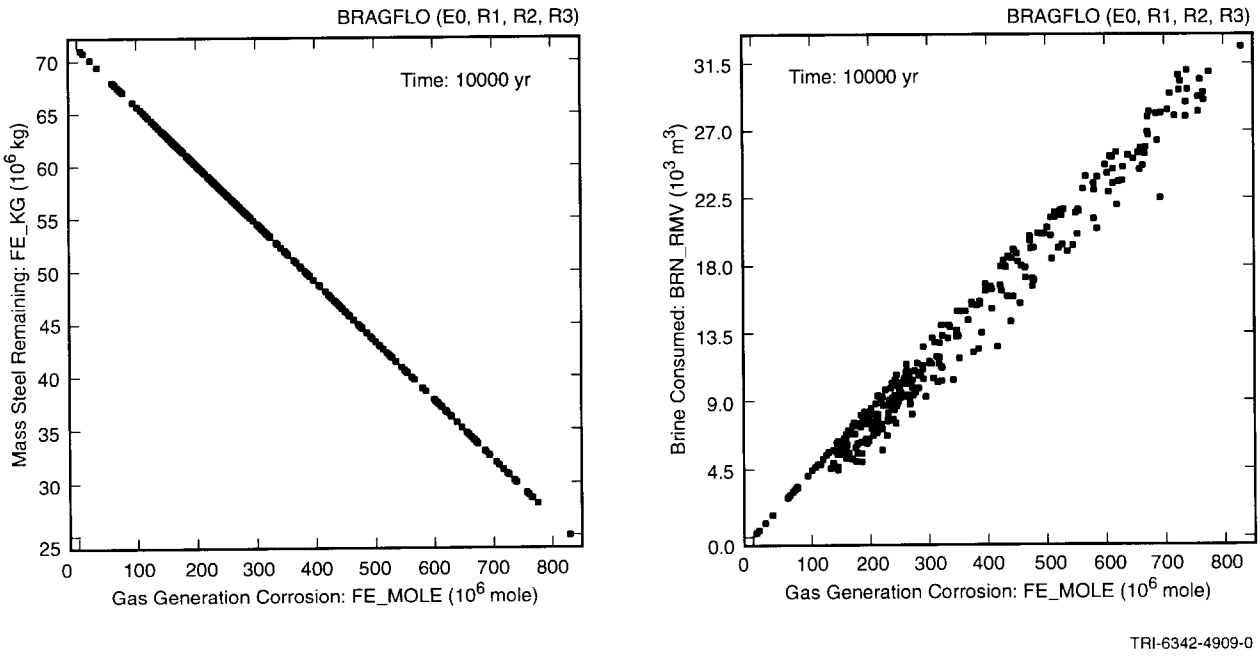

Fig. 7.3.8. Scatterplots for amount of gas generated by corrosion (*FE_MOLE*), amount of steel remaining in the repository (*FE_KG*) and amount of brine consumed by corrosion (*BRN_RMV*) at 10,000 yr under undisturbed conditions. The scatterplot for amount of brine removed should actually be a straight line, with the resolution at which computational results were stored introducing the scatter in the plot.

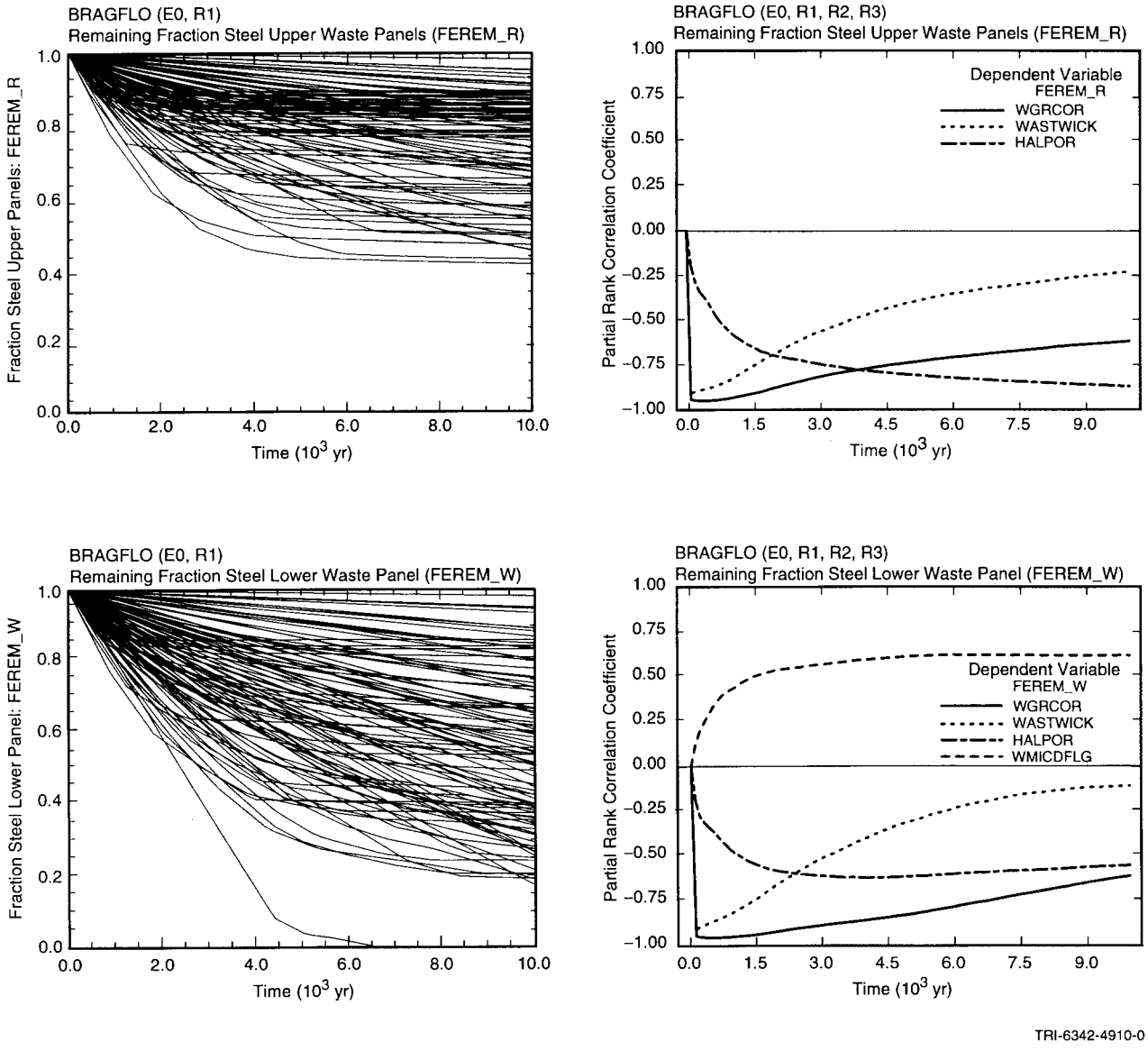

Fig. 7.3.9. Uncertainty and sensitivity analysis results for fraction of steel remaining in upper waste panels (*FEREM_R*) (upper frames) and lower waste panel (*FEREM_W*) (lower frames) under undisturbed conditions.

(Fig. 7.3.9). The appearance of *WMICDFLG* in the analysis for the lower waste panel but not the upper waste panels results because reducing brine inflow from the marker beds has a greater impact on a per unit volume basis in the lower waste panel than it does in the upper waste panels. Specifically, the volume of the upper waste panels is 9 times the volume of the lower waste panel. Thus, as similar amounts of brine flow out of the marker beds at the northern and southern ends of the computational grid (Fig. 7.2.2), the lower waste panel receives approximately 9 times more brine from the marker beds for each unit of steel that it contains than is received by the upper waste panels. Due to the linkage of gas generation and removal of steel (Fig. 7.3.8) and the fact that most gas generation takes place in the upper waste panels, the PRCCs in Fig. 7.3.9 for the fraction of steel remaining in the upper waste panels and the PRCCs in Fig. 7.3.5 for gas generation from corrosion appear with the appropriate reversal in sign.

Regression analysis can also be used to investigate variable importance with respect to fraction of steel remaining in the upper and lower waste panels (Table 7.3.2). For the upper panels, *HALPOR*, *WGRCOR* and *WASTWICK* have negative effects on the fraction of steel remaining, which is consistent with the analysis with PRCCs (Fig. 7.3.9). The variable *WMICDFLG* is also indicated as having a small positive effect, which is consistent with its role in impeding brine inflow from the marker beds. Small effects are also indicated for *SHRGSSAT* and *BPINTPRS*, with the selection of *BPINTPRS* and possibly the selection of both variables being spurious. However, it is also possible that *SHRGSSAT* may affect gas and brine flow patterns within the repository. For the lower panel, *WMICDFLG*, *WGRCOR* and *HALPOR* have effects consistent with those observed in the analysis with PRCCs (Fig. 7.3.9). The variables *ANHPRM* and *HALPRM* are selected with negative regression coefficients, which corresponds to the role that these variables play in increasing brine flow to the repository (Table 7.2.3). The

Table 7.3.2. Stepwise Regression Analyses with Rank-Transformed Data for Fraction of Steel Remaining and Total Gas Generation in Upper (*FEREM_R*, *GASMOL_R*) and Lower (*FEREM_W*, *GASMOL_W*) Waste Panels at 10,000 yr Under Undisturbed Conditions

	Fraction Steel Remaining Upper Waste Panels: *FEREM_R*			Fraction Steel Remaining Lower Waste Panel: *FEREM_W*			Total Gas Generation Upper Waste Panels: *GASMOL_R*			Total Gas Generation Lower Waste Panel: *GASMOL_W*		
Step[a]	Variable[b]	SRRC[c]	R^{2d}	Variable	SRRC	R^2	Variable	SRRC	R^2	Variable	SRRC	R^2
1	*HALPOR*	−0.78	0.63	*WMICDFLG*	0.46	0.20	*WMICDFLG*	0.65	0.43	*WGRCOR*	0.47	0.23
2	*WGRCOR*	−0.35	0.75	*WGRCOR*	−0.45	0.41	*HALPOR*	0.58	0.77	*HALPOR*	0.45	0.44
3	*WMICDFLG*	0.12	0.76	*HALPOR*	−0.38	0.56	*WGRCOR*	0.24	0.83	*ANHPRM*	0.33	0.55
4	*WASTWICK*	−0.10	0.77	*ANHPRM*	−0.25	0.63	*WASTWICK*	0.07	0.83	*WMICDFLG*	0.17	0.58
5	*SHRGSSAT*	−0.08	0.78	*HALPRM*	−0.09	0.63	*SHRGSSAT*	0.06	0.83	*HALPRM*	0.12	0.59
6	*BPINTPRS*	−0.06	0.78	*SHRGSSAT*	−0.09	0.64				*SHRGSSAT*	0.08	0.60

[a] Steps in stepwise regression analysis.

[b] Variables listed in order of selection in regression analysis with *ANHCOMP* and *HALCOMP* excluded from entry into regression model.

[c] Standardized rank regression coefficients in final regression model.

[d] Cumulative R^2 value with entry of each variable into regression model.

selection of *SHRGSSAT* at the end of the regression may be spurious. For perspective, Fig. 7.3.10 shows scatterplots for the first three variables selected in each regression for fraction of steel remaining.

The patterns of steel consumption in the upper and lower waste panels propagate through into the patterns of gas production (Fig. 7.3.11). When microbial degradation takes place, all the cellulose in the repository is consumed by 2000 yr (Fig. 7.3.2), with the result that the time-dependent patterns of gas generation after 2000 yr are determined by corrosion. Thus, the more pronounced cessation of steel consumption in the upper waste panels than in the lower waste panel (Fig. 7.3.9) carries through to a corresponding leveling off of gas production in the upper waste panels (Fig. 7.3.11).

The dominant variables with respect to gas production in the upper and lower waste panels are *WMICDFLG*, *HALPOR*, *WGRCOR* and *WASTWICK*, although there is some difference in their relative effects between the upper and lower panels (Fig. 7.3.11). For example, *WMICDFLG* remains more important over time for gas generation in the upper panels than in the lower panel. The upper and lower panels produce similar amounts of gas by microbial degradation on a unit volume basis; however, the lower panel produces more gas due to corrosion on a unit volume basis because of greater availability of brine. As a result, *WMICDFLG* is more important with respect to gas generation in the upper panels than in the lower panel. Similarly, *HALPOR* is more important to gas generation due to corrosion in the upper panels than in the lower panel due to the reduction of the importance of *HALPOR* in the lower panel owing to the inflow of brine from the marker beds. Similar results for gas generation in the upper and lower panels are also obtained with regression analysis (Table 7.3.2).

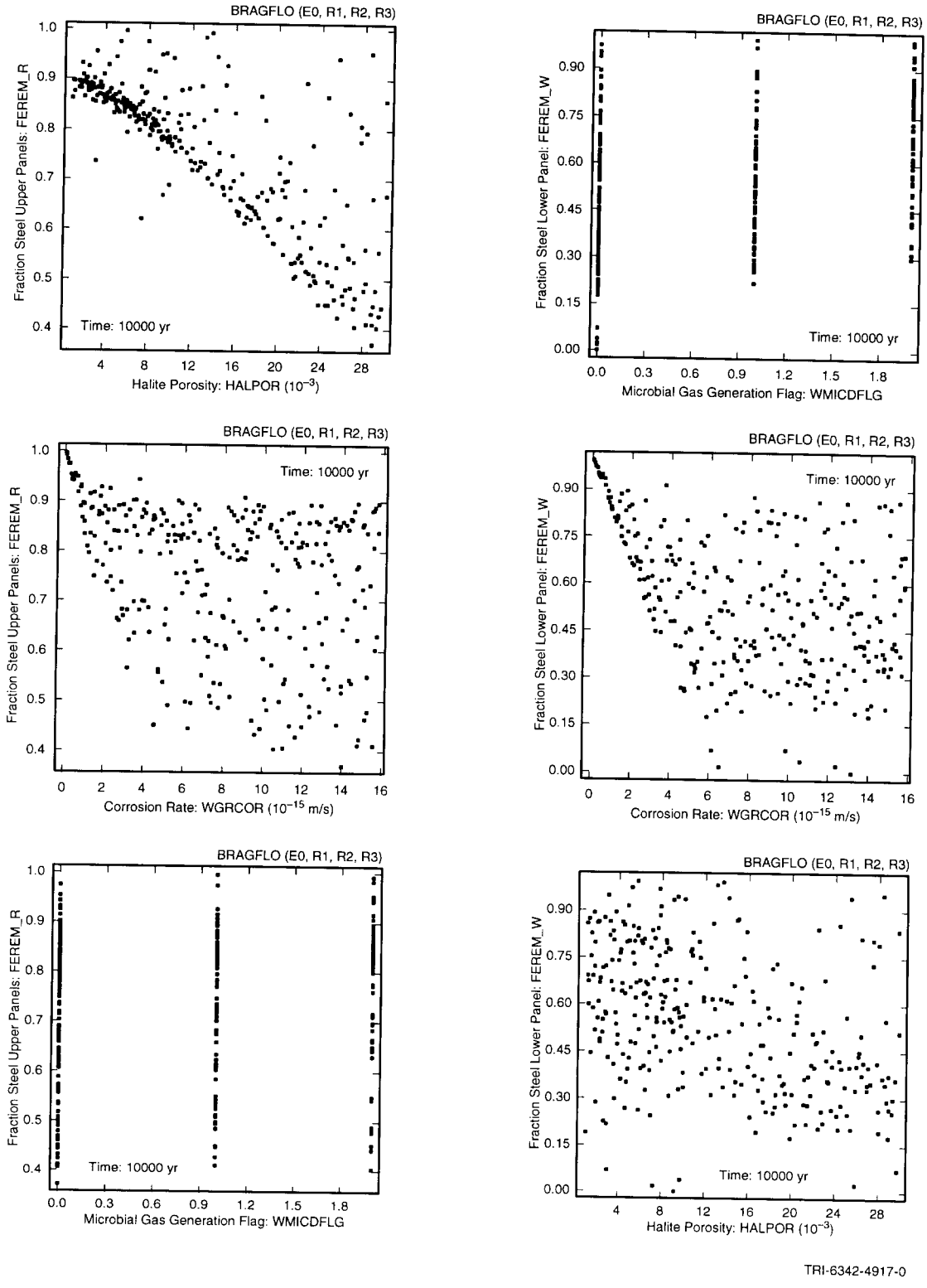

Fig. 7.3.10. Scatterplots for fraction of steel remaining in upper waste panels (*FEREM_R*) (left frames) and lower panel (*FEREM_W*) (right frames) for undisturbed conditions at 10,000 yr versus *HALPOR*, *WGRCOR* and *WMICDFLG*.

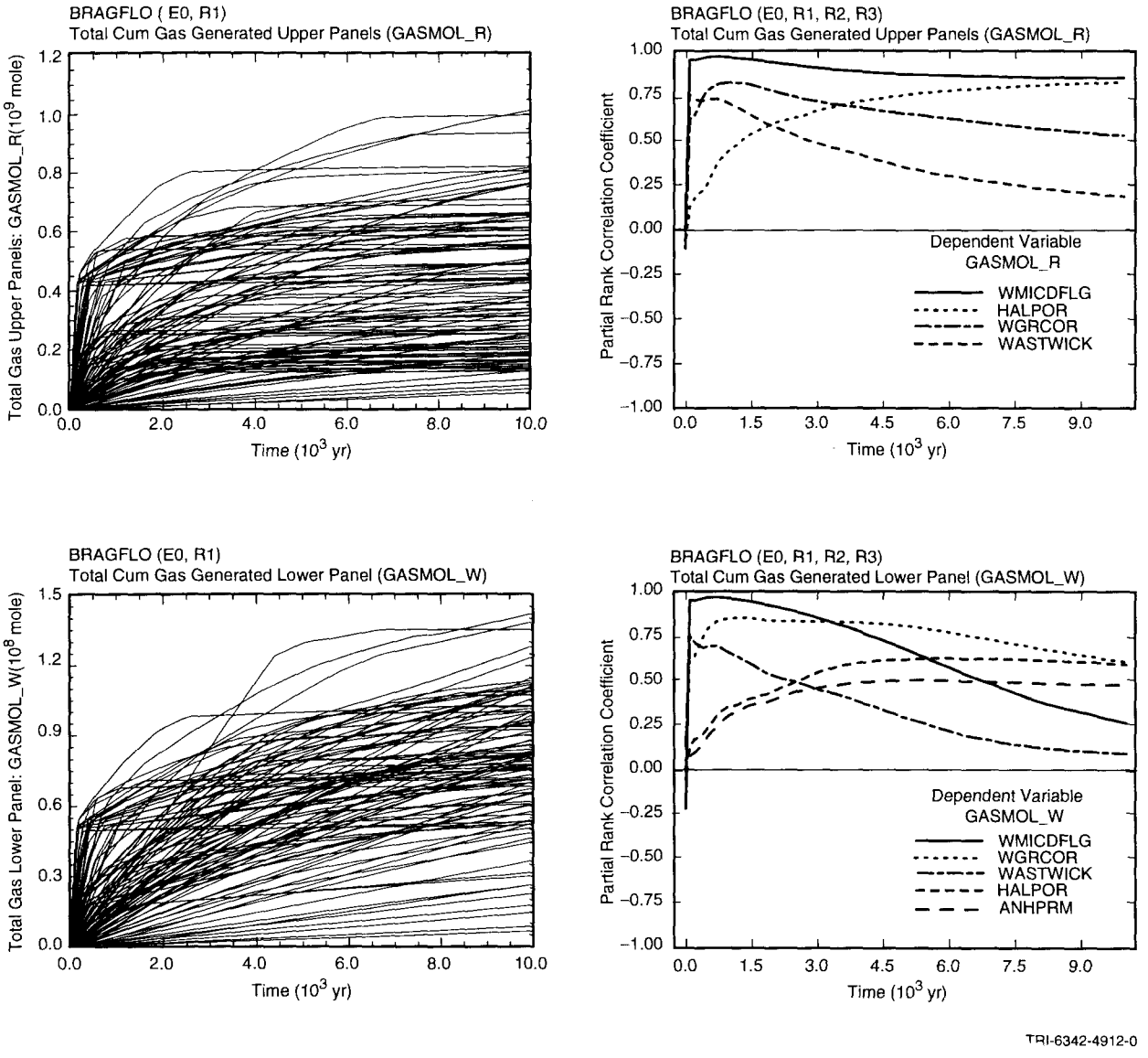

Fig. 7.3.11. Uncertainty and sensitivity analysis results for cumulative gas generation due to corrosion and microbial degradation in upper waste panels (*GASMOL_R*) (upper frames) and lower waste panel (*GASMOL_W*) (lower frames) for undisturbed conditions.

7.4 Undisturbed Conditions: Pressure

Pressure in the repository under undisturbed conditions influences the extent to which contaminated brine migrates from the repository into the marker beds and also the size of the spallings and direct brine releases associated with initial drilling intrusions into the repository. Thus, repository pressure is one of the most important results obtained from modeling brine and gas flow in the vicinity of the repository.

The pressure in the repository tends to initially increase rapidly and then to either approach an asymptote or show a decreased rate of increase (Fig. 7.4.1). The results in Fig. 7.4.1 are for the lower waste panel (Fig. 4.2.1); however, due to limited resistance to gas flow in the DRZ and panel closures, pressure is almost the same throughout the repository, operations area and experimental area. The 1996 WIPP PA was performed with three replicated LHSs of size 100, with the results for repository pressure being quite stable across replicates (Fig. 7.4.2). Thus, the distribution of this important variable that results from subjective uncertainty is being estimated quite well within the analysis.

The dominant contributor to the uncertainty in pressure is *WMICDFLG* (Fig. 7.4.1), with pressure tending to increase as *WMICDFLG* increases. As previously discussed, *WMICDFLG* controls the amount of gas generated by microbial degradation of cellulose. At early times *WGRCOR* and *WASTWICK* are also important with respect to pressure, with pressure tending to increase as each of these variables increases. Increases in *WGRCOR* and *WASTWICK* tend to increase gas pressure at early times by increasing the rate at which steel is consumed by corrosion. However, neither variable affects the total amount of corrosion that will take place, with the result that their influence on pressure tends to decrease with time. In contrast, *HALPOR* has little effect on pressure at early times, but increases steadily in importance with time. This effect results because corrosion occurs only under inundated conditions. Given that corrosion consumes brine, increased brine in the repository results in more corrosion and hence in higher pressures. As discussed in Sect. 7.2, *HALPOR* is the dominant determinant of the amount of brine that enters the repository and hence of the amount of gas produced by corrosion. The variable *HALPOR* has little or no effect on pressure at earlier times because of the availability of brine from other sources and the dominance of gas generation by the microbial degradation of cellulose. However, at later times it is the brine inflow associated with *HALPOR* that allows corrosion to continue.

There is a well-defined relationship between cumulative gas generation and repository pressure (Fig. 7.4.3), with the results at 10,000 yr showing slightly more scatter than the results at 2000 yr due to increased time for gas migration into the marker beds. The strong positive correlation between gas generation and repository pressure results in the PRCCs in Fig. 7.3.5 for total gas generation and the PRCCs in Fig. 7.4.1 for repository pressure being almost identical.

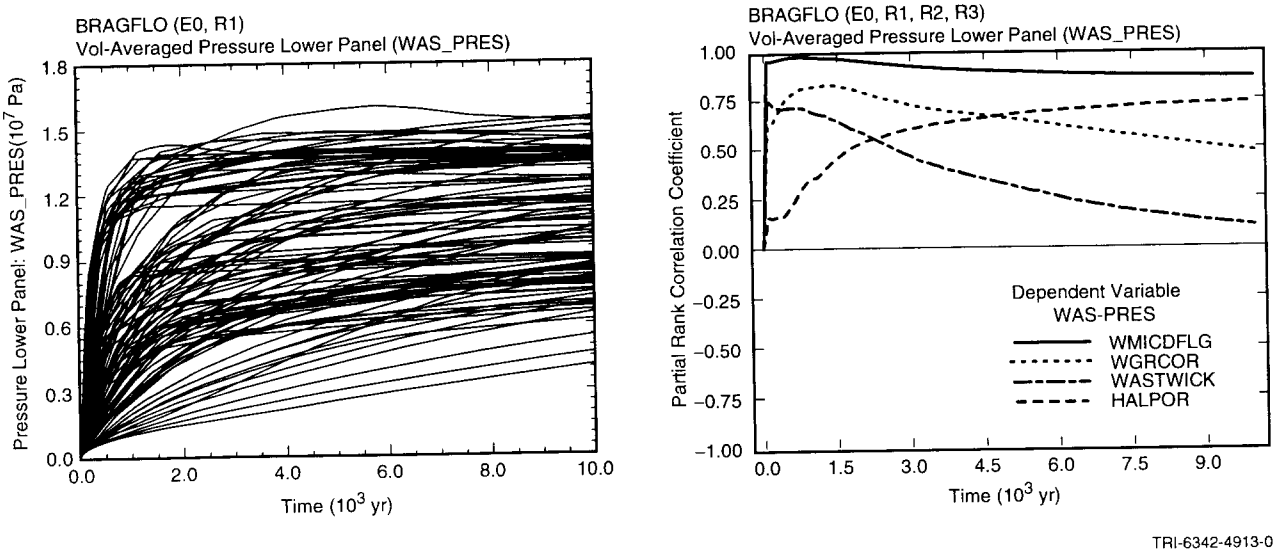

Fig. 7.4.1. Uncertainty and sensitivity analysis results for pressure in lower waste panel (*WAS_PRES*) under undisturbed conditions.

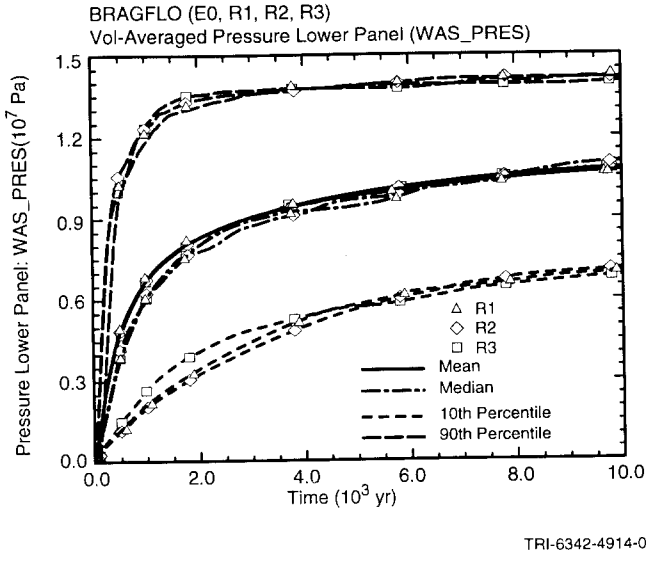

Fig. 7.4.2. Mean and percentile curves for three replicated LHSs for pressure in lower waste panel (*WAS_PRES*) under undisturbed conditions.

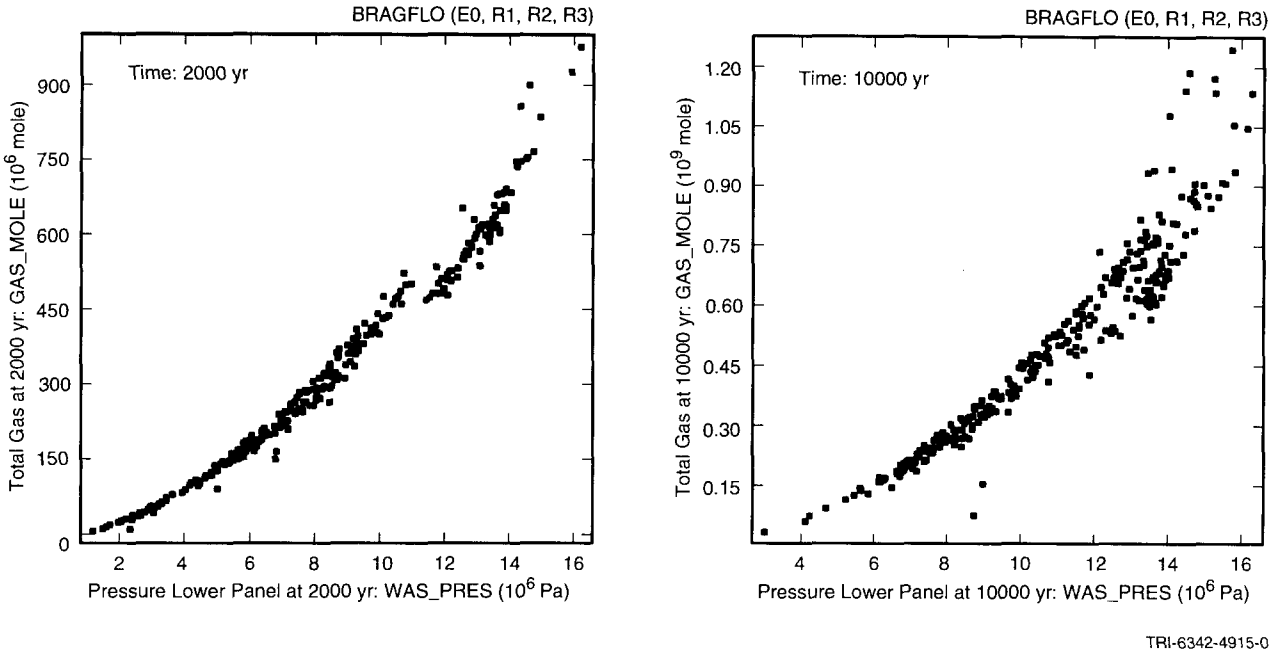

Fig. 7.4.3. Scatterplots at 2,000 and 10,000 yr for cumulative gas generated by corrosion and microbial degradation (*GAS_MOLE*) under undisturbed conditions versus pressure in repository (*WAS_PRES*).

Stepwise regression analysis (Table 7.4.1) provides an alternative to the analysis based on PRCCs in Fig. 7.4.1. The first three variables identified in the regression analysis are *WMICDFLG*, *HALPOR* and *WGRCOR*, which are also the top three variables identified in the analysis with PRCCs at 10,000 yr. In addition, the regression analysis also identifies positive effects for *ANHPRM* and *SALPRES*. Increased values for *ANHPRM* tend to increase brine flow out of the marker beds and thus increase pressure by increasing gas generation due to corrosion (Tables 7.2.3, 7.3.1). Increased values for *SALPRES* tend to reduce gas and brine movement into the marker beds and thus increase pressure in the repository. Increased values for *SHRGSSAT* are associated with increased gas generation due to corrosion (Table 7.3.1) and thus increased gas pressure in the repository; however, the selection of *SHRGSSAT* in Table 7.3.1 may be spurious. It is also possible that *SHRGSSAT* may effect gas and brine movement across the computational cells associated with the shaft (i.e., regions 10, 11 in Fig. 4.2.1). Because of the strong positive correlation between gas generation and pressure (Fig. 7.4.3), the regression analysis in Table 7.4.1 for repository pressure and the regression analysis in Table 7.3.1 for total gas generation are very similar.

Table 7.4.1. Stepwise Regression Analysis with Rank-Transformed Data for Pressure in the Repository (*WAS_PRES*) at 10,000 yr Under Undisturbed Conditions

Step[a]	Variable[b]	SRRC[c]	R^{2}[d]
1	*WMICDFLG*	0.71	0.52
2	*HALPOR*	0.45	0.73
3	*WGRCOR*	0.23	0.79
4	*ANHPRM*	0.11	0.80
5	*SALPRES*	0.07	0.80
6	*SHRGSSAT*	0.06	0.81

[a] Steps in stepwise regression analysis.

[b] Variables listed in order of selection in regression analysis with *ANHCOMP* and *HALCOMP* excluded from entry into regression model.

[c] Standardized rank regression coefficients in final regression model.

[d] Cumulative R^2 value with entry of each variable into regression model.

Pore volume in the repository (Fig. 7.4.4) changes in response to changes in pressure (Fig. 7.4.5). Due to the strong positive correlation between pore volume and pressure, sensitivity analysis for pore volume produces results similar to those obtained for repository pressure (Fig. 7.4.1, Table 7.4.1). The coupling between pore volume and pressure is implemented in the calculation through relationships determined with the SANTOS program (Sect. 4.2.3).

This presentation primarily emphasizes uncertainty and sensitivity analysis results that are obtained by considering the collective behavior of the 300 LHS elements associated with replicates R1, R2 and R3. In the formal uncertainty and sensitivity analysis procedures in use, the behavior of individual sample elements is considered only in the context of patterns that emerge from the collective behavior of all sample elements. However, it is also informative to consider the behavior of results associated with individual sample elements because this allows an examination of specific analysis outcomes at a level of resolution that is different from that considered in the formal uncertainty and sensitivity analysis. Unfortunately, the number of individual analysis outcomes that can be subjected to detailed examination is necessarily limited. In particular, as 300 sample elements are available and there are 100s of predicted results that could be examined for each sample element, all potential results of interest cannot be individually examined. None the less, selected results will be given individual examinations to help develop insight into the behavior of gas and brine in the vicinity of the repository.

As an example, the interplay between gas generation, repository pressure and repository pore volume for sample elements 37 and 40 of replicate R1 is shown in Fig. 7.4.6. For both sample elements, pressure (*WAS_PRES*, *REP_PRES*) initially increases rapidly and then levels off; also, pressure in the lower waste panel (*WAS_PRES*) and pressure in the upper waste panels (*REP_PRES*) are essentially the same. Further, both sample elements show

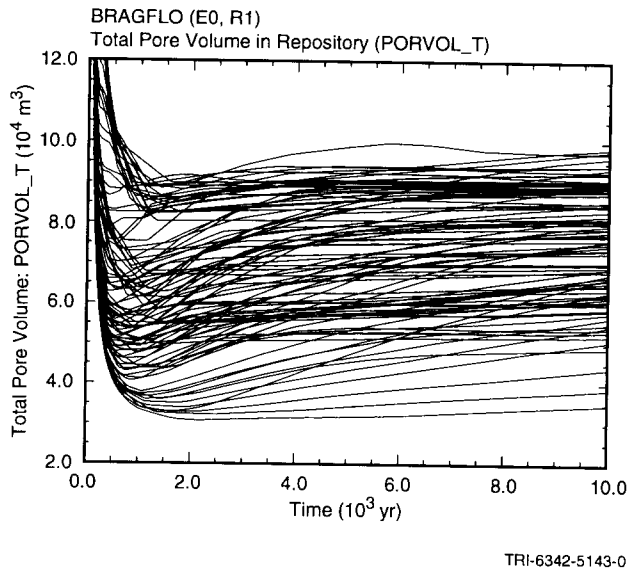

Fig. 7.4.4. Total pore volume in repository (*PORVOL_T*) under undisturbed conditions.

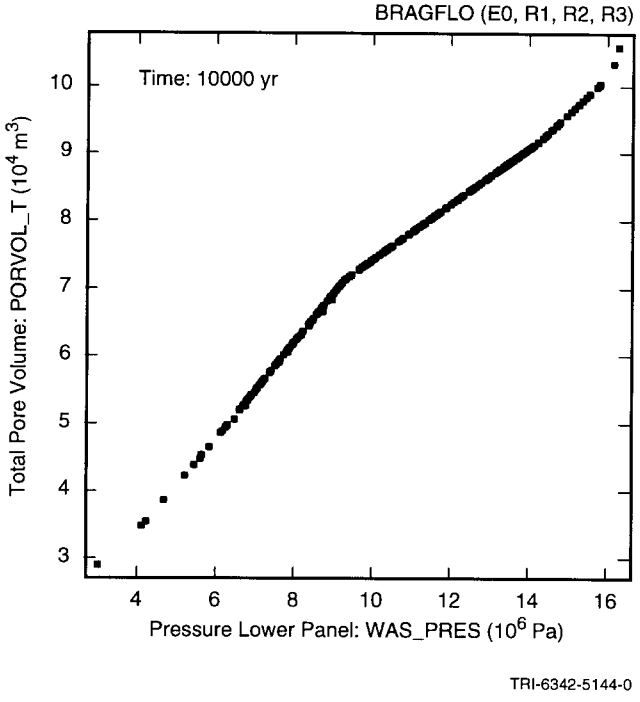

Fig. 7.4.5. Scatterplot of pressure in repository (*WAS_PRES*) at 10,000 yr under undisturbed conditions versus total pore volume in repository (*PORVOL_T*).

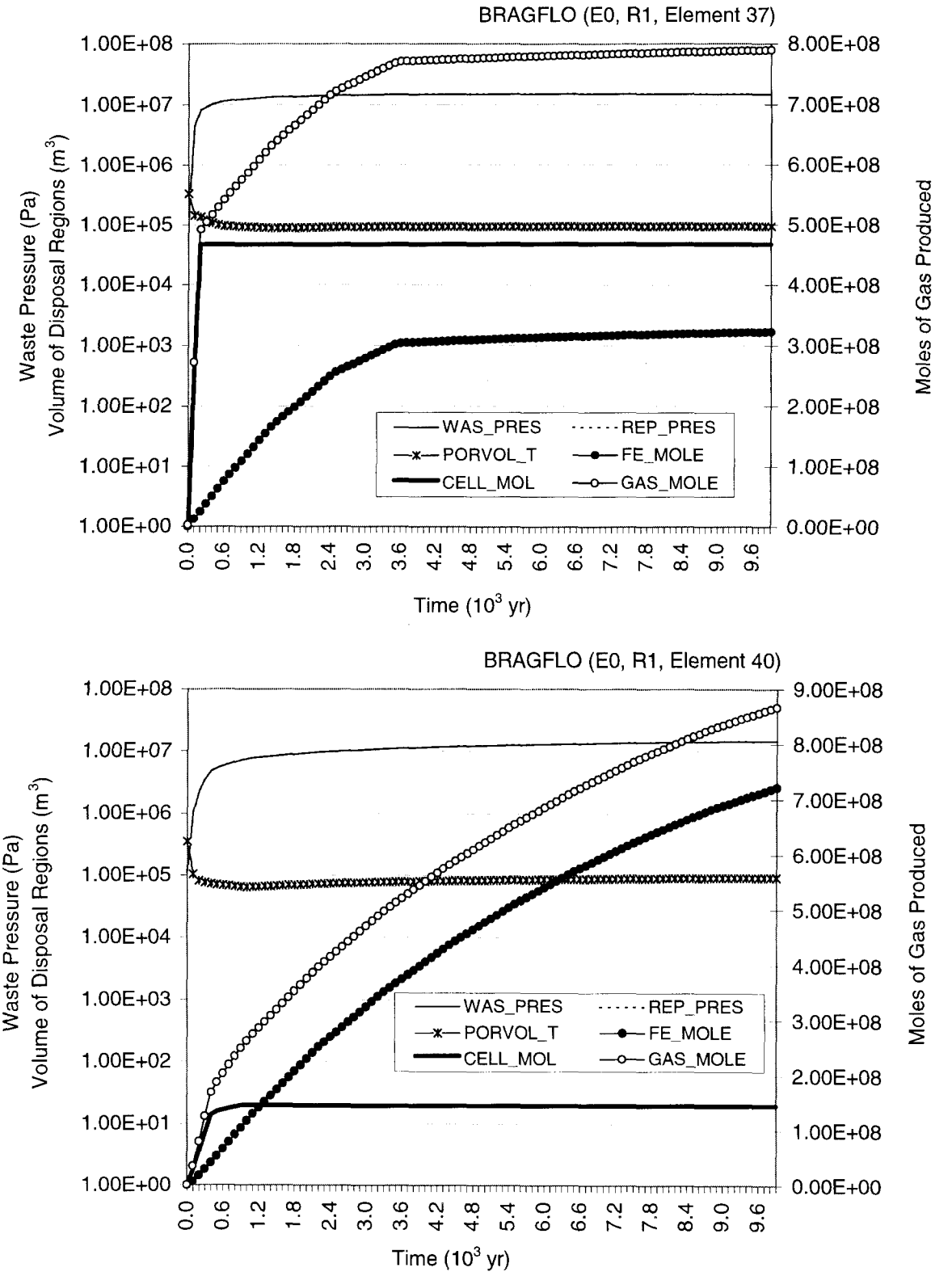

Fig. 7.4.6. Pressure (*WAS_PRES*, *REP_PRES*), pore volume (*PORVOL_T*), and gas generation (*FE_MOLE*, *CELL_MOL*, *GAS_MOLE*) for repository under undisturbed conditions for sample elements 37 and 40 of replicate R1.

similar patterns of microbial gas generation (*CELL_MOL*), with all microbial gas generation completed within 500 yr. The pattern for gas generation due to corrosion (*FE_MOLE*) is somewhat different between the two sample elements, with gas generation due to corrosion for element 37 being less than that due to microbial degradation and also almost ceasing after 3600 yr and gas generation due to corrosion for element 40 being considerably larger than that due to microbial degradation and continuing at an almost constant rate over the entire 10,000 yr period. For both sample elements, total pore volume in the repository (*PORVOL_T*) tracks repository pressure. The following patterns appearing in Fig. 7.4.6 are common to all sample elements for E0 conditions: (1) pressures in the upper and lower waste panels are similar, (2) repository pressure increases monotonically through time, (3) repository pressure and pore volume track each other very closely, and (4) microbial gas generation takes place very quickly and then stops.

7.5 Undisturbed Conditions: Brine Saturation

Unlike pressure, there is considerable variation between the brine saturation conditions at the southern and northern ends of the repository (Fig. 7.5.1). At both ends, brine saturation increases rapidly in the first 50 to 1000 yr due to brine flow from the DRZ (Fig. 7.2.1) and reduction in pore volume due to compaction of the waste (Fig. 7.4.4). After this period of rapid increase, brine saturation tends to decrease as brine is consumed more rapidly by corrosion than it is replaced by inflow. Due to the computational grid in use (Fig. 4.2.1), the lower waste panel receives more brine inflow from the marker beds relative to its size than the upper waste panels (Fig. 7.2.2). The lower panel is also at the downdip end of the repository, with the result that it can also receive brine flowing down from the upper panels. As a result, the lower panel receives more brine on a unit volume basis than the upper panels and thus tends to have a higher brine saturation.

Brine saturation is dropping to zero for some sample elements, with this tending to occur less often for the lower waste panel than for the upper waste panels (Fig. 7.5.1). Further, brine saturation is more likely to remain at zero for the upper waste panels than the lower waste panel. When brine saturation goes to zero in a given computational cell (Fig. 4.2.3), corrosion stops but will resume if brine saturation subsequently increases. The complete cessation of corrosion is indicated by the level steel fraction curves in Fig. 7.3.9, with such cessation occurring for more sample elements in the upper waste panels than in the lower waste panel.

The estimated mean and percentile curves for brine saturation show less stability across replicates than the curves for pressure (Figs. 7.4.2, 7.5.2). This reduced stability results from a limited number of sample elements producing very high brine saturations while most sample elements produce much lower brine saturations (Fig. 7.5.1).

The dominant variables with respect to the uncertainty in brine saturation in the lower waste panel are *HALPOR*, *WMICDFLG*, *WGRCOR*, *WASTWICK* and *ANHPRM* (Fig. 7.5.1). The positive effect for *HALPOR* results because

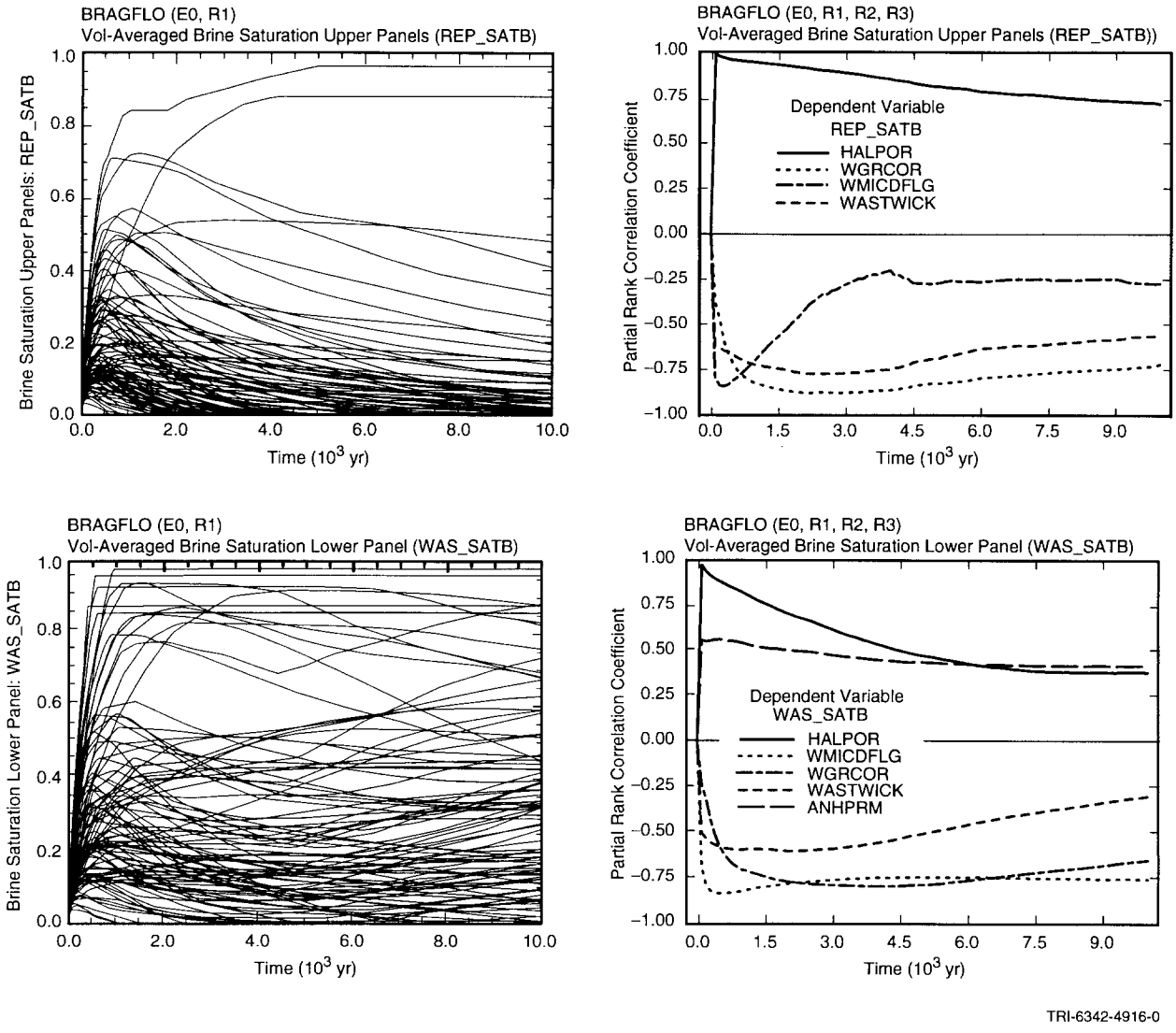

Fig. 7.5.1. Uncertainty and sensitivity analysis results for brine saturation in upper waste panels (*REP_SATB*) (upper frames) and lower waste panel (*WAS_SATB*) (lower frames) under undisturbed conditions.

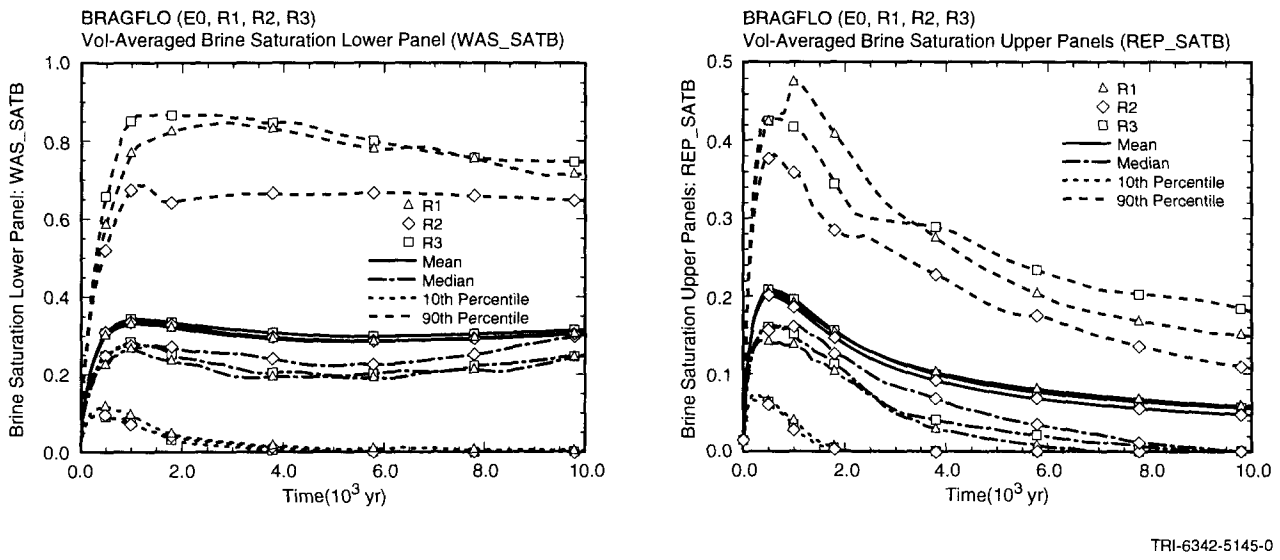

Fig. 7.5.2. Percentile curves for three replicated LHSs for brine saturation in the lower (*WAS_SATB*) and upper waste panels (*REP_SATB*) under undisturbed conditions.

increasing *HALPOR* increases the flow of brine into the lower waste panel from the DRZ in the first 50 to 100 yr of the calculation and thus contributes to the rapid rise in brine saturation during this early time period (Fig. 7.5.1). However, some of this rapid initial increase in brine saturation is also due to the compaction of the repository at early times (Fig. 7.4.4). The negative effect for *WMICDFLG* results because increasing *WMICDFLG* increases pressure in the repository, which in turn increases pore volume and decreases brine inflow from the marker beds. Both of the preceding effects will tend to reduce brine saturation. The negative effects for *WGRCOR* and *WASTWICK* result from increasing the rate at which brine is consumed by corrosion, which in turn tends to reduce brine saturation by both removing brine and increasing pore volume due to increased pressure. Finally, the positive effect for *ANHPRM* results because increasing *ANHPRM* increases brine flow from the marker beds and thus increases saturation in the lower waste panel.

Similar effects are also indicated for *HALPOR*, *WMICDFLG*, *WGRCOR* and *WASTWICK* in the analysis for brine saturation in the upper waste panels (Fig. 7.5.1). However, the patterns of importance for *HALPOR* and *WMICDFLG* are changed, with *HALPOR* showing greater importance over the entire 10,000 yr period than for the lower waste panel and *WMICDFLG* showing a significant effect at only early times. These changes occur because brine inflow from the marker beds is more important in determining saturation in the lower waste panel than in the upper waste panels, with the result that *WMICDFLG* has more influence through time on the saturation conditions in the lower waste panel than on the saturation conditions in the upper waste panels. Because *WMICDFLG* has less

effect through time on the saturation conditions in the upper panels, *HALPOR* will correspondingly tend to remain more important through time.

Regression analysis provides an alternative way to investigate the effect of uncertain variables on brine saturation in the upper and lower waste panels (Table 7.5.1) and produces results similar to those obtained with PRCCs (Fig. 7.5.1). For the lower panel, the variables *HALPOR*, *WMICDFLG*, *WGRCOR*, *WASTWICK* and *ANHPRM* identified with PRCCs are also identified in the regression analysis with effects of the same sign (i.e., saturation increases as *HALPOR* and *ANHPRM* increase and saturation decreases as *WMICDFLG*, *WGRCOR* and *WASTWICK* increase). Further, the regression analysis identifies *WRBRNSAT* and *HALPRM* as having negative and positive effects, respectively, on brine saturation in the lower panel. The positive effect for *HALPRM* results because increasing *HALPRM* tends to increase brine flow into the repository. The reason for the negative effect associated with *WRBRNSAT* is not clear; intuitively, it seems like increasing *WRBRNSAT* should increase brine saturation. A possibility is that increasing *WRBRNSAT* makes it more difficult for brine to flow into the repository as brine saturation is reduced below *WRBRNSAT* in individual computational cells due to consumption in the corrosion process. Another possibility is that the use of brine saturation and *WASTWICK* to define an effective saturation for the implementation of corrosion (i.e., $S_{b,eff}$ in Eq. (4.2.71)) may result in the small negative effect observed for *WRBRNSAT.*

For the upper waste panels, the variables *HALPOR*, *WGRCOR*, *WMICDFLG* and *WASTWICK* are identified in both the PRCC analysis (Fig. 7.5.1) and the regression analysis (Table 7.5.1) as having similar effects on brine saturation. In addition, the regression analysis also identifies *WRBRNSAT*, *HALPRM* and *ANHPRM*. The positive effects for *HALPRM* and *ANHPRM* result from increasing brine inflow to the repository. It is also possible that increasing *HALPRM* and *ANHPRM* may increase brine saturation by increasing gas movement away from the repository, which would reduce pressure and thereby reduce pore volume and thus increase brine saturation. As for the lower waste panel, the reason for the selection of *WRBRNSAT* with a negative regression coefficient is not immediately apparent. For perspective, scatterplots for the top three variables in each of the regression analyses in Table 7.5.1 are shown in Fig. 7.5.3.

In addition to brine saturation, brine volume in the waste panels is also important because it influences the amount of dissolved, and hence mobile, radionuclides in the repository. Volume of brine in the upper waste panels tends to increase at very early times (i.e., in the first few hundred years) and then decrease monotonically (Fig. 7.5.4). In contrast, brine volume in the lower panel shows a more complex pattern of behavior, with brine volume tending to increase over the entire 10,000 yr period for some sample elements and displaying a pattern of early increase followed by monotonic decrease for other sample elements (Fig. 7.5.4).

Table 7.5.1. Stepwise Regression Analyses with Rank-Transformed Data for Brine Saturation in the Upper (*REP_SATB*) and Lower (*WAS_SATB*) Waste Panels at 10,000 yr Under Undisturbed Conditions

	Brine Saturation Upper Waste Panels: *REP_SATB*			Brine Saturation Lower Waste Panel: *WAS_SATB*		
Step[a]	Variable[b]	SRRC[c]	R^{2d}	Variable	SRRC	R^2
1	*HALPOR*	0.53	0.27	*WMICDFLG*	−0.59	0.39
2	*WGRCOR*	−0.53	0.55	*WGRCOR*	−0.43	0.57
3	*WASTWICK*	−0.35	0.67	*ANHPRM*	0.23	0.62
4	*WMICDFLG*	−0.15	0.70	*HALPOR*	0.21	0.66
5	*WRBRNSAT*	−0.10	0.71	*WRBRNSAT*	−0.18	0.69
6	*HALPRM*	0.09	0.71	*WASTWICK*	−0.16	0.72
7	*ANHPRM*	0.08	0.72	*HALPRM*	0.11	0.73

[a] Steps in stepwise regression analysis.

[b] Variables listed in order of selection in regression analysis with *ANHCOMP* and *HALCOMP* excluded from entry into regression model.

[c] Standardized rank regression coefficients in final regression model.

[d] Cumulative R^2 value with entry of each variable into regression model.

The dominant variables with respect to brine volume in the upper panels identified by PRCCs are *HALPOR*, *WGRCOR* and *WASTWICK*, with brine volume tending to increase as *HALPOR* increases and decrease as *WGRCOR* and *WASTWICK* increase (Fig. 7.5.4). These effects result because *HALPOR* influences the amount of brine that enters the repository due to drainage from the DRZ (Fig. 7.2.3, Table 7.2.3) and *WGRCOR* and *WASTWICK* influence the rate at which brine is consumed by corrosion (Fig. 7.3.7, Table 7.3.2, with fraction of steel remaining having a rank correlation of −1 with amount of brine consumed). The negative effect for *SALPRES* at early times is probably spurious and results from *HALPOR* having a PRCC close to 1.

Regression analysis provides an alternative determination of variable importance for volume of brine in upper panels (Table 7.5.2) and also identifies *HALPOR*, *WGRCOR* and *WASTWICK* as important variables with similar effects as in the analysis with PRCCs. In addition, the analysis indicates that brine volume increases as *ANHPRM* and *HALPRM* increase and decreases as *WMICDFLG* and *WRBRNSAT* increase. The effects of these variables have been previously discussed in the context of brine saturation. Indeed, the sensitivity analyses for brine saturation (Fig. 7.5.1, Table 7.5.1) and brine volume (Fig. 7.5.4, Table 7.5.2) are very similar due to the substantial correlations that exist between brine saturation and brine volume in the upper and lower waste panels (Fig. 7.5.5).

As for the upper waste panels, the sensitivity analyses for brine volume in the lower panel (Fig. 7.5.4, Table 7.5.2) are very similar to the corresponding results for brine saturation in the lower panel (Fig. 7.5.1, Table 7.5.1). In particular, brine volume tends to increase as *HALPOR*, *ANHPRM* and *HALPRM* increase and tends to decrease as *WMICDFLG*, *WGRCOR*, *WRBRNSAT* and *WASTWICK* increase, with these effects having been previously discussed in conjunction with brine saturation.

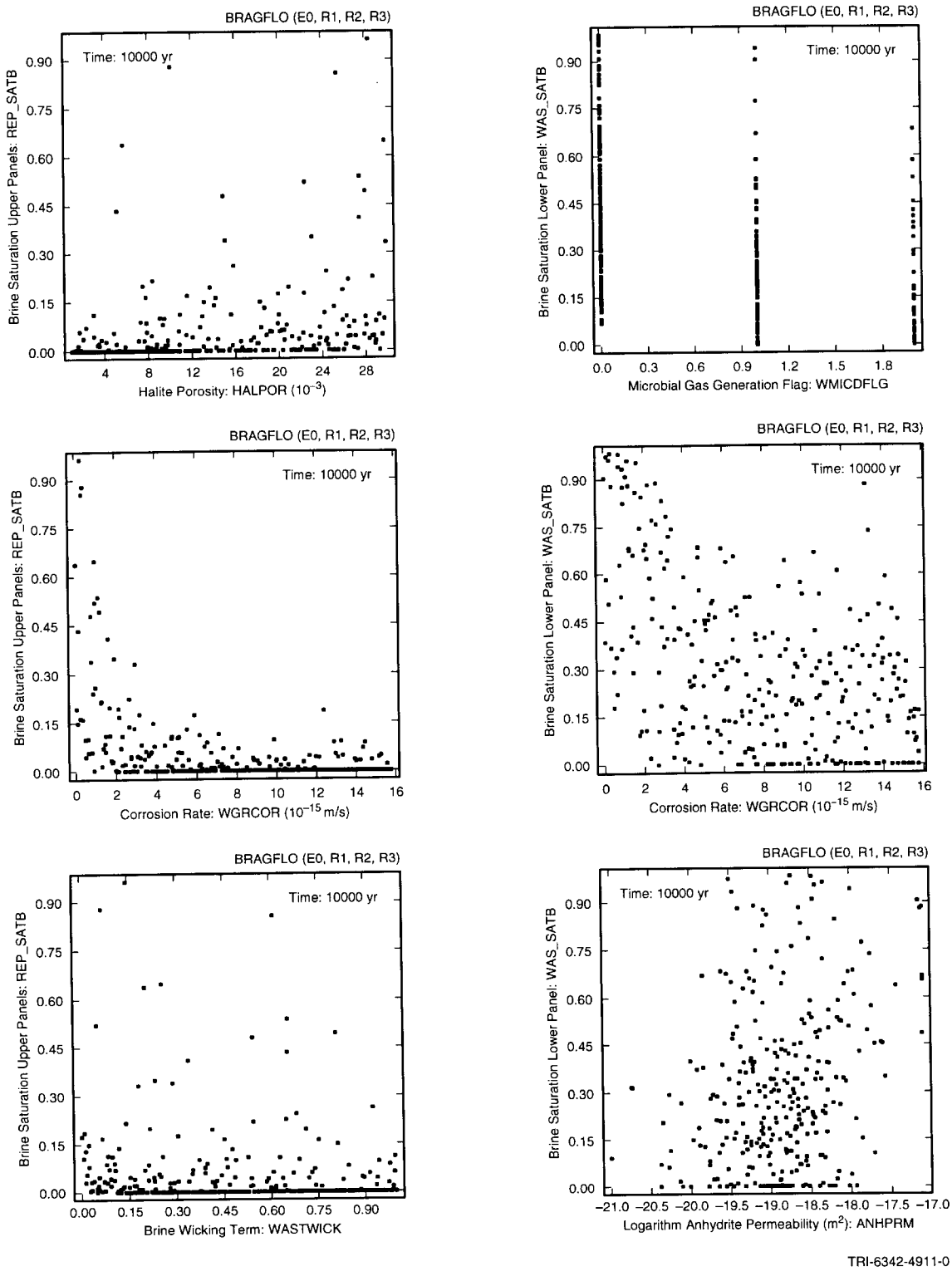

Fig. 7.5.3. Scatterplots for brine saturation in upper waste panels (*REP_SATB*) (left frames) and lower waste panel (*WAS_SATB*) (right frames) for undisturbed conditions at 10,000 yr versus *HALPOR*, *WGRCOR*, *WASTWICK*, *WMICDFLG* and *ANHPRM*.

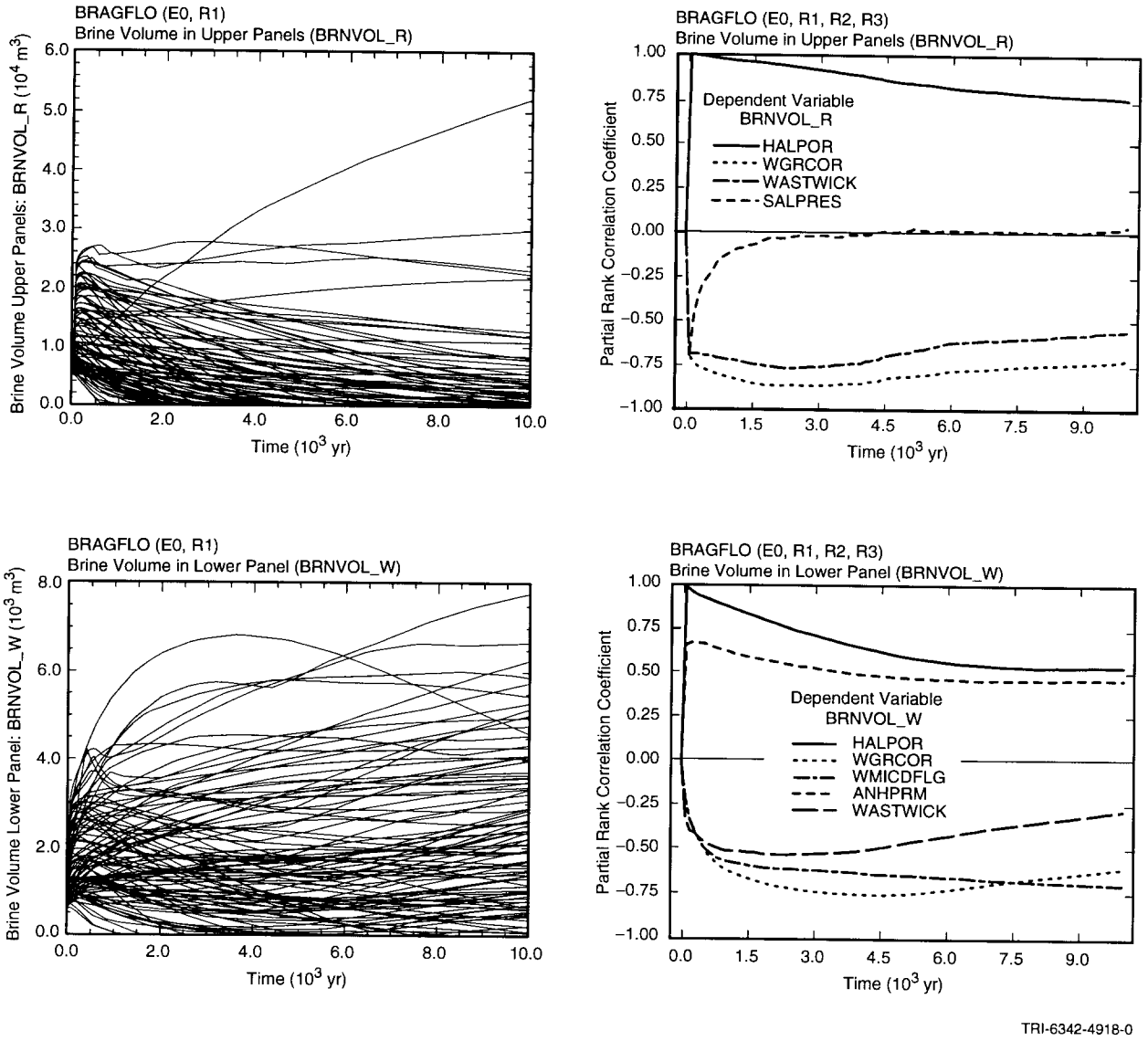

Fig. 7.5.4. Uncertainty and sensitivity analysis results for brine volume in upper waste panels (*BRNVOL_R*) (upper frames) and lower waste panel (*BRNWOL_W*) (lower frames) under undisturbed conditions.

Table 7.5.2. Stepwise Regression Analyses with Rank-Transformed Data for Brine Volume in the Upper (*BRNVOL_R*) and Lower (*BRNVOL_W*) Waste Panels at 10,000 yr Under Undisturbed Conditions

	Brine Volume Upper Waste Panels: *BRNVOL_R*			Brine Volume Lower Waste Panel: *BRNVOL_W*		
Step[a]	Variable[b]	SRRC[c]	R^{2d}	Variable	SRRC	R^2
1	*HALPOR*	0.57	0.31	*WMICDFLG*	−0.52	0.30
2	*WGRCOR*	−0.51	0.57	*WGRCOR*	−0.39	0.44
3	*WASTWICK*	−0.34	0.69	*HALPOR*	0.33	0.55
4	*WMICDFLG*	−0.12	0.70	*ANHPRM*	0.28	0.63
5	*ANHPRM*	0.10	0.71	*WRBRNSAT*	−0.20	0.67
6	*WRBRNSAT*	−0.10	0.72	*WASTWICK*	−0.15	0.69
7	*HALPRM*	−0.09	0.73	*HALPRM*	0.13	0.71

[a] Steps in stepwise regression analysis.

[b] Variables listed in order of selection in regression analysis with *ANHCOMP* and *HALCOMP* excluded from entry into regression model.

[c] Standardized rank regression coefficients in final regression model.

[d] Cumulative R^2 value with entry of each variable into regression model.

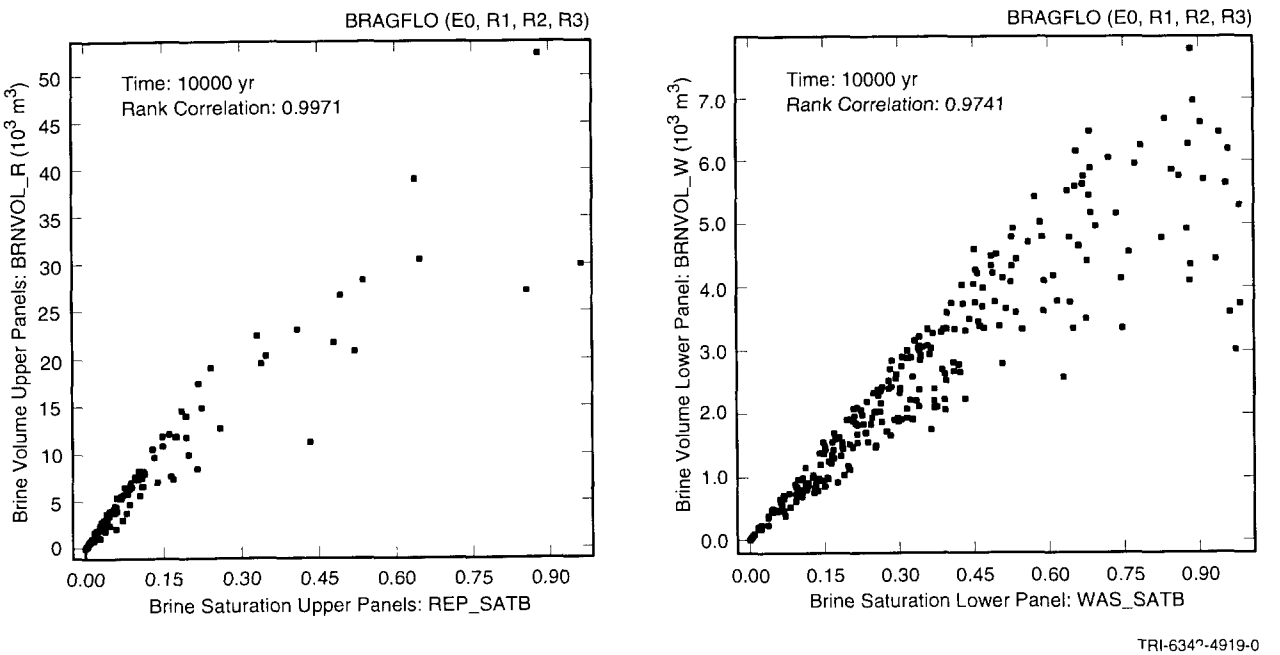

Fig. 7.5.5. Scatterplots for brine saturation and brine volume in upper (*BRNVOL_R, REP_SATB*) and lower (*BRNVOL_W, WAS_SATB*) waste panels under undisturbed conditions at 10,000 yr.

For perspective, time-dependent gas saturations (*REP_SATG*, *WAS_SATG*) and fractions of initial steel inventory remaining (*FEREM_R*, *FEREM_W*) in the upper and lower waste panels for sample elements 37 and 40 of replicate R1 are shown in Fig. 7.5.6. For sample element 37, the gas saturations go to 1 in both the upper (*REP_SATG*) and lower (*WAS_SATG*) waste panels, which is equivalent to the brine saturation going to 0. As the fraction of remaining steel ceases to decrease in the upper panels (*FEREM_R*), no ongoing corrosion is occurring in these panels. However, given that the fraction of remaining steel continues to decrease in the lower waste panel (*FEREM_W*), corrosion is continuing over the entire 10,000 yr period in this panel. As the gas saturation (*WAS_SATG*) is staying at 1, brine must be flowing into the lower waste panel, with this inflow being consumed by corrosion as it occurs. In contrast, the gas saturations remain below 1 in both the upper and lower panels for sample element 40, with the result that gas generation due to corrosion takes place in both panels over the entire 10,000 yr period under consideration.

Time-dependent pore volumes (*PORVOL_R*, *PORVOL_W*) and brine volumes (*BRNVOL_R*, *BRNVOL_W*) are shown in Fig. 7.5.7. For sample element 37, brine is almost completely removed from both the upper and lower waste panels, which is consistent with gas saturations (*REP_SATG*, *WAS_SATG*) close to 1 in Fig. 7.5.6. However, as gas generation due to corrosion continues over the entire 10,000 yr period for this sample element (see *FE_MOLE* in Fig. 7.4.7 and *FEREM_W* in Fig. 7.5.6 for sample element 37), a small amount of brine is entering the lower waste panel to replace the brine that is being consumed by corrosion. For sample element 40, a substantial amount of brine is present in the waste panels over the entire 10,000 yr period (Fig. 7.5.7), with the result that gas generation due to corrosion also continues over this time period (Figs. 7.4.6, 7.5.6).

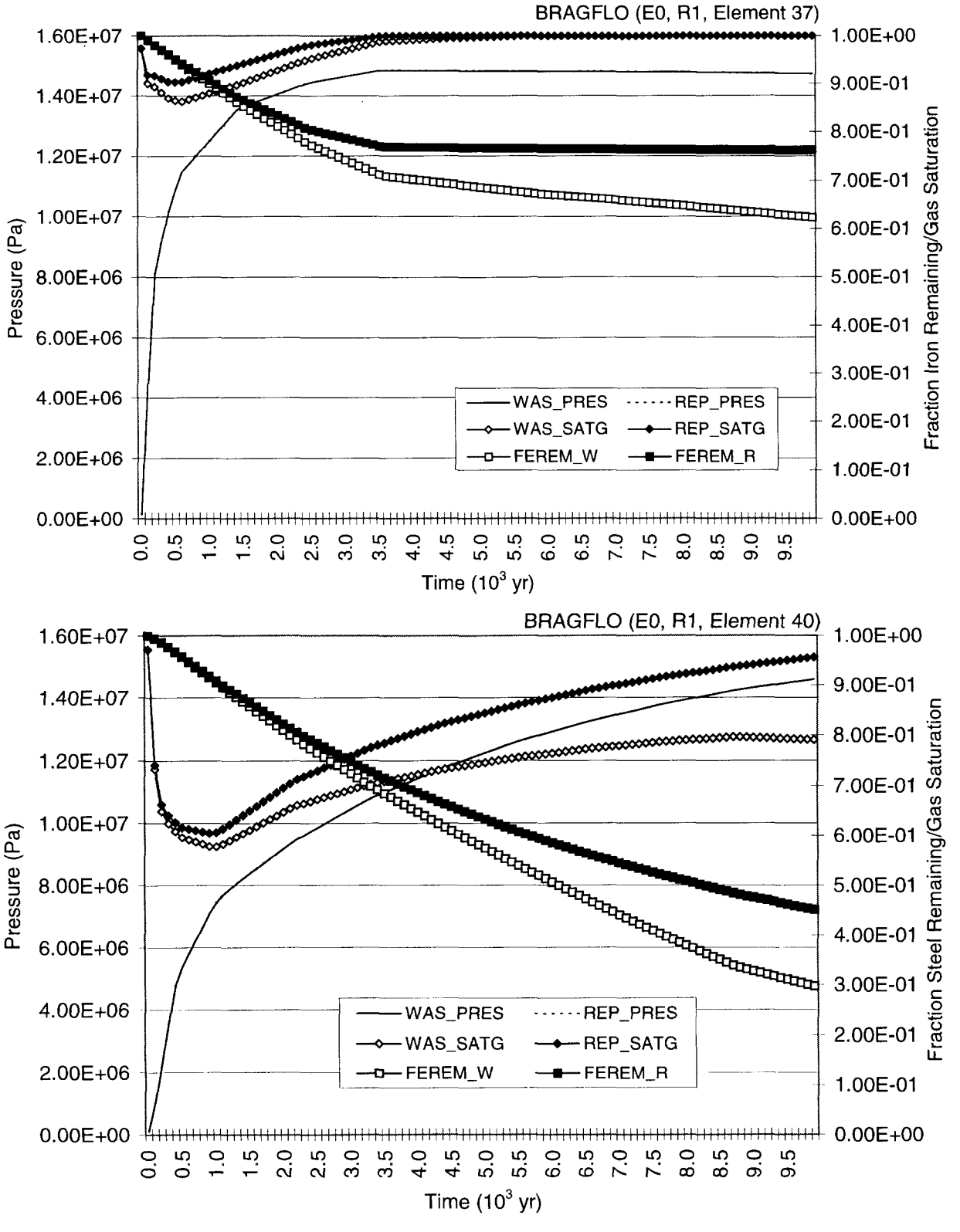

Fig. 7.5.6. Pressure (*REP_PRES*, *WAS_PRES*), gas saturation (*REP_SATG*, *WAS_SATG*) and fraction of initial steel inventory remaining (*FEREM_R*, *FEREM_W*) in upper and lower waste panels under undisturbed conditions for sample elements 37 and 40 in replicate R1.

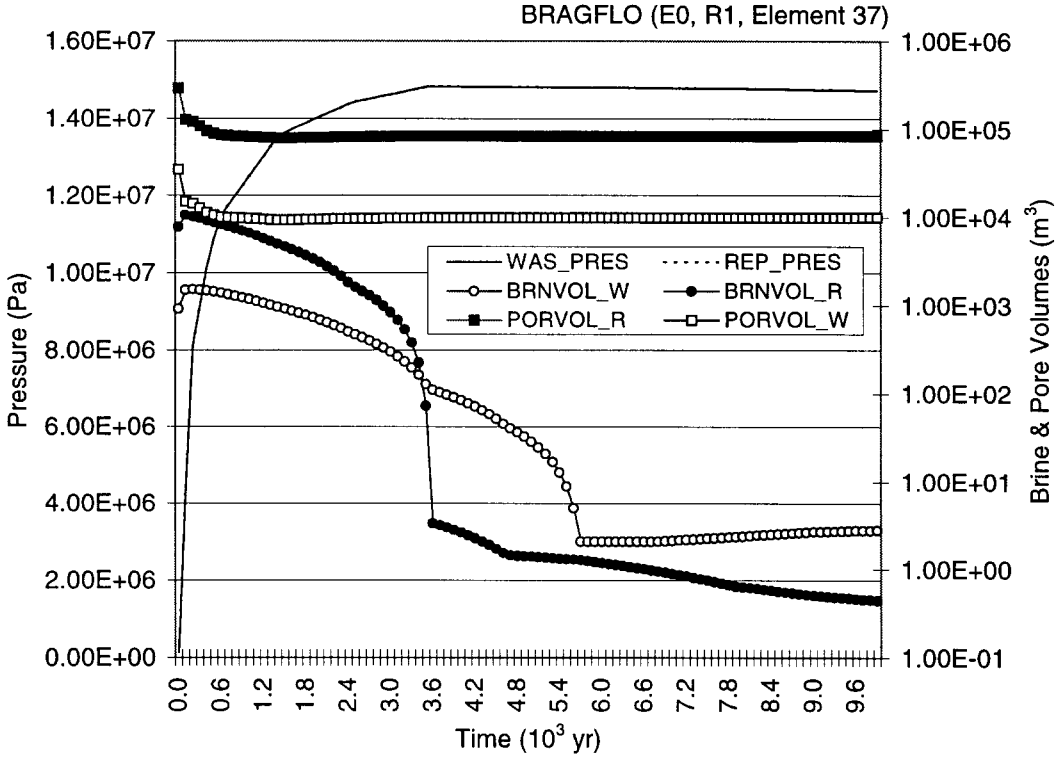

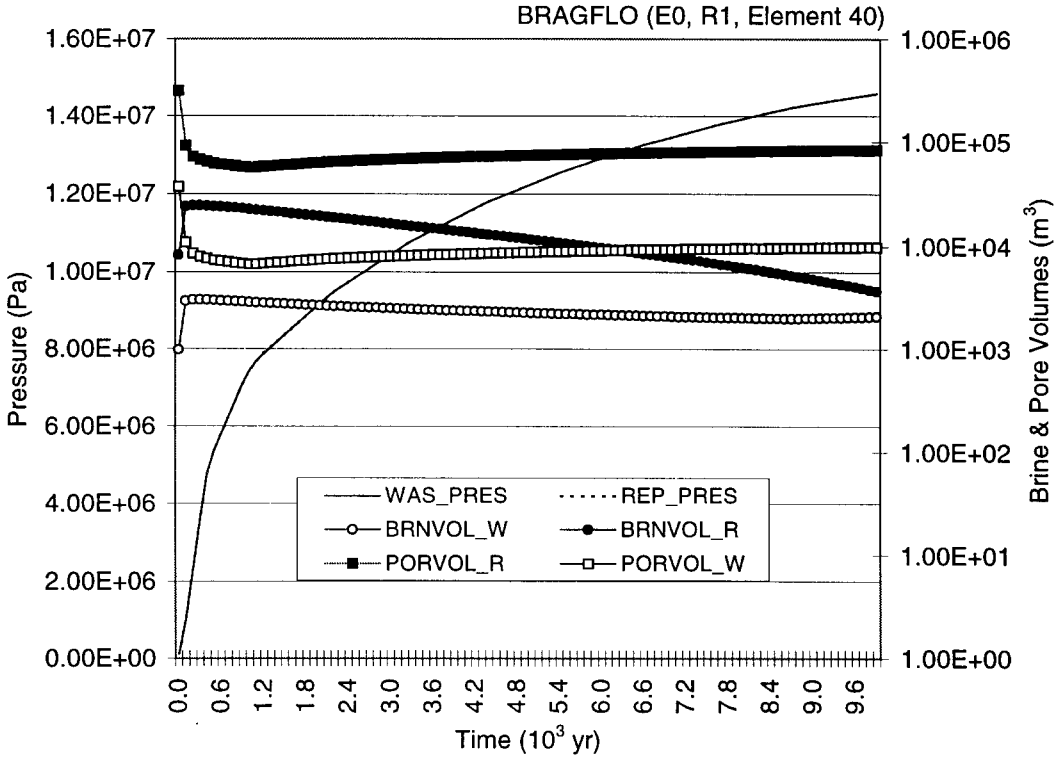

Fig. 7.5.7. Pressure (*REP_PRES*, *WAS_PRES*), pore volume (*PORVOL_R*, *PORVOL_W*) and brine volume (*BRNVOL_R*, *BRNVOL_W*) in upper and lower waste panels under undisturbed conditions for sample elements 37 and 40 of replicate R1.

7.6 Undisturbed Conditions: Brine and Gas Outflow

The anhydrite marker beds provide a possible pathway by which brine can flow away from the repository (Fig. 7.6.1). However, the amount of brine that leaves the repository through the marker beds (i.e., at the boundary between the marker beds and the DRZ) tends to be smaller than the amount of brine that enters by this pathway (i.e., compare Figs. 7.2.1 and 7.6.1). Most sample elements result in no brine flow away from the repository in the marker beds (i.e., less than half of the sample elements result in nonzero cumulative brine flows in Fig. 7.6.1).

The largest brine flows away from the repository take place in MB 139, with the next largest flows taking place in MB 138 and the smallest flows taking place in anhydrite layers A and B (Fig. 7.6.2). Further, the brine flows from the repository into the shaft tend to be intermediate in size between those into MB 139 and 138 (Fig. 7.6.2), although the largest flows into MB 138 are larger than the largest flows into the shaft.

The PRCCs in Fig. 7.6.1 indicate that *WMICDFLG* and *HALPOR* are the two most important variables with respect to brine flow away from the repository, with this flow tending to increase as each of these variables increases. Increasing each of these variables increases gas generation and thus pressure in the repository, which in turn increases the pressure gradient into the marker beds. The scatterplots in Fig. 7.6.3 provide a summary of the effects of *WMICDFLG* and *HALPOR* at 10,000 yr.

The variables *WMICDFLG* and *HALPOR* are also the most important variables for brine movement into the individual marker beds (Table 7.6.1). In addition, small effects are indicated for several other variables. Increasing *WGRCOR* and *WASTWICK* tends to increase brine movement into the marker beds due to their role in increasing pressure, and increasing *SALPRES* tends to decrease movement into the marker beds by increasing marker bed pressure. Positive effects are also indicated for *ANHPRM* and *HALPRM*. These two variables potentially play a dual role by initially increasing brine inflow to the repository and thus pressure due to gas generation by corrosion, and then by reducing resistance to brine flow away from the repository as pressure increases. The individual regression models tend to have relatively low R^2 values (i.e., 0.51 to 0.62) due to the large number of vectors in which no brine flow into the marker beds takes place (Fig. 7.6.3).

The last regression in Table 7.6.1 is for brine movement in the shaft away from the repository at the top of the DRZ. The size of the movements is small and typically around 10 m^3 (Fig. 7.6.2). A number of variables are identified as affecting this movement but the final regression model has an R^2 of only 0.58. The two most important variables are *WMICDFLG* and *SHRGSSAT*, with brine flow away from the repository tending to increase as each of these variables increases. Increasing *WMICDFLG* increases pressure in the repository and hence the movement of brine away from the repository. Increasing *SHRGSSAT* changes brine flow patterns in the vicinity of the shaft. For perspective, scatterplots for *WMICDFLG* and *SHRGSSAT* are presented in Fig. 7.6.4, with the positive effects indicated in the regression model apparent but weak.

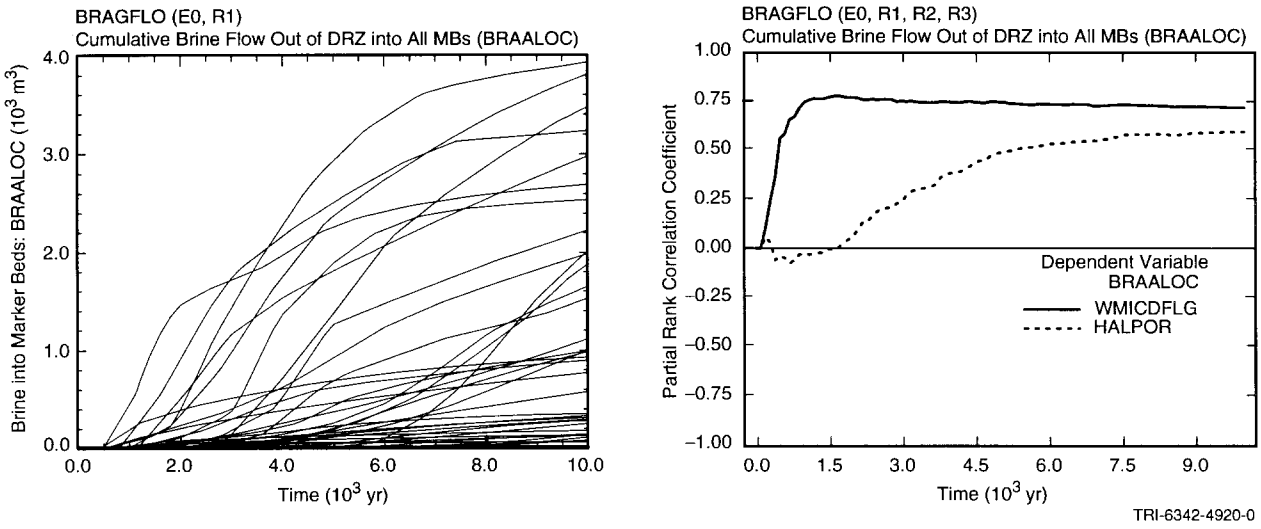

Fig. 7.6.1. Uncertainty and sensitivity analysis results for cumulative brine flow into marker beds away from repository (*BRAALOC*) under undisturbed conditions.

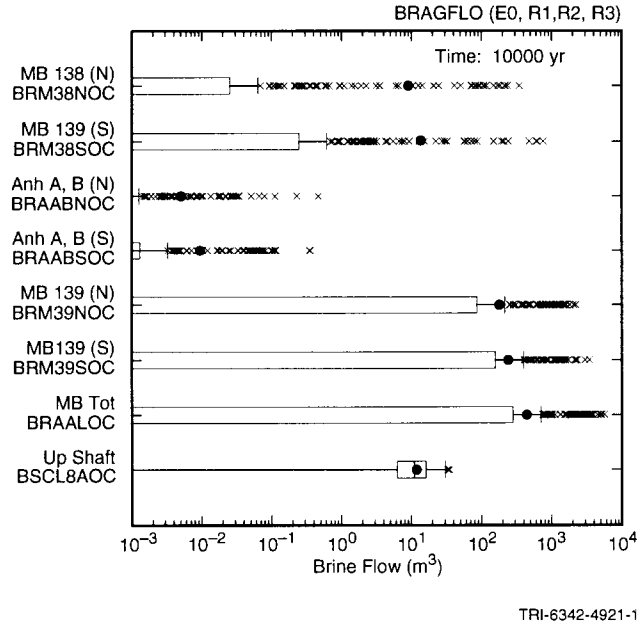

Fig. 7.6.2. Cumulative brine flow over 10,000 yr away from repository in marker beds (*BRM38NOC*, *BRM38SOC*, *BRAABNOC*, *BRAABSOC*, *BRM39NOC*, *BRM39SOC*, *BRAALOC*) and up shaft (*BSCL8AOC*) under undisturbed conditions.

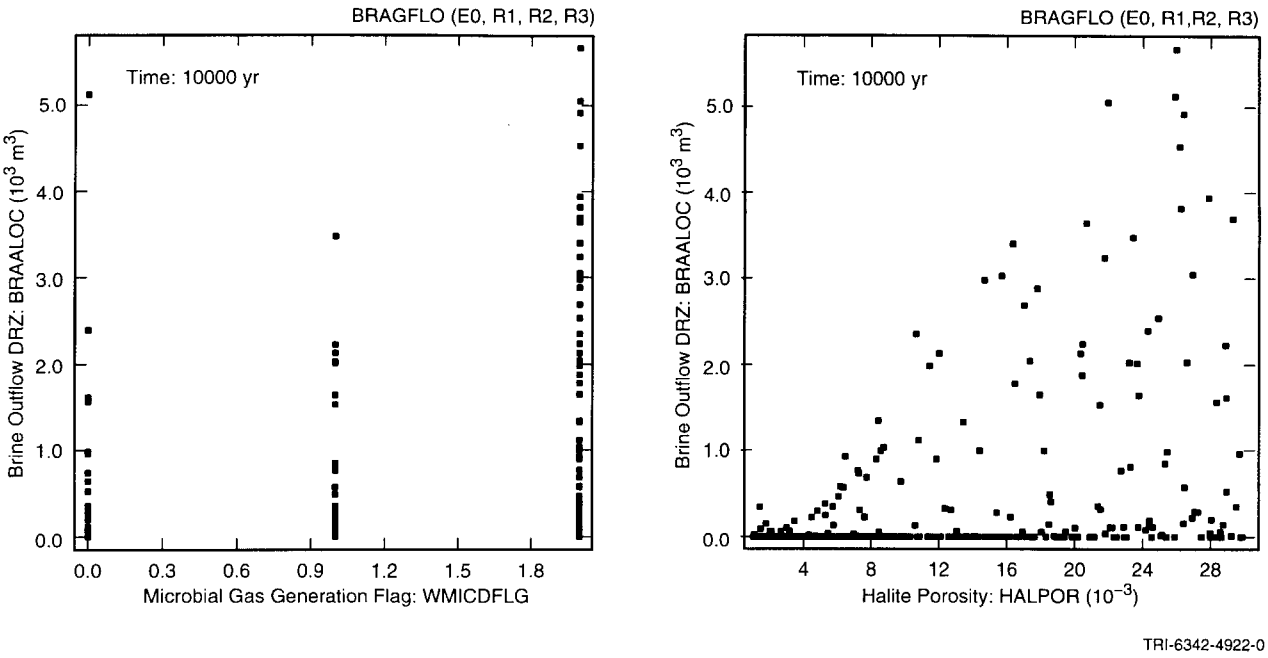

Fig. 7.6.3. Scatterplots for cumulative brine flow away from the repository over 10,000 yr in marker beds (*BRAALOC*) under undisturbed conditions versus *WMICDFLG* and *HALPOR*.

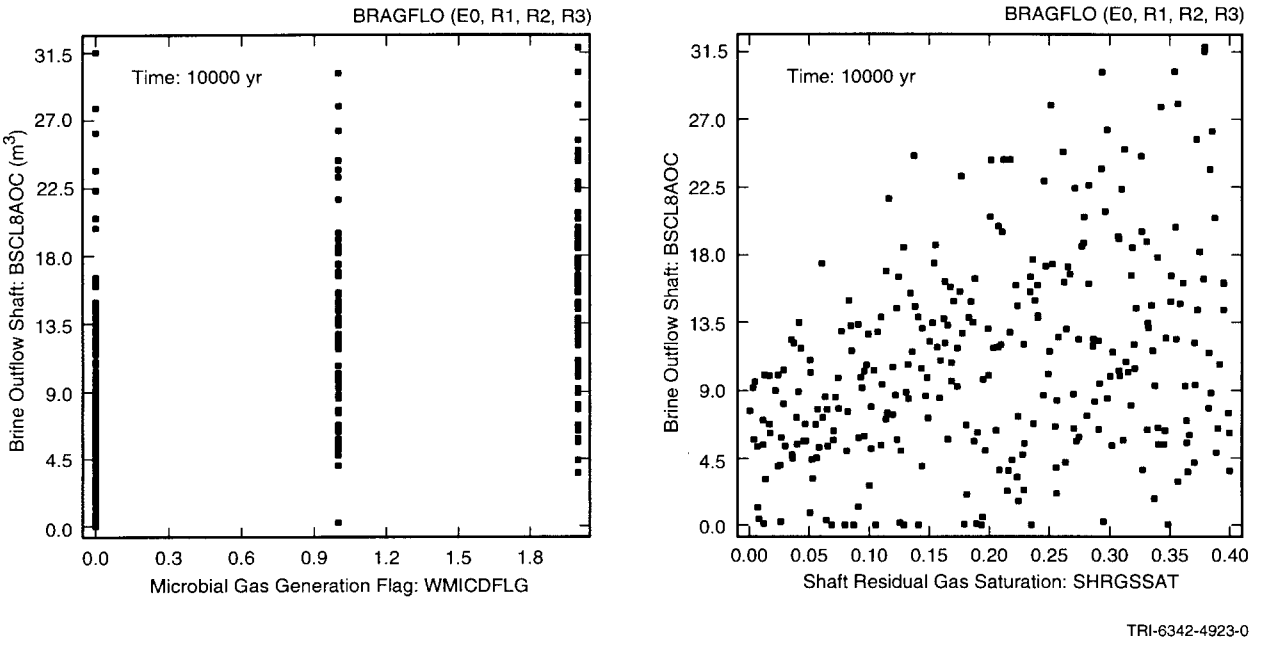

Fig. 7.6.4. Scatterplots for cumulative brine flow in shaft at boundary of DRZ and intact halite (*BSCL8AOC*) over 10,000 yr under undisturbed conditions versus *WMICDFLG* and *SHRGSSAT*.

Table 7.6.1. Stepwise Regression Analyses with Rank-Transformed Data for Cumulative Brine Flow over 10,000 yr away from Repository in Marker Beds (*BRM38NOC*, *BRM38SOC*, *BRAABNOC*, *BRAABSOC*, *BRM39NOC*, *BRM39SOC*, *BRAALOC*) and up shaft (*BSCL8AOC*) Under Undisturbed Conditions

	MB 138 North: *BRM38NOC*			MB 138 South: *BRM38SOC*			Anh a and b North: *BRAABNOC*			Anh a and b South: *BRAABSOC*		
Step[a]	Variable[b]	SRRC[c]	R^{2d}	Variable	SRRC	R^2	Variable	SRRC	R^2	Variable	SRRC	R^2
1	*WMICDFLG*	0.57	0.32	*WMICDFLG*	0.55	0.30	*WMICDFLG*	0.57	0.31	*WMICDFLG*	0.57	0.31
2	*HALPOR*	0.33	0.43	*HALPOR*	0.35	0.42	*HALPOR*	0.48	0.55	*HALPOR*	0.44	0.51
3	*SALPRES*	−0.18	0.47	*ANHPRM*	0.17	0.45	*WGRCOR*	0.18	0.58	*WGRCOR*	0.17	0.54
4	*ANHPRM*	0.17	0.49	*WGRCOR*	0.16	0.48	*SALPRES*	−0.15	0.60	*SALPRES*	−0.15	0.56
5	*WGRCOR*	0.14	0.51	*SALPRES*	−0.16	0.51	*HALPRM*	0.09	0.61	*ANHPRM*	0.12	0.57
6	*WASTWICK*	0.10	0.52							*HALPRM*	0.09	0.58

	MB 139 North: *BRM39NOC*			MB 139 South: *BRM39SOC*			MBs Total: *BRAALOC*			Up Shaft: *BSCL8AOC*		
Step[a]	Variable[b]	SRRC[c]	R^{2d}	Variable	SRRC	R^2	Variable	SRRC	R^2	Variable	SRRC	R^2
1	*WMICDFLG*	0.59	0.34	*WMICDFLG*	0.61	0.37	*WMICDFLG*	0.61	0.36	*WMICDFLG*	0.48	0.25
2	*HALPOR*	0.45	0.55	*HALPOR*	0.40	0.53	*HALPOR*	0.44	0.56	*SHRGSSAT*	0.33	0.36
3	*WGRCOR*	0.19	0.58	*WGRCOR*	0.18	0.56	*WGRCOR*	0.19	0.59	*HALPRM*	−0.25	0.42
4	*SALPRES*	−0.15	0.61	*SALPRES*	−0.15	0.59	*SALPRES*	−0.15	0.61	*HALPOR*	0.24	0.48
5	*HALPRM*	0.09	0.61				*HALPRM*	0.09	0.62	*WGRCOR*	0.20	0.52
										SHPRMHAL	0.18	0.55
										WASTWICK	0.09	0.56
										SHBCEXP	0.10	0.57
										ANHBCVGP	0.09	0.58

[a]Steps in stepwise regression analysis.

[b] Variables listed in order of selection in regression analysis with *ANHCOMP* and *HALCOMP* excluded from entry into regression model.

[c] Standardized rank regression coefficients in final regression model.

[d] Cumulative R^2 value with entry of each variable into regression model.

Brine flow away from the repository in the marker beds provides a potential mechanism for radionuclide transport to the accessible environment. However, flows across the land withdrawal boundary (i.e., the subsurface boundary of the accessible enviornment) away from the repository are zero or very small for most sample elements (Figs. 7.6.5, 7.6.6). Generally, more flow crosses the land withdrawal boundary moving away from the repository to the north than to the south (Fig. 7.6.6). However, it is a mistake to assume that the brine flows in Fig. 7.6.6 crossing the land withdrawal boundary originated in the repository. The pressurization of the marker beds can cause the movement across the land withdrawal boundary of brine that was initially present in the marker beds and has never had contact with the waste. For perspective, cumulative flows from the shaft into the Rustler Formation are also shown (Fig. 7.6.6). Again, it is a mistake to assume that these flows necessarily originated in the repository.

The dominant variable affecting brine flow in the marker beds across the land withdrawal boundary away from the repository is *ANHPRM*, with this flow tending to increase as *ANHPRM* increases due to reduced resistance to flow (Fig. 7.6.5, Table 7.6.2). The regressions for flow to the south (Table 7.6.2) have low R^2 values (i.e., 0.20 to

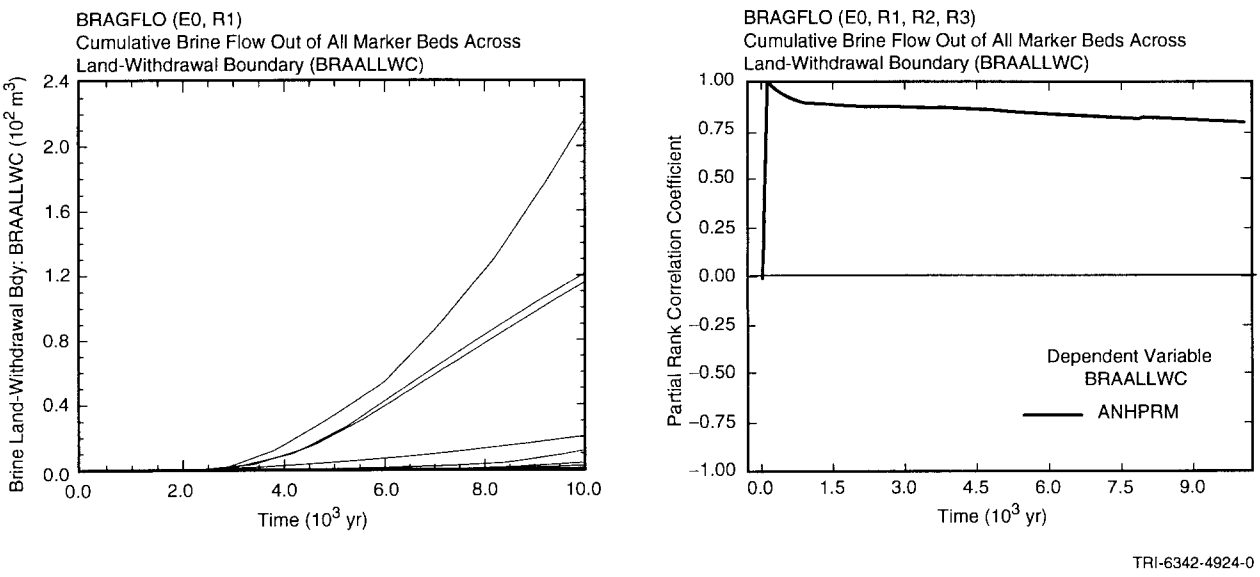

Fig. 7.6.5. Uncertainty and sensitivity analysis results for cumulative brine flow in marker beds across land withdrawal boundary away from repository (*BRAALLWC*) under undisturbed conditions.

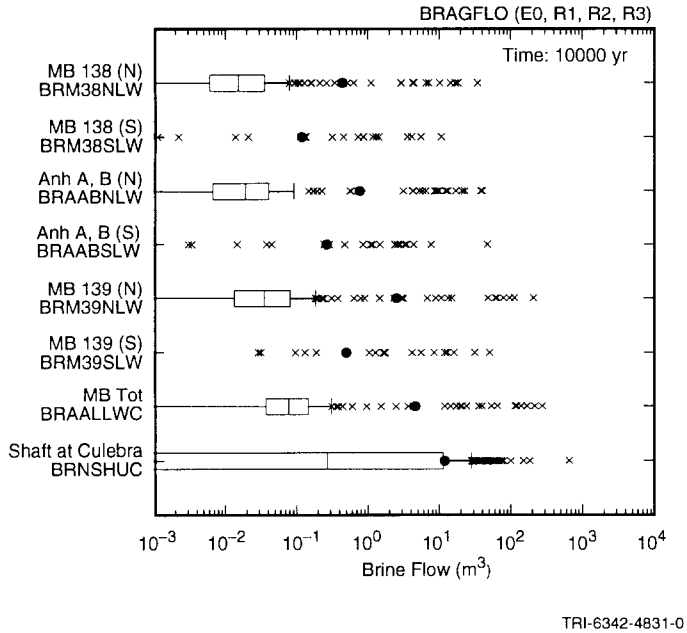

Fig. 7.6.6. Cumulative brine flow over 10,000 yr away from repository in individual marker beds at land withdrawal boundary (*BRM38NLW*, *BRM38SLW*, *BRAABNLW*, *BRAABSLW*, *BRM39NLW*, *BRM39SLW*, *BRAALLWC*) and in shaft at boundary with Rustler Formation (*BRNSHUC*) under undisturbed conditions.

Table 7.6.2. Stepwise Regression Analyses with Rank-Transformed Data for Cumulative Brine Flow over 10,000 yr Away From Repository in Individual Marker Beds at Land Withdrawal Boundary Away from Repository (*BRM38NLW*, *BRM38SLW*, *BRAABNLW*, *BRAABSLW*, *BRM39NLW*, *BRM39SLW*, *BRAALLWC*) and in Shaft at Boundary with Rustler Formation (*BRNSHUC*) Under Undisturbed Conditions

	MB 138 North: *BRM38NLW*			MB 138 South: *BRM38SLW*			Anh a and b North: *BRAABNLW*			Anh a and b South: *BRAABSLW*		
Step[a]	Variable[b]	SRRC[c]	R^{2d}	Variable	SRRC	R^2	Variable	SRRC	R^2	Variable	SRRC	R^2
1	*ANHPRM*	0.88	0.78	*WMICDFLG*	0.30	0.09	*ANHPRM*	0.70	0.50	*WMICDFLG*	0.31	0.10
2	*WMICDFLG*	0.12	0.79	*ANHPRM*	0.23	0.14	*WMICDFLG*	0.19	0.54	*ANHPRM*	0.22	0.15
3	*HALPOR*	0.08	0.80	*HALPOR*	0.16	0.17	*HALPRM*	0.18	0.57	*HALPOR*	0.16	0.17
4				*ANHBCVGP*	−0.16	0.19	*WRGSSAT*	−0.11	0.58	*ANHBCVGP*	−0.16	0.20
5				*SALPRES*	−0.14	0.21	*ANHBCVGP*	−0.09	0.59	*SALPRES*	−0.14	0.22
6				*WASTWICK*	0.13	0.23						

	MB 139 North: *BRM39NLW*			MB 139 South: *BRM39SLW*			MBs Total: *BRAALLWC*			Shaft to Culebra: *BRNSHUC*		
Step	Variable	SRRC	R^2	Variable	SRRC	R^2	Variable	SRRC	R^2	Variable	SRRC	R^2
1	*HALPRM*	0.37	0.13	*WMICDFLG*	0.30	0.10	*ANHPRM*	0.72	0.53	*SHPRMCLY*	0.72	0.51
2	*ANHPRM*	0.34	0.25	*ANHPRM*	0.26	0.16	*HALPRM*	0.24	0.59	*HALPRM*	0.49	0.75
3	*WMICDFLG*	0.22	0.30	*WASTWICK*	0.16	0.19	*WMICDFLG*	0.19	0.63	*SHPRMHAL*	0.19	0.79
4	*ANHBCVGP*	−0.14	0.32	*HALPOR*	0.13	0.20	*ANHBCVGP*	−0.09	0.63	*WMICDFLG*	0.07	0.79
5	*WASTWICK*	0.12	0.33				*WASTWICK*	0.08	0.64	*SALPRES*	0.07	0.80
6							*WRGSSAT*	−0.08	0.65			

[a] Steps in stepwise regression analysis.

[b] Variables listed in order of selection in regression analysis with *ANHCOMP* and *HALCOMP* excluded from entry into regression model.

[c] Standardized rank regression coefficients in final regression model.

[d] Cumulative R^2 value with entry of each variable into regression model.

0.23) due to the large number of zero results (Fig. 7.6.6). Similarly, the models for flow to the north and also for total flow are also rather poor with R^2 values of 0.80, 0.59, 0.33 and 0.65 (Table 7.6.2) due to the large number of zero or very small flows (Fig. 7.6.7). However, when flow does occur, it takes place for larger values of *ANHPRM* and also tends to increase as *ANHPRM* increases (Fig. 7.6.7).

The last regression in Table 7.6.2 is for brine flow out of the shaft into the Culebra. Brine flow out of the shaft is much greater than brine flow into the shaft at the repository (Figs. 7.6.2, 7.6.6). Thus, most of the brine exiting the shaft into the Culebra did not enter the shaft directly from the repository. The variables *SHPRMCLY* and *SHPRMHAL* appear in the regression model with positive regression coefficients because increasing their values reduces resistance to flow. The variables *HALPRM* and *SALPRES* appear in the regression model with positive regression coefficients because increasing their values tends to increase brine movement from the Salado halite to the shaft. Finally, *WMICDFLG* also appears in the regression model with a positive coefficient because increasing its values tends to increase repository pressure and thus increase brine movement away from the repository.

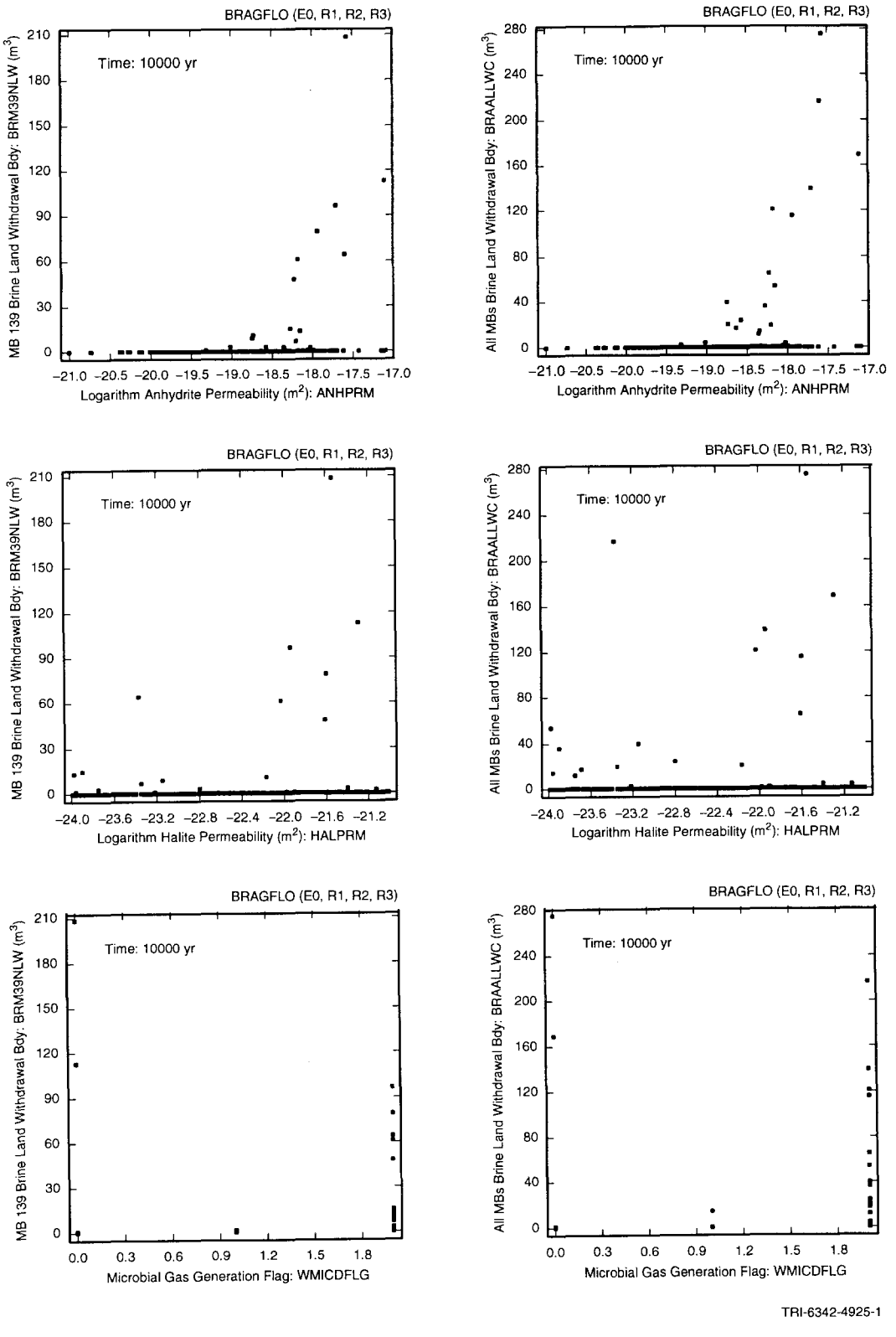

Fig. 7.6.7. Scatterplots for cumulative brine flow in marker beds across land withdrawal boundary away from repository over 10,000 yr for MB 139 North (*BRM39NLW*) (left frames) and all marker beds (*BRAALLWC*) (right frames) versus (*ANHPRM*), (*HALPOR*) and (*WMICDFLG*).

Gas flow can also take place in the anhydrite marker beds away from the repository, although little appreciable gas movement takes place for most sample elements (Fig. 7.6.8). Most gas movement in the individual marker beds tends to take place to the north (Fig. 7.6.9). In particular, MB 139 South experiences little gas inflow due to the tendency of brine to drain to its interface with the DRZ (Fig. 7.6.9).

The dominant variable in determining the amount of gas that moves away from the repository is *WMICDFLG*, with gas movement tending to increase as *WMICDFLG* increases due to increased repository pressure (Fig. 7.6.8, Table 7.6.3). In addition, gas movement tends to increase with increasing values for *HALPOR*, *WGRCOR* and *ANHPRM*, and to decrease with increasing values for *ANHBCVGP* and *SALPRES*. Increasing *HALPOR* and *WGRCOR* increases gas generation and hence pressure in the repository. Increasing *ANHPRM* increases repository pressure by increasing gas generation due to corrosion and also reduces resistance to gas flow into the marker beds. In contrast, increasing *SALPRES* reduces gas flow into the marker beds by increasing the pressure within the marker beds. The negative effect for *ANHBCVGP* indicates that gas is more likely to move into the marker beds when the Brooks-Corey model is in use. The very low R^2 value for gas movement into MB 139 South (i.e., 0.28) results from the large number of sample elements in which no gas movement takes place (Fig. 7.6.9). Scatterplots for the three most important variables with respect to gas movement away from the repository (i.e., *WMICDFLG*, *HALPOR* and *ANHBCVGP*) are given in Fig. 7.6.10, with the positive effects for *WMICDFLG* and *HALPOR* and the negative effect for *ANHBCVGP* being discernible within these plots.

Very little gas movement takes place through the shaft to the Culebra (Fig. 7.6.9). Due to the large number of zero and very small (i.e., probably numerical noise) results, the corresponding regression analysis (Table 7.6.3) produces rather poor results (i.e., $R^2 = 0.49$). However, examination of scatterplots shows the nonzero gas releases tend to be associated with small values for *SHRGSSAT* (Fig. 7.6.11).

The increased pressurization of the marker beds that results from gas generation in the repository can cause the marker beds to fracture and increase in pore volume (Fig. 7.6.12). However, pressure induced fracturing does not occur for most sample elements. Fracturing occurs almost equally to the north and south of the repository, with perhaps a slight tendency towards a greater increase in fracture-induced pore volume to the north (Fig. 7.6.13). Due to changes in pressure, the additional pore volume associated with fracturing can both increase and decrease with time (Fig. 7.6.12).

Due to its influence on volume of gas generated and hence repository pressure, *WMICDFLG* is the most important variable with respect to pore volume increase due to fracturing, with pore volume tending to increase as *WMICDFLG* increases (Fig. 7.6.12, Table 7.6.4). In addition, pore volume tends to increase as *HALPOR* and *WGRCOR* increase due to increased gas generation and to decrease as *SALPRES* increases due to reduced gas and

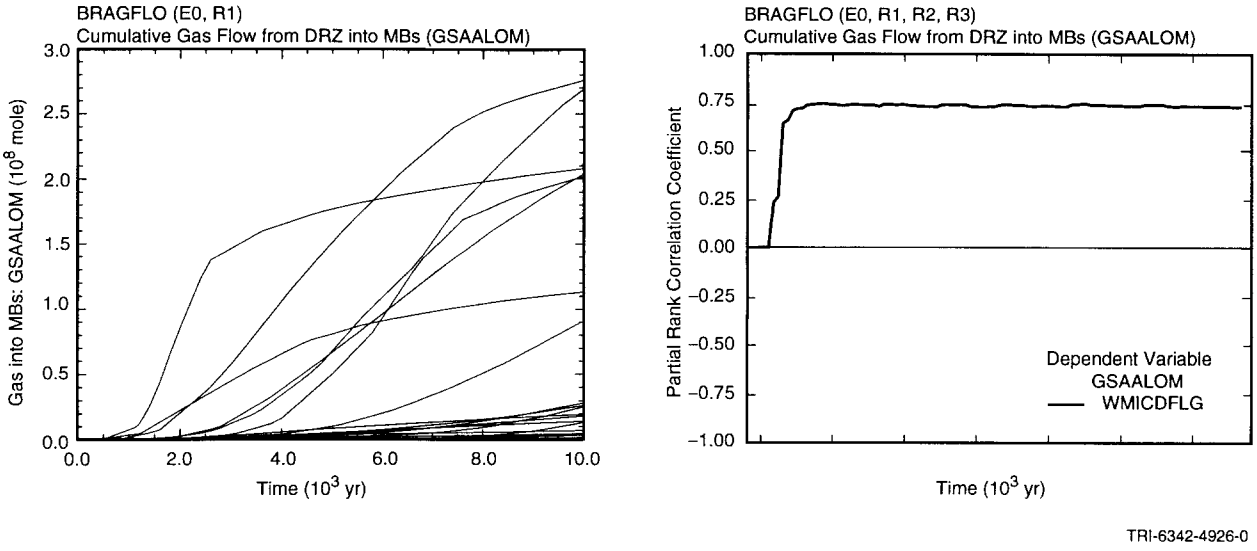

Fig. 7.6.8. Uncertainty and sensitivity analysis results for cumulative gas flow into marker beds away from repository (*GSAALOM*) under undisturbed conditions.

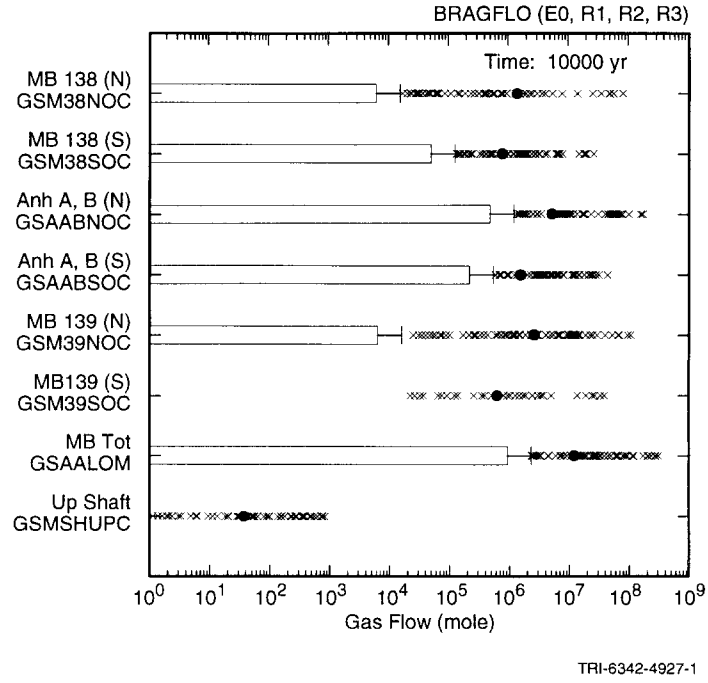

Fig. 7.6.9. Cumulative gas flows over 10,000 yr away from repository in individual marker beds (*GSM38NOC*, *GSM38SOC*, *GSAABNOC*, *GSAABSOC*, *GSM39NOC*, *GSM39SOC*, *GSAALOM*) and in shaft at boundary with Rustler Formation (*GSMSHUPC*) under undisturbed conditions.

Table 7.6.3. Stepwise Regression Analyses with Rank-Transformed Data for Cumulative Gas Flows over 10,000 yr Away From Repository in Individual Marker Beds (*GSM38NOC*, *GSM38SOC*, *GSAABNOC*, *GSAABSOC*, *GSM39NOC*, *GSM39SOC*, *GSAALOM*) and in Shaft at Boundary with Rustler Formation (*GSMSHUPC*) Under Undisturbed Conditions

	MB 138 North: *GSM38NOC*			MB 138 South: *GSM38SOC*			Anh a and b North: *GSAABNOC*			Anh a and b South: *GSAABSOC*		
Step[a]	Variable[b]	SRRC[c]	R^{2d}	Variable	SRRC	R^2	Variable	SRRC	R^2	Variable	SRRC	R^2
1	*WMICDFLG*	0.59	0.35	*WMICDFLG*	0.59	0.35	*WMICDFLG*	0.60	0.37	*WMICDFLG*	0.59	0.36
2	*HALPOR*	0.26	0.43	*HALPOR*	0.29	0.44	*HALPOR*	0.33	0.49	*HALPOR*	0.32	0.46
3	*ANHBCVGP*	−0.28	0.50	*ANHBCVGP*	−0.24	0.50	*ANHBCVGP*	−0.22	0.53	*ANHBCVGP*	−0.20	0.50
4	*WGRCOR*	0.19	0.54	*WGRCOR*	0.15	0.52	*WGRCOR*	0.19	0.57	*WGRCOR*	0.16	0.52
5	*SALPRES*	−0.16	0.56	*ANHPRM*	0.15	0.54	*ANHPRM*	0.17	0.60	*SALPRES*	−0.16	0.55
6	*HALPRM*	0.16	0.58	*SALPRES*	−0.15	0.56	*SALPRES*	−0.10	0.61	*ANHPRM*	0.13	0.57
7	*SHRGSSAT*	0.10	0.59	*HALPRM*	0.13	0.58						
8				*SHRGSSAT*	0.09	0.58						

	MB 139 North: *GSM39NOC*			MB 139 South: *GSM39SOC*			MBs Total: *GSAALOM*			Up Shaft at Rustler: *GSMSHUPC*		
Step	Variable	SRRC	R^2	Variable	SRRC	R^2	Variable	SRRC	R^2	Variable	SRRC	R^2
1	*WMICDFLG*	0.66	0.44	*WMICDFLG*	0.49	0.24	*WMICDFLG*	0.61	0.38	*SHPRMCON*	−0.43	0.20
2	*ANHBCVGP*	−0.18	0.47	*SALPRES*	−0.17	0.27	*HALPOR*	0.34	0.50	*SHRGSSAT*	−0.41	0.37
3	*ANHPRM*	0.15	0.50	*WGRCOR*	0.13	0.28	*ANHBCVGP*	−0.22	0.54	*SHPRMCLY*	0.35	0.49
4	*SALPRES*	−0.13	0.51				*WGRCOR*	0.20	0.58			
5	*WGRCOR*	0.11	0.53				*ANHPRM*	0.15	0.61			
6							*SALPRES*	−0.11	0.62			

[a] Steps in stepwise regression analysis.

[b] Variables listed in order of selection in regression analysis with *ANHCOMP* and *HALCOMP* excluded from entry into regression model.

[c] Standardized rank regression coefficients in final regression model.

[d] Cumulative R^2 value with entry of each variable into regression model.

brine inflow to the marker beds (Table 7.6.4). However, the R^2 values for the individual regression models tend to be low (i.e., 0.31 to 0.49 in Table 7.6.4) due to the large number of observations that result in no increase in pore volume. Scatterplots for the effects of *WMICDFLG*, *HALPOR*, *SALPRES* and *WGRCOR* on pore volume increase at 10,000 yr are shown in Fig. 7.6.14, with the two strongest trends involving *WMICDFLG* and *HALPOR*.

Fracturing is of concern because it can create zones of enhanced permeability between the repository and the boundary with the accessible environment (i.e., the land withdrawal boundary), which is 2.75 km from the repository. The longest observed fractures were approximately 2 km in length (Table 7.6.5) and thus did not reach the accessible environment. Further, most sample elements result in no fracturing of the marker beds (Table 7.6.5). As for fracture volume, fracture length can both increase and decrease with time due to changes in pressure (Fig. 7.6.15).

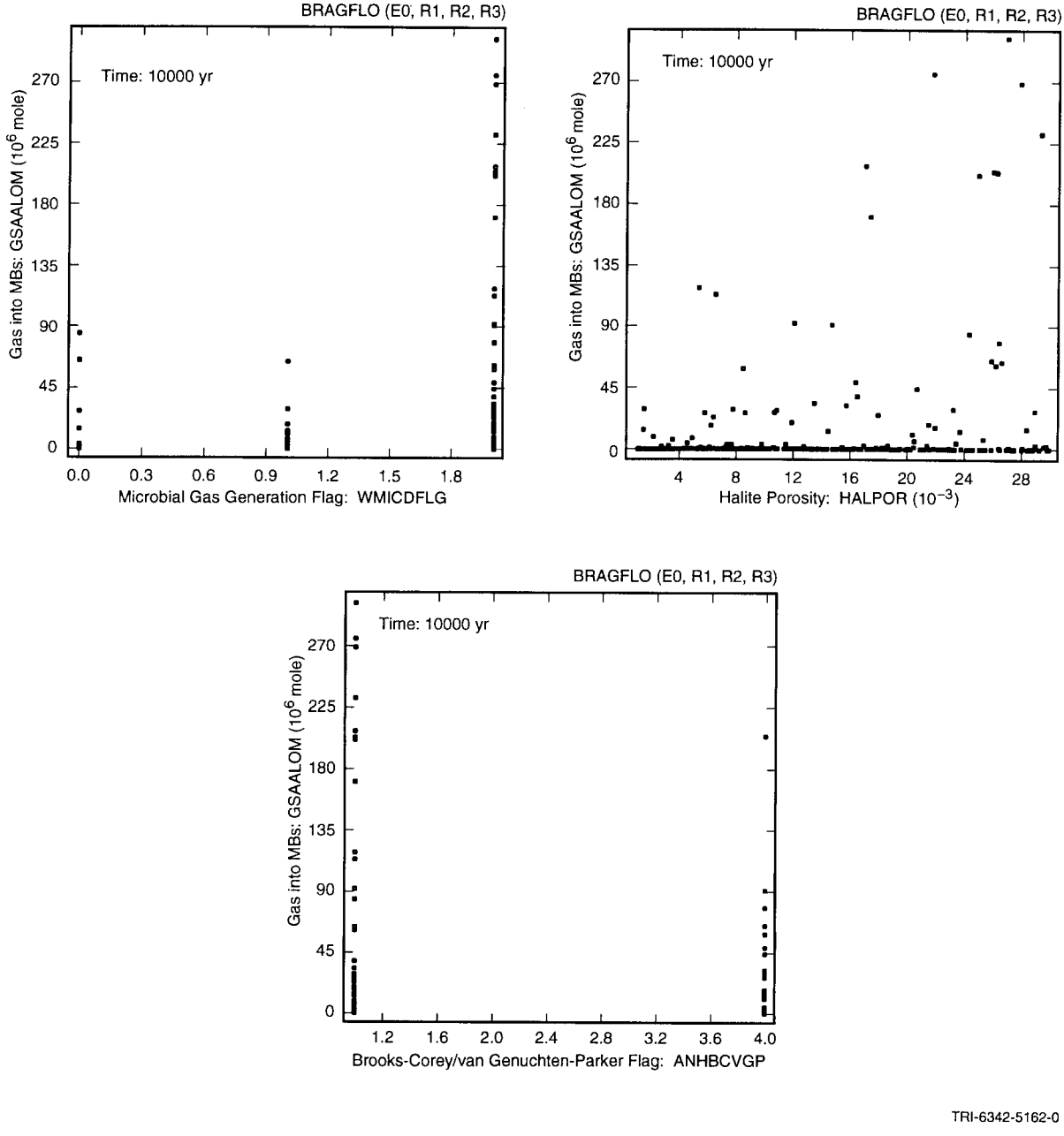

Fig. 7.6.10. Scatterplots for cumulative gas flow in marker beds away from repository (*GSAALOM*) under undisturbed conditions over 10,000 yr versus *WMICDFLG*, *HALPOR* and *ANHBCVGP*.

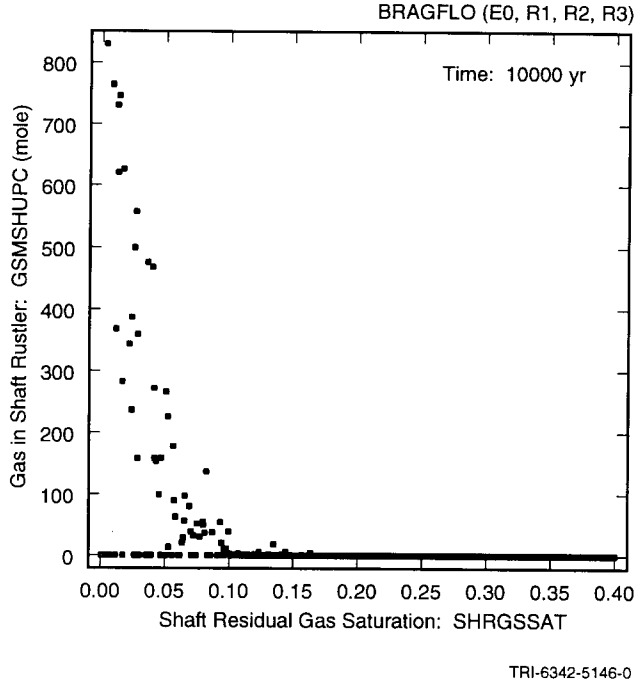

Fig. 7.6.11. Scatterplots for cumulative gas flow in shaft away from repository at boundary with Rustler Formation (*GSMSHUPC*) under undisturbed conditions over 10,000 yr versus *SHRGSSAT*.

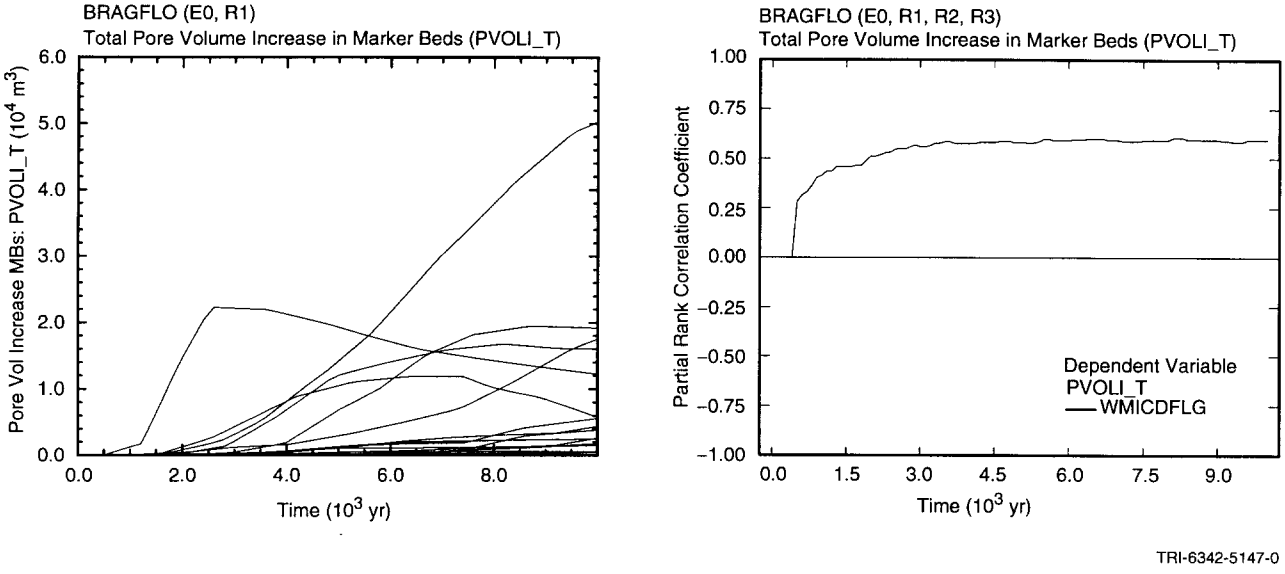

Fig. 7.6.12. Uncertainty and sensitivity analysis results for total pore volume increase in marker beds (*PVOLI_T*) under undisturbed conditions.

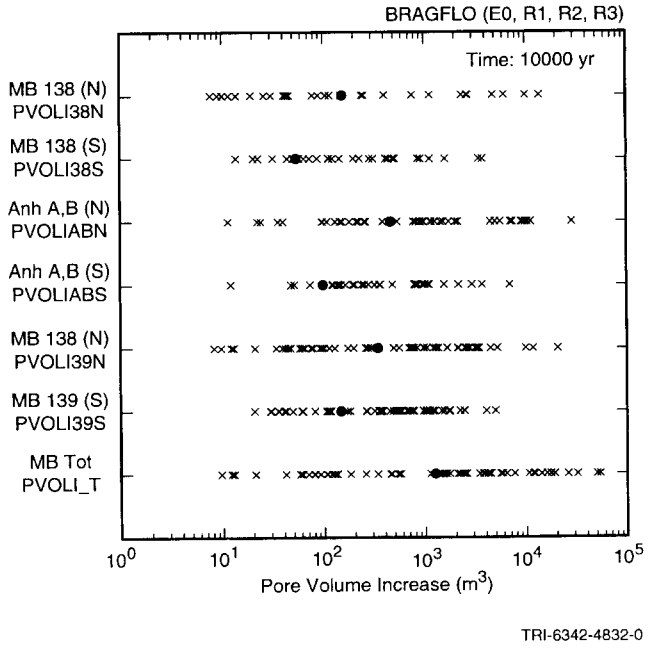

Fig. 7.6.13. Pore volume increase due to fracturing in individual marker beds (*PVOLI38N*, *PVOLI38S*, *PVOLIABN*, *PVOLIABS*, *PVOLI39N*, *PVOLI39S*, *PVOLI_T*) at 10,000 yr under undisturbed conditions.

Table 7.6.4. Stepwise Regression Analyses with Rank-Transformed Data for Pore Volume Increase Due to Fracturing in Individual Marker (*PVOLI38N*, *PVOLI38S*, *PVOLIABN*, *PVOLIABS*, *PVOLI39N*, *PVOLI39S*, *PVOLI_T*) Beds at 10,000 yr Under Undisturbed Conditions

	MB 138 North: *PVOLI38N*			MB 138 South: *PVOLI38S*			Anh a and b North: *PVOLIABN*			Anh a and b South: *PVOLIABS*		
Step[a]	Variable[b]	SRRC[c]	R^{2d}	Variable	SRRC	R^2	Variable	SRRC	R^2	Variable	SRRC	R^2
1	*WMICDFLG*	0.42	0.16	*WMICDFLG*	0.42	0.17	*WMICDFLG*	0.49	0.24	*WMICDFLG*	0.44	0.19
2	*HALPOR*	0.29	0.25	*HALPOR*	0.29	0.26	*HALPOR*	0.28	0.32	*HALPOR*	0.30	0.28
3	*SALPRES*	−0.20	0.29	*SALPRES*	−0.20	0.30	*SALPRES*	−0.24	0.38	*SALPRES*	−0.18	0.31
4	*WGRCOR*	0.13	0.31	*WGRCOR*	0.13	0.32	*WGRCOR*	0.12	0.39	*WGRCOR*	0.12	0.33
5							*SHRGSSAT*	0.11	0.41	*SHRGSSAT*	0.12	0.34
6							*HALPRM*	−0.11	0.42			

	MB 139 North: *PVOLI39N*			MB 139 South: *PVOLI39S*			MBs Total: *PVOLI_T*		
Step	Variable	SRRC	R^2	Variable	SRRC	R^2	Variable	SRRC	R^2
1	*WMICDFLG*	0.53	0.27	*WMICDFLG*	0.52	0.26	*WMICDFLG*	0.54	0.28
2	*HALPOR*	0.37	0.41	*HALPOR*	0.34	0.38	*HALPOR*	0.37	0.42
3	*SALPRES*	−0.21	0.45	*SALPRES*	−0.21	0.42	*SALPRES*	−0.20	0.46
4	*WGRCOR*	0.15	0.47	*WGRCOR*	0.14	0.44	*WGRCOR*	0.16	0.49

[a] Steps in stepwise regression analysis.

[b] Variables listed in order of selection in regression analysis with *ANHCOMP* and *HALCOMP* excluded from entry into regression model.

[c] Standardized rank regression coefficients in final regression model.

[d] Cumulative R^2 value with entry of each variable into regression model.

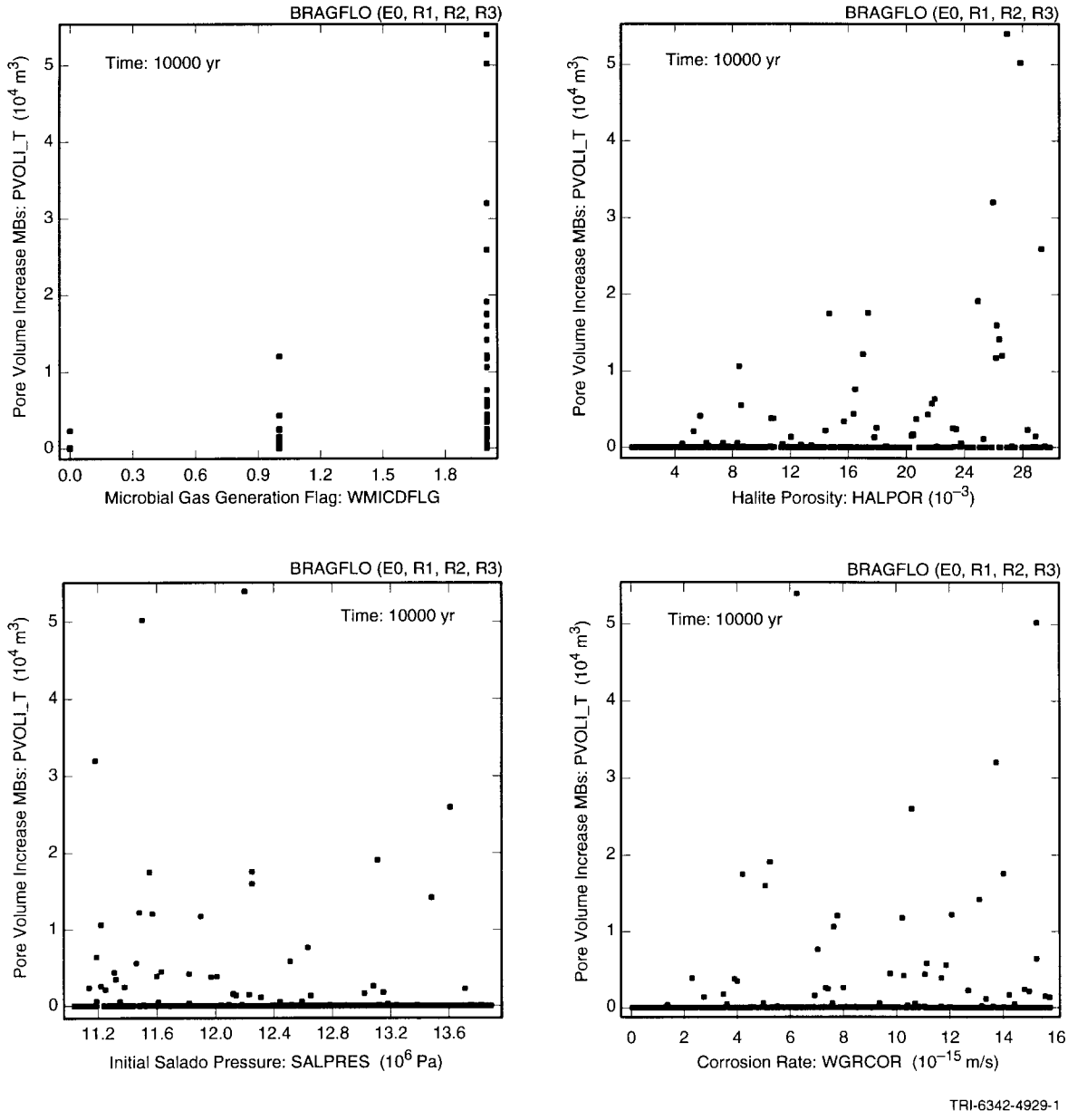

Fig. 7.6.14. Scatterplots for total pore volume increase due to fracturing in marker beds (*PVOLI_T*) at 10,000 yr under undisturbed conditions versus *WMICDFLG*, *HALPOR*, *SALPRES* and *WGRCOR*.

Table 7.6.5. Number of Observations Producing Fracture Zones of Different Lengths in Individual Marker Beds (*FRACX38N*, *FRACX38S*, *FRACXABN*, *FRACXABS*, *FRACX39N*, *FRACX39S*) at 10,000 yr under Undisturbed Conditions

	Fracture Distance					
Marker Bed	5 m	30 m	100 m	400 m	1030 m	1900 m
MB 138 (N): *FRACX38N*	0[a]	9	10	5	2	5
MB 138 (S): *FRACX38S*	0	6	14	6	5	0
Anh A,B (N): *FRACXABN*	1	6	11	14	7	5
Anh A,B (S): *FRACXABS*	1	6	12	12	2	0
MB 139 (N): *FRACX39N*	10	15	19	16	3	0
MB 139 (S): *FRACX39S*	8	15	25	5	1	0

[a] Number of observations out of 300

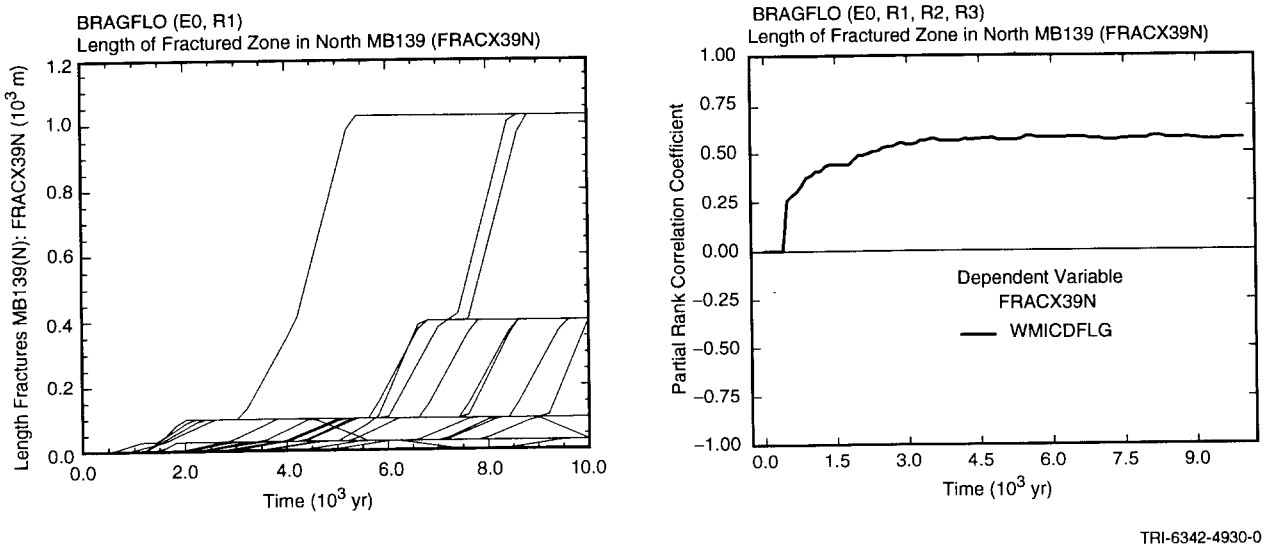

Fig. 7.6.15. Uncertainty and sensitivity analysis results for length of fracture zone in north MB 139 (*FRACX39N*) under undisturbed conditions.

Fracture volume (Fig. 7.6.13) and length (Table 7.6.5) are highly correlated. Specifically, rank correlations of 0.9999, 0.9994, 0.9997, 0.9996, 0.9991 and 0.9987 exist between fracture volume and length for MB 138 North, MB 138 South, Anhydrites a and b North, Anhydrites a and b South, MB 139 North, and MB 139 South. Thus, the sensitivity analysis results obtained for fracture volume (Table 7.6.4, Fig. 7.6.14) also apply to fracture length.

As an example, the brine and gas flows from the marker beds into the repository (*BRAALIC, GSAALIM*) and also from the repository into the marker beds (*BRAALOC, GSAALOM*) are summarized for sample elements 37 and 40 of replicate R1 in Fig. 7.6.16. Both sample elements have relatively small brine flows from the marker beds to the repository (~800 m^3 for element 37 and ~390 m^3 for element 40), with brine flow continuing over a longer period of time for element 40 than element 37. Brine flows into the marker beds (~900 m^3 for element 37 and ~140 m^3 for element 40) also occur once the pressure in the repository has risen to a sufficiently high level. A substantial gas flow into the marker beds occurs for sample element 37 but no gas flow occurs for element 40, which is why pressure levels off at an asymptote for element 37 but not for element 40. No gas flow takes place from the marker beds to the repository for either sample element.

A more detailed representation of the brine flows out of and into the individual marker beds is given in Fig. 7.6.17 for sample elements 37 and 40 of replicate R1. Most of the brine flow out of the marker beds and all of the brine flow into the marker beds are associated with MB 139.

A more detailed representation of the gas flows into the individual marker beds is given in Fig. 7.6.18. As no such flows occurred for sample element 40, the gas flows associated with sample element 14 are presented as an additional example. For sample element 14, the orderings of the gas flows out of the repository are *GSAABNOM* > *GSM38NOM* > *GSM39NOM* at the northern end of the repository and *GSM39SOM* > *GSAABSOM* > *GSM38SOM* at the southern end of the repository. For sample element 37, the corresponding orderings are *GSAABNOM* > *GSM39NOM* > *GSM38NOM* and *GSAABSOM* > *GSM38SOM* > *SGM39SOM* $\doteq$ 0 mol, respectively. Most sample elements result in no gas movement into the marker beds. When such movement does occur, the largest movements are typically in Anhydrites a and b (Fig. 7.6.9).

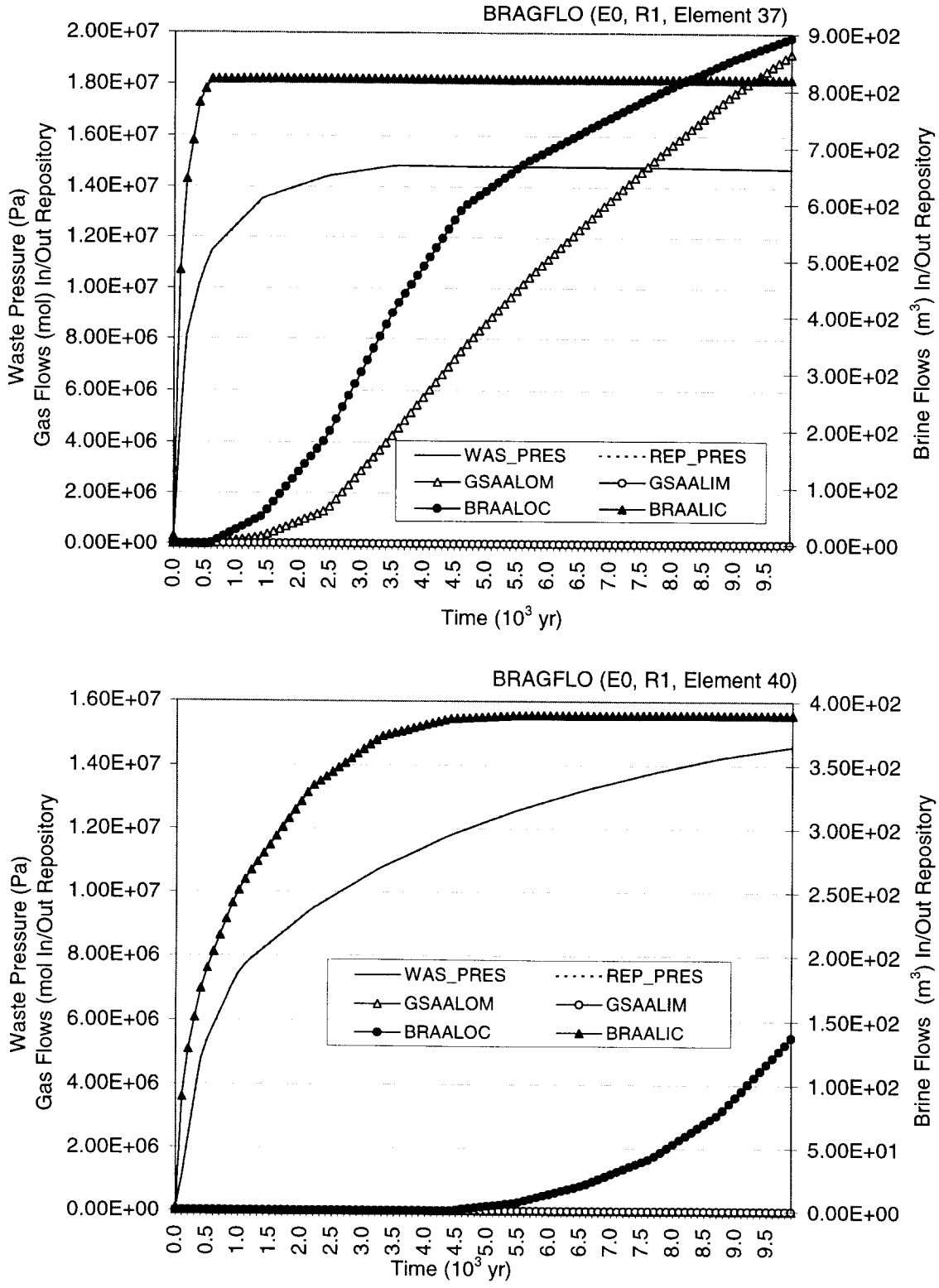

Fig. 7.6.16. Pressure (*REP_PRES*, *WAS_PRES*), brine flow from marker beds to repository (*BRAALIC*), brine flow from repository to markerbeds (*BRAALOC*), gas flow from marker beds to repository (*GSAALIM*), and gas flow from repository to marker beds (*GSAALOM*) under undisturbed conditions for sample elements 37 and 40 of replicate R1.

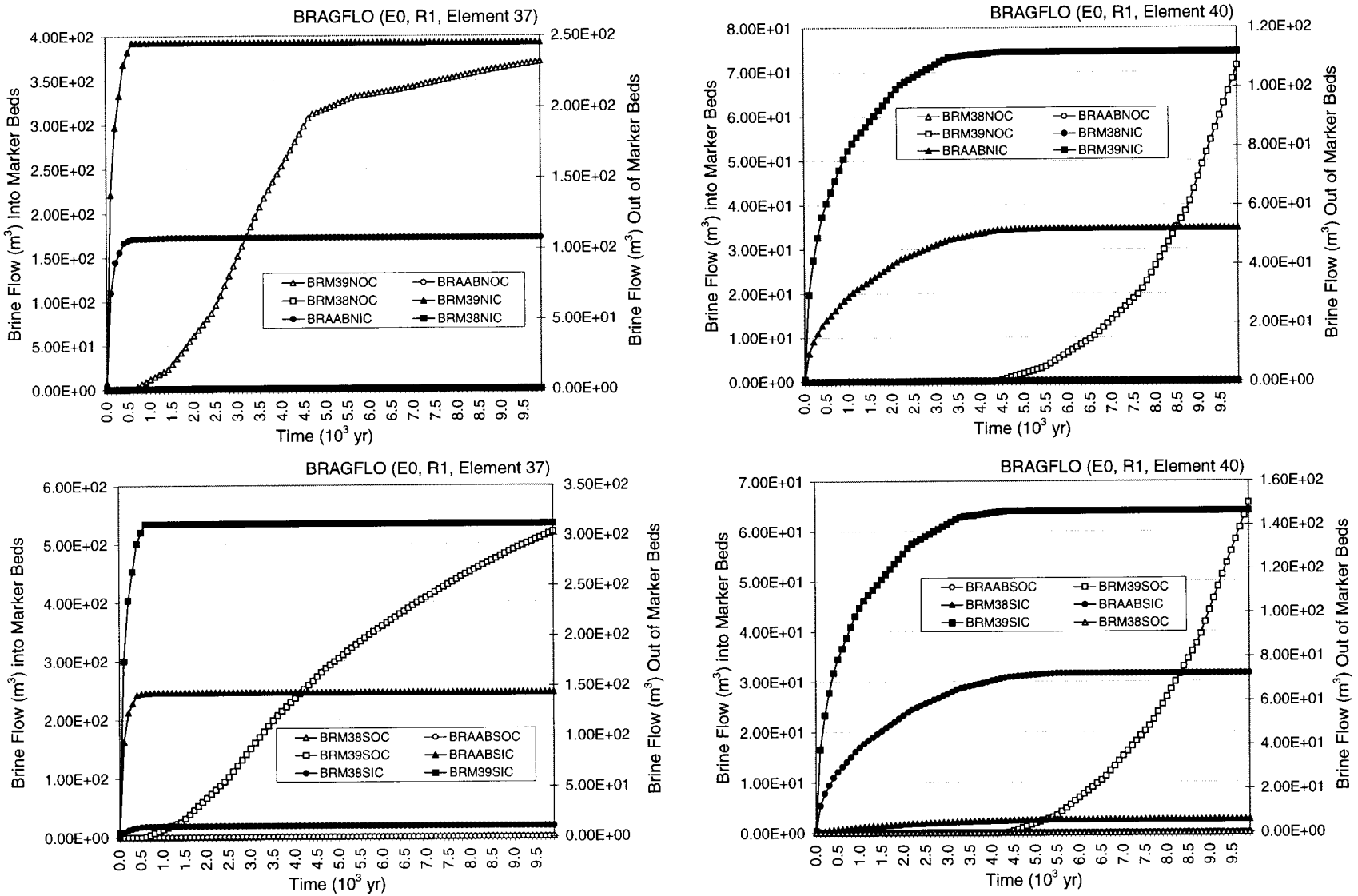

Fig. 7.6.17. Brine flows from marker beds into repository (*BRM38NIC*, *BRM38SIC*, *BRAABNIC*, *BRAABSIC*, *BRM39NIC*, *BRM39SIC*) and from repository into marker beds (*BRM38NOC*, *BRM38SOC*, *BRAABNOC*, *BRAABSOC*, *BRM39NOC*, *BRM39SOC*) under undisturbed conditions for sample elements 37 and 40 of replicate R1.

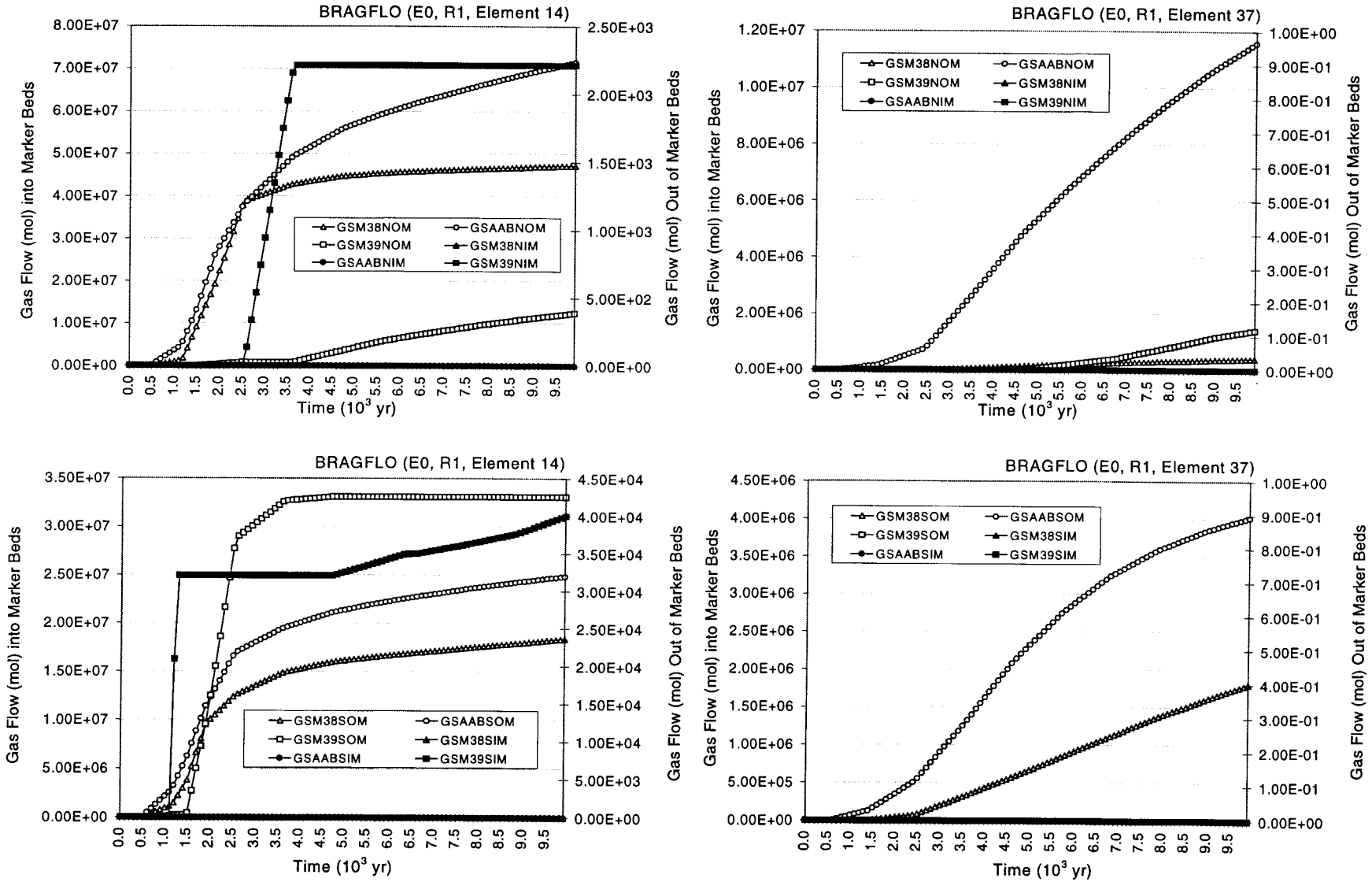

Fig. 7.6.18. Gas flows from marker beds into repository (*GSM38NIC*, *GSM38SIC*, *GSAABNIC*, *GSAABSIC*, *GSM39NIC*, *GSM39SIC*) and from repository into marker beds (*GSM38NOC*, *GSM38SOC*, *GSAABNOC*, *GSAABSOC*, *GSM39NOC*, *GSM39SOC*) under undisturbed conditions for sample elements 14 and 37 of replicate R1.

8. Fluid Flow in Vicinity of Repository: Disturbed Conditions

8.1 Overview

This chapter presents uncertainty and sensitivity analysis results for fluid flow in the vicinity of the repository under disturbed conditions. These results were calculated with BRAGFLO for the three replicated samples (i.e., R1, R2, R3) indicated in Eq. (6.5.1). In particular, the following cases in Table 6.9.1 will be presented: an E1 intrusion at 1000 yr, an E2 intrusion at 1000 yr, and an E2E1 intrusion with the E2 intrusion at 800 yr and the E1 intrusion at 2000 yr. Calculations were also performed for E1 and E2 intrusions at 350 yr (Table 6.9.1). However, as the results for fluid flow in the vicinity of the repository for intrusions at 350 yr are similar to those for intrusions at 1000 yr, the results for intrusions at 350 yr will not be presented. The following topics related to conditions in the repository are considered: brine inflow (Sect. 8.2), gas generation (Sect. 8.3), pressure (Sect. 8.4), saturation (Sect. 8.5), brine and gas flow in an intruding borehole (Sect. 8.6), brine and gas flow in marker beds (Sect. 8.7), behavior of brine pocket (Sect. 8.8), brine flow within repository and DRZ (Sect. 8.9), and behavior of E2E1 intrusions (Sect. 8.10). As in each section of Chapt. 7, a number of specific results calculated by BRAGFLO are examined with techniques based on examination of scatterplots, partial correlation coefficients, and stepwise regression analyses (Sect. 6.10). The specific BRAGFLO results considered are listed in Tables 7.1.1 and 8.1.1, which can be used to obtain exact definitions of the individual variables under consideration.

As in Chapt. 7, the sensitivity analysis results presented in this chapter are based on all 300 observations (i.e., replicates R1, R2 and R3 are pooled for the performance of sensitivity analyses with scatterplots, correlation coefficients and stepwise regression analyses). This permits the sensitivity analysis results to be based on all available information. Similarly, summaries of uncertainty based on box plots also use all 300 observations. In contrast, distributions of time-dependent results are typically shown for only replicate R1 to avoid the presentation of plots with so many individual curves that they are unreadable. However, mean and percentile curves are obtained from all 300 observations.

The chapter concludes with results of BRAGFLO calculations for multiple E1 intrusions (Sect. 8.11). These results are not listed in Table 6.9.1 and were not used in CCDF construction in the 1996 WIPP PA. Rather, these calculations were performed to provide perspective on the possible effects of multiple E1 intrusions when a block of CPU time became available after the computational plan for CCDF construction had been finalized.

Table 8.1.1. Results Calculated by BRAGFLO Considered in Uncertainty and Sensitivity Analyses for Fluid Flow in the Vicinity of the Repository Under Disturbed (i.e., E1, E2, E2E1) Conditions in Addition to the Results in Table 7.1.1

Result	Description
B_P_PRES	Volume-averaged pressure (Pa) in brine pocket (i.e., in Cells 1007-1023 in Fig. 4.2.3)
BNBHDNUZ	Cumulative brine flow (m^3) down borehole at MB 138 (i.e., from Cell 223 to Cell 575 in Fig. 4.2.3)
BNBHLDRZ	Cumulative brine flow (m^3) up borehole at bottom of lower DRZ (i.e., from Cell 78 to Cell 439 in Fig. 4.2.3)
BNBHUDRZ	Cumulative brine flow (m^3) up borehole at top of DRZ (i.e., from Cell 513 to Cell 575 in Fig. 4.2.3)
BRAPSNOC	Cumulative brine flow (m^3) out of DRZ above panel seal to north (i.e., from Cells 475, 489, 503, 517 to Cells 476, 490, 504, 518
BRAPSSOC	Cumulative brine flow (m^3) out of DRZ above panel seal to south (i.e., from Cells 475, 489, 503, 517 to Cells 474, 488, 502, 516 in Fig. 4.2.3)
BRBPSNOC	Cumulative brine flow (m^3) out of DRZ column below panel seal to north (i.e., from Cells 443, 457 to Cells 444, 458 in Fig. 4.2.3)
BRBPSSOC	Cumulative brine flow (m^3) out of DRZ column below panel seal to south (i.e., from Cells 443, 457 to Cells 442, 456 in Fig. 4.2.3)
BRNPSIRC	Cumulative brine flow (m^3) across panel seal into upper waste panels (i.e., from Cells 638, 639, 640 to Cells 617, 620, 623 in Fig. 4.2.3)
BRNPSIWC	Cumulative brine flow (m^3) across panel seal into lower waste panel (i.e., from Cells 638, 639, 640 to Cells 602, 609, 616 in Fig. 4.2.3)
BRNVOL_B	Brine volume (m^3) in brine pocket (i.e., in Cells 1007-1023 in Fig. 4.2.3)
GASBHUDZ	Cumulative gas flow (m^3 at standard temperature and pressure; *GASBHUDZ* = 0.02463 m^3/mol * *GSMBUDZ*) up borehole at top of DRZ (i.e., from Cell 513 to Cell 575 in Fig. 4.2.3)
GSMBHUDZ	Cumulative gas flow (mol) up borehole at top of DRZ (i.e., from Cell 513 to Cell 575 in Fig. 4.2.3)

8.2 Disturbed Conditions: Brine Inflow for E1 and E2 Intrusions

For undisturbed (i.e., E0) conditions, the two main pathways by which brine enters the repository are flow from the Salado Formation through the anhydrite marker beds and drainage from the DRZ (Sect. 7.2). For E2 intrusions (i.e., drilling intrusions that pass through the repository but do not penetrate pressurized brine in the Castile Formation), an additional pathway is provided by brine flow down the intruding borehole from overlying formations;

for E1 intrusions (i.e., drilling intrusions that pass through the repository and penetrate pressurized brine in the Castile Formation), two additional pathways are provided by brine flow down the intruding borehole from overlying formations and brine flow up the borehole from a pressurized brine pocket in the Castile Formation.

For brine inflow from the marker beds, E0, E1 and E2 conditions produce similar results (Figs. 7.2.1, 8.2.1), with the inflows for E1 and E2 intrusions tending to be somewhat larger than the inflows for E0 conditions (Fig. 8.2.2). This difference results because E1 and E2 intrusions result in lower repository pressures (Sect. 8.4), which in turn result in reduced resistance to brine flow toward the repository and hence greater brine flow out of the marker beds. The dominant variables affecting brine flow from the marker beds are *ANHPRM, HALPRM,* and *WMICDFLG* (Fig. 8.2.1). The positive effects for *ANHPRM* and *HALPRM* result from reducing resistance to flow in the anhydrite and halite, respectively. The negative effect for *WMICDFLG* results from increasing pressure in the repository before the drilling intrusion at 1000 yr and thus increasing resistance to flow out of the marker beds. A positive effect is also indicated for *BHPRM* after the E2 intrusion, with this effect resulting from reduced pressure in the repository and hence reduced resistance to flow out of the marker beds (Sect. 8.4).

Stepwise regression provides another way to investigate the effects of uncertain variables on brine flow from the marker beds (Table 8.2.1). The first regression, E0: 0 - 1000 yr, in Table 8.2.1 is for cumulative brine flow out of the marker beds under undisturbed conditions in the first 1000 yr after repository closure, which is also the flow that occurs over this time period for E1 and E2 intrusions at 1000 yr. The dominant variable is *ANHPRM*, with brine flow out of the marker beds increasing as *ANHPRM* increases because of reduced resistance to flow. In addition, positive effects are indicated for *HALPRM* and *SALPRES*, with increasing values for *HALPRM* decreasing resistance to brine flow out of the halite into the marker beds and increasing values for *SALPRES* increasing the pressure gradient towards the repository. Negative effects are indicated for *WMICDFLG, WASTWICK, WGRCOR* and *WGRMICI* due to the role that these variables play in increasing gas generation and hence pressure in the repository (Sect. 7.4).

Regression results for cumulative brine inflow from 1000 to 10,000 yr after a drilling intrusion at 1000 yr are presented under the headings E2: 1000 - 10,000 yr and E1: 1000 - 10,000 yr for E2 and E1 intrusions, respectively. For both intrusion types, *ANHPRM, SALPRES* and *HALPRM* have similar effects to those observed for undisturbed conditions, although *ANHPRM* can now account for more of the uncertainty (i.e., $R^2 = 0.81, 0.80$ for E2, E1: 1000 - 10,000 yr versus $R^2 = 0.58$ for E0: 0 - 1000 yr) in brine inflow due to the reduction in repository pressure resulting from the venting of gas through the borehole. Consistent with this, *BHPRM* has a positive effect on brine inflow from the marker beds for both intrusion types because increasing *BHPRM* tends to increase gas flow up the borehole and thus reduce repository pressure. Small negative effects are indicated for *WMICDFLG* and *BPCOMP* for the E2 and E1 intrusions, respectively, with both variables tending to increase pressure in the repository and thus reduce brine inflow from the marker beds.

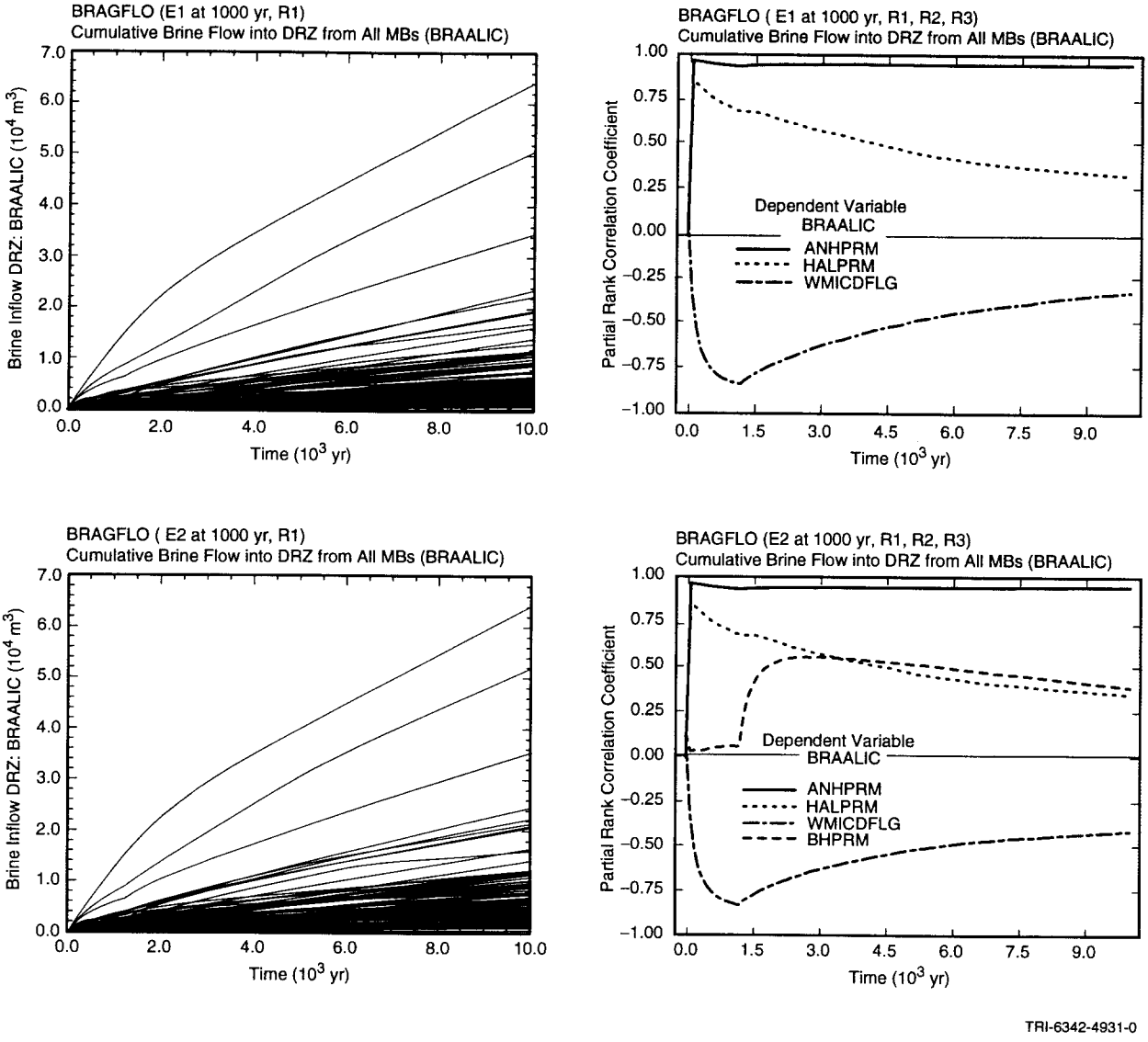

Fig. 8.2.1. Uncertainty and sensitivity analysis results for cumulative brine flow from anhydrite marker beds (*BRAALIC*) for E1 and E2 intrusions at 1000 yr into lower waste panel.

Table 8.2.1. Stepwise Regression Analyses with Rank-Transformed Data for Cumulative Brine Flow from Anhydrite Marker Beds (*BRAALIC*) for E1 and E2 Intrusions at 1000 yr into Lower Waste Panel

	E0: 0 - 1000 yr			E2: 1000 - 10,000 yr			E2: 0 - 10,000 yr			E1: 1000 - 10,000 yr		
Step[a]	Variable[b]	SRRC[c]	R^{2d}	Variable	SRRC	R^2	Variable	SRRC	R^2	Variable	SRRC	R^2
1	*ANHPRM*	0.73	0.58	*ANHPRM*	0.90	0.81	*ANHPRM*	0.91	0.83	*ANHPRM*	0.89	0.80
2	*WMICDFLG*	−0.45	0.79	*BHPRM*	0.16	0.84	*WMICDFLG*	−0.15	0.85	*BHPRM*	0.14	0.82
3	*HALPRM*	0.29	0.88	*WMICDFLG*	−0.10	0.85	*BHPRM*	0.13	0.87	*SALPRES*	0.12	0.83
4	*WASTWICK*	−0.11	0.89	*SALPRES*	0.10	0.86	*HALPRM*	0.12	0.88	*BPCOMP*	−0.10	0.84
5	*SALPRES*	0.08	0.90	*HALPRM*	0.08	0.86	*SALPRES*	0.10	0.89	*HALPRM*	0.08	0.85
6	*WGRCOR*	−0.07	0.90				*WGRCOR*	−0.05	0.90			
7	*WGRMICI*	−0.07	0.91									

	E1: 0 - 10,000 yr			(E2: 0 - 10,000 yr) − (E0: 0 - 10,000 yr)			(E1: 0 - 10,000 yr) − (E0: 0 - 10,000 yr)			(E2: 0 - 10,000 yr) − (E1: 0 - 10,000 yr)		
Step	Variable	SRRC	R^2	Variable	SRRC	R^2	Variable	SRRC	R^2	Variable	SRRC	R^2
1	*ANHPRM*	0.91	0.83	*ANHPRM*	0.74	0.55	*ANHPRM*	0.64	0.43	*BPCOMP*	0.57	0.32
2	*HALPRM*	0.12	0.84	*WMICDFLG*	0.27	0.63	*WMICDFLG*	0.32	0.54	*ANHPRM*	0.32	0.41
3	*BHPRM*	0.12	0.86	*WGRCOR*	0.16	0.65	*WGRCOR*	0.22	0.58	*BHPRM*	0.25	0.48
4	*SALPRES*	0.12	0.87	*BHPRM*	0.13	0.67	*BPCOMP*	−0.15	0.61	*WMICDFLG*	−0.27	0.54
5	*WMICDFLG*	−0.12	0.88	*HALPOR*	0.12	0.68	*HALPOR*	0.12	0.62	*BPINTPRS*	0.14	0.56
6	*BPCOMP*	−0.09	0.89				*BHPRM*	0.10	0.63	*BPVOL*	0.11	0.57
							BPVOL	−0.09	0.64			
							WASTWICK	0.08	0.65			

[a] Steps in stepwise regression analysis.

[b] Variables listed in order of selection in regression analysis with *ANHCOMP* and *HALCOMP* excluded from entry into regression model.

[c] Standardized rank regression coefficients in final regression model.

[d] Cumulative R^2 value with entry of each variable into regression model.

Results for the entire 10,000 yr period (i.e., E2: 0 - 10,000 yr, E1: 0 - 10,000 yr in Table 8.2.1) are consistent with those previously observed for the periods 0 - 1000 yr and 1000 - 10,000 yr. In particular, the dominant variable is *ANHPRM*, with small positive effects indicated for *BHPRM, HALPRM* and *SALPRES*, and small negative effects indicated for *WMICDFLG, WGRCOR* and *BPCOMP*.

The last three regressions in Table 8.2.1 are for the differences between brine inflow for E2 and E0, E1 and E0, and E2 and E1 intrusions (see Fig. 8.2.2 for scatterplots of the flows associated with E0, E1 and E2 intrusions). The differences in brine inflows between E2 and E1 intrusions and undisturbed (i.e., E0) conditions are dominated by *ANHPRM*, with the difference between flows for disturbed and undisturbed conditions tending to increase as *ANHPRM* increases. This effect occurs because the potential of higher values of *ANHPRM* to allow more brine inflow to the repository is realized to a greater extent under the lower repository pressure conditions associated with E1 and E2 intrusions. Additional small effects are indicated for a number of variables. The difference between E2

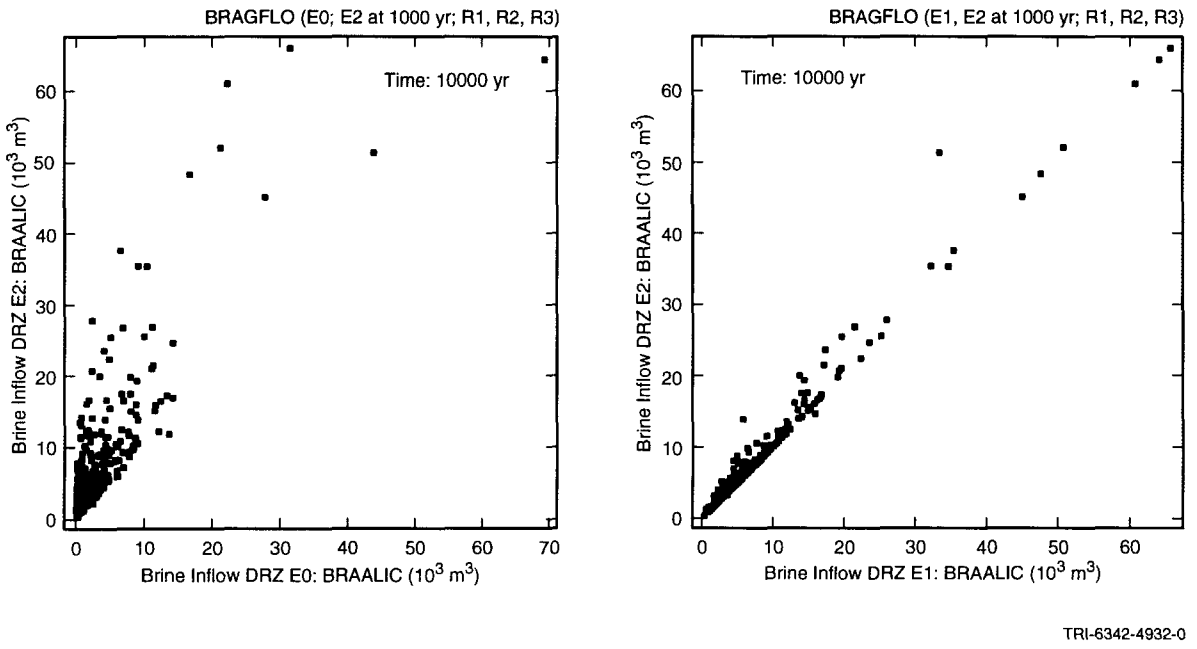

Fig. 8.2.2. Scatterplots for cumulative brine flow from anhydrite marker beds (*BRAALIC*) over 10,000 yr for E0 conditions, an E1 intrusion at 1000 yr into lower waste panel, and an E2 intrusion at 1000 yr into lower waste panel.

and E1 flows is dominated by *BPCOMP*, with this difference tending to increase as *BPCOMP* increases. This behavior occurs because increasing *BPCOMP* increases brine inflow from the brine pocket to the repository and thus pressure in the repository, with the result that brine inflow from the marker beds is reduced. Smaller effects are indicated for several additional variables. However, the differences between brine inflows from the marker beds for E1 and E2 intrusions are rather small (Fig. 8.2.2).

A more detailed summary of brine inflow can be obtained by examining the flows associated with individual marker beds (Figs. 8.2.3, 8.2.4). In general, the patterns for E1 and E2 intrusion are similar to those already observed for E0 conditions (Fig. 7.2.2), although the flows for disturbed conditions tend to be somewhat higher due to reduced repository pressures as previously discussed. The regression analyses for brine flows out of the individual marker beds are presented in Tables 8.2.2 and 8.2.3. These analyses are consistent with previously presented results (Tables 7.2.4, 8.2.1) and will not be discussed.

Unlike brine flow from the marker beds, there is often considerable difference in cumulative brineflow into the repository for E0, E1 and E2 conditions (Figs. 7.2.1, 8.2.5). For the E2 intrusion, the cumulative brine inflow increases relative to that observed for undisturbed conditions due to brine flow down the intruding borehole (Fig. 8.2.6). Due to the assumption of a borehole plug at the Rustler/Salado interface with a 200 yr life expectancy

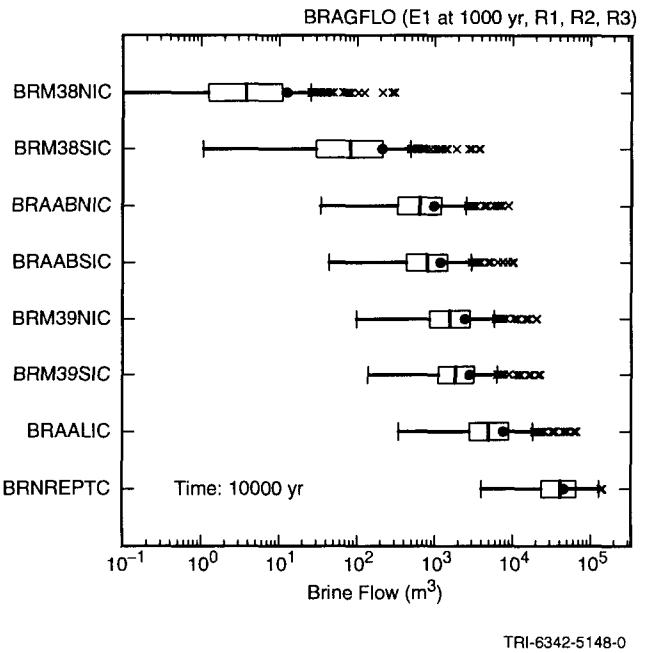

Fig. 8.2.3. Cumulative brine flow over 10,000 yr into DRZ (*BRM38NIC*, *BRM38SIC*, *BRAABNIC*, *BRAABSIC*, *BRM39NIC*, *BRM39SIC*) and into repository (*BRNREPTC*) for an E1 intrusion at 1000 yr into lower waste panel.

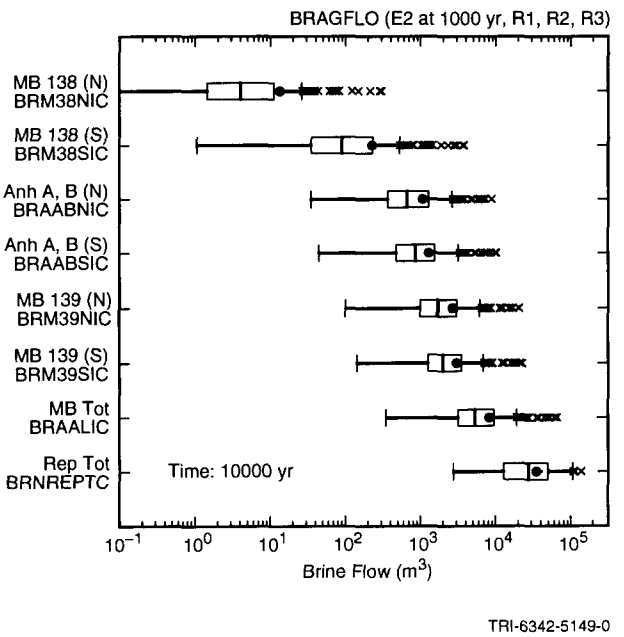

Fig. 8.2.4. Cumulative brine flow over 10,000 yr into DRZ (*BRM38NIC*, *BRM38SIC*, *BRAABNIC*, *BRAABSIC*, *BRM39NIC*, *BRM39SIC*) and into repository (*BRNREPTC*) for an E2 intrusion at 1000 yr into lower waste panel.

Table 8.2.2. Stepwise Regression Analyses with Rank-Transformed Data for Cumulative Brine Flow over 10,000 yr into Repository from Individual Marker Beds (*BRM38NIC*, *BRM38SIC*, *BRAABNIC*, *BRAABSIC*, *BRM39NIC*, *BRM39SIC*) for an E1 Intrusion at 1000 yr into Lower Waste Panel

	MB 138 North: *BRM38NIC*			MB 138 South: *BRM38SIC*			Anh A, B North: *BRAABNIC*			Anh A, B South: *BRAABSIC*		
Step[a]	Variable[b]	SRRC[c]	R^{2d}	Variable	SRRC	R^2	Variable	SRRC	R^2	Variable	SRRC	R^2
1	*ANHPRM*	0.91	0.81	*ANHPRM*	0.90	0.80	*ANHPRM*	0.89	0.78	*ANHPRM*	0.89	0.79
2	*HALPRM*	−0.31	0.91	*HALPRM*	−0.29	0.89	*WMICDFLG*	−0.22	0.83	*WMICDFLG*	−0.18	0.82
3	*WMICDFLG*	−0.11	0.92	*WMICDFLG*	−0.13	0.90	*BHPRM*	0.12	0.85	*BHPRM*	0.12	0.83
4	*SALPRES*	0.08	0.92	*BHPRM*	0.08	0.91	*SALPRES*	0.11	0.86	*SALPRES*	0.10	0.84
5	*BHPRM*	0.07	0.93	*SALPRES*	0.08	0.91	*BPCOMP*	−0.08	0.86	*BPCOMP*	−0.10	0.85
6	*BPCOMP*	−0.06	0.93	*BPCOMP*	−0.06	0.92						

	MB 139 North: *BRM39NIC*			MB 139 South: *BRM39SIC*		
Step	Variable	SRRC	R^2	Variable	SRRC	R^2
1	*ANHPRM*	0.91	0.83	*ANHPRM*	0.89	0.79
2	*HALPRM*	0.13	0.85	*HALPRM*	0.21	0.83
3	*BHPRM*	0.12	0.86	*SALPRES*	0.12	0.85
4	*SALPRES*	0.11	0.88	*BHPRM*	0.12	0.86
5	*WMICDFLG*	−0.10	0.89	*BPCOMP*	−0.09	0.87
6	*BPCOMP*	−0.08	0.89	*WMICDFLG*	−0.08	0.88

[a] Steps in stepwise regression analysis.

[b] Variables listed in order of selection in regression analysis with *ANHCOMP* and *HALCOMP* excluded from entry into regression model.

[c] Standardized rank regression coefficients in final regression model.

[d] Cumulative R^2 value with entry of each variable into regression model.

(Table 4.3.8), this flow does not begin until 200 yr after the drilling intrusion. For the E1 intrusion, the cumulative brine inflow increases relative to that observed for undisturbed conditions due to both brine flow down the intruding borehole (Fig. 8.2.6) and brine flow up the intruding borehole from the brine pocket (Fig. 8.2.7). The sharp increases in cumulative brine flow for E1 intrusions (Figs. 8.2.5, 8.2.7) take place during the 200 yr period (i.e., from 1000 to 1200 yr) during which an open borehole is assumed to exist between the brine pocket and the repository (Table 4.3.8). In the computational implementation of the analysis, this section of the borehole is assigned a permeability of 10^{-9} m^2. After 1200 yr, the effects of flow down the borehole are also apparent for E1 intrusions (Figs. 8.2.5, 8.2.6).

Prior to 1000 yr, the sensitivity analysis results for cumulative brine flow into the repository for E0, E1 and E2 conditions are the same (Figs. 7.2.3, 8.2.5), with *HALPOR* being the dominant variable. After 1000 yr, *HALPOR* is gradually exceeded by *BHPRM* in importance for disturbed conditions due to the role of *BHPRM* in controlling brine flow in the borehole. This flow takes place both down the borehole from overlying formation (Fig 8.2.6) and, for the E1 intrusion, up the borehole from the brine pocket (Fig. 8.2.7). For flow down the borehole into the repository, *BHPRM* is the dominant variable for both E1 and E2 intrusions (Fig. 8.2.6), with this effect resulting because

Table 8.2.3. Stepwise Regression Analyses with Rank-Transformed Data for Cumulative Brine Flow over 10,000 yr into Repository from Individual Marker Beds (*BRM38NIC*, *BRM38SIC*, *BRAABNIC*, *BRAABSIC*, *BRM39NIC*, *BRM39SIC*) for an E2 Intrusion at 1000 yr into Lower Waste Panel

	MB 138 North: *BRM38NIC*			MB 138 South: *BRM38SIC*			Anh A, B North: *BRAABNIC*			Anh A, B South: *BRAABSIC*		
Step[a]	Variable[b]	SRRC[c]	R^{2d}	Variable	SRRC	R^2	Variable	SRRC	R^2	Variable	SRRC	R^2
1	*ANHPRM*	0.90	0.81	*ANHPRM*	0.90	0.80	*ANHPRM*	0.89	0.78	*ANHPRM*	0.89	0.78
2	*HALPRM*	−0.32	0.90	*HALPRM*	−0.30	0.89	*WMICDFLG*	−0.26	0.84	*WMICDFLG*	−0.23	0.83
3	*WMICDFLG*	−0.13	0.92	*WMICDFLG*	−0.15	0.91	*BHPRM*	0.13	0.86	*BHPRM*	0.14	0.85
4	*BHPRM*	0.08	0.93	*BHPRM*	0.09	0.92	*SALPRES*	0.10	0.87	*SALPRES*	0.09	0.85
5	*SALPRES*	0.07	0.93	*SALPRES*	0.06	0.92	*WGRCOR*	−0.05	0.87			

	MB 139 North: *BRM39NIC*			MB 139 South: *BRM39SIC*		
Step	Variable	SRRC	R^2	Variable	SRRC	R^2
1	*ANHPRM*	0.91	0.83	*ANHPRM*	0.89	0.80
2	*HALPRM*	0.13	0.85	*HALPRM*	0.21	0.84
3	*BHPRM*	0.14	0.87	*BHPRM*	0.13	0.86
4	*WMICDFLG*	−0.13	0.89	*WMICDFLG*	−0.11	0.87
5	*SALPRES*	0.10	0.89	*SALPRES*	0.10	0.88
6	*WGRCOR*	−0.05	0.90			

[a] Steps in stepwise regression analysis.

[b] Variables listed in order of selection in regression analysis with *ANHCOMP* and *HALCOMP* excluded from entry into regression model.

[c] Standardized rank regression coefficients in final regression model.

[d] Cumulative R^2 value with entry of each variable into regression model.

increasing *BHPRM* reduces resistance to flow in the borehole. A brief negative effect is indicated for *WMICDFLG* shortly after 1200 yr (Fig. 8.2.6) due to the obstruction of brine inflow by the rapid venting of gas when the repository is at high pressure. As a reminder, *WMICDFLG* is the dominant variable with respect to the uncertainty in repository pressure under undisturbed conditions (Fig. 7.4.1, Table 7.4.1).

The variable *WMICDFLG* also shows a negative effect on total brine inflow to the repository after 1200 yr for the E1 intrusion that is not present for the E2 intrusion (Fig. 8.2.5). This behavior results because large flows of brine can take place from the brine pocket to the repository for an E1 intrusion from 1000 to 1200 yr, during which period an open borehole is assumed to connect the brine pocket and the repository (Fig. 8.2.5). However, this flow will not take place when the repository pressure is too high (Fig. 8.2.8). Thus, the negative effect for *WMICDFLG* again results from its dominant role in determining the uncertainty in repository pressure. This effect results in the negative PRCC for *WMICDFLG* for cumulative brine flow from the brine pocket (Fig. 8.2.7) and thus in the negative PRCC for cumulative brine flow into the repository (Fig. 8.2.6). In addition to the negative effect of *WMICDFLG*, the variables *BPCOMP* and *BHPRM* have positive effects on cumulative brine flow from the brine pocket to the repository. Specifically, increasing *BPCOMP* increases the amount of brine that leaves the brine pocket for each unit drop in pressure, and increasing *BHPRM* both reduces the pressure in the repository and reduces resistance to flow between the brine pocket and the repository.

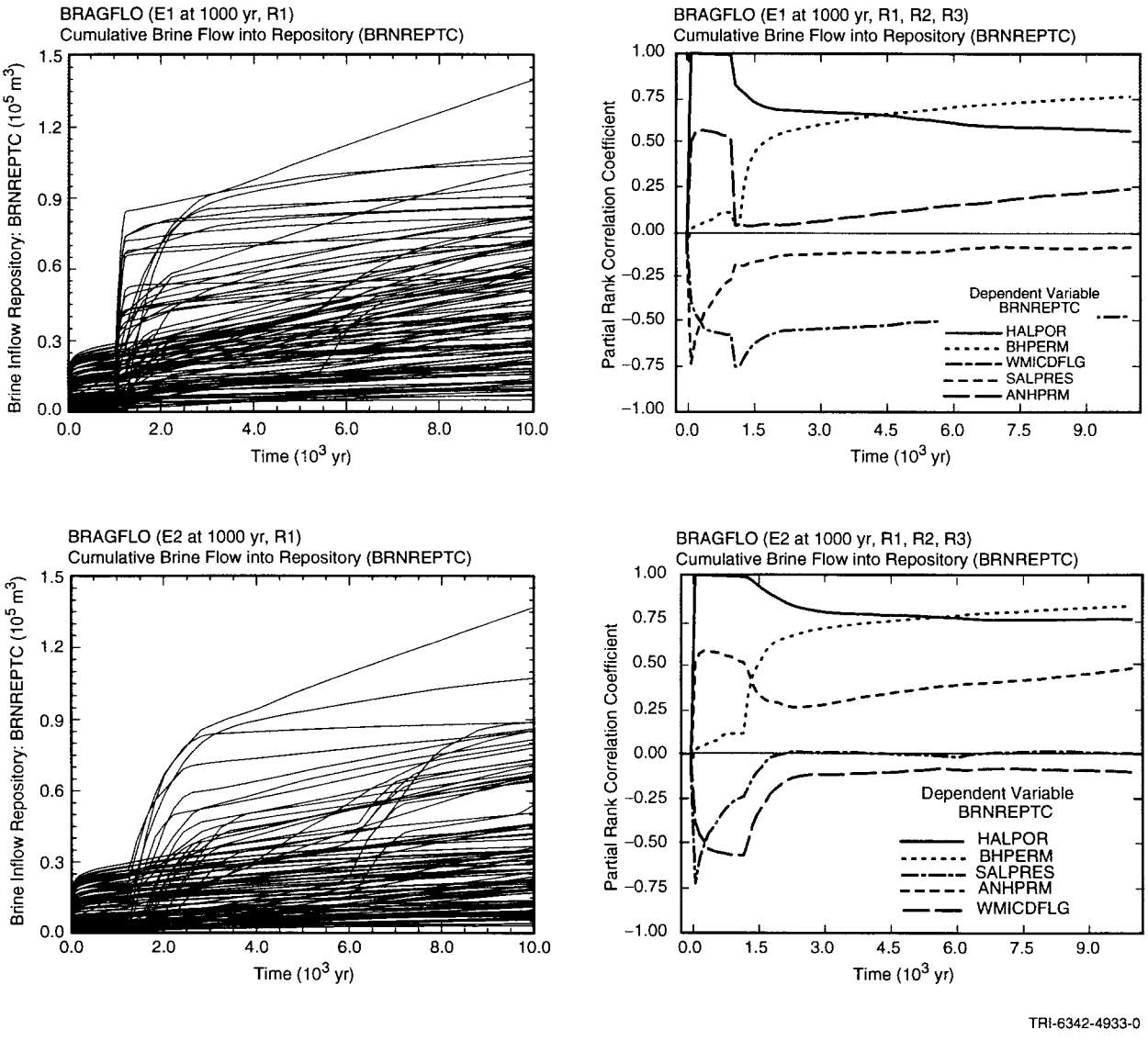

Fig. 8.2.5. Uncertainty and sensitivity analysis results for cumulative brine flow into repository (*BRNREPTC*) for E1 and E2 intrusions at 1000 yr into lower waste panel.

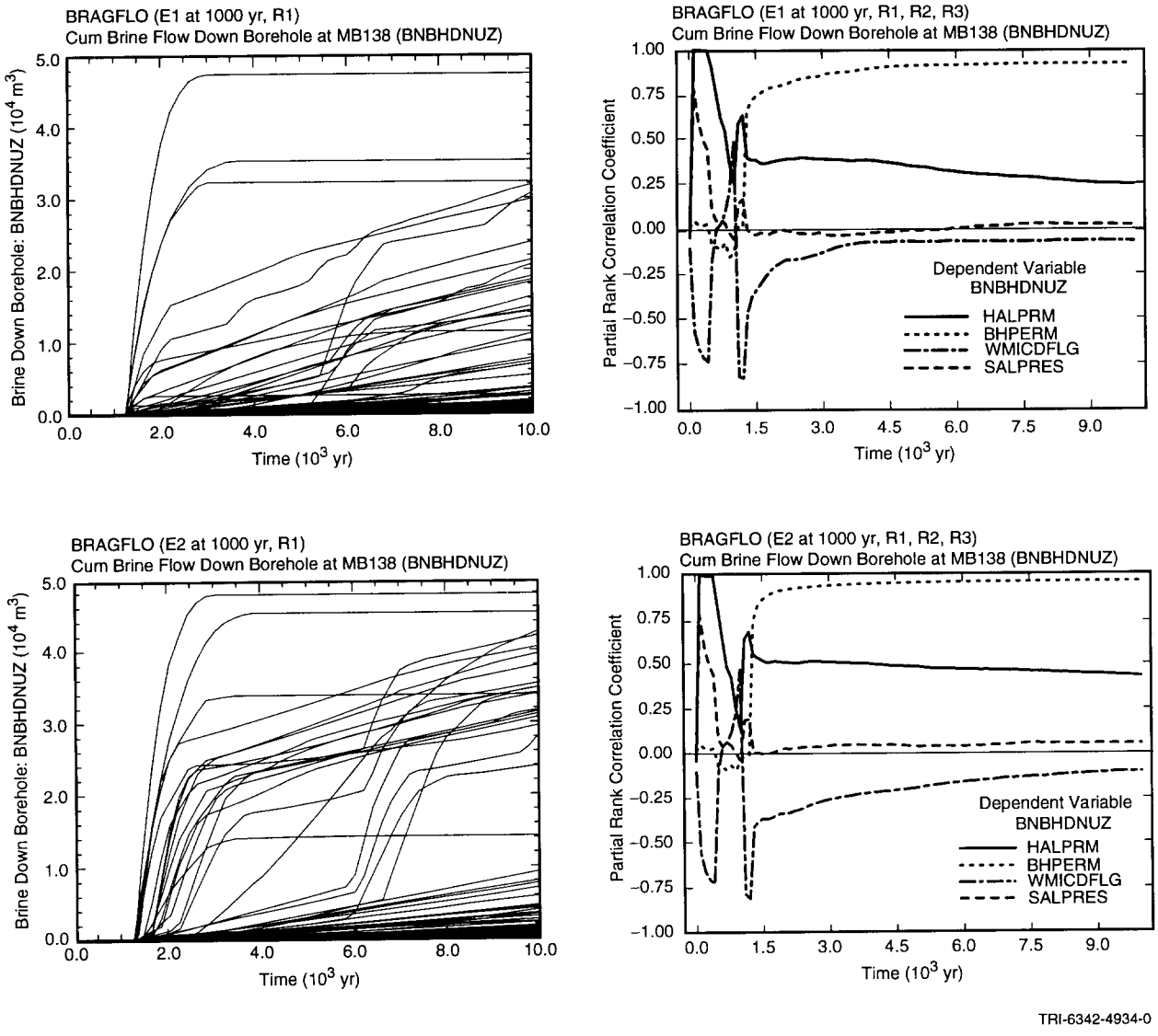

Fig. 8.2.6. Uncertainty and sensitivity analysis results for cumulative brine flow down borehole (*BNBHDNUZ*) for E1 and E2 intrusions at 1000 yr into lower waste panel.

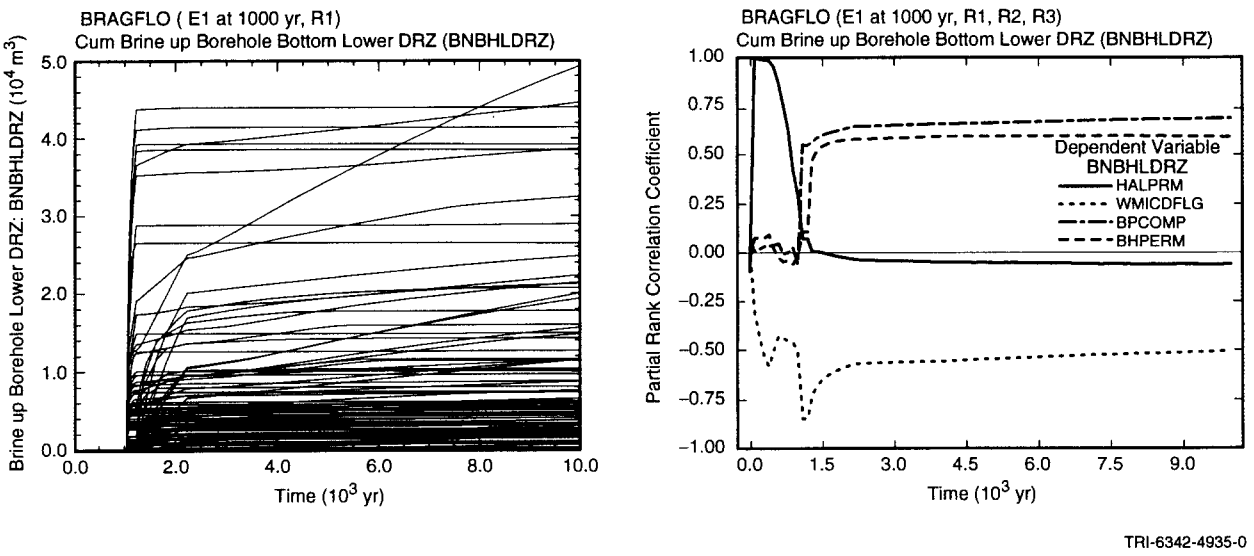

Fig. 8.2.7. Uncertainty and sensitivity analysis results for cumulative brine flow up borehole from brine pocket into bottom of lower DRZ (*BNBHLDRZ*) for E1 intrusion at 1000 yr into lower waste panel.

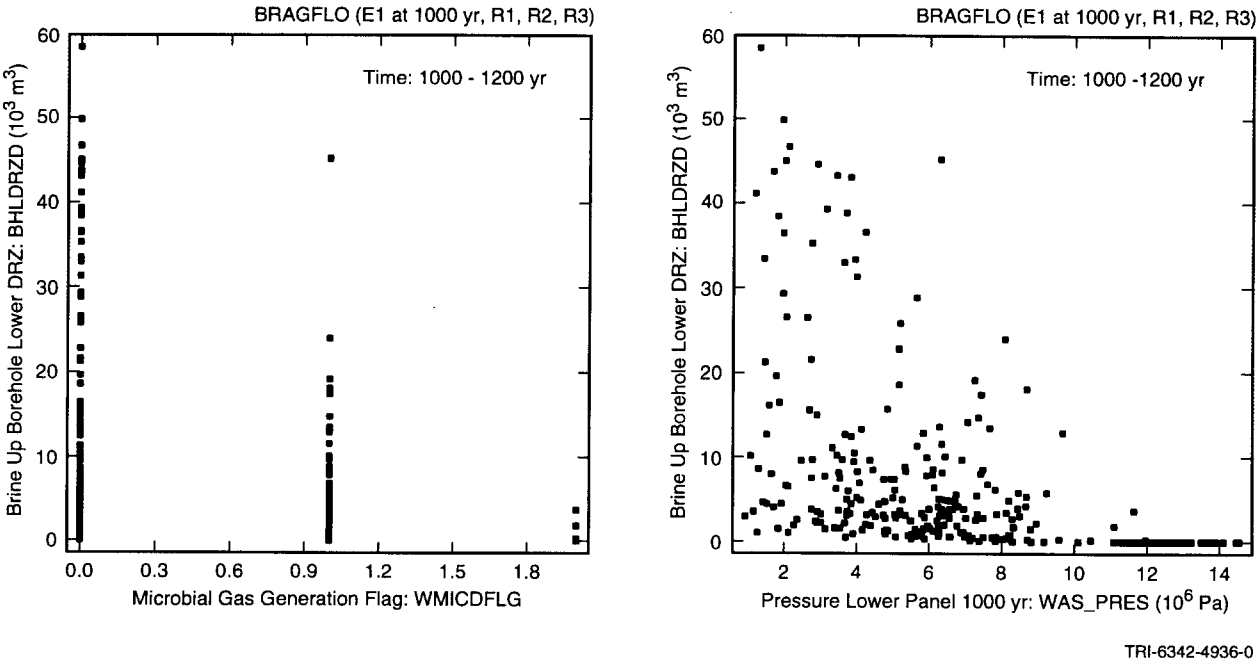

Fig. 8.2.8. Scatterplots for brine flow out of the brine pocket between 1000 and 1200 yr (*BHLDRZD* = *BNBHLDRZ* at 1200 yr – *BNBHLDRZ* at 1000 yr) versus *WMICDFLG* and repository pressure at 1000 yr (*WAS_PRES* at 1000 yr) for an E1 intrusion into lower waste panel at 1000 yr.

Stepwise regression analysis provides an alternative to the sensitivity analysis based on PRCCs in Figs. 8.2.5 - 8.2.6 (Table 8.2.4). Under undisturbed conditions from 0 to 1000 yr, brine inflow to the repository is dominated by *HALPOR*. After an E2 intrusion at 1000 yr, the dominant variable is *BHPRM*, with cumulative brine inflow increasing as *BHPRM* increases. This effect happens for two reasons. First, increasing *BHPRM* reduces repository pressure and thus allows more brine inflow from the marker beds. Second, increasing *BHPRM* allows more brine to flow down the borehole and into the repository. After *BHPRM*, positive effects are indicated for *ANHPRM*, *HALPOR* and *HALPRM*, with these variables increasing brine flow from the marker beds, DRZ and Salado halite, respectively. Finally, a small negative effect is indicated for *WRBRNSAT* and results because increasing *WRBRNSAT* decreases brine mobility within the repository and thus decreases the inflow of brine to the repository to replace brine that has moved to a new location. The E2 results for 0 to 10,000 yr are similar to those for 1000 to 10,000 yr with the exception that *HALPOR* is more important from 0 to 10,000 yr than from 1000 to 10,000 yr due to its influence on brine drainage from the DRZ at early times.

Table 8.2.4. Stepwise Regression Analyses with Rank-Transformed Data for Cumulative Brine Flow into Repository (*BRNREPTC*) for E1 and E2 Intrusions at 1000 yr into Lower Waste Panel

	E0: 0 - 1000 yr			E2: 1000 - 10,000 yr			E2: 0 - 10,000 yr			E1: 1000 - 10,000 yr		
Step[a]	Variable[b]	SRRC[c]	R^{2d}	Variable	SRRC	R^2	Variable	SRRC	R^2	Variable	SRRC	R^2
1	*HALPOR*	0.98	0.96	*BHPRM*	0.79	0.62	*BHPRM*	0.66	0.44	*BHPRM*	0.66	0.43
2	*WMICDFLG*	−0.10	0.97	*ANHPRM*	0.32	0.73	*HALPOR*	0.51	0.70	*BPCOMP*	0.42	0.60
3	*ANHPRM*	0.08	0.97	*HALPOR*	0.24	0.78	*ANHPRM*	0.24	0.76	*WMICDFLG*	−0.27	0.67
4	*HALPRM*	0.05	0.97	*HALPRM*	0.16	0.81	*HALPRM*	0.15	0.78	*BPVOL*	0.16	0.70
5	*WRBRNSAT*	−0.04	0.98	*WRBRNSAT*	−0.08	0.82	*WRBRNSAT*	−0.07	0.79	*ANHPRM*	0.14	0.72
6	*WASTWICK*	−0.04	0.98							*BPINTPRS*	0.09	0.72
7	*SALPRES*	−0.04	0.98							*WGRCOR*	−0.08	0.73
8	*WGRCOR*	−0.03	0.98									

	E1: 0 - 10,000 yr			(E2: 0 - 10,000 yr) − (E0: 0 - 10,000 yr)			(E1: 0 - 10,000 yr) − (E0: 0 - 10,000 yr)			(E1: 0 - 10,000 yr) − (E2: 0 - 10,000 yr)		
Step	Variable	SRRC	R^2	Variable	SRRC	R^2	Variable	SRRC	R^2	Variable	SRRC	R^2
1	*BHPRM*	0.58	0.34	*BHPRM*	0.83	0.69	*BHPRM*	0.68	0.46	*BPCOMP*	0.46	0.21
2	*BPCOMP*	0.38	0.49	*ANHPRM*	0.27	0.76	*BPCOMP*	0.45	0.67	*WMICDFLG*	−0.34	0.32
3	*HALPOR*	0.34	0.61	*WMICDFLG*	0.20	0.80	*WMICDFLG*	−0.18	0.70	*BHPRM*	−0.16	0.34
4	*WMICDFLG*	−0.27	0.68	*HALPRM*	0.11	0.81	*BPVOL*	0.15	0.72	*BPINTPRS*	0.15	0.36
5	*BPVOL*	0.17	0.70	*WGRCOR*	0.10	0.82	*BPINTPRS*	0.11	0.73	*BPVOL*	0.13	0.38
6	*ANHPRM*	0.12	0.72	*WASTWICK*	0.06	0.82	*ANHPRM*	0.10	0.74	*WASTWICK*	−0.11	0.39
7	*BPINTPRS*	0.09	0.72									
8	*HALPRM*	0.08	0.73									

[a] Steps in stepwise regression analysis.

[b] Variables listed in order of selection in regression analysis with *ANHCOMP* and *HALCOMP* excluded from entry into regression model.

[c] Standardized rank regression coefficients in final regression model.

[d] Cumulative R^2 value with entry of each variable into regression model.

After an E1 intrusion at 1000 yr, the dominant variable is again *BHPRM* for reasons similar to those for the E2 intrusion. Further, brine can also flow into the repository from the brine pocket after an E1 intrusion, with the result that *BPCOMP, BPVOL* and *BPINTPRS* appear in the regression model with positive coefficients. Of these, *BPCOMP* is the most important. A positive effect is also indicated for *ANHPRM* because of its role in controlling brine flow from the marker beds, and negative effects are indicated for *WMICDFLG* and *WGRCOR* because of their role in controlling repository pressure. As for the E2 intrusion, the results for 0 to 10,000 yr for the E1 intrusion are similar to those for 1000 to 10,000 yr, with the same exception that *HALPOR* is more important from 0 to 10,000 yr than from 1000 to 10,000 yr.

The final regressions in Table 8.2.4 are for the differences between brine inflow to the repository for E2 and E0, E1 and E0, and E1 and E2 intrusions. The differences between E2 and E1 intrusions and undisturbed (i.e., E0) conditions are dominated by *BHPRM* because increasing *BHPRM* reduces pressure in the repository and resistance to brine flow in the borehole. For the E2 intrusion, the difference also increases as *ANHPRM, WMICDFLG, HALPRM, WGRCOR* and *WASTWICK* increase. The positive effects for *ANHPRM* and *HALPRM* result from increasing flow into the repository from the marker beds after the intrusion. The positive effects for *WMICDFLG, WGRCOR* and *WASTWICK* result from increasing repository pressure and thus reducing brine inflow from the marker beds under undisturbed conditions. For the E1 intrusion, the difference also increases as *BPCOMP, BPVOL, BPINTPRS* and *ANHPRM* increase and decreases as *WMICDFLG* increases. The positive effects for *BPCOMP, BPVOL* and *BPINTPRS* result from increasing brine flow from the brine pocket, and the negative effect for *WMICDFLG* results from decreasing flow from the brine pocket between 1000 and 1200 yr when an open borehole exists beneath the repository (Fig. 8.2.8). The positive effect for *ANHPRM* results from increased flow out of the marker beds due to reduced pressure in the repository after an E1 pressure.

The dominant variable in determining the difference in brine flow into the repository for E1 and E2 intrusions is *BPCOMP*, with this difference tending to increase as *BPCOMP* increases. In addition, negative effects are indicated for *WMICDFLG, BHPRM* and *WASTWICK*, and positive effects are indicated for *BPINTPRS* and *BPVOL*. The negative effects for *WMICDFLG* and *WASTWICK* result from increasing repository pressure and thus reducing flow from the brine pocket between 1000 and 1200 yr (Fig. 8.2.8). The negative effect for *BHPRM* results because little brine flow down the borehole occurs for small values of *BHPRM*, in which case brine flow from the brine pocket dominates the difference in flows between E1 and E2 intrusions; at large values of *BHPRM*, so much brine flows down the borehole that the repository saturates and rises to hydrostatic pressure, which reduces brine inflow from the brine pocket (see Sect. 8.4 for additional discussion). The positive effects for *BPINTPRS* and *BPVOL* result from their role in increasing flow from the brine pocket. However, the final regression model has an R^2 value of only 0.39. Thus, the examination of scatterplots is advisable to obtain a better feeling for the processes involved in determining this difference (Fig. 8.2.9). The dominant roles played by *BPCOMP* and *BHPRM* and the lesser role played by *WMICDFLG* are clearly indicated by the scatterplots in Fig. 8.2.9. The primary differences in brine inflow

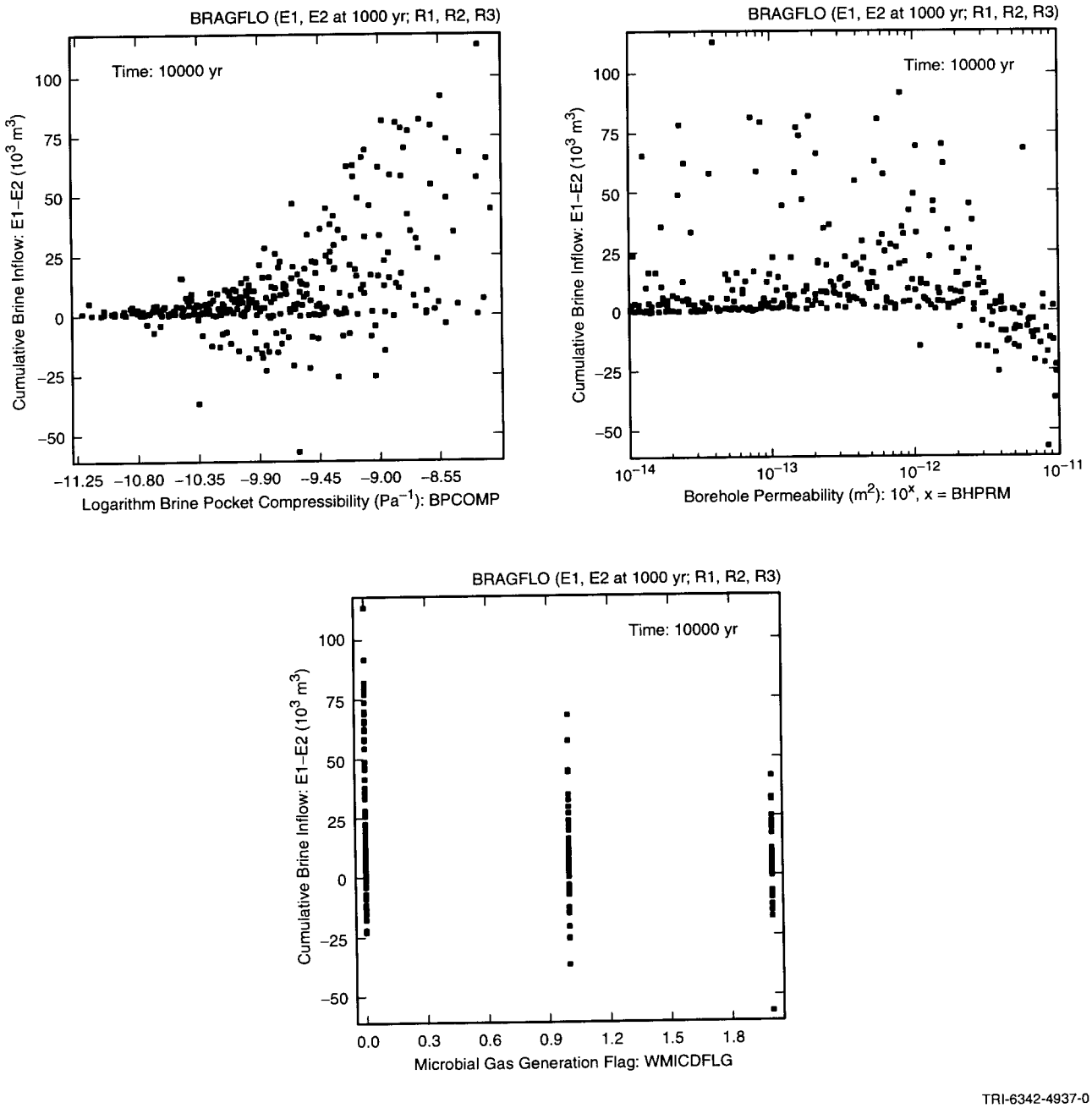

Fig. 8.2.9. Scatterplots for cumulative brine inflow into the repository (*BRNREPTC*) over 10,000 yr for an E1 intrusion at 1000 yr into lower waste panel minus cumulative brine inflow into the repository over 10,000 yr for an E2 intrusion at 1000 yr into lower waste panel (i.e., (E1: 0 - 10,000 yr) – (E2: 0 - 10,000 yr) in Table 8.2.4) versus *BPCOMP, BHPRM* and *WMICDFLG*.

to the repository for undisturbed (i.e., E0) and disturbed (i.e., E1, E2) conditions derive from brine flow in the intruding borehole. For the E2 intrusion, flow down the borehole into the repository is dominated by *BHPRM* (Table 8.2.5, Fig. 8.2.10). Similarly, brine flow down the borehole for an E1 intrusion is also dominated by *BHPRM*, although increasing values for *BPCOMP* tend to decrease the amount of flow down the borehole (Table 8.2.5, Fig. 8.2.10) by increasing the amount of repository pore volume that will be filled by brine from the brine pocket.

The difference in flow down the borehole for E2 and E1 intrusions is dominated by *BHPRM* and *BPCOMP* (Table 8.2.5, Fig. 8.2.11). In general, E2 intrusions tend to have more flow down the borehole than E1 intrusions due to the absence of flow from the brine pocket. The most important variable with respect to flow from the brine pocket is *BPCOMP*, with the flow tending to increase as *BPCOMP* increases (Table 8.2.5, Fig. 8.2.12). As a result, increasing *BPCOMP* tends to increase the difference between brine flow down the borehole for E2 and E1 intrusions.

Table 8.2.5. Stepwise Regression Analyses with Rank-Transformed Data for Cumulative Brine Flow Through Borehole into DRZ (*BNBHDNUZ, BNBHLDRZ*) over 10,000 yr for E1 and E2 Intrusions at 1000 yr into Lower Waste Panel

	E2: Upper DRZ			E1: Upper DRZ			(E2: Upper DRZ) – (E1: Upper DRZ)			E1: Lower DRZ		
Step[a]	Variable[b]	SRRC[c]	R^{2d}	Variable	SRRC	R^2	Variable	SRRC	R^2	Variable	SRRC	R^2
1	*BHPRM*	0.95	0.90	*BHPRM*	0.90	0.81	*BHPRM*	0.69	0.48	*BPCOMP*	0.72	0.52
2	*HALPRM*	0.13	0.92	*BPCOMP*	–0.11	0.82	*BPCOMP*	0.20	0.52	*BHPRM*	0.34	0.64
3	*HALPOR*	–0.06	0.92	*HALPRM*	0.10	0.83	*HALPOR*	–0.11	0.53	*WMICDFLG*	–0.28	0.71
4	*ANHPRM*	–0.06	0.92	*HALPOR*	–0.08	0.84	*SHPRMASP*	–0.10	0.54	*BPVOL*	0.16	0.74
5	*WRGSSAT*	–0.04	0.93	*BPINTPRS*	–0.06	0.84				*BPINTPRS*	0.12	0.75
6										*SHRBRSAT*	–0.07	0.76
										ANHPRM	–0.07	0.76

[a] Steps in stepwise regression analysis.

[b] Variables listed in order of selection in regression analysis with *ANHCOMP* and *HALCOMP* excluded from entry into regression model.

[c] Standardized rank regression coefficients in final regression model.

[d] Cumulative R^2 value with entry of each variable into regression model.

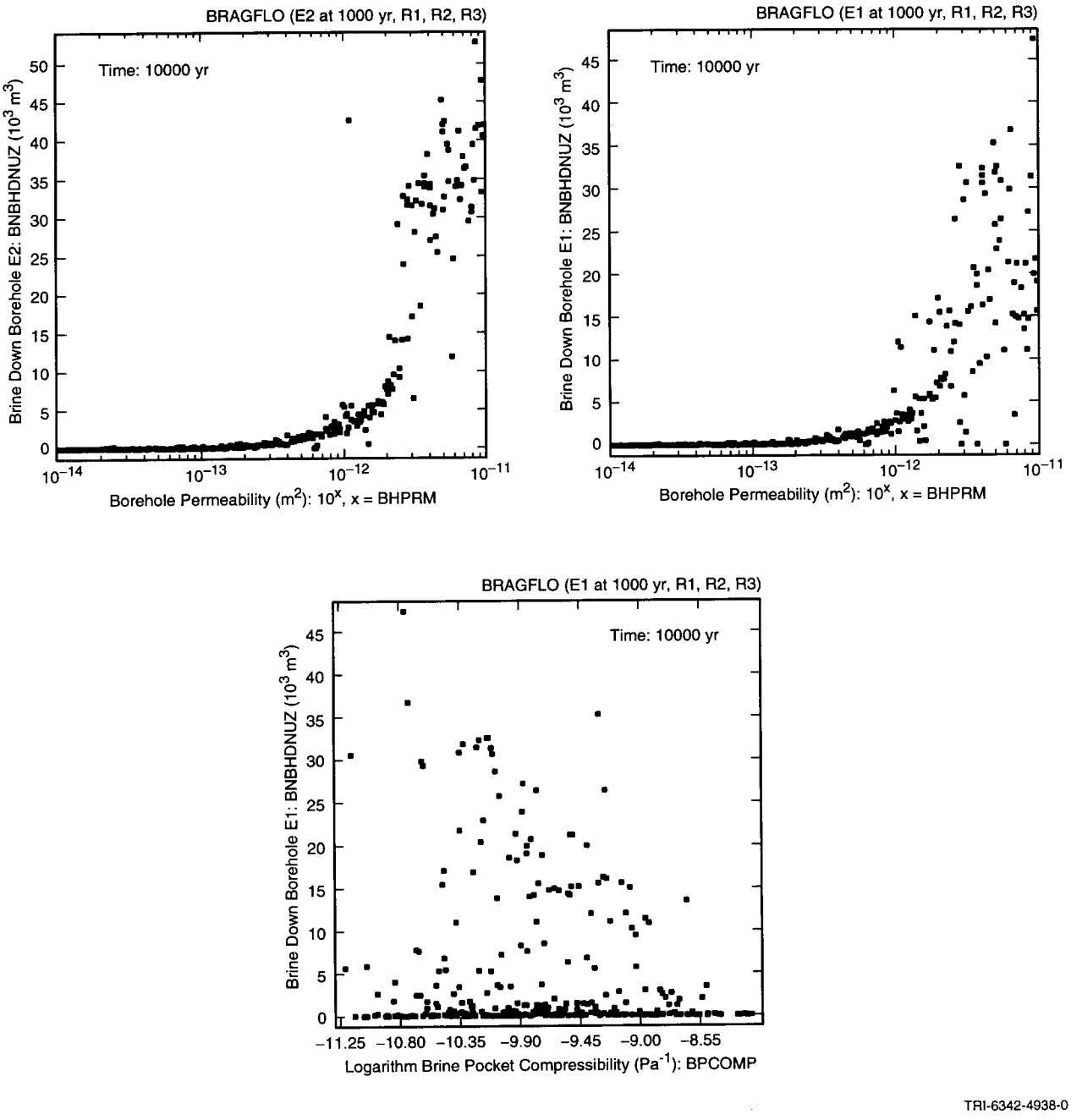

Fig. 8.2.10. Scatterplots for cumulative brine flow through borehole into upper DRZ (*BNBHDNUZ*) over 10,000 yr for E1 and E2 intrusions at 1000 yr into lower waste panel versus *BHPRM* and *BPCOMP*.

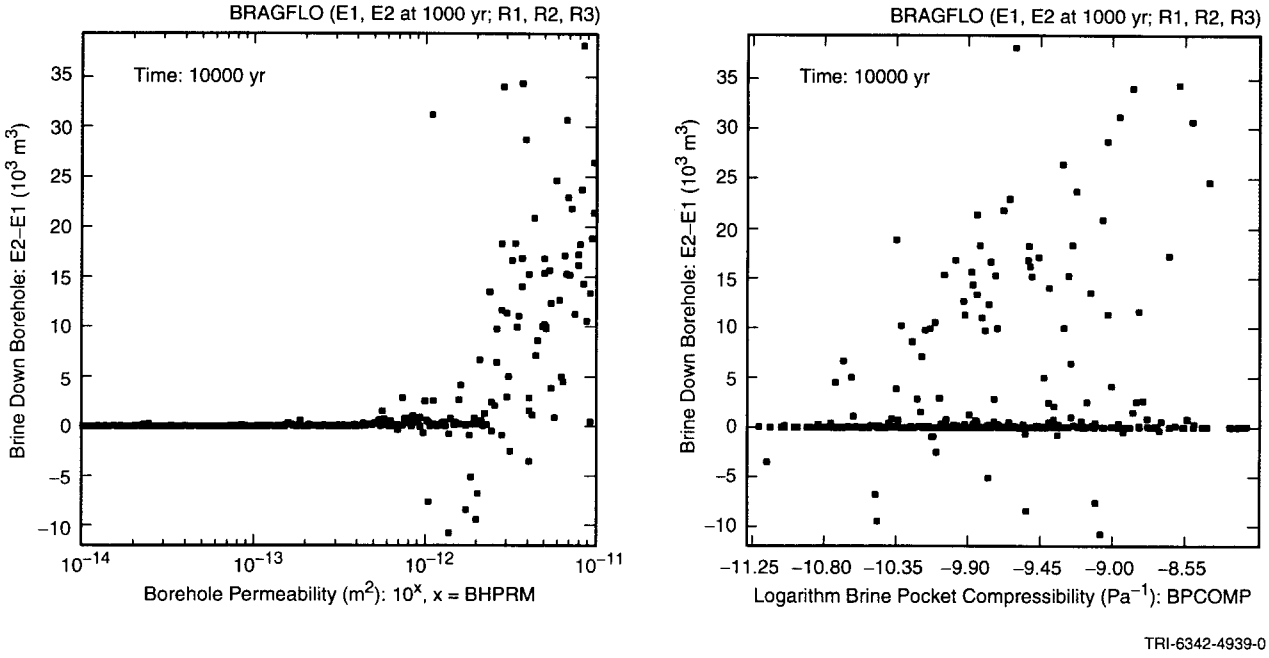

Fig. 8.2.11. Scatterplots for cumulative brine flow down a borehole into the upper DRZ (*BNBHDNUZ*) over 10,000 yr for an E2 intrusion at 1000 yr into lower waste panel minus cumulative brine flow down a borehole into the upper DRZ over 10,000 yr for an E1 at 1000 yr into lower waste panel (i.e., (E2: Upper DRZ) – (E1: Upper DRZ) in Table 8.2.5) versus *BHPRM* and *BPCOMP*.

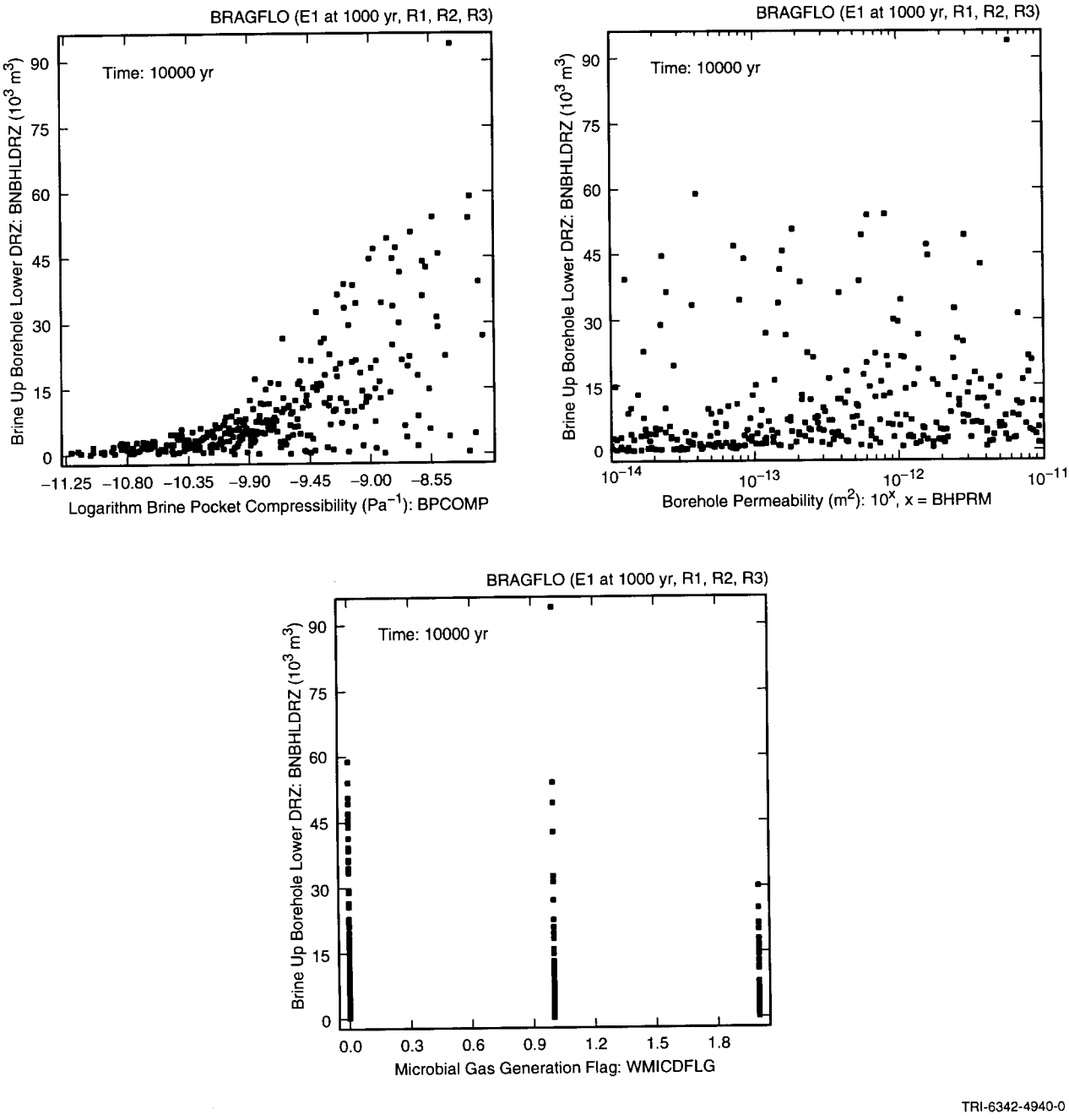

Fig. 8.2.12. Scatterplots for cumulative brine flow from borehole into lower DRZ (*BNBHLDRZ*) over 10,000 yr for an E1 intrusion at 1000 yr into lower waste panel versus *BPCOMP*, *BHPRM* and *WMICDFLG*.

8.3 Disturbed Conditions: Gas Generation for E1 and E2 Intrusions

As most of the cellulose is consumed by microbial action by 1000 yr for undisturbed conditions (Fig. 7.3.2), there is not a significant difference between gas generation due to microbial degradation under disturbed and undisturbed conditions. However, disturbed conditions result in greater gas generation from corrosion due to the increased amount of brine entering the repository (Figs. 8.3.1, 8.3.2).

Gas generation due to corrosion for E1 and E2 intrusions is dominated by *WGRCOR*, *WASTWICK*, *HALPOR* and *BHPRM*, with gas generation tending to increase as each of these variables increases (Fig. 8.3.1). The positive effect for *WGRCOR* results from increasing the rate at which steel is consumed by corrosion, and the positive effects for *WASTWICK*, *HALPOR* and *BHPRM* result from increasing the amount of brine available for the corrosion process. Similar results were obtained in the PRCC analysis for gas generation under undisturbed conditions except that *BHPRM* was not a relevant variable (Fig. 7.3.5).

Similar results were also obtained in stepwise regression analyses for total gas generation due to corrosion over 10,000 yr for E1 and E2 intrusions (Table 8.3.1). For both intrusion modes, the three dominant variables are *HALPOR*, *WGRCOR* and *BHPRM*, with smaller effects indicated for several additional variables. For perspective, scatterplots for *HALPOR*, *WGRCOR* and *BHPRM* for the E2 intrusion are shown in Fig. 8.3.3.

More gas is produced by E1 and E2 intrusions than for E0 (i.e., undisturbed) conditions; further, sometimes the amount of gas produced under E1 conditions exceeds that produced under E2 conditions and sometimes the reverse is true (Fig. 8.3.2). The dominant variables in determining the difference in the amount of gas produced under E1 or E2 conditions and the amount of gas produced under E0 conditions are *BHPRM* and *WGRCOR*, with this difference tending to increase as each of these variables increases. The positive effect for *BHPRM* results from increasing the amount of brine entering the repository, and the positive effect for *WGRCOR* results from increasing the rate at which this brine is consumed by corrosion. Smaller effects are also indicated for several additional variables. For the E2 intrusions, the difference also tends to increase as *ANHPRM* and *WMICDFLG* increase because increasing *ANHPRM* allows more brine to flow into the repository under the decreased pressures associated with the E2 intrusion and increasing *WMICDFLG* elevates repository pressure under E0 conditions and thus tends to reduce the amount of brine flowing into the repository. For the E1 intrusion, increasing *BPCOMP* and *BPINTPRS* increases the amount of brine flowing into the repository from the brine pocket, increasing *HALPOR* makes it less likely that corrosion will be brine limited under E0 conditions, and increasing *WMICDFLG* tends to exclude brine under E0 conditions.

The first three variables selected in the regression analysis for the difference between gas generation due to corrosion for E1 and E2 intrusions are *BPCOMP*, *BHPRM* and *WMICDFLG*, with this difference tending to increase

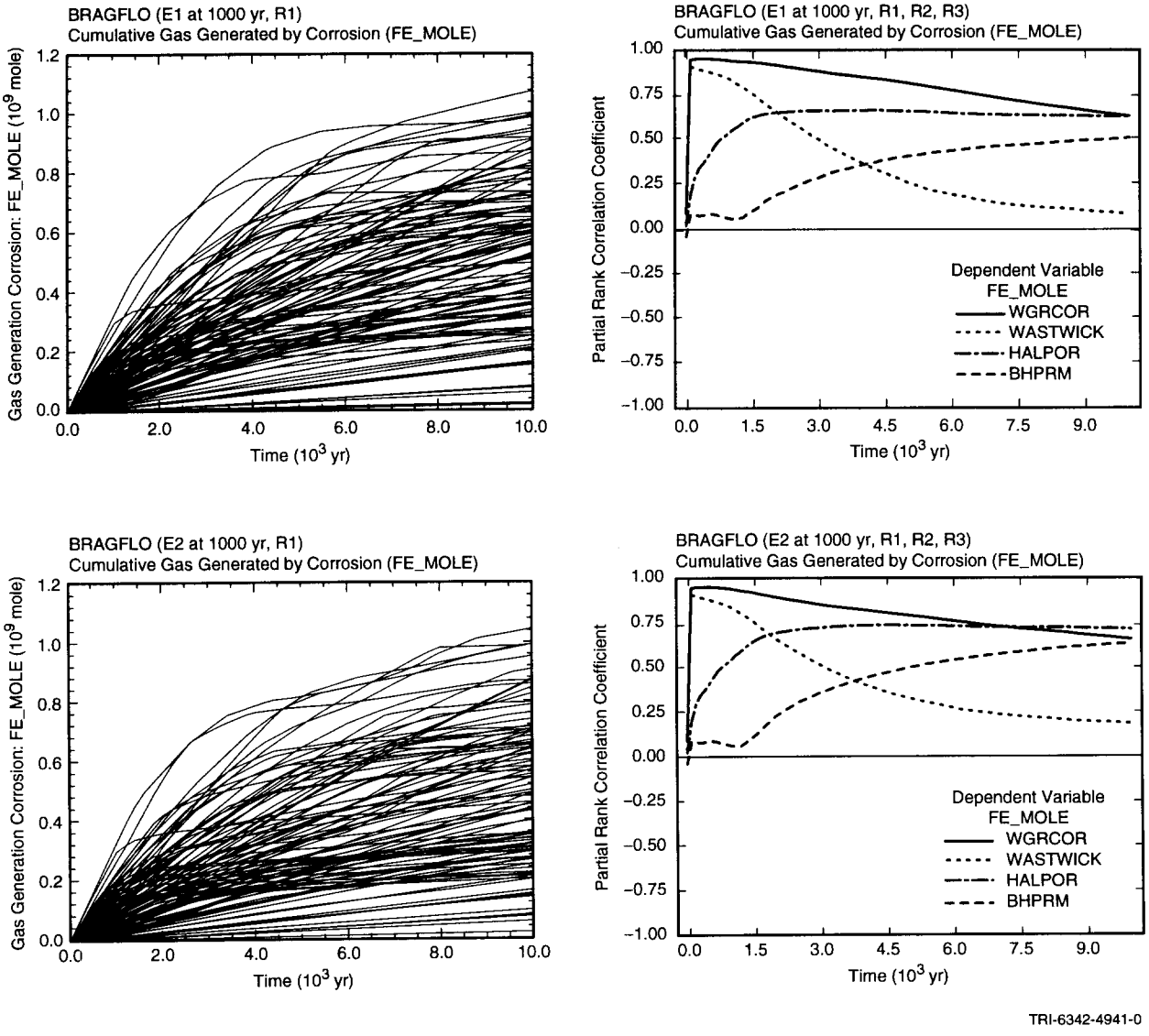

Fig. 8.3.1. Uncertainty and sensitivity analysis results for cumulative gas generation due to corrosion (*FE_MOLE*) for E1 and E2 intrusions at 1000 yr into lower waste panel.

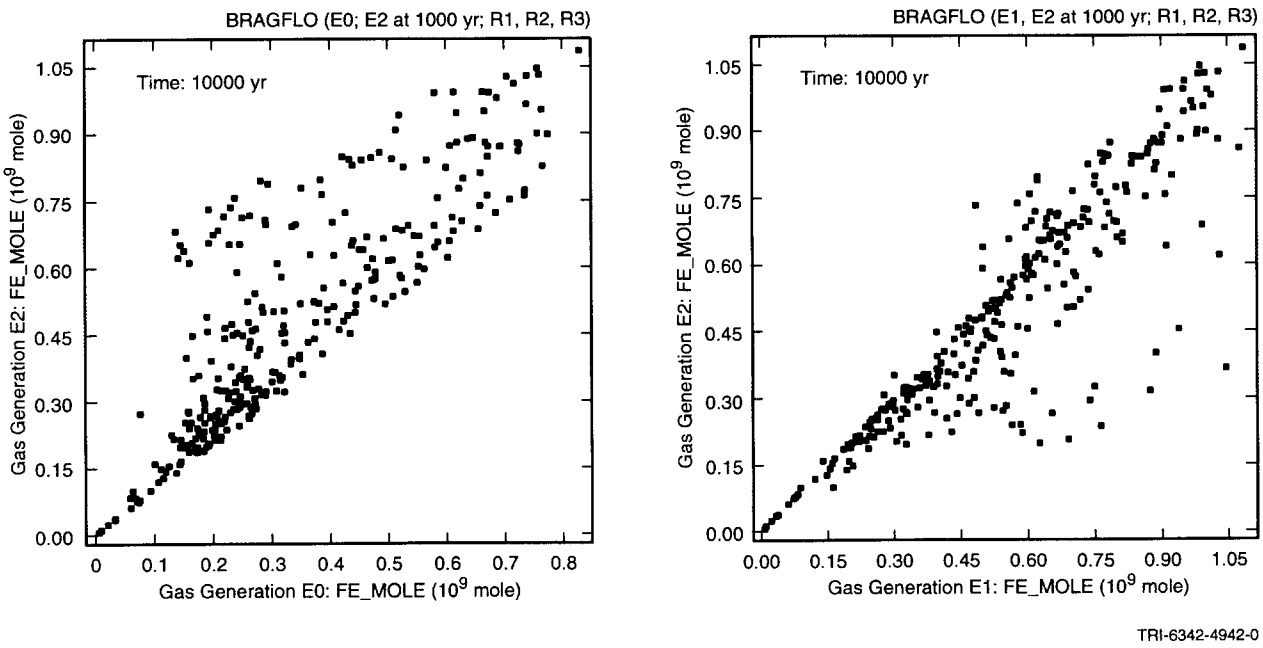

Fig. 8.3.2. Scatterplots for cumulative gas generation over 10,000 yr due to corrosion (*FE_MOLE*) for E0 conditions, an E1 intrusion at 1000 yr into lower waste panel, and an E2 intrusion at 1000 yr into lower waste panel.

as *BPCOMP* increases and tending to decrease as *BHPRM* and *WMICDFLG* increase (Table 8.3.1). The positive effect for *BPCOMP* results from allowing more brine flow from the brine pocket to the repository for E1 intrusions; the negative effect for *BHPRM* results from allowing more brine flow into the repository from overlying formations for E2 intrusions, and the negative effect for *WMICDFLG* results from reducing brine flow from the brine pocket to the repository during the 200 yr period immediately following an E1 intrusion in which an open borehole is assumed to exist between the brine pocket and the repository (Fig. 8.2.8). After *BPCOMP*, *BHPRM* and *WMICDFLG*, the regression model selects an additional 6 variables. However, the final regression model has an R^2 of only 0.36, which indicates a rather poor fit to the data. In such cases, an examination of scatterplots is often informative (Fig. 8.3.4).

The scatterplots in Fig. 8.3.4 show patterns involving *BPCOMP*, *BHPRM* and *WMICDFLG* that are consistent with the signs of the regression coefficients in Table 8.3.1. In particular, the difference in gas generation for E1 and E2 conditions tends to increase as *BPCOMP* increases and to decrease as *BHPRM* and *WMICDFLG* increase. However, *BHPRM* shows a complex pattern with the difference only being affected by the largest values of *BHPRM*. This pattern cannot be captured by the linear regression techniques in use, which results in a low R^2 value for the final regression model. As discussed in Sect. 8.4, the indicated effect for *BHPRM* results from the tendency of the intruded waste panel to fill with brine for large values of *BHPRM*.

Table 8.3.1. Stepwise Regression Analyses with Rank-Transformed Data for Gas Generation Due to Corrosion (*FE_MOLE*) and Total (i.e., Corrosion and Microbial) Gas Generation (*GAS_MOLE*) for E1 and E2 Intrusions at 1000 yr into Lower Waste Panel

	Gas, Corrosion E2: 0 - 10,000 yr			Gas, Corrosion E1: 0 - 10,000 yr			Gas, Corrosion (E2: 0 - 10,000 yr) – (E0: 0 - 10,000 yr)			Gas, Corrosion (E1: 0 - 10,000 yr) – (E0: 0 - 10,000 yr)		
Step[a]	Variable[b]	SRRC[c]	R^{2d}	Variable	SRRC	R^2	Variable	SRRC	R^2	Variable	SRRC	R^2
1	*HALPOR*	0.52	0.29	*HALPOR*	0.47	0.23	*BHPRM*	0.73	0.54	*BHPRM*	0.56	0.31
2	*WGRCOR*	0.45	0.49	*WGRCOR*	0.47	0.45	*WGRCOR*	0.37	0.68	*WGRCOR*	0.39	0.46
3	*BHPRM*	0.42	0.67	*BHPRM*	0.34	0.57	*ANHPRM*	0.19	0.71	*BPCOMP*	0.27	0.53
4	*ANHPRM*	0.13	0.69	*WMICDFLG*	–0.19	0.61	*WMICDFLG*	0.10	0.72	*HALPOR*	–0.15	0.55
5	*WASTWICK*	0.09	0.70	*BPPRM*	–0.16	0.63				*WMICDFLG*	–0.11	0.57
6	*SHRGSSAT*	0.08	0.70	*BPINTPRS*	0.10	0.64				*BPINTPRS*	0.10	0.58
7	*WMICDFLG*	–0.08	0.71									

	Gas, Corrosion (E1: 0-10,000 yr) – (E2: 0 - 10,000 yr)			Gas, Total E2: 0 - 10,000 yr			Gas, Total E1: 0 - 10,000 yr		
Step	Variable	SRRC	R^2	Variable	SRRC	R^2	Variable	SRRC	R^2
1	*BPCOMP*	0.32	0.10	*WMICDFLG*	0.53	0.28	*WMICDFLG*	0.44	0.22
2	*BHPRM*	–0.29	0.18	*HALPOR*	0.44	0.48	*WGRCOR*	0.41	0.40
3	*WMICDFLG*	–0.28	0.25	*WGRCOR*	0.36	0.61	*HALPOR*	0.41	0.57
4	*HALPRM*	–0.17	0.28	*BHPRM*	0.34	0.72	*BHPRM*	0.28	0.64
5	*HALPOR*	–0.15	0.30	*ANHPRM*	0.13	0.74	*BPCOMP*	0.13	0.66
6	*ANHPRM*	–0.13	0.32	*HALPRM*	0.07	0.75	*BPINTPRS*	0.09	0.67
7	*BPINTPRS*	0.13	0.34				*ANHPRM*	0.08	0.68
8	*WGRCOR*	0.12	0.35						
9	*WASTWICK*	–0.11	0.36						

[a] Steps in stepwise regression analysis.

[b] Variables listed in order of selection in regression analysis with *ANHCOMP* and *HALCOMP* excluded from entry into regression model.

[c] Standardized rank regression coefficients in final regression model.

[d] Cumulative R^2 value with entry of each variable into regression model.

Due to the effects of corrosion, total gas generation for E1 and E2 intrusions is also elevated relative to that observed for undisturbed conditions (Figs. 7.3.4, 8.3.5, 8.3.6). Now, *WMICDFLG* appears as an important variable (Fig. 8.3.5, Table 8.3.1) in addition to *WGRCOR*, *WASTWICK*, *HALPOR* and *BHPRM*, which were also identified when only gas generation due to corrosion was considered (Fig. 8.3.1, Table 8.3.1). As previously discussed, *WMICDFLG* controls the amount of gas generated by the microbial degradation of cellulose.

The effects of the drilling intrusion are more apparent when gas generation in the intruded panel and the rest of the repository are compared. Specifically, the intruded panel often has its entire steel inventory consumed by corrosion (Figs. 8.3.7, 8.3.8), which does not occur for the remainder of the repository in intrusion scenarios (Figs. 8.3.7, 8.3.8) or for the unintruded repository (Fig. 7.3.9).

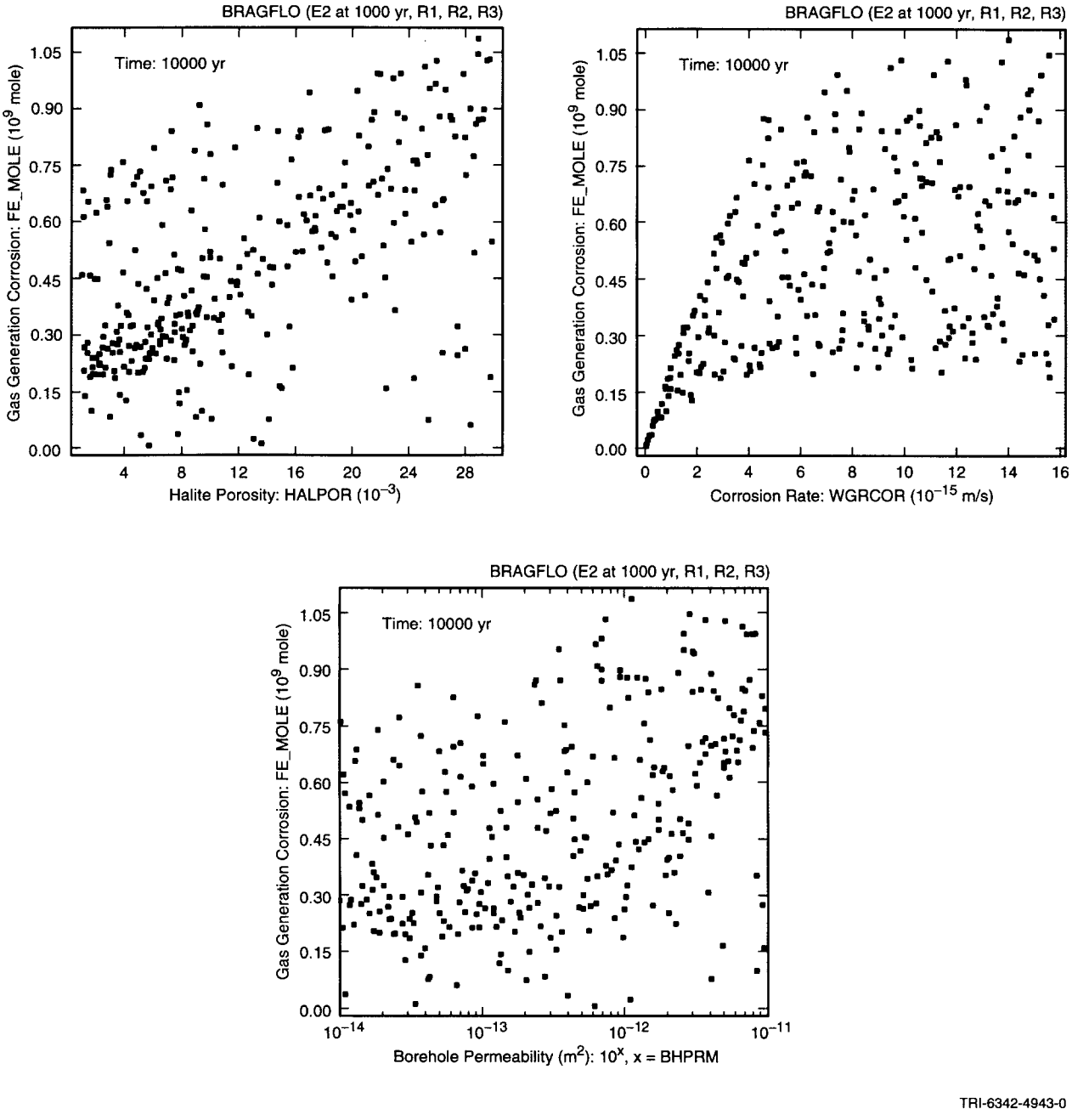

Fig. 8.3.3. Scatterplots for cumulative gas generation due to corrosion (*FE_MOLE*) at 10,000 yr for an E2 intrusion at 1000 yr into lower waste panel versus *HALPOR*, *WGRCOR* and *BHPRM*.

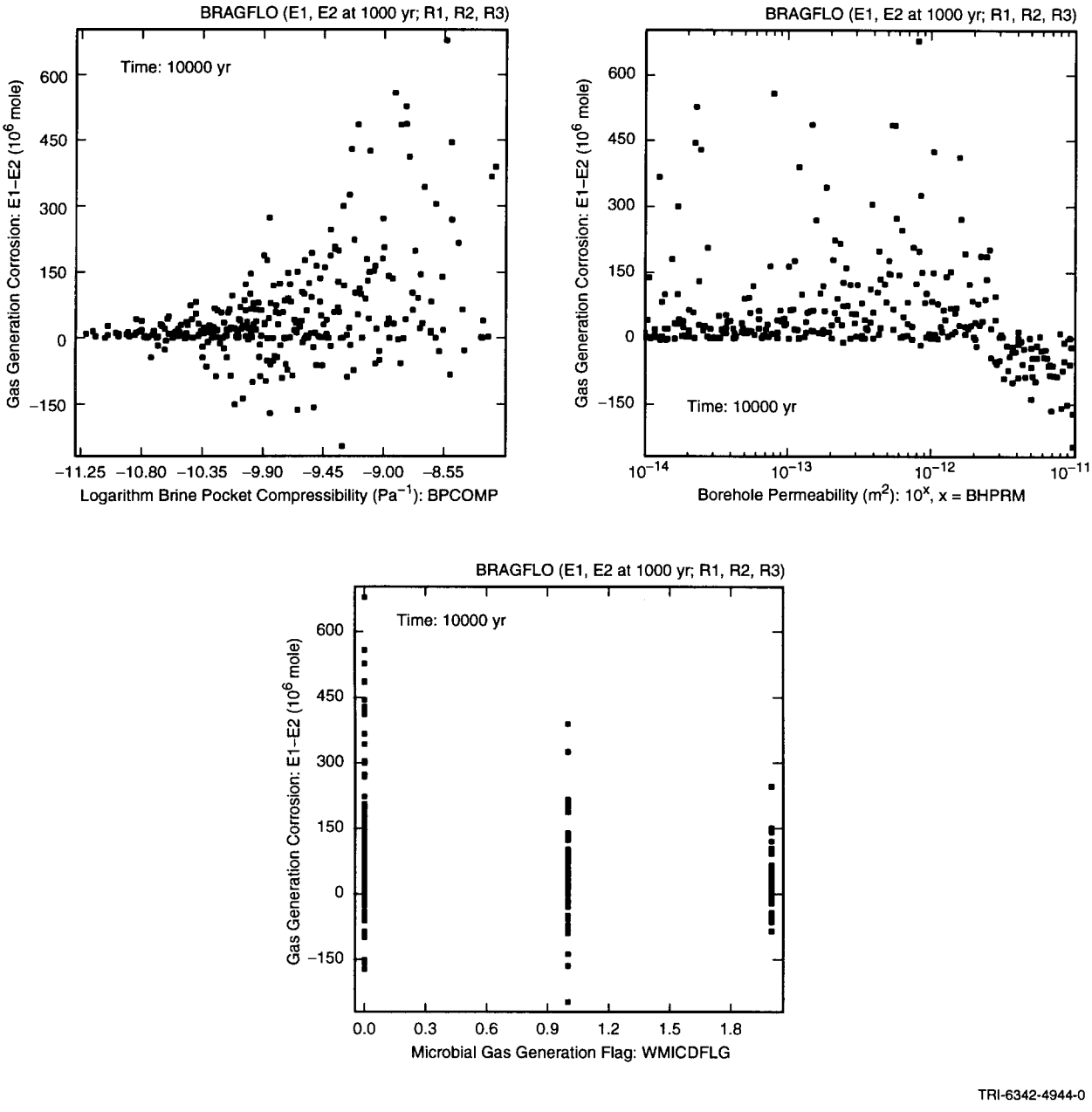

Fig. 8.3.4. Scatterplots for difference between cumulative gas generation due to corrosion (*FE_MOLE*) over 10,000 yr for E1 and E2 intrusions at 1000 yr into lower waste panel (i.e., (E1: 0 - 10,000 yr) – (E2: 0 - 10,000 yr) in Table 8.3.1) versus *BPCOMP*, *BHPRM* and *WMICDFLG*.

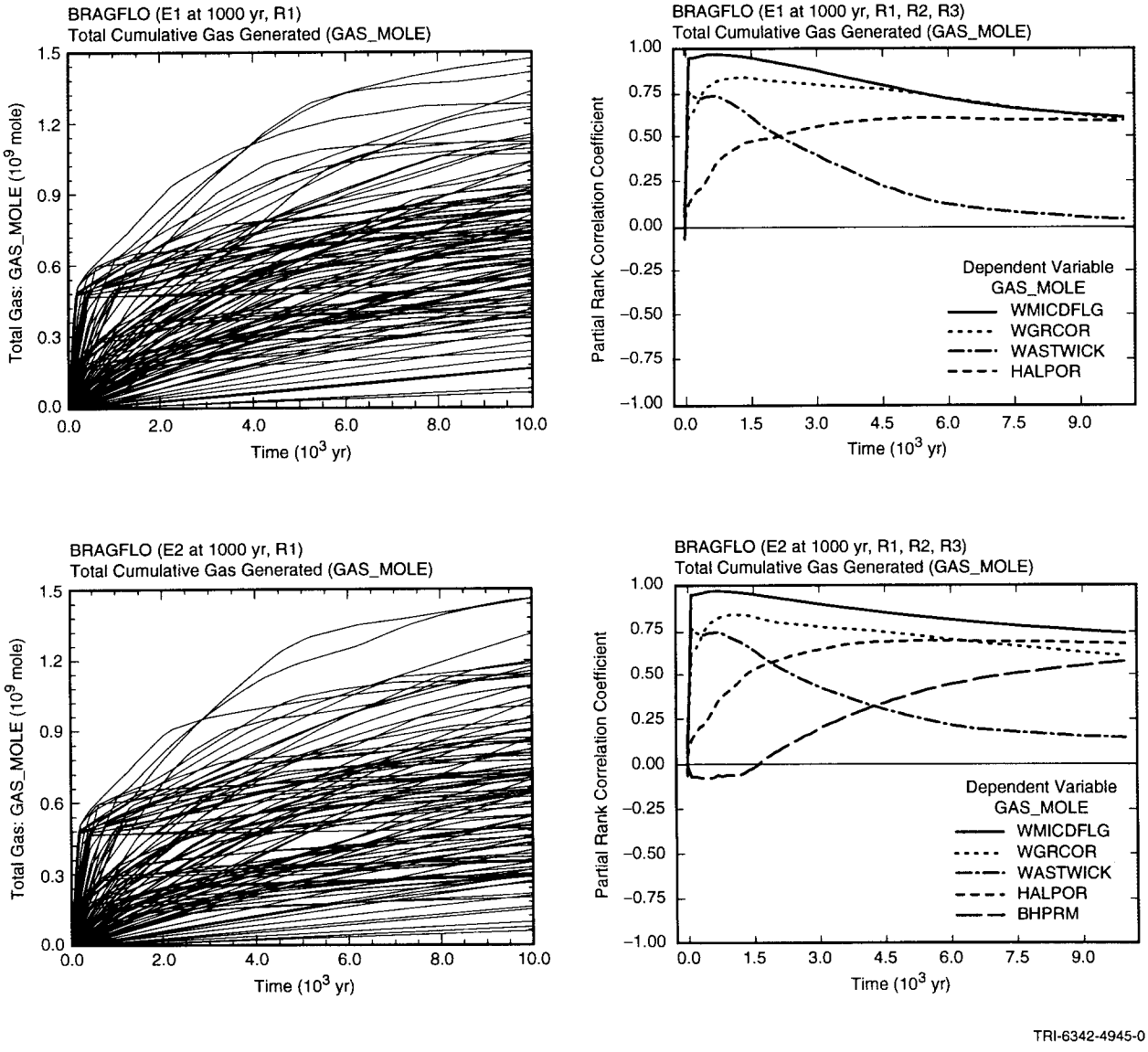

Fig. 8.3.5. Uncertainty and sensitivity analysis results for cumulative gas generation due to corrosion and microbial degradation (*GAS_MOLE*) for E1 and E2 intrusions at 1000 yr into lower waste panel.

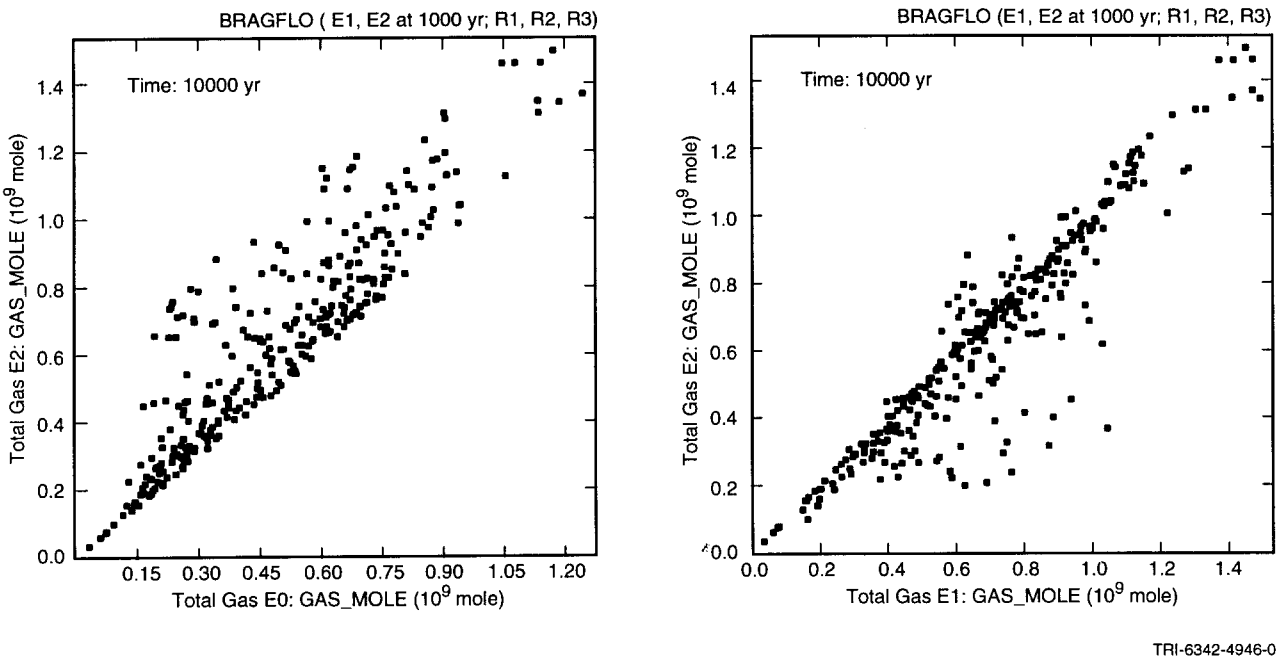

Fig. 8.3.6. Scatterplots for cumulative gas generation due to corrosion and microbial degradation (*GAS_MOLE*) at 10,000 yr for E0 conditions, an E1 intrusion at 1000 yr into lower waste panel, and an E2 intrusion at 1000 yr into lower waste panel.

There is a linear relationship between the amount of steel consumed by corrosion and the amount of gas generated (Fig. 7.3.8). As a result, the same variables that are identified as affecting the amount of gas generated by corrosion (i.e., *WGRCOR*, *WASTWICK*, *HALPOR*, *BHPRM* in Fig. 8.3.1) are also identified as affecting the amount of steel remaining in the upper and lower waste panels (Figs. 8.3.7, 8.3.8). Because the fraction of steel remaining rather than the fraction of steel consumed by corrosion appears in Figs. 8.3.7 and 8.3.8, the signs on the PRCCs in these two figures are reversed from the signs in Fig. 8.3.1.

Stepwise regression analysis provides a supplement to the sensitivity results based on PRCCs in Figs. 8.3.7 and 8.3.8 (Table 8.3.2). The dependent variables in Table 8.3.2 are fractions of steel consumed by corrosion under different sets of conditions; regressions for amounts of gas generated by corrosion would produce the same results. For the first 1000 yr in both the upper and lower waste panels, the dominant variable is *WGRCOR*, with the fraction of steel consumed tending to increase as *WGRCOR* increases. In addition, positive effects are indicated for *WASTWICK*, *HALPOR* and *SHRGSSAT* for the first 1000 yr in both the upper and lower waste panels and a negative effect is indicated for *WMICDFLG*, with increasing values for *WASTWICK* and *HALPOR* tending to increase the amount of brine available to the corrosion process, increasing values for *WMICDFLG* tending to decrease the

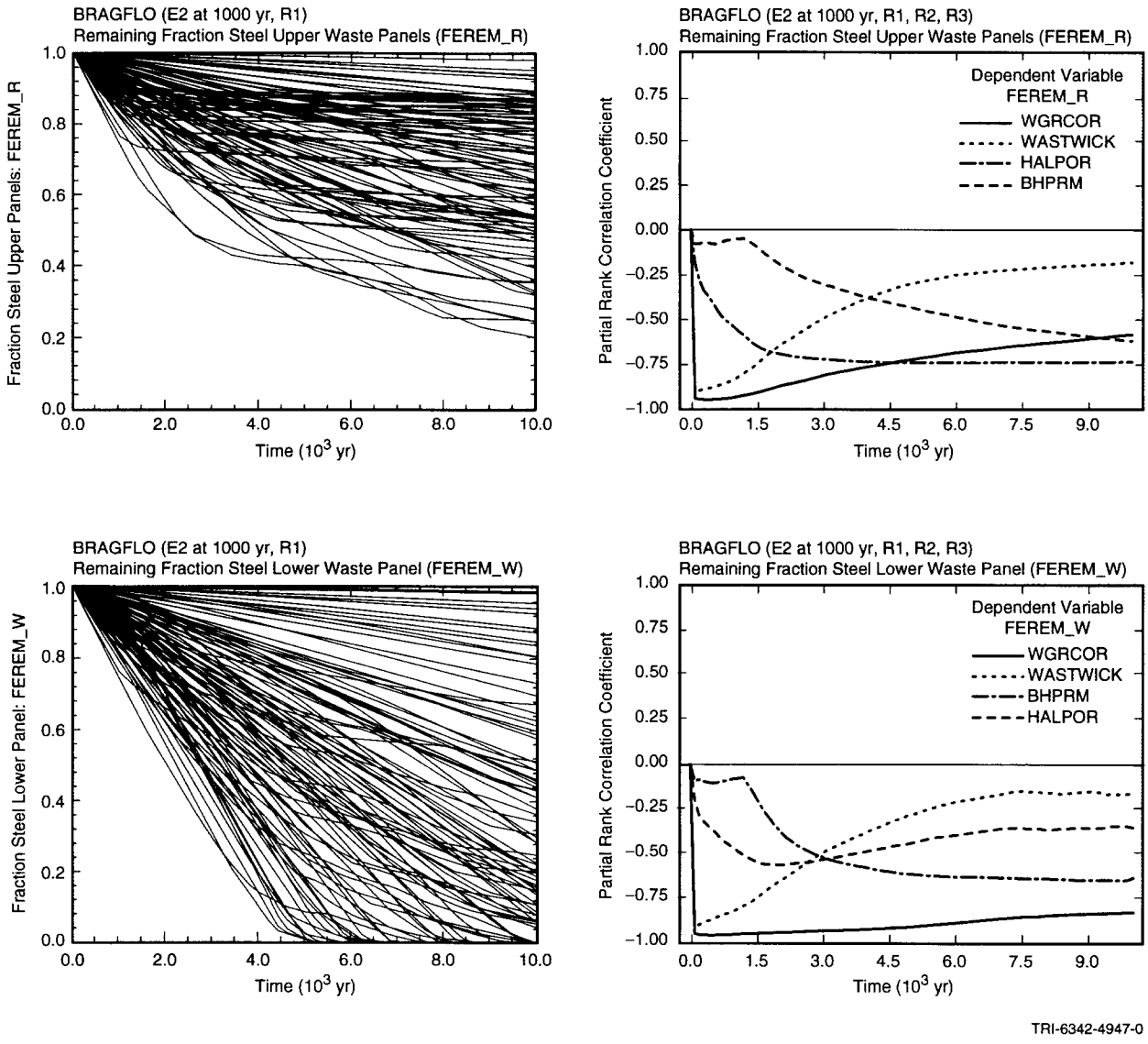

Fig. 8.3.7. Uncertainty and sensitivity analysis results for fraction of steel remaining in upper waste panels (*FEREM_R*) (upper frames) and lower waste panel (*FEREM_W*) (lower frames) for an E2 intrusion at 1000 yr into lower waste panel.

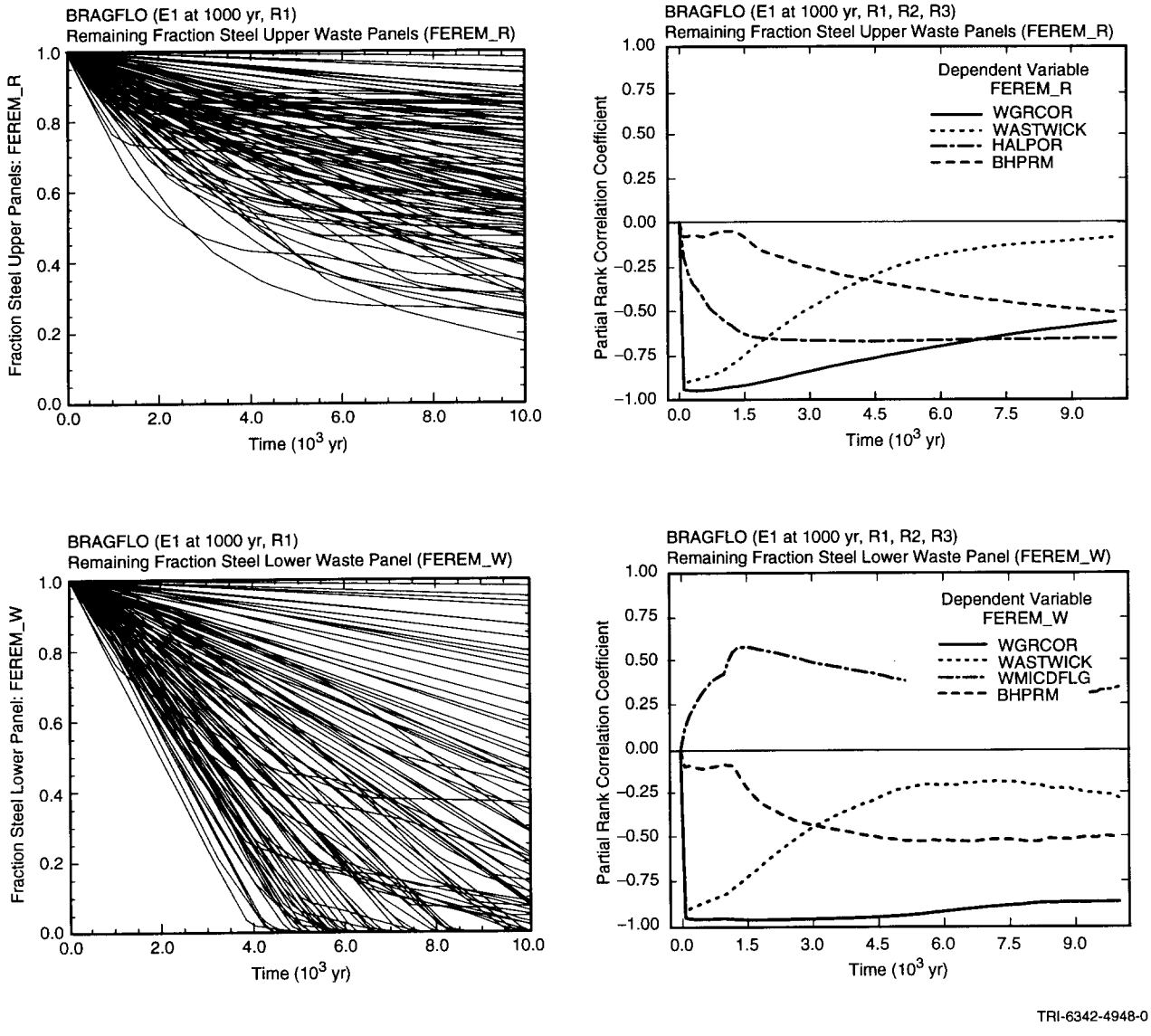

Fig. 8.3.8. Uncertainty and sensitivity analysis results for fraction of steel remaining in upper waste panels (*FEREM_R*) (upper frames) and lower waste panel (*FEREM_W*) (lower frames) for an E1 intrusion at 1000 yr into lower waste panel.

Table 8.3.2. Stepwise Regression Analyses with Rank-Transformed Data for Fraction of Steel Consumed in Upper and Lower Waste Panels (1–*FEREM_R*, 1–*FEREM_W*) for E1 and E2 Intrusions at 1000 yr into Lower Waste Panel

	Upper Waste Panels E2: 0 - 1000 yr			Upper Waste Panels E2: 1000 - 10,000 yr			Upper Waste Panels E2: 0 - 10,000 yr			Upper Waste Panels E1: 1000 - 10,000 yr		
Step[a]	Variable[b]	SRRC[c]	R^{2d}	Variable	SRRC	R^2	Variable	SRRC	R^2	Variable	SRRC	R^2
1	*WGRCOR*	0.81	0.64	*HALPOR*	0.59	0.35	*HALPOR*	0.58	0.35	*HALPOR*	0.51	0.27
2	*WASTWICK*	0.46	0.85	*BHPRM*	0.47	0.58	*BHPRM*	0.42	0.52	*BHPRM*	0.38	0.42
3	*HALPOR*	0.20	0.89	*WGRCOR*	0.17	0.60	*WGRCOR*	0.38	0.67	*WGRCOR*	0.22	0.47
4	*WMICDFLG*	−0.09	0.90	*ANHPRM*	0.12	0.62	*ANHPRM*	0.12	0.68	*WMICDFLG*	−0.20	0.50
5	*SHRGSSAT*	0.05	0.90	*HALPRM*	0.09	0.63	*WASTWICK*	0.09	0.69	*BPPRM*	−0.18	0.54
6							*HALPRM*	0.08	0.70	*BPINTPRS*	0.11	0.55
7							*SHRGSSAT*	0.08	0.70			

	Upper Waste Panels E1: 0 - 10,000 yr			Upper Waste Panels (E1: 0 - 10,000 yr) – (E2: 0 - 10,000 yr)			Lower Waste Panel E2: 0 - 1000 yr			Lower Waste Panel E2: 1000 - 10,000 yr		
Step	Variable	SRRC	R^2	Variable	SRRC	R^2	Variable	SRRC	R^2	Variable	SRRC	R^2
1	*HALPOR*	0.51	0.27	*BPCOMP*	0.31	0.09	*WGRCOR*	0.85	0.71	*WGRCOR*	0.55	0.31
2	*WGRCOR*	0.40	0.43	*WMICDFLG*	−0.30	0.17	*WASTWICK*	0.40	0.86	*BHPRM*	0.45	0.50
3	*BHPRM*	0.35	0.56	*BHPRM*	−0.22	0.22	*HALPOR*	0.15	0.89	*ANHPRM*	0.14	0.52
4	*WMICDFLG*	−0.20	0.59	*HALPRM*	−0.17	0.25	*WMICDFLG*	−0.14	0.91	*WASTWICK*	−0.12	0.54
5	*BPPRM*	−0.17	0.62	*WASTWICK*	−0.13	0.26	*ANHPRM*	0.09	0.91	*SHRGSSAT*	0.10	0.55
6	*BPINTPRS*	0.10	0.63	*BPINTPRS*	0.12	0.28	*SHRGSSAT*	0.04	0.92	*SHPRMCON*	−0.10	0.55
7										*BPVOL*	−0.09	0.56

	Lower Waste Panel E2: 0 - 10,000 yr			Lower Waste Panel E1: 1000 - 10,000 yr			Lower Waste Panel E1: 0 - 10,000 yr			Lower Waste Panel (E1: 0 - 10,000 yr) – (E2: 0 - 10,000 yr)		
Step	Variable	SRRC	R^2	Variable	SRRC	R^2	Variable	SRRC	R^2	Variable	SRRC	R^2
1	*WGRCOR*	0.71	0.51	*WGRCOR*	0.57	0.33	*WGRCOR*	0.79	0.62	*BHPRM*	−0.43	0.19
2	*BHPRM*	0.39	0.66	*BHPRM*	0.28	0.41	*BHPRM*	0.26	0.68	*HALPOR*	−0.37	0.32
3	*HALPOR*	0.18	0.70	*WASTWICK*	−0.22	0.45	*WMICDFLG*	−0.18	0.71	*ANHPRM*	−0.30	0.42
4	*ANHPRM*	0.17	0.72				*WASTWICK*	0.13	0.73	*BPINTPRS*	0.14	0.44
5	*WMICDFLG*	−0.11	0.74				*HALPOR*	0.12	0.75	*HALPRM*	−0.12	0.45
6	*WASTWICK*	0.08	0.74				*SHRGSSAT*	0.08	0.75	*WMICDFLG*	−0.11	0.46
7							*BPINTPRS*	0.08	0.76			
8							*ANHPRM*	0.07	0.76			

[a] Steps in stepwise regression analysis.

[b] Variables listed in order of selection in regression analysis with *ANHCOMP* and *HALCOMP* excluded from entry into regression model.

[c] Standardized rank regression coefficients in final regression model.

[d] Cumulative R^2 value with entry of each variable into regression model.

amount of brine available to the corrosion process, and increasing values of *SHRGSSAT* tending to alter patterns of gas and brine flow across the part of the computational grid corresponding to the shaft within the repository and DRZ (i.e., Regions 10 and 11, Fig. 4.2.1). Also, a small positive effect for *ANHPRM* is indicated in the lower panel due to its role in enhancing brine flow from the marker beds.

For E2 intrusions between 1000 and 10,000 yr, *HALPOR* is the most important variable for the upper waste panels and *WGRCOR* is the most important variable for the lower waste panel (Table 8.3.2). For both upper and lower panels, *BHPRM* is the second variable selected in the regression analysis. The upper panels receive less of the brine flowing down the borehole than the lower panel. As a result, the amount of brine entering by drainage from the DRZ, which is determined by *HALPOR*, is the most important variable in determining the amount of steel that will be consumed by corrosion. In contrast, the lower panel receives more brine inflow on a unit volume basis than the upper panels and the amount of steel consumed is dominated by how fast this brine can be used in the corrosion process, with this rate dominated by *WGRCOR*. The variable *BHPRM* has a positive effect due to its role in increasing both brine flow down the borehole and out of the marker beds. The variable *ANHPRM* also has a positive effect in both regressions due to its role in increasing brine flow out of the marker beds. The appearance of *WASTWICK* with a negative regression coefficient for the lower waste panel results because increasing *WASTWICK* increases steel consumption in the first 1000 yr and thus reduces the amount of steel that can be consumed between 1000 and 10,000 yr. Several other variables (i.e., *HALPRM*, *SHRGSSAT*, *SHPRMCON*, *BPVOL*) are indicated as having small effects. Increasing *HALPRM* tends to increase brine flow out of the marker beds (Table 8.2.1). The variables *SHRGSSAT* and *SHPRMCON* affect gas and brine flow across the part of the computational grid corresponding to the shaft within the repository and DRZ (i.e., Regions 10 and 11, Fig. 4.2.1). The appearance of *BPVOL* is spurious.

The regressions for E2 intrusions between 1000 and 10,000 yr have relatively low R^2 values (i.e., 0.63, 0.56) due to patterns of the form shown by the scatterplots in Fig. 8.3.9. Specifically, the left and right columns in Fig. 8.3.9 display scatterplots for the first three variables selected in the regression analyses in Table 8.3.2 for steel consumption between 1000 and 10,000 yr in the upper and lower waste panels, respectively. For the upper waste panels, the positive trends indicated in the scatterplots for *HALPOR*, *BHPRM* and *WGRCOR* are consistent with the positive regression coefficients in Table 8.3.2. However, the patterns are fairly diffuse, and the fact that corrosion ceases in the absence of brine is producing patterns that are difficult to capture with a linear regression model. In particular, a well-defined relationship between steel consumption and *WGRCOR* can be seen for small values of *WGRCOR*, with this pattern then becoming very diffuse for larger values of *WGRCOR* due to brine exhaustion. For the lower waste panel, a much stronger relationship between gas generation and *WGRCOR* can be seen because the extensive brine flow into the lower waste panel makes it unlikely that corrosion will cease due to brine exhaustion. The leveling off and actual decrease in the fraction of steel consumed for larger values of *WGRCOR* occurs because

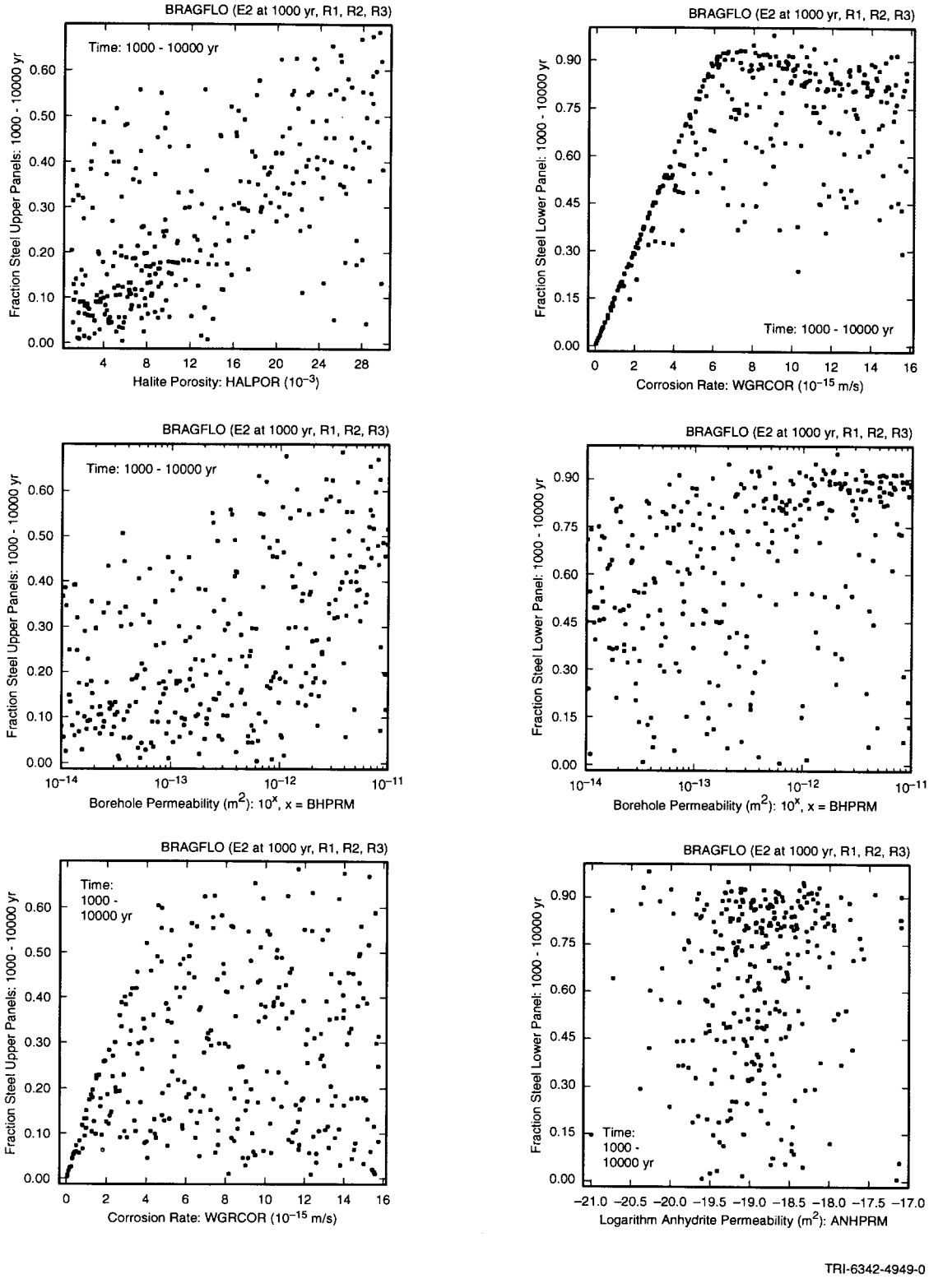

Fig. 8.3.9. Scatterplots for fraction of steel consumed in upper waste panels (1–*FEREM_R*) (left frames) and lower waste panel (1–*FEREM_W*) (right frames) between 1000 and 10,000 yr for an E2 intrusion at 1000 yr into lower waste panel versus *HALPOR*, *WGRCOR*, *BHPRM*, and *ANHPRM*.

large values of *WGRCOR* result in more steel consumption in the first 1000 yr and hence in less steel being available for consumption between 1000 and 10,000 yr. For small values of *WGRCOR*, corrosion is not limited by the steel inventory and so the loss of steel during the first 1000 yr has no effect on the fraction of steel consumed by corrosion between 1000 and 10,000 yr. As for the upper waste panels, the relationships between the fraction of steel consumed by corrosion and the sampled variables are too complex to be captured by a linear regression model.

When the entire 10,000 yr period is considered for E2 intrusions, *HALPOR* is the dominant variable with respect to fraction of steel consumed in the upper panels (Table 8.3.2), and *WGRCOR* is the dominant variable with respect to the fraction of steel consumed in the lower panel (Table 8.3.2, Figure 8.3.10). The greater availability of brine in the lower waste panel results in the fraction of steel consumed by corrosion being dominated by the rate at which corrosion takes place (Fig. 8.3.10). The larger values for *WGRCOR* result in a complete consumption of the steel if adequate brine is present (Fig. 8.3.10). Overall, the patterns of variable influence are consistent with those previously observed and discussed for the 0 - 1000 yr and 1000 - 10,000 yr time periods.

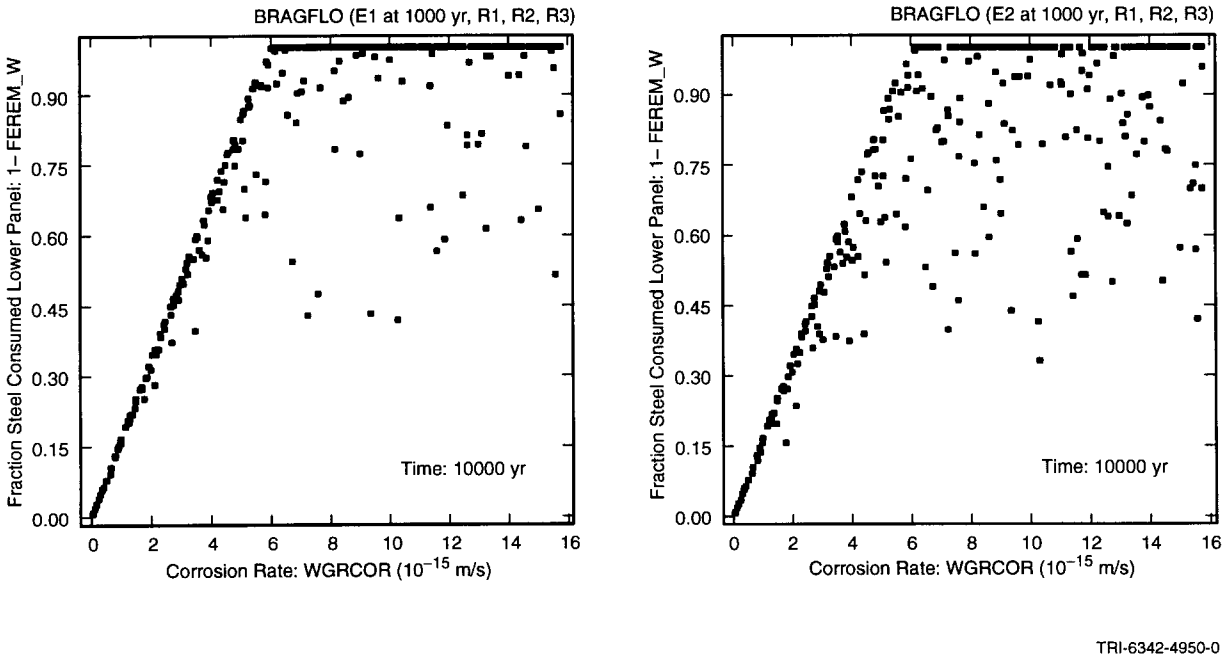

Fig. 8.3.10. Scatterplots for fraction of steel in lower waste panel consumed by corrosion (1–*FEREM_W*) over 10,000 yr for E1 and E2 intrusions at 1000 yr into lower waste panel versus *WGRCOR*.

The 0 - 1000 yr results are identical for E1 and E2 intrusions at 1000 yr (Table 8.3.2). For the upper waste panels over the interval 1000 - 10,000 yr, the analyses for E1 and E2 intrusions both select *HALPOR*, *BHPRM* and *WGRCOR* as the first three variables in the regression model (Table 8.3.2) for reasons previously discussed. The analysis for the E1 intrusion then selects *WMICDFLG*, *BPPRM* and *BPINTPRS*. The selection of *WMICDFLG* with a negative regression coefficient results because of the role that *WMICDFLG* plays in reducing and/or stopping brine flow from the brine pocket to the repository in the 200 yr period between the occurrence of the drilling intrusion and the failure of the plug at the Rustler/Salado interface (Fig. 8.2.8). The appearance of *BPPRM* with a negative regression coefficient is counterintuitive; however, *BPCOMP* and *BPPRM* were sampled with a rank correlation of -0.75, which can cause unanticipated patterns in a regression analysis. The variable *BPINTPRS* appears with a positive regression coefficient because increasing its value tends to increase brine flow from the brine pocket to the repository.

For the lower waste panel over the interval 1000 - 10,000 yr, the regression analysis for the E1 intrusion selects *WGRCOR*, *BHPRM* and *WASTWICK* and produces a model with an R^2 value of only 0.45 (Table 8.3.2). This poor fit is resulting from patterns that cannot be captured by the regression model in use (Fig. 8.3.11). Specifically, the linear relationship for small values of *WGRCOR* followed by an asymptote for larger values is too complex for a simple linear regression model to duplicate.

The variable *BPCOMP* was identified as being important with respect to the amount of brine that flows from the brine pocket to the repository for an E1 intrusion (Table 8.2.5, Fig. 8.2.12). However, *BPCOMP* does not appear in the sensitivity analyses for the amount of steel consumed by corrosion subsequent to an E1 intrusion (Fig. 8.3.8, Table 8.3.2). Given the large amount of brine that typically enters the repository for an E1 intrusion, the importance of *BPCOMP* with respect to the amount of brine entering the repository is lost due to the dominant effect of *WGRCOR* in determining the rate at which this brine is consumed (Figs. 8.3.11, 8.3.12). A similar pattern occurs for E2 intrusions, where *BHPRM* controls the amount of brine flowing down a borehole into the repository (Table 8.2.4, Fig. 8.2.10) and the amount of steel consumed by corrosion subsequent to an intrusion is dominated by *WGRCOR* (Fig. 8.3.9).

For steel consumption in the upper waste panels over the entire 10,000 yr period with an E1 intrusion at 1000 yr, the same variables are identified as for steel consumption from 1000 to 10,000 yr (Table 8.3.2), which is consistent with the result that most steel consumption occurs after 1000 yr (Fig. 8.3.8). For steel consumption in the upper waste panels, the analyses for both E1 and E2 intrusions identify *HALPOR*, *WGRCOR* and *BHPRM* as the top three variables. Interestingly, the regression analysis for steel consumption in the lower waste panel over the entire 10,000 yr period with an E1 intrusion at 1000 yr is considerably more successful than the corresponding analysis for steel consumption between 1000 and 10,000 yr (i.e., a model with 8 variables and an R^2 of 0.76 versus a model with 3 variables and an R^2 of 0.45). This difference arises from the difficulty of capturing the effects of a complete

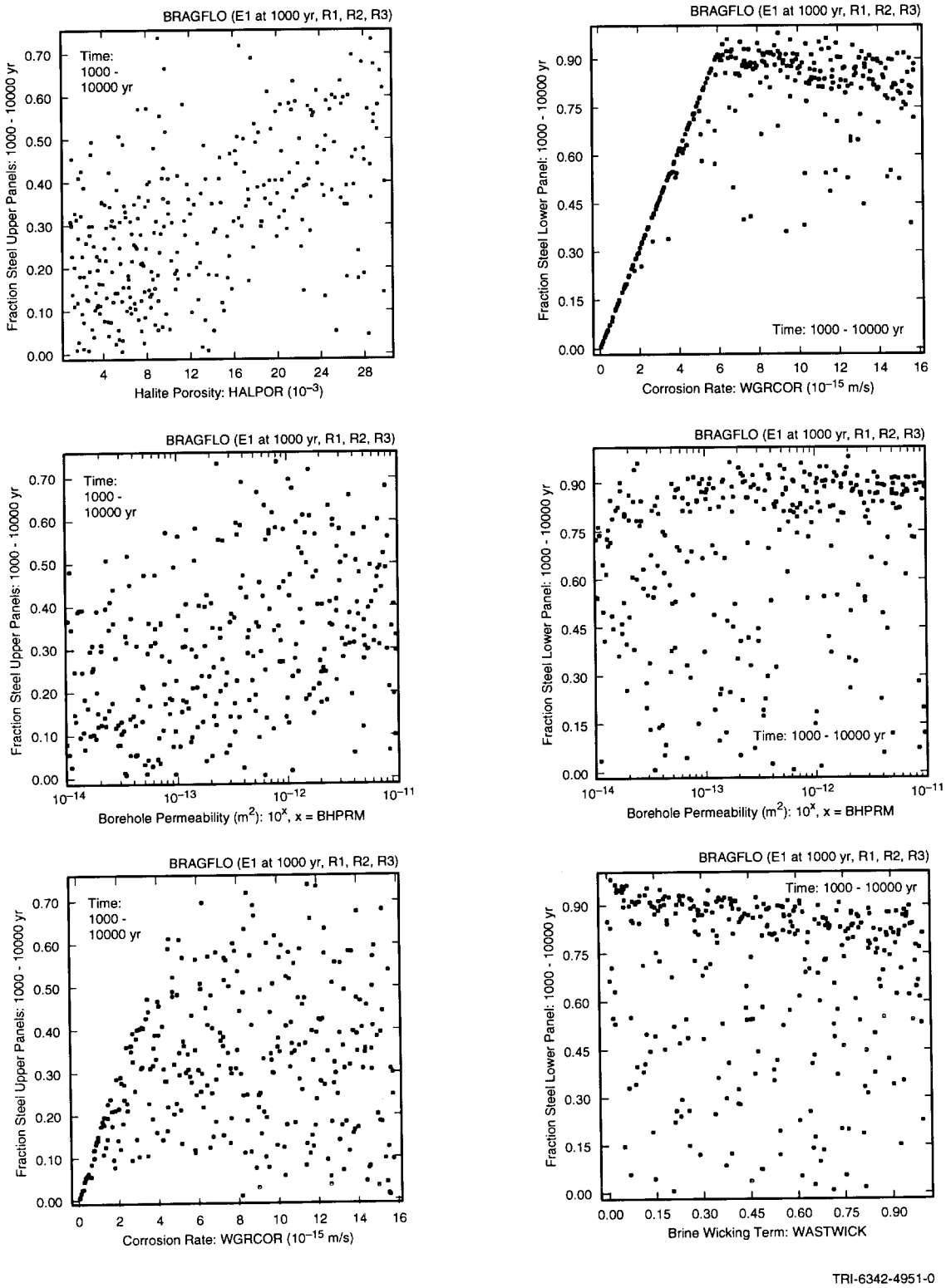

Fig. 8.3.11. Scatterplots for fraction of steel in upper waste panels (1–*FEREM_R*) (left frames) and lower waste panel (1–*FEREM_W*) (right frames) consumed by corrosion between 1000 and 10,000 yr for an E1 intrusion at 1000 yr into lower waste panel versus *HALPOR*, *WGRCOR*, *BHPRM* and *WASTWICK*.

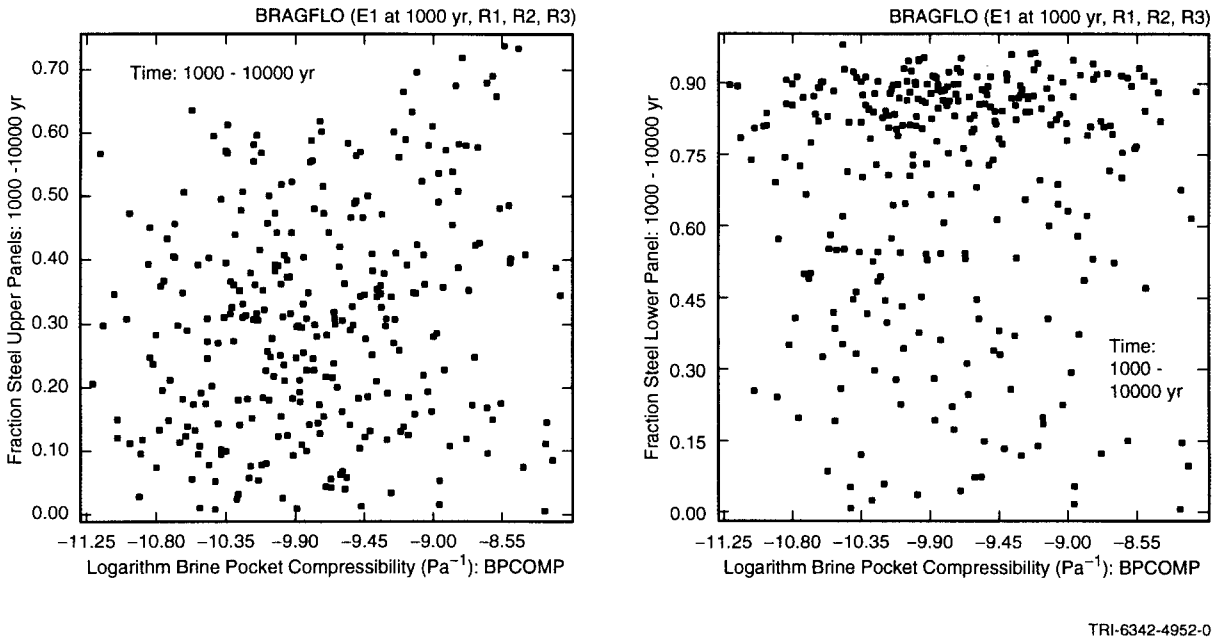

Fig. 8.3.12. Scatterplots for fraction of steel consumed in upper (1–*FEREM_R*) and lower (1–*FEREM_W*) waste panels between 1000 and 10,000 yr for an E1 intrusion at 1000 yr into lower waste panel versus *BPCOMP*.

consumption of the remaining steel inventory between 1000 and 10,000 yr (Figs. 8.3.8, 8.3.11). The dominant variable for steel consumption in the lower waste panel with an E1 intrusion at 1000 yr is *WGRCOR*, which is consistent with the corresponding scatterplot in Fig. 8.3.10. The remaining 7 variables in the regression model (i.e., *BHPRM*, *WASTWICK*, *HALPOR*, *SHRGSSAT*, *BPINTPRS* and *ANHPRM* with positive regression coefficients and *WMICDFLG* with a negative regression coefficient) have considerably smaller effects than *WGRCOR* and have been discussed previously for results in the 0 - 1000 yr and 1000 - 10,000 yr time intervals.

Regression analyses were also performed for the upper and lower waste panels for the difference between fraction of steel consumed for E1 and E2 intrusions at 1000 yr (Table 8.3.2). However, neither regression was very successful in identifying the variables that determine these differences (i.e., R^2 values of 0.28 and 0.46). For perspective, scatterplots of the variables used to define the indicated differences for the upper and lower waste panels are shown in Fig. 8.3.13. The basic problem is that the underlying patterns are too complicated to be captured by a simple regression model (Fig. 8.3.14). For the upper waste panels, *BPCOMP*, *BHPRM*, *WMICDFLG* and *HALPOR* interact to determine the difference between steel consumption for E1 and E2 intrusions (Fig. 8.3.14). Large values for *BPCOMP* tend to increase the difference because of increased brine flow from the brine pocket. Similarly, large values of *WMICDFLG* tend to decrease the difference because of decreased flow from the brine pocket. Small

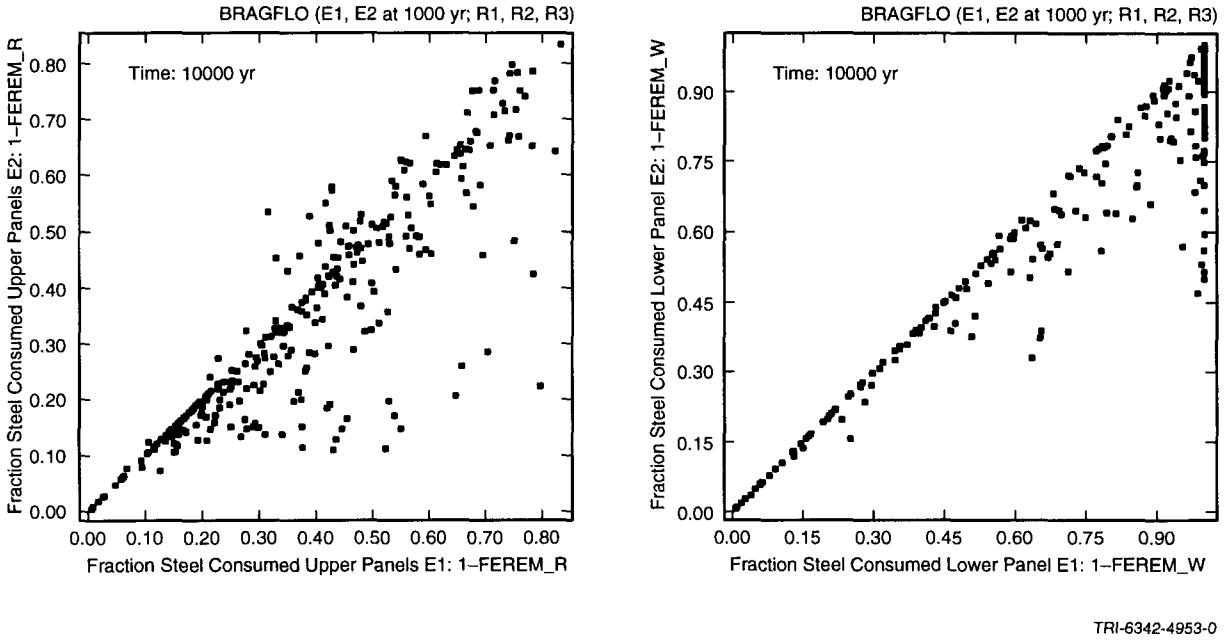

Fig. 8.3.13. Scatterplots for fraction of steel in upper (1–*FEREM_R*) and lower (1–*FEREM_W*) waste panels consumed by corrosion for E1 and E2 intrusions at 1000 yr into lower waste panel.

values for *HALPOR* tend to increase the difference because drainage from the DRZ is a more important brine source for the E2 than the E1 intrusion. Finally, the cases where steel consumption for the E2 intrusion exceeds steel consumption for the E1 intrusion are associated exclusively with the largest values for *BHPRM*.

For the lower waste panel, *BPCOMP*, *BHPRM*, *WMICDFLG* and *HALPOR* again determine the difference between steel consumption for E1 and E2 intrusions (Fig. 8.3.15). In contrast to the upper waste panels where positive and negative differences occur over the entire range of steel consumption (Fig. 8.3.13), steel consumption under E1 conditions always equals or exceeds the consumption under E2 conditions for the lower waste panel (Fig. 8.3.13). Further, the largest differences are strongly concentrated near a consumption fraction of 1 for the E1 intrusion (Fig. 8.3.13). When corrosion rates are small, E1 and E2 intrusions result in corrosion of similar amounts of steel (Fig. 8.3.10) because there is no exhaustion of the available brine. At higher corrosion rates, the amount of steel that can be consumed by corrosion becomes limited by the amount of available brine, which is why the E1 intrusion often results in the consumption of more steel in the lower waste panel than does the E2 intrusion (Fig. 8.3.13). This pattern is consistent with the scatterplots for the lower waste panel in Fig. 8.3.15. Specifically, increasing *BPCOMP* increases the difference between the fraction of steel consumed under E1 and E2 conditions because it increases the amount of brine present under E1 conditions. Similarly, increasing each of *BHPRM* and *HALPOR* tends to increase the amount of brine present under E2 conditions and thus reduce the difference between the fraction of steel consumed under E1 and E2 conditions. Finally, increasing *WMICDFLG* tends to reduce the

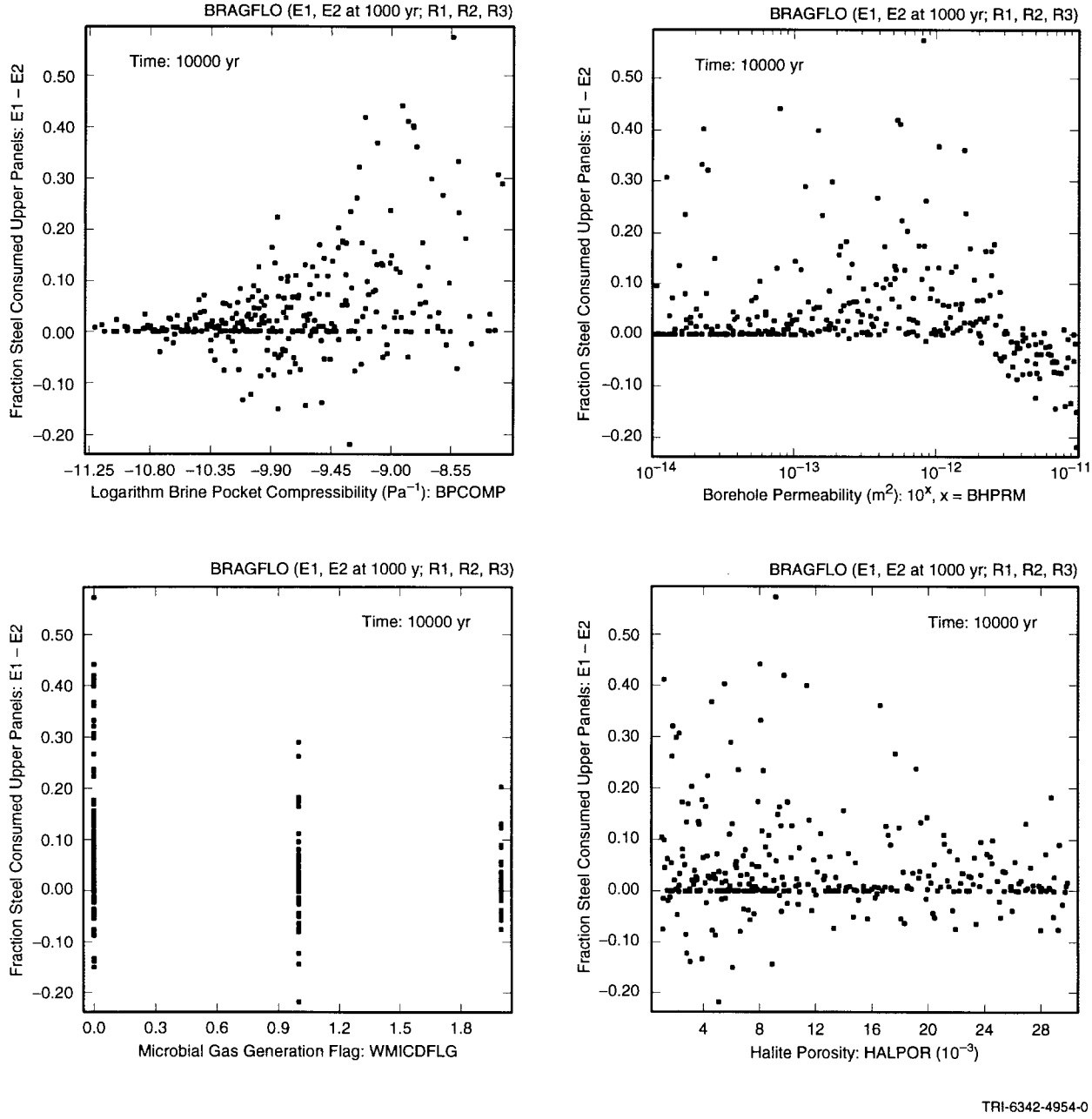

Fig. 8.3.14. Scatterplots for differences in fractions of steel consumed by corrosion in upper waste panels (1–*FEREM_R*) for E1 and E2 intrusions at 1000 yr into lower waste panel (i.e., Upper Waste Panels, (E1: 0 - 10,000 yr) - (E2: 0 - 10,000 yr) in Table 8.3.2) versus *BPCOMP*, *BHPRM*, *WMICDFLG* and *HALPOR*.

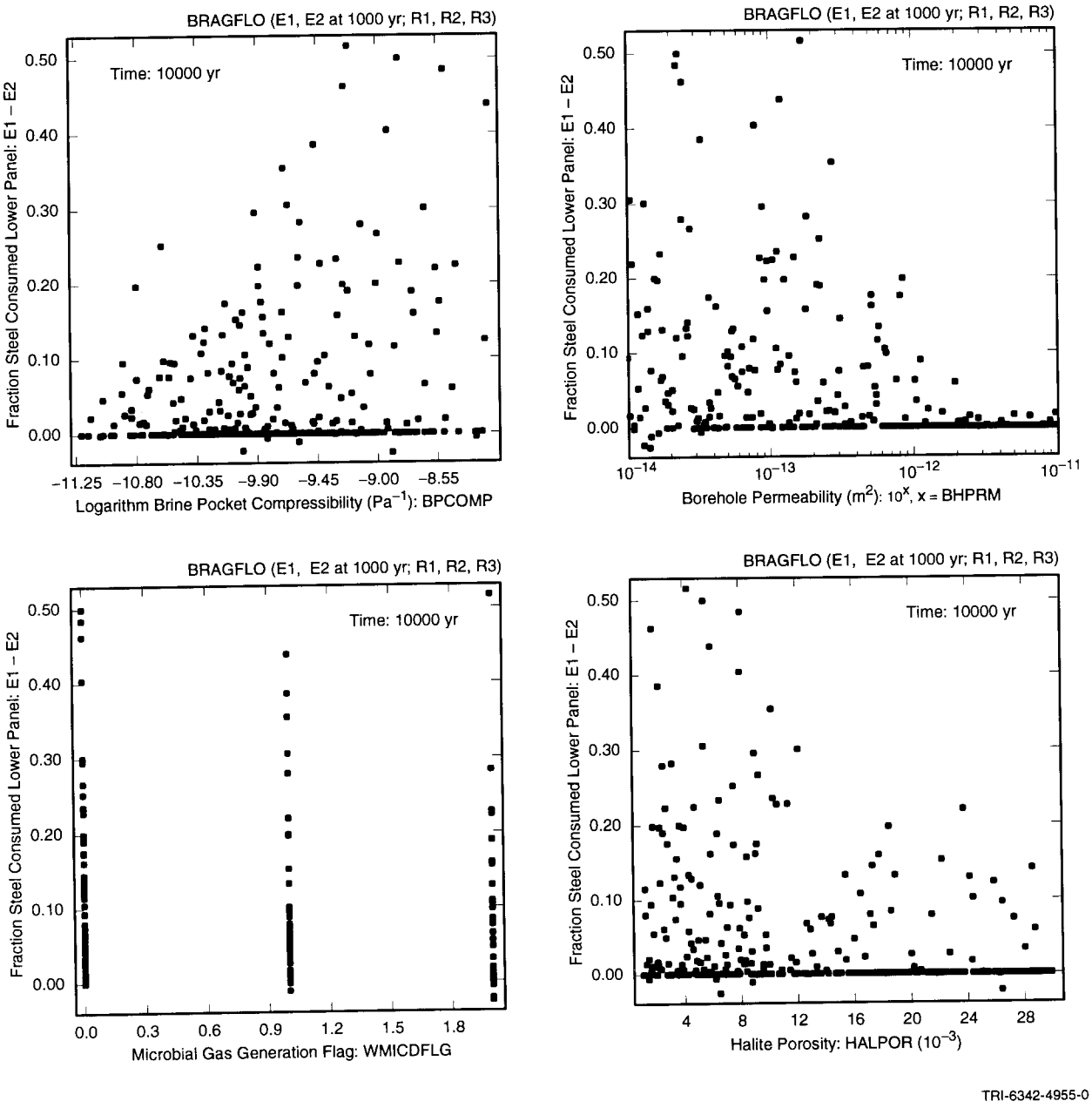

Fig. 8.3.15. Scatterplots for differences in fractions of steel consumed by corrosion in lower waste panels (1–*FEREM_W*) for E1 and E2 intrusions at 1000 yr into lower waste panel (i.e., Lower Waste Panel, (E1: 0 - 10,000 yr) - (E2: 0 - 10,000 yr) in Table 8.3.2) versus *BPCOMP*, *BHPRM*, *WMICDFLG* and *HALPOR*.

amount of brine present under E1 conditions and thus reduce the difference between the fraction of steel consumed under E1 and E2 conditions. However, the large number of observations for which steel consumption in the lower waste panel is the same for E1 and E2 intrusions creates a pattern that cannot be captured by a simple regression model, which is why the corresponding regression in Table 8.3.2 has an R^2 value of only 0.46.

The increased brine inflow, and hence increased corrosion, results in the increased gas generation observed for E1 and E2 intrusions relative to that observed for undisturbed conditions (Figs. 8.3.2, 8.3.6). Due to the different patterns of brine inflow, and hence corrosion, in the upper and lower waste panels, there are also different patterns of gas generation (Figs. 8.3.16, 8.3.17). In particular, gas generation in the lower waste panel ceases for some sample elements due to a complete consumption of the steel inventory (Figs. 8.3.7, 8.3.8). In contrast, the steel inventory is not depleted in the upper waste panels (Figs. 8.3.7, 8.3.8) and so gas generation continues over the entire 10,000 yr period unless there is no brine in the upper waste panels.

The PRCCs in Figs. 8.3.16 and 8.3.17 for cumulative gas generation consistently show *WMICDFLG* to be the dominant variable due to its role in determining the amount of gas generated by microbial degradation of cellulose. After *WMICDFLG*, the selected variables are consistent with those obtained in Figs. 8.3.7 and 8.3.8 for fraction of steel remaining, with the appropriate reversal in sign. For completeness, Table 8.3.3 presents the same regression analyses for total gas generation as presented in Table 8.3.2 for amount of steel consumed. The results in Tables 8.3.2 and 8.3.3 are generally the same with the appropriate addition of *WMICDFLG* due to its role in influencing microbial gas generation.

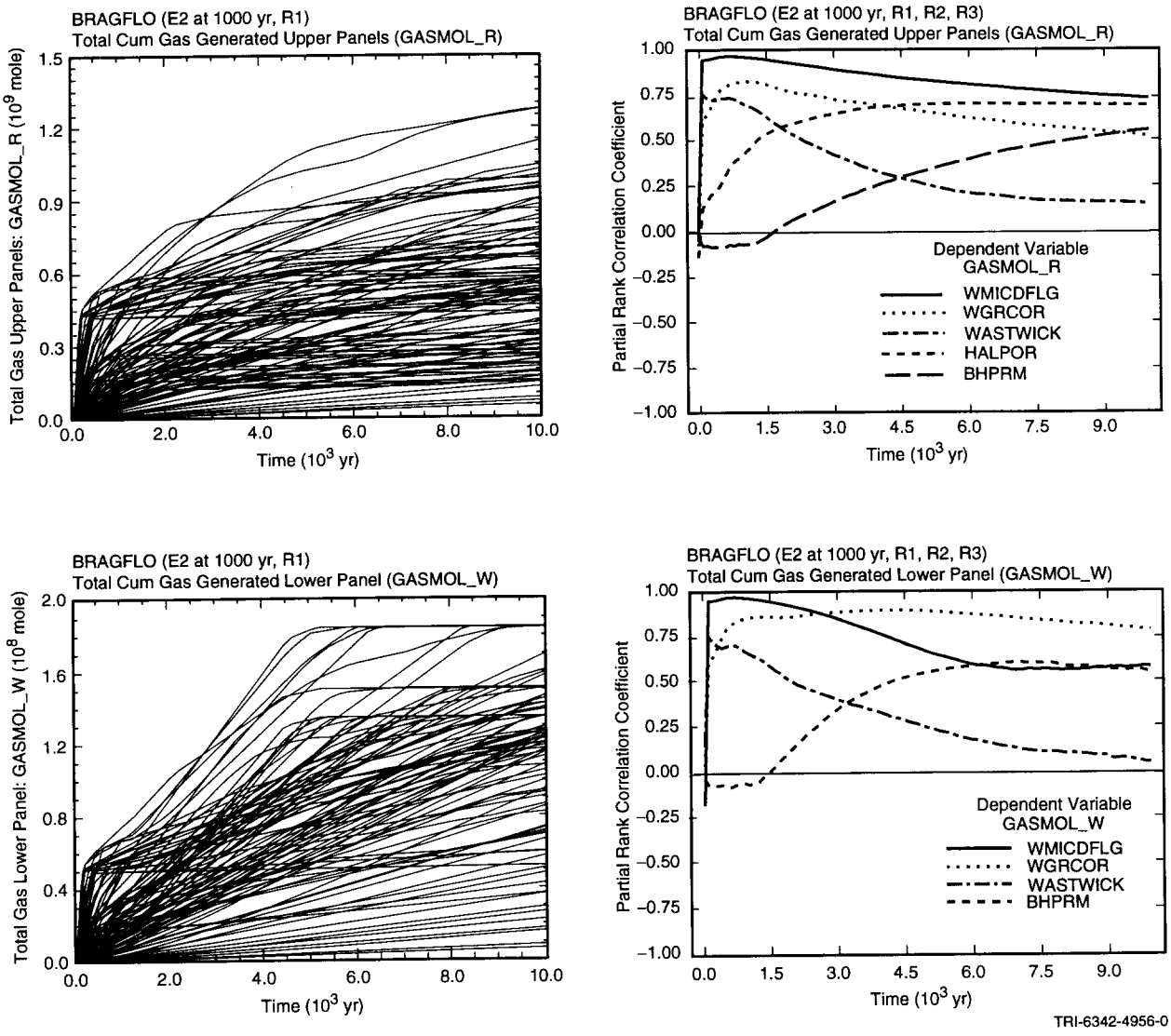

Fig. 8.3.16. Uncertainty and sensitivity analysis results for cumulative gas generation due to corrosion and microbial degradation in upper waste panels (*GSMOL_R*) (upper frames) and lower waste panel (*GASMOL_W*) (lower frames) for an E2 intrusion at 1000 yr into lower waste panel.

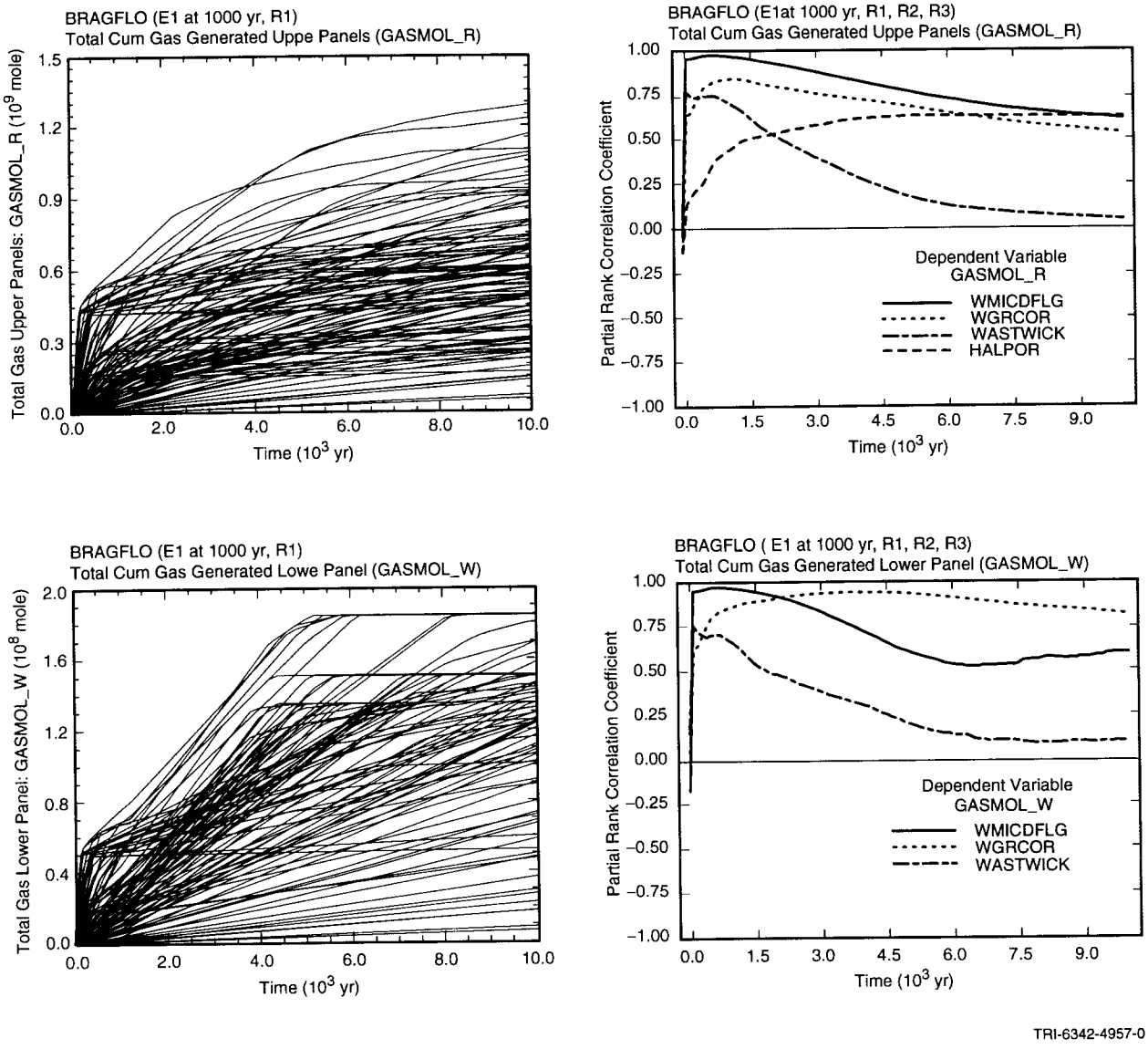

Fig. 8.3.17. Uncertainty and sensitivity analysis results for cumulative gas generation due to corrosion and microbial degradation in upper waste panels (*GASMOL_R*) (upper frames) and lower waste panel (*GASMOL_W*) (lower frames) for an E1 intrusion at 1000 yr into lower waste panel.

Table 8.3.3. Stepwise Regression Analyses with Rank-Transformed Data for Amount of Gas Generated over 10,000 yr Due to Corrosion and Microbial Degradation in Upper (*GASMOL_R*) and Lower (*GASMOL_W*) Waste Panels for E1 and E2 Intrusions at 1000 yr into Lower Waste Panel

	Upper Waste Panels E2: 0 - 1000 yr			Upper Waste Panels E2: 1000 - 10,000 yr			Upper Waste Panels E2: 0 - 10,000 yr			Upper Waste Panels E1: 1000 - 10,000 yr		
Step[a]	Variable[b]	SRRC[c]	R^{2d}	Variable	SRRC	R^2	Variable	SRRC	R^2	Variable	SRRC	R^2
1	*WMICDFLG*	0.86	0.76	*HALPOR*	0.58	0.35	*WMICDFLG*	0.54	0.30	*HALPOR*	0.51	0.27
2	*WGRCOR*	0.34	0.88	*BHPRM*	0.47	0.57	*HALPOR*	0.47	0.52	*BHPRM*	0.38	0.41
3	*WASTWICK*	0.23	0.93	*WGRCOR*	0.17	0.60	*BHPRM*	0.33	0.63	*WGRCOR*	0.23	0.47
4	*HALPOR*	0.11	0.94	*ANHPRM*	0.12	0.61	*WGRCOR*	0.30	0.72	*BPPRM*	−0.17	0.50
5	*WGRMICI*	0.04	0.94				*ANHPRM*	0.12	0.74	*WMICDFLG*	−0.18	0.53
6	*ANHBCUGP*	−0.03	0.94				*HALPRM*	0.08	0.74	*BPINTPRS*	0.12	0.54
7	*ANHPRM*	0.03	0.94				*WASTWICK*	0.07	0.75			

	Upper Waste Panels E1: 0 - 10,000 yr			Upper Waste Panels (E1: 0 - 10,000 yr) − (E2: 0 - 10,000 yr)			Lower Waste Panel E2: 0 - 1000 yr			Lower Waste Panel E2: 1000 - 10,000 yr		
Step	Variable	SRRC	R^2	Variable	SRRC	R^2	Variable	SRRC	R^2	Variable	SRRC	R^2
1	*WMICDFLG*	0.45	0.22	*BPCOMP*	0.31	0.09	*WMICDFLG*	0.84	0.73	*WGRCOR*	0.55	0.31
2	*HALPOR*	0.45	0.43	*WMICDFLG*	−0.30	0.17	*WGRCOR*	0.39	0.88	*BHPRM*	0.44	0.51
3	*WGRCOR*	0.35	0.55	*BHPRM*	−0.22	0.22	*WASTWICK*	0.21	0.93	*ANHPRM*	0.14	0.53
4	*BHPRM*	0.28	0.63	*HALPRM*	−0.17	0.25	*HALPOR*	0.09	0.93	*WASTWICK*	−0.12	0.54
5	*BPCOMP*	0.13	0.65	*WASTWICK*	−0.13	0.26	*ANHPRM*	0.07	0.94	*SHRGSSAT*	0.10	0.55
6	*BPINTPRS*	0.09	0.66	*BPINTPRS*	0.12	0.28	*WGRMICI*	0.03	0.94			

	Lower Waste Panel E2: 0 - 10,000 yr			Lower Waste Panel E1: 1000 - 10,000 yr			Lower Waste Panel E1: 0 - 10,000 yr			Lower Waste Panel (E1: 0 - 10,000 yr) − (E2: 0 - 10,000 yr)		
Step	Variable	SRRC	R^2	Variable	SRRC	R^2	Variable	SRRC	R^2	Variable	SRRC	R^2
1	*WGRCOR*	0.63	0.42	*WGRCOR*	0.58	0.34	*WGRCOR*	0.70	0.50	*BHPRM*	−0.43	0.19
2	*WMICDFLG*	0.38	0.56	*BHPRM*	0.28	0.42	*WMICDFLG*	0.39	0.66	*HALPOR*	−0.36	0.32
3	*BHPRM*	0.33	0.68	*WASTWICK*	−0.22	0.46	*BHPRM*	0.22	0.71	*ANHPRM*	−0.30	0.42
4	*ANHPRM*	0.15	0.70	*SHRGSSAT*	0.11	0.47	*ANHBCVGP*	−0.08	0.71	*BPINTPRS*	0.13	0.44
5	*HALPOR*	0.13	0.72				*BPPRM*	−0.07	0.72	*HALPRM*	−0.12	0.45
6	*SHRGSSAT*	0.08	0.72				*SHRGSSAT*	0.07	0.72	*WMICDFLG*	−0.11	0.46
										ANRGSSAT	0.10	0.47

[a] Steps in stepwise regression analysis.

[b] Variables listed in order of selection in regression analysis with *ANHCOMP* and *HALCOMP* excluded from entry into regression model.

[c] Standardized rank regression coefficients in final regression model.

[d] Cumulative R^2 value with entry of each variable into regression model.

8.4 Disturbed Conditions: Pressure for E1 and E2 Intrusions

Pressure in the repository under undisturbed conditions tends to increase monotonically towards an asymptote for each sample element (Fig. 7.4.1), with the value of this asymptote determined primarily by the amount of gas generated by corrosion and microbial degradation (Fig. 7.4.3). A very different pattern is exhibited under disturbed conditions, with pressure tending to decrease rapidly after a drilling intrusion (Fig. 8.4.1). The results in Fig. 8.4.1 are for pressure in the lower waste panel; the pressure histories for the upper waste panels are very similar (Fig. 8.4.2).

Due to the assumption of a borehole plug with a life expectancy of 200 yr at the Rustler/Salado interface (Table 4.2.8), the E2 intrusion at 1000 yr has no effect on repository pressure until 1200 yr. In contrast, the E1 intrusion is modeled with an open borehole (i.e., with a permeability of 10^{-9} m^2) between the plug and the brine pocket during this 200 yr period, with the result that the potential for flow between the brine pocket and the repository exists. The effects of this flow can be seen in the rapidly changing pressures between 1000 and 1200 yr for some sample elements for the E1 intrusion (Fig. 8.4.3). However, the highest repository pressures show little change from 1000 to 1200 yr because these pressures are sufficiently high to prevent brine flow from the brine pocket to the repository (Fig. 8.2.8). These high repository pressures tend to be associated with large values for *WMICDFLG* (Fig. 8.4.4). Sample elements with low pressures at 1000 yr often undergo a sudden increase in pressure immediately after the drilling intrusion, with this pressure then decreasing over the next 200 yr (Fig. 8.4.3) due to brine and gas flow through the DRZ and the panel closures to the remainder of the repository. The effect of the DRZ and panel closures in spreading out the pressure pulse due to penetration of a brine pocket can be seen in the slow monotonic increase in pressure in the rest of the repository in contrast with the sharp increase in pressure in the waste panel associated with the intrusion into the brine pocket (Fig. 8.4.3). Repository pressure undergoes a rapid decrease after failure of the plug at the Rustler/Salado interface at 1200 yr due to gas outflow (Fig. 8.4.1).

The PRCCs in Fig. 8.4.1 prior to 1000 yr are the same as those in Fig. 7.4.1 for undisturbed conditions. At 1000 yr, pressure in the repository is dominated by *WMICDFLG* and other variables (i.e., *WGRCOR*, *WASTWICK*, *HALPOR*, *ANHPRM*, *WGRMICI*) that influence gas generation under undisturbed conditions (Figs. 8.4.1, 8.4.4, Table 8.4.1). Immediately after 1200 yr, *BHPRM* shows a negative effect on pressure because gas flow up the borehole increases with increasing values for *BHPRM*. However, the PRCCs in Fig. 8.4.1 and regression analyses in Table 8.4.1 are not very successful in identifying the variables dominating the uncertainty in pressure after 1200 yr (e.g., the two regressions in Table 8.4.1 for pressure at 10,000 yr have R^2 values of only 0.20 and 0.25).

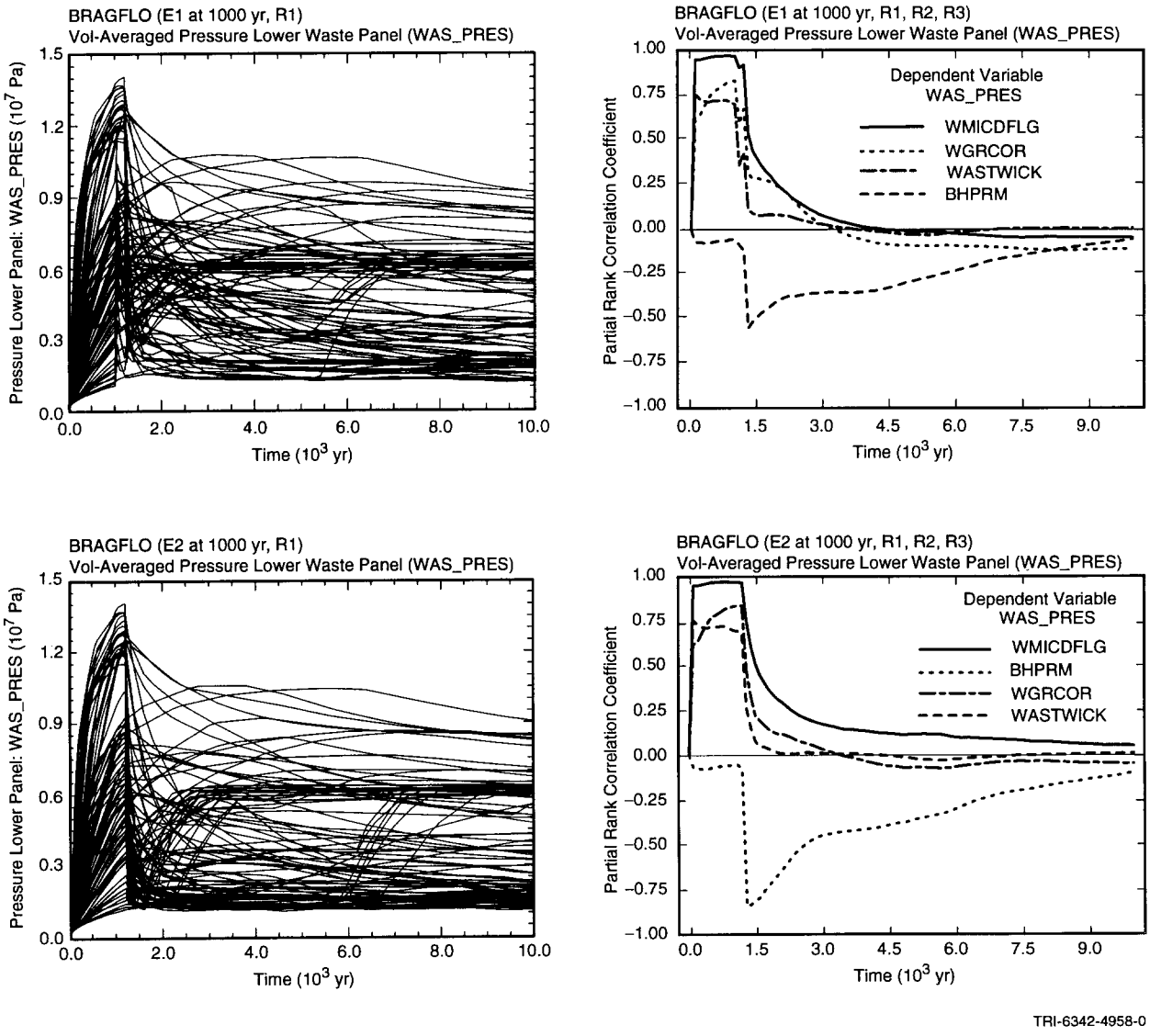

Fig. 8.4.1. Uncertainty and sensitivity analysis results for repository pressure (*WAS_PRES*) for E1 and E2 intrusions into lower waste panel at 1000 yr.

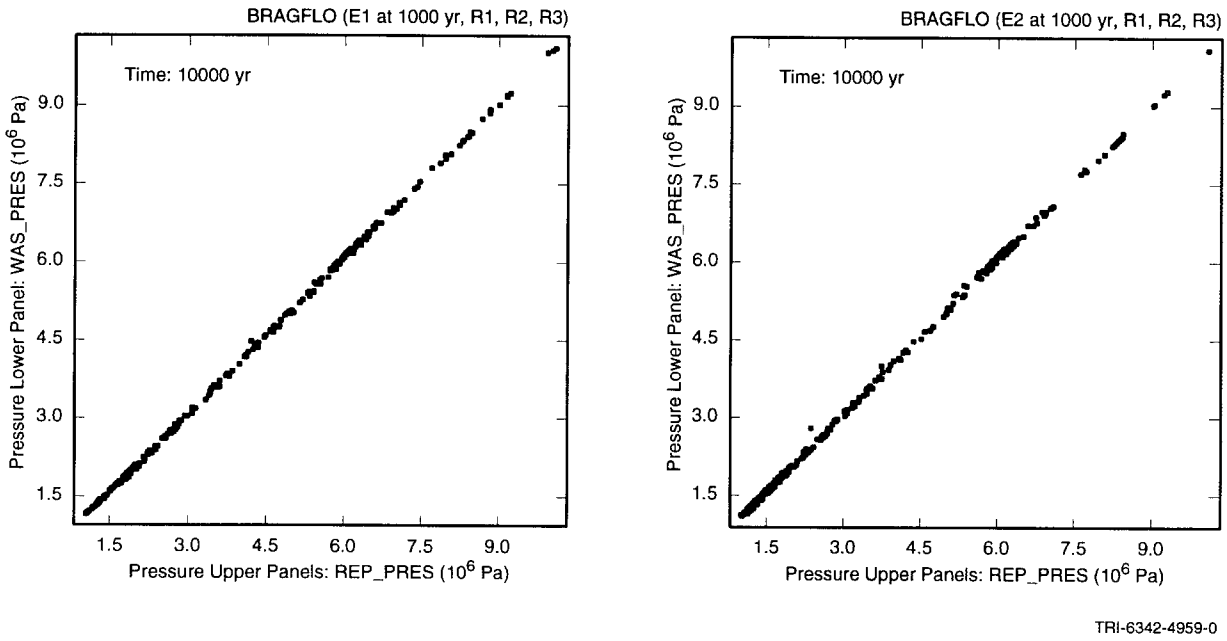

Fig. 8.4.2. Scatterplots for repository pressure in upper (*REP_PRES*) and lower (*WAS_PRES*) waste panels at 10,000 yr for E1 and E2 intrusions into lower waste panel at 1000 yr.

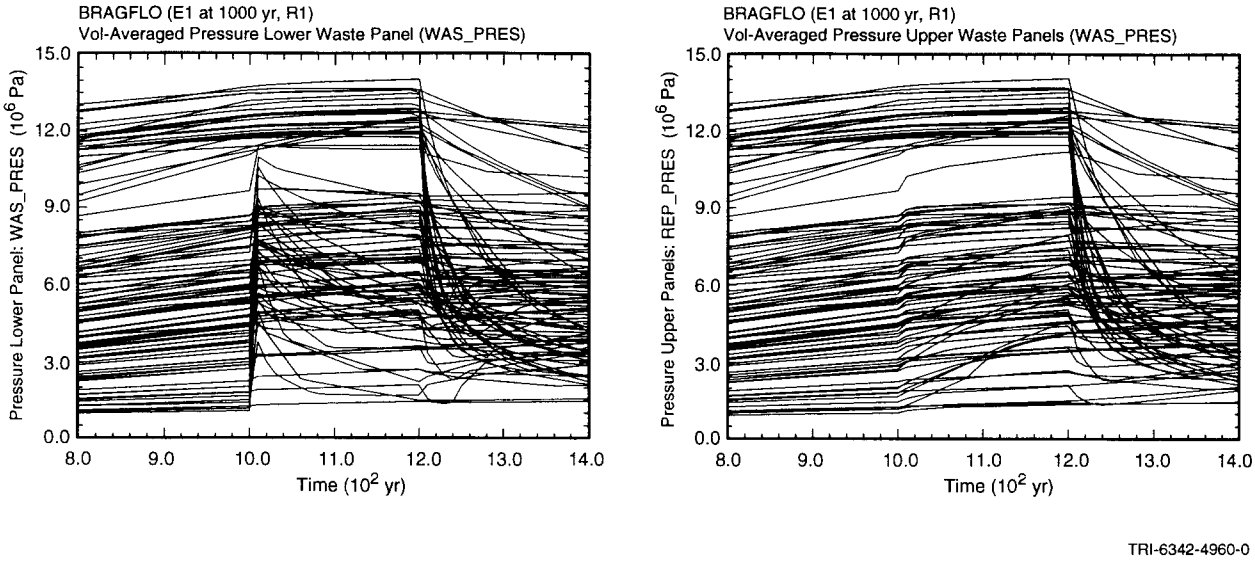

Fig. 8.4.3. Pressure in waste panel (*WAS_PRES*) penetrated by an E1 intrusion at 1000 yr (i.e., the lower waste panel) and in rest of repository (*REP_PRES*) (i.e., the upper waste panels).

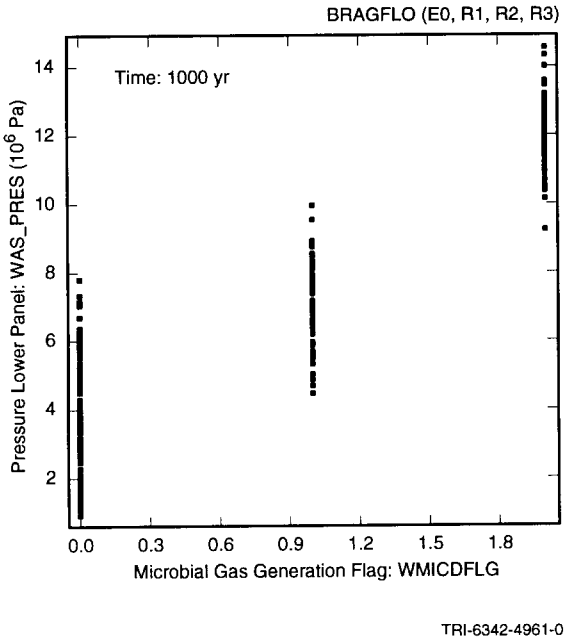

Fig. 8.4.4. Scatterplot for repository pressure (*WAS_PRES*) at 1000 yr under undisturbed conditions versus *WMICDFLG*.

Table 8.4.1. Stepwise Regression Analyses with Rank-Transformed Data for Pressure in Lower Waste Panel (*WAS_PRES*) for E1 and E2 Intrusions into Lower Waste Panel at 1000 yr

	E2: 1000 yr			E2: 10,000 yr			E1: 10,000 yr		
Step[a]	Variable[b]	SRRC[c]	R^{2d}	Variable	SRRC	R^2	Variable	SRRC	R^2
1	*WMICDFLG*	0.87	0.78	*HALPRM*	0.36	0.13	*HALPRM*	0.36	0.12
2	*WGRCOR*	0.33	0.89	*ANHPRM*	0.24	0.19	*BPCOMP*	0.22	0.17
3	*WASTWICK*	0.21	0.94	*HALPOR*	0.14	0.20	*ANHPRM*	0.18	0.20
4	*HALPOR*	0.08	0.94				*BPVOL*	0.17	0.23
5	*ANHPRM*	0.05	0.95				*HALPOR*	0.15	0.25
6	*WGRMICI*	0.04	0.95						

[a] Steps in stepwise regression analysis.

[b] Variables listed in order of selection in regression analysis with *ANHCOMP* and *HALCOMP* excluded from entry into regression model.

[c] Standardized rank regression coefficients in final regression model.

[d] Cumulative R^2 value with entry of each variable into regression model.

The poor performance of the sensitivity measures after 1200 yr is due to patterns that cannot be identified by the regression-based procedures in use. In particular, repository pressure is dominated by *BHPRM* after 1200 yr (Fig. 8.4.5). Pressure tends to decrease as *BHPRM* increases until a value of approximately $10^{-11.6}$ m^2 (2.5×10^{-12} m^2) is reached; at this point, pressure jumps to approximately 6×10^6 Pa, which is hydrostatic pressure at repository depth. The patterns in Fig. 8.4.5 result from an interplay of gas and brine flow in the borehole. At low permeabilities, little gas can flow out the borehole and so pressures remain high. As *BHPRM* increases, more gas can flow out the borehole and so pressure decreases. In particular, pressure stays relatively low (i.e., ~ 1.5 to 3.0×10^6 Pa) at intermediate values for *BHPRM* because a continuous brine column is not established between the repository and overlying formations. As *BHPRM* increases, more brine flows down the borehole and the repository fills with brine at higher values of *BHPRM*. When this occurs, a continuous brine column is established between the repository and overlying formation, with the result that repository pressure then jumps to hydrostatic pressure.

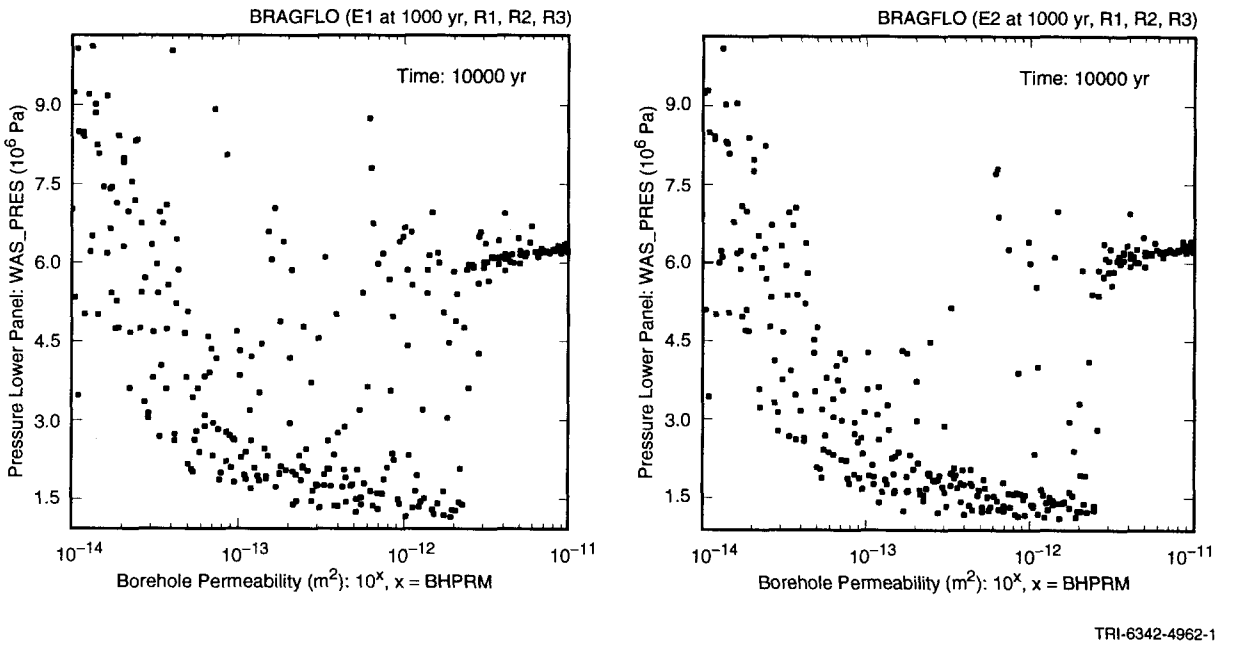

Fig. 8.4.5. Scatterplots for repository pressure (*WAS_PRES*) at 10,000 yr versus *BHPRM* for E1 and E2 intrusions at 1000 yr into lower waste panel.

Total pore volume in the repository is shown in Fig. 8.4.6. Pore volume tracks pressure very closely (Fig. 7.4.5). As a result, pore volume is influenced by the same variables as repository pressure, with *BHPRM* being the dominant variable (Fig. 8.4.5). Due to the lower pressures, pore volume under disturbed conditions is lower than pore volume under undisturbed conditions (Figs. 7.4.4, 8.4.6).

As an example, the interplay between gas generation, repository pressure and repository volume for E1 and E2 intrusions at 1000 yr and sample elements 14 and 40 of replicate R1 are shown in Fig. 8.4.7. For both sample elements and both intrusion modes, pressures in the lower (*WAS_PRES*) and upper (*REP_PRES*) waste panels are indistinguishable at the level of resolution used in the plots. Further, pressure increases monotonically until the borehole plugs fail 200 yr after the drilling intrusion (i.e., at 1200 yr) and then undergoes a decrease. The exact pattern of this decrease depends on whether an E1 or E2 intrusion is under consideration and also on particular parameter values (e.g., *BHPRM*) used in the individual calculations. After a period of rapid decrease at the beginning of the calculation due to compaction of the repository, repository volume (*PORVOL_T*) tends to track repository pressure closely. In particular, pore volume decreases as the pressure decreases after the borehole plugs fail at 1200 yr. Gas generation due to microbial degradation of cellulose (*CELL_MOL*) ceases after a few 100 yr due to exhaustion of the cellulose inventory. In contrast, gas generation due to corrosion (*FE_MOLE*) continues over the entire 10,000 yr period, with gas generation for the E1 intrusions tending to exceed gas generation for the E2 intrusions due to the greater availability of brine.

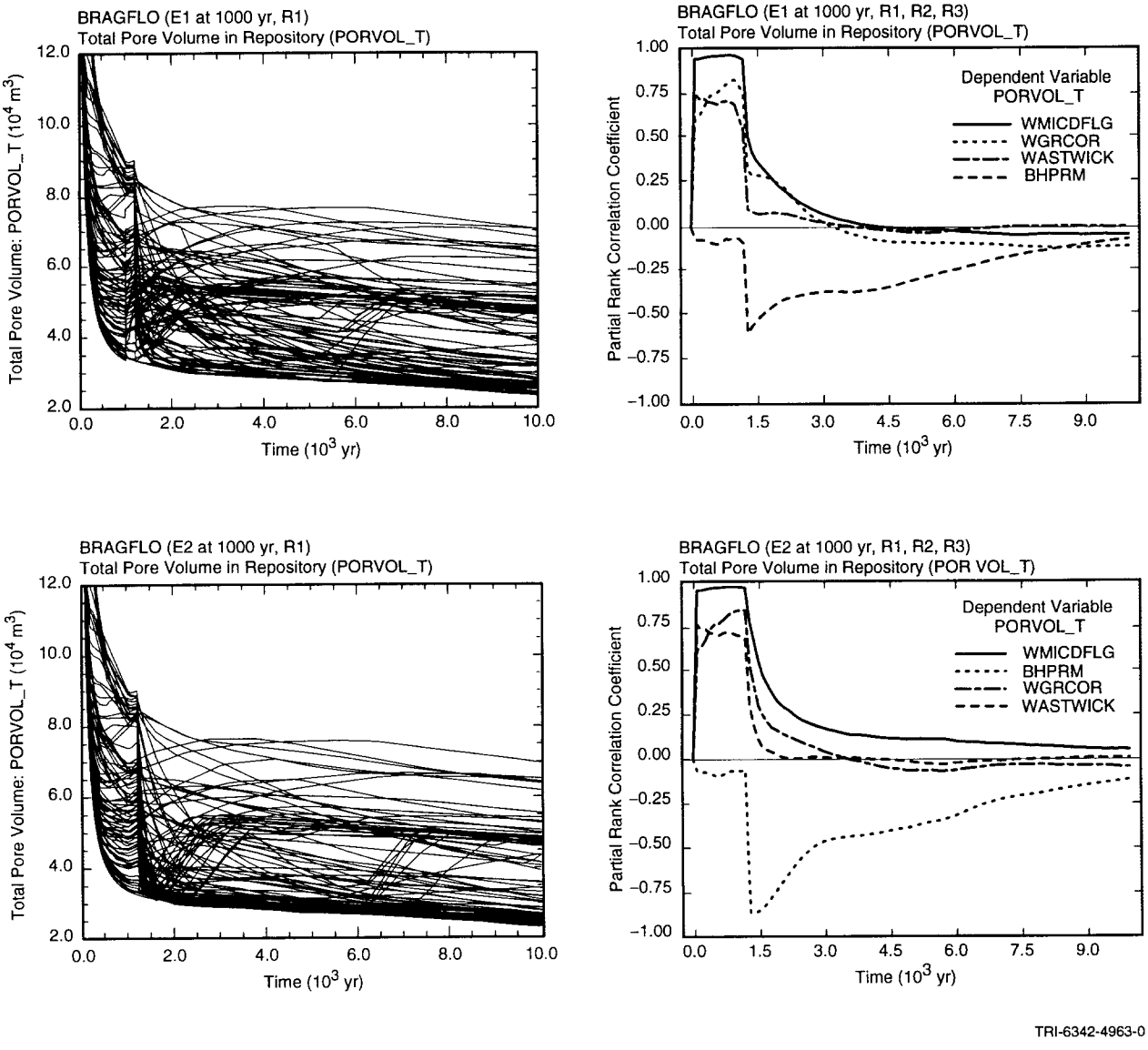

Fig. 8.4.6. Uncertainty and sensitivity analysis results for total pore volume in repository (*PORVOL_T*) for E1 and E2 intrusions into lower waste panel at 1000 yr.

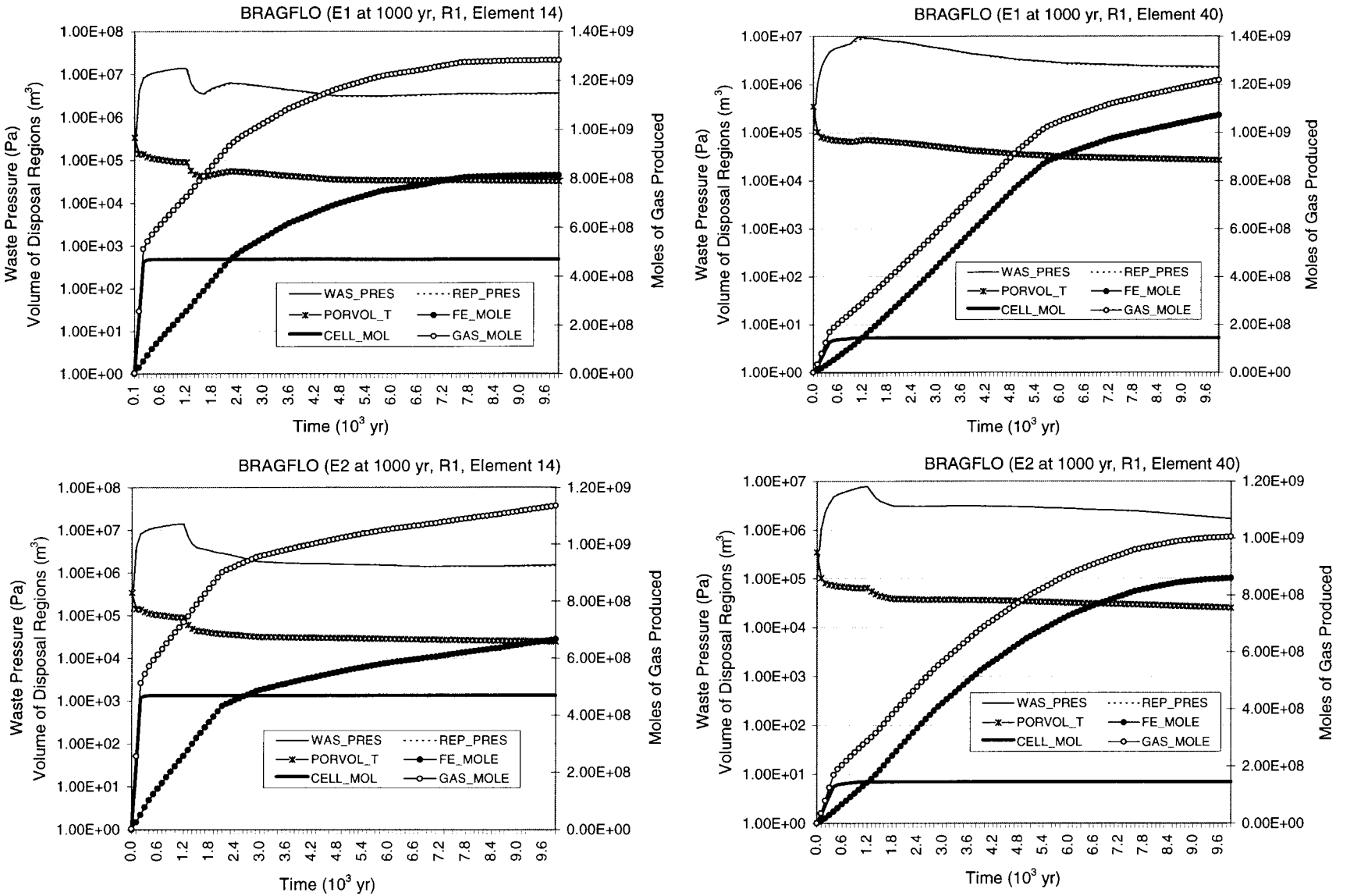

Fig. 8.4.7. Pressure (*WAS_PRES*, *REP_PRES*), pore volume (*PORVOL_T*), and gas generation (*FE_MOLE*, *CELL_MOL*, *GAS_MOLE*) for repository under disturbed conditions (i.e., E1 and E2 intrusions into the lower waste panel at 1000 yr) for sample elements 14 and 40 of replicate R1.

8.5 Disturbed Conditions: Saturation for E1 and E2 Intrusions

The occurrence of a drilling intrusion can have a significant effect on the brine saturation in both the upper and lower waste panels (Figs. 8.5.1, 8.5.2). In particular, the tendency is to increase the saturation due to (1) increased flow from the marker beds (Fig. 8.2.2), (2) flow down the borehole from overlying formations (Fig. 8.2.6), and (3) flow up from the brine pocket in the event of an E1 intrusion (Fig. 8.2.7). Although saturation tends to increase throughout the repository, the effect is particularly pronounced in the intruded panel (Figs. 8.5.1, 8.5.2), which is the lower waste panel in the calculations reported in this section. As indicated by the horizontal brine saturation curves in Figs. 8.5.1 and 8.5.2, the intruded panel often becomes fully brine saturated subject to the limitations imposed by the residual gas saturation (*WGRSSAT*). Due to the brine flow from the brine pocket, the intruded panel is more likely to become fully brine saturated for an E1 intrusion than for an E2 intrusion.

As indicated by the PRCCs in Fig. 8.5.1, the uncertainty in the brine saturation in the unintruded (i.e., upper) waste panels after an E2 intrusion is determined by *HALPOR*, *BHPRM*, *WGRCOR* and *WASTWICK*, with saturation tending to increase as *HALPOR* and *BHPRM* increase and tending to decrease as *WGRCOR* and *WASTWICK* increase. The positive effects for *HALPOR* and *BHPRM* result because increasing each of these variables allows more brine to enter the waste panels. The negative effects for *WGRCOR* and *WASTWICK* result because increasing each of these variables increases the rate at which brine is consumed by corrosion, which in turn has two effects on saturation. First, the direct loss of brine reduces saturation. Second, the generation of gas by corrosion increases repository pressure, which in turn tends to increase repository porosity due to pore space expansion and thus reduce brine saturation. Together, these two effects result in a reduced amount of brine occupying an increased pore volume. Pore space expansion due to increased pressure is also why *WMICDFLG* appears as an important variable prior to the intrusion and then drops to having no effect as the gas generation by microbial degradation is vented after the drilling intrusion. As a reminder, most microbial gas generation ends by 1000 yr (Figs. 7.3.1, 7.3.2).

As an alternative analysis for brine saturation in the upper waste panels after an E2 intrusion, regression results for saturation at 10,000 yr are presented in Table 8.5.1. As in the PRCC analysis (Fig. 8.5.1), positive effects are indicated for *BHPRM* and *HALPOR* and negative effects are indicated for *WGRCOR* and *WASTWICK*. In addition, small positive effects are indicated for *ANHPRM* and *HALPRM* because increasing each of these variables tends to increase brine flow out of the anhydrite marker beds (Tables 8.2.1, 8.2.2). Small values for *BHPRM* and *HALPOR* often result in a complete consumption of the brine in the upper waste panels (i.e., a brine saturation of zero); a similar pattern also occurs for large values of *WGRCOR* (Fig. 8.5.3). A similar but less pronounced pattern also occurs for *ANHPRM*, with smaller values tending to be associated with zero brine saturations. A small negative effect is indicated for *SHRGSSAT* (Table 8.5.1), probably due to its role in affecting gas and brine flow across the part of the computational grid in the repository and DRZ that corresponds to the shaft.

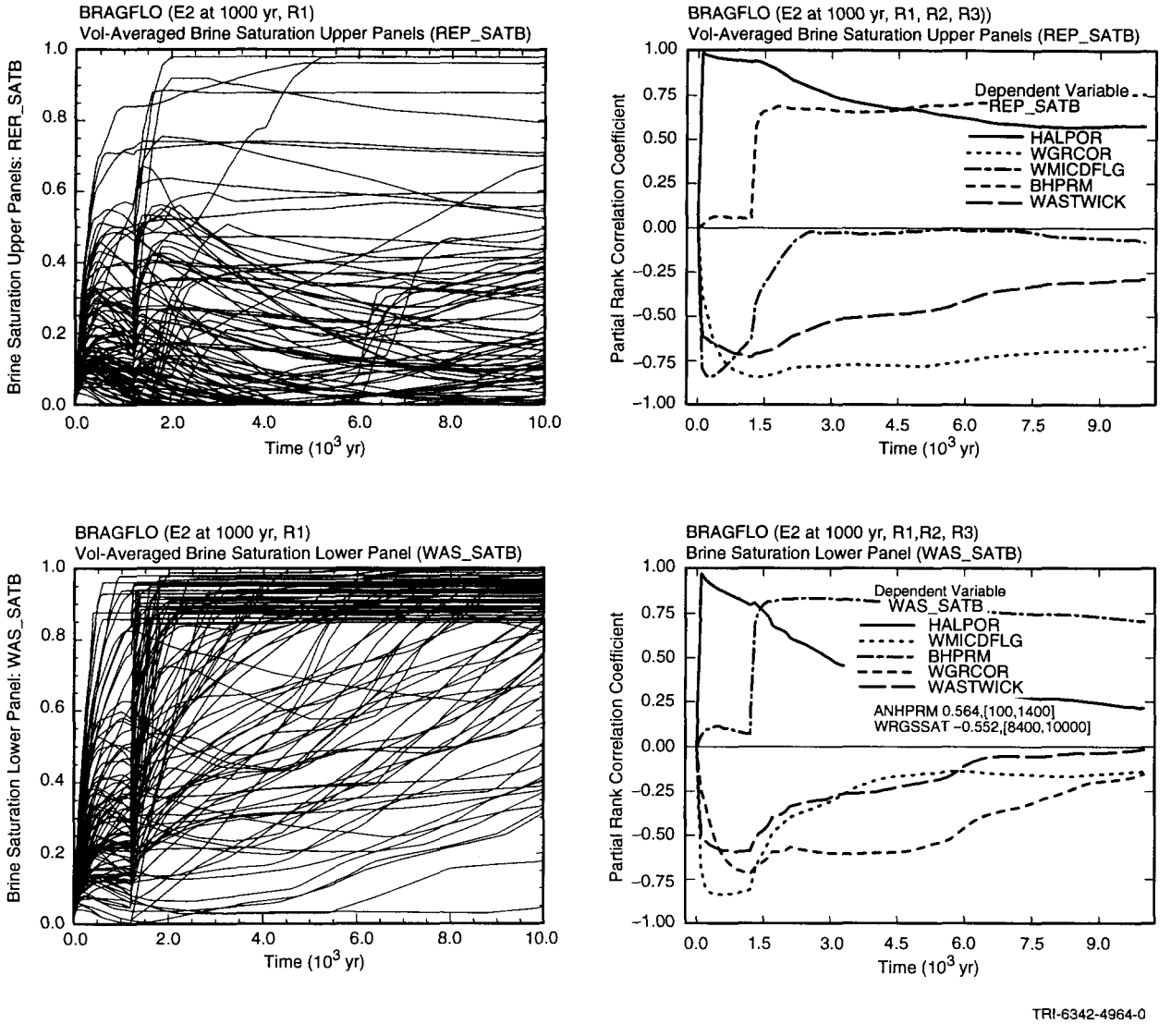

Fig. 8.5.1. Uncertainty and sensitivity analysis results for brine saturation in upper (*REP_SATB*) and lower (*WAS_SATB*) waste panels for an E2 intrusion at 1000 yr into lower waste panel (Note: Plots for PRCCs show all variables that have a PRCC that exceeds 0.5 in absolute value at some point in time, with the PRCCs for the variables with the five largest, in absolute value, PRCCs being plotted and the maximum, in absolute value, PRCCs being shown for the remaining variables together with the intervals over which the PRCCs exceed 0.5 in absolute value; e.g., the maximum of the absolute value of the PRCC between *WAS_SATB* and *WRGSSAT* for the E2 intrusion is 0.552 and this PRCC exceeds 0.5 in absolute value over the time interval [8400, 10,000 yr].)

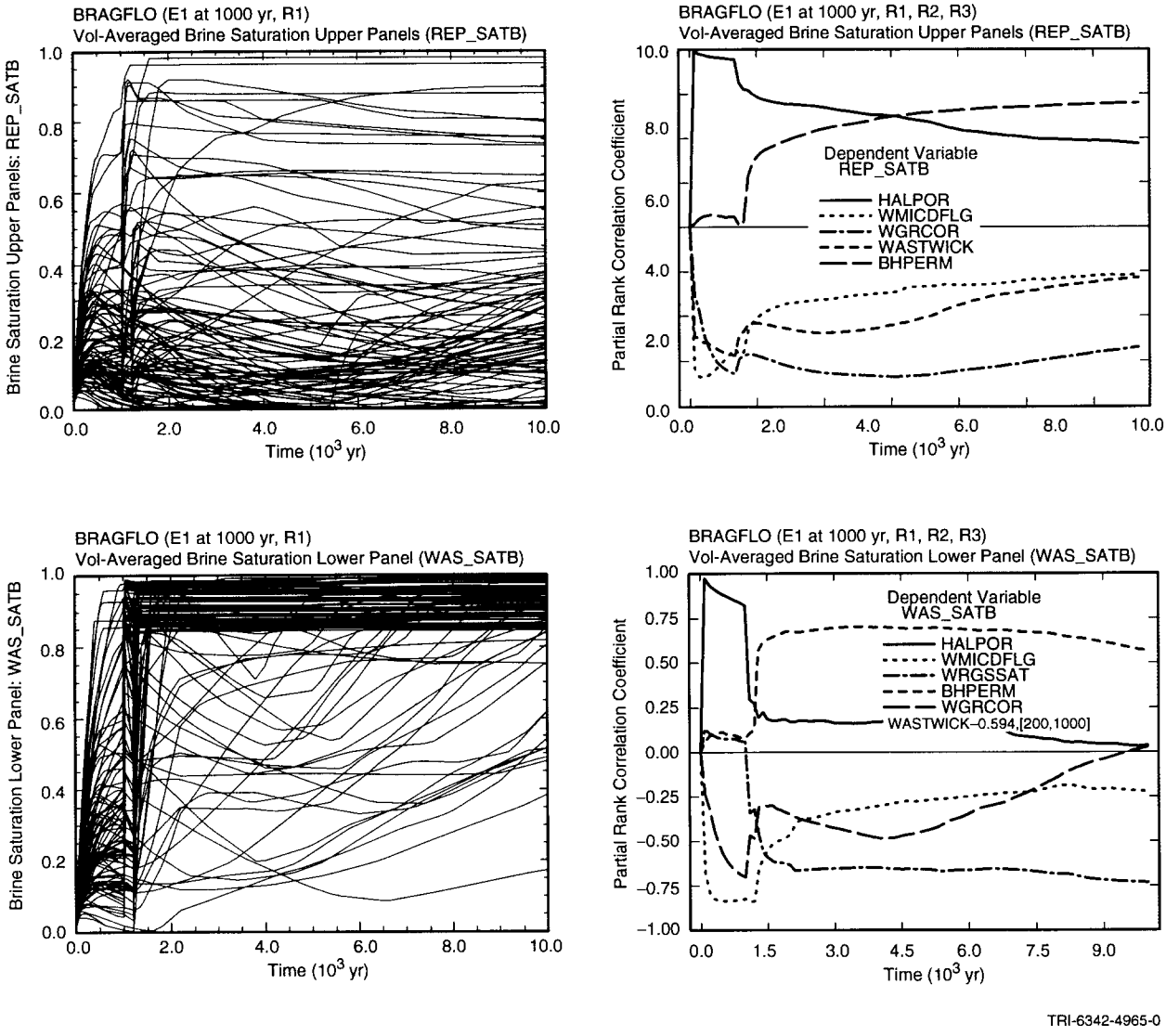

Fig. 8.5.2. Uncertainty and sensitivity analysis results for brine saturation in upper (*REP_SATB*) and lower (*WAS_SATB*) waste panels for an E1 intrusion at 1000 yr into lower waste panel (See Note, Fig. 8.5.1).

Table 8.5.1. Stepwise Regression Analyses with Rank-Transformed Data for Brine Saturations in Upper (*REP_SATB*) and Lower (*WAS_SATB*) Waste Panels at 10,000 yr for E1 and E2 Intrusions at 1000 yr into Lower Waste Panel

	E2: Upper Waste Panel			E2: Lower Waste Panel			E1: Upper Waste Panel			E1: Lower Waste Panel		
Step[a]	Variable[b]	SRRC[c]	R^{2d}	Variable	SRRC	R^2	Variable	SRRC	R^2	Variable	SRRC	R^2
1	*BHPRM*	0.58	0.34	*BHPRM*	0.59	0.36	*BHPRM*	0.52	0.26	*WRGSSAT*	−0.64	0.42
2	*WGRCOR*	−0.44	0.52	*WRGSSAT*	−0.40	0.52	*WGRCOR*	−0.48	0.48	*BHPRM*	0.41	0.58
3	*HALPOR*	0.35	0.64	*ANHPRM*	0.23	0.57	*HALPOR*	0.28	0.56	*BPCOMP*	0.14	0.60
4	*ANHPRM*	0.20	0.68	*HALPOR*	0.13	0.59	*BPCOMP*	0.26	0.62	*WMICDFLG*	−0.12	0.62
5	*WASTWICK*	−0.15	0.70	*SHPRMHAL*	−0.12	0.60	*WASTWICK*	−0.16	0.65	*ANHPRM*	0.11	0.63
6	*HALPRM*	0.14	0.72	*WGRCOR*	−0.10	0.61	*WMICDFLG*	−0.15	0.67			
7	*SHRGSSAT*	−0.08	0.73				*BPVOL*	0.11	0.68			
8							*ANHPRM*	0.11	0.69			
9							*SHRGSSAT*	−0.10	0.70			

[a] Steps in stepwise regression analysis.

[b] Variables listed in order of selection in regression analysis with *ANHCOMP* and *HALCOMP* excluded from entry into regression model.

[c] Standardized rank regression coefficients in final regression model.

[d] Cumulative R^2 value with entry of each variable into regression model.

For brine saturation in the lower (i.e., intruded) waste panel after an E2 intrusion at 1000 yr, the PRCCs in Fig. 8.5.1 indicate positive effects for *BHPRM* and *HALPOR*, negative effects for *WGRCOR* and *WRGSSAT*, and negative, rapidly decreasing effects for *WMICDFLG* and *WASTWICK*. The corresponding regression analysis for brine saturation at 10,000 yr indicates positive effects for *BHPRM*, *ANHPRM* and *HALPOR*, and negative effects for *WRGSSAT*, *SHPRMHAL* and *WGRCOR* (Table 8.5.1). However, the final regression model has an R^2 of only 0.61. Given the structure of the individual curves in Fig. 8.5.1, it is useful to examine an appropriate set of scatterplots to determine what is giving rise to the patterns in Fig. 8.5.1 and how these patterns may be affecting the PRCC and stepwise regression analyses (Fig. 8.5.4).

As the scatterplots in Fig. 8.5.4 show, saturation tends to increase as each of *BHPRM*, *ANHPRM* and *HALPOR* increases. These effects result because increasing each of these variables increases brine inflow to the intruded panel. Of these three variables, *BHPRM* has the largest effect because of its role in both reducing pressure in the repository, which increases brine flow out of the marker beds, and allowing brine flow down the intruding borehole. However, due to the large amount of brine inflow, the panel tends to completely fill with brine, with the result that the primary determinant of brine saturation is the residual gas saturation *WRGSSAT*. The dominant role played by *WRGSSAT* in determining brine saturation can be seen in the straight line of points in the corresponding scatterplot in Fig. 8.5.4.

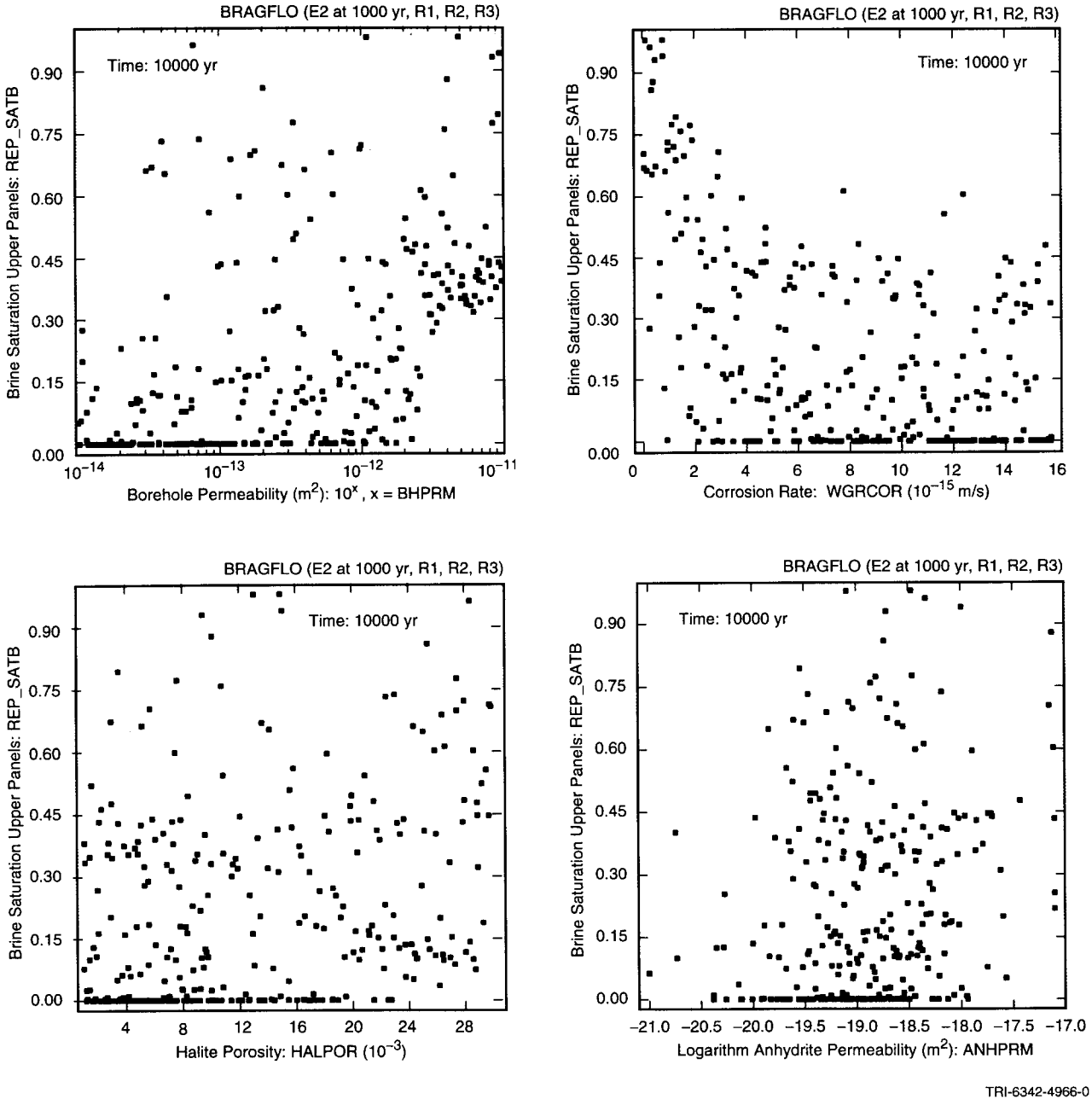

Fig. 8.5.3. Scatterplots for brine saturation in upper waste panels (*REP_SATB*) at 10,000 yr for an E2 intrusion at 1000 yr into lower waste panel versus *BHPRM*, *WGRCOR*, *HALPOR* and *ANHPRM*.

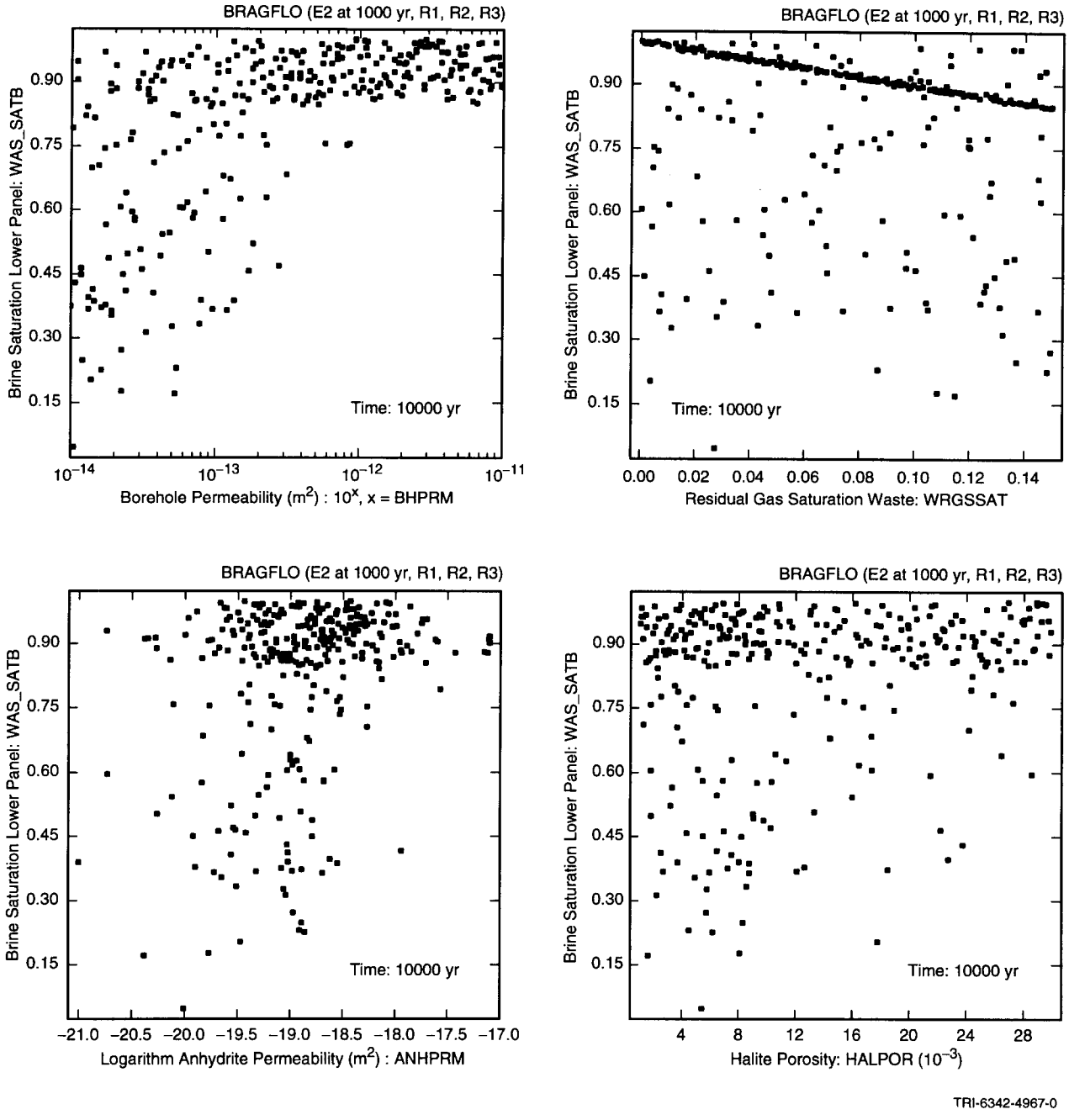

Fig. 8.5.4. Scatterplots for brine saturation in lower waste panel (*WAS_SATB*) at 10,000 yr for an E2 intrusion at 1000 yr into lower waste panel versus *BHPRM*, *WRGSSAT*, *ANHPRM* and *HALPOR*.

The uncertainty and sensitivity analysis results for brine saturation subsequent to an E1 intrusion are similar to the corresponding results for an E2 intrusion (Figs. 8.5.1, 8.5.2, Table 8.5.1). Overall, the brine saturations tend to be somewhat higher for the E1 intrusion due to the additional brine inflow from the brine pocket. The role of the brine pocket for E1 intrusions can be seen in the regressions in Table 8.5.1 in the appearance of *BPCOMP* and *BPVOL* with positive regression coefficients and the appearance of *WMICDFLG* with a negative regression coefficient. As indicated by the small changes in R^2 values with the entry of these variables into the regression models, they are not having large effects on saturation, which is consistent with the similarity of the results for E2 and E1 intrusions in Figs. 8.5.1 and 8.5.2.

A result closely related to brine saturation is the volume of brine contained in the repository (Figs. 8.5.5, 8.5.6). As indicated by the PRCCs in Fig. 8.5.5, brine volume in the upper (i.e., unintruded) waste panels subsequent to an E2 intrusion tends to increase as *BHPRM* and *HALPOR* increase and tends to decrease as *WGRCOR* and *WASTWICK* increase. Increasing each of *HALPOR* and *BHPRM* tends to increase the amount of brine entering the upper waste panels, and increasing each of *WGRCOR* and *WASTWICK* tends to increase the amount of brine being consumed by corrosion. These effects are consistent with the regression results and scatterplots for brine volume in the upper waste panels subsequent to an E2 intrusion (Table 8.5.2, Fig. 8.5.7). In addition to *BHPRM*, *HALPOR*, *WGRCOR* and *WASTWICK*, the regression analysis for brine volume at 10,000 yr also indicates small positive effects for *ANHPRM* and *HALPRM* and a small negative effect for *WRBRNSAT*. The positive effects for *ANHPRM* and *HALPRM* result from their role in influencing the amount of brine that flows from the marker beds to the repository (Table 8.2.2). The negative effect for *WRBRNSAT* probably results from its role in influencing brine flow patterns within the repository. The effects indicated for *BHPRM*, *WGRCOR* and *HALPOR* on brine saturation in the upper waste panels are consistent with the corresponding scatterplots in Fig. 8.5.7. The scatterplot for *BHPRM* shows a well-defined pattern, with a sudden jump in brine volume at $10^x \doteq 10^{-11.6}$ m^2, x = *BHPRM*. As discussed in Sect. 8.4, this jump corresponds to the lower waste panel becoming fully brine saturated.

For the lower (i.e., intruded) waste panel after an E2 intrusion at 1000 yr, PRCCs indicate small positive effects for *BHPRM*, *ANHPRM* and *HALPOR* and a small negative effect for *WGRCOR* (Fig. 8.5.5). However, the PRCCs tend to be small (e.g., all PRCCs are less than 0.5 in absolute value by 10,000 yr). The corresponding regression model in Table 8.5.2 has an R^2 value of only 0.44 and thus is also not very successful in accounting for the uncertainty in brine volume. As examination of Fig. 8.5.7 shows, the poor performance of regression-based results derives from a complex pattern of behavior involving *BHPRM*. In particular, three distinct regimes of behavior can be seen. Above $10^x \doteq 10^{-11.6}$ m^2, x = *BHPRM*, brine volumes are clustered around 5×10^3 m^3; as discussed in Sect. 8.4 and illustrated in Fig. 8.4.5, these volumes are associated with the repository being at hydrostatic pressure. Between $10^x \doteq 10^{-12.6}$ m^2 and $10^x \doteq 10^{-11.6}$ m^2, x = *BHPRM*, volumes are clustered around 2.4×10^3 m^3; as shown in Fig. 8.4.5, these volumes are associated with low pressures in the repository. Below $10^x \doteq 10^{-12.6}$ m^2,

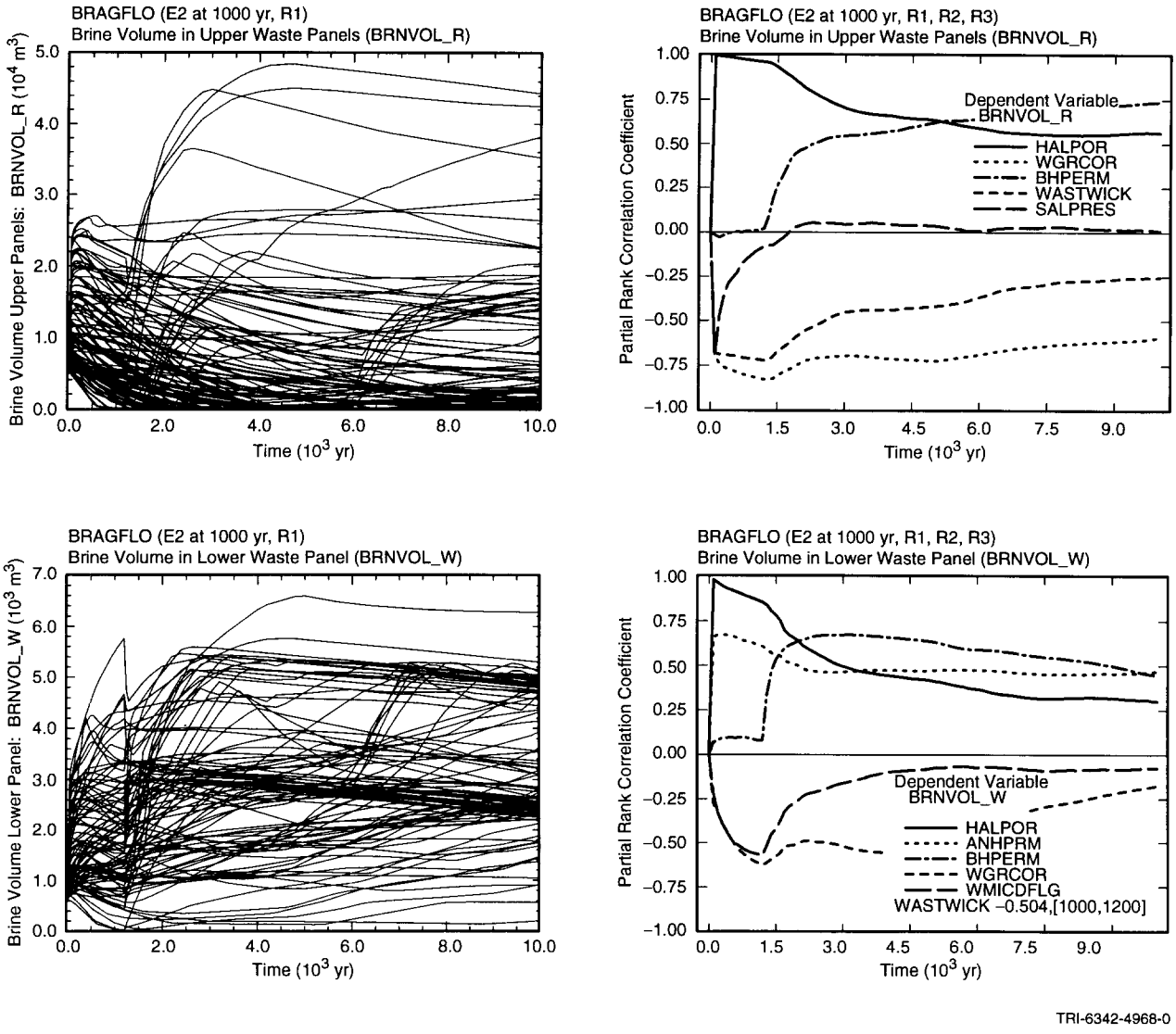

Fig. 8.5.5. Uncertainty and sensitivity analysis results for brine volume in upper (*BRNVOL_R*) and lower (*BRNVOL_W*) waste panels for an E2 intrusion at 1000 yr into lower waste panel (See Note, Fig. 8.5.1).

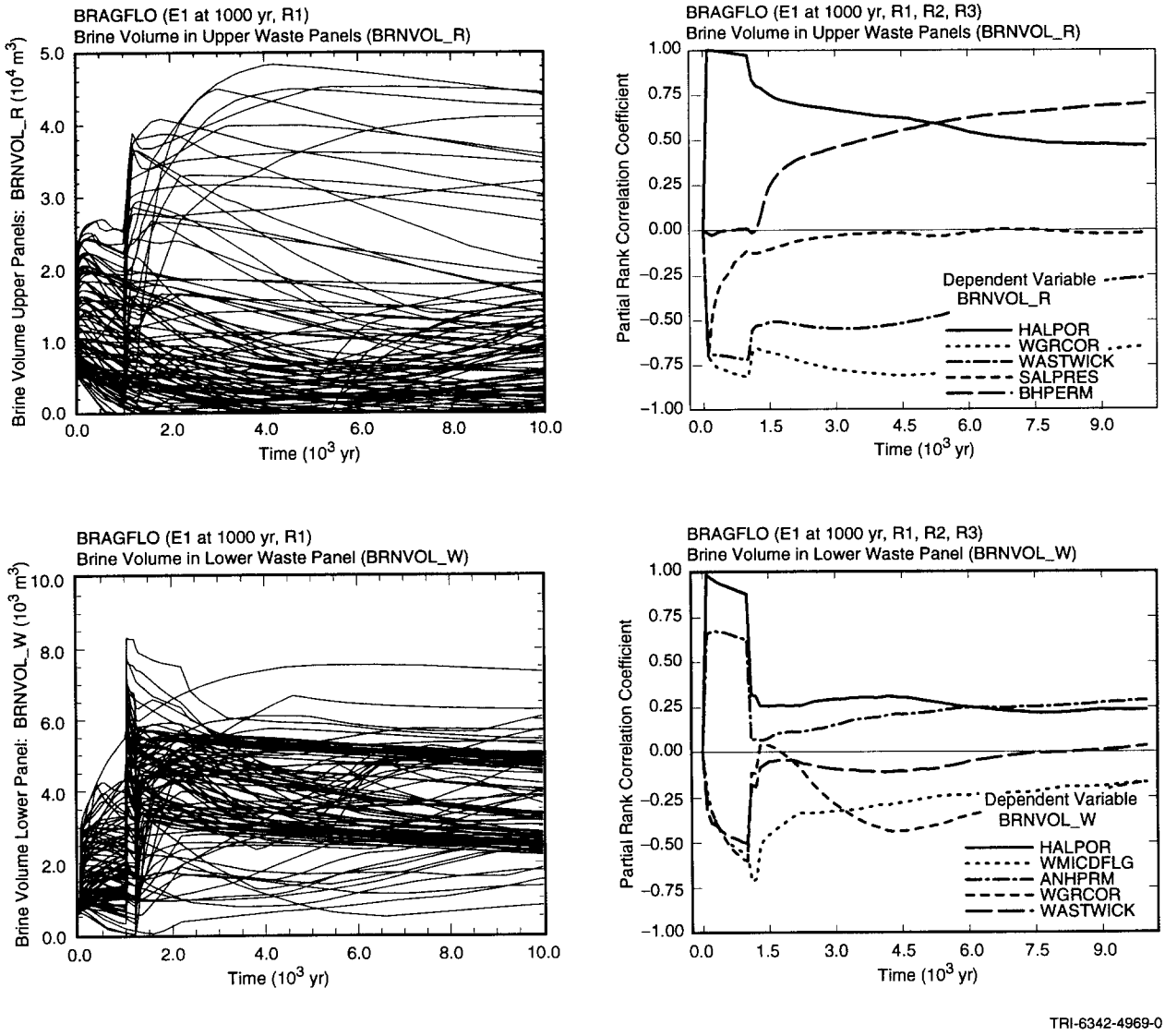

Fig. 8.5.6. Uncertainty and sensitivity analysis results for brine volume in upper (*BRNVOL_R*) and lower (*BRNVOL_W*) waste panels for an E1 intrusion at 1000 yr into lower waste panel.

Table 8.5.2. Stepwise Regression Analyses with Rank-Transformed Data for Brine Volumes in Upper (*BRNVOL_R*) and Lower (*BRNVOL_W*) Waste Panels at 10,000 yr for E1 and E2 Intrusions at 1000 yr into Lower Waste Panel

	E2: Upper Waste Panel			E2: Lower Waste Panel			E1: Upper Waste Panel			E1: Lower Waste Panel		
Step[a]	Variable[b]	SRRC[c]	R^{2d}	Variable	SRRC	R^2	Variable	SRRC	R^2	Variable	SRRC	R^2
1	*BHPRM*	0.58	0.33	*ANHPRM*	0.38	0.15	*BHPRM*	0.52	0.27	*BPCOMP*	0.28	0.08
2	*WGRCOR*	−0.38	0.47	*BHPRM*	0.37	0.28	*WGRCOR*	−0.44	0.45	*HALPRM*	0.28	0.15
3	*HALPOR*	0.36	0.60	*HALPRM*	0.26	0.35	*HALPOR*	0.28	0.53	*ANHPRM*	0.23	0.20
4	*ANHPRM*	0.21	0.64	*HALPOR*	0.23	0.40	*BPCOMP*	0.28	0.60	*BHPRM*	0.21	0.25
5	*HALPRM*	0.17	0.67	*WGRCOR*	−0.13	0.42	*WMICDFLG*	−0.16	0.63	*HALPOR*	0.18	0.28
6	*WASTWICK*	−0.14	0.69	*WRGSSAT*	−0.11	0.43	*WASTWICK*	−0.14	0.65	*WRGSSAT*	−0.15	0.30
7	*WRBRNSAT*	−0.08	0.70	*WRBRNSAT*	−0.11	0.44	*BPVOL*	0.15	0.67	*BPVOL*	0.15	0.32
8							*ANHPRM*	0.13	0.69	*WMICDFLG*	−0.14	0.34
9							*SHRGSSAT*	−0.10	0.70	*BPINTPRS*	0.13	0.36
10							*HALPRM*	0.10	0.70	*WGRCOR*	−0.12	0.37

[a] Steps in stepwise regression analysis.

[b] Variables listed in order of selection in regression analysis with *ANHCOMP* and *HALCOMP* excluded from entry into regression model.

[c] Standardized rank regression coefficients in final regression model.

[d] Cumulative R^2 value with entry of each variable into regression model.

x = *BHPRM*, these volumes show a wide range of possible values, with this wide range corresponding to the similarly wide range of values for repository pressure (Fig. 8.4.5). Thus, there is a close, but complex, link between repository pressure and volume of brine contained in the intruded waste panel (Fig. 8.5.8). In particular, *BHPRM* is the dominant variable in determining both pressure and brine volume in the intruded panel (Figs. 8.4.5, 8.5.7) after an E2 intrusion.

Brine volume in the upper (i.e., unintruded) waste panels subsequent to an E1 intrusion behaves in a similar manner to that observed subsequent to an E2 intrusion (Figs. 8.5.5, 8.5.6). As for the E2 intrusion, (1) brine volume tends to decrease with time but may show an increase at very late times, (2) positive effects are indicated for *BHPRM* and *HALPOR*, and (3) negative effects are indicated for *WGRCOR* and *WASTWICK* (Fig. 8.5.5). The regression models for brine volume in the upper waste panels after E1 and E2 intrusions are also similar (Table 8.5.2), although the model for the E1 intrusion shows the effects of variables that affect the brine pocket (i.e., positive effects for *BPCOMP* and *BPVOL*). The scatterplots for brine volume in the upper waste panels subsequent to an E1 intrusion are similar to the corresponding scatterplots in Fig. 8.5.7 for brine volume subsequent to an E2 intrusion.

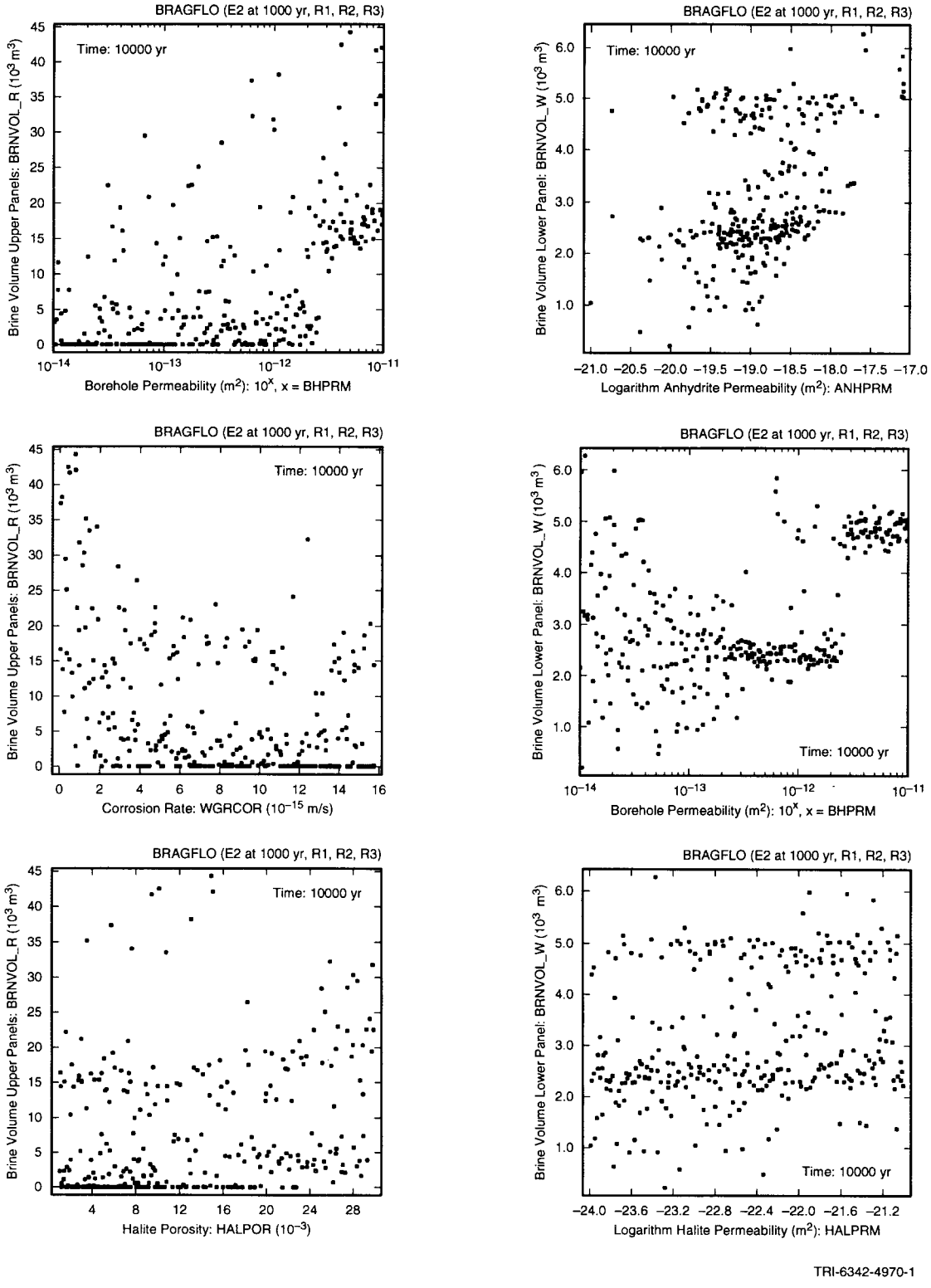

Fig. 8.5.7. Scatterplots for brine volume in upper waste panels (*BRNVOL_R*) versus *BHPRM*, *WGRCOR* and *HALPOR* (left frames) and brine volume in lower waste panel (*BRNVOL_W*) versus *ANHPRM*, *BHPRM* and *HALPRM* (right frames) at 10,000 yr for an E2 intrusion at 1000 yr into lower waste panel.

Brine volume in the lower (i.e., intruded) waste panel subsequent to an E1 intrusion also behaves similarly to brine volume subsequent to an E2 intrusion (Figs. 8.5.5, 8.5.6). Specifically, brine volume tends to cluster around values of 5×10^3 m^3 and 2.5×10^3 m^3 (Fig. 8.5.6); the corresponding values for the E2 intrusion are 5×10^3 m^3 and 2.4×10^3 m^3 (Fig. 8.5.5). For the E1 intrusion, the PRCC analysis is poor, with all variables having PRCCs less than 0.3 in absolute value after the drilling intrusion at 1000 yr (Fig. 8.5.7). The regression analysis is also poor, with an R^2 value of only 0.37 (Table 8.5.2). This poor performance occurs because a complex relationship exist between brine volume and *BHPRM*. Thus, as for the E2 intrusion, brine volume and repository pressure are being controlled by *BHPRM* (Figs. 8.4.5, 8.5.8, 8.5.9).

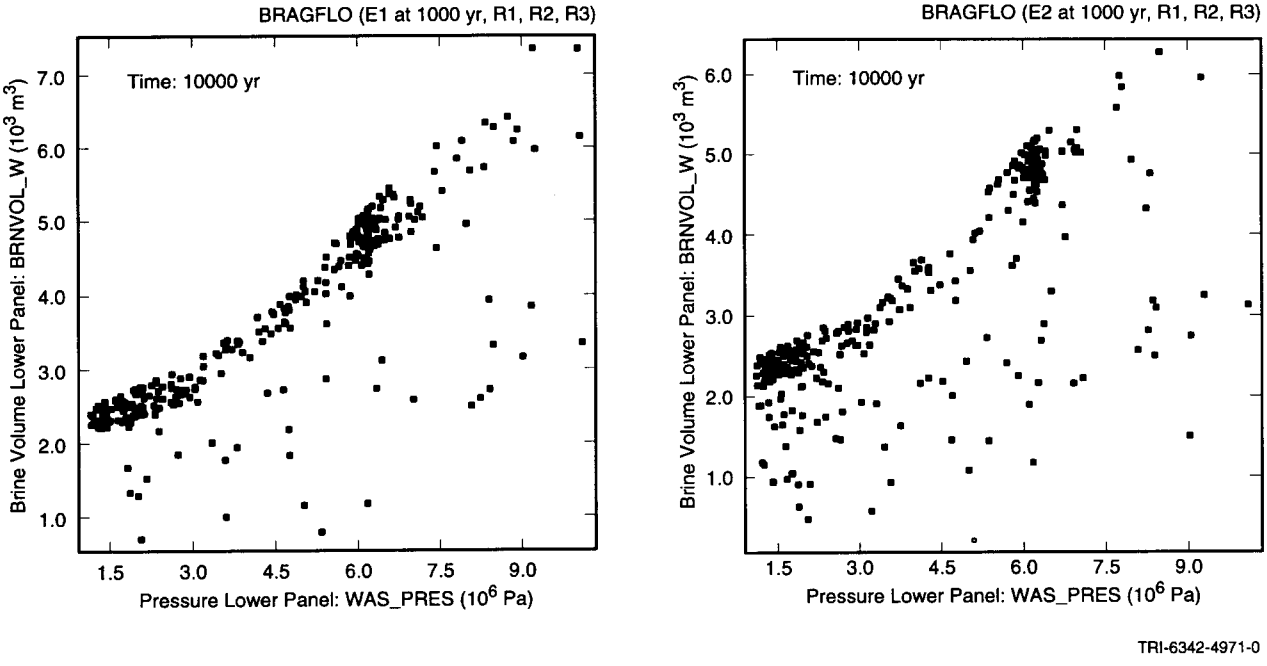

Fig. 8.5.8. Scatterplots for repository pressure (*WAS_PRES*) at 10,000 yr versus brine volume in lower waste panel (*BRNVOL_W*) for E1 and E2 intrusions at 1000 yr into lower waste panel.

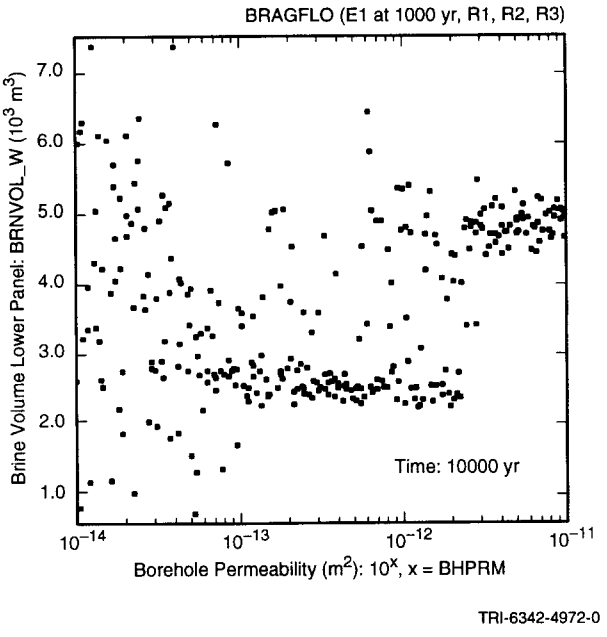

Fig. 8.5.9. Scatterplot for brine volume in lower waste panel (*BRNVOL_W*) at 10,000 yr for an E1 intrusion at 1000 yr into lower waste panel versus *BHPRM*.

8.6 Disturbed Conditions: Brine and Gas Flow in Borehole for E1 and E2 Intrusions

The defining characteristics of disturbed conditions result from brine and gas flow in the intruding borehole. A borehole plug at the Rustler/Salado interface is assumed to be effective for 200 yr after a drilling intrusion through the repository (Table 4.2.8). After the failure of this plug, repository pressure drops rapidly (Fig. 8.4.1) due to gas flow up the intruding borehole (Fig. 8.6.1). After an initial rapid venting of gas, the flow rate tends to continue at a slower rate as additional gas is generated by the corrosion of steel.

Prior to the drilling intrusion, a very small amount of gas moves into the undisturbed halite at the edge of the DRZ in the computational cell that will become part of the borehole (i.e., Cell 575 in Fig. 4.2.3). The amount of movement that takes place is dominated by the indicator variable *ANHBCVGP*, with less gas movement taking place into Cell 575 when the van Genuchten-Parker model (*ANHBCVGP* = 1) is used (Fig. 8.6.1). The preceding statement is made because of the negative PRCC shown for *ANHBCVGP* (Fig. 8.6.1) between 0 and 1000 yr. However, the actual magnitude of this movement is very small and of no consequence to the analysis and is mentioned only because of the appearance of the PRCC for *ANHBCVGP* prior to 1000 yr in Fig. 8.6.1.

For the E2 intrusion, the amount of gas vented within a few hundred years of the plug failure is dominated by *WMICDFLG*, *BHPRM*, *WGRCOR* and *WASTWICK*, with the amount of gas moving up the borehole tending to increase as each of these variables increases (Fig. 8.6.1). The positive effects for *WMICDFLG*, *WGRCOR* and *WASTWICK* result from increasing the amount of gas in the repository at the time of the intrusion, and the positive effect for *BHPRM* results from reducing the resistance to gas flow in the borehole.

After the first few hundred years, *WMICDFLG*, *BHPRM* and *WGRCOR* continue to show positive effects on the cumulative gas release for an E2 intrusion (Fig. 8.6.1). For *WMICDFLG*, this continuing importance to cumulative gas release is indicative of the large gas release that takes place immediately after the drilling intrusion (Fig. 8.6.1) and the importance of *WMICDFLG* in determining the size of this release. As a reminder, *WMICDFLG* only affects microbial gas generation, which is often completed by 1000 yr and almost always completed by 2000 yr (Fig. 7.3.1). At later times, a positive effect is also indicated for *HALPOR* due to its role in influencing gas generation due to corrosion (Fig. 8.6.1, also see Figs. 8.3.1, 8.3.3, 8.3.5, 8.3.16).

The PRCC results for gas flow up the borehole after an E1 intrusion are similar to those obtained for the E2 intrusion (Fig. 8.6.1). In particular, positive effects are indicated for *WMICDFLG*, *WGRCOR* and *BHPRM*.

Similar results are also obtained in a stepwise regression analysis for cumulative gas flow up the borehole subsequent to an E2 intrusion (Table 8.6.1). Specifically, gas flow up the borehole tends to increase as each of *WMICDFLG*, *BHPRM*, *HALPOR*, *WGRCOR*, *ANHPRM* and *SHRGSSAT* increases. The roles of these variables

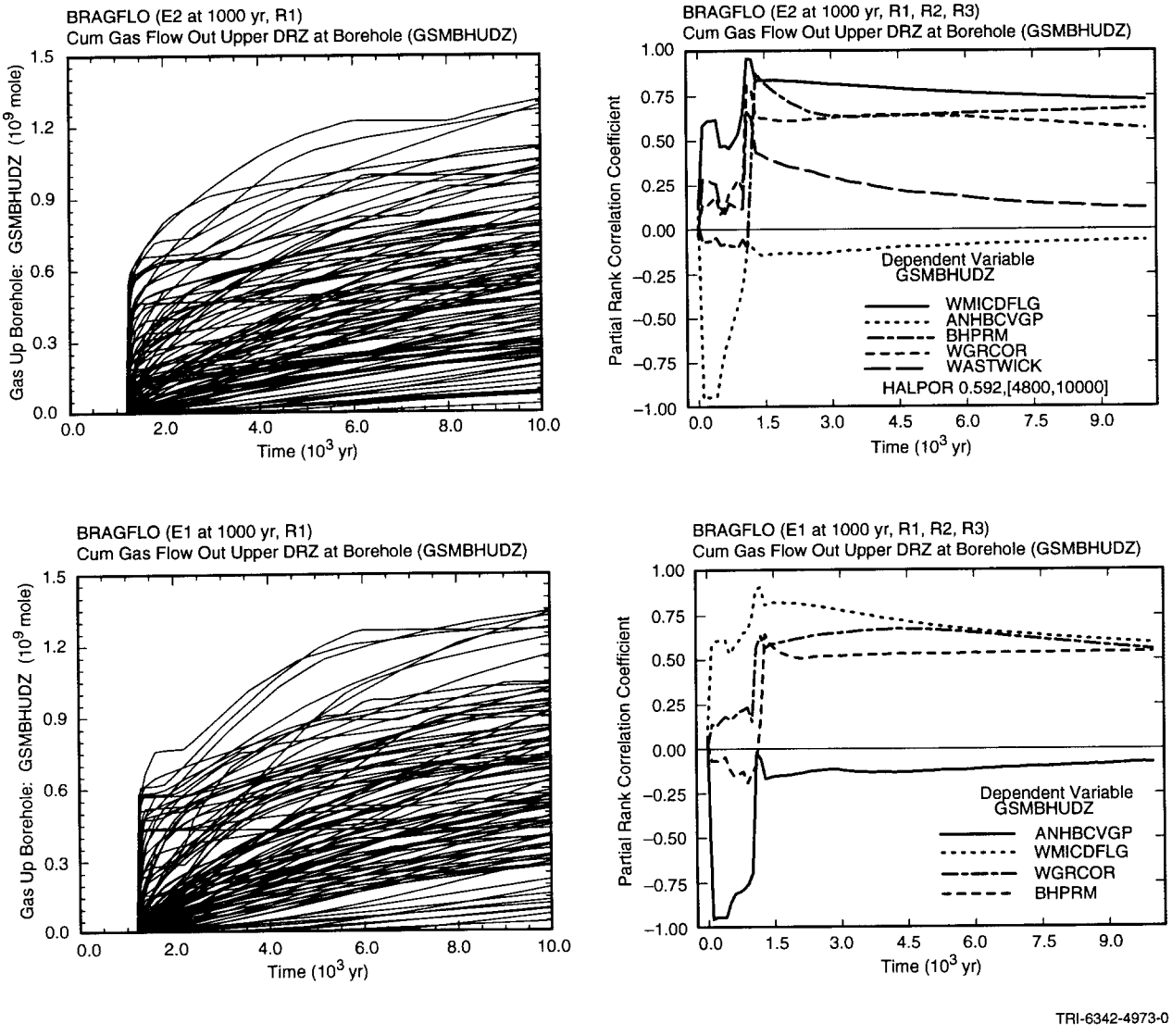

Fig. 8.6.1. Uncertainty and sensitivity analysis results for cumulative gas flow up borehole at top of DRZ (*GSMBHUDZ*) for E1 and E2 intrusions at 1000 yr into lower waste panel (See Note, Fig. 8.5.1).

Table 8.6.1. Stepwise Regression Analyses with Rank-Transformed Data for Cumulative Gas (*GSMBHUDZ*) and Brine (*BNBHUDRZ*) Flow over 10,000 yr up Borehole at Top of DRZ for E1 and E2 Intrusions at 1000 yr into Lower Waste Panel

	E2: Gas Flow			E1: Gas Flow			E2: Brine Flow			E1: Brine Flow		
Step[a]	Variable[b]	SRRC[c]	R^{2d}	Variable	SRRC	R^2	Variable	SRRC	R^2	Variable	SRRC	R^2
1	*WMICDFLG*	0.53	0.29	*WMICDFLG*	0.46	0.22	*HALPRM*	−0.48	0.25	*BPCOMP*	0.48	0.21
2	*BHPRM*	0.44	0.49	*WGRCOR*	0.39	0.37	*WMICDFLG*	0.35	0.36	*WMICDFLG*	−0.42	0.38
3	*HALPOR*	0.35	0.62	*BHPRM*	0.37	0.52	*HALPOR*	0.25	0.42	*BHPRM*	0.36	0.51
4	*WGRCOR*	0.33	0.73	*HALPOR*	0.31	0.61	*ANHBCVGP*	0.22	0.46	*BPINTPRS*	0.18	0.54
5	*ANHPRM*	0.11	0.74	*BPPRM*	−0.11	0.62	*BHPRM*	0.13	0.48	*WGRCOR*	−0.19	0.58
6	*SHRGSSAT*	0.08	0.75	*HALPRM*	−0.10	0.63	*WGRCOR*	−0.13	0.50	*HALPRM*	−0.12	0.59
7										*WASTWICK*	−0.12	0.60
8										*ANHBCVGP*	0.11	0.61
9										*HALPOR*	0.10	0.62

[a] Steps in stepwise regression analysis.

[b] Variables listed in order of selection in regression analysis with *ANHCOMP* and *HALCOMP* excluded from entry into regression model.

[c] Standardized rank regression coefficients in final regression model.

[d] Cumulative R^2 value with entry of each variable into regression model.

have been discussed previously. Specifically, increasing *WMICDFLG* increases microbial gas generation; increasing *BHPRM* both reduces resistance to gas flow up the borehole and allows more brine to enter the repository by flow down the borehole and out of the marker beds; increasing *HALPOR* and *ANHPRM* increases brine flow into the repository by increasing brine flow out of the DRZ and the marker beds, respectively; increasing *WGRCOR* increases gas generation; and increasing *SHRGSSAT* alters brine and gas flow patterns within the repository. For perspective, the corresponding scatterplots for *WMICDFLG*, *BHPRM*, *HALPOR* and *WGRCOR* are given in Fig. 8.6.2.

The regression analysis results for cumulative gas flow up the borehole subsequent to an E1 intrusion are similar to those obtained for an E2 intrusion (Table 8.6.1), although the final R^2 value tends to be somewhat lower (i.e., 0.63 versus 0.75). The same top four variables are picked in both analyses (i.e., *WMICDFLG*, *WGRCOR*, *BHPRM* and *HALPOR*). The selection of *BPPRM* with a negative regression coefficient is counterintuitive but may result from the rank correlation of −0.75 assigned to *BPCOMP* and *BPPRM*; in any event, the effect indicated for *BPPRM* is small (i.e., the inclusion of *BPPRM* in the regression model changes the R^2 value from 0.61 to 0.62).

Unlike the extensive gas flows up an intruding borehole (Fig. 8.6.1), most sample elements result in no brine flow up the intruding borehole (Fig. 8.6.3). Due to flow from the brine pocket (Fig. 8.2.7), the E1 intrusion usually results in more brine flow up the borehole than the E2 intrusion when such flow occurs; however, the typical case is no flow for both E1 and E2 intrusions. In contrast to the general importance of the E1 intrusion with respect to brine flow up the borehole, the largest such flow for replicate R1 actually results from brine inflow from the marker beds (i.e., compare the largest cumulative flow curves for E1 and E2 intrusions in Fig. 8.6.3).

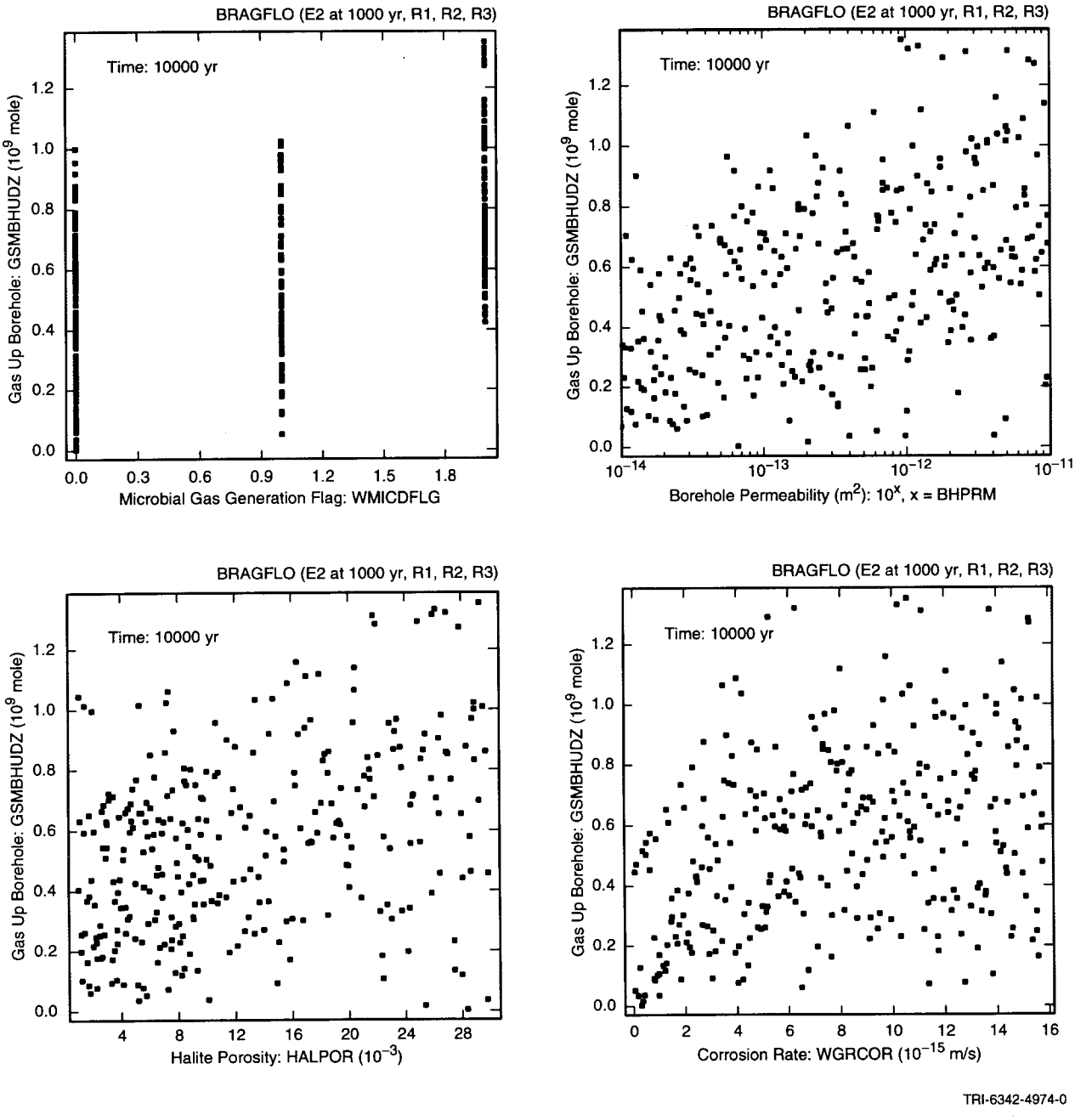

Fig. 8.6.2. Scatterplots for cumulative gas flow up a borehole (*GSMBHUDZ*) over 10,000 yr subsequent to an E2 intrusion at 1000 yr into the lower waste panel versus *WMICDFLG*, *BHPRM*, *HALPOR* and *WGRCOR*.

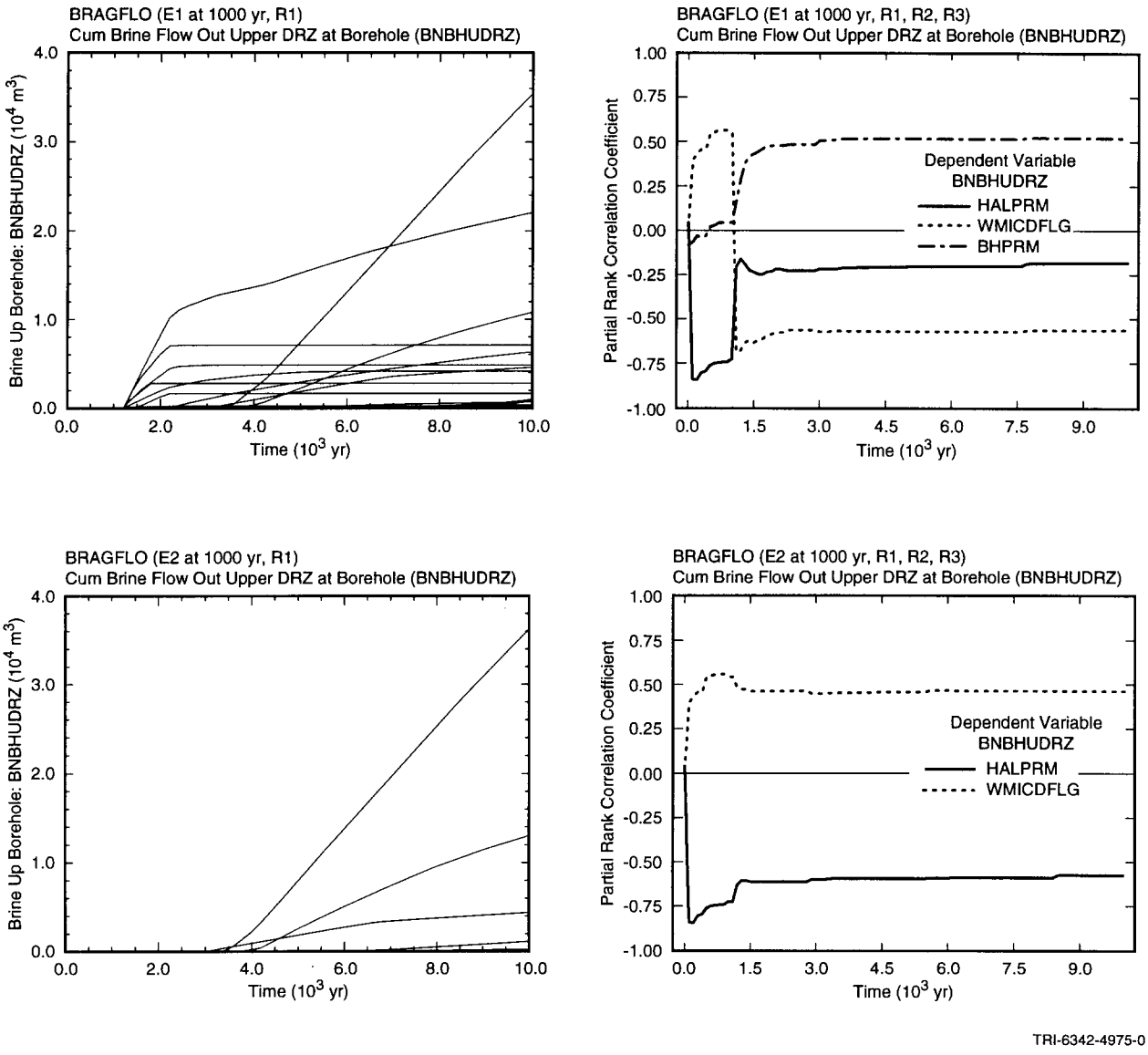

Fig. 8.6.3. Uncertainty and sensitivity analysis results for cumulative brine flow up borehole at top of DRZ (*BNBHUDRZ*) for E1 and E2 intrusions at 1000 yr into lower waste panel.

The PRCCs in Fig. 8.6.3 and also the regression analyses in Table 8.6.1 are probably not very good indicators of variable importance for brine flow up the intruding borehole due to the large number of zero flows. In particular, the regression analyses for E2 and E1 intrusions have R^2 values of only 0.50 and 0.63. Due to the large number of zero flows, examination of scatterplots provides a more reliable indication of variable importance. For the E2 intrusion, brine flow up the intruding borehole tends to be associated with large values for *BHPRM* and *ANHPRM* and small values for *WGRCOR* (Fig. 8.6.4). The positive effect for *BHPRM* results because increasing *BHPRM* permits more brine to enter the repository due to flow both down the borehole and out of the marker beds and also reduces resistance to flow up the borehole should the intruded waste panel fill with brine. The positive effect for *ANHPRM* results because increasing *ANHPRM* results in more brine flow out of the marker beds. Finally, the negative effect for *WGRCOR* results because increasing *WGRCOR* causes more brine to be removed by corrosion and thus reduces the amount of brine available for flow up the borehole; also, flow up the borehole of the additional gas produced for large values of *WGRCOR* may impede brine flow in the borehole.

For the E1 intrusion, brine flow up the intruding borehole tends to be associated with large values for *BHPRM* and *BPCOMP* and with small values for *WMICDFLG* (Fig. 8.6.5). The positive effects for *BHPRM* result for the reasons just indicated for the E2 intrusion and also because increasing *BHPRM* reduces resistance to brine flow in the borehole between the brine pocket and the repository (Fig. 8.2.12). The positive effect for *BPCOMP* results because increasing *BPCOMP* increases the amount of brine that leaves the brine pocket for each unit drop in pressure (Fig. 8.2.12). Finally, the negative effect for *WMICDFLG* results because large values for *WMICDFLG* prevent brine movement from the brine pocket to the repository during the 200 yr period that an open borehole exists between these two locations (Fig. 8.2.8), which in turn means more brine from other sources is required to fill the intruded panel before brine flow up the borehole can begin.

There is a complex interplay between repository pressure and borehole permeability (Fig. 8.4.5) that derives from interdependencies between brine and gas flow into and out of the repository in an intruding borehole. Several figures show patterns of pressure (Fig. 8.4.1), gas flow (Fig. 8.6.1) and brine flow (Figs. 8.2.6, 8.2.7, 8.6.3) associated with E1 and E2 intrusions. However, these figures do not fully indicate the complexity of the interactions between pressure, gas flow and brine flow. This complexity can be best recognized from examination of plots that show time-dependent pressures, gas flows and brine flows on a single plot frame for individual sample elements (Fig. 8.6.6, Table 8.6.2).

The complex patterns involving pressure, brine flow and gas flow in Fig. 8.6.6 result because high permeability boreholes facilitate gas flow out of the repository and brine flow both into and out of the repository, with the lower (i.e., intruded) waste panel eventually becoming brine saturated and thus reaching hydrostatic pressure (Figs. 8.4.5, 8.5.1, 8.5.2). Low permeability boreholes are less conducive to brine and gas flow, which in turn results in less

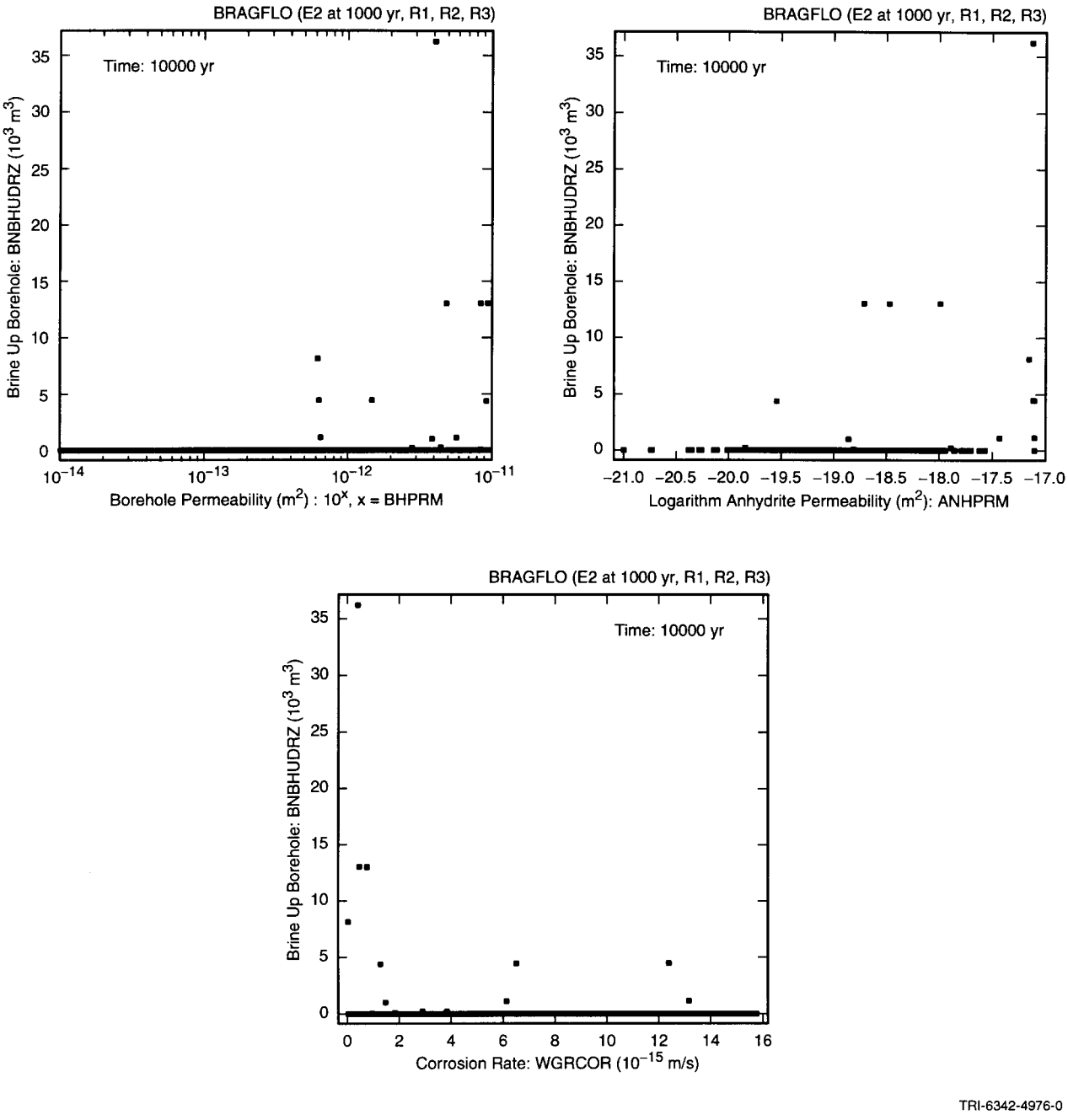

Fig. 8.6.4. Scatterplots for cumulative brine flow up borehole (*BNBHUDRZ*) over 10,000 yr for an E2 intrusion at 1000 yr into lower waste panel versus *BHPRM*, *ANHPRM* and *WGRCOR*.

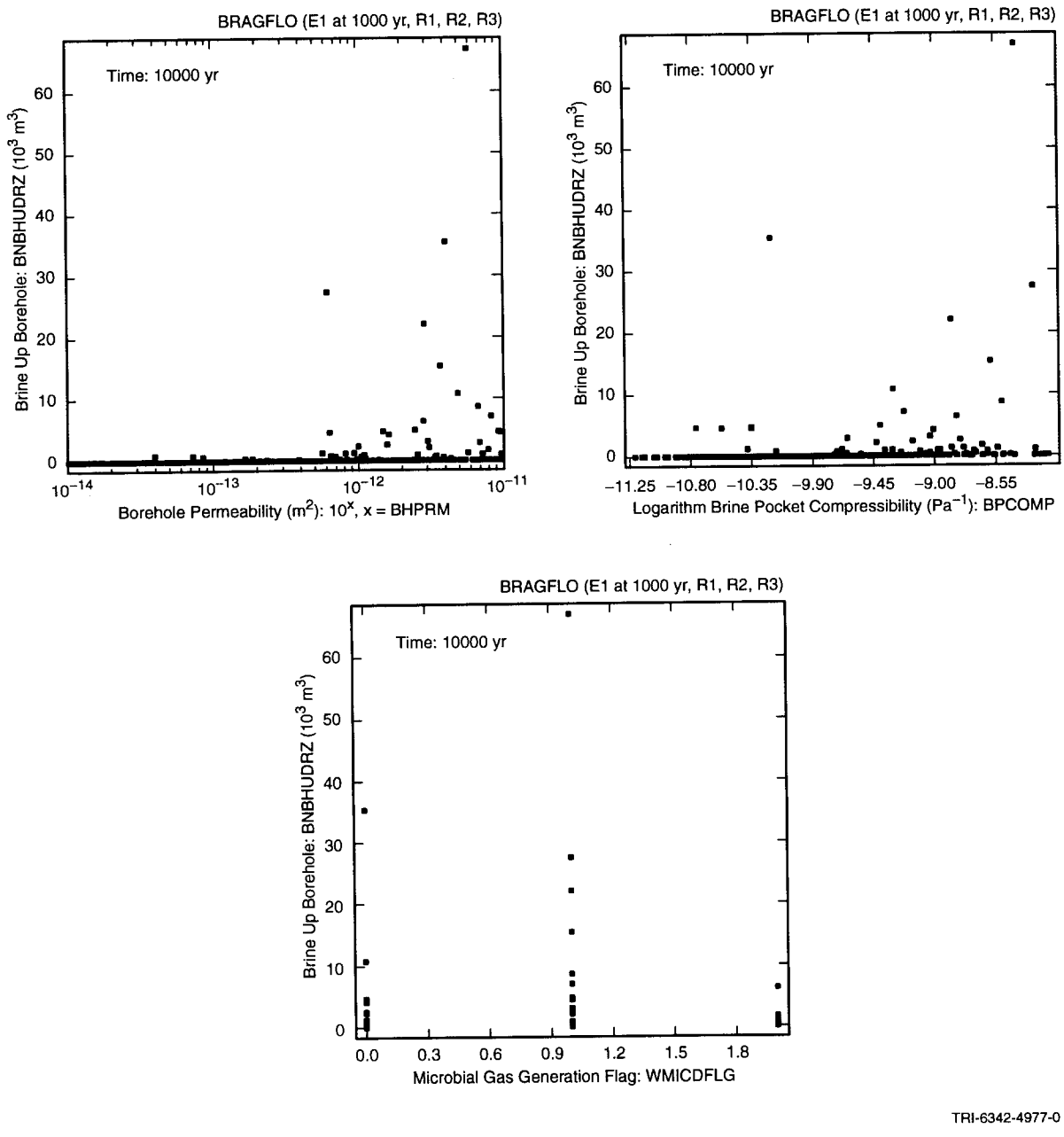

Fig. 8.6.5. Scatterplots for cumulative brine flow up borehole (*BNBHUDRZ*) over 10,000 yr for an E1 intrusion at 10,000 yr into lower waste panel versus *BHPRM*, *BPCOMP* and *WMICDFLG*.

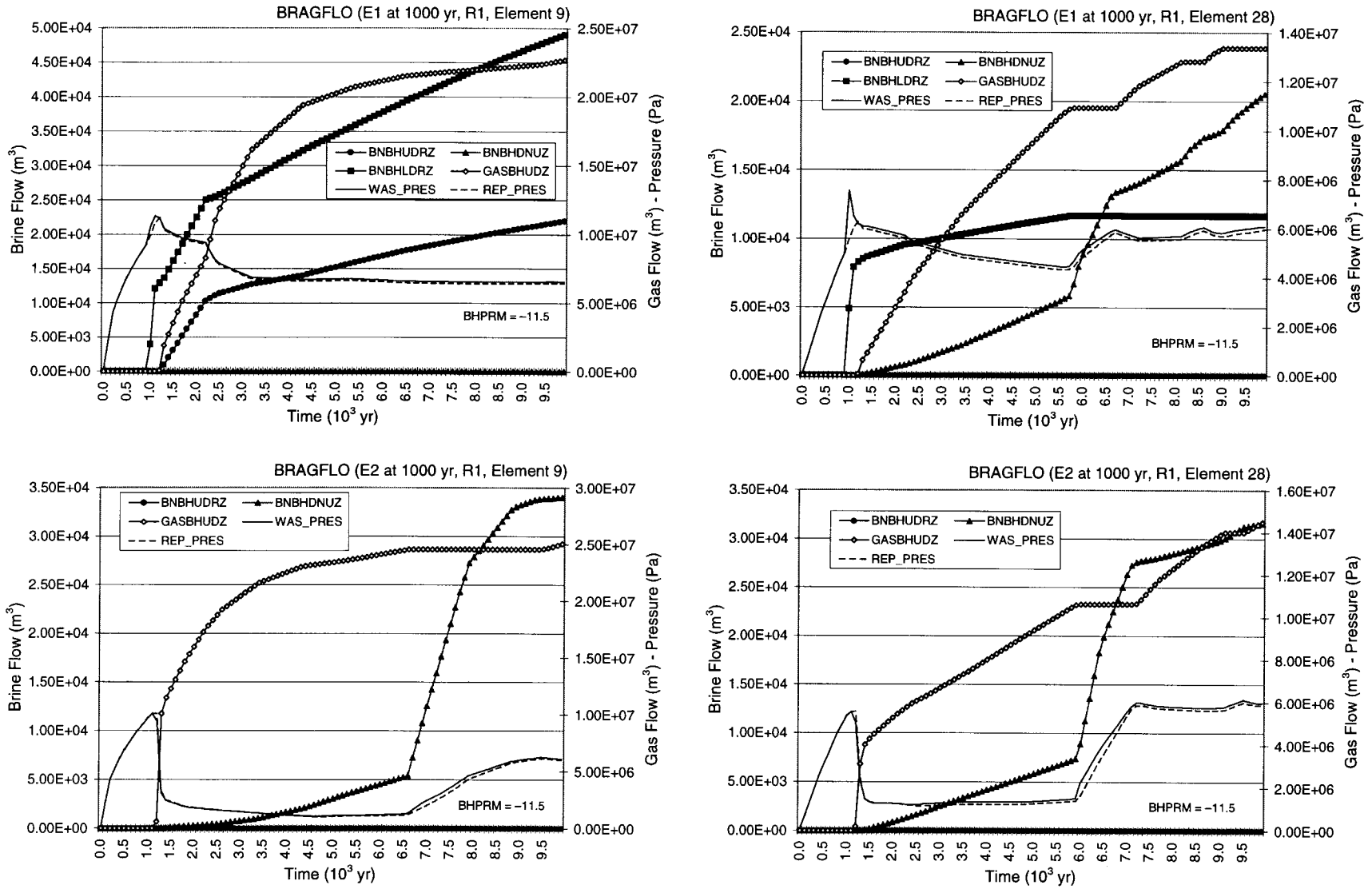

Fig. 8.6.6 Repository pressure (*WAS_PRES*, *REP_PRES*) and brine and gas flow (*BNBHUDRZ*, *BNBHDNUZ*, *BNBHLDRZ*, *GASBHUDZ*) in high permeability boreholes associated with E1 and E2 intrusions at 1000 yr into the lower waste panel for sample elements 9, 28, 39, 72, 74 and 82 of replicate R1.

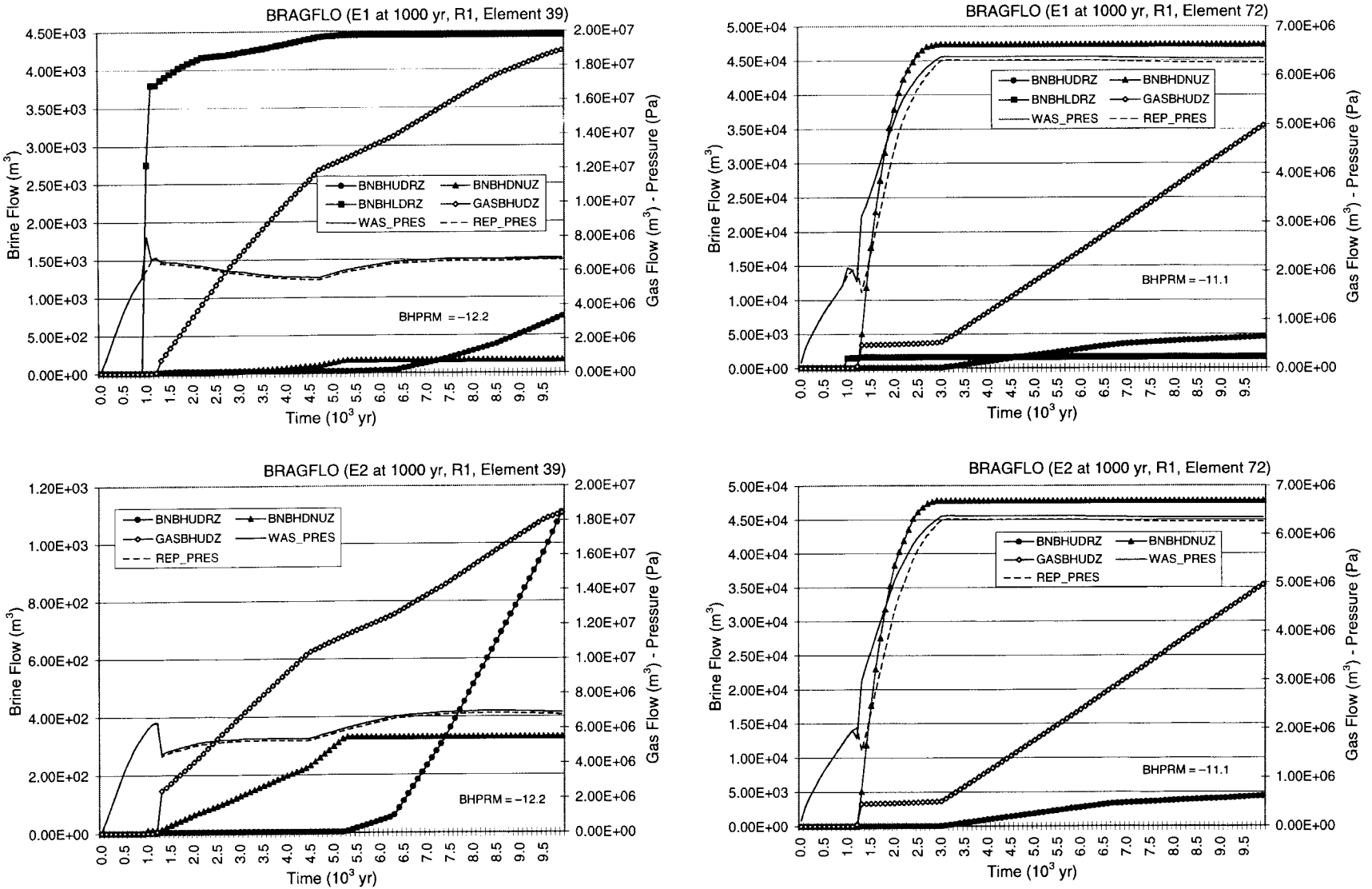

Fig. 8.6.6 Repository pressure (*WAS_PRES*, *REP_PRES*) and brine and gas flow (*BNBHUDRZ*, *BNBHDNUZ*, *BNBHLDRZ*, *GASBHUDZ*) in high permeability boreholes associated with E1 and E2 intrusions at 1000 yr into the lower waste panel for sample elements 9, 28, 39, 72, 74 and 82 of replicate R1. (Continued)

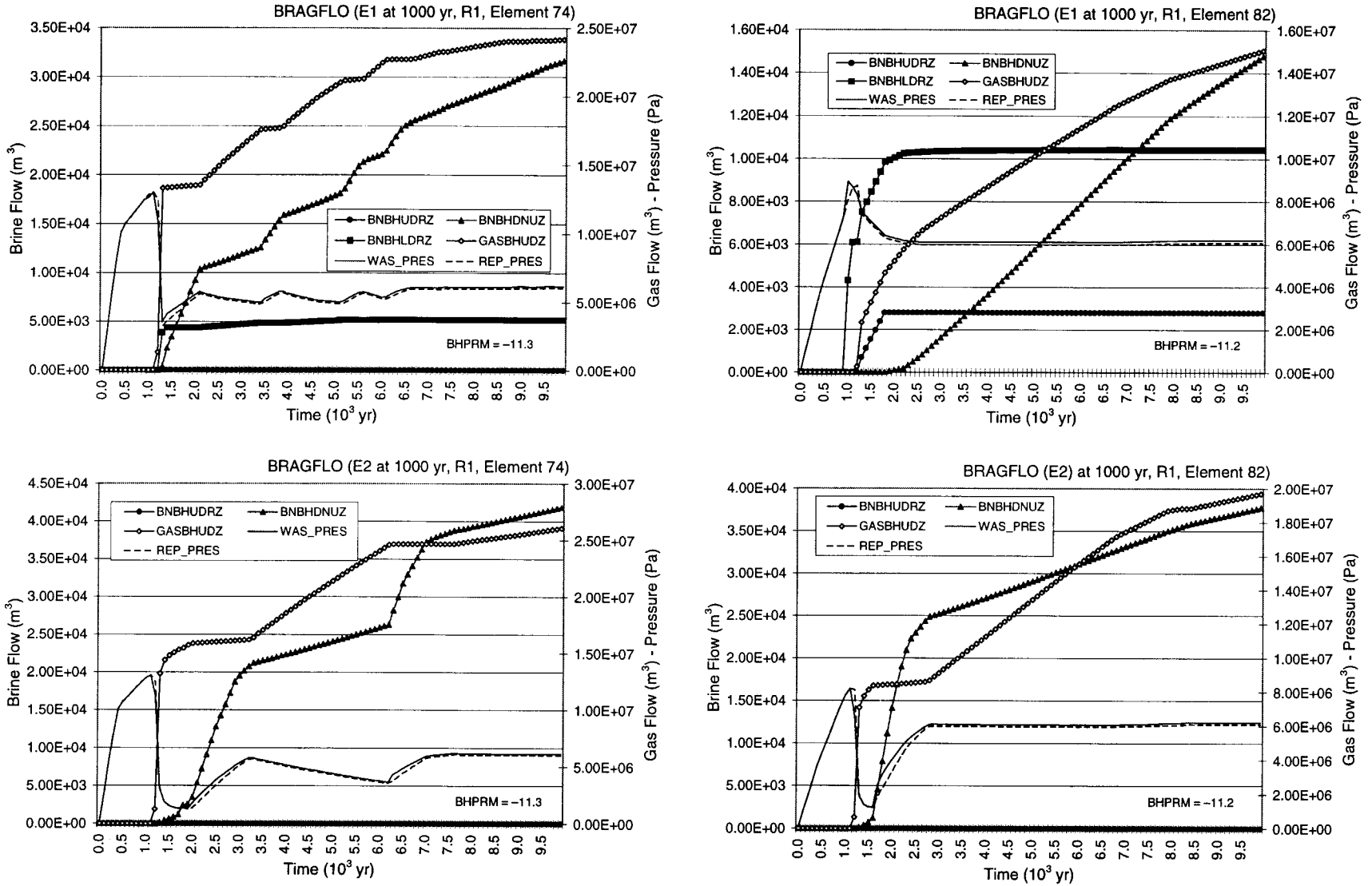

Fig. 8.6.6 Repository pressure (*WAS_PRES*, *REP_PRES*) and brine and gas flow (*BNBHUDRZ*, *BNBHDNUZ*, *BNBHLDRZ*, *GASBHUDZ*) in high permeability boreholes associated with E1 and E2 intrusions at 1000 yr into the lower waste panel for sample elements 9, 28, 39, 72, 74 and 82 of replicate R1. (Continued)

Table 8.6.2. Summary Discussion of Plots in Fig. 8.6.6 for Repository Pressure (*WAS_PRES*, *REP_PRES*) and Brine and Gas Flow (*BNBHUDRZ*, *BNBHDNUZ*, *BNBHLDRZ*, *GASBHUDZ*) in High Permeability Boreholes Associated with E1 and E2 Intrusions at 1000 yr into the Lower Waste Panel for Sample Elements 9, 28, 39, 72, 74 and 82 of Replicate R1

Sample Element 9
E1 Intrusion: Brine flow from brine pocket to repository (*BNBHLDRZ*) very rapid during period from 1000 to 1200 yr when open borehole exists between brine pocket and repository, with this flow decreasing between 1200 and 2200 yr and again after 2200 yr due to decreases in borehole permeability (Table 4.2.8). Brine and gas flows up borehole (*BNBHUDRZ*, *GASBHUDZ*) begin when borehole plugs fail at 1200 yr (Table 4.2.8), with brine flow up the borehole closely following brine flow from the brine pocket. No flow down the borehole from the Culebra and overlying formations to the repository (*BNBHDNUZ*) takes place. Pressures in upper and lower panels (*REP_PRES*, *WAS_PRES*) are similar and slowly decrease towards hydrostatic pressure (6.3×10^6) Pa) subsequent to the plug failures at 1200 yr. *E2 Intrusion*: Pressure (*REP_PRES*, *WAS_PRES*) drops rapidly when borehole plugs fail at 1200 yr due to gas flow up borehole (*GASBHUDZ*). Unlike the E1 intrusion, substantial brine flow down borehole (*BNBHDNUZ*) occurs, with this flow being initially small and then increasing as gas flow up the borehole decreases. At approximately 6600 yr, gas flow up the borehole ceases, the rate of brine flow down the borehole increases sharply, and pressures in the repository rise to hydrostatic pressure. As hydrostatic pressure is reached, brine flow down the borehole decreases and gas flow up the borehole resumes. No brine flow up the borehole from the repository (*BNBHUDRZ*) takes place.
Sample Element 28
E1 Intrusion: Brine flow from brine pocket to repository (*BNBHLDRZ*) is very rapid during period from 1000 to 1200 yr, with reductions in the flow rate at 1200 and 2200 yr and a complete cessation at approximately 5700 yr. The cessation of brine flow from the brine pocket also corresponds to a cessation of gas flow up the borehole (*GASBHUDZ*) and initiation of increases in brine flow down the borehole (*BNBHDNUZ*) and pressure in the repository (*REP_PRES*, *WAS_PRES*). Pressure reaches hydrostatic pressure at approximately 6900 yr, at which point the brine flow down the borehole decreases, gas flow up the borehole resumes, and a small decrease in repository pressure begins. A decrease in gas flow up the borehole and an increase in brine flow down the borehole results in an increase in repository pressure at approximately 8700 yr, with pressure subsequently dropping as gas flow up the borehole resumes and then beginning to rise again at approximately 9000 yr when gas flow again stops. Pressure in the lower waste panel (*WAS_PRES*) but not pressure in the upper waste panels (*REP_PRES*) shows a sharp spike between 1000 and 1200 yr due to brine flow up the open borehole connecting the brine pocket and the repository. No brine up the borehole from the repository (*BNBHUDRZ*) takes place. *E2 Intrusion*: Behavior is similar to that observed for the E2 intrusion for sample element 9 with peaks in repository pressure (*REP_PRES*, *WAS_PRES*) at approximately 7200 and 9600 yr in association with changes in the rates at which gas flows up the borehole (*GASBHUDZ*) and brine flows down the borehole (*BNBHDUZ*).
Sample Element 39
E1 Intrusion: Brine flow from brine pocket to repository (*BNBHLDRZ*) is very rapid during period from 1000 to 1200 yr, with reductions in the flow rate at 1200 and 2200 yr and a complete cessation at ~5100 yr. Gas flow up the borehole (*GASBHUDZ*) decreases at approximately the same time as brine flow from the brine pocket ceases, with this decrease being accompanied by a short period of brine flow down the borehole (*BNBHDUZ*). Brineflow down the borehole ceases at ~5400 yr and a small brine flow up the borehole (*BNBHUDRZ*) begins at ~6300 yr.

Table 8.6.2. Summary Discussion of Plots in Fig. 8.6.6 for Repository Pressure (*WAS_PRES*, *REP_PRES*) and Brine and Gas Flow (*BNBHUDRZ*, *BNBHDNUZ*, *BNBHLDRZ*, *GASBHUDZ*) in High Permeability Boreholes Associated with E1 and E2 Intrusions at 1000 yr into the Lower Waste Panel for Sample Elements 9, 28, 39, 72, 74 and 82 of Replicate R1 (Continued)

Repository pressure (*REP_PRES*, *WAS_PRES*) was approximately at hydrostatic pressure at the time of the drilling intrusion and shows little variation subsequent to the drilling intrusion, although a small spike in the lower waste panel pressure (*WAS_PRES*) occurs at the time of the drilling intrusion and repository pressure changes from decreasing to increasing at ~4800 yr when the rate of gas flow up the borehole decreases. *E2 Intrusion*: Gas flow up the borehole (*GASBHUDZ*) and brine flow down the borehole (*BNBHDNUZ*) begins when the borehole plugs fail at 1200 yr. Repository pressure (*REP_PRES*, *WAS_PRES*) shows a sudden drop when the plugs fail at 1200 yr and then increases monotonically through time towards hydrostatic pressure. At ~5400 yr, brine flow down the borehole ceases and brine flow up the borehole (*BNBHUDRZ*) begins. The complexity of the interactions between brine and gas flow in the borehole is indicated by the prediction of more brine flow up the borehole for the E2 intrusion (~1100 m^3) and than for the E1 intrusion (~750 m^3).
Sample Element 72
E1 Intrusion: Repository pressure (*REP_PRES*, *WAS_PRES*) is low at time of drilling intrusion (~1.9×10^6 Pa); further, only a small pulse of brine takes place from the brine pocket to the repository (*BNBHLDRZ*) at the time of the drilling intrusion. After 1200 yr, a substantial brine flow down the borehole (*BNBHDNUZ*) takes place and suppresses gas flow up the borehole (*GASBHUDZ*). At ~3200 yr, the repository reaches hydrostatic pressure, brine flow down the borehole ceases, and both gas flow (*GASBHUDZ*) and brine flow (*BNBHUDRZ*) up the borehole begin and then continue at constant rates for the remainder of the calculation. *E2 Intrusion*: Except for small brine flow from brine pocket, results for the E2 intrusion are the same as those for the E1 intrusion.
Sample Element 74
Sample element 74 is included as an example because of the well-defined patterns involving gas flow up the borehole (*GASBHUDZ*), brine flow down the borehole (*BNBHDNUZ*) and repository pressure (*REP_PRES*, *WAS_PRES*) displayed for both E1 and E2 intrusions.
Sample Element 82
E1 Intrusion: Brine flow from the brine pocket to the repository (*BNBHLDRZ*) is very rapid during the period from 1000 to 1200 yr, shows a decreased rate from 1200 to 2200 yr, and then ceases after 2200 yr. Repository pressure (*REP_PRES*, *WAS_PRES*) undergoes a small perturbation between 1000 and 1200 yr and then decreases monotonically towards hydrostatic pressure after 1200 yr. Flows of brine (*BNBHUDRZ*) and gas (*GASBHUDZ*) take place up the borehole between 1200 and ~1900 yr, with the brine flow ceasing at ~1900 yr and the gas flow continuing for the remainder of the calculation. Brine flow down the borehole (*BNBHDNUZ*) begins at ~1900 yr when brine flow up the borehole ceases and continues for the remainder of the calculation. *E2 Intrusion*: Repository pressure (*REP_PRES*, *WAS_PRES*) drops rapidly after 1200 yr due to gas flow up the borehole (*GASBHUDZ*). At ~1500 yr, gas flow up the borehole ceases and is replaced by rapid brine flow down the borehole (*BNBHDNUZ*). Hydrostatic pressure is reached at ~2900 yr, at which point brine flow down the borehole decreases and gas flow up the borehole resumes. No brine flow up the borehole (*BNBHDNUZ*) takes place.

complex patterns involving pressure, brine flow and gas flow (Fig. 8.6.7). In particular, the complex patterns leading to convergence to hydrostatic pressure typically occur only for borehole permeabilities above ~2×10^{-12} m^2 (i.e., $BHPRM \doteq -11.6$) (Fig. 8.4.5).

Brine and gas flow in an intruding borehole also has significant effects on gas and brine saturations in the repository and on the consumption of steel by corrosion (Figs. 8.6.8, 8.6.9, Table 8.6.3). In particular, the gas outflow and brine inflow associated with a drilling intrusion often results in significant differences in the saturations and corrosion rates in the lower and upper waste panels and also in the saturations and corrosion rates for E1 and E2 intrusions.

Brine volume and total pore volume in the repository are also closely tied to repository pressure and to gas and brine flow in an intruding borehole (Fig. 8.6.9). For E1 and E2 intrusions associated with sample element 14, repository volume (*PORVOL_R*, *PORVOL_W*) decreases as repository pressure (*REP_PRES*, *WAS_PRES*) decreases after the borehole plugs fail at 1200 yr. For sample element 40, pressure continues to rise after 1200 yr for the E1 intrusion and so pore volume also rises until pressure begins to decrease at ~1600 yr; in contrast, pressure decreases after 1200 yr for the E2 intrusion and so pore volume also decreases. For the E1 intrusion associated with sample element 14, sufficient brine inflow occurs to rapidly saturate the lower waste panel (i.e., pore volume, *PORVOL_W*, and brine volume, *BRNVOL_W*, are the same after ~1600 yr) and also to prevent the brine in the upper waste panels (*BRNVOL_R*) from being completely depleted by corrosion; in contrast, the E2 intrusion experiences less brine inflow, with the result that the lower waste panel does not become brine saturated until ~8000 yr and the upper waste panels are depleted of brine by ~3200 yr. Similar but less pronounced patterns also occur for sample element 40. In particular, the lower waste panel rapidly saturates after 1200 yr and the brine volume in the upper waste panels remains high for the E1 intrusion; the lower waste panel saturates more slowly after the E2 intrusion and the brine saturation in the upper waste panels remains low, although the brine is not completely depleted as was the case for the E2 intrusion for sample element 14.

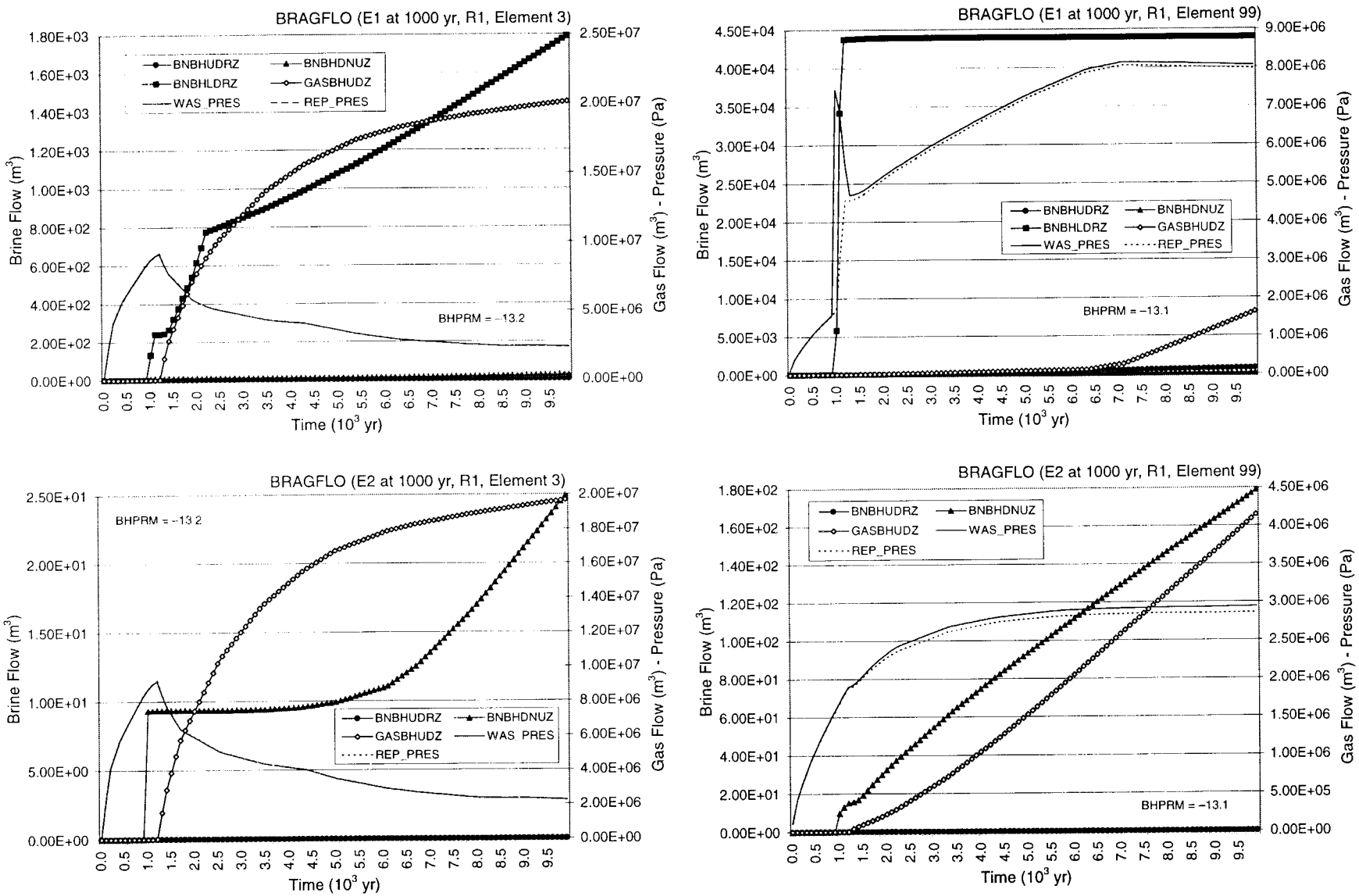

Fig. 8.6.7 Repository pressure (*WAS_PRES*, *REP_PRES*) and brine and gas flow (*BNBHUDRZ*, *BNBHDNUZ*, *BNBHLDRZ*, *GASBHUDZ*) in low permeability boreholes associated with E1 and E2 intrusions at 1000 yr into the lower waste panels for sample elements 3 and 99 of replicate R1.

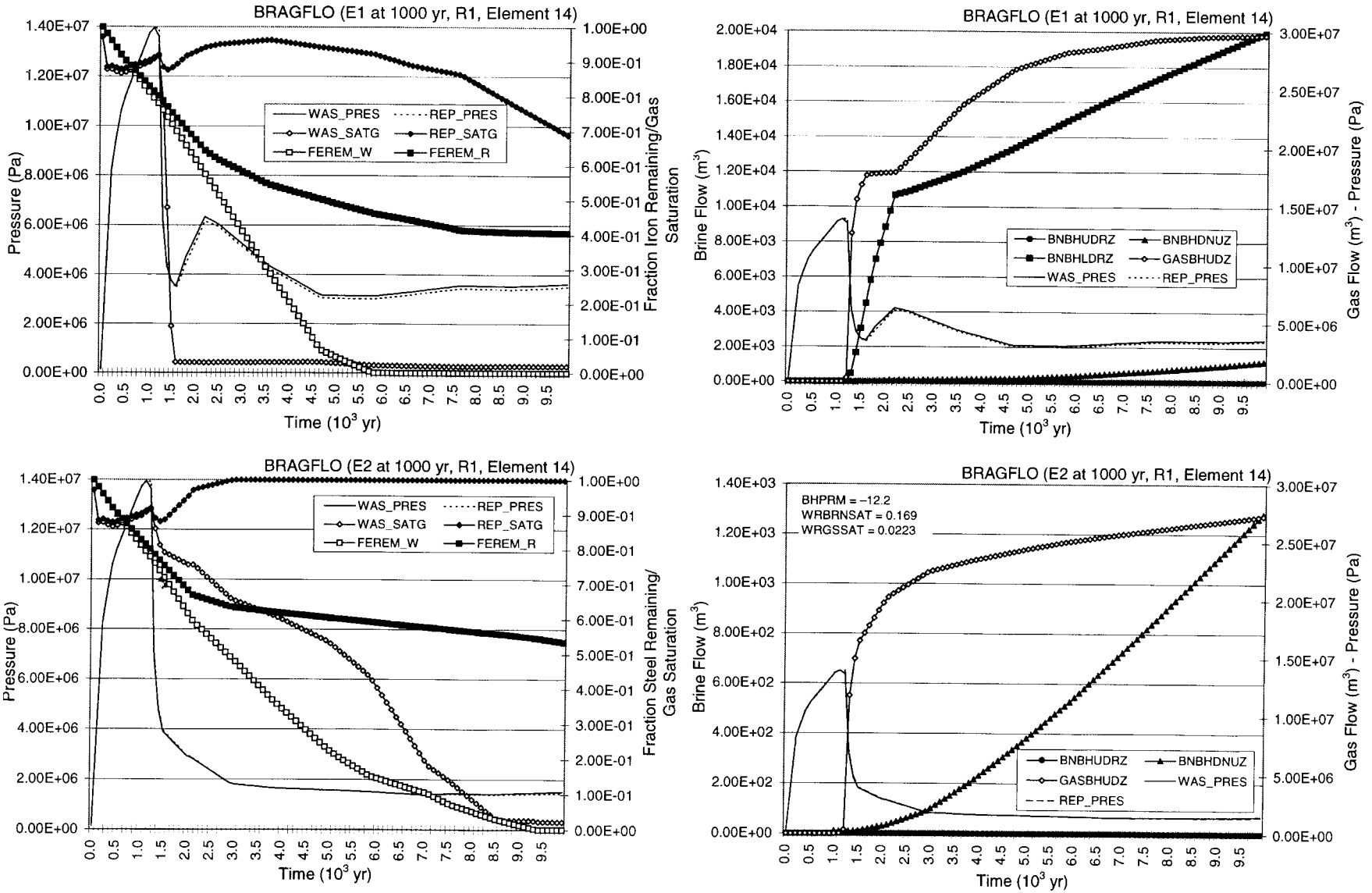

Fig. 8.6.8 Repository pressure (*WAS_PRES*, *REP_PRES*), brine and gas flows in intruding boreholes (*BNBHUDRZ*, *BNBHDNUZ*, *BNBHLDRZ*, *GASBHUDZ*), gas saturation (*WAS_SATG*, *REP_SATG*), and fraction of steel remaining (*FEREM_W*, *FEREM_R*) associated with E1 and E2 intrusions at 1000 yr into the lower waste panel for sample elements 14 and 40 of replicate R1.

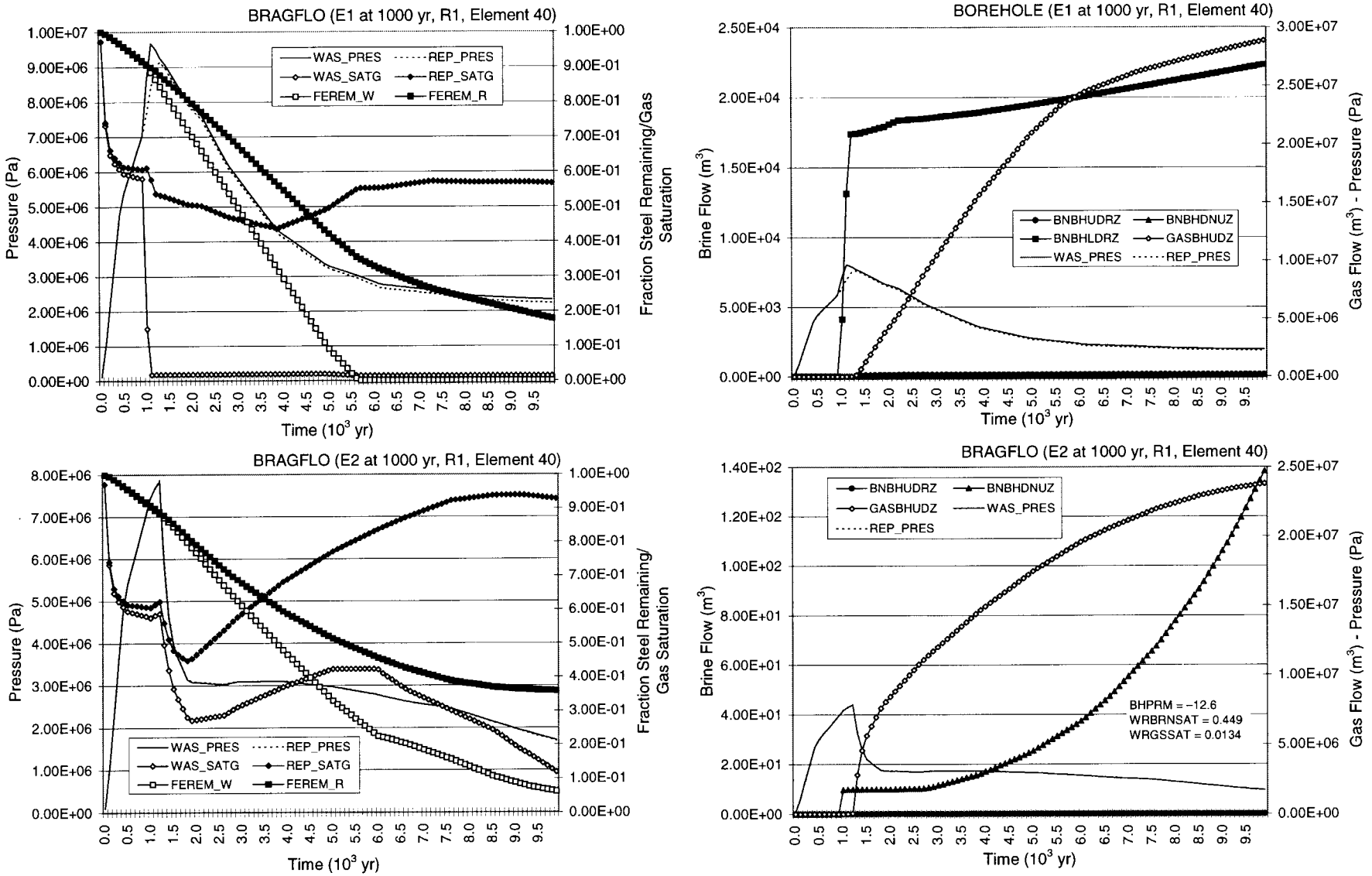

Fig. 8.6.8 Repository pressure (*WAS_PRES*, *REP_PRES*), brine and gas flows in intruding boreholes (*BNBHUDRZ*, *BNBHDNUZ*, *BNBHLDRZ*, *GASBHUDZ*), gas saturation (*WAS_SATG*, *REP_SATG*), and fraction of steel remaining (*FEREM_W*, *FEREM_R*) associated with E1 and E2 intrusions at 1000 yr into the lower waste panel for sample elements 14 and 40 of replicate R1. (Continued)

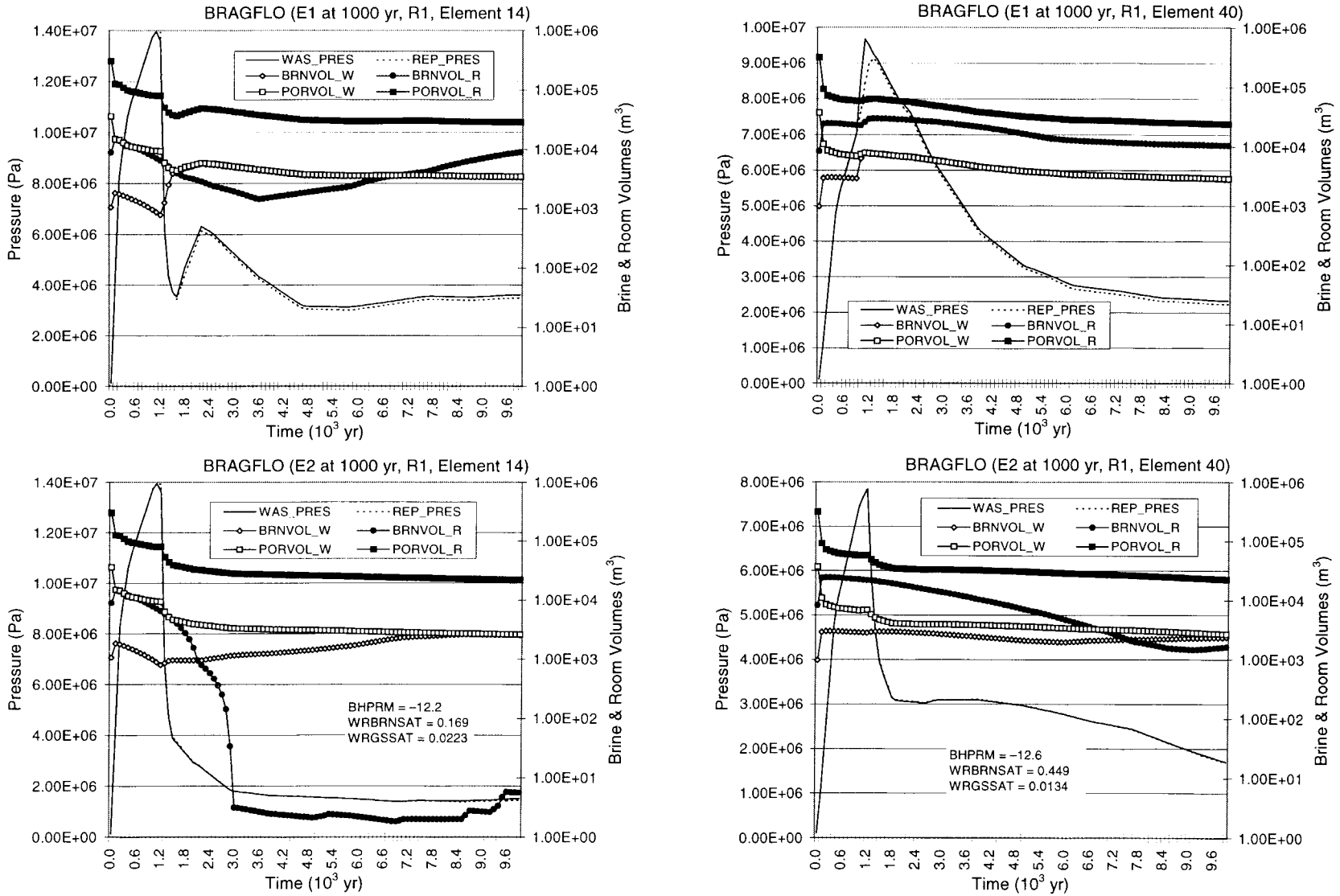

Fig. 8.6.9 Repository pressure (*REP_PRES*, *WAS_PRES*), pore volume (*PORVOL_R*, *PORVOL_W*) and brine volume (*BRNVOL_R*, *BRNVOL_W*) in upper and lower waste panels associated with E1 and E2 intrusions at 1000 yr into the lower waste panel for sample elements 14 and 40 of replicate R1.

Table 8.6.3. Summary Discussion of Plots in Fig. 8.6.8 for Repository Pressure (*WAS_PRES*, *REP_PRES*), Brine and Gas Flows in Intruding Boreholes (*BNBHUDRZ*, *BNBHDNUZ*, *BNBHLDRZ*, *GASBHUDZ*), Gas Saturation (*WAS_SATG*, *REP_SATG*), and Fraction of Steel Remaining (*FEREM_W*, *FEREM_R*) Associated with E1 and E2 Intrusions at 1000 yr Into the Lower Waste Panel for Sample Elements 14 and 40 of Replicate R1

Sample Element 14
E1 Intrusion: Rapid gas flow up borehole (*GASBHUDZ*) occurs after borehole plugs fail at 1200 yr, with result that repository pressure (*REP_PRES*, *WAS_PRES*) drops rapidly. No brine flow from brine pocket to repository (*BNBHLDRZ*) occurs between 1000 and 1200 yr when open borehole exists between brine pocket and repository due to high repository pressure (~1.4×10^7 Pa). As repository pressure decreases after 1200 yr, brine flows rapidly from the brine pocket to the repository, with a reduced flow rate after 2200 yr due to decreased borehole permeability (Table 4.2.8). Due to gas outflow and brine inflow, gas saturation in the lower (i.e., intruded) waste panel (*WAS_SATG*) drops rapidly to residual gas saturation (*WRGSSAT* = 2.23×10^{-2}), with the large amount of brine present resulting in complete corrosion of the steel in the lower waste panel (*FEREM_W*) by ~5800 yr. The upper waste panels receive less brine on a unit volume basis than the lower waste panel, with the result that gas saturation (*REP_SATG*) remains high and complete corrosion of the steel inventory (*FEREM_R*) does not occur.
E2 Intrusion: After borehole plugs fail at 1200 yr, rapid gas flow up the borehole (*GASBHUDZ*) takes place, pressure in the repository (*REP_PRES*, *WAS_PRES*) drops rapidly, and brine flow down the borehole (*BNBHUDRZ*) begins. Gas saturation in lower waste panel (*WAS_SATG*) decreases more slowly than for the E1 intrusion due to the absence of brine inflow from the brine pocket, with both residual gas saturation being reached and complete consumption of steel (*FEREM_W*) taking place by ~9500 yr. After ~3000 yr, gas saturation in the upper waste panels (*REP_SATB*) is ~1.0, although the continued decrease in the steel inventory (*FEREM_R*) indicates that some brine is flowing into the upper waste panels and then being immediately consumed in the corrosion of steel.
Sample Element 40
E1 Intrusion: Small spike in pressure in lower (i.e., intruded) waste panel (*WAS_PRES*) occurs between 1000 and 1200 yr, with repository pressure (*REP_PRES*, *WAS_PRES*) slowly decreasing after the borehole plugs fail at 1200 yr. Brine flows rapidly from the brine pocket to the repository (*BNBHLDRZ*) between 1000 and 1200 yr, with reduced rates of flow between 1200 and 2200 yr and after 2200 yr. Flow of brine from brine pocket to repository between 1000 and 1200 yr causes gas saturation in lower waste panel (*WAS_SATG*) to rapidly drop to residual gas saturation (*WRGSSAT* = 1.34×10^{-2}). Gas flow out of the repository (*GASBHUDZ*) begins at ~1500 yr and continues at a constant rate until ~5700 yr, at which time the flow rate is reduced due to complete corrosion of the steel in the lower waste panel (*FEREM_W*) and a reduction in the rate of corrosion in the upper waste panels (*FEREM_R*). Unlike the lower waste panel, gas saturation in the upper waste panels (*REP_SATG*) does not approach residual gas saturation and all steel (*FEREM_R*) is not consumed by corrosion.
E2 Intrusion: Pressure in repository (*REP_PRES*, *WAS_PRES*) drops more sharply after the borehole seals fail than is the case for the E1 intrusion; thus, brine flow from the brine pocket is reducing the rate of pressure decrease in the repository for the E1 intrusion. Unlike the E1 intrusion, gas saturation in the lower waste panel (*WAS_SATG*) does not reach residual gas saturation and all steel in the lower waste panel (*FEREM_R*) is not consumed by corrosion, although the trend is towards residual gas saturation and consumption of all steel. Further, gas saturation (*REP_SATG*) and fraction of steel remaining (*FEREM_R*) in the upper waste panels are higher for the E2 than the E1 intrusion due to the absence of brine flow from the brine pocket (*BNBHLDRZ*).

8.7 Disturbed Conditions: Brine and Gas Flow into Marker Beds for E1 and E2 Intrusions

Very little gas and brine flow takes place into the marker beds subsequent to a drilling intrusion due to the reduced pressures in the repository (Sect. 8.4). As a single example, the brine and gas flows into and out of the marker beds for an E1 intrusion are shown in Fig. 8.7.1. Prior to the failure of the borehole plugs at 1200 yr, gas and brine flow from the repository into the marker beds. After the plugs fail and the pressure in the repository drops, the flows reverse, with gas and brine now flowing from the marker beds to the repository. A detailed representation of the flows into and out of the individual marker beds is given in Fig. 8.7.2, with the brine flows primarily associated with Marker Bed 139 and the gas flows primarily associated with Marker Bed 138 and Anhydrite A and B.

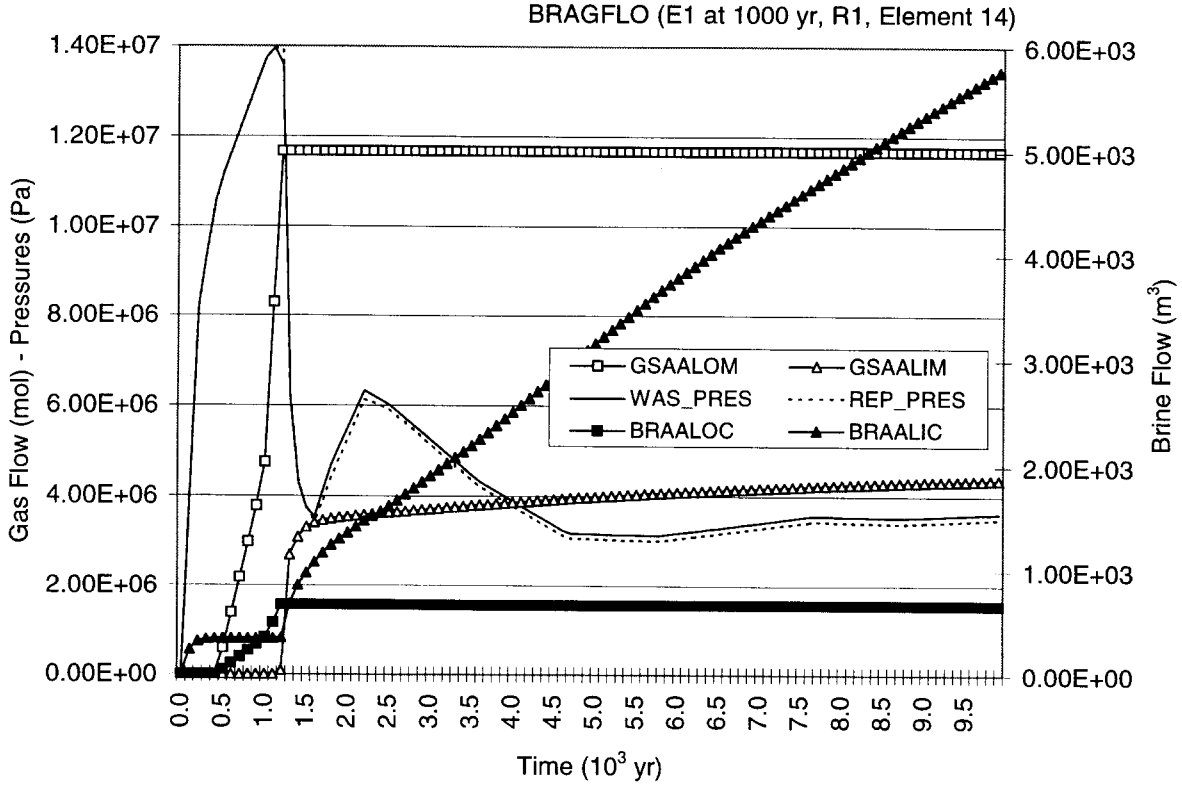

Fig. 8.7.1 Pressure (*REP_PRES*, *WAS_PRES*), brine flow from marker beds to repository (*BRAALIC*), brine flow from repository to marker beds (*BRAALOC*), gas flow from marker beds to repository (*GSAALIM*), and gas flow from repository to marker beds (*GSAALOM*) for an E1 intrusion at 1000 yr into the lower waste panel and sample element 14 of replicate R1; the corresponding E2 intrusion produces similar results.

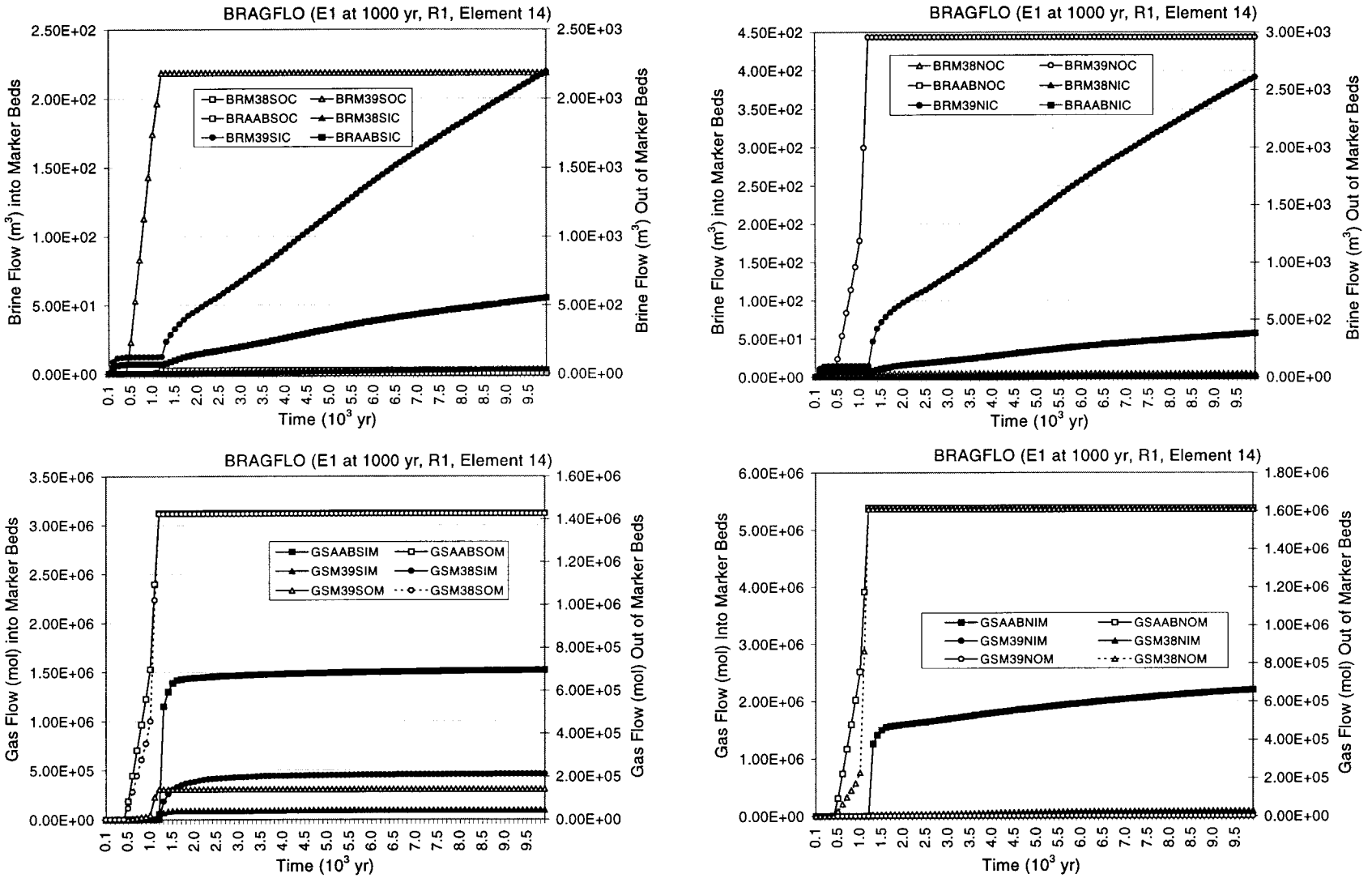

Fig. 8.7.2 Brine flow from marker beds to repository (*BRM38NIC*, *BRM39NIC*, *BRAABNIC*, *BRM38SIC*, *BRM39SIC*, *BRAABSIC*), brine flow from repository to marker beds (*BRM38NOC*, *BRM39NOC*, *BRAABNOC*, *BRM38SOC*, *BRM39SOC*, *BRAABSOC*), gas flow from marker beds to repository (*GSM38NOM*, *GSM39NOM*, *GSAABNOM*, *GSM38SOM*, *GSM39SOM*, *GSAABSOM*) and gas flow from repository to marker beds (*GSM38NIM*, *GSM39NIM*, *GSAABNIM*, *GSM38SIM*, *GSM39SIM*, *GSAABSIM*) for an E1 intrusion at 1000 yr into the lower waste panel and sample element 14 of replicate R1.

8.8 Disturbed Conditions: Behavior of Brine Pocket for E1 Intrusions

As discussed in Sect. 8.2, brine flow from a region of pressurized brine (i.e., a brine pocket) is an important potential source of brine to the repository for E1 intrusions. The behavior of a brine pocket subsequent to a drilling intrusion is now considered in more detail.

The pressure behavior of the brine pocket is quite dynamic subsequent to a drilling intrusion (Fig. 8.8.1). For 200 yr after the intrusion, an open borehole (i.e., permeability of 10^{-9} m^2) is assumed to exist between the brine pocket and the repository and an impermeable plug is assumed to exist at the Rustler/Salado interface (Table 4.2.8). This results in rapid changes of pressure in both the brine pocket and the repository (Figs. 8.4.1, 8.8.1). During this period, the pressure in the repository typically increases (Fig. 8.4.3) and the pressure in the brine pocket decreases (Figs. 8.8.1, 8.8.2). These changes in pressure tend to be accompanied by a surge of brine from the brine pocket to the repository (Fig. 8.2.7), with these surges resulting in a corresponding decrease in the volume of brine contained in the brine pocket (Fig. 8.8.1). Typically, most of the brine flow out of the brine pocket takes place during these initial surges (Figs. 8.2.7, 8.8.1). However, brine flow from the brine pocket to the repository will not take place when the pressure in the repository is sufficiently high relative to the pressure in the brine pocket (Fig. 8.2.8). This behavior can be seen in the higher repository pressure curves in Fig. 8.4.3, which are essentially unaffected by the penetration of the brine pocket. This stoppage of flow due to high repository pressures is why the largest brine pocket volumes in Fig. 8.8.1 show little change after penetration by a drilling intrusion.

After 200 yr, the plug at the Rustler/Salado interface is assumed to fail and the entire borehole is assigned a permeability of 10^x, $x = BHPRM$. At this point, gas can escape from the repository to overlying formations, which causes a rapid drop in repository pressure (Figs. 8.4.1, 8.4.3). From this point on, there is no longer an open borehole between the repository and the brine pocket (Table 4.2.8). Rather, this portion of the borehole is assumed to have a permeability of 10^x, $x = BHPRM$, for the next 1000 yr. This change in permeability produces a complex pattern of pressure behavior in the brine pocket, with pressure sometimes continuing to decrease as more brine flows out of the brine pocket and at other times increasing towards hydrostatic pressure due to the filling of the repository with brine and the resultant formation of a continuous brine-filled connection with overlying formations. Some sample elements that experienced no brine outflow from the brine pocket during the first 200 yr after the intrusion due to high pressures in the repository now show such outflow as a result of reduced repository pressure (Fig. 8.8.1).

After 1000 yr (i.e., 1200 yr after the drilling intrusion), the permeability in the borehole between the repository and the brine pocket is reduced from 10^x, $x = BHPRM$, to 10^x, $x = BHPRM - 1$ (i.e., permeability is reduced by an order of magnitude), which tends to reduce brine flow from the brine pocket to the repository (Table 4.2.8). This effect can be seen in the decreased slope of some of the brine pocket volume curves at 2200 yr (Fig. 8.8.1). However, many sample elements show little, if any, change in brine pocket volume after the initial brine outflow immediately after the drilling intrusion.

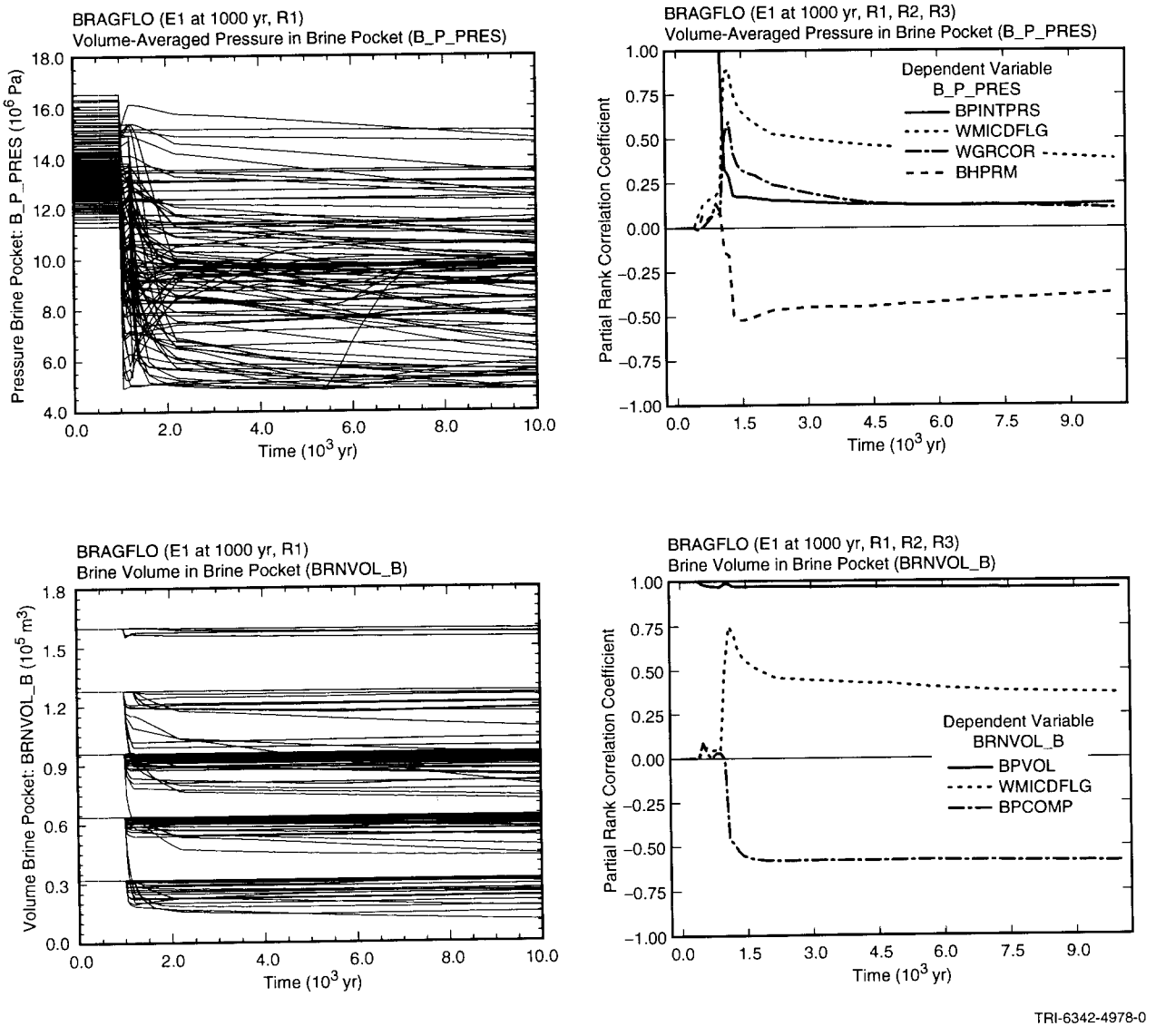

Fig. 8.8.1. Uncertainty and sensitivity analysis results for pressure (*B_P_PRES*) and brine volume (*BRNVOL_B*) in brine pocket for an E1 intrusion at 1000 yr into lower waste panel.

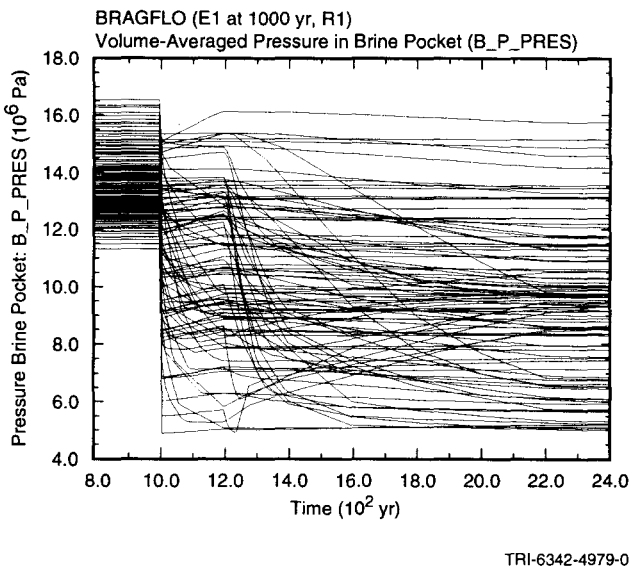

Fig. 8.8.2. Pressure in brine pocket (*B_P_PRES*) for an E1 intrusion at 1000 yr into lower waste panel (enlargement of pressure results in Fig. 8.8.1 from 800 to 2400 yr).

Before the intrusion at 1000 yr, brine pressure is completely dominated by *BPINTPRS*, which has a PRCC of 1 (Fig. 8.8.1). Immediately after the intrusion, positive effects are indicated for *WMICDFLG* and *WGRCOR*. Both of these variables tend to increase repository pressure at 1000 yr (Fig. 8.4.1, Table 8.4.1) and thus reduce brine flow from, and thus pressure change in, the brine pocket. After 1000 yr, the initial pressure *BPINTPRS* has little effect on brine pocket pressure; thus, the brine pocket tends to rapidly "forget" its initial pressure conditions. The importance of *WMICDFLG* and *WGRCOR* also rapidly decreases after failure of the plug at the Rustler/Salado interface allows gas to flow out of the repository. The variable with the largest PRCC at later times is *BHPRM*. The negative effect indicated for *BHPRM* indicates that brine pocket pressure tends to decrease as *BHPRM* increases. However, the effect is rather weak as the PRCC is mostly less than 0.5 in absolute value. As will be discussed later, the underlying relationship between *BHPRM* and brine pocket pressure is too complex to be adequately captured by a PRCC.

The stepwise regression analysis in Table 8.8.1 for pressure at 10,000 yr provides an alternate analysis of the variables affecting brine pocket pressure subsequent to a drilling intrusion. The first variable selected in the regression analysis is *BPCOMP*, with pressure tending to increase as *BPCOMP* increases. This positive relationship between *BPCOMP* and pressure results because increasing *BPCOMP* increases the amount of brine that will leave the brine pocket for a unit drop in pressure. As a result, larger values for *BPCOMP* produce a given quantity of brine with a smaller drop in brine pocket pressure than smaller values for *BPCOMP*. Although *BPCOMP* by itself produces a regression model with an R^2 value of only 0.20, the positive relationship between *BPCOMP* and pressure

Table 8.8.1. Stepwise Regression Analyses with Rank-Transformed Data for Pressure (*B_P_PRES*) and Brine Volume (*BRNVOL_B*) Associated with a Pressurized Brine Pocket at 10,000 yr for an E1 Intrusion at 1000 yr into Lower Waste Panel

	Pressure			Volume		
Step[a]	Variable[b]	SRRC[c]	R^{2d}	Variable	SRRC	R^2
1	*BPCOMP*	0.43	0.20	*BPVOL*	0.92	0.82
2	*WMICDFLG*	0.31	0.30	*BPCOMP*	−0.29	0.90
3	*BHPRM*	−0.27	0.37	*WMICDFLG*	0.11	0.91
4	*BPVOL*	0.24	0.42	*BHPRM*	−0.07	0.92
5	*HALPRM*	0.15	0.44	*BPINTPRS*	−0.06	0.92
6				*WASTWICK*	0.05	0.92
7				*ANHPRM*	0.04	0.93

[a] Steps in stepwise regression analysis.

[b] Variables listed in order of selection in regression analysis with *ANHCOMP* and *HALCOMP* excluded from entry into regression model.

[c] Standardized rank regression coefficients in final regression model.

[d] Cumulative R^2 value with entry of each variable into regression model.

can be clearly seen in the corresponding scatterplot (Fig. 8.8.3). However, this effect is not large enough to meet the screening criteria to appear in Fig. 8.8.1 (i.e., a PRCC with an absolute value of at least 0.5 at some point in time). After *BPCOMP*, the regression analysis selects *WMICDFLG* with a negative regression coefficient. As previously discussed, this effect results from the role of *WMICDFLG* in suppressing flow from the brine pocket in the first 200 yr after the drilling intrusion. The negative effect associated with *WMICDFLG* can be seen in the corresponding scatterplot (Fig. 8.8.3). The next variable selected in the regression analysis is *BHPRM*, with the pressure tending to decrease as *BHPRM* increases. This is consistent with the general pattern shown by the scatterplot in Fig. 8.8.3. However, the overall pattern is more complex than simply some noise around an overall linear trend. In particular, the largest values of *BHPRM* have brine pocket pressures in the vicinity of 1×10^7 Pa, which corresponds to hydrostatic pressure. Analogous behavior was observed for repository pressure, with this pressure tending to hydrostatic pressure for the largest values of *BHPRM* due to the establishment of a continuous brine connection with overlying formations (Fig. 8.4.5). This complex pattern of behavior is why *BHPRM* appears in Fig. 8.8.1 with a negative but rather small PRCC. The last two variables selected in the regression analysis are *BPVOL* and *HALPRM*, with pressure tending to increase as each of these variables increases. The positive effect for *BPVOL* results because larger brine pockets will tend to depressurize more slowly than smaller brine pockets and can be barely discerned in the corresponding scatterplot (Fig. 8.8.3). The reason for the positive effect associated with *HALPRM* is not apparent and cannot be discerned in the corresponding scatterplot (not shown).

Overall, neither the PRCC analysis in Fig. 8.8.1 nor the stepwise regression analysis in Table 8.8.1 for brine pocket pressure is particularly good. The underlying reason is that the relationships between pressure and the sampled variables are too complex to be captured by the linear models that underlie these techniques. In particular, a complex, nonmonotonic relationship exists between pressure and *BHPRM* (Fig. 8.8.3). Similar relationships were encountered in the analysis of repository pressure subsequent to E1 and E2 intrusions (Fig. 8.4.5).

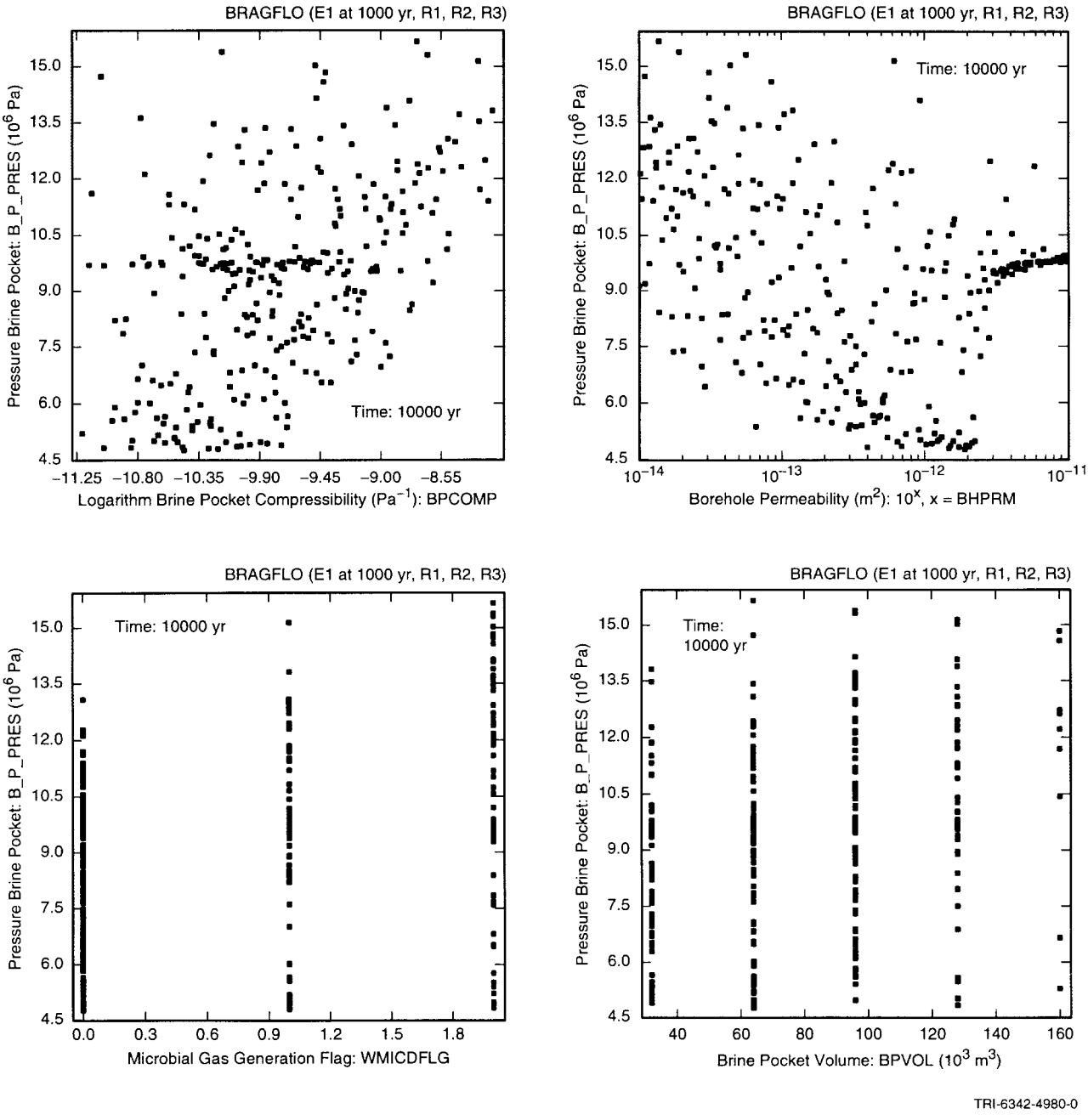

Fig. 8.8.3. Scatterplots for brine pocket pressure (*B_P_PRES*) at 10,000 yr versus *BPCOMP*, *BHPRM*, *WMICDFLG* and *BPVOL* for an E1 intrusion at 1000 yr into lower waste panel.

The dominant variable with respect to brine volume in the brine pocket is *BPVOL* (Fig. 8.8.1), which is consistent with the rather small changes in brine pocket volume subsequent to a drilling intrusion. Specifically, the changes in volume due to brine outflow are typically smaller than the differences in initial volumes defined by *BPVOL*. A positive effect is indicated for *WMICDFLG*, which results from its previously discussed role in suppressing outflow from the brine pocket in the first 200 yr after the drilling intrusion. A negative effect is also indicated for *BPCOMP* and results because increasing *BPCOMP* increases the amount of brine that flows out of the brine pocket for a given drop in pressure. The regression analysis for brine volume is quite successful (Table 8.8.1). The initial volume *BPVOL* produces a regression model with an R^2 value of 0.82, which is consistent with its large PRCC (Fig. 8.8.1). Next, *BPCOMP* is selected with a negative regression coefficient, which is again consistent with the PRCC analysis (Fig. 8.8.1). Together *BPVOL* and *BPCOMP* produce a regression model with an R^2 value of 0.90 and thus can account for most of the uncertainty in volume. After *BPVOL* and *BPCOMP*, the regression analysis selects *WMICDFLG*, *WASTWICK* and *ANHPRM* with positive regression coefficients and *BHPRM* and *BPINTPRS* with negative regression coefficients. The positive effects for *WMICDFLG*, *WASTWICK* and *ANHPRM* result from increasing pressure in the repository in the first 200 yr after the drilling intrusion and thus reducing brine flow from the brine pocket to the repository. The negative effects for *BHPRM* and *BPINTPRS* result from reducing resistance to flow in the borehole and increasing the pressure gradient between the brine pocket and the repository, respectively. However, the effects of *WMICDFLG*, *BHPRM*, *BPINTPRS*, *WASTWICK* and *ANHPRM* are small and only increase the R^2 value for the regression model from 0.90 to 0.93. For perspective, the scatterplots for *BPVOL* and *BPCOMP* are given in Fig. 8.8.4.

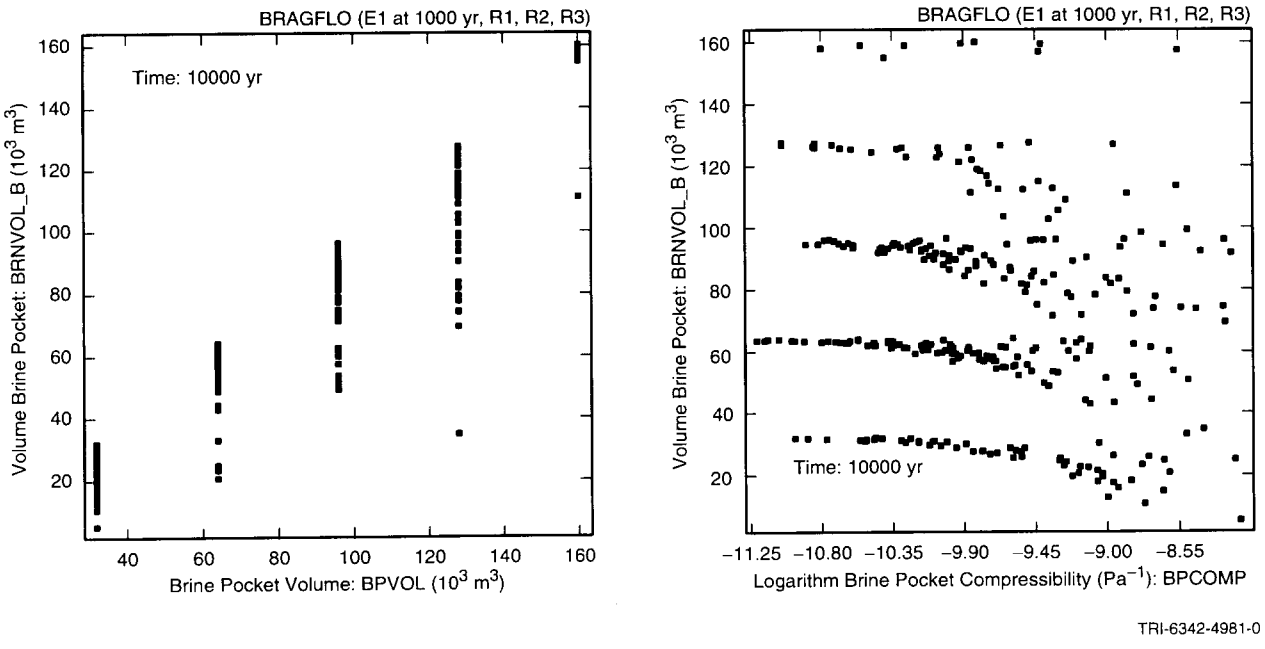

Fig. 8.8.4. Scatterplots for brine volume in pressurized brine pocket (*BRNVOL_B*) at 10,000 yr versus *BPVOL* and *BPCOMP* for an E1 intrusion at 1000 yr into lower waste panel.

8.9 Disturbed Conditions: Brine Flow in Repository and DRZ for E1 and E2 Intrusions

Under undisturbed conditions, most brine flow in the repository is from the north (i.e., updip) end to the south (i.e., downdip) end (Fig. 8.9.1). Most of this flow takes place through the panel seal and in the DRZ below the panel, with little flow taking place through the DRZ above the panel seal (Fig. 8.9.1). Very little flow takes place from the south end of the repository to the north end (Fig. 8.9.2).

For E1 and E2 intrusions into the lower waste panel, the predominant flow is still from the north to the south, with little flow taking place through the DRZ above the panel seal (Fig. 8.9.1). A sudden surge of flow from north to south takes place through the panel seal and in the DRZ below the panel seal immediately after the failure of the plugs in the borehole at 1200 yr (Fig. 8.9.2). This surge is more pronounced for the E2 than the E1 intrusion because brine flowing up from the brine pocket for the E1 intrusion (Fig. 8.2.7) tends to reduce brine movement into the lower waste panel from the north end of the repository relative to the movement that takes place in the presence of an E2 intrusion.

The E1 and E2 intrusions result in more brine flows from south to north than is the case for undisturbed conditions (Fig. 8.9.2). For E2 intrusions, these flows do not begin until after the plugs in the borehole fail at 1200 yr, which implies that much of the brine flowing from the lower waste panel to other areas in the repository and the DRZ has entered the repository by flowing down the intruding borehole (Fig. 8.2.6). For E1 intrusions, these flows often begin when the drilling intrusion occurs at 1000 yr, which implies that the sudden pulse of brine from the lower waste panel to other areas in the repository and the DRZ has entered the repository by flowing up from the brine pocket (Fig. 8.2.7).

The E1 and E2 intrusions often result in brine flow from the south to the north in the DRZ above the panel seal (Fig. 8.9.2). For the E1 intrusion, this brine often originates from the brine pocket as indicated by the surge in such flows at 1000 yr. For the E2 intrusion, this brine has flowed down the borehole and has probably been diverted through the DRZ without ever having been in contact with waste.

Sudden increases sometimes occur for cumulative brine flow from the vicinity of the lower waste panel to the rest of the repository, with these increases being particularly noticeable for the E2 intrusion at around 2000 and 6000 yr (Fig. 8.9.2). These increases are occurring when the lower waste panel becomes brine saturated due to brine flow down the borehole and undergoes an associated rapid increase in pressure (Sect. 8.4). This increased pressure then results in a pressure gradient that increases the rate at which brine flows away from the vicinity of the lower waste panel.

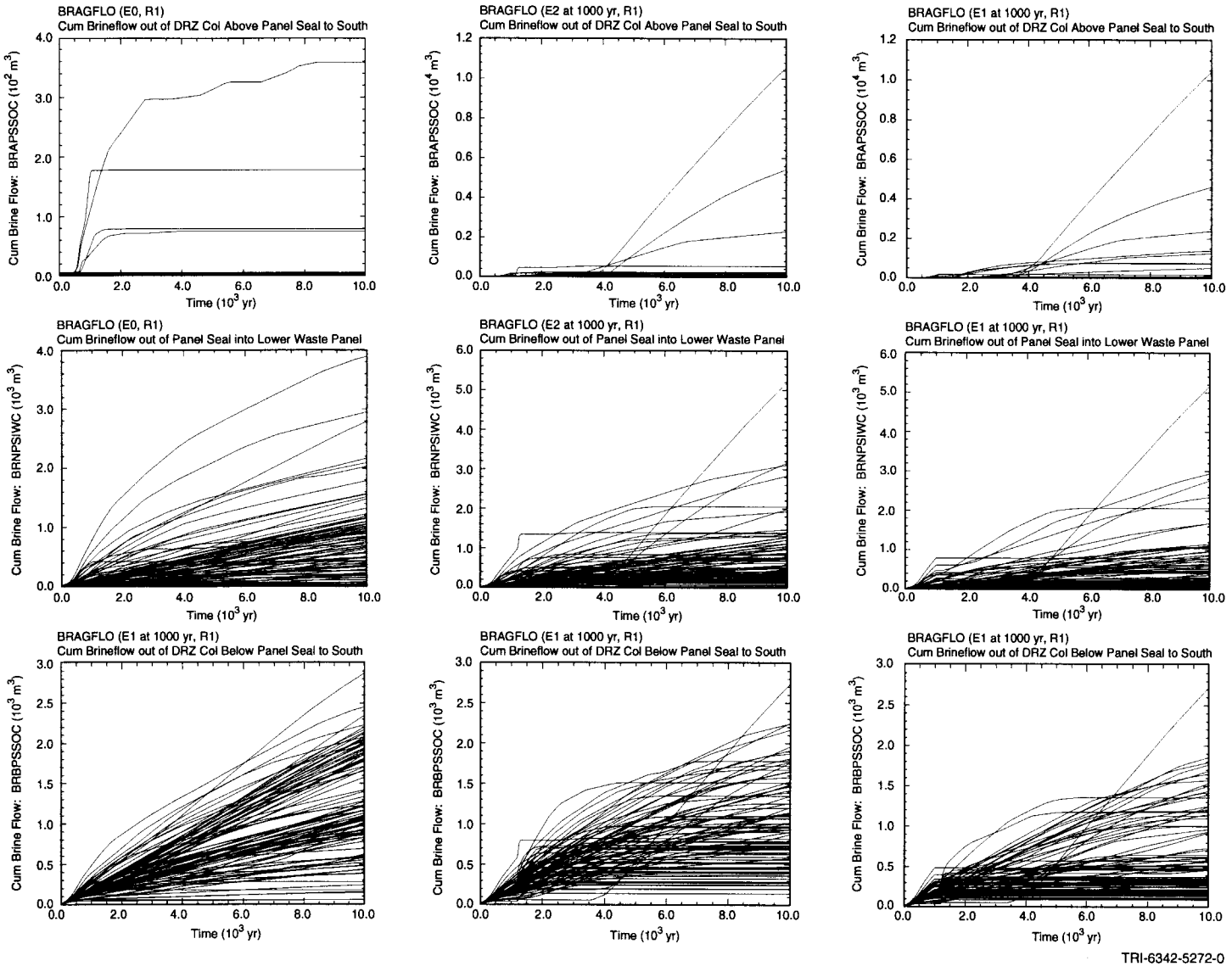

Fig. 8.9.1 Cumulative brine flow in repository and DRZ from north (i.e., updip) end of repository to south (i.e., downdip) end of repository (*BRAPSSOC*, *BRNPSIWC*, *BRBPSSOC*) for E0 (i.e., undisturbed) conditions (left column), an E2 intrusion at 1000 yr into the lower waste panel (middle column), and an E1 intrusion at 1000 yr into the lower waste panel (right column).

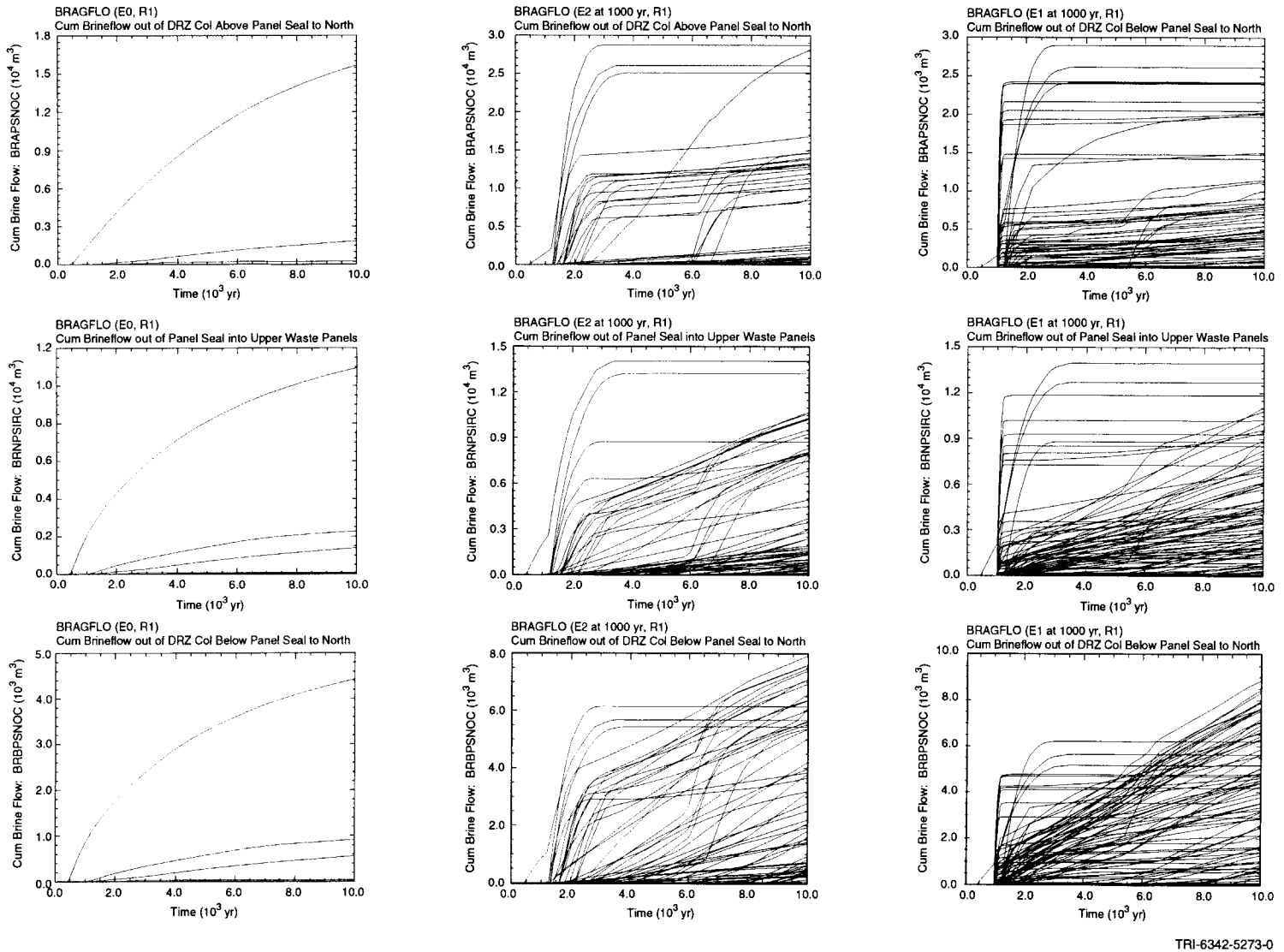

Fig. 8.9.2 Cumulative brine flow in repository and DRZ from south (i.e., downdip) end of repository to north (i.e., updip) end of repository (*BRAPSNOC*, *BRNPSIRC*, *BRBPSNOC*) for E0 (i.e., undisturbed) conditions (left column), an E2 intrusion at 1000 yr into the lower waste panel (middle column), and an E1 intrusion at 1000 yr into the lower waste panel (right column).

8.10 Disturbed Conditions: E2E1 Intrusions

Thus far, this chapter has focused on E1 and E2 intrusions. Calculations were also performed for E2E1 intrusions, with the E2 intrusion occurring at 800 yr and the E1 intrusion occurring at 2000 yr (Table 8.10.1). This calculation was performed with the same computational grid used for E1 and E2 intrusions (Figs. 4.2.1 - 4.2.3), which required use of the same computational cells to represent both drilling intrusions (i.e., region 1 in Fig. 4.2.1). This dual usage was accomplished through the definition of appropriate time-dependent borehole permeabilities (Table 8.10.1).

Table 8.10.1. Permeabilities Used with BRAGFLO Calculations for E2E1 Intrusions with the E2 Intrusion Occurring at 800 yr and the E1 Intrusion Occurring at 2000 yr

Time	Assigned Permeabilities
800 - 1000 yr	Concrete plugs assumed to be emplaced at the Santa Rosa Fm (i.e., a surface plug with a length of 15.76 m; corresponds to Cells 905, 937 in Fig. 4.2.3) and the Unnamed Mbr of the Rustler Fm (i.e., a plug at top of Salado Fm with a length of 36 m; corresponds to Cell 681 in Fig. 4.2.3). Concrete plugs assumed to have a permeability of $k = 5 \times 10^{-17}$ m^2; remainder of borehole (i.e., to bottom of DRZ) assumed to have a permeability of 1×10^{-9} m^2.
1000 - 2000 yr	Concrete plugs are assumed to fail after 200 yr (U.S. DOE 1995b) and entire borehole is assigned a permeability typical of silty sand, i.e., $k = 10^x$ m^2, $x = BHPRM$, where $BHPRM$ is an uncertain input to the analysis (see Sect. 5.2).
2000 - 2200 yr	Permeability above repository left at $k = 10^x$, $x = BHPRM$, and corresponds to permeability in borehole associated with original E2 intrusion. Permeability below repository set to 1×10^{-9} m^2 and corresponds to permeability in borehole associated with E1 intrusion at 2000 yr. Concrete plugs emplaced at the Santa Rosa Fm and the Unnamed Mbr of the Rustler Fm are assumed to prevent flow above the repository in the borehole associated with the E1 intrusion.
2200 - 3200 yr	Permeability above repository set to $k = 2 \bullet 10^x$, $x = BHPRM$, to incorporate effects of both boreholes after failure of concrete plugs at 2200 yr in borehole associated with E1 intrusion. Permeability below repository set to $k = 10^x$, $x = BHPRM$, to incorporate effects of E1 intrusion.
> 3200 yr	Permeability reduced by one order of magnitude in Salado Fm beneath repository due to creep closure of borehole (Thompson et al. 1996) (i.e., $k = 10^x/10$, $x = BHPRM$, in Cells 1010, 985, 12, 45, 78 of Fig. 4.2.3). No changes are made within and above the lower DRZ.

Overall, the results obtained for the E2E1 intrusion are similar to the results obtained for E1 and E2 intrusions. For example, total brine flow into the repository for the E2E1 intrusion (Fig. 8.10.1) shows a pattern that is a composite of the patterns shown for E1 and E2 intrusions (Fig. 8.2.5). Specifically, the E2 intrusion results in substantial brine flows down the intruding borehole for a few sample elements, which can be seen in the increased flows between 1000 and 2000 yr in Fig. 8.10.1 for those sample elements; a similar pattern can be seen in Fig. 8.2.5 for the E2 intrusion. Then, a sharp jump in cumulative inflow for the E2E1 intrusion occurs at 2000 yr due to flow from the brine pocket; again, the same pattern can be seen in Fig. 8.2.5 for the E1 intrusion. Overall, the surge in inflow at the time of the E1 intrusion for an E2E1 event is somewhat larger than the surge for an isolated E1 (Figs. 8.2.5, 8.2.7, 8.10.1). This behavior occurs because the initial E2 intrusion reduces pressure in the repository and thus results in less resistance to flow from the brine pocket to the repository during the 200 yr period that an open borehole (i.e., permeability of 1×10^{-9} m^2) connects the repository and the brine pocket. Most brine flow from the brine pocket to the repository takes place during this 200 yr interval (Figs. 8.2.5, 8.2.7, 8.10.1). Brine flow down the intruding borehole and into the repository is similar for E1, E2 and E2E1 intrusions (Figs. 8.2.6, 8.10.1).

Total gas generation is similar for E1, E2 and E2E1 intrusions (Figs. 8.3.5, 8.10.2). The microbial gas generation is essentially the same for all cases, with most of the cellulose inventory being consumed in the first 1000 yr (Figs. 7.3.1, 7.3.2). The E2E1 intrusion produces somewhat more gas due to corrosion (Figs. 8.3.5, 8.10.2) owing to the slightly greater inflows of brine from the brine pocket as discussed in the preceding paragraph.

Due to its influence on spallings and direct brine releases, repository pressure is one of the most important results calculated by BRAGFLO. As might be anticipated, repository pressure for E2E1 intrusions displays a pattern similar to that already observed for E1 and E2 intrusions (Figs. 8.4.1, 8.10.3). Specifically, pressure drops rapidly at the time of failure for the borehole plugs associated with the initial E2 intrusion (i.e., at 1000 yr); then, a sudden rise in pressure occurs at the time of the subsequent E1 intrusion (i.e., at 2000 yr). After the E1 intrusion, repository pressure is controlled almost entirely by borehole permeability (i.e., $k = 10^x$, $x = BHPRM$) (Fig. 8.4.5).

Due to its influence on direct brine releases, repository brine saturation is another important result calculated by BRAGFLO. Again, the brine saturation results for E2E1 intrusions are similar to those observed for E1 and E2 intrusions (Figs. 8.5.1, 8.5.2, 8.10.4). In particular, brine saturation starts rising after the E2 intrusion and then shows a sharp jump after the E1 intrusion (Fig. 8.10.4). This behavior is particularly pronounced in the lower (i.e., intruded) waste panel, which often reaches full brine saturation as indicated by the horizontal brine saturation curves. In contrast, the upper (i.e., unintruded) waste panels typically remain substantially below full brine saturation.

Brine volume in the repository is a potentially important variable because it influences the amount of radionuclides that can be dissolved in brine. Again, E1, E2 and E2E1 intrusions display similar brine volume patterns (Figs. 8.5.5, 8.5.6, 8.10.5). The brine volume tends to increase after an intrusion, with this effect being

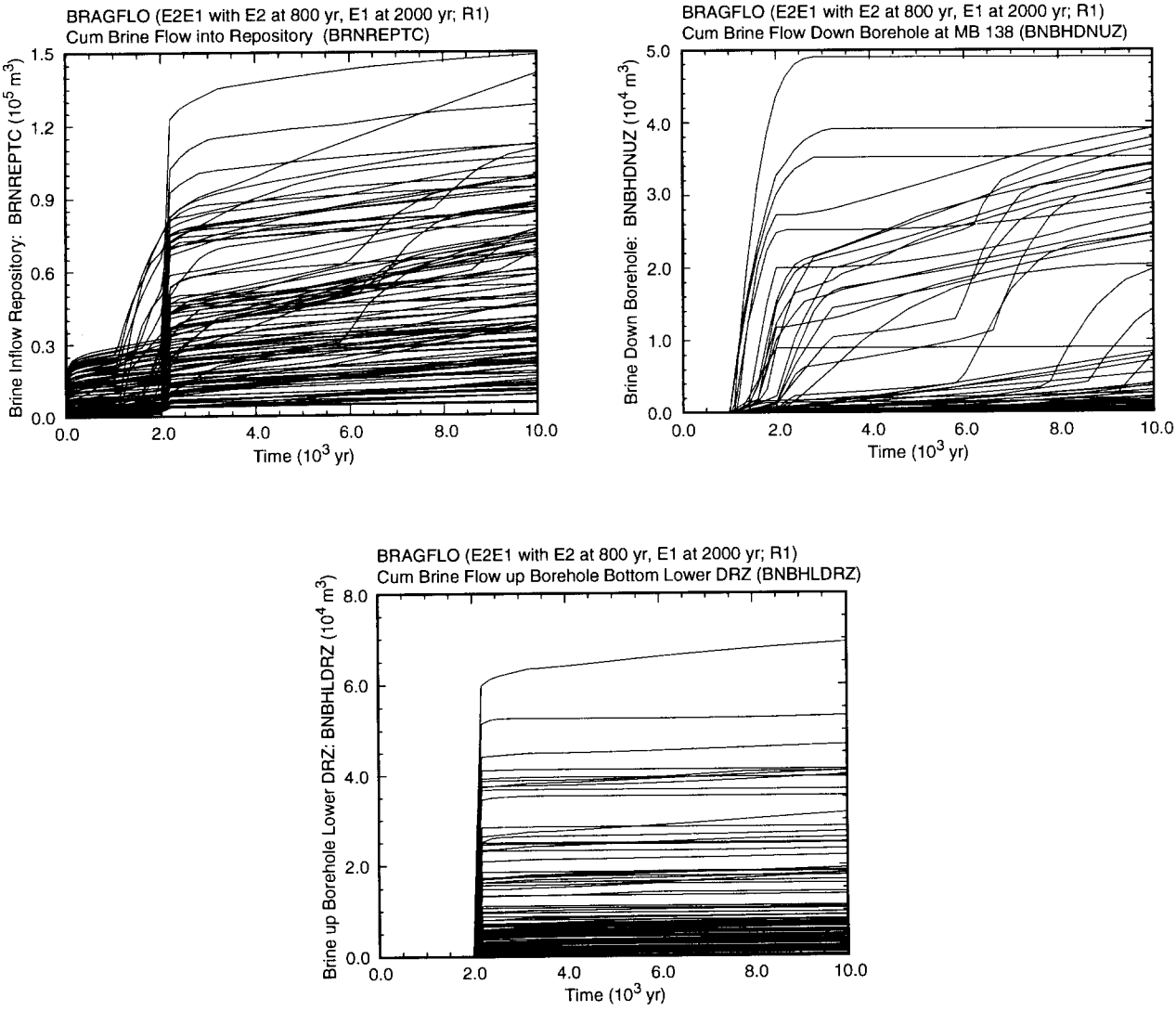

Fig. 8.10.1. Cumulative brine flow into repository (*BRNREPTC*), cumulative brine flow down intruding boreholes (*BNBHDNUZ*), and cumulative brine flow into bottom of DRZ from brine pocket (*BNBHLDRZ*) for an E2E1 intrusion into lower waste panel with the E2 intrusion at 800 yr and the E1 intrusion at 2000 yr.

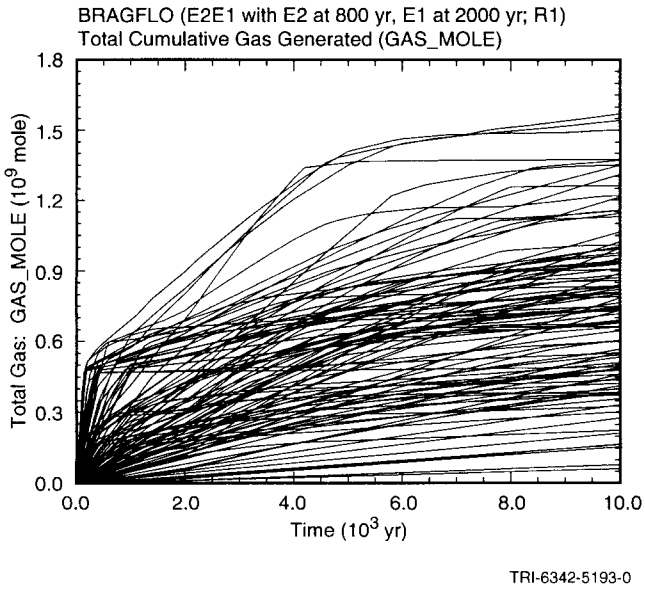

Fig. 8.10.2. Cumulative gas generation due to corrosion and microbial degradation (*GAS_MOLE*) for an E2E1 intrusion into lower waste panel with the E2 intrusion at 800 yr and the E1 intrusion at 2000 yr.

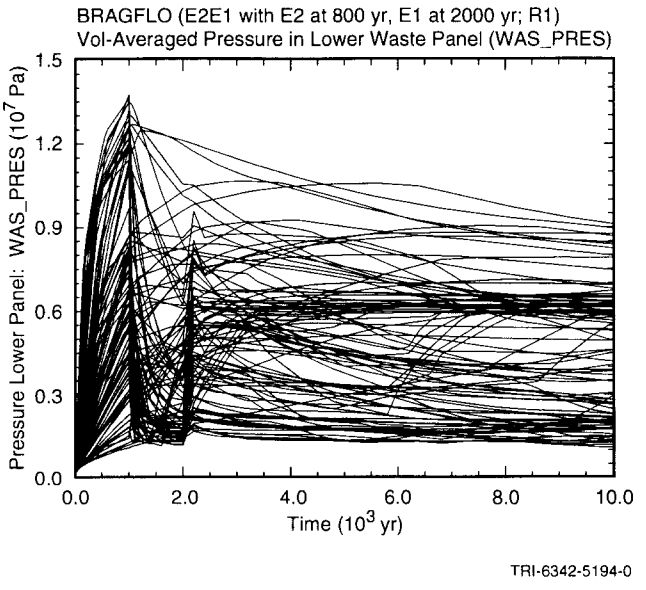

Fig. 8.10.3. Repository pressure (*WAS_PRES*) for an E2E1 intrusion into lower waste panel with the E2 intrusion at 800 yr and the E1 intrusion at 2000 yr.

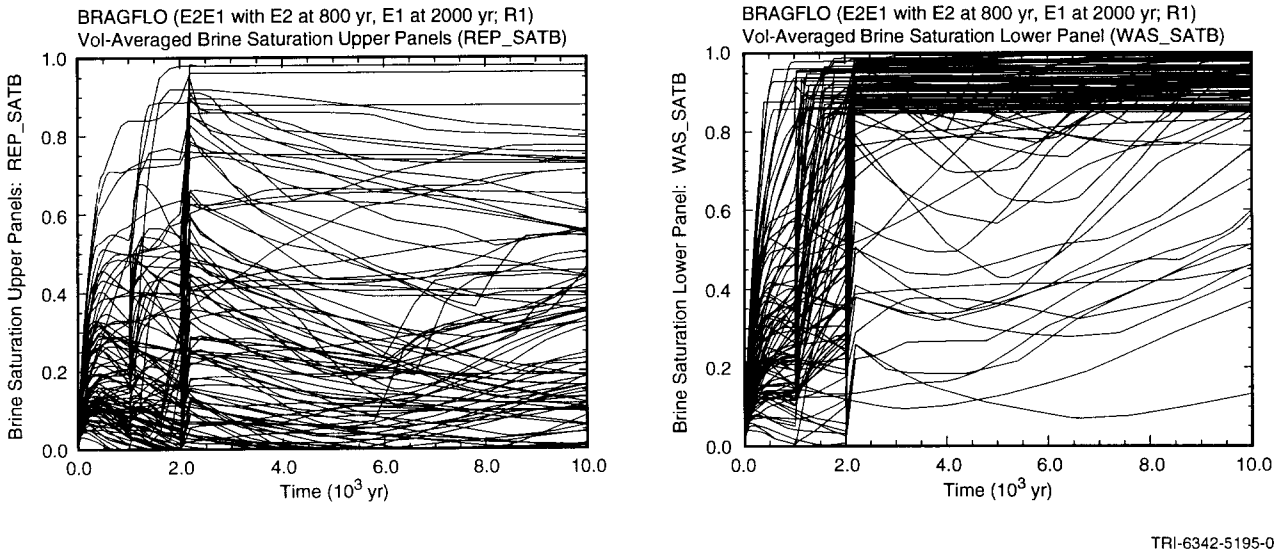

Fig. 8.10.4. Brine saturation in upper (*REP_SATB*) and lower (*WAS_SATB*) waste panels for an E2E1 intrusion into lower waste panel with the E2 intrusion at 800 yr and the E1 intrusion at 2000 yr.

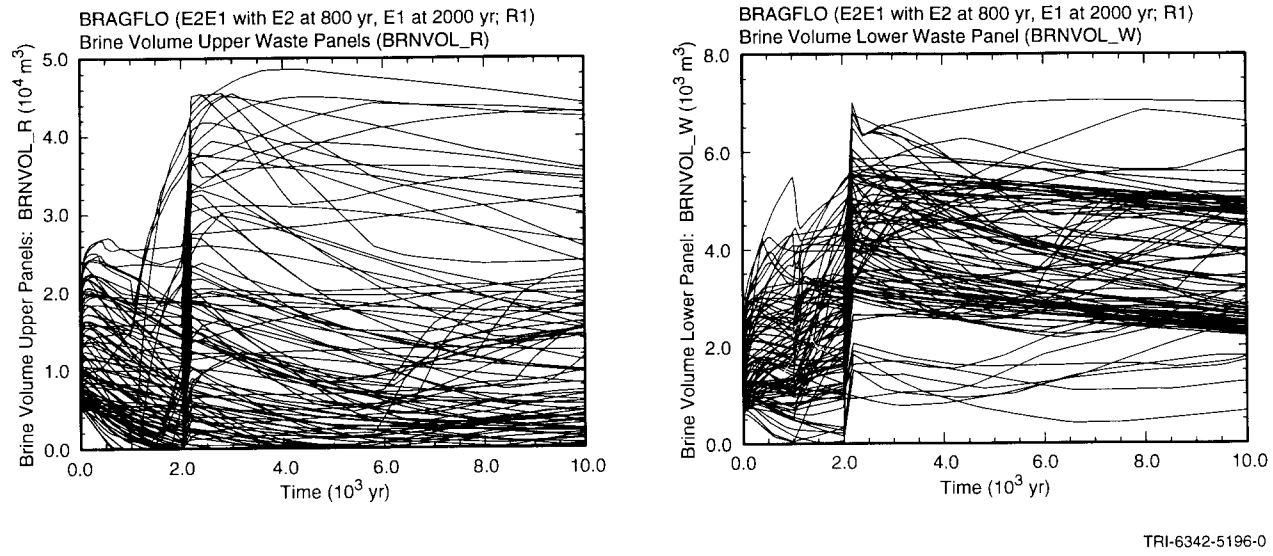

Fig. 8.10.5. Brine volume in upper (*BRNVOL_R*) and lower (*BRNVOL_W*) waste panels for an E2E1 intrusion into lower waste panel with the E2 intrusion at 800 yr and the E1 intrusion at 2000 yr.

more pronounced in the lower (i.e., intruded) waste panel than in the upper (i.e., unintruded) waste panels and also more pronounced subsequent to an E1 intrusion. The brine volumes subsequent to an isolated E1 intrusion (Fig. 8.5.6) are very similar to those subsequent to an E1 intrusion associated with an E2E1 intrusion (Fig. 8.10.5). The brine volumes in the intruded waste panel are almost entirely controlled by borehole permeability (i.e., $k = 10^x$, $x =$ *BHPRM*) (Figs. 8.5.7, 8.5.9) and are very closed linked to repository pressure (Fig. 8.5.8), which is also controlled by *BHPRM* (Fig. 8.4.5).

Brine flow up an intruding borehole is the primary mechanism by which radionuclides can be released from the repository to the Culebra Dolomite. These releases are similar for an isolated E1 intrusion and an E1 intrusion subsequent to an E2 intrusion in the same waste panel (Figs. 8.6.3, 8.10.6), although the degree of similarity will be at least partially influenced by the timing of the individual intrusions. However, the preceding E2 intrusion does not radically change the character of the brine flows associated with a subsequent E1 intrusion. In particular, most of the modeled E2E1 intrusions result in no meaningful brine flows from the repository to the Culebra, as is also the case for E1 intrusions (Figs. 8.6.3, 8.10.6). Several of the larger brine releases are actually coming from brine outflow from the anhydrite marker beds (Fig. 8.6.3).

The behavior of the brine pocket for an E1 intrusion and an E2E1 intrusion are similar, although there are some observable differences (Figs. 8.8.1, 8.10.7). For the E2E1 intrusion, the repository is at lower pressure at the time of the E1 intrusion than is the case for an isolated E1 intrusion, with the result that there is less resistance to brine flow from the brine pocket to the repository. This lessened resistance results in more rapid and greater decreases in brine pocket pressure for the E2E1 intrusion than is the case for an isolated E1 intrusion (Figs. 8.8.1, 8.10.7). Also, the lessened resistance results in greater decreases in brine pocket volume for E2E1 intrusions than for isolated E1 intrusions (Figs. 8.8.1, 8.10.7). In particular, some sample elements that show little or no decrease in brine pocket volume for an isolated E1 intrusion show a substantial decrease for an E2E1 intrusion (Figs. 8.8.1, 8.10.7).

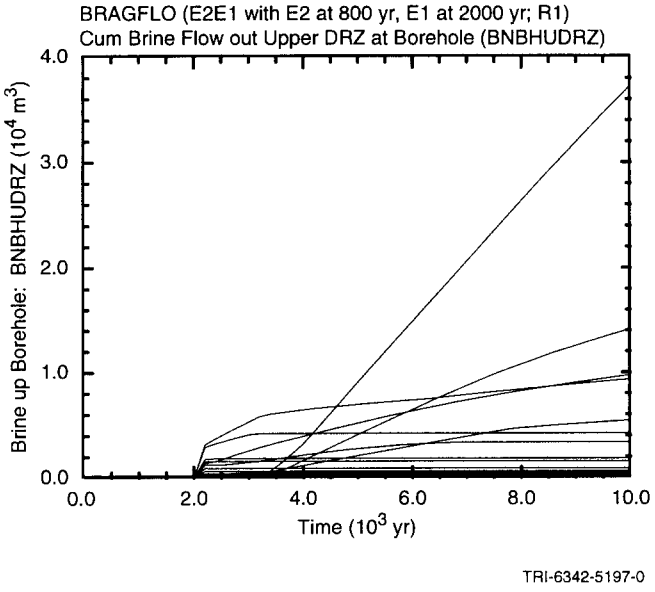

Fig. 8.10.6. Cumulative brine flow up borehole at top of DRZ (*BNBHUDRZ*) for an E2E1 intrusion into lower waste panel with the E2 intrusion at 800 yr and the E1 intrusion at 2000 yr.

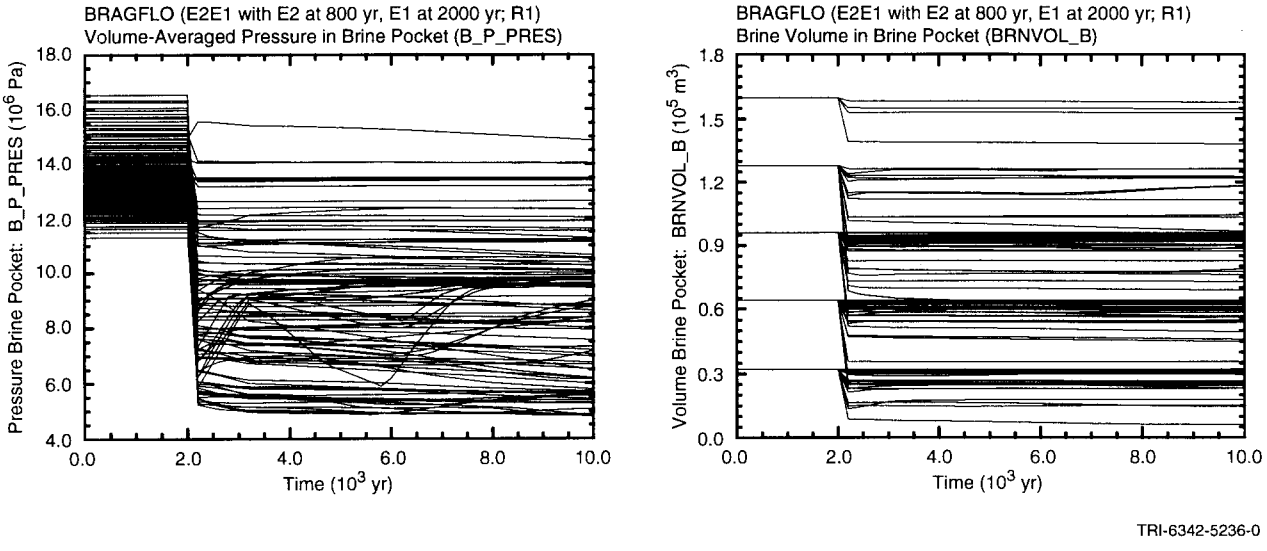

Fig. 8.10.7. Pressure (*B_P_PRES*) and brine volume (*BRNVOL_B*) in brine pocket for an E2E1 intrusion into lower waste panel with the E2 intrusion at 800 yr and the E1 intrusion at 2000 yr.

8.11 Disturbed Conditions: Multiple E1 Intrusions

An additional set of calculations was also performed to gain insights into the behavior of the repository subsequent to multiple E1 intrusions. In these calculations, E1 intrusions occur into the lower waste panel (i.e., region 23 in Fig. 4.2.1) at 1000, 2200, 3400, 4600 and 5800 yr. These multiple intrusions are represented with region 1 in Fig. 4.2.1, with the initial intrusion at 1000 yr modeled identically to the E1 intrusion at 1000 yr in Table 6.9.1 out to 2200 yr (i.e., the E1 intrusion presented in this chapter). Then, modifications are made to the properties of region 1 to incorporate the effects of the second intrusion. In particular, the permeability of the borehole from the repository to the brine pocket is reset to 1×10^{-9} m^2 and all other properties of the borehole are left unchanged. At 2400 yr, the properties of region 1 are again reset to incorporate the failure of the plugs above the repository and the decrease in borehole permeability below the repository. In particular, the borehole associated with the drilling intrusion at 2200 is assigned a permeability of k_2, where k_2 is randomly sampled from a loguniform distribution from 1×10^{-14} to 1×10^{-11} m^2. Then, the permeability k_A of the borehole within and above the repository is assigned a value of

$$k_A = k_1 + k_2 \tag{8.11.1}$$

where $k_1 = 10^x$, $x = BHPRM$, and the permeability k_B of the borehole below the repository is assigned a value of

$$k_B = (k_1/10) + k_2. \tag{8.11.2}$$

These permeabilities are used for region 1 (Fig. 4.2.1) until the third intrusion occurs at 3400 yr, when the process repeats itself with new permeabilities being assigned as described in Table 8.11.1.

Overall, the results obtained for multiple E1 intrusions are similar to those obtained for a single E1 intrusion. In particular, there is a surge of brine into the repository when the first E1 intrusion occurs, followed by smaller surges for each additional E1 intrusion (Figs. 8.2.5, 8.2.6, 8.2.7, 8.11.1). Due to decreasing pressure and brine volume in the brine pocket, the flows of brine from the brine pocket to the repository tend to decrease with each successive E1 intrusion (Fig. 8.11.1). However, the brine surge associated with the second E1 intrusion is sometimes larger than the brine surge associated with the first E1 intrusion due to reduced pressures in the repository subsequent to the failure of the borehole plugs associated with the first E1 intrusion. Most of the brine flows from the brine pocket to the repository take place during the 200 yr period in which a borehole with a permeability of 1×10^{-9} m^2 is assumed to exist between the brine pocket and the repository (Fig. 8.11.1).

Repository pressure drops rapidly after the first E1 intrusion (Figs. 8.4.1, 8.11.2). Subsequent intrusions may cause an increase in pressure during the 200 yr period in which a borehole with a permeability of 1×10^{-9} m^2 exists

Table 8.11.1. Definition of Permeabilities for Use with Multiple E1 Intrusions

Time	Assigned Permeabilities
1000 - 1200 yr	First intrusion occurs at 1000 yr. Concrete plugs assumed to be emplaced at the Santa Rosa Fm (i.e., a surface plug with a length of 15.76 m; corresponds to Cells 905, 937 in Fig. 4.2.3) and the Unnamed Mbr of the Rustler Fm (i.e., a plug at top of Salado Fm with a length of 36 m; corresponds to Cell 681 in Fig. 4.2.3). Concrete plugs assumed to have a permeability of $k = 5 \times 10^{-17}$ m^2; remainder of borehole assumed to have a permeability of 1×10^{-9} m^2.
1200 - 2200 yr	Concrete plugs assumed to fail at 1200 yr (U.S. DOE 1995b) and entire borehole is assigned a permeability typical of silty sand, i.e., $k_1 = 10^x$ m^2, $x = BHPRM$, where *BHPRM* is an uncertain input to the analysis (see Sect. 5.2).
2200 - 2400 yr	Second intrusion occurs at 2200 yr with same assumed plug configuration as first intrusion. Implemented in analysis by leaving permeability of borehole in and above repository unchanged (i.e., at $k_1 = 10^x$ m^2, $x = BHPRM$) and redefining permeability of borehole below the repository (i.e., in Cells 1010, 985, 12, 45, 78, 439, 453 in Fig. 4.2.3) to be $k = 1 \times 10^{-9}$ m^2.
2400 - 3400 yr	Concrete plugs associated with second intrusion fail at 2400 yr. Borehole associated with second intrusion assumed to have a permeability k_2, where k_2 is randomly sampled from the range [1×10^{-14}, 1×10^{-11} m^2] with a loguniform distribution. Borehole within and above repository is assigned a permeability of $k_A = k_1 + k_2$, and borehole below repository is assigned a permeability of $k_B = k_1/10 + k_2$.
3400 - 3600 yr	Third intrusion occurs at 3400 yr. with same assumed plug configuration as first intrusion. Implemented in analysis by leaving permeability of borehole in and above repository unchanged (i.e., at $k_A = k_1 + k_2$) and redefining permeability of borehole below the repository to be $k_B = 10^{-9}$ m^2.
3600 - 4600 yr	Concrete plugs associated with third intrusion fail at 3600 yr. Borehole associated with second intrusion assumed to have a permeability k_3, where k_3 is randomly sampled from the range [1×10^{-14}, 1×10^{-11} m^2] with a loguniform distribution. Borehole within and above repository is assigned a permeability of $k_A = k_1 + k_2 + k_3$, and borehole below repository is assigned a permeability of $k_B = (k_1 + k_2)/10 + k_3$.
4600 - 4800 yr	Fourth intrusion occurs at 4600 yr. Assignment of borehole permeabilities between 4600 and 4800 yr analogous to assignment between 3400 and 3600 yr for third intrusion (i.e., $k_A = k_1 + k_2 + k_3$ and $k_B = 1 \times 10^{-9}$ m^2).
4800 - 5800 yr	Concrete plugs associated with fourth intrusion fail at 4800 yr. Assignment of borehole permeabilities between 4800 and 5800 yr analogous to assignment between 3600 and 4600 yr for third intrusion (i.e., $k_A = k_1 + k_2 + k_3 + k_4$ and $k_B = (k_1 + k_2 + k_3)/10 + k_4$).
5800 - 6000 yr	Fifth intrusion occurs at 5800 yr. Assignment of borehole permeabilities between 5800 and 6000 yr analogous to assignment between 3400 and 3600 yr for third intrusion (i.e., $k_A = k_1 + k_2 + k_3 + k_4$ and $k_B = 1 \times 10^{-9}$ m^2).

Table 8.11.1. Definition of Permeabilities for Use with Multiple E1 Intrusions (Continued)

Time	Assigned Permeabilities
6000 - 10, 00 yr	Concrete plugs associated with fifth intrusion fail at 6000 yr. Assignment of borehole permeabilities between 6000 and 10,000 yr analogous to assignment between 3600 and 4600 yr for third intrusion (i.e., $k_A = k_1 + k_2 + k_3 + k_4 + k_5$ and $k_B = (k_1 + k_2 + k_3 + k_4)/10 + k_5$).

between the brine pocket and the repository. However, the size of these pressure increases tends to decrease with successive E1 intrusions, with repository pressure approaching an asymptote that corresponds to hydrostatic pressure (Fig. 8.11.2). The pressure curves that show a sudden monotonic increase to a pressure of approximately 6×10^6 Pa correspond to the pressure increase that occurs when the repository fills with brine due to brine flow down the intruding boreholes (Sect. 8.4).

The multiple E1 intrusions cause the intruded waste panel to become fully brine saturated for almost all sample elements (Fig. 8.11.3). In contrast, more sample elements remain below full brine saturation for E1 and E2E1 intrusions (Figs. 8.5.2, 8.10.4), although even in these cases the majority of sample elements result in full brine saturation in the intruded panel. The brine saturation in the unintruded (i.e., upper) waste panels for multiple E1 intrusions tends to remain substantially below full brine saturation (Fig. 8.11.3); similar saturations in the unintruded waste panels occur for E1 and E2E1 intrusions (Figs. 8.5.2, 8.10.4), although the saturations for the multiple E1 intrusions tend to be somewhat higher.

Brine volumes in the repository behave similarly for E1, E2E1 and multiple E1 intrusions (Figs. 8.5.6, 8.10.5, 8.11.4), with the volumes associated with multiple E1 intrusions tending to be somewhat higher than those associated with E1 and E2E1 intrusions. The intruded panel typically establishes a brine-filled connection through the intruding boreholes with the Culebra Dolomite and becomes fully brine saturated. As a result, brine volume is a function of pore volume, which in turn is a function of repository pressure (Fig. 8.5.8). The unintruded waste panels typically remain below full brine saturation (Figs. 8.5.2, 8.10.4, 8.11.3) and thus show more uncertainty in the volume of brine that they contain (Figs. 8.5.6, 8.10.5, 8.11.4).

Brine flow up the intruding boreholes is similar for E1, E2E1 and multiple E1 intrusions (Figs. 8.6.3, 8.10.6, 8.11.5), with a slight tendency for the flows associated with multiple E1 intrusions to be larger than the flows associated with E2E1 intrusions and for the flows associated with E2E1 intrusions to be larger than the flows associated with E1 intrusions. For the 100 sample elements in replicate R1, only one results in a substantial difference in cumulative flow for multiple E1 and E2E1 intrusions (Figs. 8.10.6, 8.11.5). The most significant aspect

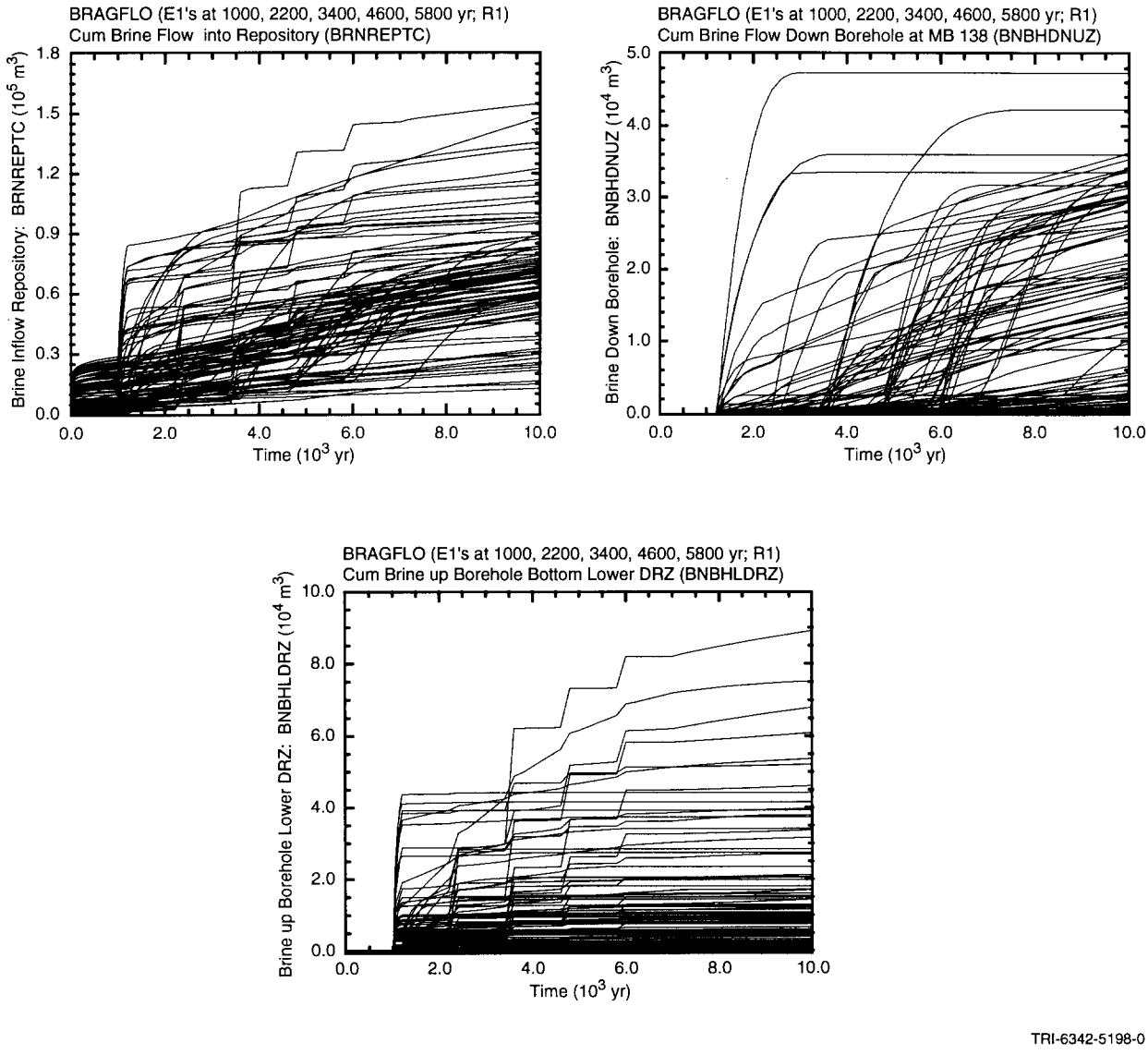

Fig. 8.11.1. Cumulative brine flow into repository (*BRNREPTC*), cumulative brine flow down intruding boreholes (*BNBHDNUZ*), and cumulative brine flow into bottom of DRZ from brine pocket (*BNBHLDRZ*) for multiple E1 intrusions into lower waste panel at 1000, 2200, 3400, 4600 and 5800 yr.

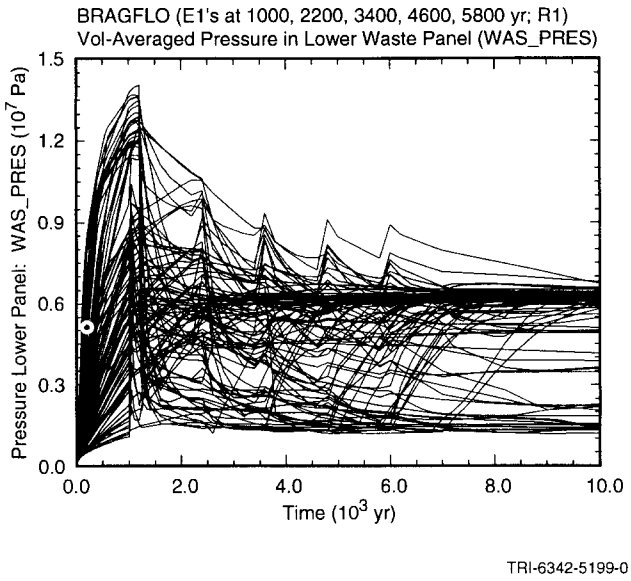

Fig. 8.11.2. Repository pressure (*WAS_PRES*) for multiple E1 intrusions into lower waste panel at 1000, 2200, 3400, 4600 and 5800 yr.

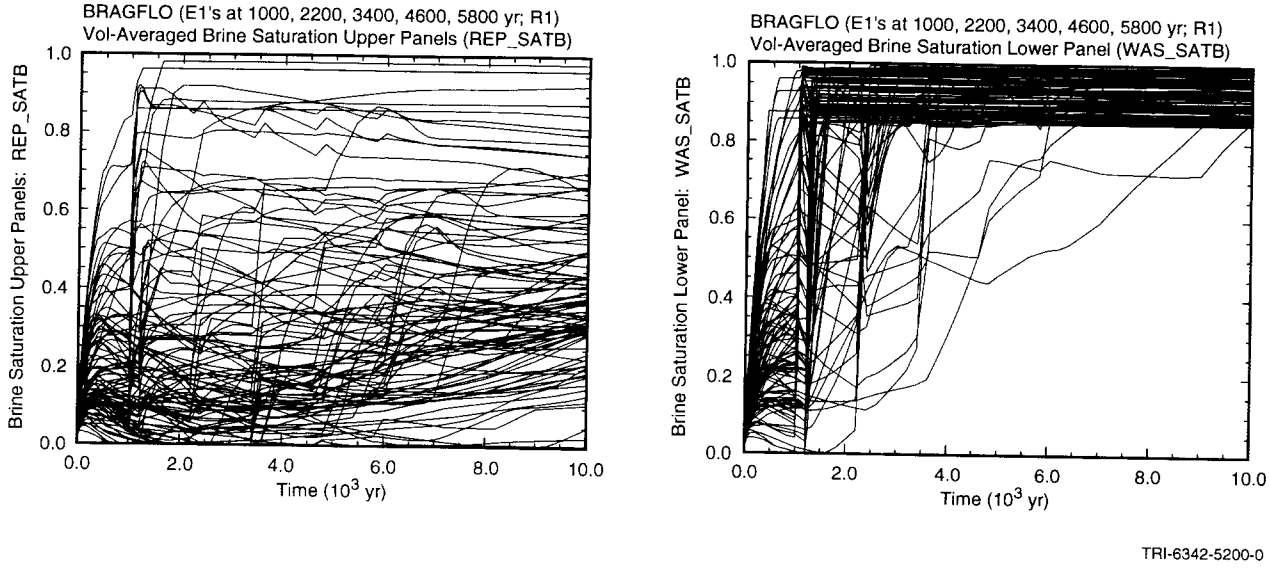

Fig. 8.11.3. Brine saturation in upper (*REP_SATB*) and lower (*WAS_SATB*) waste panels for multiple E1 intrusions into lower waste panel at 1000, 2200, 3400, 4600 and 5800 yr.

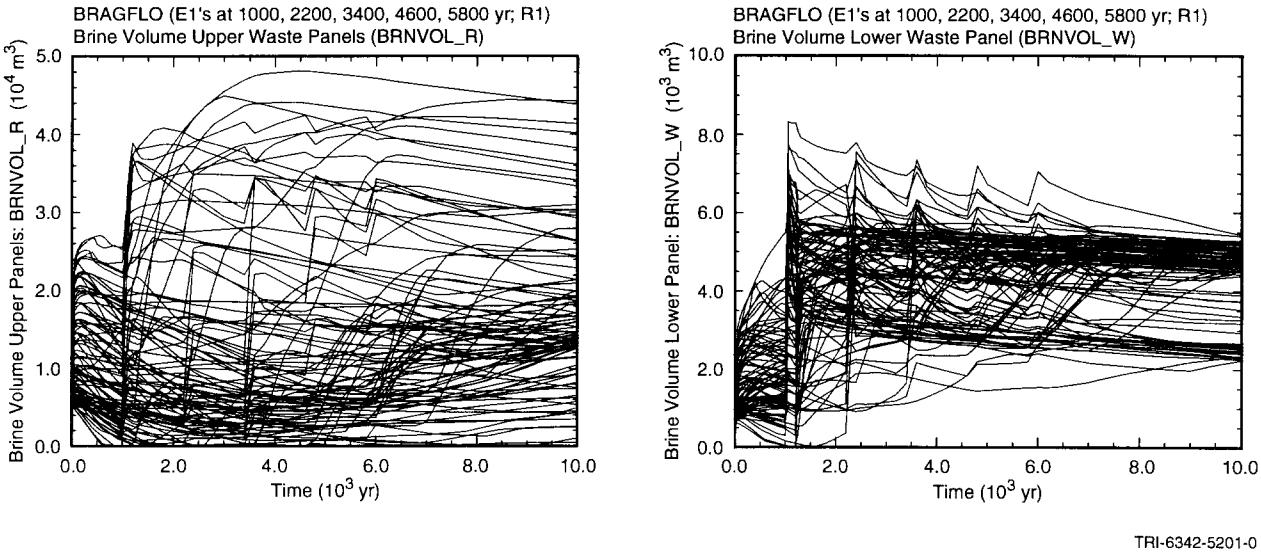

Fig. 8.11.4. Brine volume in upper (*BRNVOL_R*) and lower (*BRNVOL_W*) waste panels for multiple E1 intrusions into lower waste panel at 1000, 2200, 3400, 4600 and 5800 yr.

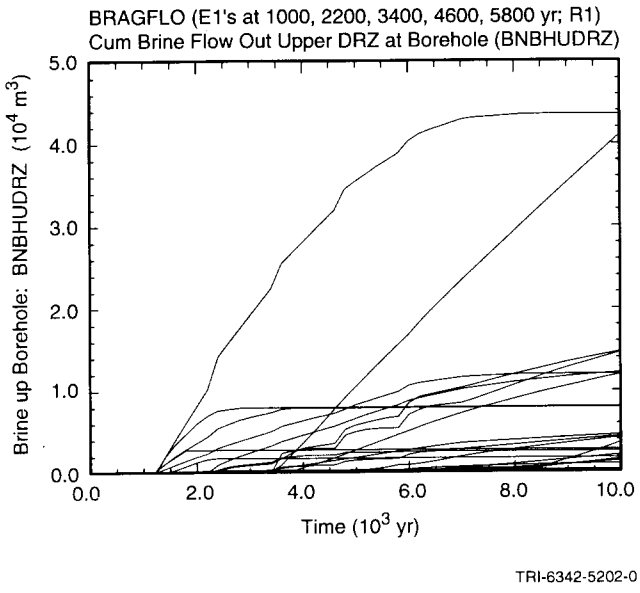

Fig. 8.11.5. Cumulative brine flow up borehole at top of DRZ (*BNBHUDRZ*) for multiple E1 intrusions into lower waste panel at 1000, 2200, 3400, 4600 and 5800 yr.

9. Direct Release to Accessible Environment: Cuttings, Cavings and Spallings

9.1 Cuttings and Cavings: Uncertainty and Sensitivity Analysis

Drilling intrusions through the waste panels can penetrate CH- or RH-TRU waste (Sect. 4.5). Specifically, the probabilities that a single intrusion through a waste panel will encounter CH- or RH-TRU waste are 0.876 and 0.124, respectively (Sect. 3.7). As the penetration of CH-TRU waste is more likely than the penetration of RH-TRU waste and the average concentrations of CH-TRU waste are similar to those for RH-TRU waste (Fig. 9.1.1), the cuttings and cavings release is dominated by CH-TRU waste.

The volume of material removed by a drilling intrusion through RH-TRU waste is fixed at 0.039 m^3 (i.e., the drill bit diameter is fixed at 0.31115 m, which yields an intersection area of 0.076 m^2, and the effective height of RH-TRU waste is assumed to be 0.509 m) (Sect. 4.5.2). However, uncertainty in inputs used in the 1996 WIPP PA results in the volume of material removed by cuttings and cavings due to a drilling intrusion through CH-TRU waste ranging from approximately 0.4 m^3 to 3 m^3 (Fig. 9.1.2). The volumes in Fig. 9.1.2 and also the volume indicated above for RH-TRU waste are the original (i.e., uncompacted) volumes of the removed waste. The use of uncompacted volumes simplifies the calculation of the radionuclide concentrations used in the determination of cuttings releases and permits a combining of removal volumes for intrusions at different times. The uncertainty in the volume of CH-TRU waste removed as cuttings and cavings is determined by the variable *WTAUFAIL* (Fig. 9.1.3).

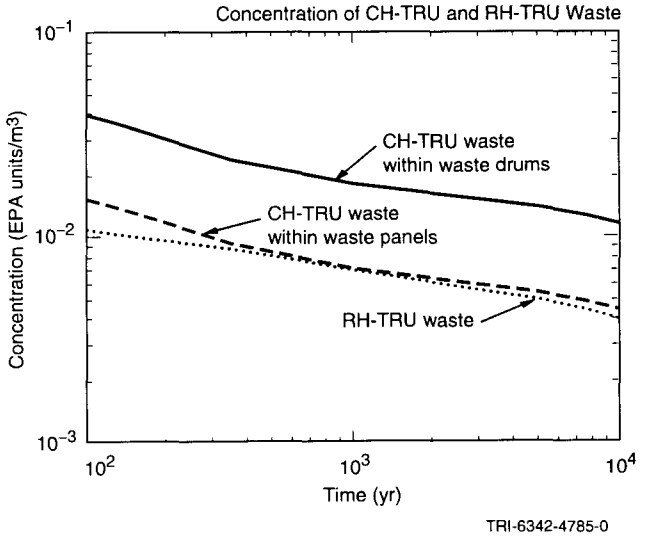

Fig. 9.1.1. Concentration (EPA units/m^3) of CH- and RH-TRU waste.

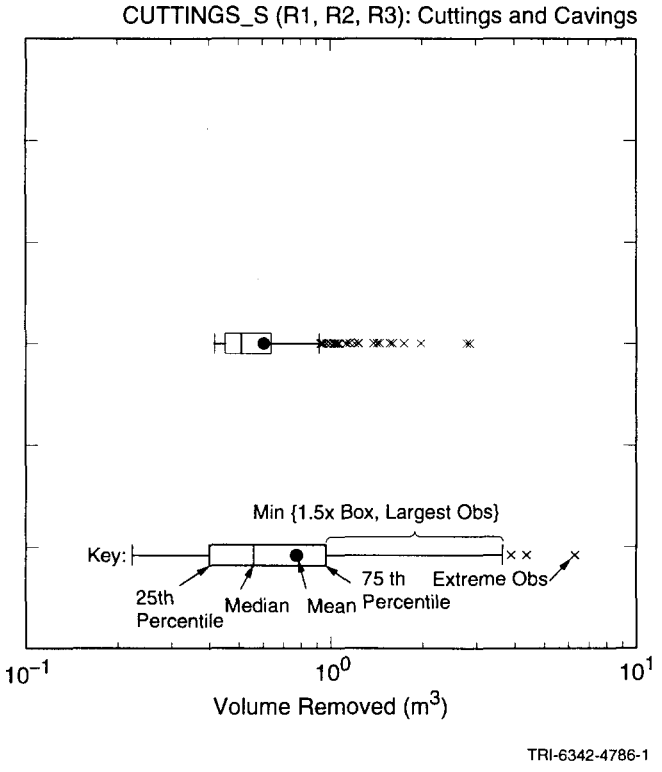

Fig. 9.1.2. Distribution of original (i.e., uncompacted) volume removed due to cuttings and cavings by a single drilling intrusion through CH-TRU waste.

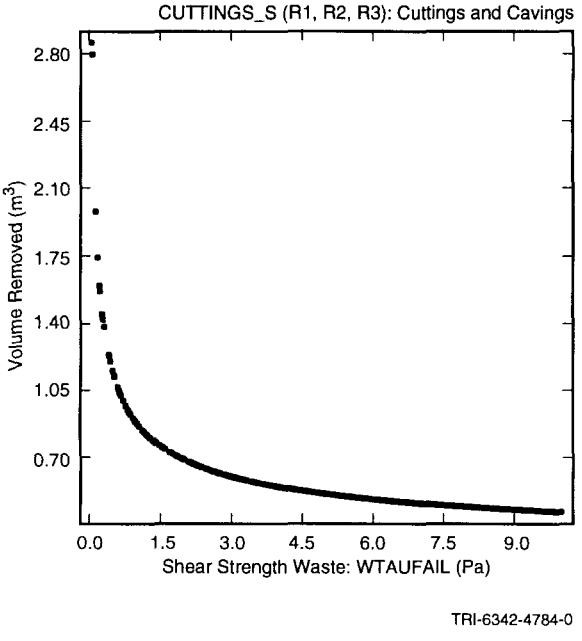

Fig. 9.1.3. Scatterplot for volume of material removed from repository due to cuttings and cavings by a single drilling intrusion through CH-TRU waste versus shear resistance for erosion (*WTAUFAIL*).

9.2 Cuttings and Cavings: CCDFs

Complementary cumulative distribution functions (CCDFs) are constructed conditionally on individual LHS elements by randomly sampling futures $\mathbf{x}_{st}$ of the form shown in Eq. (2.2.2) (Sect. 6.6). For each sampled future, a normalized release is then estimated for the particular release mode under consideration, which is cuttings and cavings removal in this section. Once the normalized releases are available, construction of the corresponding CCDF is straightforward (Sect. 6.7).

The cuttings and cavings release for a given drilling intrusion is the product of the volume of waste removed (m^3) and the radionuclide concentration (EPA units/m^3) in the removed waste. For RH-TRU waste, the indicated concentration corresponds to the concentrations plotted in Fig. 9.1.1 (see $C_{RH}(k)$ in Table 9.2.1). For CH-TRU waste, the situation is more complex due to the presence of 569 waste streams (i.e., distinct types of waste), with each of the waste drums placed in the repository containing waste from only one waste stream (see $C_{CH}(j, \tau_k)$, $P_{CH}(j)$ in Table 9.2.1). As a result, a single drilling intrusion through CH-TRU waste can intersect several different waste streams. Given that waste drums containing CH-TRU waste are stacked three high in the repository, the

Table 9.2.1. Results Available for Use in CCDF Construction for Cuttings and Cavings Removal

$C_{CH}(j, \tau_k)$	=	concentration (EPA units/m^3) in CH-TRU waste stream j, j = 1, 2, ..., 569, at time τ_k, where τ_k, k = 1, 2, 3, 4, 5, 6, 7, 8, 9, corresponds to 100, 125, 175, 350, 1000, 3000, 5000, 7500 and 10,000 yr, respectively. Value: See Table 3.7.1, Fig. 3.7.1. Source: U.S. DOE 1995a, Sanchez et al. 1997.
$P_{CH}(j)$	=	probability that a randomly sampled drum of CH-TRU waste will come from waste stream j, j = 1, 2, ..., 569. Value: See Table 3.7.1, Fig. 3.7.1. Source: U.S. DOE 1995a, Sanchez et al. 1997.
A_{CH}	=	area (m^2) through CH-TRU waste removed due to cuttings and cavings associated with a single drilling intrusion. Source: CUTTINGS_S.
H_{CH}	=	height (m) of waste panels used for disposal of CH-TRU waste. Value: 3.96 m. Source: WIPP design.
F_{CH}	=	fraction of volume removed by drilling intrusion through CH-TRU waste that is actually waste. Value: 0.386 = (volume of CH-TRU waste) / (volume of waste panels) = (1.685×10^5 m^3 / 4.36×10^5 m^3). Source: WIPP design, U.S. DOE 1995a.
$C_{RH}(\tau_k)$	=	concentration (EPA units/m^3) in RH-TRU waste at time τ_k, with τ_k corresponding to the same times used with $C_{CH}(j, \tau_k)$ for CH-TRU waste. Value: See Fig. 9.1.1. Source: U.S. DOE 1995a, Sanchez et al. 1997.
A_{RH}	=	same as A_{CH} but for RH-TRU waste. Value: 0.076 m^2 = π (drillbit diamater/2)^2 = π (0.31115/2)^2. Rationale: Little erosion around the drillbit takes place for intrusions through RH-TRU waste.
H_{RH}	=	same as H_{CH} but for RH-TRU waste. Value: 0.509 m. Source: Tierney 1996b.
F_{RH}	=	Same as F_{CH} but for RH-TRU waste. Value: 1. Rationale: Consistent with emplacement procedure for RH-TRU waste and definition of H_{RH}.

concentration of CH-TRU waste associated with a specific intrusion is taken to be the average of the concentrations associated with three randomly selected waste streams (Sect. 3.7), which results in considerable variability in the size of the cuttings and cavings releases for individual intrusions (Fig. 9.2.1).

For a given future $\mathbf{x}_{st}$ of the form shown in Eq. (2.2.2), the cuttings and cavings release to the accessible environment is given by

$$f_C(\mathbf{x}_{st}) = \sum_{i=1}^{n} rC_i, \tag{9.2.1}$$

where

$$\begin{aligned} rC_i &= 0 && \text{if } \mathbf{a}_i \sim \text{no waste} \\ &= A_{CH}\, H_{CH}\, F_{CH} \left\{ \sum_{r=1}^{3} C_{CH}[j(i,r), t_i] / 3 \right\} && \text{if } \mathbf{a}_i \sim \text{CH-TRU waste} \\ &= A_{RH}\, H_{RH}\, F_{RH}\, C_{RH}(t_i) && \text{if } \mathbf{a}_i \sim \text{RH-TRU waste} \end{aligned}$$

$j(i, r)$ = an integer randomly selected from 1, 2, ..., 569 for r = 1, 2, 3 in consistency with the probabilities $P_{CH}(j), j = 1, 2, \ldots, 569$,

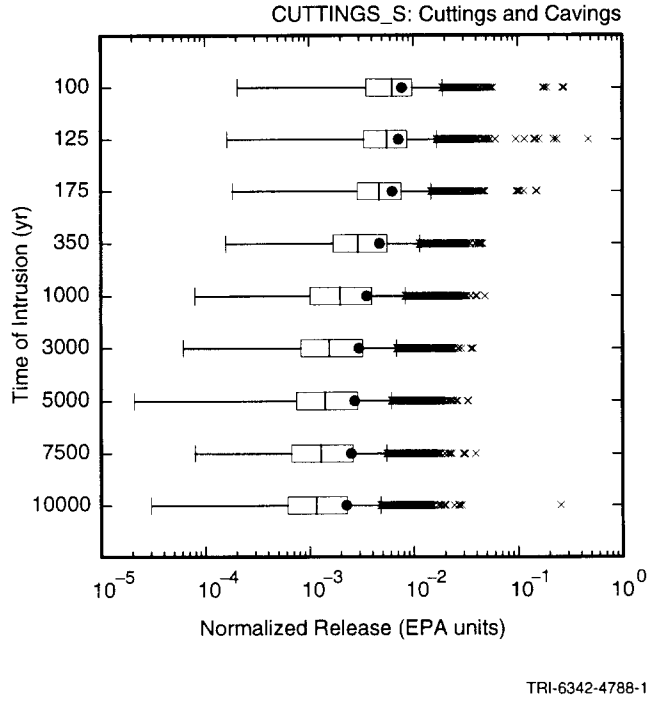

Fig. 9.2.1. Distribution of normalized release to accessible environment for cuttings and cavings removal from CH-TRU waste due to variation in intersected waste streams. Results calculated with median volume from Fig. 9.1.2 (i.e., 0.508 m^3), 38.6% of removed volume assumed to be CH-TRU waste, and a sample of size 10,000 at each time.

and all remaining symbols are defined in Table 9.2.1. The above summation from $r = 1$ to $r = 3$ corresponds to the determination of an average concentration over three randomly selected waste streams. Further, the appearance of t_i in $C_{CH}[j(i, r), t_i]$ and $C_{RH}(t_i)$ implies linear interpolation between the actual time values in Table 9.2.1 at which C_{CH} and C_{RH} are available.

For each LHS element, $nS = 10{,}000$ futures are randomly selected (Sect. 6.6) and the corresponding cuttings and cavings releases are determined as shown in Eq. (9.2.1). The resultant CCDFs (Sect. 6.7) for cuttings and cavings releases to the accessible environment are then constructed (Fig. 9.2.2). In Fig. 9.2.2 and other similar figures in this presentation, the left frame shows the distribution of CCDFs obtained with the first of the three replicated LHSs (i.e., replicate R1; see Sect. 6.5), and the right frame shows the mean and percentile curves that result from pooling all three replicates (i.e., replicates R1, R2 and R3) to obtain a sample of size 300. All the CCDFs fall below the boundary line specified in 191.13(a). Further, the distribution of CCDFs is relatively tight, and the estimates for the mean and percentile curves are quite stable (Fig. 9.2.3; see Sect. 6.4). Indeed, the three estimates for the mean and percentile curves are essentially indistinguishable at the plotting resolution of Fig. 9.2.3.

In Fig. 9.2.2 and other similar figures in this presentation, CCDFs end at the largest observed consequence value. From there, they drop vertically to zero; this drop is not shown to avoid a solid mass of vertical lines beneath the lowest observed exceedance probabilities (see Sect. 6.7, Fig. 6.7.6). Once a CCDF reaches zero on the probability axis (i.e., the ordinate), it continues right along the consequence axis (i.e., the abscissa). As a result, the mean CCDF has nonzero exceedance probabilities that fall below the nonzero exceedance probabilities of the individual CCDFs that were averaged in its construction. Similar plotting conventions hold for the quantile curves.

As volume of removed waste (i.e., $A_{CH}\, H_{CH}$ as used in conjunction with Eq. (9.2.1)) is the only quantity used in the determination of cuttings and cavings releases that is affected by variables in the LHS, the uncertainty in the CCDFs shown in Fig. 9.2.2 is due entirely to *WTAUFAIL* (Fig. 9.1.3). This assertion can be checked by reducing each CCDF for cuttings and cavings removal to an expected value and then regressing this expected value on the sampled variables. The outcome of this calculation is the rank-regression model

$$\bar{y}_C = 300.8 - 0.9989\ WTAUFAIL \tag{9.2.2}$$

with an R^2 value of 0.9979, where $\bar{y}_C$ designates the expected value associated with a CCDF for cuttings and cavings removal. Thus, *WTAUFAIL* is indeed the only variable that affects the CCDFs for cuttings and cavings removal. The corresponding scatterplot appears in Fig. 9.2.4.

The CCDFs in Fig. 9.2.2 are for normalized release, which is not a very intuitive quantity. To help provide perspective, CCDFs for volume of material brought to the surface (i.e., the quantity obtained from Eq. (9.2.1) when F_{CH}, C_{CH}, F_{RH} and C_{RH} are equal to 1) can also be constructed (Fig. 9.2.5). The release of more than 10 m^3 of material over 10,000 yr is unlikely.

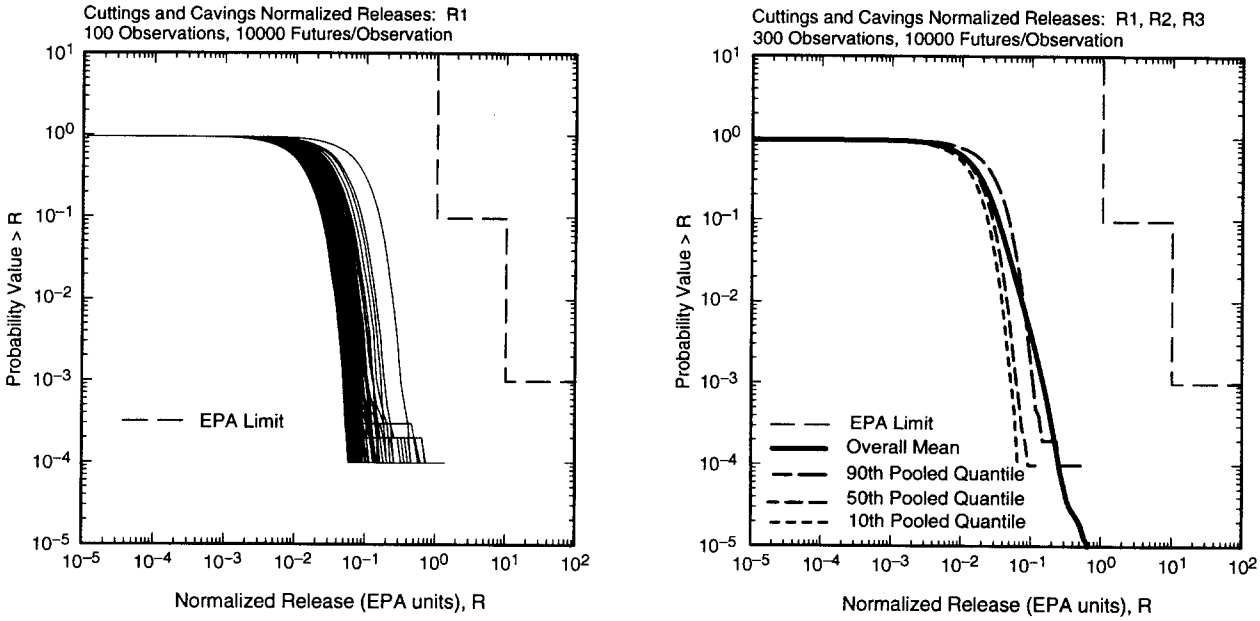

Fig. 9.2.2. Distribution of CCDFs for normalized release to accessible environment over 10,000 yr due to cuttings and cavings: CCDFs for replicate R1 (left frame), and mean and percentile curves obtained by pooling replicates R1, R2 and R3 (right frame).

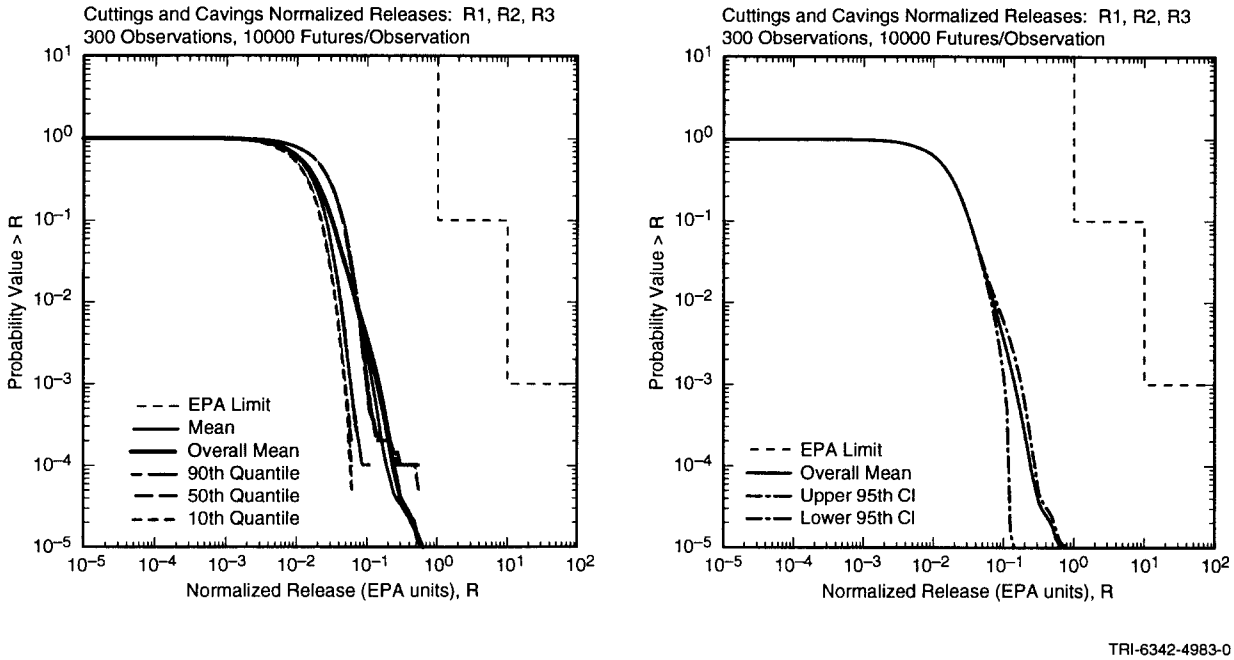

Fig. 9.2.3. Outcome of replicated sampling for distribution of CCDFs for normalized release to the accessible environment over 10,000 yr due to cuttings and cavings: mean and percentile curves for individual replicates (left frame) and confidence intervals (CIs) on mean curve obtained from the three replicates (right frame).

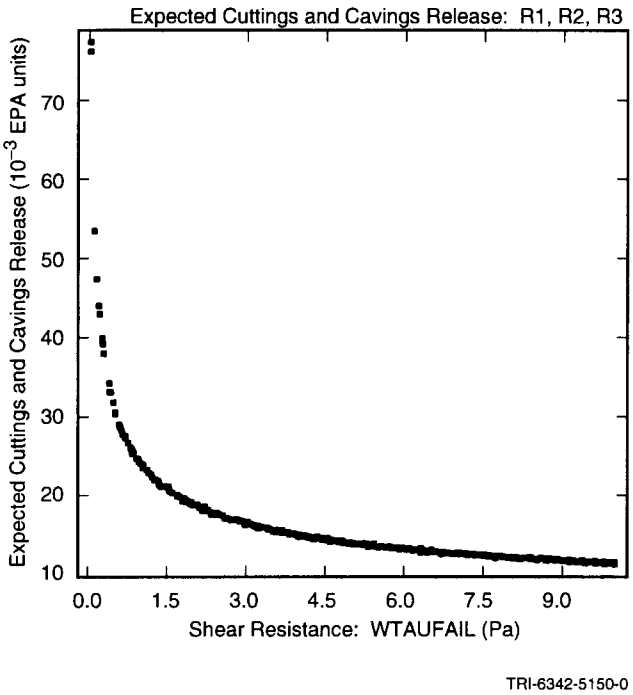

Fig. 9.2.4. Scatterplot for expected cuttings and cavings release for individual CCDFs versus *WTAUFAIL*.

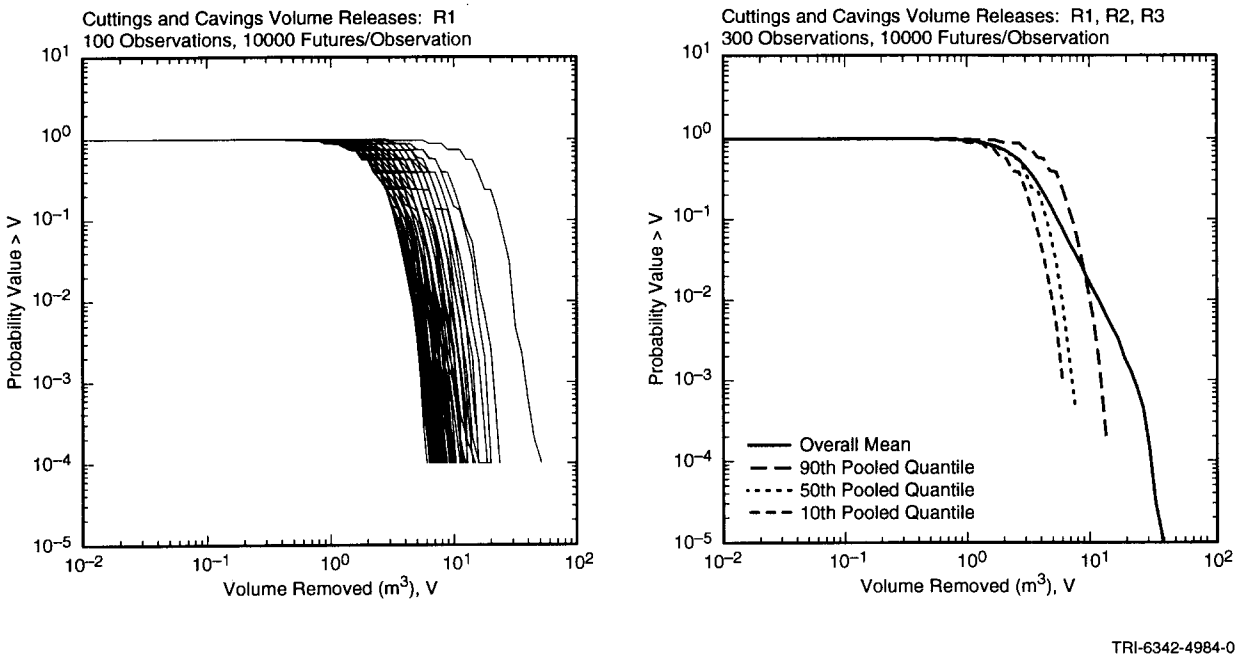

Fig. 9.2.5. Distribution of CCDFs for volume of material removed to accessible environment over 10,000 yr due to cuttings and cavings: CCDFs for replicate R1 (left frame), and mean and percentile curves obtained by pooling replicates R1, R2 and R3 (right frame).

9.3 Spallings: Uncertainty and Sensitivity Analysis

Drilling intrusions through CH-TRU waste can also produce spallings releases, which are releases of solid material due to rapid gas movement toward a borehole at the time of intrusion (Sect. 4.6). Due to the low permeability of the region surrounding each RH-TRU waste canister, intrusions into RH-TRU waste are assumed not to produce spallings releases.

The spallings model predicts a release of solid material. For computational convenience and also for comparability with cuttings results, the released volume of material is reported as volume of original, uncompacted material emplaced in the repository. For a given drilling intrusion, this volume is multiplied by the average concentration (EPA units/m^3) of CH-TRU waste in the waste panels (Fig. 9.1.1) at the time of the intrusion to produce the spallings release.

The size of the spallings release is sensitive to the pressure in the repository at the time of the associated drilling intrusion. In turn, pressure is dependent on both the time of a drilling intrusion and whether or not that drilling intrusion has been preceded by earlier intrusions. Due to the 1° dip of the repository, it is also possible that conditions influencing spallings may differ between upper panels (i.e., panels 1, 2, 3, 6, 7, 8, 9 in Fig. 3.2.1) and lower panels (i.e., panels 4, 5, 10 in Fig. 3.2.1).

For initial intrusions into the repository, spallings calculations were performed for intrusions at 100, 350, 1000, 3000, 5000 and 10,000 yr and also for intrusions into upper (U) and lower (L) waste panels (Fig. 9.3.1). Early intrusions often produced no releases, with the number of nonzero releases increasing with time due to increasing pressure in the repository (Fig. 9.3.2; also see Fig. 7.4.1). The spallings model incorporates the assumption that no spallings release will take place when the repository pressure is less than 8 MPa, which results in the switch from zero to nonzero spallings releases in Fig. 9.3.2. This switch results because a column of salt-saturated drilling fluid that extends from the land surface to the repository would exert a pressure of approximately 8 MPa (Stoelzel and O'Brien 1996); thus, 8 MPa is the minimum pressure that must be exceeded before repository fluids will displace the drilling fluid. The volume of the spallings release is between approximately 0.5 and 4 m^3 and the corresponding normalized release is between approximately 3×10^{-3} and 2×10^{-2} EPA release units. The releases from intrusions into an upper or lower panel at the same time are essentially identical (Fig. 9.3.1), with this equality resulting because pressure was essentially equal throughout the repository (Fig. 8.4.2) and the effects of brine saturation were not incorporated into the spallings model.

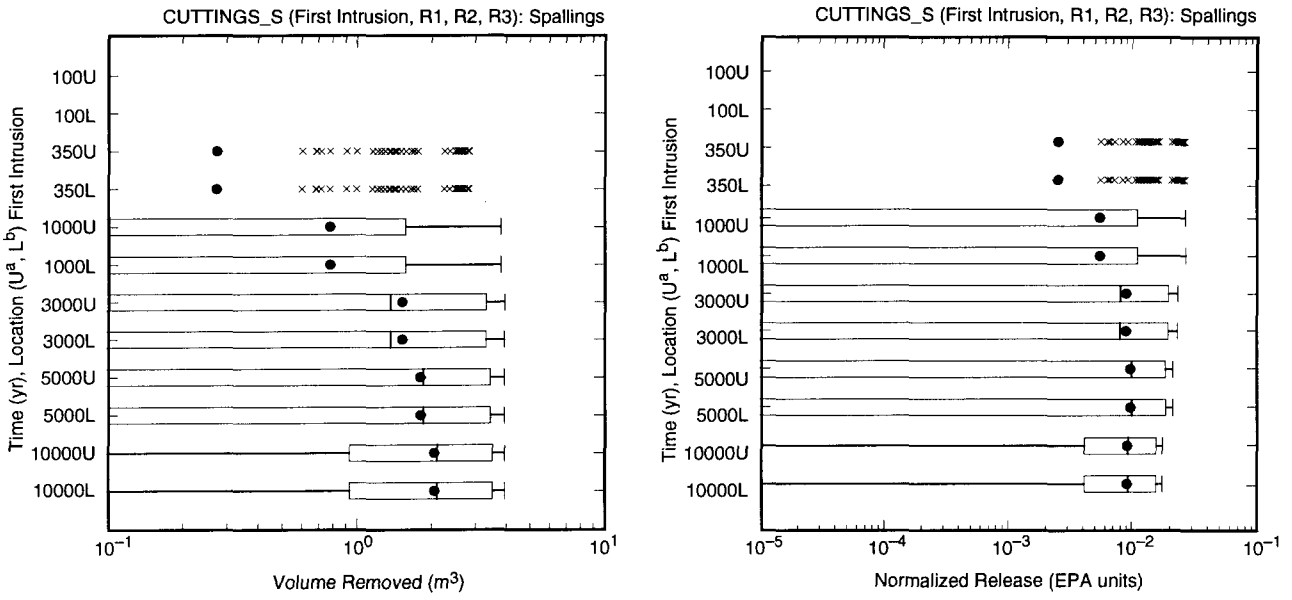

Fig. 9.3.1. Distribution of original (i.e., uncompacted) volume removed and normalized release due to spallings for a single drilling intrusion into a previously unintruded repository that encounters CH-TRU waste.

Although pressure determines whether or not a nonzero spallings release takes place, it has little effect on the actual size of the release (Fig. 9.3.2). Rather, given that a nonzero release takes place, the variable *WPRTDIAM* determines the actual size of this release (Fig. 9.3.3). Specifically, the size of the release increases as *WPRTDIAM* decreases.

At a value of $WPRTDIAM \doteq 2.5 \times 10^{-3}$ m^3 there is a noticeable change in behavior, with the volume of released material suddenly changing from approximately 2.5 m^3 to a range of values bounded below by approximately 3.2 m^3 (Figs. 9.3.3, 9.3.4). Further, below $WPRTDIAM \doteq 2.5 \times 10^{-3}$ m^3, there is a stronger relationship between pressure and volume of released material than exists at higher values of *WPRTDIAM* (Fig. 9.3.2). This discontinuity is due to an abrupt change in the coefficient of drag for particles at a Reynolds number (*Re*) of 2×10^5. Above $Re = 2 \times 10^5$, the boundary layer on the forward surface of smooth spheres changes from laminar to turbulent flow and tends to move the boundary layer point of separation downstream. This causes the size of the wake to decrease and reduces pressure drag, which results in the observed discontinuity and larger releases for small values of *WPRTDIAM* (Fox and McDonald, 1973, pp. 404-408).

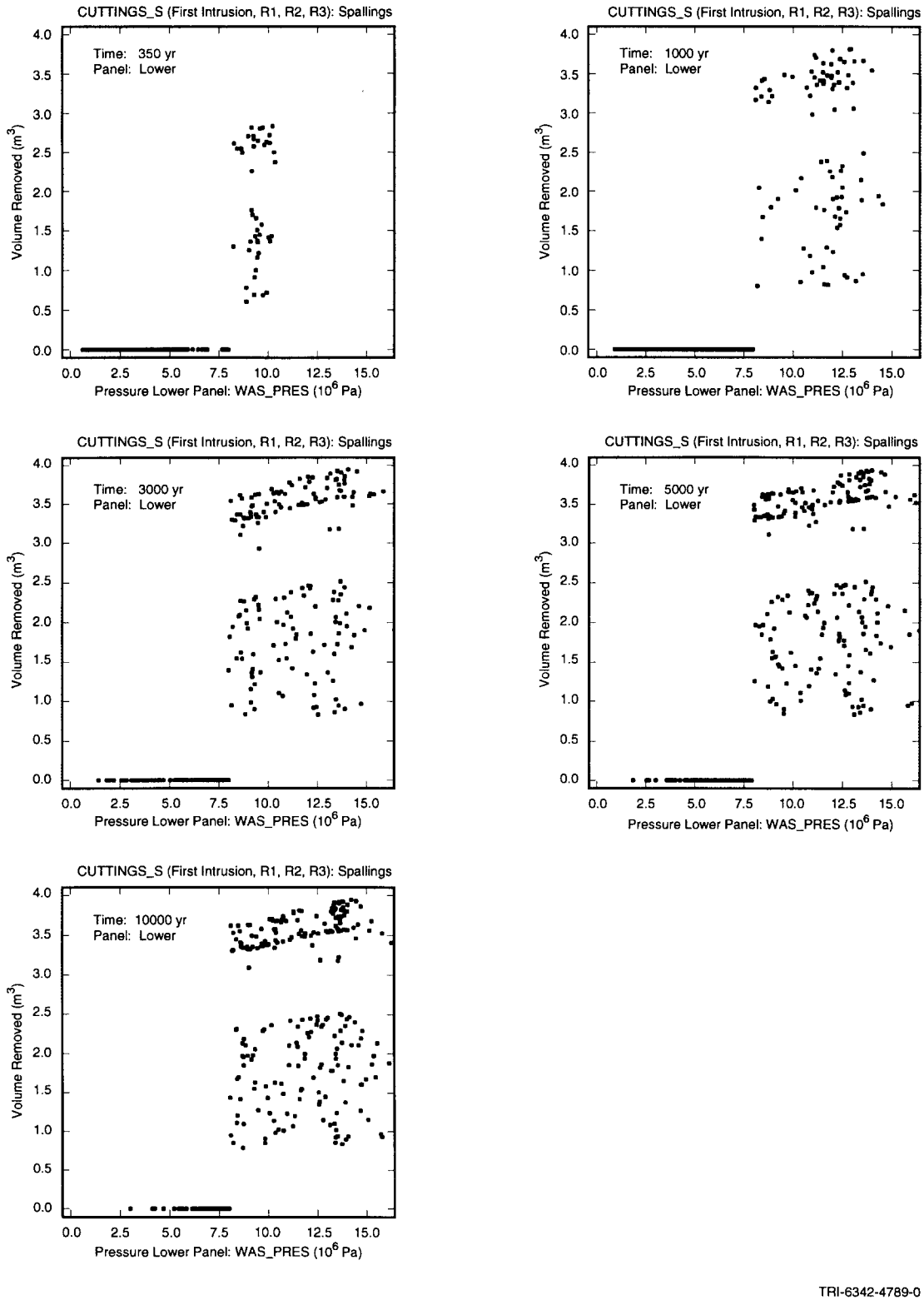

Fig. 9.3.2. Scatterplots for volume of material removed from repository due to spallings resulting from a single drilling intrusion into a previously unintruded repository that passes through CH-TRU waste in a lower waste panel versus pressure (*WAS_PRES*) in repository.

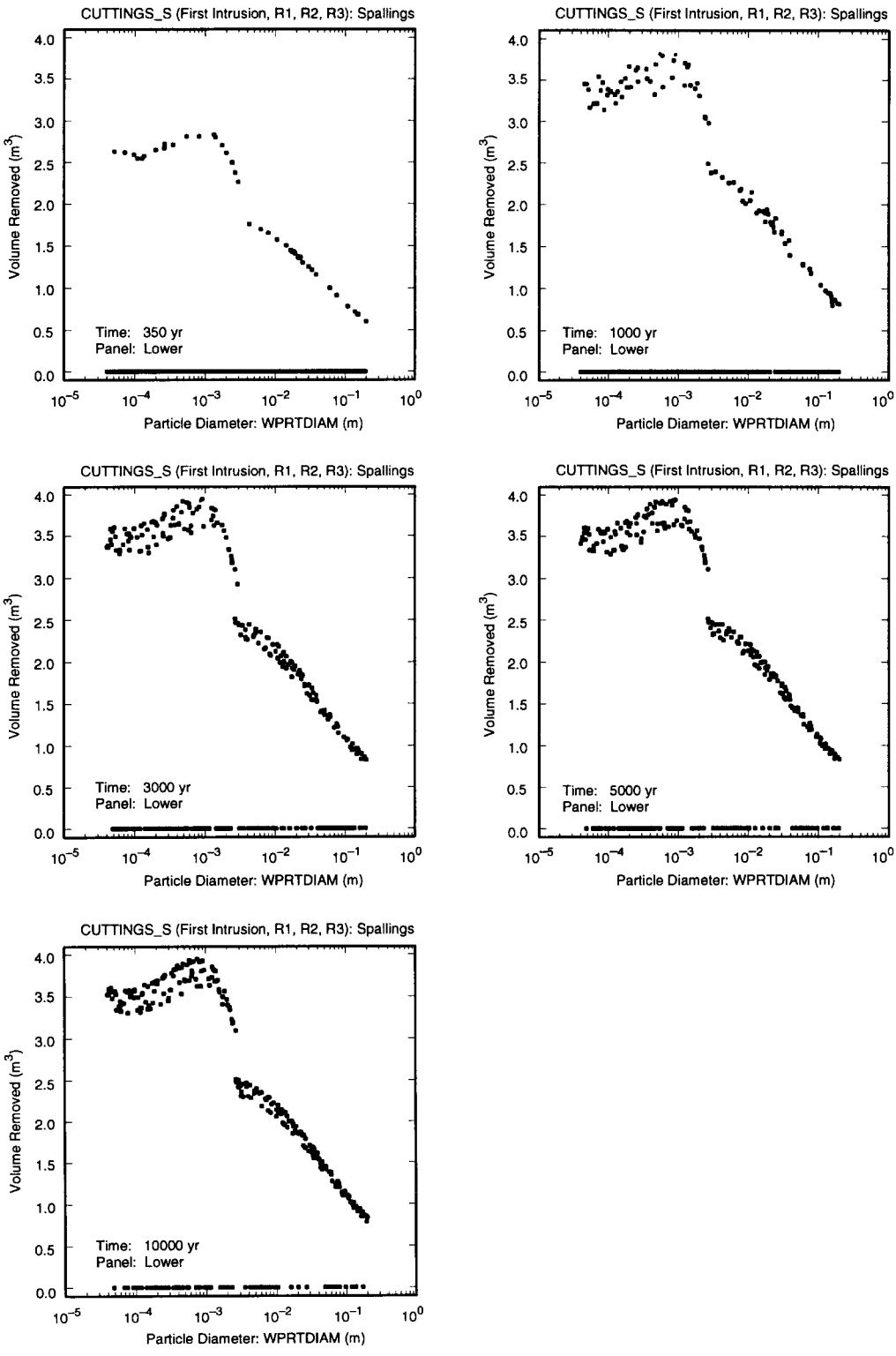

Fig. 9.3.3. Scatterplots for volume of material removed from repository due to spallings resulting from a single drilling intrusion into a previously unintruded repository that passes through CH-TRU waste in a lower waste panel versus diameter of particles available for removal by spallings (*WPRTDIAM*).

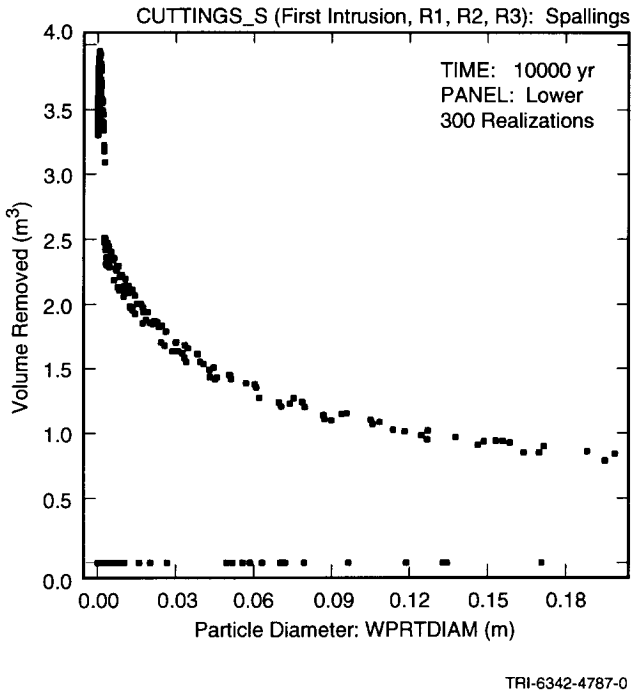

Fig. 9.3.4. Scatterplot for volume of material removed from repository due to spallings resulting from a single drilling intrusion at 10,000 yr into a previously unintruded repository that passes through CH-TRU waste in a lower waste panel versus diameter of particles available for removal by spallings (*WPRTDIAM*).

The patterns involving spallings release, pressure and *WPRTDIAM* are clearly revealed in a three dimensional scatterplot, with no release taking place for pressures below 8 MPa and the size of the release depending on *WPRTDIAM* for pressures above 8 MPa (Fig. 9.3.5).

Spallings calculations were also performed for intrusions subsequent to an initial intrusion into the repository for the following cases: (1) An initial E1 intrusion at 350 yr followed by a second intrusion at 550, 750, 2000, 4000 or 10,000 yr (Fig. 9.3.5), (2) An initial E1 intrusion at 1000 yr followed by a second intrusion at 1200, 1400, 3000, 5000 or 10,000 yr (Fig. 9.3.5), (3) An initial E2 intrusion at 350 yr followed by a second intrusion at 550, 750, 2000, 4000 or 10,000 yr (Fig. 9.3.6), and (4) An initial E2 intrusion at 1000 yr followed by a second intrusion at 1200, 1400, 3000, 5000 or 10,000 yr (Fig. 9.3.7). Further, spallings releases were calculated for two cases for each of the second intrusion times: (1) Intrusion into the same waste panel as the first intrusion, and (2) Intrusion into a different waste panel than the first intrusion. Intrusion times 200 and 400 yrs after the initial intrusion time (i.e., 550 and 750 yr for an initial intrusion at 350 yr, and 1200 and 1400 yr for an initial intrusion at 1000 yr) were selected to give results just before and after the borehole plug at the Rustler/Salado interface is assumed to fail for plugging patterns 2 and 3 (Sect. 3.6, Table 4.2.8). Wider time intervals were used at later times because gas pressure tends to change rather slowly at later times (Figs. 7.4.1, 8.4.1), thus allowing larger times between calculations. The distinction between intrusion into same and different panels was made because of the possible effects of the resistance to flow between waste panels due to the presence of panel closures and the occurrence of brine flow down a borehole into the intruded panel.

Scatterplots for second intrusions equivalent to those in Figs. 9.3.2 and 9.3.5 for initial intrusions show exactly the same patterns, with the occurrence of a spallings release depending on whether or not the pressure is above 8 MPa and the actual size of the release depending on *WPRTDIAM*. For most sample elements, there is no spallings release for the second intrusion because the pressure is less than 8 MPa (Fig. 8.4.1). As discussed in Sect. 8.4, this reduced pressure is due primarily to borehole permeability (i.e., $k = 10^x$, $x = BHPRM$). The greatest number of nonzero spallings releases occurs when the second intrusion is 200 yr after the first intrusion because the borehole plug at the Rustler/Salado interface is yet to fail (Table 4.2.8) and, as a result, the pressure has not been reduced by gas flow up the first borehole.

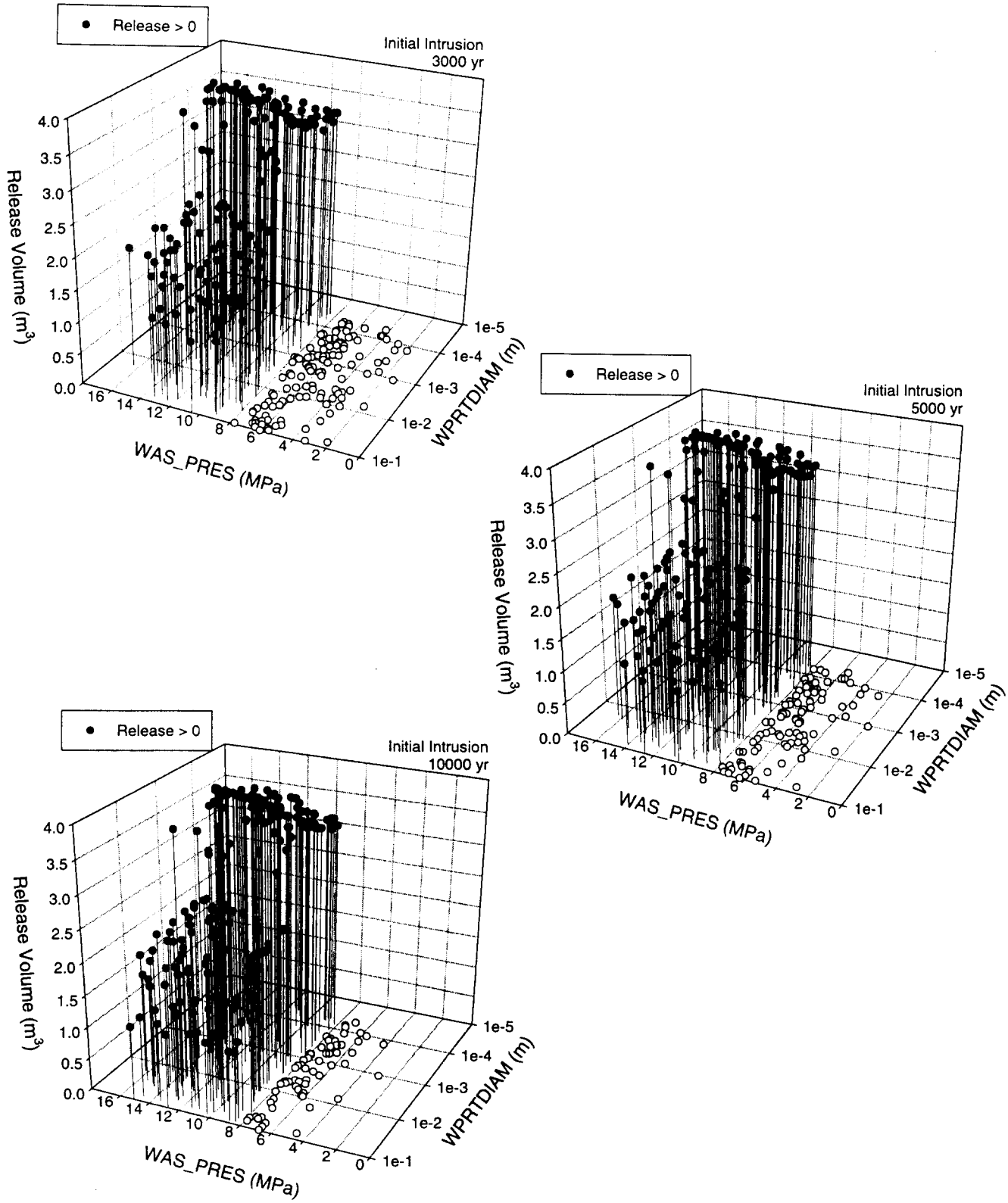

Fig. 9.3.5. Three dimensional scatterplots for volume of material removed from repository due to spallings resulting from a single drilling intrusion into a previously unintruded repository that passes through CH-TRU waste in a lower waste panel versus pressure (*WAS_PRES*) and diameter of particles available for removal by spallings (*WPRTDIAM*).

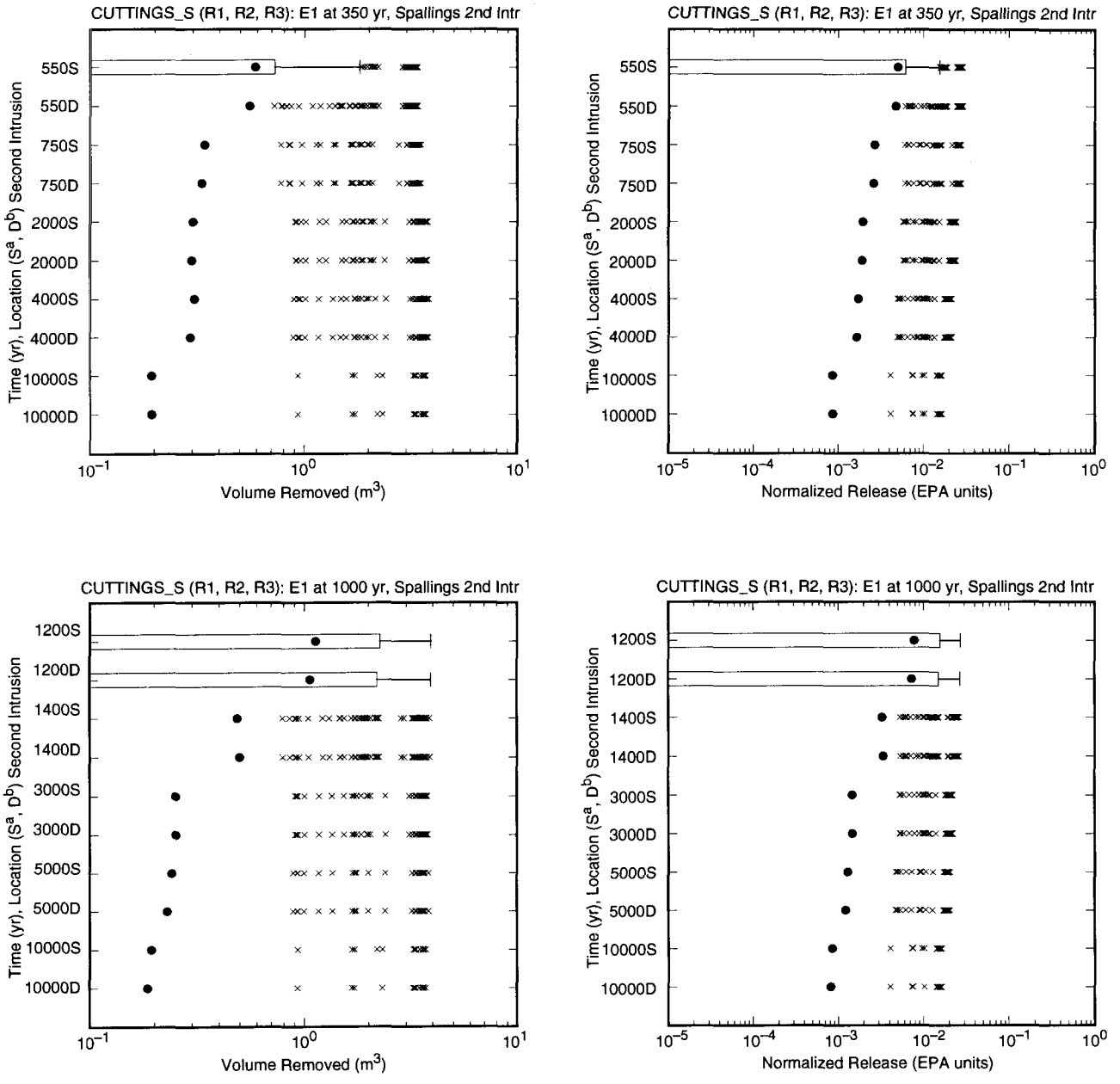

[a]S Signifies Second Intrusion Occurs in Same (S) Waste Panel as First Intrusion

[b]D Signifies Second Intrusion Occurs in Different (D) Waste Panel than First Intrusion

TRI-6342-4782-0

Fig. 9.3.6. Distribution of original (i.e., uncompacted) volume removed and normalized release due to spallings for the second drilling intrusion into CH-TRU waste after an initial E1 intrusion at 350 or 1000 yr.

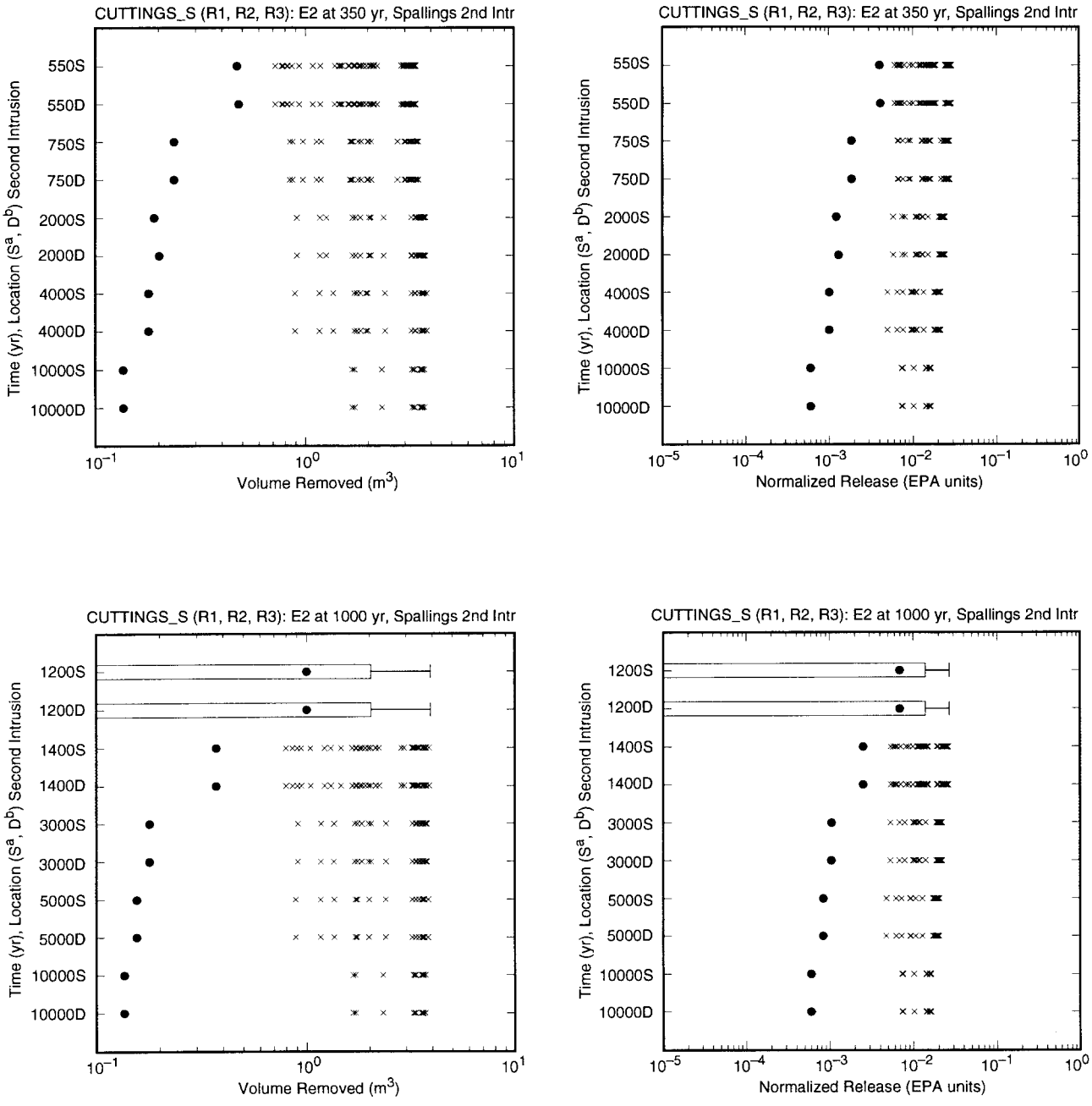

[a]S Signifies Second Intrusion Occurs in Same (S) Waste Panel as First Intrusion
[b]D Signifies Second Intrusion Occurs in Different (D) Waste Panel than First Intrusion

TRI-6342-4783-0

Fig. 9.3.7. Distribution of original (i.e., uncompacted) volume removed and normalized release due to spallings for the second drilling intrusion into CH-TRU waste after an initial E2 intrusion at 350 or 1000 yr.

9.4 Spallings: CCDFs

As for cuttings, each LHS element leads to a CCDF for spallings releases that is obtained by randomly sampling futures of the form in Eq. (2.2.2) and then constructing the corresponding spallings release for each future. This construction is based on the volumes of material (m^3) released by spallings under different conditions and the radionuclide concentration (EPA units/m^3) in that material (Table 9.4.1).

For each sampled intrusion time, radionuclide concentration can be obtained by interpolating on $C_{CH}(\tau_k)$. Further, for an initial intrusion, the volume of released material can be obtained by interpolating on $VS_{E0,U}(\tau_k)$ and $VS_{E0,L}(\tau_k)$. Obtaining results for second and subsequent intrusions is more difficult for two reasons. First, results are available for initial intrusions at only 350 and 1000 yr. Second, results are available for second intrusions but not for subsequent intrusions.

The availability of results for initial intrusions at only 350 and 1000 yr is handled by extending these results to initial intrusions at other times on the basis of the assumption that elapsed time from the first to the second intrusion (i.e., $\Delta\tau_{jk}$) is the primary determinant of the spallings release for the second intrusion. Specifically, the following assignments are made:

$$VS_{E1,S}(\tau, \Delta\tau_{1k}) = VS_{E1,S}(\tau_1, \Delta\tau_{1k}) \tag{9.4.1}$$

for $100 \le \tau \le \tau_1 = 350$ yr, and

$$VS_{E1,S}(\tau, \Delta\tau_{2k}) = VS_{E1,S}(\tau_2, \Delta\tau_{2k}) \tag{9.4.2}$$

for $\tau_2 = 1000 \le \tau \le 10{,}000$ yr. Similar assignments are also made for $VS_{E1,D}$, $VS_{E2,S}$ and $VS_{E2,D}$. The lack of results for more than two intrusions is handled by assuming that spallings releases for third and subsequent intrusions can be estimated by ignoring intermediate intrusions and treating the initial intrusion and the particular subsequent intrusion under consideration as if they were the only two intrusions in existence (Table 9.4.1).

Table 9.4.1. Results Available for Use in CCDF Construction for Spallings Releases

$C_{CH}(\tau_k)$	=	concentration (EPA units/m^3) in CH-TRU waste at time τ_k, where τ_k, k = 1, 2, ..., 9, corresponds to 100, 125, 175, 350, 1000, 3000, 5000, 7500 and 10,000 yr, respectively. See curve "CH-TRU waste within waste panels" in Fig. 9.1.1. Source: U.S. DOE 1995a, Sanchez et al. 1997.
$VS_{E0,U}(\tau_k)$	=	volume (m^3) of original (i.e., uncompacted) material released by a drilling intrusion into a previously unintruded repository at time τ_k that encounters CH-TRU waste in an upper waste panel, where τ_k, k = 1, 2, ..., 6 corresponds to 100, 350, 1000, 3000, 5000 and 10,000 yr, respectively. See Fig. 9.3.1. Source: CUTTINGS_S.
$VS_{E0,L}(\tau_k)$	=	same as $VS_{E0,U}(\tau_k)$ but for intrusion into a lower waste panel. See Fig. 9.3.1.
$VS_{E1,S}(\tau_j, \Delta\tau_{jk})$	=	volume (m^3) of original (i.e., uncompacted) material released by second drilling intrusion at time $\tau_j + \Delta\tau_{jk}$ into the same waste panel penetrated by an initial E1 intrusion at time τ_j, where (1) τ_j, j = 1, 2, corresponds to 350 and 1000 yr; (2) $\tau_1 + \Delta\tau_{1k}$, k = 1, 2, ..., 7, corresponds to 350, 550, 750, 2000, 4000, 10,000, and 10,250 yr (i.e., $\Delta\tau_{1k}$ = 0, 200, 400, 1650, 3650, 9650, 9900 yr), results for k = 2, 3, ..., 6 are summarized in Fig. 9.3.6, $VS_{E1,S}(\tau_1, \Delta\tau_{11}) = VS_{E1,S}(\tau_1, \Delta\tau_{12})$ (i.e., $VS_{E1,S}$ (350, 0) = $VS_{E1,S}$ (350, 200)), and $VS_{E1,S}(\tau_1, \Delta\tau_{16}) = VS_{E1,S}(\tau_1, \Delta\tau_{17})$ (i.e., $VS_{E1,S}$ (350, 9650) = $VS_{E1,S}$ (350, 9900)), and (3) $\tau_2 + \Delta\tau_{2k}$, k = 1, 2, ..., 6, corresponds to 1000, 1200, 1400, 3000, 5000 and 10,000 yr (i.e., $\Delta\tau_{2k}$ = 0, 200, 400, 1000, 4000, 9000 yr), results for k = 2, 3, ..., 6 are summarized in Fig. 9.3.6, and $VS_{E1,S}(\tau_2, \Delta\tau_{21}) = VS_{E1,S}(\tau_2, \Delta\tau_{22})$ (i.e., $VS_{E1,S}$ (1000, 0) = $VS_{E1,S}$ (1000, 200)). Source: CUTTINGS_S. The assignments $VS_{E1,S}$ (350, 0) = $VS_{E1,S}$ (350, 200) and $VS_{E1,S}$ (1000, 0) = $VS_{E1,S}$ (1000, 200) are made to bracket the time period between the occurrence of the first drilling intrusion and the failure of the plug at the Rustler/Salado interface; the assignment $VS_{E1,S}$ (350, 9650) = $VS_{E1,S}$ (350, 9900) is made to facilitate the use of $VS_{E1,S}(\tau_1, \Delta\tau_{1k})$ for initial intrusions before τ_1 = 350 yr.
$VS_{E1,D}(\tau_j, \Delta\tau_{jk})$	=	same as $VS_{E1,S}(\tau_j, \Delta\tau_{jk})$ but for intrusion into different waste panel. See Fig. 9.3.6.
$VS_{E2,S}(\tau_j, \Delta\tau_{jk})$	=	same as $VS_{E1,S}(\tau_j, \Delta\tau_{jk})$ but for initial E2 intrusion. See Fig. 9.3.7.
$VS_{E2,D}(\tau_j, \Delta\tau_{jk})$	=	same as $VS_{E1,D}(\tau_j, \Delta\tau_{jk})$ but for initial E2 intrusion. See Fig. 9.3.7.

For each LHS element, nS = 10,000 futures are randomly selected and the corresponding spallings releases are determined as shown in Table 9.4.2. As an aside, the same 10,000 futures are used for all CCDF constructions for a given LHS element, which ultimately permits the combining of all release modes (i.e., cuttings and cavings, spallings, direct brine release, groundwater transport) into a single CCDF. The resultant CCDFs for spallings releases to the accessible environment are then constructed (Fig. 9.4.1). All the CCDFs fall below the boundary line specified in 191.13(a). Overall, the CCDFs tend to be farther from the boundary line and also more scattered than the CCDFs for cuttings and cavings (Fig. 9.2.2), with 18 out of 100 CCDFs being degenerate (i.e., having no nonzero releases) for the first replicate. However, the distribution is still quite stable across the three replicates (Fig. 9.4.2).

The division of the CCDFs in Fig. 9.2.2 into four distinct groups depends on when an initial intrusion into the repository will produce nonzero releases. With the drilling rate into the excavated regions of the repository given by $\lambda = 6.14 \times 10^{-6}$ yr^{-1} during the 600 yr of passive institutional controls (i.e., $(2.94 \times 10^{-5}$ yr$^{-1})$ (0.209); see Sects. 3.2, 3.4) and by $\lambda = 6.14 \times 10^{-4}$ yr^{-1} after passive institutional controls are assumed to have ended (i.e., $(2.94 \times 10^{-3}$ yr$^{-1})$ (0.209); see Sects. 3.2, 3.3), the probabilities of no drilling intrusions by 1000, 3000 and 5000 yrs are given by 0.83, 0.24 and 0.071, respectively. These probabilities approximately correspond to where the three lower groups of CCDFs emerge from the ordinate, with these groups resulting from sample elements in which repository pressure has not reached 8 MPa by 1000, 3000 and 5000 yr, respectively. The upper most group of CCDFs emerges at approximately 1, which implies that initial intrusions at all times for the corresponding LHS elements are producing nonzero releases. Probabilities above are actually overestimates because spallings only gives releases for intrusions into CH-TRU waste. The CCDFs tend to emerge at lower probabilities because there is no guarantee that the specified time will actually have nonzero releases associated with it.

The primary determinant of the uncertainty in the CCDFs in Fig. 9.4.1 is the pressure conditions in repository (Fig. 9.3.2), with no spallings releases taking place at pressures less than 8 MPa. Given that the pressure is above 8 MPa, the uncertainty in the spallings release is determined by *WPRTDIAM* (Fig. 9.3.3).

To provide additional perspective, CCDFs for volume of material released by spallings (i.e., the quantity obtained from Table 9.4.2 when C_{CH} is set to 1) can also be constructed (Fig. 9.4.3). Similarly to cuttings, the release of more than 10 m^3 of material over 10,000 yr is unlikely.

As was done for the cuttings CCDFs, a sensitivity analysis can be performed on the expected spallings releases associated with each CCDF (Table 9.4.3). The regressions for volume and normalized release are almost identical. The most important variable is *WMICDFLG*, with expected releases tending to increase with increasing values of *WMICDFLG* due to the important influence of this variable on the pressure in the repository at the time of the first drilling intrusion (Fig. 7.4.1, Table 7.4.1). Positive effects are also indicated for *HALPOR*, *WGRCOR*, *HALPRM*,

Table 9.4.2. Determination of Spallings Release $f_{SP}(\mathbf{x}_{st})$ for an Arbitrary Future $\mathbf{x}_{st}$ of Form in Eq. (2.2.2)

Notation:

nH_i = number of intrusions prior to intrusion i that penetrate pressurized brine and use plugging pattern 2 (i.e., two discrete plugs)

nD = number of intrusions required to deplete brine pocket (see *BPVOL* in Table 5.2.1 for definition of nD)

$\tilde{b}_i$ = 0 if intrusion i into (1) nonexcavated area or (2) excavated area and plugging pattern 1 used (i.e., continuous plug)

= 1 if intrusion i into excavated area, penetrates pressurized brine, plugging pattern 2 used, and $nH_i \le nD$

= 2 if intrusion i into excavated area and either (1) penetrates pressurized brine, plugging pattern 2 used, and $nH_i > nD$, (2) does not penetrate pressurized brine and plugging pattern 2 used, or (3) plugging pattern 3 used (i.e., three discrete plugs)

Release rSP_i for intrusion into nonexcavated area at time t_i: $rSP_i = 0$.

Release rSP_i for intrusion into pressurized repository at time t_i (i.e., $i = 1$ or $\tilde{b}_j = 0$ for $j = 1, 2, \ldots, i-1$):

$$rSP_i = \begin{cases} 0 & \text{if intrusion penetrates RH-TRU waste} \\ C_{CH}(t_i)^{a}\, VS_{E0,U}(t_i) & \text{if } l_i \text{ in upper waste panel} \\ C_{CH}(t_i)\, VS_{E0,L}(t_i) & \text{if } l_i \text{ in lower waste panel.} \end{cases}$$

Release rSP_i for intrusion into a depressurized repository at time t_i with no E1 intrusion in first $i-1$ intrusions (i.e., $\tilde{b}_k = 0$ for $k = 1, 2, \ldots, j-1$, $\tilde{b}_j = 2$, $\tilde{b}_k \ne 1$ for $k = j+1, j+2, \ldots, i-1$):

$$rSP_i = \begin{cases} 0 & \text{if intrusion penetrates RH-TRU waste} \\ C_{CH}(t_i)\, VS_{E2,S}(t_j, t_i - t_j)^{b} & \text{if } l_j, l_i \text{ in same waste panel} \\ C_{CH}(t_i)\, VS_{E2,D}(t_j, t_i - t_j) & \text{if } l_j, l_i \text{ in different waste panels.} \end{cases}$$

Release rSP_i for intrusion into a depressurized repository at time t_i with first E1 intrusion at time $t_j < t_i$ (i.e., $\tilde{b}_k \ne 1$ for $k = 1, 2, \ldots, j-1$, $b_j = 1$):

$$rSP_i = \begin{cases} 0 & \text{if intrusion penetrates RH-TRU waste} \\ C_{CH}(t_i)\, VS_{E1,S}(t_j, t_i - t_j) & \text{if } l_j, l_i \text{ in same waste panel} \\ C_{CH}(t_i)\, VS_{E1,D}(t_j, t_i - t_j) & \text{if } l_j, l_i \text{ in different waste panels.} \end{cases}$$

Spallings release $f_{SP}(\mathbf{x}_{st})$:

$$f_{SP}(\mathbf{x}_{st}) = \sum_{i=1}^{n} rSP_i$$

[a] Here and elsewhere, appearance of an undefined time implies linear interpolation between defined times in Table 9.4.1.

[b] Here and elsewhere, appearance of two undefined times implies two-dimensional linear interpolation between defined times in Table 9.4.1.

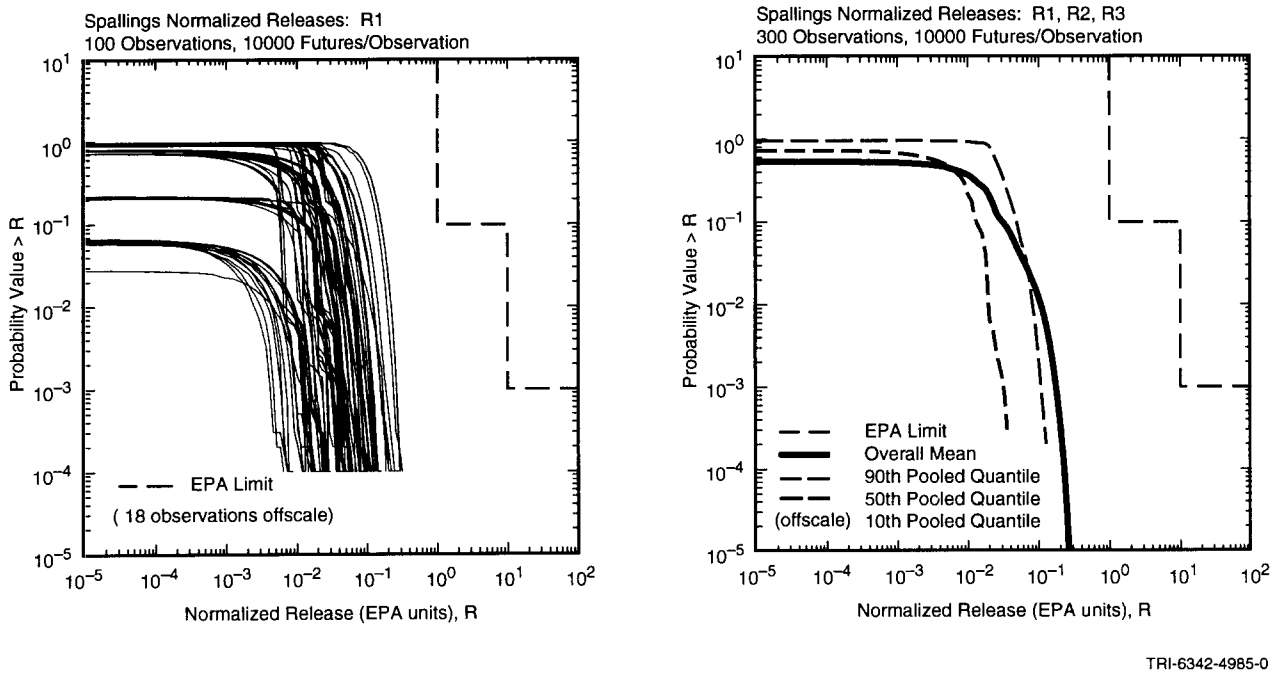

Fig. 9.4.1. Distribution of CCDFs for normalized release to accessible environment over 10,000 yr due to spallings: CCDFs for replicate R1 (left frame), and mean and percentile curves obtained by pooling replicates R1, R2 and R3 (right frame).

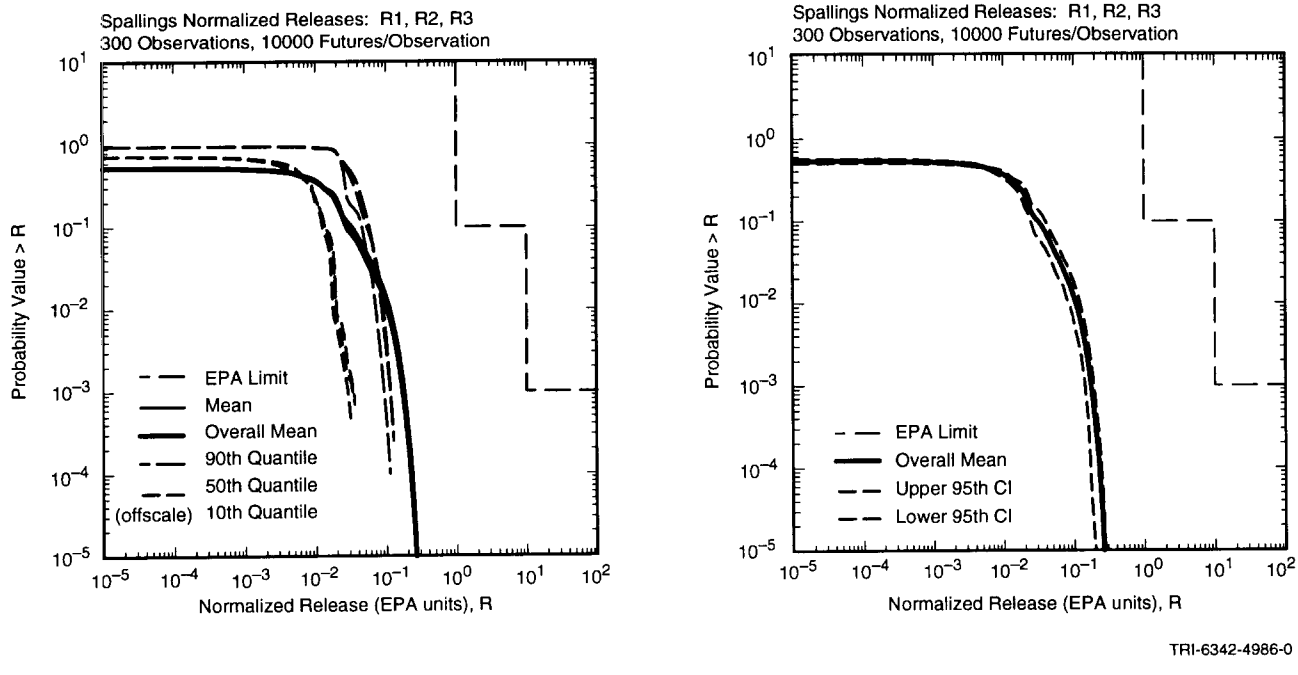

Fig. 9.4.2. Outcome of replicated sampling for distribution of CCDFs for normalized release to the accessible environment over 10,000 yr due to spallings: mean and percentile curves for individual replicates (left frame) and confidence intervals (CIs) on mean curve obtained from the three replicates (right frame).

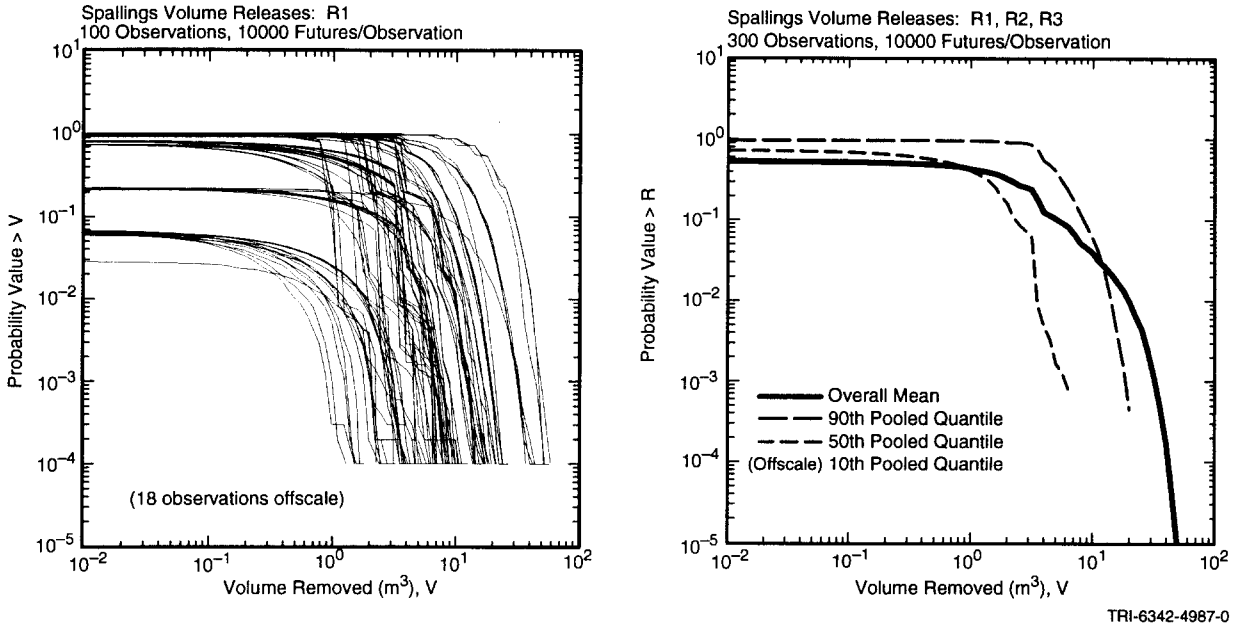

Fig. 9.4.3. Distribution of CCDFs for volume of material removed to accessible environment over 10,000 yr due to spallings: CCDFs for replicate R1 (left frame), and mean and percentile curves obtained by pooling replicates R1, R2 and R3 (right frame).

Table 9.4.3. Stepwise Regression Analyses with Rank-Transformed Data for Expected Volume and Expected Normalized Release Associated with Individual CCDFs for Spallings

	Expected Volume			Expected Normalized Release		
Step[a]	Variable[b]	SRRC[c]	R^2	Variable	SRRC	R^2
1	*WMICDFLG*	0.70	0.51	*WMICDFLG*	0.72	0.53
2	*HALPOR*	0.26	0.58	*HALPOR*	0.26	0.60
3	*WGRCOR*	0.25	0.64	*WGRCOR*	0.24	0.66
4	*BHPRM*	−0.21	0.68	*BHPRM*	−0.20	0.70
5	*WPRTDIAM*	−0.19	0.72	*WPRTDIAM*	−0.19	0.73
6	*HALPRM*	0.14	0.74	*HALPRM*	0.13	0.75
7	*WASTWICK*	0.11	0.75	*WASTWICK*	0.11	0.76
8	*ANHPRM*	0.10	0.76	*ANHPRM*	0.10	0.77

[a] Steps in stepwise regression analysis.

[b] Variables listed in order of selection in regression analysis with *ANHCOMP* and *HALCOMP* excluded from entry into regression model.

[c] Standardized rank regression coefficients in final regression model.

[d] Cumulative R^2 value with entry of each variable into regression model.

WASTWICK and *ANHPRM*, with these effects resulting because increasing each of these variables also tends to increase pressure in the repository at the time of the first drilling intrusion (Fig. 7.4.1, Table 7.4.1). Negative effects are indicated for *BHPRM* and *WPRTDIAM*. Increasing *BHPRM* tends to reduce the pressure in the repository below the 8 MPa threshold required for a spallings release (Fig. 8.4.5) and thus to reduce or eliminate spallings releases due to intrusions subsequent to the initial intrusion into the repository. Increasing *WPRTDIAM* tends to decrease the size of the spallings release for a single intrusion (Fig. 9.3.3) and thus to reduce the expected releases.

The examination of scatterplots provides additional perspective on the factors that affect the expected spallings releases (Fig. 9.4.4). The tendency of the spallings release to increase with increasing microbial gas generation is readily seen in the corresponding scatterplot. Also, the zero spallings releases tend to be associated with the smaller values for *HALPOR*. In contrast, the largest spallings releases tend to be associated with the smaller values for *BHPRM* and *WPRTDIAM*.

Another way to perform a sensitivity analysis on a distribution of CCDFs is by calculating PRCCs between the exceedance probabilities associated with individual consequence values on the abscissa and the sampled variables. The resulting PRCCs can then be plotted above the consequence values at which they were calculated. The outcomes of an analysis of this type for the CCDFs for spallings volume (Fig. 9.4.3) and normalized release (Fig. 9.4.1) appear in Fig. 9.4.5. The exceedance probabilities for a given volume or normalized release tends to increase as each of *WMICDFLG*, *HALPOR* and *WGRCOR* increases. These positive effects result because increasing each of these variables tends to increase the pressure in the repository at the time of the first drilling intrusion. The negative effect for *WPRTDIAM* results because increasing particle diameter tends to decrease the size of the spallings releases associated with individual drilling intrusions (Fig. 9.3.4). The negative effect for *BHPRM* results because increasing *BHPRM* tends to decrease the pressure in the repository after an initial drilling intrusion (Fig. 8.4.5) and thus reduce the likelihood that second and subsequent drilling intrusions will produce spallings releases (Fig. 9.3.2).

The spallings releases for individual futures were constructed with the assumption that each intrusion could result in a spallings release (Table 9.4.2). However, releases after the first intrusion only occur if the pressure in the repository remains above 8 MPa. The pressure in the repository subsequent to an intrusion is very dependent on the borehole permeability (Fig. 8.4.5). In the present analysis, there is no variation in the permeability in a borehole above the repository for plugging patterns 2 and 3; specifically, all boreholes for a given LHS element are assumed to have the same permeability. As the repository rapidly drops below 8 MPa unless a borehole has a very low permeability, it is probably unreasonable to assume that the pressure in the repository after multiple intrusions has the same value as after a single intrusion. Rather, once a higher permeability borehole occurs, the pressure would drop below 8 MPa and no additional spallings releases would take place. Inclusion of this depressurization mechanism in the analysis would substantially reduce the spallings releases (Fig. 9.4.6).

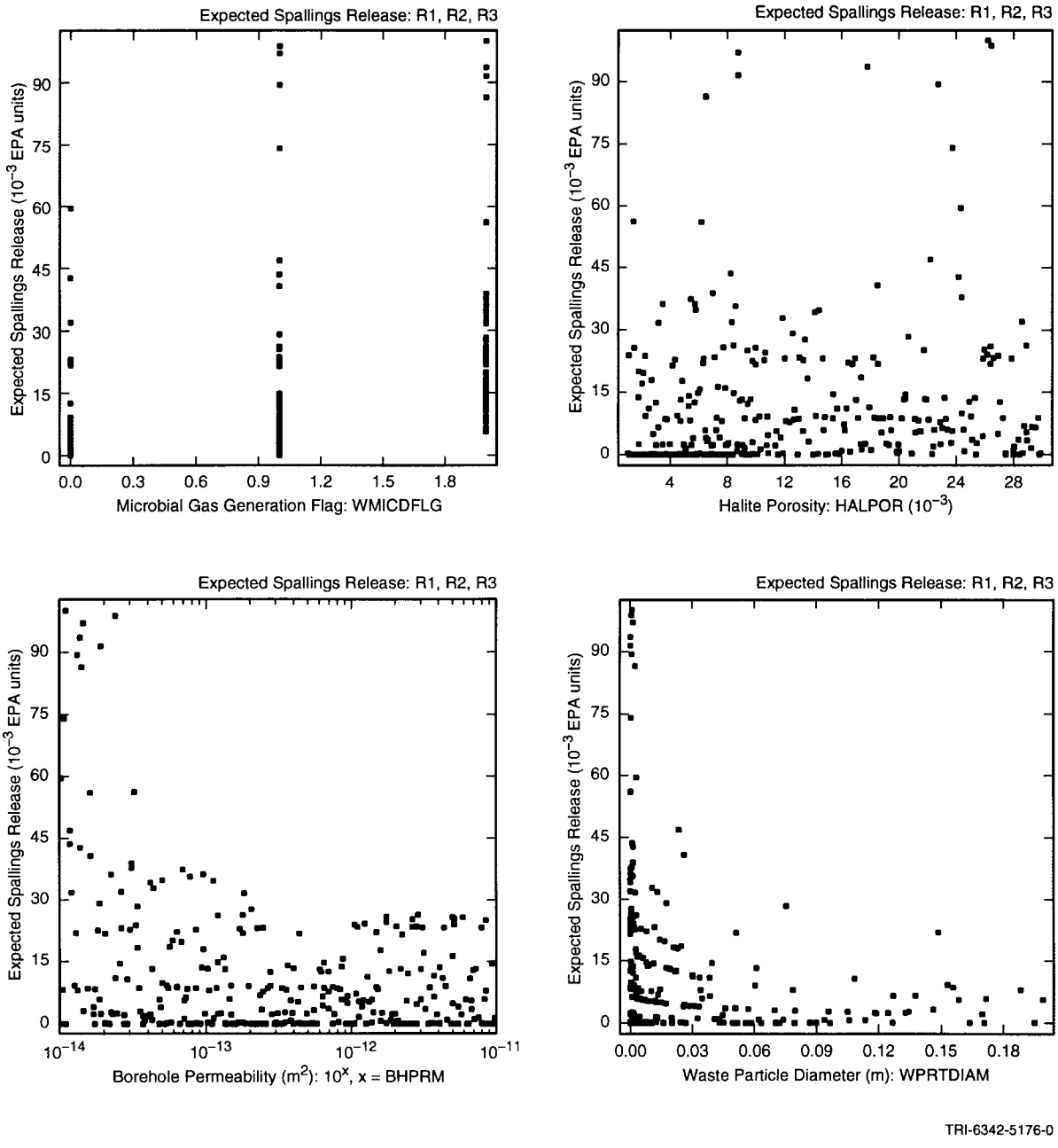

Fig. 9.4.4. Scatterplots for expected normalized releases associated with individual CCDFs for spallings versus *WMICDFLG*, *HALPOR*, *BHPRM*, and *WPRTDIAM*.

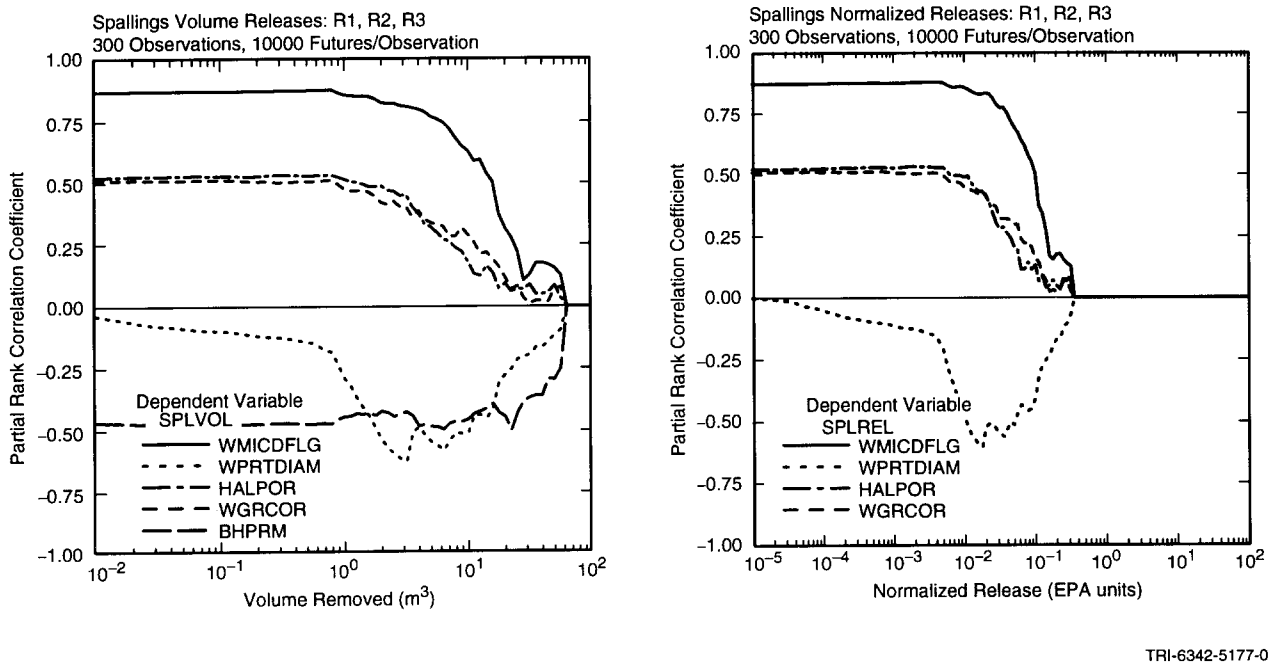

Fig. 9.4.5. Sensitivity analysis based on PRCCs for CCDFs for volume removed and normalized release due to spallings.

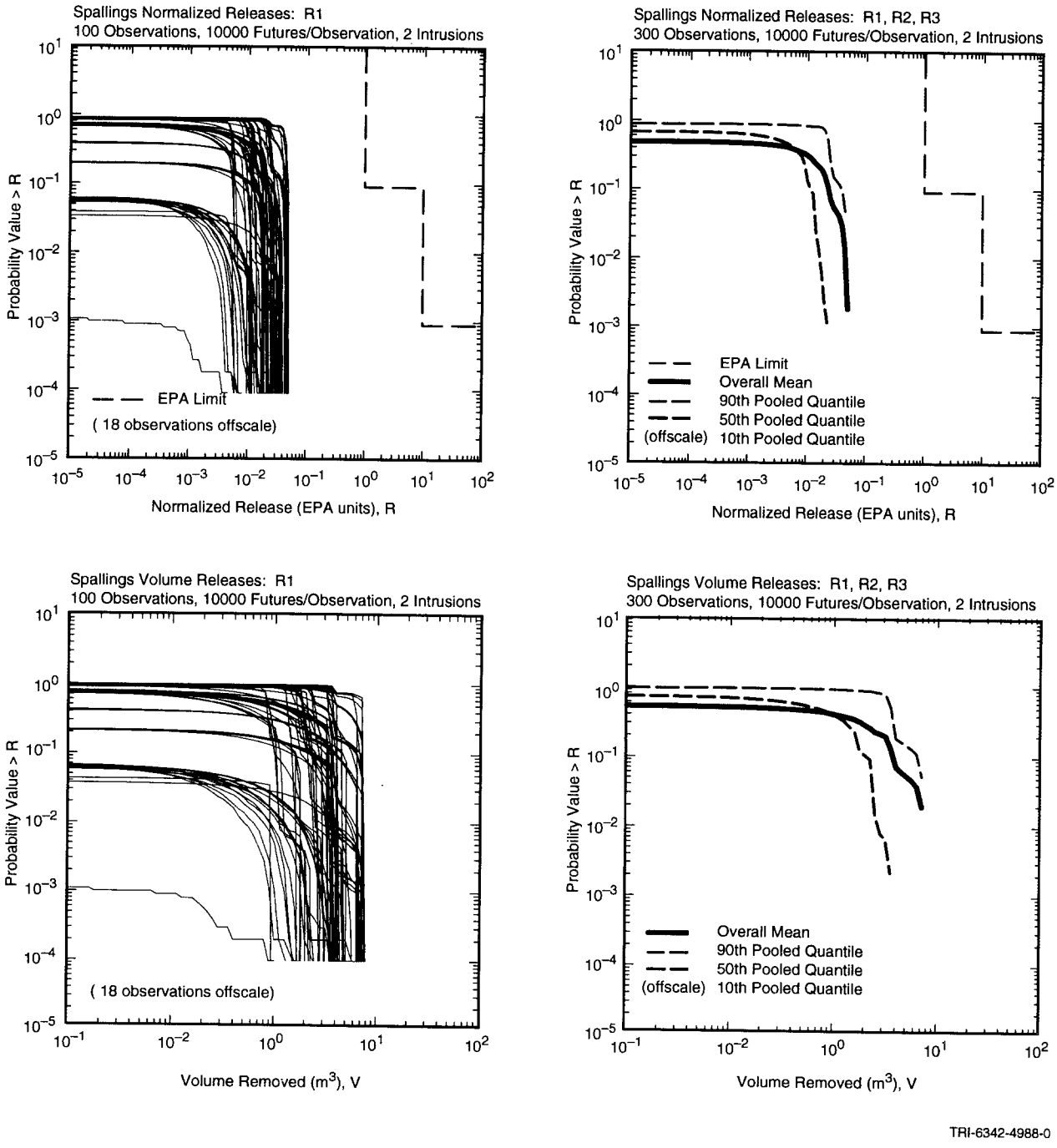

Fig. 9.4.6. Distributions of CCDFs for normalized release to accessible environment and volume of material removed to accessible environment over 10,000 yr due to spallings with the assumption that spallings releases will only take place for the first two drilling intrusions into the repository: CCDFs for replicate R1 (left frames), and mean and percentile curves obtained by pooling replicates R1, R2 and R3 (right frames).

10. Direct Release to Accessible Environment: Direct Brine Release

10.1 Direct Brine Release: Uncertainty and Sensitivity Analysis

Drilling intrusions through CH-TRU waste can produce direct brine releases, which are releases of brine, and hence dissolved radionuclides, due to rapid fluid movement toward a borehole at the time of intrusion (Sect. 4.7). Due to the low permeability of the region surrounding each RH-TRU waste canister, intrusions into RH-TRU waste are assumed not to produce direct brine releases.

The direct brine release model predicts time-dependent releases of brine and gas (Figs. 7 and 11, Stoelzel and O'Brien 1996). For a given drilling intrusion, the volume of released brine (m^3) is multiplied by the concentration (EPA units/m^3) of dissolved radionuclides in CH-TRU waste (Sect. 10.2) at the time of the intrusion to produce the direct brine release. Prior to an E1 intrusion, solubilities associated with brines derived from the Salado Formation are used; after an E1 intrusion, solubilities associated with brines derived from the Castile Formation are used.

The amount of brine associated with a direct brine release is sensitive to both the pressure and brine saturation in the vicinity of the drilling intrusion. In turn, pressure and saturation are dependent on both the time of a drilling intrusion and whether or not the drilling intrusion has been preceded by earlier intrusions. Due to the 1° dip of the repository, it is also possible that conditions influencing direct brine release may differ between upper panels (i.e., panels 1, 2, 3, 6, 7, 8, 9 in Fig. 3.2.1) and lower panels (i.e., panels 4, 5, 10 in Fig. 3.2.1).

The preceding considerations involving the time and location of drilling intrusions also affect spallings releases. Therefore, direct brine release calculations were performed for the same times as spallings calculations. Specifically, direct brine release calculations were performed for initial intrusions at 100, 350, 1000, 3000, 5000 and 10,000 yr and also for intrusions into upper (U) and lower (L) waste panels (Fig. 10.1.1). Most LHS elements produce no releases. Further, most of the nonzero releases occurred for intrusions into the lower waste panel.

Examination of the results for intrusion into the lower waste panel shows that nonzero brine releases tend to be associated with larger values for brine saturation and intermediate values for pressure (Fig. 10.1.2). The largest gas pressures tend to be associated with low brine saturations (Fig. 10.1.3) due to the consumption of brine in the corrosion of steel and hence result in no direct brine releases. As pressure is almost constant throughout the repository (Fig. 8.4.2), the greater number of zero releases for intrusions into the upper waste panels is due to lower brine saturation (Fig. 7.5.1). When a nonzero brine release does occur, the size of the corresponding normalized release tends to increase as the dissolved radionuclide concentration in the brine increases (Fig. 10.1.4).

An alternate way to view the results in Figs. 10.1.2 and 10.1.3 is to use three dimensional plots. Then, the interplay between brine release, saturation and pressure can be seen in a single plot (Fig. 10.1.5).

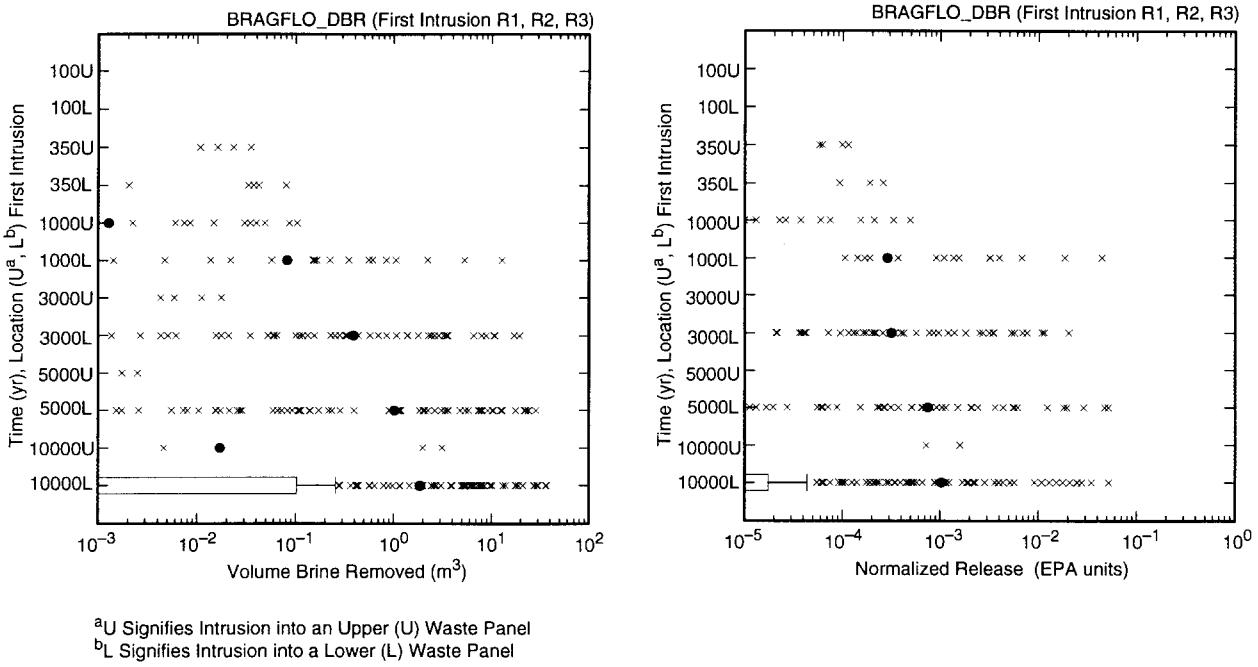

[a]U Signifies Intrusion into an Upper (U) Waste Panel
[b]L Signifies Intrusion into a Lower (L) Waste Panel

TRI-6342-4775-1

Fig. 10.1.1. Distribution of brine release and normalized release due to direct brine release for a single drilling intrusion into a previously unintruded repository.

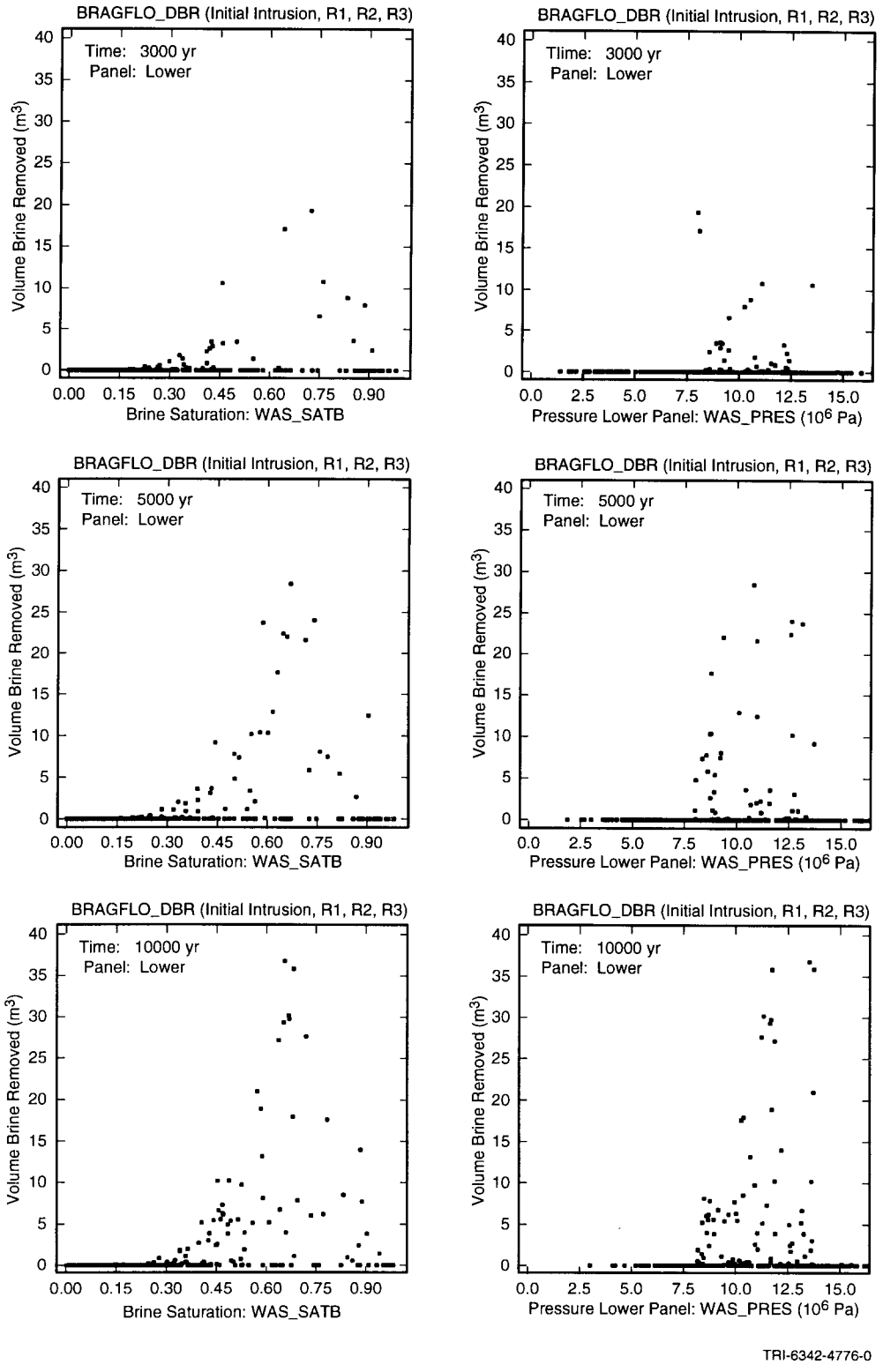

Fig. 10.1.2. Scatterplots for volume of brine removed from repository due to direct brine release resulting from a single drilling intrusion into a previously unintruded repository that passes through CH-TRU waste in a lower waste panel versus brine saturation (*WAS_SATB*) and pressure (*WAS_PRES*) in that panel.

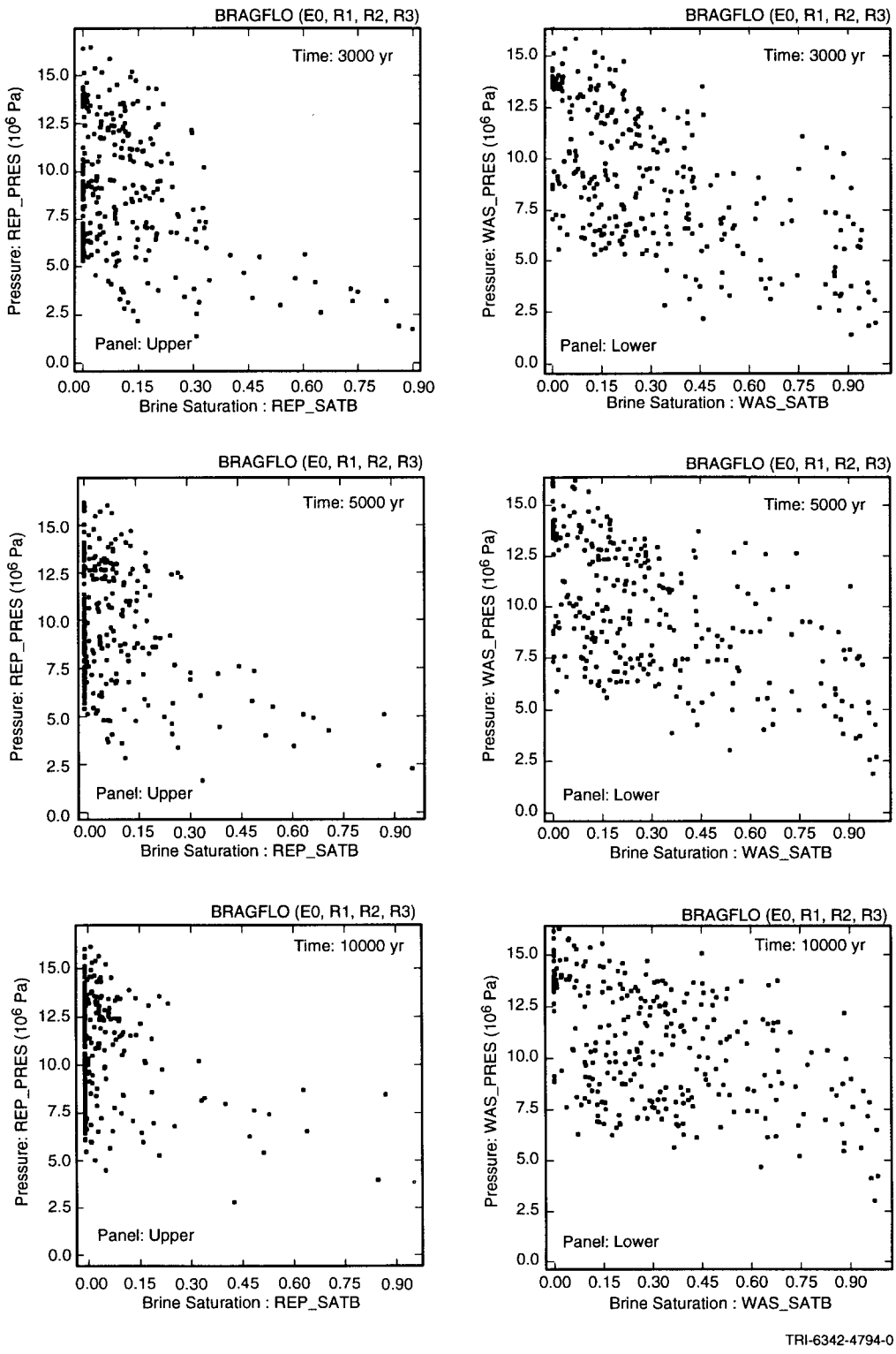

Fig. 10.1.3. Scatterplots for brine saturation versus pressure (Pa) in upper and lower waste panels of undisturbed repository.

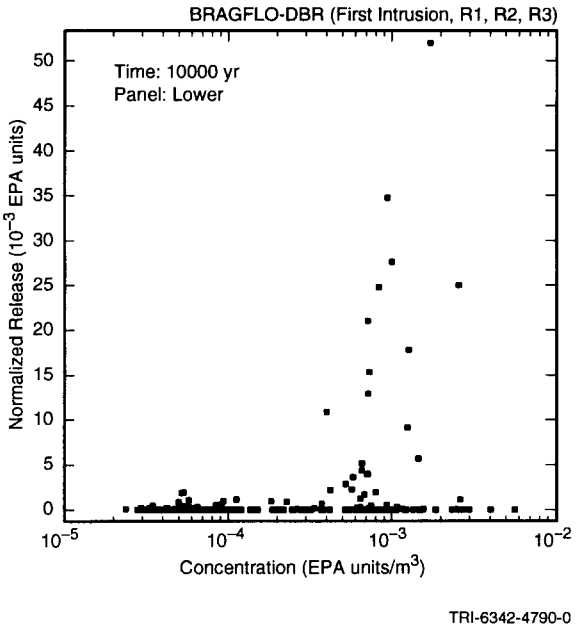

Fig. 10.1.4. Scatterplot for normalized release from repository due to direct brine release resulting from a single drilling intrusion at 10,000 yr into a previously unintruded repository that passes through CH-TRU waste in a lower waste panel versus radionuclide concentration at 10,000 yr.

Direct brine release calculations were also performed for intrusions subsequent to an initial intrusion for the same intrusion combinations as used for spallings (Figs. 10.1.6, 10.1.7). As for initial intrusions, most LHS elements result in no brine release for second intrusions. Due to the effects of the brine pocket, intrusions subsequent to an E1 intrusion tend to have more nonzero releases than intrusions subsequent to an E2 intrusion. Further, intrusions into the same waste panel tend to result in larger releases than intrusions into different waste panels. As pressure is almost constant throughout the repository (Fig. 8.4.2), the greater number of zero releases from intrusions into different waste panels is due to lower brine saturation. However, it should be recognized that, in the computational implementation of the analysis, what is described as two intrusions into the same panel is actually two intrusions into the same lower panel, and what is described as two intrusions into different panels actually consists of an initial intrusion into a lower waste panel and a subsequent intrusion into an upper waste panel (Fig. 4.7.1).

Borehole permeability (i.e., $k = 10^x$, $x = BHPRM$), brine saturation and repository pressure interact to determine the volume of brine released by a second drilling intrusion (Fig. 10.1.8). Specifically, direct brine releases for second intrusions tend to be associated with higher brine saturations, higher pressures, and lower borehole permeabilities. Further, the higher pressures tend to be associated with the lower borehole permeabilities (Fig. 8.4.5). High brine saturations are often associated with high values for borehole permeability (Fig. 8.5.3, 8.5.4). However, this combination of high saturation and high borehole permeability does not result in a spallings release for a second or subsequent intrusion because the repository pressure is too low (Fig. 8.4.5).

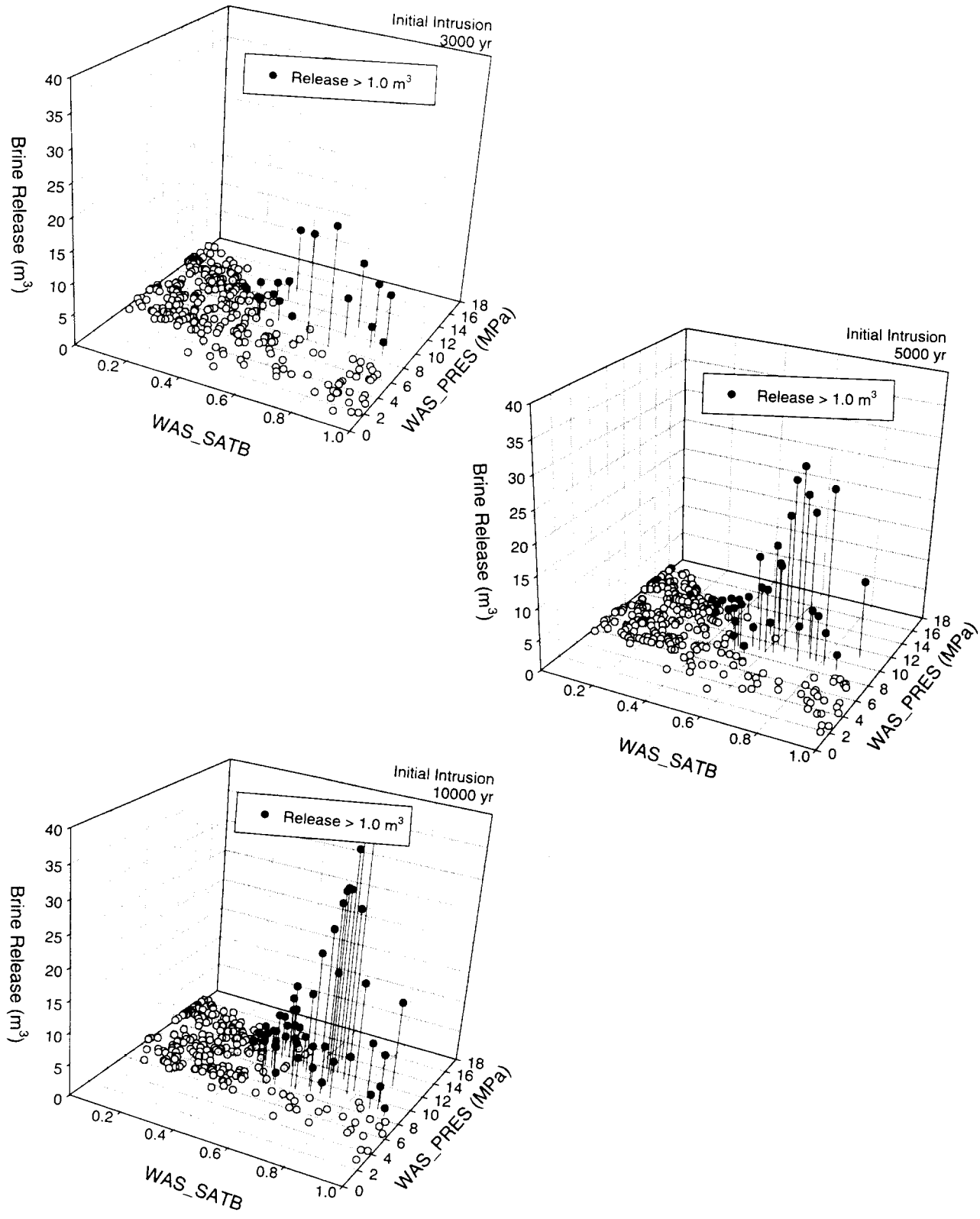

Fig. 10.1.5. Three dimensional scatterplots for volume of brine removed due to direct brine release resulting from a single drilling intrusion into a previously unintruded repository that passes through CH-TRU waste in a lower waste panel, brine saturation (*WAS_SATB*) and pressure (*WAS_PRES*).

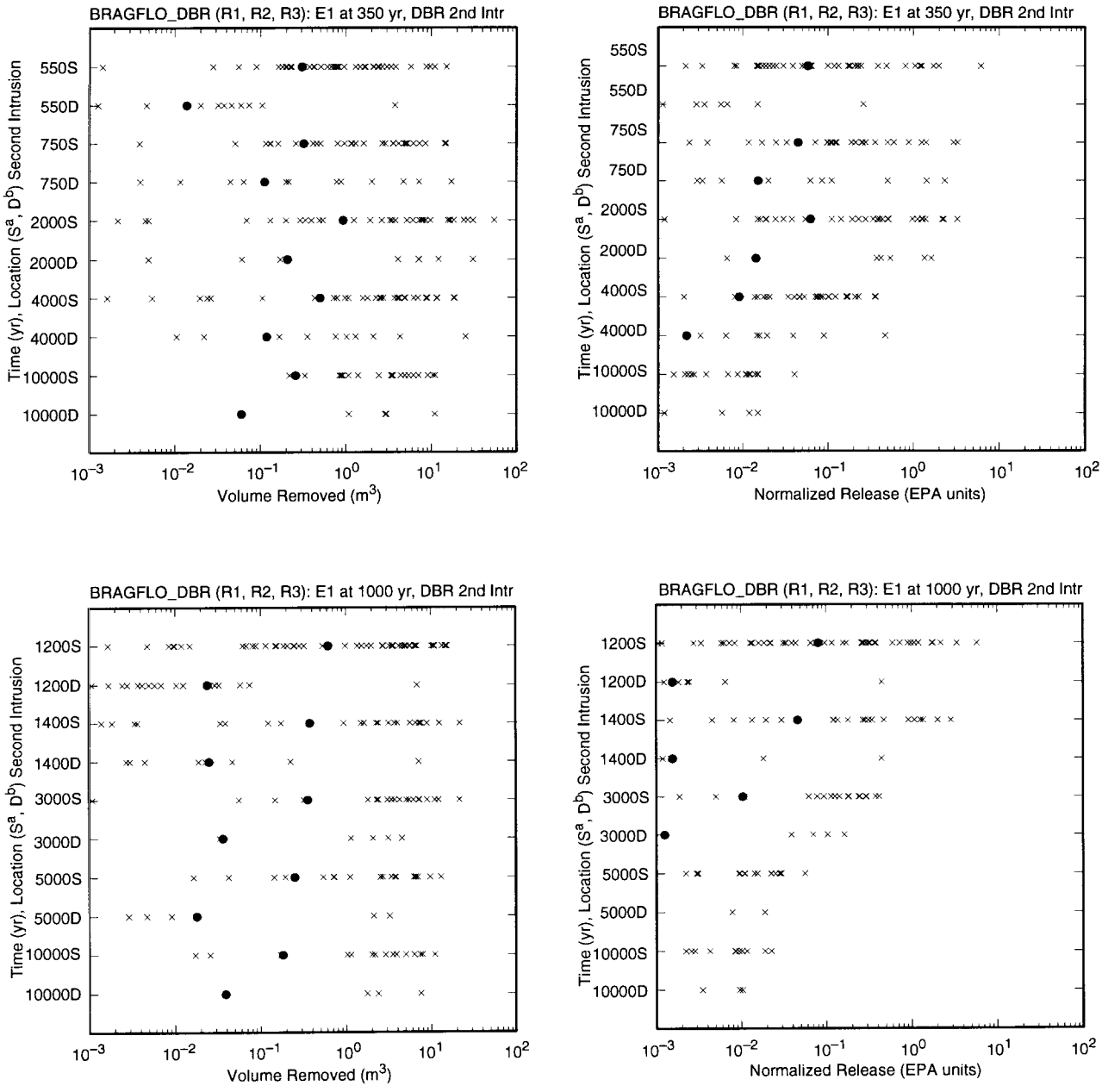

[a]S Signifies Second Intrusion Occurs in Same (S) Waste Panel as First Intrusion
[b]D Signifies Second Intrusion Occurs in Different (D) Waste Panel than First Intrusion

TRI-6342-4791-1

Fig. 10.1.6. Distribution of brine release and normalized release due to direct brine release for the second drilling intrusion into CH-TRU waste after an initial E1 intrusion at 350 or 1000 yr.

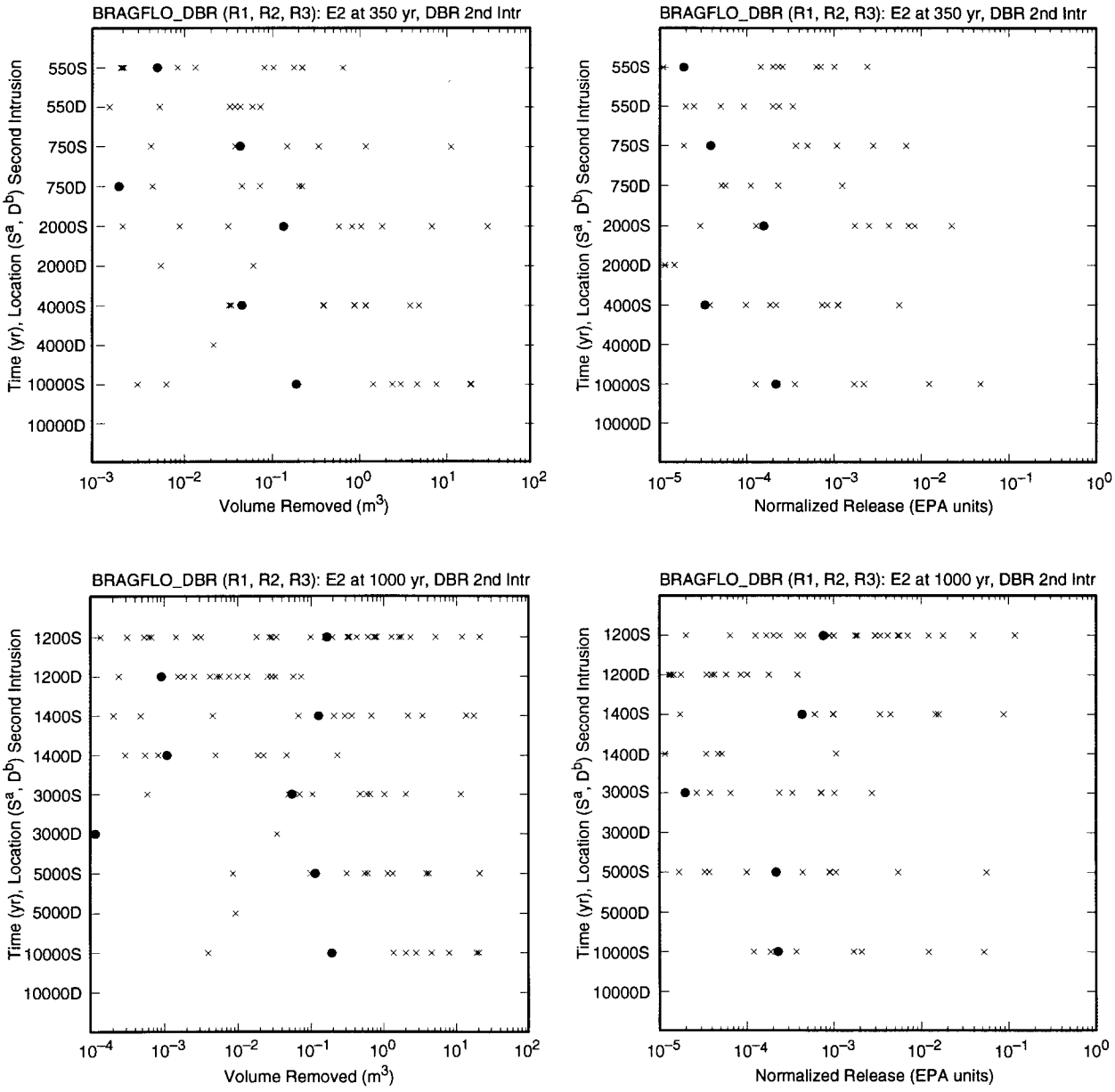

[a]S Signifies Second Intrusion Occurs in Same (S) Waste Panel as First Intrusion

[b]D Signifies Second Intrusion Occurs in Different (D) Waste Panel than First Intrusion

TRI-6342-4793-1

Fig. 10.1.7. Distribution of brine release and normalized release due to direct brine release for the second drilling intrusion into CH-TRU waste after an initial E2 intrusion at 350 or 1000 yr.

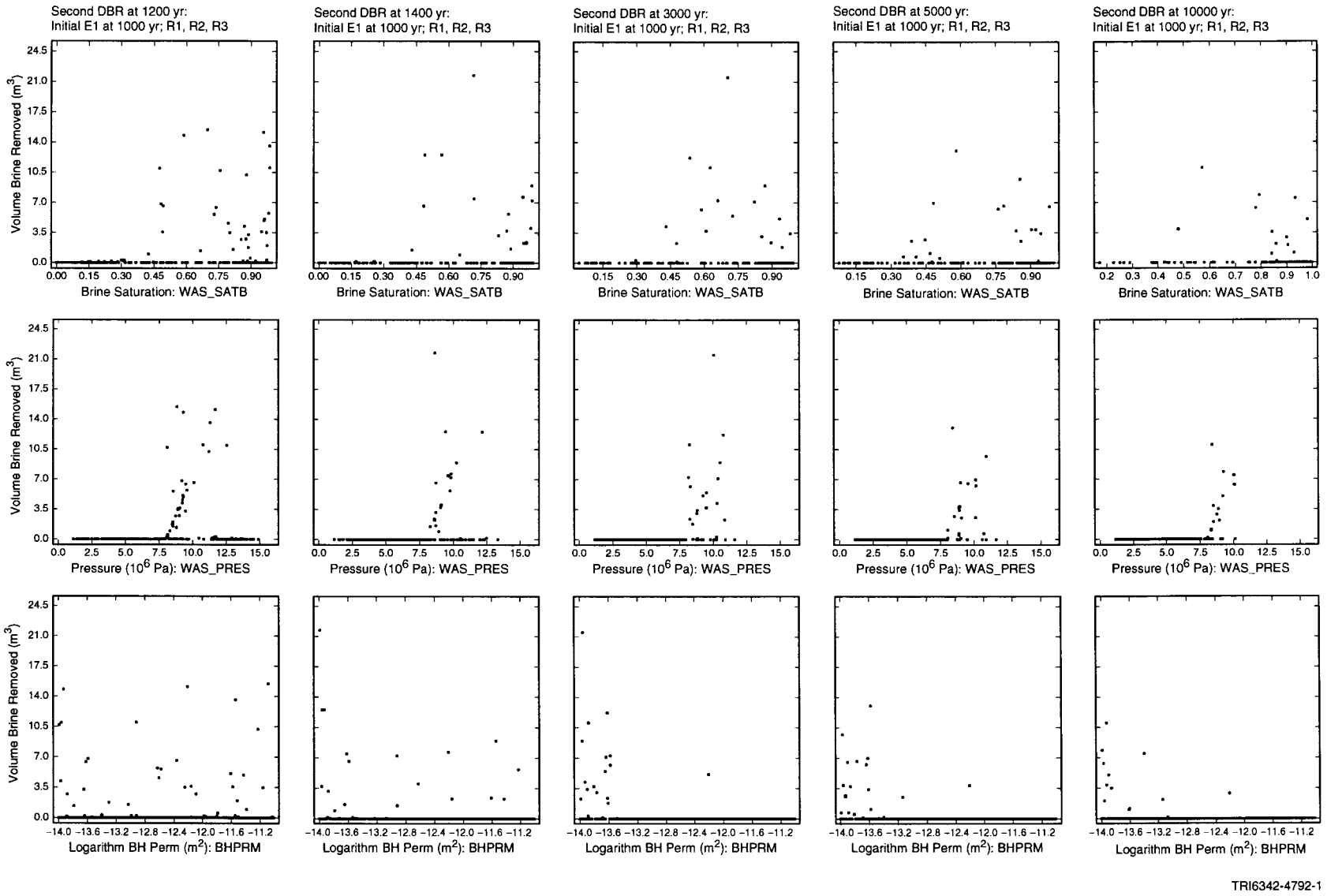

Fig. 10.1.8. Scatterplots for volume of brine removed from repository due to direct brine release resulting from second drilling intrusion into CH-TRU waste in same waste panel as an initial E1 intrusion versus brine saturation (*WAS_SATB*), pressure (*WAS_PRES*) and logarithm of borehole permeability (*BHPRM*).

10.2 Solubility: Uncertainty and Sensitivity Analysis

Given that a nonzero brine release takes place, radionuclide solubility is a major determinant of the size of a direct brine release (Fig. 10.1.4). The solubilities used in determining a direct brine release (see S_T in Table 4.3.1) depend on whether the conditions in the repository are dominated by brine from the Salado Formation (left frame, Fig. 10.2.1) or brine from the Castile formation (right frame, Fig. 10.2.1). For the 1996 WIPP PA, releases from a previously unintruded repository and also releases not preceded by an E1 intrusion use the Salado-dominated solubilities; releases after an E1 intrusion use the Castile-dominated solubilities. Thus, the normalized releases in Figs. 10.1.1 and 10.1.7 were calculated with the appropriate time-dependent solubilities from the left frame of Fig. 10.2.1; similarly, the normalized releases in Fig. 10.1.6 were calculated with the appropriate time-dependent solubilities from the right frame of Fig. 10.2.1.

Each curve in Fig. 10.2.1 results from one LHS element and derives from the values of several uncertain variables as indicated in Table 4.3.1. The noticeable downward shift of the solubility curves in Fig. 10.2.1 results when the number of EPA units in solution changes from being dominated by Am-241 to being dominated by Pu-239. A similar but less conspicuous shift also takes place at earlier times in the left frame of Fig. 10.2.1 when the number of EPA units in solution changes from being dominated by Pu-238 to being dominated by Am-241.

For the 1996 WIPP PA, MgO is assumed to be added to the waste panels as a backfill to remove CO_2 generated by microbial action and thereby to reduce solubilities by increasing the pH in the waste panels. In the absence of MgO, radionuclide solubilities tend to be higher (Fig. 10.2.2). The real difference between the solubilities in Figs. 10.2.1 and 10.2.2 is not the presence or absence of MgO in the repository but rather the presence or absence of CO_2 produced by microbial degradation of cellulosics (Stockman et al. 1996).

The maximum solubilities in the absence of MgO are increased relative to the maximum solubilities in the presence of MgO. However, the minimum solubilities with and without MgO are similar. This pattern occurs because a degree of belief probability of 0.5 was assigned to the occurrence of the microbial degradation of cellulose in the 1996 WIPP PA (see *WMICDFLG* in Table 5.2.1). As a result, the presence or absence of MgO has no effect on the solubilities associated with half of the LHS elements because no microbial degradation of celluloses is assumed to be equivalent to the absence of CO_2, which results in half the solubility curves in Fig. 10.2.2 being identical to curves for the corresponding LHS elements in Fig. 10.2.1. Specifically, if microbial degradation of celluloses does not take for a given LHS element, then the presence or absence of MgO does not affect the solubilities for that element. The presence or absence of microbial degradation is the cause of the two groups of solubility curves in the right frame of Fig. 10.2.2.

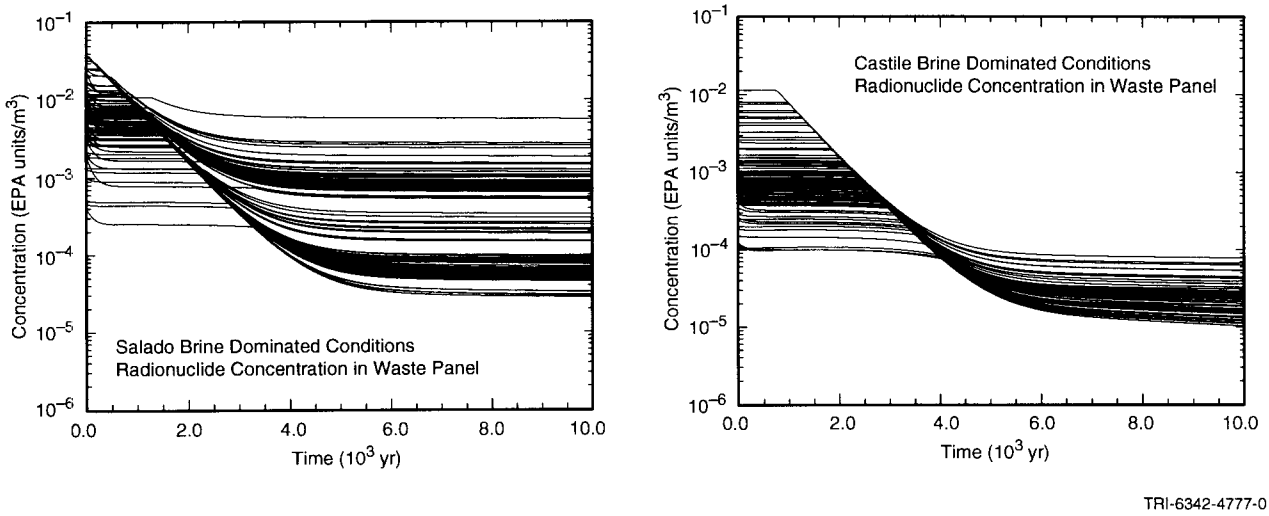

Fig. 10.2.1. Radionuclide concentration (EPA units/m^3) in repository brine with MgO backfill.

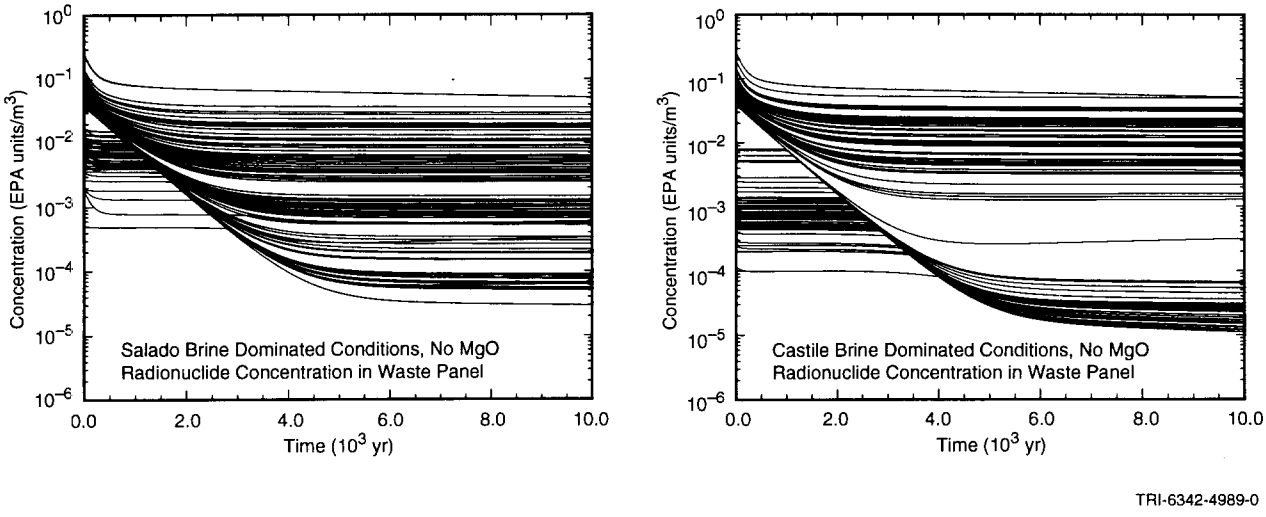

Fig. 10.2.2. Radionuclide concentration (EPA units/m^3) in repository brine without MgO backfill.

10.3 Direct Brine Release: CCDFs

As for cuttings and spallings, each LHS element leads to a CCDF for direct brine releases that is obtained by randomly sampling futures of the form in Eq. (2.2.2) and then constructing the corresponding direct brine release for each future. This construction is based on the volumes of brine (m^3) brought to the surface by direct brine release under different conditions and the radionuclide concentration (EPA units/m^3) in that brine (Table 10.3.1). The structure of the results in Table 10.3.1 for brine releases from direct brine release is the same as the structure of the results in Table 9.4.1 for solid material releases from spallings.

For each sampled intrusion time, radionuclide concentration can be obtained by interpolating on $C_{E0}(\tau_k)$ and $C_{E1}(\tau_k)$ as appropriate (Table 10.3.1). Specifically, $C_{E0}(\tau_k)$ is used before any Castile brine has entered the repository due to an E1 intrusion, and $C_{E1}(\tau_k)$ is used after an E1 intrusion has allowed Castile brine to enter the repository. Further, for an initial intrusion, the volume of released brine can be obtained by interpolating on $VB_{E0,U}(\tau_k)$ and $VB_{E0,L}(\tau_k)$.

As for spallings, obtaining results for second and subsequent intrusions is more difficult for two reasons. First, results are available for initial intrusions at only 350 and 1000 yr. Second, results are available for second intrusions but not for subsequent intrusions. The availability of results for initial intrusions at only 350 and 1000 yr is handled by extending these results to initial intrusions at other times on the basis of the assumption that elapsed time from the first to the second intrusion (i.e., $\Delta\tau_{jk}$) is the primary determinant of the direct brine release for the second intrusion. Specifically, the following assignments are made:

$$VB_{E1,S}(\tau, \Delta\tau_{1k}) = VB_{E1,S}(\tau_1, \Delta\tau_{1k}) \tag{10.3.1}$$

for $100 \le \tau \le \tau_1 = 350$ yr, and

$$VB_{E1,S}(\tau, \Delta\tau_{2k}) = VB_{E1,S}(\tau_2, \Delta\tau_{2k}) \tag{10.3.2}$$

for $\tau_2 = 1000 \le \tau \le 10{,}000$ yr. Similar assignments are also made for $VB_{E1,D}$, $VB_{E2,S}$ and $VB_{E2,D}$. The lack of results for more than two intrusions is handled by assuming that direct brine releases for third and subsequent intrusions can be estimated by ignoring intermediate intrusions and treating the initial intrusion and the particular subsequent intrusion under consideration as if they were the only two intrusions in existence (Table 10.3.2).

For each LHS element, nS = 10,000 futures are randomly selected and the corresponding direct brine releases are determined as shown in Table 10.3.2. The resultant CCDFs for direct brine releases to the accessible environment are then constructed (Fig. 10.3.1). All the CCDFs fall below the boundary line specified in 191.13(a). Overall, the CCDFs tend to be farther from the boundary line and also more scattered than the CCDFs for cuttings and spallings (Figs. 9.2.2, 9.4.1, with 51 out of 100 CCDFs for replicate R1 involving no releases that exceed 10^{-5} EPA units). However, the distribution is still stable across the three replicates (Fig. 10.3.2).

Table 10.3.1. Results Available for Use in CCDF Construction for Direct Brine Releases

$C_{E0}(\tau_k)$	=	concentration (EPA units/m^3) in brine in the repository under undisturbed conditions at time τ_k, where τ_k, k = 1, 2, ..., 9, corresponds to 100, 125, 175, 350, 1000, 3000, 5000, 7500 and 10,000 yr. Based on solubilities (*WSOLAM3S*, *WSOLPU3S*, *WSOLPU4S*, *WSOLU4S*, *WSOLU6S*, *WSOLTH4S*) and chemical conditions (*WOXSTAT*) for repository dominated by Salado brine; see Table 4.3.1 and left frame, Fig. 10.2.1. Source: PANEL
$C_{E1}(\tau_k)$	=	concentration (EPA units/m^3) in brine in the repository subsequent to an E1 intrusion at time τ_k, where τ_k, k = 1, 2, ..., 9, corresponds to 100, 125, 175, 350, 1000, 3000, 5000, 7500 and 10,000 yr. Based on solubilities (*WSOLAM3C*, *WSOLPU3C*, *WSOLPU4C*, *WSOLU6C*) and chemical conditions (*WPHUMOX3*, *WOXSTAT*) for repository dominated by Castile brine; see Table 4.3.1 and right frame, Fig. 4.3.1. Source: PANEL
$VB_{E0,U}(\tau_k)$	=	volume (m^3) of brine released by a drilling intrusion into a previously unintruded repository at time τ_k that encounters CH-TRU waste in an upper waste panel, where τ_k, k = 1, 2, ..., 6, corresponds to 100, 350, 1000, 3000, 5000 and 10,000 yr, respectively. See Fig. 10.1.1. Source: BRAGFLO_DBR.
$VB_{E0,L}(\tau_k)$	=	Same as $VB_{E0,U}(\tau_k)$ but for intrusion into a lower waste panel. See Fig. 10.1.1.
$VB_{E1,S}(\tau_j, \Delta\tau_{jk})$	=	volume (m^3) of brine released by second drilling intrusion at time $\tau_j + \Delta\tau_{jk}$ into the same waste panel penetrated by an initial E1 intrusion at time τ_j, where (1) τ_j, j = 1, 2, corresponds to 350 and 1000 yr, (2) $\tau_1 + \Delta\tau_{1k}$, k = 1, 2, ..., 7, corresponds to 350, 550, 750, 2000, 4000, 10,000 and 10,250 yr (i.e., $\Delta\tau_{1k}$ = 0, 200, 400, 1650, 3650, 9650, 9900 yr), results for k = 2, 3, ..., 6 are summarized in Fig. 10.1.6, $VB_{E1,S}(\tau_1, \Delta\tau_{11}) = VB_{E1,S}(\tau_1, \Delta\tau_{12})$ (i.e., $VB_{E1,S}$ (350,0) = $VB_{E1,S}$ (350, 200)), and $VB_{E1,S}(\tau_1, \Delta\tau_{16}) = VB_{E1,S}(\tau_1, \Delta\tau_{17})$ (i.e., $VB_{E1,S}$ (350, 9650) = $VB_{E1,S}$ (350, 9900), and (3) $\tau_2 + \Delta\tau_{2k}$, k = 1, 2, ..., 6, corresponds to 1000, 1200, 1400, 3000, 5000 and 10,000 yr (i.e., $\Delta\tau_{2k}$ = 0, 200, 400, 1000, 4000, 9000 yr), results for k = 2, 3, ..., 6 are summarized in Fig. 10.1.6, and $VB_{E1,S}(\tau_1, \Delta\tau_{21}) = VB_{E1,S}(\tau_1, \Delta\tau_{22})$ (i.e., $VB_{E1,S}$ (1000, 0) = $VB_{E1,S}$ (1000, 200)). Source: BRAGFLO_DBR. The assignments $VB_{E1,S}$ (350, 0) = $VB_{E1,S}$ (350, 200) and $VB_{E1,S}$ (1000, 0) = $VB_{E1,S}$ (1000, 200) are made to bracket the time period between the occurrence of the first drilling intrusion and the failure of the plug at the Rustler/Salado interface; the assignment $VB_{E1,S}$ (350, 9650) = $VB_{E1,S}$ (350, 9900) is made to facilitate the use of $VB_{E1,S}(\tau_1, \Delta\tau_{1k})$ for initial intrusions before τ_1 = 350 yr.
$VB_{E1,D}(\tau_j, \Delta\tau_{jk})$	=	same as $VB_{E1,S}(\tau_j, \Delta\tau_{jk})$ but for intrusion into different waste panel. See Fig. 10.1.6.
$VB_{E2,S}(\tau_j, \Delta\tau_{jk})$	=	same as $VB_{E1,S}(\tau_j, \Delta\tau_{jk})$ but for initial E2 intrusion. See Fig. 10.1.7.
$VB_{E2,D}(\tau_j, \Delta\tau_{jk})$	=	same as $VB_{E1,D}(\tau_j, \Delta\tau_{jk})$ but for initial E2 intrusion. See Fig. 10.1.7.

Table 10.3.2. Determination of Direct Brine Release $f_{DB}(\mathbf{x}_{st})$ for an Arbitrary Future $\mathbf{x}_{st}$ of Form in Eq. (2.2.2)

Release rDB_i for intrusion into nonexcavated area at time t_i: $rDB_i = 0$

Release rDB_i for intrusion into pressurized repository at time t_i (i.e., $i = 1$ or $\tilde{b}_j = 0$[a] for $j = 1, 2, \ldots, i-1$):

rDB_i	= 0	if intrusion penetrates RH-TRU waste
	= $C_{E0}(t_i)$[b] $VB_{E0,U}(t_i)$	if l_i in upper waste panel
	= $C_{E0}(t_i)$ $VB_{E0,L}(t_i)$	if l_i in upper waste panel.

Release rDB_i for intrusion into a depressurized repository at time t_i with no E1 intrusion in first $i-1$ intrusions (i.e., $\tilde{b}_k = 0$ for $k = 1, 2, \ldots, j-1$, $\tilde{b}_j = 2$, $\tilde{b}_k \neq 1$ for $k = j+1, j+2, \ldots, i-1$):

rDB_i	= 0	if intrusion penetrates RH-TRU waste
	= $C_{E0}(t_i)$ $VB_{E2,S}(t_j, t_i - t_j)$[c]	if l_j, l_i in same waste panel
	= $C_{E0}(t_i)$ $VB_{E2,D}(t_j, t_i - t_j)$	if l_j, l_i in different waste panels.

Release rDB_i for intrusion into a depressurized repository at time t_i with first E1 intrusion at time $t_j < t_i$ (i.e., $\tilde{b}_k \neq 1$ for $k = 1, 2, \ldots, j-1$, $\tilde{b}_j = 1$):

rDB_i	= 0	if intrusion penetrates RH-TRU waste
	= $C_{E1}(t_i)$ $VB_{E1,S}(t_j, t_i - t_j)$	if l_j, l_i in same waste panel
	= $C_{E1}(t_i)$ $VB_{E1,D}(t_j, t_i - t_j)$	if l_j, l_i in different waste panels.

Spallings release $f_{BL}(\mathbf{x}_{st})$:

$$f_{DB}(\mathbf{x}_{st}) = \sum_{i=1}^{n} rDB_i$$

[a] See Table 9.4.2 for definition of $\tilde{b}_j = 0, 1, 2$.

[b] Here and elsewhere, appearance of an undefined time implies linear interpolation between defined times in Table 10.3.1.

[c] Here and elsewhere, appearance of two undefined times implies two-dimensional linear interpolation between defined times in Table 10.3.1.

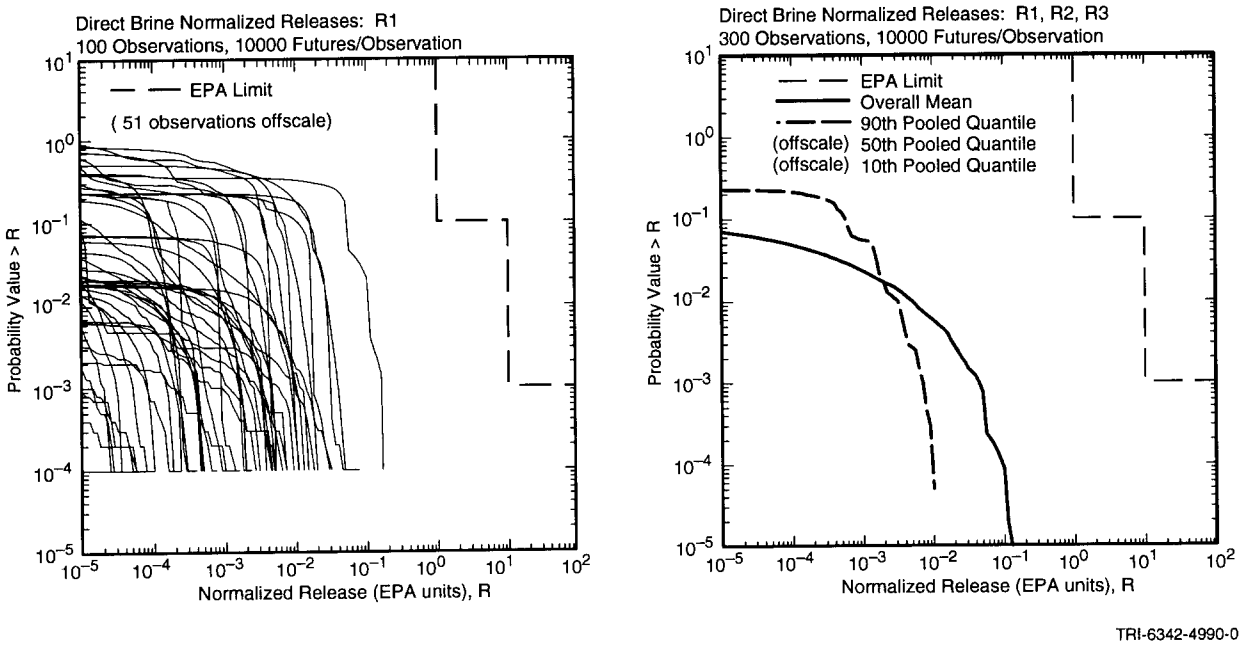

Fig. 10.3.1. Distribution of CCDFs for normalized release to accessible environment over 10,000 yr due to direct brine release: CCDFs for replicate R1 (left frame), and mean and percentile curves obtained by pooling replicates R1, R2 and R3 (right frame).

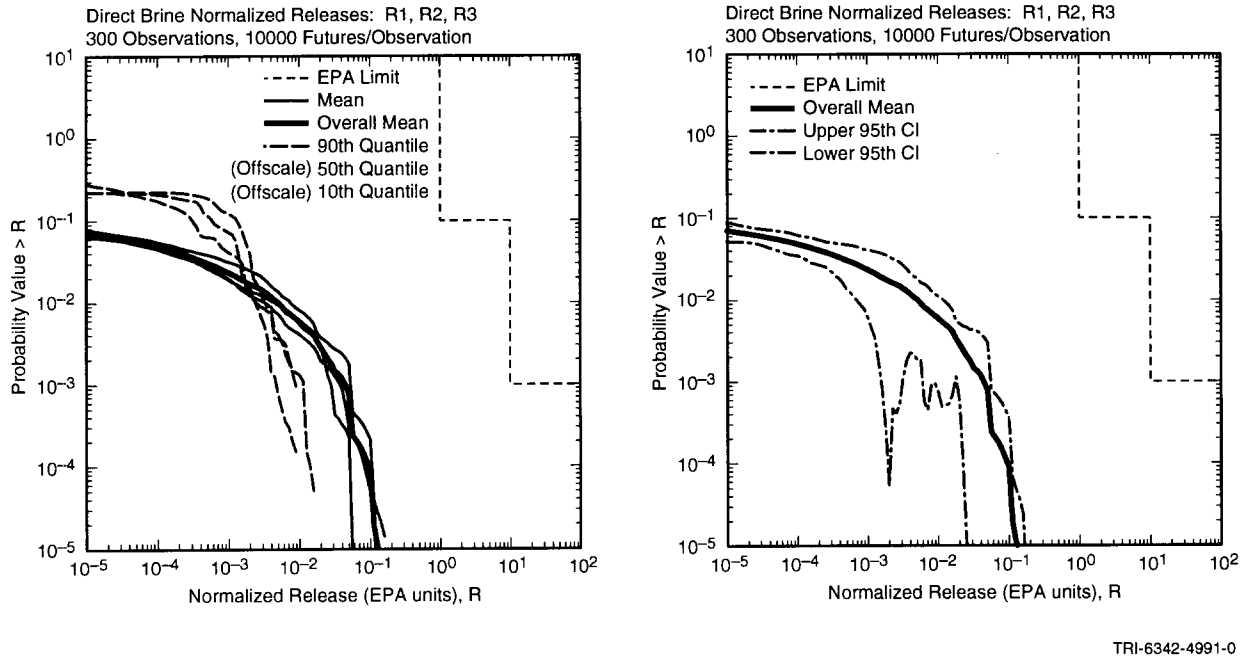

Fig. 10.3.2. Outcome of replicated sampling for distribution of CCDFs for normalized release to the accessible environment over 10,000 yr due to direct brine release: mean and percentile curves for individual replicates (left frame) and confidence intervals (CIs) on mean curve obtained from the three replicates (right frame).

The primary determinants of the uncertainty in the CCDFs in Fig. 10.3.1 are the pressure and brine saturation conditions in the repository, with no direct brine releases taking place for low brine saturation (Figs. 10.1.2, 10.1.5, 10.1.8) and also no releases taking place for low pressures (Figs. 10.1.2, 10.1.5, 10.1.8). For undisturbed conditions, pressure is primarily influenced by factors related to gas generation (i.e., *WMICDFLG*, *WGRCOR*, *WASTWICK*, *HALPOR* and *ANHPRM* as indicated in Fig. 7.4.1 and Table 7.4.1); similarly, brine saturation is also primarily influenced by factors related to brine inflow and gas generation (i.e., *HALPOR*, *WMICDFLG*, *WGRCOR*, *WASTWICK*, and *ANHPRM* as indicated in Fig. 7.5.1 and Table 7.5.1). Subsequent to a drilling intrusion, pressure and saturation are determined primarily by borehole permeability (Figs. 8.4.5, 8.5.3, 8.5.4).

To provide additional perspective, CCDFs for volume of brine released by direct brine release (i.e., the quantity obtained from Table 10.3.2 when C_{E0} and C_{E1} are set to 1) can also be constructed (Fig. 10.3.3). Similarly to cuttings and spallings (Figs. 9.2.5, 9.4.3), the release of more than 10 m^3 of material (i.e., brine) over 10,000 yr is unlikely.

As was done for the cuttings and spallings CCDFs, a sensitivity analysis can be performed on the expected direct brine releases associated with each CCDF (Table 10.3.3). The dominant variables are *WRBRNSAT* and *HALPOR*, with the size of the release tending to decrease as *WRBRNSAT* increases and to increase as *HALPOR* increases. The negative effect for *WRBRNSAT* results from reducing the amount of brine that can take part in a direct brine release, and the positive effect for *HALPOR* results from increasing the amount of brine in the repository and thus also increasing the pressure in the repository under undisturbed conditions. Small positive effects are also indicated for *ANHPRM*, *BPCOMP*, *HALPRM*, *BPINTPRS* and *BPVOL*. However, the final regression models have R^2 values of only 0.49 and 0.50. Thus, these models are not very effective in accounting for the uncertainty in the analysis outcomes. This lack of resolution is due to the large number of sample elements that have no direct brine release. For example, the effects of *WRBRNSAT* and *HALPOR* can be readily seen in the scatterplots in Fig. 10.3.4; however, these effects tend to be obscured by the large number of zero releases. As a reminder, direct brine releases can only take place when the repository is at a pressure that exceeds 8 MPa.

The regressions in Table 10.3.3 included the solubilities of the individual elements as candidate independent variables (see Tables 4.3.1, 10.3.4). However, none of these solubilities were selected in the regression analysis. Basically, the uncertainty in whether or not a direct brine release takes place is swamping out the uncertainty induced by the solubilities when a release does take place. Also, borehole permeability (i.e., $k = 10^x$, $x = BHPRM$) appears to have little effect on the expected release for direct brine release (Fig. 10.3.5); again, this is probably due to the dominant role played by the uncertainty in whether or not a direct brine release occurs at all.

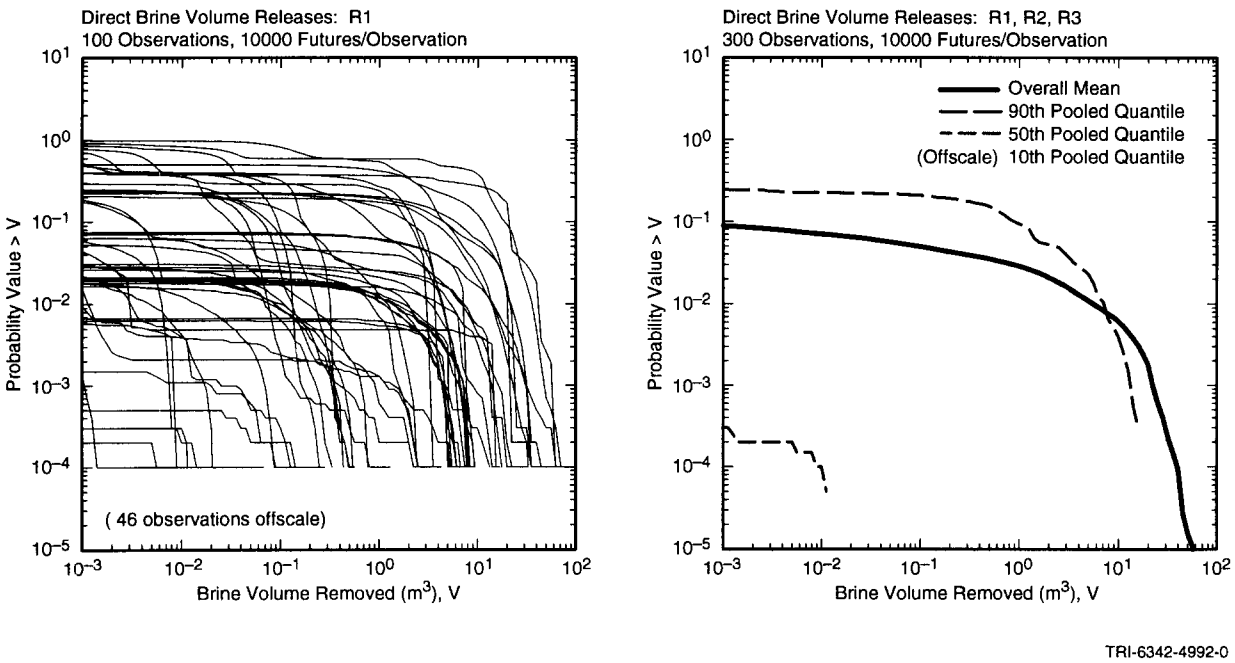

Fig. 10.3.3. Distribution of CCDFs for volume of brine removed to accessible environment over 10,000 yr due to direct brine release: CCDFs for replicate R1 (left frame), and mean and percentile curves obtained by pooling replicates R1, R2 and R3 (right frame).

Table 10.3.3. Stepwise Regression Analyses with Rank-Transformed Data for Expected Volume and Expected Normalized Release Associated with Individual CCDFs for Direct Brine Release

	Expected Volume			Expected Normalized Release		
Step[a]	Variable[b]	SRRC[c]	R^{2d}	Variable	SRRC	R^2
1	*WRBRNSAT*	−0.44	0.19	*WRBRNSAT*	−0.46	0.21
2	*HALPOR*	0.35	0.32	*HALPOR*	0.37	0.35
3	*ANHPRM*	0.28	0.39	*ANHPRM*	0.27	0.42
4	*BPCOMP*	0.22	0.44	*BPCOMP*	0.20	0.46
5	*HALPRM*	0.15	0.46	*BPINTPRS*	0.14	0.48
6	*BPINTPRS*	0.14	0.48	*HALPRM*	0.14	0.50
7	*BPVOL*	0.11	0.49			

[a] Steps in stepwise regression analysis.

[b] Variables listed in order of selection in regression analysis with *ANHCOMP* and *HALCOMP* excluded from entry into regression model.

[c] Standardized rank regression coefficients in final regression model.

[d] Cumulative R^2 value with entry of each variable into regression model.

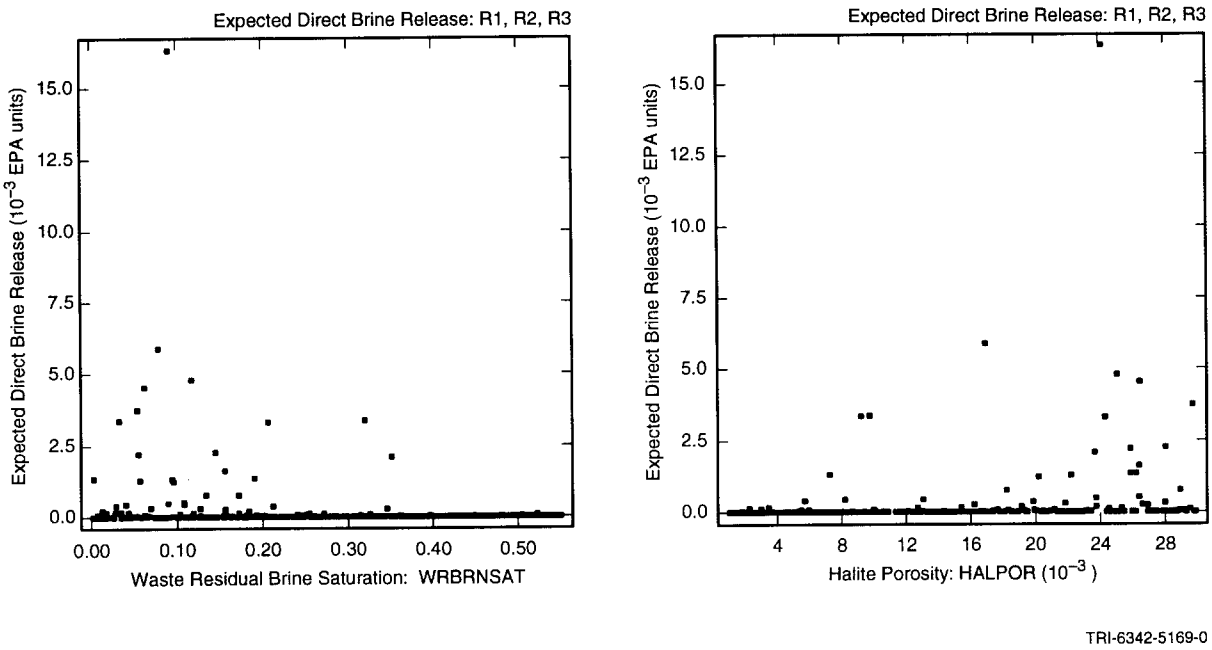

Fig. 10.3.4. Scatterplots for expected normalized releases associated with individual CCDFs for direct brine release versus *WRBRNSAT* and *HALPOR*.

Table 10.3.4 Solubilities Used in Sensitivity Studies Associated with Releases from the Repository (see Table 4.3.1 for definitions of individual solubilities)

Variable	Definition
SOLAMC	Solubility (mol/l) of americium in Castile brine.
SOLPUC	Solubility (mol/l) of plutonium in Castile brine.
SOLTHC	Solubility (mol/l) of thorium in Castile brine.
SOLUC	Solubility (mol/l) of uranium in Castile brine.
SOLAMS	Solubility (mol/l) of americium in Salado brine.
SOLPUS	Solubility (mol/l) of plutonium in Salado brine.
SOLTHS	Solubility (mol/l) of thorium in Salado brine.
SOLUS	Solubility (mol/l) of uranium in Salado brine.

The direct brine releases for individual futures were constructed with the assumption that each intrusion could result in a direct brine release (Table 10.3.2). However, releases after the first intrusion only occur if the pressure in the repository remains above 8 MPa (Fig. 10.1.8). The pressure in the repository subsequent to an intrusion is very dependent on the borehole permeability (Fig. 8.4.5). In turn, this means that the occurrence of direct brine releases subsequent to an initial intrusion is also very dependent on borehole permeability (Fig. 10.1.8). In the present analysis, there is no variation in the permeability in a borehole above the repository for plugging patterns 2 and 3; specifically, all boreholes for a given LHS element are assumed to have the same permeability. As the repository rapidly drops below 8 MPa unless a borehole has a very low permeability, it is probably unreasonable to assume that the pressure in the repository after multiple intrusions has the same value as after a single intrusion. Rather, once a higher permeability borehole occurs, the pressure would drop below 8 MPa and no additional direct brine releases would take place. Inclusion of this depressurization mechanism in the analysis would reduce the direct brine releases (Fig. 10.3.6). However, the differences between the CCDFs with no cutoff (Fig. 10.3.1) and the CCDFs with a two drilling intrusion cutoff (Fig. 10.3.6) are not large, which is consistent with the limited effect indicated for *BHPRM* in Fig. 10.3.5.

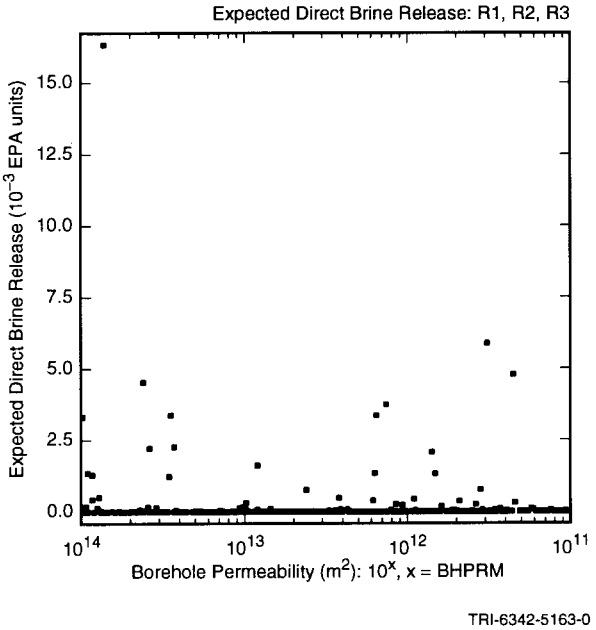

Fig. 10.3.5. Scatterplot for expected normalized releases associated with individual CCDFs for direct brine release versus *BHPRM*.

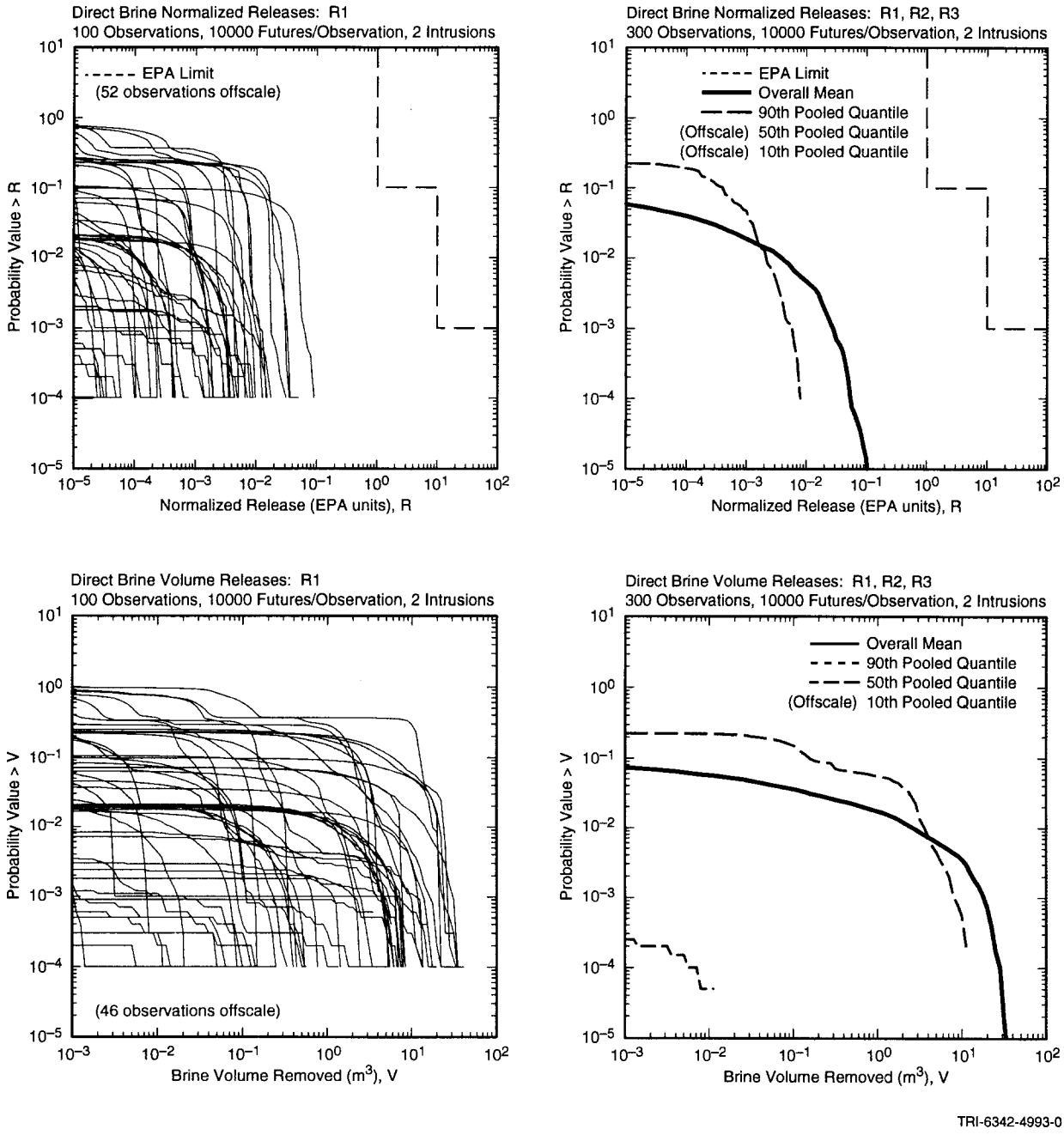

Fig. 10.3.6. Distributions of CCDFs for normalized release to accessible environment and volume of brine removed to accessible environment over 10,000 yr due to direct brine release with the assumption that direct brine releases will only take place for the first two drilling intrusions into the repository: CCDFs for replicate R1 (left frames), and mean and percentile curves obtained by pooling replicates R1, R2 and R3 (right frames).

11. Release from Repository

11.1 Release to Culebra: Uncertainty and Sensitivity Analysis

Radionuclide releases to the Culebra Dolomite were calculated with the NUTS and PANEL programs (Sects. 4.3, 4.4). In turn, these programs used brine flow patterns calculated by BRAGFLO as input (Sects. 4.2, 6.9; Chapts. 7, 8).

Six sets of BRAGFLO calculations were used to support the estimation of radionuclide releases to the Culebra: E0 (i.e., undisturbed conditions), E1 intrusion at 350 yr, E1 intrusion at 1000 yr, E2 intrusion at 350 yr, E2 intrusion at 1000 yr, and E2E1 intrusion with the E2 intrusion at 800 yr and the E1 intrusion at 2000 yr (Table 11.1.1). In turn, the preceding BRAGFLO calculations were used to supply brine flows for use in calculations with NUTS or PANEL (Table 11.1.1). In particular, the BRAGFLO results for E0 conditions were used as input to calculations with NUTS for radionuclide transport under undisturbed conditions. Further, the BRAGFLO results for E1 and E2 intrusions at 350 yr were used as input to NUTS calculations for intrusions at 100 yr and also at 350 yr. For the 100 yr intrusion, the flow pattern used in NUTS subsequent to the intrusion is assumed to be the same as the flow pattern predicted by BRAGFLO subsequent to an intrusion at 350 yr. Similarly, the BRAGFLO results for E1 and E2 intrusions at 1000 yr were used as input to NUTS calculations for intrusions at 1000, 3000, 5000, 7000 and 9000 yr, with the calculations for transport subsequent to intrusions at 3000, 5000, 7000 and 9000 yr performed with the flow patterns obtained from 1000 yr on in the BRAGFLO calculations. As described in Table 6.9.1, each potential NUTS calculation was preceded by a preliminary screening calculation to determine if a full NUTS calculation was required, with full NUTS calculations only being performed for sample elements that had the potential to result in radionuclide releases to the Culebra or the accessible environment. Finally, the BRAGFLO results for the E2E1 intrusion were used as input to PANEL for calculations in which the second (i.e., E1) intrusion was assumed to be in place at 100, 350, 1000, 2000, 4000, 6000 and 9000 yr. Again, the assumption is made that the flow patterns after the intrusions at 100, 350, 1000, 4000, 6000 and 9000 yr are the same as the flow patterns after 2000 yr in the BRAGFLO calculation for the E2E1 intrusion.

Radionuclide release from the repository to the Culebra depends on both the amount of brine flow and the amount of radionuclide that can be transported in this flow. Radionuclides are assumed to exist in five states that can be transported from the repository by flowing groundwater: dissolved, humic colloids, microbial colloids, mineral fragment colloids, and actinide intrinsic colloids. Typically, the concentration in each of these states is a function of one or more sampled variables (Table 4.3.1, Fig. 11.1.1). The "Total" concentrations in Fig. 11.1.1 are the concentrations used in the NUTS and PANEL calculations to determine releases from the repository to the Culebra. In the computational implementation of the analysis, the concentrations in Fig. 11.1.1 are only realized in individual

Table 11.1.1 Calculations Performed with BRAGFLO, NUTS and PANEL to Estimate Radionuclide Releases to the Culebra Dolomite

BRAGFLO Calculation	NUTS/PANEL Calculations
E0	NUTS: E0 (no release to Culebra)
E1 at 350 yr	NUTS: E1 at 100, 350 yr
E1 at 1000 yr	NUTS: E1 at 1000, 3000, 5000, 7000, 9000 yr
E2 at 350 yr	NUTS: E2 at 100, 350 yr
E2 at 1000 yr	NUTS: E2 at 1000, 3000, 5000, 7000, 9000 yr
E2E1 with E2 at 800 yr and E1 at 2000 yr	PANEL: E2E1 at 100, 350, 1000, 2000, 4000, 6000, 9000 yr (Note: an E2E1 intrusion is the same as the E1E2 intrusion referred to in the CCA)

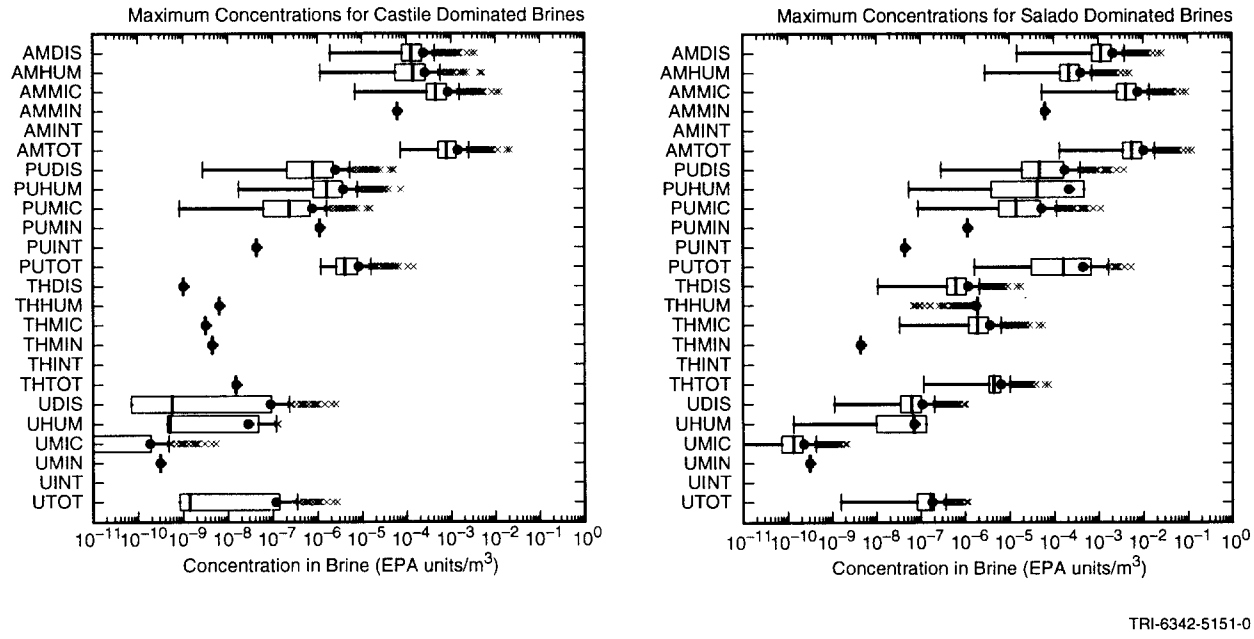

Fig. 11.1.1. Elemental concentrations (EPA units/m^3) in Salado and Castile brines (key: Am, Pu, Th, U correspond to americium, plutonium, thorium, uranium; DIS, HUM, MIC, MIN, INT, TOT correspond to dissolved, humic colloids, microbial colloids, mineral fragment colloids, actinide intrinsic colloids and total).

computational cells if there is adequate inventory in the cell to produce this concentration; otherwise, the concentration is set by assuming all of the relevant element is present in the brine contained in that cell. The effect of inventory depletion due to radioactive decay can be seen in the structure of the total concentration curves in Fig. 10.2.1. Further, the concentrations are a function of whether repository conditions are dominated by Salado or Castile brine (Table 4.3.1).

Radionuclide releases to the Culebra only occur for sample elements for which BRAGFLO predicts nonzero brine flows from the repository to the Culebra. For most sample elements, brine flow from the repository is zero or very small (Fig. 8.6.3) and so little or no radionuclide transport takes place (Fig. 11.1.2). For E1 and E2E1 intrusions, most of the release takes place over a relatively short period of time and then continues at a reduced rate or stops entirely. This behavior results from (1) an initial 200 yr period during which an open borehole exists between the repository and the brine pocket, (2) a subsequent 1000 yr period in which the borehole over its entire length has permeability $k = 10^x$, $x = BHPRM$, and (3) a reduction of the permeability below the repository to $k = 10^x/10$, $x = BHPRM$, after 1200 yr (Table 4.2.8). For the E2E1 intrusion and a few sample elements, a release occurs before the E1 intrusion due to brine flow up the borehole associated with the preceding E2 intrusion. Most sample elements result in little or no release for E1 and E2E1 intrusions due to limited brine flow (Fig 8.6.3). Even fewer sample elements result in releases for E2 intrusions; again, this is due to limited brine flow from the repository to the Culebra (Fig. 8.6.3). However, given equal-sized brine flows, an E2 intrusion will produce a larger release than an E1 or E2E1 intrusion because solubilities in Salado-dominated brines are higher than solubilities in Castile-dominated brines (Fig. 11.1.1). This behavior results in the largest release curves in Fig. 11.1.2 for E2 intrusions exceeding the largest release curves for E1 and E2E1 intrusions.

Results are presented in Fig. 11.1.2 for only two of the intrusion times used in the NUTS and PANEL calculations indicated in Table 11.1.1. A summary of the cumulative releases over 10,000 yr for all intrusion times is given in Fig. 11.1.3. As should be the case, the size of the release decreases with increasing intrusion time due to increased time for radioactive decay and decreased time for transport from the repository to the Culebra. However, at all times, most sample elements result in no significant releases to the Culebra.

The total normalized releases in Figs. 11.1.2 and 11.1.3 are based on Am-241, Pu-238, Pu-239, U-234 and Th-230 (Figs. 11.1.4, 11.1.5, 11.1.6). At early times (i.e., 100 and 350 yr), the release tends to be dominated by Am-241, with an additional contribution from Pu-238 at very early times. With increasing time, Am-241 is lost due to decay and the release is dominated by Pu-239 due to its long half life and large inventory.

The occurrence of releases for E2 intrusions is dominated by *BHPRM* (Fig. 11.1.7). For small values of *BHPRM*, there is not enough flow down the borehole to fill the intruded waste panel with brine and so a release up the borehole to the Culebra will not take place (Sect. 8.4). A similar effect also occurs for *ANHPRM* (Fig. 11.1.7).

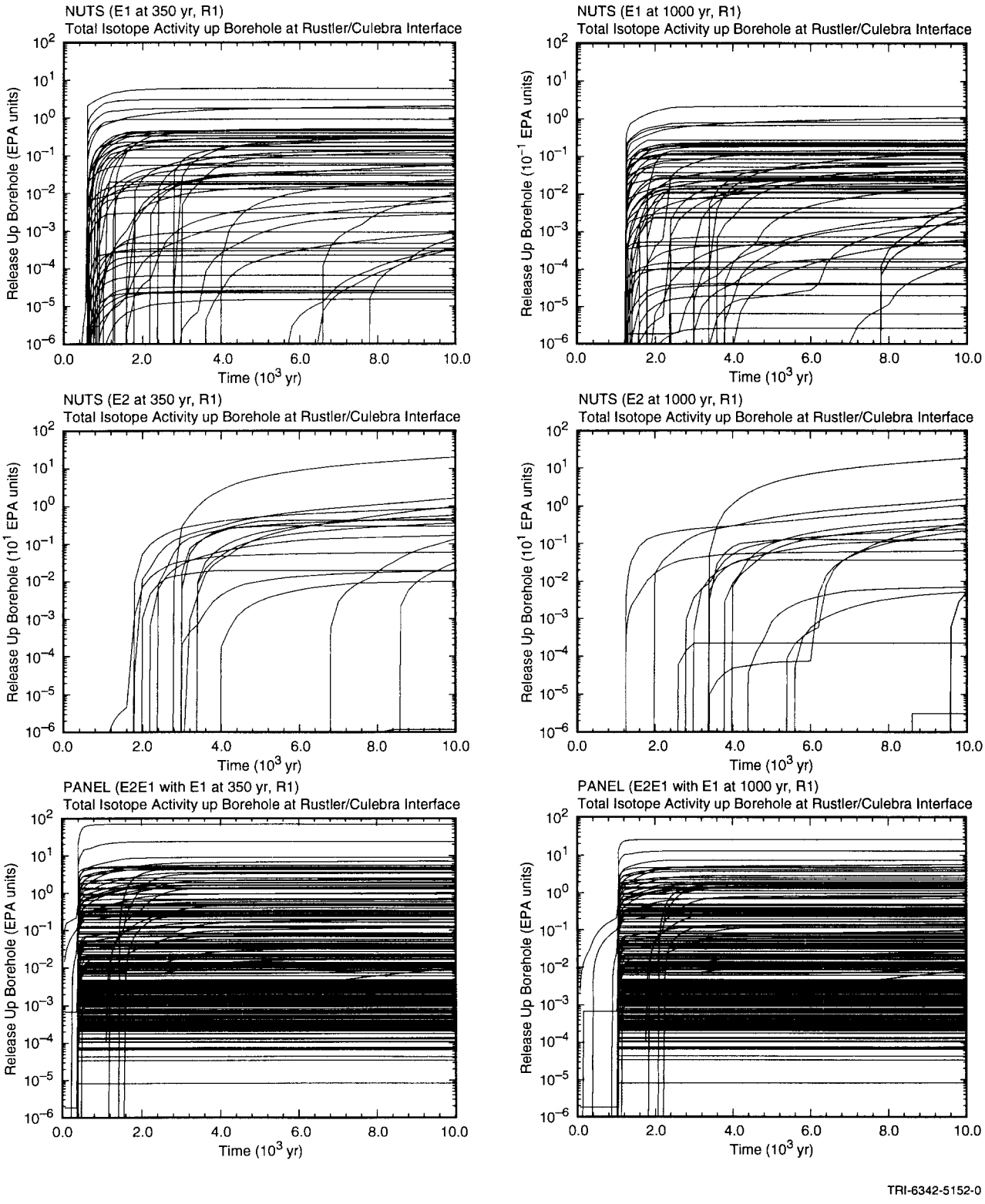

Fig. 11.1.2. Cumulative normalized release from repository to Culebra Dolomite for E1, E2 and E2E1 intrusions at 350 and 1000 yr.

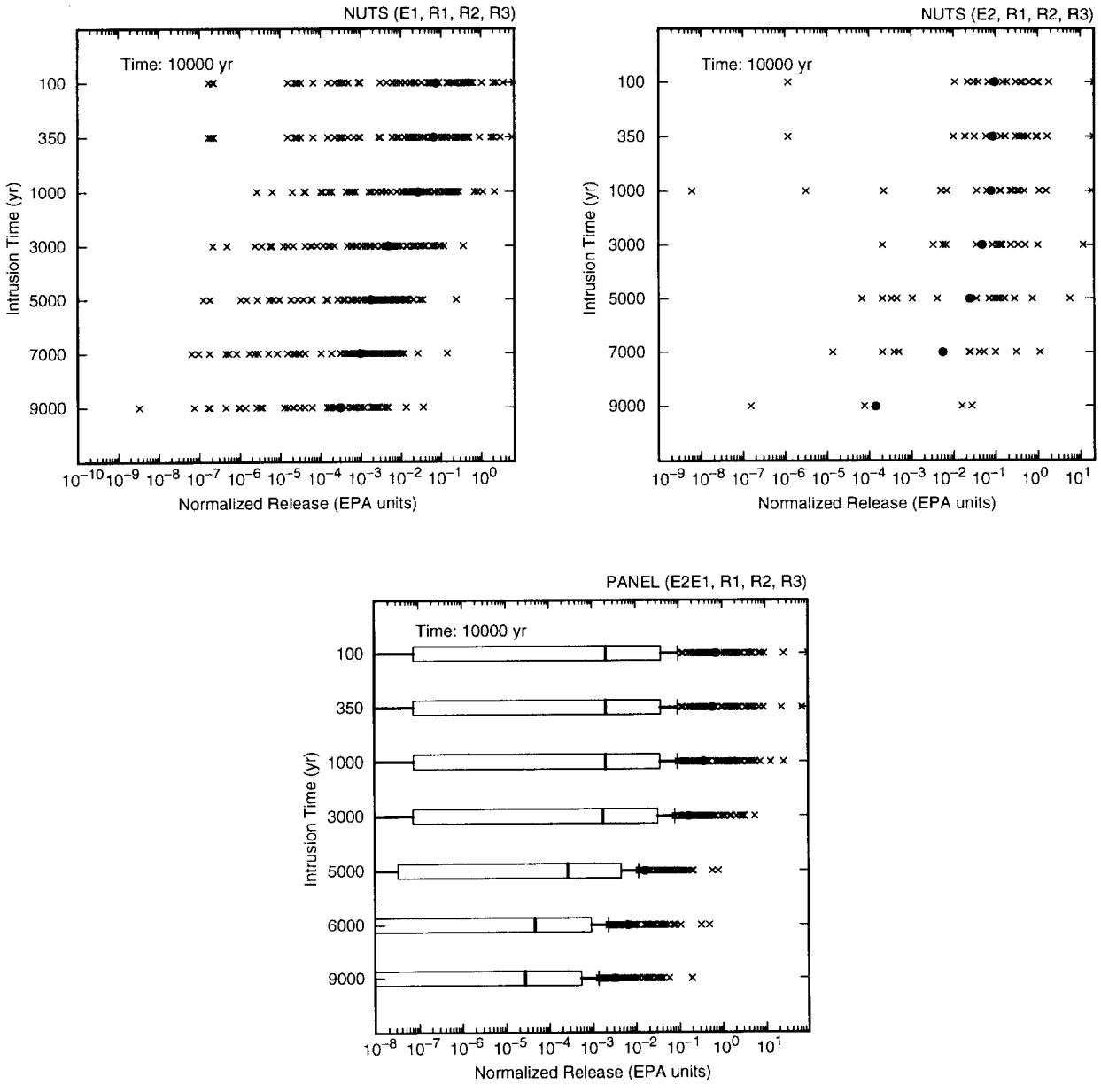

Fig. 11.1.3. Cumulative normalized releases over 10,000 yr from repository to Culebra Dolomite for E1, E2 and E2E1 intrusions, with the indicated intrusion times corresponding to the time of the E1 intrusion for the E2E1 intrusion.

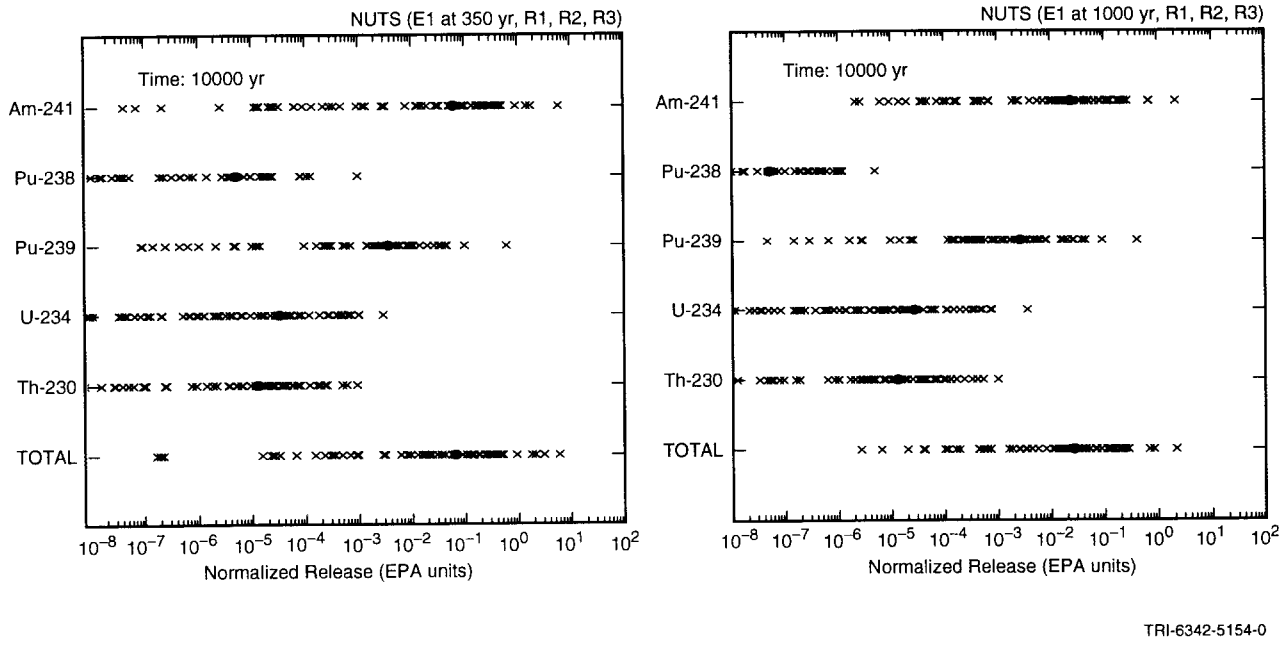

Fig. 11.1.4. Cumulative normalized releases of individual isotopes over 10,000 yr from repository to Culebra Dolomite for E1 intrusions at 350 and 1000 yr.

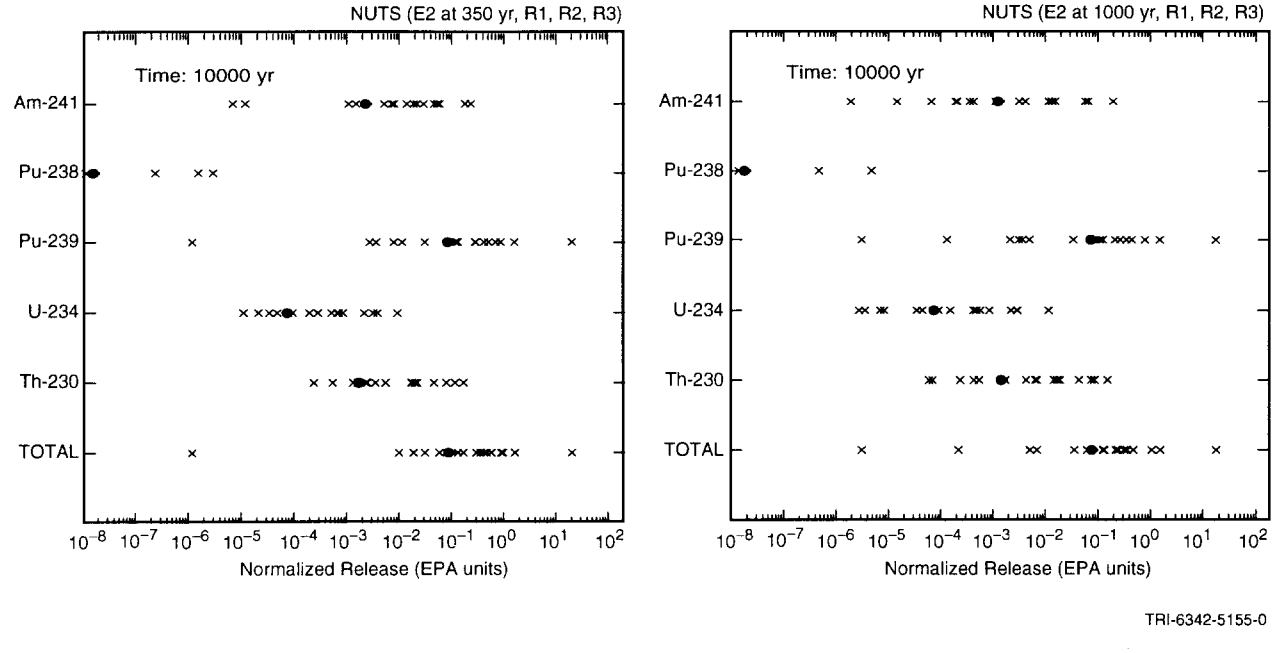

Fig. 11.1.5. Cumulative normalized releases of individual isotopes over 10,000 yr from repository to Culebra Dolomite for E2 intrusions at 350 and 1000 yr.

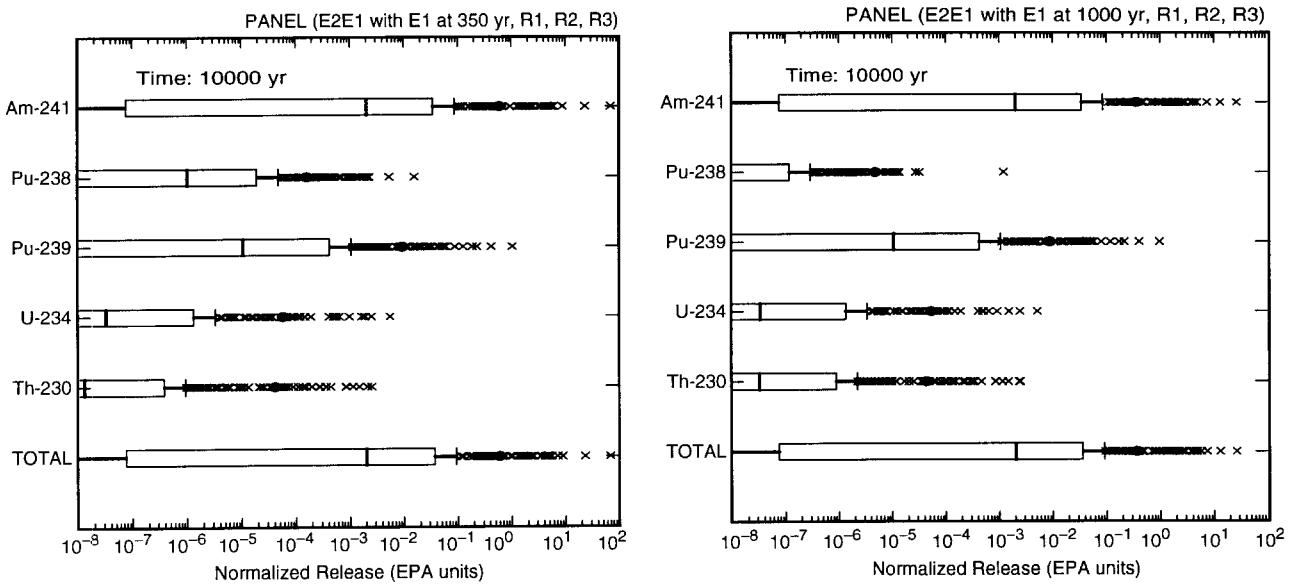

Fig. 11.1.6. Cumulative normalized releases of individual isotopes over 10,000 yr from repository to Culebra Dolomite for E2E1 intrusions with the E1 intrusion at 350 and 1000 yr.

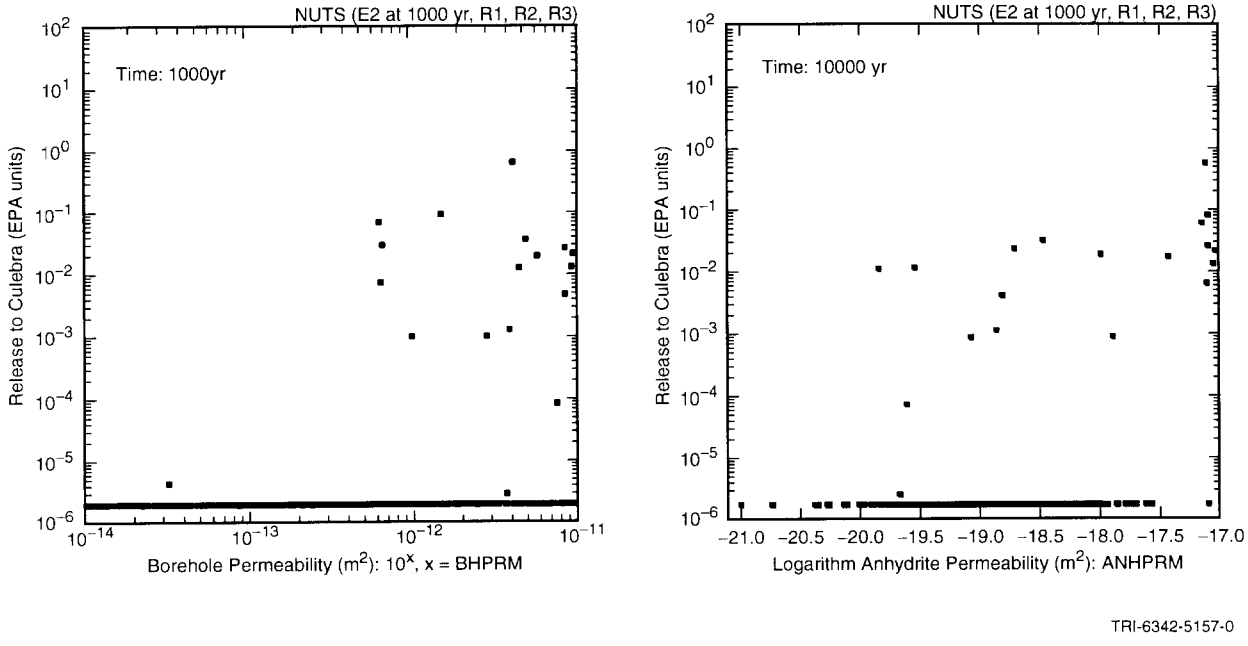

Fig. 11.1.7. Scatterplots for normalized release to Culebra Dolomite over 10,000 yr for an E2 intrusion at 1000 yr versus *BHPRM* and *ANHPRM*.

For E1 intrusions, releases tend to be associated with larger values for *BPCOMP* (Fig. 11.1.8). This association occurs because increasing *BPCOMP* tends to increase the brine flows from the brine pocket to the repository (Fig. 8.2.12), thus increasing the likelihood that the intruded waste panel will fill with brine. There is also a tendency for the size of the release to the Culebra to increase as *BHPRM* increases (Fig. 11.1.8). This effect results because increasing *BHPRM* increases both the amount of brine that flows down the borehole from overlying formations and the amount of brine that flows up the borehole from the brine pocket. However, due to the effects of *BPCOMP*, less influence is exerted by *BHPRM* in determining whether or not a release occurs than is the case for the E2 intrusion.

Due to the large number of zero releases, a stepwise regression analysis is not very revealing as a sensitivity analysis procedure for E1 and E2 intrusions. However, the greater number of nonzero releases associated with E2E1 intrusions makes stepwise regression analysis a possibility for this intrusion mode (Table 11.1.2). In constructing the regression models in Table 11.1.2, the candidate independent variables included the original sampled variables and also the solubilities for individual elements (Table 10.3.4). As a reminder, elemental solubilities change as a function of brine type (i.e., Salado or Castile) and several sampled variables (Table 4.3.1). By including the actual solubilities used in the PANEL calculations for E2E1 intrusions rather than only the sampled variables, the effects of the actual solubility used in the calculation will be shown. In interpreting the analysis results, two properties of the analysis should be kept in mind. First, calculations for E2E1 intrusions use the solubilities for Castile brine. Second,

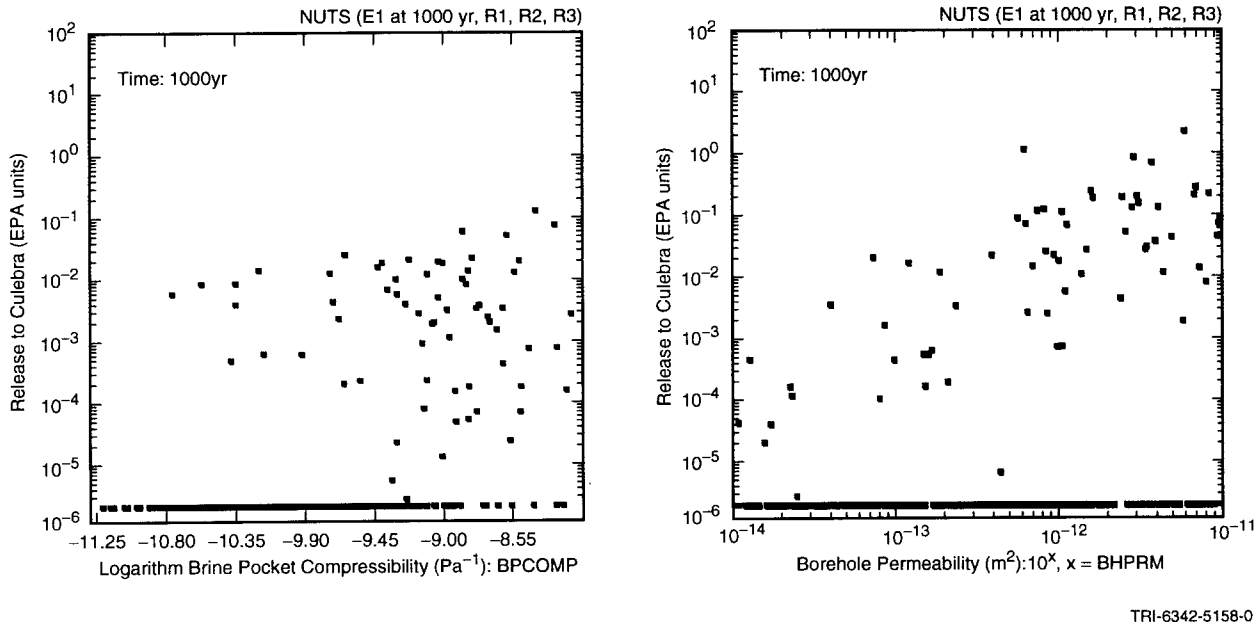

Fig. 11.1.8. Scatterplots for normalized release to Culebra Dolomite over 10,000 yr for an E1 intrusion at 1000 yr versus *BPCOMP* and *BHPRM*.

Table 11.1.2 Stepwise Regression Analyses with Rank-Transformed Data for Cumulative Radionuclide Releases over 10,000 yr from the Repository to the Culebra Dolomite for an E2E1 Intrusion with the E1 Intrusion Occurring at 1000 yr

	Am-241			Pu-238			Pu-239			U-234		
Step[a]	Variable[b]	SRRC[c]	R^{2d}	Variable	SRRC	R^2	Variable	SRRC	R^2	Variable	SRRC	R^2
1	*BHPRM*	0.61	0.37	*BHPRM*	0.57	0.34	*BHPRM*	0.59	0.36	*BHPRM*	0.58	0.35
2	*BPCOMP*	0.52	0.64	*BPCOMP*	0.54	0.63	*BPCOMP*	0.52	0.63	*BPCOMP*	0.45	0.55
3	*SOLAMC*	0.20	0.68	*SOLPUC*	0.18	0.67	*SOLPUC*	0.16	0.66	*SOLUC*	0.36	0.69
4	*BPINTPRS*	0.17	0.70	*BPINTPRS*	0.16	0.69	*WGRCOR*	−0.16	0.68	*BPINTPRS*	0.17	0.71
5	*WGRCOR*	−0.14	0.72	*BPVOL*	0.12	0.70	*BPINTPRS*	0.16	0.70	*WGRCOR*	−0.12	0.72
6	*BPVOL*	0.12	0.74	*WGRCOR*	−0.09	0.71	*BPVOL*	0.12	0.72	*BPVOL*	0.12	0.74
7	*ANHPRM*	0.10	0.74	*WMICDFLG*	−0.08	0.72	*ANHPRM*	0.09	0.73	*ANHPRM*	0.11	0.75
8	*WMICDFLG*	−0.07	0.75	*ANHPRM*	0.08	0.73	*WMICDFLG*	−0.10	0.74	*WMICDFLG*	−0.10	0.76

	Th-230			Total		
Step[a]	Variable[b]	SRRC[c]	R^{2d}	Variable	SRRC	R^2
1	*BHPRM*	0.60	0.36	*BHPRM*	0.61	0.37
2	*BPCOMP*	0.54	0.65	*BPCOMP*	0.52	0.64
3	*WGRCOR*	−0.16	0.68	*SOLAMC*	0.19	0.67
4	*BPINTPRS*	0.17	0.70	*BPINTPRS*	0.17	0.70
5	*BPVOL*	0.13	0.72	*WGRCOR*	−0.14	0.72
6	*ANHPRM*	0.10	0.73	*BPVOL*	0.12	0.73
7	*WMICDFLG*	−0.10	0.74	*ANHPRM*	0.10	0.74
8				*WMICDFLG*	−0.07	0.75

[a] Steps in stepwise regression analysis.

[b] Variables listed in order of selection in regression analysis with *ANHCOMP* and *HALCOMP* excluded from entry into regression model.

[c] Standardized rank regression coefficients in final regression model.

[d] Cumulative R^2 value with entry of each variable into regression model.

the solubilities in Tables 4.3.1 and 11.1.2 are only realized if there is a sufficient quantity of the element in the waste panel; otherwise, the amount of material that can go into solution is limited by the amount present. Such inventory limits occur for both Am-241 and Pu-238.

The regressions in Table 11.1.2 for the individual radionuclides and also for the total release in EPA units are very similar. In particular, the releases are dominated by *BHPRM* and *BPCOMP*, with the size of the release tending to increase as each of these variables increases. These positive effects result because increasing *BHPRM* tends to increase the rate at which the intruded waste panel fills with brine due to flow down the borehole, and increasing *BPCOMP* tends to increase the rate at which the intruded waste panel fills with brine due to flow up the borehole from the brine pocket. Also, increasing *BHPRM* reduces resistance to flow in the borehole from the brine pocket to the waste panel and also from the waste panel to the Culebra. The third variable selected in most analyses is the solubility for the radionuclide under consideration (i.e., *SOLAMC*, *SOLPUC* or *SOLUC*), with release size tending to increase as solubility increases. However, the effect of solubility is less than that of *BHPRM* and *BPCOMP*, which is

due in part to the significant number of observations that have no brine flow, and hence no radionuclide release, to the Culebra.

In addition, positive effects are indicated for *BPINTPRS*, *BPVOL* and *ANHPRM*, and negative effects are indicated for *WGRCOR* and *WMICDFLG* (Table 11.1.2). Increasing *BPINTPRS* and *BPVOL* increases the amount of brine that flows from the brine pocket to the repository (Table 8.2.5), and increasing *ANHPRM* increases the amount of brine that flows from the anhydrite marker beds to the repository (Tables 8.2.2, 8.2.3). In both cases, the ultimate effect is to increase the rate at which the intruded waste panel fills with brine. In contrast, increasing *WGRCOR* and *WMICDFLG* decreases the rate at which the waste panel fills with brine. For *WGRCOR*, this effect results from an increased loss of brine due to corrosion; it is also possible that the resultant increased gas flow up the borehole may retard the filling of the waste panel due to brine flow down the borehole. For *WMICDFLG*, the negative effect results primarily from reduced brine flow during the initial 200 yr period that an open borehole is assumed to exist between the brine pocket and the waste panel (Fig. 8.2.8).

For perspective, scatterplots for *BHPRM*, *BPCOMP*, and the Am-241 release are given in Fig. 11.1.9. No releases tend to result for small values of *BHPRM* and *BPCOMP* due to a failure to fill the intruded waste panel with brine. Further, given that a release takes place, the size of this release tends to increase as each of *BHPRM* and *BPCOMP* increases. Similar patterns also occur for the other radionuclides and the total release. The uncertainty that derives from *BHPRM* and *BPCOMP* tends to swamp out the uncertainty associated with solubilities (Fig. 11.1.10). In particular, although a positive relationship can be discerned between solubility and the size of the nonzero releases, there is a large amount of variation around this trend.

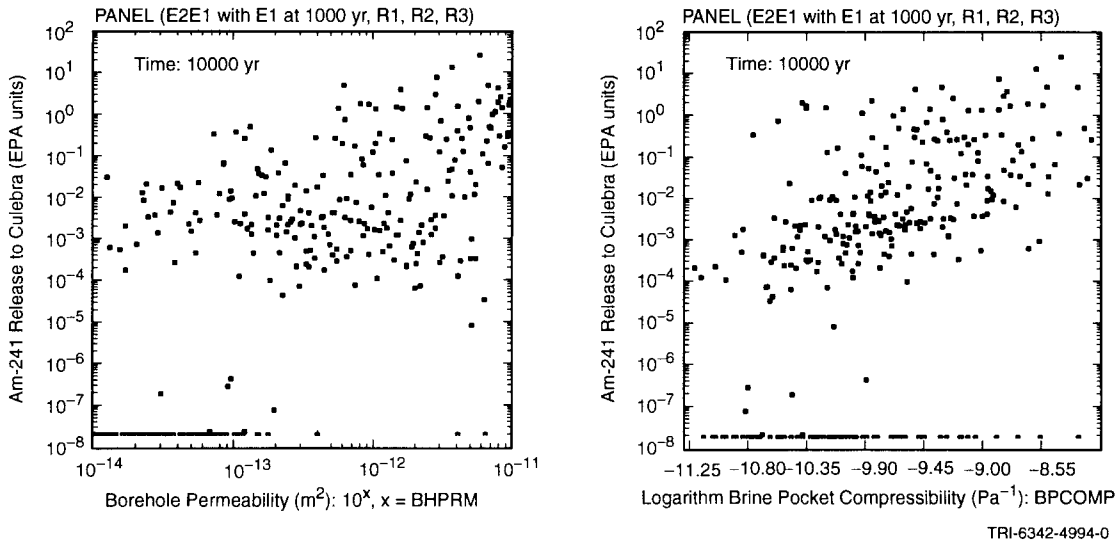

Fig. 11.1.9. Scatterplots for normalized release of Am-241 to Culebra Dolomite over 10,000 yr for an E2E1 intrusion with the E1 intrusion occurring at 1000 yr versus *BHPRM* and *BPCOMP*.

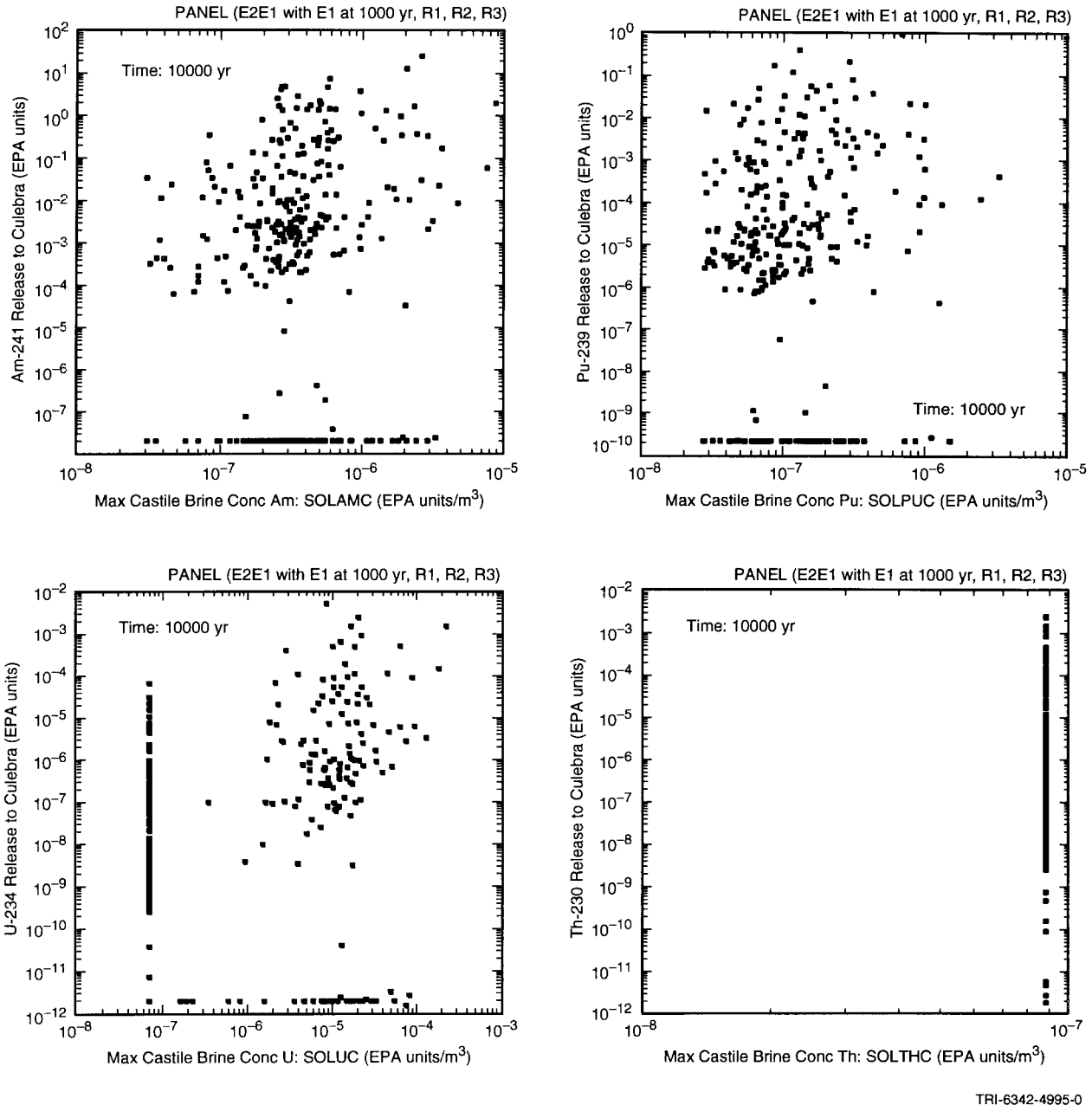

Fig. 11.1.10. Scatterplots for normalized release of individual radionuclides (i.e., Am-241, Pu-239, U-234, Th-230) to Culebra Dolomite over 10,000 yr for an E2E1 intrusion with the E1 intrusion occurring at 1000 yr versus the solubility for the individual radionuclides (i.e., *SOLAMC*, *SOLPUC*, *SOLUC*, *SOLTHC* in Table 10.3.4).

11.2 Release to Culebra: CCDFs

The CCDFs for release to the accessible environment are constructed conditionally on individual LHS elements by randomly sampling futures of the form in Eq. (2.2.2). The outcomes of this procedure for cuttings, spallings and direct brine release are presented in Sects. 9.2, 9.4 and 10.3. For groundwater releases to the accessible environment due to transport through the Culebra, a two-step procedure is used. First, time-dependent release rates to the Culebra are constructed for each isotope and each randomly sampled future (Tables 11.2.1, 11.2.2). Second, these release rates are then used in conjunction with SECOTP2D results (Sects. 4.8, 4.9) to estimate a normalized release to the accessible environment for each randomly sampled future (Sect. 13.2). Once these normalized releases are estimated, construction of the CCDF for transport through the Culebra to the accessible environment is straightforward.

The actual radionuclide releases into the Culebra calculated with NUTS and PANEL use the "Total" concentrations in Fig. 11.1.1. The division of the release into dissolved and colloidal components in Table 11.2.2 is done to facilitate transport calculations in the Culebra and has no effect on the release into the Culebra. The fractions *fCE0*, *fCE1* and *fCE2* in Table 11.2.1 are used to partition the release into the Culebra back into its dissolved and colloidal components. Humic colloids are assumed to transport exactly the same as dissolved radionuclides (Papenguth 1996), with the result that *fCE0*, *fCE1* and *fCE2* are set to 0 for humic colloids. In the computational implementation of the analysis for transport in the Culebra described in Sect. 12.2, this results in the same SECOTP2D results being used for both dissolved radionuclides and humic colloids. Values for *fCE1* and *fCE2* are obtained by forming the ratio of corresponding colloidal and total concentrations in Fig. 11.1.1 (Fig. 11.2.1). As E0 and E2 conditions are both dominated by Salado brine, *fCE0* is assumed to equal corresponding values for *fCE2*, although the definition of *fCE0* has no impact on the analysis because no releases to the Culebra occur for undisturbed conditions.

Conditional on a given LHS element and a given future of the form in Eq. (2.2.2), $cRT(j, k, 10{,}000)$ in Table 11.2.2 gives the total cumulative release to the Culebra over 10,000 yr of element k of decay chain j. These individual releases can then be converted into a total normalized release, which is used in the construction of the corresponding CCDF for normalized release to the Culebra. This construction follows the same procedure and uses the same randomly-sampled futures as used in Sects. 9.2, 9.4 and 10.3 to construct CCDFs for cuttings, spallings and direct brine release. Specifically, 10,000 randomly-sampled futures are generated for each LHS element; the corresponding 10,000 normalized releases to the Culebra are evaluated, and the resultant CCDF is constructed (Fig. 11.2.2), which results in 100 CCDFs for each of the three replicates.

With one exception, all the CCDFs in the left frame of Fig. 11.2.2 fall beneath the boundary line for release to the accessible environment. As a reminder, a release to the Culebra at the repository is not a release to the accessible environment. The boundary line specified in 40 CFR 191.13(a) is referred to to help the reader assess how much

Table 11.2.1. Results Available for Use in CCDF Construction for Radionuclide Releases into the Culebra Dolomite

---

$rE0(j, k, \omega_l)$ = cumulative release (kg) of element k of decay chain j (See Eq. (4.3.18)) from the repository to the Culebra under undisturbed (i.e., E0) conditions from time 0 yr (i.e., closure of repository) through time ω_l, ω_l = 100, 150, 200, ..., 10,000 yr (i.e., $\omega_{l+1} = \omega_l + 50$ yr for $l \geq 1$), due to brine flow. Source: NUTS (See Table 11.1.1).

$rE1(\tau_i, j, k, \omega_l)$ = cumulative release (kg) of element k of decay chain j (See Eq. (4.3.18)) from the repository to the Culebra from time τ_i to time ω_l, $\omega_l = \tau_i + 50$ yr, $\tau_i + 100$ yr, ..., 10,000 yr, due to brine flow with an E1 intrusion occurring at time τ_i, τ_i = 100, 350, 1000, 3000, 5000, 7000, 9000 yr. Source: NUTS (See Table 11.1.1).

$rE2(\tau_i, j, k, \omega_l)$ = cumulative release (kg) of element k of decay chain j (See Eq. (4.3.18)) from the repository to the Culebra from time τ_i to time ω_l, $\omega_l = \tau_i + 50$ yr, $\tau_i + 100$ yr, ..., 10,000 yr, due to brine flow with an E2 intrusion occurring at time τ_i, τ_i = 100, 350, 1000, 3000, 5000, 7000, 9000 yr. Source: NUTS (See Table 11.1.1).

$rE21(\tau_i, j, k, \omega_l)$ = cumulative release (kg) of element k of decay chain j (See Eq. (4.3.18)) from the repository to the Culebra from time τ_i to time ω_l, $\omega_l = \tau_i + 50$ yr, $\tau_i + 100$ yr, ..., 10,000 yr, due to brine flow with an E2E1 intrusion occurring at time τ_i, τ_i = 100, 350, 1000, 4000, 6000, 9000 yr. Source: PANEL (See Table 11.1.1).

$fCE0(s, j, k)$ = fraction of element k of decay chain j (See Eq. (4.3.18)) attached to colloid specie s under undisturbed (i.e., E0) conditions (See Table 4.3.1).

$fCE1(s, j, k)$, $fCE2(s, j, k)$: same as $fCE0(s, j, k)$ but for conditions subsequent to E1 and E2 intrusions, respectively.

Table 11.2.2. Construction of Radionuclide Releases into the Culebra Dolomite for an Arbitrary Future $\mathbf{x}_{st}$ of Form in Eq. (2.2.2)

Notation:

nC = number of colloid species (i.e., $nC = 4$; see Table 4.3.1)

nP = number of waste panels (i.e., $nP = 10$; see Fig. 3.2.1)

$nI(p)$ = number of drilling intrusions into waste panel p, $p = 1, 2, \ldots, nP$, with potential for brine flow from repository to Culebra (i.e., drilling intrusions for which $\tilde{b}_i = 1$ or 2[a] and l_i is associated with waste panel p; see Sects. 3.3, 3.4)

t_{pi} = time (yr) of i^{th} drilling intrusion into waste panel p, $i = 1, 2, \ldots, nI(p)$, $p = 1, 2, \ldots, nP$, with potential for brine flow from repository to Culebra (see Sect. 3.2)

$nE1(p)$ = number of E1 intrusions into waste panel p (i.e., intrusions for which $\tilde{b}_i = 1$; see Sect. 3.5))

$nE2(p)$ = number of E2 intrusions into waste panel p (i.e., intrusions for which $\tilde{b}_i = 2$; see Sect. 3.5))

$nE21(p)$ = number of E2E1 intrusions into waste panel p (see $tE21_{pj}$ below)

$tE1_{pj}$ = time (yr) of j^{th} E1 intrusion into waste panel p, $j = 1, 2, \ldots, nE1(p)$

$tE2_{pj}$ = time (yr) of j^{th} E2 intrusion into waste panel p, $j = 1, 2, \ldots, nE2(p)$

$tE21_{p1}$ = time (yr) of 1st E2E1 intrusion into waste panel p (i.e., time when two or more drilling intrusions have penetrated waste panel p, of which at least one encounters pressurized brine in the Castile Formation; specifically, $\tilde{b}_i = 1$ or 2 for each intrusion and $\tilde{b}_i = 1$ for at least one intrusion)

$tE21_{pj}$ = time (yr) of each E1 intrusion (i.e., $\tilde{b}_i = 1$) into waste panel p subsequent to $tE21_{p1}$, $j = 2, 3, \ldots, nE21(p)$ (i.e., $tE1_{pj}$, $j = 2, 3, \ldots, nE1(p)$ if $tE21_{p1} < tE1_{p2}$ and $tE1_{pj}$, $j = 3, 4, \ldots, nE1(p)$ if $tE21_{p1} = tE1_{p2}$)

Cumulative release to Culebra:

$cRD_p(j, k, t)$ = cumulative dissolved release (kg) to Culebra through time t of element k of decay chain j from waste panel p

$= 0$ if $t \le t_{p1}$

$$= \left[1 - \sum_{s=1}^{nC} fCE1(s, j, k)\right] rE1\left(t_{p1}, j, k, t\right)^{b} \qquad \text{if } tE1_{p1} = t_{p1} < t \le t_{p2}$$

$$= \left[1 - \sum_{s=1}^{nC} fCE2(s, j, k)\right] rE2\left(t_{p1}, j, k, t\right) \qquad \text{if } tE2_{p1} = t_{p1} < t \le tE1_{p1}$$

Table 11.2.2. Construction of Radionuclide Releases into the Culebra Dolomite for an Arbitrary Future $\mathbf{x}_{st}$ of Form in Eq. (2.2.2) (continued)

$$= cRD_p\left(j, k, tE2l_{pm}\right) + \left[1 - \sum_{s=1}^{nC} fCE1(s, j, k)\right] rE2l\left(tE2l_{pm}, j, k, t\right)$$

if $tE2l_{pm} < t \le tE2l_{p,m+1}$, $m = 1, 2, \ldots, nE2l(p)$

$cRD(j, k, t)$ = cumulative dissolved release (kg) from repository to Culebra through time t of element k of decay chain j

$$= \left[1 - \sum_{s=1}^{nC} fCE0(s, j, k)\right] rE0(j, k, t)^c \qquad \text{if } t \le t_1$$

$$= cRD(j, k, t_1) + \sum_{p=1}^{nP} cRD_p(j, k, t) \qquad \text{if } t > t_1$$

$cRC_p(s, j, k, t)$ = cumulative release (kg) from waste panel p to Culebra through time t of element k of decay chain j sorbed to colloid specie s

$$= 0 \qquad \text{if } t \le t_{p1}$$

$$= fCE1(s, j, k)\, rE1\left(t_{p1}, j, k, t\right) \qquad \text{if } tE1_{p1} = t_{p1} < t \le t_{p2}$$

$$= fCE2(s, j, k)\, rE2\left(t_{p1}, j, k, t\right) \qquad \text{if } tE2_{p1} = t_{p1} < t \le tE1_{p1}$$

$$= cRC_p\left(s, j, k, tE2l_{pm}\right) + fCE1(s, j, k)\, rE2l\left(tE2l_{pm}, j, k, t\right)$$

if $tE2l_{pm} < t \le tE2l_{p,m+1}$, $m = 1, 2, \ldots, nE2l(p)$

$cRC(s, j, k, t)$ = cumulative release (kg) from repository to Culebra through time t of element k of decay chain j sorbed to colloid specie s

$$= fCE0(s, j, k)\ rE0(j, k, t) \qquad \text{if } t \le t_1$$

$$= cRC(s, j, k, t_1) + \sum_{p=1}^{nP} cRC_p(s, j, k, t) \qquad \text{if } t > t_1$$

$cRT(j, k, t)$ = total cumulative release (kg) to Culebra through time t of element k of decay chain j

$$= cRD(j, k, t) + \sum_{s=1}^{nC} cRC(s, j, k, t)$$

[a] See Table 9.4.2 for definition of $\tilde{b}_i = 0, 1, 2$.

[b] Here and elsewhere, appearance of two undefined times implies two-dimensional linear interpolation between defined times in Table 11.1.1.

[c] Here and elsewhere, appearance of an undefined time implies linear interpolation between defined times in Table 11.1.1.

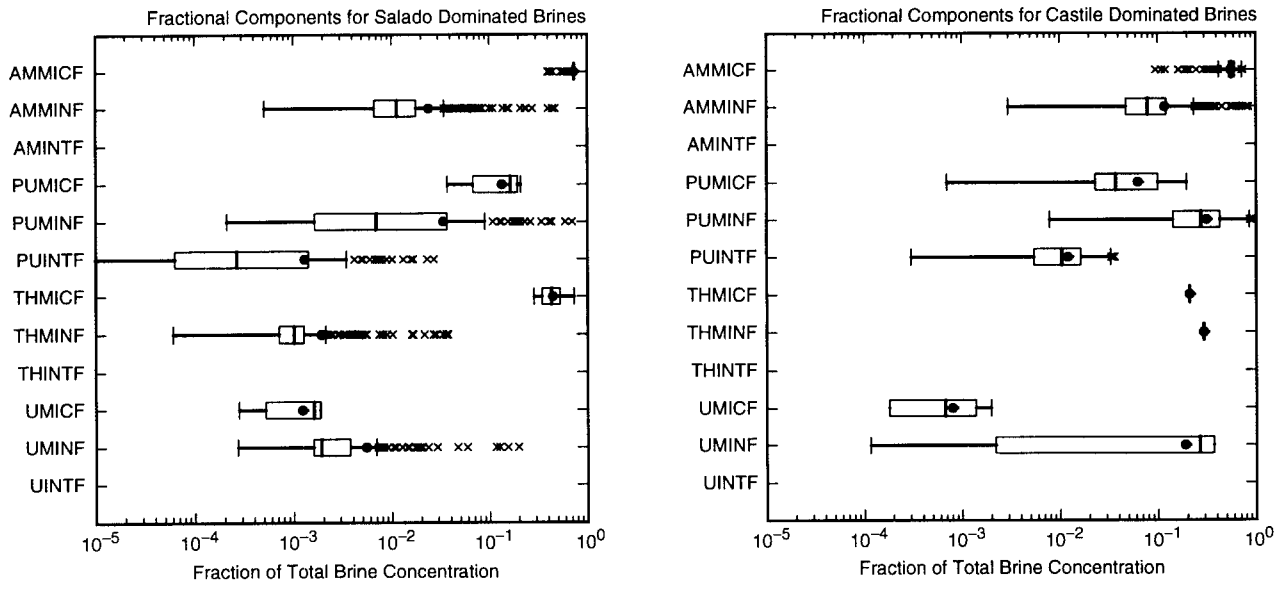

Fig. 11.2.1. Fraction of total radionuclide concentration in brine (EPA units/m^3) attached to microbial, mineral fragment and actinide intrinsic colloids (key: Am, Pu, Th, U correspond to americium, plutonium, thorium, uranium; MICF, MINF, INTF correspond to microbial fraction, mineral fragment fraction, actinide intrinsic fraction).

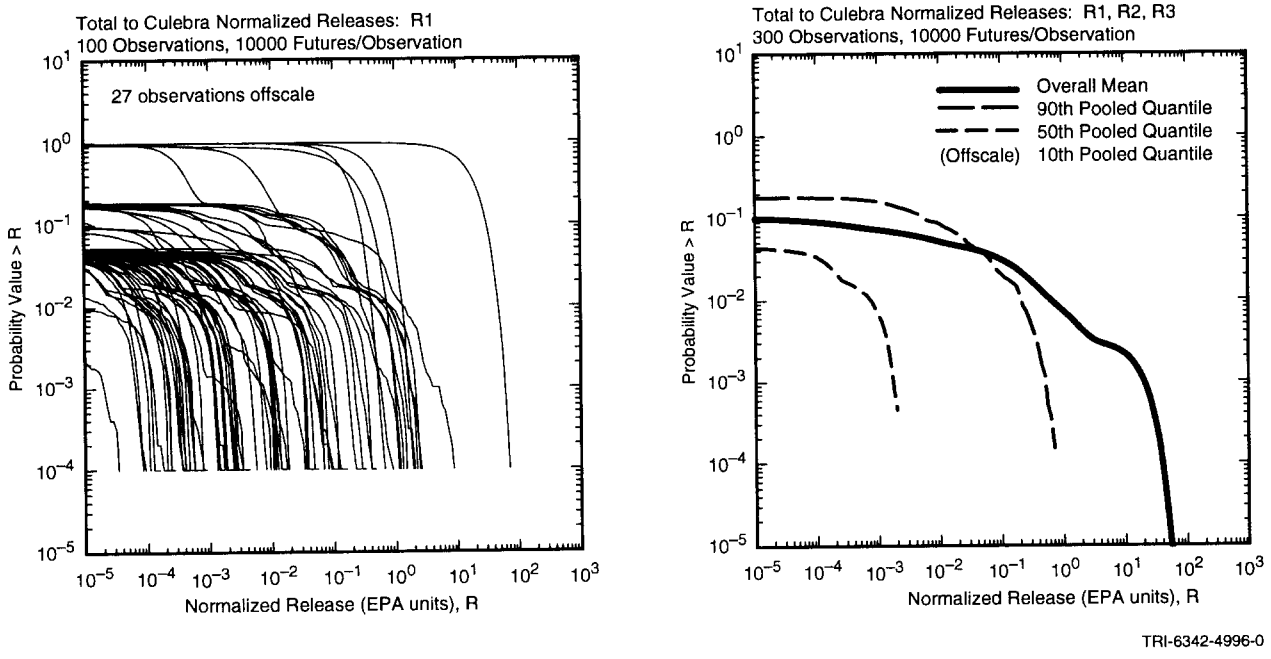

Fig. 11.2.2. Distribution of CCDFs for normalized release to Culebra Dolomite over 10,000 yr: CCDFs for replicate R1 (left frame), and mean and percentile curves obtained by pooling replicates R1, R2 and R3 (right frame).

attenuation might be required during transport in the Culebra to result in compliance. As shown by Fig. 11.2.2, most sample elements produce releases into the Culebra that would require no attenuation to be in compliance with 40 CFR 191.13(a). A similar pattern is also shown by the other two replicates (Fig. 11.2.3), with three CCDFs crossing the boundary line for replicate R2 and no CCDFs crossing for replicate R3 (although 2 CCDFs come close to the boundary line).

The distributions of CCDFs in Figs. 11.2.2 and 11.2.3 show a distinct structure, with one group (Group 1) of CCDFs emerging from the ordinate at a probability close to 1, another group (Group 2) emerging at a probability close to 0.25, and a final group (Group 3) emerging at probabilities close to 0.15. There are only a few Group 1 CCDFs. These CCDFs result from sample elements that have a nonzero E2 release. Their relatively low likelihood of occurring (i.e., 15 out of 300 sample elements) results because most sample elements result in no brine release, and hence no radionuclide release, to the Culebra for E2 intrusions. However, due to the high drilling rate, an E2 release to the Culebra is almost certain to take place (i.e., a probability very close to 1) if E2 intrusions result in brine flow from the repository to the Culebra. The relatively large releases for Group 1 CCDFs derives from two sources. First, releases for E2 intrusions are calculated with the solubilities for Salado dominated brines, which tend to be higher than the solubilities for Castile dominated brines (Fig. 10.2.1). Second, an additional E2 release is included for the first intrusion into each waste panel for a given future $\mathbf{x}_{st}$ (Table 11.2.2). As a result, the release to the Culebra for a typical future $\mathbf{x}_{st}$ will be the sum of a number of individual E2 releases. Again, the high drilling rate results in most futures involving intrusions into a number of different waste panels (Table 3.2.1).

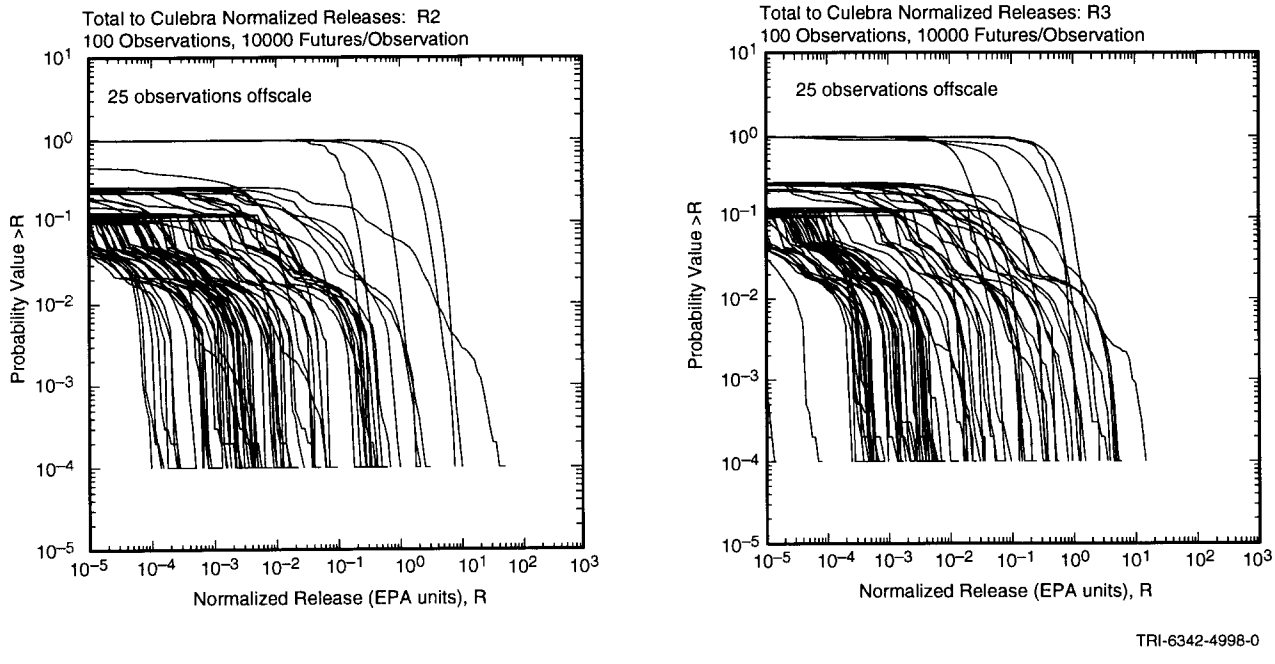

Fig. 11.2.3. Distributions of CCDFs for normalized release to the Culebra Dolomite over 10,000 yr for replicates R2 (left frame) and R3 (right frame).

The Group 2 CCDFs result from LHS elements that have E1 releases to the Culebra but no E2 releases. As the probability of a given drilling intrusion penetrating pressured brine is 0.08 (actually, an E1 intrusion only occurs if the borehole penetrates a nondepleted pressurized brine pocket and plugging pattern 2 is used, which makes the effective probability of penetrating pressurized brine approximately (0.08)(0.68) $\doteq$ 0.05; see Sects. 3.5, 3.6), these CCDFs emerge from the ordinate at a lower probability than the Group 1 CCDFs. The Group 2 CCDFs tend to have smaller releases than the Group 1 CCDFs for two reasons. First, the E1 releases used in the construction of the Group 2 CCDFs are calculated with solubilities for Castile dominated brine, which tend to be lower than the solubilities for Salado dominated brine used in the calculation of E2 releases (Fig. 10.2.1). Second, the likelihood of futures $\mathbf{x}_{st}$ that have multiple intrusions that give rise to releases to the Culebra is less for the Group 2 CCDFs than for the Group 1 CCDFs. Each E1 intrusion associated with a future $\mathbf{x}_{st}$ gives rise to either an E1 or an E2E1 release (Table 11.2.2). However, because the probability of penetrating pressurized brine is 0.08, a given future will not have very many intrusions that penetrate pressurized brine (Table 3.5.1). In contrast, the typical future will have many E2 intrusions that penetrate different waste panels.

The Group 3 CCDFs result from LHS elements that have E2E1 releases but no E1 or E2 releases. Because E2E1 releases require two drilling intrusions into a waste panel with at least one of these intrusions penetrating pressurized brine, the Group 3 CCDFs emerge from the ordinate at a lower probability than the Group 2 CCDFs. As for the Group 2 CCDFs, the releases for Group 3 CCDFs are calculated with solubilities for Castile dominated brines. Due to the requirement for multiple drilling intrusions into a single waste panel to produce an E2E1 release (Table 11.2.2), individual futures are less likely to have multiple releases in the construction of Group 3 CCDFs than in the construction of Group 2 CCDFs.

The Group 3 CCDFs show an interesting structure, with most CCDFs having an abrupt change in slope at probabilities of approximately 0.04 and 0.02. As examination of Fig. 11.2.4 shows, this behavior is due to Am-241, with the Am-241 CCDFs in Fig. 11.2.4 showing a pattern that exactly matches the indicated changes in slope for the total release in Figs. 11.2.2 and 11.2.3. These changes in slope are probably resulting from a change in the dissolved concentration of Am-241 from being solubility limited (i.e., by *SOLAMC*) to being inventory limited (Fig. 10.2.1). When concentration is solubility limited, the size of an E2E1 release changes smoothly as a function of the time of the intrusion that produces the E2E1 conditions; similarly when concentration is inventory limited, the size of an E2E1 release again changes smoothly as a function of the time of the intrusion that produces the E2E1 conditions. It is the switch from futures with releases dominated by inventory limited concentrations to futures with releases dominated by solubility limited concentrations that may be producing the changes in slope. It is also possible that the pattern may be due in part to futures that have different numbers of E2E1 intrusions.

The 90^{th} and 50^{th} quantile curves for release to the Culebra are quite stable across the three replicates (Fig. 11.2.5); the 10^{th} quantile is degenerate for all three replicates (i.e., replicates R1, R2 and R3 produce 27, 25 and 25 degenerate CCDFs, respectively). In contrast, the location of the mean for releases above 0.1 EPA units

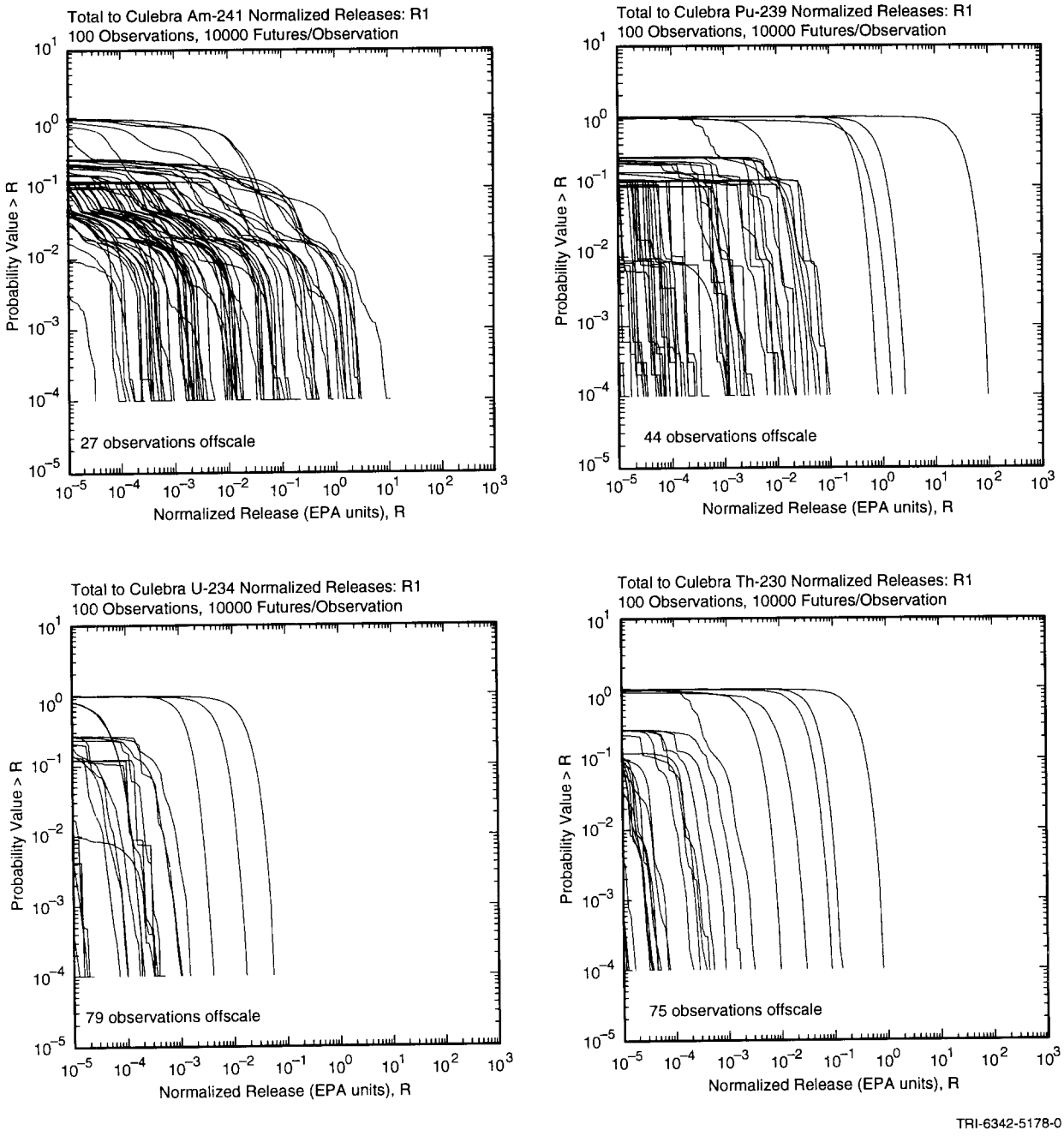

Fig. 11.2.4. Distributions of CCDFs for replicate R1 for normalized release of individual radionuclides (dissolved and colloidally-transported) to Culebra Dolomite over 10,000 yr.

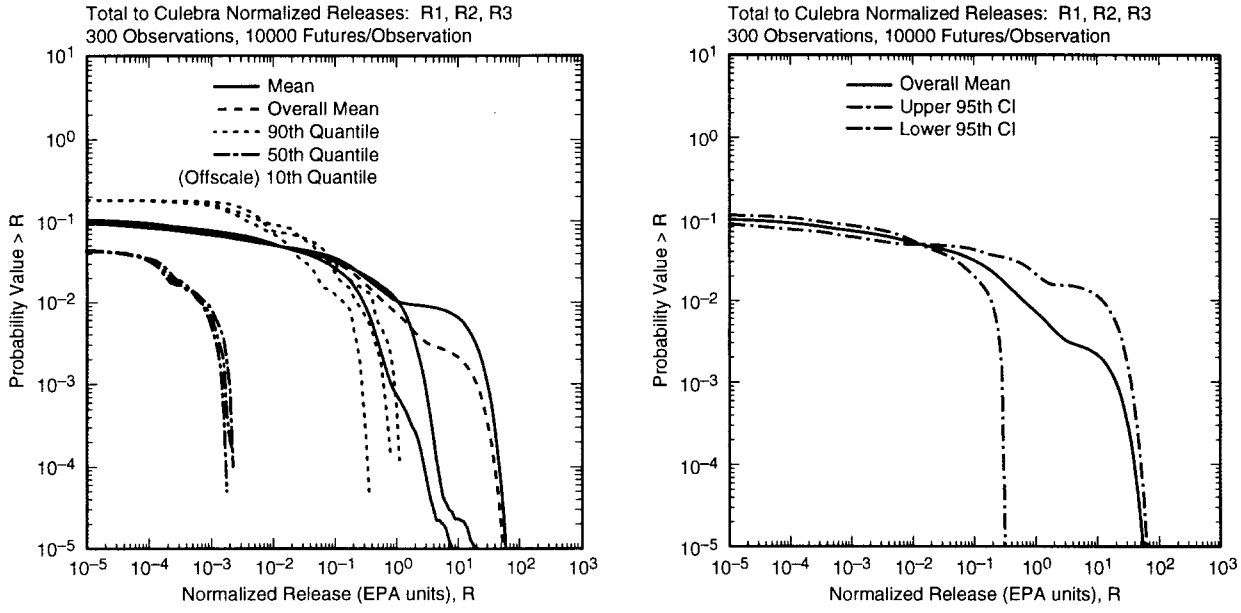

Fig. 11.2.5. Outcome of replicated sampling for distribution of CCDFs for normalized release to the Culebra Dolomite over 10,000 yr: mean and percentile curves for individual replicates (left frame) and confidence intervals (CIs) on mean curve obtained from the three replicates (right frame).

shows a considerable amount of variability across the three replicates (Fig. 11.2.5). The mean above about 1.0 EPA units for each replicate is being determined by a few (i.e., 1, 2 or 3) CCDFs. As a result, the means for the individual replicates and the mean across all three replicates are being determined by a few outliers and, thus, tend to be unstable. The nonrepresentativeness of the means for release to the Culebra provides an indication of why means associated with skewed distributions are not very informative quantities. Typically, selected quantiles provide more insight into the nature of a distribution, and especially a skewed distribution, than a mean.

As shown by the distributions in Fig. 11.2.4, Am-241 and Pu-239 are the dominant contributors to the CCDFs for release to the Culebra, with the largest releases coming from Pu-239. Lesser contributions are made by Th-230 and U-234, with the contribution from Th-230 tending to be larger than that from U-234.

As was done for the cuttings, spallings and blowout release CCDFs, a sensitivity analysis can be performed on the expected release to the Culebra for the CCDFs for the individual isotopes and also for the CCDFs for total release (Table 11.2.3). The dominant variables are *BHPRM* and *BPCOMP*, with these variables consistently selected first and second in the regression analyses in Table 11.2.3. The expected values increase as each of *BHPRM* and *BPCOMP* increases. The positive effect for *BHPRM* results from facilitating the filling of the repository due to brine flow down an intruding borehole and reducing resistance to flow both into the repository from a brine pocket and from the repository to the Culebra. The positive effect for *BPCOMP* results from increasing

Table 11.2.3. Stepwise Regression Analyses with Rank-Transformed Data for Expected Normalized Release Associated with Individual CCDFs for Release to Culebra Dolomite

	Am-241			Pu-239			U-234			Th-230		
Step[a]	Variable[b]	SRRC[c]	R^{2d}	Variable	SRRC	R^2	Variable	SRRC	R^2	Variable	SRRC	R^2
1	*BHPRM*	0.62	0.38	*BHPRM*	0.61	0.37	*BHPRM*	0.59	0.36	*BHPRM*	0.61	0.37
2	*BPCOMP*	0.56	0.69	*BPCOMP*	0.52	0.65	*BPCOMP*	0.46	0.57	*BPCOMP*	0.55	0.68
3	*BPINTPRS*	0.17	0.71	*WGRCOR*	−0.15	0.67	*SOLUC*	0.31	0.68	*WGRCOR*	−0.15	0.70
4	*SOLAMC*	0.13	0.73	*SOLPUC*	0.13	0.69	*BPINTPRS*	0.16	0.70	*BPINTPRS*	0.16	0.72
5	*BPVOL*	−0.13	0.74	*BPINTPRS*	0.15	0.71	*WMICDFLG*	−0.12	0.72	*BPVOL*	0.13	0.74
6	*WGRCOR*	−0.12	0.76	*BPVOL*	0.13	0.72	*ANHPRM*	0.13	0.73	*WMICDFLG*	−0.12	0.75
7	*ANHPRM*	0.10	0.77	*WMICDFLG*	−0.11	0.74	*BPVOL*	0.12	0.74	*ANHPRM*	0.11	0.77
8	*WMICDFLG*	−0.09	0.78	*ANHPRM*	0.11	0.75	*WGRCOR*	−0.12	0.76			
9				*WASTWICK*	−0.07	0.75						

	Total		
Step[a]	Variable[b]	SRRC[c]	R^{2d}
1	*BHPRM*	0.62	0.38
2	*BPCOMP*	0.54	0.67
3	*BPINTPRS*	0.17	0.70
4	*WGRCOR*	−0.14	0.72
5	*BPVOL*	0.12	0.73
6	*ANHPRM*	0.11	0.74
7	*SOLAMC*	0.11	0.75
8	*WMICDFLG*	−0.10	0.76

[a] Steps in stepwise regression analysis.

[b] Variables listed in order of selection in regression analysis with *ANHCOMP* and *HALCOMP* excluded from entry into regression model.

[c] Standardized rank regression coefficients in final regression model.

[d] Cumulative R^2 value with entry of each variable into regression model.

brine flow from a brine pocket to the repository and then from the repository to the Culebra. Typically, small positive effects are indicated for the solubilities for the individual elements (i.e., *SOLAMC*, *SOLPU*, *SOLUC*). As most releases occur in association with drilling intrusions involving pressurized brine, it is the solubilities for Castile dominated brines that are being selected in the regression analyses. In addition, positive effects are also indicated for *BPINTPRS*, *BPVOL* and *ANHPRM*. Increasing each of these variables tends to increase the amount of brine entering the repository (Table 8.2.4). Negative effects are indicated for *WGRCOR* and *WMICDFLG*. Increasing *WGRCOR* tends to decrease the amount of brine in the repository by increasing the amount of brine that is consumed by corrosion. Increasing *WMICDFLG* tends to decrease the amount of brine in the repository by preventing brine flow from the brine pocket to the repository during the 200 yr period subsequent to an E1 intrusion in which an open borehole exists between the repository and the brine pocket (Fig. 8.2.8).

For perspective, scatterplots involving *BHPRM*, *BPCOMP* and total release to the Culebra are given in Fig. 11.2.6. In consistency with the regression results (Table 11.2.3), the release tends to increase as *BHPRM* and *BPCOMP* increase. Further, zero releases tend to be associated with small values for these variables, with the association being more pronounced for small values of *BHPRM*.

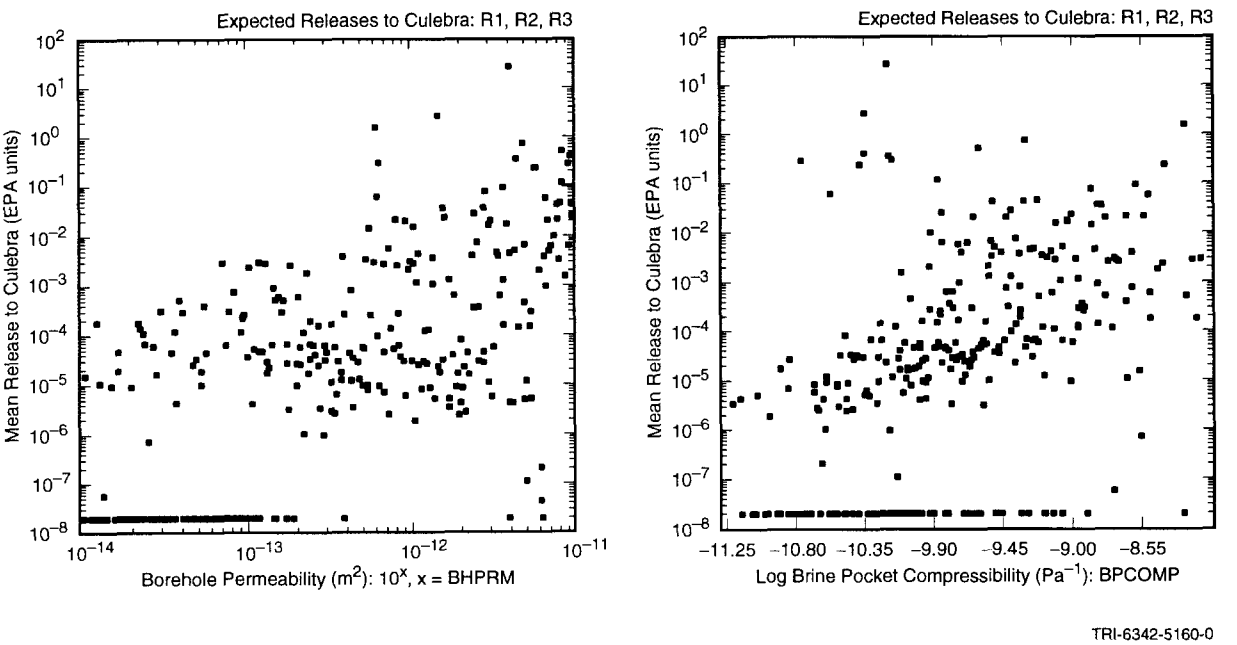

Fig. 11.2.6. Scatterplots for expected normalized releases associated with individual CCDFs for total release to the Culebra Dolomite versus *BHPRM* and *BPCOMP*.

11.3 Other Release Pathways

No releases occurred above the Culebra due to brine flow up the shaft or a borehole. No substantive releases to the marker beds were observed (Fig. 11.3.1); further, no numerically significant releases to the accessible environment due to transport through marker beds took place.

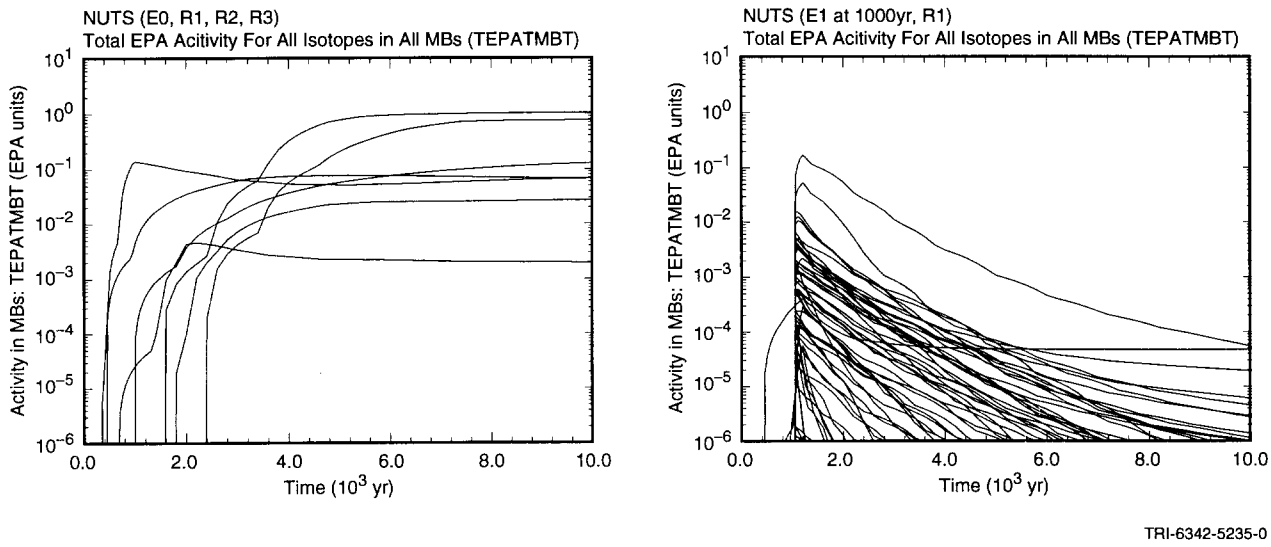

Fig. 11.3.1. Normalized inventory in marker beds (*TEPATMBT*) for undisturbed conditions (left frame) and an E1 intrusion at 1000 yr into lower waste panel (right frame).

12. Transport in Culebra

12.1 Fluid Flow in Culebra

Fluid flow calculations for the Culebra were performed with the SECOFL2D program (Sect 4.8) for three different sets of conditions: no mining, partial mining and full mining. These designations refer to the extent that commercially viable potash reserves in the vicinity of the WIPP are mined (Wallace 1996a). Specifically, no mining indicates no mining of potash reserves within the region associated with the computational grids used with SECOFL2D and SECOTP2D. Partial and full mining indicate mining all reserves outside the land withdrawal boundary (Fig. 4.8.1) and all reserves both inside and outside the land withdrawal boundary (Fig. 4.8.2), respectively. Criteria in 40 CFR 194 specify that partial mining shall be assumed to have taken place by time of closure of the repository (i.e., $t = 0$) and also that full mining will take place at time t_{min} (Sect. 3.8). Thus, only calculations for partial and full mining are relevant with respect to assessing compliance with 40 CFR 191. However, flow calculations for no mining were also performed to provide perspective on the results obtained for partial and full mining.

The only sampled variable that affects the no mining calculations with SECOFL2D is *CTRAN* (Table 5.2.1), which determines the transmissivity field used for the Culebra. For the partially and fully mined cases, the calculations involve two sampled variables: *CTRAN* and *CTRANSFM*. The variable *CTRANSFM* is a multiplier on the parts of the transmissivity field associated with *CTRAN* that are assumed to be affected by partial and full mining, respectively (Figs. 4.8.1, 4.8.2). The use of *CTRANSFM* in the analysis is specified in 40 CFR 194.

SECOFL2D calculations were first performed on a regional computational grid (Fig. 4.8.4). Interpolation on the pressures (i.e., heads) obtained from this calculation were then used to set the boundary conditions for calculations on a local grid (Fig. 4.8.5). The flow field obtained from the calculation on the local grid was then used as input to SECOTP2D for the radionuclide transport calculations.

As the 1996 WIPP PA used a total of 300 sample elements, and calculations were required for both partially and fully mined conditions, 600 pairs (i.e., on regional and local grids) of SECOFL2D calculations were required. As a reminder, only 100 unique transmissivity fields were generated for use in the 1996 WIPP PA. These fields are indexed by *CTRAN* as described in Table 5.2.1. However, 600 unique transmissivity fields result from the consideration of full and partial mining and the multiplier *CTRANSFM*. In addition, 100 pairs of calculations were also performed with the assumption of no mining. Specifically, these calculations were performed with the transmissivity fields associated with *CTRAN* without use of the multiplier defined by *CTRANSFM*. Given that 40 CFR 194 requires that partial mining be assumed to occur before closure of the repository, only the results for partial and full mining are needed for direct use in CCDF construction.

The actual result of the SECOFL2D calculation that is passed on to SECOTP2D is a spatially-dependent velocity vector (i.e., velocity field) $\mathbf{v}(x,y)$. A total of 700 such vector functions were generated. Examples of three of these vector functions are given in Fig. 12.1.1.

The presentation and comparison of 700 vector functions is difficult. One way to make such a presentation and comparison is to use summary quantities as surrogates for the vector functions. The flow path and travel time of a nonreactive, nonsorbing particle released into the velocity field defined by $\mathbf{v}(x,y)$ are such summary results and can be calculated by the TRACKER program, which is part of the SECO suite of programs (Roache 1993.).

Each velocity field $\mathbf{v}(x,y)$ calculated by SECOFL2D results in a different travel path for a nonreactive, nonsorbing particle released at the center of the repository (Fig. 12.1.2). The different values for $\mathbf{v}(x,y)$ can result in quite different travel paths. In particular, significant shifting of the travel paths occurs for some sample elements for fully mined conditions.

The velocity fields $\mathbf{v}(x,y)$ can also be compared on the basis of travel times. Specifically, TRACKER was used to obtain travel times in the Culebra from the center of the repository to the boundary with the accessible environment (Fig. 12.1.3). The travel times in Fig. 12.1.3 were calculated with the porosity of the Culebra set to 1; technically, this means that the travel times were calculated with the Darcy velocity predicted for the Culebra by SECOFL2D rather than with the pore velocity. This is acceptable because the predicted travel times are only useful for comparing the relative effects of different values of $\mathbf{v}(x,y)$ on travel time and are not intended to be indicative of actual travel times within the Culebra. In particular, radionuclide transport within the Culebra is believed to be appropriately represented by a dual porosity model (Sect. 4.9). The travel times presented in Fig. 12.1.3 do not include the effects of rapid flow through the advective medium (i.e., the fractures), diffusion into the surrounding matrix, sorption, or dispersion. Thus, no matter what porosity is used, the resulting travel times do not characterize radionuclide transport in the Culebra. However, the travel times do give an idea as to whether or not the different ways of defining $\mathbf{v}(x,y)$ (i.e., unmined, partially mined, fully mined) speeds up or slows down movement in the Culebra. Rather surprisingly, the unmined conditions tend to give rise to faster travel times than partially mined or fully mined conditions. However, depending on the individual observations, the fastest travel time can be associated with any one of the three conditions. Thus, the assumptions about potash mining and its effects on transmissivity specified in 40 CFR 194 do affect transport in the Culebra, but perhaps not in the manner originally expected.

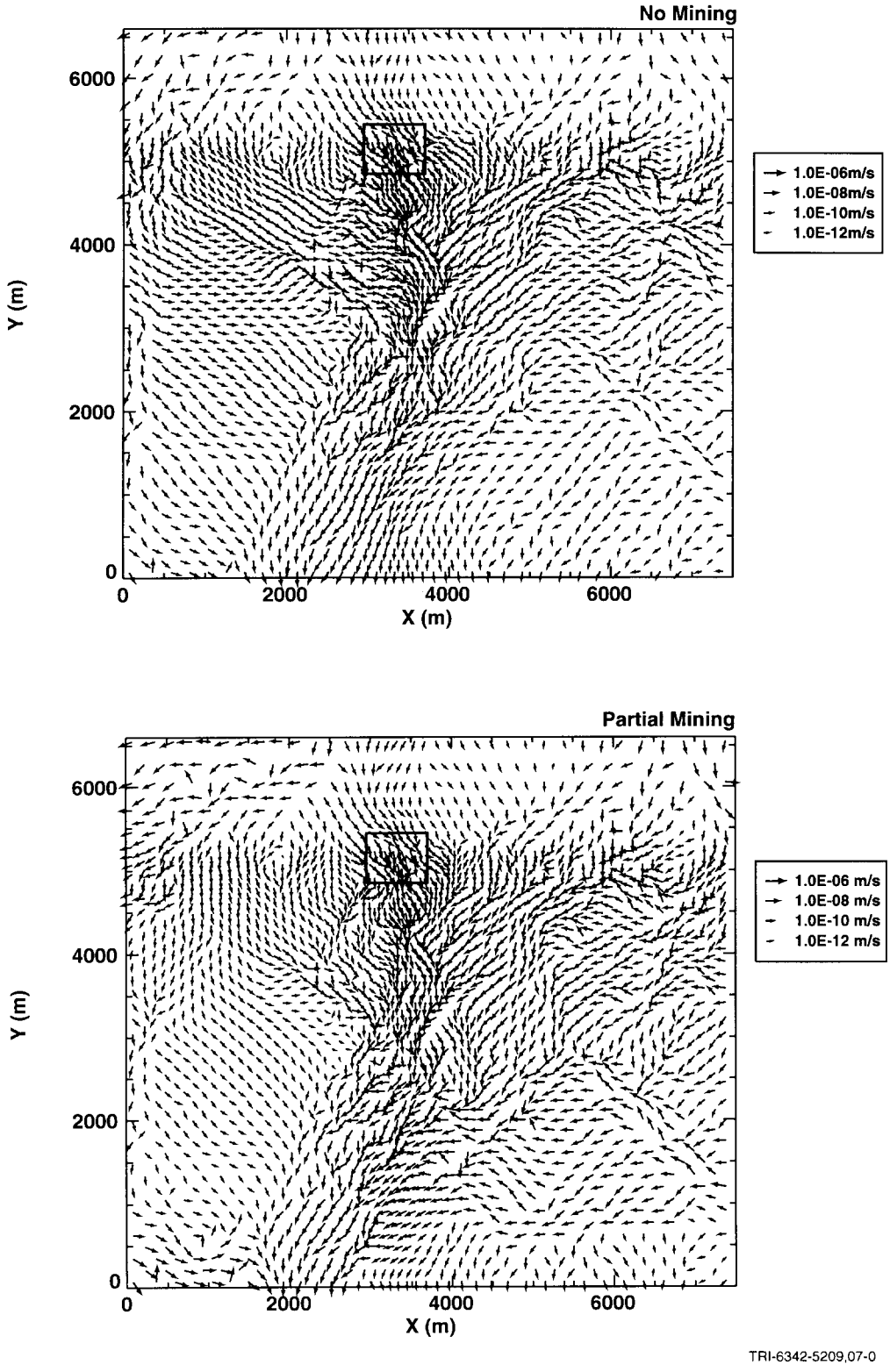

Fig. 12.1.1. Velocity field calculated by SECOFL2D for sample element 40 in replicate 1 for unmined, partially mined and fully mined conditions.

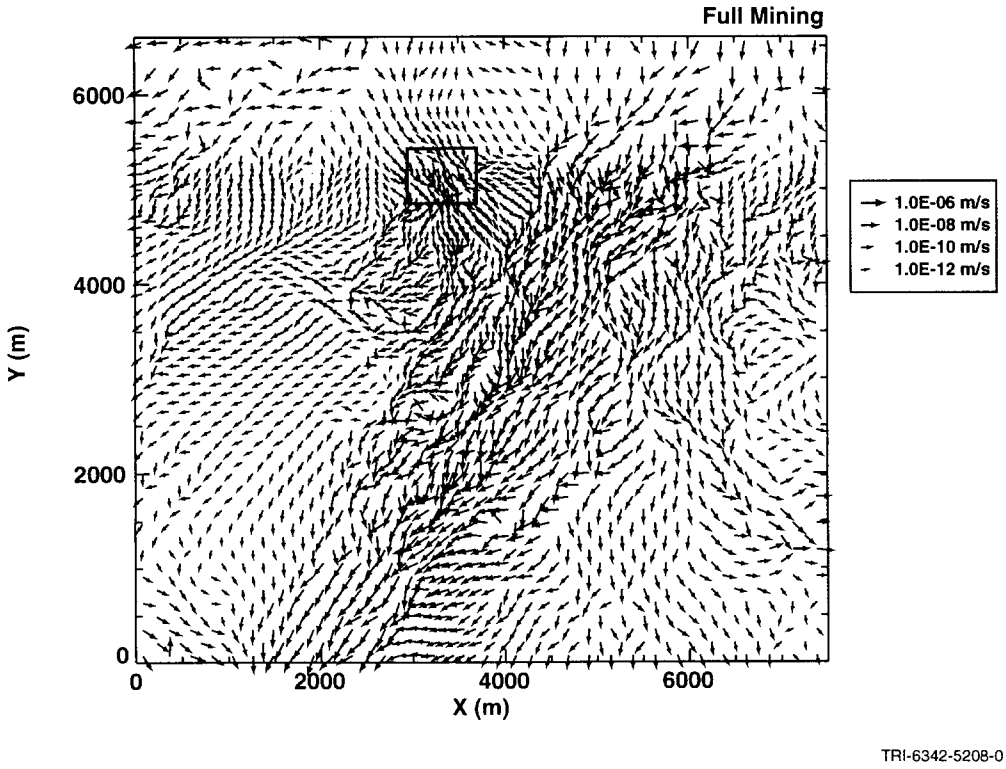

Fig. 12.1.1. Velocity field calculated by SECOFL2D for sample element 40 in replicate 1 for unmined, partially mined and fully mined conditions (continued).

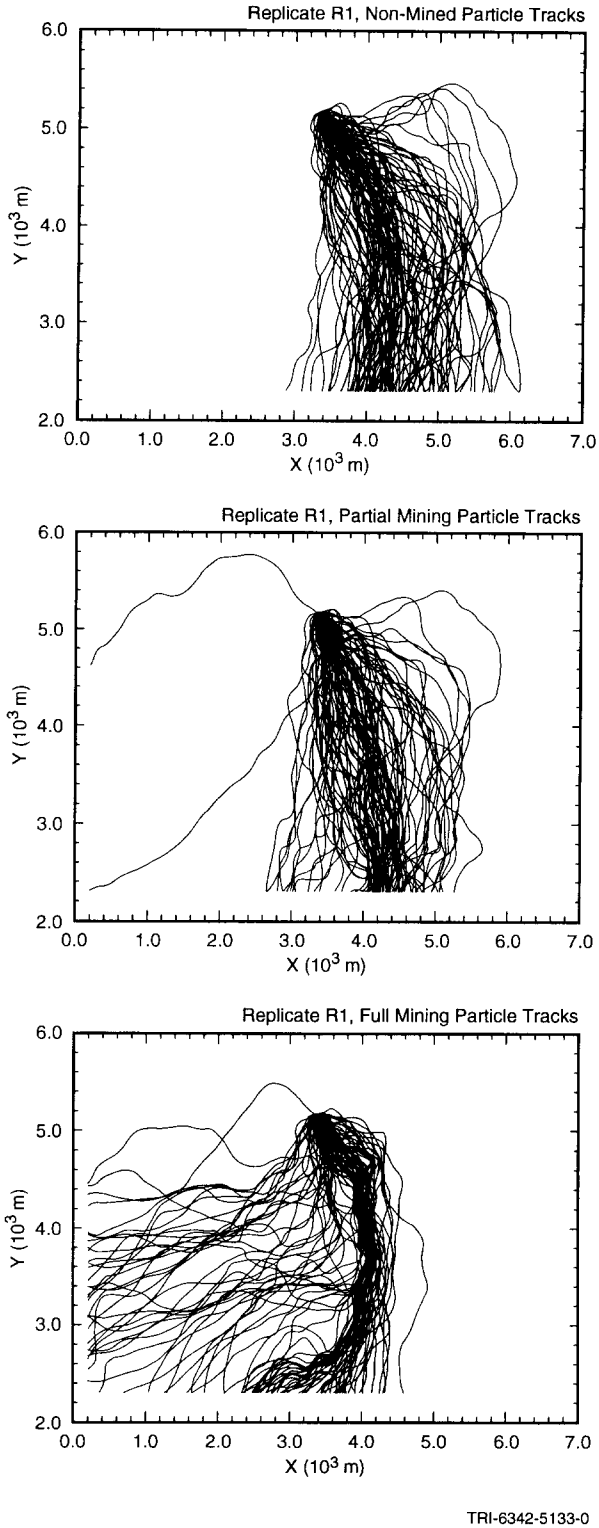

Fig. 12.1.2. Travel paths for nonreactive, nonsorbing particle released at center of repository for different values of $\mathbf{v}(x,y)$ for unmined, partially mined and fully mined conditions.

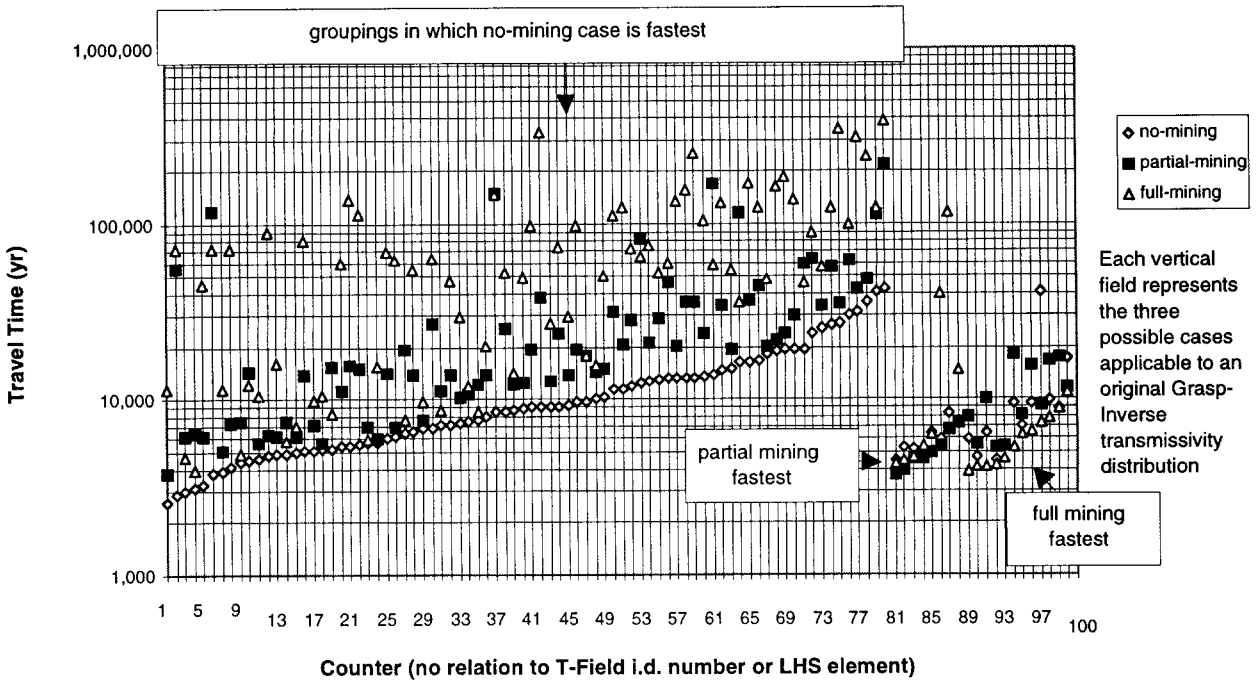

Fig. 12.1.3. Travel times to accessible environment for nonreactive, nonsorbing particles released at center of repository for different values of velocity field $\mathbf{v}(x,y)$ for unmined, partially mined and fully mined conditions for 100 sample elements in replicate R1. These travel times should not be interpreted as being representative of actual radionuclide transport times (see text).

12.2 Transport in Culebra: Computational Strategy

Without careful planning, the computational cost of performing SECOTP2D calculations (Sect. 4.9) for radionuclide movement in the Culebra would be prohibitive. In concept, a set of calculations is required for each randomly sampled future. As 300 LHS elements are under consideration (i.e., 3 replicates of 100 elements each) and 10,000 randomly sampled futures are evaluated for each LHS element, a total of 3×10^6 sets of SECOTP2D calculations result. In addition, 4 radionuclides are considered for transport in the Culebra (i.e., Am-241, Pu-239, U-234, Th-230), with these radionuclides present in both dissolved and colloidal (i.e., humic, microbial, mineral fragment, actinide intrinsic) states; Pu-238 was not transported in the Culebra due to its short half-life. This potentially places an additional multiplier of 15 (i.e., three decay chains and 5 states) on the number of SECOTP2D calculations. Finally, there is the need to alter the Culebra flow field at time t_{min}, which adds an additional complication to the analysis. The performance of 4.5×10^7 SECOTP2D calculations with time-varying source rates and flow fields was not considered to be an option. Actually, even this number was arrived at by trimming the number of radionuclides and colloidal states to be considered.

A more computationally efficient approach was needed than simply performing every possible calculation. This approach was provided by taking advantage of the linearity of the system of partial differential equations that underlies SECOTP2D. Because of this linearity, transport calculations can be performed for unit releases to the Culebra at 0 yr and then used to construct transport results for arbitrary time-dependent releases into the Culebra. In concept, 16 SECOTP2D calculations are required for each LHS element (Table 12.2.1). Radionuclide transport through the Culebra to the accessible environment for each of the 10,000 randomly sampled futures associated with an LHS element can then be constructed from the results of these 16 calculations (Table 12.2.1). Colloidally transported radionuclides are assumed to remain associated with their colloid carriers throughout transport in the Culebra. Because of this, SECOTP2D calculations need only be performed for the colloid carriers as indicated in Table 12.2.1; then, the effects of radioactive decay and daughter growth can be incorporated into the transport results by an appropriate application of the Bateman equations (Bateman 1910).

The results *uDP*, *uDF*, *uCP* and *uCF* in Table 12.2.2 are the outcomes of the SECOTP2D calculations. For notational convenience, *uDP* and *uDF* are defined as being the release through 10,000 yr (i.e., τ_{nTl+1}) for a unit release over the time interval $[\tau_m, \tau_{m+1}]$. Computationally, these results are obtained from the SECOTP2D calculations for a unit release over time interval $[\tau_1, \tau_2]$ and transport through time $\tau_2 + (10{,}000 - \tau_{m+1})$. Experimental results indicate that microbial and mineral fragment colloids will undergo very little transport in the Culebra due to filtration effects (Lucero et al. 1996, Papenguth 1996). Thus, the release of these colloids and their associated radionuclides to the accessible environment due to transport through the Culebra was assumed to be 0 in the 1996 WIPP PA (i.e., *uCP* and *uCF* in Table 12.2.2 were assumed to be 0 for these colloids). Actinide intrinsic colloids were found to exist in insignificant quantities and thus were not considered for transport in the Culebra. Humic colloids were found to transport similarly to dissolved radionuclides (Papenguth 1996). As a result, humic colloids were not treated explicitly in the calculations (i.e., *fCE0*, *fCE1* and *fCE2* in Table 11.2.1 were set to 0 for humic colloids).

Due to the preceding simplifications, SECOTP2D results were only needed for dissolved radionuclides (i.e., calculations 1-8 in Table 12.2.1). For computational efficiency, these calculations were performed for partially and fully mined conditions, with all radionuclides (i.e., Am-241, Pu-239, U-234, Th-230) incorporated into each calculation. Thus, a total of 600 SECOTP2D calculations were actually performed (i.e., 300 for partially mined conditions and 300 for fully mined conditions). In each calculation, a 1 kg release of each radionuclide (i.e., Am-241, Pu-239, U-234, Th-230) is assumed to take place between 0 and 50 yr and then the transport of this release through 10,000 yr is calculated. For the unit release of U-234, the transport of both U-234 and its daughter Th-230 is modeled. In addition, the transport of a separate unit release of Th-230 is also modeled. This separation is needed to define *uDP* and *uDF* in Table 12.2.2 for U-234 and Th-230.

Table 12.2.1. Potential SECOTP2D Calculations for a Single LHS Element

SECOTP2D Calculations	Description
1,2	Dissolved Am-241 for partially and fully mined conditions
3,4	Dissolved Pu-239 for partially and fully mined conditions
5,6	Dissolved U-234, Th-230 for partially and fully mined conditions
7,8	Dissolved Th-230 for partially and fully mined conditions
9,10	Humic colloids for partially and fully mined conditions
11,12	Microbial colloids for partially and fully mined conditions
13,14	Mineral fragment colloids for partially and fully mined conditions
15,16	Actinide intrinsic colloids for partially and fully mined conditions

Table 12.2.2. Results Available for Use in CCDF Construction for Radionuclide Releases Resulting from Groundwater Transport through the Culebra Dolomite

τ_m = times (yr) used to record results of unit release calculations with SECOTP2D for the Culebra, m = 1, 2, ..., $nTI + 1 = 201$ with $\tau_1 = 0$ yr and $\Delta\tau_m = 50$ yr

nTI = number of time intervals $[\tau_m, \tau_{m+1}]$, $m = 1, 2, \ldots, nTI$, defined by τ_m, $m = 1, 2, \ldots, nTI + 1$

$uDP(j, k, l, \tau_m)$= release (kg) to accessible environment of element l of decay chain j resulting from a 1 kg dissolved release of element k of decay chain j to the Culebra over time interval $[\tau_m, \tau_{m+1}]$ and subsequent transport under partially mined conditions between τ_m and 10,000 yr. Source: SECOTP2D (see Table 6.9.1).

$uDF(j, k, l, \tau_m)$= release (kg) to accessible environment of element l of decay chain j resulting from a 1 kg dissolved release of element k of decay chain j to the Culebra over time interval $[\tau_m, \tau_{m+1}]$ and subsequent transport under fully mined conditions between τ_m and 10,000 yr. Source: SECOTP2D (see Table 6.9.1).

$uCP(s, \tau_1)$ = cumulative release (kg) to accessible environment through time τ_l of colloid specie s due to a 1 kg release of colloid specie s to the Culebra over time interval $[\tau_1, \tau_2]$ and subsequent transport under partially mined conditions. Assumed to be 0; otherwise, would be calculated with SECOTP2D.

$uCF(s, \tau_1)$ = cumulative release (kg) to accessible environment through time τ_l of colloid specie s due to a 1 kg release of colloid specie s to the Culebra over time interval $[\tau_1, \tau_2]$ and subsequent transport under fully mined conditions. Assumed to be 0; otherwise, would be calculated with SECOTP2D.

Once the transport results in Table 12.2.2 are available, the releases to the accessible environment for individual futures $\mathbf{x}_{st}$ due to transport through the Culebra can be calculated as shown in Table 12.2.3, with this calculation also requiring the releases into the Culebra defined in Table 11.2.2.

Table 12.2.3. Calculation of Groundwater Transport Release $f_{ST}(\mathbf{x}_{st})$ through the Culebra Dolomite for an Arbitrary Future $\mathbf{x}_{st}$ of form in Eq. (2.2.2)

Notation:

$cKM(j, k)$ = conversion factor from kg to moles (mole/kg) for element k of decay chain j

$cMK(j, k)$ = conversion factor from moles to kg (kg/mole) for element k of decay chain j [$=1/cKM(j, k)$]

$cKC(j, k)$ = conversion factor from kg to Ci (Ci/kg) for element k of decay chain j

$\lambda(j, k)$ = decay constant (yr^{-1}) for element k of decay chain j

nDC = number of decay chains

$nM(j)$ = number of members in decay chain j

$rL(j, k)$ = EPA release limit (Ci) for element k of decay chain j

tI = total inventory (Ci) of α-emitting radionuclides placed in repository with halflives that exceed 20 yr

nC = number of colloid species

Dissolved release $rD(j, k)$ of element k of decay chain j:

$uD(j, k, l, \tau_m)$ = release (kg) to accessible environment of element l of decay chain j resulting from a 1 kg dissolved release of element k of decay chain j to the Culebra over time interval $[\tau_m, \tau_{m+1}]$

$$= \begin{cases} uDP(j, k, l, \tau_m) & \text{if } \tau_{m+1} < t_{min} \quad \text{(See Table 12.2.2)} \\ uDF(j, k, l, \tau_m) & \text{if } \tau_{m+1} \geq t_{min} \quad \text{(See Table 12.2.2)} \end{cases}$$

$dRD(j, k, \tau_m, \tau_{m+1})$ = dissolved release (kg) to Culebra of element k of decay chain j over time interval $[\tau_m, \tau_{m+1}]$

$$= cRD(j, k, \tau_{m+1}) - cRD(j, k, \tau_m) \quad \text{(see Table 11.2.2)}$$

$rD(j, k)$ = release (kg) to accessible environment of element k of decay chain j resulting from dissolved releases into the Culebra

$$= \sum_{m=1}^{nTI} \sum_{p=1}^{k} dRD(j, p, \tau_m, \tau_{m+1})\, uD(j, p, k, \tau_m)$$

Table 12.2.3. Calculation of Groundwater Transport Release f_{ST} ($\mathbf{x}_{st}$) through the Culebra Dolomite for an Arbitrary Future $\mathbf{x}_{st}$ of form in Eq. (2.2.2) (continued)

Colloidal release $rC(j, k)$ of element k of decay chain j:

$uC(s, \tau_1, \tau_m)$ = release (kg) to accessible environment of colloid specie s over time interval $[\tau_m, \tau_{m+1}]$ resulting from a 1 kg release of colloid specie s to the Culebra over time interval $[\tau_l, \tau_{l+1}]$

$$= \begin{cases} uCP(s, \tau_{m+1-l}) - uCP(s, \tau_{m-l}) & \text{if } \tau_{m+1} < t_{min} \quad \text{(See Table 12.2.2)} \\ uCF(s, \tau_{m+1-l}) - uCF(s, \tau_{m-l}) & \text{if } \tau_{m+1} \geq t_{min} \quad \text{(See Table 12.2.2)} \end{cases}$$

$dRC(s, j, k, \tau_1)$ = amount (kg) of element k of decay chain j attached to colloid specie s released to Culebra over time interval $[\tau_l, \tau_{l+1}]$

$$= cRC(s, j, k, \tau_{l+1}) - cRC(s, j, k, \tau_l) \qquad \text{(see Table 11.2.2)}$$

$aC(s, j, k, \tau_1, \tau_m)$ = amount (kg) of element k of decay chain j attached to colloid specie s over time interval $[\tau_m, \tau_{m+1}]$ due to releases over time interval $[\tau_l, \tau_{l+1}]$

$$= \left\{ \sum_{p=1}^{k} \left(\sum_{q=p}^{k} \left[\frac{\left[\prod_{r=p}^{k} \lambda(j, r) \right] / \lambda(j, k)}{\prod_{\substack{s=p \\ s \neq q}}^{k} [\lambda(j, s) - \lambda(j, q)]} \right] \bullet \exp\left[-\lambda(j, q) \left(\frac{\tau_m + \tau_{m+1}}{2} - \frac{\tau_l + \tau_{l+1}}{2} \right) \right] \right) \right.$$

$$\left. \bullet \, dRC(s, j, p, \tau_1)\, cKM(j, p) \right\} cMK(j, k)$$

$rCI(s, j, k, \tau_m)$ = amount (kg) of element k of decay chain j attached to colloid specie s released to accessible environment over time interval $[\tau_m, \tau_{m+1}]$

$$= \sum_{l=1}^{m} aC(s, j, k, \tau_1, \tau_m)\, uC(s, \tau_1, \tau_m)$$

$rC(j, k)$ = release (kg) to accessible environment of element k of decay chain j resulting from colloidal releases into the Culebra

Table 12.2.3. Calculation of Groundwater Transport Release f_{ST} ($\mathbf{x}_{st}$) through the Culebra Dolomite for an Arbitrary Future $\mathbf{x}_{st}$ of form in Eq. (2.2.2) (continued)

$$= \sum_{s=1}^{nC} \sum_{m=1}^{nTI} rCI(s, j, k, \tau_m)$$

Evaluation of $f_{ST}(\mathbf{x}_{st})$:

$$f_{ST}(\mathbf{x}_{st}) = \sum_{j=1}^{nDC} \sum_{k=1}^{nM(j)} \left\{ \frac{[rD(j,k) + rC(j,k)]\, cKC(j,k)}{rL(j,k)} \right\} \left\{ \frac{10^6 \text{ Ci}}{tI} \right\}$$

12.3 Transport in Culebra: Initial Results

Of the 300 LHS elements under consideration, only element 33 of replicate R3 produced nonzero releases to the accessible environment, with releases only occurring for U-234 (Fig. 12.3.1). For all other sample elements and all radionuclides, no release to the accessible environment occurred for either partially or fully mined conditions.

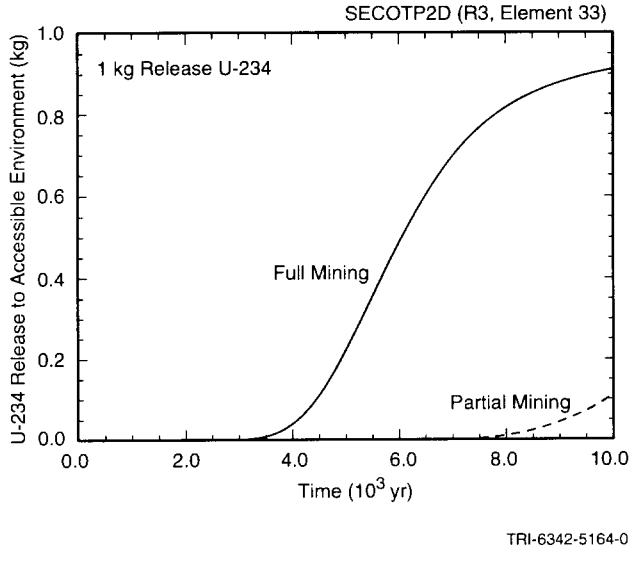

Fig. 12.3.1. Cumulative transport to accessible environment under partially mined and fully mined conditions for LHS element 33 of replicate R3 for unit release (1 kg) of U-234 to the Culebra over the time interval [0, 50 yr].

12.4 Transport in Culebra: CCDFs

In concept, the CCDFs for radionuclide transport through the Culebra to the accessible environment can be constructed in the same manner as the CCDFs for cuttings (Fig. 9.2.2), spallings (Fig. 9.4.1), direct brine release (Fig. 10.3.1), and release to the Culebra (Fig. 11.2.2). The only difference is the use of $f_{ST}(\mathbf{x}_{st})$ in Table 12.2.3 for each sampled future rather than the total normalized release associated with one of the other release modes.

For 299 of the LHS elements, the resulting CCDFs are degenerate (i.e., a probability of 0 of exceeding a normalized release of 0) because releases to the Culebra, if they occur, do not transport through to the accessible environment in the 10,000 yr period of interest. For element 33 of replicate R3, releases of U-234 to the Culebra have the potential to transport to the accessible environment (Fig. 12.3.1). However, no such releases occur, and so the resultant CCDF is again degenerate. Thus, all 300 CCDFs for transport through the Culebra to the accessible environment are degenerate.

12.5 Transport in Culebra: Additional Results

Due to the zero releases, the SECOTP2D results described in Sect. 12.3 do not provide suitable input for a sensitivity analysis. Therefore, to observe the effects of sampled (i.e., uncertain) variables on Culebra transport, SECOTP2D calculations were performed on a much smaller computational grid (Fig. 12.5.1) than the grid used to assess transport to the accessible environment (Fig. 4.8.5). In particular, transport was calculated across boundaries 3, 5, 7 and 10 m from the release point into the Culebra (Fig. 12.5.1) for U-234, which was selected for analysis because it is the least retarded of the radionuclides considered in the 1996 WIPP PA. Further, calculations were performed for the partially mined transmissivity fields calculated for replicate R1. The associated flow field calculated by SECOFL2D for each sample element is spatially variable. However, due to the small size of the computational grid in use (Fig. 12.5.1), a single constant velocity was interpolated from the spatially variable flow field for each sample element and used to define fluid flow. The calculations were performed for the 100 sample elements in replicate R1.

The releases (i.e., kilograms or fraction of initial release) over 10,000 yr across the four boundaries in Fig. 12.5.1 range from 0 to close to 1 (Fig. 12.5.2). Even at the small distances under consideration (i.e., 3, 5, 7, 10 m), a significant number of the sample elements result in little transport across the boundaries.

There is significant uncertainty in the cumulative release curves in Fig. 12.5.2. One way to assess the sources of this uncertainty is by calculating PRCCs between the cumulative releases and the relevant sampled variables (Table 12.5.1). Due to their definitions and use within the analysis, significant correlations can potentially exist between *CMTRXPOR*, *CMRTRDU*, *CVEL*, *CVELCF*, *CVELSC*, *CULCLIM* and *WOXSTAT*. To eliminate the loss of information that results from the calculation of partial correlation coefficients in the presence of correlated variables,

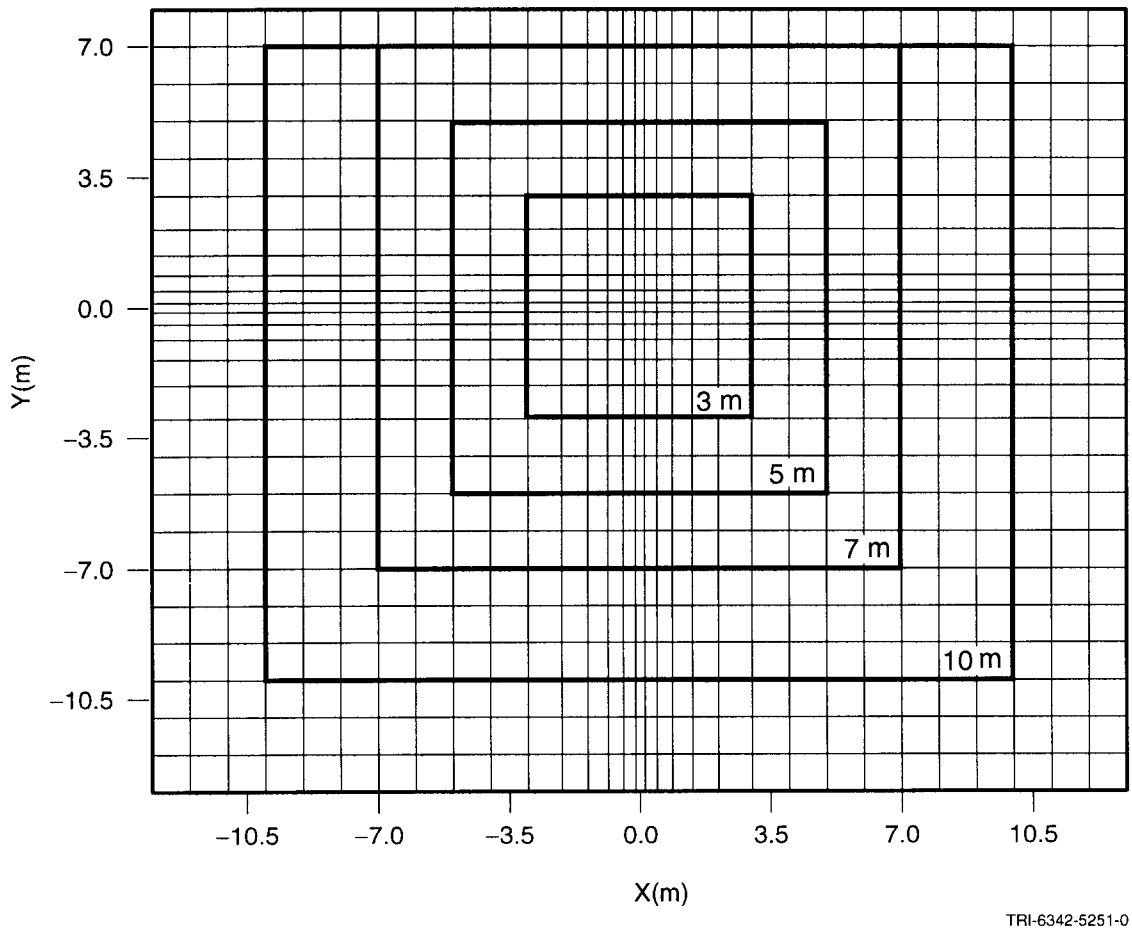

Fig. 12.5.1. Computational grid used in sensitivity analysis of SECOTP2D results.

only *CFRCSP*, *CMRTRDU* and *CVEL* were used in the calculation of PRCCs. As should be the case, release tends to increase as fluid velocity (*CVEL*) and fracture spacing (*CFRCSP*) increase and tends to decrease as matrix retardation (*CMRTRDU*) increases (Fig. 12.5.3). The positive effect for *CFRCSP* results because increasing *CFRCSP* decreases the surface area available for diffusion into the matrix and thus reduces radionuclide movement from the fractures into the surrounding matrix.

The cumulative releases over 10,000 yr in Fig. 12.5.2 can also be summarized with box plots (Fig. 12.5.4). For most sample elements, these releases are small. The median values for 3 and 5 m are approximately 0.06 and 0.0006, and the median values for 7 and 10 m are less than 1×10^{-5}. The means are between 0.1 and 0.4 and are dominated by the few largest values. The rapid attenuation indicated in Figs. 12.5.2 and 12.5.4 is why there is little radionuclide transport in the Culebra to the boundary with the accessible environment within the 10,000 yr period under consideration.

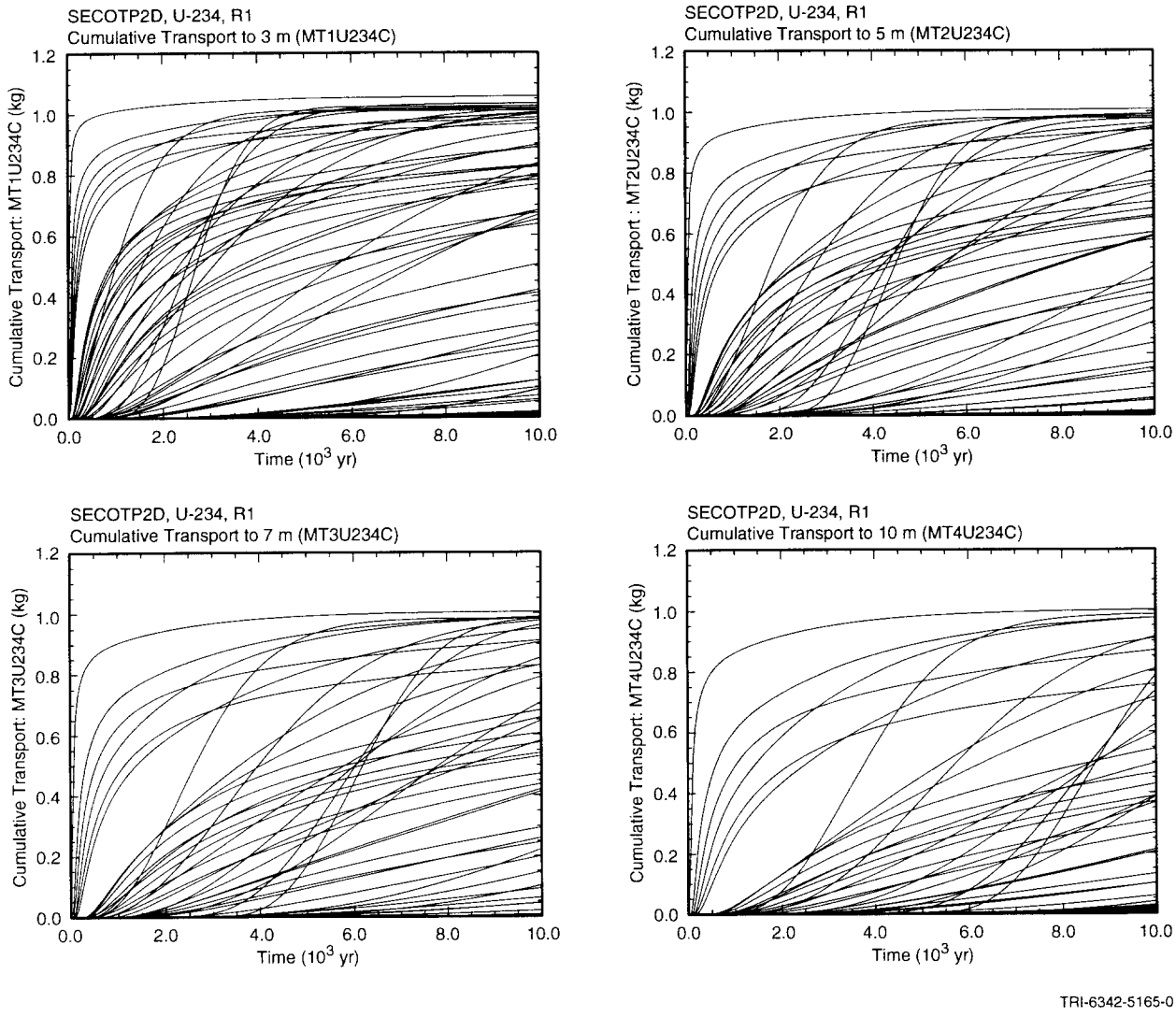

Fig. 12.5.2. Cumulative U-234 releases to the 3, 5, 7 and 10 m boundaries in Fig. 12.5.1 for 1 kg release over time interval [0, 50 yr].

Table 12.5.1. Independent Variables Considered for Potential Inclusion in Sensitivity Analysis of U-234 Transport in Culebra Dolomite

Variable	Description
CFRCSP	Culebra fracture spacing (m). Defined in Table 5.2.1
CFRCPOR	Culebra fracture porosity. Defined in Table 5.2.1
CMTRXPOR	Culebra matrix porosity. Defined in Table 5.2.1
CMRTRDU	Culebra matrix retardation for uranium. Defined by *CMRTRDU* = 1 + [2800 kg/m^3 (1 – *CMTRXPOR*) K_d (*WOXSTAT*)] / *CMTRXPOR* with K_d (*WOXSTAT*) = *CMKDU*4 if *WOXSTAT* = 0 and K_d (*WOXSTAT*) = *CMKDU*6 if *WOXSTAT* = 1.
CVEL	Norm of fluid velocity vector calculated by SECOFL2D under partially mined conditions at release point into Culebra and used in SECOTP2D calculations (m/s).
CVELCF	Norm of fluid velocity vector multiplied by climate scale factor (m/s): *CVELCF* = *CVEL CULCLIM*
CVELSC	Norm of scaled fluid velocity within fracture s (m/s): *CVELSC* = *CVEL CULCLIM* / *CFRCPOR*
CULCLIM	Climate scale factor for Culebra flow field. Defined in Table 5.2.1
WOXSTAT	Pointer variable for elemental oxidation states. Defined in Table 5.2.1

As shown by the stepwise regressions in Table 12.5.2, the two dominant variables for U-234 transport over 10,000 yr are *CMRTRDU* and *CVEL*, with transport tending to decrease as *CMRTRDU* increases and tending to increase as *CVEL* increases. These same patterns were also observed in the analyses with PRCCs (Fig. 12.5.3). Lesser effects are indicated for *CFRCSP* and *WOXSTAT*. The small positive effect for *CFRCSP* results from increasing the surface area available for diffusion into the matrix. The positive effect for *WOXSTAT* results from its role in determining the distribution coefficients for use in the definition of *CMRTRDU* (Table 12.5.1). In particular, smaller distribution coefficients are associated with *WOXSTAT* = 1; in turn, this results in smaller values for *CMRTRDU* and hence the positive effect for *WOXSTAT* in Table 12.5.2. The use of *WOXSTAT* in the definition of *CMRTRDU* results in a rank correlation of –0.8661 between *WOXSTAT* and *CMRTRDU*, which is the cause of the instability in the regression coefficients for *WOXSTAT* and *CMRTRDU* in Table 12.5.2.

Additional perspective is provided by the scatterplots in Fig. 12.5.5 for U-234 transport across the 3 and 10 m boundaries in Fig. 12.5.1. The tendency of the release to decrease with increasing values for *CMRTRDU* is clearly evident. The division of *CMRTRDU* into a range of values below 10^3 and a range of values above 10^4 is due to *WOXSTAT* (see *CMRTRDU* in Table 12.5.1), with the smaller values corresponding to the use of *CMKDU*6 to define *CMRTRDU* (i.e., *WOXSTAT* = 1) and the larger values corresponding to the use of *CMKDU*4 to define *CMRTRDU*

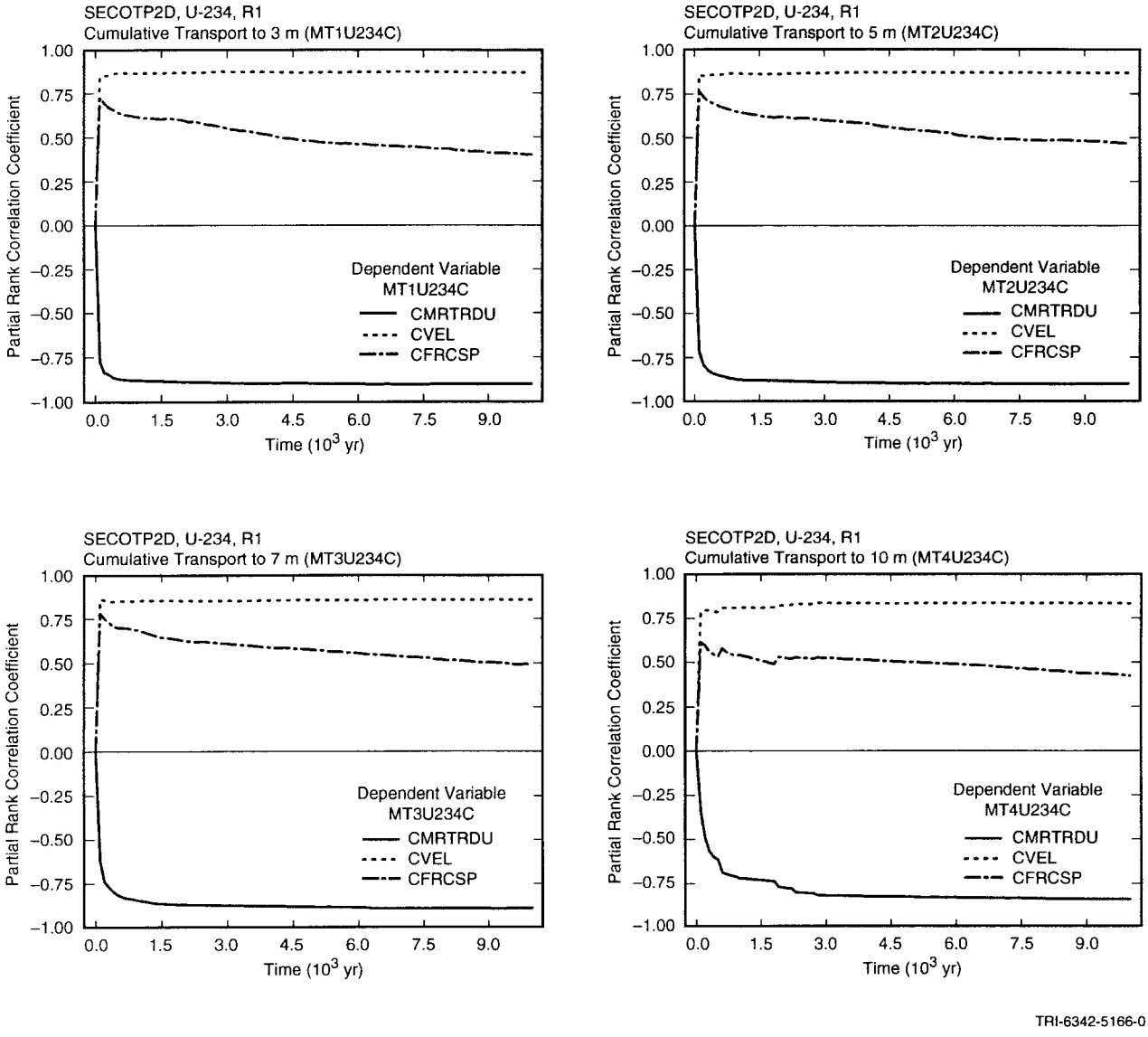

Fig. 12.5.3. Partial rank correlation coefficients (PRCCs) for cumulative U-234 releases across boundaries 3, 5, 7 and 10 m from release point into Culebra Dolomite for 1 kg release over time interval [0, 50 yr].

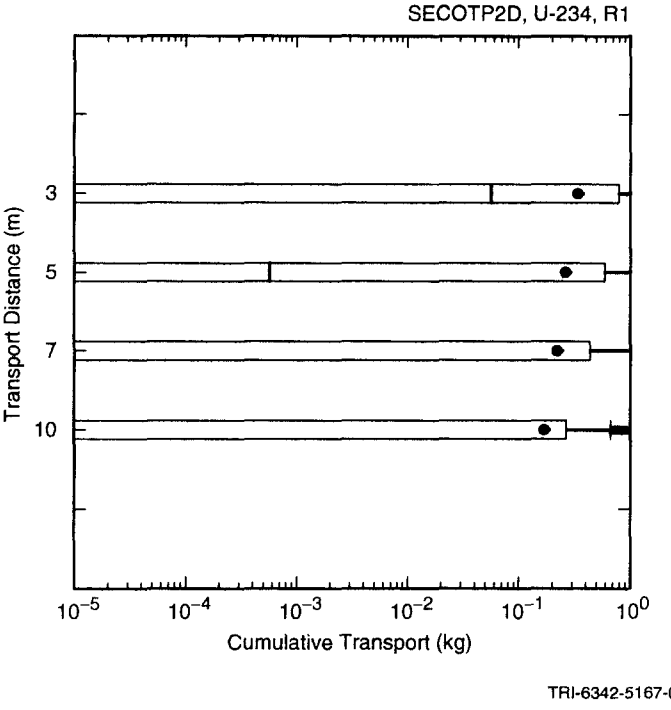

Fig. 12.5.4. Cumulative transport over 10,000 yr of U-234 across the 3, 5, 7 and 10 m boundaries in Fig. 12.5.1 for a 1 kg release over the time interval [0, 50 yr].

Table 12.5.2. Stepwise Regression Analyses with Rank-Transformed Data and Independent Variables in Table 12.5.1 for Cumulative Transport of U-234 over 10,000 yr Across the 3, 5, 7 and 10 m Boundaries in Fig. 12.5.1 for a 1 kg Release over the Time Interval [0, 50 yr]

	3 m			5 m			7 m			10 m		
Step[a]	Variable[b]	SRRC[c]	R^{2d}	Variable	SRRC	R^2	Variable	SRRC	R^2	Variable	SRRC	R^2
1	*CMRTRDU*	−0.44	0.51	*CMRTRDU*	−0.41	0.50	*CMRTRDU*	−0.40	0.48	*CMRTRDU*	−0.41	0.41
2	*CVEL*	0.58	0.86	*CVEL*	0.59	0.86	*CVEL*	0.58	0.84	*CVEL*	0.61	0.80
3	*CFRCSP*	0.16	0.89	*CFRCSP*	0.19	0.89	*CFRCSP*	0.21	0.88	*CFRCSP*	0.20	0.84
4	*WOXSTAT*	0.31	0.91	*WOXSTAT*	0.32	0.91	*WOXSTAT*	0.37	0.90	*WOXSTAT*	0.29	0.85

[a] Steps in stepwise regression analysis.

[b] Variables listed in order of selection in regression analysis.

[c] Standardized rank regression coefficients in final regression model.

[d] Cumulative R^2 value with entry of each variable into regression model.

(i.e., *WOXSTAT* = 0). The larger values for *CMRTRDU* (i.e., *WOXSTAT* = 0, which implies use of *CMKDU4*) result in almost no transport across the 10 m boundary. The positive effect of *CVEL* on transport is evident but less strong than the negative effect of *CMRTRDU*.

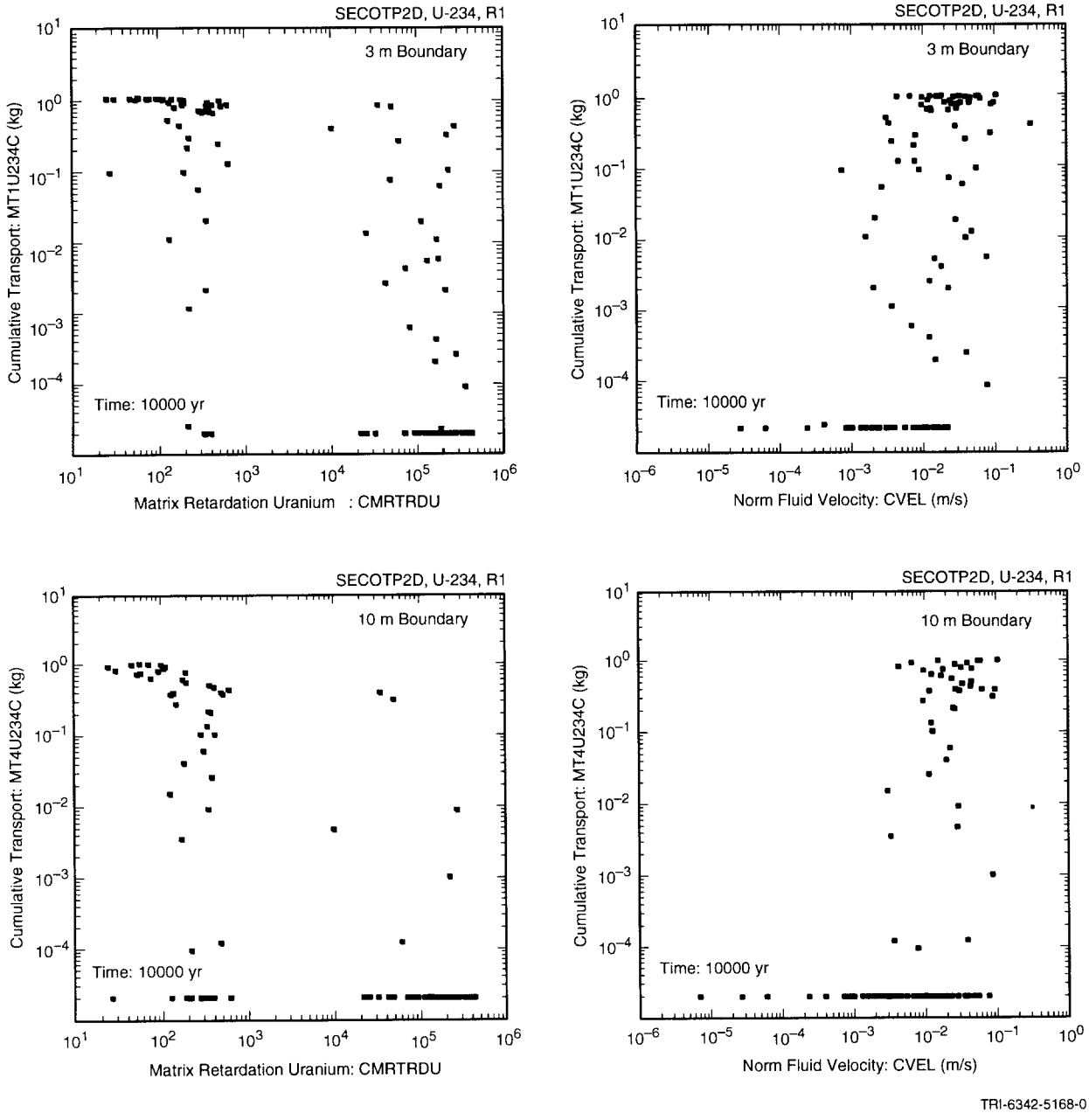

Fig. 12.5.5. Scatterplots for cumulative transport over 10,000 yr of U-234 across the 3 and 10 m boundaries in Fig. 12.5.1 for 1 kg release over time interval [0, 50 yr] versus *CMRTRDU* and *CVEL*.

13. Total Release to Accessible Environment

13.1 Total Release: Individual Futures

Each sampled future of the form indicated in Eq. (2.2.2) requires the determination of a normalized release to the accessible environment. Determination of this release corresponds to evaluation of the function f in Eq. (4.1.1). Of the functions appearing in Eq. (4.1.1), only f_C, f_{DBR} and f_{SP} produced nonzero results when evaluated with the 300 LHS elements used in the 1996 WIPP PA. Thus, in this PA, f can be viewed as a function of the form

$$f(\mathbf{x}_{st}) = f_C(\mathbf{x}_{st}) + f_{SP}\left[\mathbf{x}_{st}, f_B(\mathbf{x}_{st})\right] + f_{DBR}\left\{\mathbf{x}_{st}, f_{SP}\left[\mathbf{x}_{st}, f_B(\mathbf{x}_{st})\right], f_B(\mathbf{x}_{st})\right\} \tag{13.1.1}$$

for the determination of total release to the accessible environment.

As previously discussed, CCDFs are constructed by randomly sampling individual futures $\mathbf{x}_{st,i}$, $i = 1, 2, \ldots, nS = 10{,}000$ (Sect. 6.7). The total release for each future $\mathbf{x}_{st,i}$ is then given by

$$f(\mathbf{x}_{st,i}) = f_C(\mathbf{x}_{st,i}) + f_{SP}\left[\mathbf{x}_{st,i}, f_B(\mathbf{x}_{st,i})\right] + f_{DBR}\left\{\mathbf{x}_{st,i}, f_{SP}\left[\mathbf{x}_{st,i}, f_B(\mathbf{x}_{st,i})\right], f_B(\mathbf{x}_{st,i})\right\}. \tag{13.1.2}$$

The specific procedures used to obtain f_C, f_{SP} and f_{DBR} in the 1996 WIPP PA are described in Sects. 9.2, 9.4 and 10.3, respectively.

13.2 Total Release: CCDFs

The CCDFs for total release are constructed with the release values indicated in Eq. (13.1.2). The outcome is a distribution of CCDFs that falls substantially below the limit specified in 40 CFR 191 (Fig. 13.2.1). The dominant contributor to total release is cuttings removal (i.e., f_C) (Fig. 9.2.2); a substantial contribution is also made by spallings (i.e., f_{SP}) for some LHS elements (Fig. 9.4.1). Direct brine release (i.e., f_{DB}) is a small, and often zero, contributor to the total release (Fig. 10.3.1). The appearance of the 90th quantile substantially below and to the left of the boundary line specified in 40 CFR 191 is indicative of a high confidence that the WIPP does indeed meet this regulation (Fig. 13.2.1).

The three replicated LHSs provide a check on the stability of the results in Fig. 13.2.1 (Fig. 13.2.2). Reassuringly, the estimated mean and quantiles are quite stable across the three replicates and a tight confidence interval is obtained for the mean. Similar stability was also observed for the cuttings (Fig. 9.2.3), spallings (Fig. 9.4.2) and direct brine release (Fig. 10.3.2) CCDFs.

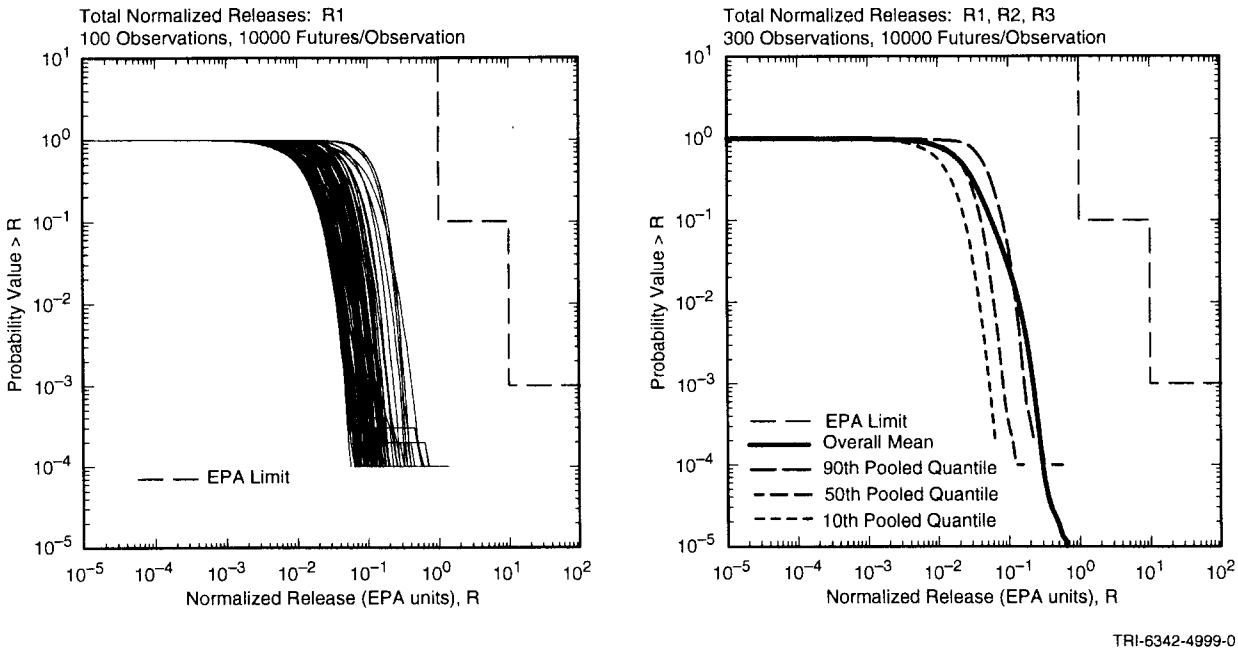

Fig. 13.2.1. Distribution of CCDFs for total normalized release to accessible environment over 10,000 yr due to cuttings and cavings, spallings and direct brine release: CCDFs for replicate R1 (left frame), and mean and percentile curves obtained by pooling replicates R1, R2 and R3 (right frame).

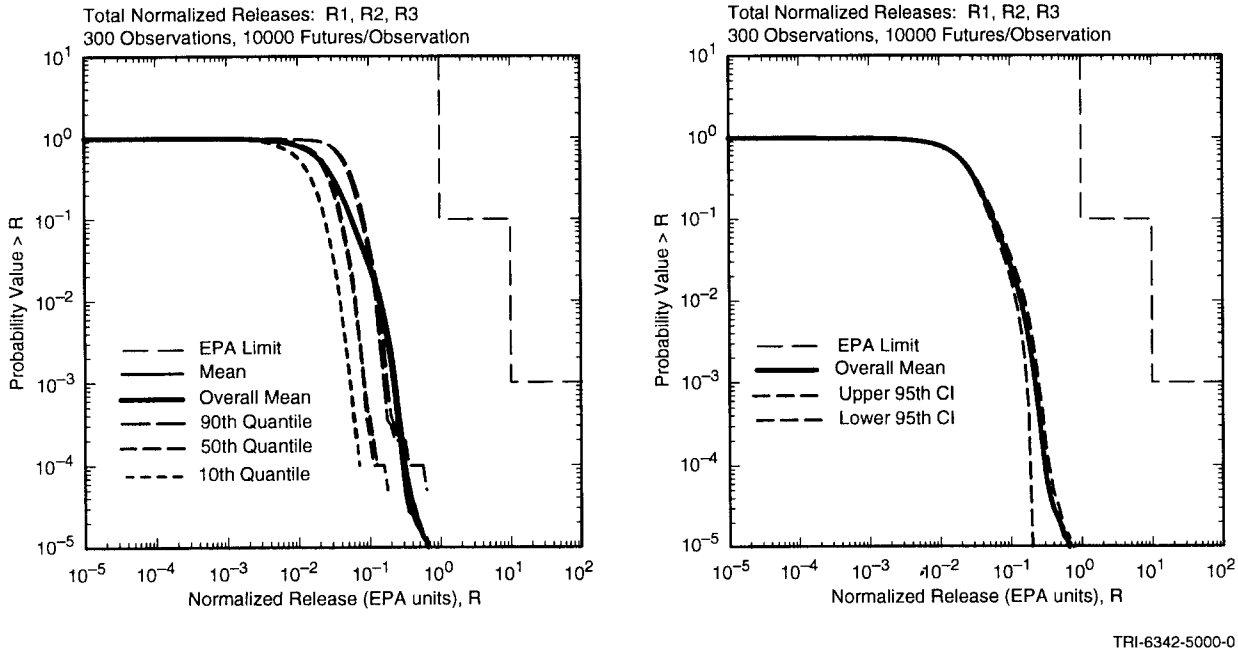

Fig. 13.2.2. Outcome of replicated sampling for distribution of CCDFs for total normalized release to the accessible environment over 10,000 yr due to cuttings and cavings, spallings and direct brine release: mean and percentile curves for individual replicates (left frame) and confidence intervals (CIs) on mean curve obtained from the three replicates (right frame).

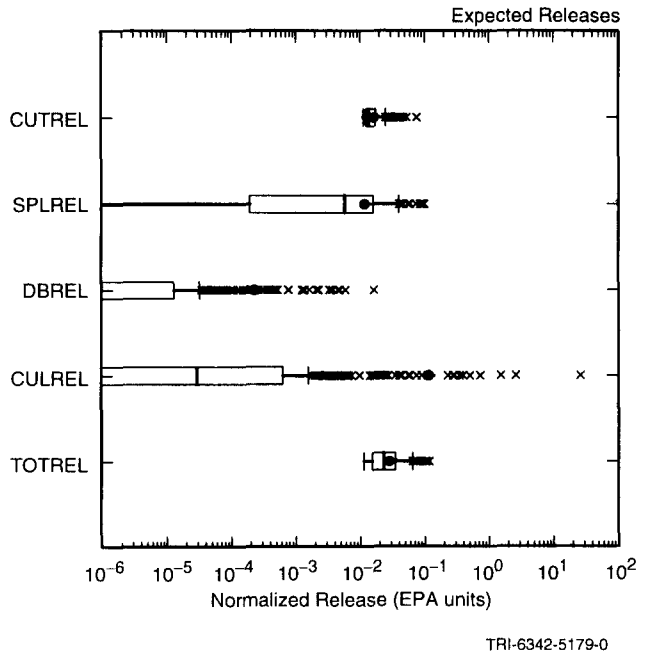

Fig. 13.2.3. Distribution of expected values for total normalized release due to (1) cuttings and cavings (*CUTREL*), (2) spallings (*SPLREL*), (3) direct brine release (*DBREL*), (4) groundwater transport to Culebra (*CULREL*), and (5) cuttings and cavings, spallings and direct brine release combined (*TOTREL*).

The CCDFs for total release can be reduced to expected values (Fig. 13.2.3). Comparison of expected values for cuttings, spallings, direct brine release and total release shows that the total release is dominated by cuttings. For a few LHS elements, the release to the Culebra exceeds the total release due to cuttings, spallings and direct brine release. However, these releases were not transported through the Culebra to the accessible environment.

Stepwise regression analysis can be used to determine the dominant contributors to the expected value for total release due to cuttings, spallings and direct brine release (Table 13.2.1). The two dominant variables with respect to uncertainty in the expected total release are *WMICDFLG* and *WTAUFAIL*, with the size of the expected release tending to increase as *WMICDFLG* increases and tending to decrease as *WTAUFAIL* increases. The positive effect for *WMICDFLG* results from its influence on the size of the spallings release (Table 9.4.3, Fig. 9.4.4), and the negative effect for *WTAUFAIL* results from its influence on the size of the cuttings release (Eq. (9.2.2), Fig. 9.2.4). As a reminder, the total release is completely dominated by spallings and cuttings (Fig. 13.2.3), with *WMICDFLG* and *WTAUFAIL* being the dominant contributors to the uncertainty in these two release modes. The remaining seven variables in the regression model (i.e., *WGRCOR*, *WPRTDIAM*, *HALPOR*, *BHPRM*, *HALPRM*, *WASTWICK*, *ANHPRM*) appear primarily because of their effects on the spallings release. Indeed, these are exactly the same seven variables selected after *WMICDFLG* in the regression analysis for spallings releases (Table 9.4.3). A discussion of the effects of these variables is provided in conjunction with Table 9.4.3.

For perspective, scatterplots involving *WMICDFLG*, *WTAUFAIL*, *WPRTDIAM* and *BHPRM* are presented in Fig. 13.2.4. The tendency of the expected release to increase with increasing values for *WMICDFLG* and to decrease with increasing values for *WPRTDIAM* can be seen in the corresponding scatterplots. The scatterplot for *WTAUFAIL* clearly shows the interplay of the spallings and cuttings components of the total release. The scatterplot is bounded below by points that correspond to LHS elements in which the cuttings release is much larger than the spallings release (see Fig. 9.2.4 for the corresponding scatterplot for cuttings releases only); LHS elements in which spallings is a significant contributor to the total release produce points above this lower curve. The scatterplots for *WPRTDIAM* and *BHPRM* show a tendency for the largest releases to be associated with small values for *WPRTDIAM* and *BHPRM*, with these associations resulting from the effects of *WPRTDIAM* and *BHPRM* on the size of the spallings release (see Sect. 9.4).

As for spallings (Fig. 9.4.5), an alternative investigation of the effects of uncertainty on the CCDFs in Fig. 13.2.1 is provided by PRCCs (Fig. 13.2.5). Specifically, the probability of exceeding a given release tends to go up as *WMICDFLG* increases and tends to go down as *WTAUFAIL* increases. The basis of these effects is discussed in conjunction with Table 13.2.1, with *WMICDFLG* and *WTAUFAIL* being the first two variables selected in the stepwise regression analysis summarized in Table 13.2.1.

Table 13.2.1. Stepwise Regression Analysis with Rank-Transformed Data for Expected Normalized Release Associated with Individual CCDFs for Total Release Due to Cuttings and Cavings, Spallings and Direct Brine Release

	Expected Normalized Release		
Step[a]	Variable[b]	SRRC[c]	R^{2d}
1	*WMICDFLG*	0.60	0.40
2	*WTAUFAIL*	−0.39	0.55
3	*WGRCOR*	0.21	0.59
4	*WPRTDIAM*	−0.19	0.63
5	*HALPOR*	0.17	0.65
6	*BHPRM*	−0.17	0.68
7	*HALPRM*	0.16	0.71
8	*WASTWICK*	0.11	0.72
9	*ANHPRM*	0.09	0.73

[a] Steps in stepwise regression analysis.

[b] Variables listed in order of selection in regression analysis with *ANHCOMP* and *HALCOMP* excluded from entry into regression model.

[c] Standardized rank regression coefficients in final regression model.

[d] Cumulative R^2 value with entry of each variable into regression model.

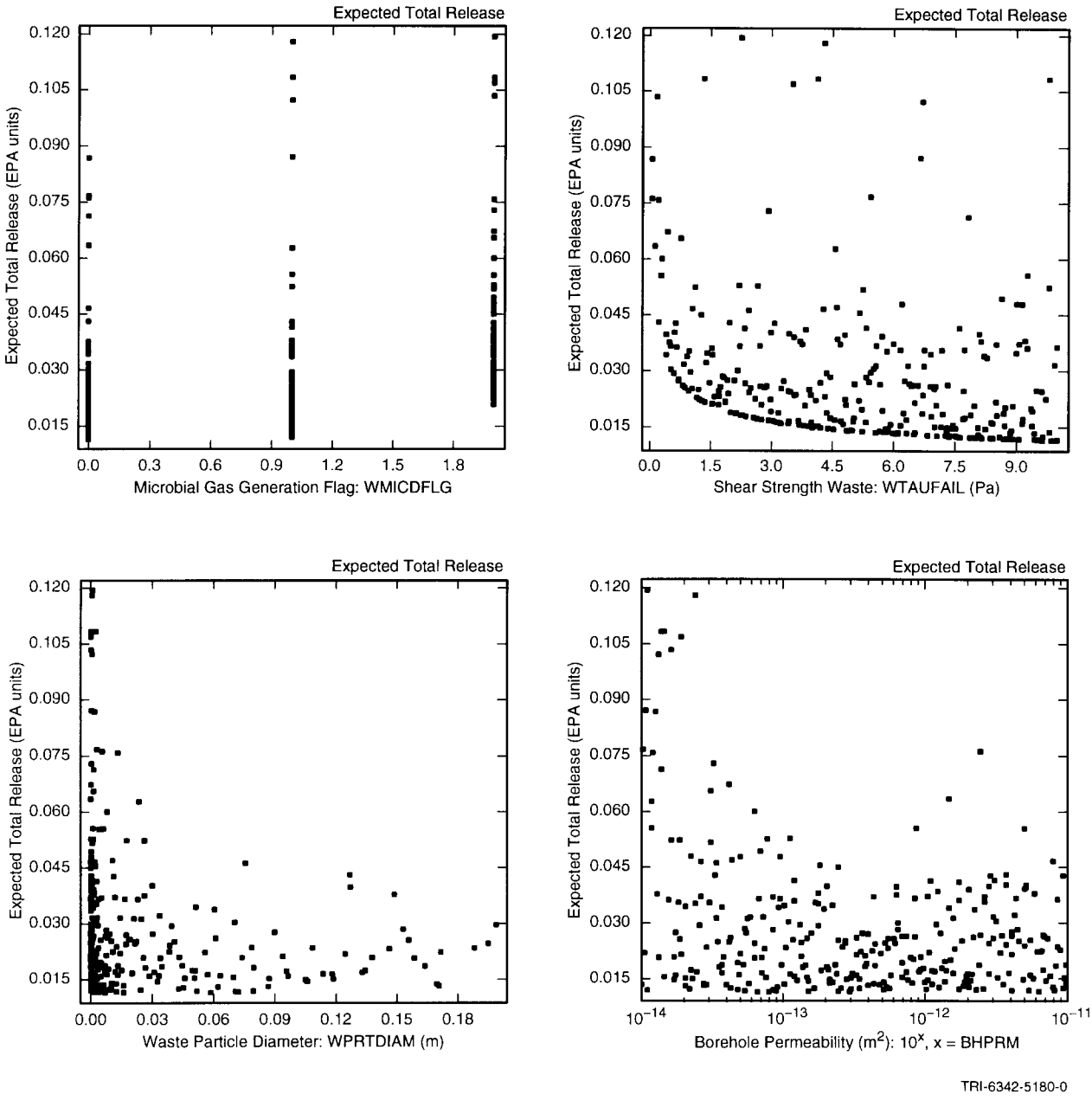

Fig. 13.2.4. Scatterplots for expected normalized releases associated with individual CCDFs for total release due to cuttings and cavings, spallings and direct brine release versus *WMICDFLG*, *WTAUFAIL*, *WPRTDIAM* and *BHPRM*.

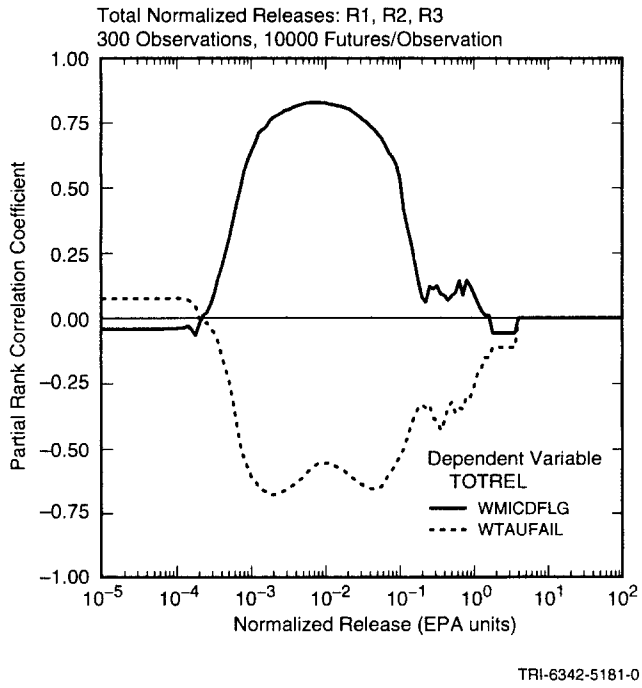

Fig. 13.2.5. Sensitivity analysis based on PRCCs for CCDFs for total normalized release to the accessible environment due to cuttings and cavings, spallings and direct brine release.

14. REFERENCES

Abdul Khader, M.H., and H.S. Rao. 1974. "Flow Through Annulus with Large Radial Clearance," *American Society of Civil Engineers, Journal of the Hydraulics Division.* Vol. 100, no. HY1, 25-39.

Allen, B.C., T.R. Covington, and H.J. Clewell. 1996. "Investigation of the Impact of Pharmacokinetic Variability and Uncertainty on Risks Predicted with a Pharmacokinetic Model for Chloroform," *Toxicology.* Vol. 111, no. 1-3, 289-303.

Allen, D.M. 1971. "The Prediction Sum of Squares as a Criterion for Selecting Predictor Variables." Report No. 23. Lexington, KY: University of Kentucky, Department of Statistics.

Anderson, E., P.F. Deisler, Jr., D. McCallum, C. St. Hilaire, H.L. Spitzer, H. Strauss, J.D. Wilson, and R. Zimmerman. 1993. "Key Issues in Carcinogen Risk Assessment Guidelines, Society for Risk Analysis," *Risk Analysis.* Vol. 13, no. 4, 379–382.

Anderson, T.W. 1984. *An Introduction to Multivariate Statistical Analysis.* 2nd ed. New York, NY: John Wiley & Sons.

Apostolakis, G.E. 1989. "Uncertainty in Probabilistic Risk Assessment," *Nuclear Engineering and Design.* Vol. 115, 173-179.

Apostolakis, G. 1990. "The Concept of Probability in Safety Assessments of Technological Systems," *Science.* Vol. 250, no. 4986, 1359-1364.

Aziz, K., and A. Settari. 1979. *Petroleum Reservoir Simulation.* London: Applied Science Publishers; New York: Elsevier.

Bateman, H. 1910. "The Solution of a System of Differential Equations Occurring in the Theory of Radio-active Transformations," *Proceedings of the Cambridge Philosophical Society.* Vol. 15, pt. 5, 423-427.

Bean, J.E., M.E. Lord, D.A. McArthur, R.J. MacKinnon, J.D. Miller, and J.D. Schreiber. 1996. "Analysis Package for the Salado Flow Calculations (Task 1) of the Performance Assessment Analysis Supporting the Compliance Certification Application (CCA)." Analysis Package. Albuquerque, NM: Sandia National Laboratories. Sandia WIPP Central Files WPO # 40514.

Bear, J. 1972. *Dynamics of Fluids in Porous Media.* New York, NY: Dover Publications.

Bechtel National, Inc. 1986. *Waste Isolation Pilot Plant Design Validation Final Report.* DOE/WIPP-86-010. Prepared for the U.S. Department of Energy. San Francisco, CA: Bechtel National, Inc. (Available from the National Technical Information Service (NTIS), Springfield, VA as DE87003412/XAB.)

Belsley, D.A., E. Kuh, and R.E. Welsch. 1980. *Regression Diagnostics: Identifying Influential Data and Sources of Collinearity.* New York, NY: John Wiley & Sons.

Berglund, J.W. 1992. *Mechanisms Governing the Direct Removal of Wastes from the Waste Isolation Pilot Plant Repository Caused by Exploratory Drilling.* SAND92-7295. Albuquerque, NM: Sandia National Laboratories.

Berglund, J.W. 1996a. "Analysis Package for the Cuttings and Spallings Calculations (Task 5 and 6) of the Performance Assessment Calculation Supporting the Compliance Certification Application (CCA), AP-015 and AP-016." Analysis package. Albuquerque, NM: Sandia National Laboratories. Sandia Central Files WPO # 40521.

Berglund, J. 1996b. "Parameters Required for the CUTTINGS_S Code for Use in WIPP Performance Assessment." Memo to M.S. Tierney, April 1, 1996. Albuquerque, NM: Sandia National Laboratories. Sandia WIPP Central Files WPO # 36766.

Berglund, J. 1996c. "Effective Shear Resistance to Erosion TAUFAIL." Memo to B.M. Butcher, October 28, 1996. Albuquerque, NM: Sandia National Laboratories. Sandia WIPP Central Files WPO # 35695 attachment.

Berglund, J.W., J.S. Rath, and R.A. Cole. 1996. "CUTTING_S User's Manual, Version 5.03." Albuquerque: University of New Mexico, New Mexico Engineering Research Institute. Sandia WIPP Central Files WPO # 37765.

Bertram-Howery, S.G., M.G. Marietta, R.P. Rechard, P.N. Swift, D.R. Anderson, B.L. Baker, J.E. Bean, Jr., W. Beyeler, K.F. Brinster, R.V. Guzowski, J.C. Helton, R.D. McCurley, D.K. Rudeen, J.D. Schreiber, and P. Vaughn. 1990. *Preliminary Comparison with 40 CFR Part 191, Subpart B for the Waste Isolation Pilot Plant, December 1990.* SAND90-2347. Albuquerque, NM: Sandia National Laboratories.

Bilgen, E., R. Boulos, and A.C. Akgungor. 1973. "Leakage and Frictional Characteristics of Turbulent Helical Flow In Fine Clearance," *Journal of Fluids Engineering. Transactions of the ASME. Series I.* Vol. 95, no. 4, 493-497.

Binder, R.C. 1958. *Advanced Fluid Mechanics.* Englewood Cliffs, NJ: Prentice-Hall, Inc. Vol. 1, p. 63.

BIR (Baseline Inventory Report). 1996. *Transuranic Waste Baseline Inventory Report (Revision 3).* DOE/CAO-95-1121. Carlsbad, NM: U.S. Department of Energy. (Available from the National Technical Information Service (NTIS), Springfield, VA as DE96012535/XAB.)

Bogen, K.T. and R.C. Spear. 1987. "Integrating Uncertainty and Interindividual Variability in Environmental Risk Assessment," *Risk Analysis.* Vol. 7, no. 4, 427–436.

Brattin, W.J., T.M. Barry, and N. Chiu. 1996. "Monte Carlo Modeling with Uncertain Probability Density Functions," *Human and Ecological Risk Assessment.* Vol. 2, no. 4, 820-840.

Breeding, R.J., J.C. Helton, E.D. Gorham, and F.T. Harper. 1992. "Summary Description of the Methods Used in the Probabilistic Risk Assessments for NUREG-1150," *Nuclear Engineering and Design.* Vol. 135, no. 1, 1-27.

Brill, J.P., and H.D. Beggs. 1986. *Two-Phase Flow in Pipes.* 5th ed., first printing. Tulsa, OK: University of Tulsa.

Broc, R., ed. 1982. *Drilling Mud and Cement Slurry Rheology Manual.* Houston, TX: Gulf Publishing Company; Paris: Editions Techni. p.

Brooks, R.H., and A.T. Corey. 1964. "Hydraulic Properties of Porous Media." Hydrology Paper No. 3. Fort Collins, CO: Colorado State University. Sandia WIPP Central Files WPO # 41117.

Brush, L.H. 1995. "Systems Prioritization Method - Iteration 2 Baseline Position Paper: Gas Generation in the Waste Isolation Pilot Plant." Albuquerque, NM: Sandia National Laboratories. Sandia WIPP Central Files WPO # 28740.

Brush, L.H. 1998a. "Revised Free-Solution Tracer Diffusion Coefficients (D_{sol} S) for Dissolved Pu, Am, U, Th, Np, Cm, and Ra in Boreholes and the Culebra for Use in PA Calculations to Support the WIPP CCA," *Laboratory Column Experiments for Radionuclide Adsorption Studies of the Culebra Dolomite Member of the Rustler Formation.* D.A. Lucero, G.O. Brown, and C.E. Heath. SAND97-1763. Albuquerque, NM: Sandia National Laboratories. D-4 through D-8.

Brush, L.H. 1998b. "Ranges and Probability Distributions of K_ds for Dissolved Pu, Am, U, Th, and Np in the Culebra for the PA Calculations to Support the WIPP CCA," *Laboratory Column Experiments for Radionuclide*

Adsorption Studies of the Culebra Dolomite Member of the Rustler Formation. D.A. Lucero, G.O. Brown, and C.E. Heath. SAND97-1763. Albuquerque, NM: Sandia National Laboratories. D-9 through D-105.

Brush, L.H., and L.J. Storz. 1996. "Revised Ranges and Probability Distributions of K_ds for Dissolved Pu, Am, U, Th, and Np in Culebra for the PA Calculations to Support the WIPP CCA." Memo to M.S. Tierney, July 24, 1996. Albuquerque, NM: Sandia National Laboratories. Sandia WIPP Central Files WPO # 41561.

Bynum, R.V. 1996. "Revised Update of Uncertainty Range and Distribution for Actinide Solubility to be Used in CCA NUTS Calculations." Memo to M.S. Tierney and C. Stockman, May 23, 1996. Albuquerque, NM: Sandia National Laboratories. Sandia WIPP Central Files WPO # 37791.

Bynum, R.V., C. Stockman, Y. Wang, A. Peterson, J. Krumhansl, J. Nowak, J. Cotton, M.S.Y. Chu, and S.J. Patchett. 1997. "Implementation of Chemical Controls Through a Backfill System for the Waste Isolation Pilot Plant (WIPP)," *Proceedings of the Sixth International Conference on Radioactive Waste Management and Environmental Remediation, ICEM '97, Singapore, October 12-16, 1997.* SAND96-2656C. Eds. R. Baker, S. Slate, and G. Benda. New York, NY: American Society of Mechanical Engineers. 357-361.

Chappelear, J.E., and A.S. Williamson. 1981. "Representing Wells in Numerical Reservoir Simulation—2. Implementation," *SPEJ Society of Petroleum Engineers Journal.* Vol. 21, no. 3, 339-344.

Cheremisinoff, N.P., and P.N. Cheremisinoff. 1984. *Hydrodynamics of Gas-Solids Fluidization.* Houston, TX: Gulf Publishing Co.

Christian-Frear, T.L. 1996a. "Salado Halite Rock Compressibility from Room Q Analysis." Records Packages. Albuquerque, NM: Sandia National Laboratories. Sandia WIPP Central Files WPO # 30598, WPO # 31220.

Christian-Frear, T.L. 1996b. "Salado Halite Permeability from Room Q Analysis." Records Package. Albuquerque, NM: Sandia National Laboratories. Sandia WIPP Central Files WPO # 30721.

Conover, W.J. 1980. *Practical Nonparametric Statistics.* 2nd ed. New York, NY: John Wiley & Sons.

Cook, D.R., and S. Weisberg. 1982. *Residuals and Influence in Regression.* New York, NY: Chapman and Hall.

Corbet, T. and P. Swift. 1996a. "Distribution for Non-Salado Parameter for SECOFL2D: Climate Index." Memo to M.S. Tierney, April 12, 1996. Albuquerque, NM: Sandia National Laboratories. Sandia WIPP Central Files WPO # 36425, Segment 2.

Corbet, T., and P. Swift. 1996b. "Parameters Required for SECOFL2D: Climate Index." Record Package. Albuquerque, NM: Sandia National Laboratories. Sandia WIPP Central Files WPO # 36425.

Cox, D.C. and P. Baybutt. 1982. "Limit Lines for Risk," *Nuclear Technology.* Vol. 57, no. 3, 320-330.

Daniel, C., F.S. Wood, and J.W. Gorman. 1980. *Fitting Equations to Data: Computer Analysis of Multifactor Data.* 2nd ed. New York, NY: John Wiley & Sons.

Darley, H.C.H. 1969. "A Laboratory Investigation of Borehole Stability," *JPT Journal of Petroleum Technology.* July 1969, 883-892.

Darley, H.C.H., and G.R. Gray. 1988. *Composition and Properties of Drilling and Completion Fluids.* 5th ed. Houston, TX: Gulf Publishing Company.

Davies, P., and R. Beauheim. 1996. "Changes to the Parameter Records Package and Form # 464 for Far-Field Permeability of Salado Halites." Memo to M. Tierney, March 7, 1996. Albuquerque, NM: Sandia National Laboratories. Sandia WIPP Central Files WPO # 36772.

Dendy, J.E., Jr., S.F. McCormick, J.W. Ruge, T.F. Russell, and S. Schaffer. 1989. "Multigrid Methods for Three-Dimensional Petroleum Reservoir Simulation," *Proceedings, 10th Symposium on Reservoir Simulation, Houston, TX. February 6-8, 1989.* Ed. J.E. Killough. SPE 18409. Richardson, TX: Society of Petroleum Engineers of the American Institute of Mining, Metallurgical and Petroleum Engineers. 19-25.

Dendy, J.E., Jr., M.P. Ida, and J.M. Rutledge. 1992. "A Semicoarsening Multigrid Algorithm for SIMD Machines," *SIAM Journal on Scientific and Statistical Computing.* Vol. 13, no. 6, 1460-1469.

Domski, P. 1996a. "Salado: Halite Permeability." Records Package. Albuquerque, NM: Sandia National Laboratories. Sandia WIPP Central Files WPO # 31218.

Domski, P. 1996b. "Salado: Halite Pressure." Records Package. Albuquerque, NM: Sandia National Laboratories. Sandia WIPP Central Files WPO # 31221.

Draper, N.R, and H. Smith. 1981. *Applied Regression Analysis.* 2nd ed. New York, NY: John Wiley & Sons.

Drez, P. 1996. "Preliminary Estimate for SNL/NM Performance Assessment Calculations of Nitrate, Sulfate, and Phosphate Content in Transuranic Solidified Wastes Destined for Disposal in WIPP." Carlsbad Technical Assistance Contractors. Memo, 1/26/96. (Reproduced as Memorandum from D. Watkins to L. Shephard Dated Feb. 20, 1996, in App. B-6 of U.S. Department of Energy. 1996. *Transuranic Waste Baseline Inventory Report (Revision 3).* DOE/CAO-95-1121, Revision 3. Carlsbad, NM: U.S. Department of Energy, Carlsbad Area Office.)

Eisenhart, C. 1964. "The Meaning of 'Least' in Least Squares," *Journal of the Washington Academy of Science.* Vol. 54, 24-33.

Ely, J.F. and M.L. Huber. 1992. *NIST Thermophysical Properties of Hydrocarbon Mixtures Database (SUPERTRAPP), Version 1.0, User's Guide.* Gaithersburg, MD: U.S. Department of Commerce, National Institute of Standards and Technology, Standard Reference Data Program. Sandia WIPP Central Files WPO # 42589.

Farmer, F.R. 1967. "Reactor Safety and Siting: A Proposed Risk Criterion," *Nuclear Safety.* Vol. 8, no. 6, 539-548.

Feller, W. 1971. *An Introduction to Probability Theory and Its Applications.* 2nd ed. New York, NY: John Wiley & Sons. Vol. 2.

Finkel, A.M. 1990. *Confronting Uncertainty in Risk Management: A Guide for Decision-Makers. A Report.* Washington, DC: Center for Risk Management, Resources for the Future.

Fletcher, C.A.J. 1988. *Computational Techniques for Fluid Dynamics.* 2nd ed. Berlin; New York: Springer-Verlag. Vols. 1-2.

Fogarty, M.J., A.A. Rosenberg, and M.P. Sissenwine. 1992. "Fisheries Risk Assessment: Sources of Uncertainty," *Environmental Science & Technology.* Vol. 26, no. 3, 440-447.

Fox, R.W., and A.T. McDonald. 1973. *Introduction to Fluid Mechanics.* New York, NY: John Wiley & Sons.

Francis, A.J., J.B. Gillow, and M.R. Giles. 1997. *Microbial Gas Generation Under Expected Waste Isolation Pilot Plant Repository Conditions.* SAND96-2582. Albuquerque, NM: Sandia National Laboratories.

Freeze, G.F. 1996a. "Non-Salado: Castile Brine Reservoir Rock Compressibility." Records Package. Albuquerque, NM: Sandia National Laboratories. Sandia WIPP Central Files WPO # 31084.

Freeze, G.F. 1996b. "Non-Salado: Castile Brine Reservoir Permeability." Records Package. Albuquerque, NM: Sandia National Laboratories. Sandia WIPP Central Files WPO # 31070.

Freeze, G., and K. Larson. 1996. "Initial Pressure in the Castile Brine Reservoir." Memo to M. Tierney, March 20, 1996. Albuquerque, NM: Sandia National Laboratories. Sandia WIPP Central Files WPO # 37148.

Freeze, G.A., K.W. Larson, and P.B. Davies. 1995. *Coupled Multiphase Flow and Closure Analysis of Repository Response to Waste-Generated Gas at the Waste Isolation Pilot Plant (WIPP).* SAND93-1986. Albuquerque, NM: Sandia National Laboratories.

Freeze, R.A., and J.A. Cherry. 1979. *Groundwater.* Englewood Cliffs, NJ: Prentice-Hall, Inc.

Frey, H.C., and D.S. Rhodes. 1996. "Characterizing, Simulating, and Analyzing Variability and Uncertainty: An Illustration of Methods Using an Air Toxics Emissions Example," *Human and Ecological Risk Assessment.* Vol. 2, no. 4, 762-797.

Gatlin, C. 1960. *Petroleum Engineering: Drilling and Well Completions.* Englewood Cliffs, NJ: Prentice-Hall, Inc.

Golub, G.H., and C.F. van Loan. 1983. *Matrix Computations.* Baltimore, MD: Johns Hopkins University Press.

Graboski, M.S., and T.E. Daubert. 1979. "A Modified Soave Equation of State for Phase Equilibrium Calculations. 3: Systems Containing Hydrogen," *Industrial and Engineering Chemistry. Process Design and Development.* Vol. 18, 300-306.

Haberman, J.H., and D.J. Frydrych. 1988. "Corrosion Studies of A216 Grade WCA Steel in Hydrothermal Magnesium-Containing Brines," *Scientific Basis for Nuclear Waste Management XI, Materials Research Society Symposium Proceedings, Boston, MA, November 30 - December 3, 1987.* Eds. M.J. Apted and R.E. Westerman. Pittsburgh, PA: Materials Research Society Vol. 112, 761-772.

Hacking, I. 1975. *The Emergence of Probability: A Philosophical Study of Early Ideas About Probability, Induction and Statistical Inference.* London; New York: Cambridge University Press.

Hamby, D.M. 1994. "A Review of Techniques for Parameter Sensitivity Analysis of Environmental Models," *Environmental Monitoring and Assessment.* Vol. 32, no. 2, 135-154.

Harter, H.L. 1983. "Least Squares," *Encyclopedia of Statistical Sciences.* Vol. 4: Icing the Tails to Limit Theorems. Eds. S. Kotz, N.L. Johnson, and C.B. Read. New York, NY: John Wiley & Sons. Vol. 4, 593-598.

Hattis, D., and K. Silver. 1994. "Human Interindividual Variability—A Major Source of Uncertainty in Assessing Risks for Noncancer Health Effects," *Risk Analysis.* Vol. 14, no. 4, 421–431.

Helton, J.C. 1993a. "Risk, Uncertainty in Risk, and the EPA Release Limits for Radioactive Waste Disposal," *Nuclear Technology.* Vol. 101, no. 1, 18-39. (Also available as SAND91-1255J.)

Helton, J.C. 1993b. "Drilling Intrusion Probabilities for Use in Performance Assessment for Radioactive Waste Disposal," *Reliability Engineering and System Safety.* Vol. 40, no. 3, 259-275.

Helton, J.C. 1993c. "Uncertainty and Sensitivity Analysis Techniques for Use in Performance Assessment for Radioactive Waste Disposal," *Reliability Engineering and System Safety.* Vol. 42, no. 2-3, 327-367.

Helton, J.C. 1994. "Treatment of Uncertainty in Performance Assessments for Complex Systems," *Risk Analysis.* Vol. 14, no. 4, 483-511.

Helton, J.C. 1996. "Probability, Conditional Probability and Complementary Cumulative Distribution Functions in Performance Assessment for Radioactive Waste Disposal," *Reliability Engineering and System Safety.* Vol. 54, no. 2-3, 145-163.

Helton, J.C. 1997. "Uncertainty and Sensitivity Analysis in the Presence of Stochastic and Subjective Uncertainty," *Journal of Statistical Computation and Simulation.* Vol. 57, no. 1-4, 3-76.

Helton, J.C., and R.J. Breeding. 1993. "Calculation of Reactor Accident Safety Goals," *Reliability Engineering and System Safety.* Vol. 39, no. 2, 129-158.

Helton, J.C., and D.E. Burmaster. 1996. "Guest Editorial: Treatment of Aleatory and Epistemic Uncertainty in Performance Assessments for Complex Systems," *Reliability Engineering and System Safety.* Vol. 54, no. 2-3, 91-94.

Helton, J.C., and H.J. Iuzzolino. 1993. "Construction of Complementary Cumulative Distribution Functions for Comparison with the EPA Release Limits for Radioactive Waste Disposal," *Reliability Engineering and System Safety.* Vol. 40, no. 3, 277-293.

Helton, J.C., and A.W. Shiver. 1996. "A Monte Carlo Procedure for the Construction of Complementary Cumulative Distribution Functions for Comparison with the EPA Release Limits for Radioactive Waste Disposal," *Risk Analysis.* Vol. 16, no. 1, 43-55.

Helton, J.C., J.W. Garner, R.D. McCurley, and D.K. Rudeen. 1991. *Sensitivity Analysis Techniques and Results for Performance Assessment at the Waste Isolation Pilot Plant.* SAND90-7103. Albuquerque, NM: Sandia National Laboratories.

Helton, J.C., D.R. Anderson, B.L. Baker, J.E. Bean, J.W. Berglund, W. Beyeler, J.W. Garner, H.J. Iuzzolino, M.G. Marietta, R.P. Rechard, P.J. Roache, D.K. Rudeen, J.D. Schreiber, P.N. Swift, M.S. Tierney, and P. Vaughn. 1995a. "Effect of Alternative Conceptual Models in a Preliminary Performance Assessment for the Waste Isolation Pilot Plant," *Nuclear Engineering and Design.* Vol. 154, no. 3, 251-344.

Helton, J.C., J.D. Johnson, M.D. McKay, A.W. Shiver, and J.L. Sprung. 1995b. "Robustness of an Uncertainty and Sensitivity Analysis of Early Exposure Results with the MACCS Reactor Accident Consequence Model," *Reliability Engineering and System Safety.* Vol. 48, no. 2, 129-148.

Helton, J.C., D.R. Anderson, M.G. Marietta, and R.P. Rechard. 1997. "Performance Assessment for the Waste Isolation Pilot Plant: From Regulation to Calculation for 40 CFR 191.13," *Operations Research.* Vol. 45, no. 2, 157-177.

Hoffman, F.O., and J.S. Hammonds. 1994. "Propagation of Uncertainty in Risk Assessments: The Need to Distinguish Between Uncertainty Due to Lack of Knowledge and Uncertainty Due to Variability," *Risk Analysis.* Vol. 14, no. 5, 707-712.

Howard, B.A. 1996. "Performance Assessment Parameter Input." Memo to M. Marietta, February 23, 1996. Carlsbad, NM: Westinghouse Electric Corporation to Sandia National Laboratories, Albuquerque, NM. Sandia WIPP Central Files WPO # 47595.

Howarth, S.M. 1996. "Salado Halite Porosity." Records Package. Albuquerque, NM: Sandia National Laboratories. Sandia WIPP Central Files WPO # 30601.

Howarth, S.M., and T. Christian-Frear. 1997. *Porosity, Single-Phase Permeability, and Capillary Pressure Data from Preliminary Laboratory Experiments on Selected Samples from Marker Bed 139 at the Waste Isolation Pilot Plant.* SAND94-0472/1/2/3. Albuquerque, NM: Sandia National Laboratories.

Hunter, R.L. 1985. *A Regional Water Balance for the Waste Isolation Pilot Plant (WIPP) Site and Surrounding Area.* SAND84-2233. Albuquerque, NM: Sandia National Laboratories.

Hurtado, L.D. 1996. "Correction of Lambda Distribution." Memo to M. Tierney, February 12, 1996. Albuquerque, NM: Sandia National Laboratories. Sandia WIPP Central Files WPO # 32287.

Huyakorn, P.S., B.H. Lester, and J.W. Mercer. 1983. "An Efficient Finite Element Technique for Modelling Transport in Fractured Porous Media: 1. Single Species Transport," *Water Resources Research.* Vol. 19, no. 3, 841-854.

IAEA (International Atomic Energy Agency). 1989. *Evaluating the Reliability of Predictions Made Using Environmental Transfer Models.* Safety Series Report No. 100. Vienna: International Atomic Energy Agency.

Iman, R.L. 1982. "Statistical Methods for Including Uncertainties Associated with the Geologic Isolation of Radioactive Waste Which Allow for a Comparison with Licensing Criteria," *Proceedings of the Symposium on Uncertainties Associated with the Regulation of the Geologic Disposal of High-Level Radioactive Waste, March 9-13, 1981.* Ed. D.C. Kocher. NUREG/CP-0022, CONF-810372. Washington, DC: U.S. Nuclear Regulatory Commission, Directorate of Technical Information and Document Control. 145-157.

Iman, R.L., and W.J. Conover. 1979. "The Use of the Rank Transform in Regression." *Technometrics.* Vol. 21, no. 4, 499-509.

Iman, R.L., and W.J. Conover. 1982. "A Distribution-Free Approach to Inducing Rank Correlation Among Input Variables," *Communications in Statistics: Simulation and Computation.* Vol. B11, no. 3, 311-334.

Iman, R.L., and W.J. Conover. 1983. *A Modern Approach to Statistics.* New York, NY: John Wiley & Sons.

Iman, R.L., and J.M. Davenport. 1982. "Rank Correlation Plots for Use with Correlated Input Variables," *Communications in Statistics: Simulation and Computation.* Vol. B11, no. 3, 335-360.

Iman, R.L., and J.C. Helton. 1988. "An Investigation of Uncertainty and Sensitivity Analysis Techniques for Computer Models," *Risk Analysis.* Vol. 8, no. 1, 71-90.

Iman R.L., and J.C. Helton. 1991. "The Repeatability of Uncertainty and Sensitivity Analyses for Complex Probabilistic Risk Assessments," *Risk Analysis.* Vol. 11, no. 4, 591-606.

Iman, R.L., and M.J. Shortencarier. 1984. *A Fortran 77 Program and User's Guide for the Generation of Latin Hypercube and Random Samples for Use with Computer Models.* SAND83-2365. Albuquerque, NM: Sandia National Laboratories.

Iman, R.L., M.J. Shortencarier, and J.D. Johnson. 1985. *A FORTRAN 77 Program and User's Guide for the Calculation of Partial Correlation and Standardized Regression Coefficients.* NUREG/CR-4122, SAND85-0044. Albuquerque, NM: Sandia National Laboratories.

Johnson, J.D. 1997. "CCDFGF, Version 4.00, User's Manual." Albuquerque, NM: Sandia National Laboratories. Sandia WIPP Central Files WPO # 47364.

Kaplan, S. 1993. "Formalisms for Handling Phenomenological Uncertainties: The Concepts of Probability, Frequency, Variability, and Probability of Frequency," *Nuclear Technology.* Vol. 102, no. 1, 137-142.

Kaplan, S., and B.J. Garrick. 1981. "On the Quantitative Definition of Risk," *Risk Analysis.* Vol. 1, no. 1, 11-27.

Kaufmann, D.W., ed. 1960. *Sodium Chloride, The Production and Properties of Salt and Brine.* ACS Monograph 145. New York, NY: Reinhold Pub. Corp.; Washington, DC: American Chemical Society.

Kelley, V., T. Jones, and J. Ogintz. 1996a. "WIPP Seal System Parameters for Performance Assessment BRAGFLO Compliance Calculations." Internal Memo to L.D. Hurtado, January 15, 1996. Albuquerque, NM: Sandia National Laboratories. Sandia WIPP Central Files WPO # 30995.

Kelley, V.A., T.L. Jones, and J.B. Ogintz. 1996b. "WIPP Shaft Seal System Parameters Documentation to Support Performance Assessment BRAGFLO Compliance Calculations," Internal Memo to L.D. Hurtado. March 22, 1996. Albuquerque, NM: Sandia National Laboratories. Sandia WIPP Central Files WPO # 40258.

Klinkenberg, L.J. 1941. "The Permeability of Porous Media to Liquids and Gases," *API Drilling and Production Practice*. 200-213. Sandia WIPP Central Files WPO # 8556.

Knowles, M.K., D. Borns, J. Fredrich, D. Holcomb, R. Price, D. Zeuch, T. Dale, and R.S. Van Pelt. 1998. "Testing the Disturbed Zone Around a Rigid Inclusion in Salt," *Fourth Conference on the Mechanical Behavior of Salt, Montreal, Quebec, Canada, June 16-17, 1996.* Eds. M. Aubertin and H.R. Zeller. Clausthal-Zellerfield, Germany: TTP Trans Tech Publications. 175-188.

Larson, K. 1997. "Tracing the Source: The 32,000 m^3 Reservoir Volume Used in Determination of GRIDFLO Parameter Probabilities." Albuquerque, NM: Sandia National Laboratories. Sandia WIPP Central Files WPO # 44401 attachment.

LaVenue, A.M. 1996. "Analysis of the Generation of Transmissivity Fields for the Culebra Dolomite Compliance Certification Application (CCA) - AP-018 (Task 3)." Analysis Package - AP-018. Albuquerque, NM: Sandia National Laboratories. Sandia WIPP Central Files WPO # 40517.

Lee, J. 1982. *Well Testing*. SPE Textbook Series Vol. 1. New York, NY: Society of Petroleum Engineers of AIME.

Lenke, L.R., J. Berglund, and R.A. Cole. 1996. *Blowout Experiments Using Fine Grained Silica Sands in an Axisymmetric Geometry*. NMERI Report 1996/7/32250. Albuquerque, NM: New Mexico Engineering Research Institute, University of New Mexico. Sandia WIPP Central Files WPO # 43145.

Lewis, H.W., R.J. Budnitz, H.J. C. Kouts, W.B. Loewenstein, W.D. Rowe, F. von Hippel, and F. Zachariasen. 1978. *Risk Assessment Review Group Report to the U.S. Nuclear Regulatory Commission.* NUREG/CR-0400. Washington, DC: U.S. Nuclear Regulatory Commission. (Available from the NTIS as PB-286 859/4.)

Lide, D.R., ed. 1991. *CRC Handbook of Chemistry and Physics.* 72nd ed. Boca Raton, FL: CRC Press.

Lucero, D.A., Y.K. Behl, G.O. Brown, K.G. Budge, M. Dunn, A.J. Francis, J.B. Gillow, and H.W. Papenguth. 1996. "Laboratory Evaluation of Colloid Transport Under Simulated Subsurface Conditions at the Waste Isolation Pilot Plant (WIPP): 2. Large-Scale-Intact-Core Column Flow Experiments," *Experimental and Modeling Studies of Radionuclide Speciation in Real Systems.* SAND96-2741J. Albuquerque, NM: Sandia National Laboratories. Sandia WIPP Central Files WPO # 42864.

MacIntosh, D.L., G.W. Suter, II, and F.O. Hoffman. 1994. "Uses of Probabilistic Exposure Models in Ecological Risk Assessments of Contaminated Sites," *Risk Analysis*. Vol. 14, no. 4, 405-419.

MacKinnon, R.J., G. Freeze, and H. Jow. 1997. "Summary of EPA-Mandated Performance Assessment Verification Test (Replicate 1) and Comparison with the Compliance Certification Application Calculations." Technical Data Package. Albuquerque, NM: Sandia National Laboratories. Sandia WIPP Central Files WPO # 46674.

Marietta, M.G., S.G. Bertram-Howery, D.R. Anderson, K.F. Brinster, R.V. Guzowski, H. Iuzzolino, and R.P. Rechard. 1989. *Performance Assessment Methodology Demonstration: Methodology Development for Evaluating Compliance with EPA 40 CFR 191, Subpart B, for the Waste Isolation Pilot Plant.* SAND89-2027. Albuquerque, NM: Sandia National Laboratories.

Martell, M. 1996a. "Additional Information for the DRZ (Disturbed Rock Zone) Porosity." Memo to C. Lattier, November 14, 1996. Albuquerque, NM: Sandia National Laboratories. WIPP Central Files WPO # 42257.

Martell, M. 1996b. "Additional Information for the Culebra Transport Parameter Id: 843, idpram: DNSGRAIN, idmtrl: CULEBRA, WIPP Data Entry Form 464 at WPO # 32689." Memo to C. Lattier, December 10, 1996. Albuquerque, NM: Sandia National Laboratories. Sandia WIPP Central Files WPO # 32689.

Mattax, C.C., and R.L. Dalton. 1990. *Reservoir Simulation.* SPE Monograph 13. Richardson, TX: Henry L. Doherty Memorial Fund of Society of Petroleum Engineers Inc.

Mayer, G., F. Jacobs, and F.H. Wittmann. 1992. "Experimental Determination and Numerical Simulation of the Permeability of Cementitious Materials," *Nuclear Engineering and Design.* Vol. 138, no. 2, 171-177.

McCord, J. 1996. "Culebra Longitudinal Dispersivity." Albuquerque, NM: Sandia National Laboratories. Sandia WIPP Central Files WPO # 37230.

McDonald, M.G., and A.W. Harbaugh. 1988. "A Modular Three-Dimensional Finite-Difference Ground-Water Flow Model." *Techniques of Water-Resources Investigations of the United States Geological Survey, Book 6, Modeling Techniques.* TWI-06-A1. Denver, CO: U.S. Geological Survey.

McDonald, M.G., A.W. Harbaugh, B.R. Orr, and D.J. Ackerman. 1991. *A Method of Converting No-Flow Cells to Variable-Head Cells for the U.S. Geological Survey Modular Finite-Difference Ground-Water Flow Model.* Open-File Report 91-0536. Reston, VA: U.S. Geological Survey.

McKay, M.D., R.J. Beckman, and W.J. Conover. 1979. "A Comparison of Three Methods for Selecting Values of Input Variables in the Analysis of Output from a Computer Code," *Technometrics.* Vol. 21, no. 2, 239-245.

McKone, T.E. 1994. "Uncertainty and Variability in Human Exposures to Soil Contaminants Through Home-Grown Food: A Monte Carlo Assessment," *Risk Analysis.* Vol. 14, no. 4, 449-463.

McKone, T.E., and K.T. Bogen. 1991. "Predicting the Uncertainties in Risk Assessment: A California Groundwater Case Study," *Environmental Science and Technology.* Vol. 25, no. 10, 1674-1681.

McTigue, D.F. 1993. *Permeability and Hydraulic Diffusivity of Waste Isolation Pilot Plant Repository Salt Inferred from Small-Scale Brine Inflow Experiments.* SAND92-1911. Albuquerque, NM: Sandia National Laboratories.

Meigs, L. 1996a. "Non-Salado: Culebra Advective Porosity." Records Package. Albuquerque, NM: Sandia National Laboratories. Sandia WIPP Central Files WPO # 37227.

Meigs, L. 1996b. "Non-Salado: Culebra Half Matrix Block Length." Records Package. Albuquerque, NM: Sandia National Laboratories. Sandia WIPP Central Files WPO # 37225.

Meigs, L. 1996c. "Non-Salado: Diffusive Porosity for the Culebra Dolomite." Memo to J. Ramsey, June 6, 1996. Albuquerque, NM: Sandia National Laboratories. Sandia WIPP Central Files WPO # 38773.

Meigs, L. 1996d. "Non-Salado: Culebra Diffusive Porosity." Records Package. Albuquerque, NM: Sandia National Laboratories. Sandia WIPP Central Files WPO # 37228.

Meigs, L. 1996e. "Non-Salado: Diffusive Tortuosity for the Culebra Dolomite (WPO#37226)." Memo to J. Ramsey, May 16, 1996. Albuquerque, NM: Sandia National Laboratories. Sandia WIPP Central Files WPO # 38940.

Meigs, L., and J. McCord. 1996a. "Physical Transport in the Culebra Dolomite." Albuquerque, NM: Sandia National Laboratories. Sandia WIPP Central Files WPO # 37450, Segment 3.

Meigs, L., and J. McCord. 1996b. "Non-Salado: Advective Porosity for the Culebra Dolomite (WPO#37227)." Memo to J. Ramsey, June 6, 1996. Albuquerque, NM: Sandia National Laboratories. WIPP Central Files WPO # 38939.

Meigs, L., and J. McCord. 1996c. "Non-Salado: Culebra Half Matrix Block Length (WPO#37225)." Memo to J. Ramsey, June 7, 1996. Albuquerque, NM: Sandia National Laboratories. WIPP Central Files WPO # 38928.

Mendenhall, F.T., and W. Gerstle. 1995. "WIPP Anhydrite Fracture Modeling," *Systems Prioritization Method - Iteration 2 Baseline Position Paper: Disposal Room and Cutting Models.* B.M. Butcher, S.W. Webb, J.W. Berglund, and P.R. Johnson. Albuquerque, NM: Sandia National Laboratories. Sandia WIPP Central Files WPO # 39830.

Mercer, J.W. 1983. *Geohydrology of the Proposed Waste Isolation Pilot Plant Site, Los Medaños Area, Southeastern New Mexico.* Water-Resources Investigations Report 83-4016. Prepared in Cooperation with the U.S. Department of Energy. Albuquerque, NM: U.S. Geological Survey.

Munera, H.A., and G. Yadigaroglu. 1986. "On Farmer's Line, Probability Density Functions, and Overall Risk," *Nuclear Technology.* Vol. 74, no. 2, 229-232.

Myers, R.H. 1986. *Classical and Modern Regression with Applications.* Boston, MA: Duxbury Press.

NCRP (National Council on Radiation Protection and Measurements). 1996. *A Guide for Uncertainty Analysis in Dose and Risk Assessments Related to Environmental Contamination.* NCRP Commentary No. 14. Bethesda, MD: National Council on Radiation Protection and Measurements.

Neter, J., and W. Wasserman. 1974. *Applied Linear Statistical Models: Regression, Analysis of Variance, and Experimental Designs.* Homewood, IL: Richard D. Irwin.

Nowak, E.J., J.R. Tillerson, and T.M. Torres. 1990. *Initial Reference Seal System Design: Waste Isolation Pilot Plant.* SAND90-0355. Albuquerque, NM: Sandia National Laboratories.

NRC (National Research Council). 1983. *Risk Assessment in the Federal Government: Managing the Process.* Committee on the Institutional Means for Assessment of Risks to Public Health, Commission on Life Sciences. Washington, DC: National Academy Press.

NRC (National Research Council). 1993. *Issues in Risk Assessment.* Committee on Risk Assessment Methodology, Board on Environmental Studies and Toxicology, Commission on Life Sciences. Washington, DC: National Academy Press.

NRC (National Research Council). 1994. *Science and Judgment in Risk Assessment.* Committee on Risk Assessment of Hazardous Air Pollutants. Washington, DC: National Academy Press.

Obert, E. 1948. *Thermodynamics.* 1st ed. New York, NY: McGraw-Hill.

Oldroyd, J.G. 1958. "Non-Newtonian Effects in Steady Motion of Some Idealized Elastico-Viscous Liquids," *Proceedings of the Royal Society of London. Series A. Mathematical and Physical Sciences.* Vol. 245, no. 1241, 278-297. Sandia WIPP Central Files WPO # 43211.

Papenguth, H.W. 1996. "Development of Parameter Values Describing Colloidal Actinide Retardation in the Culebra Dolomite," Document in Records Package: Colloidal Actinide Retardation Parameters. Albuquerque, NM: Sandia National Laboratories. Sandia WIPP Cental Files WPO # 38173.

Papenguth, H.W., and R.C. Moore. 1996a. "Mobile-Colloidal-Actinide Source Term, 3. Humic Substances." Records Package. Albuquerque, NM: Sandia National Laboratories. Sandia WIPP Central Files WPO # 35855.

Papenguth, H.W., and R.C. Moore. 1996b. "Rationale for Definition of Parameter Values for Humic Substances." Albuquerque, NM: Sandia National Laboratories. Sandia WIPP Central Files WPO # 35855, Attachment A.

Parry, G.W. 1988. "On the Meaning of Probability in Probabilistic Safety Assessment," *Reliability Engineering and System Safety*. Vol. 23, no. 4, 309-314.

Paté-Cornell, M.E. 1986. "Probability and Uncertainty in Nuclear Safety Decisions," *Nuclear Engineering and Design*. Vol. 93, no. 2-3, 319-327.

Paté-Cornell, M.E. 1996. "Uncertainties in Risk Analysis: Six Levels of Treatment," *Reliability Engineering and System Safety*. Vol. 54, no. 2-3, 95-111.

Payne, A.C., Jr. 1992. *Analysis of the LaSalle Unit 2 Nuclear Power Plant: Risk Methods Integration and Evaluation Program (RMIEP). Summary*. SAND92-0537, Vol. 1; NUREG/CR-4832, Vol. 1. Prepared for U.S. Nuclear Regulatory Commission, Office of Nuclear Regulatory Research, Division of Safety Issue Resolution. Albuquerque, NM: Sandia National Laboratories. Vol. 1.

Payne, A.C., Jr., T.T. Sype, D.W. Whitehead, and A.W. Shiver. 1992a. *Analysis of the LaSalle Unit 2 Nuclear Power Plant: Risk Methods Integration and Evaluation Program (RMIEP). Integrated Quantification and Uncertainty Analysis*. SAND92-0537, Vol. 2; NUREG/CR-4832, Vol. 2. Prepared for U.S. Nuclear Regulatory Commission, Office of Nuclear Regulatory Research, Division of Safety Issue Resolution. Albuquerque, NM: Sandia National Laboratories. Vol. 2.

Payne, A.C., Jr., S.L. Daniel, D.W. Whitehead, T.T. Sype, S.E. Dingman, and C.J. Shaffer. 1992b. *Analysis of the LaSalle Unit 2 Nuclear Power Plant: Risk Methods Integration and Evaluation Program (RMIEP). Internal Events Accident Sequence Quantification. Main Report*. SAND92-0537, Vol. 3, pt. 1; NUREG/CR-4832, Vol. 3, pt. 1. Prepared for U.S. Nuclear Regulatory Commission, Office of Nuclear Regulatory Research, Division of Safety Issue Resolution. Albuquerque, NM: Sandia National Laboratories. Vol. 3, pt. 1.

Payne, A.C., Jr., S.L. Daniel, D.W. Whitehead, T.T. Sype, S.E. Dingman, and C.J. Shaffer. 1992c. *Analysis of the LaSalle Unit 2 Nuclear Power Plant: Risk Methods Integration and Evaluation Program (RMIEP). Internal Events Accident Sequence Quantification. Appendices*. SAND92-0537, Vol. 3, pt. 2; NUREG/CR-4832, Vol. 3, pt. 2. Prepared for U.S. Nuclear Regulatory Commission, Office of Nuclear Regulatory Research, Division of Safety Issue Resolution. Albuquerque, NM: Sandia National Laboratories. Vol. 3, pt. 2.

PLG (Pickard, Lowe and Garrick, Inc.). 1983. *Seabrook Station Probabilistic Safety Assessment*. PLG-0300. Prepared for Public Service Company of New Hampshire and Yankee Atomic Electric Company. Irvine, CA: Pickard, Lowe and Garrick, Inc. (Available from the NTIS as PB84-186949 and PB84-186931.)

PLG (Pickard, Lowe and Garrick, Inc., Westinghouse Electric Corporation, and Fauske & Associates, Inc.). 1982. *Indian Point Probabilistic Safety Study*. Prepared for the Power Authority of the State of New York and Consolidated Edison Company of New York, Inc. Irvine, CA: Pickard, Lowe and Garrick, Inc. (This 6200-page report is available at the NRC Public Document Room, 2120 L Street, NW, Lower Level, Washington, DC 20555-0001, 1-800-397-4209.).

Poettmann, F.H., and P.G. Carpenter. 1952. "Multiphase Flow of Gas, Oil, and Water Through Vertical Flow Strings with Application to the Design of Gas-lift Installations," *Drilling and Production Practice*. 257-317.

Popielak, R.S., R.L. Beauheim, S.R. Black, W.E. Coons, C.T. Ellingson, and R.L. Olsen. 1983. *Brine Reservoirs in the Castile Formation, Waste Isolation Pilot Plant (WIPP) Project, Southeastern New Mexico*. TME-3153. Albuquerque, NM: U.S. Department of Energy, Waste Isolation Pilot Plant. (Available from the NTIS as DE86004341/XAB).

Powers, D.W., J.M. Sigda, and R.M. Holt. 1996. "Probability of Intercepting a Pressurized Brine Reservoir Under the WIPP." Albuquerque, NM: Sandia National Laboratories. Sandia WIPP Central Files WPO # 40199.

Prasuhn, A.L. 1980. *Fundamentals of Fluid Mechanics*. Englewood Cliffs, NJ: Prentice-Hall, Inc.

Prausnitz, J.M. 1969. *Molecular Thermodynamics of Fluid - Phase Equilibria.* Englewood Cliffs, NJ: Prentice-Hall, Inc.

Price, P.S., S.H. Su, J.R. Harrington, and R.E. Keenan. 1996. "Uncertainty and Variation of Indirect Exposure Assessments: An Analysis of Exposure to Tetrachlorodibenzene-p-Dioxin from a Beef Consumption Pathway," *Risk Analysis.* Vol. 16, no. 2, 263-277.

Rai, S.N., D. Krewski, and S. Bartlett. 1996. "A General Framework for the Analysis of Uncertainty and Variability in Risk Assessment," *Human and Ecological Risk Assessment.* Vol. 2, no. 4, 972-989.

Raj, D. 1968. *Sampling Theory.* New York, NY: McGraw-Hill.

Ramsey, J.L., M.G. Wallace, and H.N. Jow. 1996. "Analysis Package for the Culebra Flow and Transport Calculations (Task 3) of the Performance Assessment Calculations Supporting the Compliance Certification Application (CCA), Analysis Plan 019." Analysis package. Albuquerque, NM: Sandia National Laboratories. WIPP Central Files WPO # 40516.

Rechard, R.P., H. Iuzzolino, and J.S. Sandha. 1990. *Data Used in Preliminary Performance Assessment of the Waste Isolation Pilot Plant (1990).* SAND89-2408. Albuquerque, NM: Sandia National Laboratories.

Repository Isolation Systems Department. 1996. *Waste Isolation Pilot Plant Shaft Sealing System Compliance Submittal Design Report.* SAND96-1326/1-2. Albuquerque, NM: Sandia National Laboratories. Vols. 1-2.

Risk Assessment Forum. 1997. *Guiding Principles for Monte Carlo Analysis.* M. Firestone, P. Fenner-Crisp, T. Barry, D. Bennett, S. Chang, M. Callahan, A-M. Burke, M. Olsen, J.M. Chand, P. Cirone, D. Barne, W.P. Wood and S.M. Knott. EPA/630/R-97/001. Washington, DC: Risk Assessment Forum, U.S. Environmental Protection Agency. (Available from the NTIS as PB97-188106/XAB.)

Roache, P.J. 1972. *Computational Fluid Dynamics.* Rev. printing. Albuquerque, NM: Hermosa Publishers.

Roache, P.J. 1993. "The SECO Suite of Codes for Site Performance Assessment," *High Level Radioactive Waste Management, Proceedings of the Fourth Annual International Conference, Las Vegas, NV, April 26-30, 1993.* La Grange Park, IL: American Nuclear Socieity, Inc.; New York, NY: American Socieity of Civil Engineers. Vol. 2, 1586-1594.

Roache, P.J., R.L. Blaine, and B.L. Baker. 1996. "SECOFL2D User's Manual, Version 3.03." Albuquerque, NM: Sandia National Laboratories. Sandia WIPP Central Files WPO # 37271.

Roberts, R. 1996. "Salado: Brine Compressibility." Records Package. Albuquerque, NM: Sandia National Laboratories. Sandia WIPP Central Files WPO #31174.

Robinson, T.W., and W.B. Lang. 1938. "Geology and Ground-Water Conditions of the Pecos River Valley in the Vicinity of Laguna Grande de la Sal, New Mexico, with Special Reference to the Salt Content of the River Water," *Twelfth and Thirteenth Biennial Reports of the State Engineer of New Mexico for the 23rd, 24th, 25th and 26th Fiscal Years, July 1, 1934 to July 30, 1938.* Santa Fe, NM: State Engineer. 77-100. Sandia WIPP Central Files WPO # 37942.

Romano, J.P., and A.F. Siegel. 1986. *Counterexamples in Probability and Statistics.* Monterey, CA: Wadsworth and Brooks/Cole, Advanced Books & Software.

Ross, S.M. 1987. *Introduction to Probability and Statistics for Engineers and Scientists.* New York, NY: John Wiley & Sons.

Saltelli, A., and J. Marivoet. 1990. "Non-Parametric Statistics in Sensitivity Analysis for Model Output: A Comparison of Selected Techniques," *Reliability Engineering and System Safety*. Vol. 28, no. 2, 229-253.

Sanchez, L.C., J. Liscum-Powell, J.S. Rath, and H.R. Trellue. 1997. "WIPP PA Analysis Report for EPAUNI: Estimating Probability Distribution of EPA Unit Loading in the WIPP Repository for Performance Assessment Calculations." Version 1.01. Albuquerque, NM: Sandia National Laboratories. Sandia WIPP Central Files WPO # 43843.

Saulnier, G.J., Jr., P.S. Domski, J.B. Palmer, R.M. Roberts, W.A. Stensrud, and A.L. Jensen. 1991. *WIPP Salado Hydrology Program Data Report #1*. SAND90-7000. Albuquerque, NM: Sandia National Laboratories.

Savins, J.G., and G.C. Wallick. 1966. "Viscosity Profiles, Discharge Rates, Pressures, and Torques for a Rheologically Complex Fluid in a Helical Flow," *A.I.Ch.E. Journal*. Vol. 12, no. 2, 357-363.

Schreiber, J. 1991. Hand Calculation. Attached to Form 464 for REFCON VREPOS, ID 3108. Albuquerque, NM: Sandia National Laboratories. Sandia WIPP Central Files WPO# 33276. (Dated 7/29/91 and 8/12/91).

Seber, G.A.F. 1977. *Linear Regression Analysis*. New York, NY: John Wiley & Sons.

Siegel, M.D. 1996. "Solubility Parameters for Actinide Source Term Look-Up Tables." Records package. Albuquerque, NM: Sandia National Laboratories. Sandia WIPP Central Files WPO # 35835.

Silbergeld, E.K. 1987. "Five Types of Ambiguity: Scientific Uncertainty in Risk Assessment," *Hazardous Waste and Hazardous Materials*. Vol. 4, no. 2, 139-150.

Smith, L.N., J.D. Johnson, and J.C. Helton. 1996. "Analysis Package for the CCDF Construction (Task 7) of the Performance Assessment Calculations Supporting the Compliance Certification Application (CCA), AP-AAD." Analysis Package. Albuquerque, NM: Sandia National Laboratories. Sandia WIPP Central Files WPO # 40524.

Sokolnikoff, I.S., and R.M. Redheffer. 1966. *Mathematics of Physics and Modern Engineering*. 2nd ed. New York, NY: McGraw-Hill Book Co.

Solutions Engineering. 1995. "Critical Gas Saturation Recommendations for WIPP." cc Letter Report D. O'Brien to D.M. Stoezel, November 15, 1995. Littleton, CO: Solutions Engineering. Sandia WIPP Central Files WPO # 38769.

Steinberg, H.A. 1963. "Generalized Quota Sampling," *Nuclear Science and Engineering*. Vol. 15, 142-145.

Stensrud, W.A., T.F. Dale, P.S. Domski, J.B. Palmer, R.M. Roberts, M.D. Fort, G.J. Saulnier, Jr., and A.L. Jensen. 1992. *Waste Isolation Pilot Plant Salado Hydrology Program Data Report #2*. SAND92-7072. Albuquerque, NM: Sandia National Laboratories.

Stockman, C. 1996a. "Implementation of Chemistry Parameters in PA. Reducing the Number of Sampled Parameters." Memo to M. Tierney, April 16, 1996. Albuquerque, NM: Sandia National Laboratories. Sandia WIPP Central Files WPO # 37536 attachment.

Stockman, C. 1996b. "Proposed Method of Implementation of Updated Solubility Distributions." Memo to M. Martell, May 10, 1996. Albuquerque, NM: Sandia National Laboratories. Sandia WIPP Central Files WPO # 37545.

Stockman, C.T., and R.C. Moore. 1998. "Use of Dissolved and Colloidal Actinide Parameters Within the 1996 Waste Isolation Pilot Plant Compliance Certification Application." SAND98-1062C. Albuquerque, NM: Sandia National Laboratories.

Stockman, C., A. Shinta, and J.W. Garner. 1996. "Analysis Package for the Salado Transport Calculations (Task 2) of the Performance Assessment Analysis Supporting the Compliance Certification Application (CCA), AP-023." Analysis

Package. SWCF-A:1.2.07.4.1:PA:QA:CCA. Albuquerque, NM: Sandia National Laboratories. Sandia WIPP Central Files WPO # 40515.

Stoelzel, D.M., and D.G. O'Brien. 1996. "Analysis Package for the BRAGFLO Direct Release Calculations (Task 4) of the Performance Assessment Calculations Supporting the Compliance Certification Application (CCA), AP-029, Brine Release Calculations." Analysis Package. Albuquerque, NM: Sandia National Laboratories. Sandia WIPP Central Files WPO # 40520.

Stone, C.M. 1997a. SANTOS - *A Two-Dimensional Finite Element Program for the Quasistatic, Large Deformation, Inelastic Response of Solids.* SAND90-0543. Albuquerque, NM: Sandia National Laboratories.

Stone, C.M. 1997b. *Final Disposal Room Structural Response Calculations.* SAND97-0795. Albuquerque, NM: Sandia National Laboratories.

Streeter, V.L. 1958. *Fluid Mechanics.* 2nd ed. New York, NY: McGraw-Hill.

Sweby, P.K. 1984. "High Resolution Schemes Using Flux Limiters for Hyperbolic Conservation Laws." *SIAM Journal on Numerical Analysis.* Vol. 21, no. 5, 995-1011.

Swift, P.N., K.W. Larson, and R.L. Beauheim. 1996. "Treatment of Castile Brine Reservoir in the 1996 CCA Performance Assessment." Memo to L.E. Shephard and M.S.Y. Chu, October 3, 1996. Albuquerque, NM: Sandia National Laboratories. Sandia WIPP Central Files WPO # 41885.

Telander, M.R., and R.E. Westerman. 1993. *Hydrogen Generation by Metal Corrosion in Simulated Waste Isolation Pilot Plant Environments: Progress Report for the Period November 1989 Through December 1992.* SAND92-7347. Albuquerque, NM: Sandia National Laboratories.

Telander, M.R., and R.E. Westerman. 1997. *Hydrogen Generation by Metal Corrosion in Simulated Waste Isolation Pilot Plant Environments.* SAND96-2538. Albuquerque, NM: Sandia National Laboratories.

Thompson, K.M., and J.D. Graham. 1996. "Going Beyond the Single Number: Using Probabilistic Risk Assessment to Improve Risk Management," *Human and Ecological Risk Assessment.* Vol. 2, no. 4, 1008-1034.

Thompson, T.W., W.E. Coons, J.L. Krumhansl, and F.D. Hansen. 1996. "Inadvertent Intrusion Borehole Permeability, Final Draft." August 1, 1996. Albuquerque, NM: Sandia National Laboratories. Sandia WIPP Central Files WPO # 39622.

Tierney, M.S. 1996a. "Reasons for Choice of the PROBDEG Parameter (id nos: 2824 and 2823) on February 22, 1996." Memo to file, March 29, 1996. Albuquerque, NM: Sandia National Laboratories. Sandia WIPP Central Files WPO # 34881.

Tierney, M. 1996b. "Emplaced Height of Remote Handled Waste in CCDFGF Model." WIPP Data Entry Form. Albuquerque, NM: Sandia National Laboratories. Sandia WIPP Central Files WPO # 38744.

Trauth, K. 1996. "Assessment of the Effectiveness of Passive Institutional Controls in Deterring Inadvertent Human Intrusion Into the WIPP for the Compliance Certification Calculations - Updated Information." Memo to J. Helton, June 26, 1996. Albuquerque, NM: Sandia National Laboratories. Sandia WIPP Central Files WPO # 40133.

Trauth, K.M., R.V. Guzowski, C.G. Pflum, and R.J. Rodriguez. 1996. *Effectiveness of Passive Institutional Controls in Reducing Inadvertent Human Intrusion into the Waste Isolation Pilot Plant for Use in Performance Assessments.* WIPP/CAO-96-3168, Revision 1, November 14, 1996 with Addendum of December 6, 1996. Carlsbad, NM: United States Department of Energy, Waste Isolation Pilot Plant, Carlsbad Area Office.

U.S. DOE (U.S. Department of Energy). 1980. *Final Environmental Impact Statement: Waste Isolation Pilot Plant.* DOE/EIS-0026. Washington, DC: U.S. Department of Energy, Assistant Secretary for Defense Programs. Vols. 1-2.

U.S. DOE (U.S. Department of Energy). 1990. *Final Supplement: Environmental Impact Statement, Waste Isolation Pilot Plant.* DOE/EIS-0026-FS. Washington, DC: U.S. Department of Energy, Office of Environmental Restoration and Waste Management. Vols. 1-13.

U.S. DOE (U.S. Department of Energy). 1993. *Waste Isolation Pilot Plant Strategic Plan.* DOE/EM-48063. Washington, DC: U.S. Department of Energy.

U.S. DOE (U.S. Department of Energy). 1995a. *Transuranic Waste Baseline Inventory Report (Revision 2).* DOE/CAO-95-1121, Revision 2. Carlsbad, NM: U.S. Department of Energy, Carlsbad Area Office.

U.S. DOE (U.S. Department of Energy). 1995b. *Waste Isolation Plant Sealing System Design Report.* DOE/WIPP-95-3117. Carlsbad, NM: United States Department of Energy, Waste Isolation Pilot Plant, Carlsbad Area Office.

U.S. DOE (U.S. Department of Energy). 1996. *Title 40 CFR Part 191 Compliance Certification Application for the Waste Isolation Pilot Plant.* DOE/CAO-1996-2184. Carlsbad, NM: U.S. Department of Energy, Waste Isolation Pilot Plant, Carlsbad Area Office.

U.S. EPA (U.S. Environmental Protection Agency). 1985. "40 CFR 191: Environmental Standards for the Management and Disposal of Spent Nuclear Fuel, High-Level and Transuranic Radioactive Wastes; Final Rule," *Federal Register.* Vol. 50, no. 182, 38066-38089.

U.S. EPA (U.S. Environmental Protection Agency). 1993a. "40 CFR 191: Environmental Radiation Protection Standards for the Management and Disposal of Spent Nuclear Fuel, High-Level and Transuranic Radioactive Wastes; Final Rule," *Federal Register.* Vol. 58, no. 242, 66398-66416.

U.S. EPA (U.S. Environmental Protection Agency). 1993b. *An SAB Report: Multi-Media Risk Assessment for Radon, Review of Uncertainty Analysis of Risks Associated with Exposure to Radon.* EPA-SAB-RAC-93-014. Washington, DC: U.S. Environmental Protection Agency, Science Advisory Board. Sandia WIPP Central Files WPO # 49480.

U.S. EPA (U.S. Environmental Protection Agency). 1996. "40 CFR Part 194: Criteria for the Certification and Re-Certification of the Waste Isolation Pilot Plant's Compliance With the 40 CFR Part 191 Disposal Regulations; Final Rule," *Federal Register.* Vol. 61, no. 28, 5224-5245.

U.S. NRC (U.S. Nuclear Regulatory Commission). 1975. *Reactor Safety Study—An Assessment of Accident Risks in U.S. Commercial Nuclear Power Plants.* N.C. Rasmusen. WASH-1400 (NUREG-75/014). Washington, DC: U.S. Nuclear Regulatory Commission. Vols. 1-8. (Available from the NTIS as PB-248 200.)

U.S. NRC (U.S. Nuclear Regulatory Commission). 1986. "10 CFR Part 50 Safety Goals for the Operation of Nuclear Power Plants; Policy Statement; Correction and Republication," *Federal Register.* Vol. 51, no. 162, 30028–30033.

U.S. NRC (U.S. Nuclear Regulatory Commission). 1990-1991. *Severe Accident Risks: An Assessment for Five U.S. Nuclear Power Plants.* NUREG-1150. Washington, DC: U.S. Nuclear Regulatory Commission, Office of Nuclear Regulatory Research, Division of Systems Research. Vols. 1-3.

van Genuchten, R. 1978. *Calculating the Unsaturated Hydraulic Conductivity with a New Closed-Form Analytical Model.* Report 78-WR-08. Princeton, NJ: Princeton University, Department of Civil Engineering, Water Resources Program. Sandia WIPP Central Files WPO # 49486.

Vargaftik, N.B. 1975. *Tables on the Thermophysical Properties of Liquids and Gases in Normal and Dissociated States*. 2nd ed. Washington, DC: Hemisphere Pub. Corp.; New York, NY: Distributed by Halsted Press.

Vaughn, P. 1996a. "WAS_AREA and REPOSIT SAT_RBRN Distribution." Memo with attachments to M. Tierney, February 13, 1996. Albuquerque, NM: Sandia National Laboratories. Sandia WIPP Central Files WPO # 34902.

Vaughn, P. 1996b. "Salado Borehole Diameter." Memo to M. Tierney, February 23, 1996. Albuquerque, NM: Sandia National Laboratories. Sandia WIPP Central Files WPO # 35329.

Vaughn, P., and D. McArthur. 1996. "CUMPROB Parameter Definition and Usage." Memo to M. Tierney, May 20, 1996. Albuquerque, NM: Sandia National Laboratories. Sandia WIPP Central Files WPO # 37542.

Vesely, W.E., and D.M. Rasmuson. 1984. "Uncertainties in Nuclear Probabilistic Risk Analyses," *Risk Analysis*. Vol. 4, no. 4, 313-322.

Walas, S.M. 1985. *Phase Equilibria in Chemical Engineering*. Boston, MA: Butterworth Publishers.

Walker, R.E. 1976. "Hydraulic Limits are Set by Flow Restrictions," *Oil and Gas Journal*. Vol. 74, no. 40, 86-90.

Walker, R.E., and W.E. Holman. 1971. "Computer Program Predicting Drilling-Fluid Performance," *Oil and Gas Journal*. Vol. 69, no. 13, 80-90.

Wallace, M.G. 1996a. "Phase II FEP, NS-11, 'Subsidence Associated with Mining Inside or Outside the Controlled Area.'" Records Package. Albuquerque, NM: Sandia National Laboratories. Sandia WIPP Central Files WPO # 40816.

Wallace, M.G. 1996b. "Distribution for Non-Salado Parameter for SECOFL2D: Mining Transmissivity Multiplier." Memo to M. Tierney, April 18, 1996. Albuquerque, NM: Sandia National Laboratories. Sandia WIPP Central Files WPO # 39355.

Wallace, M.G. 1996c. "Mining Transmissivity Multiplier." Records Package. Albuquerque, NM: Sandia National Laboratories. Sandia WIPP Central Files WPO # 36489.

Wallace, M. 1996d. "Distribution for Non-Salado Parameter for SECOTP2D: Fracture Tortuosity." Memo to M. Tierney, May 2, 1996. Albuquerque, NM: Sandia National Laboratories. Sandia WIPP Central Files WPO # 39365.

Wang, Y., and L. Brush. 1996a. "Estimates of Gas-Generation Parameters for the Long-Term WIPP Performance Assessment." Memo to M. Tierney, January 26, 1996. Albuquerque, NM: Sandia National Laboratories. Sandia WIPP Central Files WPO # 35162.

Wang Y., and L. Brush. 1996b. "Modify the Stoichiometric Factor y in BRAGFLO to Include the Effect of MgO Added to WIPP Repository as Backfill." Memo to M. Tierney, February 23, 1996. Albuquerque, NM: Sandia National Laboratories. Sandia WIPP Central Files WPO # 22286.

Weast, R.C., ed. 1969. *Handbook of Chemistry and Physics*. 50th ed. Cleveland, OH: Chemical Rubber Pub. Co.

Webb, S.W. 1992. "Appendix A: Uncertainty Estimates for Two-Phase Characteristic Curves for 1992 40 CFR 191 Calculations," *Preliminary Performance Assessment for the Waste Isolation Pilot Plant, December 1992. Volume 3: Model Parameters*. Sandia WIPP Project. SAND92-0700/3. Albuquerque, NM: Sandia National Laboratories. A-147 through A-155.

Weiner, R.F. 1996. "Documentation Package for Oxidation State Distribution of Actinides in the Repository." Records Package. Albuquerque, NM: Sandia National Laboratories. Sandia WIPP Central Files WPO # 35194.

Weisberg, S. 1985. *Applied Linear Regression.* 2nd ed. New York, NY: John Wiley & Sons.

Welchon, J.K., A.F. Bertuzzi, and F.H. Poettmann. 1962. "Chapter 31 Wellbore Hydraulics," *Petroleum Production Handbook.* Eds. T.C. Frick and R.W. Taylor. Dallas, TX: Society of Petroleum Engineers of AIME. 31-1 to 31-36.

Whipple, C.G. 1986. "Dealing with Uncertainty about Risk in Risk Management," *Hazards: Technology and Fairness.* Washington, DC: National Academy Press. 44-59.

Whittaker, A., ed. 1985. *Theory and Application of Drilling Fluid Hydraulics.* Boston, MA: International Human Resources Development Corporation.

Williamson, A.S., and J.E. Chappelear. 1981. "Representing Wells in Numerical Reservoir Simulation: Part 1 - Theory," "Representing Wells in Numerical Reservoir Simulation: Part 2 - Implementation." *Society of Petroleum Engineers Journal.* Vol. 21, no. 3, 323-338.

WIPP PA (Performance Assessment). 1991-1992. *Preliminary Comparison with 40 CFR Part 191, Subpart B for the Waste Isolation Pilot Plant, December 1991.* SAND91-0893/1-4. Albuquerque, NM: Sandia National Laboratories. Vols. 1-4.

WIPP PA (Performance Assessment). 1992-1993. *Preliminary Performance Assessment for the Waste Isolation Pilot Plant, December 1992.* SAND92-0700/1-5. Albuquerque, NM: Sandia National Laboratories. Vols. 1-5.

WIPP PA (Performance Assessment). 1996a. "BRAGFLO, Version 4.00, User's Manual." Albuquerque, NM: Sandia National Laboratories. Sandia WIPP Central Files WPO #30703.

WIPP PA (Performance Assessment). 1996b. "NUTS, Version 2.02, Version 5/23/96, User's Manual." Albuquerque, NM: Sandia National Laboratories. Sandia WIPP Central Files WPO #37927.

WIPP PA (Performance Assessment). 1996c. "PANEL, Version 3.60, User's Manual." Albuquerque, NM: Sandia National Laboratories. Sandia WIPP Central Files WPO #37361.

WIPP PA (Performance Assessment). 1996d. "CUTTINGS_S, Version 5.03, Version Date 4/22/96, User's Manual." Albuquerque, NM: Sandia National Laboratories. Sandia WIPP Central Files WPO #37765.

WIPP PA (Performance Assessment). 1997. "SECOTP2D, Version 1.41, User's Manual." Albuquerque, NM: Sandia National Laboratories. Sandia WIPP Central Files WPO #45734.

Yelton, W.G., Y.K. Behl, J.W. Kelly, M. Dunn, J.B. Gillow, A.J. Francis, and H.W. Papenguth. 1996. "Laboratory Evaluation of Colloidal Actinide Transport at the Waste Isolation Pilot Plant (WIPP): 1. Crushed-Dolomite Column Flow Experiments," *Experimental and Modeling Studies of Radionuclide Speciation in Real Systems.* SAND96-2894C. Albuquerque, NM: Sandia National Laboratories.

Appendix

Distributions Characterizing Subjective Uncertainty Assigned to Variables in Table 5.2.1

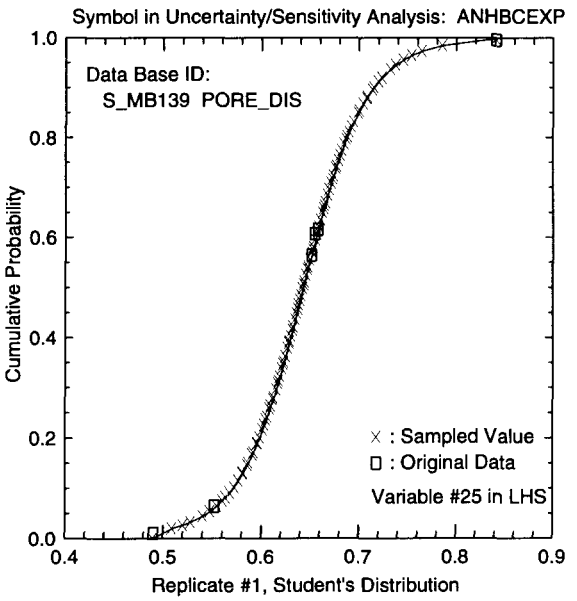

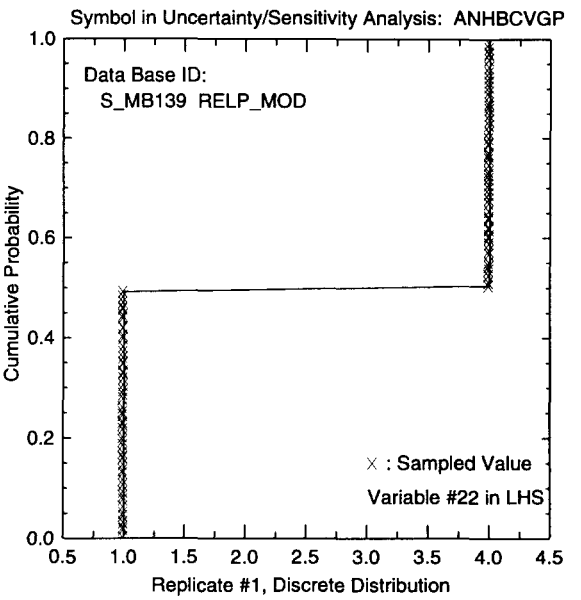

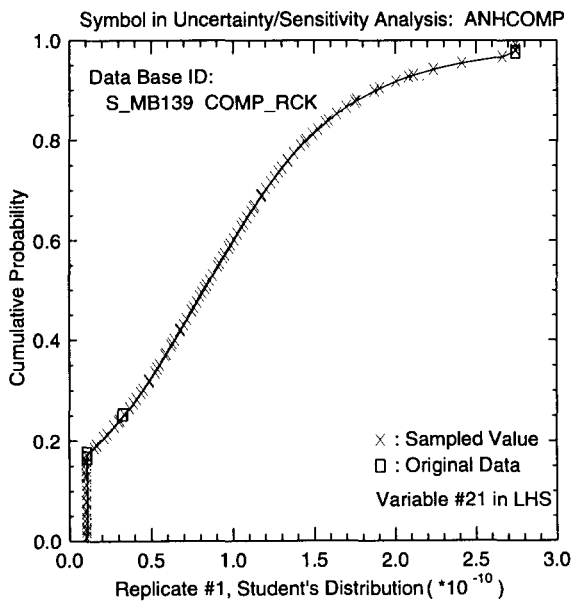

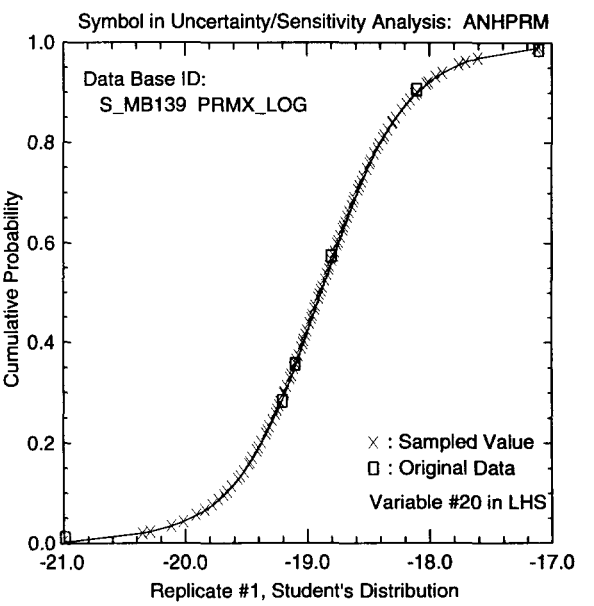

TRI-6342-5393-0

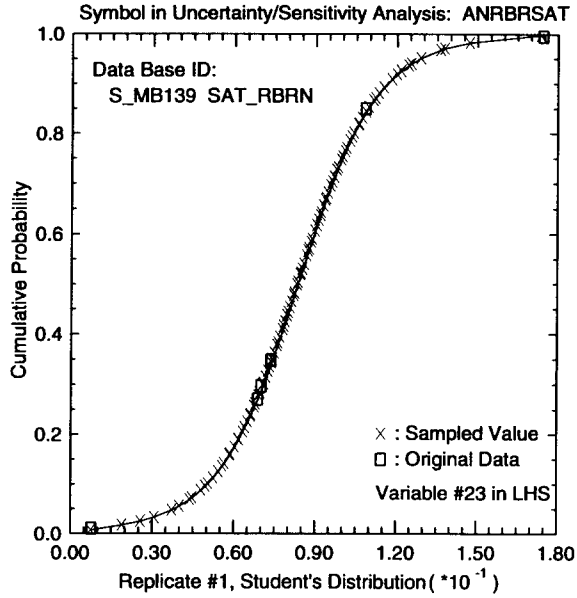

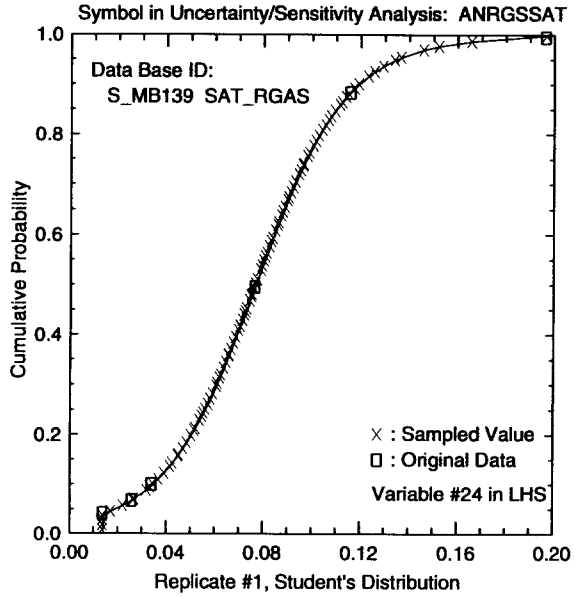

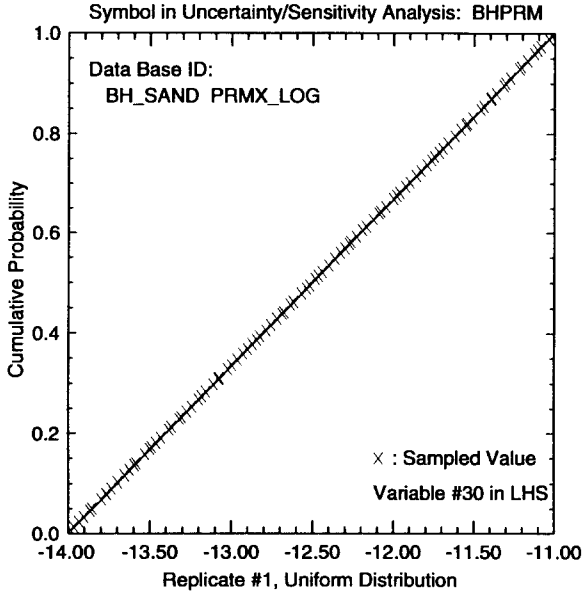

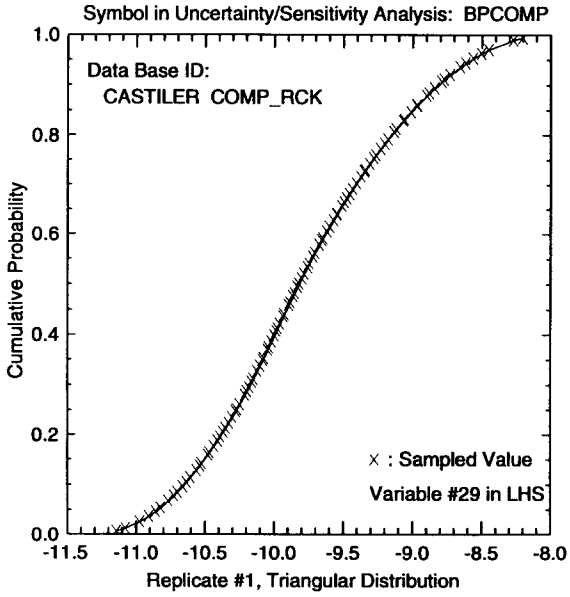

TRI-6342-5394-0

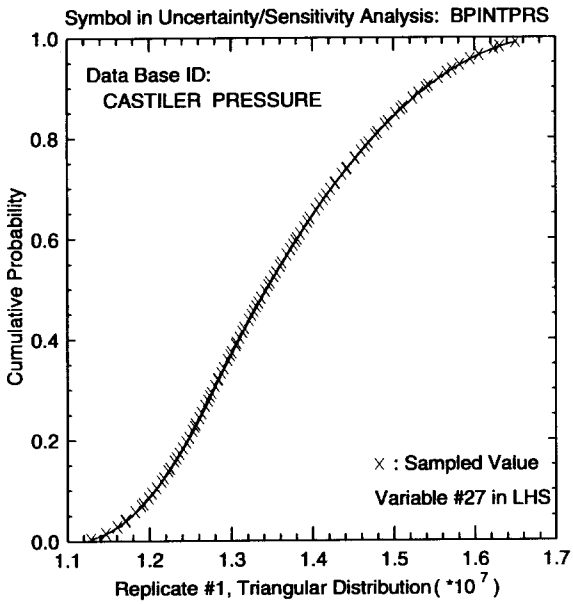

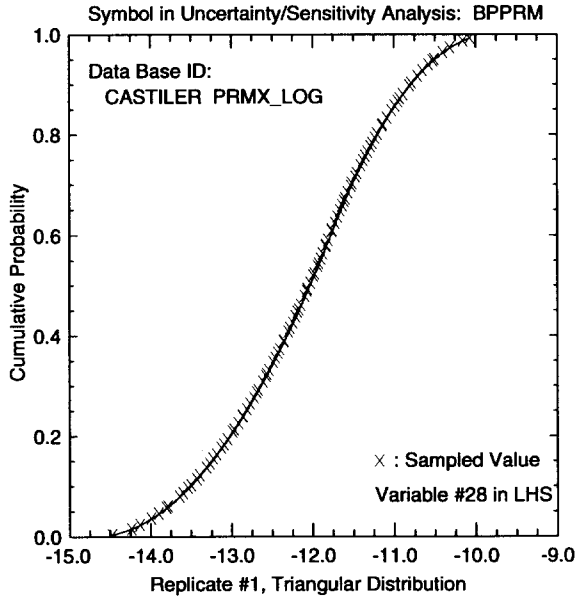

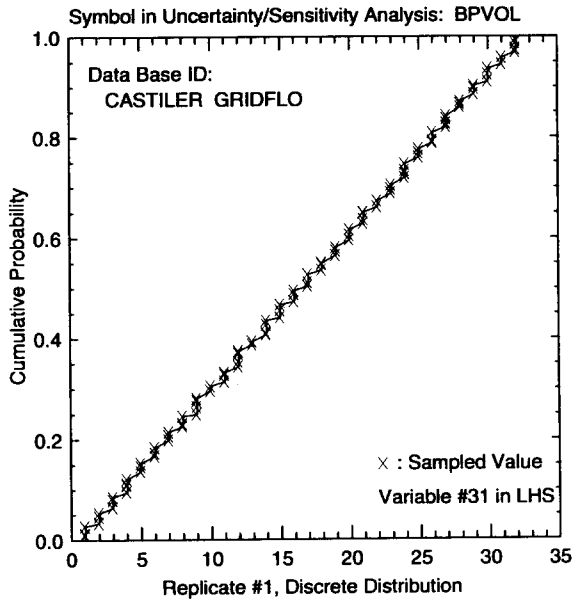

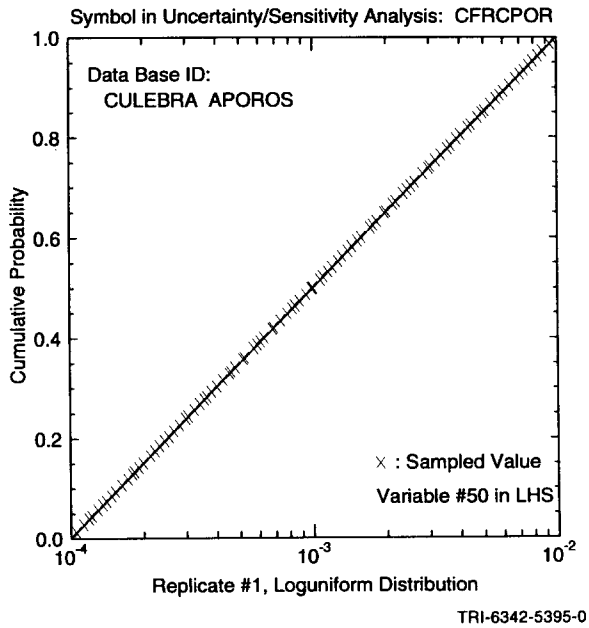

TRI-6342-5395-0

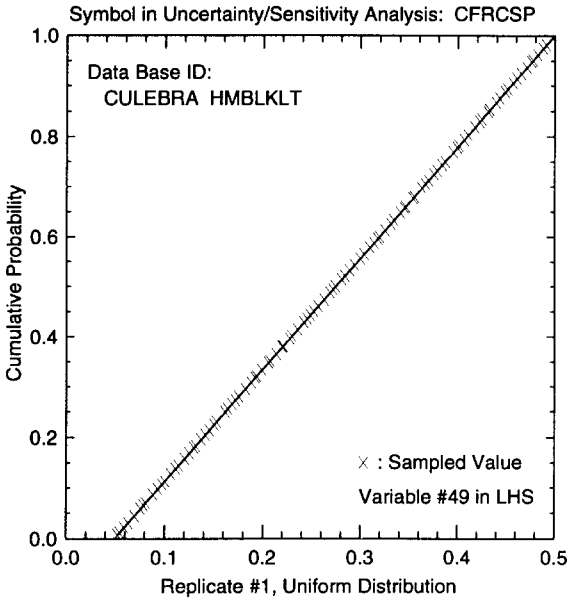

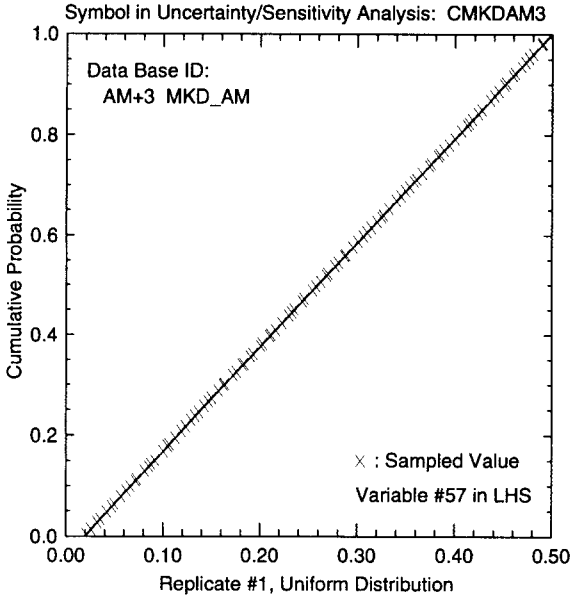

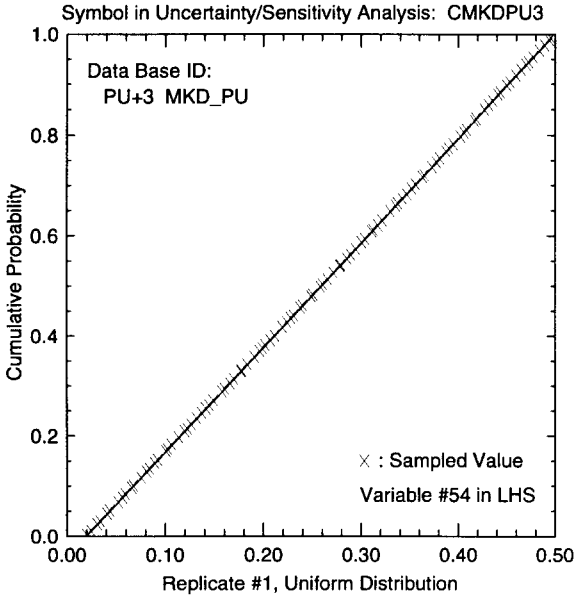

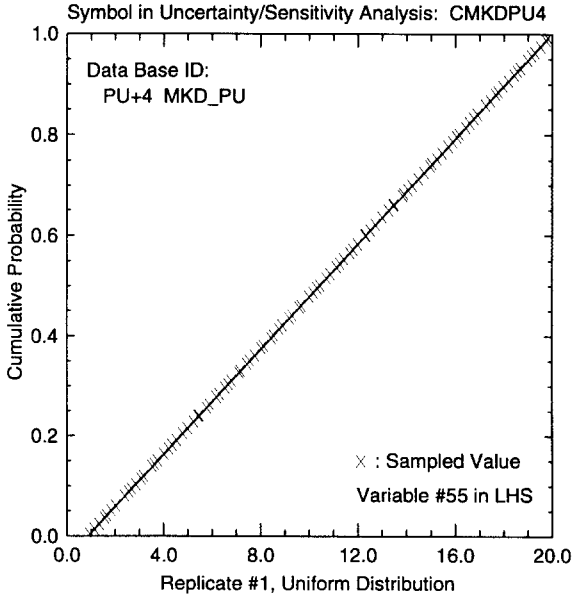

TRI-6342-5396-0

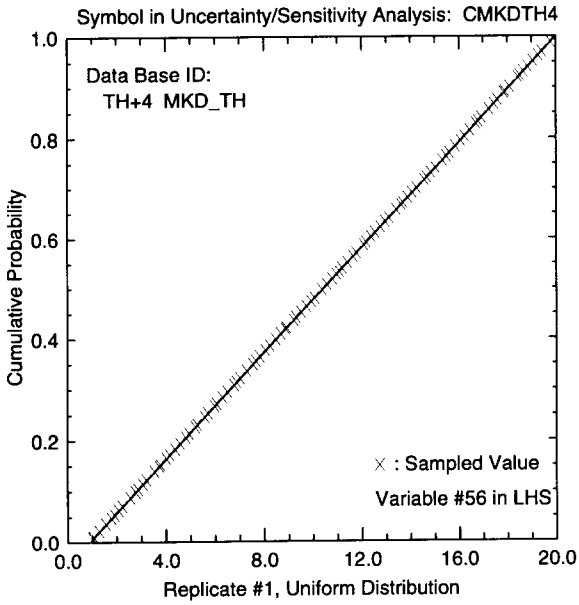

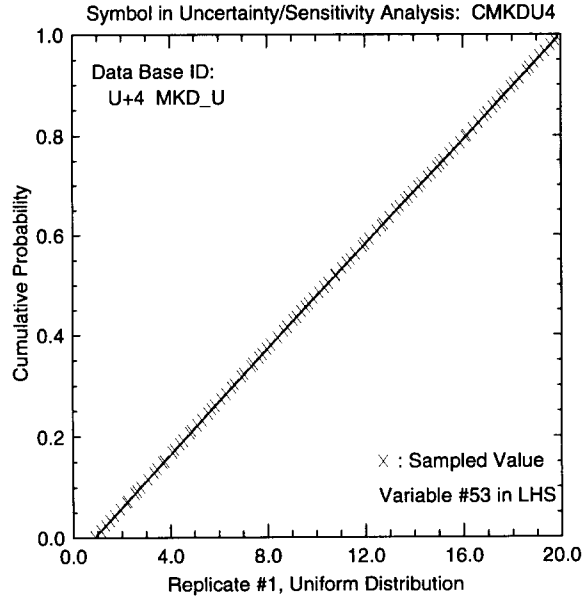

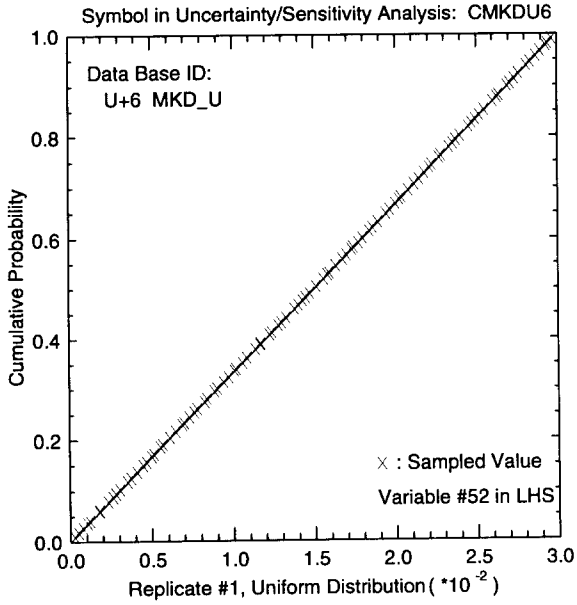

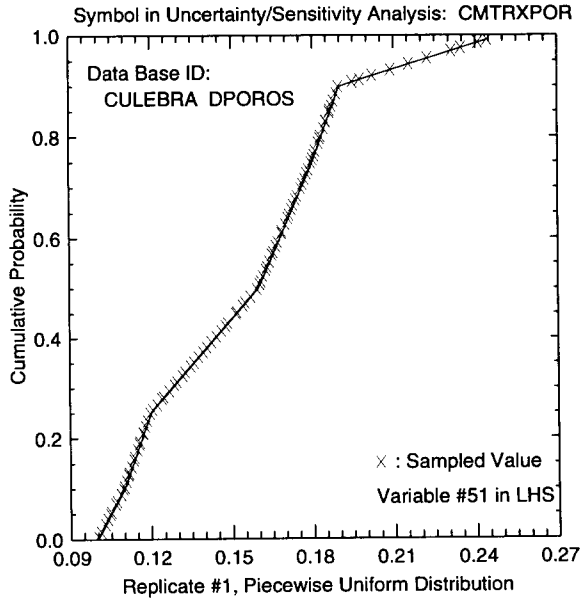

TRI-6342-5397-0

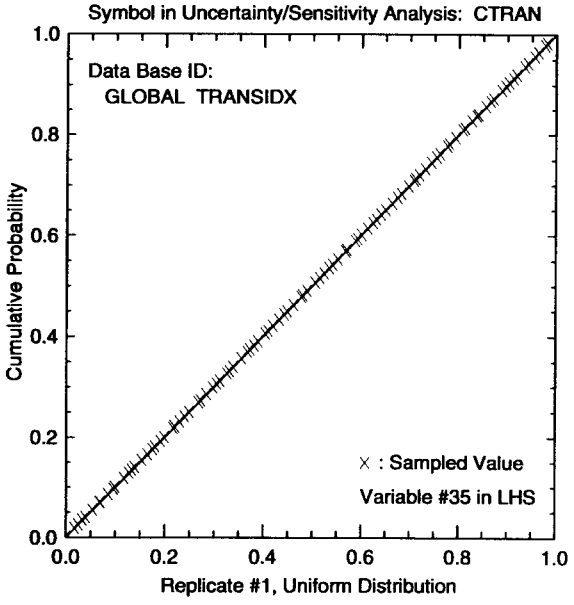

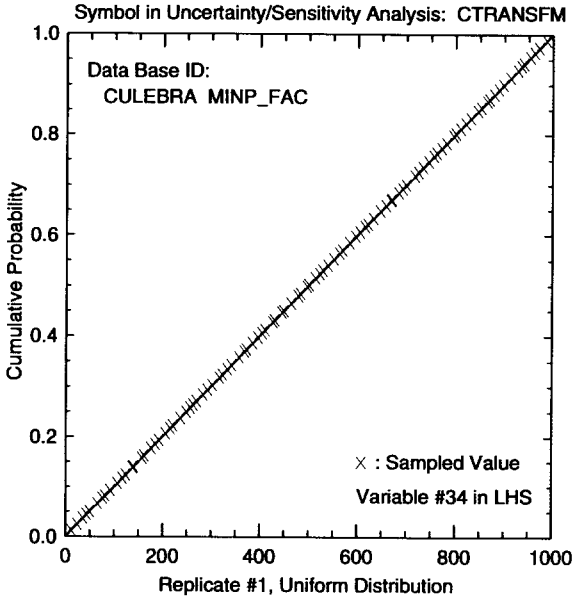

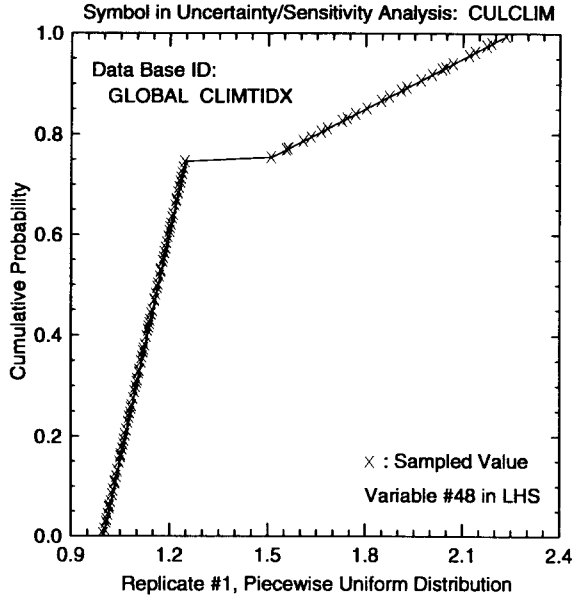

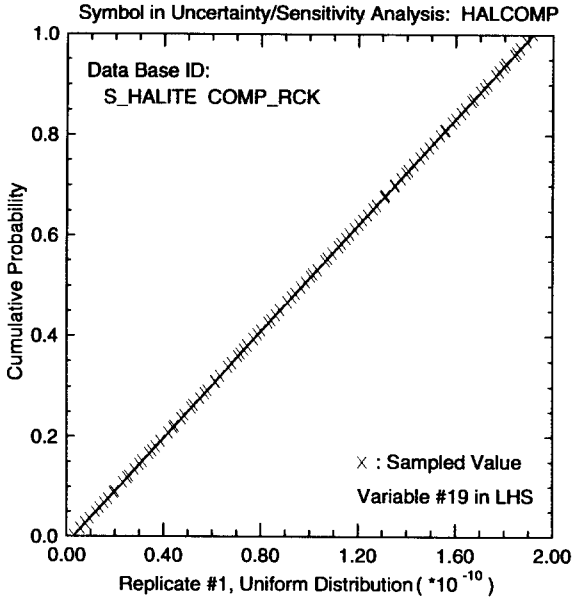

TRI-6342-5398-0

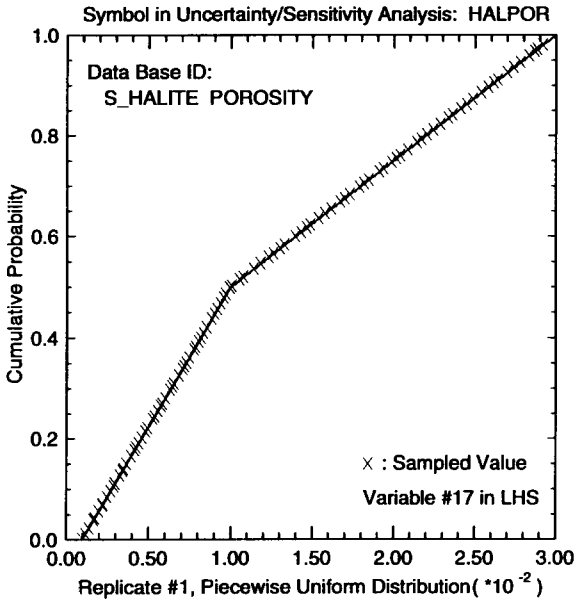

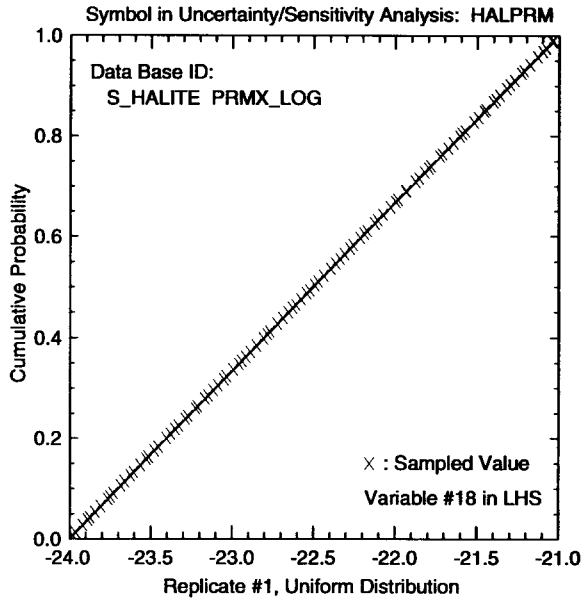

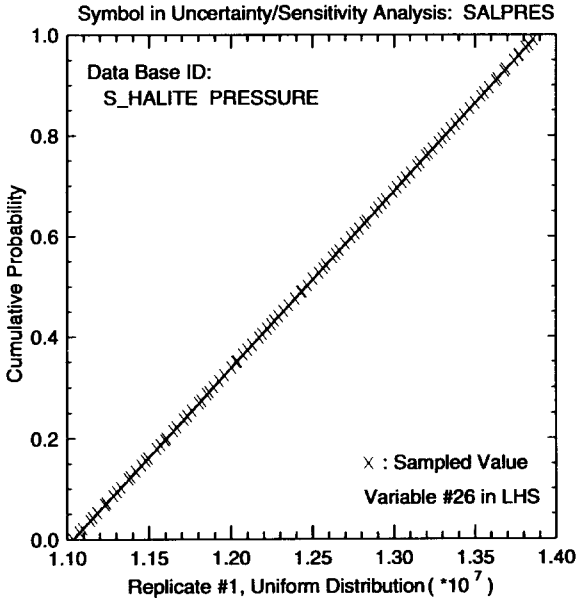

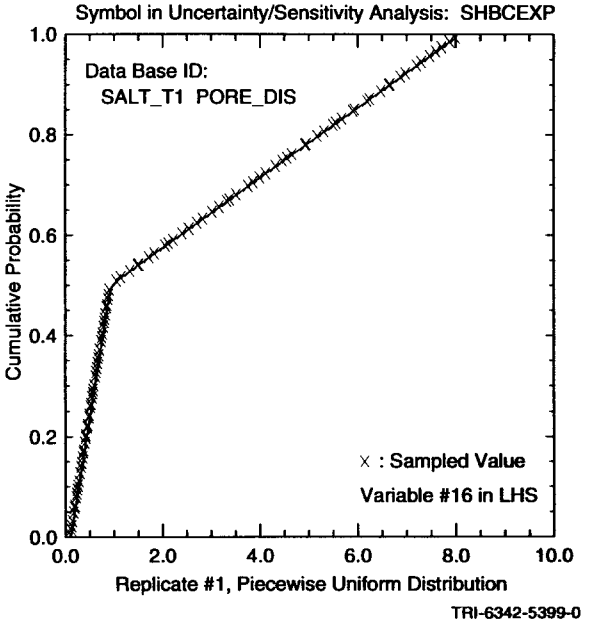

TRI-6342-5399-0

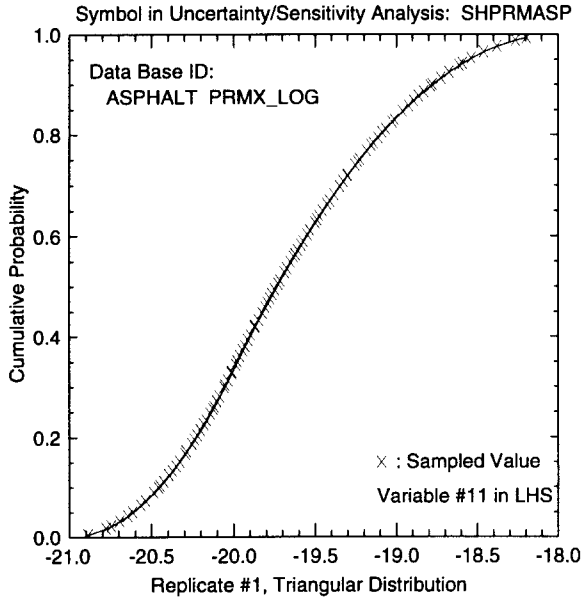

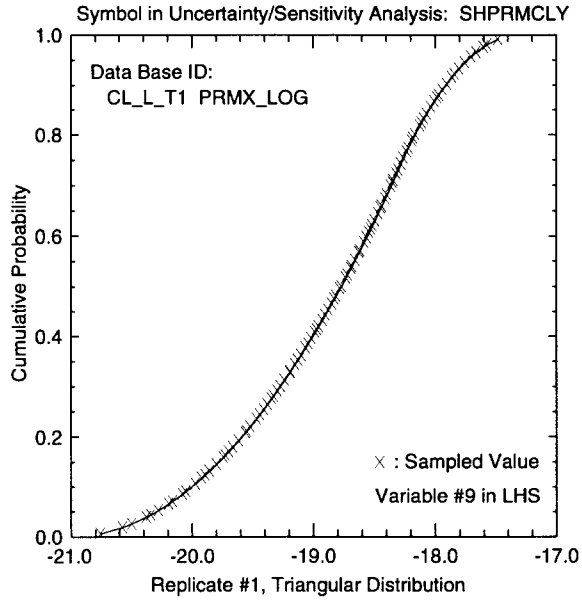

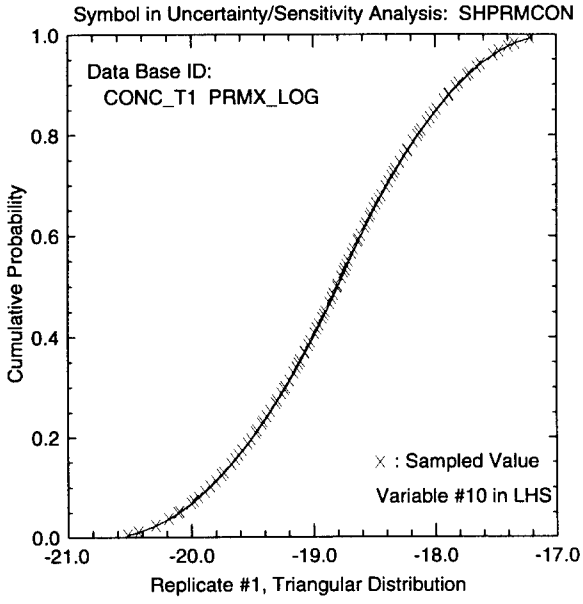

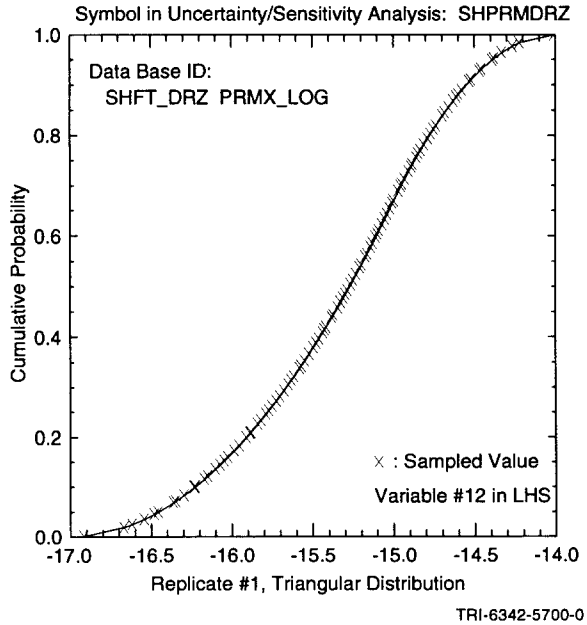

TRI-6342-5700-0

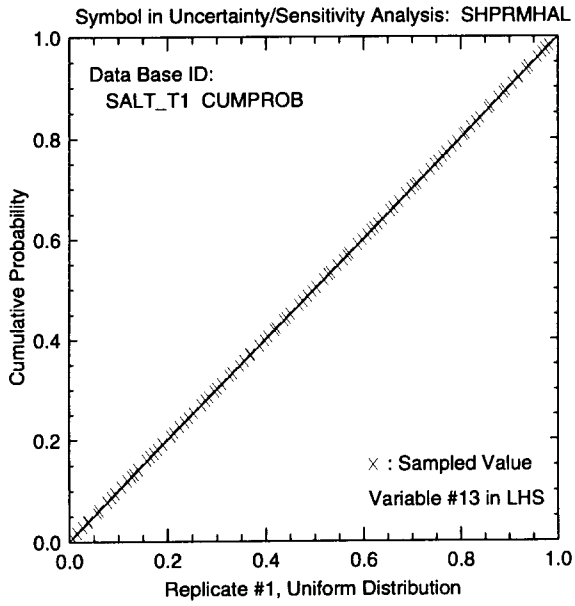

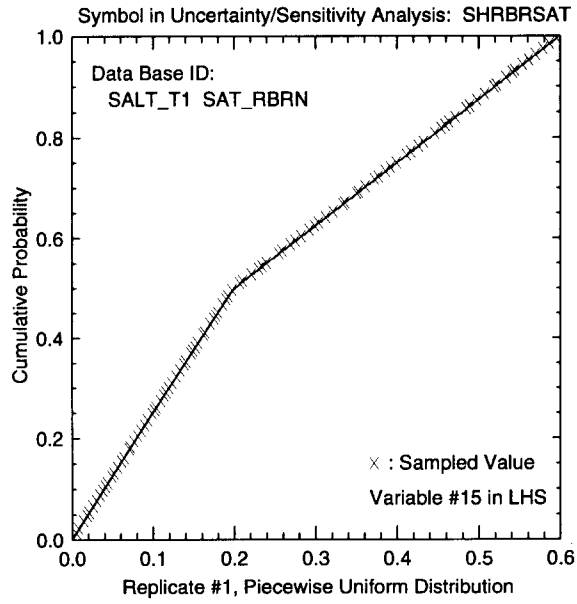

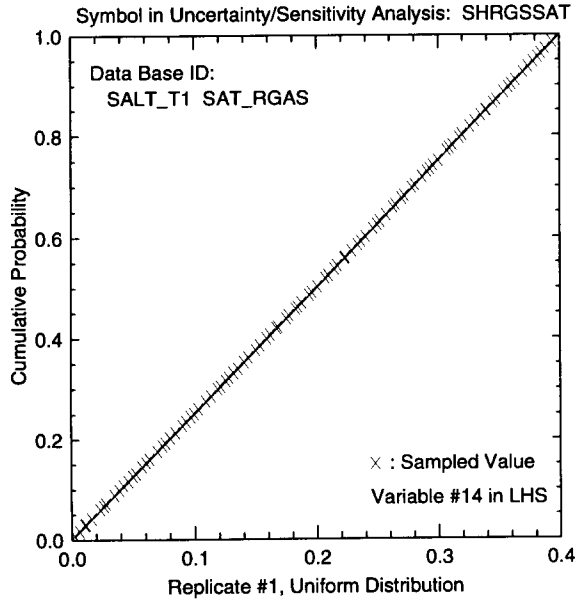

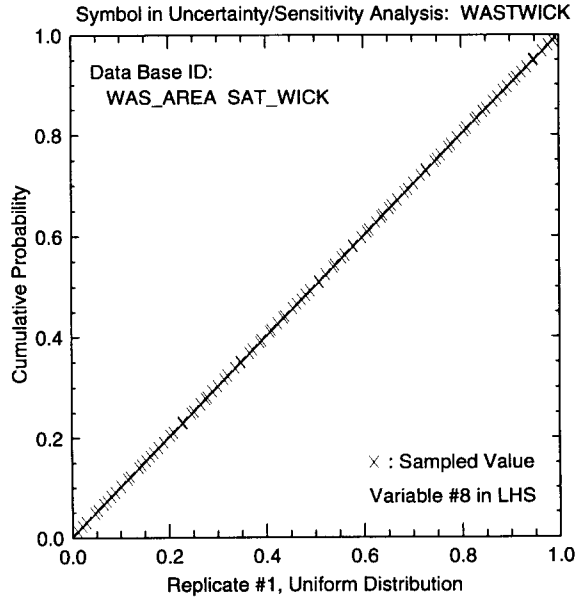

TRI-6342-5701-0

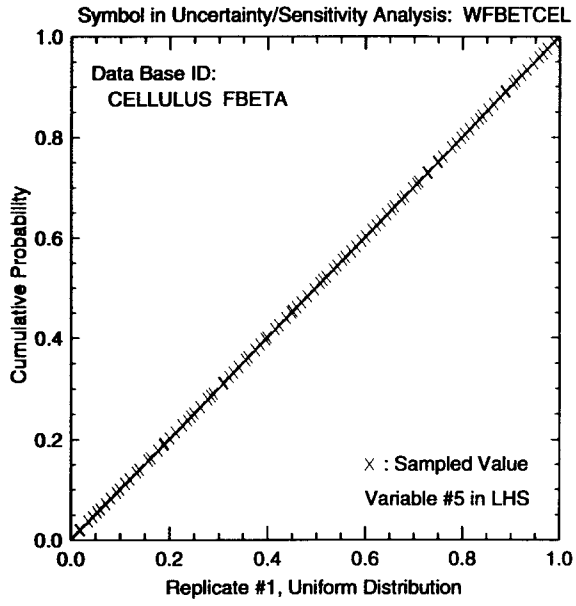

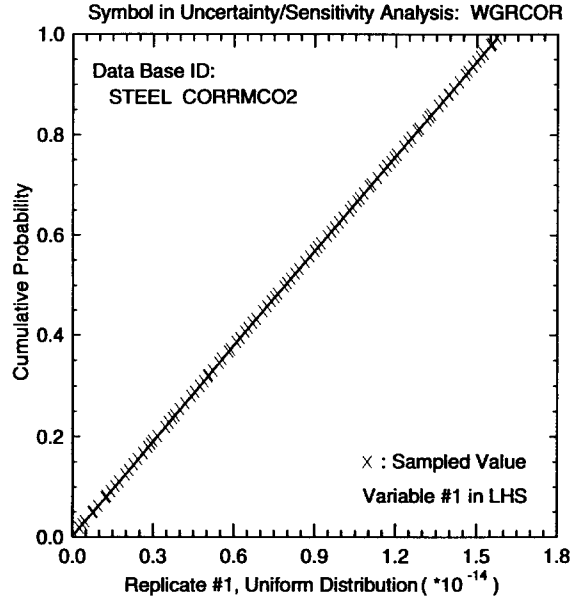

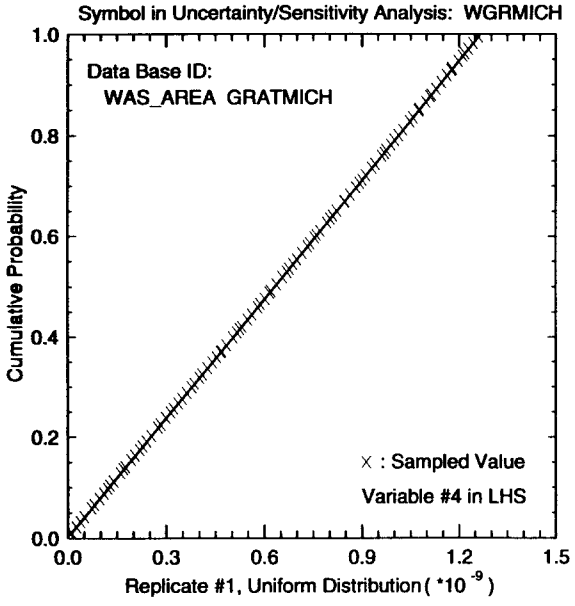

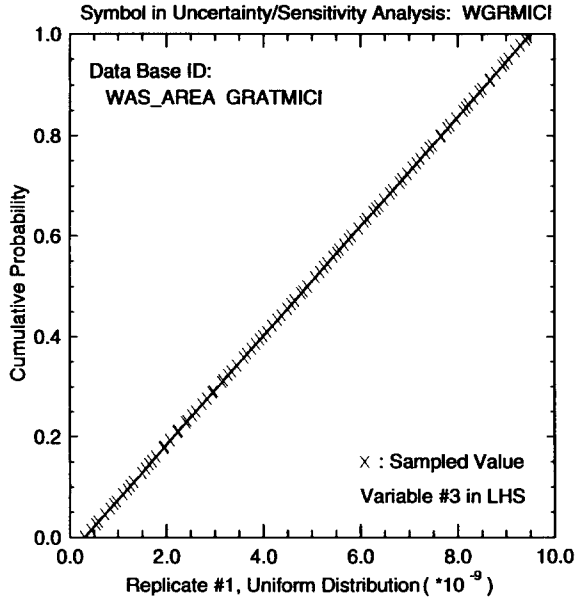

TRI-6342-5702-0

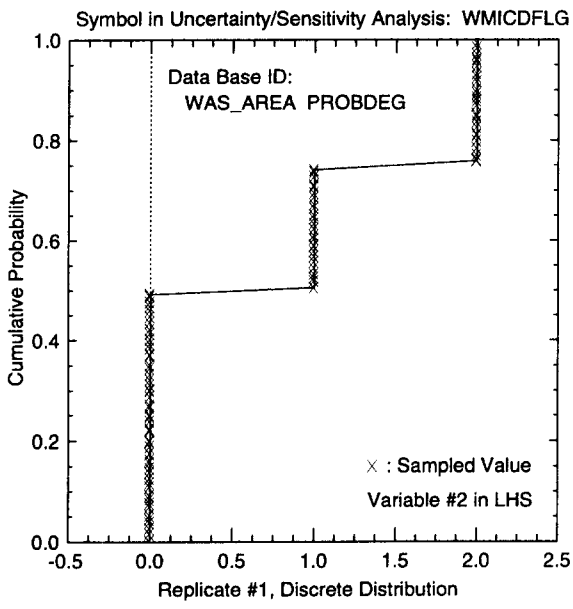

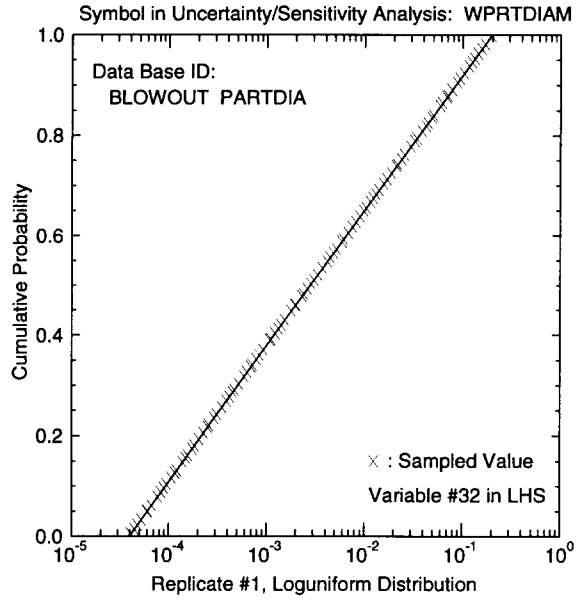

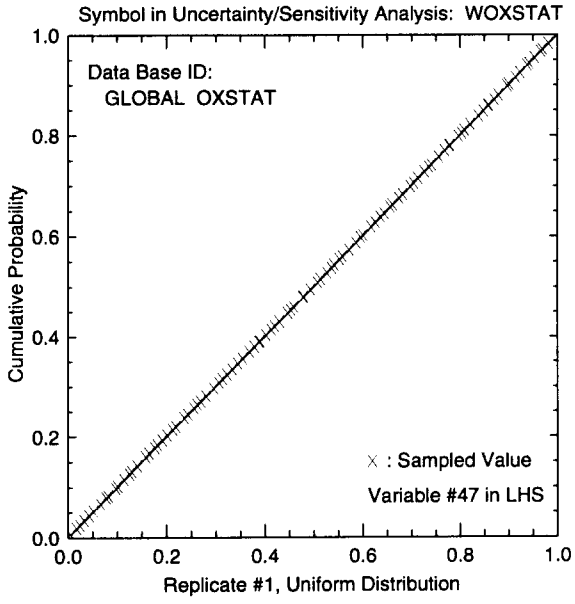

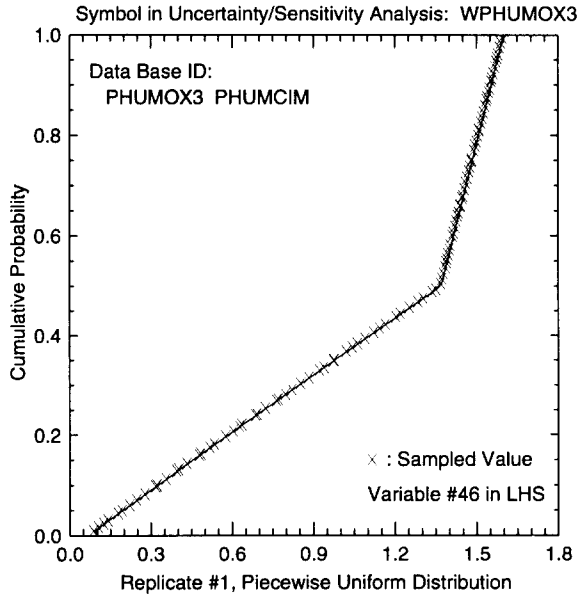

TRI-6342-5703-0

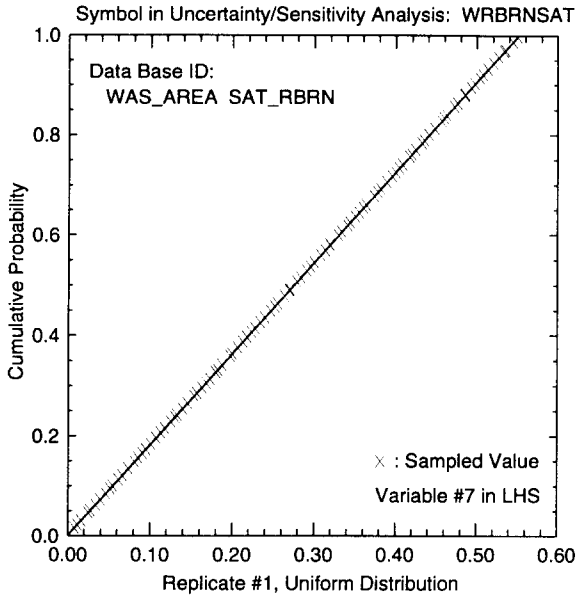

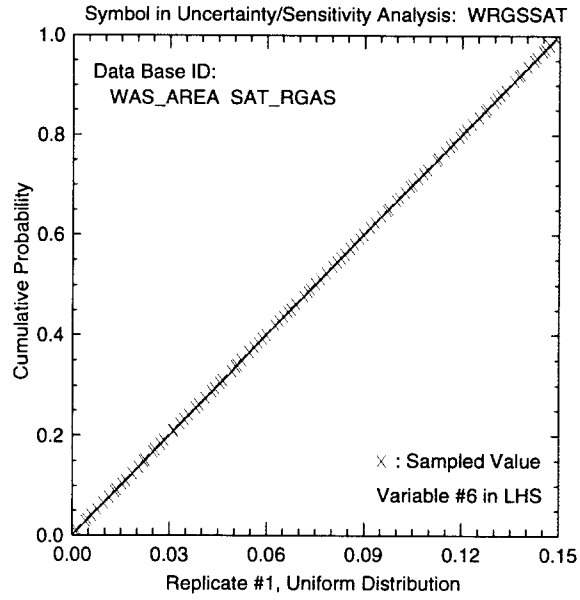

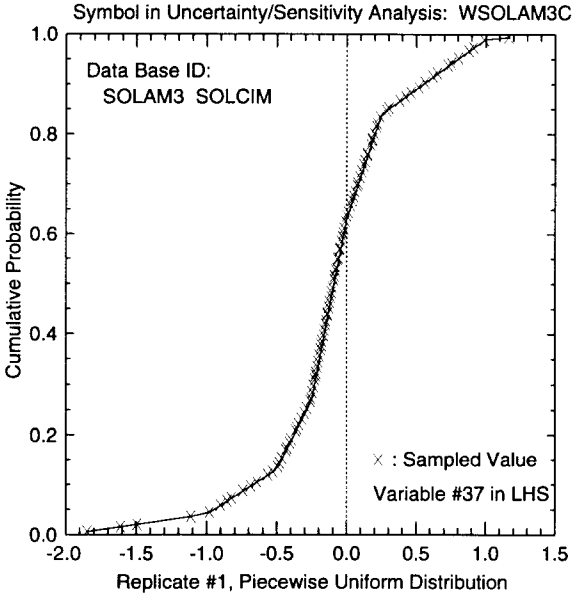

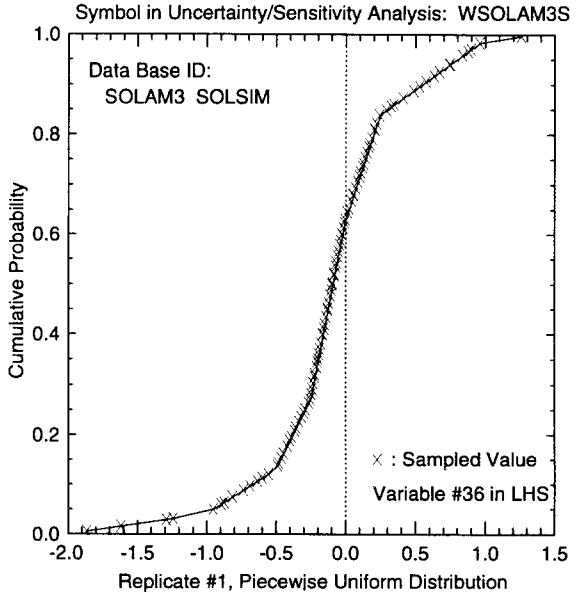

TRI-6342-5704-0

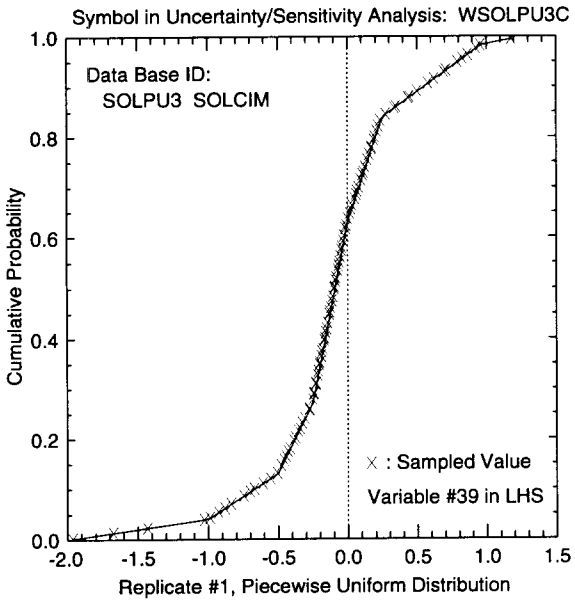

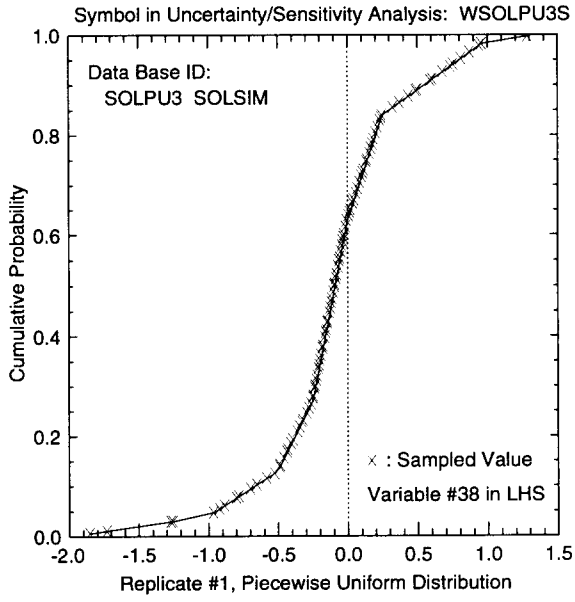

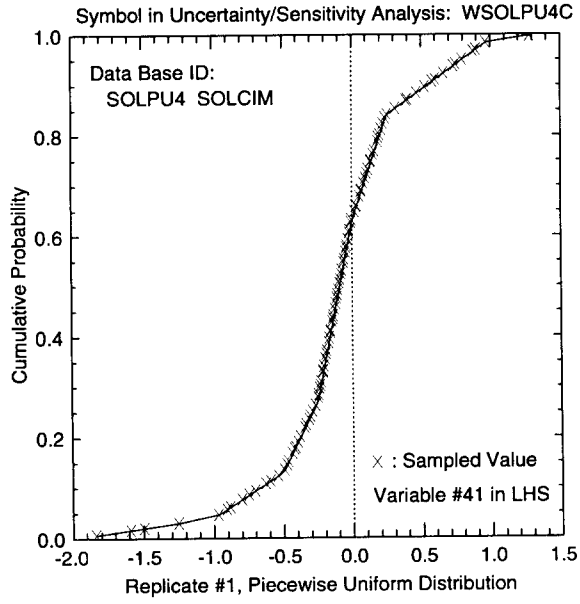

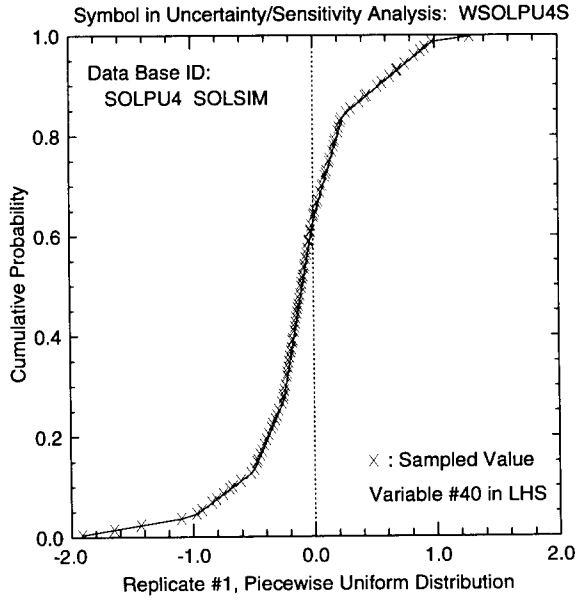

TRI-6342-5705-0

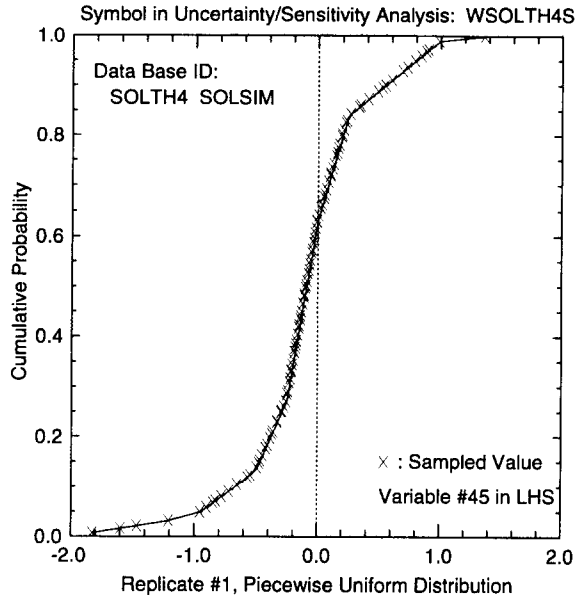

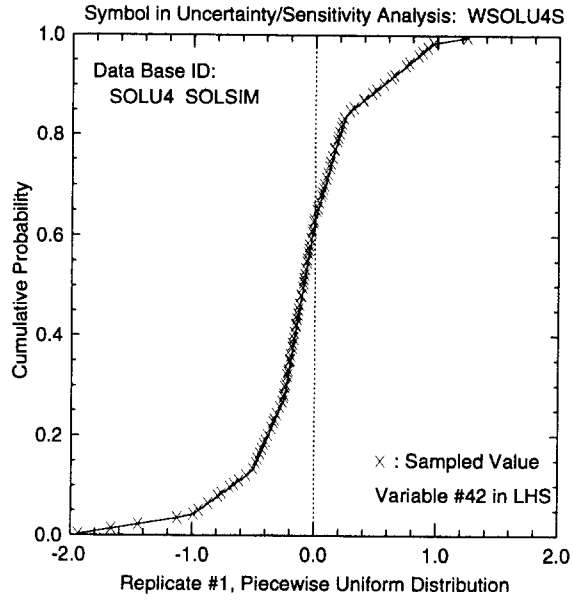

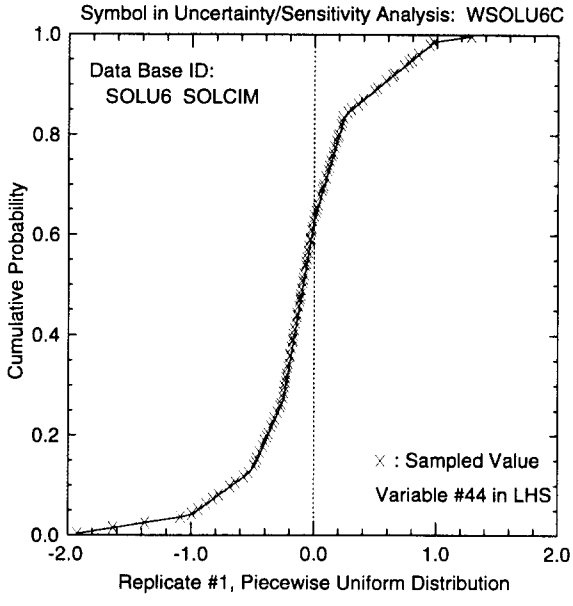

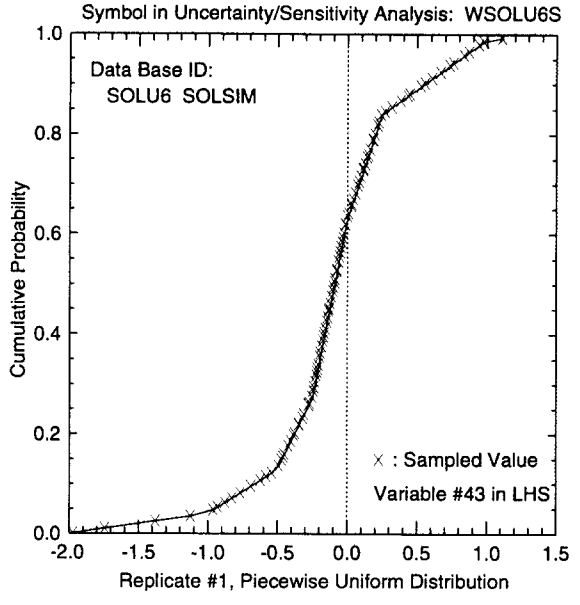

TRI-6342-5706-0

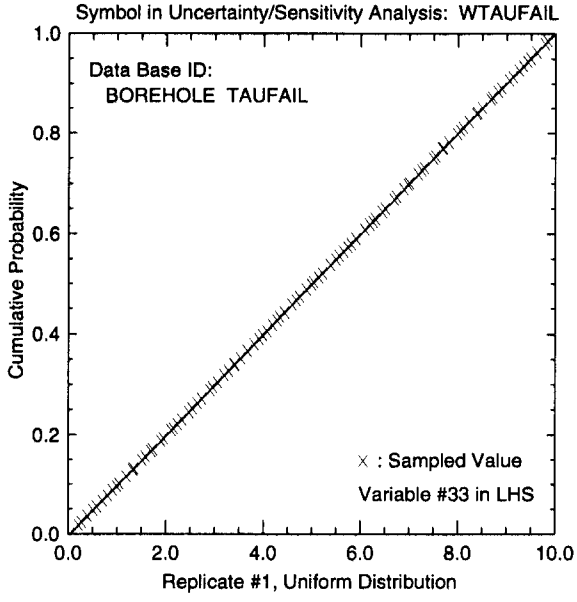

TRI-6342-5707-0

WIPP
UC721 - DISTRIBUTION LIST
SAND98-0365

Federal Agencies

US Department of Energy (4)
Office of Civilian Radioactive Waste Mgmt.
Attn: Deputy Director, RW-2
Acting Director, RW-10
Office of Human Resources & Admin.
Director, RW-30
Office of Program Mgmt. & Integ.
Director, RW-40
Office of Waste Accept., Stor., & Tran.
Forrestal Building
Washington, DC 20585

Yucca Mountain Site Characterization Office
Director, RW-3
Office of Quality Assurance
Attn: Project Director
P. O. Box 30307
Las Vegas, NV 89036-0307

US Department of Energy
Research & Waste Management Division
Attn: Director
P.O. Box E
Oak Ridge, TN 37831

US Department of Energy (5)
Carlsbad Area Office
Attn: G. T. Basabilvazo
D. Galbraith
M. McFadden
R. Lark
J. A. Mewhinney
P.O. Box 3090
Carlsbad, NM 88221-3090

US Department of Energy
Office of Environmental Restoration and
Waste Management
Attn: M. Frei, EM-30
Forrestal Building
Washington, DC 20585-0002

US Department of Energy (3)
Office of Environmental Restoration and
Waste Management
Attn: J. Juri, EM-34, Trevion II
Washington, DC 20585-0002

US Department of Energy
Office of Environmental Restoration and
Waste Management
Attn: S. Schneider, EM-342, Trevion II
Washington, DC 20585-0002

US Department of Energy (2)
Office of Environment, Safety & Health
Attn: C. Borgstrom, EH-25
R. Pelletier, EH-231
Washington, DC 20585

US Department of Energy (2)
Idaho Operations Office
Fuel Processing & Waste Mgmt. Division
785 DOE Place
Idaho Falls, ID 83402

US Environmental Protection Agency (2)
Radiation Protection Programs
Attn: M. Oge
ANR-460
Washington, DC 20460

Timothy M. Barry
Chief, Science – Policy, Planning, and
Evaluation
PM 223X U.S. EPA
Washington, DC 20460

Norman A. Eisenberg
U.S. Nuclear Regulatory Commission
Office of Nuclear Material Safety and
Safeguards
Division of Waste Management
Washington, D. C. 20555

Boards

Defense Nuclear Facilities Safety Board
Attn: D. Winters
625 Indiana Ave. NW, Suite 700
Washington, DC 20004

Nuclear Waste Technical Review Board (2)
Attn: Chairman
J.L. Cohon
2300 Clarendon Ste. 1300
Arlington, VA 22203-3367

State Agencies

Attorney General of New Mexico
P.O. Drawer 1508
Santa Fe, NM 87504-1508

Environmental Evaluation Group (3)
Attn: Library
7007 Wyoming NE
Suite F-2
Albuquerque, NM 87109

NM Environment Department (3)
Secretary of the Environment
1190 St. Francis Drive
Santa Fe, NM 87503-0968

NM Bureau of Mines & Mineral Resources
Socorro, NM 87801

Laboratories/Corporations

Battelle Pacific Northwest Laboratories
Battelle Blvd.
Richland, WA 99352

Dr. Pamela Doctor
Battelle Northwest
P.O. Box 999
Richland, WA 99352

Los Alamos National Laboratory
Attn: B. Erdal, INC-12
P.O. Box 1663
Los Alamos, NM 87544

M. D. McKay
F600
Los Alamos National Laboratory
Los Alamos, NM 87545

Max Henrion
The Decision Laboratory (IDSR)
4984 El Camino Real, Suite 105
Los Altos, CA 94022

Tech Reps, Inc. (3)
Attn: J. Chapman (1)
Loretta Robledo (2)
5000 Marble NE, Suite 222
Albuquerque, NM 87110

Westinghouse Electric Corporation (5)
Attn: Library
J. Epstein
J. Lee
B. A. Howard
R. Kehrman
P.O. Box 2078
Carlsbad, NM 88221

S. Cohen & Associates
Attn: Bill Thurber
1355 Beverly Road
McLean, VA 22101

B. John Garrick
PLG Incorporated
4590 MacArthur Blvd., Suite 400
Newport Beach, CA 92660-2027

Christopher G. Whipple
ICF Kaiser Engineers
1800 Harrison St., 7th Floor
Oakland, CA 94612-3430

Dr. Kenneth T. Bogen
LLNL/ENV SCI DIVL – 453
P. O. Box 808
Livermore, CA 94550

David E. Burmaster
ALCEON Corporation
P. O. Box 382669
Harvard Square Station
Cambridge, MA 02238-2669

Scott Ferson
Applied Biomathematics
100 North Country Road
Setauket, NY 11733

Dr. Robert J. Budnitz
Future Resources Associates
2039 Shattuck Avenue, Suite 402
Berkeley, CA 94704

Dr. Tom Cotton
JK Research Associates
2650 Park Tower Drive, Suite 800
Vienna, VA 22180

Dr. John Kessler
Electronic Power Research Institute
3412 Hillview Avenue
Palo Alto, CA 94304-1395

D. Warner North
Decision Focus Incorporated
650 Castro Street, Suite 300
Mountain View, CA 94041-2055

S. David Sevougian
Duke Engineering and Services
CRWMS M&O
1180 Town Center Drive
Las Vegas, NV 89134

Michael B. Gross
Michael Gross Enterprises
21 Tradewind Passage
Corte Madera, CA 94925

Beta Corporation Int.
Attn: E. Bonano
6613 Esther NE
Albuquerque, NM 87109

Center for Nuclear Waste Regulatory Analysis
(CNWRA)
Southwest Research Institute
Attn: B. Sagar
P. O. Drawer 28510
620 Culebra Road
San Antonio, TX 78284

Banda S. Ramarao
Duke Engineering and Services
9111 Research Blvd.
Austin, TX 78758

Senes Oak Ridge, Inc (2)
Center for Risk Analysis
Attn: Steve Bartell
F. Owen Hoffman
102 Donner Drive
Oak Ridge, TN 37810

National Academy of Sciences, WIPP Panel

Tom Kiess (15)
Staff Study Director
GF456
2101 Constitution Ave.
Washington, DC 20418

Universities

University of New Mexico
Geology Department
Attn: Library
141 Northrop Hall
Albuquerque, NM 87131

University of Washington
College of Ocean & Fishery Sciences
Attn: G. R. Heath
583 Henderson Hall, HN-15
Seattle, WA 98195

Prof. G. E. Apostolakis
Department of Nuclear Engineering
Massachusetts Institute of Technology
Cambridge, MA 02139-4307

Prof. V. M. Bier
Department of Industrial Engineering
University of Wisconsin
Madison, WI 53706

Prof. M. Elisabeth Pate-Cornell
Department of Industrial Engineering and
Management
Stanford University
Stanford, CA 94305

Prof. C. Frey
Department of Civil Engineering
Box 7908/NCSU
Raleigh, NC 27659-7908

Prof. Yacov Y. Haimes
Center for Risk Management of Engineering Systems
D111 Thornton Hall
University of Virginia
Charlottesville, VA 22901

Prof. D. B. Hattis
CENTED
Clark University
950 Main Street
Worcester, MA 01610

Prof. Ali Mosleh
Center for Reliability Engineering
University of Maryland
College Park, MD 20714-2115

Prof. T. G. Theofanous
Department of Chemical and Nuclear Engineering
University of California
Santa Barbara, CA 93106

Prof. Steve Hora
Institute of Business and Economic Studies
University of Hawaii, Hilo
523 W. Lanikaula
Hilo, HI 96720-4091

Prof. Thomas E. McKone
School of Public Health
University of California
Berkeley, CA 94270-7360

Prof. Herschel Rabitz
Princeton University
Department of Chemistry
Princeton, NJ 08544

Prof. Robert L. Winkler
Fuqua School of Business
Duke University
Durham, NC 27708-0120

F. E. Haskin
Department of Chemical and Nuclear Engineering
University of New Mexico
Albuquerque, NM 87131

Alan Gutjahr
Department of Mathematics
New Mexico Institute of Mining and Tech.
Socorro, NM 87801

Thomas H. Pigford
Department of Nuclear Engineering
4159 Etcheverry Hall
University of California
Berkeley, CA 94720

C. John Mann
Department of Geology
245 Natural History Bldg.
1301 West Green Street
University of Illinois
Urbana, IL 61801

Frank W. Schwartz
Department of Geology and Mineralogy
Ohio State University
Scott Hall
1090 Carmack Rd.
Columbus, OH 43210

David M. Hamby
University of Michigan
109 Observatory St.
Ann Arbor, MI 48109-2029

Rodney C. Ewing
Nuclear Engineering and Radiological Science
University of Michigan
Ann Arbor, MI 48109-2104

David Okrent
Mechanical and Aerospace Engineering Department
University of California
48-121 Engineering IV Building
Los Angeles, CA 90095-1587

Libraries

Thomas Brannigan Library
Attn: D. Dresp
106 W. Hadley St.
Las Cruces, NM 88001

Government Publications Department
Zimmerman Library
University of New Mexico
Albuquerque, NM 87131

New Mexico Junior College
Pannell Library
Attn: R. Hill
Lovington Highway
Hobbs, NM 88240

New Mexico State Library
Attn: N. McCallan
325 Don Gaspar
Santa Fe, NM 87503

New Mexico Tech
Martin Speere Memorial Library
Campus Street
Socorro, NM 87810

WIPP Public Reading Room
Carlsbad Public Library
101 S. Halagueno St.
Carlsbad, NM 88220

Foreign Addresses

Atomic Energy of Canada, Ltd. (2)
Whiteshell Laboratories
Attn: B. Goodwin
T. Andres
Pinawa, Manitoba, CANADA R0E 1L0

Dr. Arnold Bonne
Acting Head of the Waste Technology Section
Division of Nuclear Fuel Cycle and Waste Management
International Atomic Energy Agency
P.O. Box 100
A-1400 Vienna
AUSTRIA

Clandio Pescatori
AERI/NEA/OECD
LeSeine St. Germain
12 Boulevard des iles
92130 Issy-les-Moulineaux
FRANCE

Francois Chenevier (2)
ANDRA
Parc de la Croix Blanche
1-7 rue Jean Monnet
92298 Chatenay-Malabry Cedex
FRANCE

Claude Sombret
Centre d'Etudes Nucleaires de la Vallee Rhone
CEN/VALRHO
S.D.H.A. B.P. 171
30205 Bagnols-Sur-Ceze
FRANCE

Commissariat a L'Energie Atomique
Attn: D. Alexandre
Centre d'Etudes de Cadarache
13108 Saint Paul Lez Durance Cedex
FRANCE

Ghislain de Marsily
University Pierre et Marie Curie
Laboratorie de Geologie Applique
4, Place Jussieu
T.26 – 5e etage
75252 Paris Cedex 05
FRANCE

Bundesanstalt fur Geowissenschaften und Rohstoffe
Attn: M. Langer
Postfach 510 153
D-30631 Hannover
GERMANY

Bundesministerium fur Forschung und Technologie
Postfach 200 706
5300 Bonn 2
GERMANY

Institut fur Tieflagerung
Attn: K. Kuhn
Theodor-Heuss-Strasse 4
D-3300 Braunschweig
GERMANY

Gesellschaft fur Anlagen und Reaktorsicherheit (GRS)
Attn: B. Baltes
Schwertnergasse 1
D-50667 Cologne
GERMANY

Forschunginstitute
GRS (2)
Attn: Eduard Hofer
B. Krzykacz-Hausmann
Forschungsgelande Nebau 2
D-85748 Garching
GERMANY

Tamas Turanyi
Eotvos University (ELTE)
Po.O. Box 32
H –1518 Budapest
HUNGARY

Jan Marivoet
Centre D'Etudes de l'Energie
Nucleaire
Boeretang 200
B-2400 MOL
BELGIUM

Andrea Saltelli
European Commission
Via Fermi
21020 Ispra (VA)
ITALY

Prof. I. Papazoglou
Institie of Nuclear Technology-Radiation
Protection
N.C.S.R. Demokritos
Aghia Papakevi
153-10 Athens
GREECE

European Commission (3)
Attn: Francesca Campolongo
Karen Chan
Stefano Tarantola
JRC Ispra, ISIS
I – 21020 Ispra
ITALY

Enrico Zio
Politecnico di Milano
Via Ponzio 34/3
I –20133 Milan
ITALY

Ricardo Bolado
Polytechnical University of Madrid
Jose Gutierrez Abascal, 2
E- 28006 Madrid
SPAIN

David Rios Insua
University Rey Juan Carlos
ESCET-URJC, C. Humanes 63
E –28936 Mostoles
SPAIN

Shingo Tashiro
Japan Atomic Energy Research Institute
Tokai-Mura, Ibaraki-Ken, 319-11
JAPAN

Toshimitsu Homma
Nuclear Power Engineering Corporation
3-17-1 Toranomon, Minato-Ku
Tokyo 1015
JAPAN

Netherlands Energy Research Foundation ECN
Attn: J. Prij
3 Westerduinweg
P.O. Box 1
1755 ZG Petten
THE NETHERLANDS

Prof. Roger Cooke
Dept. of Mathematics
Delft University of Technology
P.O. Box 5031 2800 GA Delft
THE NETHERLANDS

Louis Goossens
Safety Science Group
Delft Univ. of Technology
Kanaalweg 2b
2628 EB Delft
THE NETHERLANDS

Prof. J.P.C. Kleijnen
Department of Information Systems
Tilburg University
5000 LE Tilburg
THE NETHERLANDS

A. Seebregts
ECN PO Box 1
1755 ZG Petten
THE NETHERLANDS

Willem Van Groenendaal
Tilburg University
P.O. Box 90153
NL – 5000 Le Tilburg
THE NETHERLANDS

Svensk Karnbransleforsorjning AB
Attn: F. Karlsson
Project KBS (Karnbranslesakerhet)
Box 5864
S-102 48 Stockholm
SWEDEN

Prof. S. E. Magnusson
Lund University
P.O. Box 118
22100 Lund
SWEDEN

Prof. Christian Ekberg
Chalmers University of Technology
Dept. of Nuclear Chemistry
S-41296 Goteborg
SWEDEN

Nationale Genossenschaft fur die Lagerung
Radioaktiver Abfalle (2)
Attn: S. Vomvoris
P. Zuidema
Hardstrasse 73
CH-5430 Wettingen
SWITZERLAND

AEA Technology
Attn: J. H. Rees
D5W/29 Culham Laboratory
Abington, Oxfordshire OX14 3DB
UNITED KINGDOM

AEA Technology
Attn: W. R. Rodwell
044/A31 Winfrith Technical Centre
Dorchester, Dorset DT2 8DH
UNITED KINGDOM

Daniel A. Galson
Galson Science Ltd.
35, Market Place
Oakham
Leicestershire LE15 6DT
UNITED KINGDOM

David Draper
University of Bath
Claverton Down
Bath BA2 7AY
UNITED KINGDOM

AEA Technology
Attn: J. E. Tinson
B4244 Harwell Laboratory
Didcot, Oxfordshire OX11 ORA
UNITED KINGDOM

Prof. Marian Scott
Dept. of Statistics
University of Glasgow
Glasgow G12 BQW
UNITED KINGDOM

Prof. Simon French
School of Informatics
University of Manchester
Coupland 1
Manchester M13 9pl
UNITED KINGDOM

Arthur Jones
Nat. Radio. Prot. Board
Chilton, Didcot
Oxon OX110RQ
UNITED KINGDOM

Prof. M. Newby
Dept. of Acturial Sci & Statistics
City University
Northhampton SQ
London EC1V OHB
UNITED KINGDOM

Prof. Russell Cheng
University of Kent at Canterbury
Cornwallis Building
Canterbury, Kent, CT2 7NF
UNITED KINGDOM

B.G.J. Thompson
20 Bonser Road
Twickenham
Middlesex, TW1 4RG
ENGLAND

Other

Leonard F. Konikow
US Geological Survey
431 National Center
Reston, VA 22092

Dr. Bob Andrews
1280 Town Center Dr.
Las Vegas, NV 89314

Dr. Alison Cullen
2125 North 90th Street
Seattle, WA 98103

P.S. Price
129 Oakhurst Road
Cape Elizabeth, ME 04107

Dr. Gareth Parry
19805 Bodmer Ave
Poolesville, MD 200837

Dennis Powers
Star Route Box 87
Anthony, TX 79821

Les Shephard
YMSCO
P. O. Box 30307
MS523
N. Las Vegas, NV 89036

Internal

MS	Org.	
0735	6115	P. B. Davies
0737	6831	E. J. Nowak
0737	6833	J. R. Tillerson
0737	6833	E. H. Ahrens
0779	6849	D. R. Anderson
0779	6848	H. N. Jow
0771	6801	M. Chu
0733	6832	J. T. Holmes
1395	6821	M. Marietta
0771	6000	W. D. Weart
0771	6800	F. W. Bingham
0773	6821	G. K. Froehlich
1395	6821	F. D. Hansen
0773	6821	S. M. Howarth
0773	6821	K. W. Larson
0773	6832	C. D. Leigh
0773	6800	P. N. Swift
0734	6803	L. D. Bustard
1395	6860	R. Waters
0720	6804	K. B. Sorenson
0715	6805	C. E. Olson
0715	6805	R. L. Hunter
0715	6805	P. Kaplan
1395	6811	S. Y. Pickering
1395	6821	B. L. Baker
1395	6821	M. K. Knowles
1395	6821	M-A. Martell
1395	6821	P. E. Sanchez
1395	6821	Y. Wang
0737	6831	R. V. Bynum
0733	6832	S. G. Bertram
0733	6832	L. H. Brush
0733	6832	R. V. Guzowski
0733	6832	H. W. Papenguth
0733	6832	A. C. Peterson
0733	6832	M. D. Siegel
0733	6832	K. M. Trauth
0779	6848	K. Aragon
0779	6848	J. E. Bean
0779	6848	F. J. Davis
0779	6848	L. J. Dotson
0779	6848	K. M. Economy
0779	6848	J. N. Emery
0779	6848	J. C. Helton (10)
0779	6848	J. D. Johnson
0779	6848	R. D. McCurley
0779	6848	J. D. Miller
0779	6848	D. O'Brien
0779	6848	H. C. Ogden
0779	6848	J. A. Rollstin
0779	6848	L. C. Sanchez
0779	6848	J. D. Schreiber
0779	6848	M. J. Shortencarier
0779	6848	L. N. Smith
0779	6848	M. S. Tierney
0779	6848	M. Williamson
0779	6848	T. Zimmerman
0779	6849	J. W. Berglund
0779	6849	P. J. Chen
0779	6849	M. E. Fewell
0779	6849	G. A. Freeze
0779	6849	J. W. Garner
0779	6849	L. S. Gomez
0779	6849	T. Hadgu
0779	6849	H. J. Iuzzolino
0779	6849	M. Lavenue
0779	6849	M. E. Lord
0779	6849	L. J. Rahal
0779	6849	J. L. Ramsey
0779	6849	R. P. Rechard
0779	6849	D. Rudeen
0779	6849	A. Schenker
0779	6849	A. H. Treadway
0779	6849	P. Vaughn
0779	6849	M. Wallace
0779	6849	J. A. Jones
0779	6849	J. H. Saloio
1399	6850	A. Orrell
0778	6851	H. A. Dockery
0778	6851	G. E. Barr
0778	6851	R. Aguilar
0778	6851	J. H.Gauthier
0778	6851	R. J. MacKinnon
0778	6851	M. L. Wilson
0778	6851	C. T. Stockman
1399	6853	J. J. Danneels

0735	6115	A. R. Lappin
0735	6115	R. L. Beauheim
0735	6115	T. F. Corbet
0735	6115	B. Holt
0735	6115	L. Meigs
1044	7511	A. Reiser
0731	6811	K. Hart (2)
0731	4415	NWM Library (20)
9018	8940-2	Central Technical Files
0899	4916	Technical Library (2)
0619	12690	Review and Approval Desk, For DOE/OSTI (2)